LBNL-39981
UC-411

Advanced Light Source

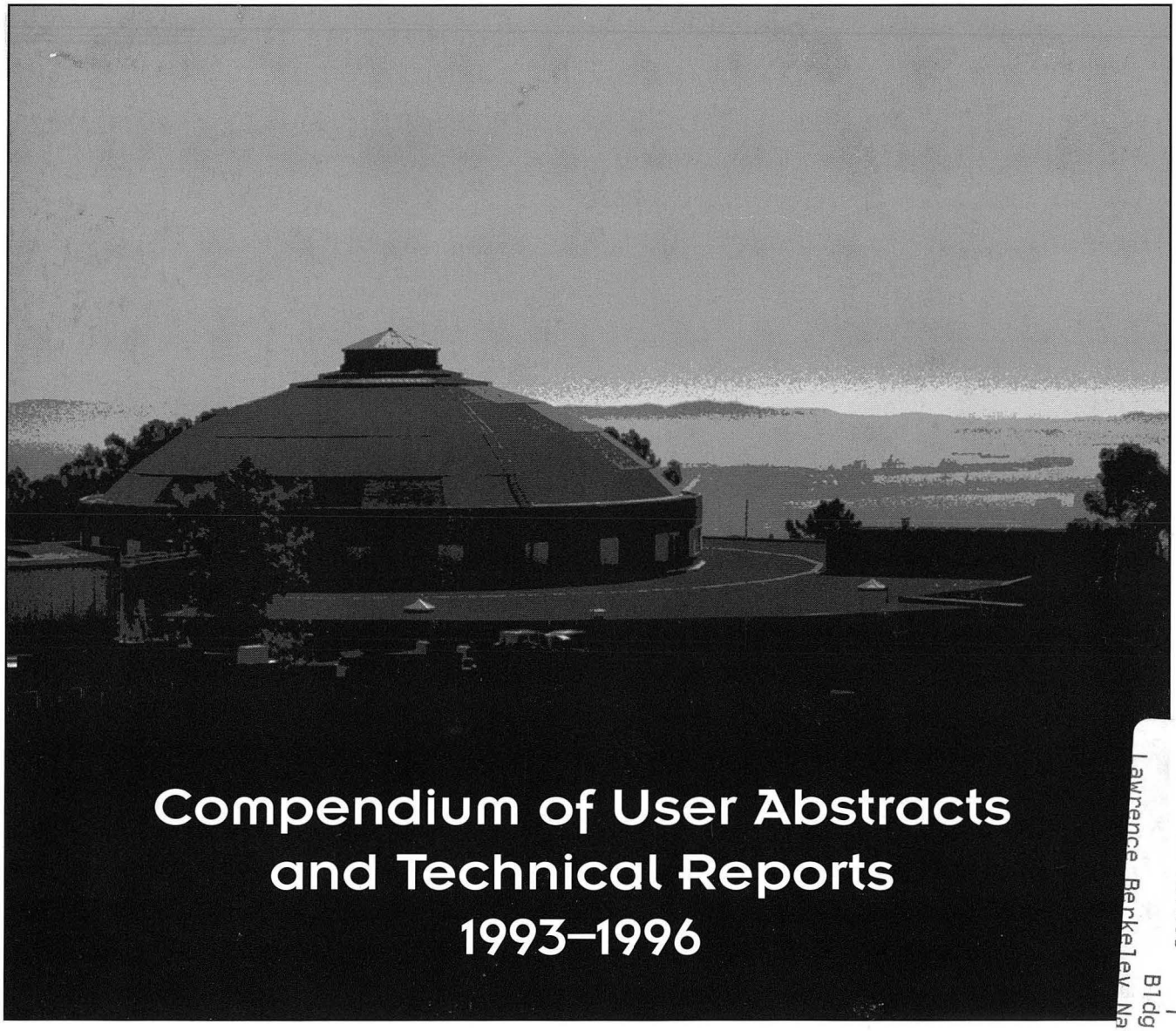

Compendium of User Abstracts and Technical Reports 1993–1996

April 1997

Ernest Orlando Lawrence Berkeley National Laboratory
University of California
Berkeley, California 94720

This volume is intended to complement the Advanced Light Source Activity Report, which presents an overview of the scientific program, ongoing research and development efforts, and operations.

Related publications available from ALS Administration

ALS Activity Report 1995

ALS Users' Handbook

The Art and Science of Magnet Design
Volume 1: A Festschrift in Honor of Klaus Halbach
Volume 2: Selected Notes of Klaus Halbach

Editors: Deborah J. Dixon, Jane Cross, Kathryn Devereaux, and Annette Greiner
Cover Design: Marilee Bailey

The editors gratefully acknowledge the work of Tina Aitkens, Bernadette Dixon, Sharon Fujimura, and other ALS staff in compiling this volume, as well as the contributions of ALS users and staff to its contents.

DISCLAIMER

Advanced Light Source

Compendium of User Abstracts and Technical Reports 1993–1996

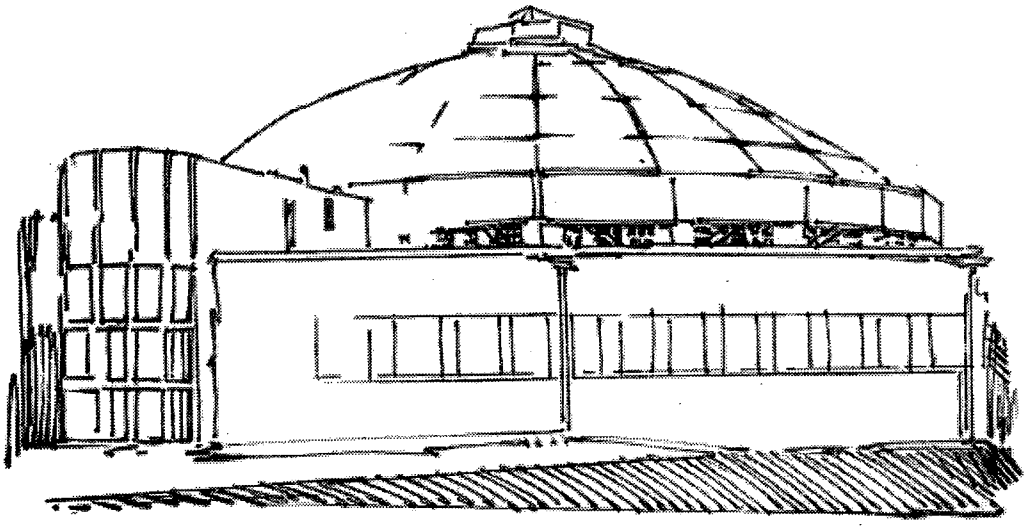

April 1997

Ernest Orlando Lawrence Berkeley National Laboratory
University of California
Berkeley, California 94720

Prepared for the U.S. Department of Energy under Contract DE-AC03-76SF00098

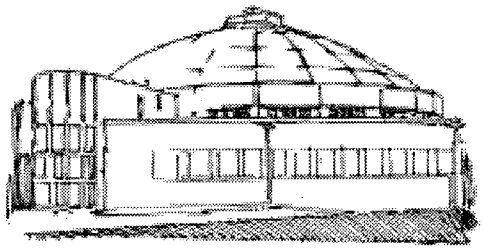

I am pleased to introduce the first Compendium of research abstracts and technical reports from the Advanced Light Source (ALS). The scientific program at the ALS started in October 1993 with a single beamline, the x-ray microprobe on Beamline 10.3.1. Since then we have commissioned beamlines at a steady pace and added significantly to the set of tools for the research community. Now twelve beamlines are in operation supporting nearly 350 users in a scientific program ranging over such diverse areas as materials science, EUV lithography, chemical dynamics, life science, and environmental science.

The research summaries within are a testament not only to the wide range of research applications at the ALS but also to the techniques and results spawned by the capabilities of a third-generation machine. The high brightness of a synchrotron source such as the ALS translates into fine spatial resolution, so x-ray microscopies of various kinds are emerging as a mainstream activity. Our users are also doing experiments which may pave the way to the future, such as the the production of femtosecond x-ray pulses with an eye toward so-called "fourth generation" light sources. As a relatively new and rapidly growing national user facility, the ALS welcomes current and potential users to work with us to continue to develop a scientific program noted for its excellence, scope, and collaborative nature.

We intend to publish the Compendium on a yearly basis as a supplement to our annual ALS Activity Report. Scientific highlights and ongoing R&D projects written for a broad audience will appear in the Activity Report. The Compendium, on the other hand, will be dedicated to more in-depth research reports by the scientists themselves, and will serve as a more detailed reference to the scientific program, related publications, and beamline information. We hope that you will reserve some space on your bookshelves for these volumes since they will offer a sequence of snapshots of progress at the ALS in years to come.

Neville Smith
ALS Scientific Program Head

Advanced Light Source

Compendium of User Abstracts and Technical Reports 1993–1996

The Advanced Light Source (ALS), a national user facility located at Ernest Orlando Lawrence Berkeley National Laboratory of the University of California, is available to researchers from academia, industry, and government laboratories. Operation of the ALS is funded by the Department of Energy's Office of Basic Energy Sciences.

This Compendium contains abstracts written by users summarizing research completed or in progress from 1993–1996, ALS technical reports describing ongoing efforts related to improvement in machine operations and research and development projects, and information on ALS beamlines planned through 1998.

Two tables of contents organize the user abstracts by beamline and by area of research, and an author index makes abstracts accessible by author and by principal investigator. Technical details for each beamline including whom to contact for additional information can be found in the beamline information section. The most current information on ALS beamlines can be found on the ALS web pages (http://www-als.lbl.gov/).

User Abstracts
Table of Contents by Beamline

Abstracts are organized by beamline. Within each beamline, abstracts describing instrumentation appear first, followed by other abstracts in alphabetical order by title. Abstracts associated with two beamlines are listed under both.

Other Abstracts

Beamline 7.0.1: Surface & Materials Science, Spectromicroscopy

Instrumentation

Other Abstracts

Beamline 8.0.1: Surface & Materials Science

Other Abstracts

Beamline 9.0.1: Atomic & Molecular Science, High-Resolution Gas-Phase Spectroscopy

Instrumentation

Other Abstracts

Beamline 9.0.2: Chemical Reaction Dynamics, Photochemistry, Photoionization Dynamics

Instrumentation

Other Abstracts

Beamline 9.3.1: Atomic, Molecular, & Materials Science

Instrumentation

Other Abstracts

Beamline 9.3.2: Chemical & Materials Science

Instrumentation

Other Abstracts

Beamline 10.3.1: Fluorescence X-Ray Microprobe

Instrumentation

Other Abstracts

Beamline 10.3.2: X-Ray Optics Development, Deep-Etch X-Ray Lithography (LIGA), Materials Science

Instrumentation

Other Abstracts

Beamline 12.0.1: EUV Lithography Optics Testing, Interferometry, Surface & Materials Science

Instrumentation

Beam Test Facility

Instrumentation

User Abstracts
Table of Contents by Subject Area

Abstracts are organized by general subject area: Atomic & Molecular Physics & Chemistry, Earth Sciences, Instrumentation, Life Sciences, Materials & Surface Science, and Technology. Within each subject area, abstracts are in alphabetical order by title. The beamlines associated with each abstract appear at the right.

Atomic & Molecular Physics & Chemistry

Earth Sciences

Instrumentation

Life Sciences

Materials & Surface Science

Technology

User Abstracts Author Index

If an author is the principal investigator for an abstract, that abstract's page number appears in bold type.

Beamline 6.1.2 Abstracts

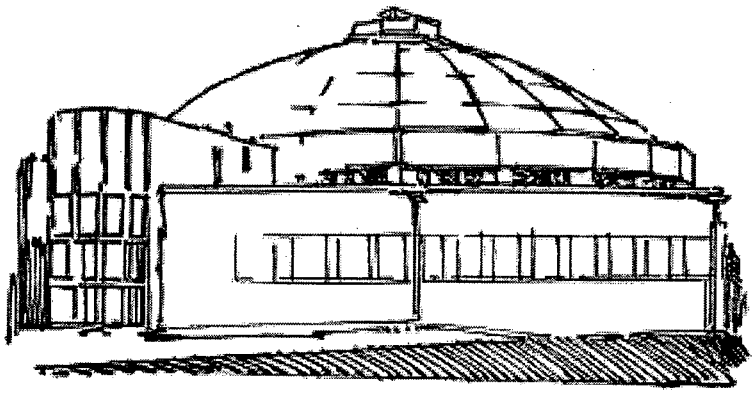

Determination of the Resolution of the X-Ray Microscope XM-1 at Beamline 6.1

John M. Heck, Werner Meyer-Ilse, and David T. Attwood
Center for X-ray Optics, Ernest Orlando Lawrence Berkeley National Laboratory,
University of California, Berkeley, California 94720, USA

INTRODUCTION

Resolution determination in x-ray microscopy is a complex issue which depends on many factors. Many different criteria and experimental setups are used to characterize resolution. Some of the important factors affecting resolution include the partial coherence and spectrum of the illumination. The purpose of this research has been to measure the resolution of XM-1 at beamline 6.1 taking into account these factors, and to compare the measurements to theoretical calculations.

The x-ray microscope XM-1, built by the Center for X-ray Optics (CXRO), has been operational since 1994 at the Advanced Light Source at E. O. Lawrence Berkeley National Laboratory. It is of the conventional (i.e. full-field) type, utilizing zone plate optics [1]. A schematic is shown in Fig. 1. ALS bending magnet radiation is focused by a condenser zone plate [2] onto a monochromator pinhole immediately in front of the sample. X-rays transmitted through the sample are focused by a micro-zone plate [3] onto a CCD camera. The pinhole and the condenser with a central stop constitute a linear monochromator. The spectral distribution of the light illuminating the sample has been calculated assuming geometrical optics.

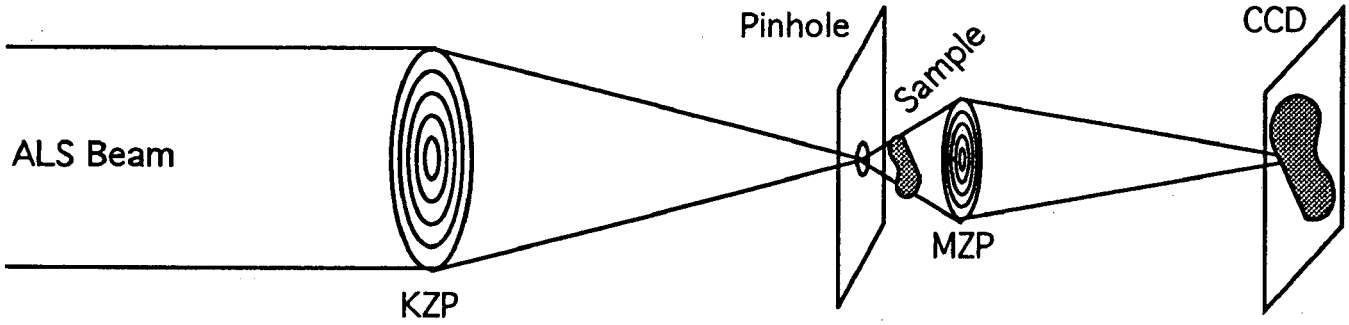

Figure 1. Schematic of the x-ray microscope XM-1 at ALS beamline 6.1

PARTIALLY COHERENT IMAGING

The partial coherence of an imaging system is of utmost importance in resolution determination, and is affected by the aperture of the condenser lenses. A coherence parameter m is defined as $m = NA_c/NA_o$, where NA_c and NA_o are the numerical apertures of the condenser and objective lenses. When $m = \infty$ or $m = 0$, the illumination is incoherent or coherent, respectively, and the image formation is linear. For any other value of m, the imaging is partially coherent, leading to nonlinear image formation. In order to calculate an image from an object under partially coherent illumination, the Hopkins theory of partial coherence [4,5] must be applied. The software package SPLAT has been developed for this purpose by A. Neureuther and K. Toh of the University of California, Berkeley [6].

There are many common criteria for characterizing resolution, the most famous of which is the Rayleigh criterion. When applied to two incoherently imaged point sources, the Rayleigh criterion gives the result that the two points are "distinguishable" when they are separated by 0.61 λ/NA. At this point, the image contrast, given by $(I_{max}-I_{min})/(I_{max}+I_{min})$ is 15.3%. For the partially coherent case, we have defined three resolution criteria which are valid for any value of *m*:

Two Point Resolution:	The point separation *d* at which the image contrast is 15.3%, regardless of the degree of coherence.
Knife Edge Resolution:	We define the knife edge resolution as the width of the 10-90% intensity transition, because when a knife edge is imaged incoherently, the intensity transition over a distance of 0.61 λ/NA is 10-90%.
Grating Resolution:	The period of the smallest grating for which the image contrast is at least 15.3%.

All three of these resolution criteria give the same numerical value as the Rayleigh criterion for two incoherent points at $m = \infty$, provided there are no central stops on the lenses.

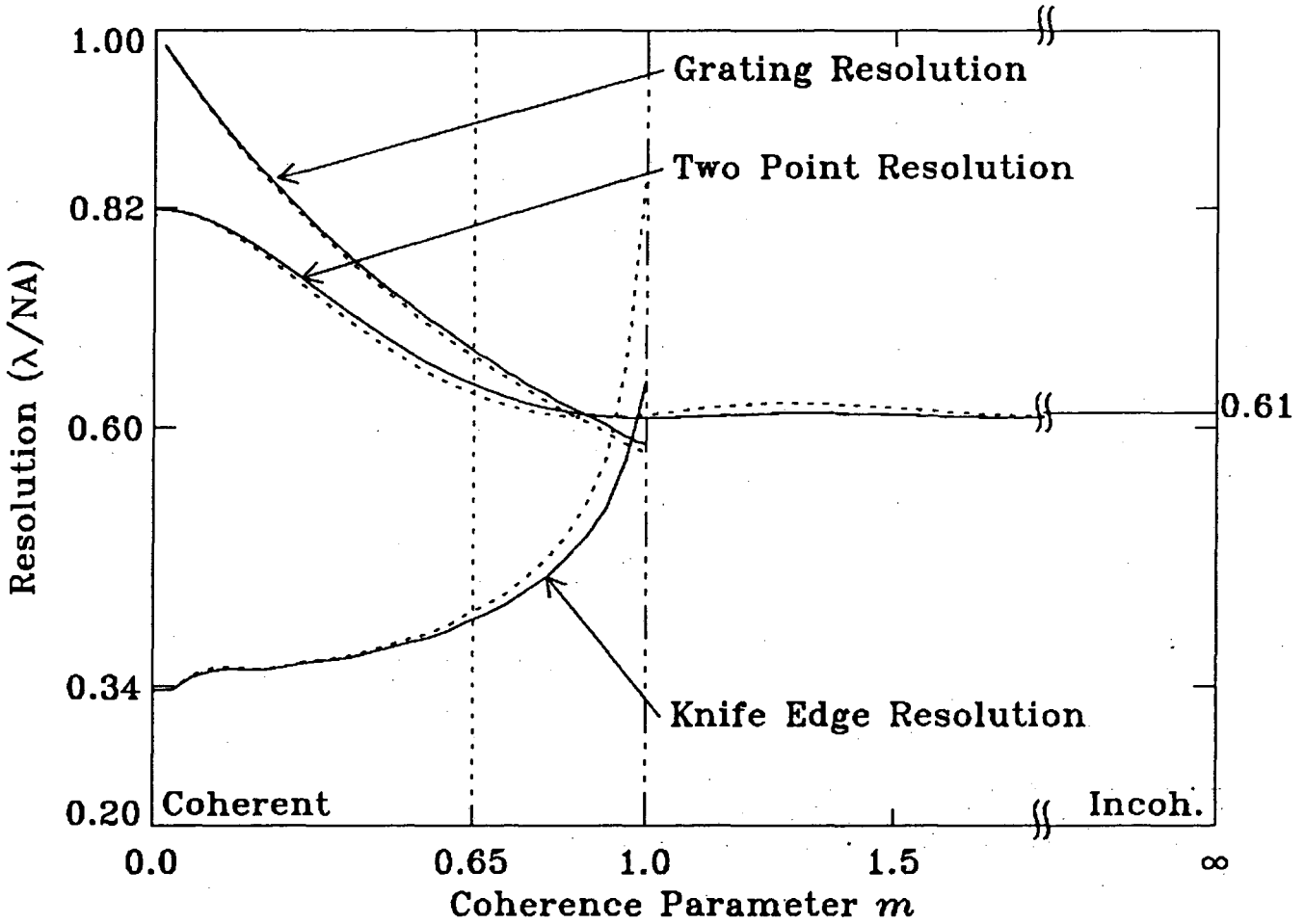

Figure 2. The effect of partial coherence on two point, knife edge, and grating resolution. The solid lines indicate no central stop on the condenser lens; the dotted lines represent a 1/3 radius central stop. The XM-1 coherence of 0.65 is marked with a dashed line.

The values of the three resolution criteria in the case of a partially coherent imaging system without aberrations are plotted as a function of *m* in Fig. 2, both with and without a central stop in the condenser. Although all of these criteria give equal values under incoherent illumination, they differ significantly as the imaging system becomes more coherent. The knife edge becomes sharper as coherence is increased, whereas the two point and grating resolutions are degraded. The central stop has little effect on the resolution. In our experiments with XM-1, the value of *m* was 0.65, which is marked with a dashed line.

XM-1 KNIFE EDGE RESOLUTION

The knife edge resolution is a useful test of instrument performance because knife edges are easy to fabricate, image, and analyze. A gold knife edge was made by Erik Anderson of CXRO by a liftoff process, imaged in XM-1, and analyzed in the following manner. First, a straight line was fittted to the edge image between the dark and light portions. Then, the intensity of every image pixel was plotted as a function of its distance to the edge. The 10-90% width of the intensity transition of these points was then measured.

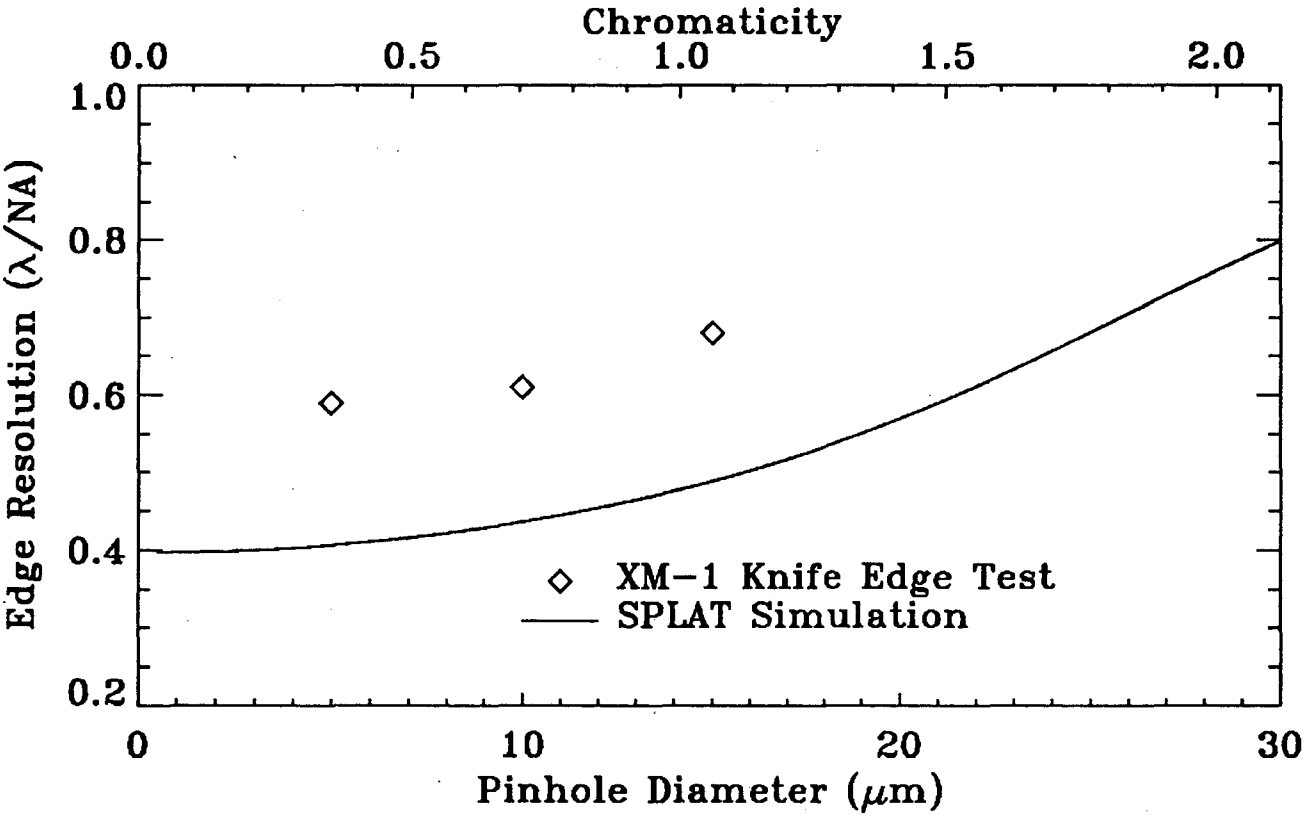

Figure 3. Knife edge resolution as a function of pinhole size and the corresponding chromaticity (=ratio of the number of zones of the micro-zone plate [N=318] to the spectral bandwidth of the illumination). The solid line is a SPLAT simulation; the diamonds represent knife edge resolution measurements with 5, 10, and 15 μm monochromator pinholes. The knife edge resolution improves gradually as the illumination becomes more monochromatic.

Knife edges were imaged with each of three monochromator pinholes, and the 10-90% edge widths were measured. The edge widths were 48, 43, and 41 nm, using the 15, 10 and 5 μm pinholes, respectively. This data is compared to a series of SPLAT simulations using the appropriate spectral

distribution due to the linear monochromator (Fig. 3). It can be seen that the data points in Fig. 3 follow the same trend as the theory, although the experimental edge width is consistently about 40% larger than the diffraction limit. The relatively constant nature of the data for small illumination bandwidths indicates that the achievement of a *spectral* resolution greater than about $\lambda/\Delta\lambda = 500$ (corresponding to a 10 μm monochromator pinhole) will not significantly affect the *spatial* resolution of the x-ray microscope. However, a high spectral resolution is desirable for spectromicroscopy.

CONCLUSIONS

The effect of partial coherence has been shown to play a major role in image formation and spatial resolution of x-ray microscopes, due to the non-linear relationship between the image and the object. With an increasing degree of coherence, knife edge images become sharper while two-point resolution is degraded. Although 10-90% edge resolution may be measured at less than 0.61 λ/NA, the actual resolution of the imaging system may be far from diffraction limited, depending on the partial coherence parameter.

The effect of the illumination spectrum has been analyzed in detail. It has been shown, both theoretically and experimentally, that an improvement in the spectral resolution beyond $\lambda/\Delta\lambda = 500$ does not significantly affect the spatial resolution. However, a high spectral resolution does allow more accurate elemental distinguishability, and makes it possible to perform spectroscopic techniques since we have the ability to tune the wavelength to various resonances in the absorption spectrum.

The knife-edge resolution of XM-1 has been measured to be 0.61 λ/NA, or about 43 nm, with a 10 μm monochromator pinhole. Although this is quite small, it is still 40% from diffraction limited. A major emphasis of future research is to determine the causes of this discrepancy and attempt to eliminate it. Some of the possible causes being investigated are zone plate thickness and aberrations.

REFERENCES

1. W. Meyer-Ilse, H. Medecki, J.T. Brown, J. M. Heck, E. H. Anderson, D. T. Attwood, this volume
2. M. Hettwer and D. Rudolph, in *X-Ray Microscopy and Spectromicroscopy*, edited by J. Thieme, G. Schmahl, E. Umbach, and D. Rudolph (Springer-Verlag, Heidelberg, Germany, 1997, in press).
3. E. Anderson and D. Kern, Springer Series in Optical Sciences **67**, *X-Ray Microscopy III*, 75-78 (1992).
4. L. Jochum and W. Meyer-Ilse, Appl. Optics **34** (22), 4944-4950 (1995).
5. H. H. Hopkins, Proc. R. Soc. London Ser. A **217**, 408-432 (1953).
6. K. H. Toh and A. R. Neureuther, SPIE **772**, *Optical Microlithography VI*, 202-209 (1987).

This work was supported by the U.S. Department of Energy, Office of Basic Energy Sciences, and the Office of Health and Environmental Research and the Laboratory Directed Research and Development Program of the E. O. Lawrence Berkeley National Laboratory under the Department of Energy contract No. DE-AC03-76SF00098.

Principal investigator: Werner Meyer-Ilse, Center for X-ray Optics, E. O. Lawrence Berkeley National Laboratory, E-Mail: W_MEYER-ILSE@LBL.GOV, Phone: (510) 486-6892.

High Spatial Resolution Soft-X-Ray Microscopy

W. Meyer-Ilse, H. Medecki, J. T. Brown, J. M. Heck, E. H. Anderson, D. T. Attwood
Center for X-ray Optics, E. O. Lawrence Berkeley National Laboratory,
University of California, Berkeley, California 94720, USA

INTRODUCTION

A new soft x-ray microscope (XM-1) with high spatial resolution has been construeted by the Center for X-ray Optics (Fig. 1). It uses bending magnet radiation from beamline 6.1 at the Advanced Light Source, and is used in a variety of projects and applications in the life and physical sciences [1]. Most of these projects are ongoing.

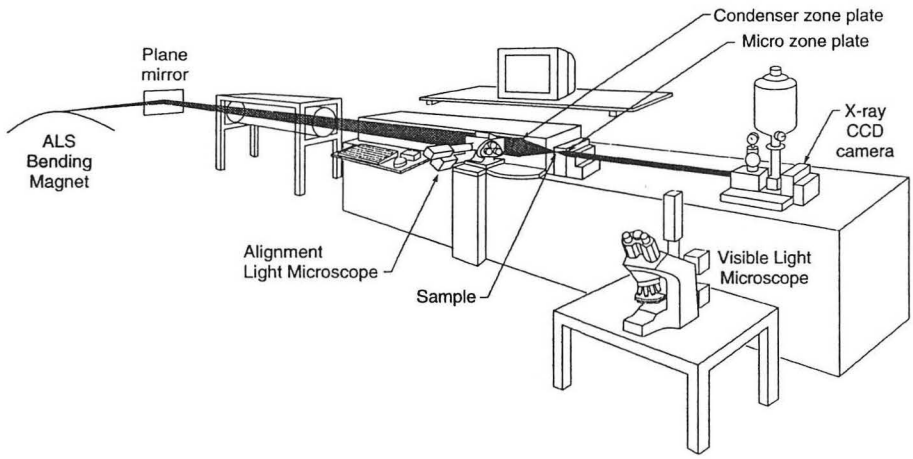

Figure 1: Schematic of the high resolution soft x-ray microscope XM-1, built and operated by the Center for X-ray Optics. Bending magnet radiation from the ALS is monochromatized and focused onto the sample with a condenser zone-plate lens [2]. X-rays transmitted through the sample are enlarged with an objective (micro-) zone plate lens and detected with an x-ray CCD camera system. Except for air gap containing the sample of about 100 microns, the x-ray optics are in vacuum. A mutual indexing system is used to position and focus the sample with an external visible light microscope.

The instrument uses zone plate lenses and achieves a resolution of 43 nm, measured over 10% to 90% intensity with a knife edge test sample [3]. X-ray microscopy permits the imaging of relatively thick samples, up to 10 μm thick, in water. XM-1 has an easy to use interface, that utilizes visible light microscopy to precisely position and focus the specimen.

BIOLOGICAL APPLICATIONS

In our most extensive study with C. Magowan (Life Sciences Division, LBNL) [4,5], the life cycle of malaria parasites (*Plasmodium falciparum*) in intact normal human red blood cells (Fig. 2) has been observed, using hundreds of images. Building on the knowledge about the parasites' normal development, abnormalities which

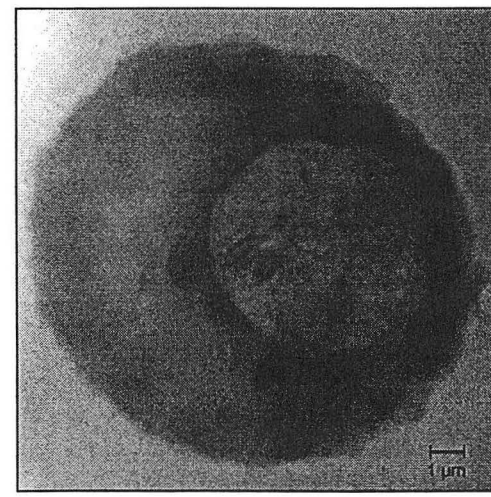

Figure 2: Malaria Parasite in a human red blood cell imaged with XM-1

occur in the parasite after protease inhibitor treatments or in erythrocytes deficient in membrane protein 4.1, have been investigated.

In a collaboration of T. Ford and A. Stead (Royal Holloway University of London, UK) structures in green alga (*Chlamydomonas*), uniquely visible with soft x-rays, have been analyzed in unfixed samples [6]. By using x-ray wavelengths near the L-absorption edges, we were able to detect trace amounts of Fe, Mg, and Co in this alga. Bacterial spores (*Bacillus subtilis)* were studied in collaboration with J. Judge (Unilever plc., UK). Structural differences between hydrated and dehydrated spores were observed and reported [7].

The uniformity of chromatin organization within the heads of sperm from several mammals was analyzed in collaboration with R. Balhorn (LLNL). Sperm chromatin is particularly well suited for imaging with x-rays. Since the DNA is packaged in a highly compacted state, x-ray images of the sperm heads show structural details that cannot be observed using other techniques. These images are providing new insight into the importance of the timely synthesis of protamine 1, one of the two nuclear proteins that package DNA in spermatids and sperm (Fig. 3).

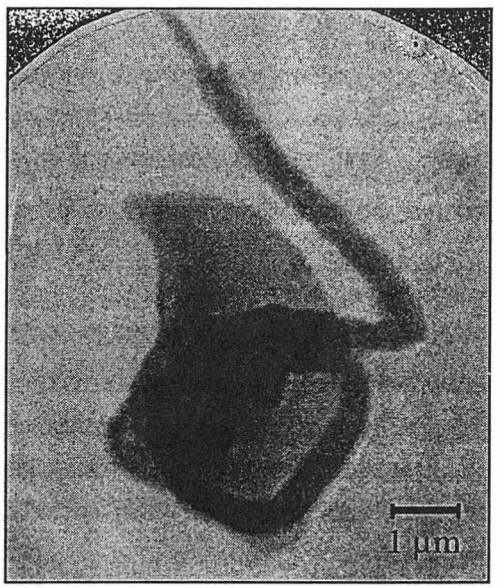

Figure 3: Transgenic sperm cell from mouse.

Cryptosporidium is a parasite commonly found in lakes and rivers contaminated with animal waste and sewage. Occasionally municipal drinking water supplies may become contaminated. The parasite oocyst is about 4 to 6 microns in size and resistant to chlorination treatment used in public water systems. Recent outbreaks of *Cryptosporidium* infections in Las Vegas (1994) and Milwaukee (1993) caused about 140 deaths and approximately 400,000 cases of severe diarrhea and vomiting. *Cryptosporidium* is important to human health because of its debilitating effects, and it can be fatal to immuno-compromised individuals. We recorded a first series of x-ray microscope images of *Cryptosporidium* prepared in the laboratory of C. Petersen (UCSF, San

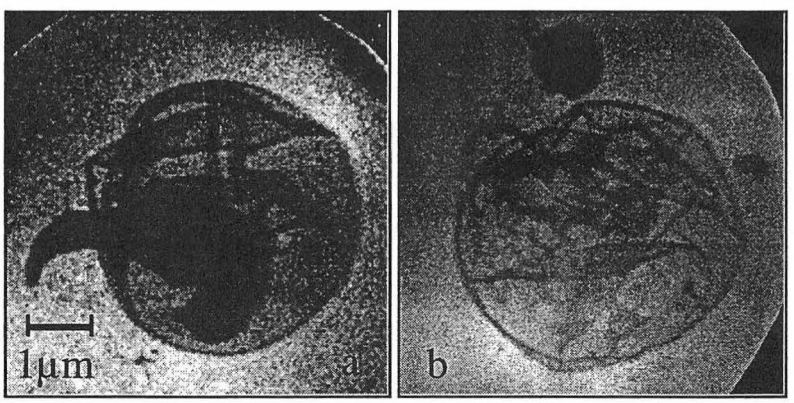

Figure 4: *Cryptosporidium.*
(a) sporozoite emerging from oocyst, (b) empty oocyst with residium.

Francisco General Hospital). These images were made from formalin fixed, wet samples. The images show a sporozoite emerging from the oocyst (Fig. 4 a) and an empty oocyst with the associated residuum (Fig. 4 b).

Other biological projects include investigations of human chromosomes (D. Arndt-Jovin, T. Jovin, Max-Planck-Institute Göttingen, Germany); mammalian cells (J. Hearst, M. Albertie, Structural Biology Division, LBNL, and S. Lelievre, Life Sciences Division, LBNL); human fibroblast cells (S. Krauss, Life Sciences Division, LBNL); human lung tissue (J. Bastacky, Life Sciences Division, LBNL); two projects with rat neurons (S. Brubaker, Univ. Oregon, Eugene and G. DeStasio, Univ. Rome, Italy); and development of lanthanide based luminescent labels (M. Moronne, Life Sciences Division, LBNL).

PHYSICAL SCIENCES APPLICATIONS

Soft x-ray microscopy is advantageous wherever high spatial resolution transmission images from samples several microns thick are required. If the sample is in a liquid environment, x-rays might be the only possible method. In addition to that, it may be possible to gain elemental or chemical information through spectromicroscopy, making x-ray transmission the method of choice in a variety of applications in materials sciences and environmental research.

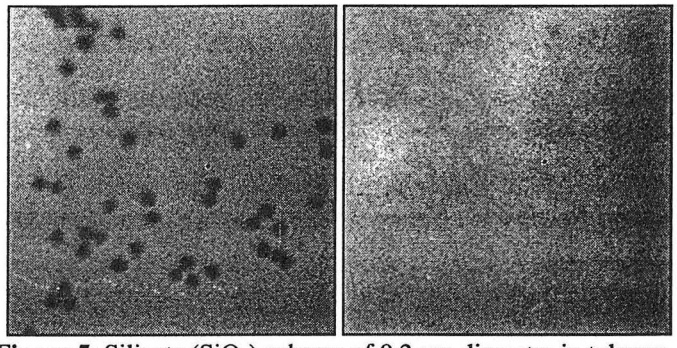

Figure 5: Silicate (SiO_x) spheres of 0.2 μm diameter in toluene. Images taken at 539 eV (left) and at 533 eV (right).

Fig. 5 shows images of silicate (SiO_x) micro-spheres suspended in toluene ($C_6H_5CH_3$; liquid at room temperature) imaged at different wavelengths near the absorption edge of the oxygen K-shell. At a photon energy of 539 eV (2.30 nm) the absorption of oxygen is at a maximum, whereas at the slightly lower photon energy of 533 eV (2.33 nm) the absorption of oxygen is negligible. As only the silicate micro-spheres contain oxygen, they are clearly visible at 2.30 nm and almost invisible (actually slightly brighter than the medium) at 2.33 nm.

In a collaboration with G. Mitchell and E. Rightor (Dow Chemical) we started to use XM-1 for a number of industrial applications. The samples investigated included different types of structured polymers with sizes that take full advantage of our spatial resolution, and latex spheres, which were imaged wet.

CONCLUSION AND OUTLOOK

The high resolution soft x-ray microscope XM-1 has gained new insights in a large variety of applications.

We are currently developing a cryogenic sample holder to be used in our soft x-ray microscope. The holder will allow us to use longer exposure times and perform multiple view imaging without increasing visible sample damage. For multiple view imaging, which provides tomographic information, a rotation stage is planned. A new electron beam writing tool (NanoWriter) is being commissioned; it will provide us with higher resolution condenser and objective zone plate lenses.

REFERENCES

1. W. Meyer-Ilse, H. Medecki, J. T. Brown, J. Heck, E. Anderson, C. Magowan, A. Stead, T. Ford, R. Balhorn, C. Petersen, D. T. Attwood, in *X-ray Microscopy and Spectromicroscopy,* J. Thieme, G. Schmahl, E. Umbach, D. Rudolph, eds. (Springer, Heidelberg 1997, in press)
2. M. Hettwer and D. Rudolph, ibid.
3. J. M. Heck, W. Meyer-Ilse, D. T. Attwood, this volume.
4. C. Magowan, J.T. Brown, N. Mohandas, W. Meyer-Ilse, this volume.
5. C. Magowan, J. T. Brown, J. Heck, M. Narla, W. Meyer-Ilse, "Developmental Anomalies of *Plasmodium falciparum* Malaria Parasites in Abnormal Erythrocytes Imaged by Soft X-ray Microscopy," submitted
6. T. W. Ford, A. M. Page, W. Meyer-Ilse, A. D. Stead, in ref. 1.
7. A. D. Stead, J. T. Brown, J. Judge, W. Meyer-Ilse, D. Neely, A. M. Page, E. Wolfrum, T. W. Ford, ibid.

This work was supported by the U.S. Department of Energy, Office of Basic Energy Sciences, and the Office of Health and Environmental Research and the Laboratory Directed Research and Development Program of the E. O. Lawrence Berkeley National Laboratory under the Department of Energy contract No. DE-AC03-76SF00098.

Principal investigator: Werner Meyer-Ilse, Center for X-ray Optics, E. O. Lawrence Berkeley National Laboratory, e-mail: W_MEYER-ILSE@LBL.GOV, Phone: (510) 486-6892.

Imaging Bacterial Spores by Soft-X-Ray Microscopy

A.D. Stead[1], T.W. Ford[1], J. Judge[2], J.T. Brown[3] and W. Meyer-Ilse[3]
[1]Biological Sciences, Royal Holloway (University of London), Egham, Surrey, TW20 0EX. UK
[2]Unilever plc, Colworth House, Sharnbrook, Beds., MK44 1LQ. UK
[3]Center for X-ray Optics, Ernest Orlando Lawrence Berkeley National Laboratory, University of California, Berkeley, California 94720, USA

INTRODUCTION

Bacterial spores are able to survive dehydration, but neither the physiological nor structural basis of this have been fully elucidated. Furthermore, once hydrated, spores often require activation before they will germinate [1]. Several treatments can be used to activate spores, but in the case of *Bacillus subtlis* the most effective is heat treatment. The physiological mechanism associated with activation is also not understood, but some workers suggest that the loss of calcium from the spores may be critical. However, just prior to germination, the spores change from being phase bright to phase dark when viewed by light microscopy.

Imaging spores by soft x-ray microscopy is possible without fixation. Thus, in contrast to electron microscopy, it is possible to compare the structure of dehydrated and hydrated spores in a manner not possible previously. A further advantage is that it is possible to monitor individual spores by phase contrast light microscopy immediately prior to imaging with soft x-rays; whereas, with both electron microscopy and biochemical studies, it is a population of spores being studied without knowledge of the phase characteristics of individual spores. This study has therefore tried to compare dehydrated and hydrated spores and to determine if there is a mass loss from individual spores as they pass the transition from being phase bright to phase dark.

METHODS

Bacterial spores (*Bacillus subtilis*) were prepared [2] and transported frozen. After thawing the spores were aliquoted and refrozen. Each experiment used a fresh aliquot. Initial experiments compared the structure of hydrated spores, to dehydrated spores and in subsequent experiments spores were activated (70° C for 30 min; phosphate-citrate buffer [50mM, pH 7.0] followed by re-suspension in nutrient broth [Oxoid] with 10mM L-alanine added and incubated at 30° C). Before, or at various times after, addition of germination media, a 2 µl sample was removed and imaged. For imaging 2 µl of the spore suspension was placed between two 120nm thick Si_3N_4 windows. The preparation was examined by phase contrast light microscopy and fields of view were selected which included phase bright, phase dark and, if possible, vegetative cells. X-ray micrographs of the spores selected with visible light were taken using the soft x-ray microscope XM-1 [3] at beamline 6.1 of the Advanced Light Source. Each field of view was photographed for comparison with the x-ray images.

RESULTS & DISCUSSION

Images of dry bacterial spores (Fig. 1) reveal little internal detail as the spores appear to be uniformly x-ray dense. Subsequent images of the same field of view show that the spores are very radiation resistant and that there is little or no reduction in the volume (Fig. 2a) of the spores and no apparent loss of mass (Fig. 2b) as determined by the calculated x-ray transmittance even when the x-ray dose exceeded $2x10^7$ Gy, a dose well above that recognized to cause structural and functional damage in several other tissues [4-7].

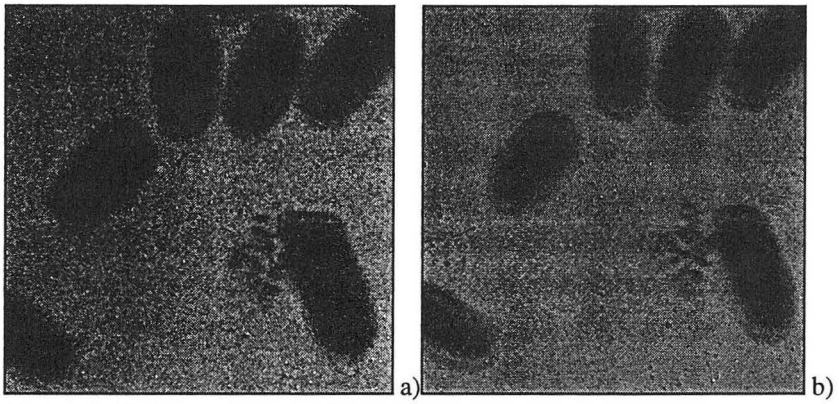

Figure 1: Soft x-ray images of dehydrated spores.
a) 2 sec exposure (0 sec prior); b) 24 sec (80 sec prior exposure).
(Image size: 4 μm x 4 μm)

By comparison, hydrated spores appear to be very radiation-sensitive and show some internal features. Using a 2 sec exposure time the spores appear to have an indistinct denser central region, although this may simply be a result of the greater thickness of the spores at their center compared to the spore margins (Fig. 3a). In subsequent exposures (Figs. 3b-d) of the same area, however, the central area is distinctly more x-ray dense than the spore periphery. Furthermore, the margins of the spores also become more x-ray dense suggesting that the spore wall is now visible, although since the images are of intact hydrated spores, the wall, and its effect on x-ray absorbency, should be present over the entire image. In fact, in images of many spores, the ends of the spores are denser than the lateral margins, thus giving the impression of 'caps.' Further imaging causes the size of the spores to be reduced, probably by contraction since the overall appearance remains similar.

Images taken with an exposure time of less than 2 sec have a very poor signal to noise ratio. This can be partially compensated for by combining data from several adjacent pixels, but this reduces the resolution that can be achieved. Nevertheless it is useful to be able do this to ascertain if either the x-ray dense central core or the spore margin is present before exposure to the x-rays or whether both are the consequence of exposure to x-rays. Images taken with exposures as short as 0.1 sec appear to show that there is indeed a small increase in x-ray absorbency at the spore margin and in the central region, suggesting that the cortex (the region between the central core and spore margins) is the most radiation-sensitive. The appearance of spores after heat activation was very similar to that of hydrated spores. However, unlike hydrated spores, there is an initial increase in spore volume before exposure to soft x-rays causes an apparent loss of spore volume (Fig. 2a). This increase in volume is also seen in images of spores which have been in growth

media overnight (Fig. 2a). It is not clear why spores should increase in volume after exposure to soft x-rays, nor why only activated and not hydrated spores should behave in this way.

When activated there are, within the spore population, two types of spores which are readily identified by phase contrast light microscopy: those which are phase dark, and those which remain phase bright. It is usually assumed that spores which are phase dark are about to germinate and that this change in phase characteristics is associated with a loss of material from the spores. Unfortunately, the transition to phase dark does not occur simultaneously, and indeed some spores seem to be very recalcitrant. This makes biochemical and conventional electron microscopy studies difficult as both require a large population of spores in which it is impossible to distinguish the phase characteristics of individual spores. Soft x-ray microscopy, as available on beamline 6.1, has the very real advantage of enabling spores to be studied by phase contrast light microscopy before imaging, at higher resolution, with soft x-rays. Images of phase bright and phase dark spores show that the transmittance of soft x-rays, through phase dark spores is much greater than through those which are phase bright (Table 1) suggesting that there has, indeed, been a considerable loss of material from those which are phase dark. In the second exposures to soft x-rays there is a marked increase in soft x-ray transmittance (Table 1) but this increase does not continue with further exposure, especially when the analysis of transmittance is concerned with only the central core (Fig. 2b).

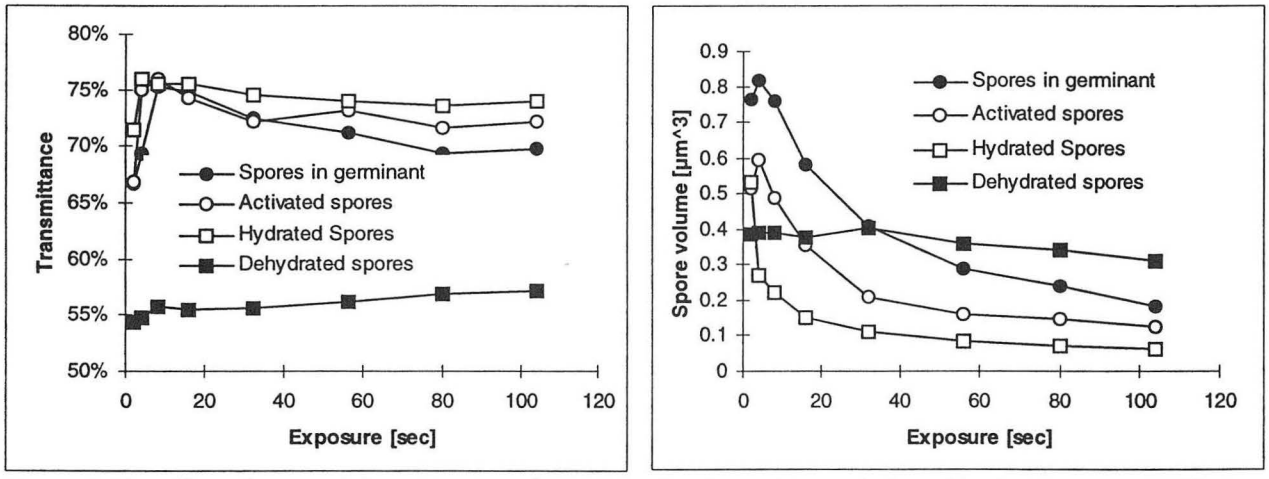

Figure 2. The effect of sequential exposure to soft x-rays on the size and transmission of bacterial spores. a) Effect on volume where spores are assumed to be a prolate spheroid, and b) effect on transmission of soft x-rays.

Table 1. Comparison of x-ray transmittance through phase bright, phase dark and vegetative cells in the initial 2sec exposure and the second 2sec exposure. In each case the the thickness of carbon (nm) required to attenuate the soft x-rays has been calculated.

	Phase bright	Phase dark	Vegetative
Initial 2sec exposure	136.6	81.3	17.8
2nd 2sec exposure	100.0	64.0	12.8

However, the fact that the percentage transmittance through phase dark spores is so much greater than that through phase bright spores indicates that the radiation dose received by phase dark spores is much lower than that received by phase bright spores. And yet, at least during initial exposures, the apparent loss of

material is as great from phase dark as from phase bright spores, showing that phase dark spores are considerably more radiation-sensitive than phase bright spores. Preliminary data show that in other respects phase bright and phase dark spores respond similarly when exposed to soft x-rays. However, relatively few phase dark spores have been examined to date due to difficulties in establishing the optimum activation and/or germination conditions at the ALS. This problem has now been overcome, and it will be of considerable interest to determine if it is calcium that is lost from the spores as they become phase dark. Biochemical analysis has shown that calcium, probably as calcium dipicolinate, is lost from populations of spores during germination [8]. However, it is not clear if this is lost only from spores that become phase dark, or whether calcium is lost from all spores regardless of their phase characteristics. Soft x-ray microscopy has the potential for resolving this question. Knowledge of the means by which some spores fail to activate and germinate is of considerable economic importance in the food industry, since bacterial spores are very resistant and may not be killed during preparation whereas vegetative bacterial cells, i.e. after germination, are relatively easy to kill. If all spores could be induced to germinate, they could be killed thereby removing the potential health hazard.

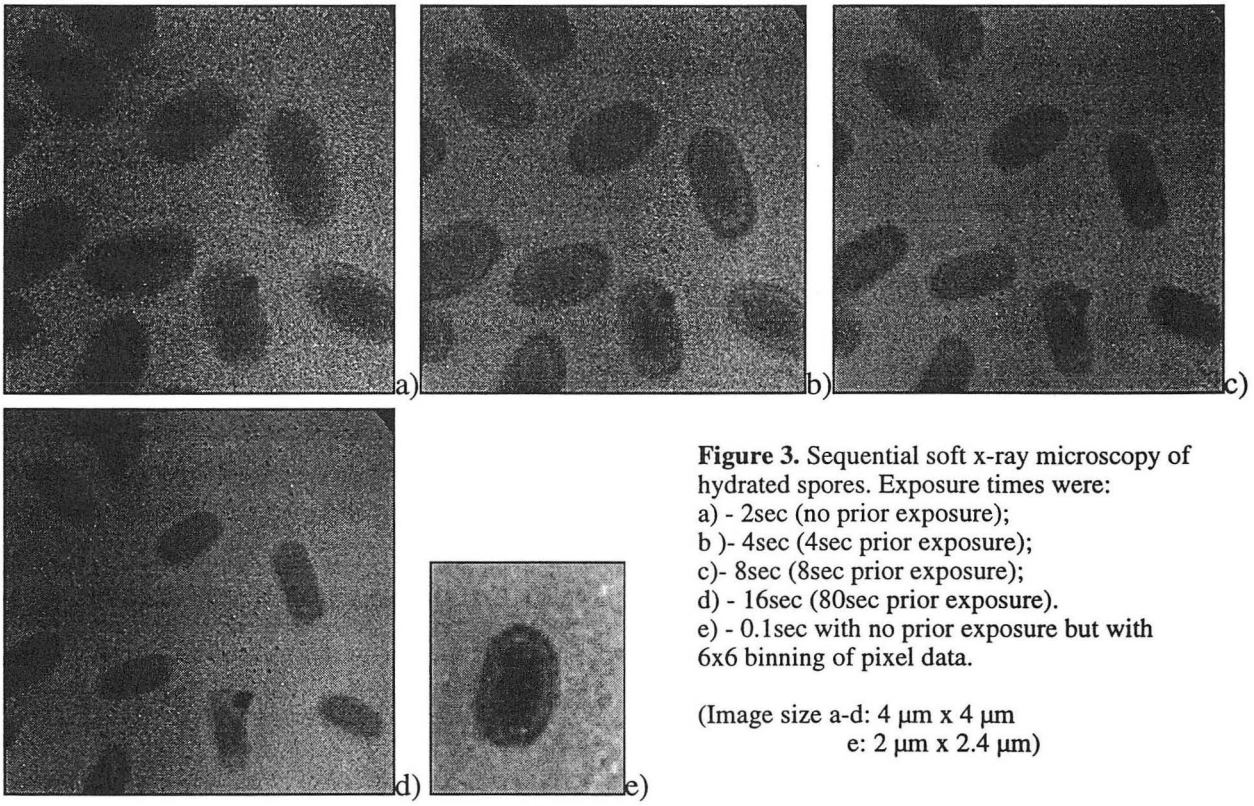

Figure 3. Sequential soft x-ray microscopy of hydrated spores. Exposure times were:
a) - 2sec (no prior exposure);
b)- 4sec (4sec prior exposure);
c)- 8sec (8sec prior exposure);
d) - 16sec (80sec prior exposure).
e) - 0.1sec with no prior exposure but with 6x6 binning of pixel data.

(Image size a-d: 4 μm x 4 μm
e: 2 μm x 2.4 μm)

The present work has demonstrated that soft x-ray microscopy can be used to gain novel information on the structural differences between dehydrated and hydrated spores due to its ability to image material in an aqueous environment. In the future, as elemental discrimination becomes feasible, the technique will be even more useful. However, this work has also shown that bacterial spores, like many other biological specimens, are very radiation sensitive, especially when hydrated, and that therefore cryo x-ray microscopy will be essential since

elemental mapping requires that at least two images, be taken, often with long exposures, one on either side of an absorption edge.

REFERENCES

1. K.J. Johnstone, Appl. Bacteriology Symp. Supp. 76, 17S (1994).
2. P.J. Coote, C.M-P. Billon, S. Pennell, P.J. McClure, D.P. Ferdinando, and M.B. Cole. J. of Microbiol. Methods 21, 193.
3. W. Meyer-Ilse, H. Medecki, L. Jochum, E. Anderson, D. Attwood, Magowan, R. Balhorn, and M. Moronne. Synchrotron Radiation News 8, 29 (1995).
4. S. Williams, X. Zhang, C. Jacobsen, J. Kirz, S. Lindaas, J. Vanthof, and S.S. Lamm. J. of Microsc. 170, 155 (1993).
5. M. Bennett, G.F. Foster, C.J. Buckley, and R.E. Burge. J. of Microsc. 172, 109 (1993).
6. T.W. Ford, A.M. Page, G.F. Foster, and A.D. Stead. SPIE Proceedings 1741, 325 (1993).
7. H. Fujisaki, S. Takahashi, H. Ohzeki, K. Sugisaki, H. Kondo, Nagata, H. Kato, and S. Ishiwata. J. of Microsc. 182, 79.
8. I.R. Scott, and D.J. Ellar. J. of Bacteriol. 135, 133 (1978).

This work has been supported by financial contributions to ADS and TWF from Unilever plc which we gratefully acknowledge, and from U.S. Department of Energy, Office of Basic Energy Sciences, and the Office of Health and Environmental Research and the Laboratory Directed Research and Development Program of the E. O. Lawrence Berkeley National Laboratory under the Department of Energy contract No. DE-AC03-76SF00098.

Principal investigator: Tony Stead, Biological Sciences, Royal Holloway (University of London),
Egham, Surrey, UK. TW20 0EX.
E-mail: A.Stead@RHBNC.AC.UK. Telephone: (44) 1784 443761; Fax: (44) 1784 470756

Imaging Mammalian Cells with Soft X Rays: The Importance of Specimen Preparation

John T. Brown and Werner Meyer-Ilse
Center for X-ray Optics, E. O. Lawrence Berkeley National Laboratory,
University of California, Berkeley, California 94720, USA

INTRODUCTION

Studies of mammalian cell structure and spatial organization are a very prominent part of modern cell biology. The interest in them as well as their size make them very accommodating subject specimens for imaging with soft x-rays using the XM-1 transmission microscope built and operated by The Center for X-ray Optics on Beam Line 6.1 at the Advanced Light Source. The purpose of these experiments was to determine if the fixative protocols normally used in electron or visible light microscopy were adequate to allow imaging cells, either fibroblasts or neurons, with minimal visible radiation damage due to imaging with soft x-rays at 2.4 nm. Two cell types were selected. Fibroblasts are easily cultured but fragile cells which are commonly used as models for the detailed study of cell physiology. Neurons are complex and sensitive cells which are difficult to prepare and to culture for study in isolation from their connections with surrounding cells. These cell types pose problems in their preparation for any microscopy. To improve the contrast and to prevent postmortem alteration of the chemistry and hence the structure of cells extracted from culture or from living organisms, fixation and staining techniques are employed in electron and visible light microscopy. It has been accepted by biologists for years that these treatments create artifacts and false structure. We have begun to develop protocols for specimens of each of these two cell types for soft x-ray microscopy which will preserve them in as near normal state as possible using minimal fixation, and make it possible to image them in either a hydrated or dried state free of secondary addition of stains or other labels.

EXPERIMENTS

Cultured WI38 human diploid fetal lung cells were used to test the efficacy of paraformaldehyde vs. glutaraldehyde fixation. The cells are useful for imaging with soft x-rays because they grow in culture attached to the surface and show a better defined nuclear morphology than other cells which have a more rounded morphology. The cells were cultured directly upon the silicon nitride membranes which are used as sample holders for x-ray imaging. The WI38 cell line is used as a model system for studies of cell senescence. Since this cell line is not transformed, we used early passage cultures. The cells of this line do not undergo apoptosis but they have a defined replicative life span in that they change their morphology and cease mitosis after a certain number of passages. Eventually their division rate in culture drops to zero. Cultures were raised in Dulbecco's Modified Eagle's medium in 37°C incubator held at 5% carbon dioxide. The medium was supplemented with 10% fetal calf serum. After 24 hours in culture the membranes

with their attached fibroblasts were rinsed in PBS then fixed at a final concentration of 2% paraformaldehyde in PBS. Following the fixation step the cells were permeabilized in 0.1% Triton X100 in PBS. A final incubation at room temperature was carried out in 1% Triton X100. Cells were washed and held in water until imaging. Cultures raised for glutaraldehyde fixation followed exactly the same protocol steps up to the fixation. Fixation was carried out at room temperature in 1% glutaraldehyde in PBS. This was followed by a 1% Triton X100 permeabilization at room temperature in PBS. Cells were then rinsed in PBS and water and kept wet until the chambers were assembled for imaging.

Primary cultures of rat cerebellar neurons were prepared to study the effects of excitatory amino acids, kainate and glutamate, on the uptake of cobalt. Cells prepared for this experiment were air dried as part of the experimental design to be imaged in the XM-1 soft x-ray transmission microscope. Primary cerebellar neuron granule cells were cultured in 10% calf serum enhanced modified Eagle's medium. They had been excised from the rat brain and were suspended in the medium and allowed to attach themselves to the silicon nitride membrane on which they were to be exposed to cobalt in solution. Cells attached to the membranes were fixed with paraformaldehyde, washed and dried. Imaging was done with the XM-1 at 2.4nm, within the water window, with exposures of a few seconds to 180 seconds. Wet samples were placed into a chamber composed of two silicon nitride windows held in a stainless steel holder which retains liquid water for over two hours. Dried samples of the neurons were placed on a silicon nitride window and they are exposed to helium during imaging.

Figure 1. Paraformaldehyde fixed, hydrated fibroblast showing radiation damage. (Image size 10 μm x 8 μm)

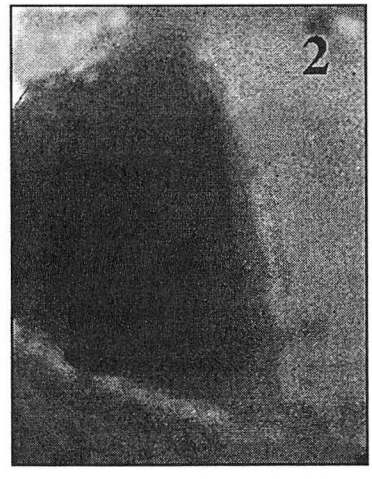

Figure 2. Rat neuron, paraformaldehyde fixed, imaged dry. (Image size 6 μm x 7 μm)

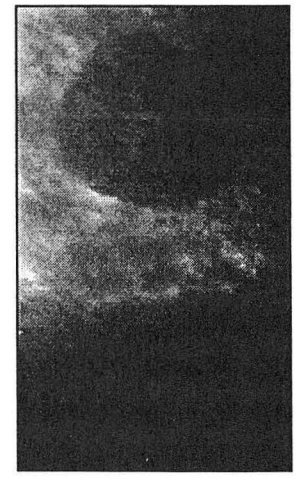

Figure 3. Nucleolus of fibroblast. Fixed with glutaraldehyde imaged hydrated. (Image size 6 μm x 11 μm)

CONCLUSIONS

These experiments show that the fixation step is critical. Paraformaldehyde fixation of WI38 fibroblasts followed by permeabilization in detergent, Triton X100, is not adequate to fix the

cells and prevent radiation damage in soft x-rays at short exposure times. Fibroblasts, maintained in the hydrated state and imaged at exposures of a few seconds, show distinct radiation damage or even complete dissolution of the cell (Fig. 1).

Paraformaldehyde has proven to be an unreliable fixative, and some substitute for it or additional treatment must be applied to make it useful for viewing hydrated specimens. Rat cerebellar neurons which have been cultured on silicon nitride membranes, paraformaldehyde fixed and dried retain their external connections which are of morphological importance. They have the ability to withstand relatively long exposures (Fig. 2).

For dried samples paraformaldehyde is a good choice. Even the most delicate and reactive cells so treated retain their external form and connections to their neighbors. One percent glutaraldehyde, a cross-linking fixative, is adequate for hydrated specimens of cultured fibroblasts where fine details of morphology are important (Fig. 3).

Experiments are continuing to solve the problems which have arisen in imaging fragile cells with soft x-rays. New procedures for fixation of fibroblasts and neurons are under way.

ACKNOWLEDGMENTS

We wish to thank Dr. Sharon Krauss and Dr. Gelsomina De Stasio for preparing specimens for imaging.

This work was supported by the U.S. Department of Energy, Office of Basic Energy Sciences, and the Office of Health and Environmental Research and the Laboratory Directed Research and Development Program of the E. O. Lawrence Berkeley National Laboratory under the Department of Energy contract No. DE-AC03-76SF00098.

Principal investigator: Werner Meyer-Ilse, Center for X-ray Optics, E. O. Lawrence Berkeley National Laboratory, E-Mail: W_MEYER-ILSE@LBL.GOV, Phone: (510) 486-6892.

In Situ Alkali-Silica Reaction Observed by X-Ray Microscopy

K.E. Kurtis,[1] P.J.M. Monteiro,[1] J.T. Brown,[2] and W. Meyer-Ilse[2]
[1]Department of Civil and Environmental Engineering, University of California, Berkeley, California 94720, USA
[2]Center for X-Ray Optics, Ernest Orlando Lawrence Berkeley National Laboratory, University of California, Berkeley, California 94720, USA

INTRODUCTION

In concrete, alkali metal ions and hydroxyl ions contributed by the cement and reactive silicates present in aggregate can participate in a destructive alkali-silica reaction (ASR). This reaction of the alkalis with the silicates produces a gel that tends to imbibe water found in the concrete pores, leading to swelling of the gel and eventual cracking of the affected concrete member. Over 104 cases of alkali-aggregate reaction in dams and spillways have been reported around the world. At present, no method exists to arrest the expansive chemical reaction which generates significant distress in the affected structures [1].

By studying the reaction of silica gel in sodium hydroxide solutions and calcium hydroxide solutions, Dent Glasser and N. Kataoka have distinguished four reactions for the silica gel/sodium hydroxide/calcium hydroxide system [2,3]:

1) dissolution of silica by hydroxyl attack,
2) reaction of surface silanol (Si-OH) groups with hydroxyl ions (OH^-) in the solution,
3) binding of the sodium cations (Na^+) and calcium cations (Ca^{++}) at negatively charged sites on the silicate surface,
4) reaction of silicate species in solution with calcium ions in solution to form calcium silicate hydrate (C-S-H).

Most existing techniques available for the examination of concrete microstructure, including ASR products, demand that samples be dried and exposed to high pressure during the observation period. These sample preparation requirements present a major disadvantage for the study of alkali-silica reaction. Given the nature of the reaction and the affect of water on its products, it is likely that the removal of water will affect the morphology, creating artifacts in the sample.

The purpose of this research is to observe and characterize the alkali-silica reaction, including each of the specific reactions identified above, in situ without introducing sample artifacts. For observation of unconditioned samples, x-ray microscopy offers an opportunity for such an examination of the alkali-silica reaction. Currently, this investigation is focusing on the effect of calcium ions on the alkali-silica reaction.

EXPERIMENT

Experiments were conducted at the x-ray microscopy XM-1, built and operated by the Center for X-ray Optics (CXRO) at beamline 6.1 at the Advanced Light Source (ALS) at the E. O. Lawrence Berkeley National Laboratory in Berkeley, California. Samples consisted of finely ground particles of reactive silica in saturated calcium hydroxide solution. Chemical-grade silica gel, ground ASR gel from the FURNAS Dam in Brazil, silica fume, and ground opal were used as the reactive silicate required for the reaction. The solution, made from double distilled, deoxygenated water, was used to simulate highly alkaline concrete pore solution which reacts with disordered siliceous aggregate. The pH of the solution was 12.2.

Samples were observed with soft x-rays at 2.4 nm wavelength at a magnification of 2400x. Images were recorded with exposures of 2 to 120 seconds. Samples were observed dry and after the addition of the alkaline solution. The effect of the solution on the silicate samples was documented over time, from five minutes after adding the solution to 2 weeks after adding the solution to the ground silicates.

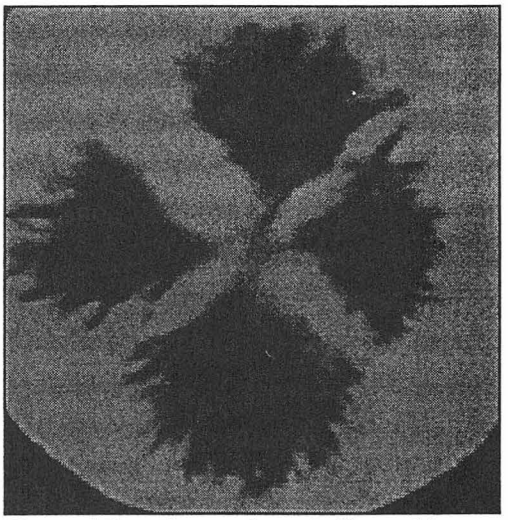

Figure 1 Reaction product of silica gel in saturated calcium hydroxide solution, 23 minutes after the solution was introduced. (Image size: 10.2 μm x 10.4 μm)
(61106105)

RESULTS

Reaction products were visible 5 to 25 minutes after the saturated calcium hydroxide solution was added to each of the silicates. Reaction of the ASR gel with the calcium ions was the fastest observed, with products visible 1 to 3 minutes after mixing. The reaction appeared to stabilize in about an hour, with no changes in the reaction products visible after that time.

Comparing the products of the reaction with the dry silicate morphology, the extent of the reaction is clear. When dry, the silicates exhibit relatively smooth, clearly defined edges. However, the products of each reaction were characterized by dendritic growth of lath like crystal structures in either a diametrical or radial pattern, exhibiting much symmetry. Crystal structure depicted in figure 1 exhibits a radial symmetry, while that in Fig. 2 is diametrical. In some instances, the growth was sparse and delicate (Fig. 1), while other structures appeared more dense (Fig. 2). It is not clear whether the reaction product is formed by a through solution or topochemical reaction.

Largely, the structures resulting from the reaction of the silicate species and the calcium ions in this investigation resemble structures described by Rashed [4] and Williamson [5]. Rashed reported similar microstructures while examining the reaction of silica fume in concrete by

scanning electron microscopy (SEM). This characteristic microstructure, termed 'sheaf of wheat' morphology, appears to result from the reaction of silicates and calcium ions in the presence of water in locations of relative emptiness, allowing such extensive crystal growth. The samples prepared for this investigation were of high solution-to-silicate ratio, which would provide space for crystal growth.

The branched crystal structure is thought to be a precursor to calcium silicate hydrate (C-S-H), a complex crystal structure which acts as a binder in concrete. The effect of the formation of a C-S-H or its precursor is not certain. It has been proposed that such a reaction product could provide additional strength to a concrete member experiencing alkali-silica reaction. If this hypothesis is confirmed, it can provide a basis for a methodology to control the expansive alkali-aggregate reaction in concrete.

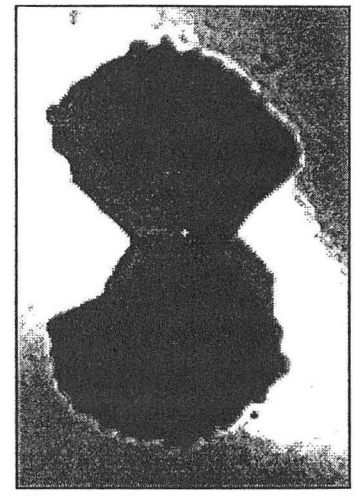

Figure 2 Sheaf of wheat morphology resulting from the reaction of alkali-silica reaction gel in saturated calcium hydroxide solution, 30 minutes after the addition of the solution.
(Image: 6.2 μm x 10.4 μm)
(61113014)

CONCLUSIONS

Saturated calcium hydroxide solution was reacted with several silicates to examine the role of calcium cations in the alkali-silica reaction in concrete. From this investigation -- which included the reaction of silica gel, alkali-silica reaction gel, silica fume, and ground opal -- it is clear that silicates react with calcium ions in the presence of hydroxyl ions and water to produce a complex crystalline microstructure characterized by bundles of lath like structure. This distinctive microstructure has been termed 'sheaf of wheat' morphology by previous authors and is thought to be a C-S-H precursor. The effect, beneficial or detrimental, of the growth of this reaction product is under investigation.

REFERENCES

1. R.G. Charlwood and Z.V. Solymar, "Long-Term Management of AAR-Affected Structures: An International Perspective", 2nd International Conference on Alkali-Aggregate Reaction in Hydroelectric Plants and Dams, Chattanooga, Tennessee, 19, (1995).
2. L.S. Dent Glasser and N. Kataoka, "The Chemistry of 'Alkali-Aggregate' Reaction", *Cement and Concrete Research*, **11**, 1-9 (1981).
3. L.S. Dent Glasser and N. Kataoka, "On the Role of Calcium in the Alkali-Aggregate Reaction", *Cement and Concrete Research*, **12**, 321-331, (1982).
4. A.M.I. Rashed, "The Microstructure of Air-entrained Concrete", UC Berkeley Dissertation, (1989).
5. R.B. Williamson, "Constitutional Supersaturation in Portland Cement Solidified by Hydration", *Journal of Crystal Growth*, **34**, 787-794, (1968).

Principal investigator: Paulo J.M. Monteiro, Department of Civil and Environmental Engineering, University of California, Berkeley. Email: paulmont@euler.berkeley.edu. Telephone: 510-643-8251.

This work has been supported by the U.S. Department of Energy, Office of Basic Energy Sciences, and the Laboratory Directed Research and Development Program of the Ernest Orlando Lawrence Berkeley National Laboratory under U.S. Department of Energy Contract No. DE-AC03-76SF00098.

The Mechanism of Cellular Secretion Studied by High Resolution Soft-X-Ray Microscopy

Billy W. Loo, Jr.[1,3,4], Werner Meyer-Ilse[2], and Stephen S. Rothman[1,3,5]

[1]Bioengineering Graduate Group,
University of California, San Francisco and Berkeley, California, USA
[2]Center for X-ray Optics, [3]Ernest Orlando Lawrence Berkeley National Laboratory,
University of California, Berkeley, California 94720, USA
[4]School of Medicine,
University of California, Davis, California 95616, USA
[5]Departments of Physiology and Stomatology,
University of California, San Francisco, California 94143, USA

INTRODUCTION

The secretion of proteins is a fundamental cellular process. The physical and biochemical mechanisms that underlie this process have been studied with the view that they can serve as a general model for how cells transport many different substances to and through their various compartments and to the external environment.

In our work, we study the secretion of digestive enzymes by the acinar cell of the mammalian pancreas. This is the classical system for studying such processes. The proteins that digest food are stored in approximately micrometer sized vesicles, zymogen granules, within these cells. There are two explanations for how these proteins are transported from within the granules to the exterior of the cell during the process of secretion. One proposes that whole granules are lost from the cell in discrete events [1], and the other proposes that partial and gradual emptying of the granules accounts for protein secretion [2]. Of course, both mechanisms may occur. We are attempting to assess to what degree each of these mechanisms account for protein secretion by the organ. In order to do so, we have been determining whether physical changes in the granules, such as mass loss, occur during secretion as the second model predicts, or if there is a simple reduction in the number of granules as predicted by the first model.

The tools that have been available to date have not allowed such an assessment. They are unable to measure quantitatively the protein content of individual structures on the size scale of zymogen granules, or subcellular organelles in general. However, the absorption of soft x-rays is highly sensitive to the content in the sample of carbon and nitrogen, the predominant components of organic molecules — in this case, the proteins contained by the granules — permitting their measurement at a resolution of tens of nanometers. Thus x-ray microscopy provides an excellent means, indeed the only means developed, of both imaging and measuring the cellular distribution of protein at the required resolutions for these and even smaller structures.

For these studies we are using the high resolution soft x-ray microscope developed and operated by the Center for X-ray Optics at LBNL on beamline 6.1 of the ALS [3]. This instrument is well suited to acquiring the large volumes of image data required to do a good statistical analysis on the characteristics of populations of zymogen granules. Thus far, we have acquired nearly 3,000 images on this instrument, corresponding to approximately 400 cells containing about 25,000 zymogen granules. The relatively large population of individual granules we have measured

should allow us to assess the changes that occur in these objects when secretion is augmented by hormonal stimulation.

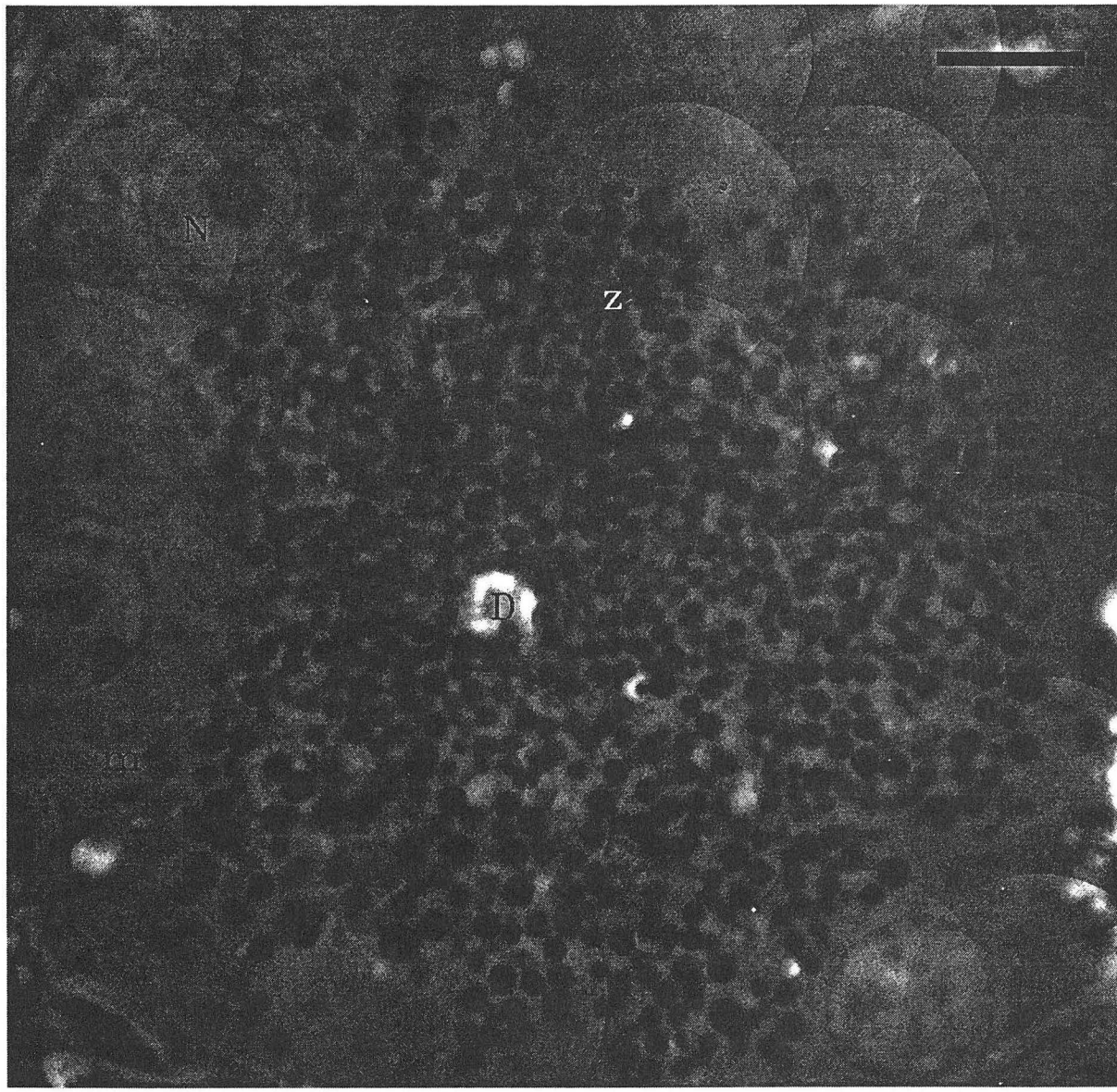

Figure 1. X-ray microscope image of a pancreatic acinus. Individual acinar cells are arrayed like pie wedges around a central ductal space (D). Dark round objects in the apex of the cells are zymogen granules (z). Also visible are cell nuclei (N) and nucleoli (n). Mitochondria (m) appear as thin, elongated objects slightly less dense than the granules. Scale bar = 5 micrometers.

EXPERIMENT

Our goal is to measure the number, size, and protein content of zymogen granules within pancreatic acinar cells, and determine how the population statistics of these parameters change with time throughout the secretion process. We hope to determine whether protein is lost from

the granules primarily by reduction in the number of granules, or by reduction in the protein content of each granule. To this end, small tissue biopsies are removed from the pancreas of rats at various time points following the administration of a drug that enhances secretion. These tissue pieces are fixed, embedded in plastic, sectioned into 0.75 micrometer slices, and imaged with the x-ray microscope. Simultaneously, overall protein secretion from the gland is monitored in fluid collected from the cannulated duct of the pancreas.

We have found this sample preparation technique, which is similar to a standard one used in histology labs, to be well suited to x-ray imaging. The infiltration of plastic into the tissue appears to be highly homogeneous and does not adversely affect the natural protein contrast in the sample. In addition, few radiation induced artifacts are observed.

In order to obtain a sufficiently large field of view for these samples, we have developed the means to tile together smaller adjacent image fields into a large composite image. The performance of the position readout scales on the sample stage results in a mean registration error of about 60 nanometers, or less than two image pixels. Fig. 1 shows a composite image of a pancreatic acinus acquired using the x-ray microscope. In addition to the zymogen granules, other features of cellular ultrastructure can be seen, including mitochondria and nuclear morphology.

Measurement of the large numbers of zymogen granules is made possible by an automated image segmentation algorithm we have developed [4] for use as a first pass analysis tool on the image data. Figure 2 shows the performance of the automated segmentation on the image of Fig. 1.

PRELIMINARY RESULTS

Although we are at the early stages in our data acquisition and analysis, our results so far appear to confirm earlier observations using electron microscopy in which zymogen granules show a decrease in mean diameter after a secretory stimulus has been administered [5,6]. In addition, with the x-ray microscope we measured what the earlier studies could not: that there is a corresponding reduction in granule protein content. Mass loss has previously been measured by x-ray microscopy in isolated zymogen granules under certain conditions [7], and the present study may indicate that the same process occurs within intact tissue as well.

Finally and significantly, the percentage decrease in granule mass appears to be approximately equal to the percentage of the whole organ's digestive protein content secreted. If verified by more detailed and extensive measurements currently underway, this would indicate that protein secretion under the conditions of this study primarily involves depletion of granules of their protein contents, rather than their loss *in toto* from the cell.

CONCLUSION

While the understanding of secretory mechanisms such as those we have been studying is central to understanding many cellular processes more generally, quantitative tools that allow for the direct measurement of protein at high resolution are only now becoming available. The x-ray microscope, particularly as it has been implemented at this facility, should help make possible

both the quantitation of protein transport at the ultrastructural level during secretion, and the acquisition and analysis of much larger volumes of samples than has been possible with existing microscopic imaging instruments.

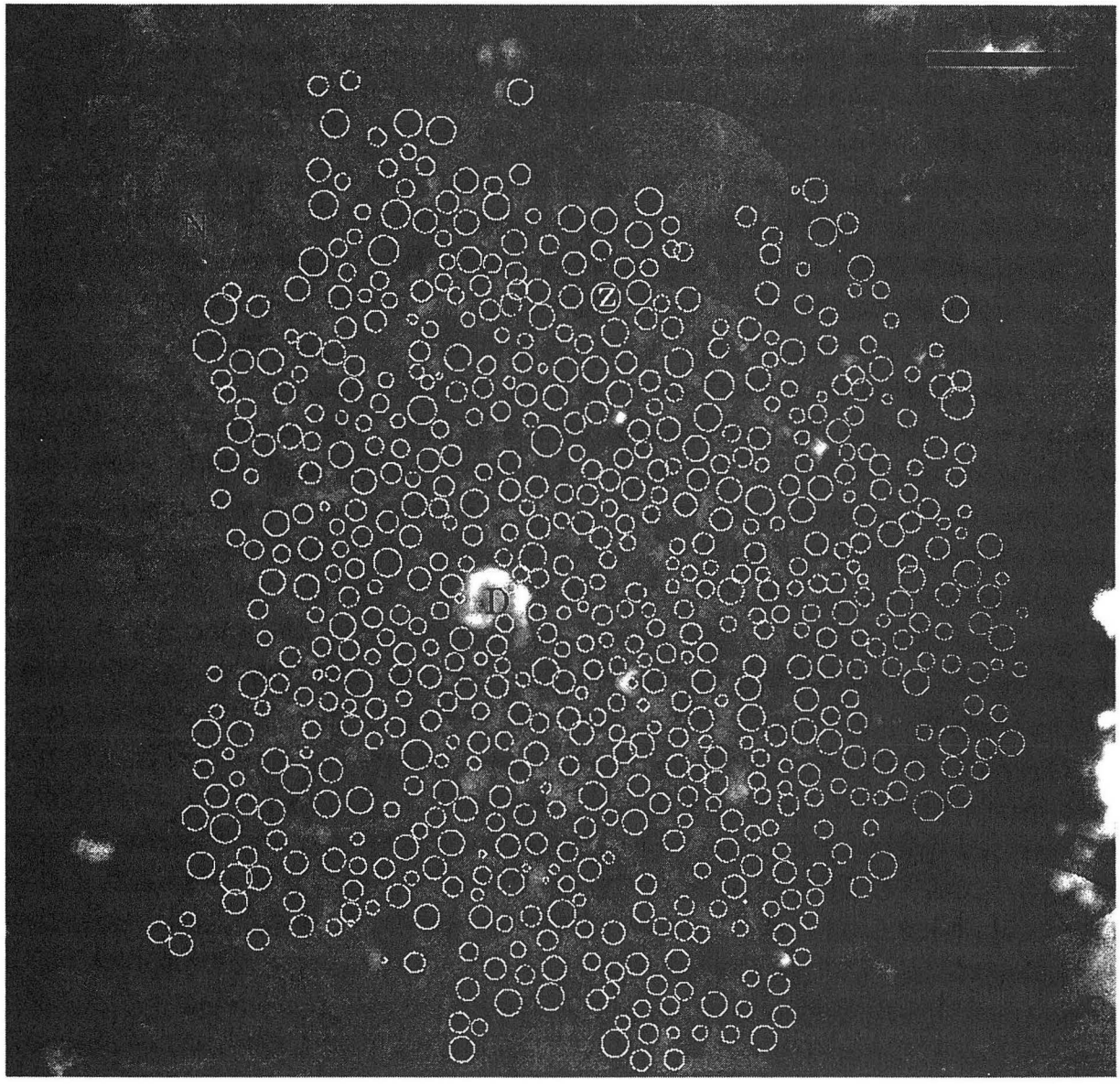

Figure 2. Automated image segmentation performed on the image of Figure 1. Objects detected by the algorithm are highlighted. Accuracy is greater than 80%. Using the algorithm as a first pass data analysis tools makes possible the measurement of the large numbers of objects required for good statistical power.

ACKNOWLEDGEMENTS

This work has been made possible by the contributions of many individuals, including staff members of the Center for X-ray Optics and the Advanced Light Source at LBNL, and the

departments of Craniofacial Histology, Stomatology, and Oral Pathology, and the Laboratory for Radiological Informatics at UCSF.

REFERENCES

1. G.E. Palade, "Intracellular aspects of the process of protein synthesis," *Science* **189**, 347-358 (1975).
2. S.S. Rothman, *Protein Secretion, A Critical Analysis Of The Vesicle Model* (Wiley, New York, 1985).
3. W. Meyer-Ilse, H. Medecki, J.T. Brown, J.M. Heck, E.H. Anderson, and D.T. Attwood, "High spatial resolution soft x-ray microscopy," this volume.
4. B.W. Loo, Jr., B. Parvin, and S.S. Rothman, "Two- and three-dimensional segmentation and measurement of particles in the analysis of microscopic digital images of biological samples," in *Three-Dimensional Microscopy: Image Acquisition and Processing III*, C.J. Cogswell, G.S. Kino, T. Wilson, Editors, Proc. SPIE **2655**, 209-215 (1996).
5. T.H. Ermak and S.S. Rothman, "Zymogen granules of pancreas decrease in size in response to feeding," *Cell and Tissue Research* **214**, 51-66 (1981).
6. A.R. Beaudoin, G. Grondin, M. Filion, and A. Lord, "Secretagogues cause a preferential discharge of large size granules in rat pancreas," *Canadian Journal of Biochemistry and Cell Biology* **62**, 1288-1292 (1984).
7. K.K. Goncz, R. Behrsing, and S.S. Rothman, "The protein content and morphogenesis of zymogen granules," *Cell and Tissue Research* **280**, 519-530 (1995).

B.W. Loo gratefully acknowledges the support of a Laboratory Graduate Fellowship from Associated Western Universities, Inc. The x-ray microscopy work was supported by the U.S. Department of Energy, Office of Basic Energy Sciences, and the Office of Health and Environmental Research and the Laboratory Directed Research and Development Program of the E. O. Lawrence Berkeley National Laboratory under the Department of Energy contract No. DE-AC03-76SF00098.

Correspondence should be addressed to: Billy W. Loo, Jr., Bioengineering Graduate Group, University of California, San Francisco and Berkeley. Email: BWLoo@lbl.gov. Telephone: 510-486-7382.

Principal investigator: Stephen S. Rothman, University of California, San Francisco.

X-Ray Dense Cellular Inclusions in the Cells of the Green Alga *Chlamydomonas reinhardtii* as seen by Soft-X-Ray Microscopy

A.D. Stead[1], T.W. Ford[1], A.M. Page[1], J.T. Brown[2] and W. Meyer- Ilse[2]

[1]Biological Sciences, Royal Holloway (University of London), Egham, Surrey, TW20 0EX. UK
[2]Center for X-ray Optics, Ernest Orlando Lawrence Berkeley National Laboratory, University of California, Berkeley, California 94720, USA

INTRODUCTION

Soft x-rays, having a greater ability to penetrate biological material than electrons, have the potential for producing images of intact, living cells. In addition, by using the so-called 'water window' area of the soft x-ray spectrum, a degree of natural contrast is introduced into the image due to differential absorption of the wavelengths by compounds with a high carbon content compared to those with a greater oxygen content. The variation in carbon concentration throughout a cell therefore generates an image which is dependent upon the carbon density within the specimen. Using soft x-ray contact microscopy we have previously examined the green alga *Chlamydomonas reinhardtii*, and the most prominent feature of the cells are the numerous x-ray absorbing spheres, But they were not seen by conventional transmission electron microscopy [1,2]. Similar structures have also been reported by the Göttingen group using their cryo transmission x-ray microscope at BESSY [3]. Despite the fact that these spheres appear to occupy up to 20% or more of the cell volume when seen by x-ray microscopy, they are not visible by transmission electron microscopy. Given the difficulties and criticisms associated with soft x-ray contact microscopy, the present study was aimed at confirming the existence of these cellular inclusions and learning more of their possible chemical composition.

METHODS

For imaging, 2 µl of the spore suspension was placed between two120nm thick, Si_3N_4 windows. After selecting fields of view using light microscopy, the field coordinates were recorded and the cells imaged with soft x-rays using XM-1 on beamline 6.1 at the ALS, Berkeley, USA [4] using monochromatic soft x-rays (2.4 nm). For investigations of the oxygen content, images of air-dried material were taken on and below the oxygen absorption resonance energy (2.325 and 2.300 nm equivalent to 533 and 539 eV).

RESULTS & DISCUSSION

Soft x-ray transmission images of hydrated *Chlamydomonas* cells show, as with soft x-ray contact microscopy, that each cell contains several x-ray dense spherical inclusions (Fig. 1a). Because these spheres are denser than the surrounding cytoplasm, it is unlikely that they could be vacuoles since the carbon content would be expected to be less in the vacuole than in the surrounding cytoplasm. If these spheres are imaged a second time, clear evidence of their

radiation sensitivity can be seen (Fig. 1b) as they appear to collapse leaving an x-ray dense deposit. This may be the membraneous material which previously surrounded these inclusions but which, when exposed to soft x-rays, is damaged such that the contents are lost and the remaining membrane then collapses. The sensitivity to soft x-ray exposure is particularly evident when the spheres were extruded from the cells by the pressure of the two silicon nitride windows (Fig. 2a-b).

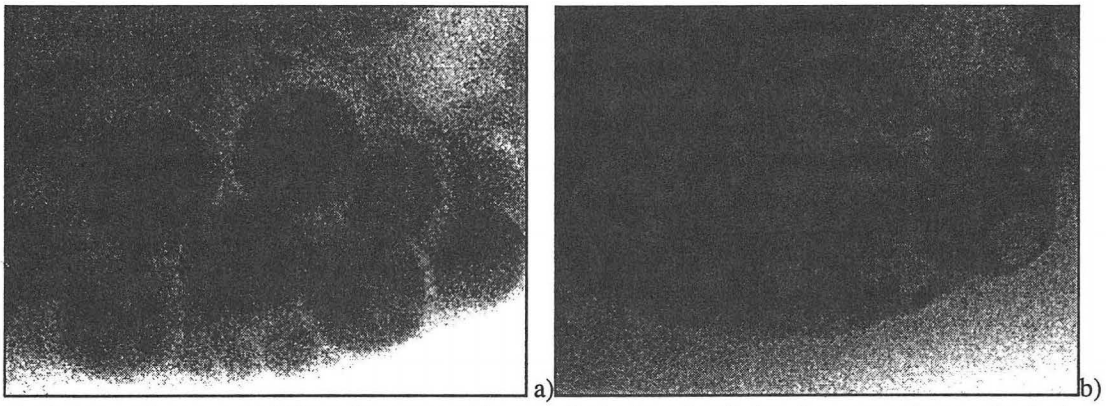

Figure 1. Soft x-ray images of *Chlamydomonas*. a) Image of a hydrated cell showing x-ray dense spherical inclusions; 1sec exposure without previous exposure. b) 2sec image taken of the same area (total pre-irradiation equal to 3sec), the spherical inclusions have collapsed but x- ray dense deposit still remains.
(Image sizes: 5.4 μm x 4 μm) (60214012/14)

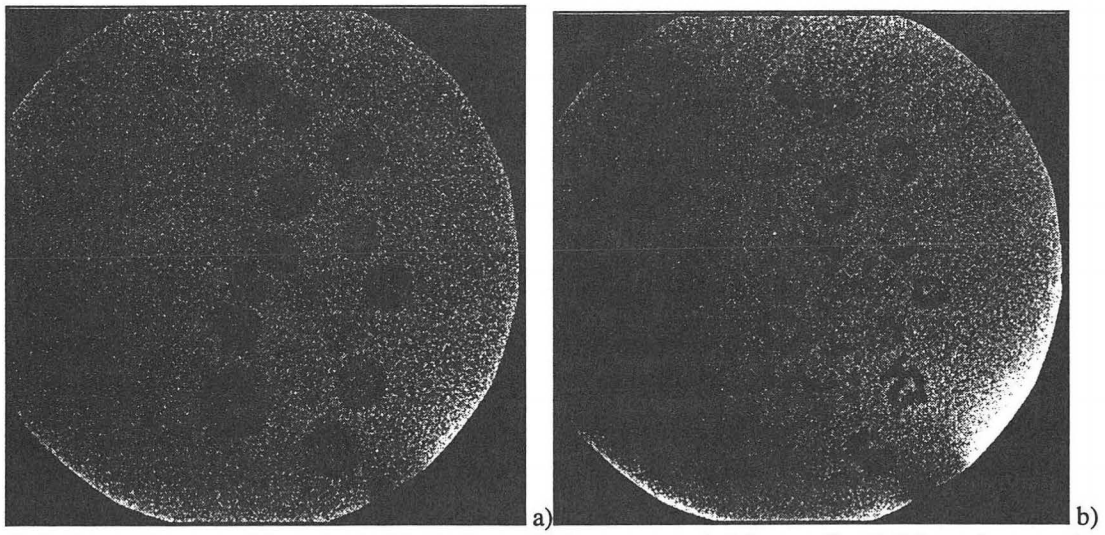

Figure 2. Soft x-ray images of the spherical inclusions which were extruded from cells of *Chlamydomonas* by the pressure of the two membranes in the specimen holder. a) Initial image; 0.2sec exposure without previous exposure. b) Second 1sec image taken of the same area (total pre-irradiation equals 1.4sec), the spherical inclusions have collapsed but x-ray dense deposit still remains.
(Image sizes: 10 μm x 10 μm) (60216048/51)

Spheres could not be identified in cells fixed in glutaraldehyde (i.e. as used in preparing for electron microscopy) since the increased density of the cytoplasm, due to the uptake of the glutaraldehyde, reduced the contrast between it and the spheres. In cells in which the increase in density was minimal, the spheres could still not be seen.

In dried material the spheres are visible when imaged at 539 eV and not at 533 eV photon energy, which indicates that oxygen is abundant in these spheres (Fig. 3). Since this material is dry the oxygen cannot be associated with the water content but other possibilities would include phosphates. There are reports of *Chlamydomonas* cells containing calcium polyphosphate granules [5], but the spheres seen in the present study appear to be too large. Furthermore, it is reported that the calcium is present in an insoluble form only in the gametes of *Chlamydomonas*, and in the vegetative cells (as used in the present study) calcium is diffuse within the cell [6]. When imaged at 2.4 nm, the amount of calcium that would be required to produce the relative x-ray absorbance of these spheres, compared to the cytoplasm, would be high. It would be expected that, if such levels of calcium existed, they would be detectable when imaging either side of the calcium edge (346 eV). However, no such absorption difference was detected (data not shown). Therefore our preliminary investigations suggest that calcium is not a major constituent of the spheres. Other possibilities could include some metal oxides since, under certain environmental conditions *Chlamydomonas* cells may accumulate metals such as manganese [7]. Once again, it is surprising that such large structures as these spheres are not seen by transmission electron microscopy.

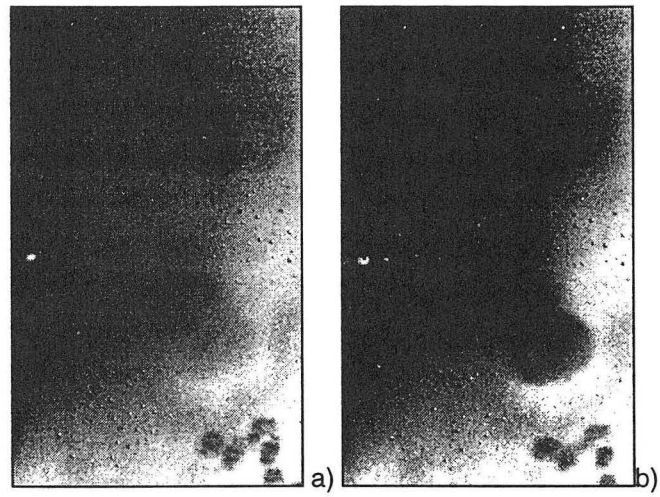

Figure 3. Soft x-ray images of dried *Chlamydomonas* cells taken below
(a: 533 eV=2.325 nm) and
at the oxygen absorption resonance
(b: 539 eV = 2.3 nm).
Image sizes: 3 μm x 5 μm. (61215051/52)

REFERENCES

1. R.A. Cotton, A.D. Stead, T.W. Ford, J.H. Fletcher, and C.E. Webb, SPIE Proceedings 1741, 204 (1993).
2. T.W. Ford, R.A. Cotton, A.M. Page, T. Tomie, T. Majima, and A.D. Stead, SPIE Proceedings 2523, 212 (1995).
3. G. Schneider, B. Niemann, P. Guttmann, D. Rudolph, and G. Schmahl, Synchrotron Radiation News 8, 19 (1995).
4. W. Meyer-Ilse, H. Medecki, L. Jochum, E. Anderson, D. Attwood, C. Magowan, R. Balhorn, and M. Moronne. Synchrotron Radiation News 8, 29 (1995).
5. M.E. Callow and L.V. Evans, British Phycological Journal 14, 327 (1979).
6. D.D. Kaska, I.C. Piscopo, and A. Gibor, Exptl. Cell. Res. 160, 371 (1985).
7. M. Siderius, A. Musgrave, H. Vandenende, H. Koerten, P. Cambier, and P. Vandermeer, J. of Phycology 32, 402 (1996).

This work has been supported by the U.S. Department of Energy, Office of Basic Energy Sciences, and the Office of Health and Environmental Research and the Laboratory Directed Research and Development Program of the E. O. Lawrence Berkeley National Laboratory under the Department of Energy contract No. DE-AC03-76SF00098.

Principal investigator: Tony Stead, Biological Sciences, Royal Holloway (University of London), Egham, Surrey, UK. TW20 0EX. E- mail: A.Stead@RHBNC.AC.UK. Telephone: (44) 1784 443761; Fax: (44) 1784 470756

X-Ray Microscopy of Human Malaria

C. Magowan, J.T. Brown[2], N. Mohandas, W. Meyer-Ilse[2]
Life Sciences Division, E. O. Lawrence Berkeley National Laboratory
University of California, Berkeley, California, 94720, USA

[2]Center for X-ray Optics, E. O. Lawrence Berkeley National Laboratory
University of California, Berkeley, California, 94720, USA

INTRODUCTION

Associations between intracellular organisms and host cells are complex and particularly difficult to examine. X-ray microscopy provides transmission images of subcellular structures in intact cells at resolutions superior to available methodologies. The spatial resolution is 50-60nm with a 1 micron depth of focus, superior to anything achievable with light microscopy. Image contrast is generated by differences in photoelectric absorption by the atoms in different areas (i.e. subcellular structures) throughout the full thickness of the sample. Absorption due to carbon dominates among all the elements in the sample at 2.4 nm x-ray wavelength. Thus images show features or structures, in a way not usually seen by other types of microscopy.

We used soft x-ray microscopy to investigate structural development of *Plasmodium falciparum* malaria parasites in normal and genetically abnormal erythrocytes, and in infected erythrocytes treated with compounds that have anti-malarial effects. X-ray microscopy showed newly elaborated structures in the cytosol of unstained, intact erythrocytes, redistribution of mass (carbon) in infected erythrocytes, and aberrant parasite morphology. Better understanding of the process of intracellular parasite maturation and the interactions between the parasite and its host erythrocyte can help device new approaches to the control of this deadly disease.

Falciparum malaria infects hundreds of millions of individuals every year, with an even greater number at risk. The World Health Organization estimates there are 300-500 million clinical cases, 800 million people at risk, and 2.7 million deaths, (1-2 million deaths of children in Africa alone) attributable to malaria every year. Malaria remains a serious public health problem, with emerging parasite resistance to many of the available, standard drug therapies, and mosquito resistance to many insecticides.

The life cycle of malaria is a complex one. Infection of the human host is initiated when a female *Anopheles* mosquito carrying the parasite introduces sporozoites during a blood meal. The sporozoites invade hepatocytes within minutes and remain there, multiplying many thousands-fold for approximately 2 weeks. Merozoites rupture cells and escape from the liver and within minutes must invade red blood cells. The parasite develops in the red blood cell through the ring stage to a trophozoite and metabolizes hemoglobin, synthesizes many new proteins, lipids and membranes to ensure its survival in the cell. At about 40 hours post-infection, the multinucleated schizont develops and at about 48 hours the red blood cell ruptures, releasing 6-24 new

merozoites which reinvade red blood cells to continue the erythrocytic cycle. The clinical symptoms (i.e. the morbidity) and the mortality of malaria are the result of this repeated rupture and re-invasion of red blood cells.

The parasite is so small, ranging from 1 to 5 or 6μ throughout the erythrocytic stages, that the resolution offered by transmitted light microscopy is inadequate to visualize the small organelles and structures within this organism. On the other hand, the thickness of the infected erythrocyte necessitates serial sectioning for examination by electron microscopy. In addition, there is significant sample preparation time involved in fixing, embedding, and sectioning the cells for electron microscopy, particularly when a large number of cells must be examined. Thus, the intraerythrocytic location of the parasite and its size make x-ray microscopy a valuable tool to investigate structural development of this pathogen.

RESULTS

We have conducted several sets of unique experiments with malaria infected red blood cells with the soft x-ray microscope XM-1, built and operated by the Center for X-ray Optics at beamline 6.1 at the ALS. We have generated the first images of the entire intraerythrocytic cycle in normal human erythrocytes and have used these to evaluate normal development of structures and organelles within the parasite as it matures. We studied hundreds of parasites in images (Fig. 1) collected at 6 hour intervals throughout the 48 hour life cycle in normal and in pathologic red blood cells showing the immature ring stage, the more mature trophozoite and the multinucleated schizont.

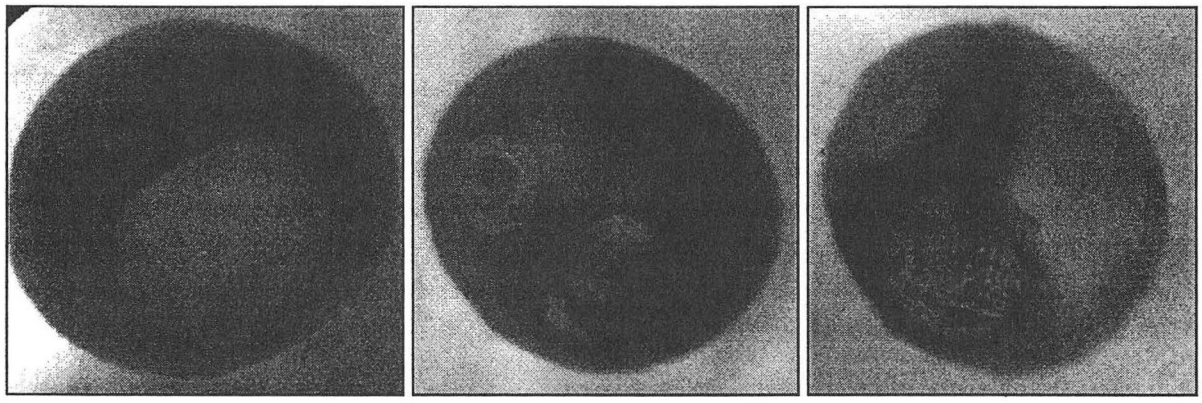

Figure 1. Life cycle of malaria in human red blood cells. The images show from left an uninfected blood cell, a newly infected cell, and a 12- hour old parasite. (Image sizes: 7 μm x 7 μm)

Data obtained with improved resolution and unique contrast from photoelectric absorption in x-ray microscopy allowed us to develop new insights into intraerythrocytic parasite development. One of the most interesting outcomes of these studies in normal red blood cells was the documentation in intact, unstained red cells, of the existence of a tubular structure surroumding the parasite and protruding into the red blood cell cytosol (Fig. 2). This tubulovesicular membrane network is thought to have a role in the import of nutrients to the parasite. Similar

structures had been visualized by fluorescent lipid labeling [1], and vesicles and clefts that are probably homologous were seen in thin section transmission electron microscopy [2], but we have now confirmed that these are not artifacts of staining or other preparative techniques which may alter such membrane bound structures.

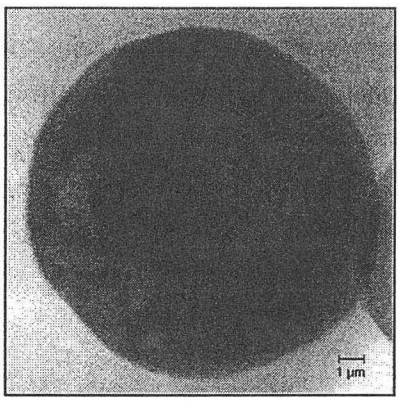

Figure 2. Tubular structure protruding from the parasite into the red blood cell cytosol seen with a young parasite.
(Image size: 7 µm x 7 µm)

We then investigated parasite development in two different unfavorable environments, protease inhibitor treated erythrocytes and genetically abnormal elliptocytes. *P. falciparum* malaria parasites transport hemoglobin from the host erythrocyte cytosol into their acidic digestive vacuoles as an energy source and to derive free amino acids for protein synthesis. Parasite cysteine and aspartic proteinases function as hemoglobinases in the parasite digestive vacuole to hydrolyze globin [3, 4]. Protease inhibitors block globin hydrolysis, causing the digestive vacuole to expand and fill with undegraded globin, ultimately resulting in death of the parasite. By bright field and electron microscopy, digestive vacuoles appear enlarged and filled with material that does not detectably differ from the contents of the red blood cell cytosol [4].

The effect of cysteine protease inhibitors on structural development of intraerythrocytic parasites has not previously been defined beyond the observation of enlarged digestive vacuoles (figure 3.). We detected increased carbon density in the vacuoles, structure surrounding the parasites, and in smaller spheres within the parasite cytoplasm.

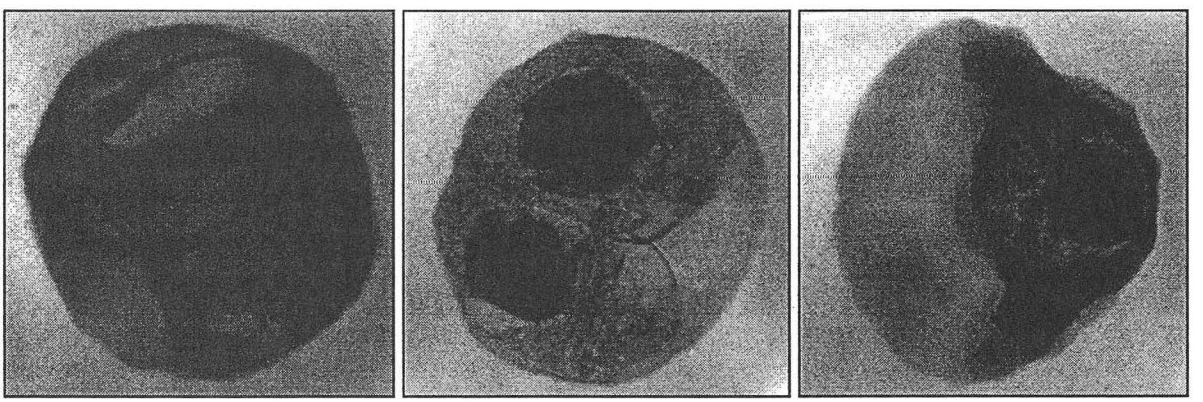

Figure 3. Protease inhibitor treated malaria parasites in human red blood cells. The image on the left shows a ZFR (ZFR courtesy of Prototec Inc., Dublin, CA) treated cell; the other two are Leupeptin treated.
(Image sizes: 7 µm x 7 µm)

A decrease in the mass of the erythrocyte cytoplasm would be expected if material were transported from the cytosol, sequestered in the parasite digestive vacuole and not replaced by equivalent mass released from the parasite. In x-ray images, obvious depletion of hemoglobin, which normally comprises >95% of the red blood cell contents, is indicated by the decreasing

carbon density of erythrocyte cytosols. The average mass of infected erythrocyte cytosols at hours 30 and 36 was reduced to approximately 50% of the mass of newly invaded red blood cells, as measured from a subset of our images. This initial data demonstrates that the translocation of hemoglobin in infected erythrocytes can be quantitated by analysis of x-ray images.

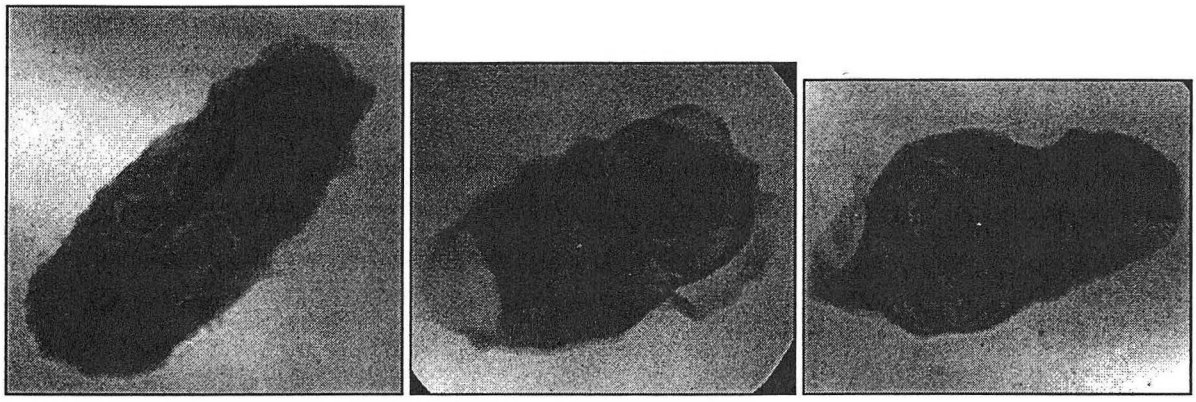

Figure 4. Malaria parasites in protein 4.1 deficient red blood cells. (Image width: 8 μm)

Red blood cell membrane abnormalities can reduce rates of infection and parasite survival [5]. Hereditary elliptocytosis is a relatively rare red blood cell disorder that can be caused by protein 4.1 deficiency. Protein 4.1 is an 80kD erythrocyte protein that binds to spectrin and actin in the erythrocyte skeleton to provide mechanical stability to the erythrocyte membrane. Erythrocytes that are totally deficient in skeletal protein 4.1 do not support the intraerythrocytic development of *P. falciparum* as well as do erythrocytes with normal membranes [5, 6]. Yet earlier investigations of parasite development in these abnormal erythrocytes did not detect morphological aberrations [6-8]. With higher resolution x-ray microscopy, it is apparent that great disorganization in parasite structure, with internal partitioning and aberrant forms, results from maturation in these abnormal erythrocytes (figure 4.). Our studies demonstrate for the first time that an abnormal erythrocyte membrane has a direct effect on the structure of intraerythrocytic *P. falciparum* parasites.

CONCLUSIONS

The previously undetected and often unexpected changes we observed in malarial parasites demonstrate that x-ray microscopy is a valuable approach to the investigation of intracellular organisms and subcellular structures in intact cells, omplementing to other microscopy technologies. We have gained new insights into intraerythrocytic development of *P. falciparum* malaria parasites, including the detection of 1) newly elaborated structures in the cytosol of unstained, intact erythrocytes, 2) redistribution of mass (carbon) in infected erythrocytes and, 3) aberrant parasite morphology in adverse environments. We have obtained unique measurements of parasites throughout their intraerythrocytic maturation, and measurements of the effects of parasitization on the red blood cell.

Investigations of normal red blood cells showed morphological anomalies in parasites treated with potential chemotherapeutic agents. Parasites that matured in erythrocytes with a membrane skeletal defect were also disorganized. We can recognize previously undetected concentrations of hemoglobin and perhaps other proteins in the abnormal digestive vacuoles. In addition, we have shown that an abnormal host erythrocyte skeleton affects structural development of parasites. This finding demonstrates conclusively for the first time that 4.1 protein of the erythrocyte membrane plays a role in normal parasite structural development.

REFERENCES

1. Elmendorf, H. G. and Haldar, K. (1994) *Plasmodium falciparum* exports the Golgi marker sphingomyelin synthase into a tubovesicular network in the cytoplasm of mature erythrocytes. J Cell Biol 124, 449-462.
2. Aikawa, M., Uni, Y., Andrutis, A. T. and Howard, R. J. (1986) Membrane-associated electron-dense material of the asexual stages of *Plasmodium falciparum*: evidence for movement from the intracellular parasite to the erythrocyte membrane. Am J Trop Med Hyg 35, 30-36.
3. Goldberg, D. E. and Slater, A. F. G. (1992) The pathway of hemoglobin degradation in malaria parasites. Parasitol Today 8, 280-83.
4. Rosenthal, P. J., McKerrow, J. H., Aikawa, M., Nagasawa, H. and Leech, J. H. (1988) A malarial cysteine proteinase is necessary for hemoglobin degradation by Plasmodium falciparum. J Clin Invest 82, 1560-1566.
5. Schulman, S., Roth, E. F. J., Cheng, B., Rybicki, A. C., Sussman, I. I., Wong, M., Wang, W., Ranney, H. M., Nagel, R. L. and Schwartz, R. S. (1990) Growth of *Plasmodium falciparum* in human erythrocytes containing abnormal membrane proteins. Proc Natl Acad Sci USA 87, 7339-7343.
6. Magowan, C., Coppel, R. L., Lau, A., Moronne, M. M., Tchernia, G. and Mohandas, N. (1995) Role of the Plasmodium falciparum mature-parasite infected erythrocyte surface antigen (MESA/PfEMP-2) in malarial infection of erythrocytes. Blood 86, 3196-3204.
7. Facer, C. A. (1995) Erythrocytes carrying mutations in spectrin and protein 4.1 show differing sensitivities to invasion by plasmodium falciparum. Parasitol Res 81, 52-57.
8. Chishti, A. H., Maalouf, G. J., Marfatia, S., Palek, J., Wang, W., Fisher, D. and Liu, S. C. (1994) Phosphorylation of protein 4.1 in Plasmodium falciparum-infected human red blood cells. Blood 83, 3339-3345.

This work was supported by the U.S. Department of Energy, Office of Basic Energy Sciences, and the Office of Health and Environmental Research and the Laboratory Directed Research and Development Program of the E. O. Lawrence Berkeley National Laboratory under the Department of Energy contract No. DE-AC03-76SF00098 and NIH grant #DK32094-10.

Principal investigator: Cathie Magowan, Life Sciences Division, E. O. Lawrence Berkeley National Laboratory. e-mail: Cathie_Magowan@macmail2.LBL.GOV, Phone: (510) 486-6439.

Beamline 6.3.2 Abstracts

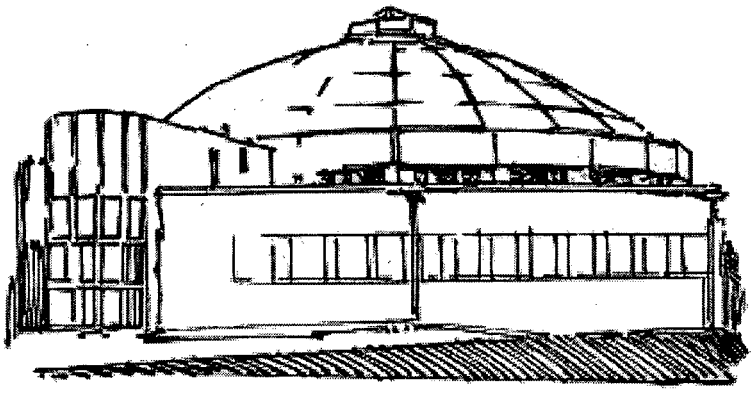

Calibration and Standards Beamline 6.3.2 at the ALS

J. H. Underwood, E. M. Gullikson, M. Koike, P. J. Batson, P. E. Denham, K. D. Franck, R. E. Tackaberry and W. F. Steele

Center for X-ray Optics, Ernest Orlando Lawrence Berkeley National Laboratory, University of California, Berkeley, California 94720, USA

INTRODUCTION

More sophisticated optics for the x-ray, soft x-ray and far ultraviolet spectral regions being developed for synchrotron radiation research and many other applications, require accurate calibration and standards facilities for measuring reflectivity of mirrors and multilayer coatings, transmission of thin films, bandpass of multilayers, efficiency of gratings or detectors, etc. For this purpose beamline 6.3.2 was built at the ALS. Its energy coverage, versatility, simplicity and convenience also make it useful for a wide range of other experiments.

BEAMLINE 6.3.2

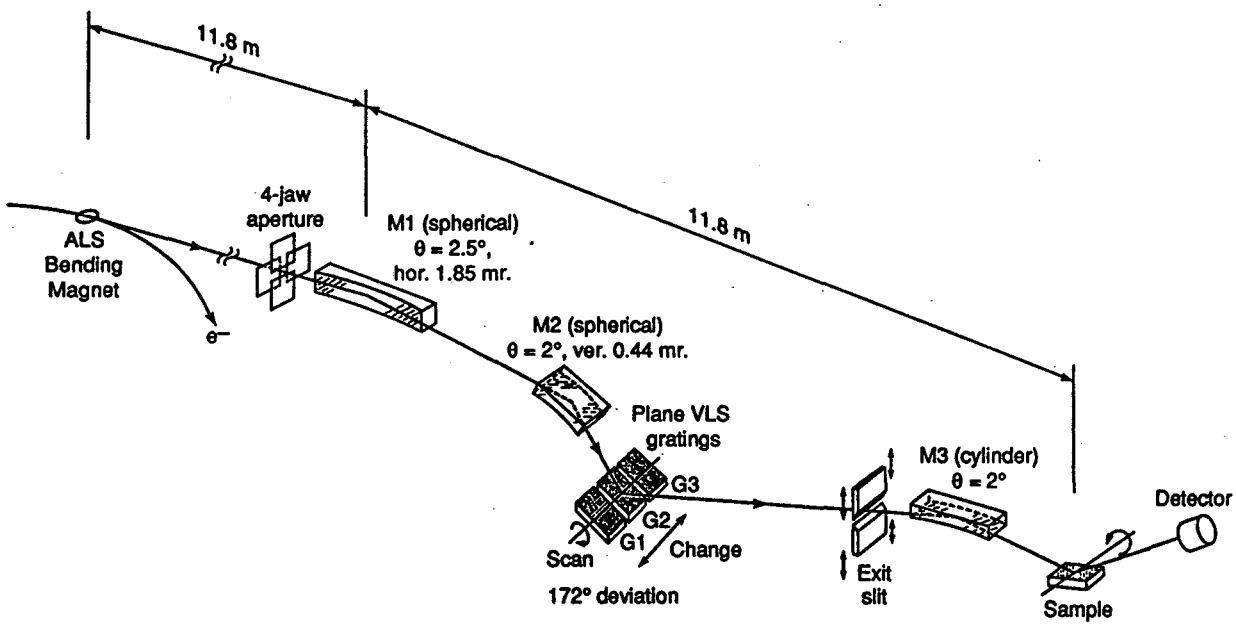

Figure 1. Schematic diagram of the layout of beamline 6.3.2 at the Advanced Light Source.

Fig. 1 is a schematic view of the beamline. The principal components are:

The **four jaw aperture** consists of four water cooled copper plates mounted on UHV feed-throughs which can be inserted into the beam as far as required to determine the horizontal and vertical acceptance.

The **horizontal focusing mirror (M1)** re-images the bending magnet source, horizontally at unit magnification, on the sample at the center of the reflectometer chamber. It is made from single crystal silicon, is gold-coated and is cooled by thermally contacting one side to a water cooled stainless steel block. This simple and effective cooling method leads to negligible thermal distortion.

The **monochromator.** Reliability of the wavelength and intensity calibrations require a high resolution, high throughput monochromator that is simple and compact, with a stable accurately determined geometry. These requirements are met by a varied line spacing plane grating monochromator [1] (VLS-PGM) design in which the grating operates in the converging light produced by a concave spherical mirror at 10:1 demagnification. The large spherical aberration of the mirror is corrected by adjusting the variation of grating ruling [2]. Because excellent source ALS stability has been achieved, an entrance slitless design carries no penalty of drifts in wavelength calibration during scans. Wavelength shifts caused by source motions arising from e.g. changes in the storage ring operation parameters, can be easily calibrated using the zero order image. This design has many practical advantages;

i) Optimization of the line space variation corrects all M2 aberrations, and the monochromator reaches resolution limited by the vertical source size of the ALS. **ii)** The demagnification allows a very short beamline, hence low cost and high mechanical stability. The increased vertical divergence allows better f-number matching for optics following the exit slit. **iii)** Wavelength is scanned by simple rotation of the grating; no other motions are needed. **iv)** Entrance slitless operation allows maximal flux collection, simplifying mechanical design and alignment and further shortening the beamline. **v)** The zero order is focused at the exit slit. This feature is extremely valuable for set-up and alignment. This image is also used to monitor vertical motions of the ALS source, to calibrate wavelength shifts. **vi)** All optical surfaces required are either plane or spherical, simplifying fabrication and reducing cost.

M2 is made from single crystal silicon. The **three interchangeable gratings** (300, 600 and 1200 l/mm), are mechanically ruled and blazed. The end of the grating sine bar can be positioned within 20 nm with a precision engraved glass scale. This allows, for example, a wavelength step size of 3 parts per million at 130 Å.

The **exit slit** can be closed to a width of a few microns to allow for the small linear dispersion. Adjustments for position, parallelism and tilt are incorporated to optimize performance; each of the four slit corners is independently actuated through a feedthrough and its position sensed to 0.1 μm by a capacitance micrometer.

The **monochromator mechanical/vacuum design** was developed to have high stability and precisely known geometry, which allows absolute wavelength calibration. The optical components are mounted on three pedestals on a baseplate *outside* the vacuum chamber. A flexible bellows surrounds each pedestal. This prevents the vacuum system from transmitting bending moments to the baseplate.

The **vertically focusing mirror (M3)** re-images the exit slit, at unit magnification, in the center of the reflectometer chamber. This mirror, polished from polycrystalline silicon, has variable elliptical curvature to re-image the slit in an auxiliary experimental chamber behind the reflectometer, or at infinity to generate parallel light.

EXPERIMENTAL FACILITIES

The **reflectometer** is a two-axis goniometer. One axis (θ-motion) carries the sample, for example a mirror, at the center of the reflectometer vacuum tank. The other (φ-motion) carries the detector on a rotating arm. Independent linear motions translate the sample in three orthogonal directions (x, y, z) with a position accuracy of 10 μm. The valve at the front of the reflectometer has a glass window to allow sample positioning and alignment at atmospheric pressure, using visible synchrotron light. The reflectometer is isolated from the monochromator by a differential ion pump and is equipped with a vibration isolated cryopump with high pumping speed to allow fast turn around of samples.

The beamline contains two **filter wheels** in which thin foils can be mounted to filter unwanted radiation or for the purpose of measuring transmission. A flange is provided at the back of the reflectometer for the attachment of additional **auxiliary experiments**.

The experiment control and data acquisition are implemented with LABVIEW™ software. All monochromator and reflectometer functions (except sample changing) and data acquisition are controlled and displayed at the workstation. The software provides the capability for scanning monochromator wavelength or energy, and for scanning any of the reflectometer motions.

SELECTED RESULTS

The beamline has been operating since February 1995, and the flux, resolution, wavelength calibration, scattered light and higher order contamination have been characterized. The monochromator resolution was measured using the spectrum of the 1s-π* vibrational states of molecular nitrogen. Fig. 2 is a (source size limited) spectrum using the 300 l/mm grating, showing a resolution of about 7000.

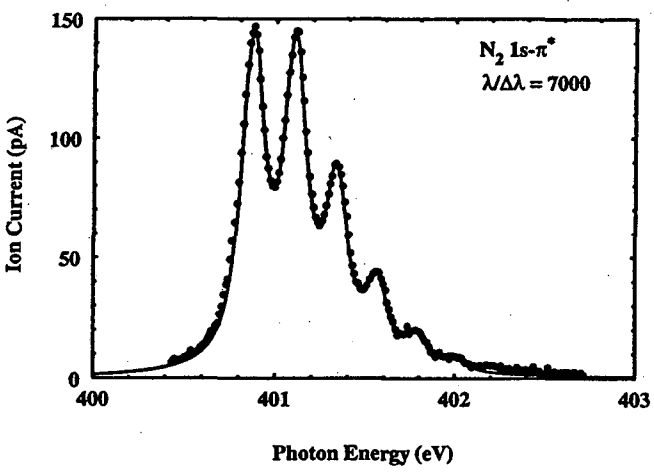

Figure 2. Absorption spectrum of N_2 gas at 30 mtorr.

Fig. 3 shows reflectivity curves of a normal incidence Mo/Si multilayer mirror. The measurements at the beamline are compared with measurements made on the identical sample at the BESSY-PTB facility in Berlin.

A more complete description of the beamline is given in reference [3].

CONCLUSIONS

Several of the other abstracts in this report volume describe work done wholly or partially at this facility. The beamline is a well-characterized and user-friendly resource which is proving itself to be useful, not only for Calibration and Standards, but for a wide variety of other investigations requiring soft x-rays in the range 50-1000eV.

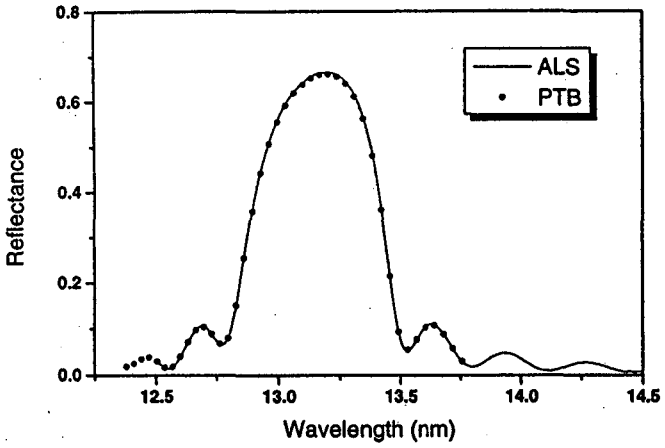

Figure 3. Reflectivity *vs.* λ of a normal incidence Mo-Si multilayer measured at Beamline 6.3.2 and BESSY-PTB in Berlin, Germany. The measurements agree in reflectivity to 0.6% and in wavelength to 0.008 Å. (Data courtesy of D. Gaines and D. Stearns, LLNL)

REFERENCES

1. M. C. Hettrick and J. H. Underwood, in *Short Wavelength Coherent Radiation: Generation and Applications*, Eds.: D. Attwood, J. Bokor, (AIP Conf. Proc. 147, 1986).
2. M. Koike, R. Beguristain, J. H. Underwood and T. Namioka, Nucl. Inst. Meth. A **347**, 273 (1994).
3. J. H. Underwood, E. M. Gullikson, M. Koike, P. J. Batson, P. E. Denham, K. D. Franck, R. E. Tackaberry and W. F. Steele; Rev. Sci. Inst. 67 (9) 1, September 1996 (CD-ROM).

This work was supported by the Advanced Lithography Program of the Department of Defense Advanced Projects Research Agency, and the Director, Office of Basic Energy Sciences, U.S. Department of Energy, under contract number DE-AC03-76SF00098

Principal investigator: J.H. Underwood, Center for X-ray Optics, Ernest Orlando Lawrence Berkeley National Laboratory. Email: underwoo@lbl.gov. Telephone: 510-486-4958

Soft-X-Ray Magneto-Optical Kerr Effect and Element-Specific Hysteresis Measurement

J.B. Kortright and M. Rice
Materials Sciences Division, Lawrence Berkeley National Laboratory, University of California, Berkeley, CA 94720, USA

INTRODUCTION

Interest in the utilization of x-ray magneto-optical properties to provide element-specific magnetic information, combined with recent development of tunable linear polarizers for spectroscopic polarization measurement,[1] have led us to the study of magneto-optical rotation (MOR) near core levels of magnetic atoms in magnetic multilayer and alloy films. Our initial observation of Faraday rotation (in transmission) demonstrated that for Fe MOR is easily measured and is larger at its L_3 resonance than in the near-visible spectral regions.[2] This work also demonstrated that the spectroscopic behavior of the MOR signal in transmission, resulting from the differential *refraction* of left- and right-circular components of a linearly polarized beam, is related to the magnetic circular dichroism (MCD), or differential *absorption*, as expected by a Kramers-Kronig transformation. Thus MCD measurements using circular polarization and MOR measurements using linear polarization can provide complementary, and in some cases equivalent, information.

On beamline 6.3.2 we have begun to investigate soft x-ray MOR in the reflection geometry, the x-ray magneto-optic Kerr effect (XMOKE). Early measurements have demonstrated the ability to measure element-specific hysteresis loops and large rotations compared to analogous near-visible measurements. We are investigating the spectral dependence of the XMOKE signal, and have initiated systematic materials studies of sputter-deposited films of Fe, Fe_xCr_{1-x} alloys, and Fe/Cr multilayers.

EXPERIMENT

A solenoidal electromagnet (Figure 1) was constructed that can be mounted onto the sample stage in the reflectometer on beamline 6.3.2 . Linearly polarized x-rays enter one end of the solenoid, reflect off of the sample centered in the magnet at glancing angle, and exit the magnet

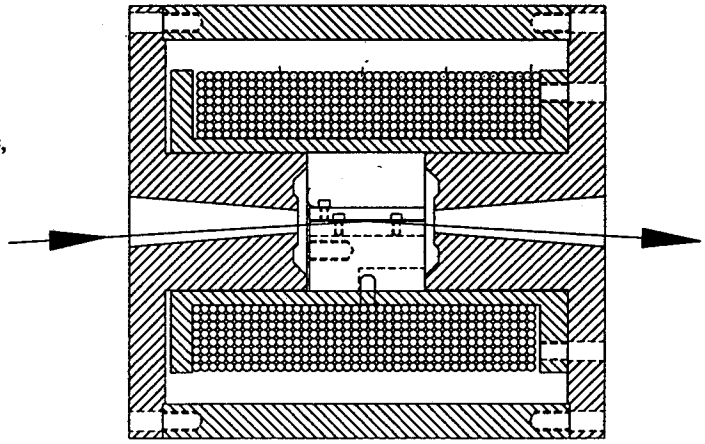

Figure 1. Solenoidal electromagnet providing variable, uniform field at the sample, which is at the center in reflection geometry.

through the other end of the solenoid. The polarization of the reflected beam then is analyzed by a tunable multilayer polarizer housed in a polarimeter[2] bolted onto the downstream port of the reflectometer. The grazing incidence angle θ was limited to $\leq 2°$ because of constraints in positioning the polarimeter on the reflectometer. An applied field of +/- 2.5 kOe can be varied continuously to produce element-specific hysteresis loops, although the uncooled magnet cannot operate continuously at such high fields.

RESULTS

A hysteresis loop measured 10 eV below the Fe L_3 line from an Fe film at 2° incidence angle is shown in Figure 2. Data have been normalized to the Kerr angle, that is the deviation of the plane of polarization produced by the magnetized sample. The measured Kerr angle of nearly 10° in the soft x-ray is over an order of magnitude larger than that measured from Fe in the near-visible region, where the maximum Kerr angle is about 0.5° at 830 nm. It is interesting that such large effects are observed so far below the L_3 line, since we know that the largest specific rotation, i.e., the rotation per unit thickness, occurs on the leading edge of the L_3 line (consistent with the Kramers-Kronig dispersion relation). This is understood by realizing that the penetration depth is a function of the optical constants which are strongly varying near the Fe $L_{2,3}$ resonances. The critical angle for total external reflection is given by $\theta_C = (2\delta)^{1/2}$ where δ is the real correction in the complex refractive index $n = 1 - \delta - i\cdot\beta$. Well away from the L_3 edge the incidence angle of 2° falls below the critical angle, severely limiting the penetration depth. In a limited region below the L_3 line δ becomes negative and total external reflection no longer occurs, leading to a much increased penetration depth. The observed XMOKE signal depends both on the specific rotation and the penetration depth, and it is the large penetration depth at 10 eV below the L_3 line that contributes to the large observed signal there, even though the specific rotation is not at its maximum. We are continuing to analyze the spectral dependence of the XMOKE signal for Fe films and other samples.

New equipment will in the future enable measurements at larger incidence angles that will increase the penetration depth by moving well above θ_C for most materials above about 100 eV. These increased penetration depths will enable studies of magnetic regions well away from the surface, including buried magnetic layers and interfaces.

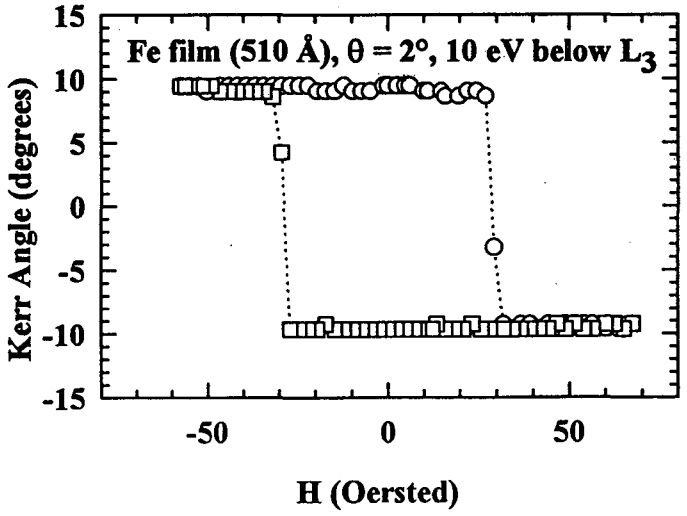

Figure 2. XMOKE hysteresis loop for an Fe film shows Kerr angles over an order of magnitude larger than observed in near-visible spectral regions. The large effects in the soft x-ray result both from the selective coupling to the empty 3d states responsible for magnetism in Fe and from large penetration depths in a limited region below the Fe L_3 edge.

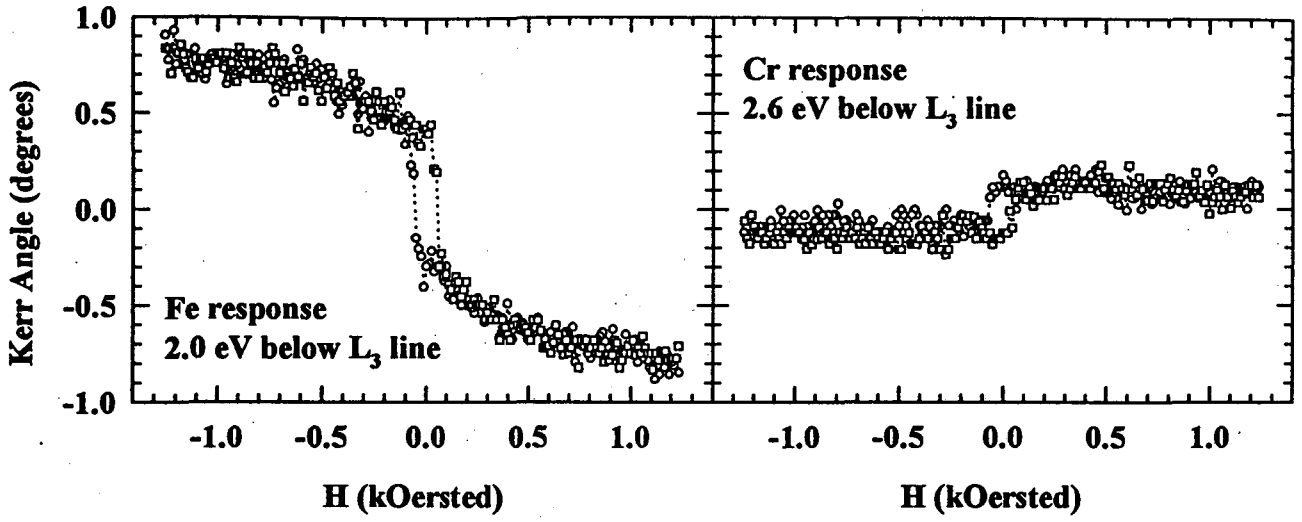

Figure 3. Hysteresis loops showing the separate Fe (left) and Cr (right) magnetization response for a sputtered, polycrystalline Fe(20Å)/Cr(19Å) multilayer. The photon energy was tuned just below each elements L_3 white line as noted. Cr exhibits a net moment oriented opposite to that of Fe. Both Cr and Fe share a common coercive feature, but only Fe shows a reversible region to higher fields prior to saturation.

Element-resolved hysteresis loops showing the separate magnetization response of Fe and Cr in an Fe/Cr multilayer sample are shown in Figure 3. Fe/Cr and similar multilayer systems have received much study recently because of the oscillatory coupling of the ferromagnetic (Fe) layers as a function of the non-ferromagnetic (Cr) layer thickness, and its influence on magneto-resistance. Our samples were grown by sputtering onto room temperature Si wafer substrates and are polycrystalline with <110> texture. The element-resolved hysteresis loops were obtained with $\theta = 2°$ and hν several eV below the respective L_3 lines as noted. Under such conditions the effective penetration depth is greater than the period of the multilayer, so that many periods contribute to the observed signal.

The individual Fe and Cr hysteresis loops provide much more information than would a traditional hysteresis measurement, that would average over the entire sample to yield the net magnetic response. The Fe signal has two distinct components. At higher applied fields is a reversible region in which the Fe magnetization traces the same path with increasing and decreasing fields but is not saturated. Together with results from other samples, this region indicates that adjacent Fe layers are not coupled ferromagnetically at this Cr layer thickness. Rather, adjacent Fe layers may show antiferromagnetic or non-colinear coupling, and the reversible change results from rotation of the magnetization in adjacent Fe layers toward the saturated (ferromagnetic) condition. The Fe loop also exhibits an open region with associated coercive field. The Cr signal exhibits only one feature, a small open loop oriented opposite to the open part of the Fe loop. Thus Cr in the sample exhibits a net moment oriented opposite to that of the Fe responsible for this part of the loop. One interpretation of these results is that the Cr moment and the coercive part of each loop result from the interface regions of the multilayer, where Fe and Cr atoms must exhibit some degree of intermixing. This interpretation is consistent with separate measurements of Fe_xCr_{1-x} alloy samples, which reveal Cr to have a moment oriented opposite to that of Fe in Fe-rich alloy samples. By itself, Cr is an antiferromagnet and shows no net moment in XMOKE measurements.

Other groups have measured element-specific hysteresis loops using soft x-ray MCD in conjunction with fluorescence detection.[3,4] Fluorescence yields are very small in the soft x-ray, and collection effieciencies are far from unity. The XMOKE technique is relatively efficient, utilizing all specularly reflected photons that have interacted with the sample.

CONCLUSIONS

These early results demonstrate that soft x-ray magneto-optical rotation measurements in the reflection geometry are possible, and offer capabilities and information complementary to other near-visible and soft x-ray magneto-optical techniques. Generalizing from our Fe result, MOR is larger at core resonances in the soft x-ray than in near-visible regions because dipole transitions provide selective coupling to the empty states associated with magnetism. Working at core resonances also provides element specificity, allowing dissection of the aggregate magnetic response of a complex sample into its constituent pieces. Through choice of incidence angle and energy, large penetration depths can allow study of regions well below the surface, including buried layers and interfaces. Relying on specular reflection, XMOKE is an efficient measurement of magnetic effects and is immune to perturbing effects of varying external fields.

Compared to the transmission (Faraday) geometry, the reflection (Kerr) geometry has added complexity in the spectral response near resonances resulting from the rapidly varying penetration depth. This will complicate the application of sum rules to XMOKE spectra to resolve spin and orbital contributions to elemental moments.

We are proceeding to build a dedicated endstation for soft x-ray MOR measurements. The new device will feature a larger electromagnet external to the vacuum to provide higher field capability, and the ability to work both in transmission geometry and in reflection geometry with incidence angles greater than 10° to increase penetration depths. MCD measurements will also be possible using this apparatus, which will make use of bending magnet and undulator beams.

ACKNOWLEDGEMENTS

Multilayers and films studied where grown in the labs of the Center for X-Ray Optics at LBNL. The electromagnet was designed by D. Humphries, and fabricated with the help of D. Kemp.

REFERENCES

1. J.B. Kortright, M. Rice, and K.D. Franck, Rev. Sci. Instrum. **66**, 1567 (1995).
2. J.B. Kortright, M. Rice, and R. Carr, Phys. Rev. B **51**, 10240 (1995).
3. C.T. Chen, Y.U. Idzerda, H.J. Lin, G. Meigs, A. Chaiken, G.A. Prinz, and G.H. Ho, Phys. Rev. B. **48**, 642 (1993).
4. V. Chakarian, Y.U. Idzerda, G. Meigs, E.E. Chaban, J.-H. Park, and C.T. Chen, Appl. Phys. Lett. **66**, 3368 (1995).

This research was supported by the Director, Office of Energy Research, Office of Basic Energy Sciences, Materials Sciences Division. of the U.S. Department of Energy under Contract No. DE-AC03-76SF00098.

Principal investigator: Jeffrey Kortright, Materials Sciences Division, Lawrence Berkeley National Laboratory
E-mail: JBKortright@lbl.gov. Telephone: (510) 486-5960.

Anisotropy of the Nitrogen Conduction States in the Group III Nitrides Studied by Polarized X-Ray Absorption

K. Lawniczak-Jablonska[1,2], T. Suski[1,3], Z. Liliental-Weber[1], E. M.Gullikson[1], J.H. Underwood[1], T. J. Drummond [4] and R.C.C. Perera[1]

[1] Lawrence Berkeley National Laboratory, Berkeley, California 94720.
[2] Institute of Physics, Polish Academy of Sciences, 02 668 Warsaw, Poland.
[3] High Pressure Research Center, Polish Academy of Sciences, 01 142 Warsaw, Poland.
[4] Sandia National Laboratory, Albuquerque , New Mexico 87185.

INTRODUCTION

Group III nitrides (AlN, GaN, and InN) consists of the semiconductors which appear recently as a basic materials for optoelectronic devices active in the visible/ ultraviolet spectrum as well as high -temperature and high -power microelectronic devices [1,2]. However, understanding of the basic physical properties leading to application is still not satisfactory. One of the reasons consists in unsufficient knowledge of the band structure of the considered semiconductors. Several theoretical studies of III-nitrides band structure have been published [3, 4, 5] but relatively few experimental studies have been carried out [4, 5,6], particularly with respect to their conduction band structure. This motivated us to examine the conduction band structure projected onto p-states of the nitrogen atoms for AlN, GaN and InN. An additional advantage of our studies is the availability of the studied nitrides in two structures, hexagonal (wurtzite) and cubic (zincblende). This offers an opportunity to gain information about the role of the anisotropy of electronic band states in determining various physical properties.

EXPERIMENT

The x-ray absorption measurements (nitrogen K-edge) were performed at the beamline 6.3.2 Advanced Lights Source (ALS), using a total photocurrent measurement technique. The high level of linear polarization (~98%) and the high resolution of new designed varied line space grating monochromator [7] made it possible to measure the nitrogen K-edge of epitaxially grown layers of III - nitrides for two geometries. In the transverse electric polarization geometry, the electric field vector of the synchrotron radiation, **E**, was perpendicular to sample normal ($\mathbf{E} \perp \mathbf{n}$) and in the transverse magnetic polarization geometry, **E** was parallel to sample normal ($\mathbf{E} \parallel \mathbf{n}$). Samples were mounted onto a conducting indium foil which was isolated from the samples holder in the ultra high vacuum reflectometer.Thickness of epitaxial layers used in our measurements was between 0.05 and 1 μm. The hexagonal GaN and InN films were grown by molecular beam epitaxy (MBE) on sapphire substrates. Electron microscopy and x-ray investigations confirm that our epitaxial hexagonal layers were oriented with the surface normal parallel to the *c*-axis. The nucleation and growth of hexagonal AlN and cubic GaN and InN films were performed in MBE system on singular (001) n+ GaAs substrates. Transmission Electron Microscopy (TEM) cross-section and x -ray diffraction studies of the two latter samples have clearly shown formation of cubic phase. However, an asymmetry of distribution of stacking faults (SF) in two perpendicular [110] directions in the cubic GaN was observed. The higher density of SF was observed for the [110] direction parallel to the major flat plane of GaAs. In the perpendicular direction much less of SFs were observed [8]. In the case of cubic InN film TEM investigations showed that subsurface layer of InN has not that much planar defects (mainly SFs) as the cubic GaN film.

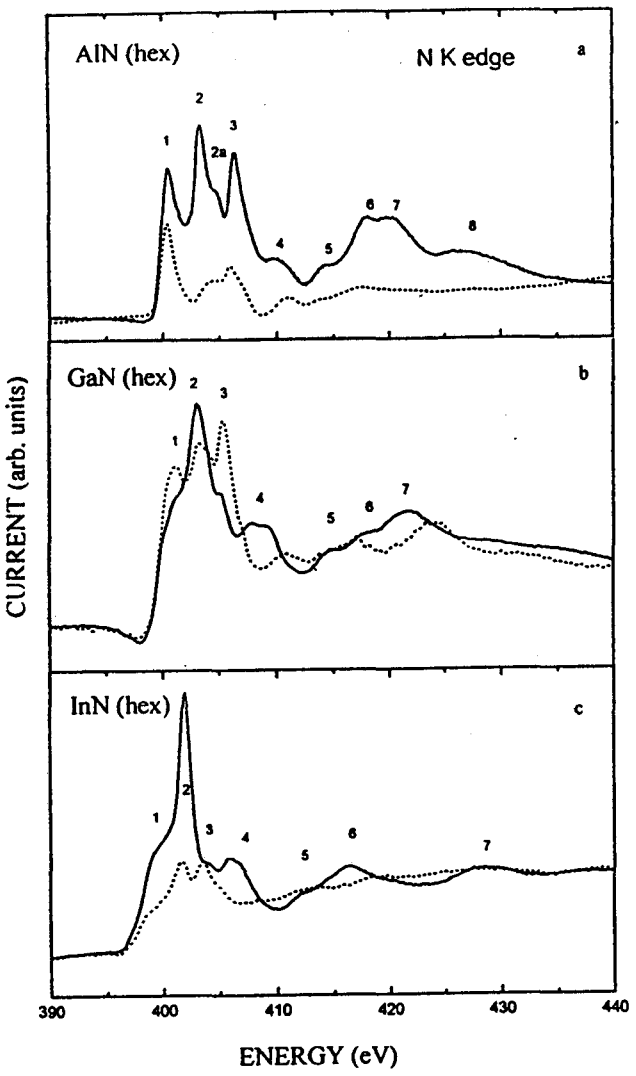

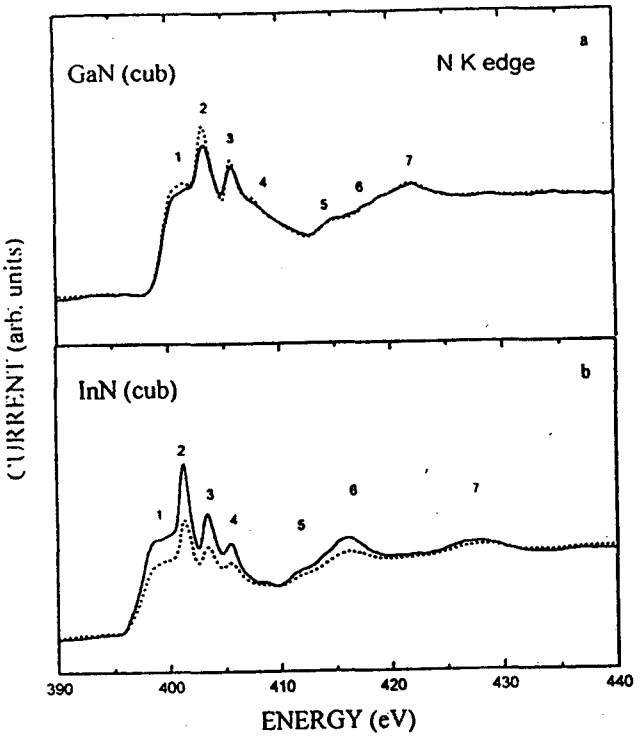

Figure 1. The N K-edges for hexagonal epitaxial layers of group III nitrides recorded for $\mathbf{E} \perp c$ (solid line) and $\mathbf{E} \parallel c$ (dashed line) polarization geometry. a) for AlN, b) for GaN , c) for InN.

Figure 2. The N K-edges for cubic epilaxial layers of group III nitrides recorded for $\mathbf{E} \perp c$ (solid line) and $\mathbf{E} \parallel c$ (dashed line) polarization geometry. a) for GaN , b) for InN.

The x-ray absorption spectra can be crystallographic orientation dependent. This is due to the scalar multiplication in the matrix element of the absorption cross-section between polarization vector of the photon and the position vector of the electron. Transition of the 1s electron to the final p_z -states is forbidden if the electric field of the absorbed light is perpendicular to the *c*-axis ($\mathbf{E} \perp c$). Whereas, transition of the 1s electron to the final p_{xy} -states is forbidden if the electric field of the absorbed light is parallel to the *c*-axis ($\mathbf{E} \parallel c$). Therefore, our absorption studies are not only element and orbital symmetry specific but also orientation dependent that means, project the particular conduction states separately along specific crystallographic directions. The nitrogen K-edge from hexagonal AlN, GaN, InN epitaxial layers measured for different polarization geometry are presented in Fig. 1. All spectra have been normalized to the same intensity level corresponding to the energy value just before the onset of the edge (where no polarization dependence was suspected). The shape and the energy position of the characteristic spectra features differs considerably in the investigated energy range (40 eV from edge) depending on the cation atom. For the same cation the shape of spectra depends on the polarization indicating the strong anisotropy of the conduction band states distribution in the *ab*-plane (p_{xy}-states) and along, the *c*-axis (p_z-states). The N K-edges from GaN and InN cubic layers are presented in Fig. 2. As can be deduced, due to isotropic arrangement of atoms, we do not expect anisotropy in the conduction states distribution for cubic layers. Indeed, the spectra in both polarizations are almost identical but different from spectra for the GaN and InN in the wurtzite structure.

CONCLUSION

Concluding, the most important finding of this studies consists in demonstrating the anisotropy of the nitrogen conduction band states for the hexagonal group-III nitrides (wurtzite structure). The anisotropy is the highest in AlN and the lowest in GaN semiconductor. InN represents the intermediate case. The detailed comparison of our data with the prediction of the theory is under preparation. It is natural to expect that our findings will inspire studies pointing out a role of this anisotropy in determination corresponding physical properties of the considered nitrides. Situation here is much less understood than in the case of e.g., high temperature superconductors where the important contribution of the conduction band anisotropy to the mechanism of the superconductivity was intensively studied [9].

ACKNOWLEDGMENTS

Authors would like to express their gratitude to Paul Denham for construction of special sample holder for the performed experiments.

REFERENCES

1. H. Sakai, T. Koide, H. Suzuki, M. Yamaguchi, S. Yamasaki, M. Koike, H. Amano and I. Akasaki, Jpn. J. Appl. Phys. 34, L1429 (1995).
2. S. Nakamura, M. Senoh, S. Nagahama, N. Iwasa, T. Yamada, T. Matsushita, H. Kiyoku, and W. Sugimoto, Jpn. J. Appl. Phys. 35, L74 (1996).
3. A. Rubio, J. L. Corkill, M. L. Cohen, E. L. Shiley and S.G. Louie, Phys. Rev. B48, 11810, (1993).
4. N.E. Christensen and I. Gorczyca, Phys. Rev. B 50, 4397 (1994).
5. W.R.L. Lambrecht and B. Segall, J. Rife, W.R. Hunter, D.K. Wickenden, Phys. Rev.51, 13516 (1995).
6. G. Martin, S. Strite, A. Botchkarev, A. Agarwal, A. Rockett and H. Morkoc, Appl. Phys.Lett. 65, 610 (1994).
7. J.H. Underwood, E.M. Gullikson, M. Koike, P.J. Batson, P.E. Denhan, K.D. Franck, R.E.Tackaberry, and W. F. Steele, Rev. Sci. Instrum., in press.
8. S. Ruvimov, Z. Liliental-Weber, T.J. Drummond, M. Hafich and S.R. Lee, Appl.Phys. Lett. subm. (1996)
9. C.T. Chen, L.H. Tjeng, J. Kwo, H. L. Kao, P. Rudolf, F. Sette, and R.M. Fleming, Phys. Rev. Let. 68, 2543 (1992).

This work was supported by the Director, Office of Energy Research, Office of Basic Energy Science, Materials Science Division of the U.S. Department of Energy under Contract No. DE-AC03-76SF00098. Authors (K. L-J and T. S.) kindly acknowledges the financial support of the Fulbright Foundation.

Principal investigator: K. Lawniczak-Jablonska, Institute of Physics, Polish Academy of Sciences, Al Lotnikow 32/46, 02 668 Warsaw, Poland. E-mail:jablo@ifpan.edu.pl. Telephone: 48-22-436034.

Chemical Reaction of Hexagonal Boron Nitride and Graphite Nanoclusters in Mechanical Milling Systems

Y. Muramatsu,[1*] S. Kashiwai,[2] T. Kaneyoshi,[2] H. Kouzuki,[2] M. Motoyama,[2] M. Grush[1], T. A. Callcott,[1] J. H. Underwood,[3] E. M. Gullikson,[3] and R. C. C. Perera[4]

[1]University of Tennessee, Knoxville, TN 37996, USA
[2]Hyogo Prefectural Institute of Industrial Research, Kobe 654, Japan
[3]Center for X-ray Optics, Ernest Orlando Lawrence Berkeley National Laboratory, University of California, Berkeley, CA 94720. USA
[4]Advanced Light Source, Ernest Orlando Lawrence Berkeley National Laboratory, University of California, Berkeley, CA 94720, USA
*permanent address: NTT Integrated Information and Energy Systems Laboratory, Tokyo 180, Japan

INTRODUCTION

Synthesis of boron-carbon-nitride (BCN) hybrid alloys has been attempted extensively by many researchers because the BCN alloys are considered an extremely hard material called "super diamond," and the industrial application for wear-resistant materials is promising [1]. A mechanical alloying (MA) method of hexagonal boron nitride (*h*-BN) with graphite has recently been studied to explore the industrial synthesis of the BCN alloys [2]. To develop the MA method for the BCN alloy synthesis, it is necessary to confirm the chemical reaction processes in the mechanical milling systems and to identify the reaction products. Therefore, we have attempted to confirm the chemical reaction process of the *h*-BN and graphite in mechanical milling systems using x-ray absorption near edge structure (XANES) methods.

EXPERIMENTAL

A mixture of *h*-BN and graphite was mechanically milled up to 160 h in an argon atmosphere to prevent oxidation. The particle size of the milled products can be estimated to be several nanometers from the x-ray diffraction peak width. Chemical stoichiometry of boron, carbon, and nitrogen was maintained as 1 : 1 : 1 during the milling. XANES spectra in B-K and N-K edges were taken at BL-6.3.2 [3] by monitoring the total photoelectron yield with the energy resolution of $E\Delta E > 5000$.

RESULTS AND DISCUSSION

XANES spectra of the mechanically milled products in the B-K edge are shown in Fig. 1. In the initial stage on the milling reaction up to the 20-h milling, the 192-eV peak is drastically enhanced. This spectral feature shows the decomposition of the hexagonal structure of *h*-BN crystal. The enhancement

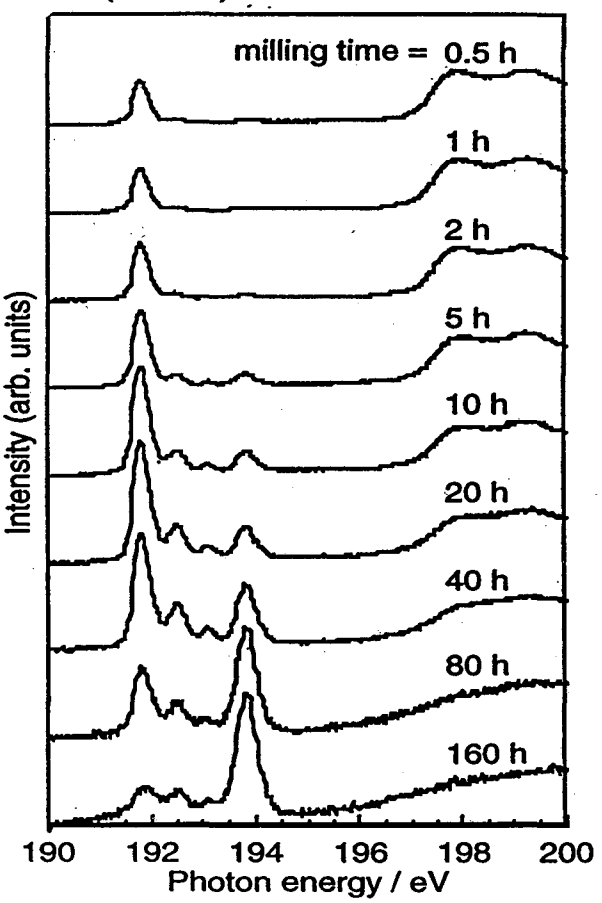

Fig. 1 B-K XANES spectra of mechanically milled mixture of *h*-BN and graphite. Milling time is from 0.5 h to 160 h.

of the 192-eV peak intensity can be explained by a B1s-B2p*(π*) transition on the boron atoms diffused with nitrogen atoms in sp^2 structure [4]. After the initial stage, the 192-eV peak decreased gradually while three other peaks appeared at 192.5, 193 and 194 eV with increasing intensity. These multiple-peak figures may show that the local environment of boron atoms is changed into an amorphous state [5]. In the final stage, the 194-eV peak becomes dominant and the B2p* edge structure in sp^3-boron atoms can be observed beyond the 196 eV region. This spectral feature shows that the conformation of boron atoms is changed from sp^2 to sp^3 structure and new chemical bonds may be formed on boron atoms by the long-term milling. XANES spectra in the N-K edge of the same samples, shown in Fig. 2, demonstrates that the local environment of nitrogen atoms is also changed by the mechanical milling. The spectral feature of the final stage of 160-h milling is similar to that of cubic BN or CNx compounds. Therefore, the conformation of nitrogen atoms is also changed from sp^2 to sp^3 structure by the long-term milling, and C-N bonds may be formed in the final stage.

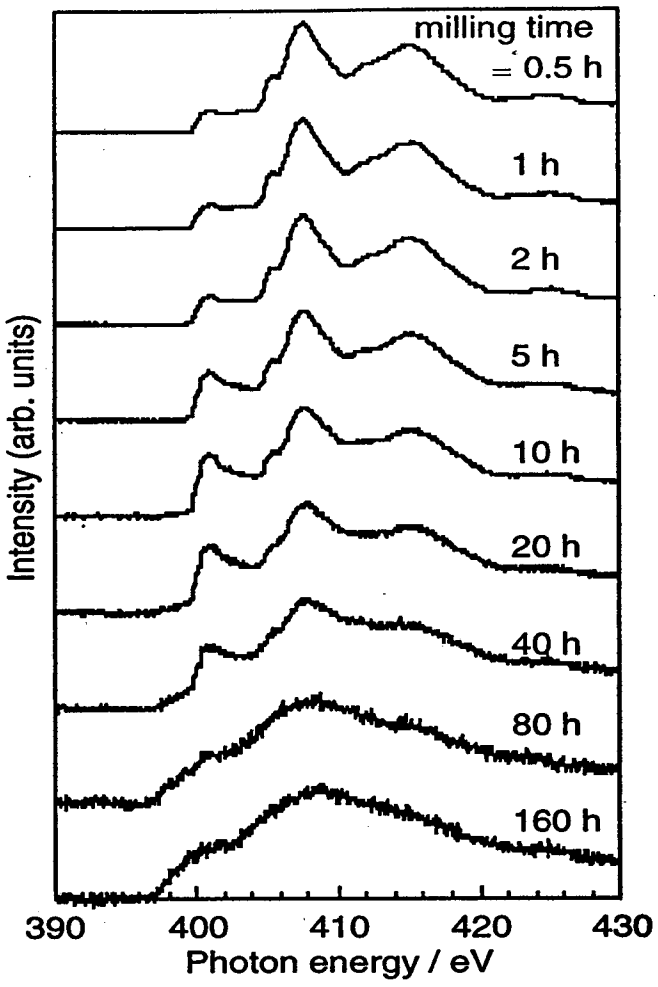

Fig. 2 N-K XANES spectra of mechanically milled mixture of h-BN and graphite. Milling time is from 0.5 h to 160h.

CONCLUSION

Mechanical milling reaction of *h*-BN with graphite consists of two steps. Amorphous BN and graphite nanoclusters are formed in the first step (up to 20-h milling). In the second step, the conformation of boron and nitrogen atoms can be changed from sp^2 into sp^3 structure, and chemical bonds among boron, carbon, and nitrogen atoms may be rearranged.

REFERENCES

1. T. Sasaki, New Diamond, **10**, 14 (1994).
2. S. Kashiwai, T. Kaneyoshi, H. Kohzuki, M. Motoyama, Advanced in X-ray Chemical Analysis Japan (in submission).
3. J. H. Underwood, E. M. Gullikson, M. Koike, P. J. Batson, P. E. Denham, K. D. Frank, R. E. Tackaberry, and W. F. Steele, Rev. Sci. Instr., **67**, 1 (1996). (CD-ROM only)
4. Y. Muramatsu, M. Oshima, J. Kawai, S. Takokoro, H. Adachi, A. Agui, S. Shin, H. Kato, H. Kohzuki, and M. Motoyama, Phys. Rev. Lett., **76**, 3846 (1996).
5. I. Jimenez, A. Jankowski, L. J. Terminello, J. A. Carlisle, D. G. J. Sutherland, G. L. Doll, J. V. Mantese, W. M. Tong, D. K. Shuh, F. J. Himpsel, Appl. Phys. Lett., **68**, 2816 (1996).

This work was supported by the Director, Office of Energy Research, Office of Basic Energy Sciences, Materials Science Division, of the U.S. Department of Energy under Contract No. DE-AC03-76F00098.

Principal investigator: Yasuji Muramatsu, The University of Tennessee (working at Advanced Light Source, Ernest Orlando Lawrence Berkeley National Laboratory), E-mail: ymuramatsu@lbl.gov or murama@ilab.ntt.co.jp

The Electronic Structure of Barium Strontium Titanate by Soft-X-Ray Absorption Spectroscopy

Y. Uehara,[1] J.H. Underwood,[2] E.M. Gullikson,[2] and R.C.C. Perera[3]

[1]Mitsubishi Electric Co., Amagasaki, Hyogo 661, Japan
[2]Center for X-ray Optics, Ernest Orlando Lawrence Berkeley National Laboratory, University of California, Berkeley, CA 94720, USA
[3]Advanced Light Source, Ernest Orlando Lawrence Berkeley National Laboratory, University of California, Berkeley, CA 94720, USA

ABSTRACT

Perovskite-type titanates, such as Strontium Titanate (STO), Barium Titanate (BTO), and Lead Titanate (PTO) have been widely studied because they show good electric and optical properties. In recent years, thin films of Barium Strontium Titanate (BST) have been paid much attention as dielectrics of dynamic random access memory (DRAM) capacitors [1]. BST is a better insulator with a higher dielectric constant than STO and can be controlled in a paraelectric phase with an appropriate ratio of Ba/Sr composition, however, few studies have been done on the electronic structure of the material. Studies of the electronic structure of such materials can be beneficial, both for fundamental physics research and for improving technological applications.

BTO is a famous ferroelectric material with a tetragonal structure, in which Ti and Ba atoms are slightly displaced from the lattice points. On the other hand, BST keeps a paraelectric phase, which means that the atoms are still at the cubic lattice points. It should be of great interest to see how this difference of the local structure around Ti atoms between BTO and BST effects the electronic structure of these two materials.

In this report, we present the Ti $L_{2,3}$ absorption spectra of STO, BTO, and BST measured with very high accuracy in energy of the absorption features.

EXPERIMENTAL

STO and BTO powders were commercially available ones with over 99.9% purity. BST powder was obtained from a commercially available sputtering target ceramic, which was purchased from Mitsubishi Materials Co. Ba/Sr molar ratio of the powder was analytically determined to be 1, and x-ray powder diffraction revealed that the material remains a cubic structure.

The x-ray absorption measurements were carried out on Beamline 6.3.2 at the Advanced Light Source (ALS), an entrance slitless bend magnet beamline equipped with a Hettrick-Underwood type varied line space (VLS) grating monochromator [2]. The energy resolution of the monochromated photons was set at E / DE = 3000 around the Ti L-edge energy region. The powder samples were spread onto an indium foil, and the absorption spectra presented in this work were obtained in step scanning the monochromator and measuring the total electron yield (photoelectron, Auger and secondary) from the sample (foil). The monochromator in BL6.3.2 was constructed and assembled in a manner that provides absolute energy measurements [2,3]. The photo-currents from the third mirror were monitored as the incident photon flux monitor.

RESULTS AND DISCUSSIONS

Figure 1 shows the x-ray absorption spectra around Ti $L_{2,3}$ edge of STO, BST, and BTO. The three spectra are quite similar to each other, and show four distinct peaks which correspond to the transition of Ti 2p3/2 - Ti 3d and Ti 2p1/2 - Ti 3d. Energy shifts of as much as 0.3 eV are observed between the peaks of STO and those of BTO, and the peaks of BST resemble the middle energy. From these results, it can be predicted that the distortion of TiO6 clusters due to the tetragonal crystal structure in BTO does not affect the fine structure of Ti 3d levels. However, the Ti - O bond length has some effects on the energy levels of those states. Besides those eminent peaks, two weak pre-edge peaks are observed on all three spectra. According to the band structure calculations [4], the lowest unoccupied molecular orbital (LUMO) is mainly formed by Ti 3d orbital in these materials. However, O 2p orbital, which is just few eV below the Ti 3d orbital, may perform as transition states for the excited Ti 2p electrons.

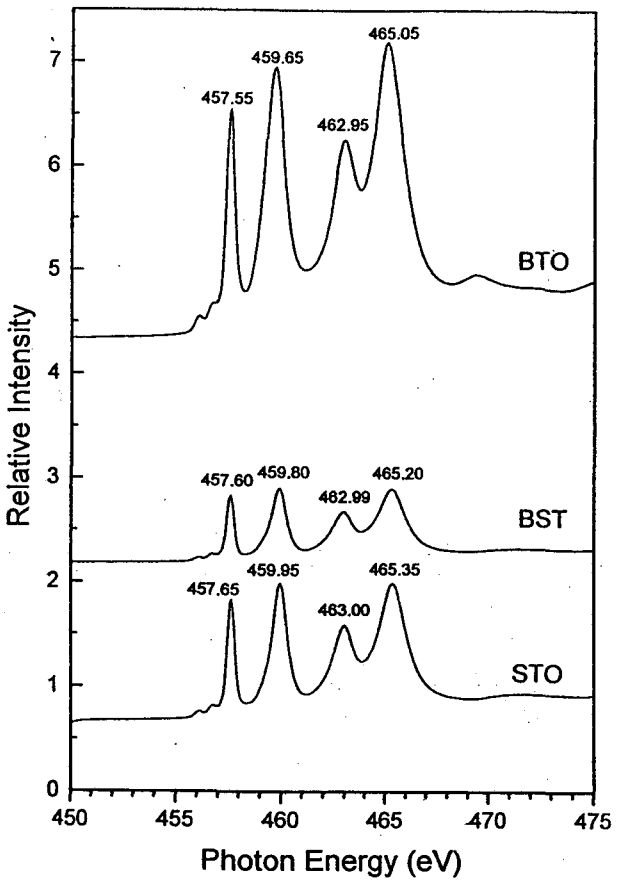

Figure 1. The Ti L-edge absorption spectra of SrTiO3 (STO), Ba0.5Sr0.5TiO3 (BST), and BaTiO3(BTO) powders. The peak energies are indicated on each peak.

REFERENCES

1. T. Horikawa, N. Mikami, T. Makita, J. Tanimura, M. Kataoka, K. Sato, M. Nunoshita:Jap. J. Appl. Phys. **32**, 4126 (1993)
2. J.H. Underwood, E.M. Gullikson, M. Koike, P.J. Batson, P.E. Denham, K.D. Franck, R.E. Tackaberry, W.F. Steele: Rev. Sci. Instrum. (in press).
3. J.J. Jia, J.H. Underwood, E.M. Gullikson, T.A. Callcott, R.C.C. Perera: J. Electron Spectrosc. and Relat. Phenom. **80**, 509 (1996)
4. T. Kamiya, T. Tanaka, T. Tsurimi, M. Daimon: Jap. J. Appl. Phys. **33**, 3965 (1994)

This work was supported by the Office of Basic Energy Science of the Department of Energy under contract No. DE-AC03-76SF00098

Principal investigator: Y. Uehara, Mitsubishi Electric Co., Amagasaki, Hyogo 661, Japan. Email: uehara@ana.edl.melco.co.jp. Fax: +81-6/497-7602.

Inner-Shell Excitation and Ionic Fragmentation of Molecules

A.P. Hitchcock[1], T. Tyliszczak[1], R.G. Cavell[2], N. Kosugi[3] and J.D. Bozek[4]

1. Dept. of Chemistry, McMaster University, Hamilton, ON L8S 4M1, Canada
2. Dept. of Chemistry, University of Alberta, Edmonton, AB T6G 2G2, Canada
3. Institute for Molecular Science, Okazaki, 444 Japan
4. Advanced Light Source, Lawrence Berkeley Lab, Berkeley, CA 94720

INTRODUCTION

Inner-shell excitation and associated decay spectroscopies are site specific probes of electronic and geometrical structure and photoionization dynamics. X-ray absorption probes the geometric and electronic structure, while time-of-flight mass spectrometry with multi-coincidence detection provides information on the photofragmentation dynamics of the initially produced inner-shell state. Auger decay of inner-shell excited and ionised states is an efficient source of multiply charged ions. The charge separation and fragmentation of these species, studied by photoelectron-photoion-photoion coincidence (also called charge separation mass spectrometry [1]) gives insights into bonding and electronic structure. In molecules, the dependence of the fragmentation process on the X-ray energy can reveal cases of site and/or state selective fragmentation. At the ALS we have examined the soft X-ray spectroscopy and ionic fragmentation of a number of molecules, including carboranes, silylenes, phosphorus halides, SF_6 and CO_2. Our work is illustrated using results from the carborane [2,3] and PF_3 [4,5] studies.

EXPERIMENT

Experiments were carried out at ALS beamlines 9.0.1 and 6.3.2. Total yield spectra were recorded using a biased channeltron (for e^-) placed close to the intersection of the X-ray beam with an effusive gas jet, or the channelplate at the end of the time-of-flight drift tube (for i^+). Mass spectra were recorded using either pulse extraction, which provides more quantitative yields, or photoelectron coincidence, which is better for investigating charge separation mechanisms. Because of relatively limited extraction fields there is significant kinetic energy discrimination in the ion and electron detectors such that lower kinetic energy species are emphasised. The time correlation among cation signals from a single core excitation event are detected using a custom-built multistop time-to-digital converter.

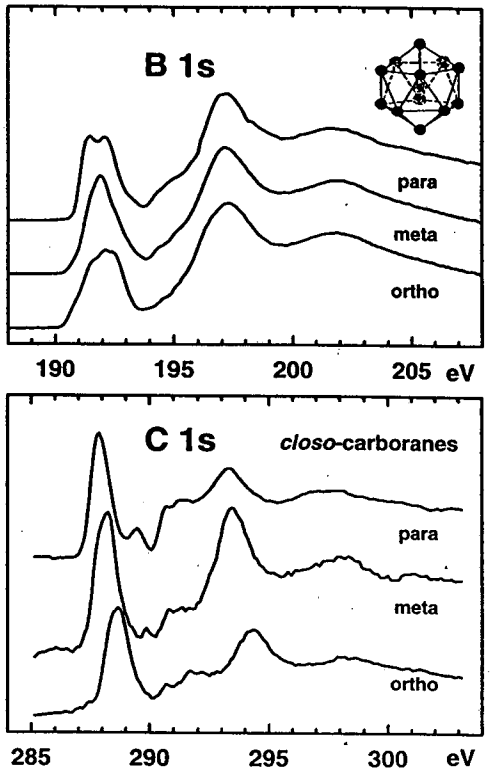

Figure 1. Total ion yield spectra of ortho-, meta- and para-carborane in the B 1s and C 1s regions.

RESULTS

A. Carboranes

The spectroscopy and ionic fragmentation of three isomeric carborane cluster compounds was measured. *closo*-1,2-orthocarborane is being used as a source compound for chemical vapour deposition (CVD) of boron carbide thin film semiconductors [6]. Understanding the electronic excitations and the preferred fragmentation pathways of this species and its meta and para isomers could help in understanding electron- and photon-induced decomposition at the molecular level. The B 1s and C 1s spectra of ortho-, meta-, and para-carborane are compared in Fig. 1. Although the overall shape appears isomerically independent, there are differences in the fine structure of the lowest energy discrete excitations. These differences have been explained by detailed comparison to *ab initio* GSCF3 calculations [2].

Sample PEPICO (electron-start time-of-flight mass spectra), PIPICO (ion auto-correlation), and PEPIPICO (multi-stop PEPICO) mass spectra of meta-carborane are given in Fig. 2. Spectra of this quality, collected at closely spaced energies in the C 1s and B 1s regions were used to generate partial ion and ion pair yields for all three species [3]. Core hole decay leads to extensive ionic fragmentation, including large amounts of multiple ionisation, almost all of which ends up as ion pairs. PIPICO (ion-ion autocorrelation) spectra of large molecules are very complex because of superposition of many ion pair signals. The PEPIPICO t_1/t_2 plot is very effective in separating these overlapping signals. Each peak in this plot is easily identified by the flight times of each ion involved.

The relatively strong signals of Y_3^+ and Y_6^+ (where Y indicates a cluster vertex, either a CH or a BH species) in the PEPICO mass spectrum can be rationalised by a greater stability of planar trigonal and octahedral structures which arise by rearrangement of the ions initially formed. Overall there is little difference among the B 1s or C 1s partial yields of the isomeric species and relatively little change in individual ion or ion pair yields aside from a major step up

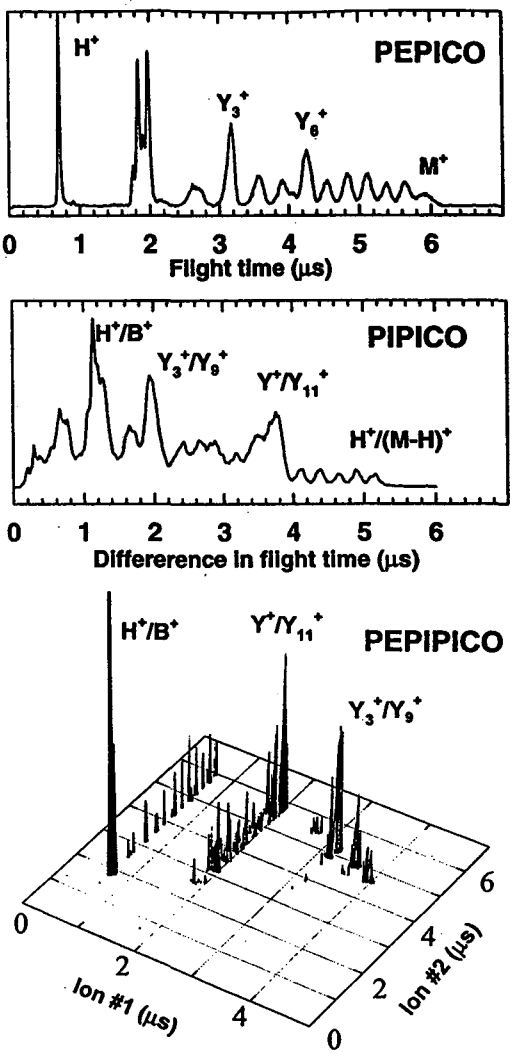

Figure 2 PEPICO, PIPICO and PEPIPICO signals of B 1s ionised meta-carborane recorded at 192 eV. The peak of the H^+/B^+ signal is off-scale by 30%.

or step down in specific channels at the onsets of B 1s core excitation and ionization. Thus any selectivity among these three species which may exist with regard to properties of boron carbide films prepared by X-ray assisted CVD [6] is likely to be associated with specificity of the chemistry of fragments rather than selectivity in the initial excitation.

B. P 2p Excited PF_3

The 2p (L_{23}) excitation spectra of third row elements and their compounds are generally characterized by the presence of two closely related manifolds of excited states, associated with the $2p_{3/2}$ (L_3) and $2p_{1/2}$ (L_2) spin-orbit coupled ion core. The spin-orbit splitting varies little among compounds of a given element. However PF_3 has an unusual P 2p spectrum in that it has a sharp line at 136.5 eV without an obvious spin-orbit partner state, although a very weak feature at 135.6 eV has been proposed as the $2p_{3/2}$ spin-orbit partner state [7]. In our study of P 2p excitation and ionic fragmentation of phosphorus compounds at the ALS we observed an unusual signature in the PF_3^+ parent ion yield (see Fig. 3), namely only a single line at 136.5 eV, with negligible intensity at 135.6 eV. This has lead to a significant clarification of the assignment of the P 2p spectrum of PF_3 and the identification of a general inner shell spectroscopic phenomenon which has previously been overlooked [4].

A complete description of P 2p excitation requires an intermediate coupling treatment with both spin-orbit interaction and electron-electron repulsion. One can interpret P 2p spectra through limiting approximations: (a) LS coupling in which spin-orbit coupling is ignored. Here core-valence exchange interaction gives rise to a singlet-triplet (S-T) splitting; (b) (jj) coupling in which the P 2p spin-orbit (S-O) splitting is assumed to be constant in all P 2p excited states (characteristic of the ion core) and core-valence exchange is ignored. These two limits must connect smoothly through the regime of intermediate coupling. Using scheme (a), if the S-T separation for a given state is small compared to the S-O splitting, transitions to this state will appear in both the "$2p_{3/2}$" and "$2p_{1/2}$" manifolds. In contrast, if the S-T splitting greatly exceeds the S-O splitting only one transition might be observed and the LS description should be more appropriate. Non-relativistic *ab initio* calculations of PF_3 were carried out using

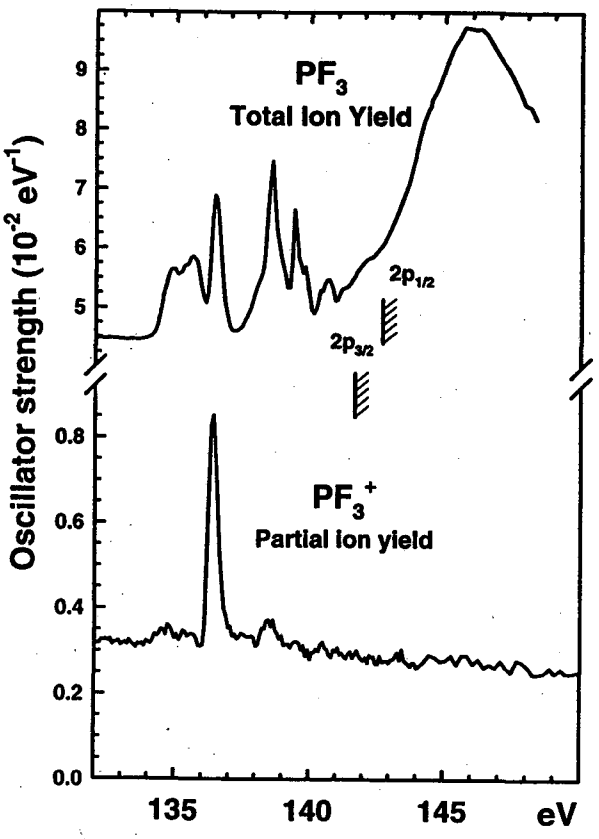

Figure 3. Comparison of the partial yield of PF_3^+ to the total ion yield spectrum of PF_3.

the GSCF3 code. These results indicate that the $(e^{-1},e)\ ^1A_1$ and $(e^{-1},e)\ ^3A_1$ P 2p excited states are separated by 2.38 eV. Since this is almost three times larger than the P 2p S-O splitting (0.9 eV), the appropriate description for this particular state must be one much closer to LS than (jj) coupling. Thus, to a good first approximation, one expects only one, not two transitions, as observed (excitation from the $^1A_1$ ground state to the $^3A_1$ P 2p excited state is spin forbidden). Alternatively one might describe the phenomenon in terms of a very large core-valence exchange interaction in the $(e^{-1}e^1)\ ^1A_1$ state such that the S-O intensity ratio is totally skewed in favor of the $2p_{1/2}$ component. The two descriptions are closely related. The existence of only one strong resonance at 136.5 eV in the PF_3^+ yield is strong support of this interpretation. A complete discussion of the time-of-flight mass spectra, partial ion yield signals, and PEPIPICO of PF_3 in the P 2p region will be presented elsewhere, in comparison to results for PCl_3 and CF_3PCl_2 [5]. Similar, single-peak P 2p excited states have been identified in PCl_3 and CF_3PCl_2 [5], and corresponding S 2p states have been identified in the S 2p spectrum of SF_6 [8].

ACKNOWLEDGEMENTS

Adam Hitchcock thanks the Advanced Light Source, AFRD, and LBNL, for their generous hospitality and financial support during a research leave in 94-95. We thank the ALS staff for their excellent operation of the facility. Special thanks are given to David Kilcoyne who designed and helped develop the time-of-flight photoionization mass spectrometer, and to Peter Dowben who motivated the carborane project and provided samples.

REFERENCES

1. J.H.D Eland, *Acc. Chem. Res.* **22**, 381 (1989).
2. Hitchcock et al, *J. Phys. Chem.* (1997) in press.
3. A.P. Hitchcock et al, *J. Phys. Chem.* in preparation
4. N. Kosugi, R.G. Cavell and A.P. Hitchcock, *Chem. Phys. Lett.* (1997) in press.
5. A.P. Hitchcock et al, *Chem. Phys.* in preparation
6. S. Lee, J. Mazurowski, G. Ramseyer, and P.A. Dowben, *J. Appl. Phys.* **72**, 4925 (1992).
7. R.N.S. Sodhi and C.E. Brion, *J. Electron Spectrosc.* **37**, 97 (1985).
8. J.T. Francis et al, *Phys. Rev. A* **52**, 4665 (1995).

This research was supported financially by NSERC (Canada), and NATO. The ALS is supported by the Director, Office of Energy Research, Office of Basic Energy Sciences, Materials Sciences Division, of the U.S. Department of Energy, under contract No. DE-AC03-76SF00098,

Principal Investigator: Adam P. Hitchcock, Dept. of Chemistry, McMaster University, Hamilton, ON L8S 4M1, Canada. Tel: (905) 525-9140 ext 24749; FAX (905) 521-2773; email: aph@mcmaster.ca

The K-Shell Auger Decay of Atomic Oxygen

W.C. Stolte[1], Y. Lu[1], J.A.R. Samson[1], O. Hemmers[2], D. Hansen[2], P. Glans[2], S.B. Whitfield[2], H. Wang[2], D.W. Lindle[2]

[1]Behlen Laboratory of Physics, University of Nebraska, Lincoln, Nebraska 68588-0111
[2]Department of Chemistry, University of Nevada, Las Vegas, Nevada 89154-4003

The aim of the present research is to understand the interaction between the ejected photoelectron and Auger electron produced by the Auger decay of a 1s hole in atomic oxygen, and to understand the influence this interaction has on the shape of the ionization cross sections. To accomplish this we have measured the relative ion yields (ions/photon) in the vicinity of the oxygen K-shell (525 - 553 eV) for O^+ and O^{2+} (Fig. 1). The measurements were performed at the ALS on beamline, 6.3.2.

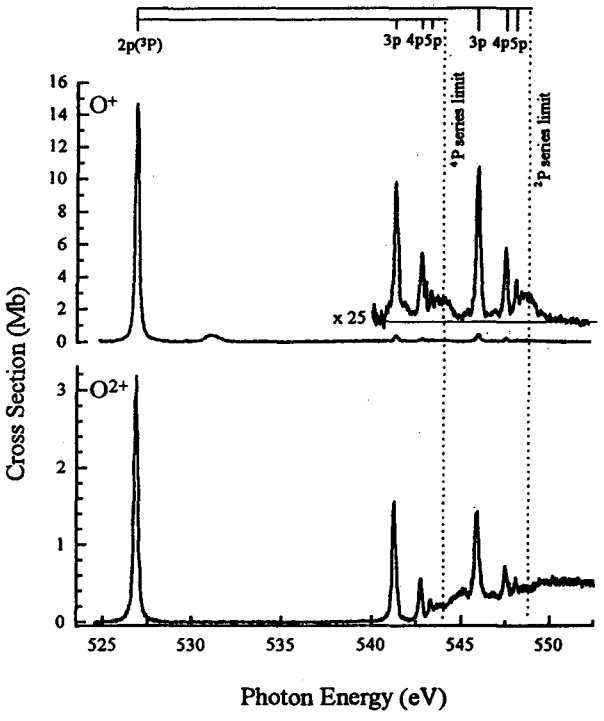

Fig. 1 Photoionization cross sections of O^+ and O^{2+} produced by the decay of a 1s hole in atomic oxygen. The resonance lines represent the transitions $1s^12s^22p^5(^3P)$, $1s^12s^22p^4(^4P)np$, and $1s^12s^22p^4(^2P)np$ with n=3-6.

The atomic oxygen was produced by passing molecular oxygen through a microwave-driven discharge. The apparatus used in the present study has been previously discussed in detail [1]. The major difference in the experimental setup was the use of a mixture of 20% molecular nitrogen and 80% molecular oxygen passing through the glass flow assembly (Fig. 2). The flow assembly consisted of a short quartz tube, coated with phosphorous pentoxide (P_2O_{10}), in which the microwave-driven discharge takes place, and a long "T" shaped, Teflon coated, Pyrex tube, which transports the atoms to the interaction region. An increase of 30% in the amount of atomic oxygen transported to the interaction region was seen when using the coated flow tubes instead of clean flow tubes. An additional Pyrex tube with a 1.5 mm orifice on one end was used to separate the high pressure discharge region from the low pressure photoionization interaction region. With the microwave-driven discharge on, a 180° electromagnetic mass analyzer, with a resolution of 1 mass in 50, was used to identify the various degrees of ionization produced. Data were taken in 5 to 20 meV steps. The photon energy scale was calibrated with respect to the O K-edge resonance features in molecular oxygen near 541 eV [2], and verified by a scan over the Ar resonance lines near the $L_{2,3}$-edge [3], which showed an error of 34 meV. A time-of-flight mass spectrometer

was used in conjunction with the microwave discharge system to determine the branching ratios between O^+ and O^{2+} at the $1s^12s^22p^5(^3P)$ resonance, 526.79 eV.

A Rydberg analysis of the two series leading to the $[1s]2s^22p^4(^4P)$ and $[1s]2s^22p^4(^2P)$ limits were obtained. This analysis shows some differences to the recently published results by Menzel *et al.* [4]. The energy position of the main $1s^12s^22p^5(^3P)$ resonance differs by approximately 1 eV from our value, all members of the $(^2P)np$ series differ by 0.3 eV, but the members of the $(^4P)np$ series agree with ours. The molecular resonance at 530.5 eV and those between 539 eV and 543 eV, measured with the microwave discharge off show identical results in both experiments.

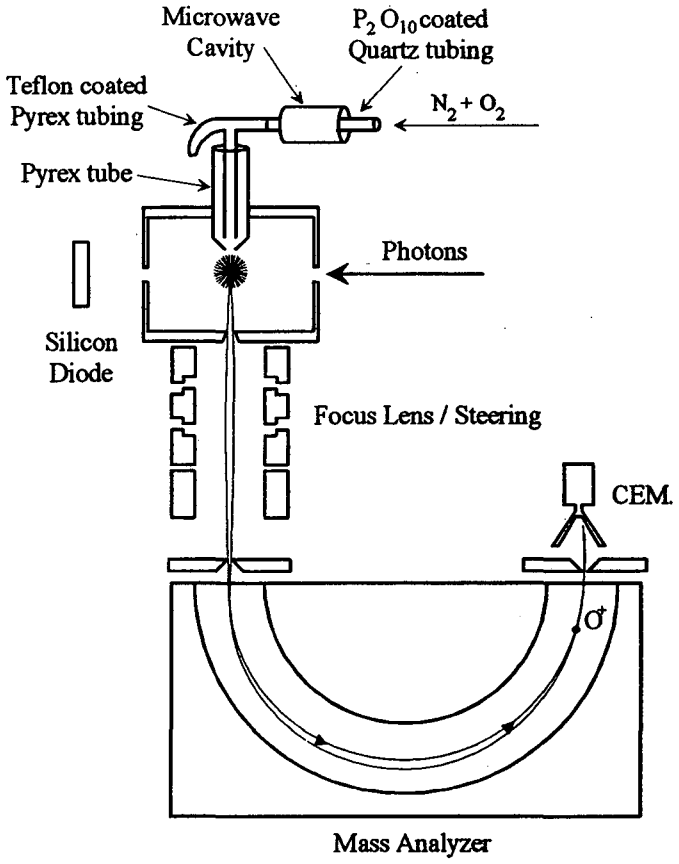

Fig. 2 Schematic diagram of the apparatus

REFERENCES

1. G.C. Angel and J.A.R. Samson, Phys. Rev. A **38**, 5578 (1988).
2. A. Yagishita, E. Shigemasa, and N. Kosugi, Phys. Rev. Lett. **72**, 3961 (1994).
3. G.C. King and F.H. Read, *Physics of Atom and Molecules*, edited by B. Crasemann (Plenum Press, New York, 1985) p. 317.
4. A. Menzel, S. Benzaid, M.O. Krause, C.D. Caldwell, U. Hergenhahn, and M. Bissen, Phys. Rev. A **54**, R991 (1996).

This research was supported by NASA under Grant No. NAGW-1751

Principle investigator: James A.R. Samson, University of Nebraska, Lincoln. Email: jsamson@unlinfo.unl.edu
Telephone: 402-472-2791

Photoemission Studies of Semiconductor Nanocrystals

K.S. Hamad, R. Roth, A.P. Alivisatos

Department of Chemistry, University of California at Berkeley, Berkeley, California 94720, USA
The Molecular Design Institute, Materials Science Division, Ernest Orlando Lawrence Berkeley National Laboratory, University of California, Berkeley, California, 94720, USA

INTRODUCTION

Semiconductor nanocrystals have been the focus of much attention in the last ten years due predominantly to their size dependent optical properties. Namely, the band gap of nanocrystals exhibits a shift to higher energy with decreasing size due to quantum confinement effects. Figure 1 shows this shift of the onset of absorption of CdSe nanocrystals. Research in this field has employed primarily optical techniques to study nanocrystals, and in this respect this system has been investigated extensively. In addition, we are able to synthesize monodisperse, crystalline particles of CdS, CdSe, Si, InP, InAs, as well as CdS/HgS/CdS and CdSe/CdS composites. However, optical spectroscopies have proven ambiguous in determining the degree to which electronic excitations are interior or surface admixtures or giving a complete picture of the density of states. Photoemission is a useful technique for understanding the electronic structure of nanocrystals and the effects of quantum confinement, chemical environments of the nanocrystals, and surface coverages. Of particular interest to us is the surface composition and structure of these particles, for we have found that much of the behavior of nanocrystals is governed by their surface [1,2]. Previously, we had performed x-ray photoelectron spectroscopy (XPS) on CdSe nanocrystals [3,4]. XPS has proven to be a powerful tool in that it allows one to determine the composition of the nanocrystal surface. Specifically, we were able to investigate the coverages of capping groups on the surface of the nanocrystals, effects of oxidation, and the

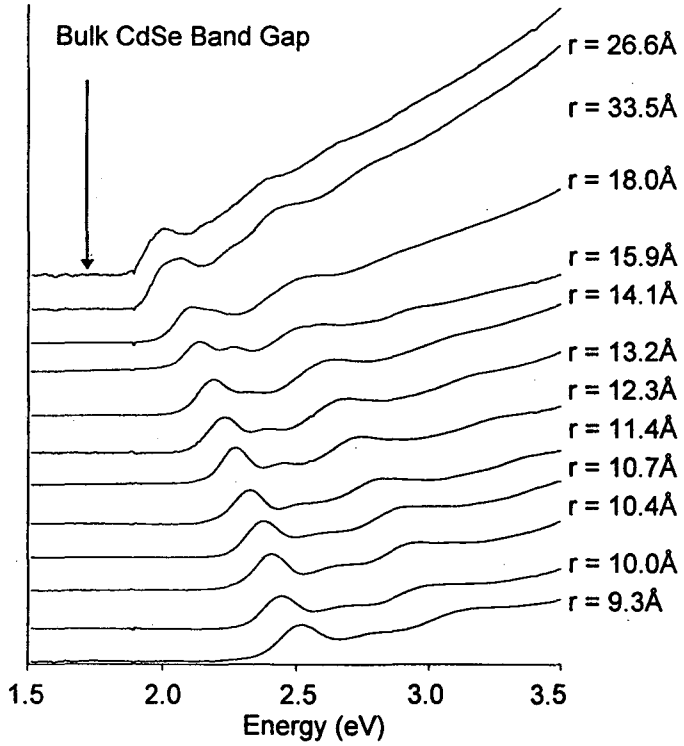

Figure 1: Optical absorption spectra of several sizes of CdSe nanocrystals.

influence of varying chemical environments by examining core level peaks and their chemical shifts.

Currently, we are employing photoemission to a further extent in order to study size effects on core level lineshape and valence band density of states. Much of this work is currently in progress both on-line as well as off-line.

EXPERIMENTAL

Recently, photoemission studies of semiconductor nanocrystals was made possible by the implementation of a novel synthetic technique [5]. Hexanedithiol chains are used as organic linkers between the nanocrystals and a metal substrate. First, these organic chains are allowed to self-assemble onto a gold layer. The samples are then placed into a nanocrystal solution which is stirred for a long period of time, allowing the crystallites to attach themselves to the exposed end of the organic chain. These organic layers make an electrical contact to nanocrystals because they provide a short pathway of approximately 10Å in length through which electrons can tunnel from a conducting substrate. Since in this form the nanocrystals do not charge, the samples are suitable for electronic spectroscopies such as photoemission.

For both studies, the photoemission experiment was performed in a ESCA chamber with a base pressure of 5×10^{-10} torr. The radiation source was either a conventional Mg anode (Kα) or synchrotron radiation from beamline 6.3.2 (bend magnet) in the range of 50-500eV. Photoelectrons were detected in a hemispherical electron energy analyzer which had a resolution of 25 meV. Ultimate resolution was determined by the radiation source, which was 695 meV for the Mg anode and ~100meV for the synchrotron beam.

INVESTIGATIONS OF CORE LINEWIDTHS AND BINDING ENERGY VERSUS SIZE

By examining the linewidths of peaks in the photoelectron spectrum, we would obtain information on the intrinsic lifetimes of charge carriers in nanocrystals. The excited photoelectron state can decay in several ways, radiatively by x-ray emission or nonradiatively by Auger or other processes. Furthermore, we speculate that these lifetimes are strongly influenced by the size of the particle: a hole created in the photoelectron process can be quenched more rapidly in larger particles due to increased interatomic electronic relaxation, or screening. We have the means to alter the size of our particles systematically, therefore we can study the hole lifetime as a function of nanocrystal size. Previously, we were unable to analyze linewidths of photoelectron peaks because the resolution of an ESCA system is limited largely by its x-ray source. Standard x-ray anodes (Mg, Al) have a resolution of approximately 750 meV, while it is estimated that intrinsic linewidths of peaks are comparable or less. Consequently, these sources are not suitable for examining lifetimes and a higher resolution light source is necessary. We can synthesize CdSe and InAs particles from 20Å to 60Å in diameter, with a size distribution as narrow as 1.5Å. Therefore, these particles are most suitable for examining the widths of the Cd and Se 3d cores of CdSe or the In 3d and As 2p cores of InAs.

The hole screening also has an effect on the core level energy. Studies on gas phase Ar clusters by Möller and co-workers show that this size-dependent hole screening shifts the binding energy of the Ar 2p level to higher energies with decreasing cluster size [6]. We have been working towards observing such an effect in our nanocrystals.

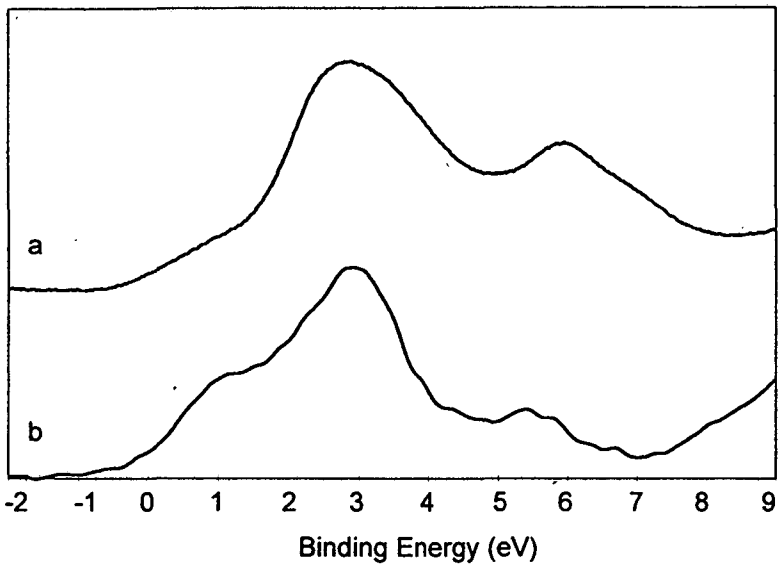

Figure 2. a.) Valence band spectrum obtained from CdSe nanocrystals on dithiol / Au substrate. b.) Spectrum obtained by subtracting dithiol / Au background.

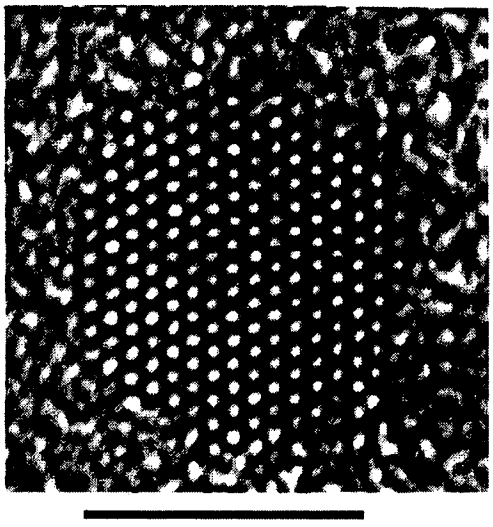

Figure 3. High Resolution TEM of CdSe nanocrystal. The bar indicates a length of 50Å.

INVESTIGATION OF VALENCE BANDS VERSUS SIZE

We are also utilizing x-ray and ultraviolet photoemission experiments to study the valence band as a function of size of the particle [7]. As the size of the nanocrystal is decreased, the valence band shifts to higher binding energy. We are interested in obtaining the density of states (DOS) in both the valence and conduction bands and seeing how they evolve as a function of the size of the nanocrystal. Optical spectroscopy is limited to examining only the gap between the valence and conduction bands within constrictions of selection rules. Photoelectron spectroscopy, however, enables one to obtain a picture of the entire valence band. In our experiments on the beam as well as off-line, we have determined a method to obtain the valence DOS of CdSe and InAs nanocrystals without the DOS from the substrate (the hexanedithiol on Au). Figure 2a shows a valence band taken of CdSe nanocrystals on a hexanedithiol substrate. The spectra in 2b is obtained by subtracting the hexanedithiol on Au background, therefore it is characteristic of the CdSe nanocrystal only. We have repeated this experiment on other substrates (for example, indium tin oxide, ITO) to confirm that this spectrum is of the nanocrystals. Thus far we have been able to do so using a conventional x-ray source, which has a resolution that obscures any size effects of the nanocrystals. We are interested in how the valence DOS evolves with the size of the particle, and seeing if it exhibits predicted 0-D behavior. If it were possible to isolate the surface DOS [8] it would be interesting to watch its evolution with size of the nanocrystal. For example, does the surface DOS reflect the approximate surface to volume ratios for a given size quantum dot? Where does it lie in energy relative to the band gap? As aforementioned, we have the chemical ability to alter the surface of the particle and thus look at which states in the valence band are affected. Another interesting property that can be obtained by UPS is the way the valence energy levels of the nanocrystal line up with the substrate Fermi level [9]. What is the offset between the Au Fermi level and the top of the valence band in CdSe? Is there band bending? These questions are necessary for the understanding of transport in these systems, and currently we are working in collaboration with the McEuen group to understand the behavior of this system [10].

ORIENTED CRYSTALLITES AND PHOTOELECTRON DIFFRACTION

Current work is underway to orient a monolayer of nanocrystals on a plane. Many [11, 12, 13] have devised novel methods to align particles on substrates such that their optical axes are oriented in a single direction relative to the plane. The nanocrystals on our self assembled monolayer samples are randomly oriented, thus their photoelectron spectra represent an averaging over a random distribution. With aligned particles we would have the potential to perform another order of photoemission experiments that would resolve the question of the nanocrystal's surface. Photoelectron diffraction (XPD) would allow us to determine the both the atomic positions (by scanning in angle) and bond lengths (by scanning in energy) of the surface atoms. Thus it would give us the most complete picture of the surface. Figure 3 shows a high resolution transmission electron micrograph of a CdSe nanocrystal. From the image, we can see the interior lattice structure, which we have determined to be identical to that of bulk CdSe. However, the image tells us nothing about the surface structure, since essentially it is a two-dimensional projection of a nanocrystal. Although we can predict beforehand what surfaces will be more stable than others, we do not know exactly what the surface looks like.

ACKNOWLEDGMENTS

This work was supported by the NSF, grant no. DMR-9505302.

REFERENCES

1. W. Hoheisel, V.L. Colvin, C.S. Johnson, A.P. Alivisatos, J. Chem. Phys. **101**, 8455 (1994).
2. N.A. Hill, K.B. Whaley, J. Chem. Phys. **99**, 3707 (1993).
3. J.E. Bowen Katari, V.L. Colvin, A.P. Alivisatos, J. Phys. Chem. **98**, 4109 (1994).
4. A.A. Guzelian, et al., J. Phys. Chem **100**, 7212 (1996).
5. V.L. Colvin, A.N. Goldstein, A.P. Alivisatos. J. Am. Chem. Soc. **114**, 5221 (1992).
6. O. Björneholm, F. Federmann, F. Fössing, T. Möller, P. Stampfli, J. Chem. Phys, 104, 1846 (1996).
7. V.L. Colvin, A.P. Alivisatos, J.G. Tobin. Phys. Rev. Lett. **66**, 2786 (1991).
8. S.B. DiCenzo, P.H. Citrin, E.H. Hartford, G.K. Wertheim. Phys. Rev. B. **34**, 1343 (1986).
9. S. Narioka, et al. Appl. Phys. Lett. **67**, 1899 (1995).
10. D.L. Klein, P.L. McEuen, J.E. Bowen Katari, R. Roth, A.P. Alivisatos, Appl. Phys. Lett. **68**, 2574 (1996).
11. Y. Golan, L. Margulis, I. Rubinstein, G. Hodes, Langmuir **8**, 749 (1992).
12. X.K. Zhao, J. Yang, L.P. McCormick, J.H. Fendler, J. Phys. Chem. **96**, 9933 (1992).
13. C.B. Murray, C.R. Kagan, M.G. Bawendi, Science **270**, 1335 (1995).

Principal investigator: A.P. Alivisatos, Material Sciences Division, Ernest Orlando Lawrence Berkeley National Laboratory. Email: alivis@uclink4.berkeley.edu. Telephone: 510-643-7371.

Postcollision Interactions in the Auger Decay of the Ar L-Shell

J.A.R. Samson,[1] W.C. Stolte,[1] Z.X. He,[1] J.N. Cutler,[1] and D. Hansen[2]
[1]Behlen Laboratory of Physics, University of Nebraska, Lincoln, NE 68588-0111, USA
[2]Department of Chemistry, University of Nevada, Las Vegas, NV 89154, USA

The photoionization cross sections for Ar^+ through Ar^{4+}, produced by the Auger decay of an inner shell 2p hole, have been measured between 242 eV and 253 eV on beamline 9.0.1 and 6.3.2 (see Fig. 1). In this study we are interested in near threshold phenomenon involving postcollision interactions (PCI), which are related to the Auger decay of a vacancy in the Ar L-shell.

During an Auger decay a postcollision interaction can occur causing the out-going photoelectron to be retarded thus losing a certain amount of energy. If the retardation is sufficiently large the photoelectron will not escape. This result produces a singly charged ion, which normally would not be present.

Such evidence of electron capture by the PCI effect was first shown clearly by Eberhardt *et al.* [1] and, with higher resolution, in the present work (see Fig. 2). However, capture of the photoelectron is expected to be 100% exactly at the $L_{2,3}$ thresholds [2]. Thus, from our results shown in Fig. 3 we would have expected the Ar^{2+} signal to be zero at threshold, but it is not! We can explain this anomoly on the basis that during the Auger decay the photoelectrons are captured into high lying excited states of Ar^+, which subsequently decay through autoionization yielding Ar^{2+}. Our predicted results for Ar^{2+} produced in this manner are shown in Fig. 3 by the shaded areas. Future work in this area will seek experimental evidence to verify this prediction.

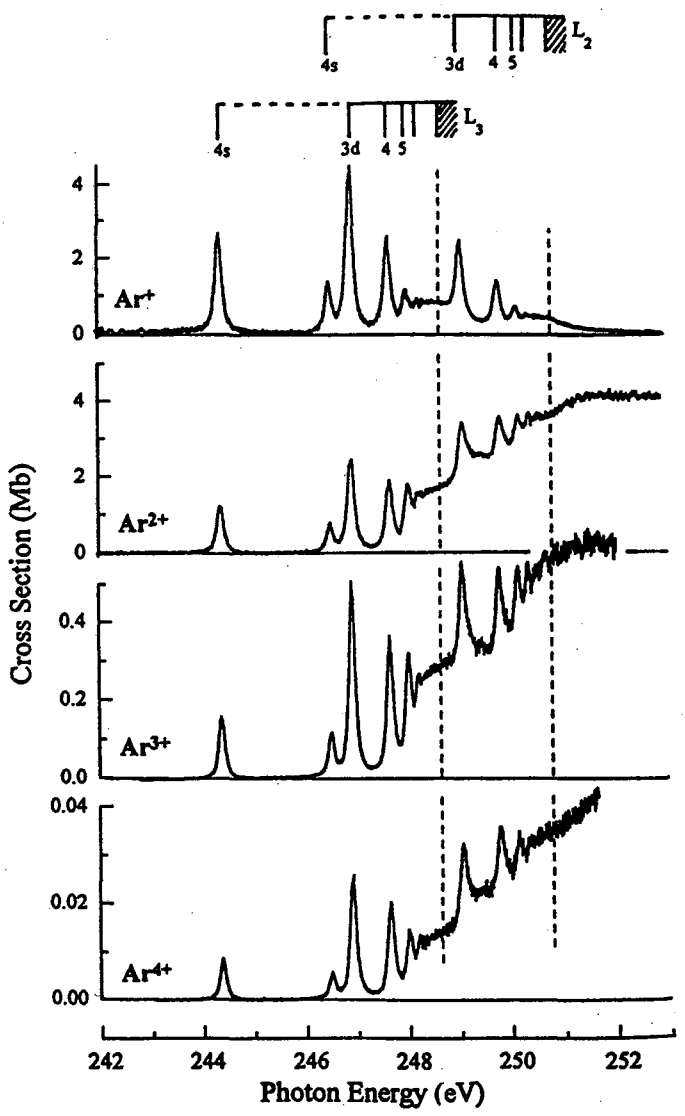

Figure 1. Photoionization cross sections of Ar^+ through Ar^{4+} produced by the decay of a $2p$ hole in argon. The resonance lines represent the transitions $2p^{-1}(3s^23p^6)nd$, $(n+1)s$, where $n \geq 3$. The instrumental resolution was 80 meV for the Ar^+ and Ar^{2+} spectra and 54 meV for Ar^{3+} and Ar^{4+}.

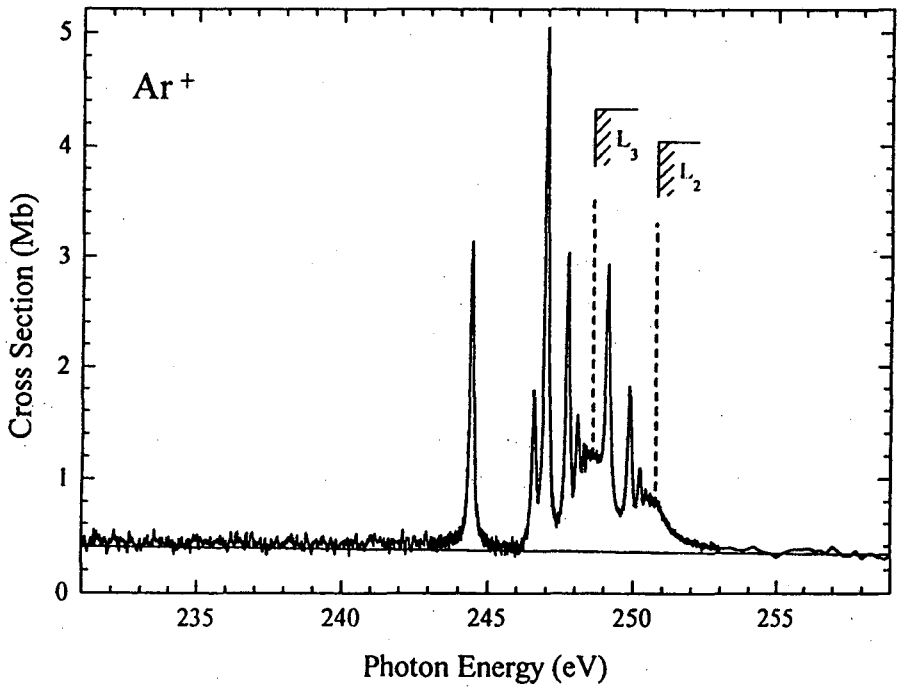

Figure 2. Photionization cross section for producing Ar^+ by ejection of a $2p$ electron. The slowly decreasing background continuum is caused by photoionization of a valence shell electron.

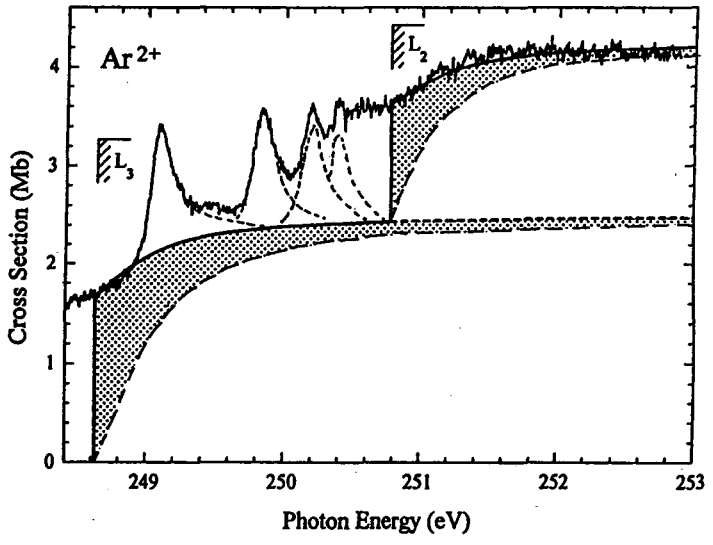

Figure 3. The Ar^{2+} continuum. The predicted Ar^{2+} yield is given by the probability function $(1 - P)$. If electron recapture is 100% at the $L_{2,3}$ thresholds ($P = 1$), then the Ar^{2+} yield is represented by the unshaded area under the dashed line. The disagreement with the experiment implies that at threshold 67% of the recaptured electrons must be emitted. That is, the Ar^{2+} yield must be represented by the curve $(1 - P)$ with $P = 0.33$ at threshold. This curve is shown by the solid line. The shaded area represents the contribution to Ar^{2+} by electron reemission.

REFERENCES

1. W. Eberhardt, S. Bernstorff, H.W. Jochims, S.B. Whitfield, and B. Crasemann, Phys. Rev. A **38**, 3808 (1988).
2. J.A.R. Samson, W.C. Stolte, Z.X. He, J.N. Cutler, and D. Hansen, Phys. Rev. A **54**, 2099 (1996).

This work was supported by the National Science Foundation under Grant No. PHY-9410716.

Principal investigator: James A.R. Samson, Behlen Laboratory of Physics, University of Nebraska. Email: jsamson@unlinfo.unl.edu. Telephone: 402-472-2791.

The Ratio of He^{2+}/He^{+} from 80 to 800 eV

J.A.R. Samson, W.C. Stolte, Z.X. He, J.N. Cutler, and Y. Lu
Behlen Laboratory of Physics, University of Nebraska, Lincoln, NE 68588-0111, USA

The importance of studying the double ionization of He by single photons lies in the fact that He presents the simplest structure for the study of electron correlation processes. Even so it has proved a challenging problem to understand and describe theoretically. Surprisingly, it has also proved difficult to agree experimentally on the absolute values of the He^{2+}/He^{+} ratios [1-7]. The availability of new synchrotron facilities with high intensity light outputs have increased the experimental activity in this area. However, by the very nature of those continuum sources systematic errors occur due to the presence of higher order spectra and great care must be exercised.

We have measured the He^{2+}/He^{+} ratios over a period of 5 years, the last three at the ALS utilizing beamlines 9.0.1 and 6.3.2. The sources of systematic errors that we have considered include, scattered light, higher order spectra, detector sensitivity to differently charged ions, discriminator levels in the counting equipment, gas purity, and stray electrons from filters and metal supports. The measurements have been made at three different synchrotron facilities with different types of monochromators and their potential for different sources of systematic errors. However, our data from all these different measurements agree within a few percent of each other, as can be seen in Fig. 1.

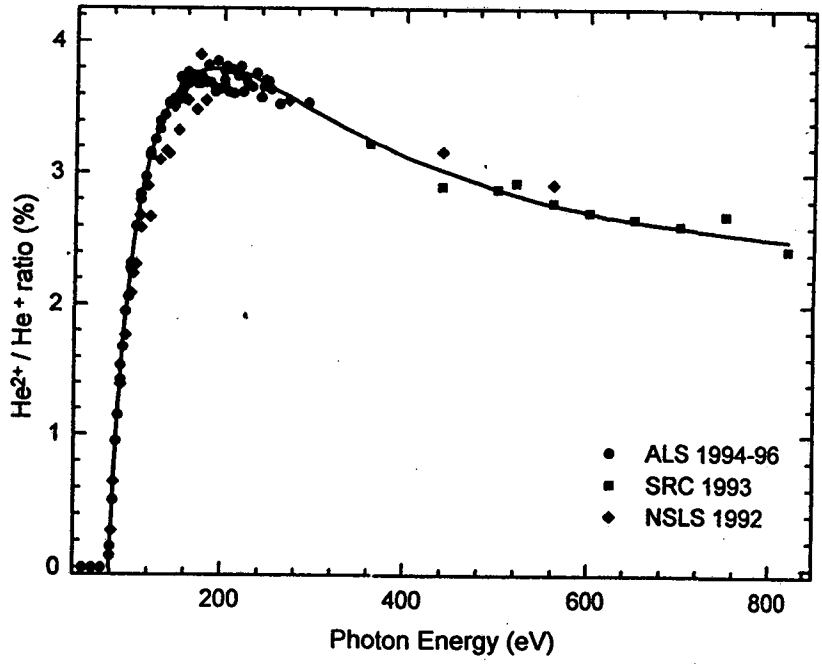

Figure 1. Measurements of the He^{2+}/He^{+} ratio taken at various synchrotron facilities.

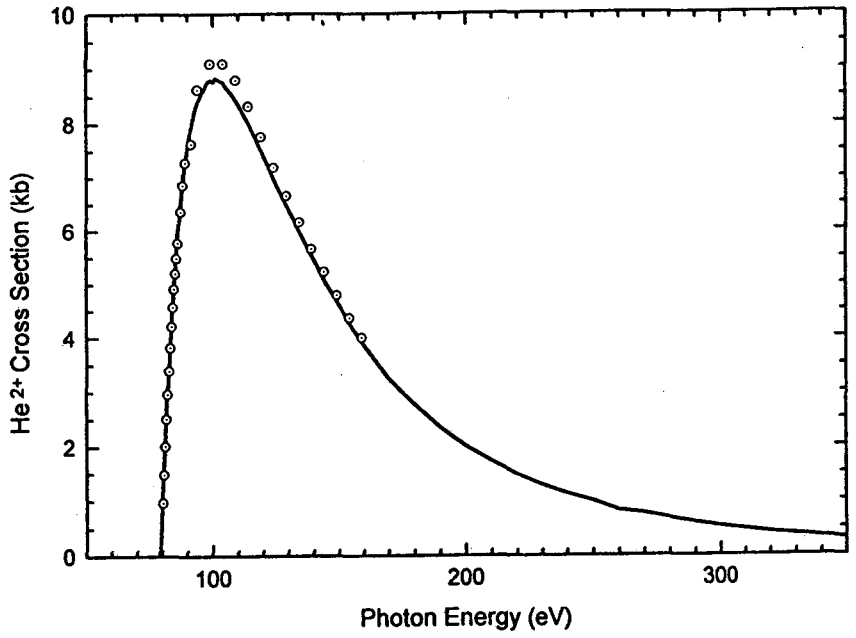

Figure 2. Photoionization cross section for He^{2+}. The solid line represents our experimental data. The open circles are the theoretical results of Pont and Shakeshaft [9].

From the above results and our precision total photoionization cross sections for He we can obtain the absolute photoionization cross section for He^{2+} [8]. These results are shown in Fig. 2 by the solid line and compred to the recent theoretical results of Pont and Shakeshaft [9]. We find similar near perfect agreement with several of the latest calculations [10-12].

REFERENCES

1. V. Schmidt, N. Sander, H. Kuntzemüller, P. Dhez, F. Wuilleumier, and E. Källne, Phys. Rev. A **13**, 1748 (1976).
2. P. Lablanquie, K. Ito, P. Morin, I. Nenner, and J.H.D. Eland, Z. Phys. D **16**, 77 (1990).
3. R. Wehlitz, F. Heiser, O. Hemmers, B. Langer, A. Menzel, and U. Becker, Phys. Rev. Letters **67**, 3764 (1991).
4. R.J. Bartlett, P.J. Walsh, Z.X. He, Y. Chung, E.M. Lee, and J.A.R. Samson, Phys. Rev. A **46**, 5574 (1992).
5. N. Berrah, F. Heiser, R. Wehlitz, J. Levin, S.B. Whitfield, J. Viefhaus, I.A. Sellin, and U. Becker, Phys. Rev. A **48**, R1733 (1993).
6. J.C. Levin, G.B. Armen, and I.A. Sellin, Phys. Rev. Letters **76**, 1220 (1996).
7. R. Dörner et al., Phys. Rev. Letters **76**, 2654 (1996).
8. J.A.R. Samson, Z.X. He, L. Yin, and G.N. Haddad, J. Phys. B **27**, 887 (1994).
9. M. Pont and R. Shakeshaft, J. Phys. B **28**, L571 (1995).
10. K.W. Meyer and C.H. Greene, Phys. Rev. A **50**, R3573, (1994).
11. A.S. Kheifets and I. Bray, Phys. Rev. A **54**, R995 (1996).
12. J.M. Rost, Phys. Rev. A **53**, R640 (1996).

This work was supported by the National Science Foundation under Grant No. PHY-9410716.

Principal investigator: James A.R. Samson, Behlen Laboratory of Physics, University of Nebraska. Email: jsamson@unlinfo.unl.edu. Telephone: 402-472-2791.

Reflectance Measurements on Clean Surfaces for the Determination of Optical Constants of Silicon in the EUV/Soft-X-Ray Range

R. Soufli[1,2] and E. M. Gullikson[2]

[1] Department of Electrical Engineering and Computer Sciences, University of California, Berkeley, California 94720, USA
[2] Center for X-ray Optics, Ernest Orlando Lawrence Berkeley National Laboratory, University of California, Berkeley, California 94720, USA

INTRODUCTION

The response of a given material to an incident electromagnetic wave is described by the energy dependent complex index of refraction $n = 1 - \delta + i\beta$. In the extreme ultraviolet (EUV)/ soft x-ray spectral region, the need for accurate determination of n is driven by activity in areas such as synchrotron based research, EUV/x-ray lithography, x-ray astronomy and plasma applications. Various methods are used in order to determine the optical constants δ, β such as reflectance measurements, angle dependent electron yield, transmission measurements, interferometry and ellipsometry. In this work, the method of angle dependent reflectance is evaluated and implemented in order to obtain the optical constants of Si in the region around the $L_{2,3}$ edge (99.8 eV). Silicon is among the materials of particular importance for practical applications in the EUV/soft x-ray range, due to its implementation as filter and spacer material in multilayer mirrors, for energies below the $L_{2,3}$ edge. The refractive index of Si in this energy range has been investigated by previous experimenters [1,2,3] using various methods. The discrepancies among their data arise mainly due to the surface quality of the samples used for measurements and the inherent difficulties of each method. Angle dependent reflectance measurements have the advantage that both δ and β may be deduced experimentally, and thus provide an important test of the tabulated values [4] of δ generated using the Kramers-Kronig relations. In addition, measurements may be performed on bulk samples without the need to fabricate the free standing thin films required for transmission measurements.

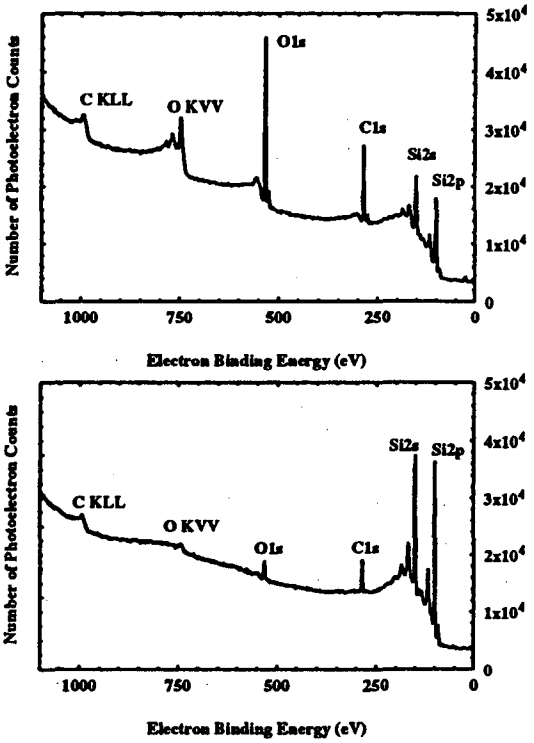

Figure 1. XPS survey scan results for a Si(111) wafer, "as received" (top) and after H-passivation (bottom).

EXPERIMENT

The samples investigated include crystalline silicon ((111) and (100) orientations) and amorphous silicon. The reliability of reflectance data depends on the quality of the sample surface. The most serious sources of error are: 1) surface roughness, 2) the presence of native oxide and organic contamination on the sample surface. For these reasons, particularly smooth samples were used and a cleaning treatment was applied to the sample surfaces, prior to the measurements. The cleaning procedure includes UV cleaning (for organic contamination removal) and subsequent HF:ethanol dipping of the samples, which results in H-passivated surfaces [5,6]. The samples were investigated before and after cleaning was applied, using the X-ray Photoelectron Spectroscopy

(XPS) method, in order to determine the effectiveness of the H-passivation technique, as shown in Fig. 1.

Two instruments were used for the reflectance measurements on the H-passivated silicon samples: 1) The EUV/soft X-ray reflectometer is described in detail in [7]. The instrument uses a laser produced plasma source and a spherical grating monochromator to produce continuously tunable radiation in the range 30<E<300 eV. 2) Beamline 6.3.2 at the ALS is described in [8]. This beamline is using radiation from a bending magnet in the energy range 50<E<1000 eV. The optics consist of a plane grating monochromator, a reflectometer chamber (10^{-8} Torr base pressure) and refocusing mirrors to provide a small spot on the sample. Data were collected in the form of reflectance curves (R vs. angle of incidence) for a number of energies in the region 50-180 eV. The reflectance data vs. angle at each energy were fitted in order to obtain the optical constants δ, β by means of a least squares fitting algorithm, using the Fresnel equation.

RESULTS

It is shown that the method of least squares fitting in order to derive the optical constants δ, β from experimental data is reliable only in regions where β is sufficiently below δ, while it is producing results with large uncertainties in the energy range where $\beta \geq \delta$, as shown in Fig. 2. The effect of the β/δ ratio in the fitting of a reflectance curve has a purely mathematical nature, thus, the above reliability criteria should apply to the fitting of reflectance data from any material in any energy range. However, the exact value of β/δ which marks the boundary between reliable and uncertain fitting should depend on the particular experimental conditions and therefore it has to be determined separately in each case.

In this experiment, reliable data are obtained in the range 50 - 90 eV (below the silicon $L_{2,3}$ edge), corresponding to $\beta/\delta \leq 0.5$. It is shown that crystalline Si exhibits structure from 60 to 80 eV, also observed in previous transmission data. Furthermore, the fitted values for δ are compared to the tabulated values [4]. It is demonstrated through the sum rule that the tabulated values in [4] should overestimate δ because of missing oscillator strength in the absorption coefficient data used. This effect is verified by the present reflectance results for δ.

The above discussion suggests that least squares fitting of reflectance data may not be a suitable method for the determination of the refractive index in certain energy regions; different techniques should be explored in the regions where the fitting algorithm becomes problematic. Particularly for silicon, there is a need for improved measurements in the region above the $L_{2,3}$ edge, where the available absorption data are poor and the reflectance method fails to provide reliable results.

ACKNOWLEDGEMENTS

The authors are thankful to J. H. Underwood for his support and gratefully acknowledge S. Irick, F. Ogletree and N. Palaio for their contributions in this experiment.

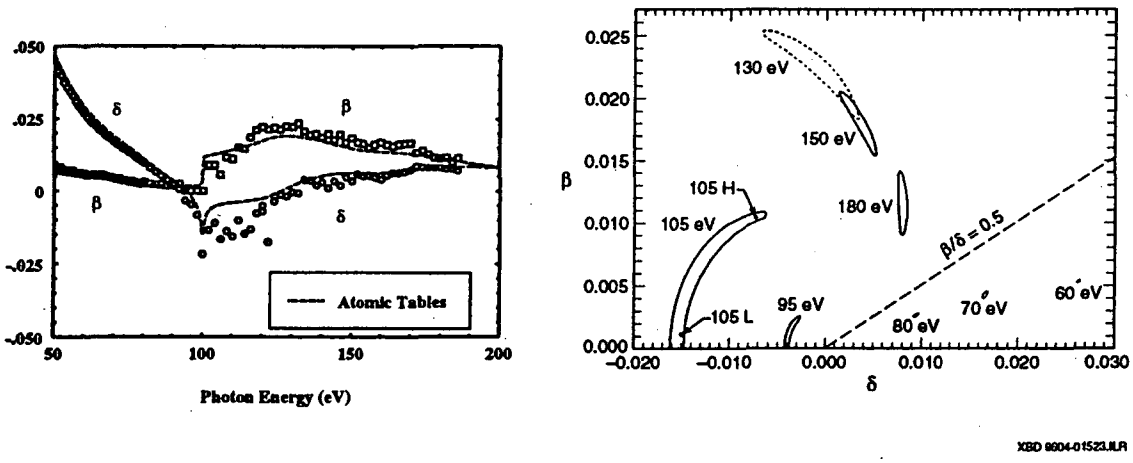

Figure 2. Left: The optical constants δ (○), β (□), for a Si(100) sample measured at the ALS beamline 6.3.2. The values for δ, β (dash) from the atomic tables [4] are also shown. Right: Contour plots of the least squared error generated with the data on the Si(100) sample. The energies shown are 60, 70, 80, 95, 105, 130, 150 and 180 eV in a $\delta - \beta$ axis system. Each contour area is enclosing the optical constant pairs fitted by the least squares algorithm within $\pm 1\sigma$ of their true values. When the contour areas become large, then the fitting is uncertain. This is true for the energies above the edge in this experiment.

REFERENCES

1. D. L. Windt, W. C. Cash, Jr., M. Scott, P. Arendt, B. Newnam, R. Fisher, A. B. Swartzlander, P. Z. Takacs and J. M. Pinneo, Appl. Opt. **27**, 279-295 (1988).
2. F. R. Bartsch, H. G. Birken, C. Kunz and R. Wolf, Semicond. Sci. Technol. **5**, 974-979 (1990).
3. E. M. Gullikson, P. Denham, S. Mrowka and J. H. Underwood, Phys. Rev. B **49**, 16283-16288 (1994).
4. B. L. Henke, E. M. Gullikson and J. C. Davis, Atomic Data and Nuclear Data Tables **54**, (1993).
5. R. W. C. Hansen, J. Wolske, D. Wallace and M. Bissen, Nuclear Instruments and Methods in Physics Research A **347**, 249 (1994).
6. J. M. C. Thornton and R. H. Williams, Physica Scripta **41**, 1047-1052 (1990).
7. E. M. Gullikson, J. H. Underwood, P. J. Batson and V. Nikitin, J. X-Ray Sci. Technol. **3**, 283-299 (1992).
8. J. H. Underwood, E. M. Gullikson, M. Koike, P. J. Batson, P. E. Denham, K. D. Franck, R. E. Tackaberry and W. F. Steele, in Conference on Synchrotron Radiation Instrumentation '95, Rev. Sci. Instrum. **67** (1996), available on CD-ROM only.

This work was supported by the Director, Office of Basic Energy Sciences, Materials Sciences Division, of the U.S. Department of Energy under Contract No. DE-AC03-76SF00098.

Principal Investigator: Regina Soufli, Center for X-Ray Optics, Ernest Orlando Lawrence Berkeley National Laboratory. Email:regina@ux5.lbl.gov. Telephone: 510-486-4079.

Resonant Magnetic Scattering of Polarized Soft X Rays

Maurizio Sacchi [1], Coryn F. Hague [2], Eric M.Gullikson [3] and Jim Underwood [3]

[1] Laboratoire pour l' Utilisation du Rayonnement Electromagnétique,
Centre Universitaire Paris-Sud, 91405 Orsay (France)

[2] Laboratoire de Chimie Physique - Matière et Rayonnement
Université Pierre et Marie Curie, 11 rue Curie, 75231 Paris Cedex 05 (France)

[3] Advanced Light Source, Ernest Orlando Lawrence Berkeley National Laboratory,
University of California, Berkeley, California 94720 (USA)

INTRODUCTION

Magnetic effects on X-ray scattering (Bragg diffraction, specular reflectivity or diffuse scattering) are a well known phenomenon [1], and they also represent a powerful tool for investigating magnetic materials since it was shown that they are strongly enhanced when the photon energy is tuned across an absorption edge (resonant process) [2]. The resonant enhancement of the magnetic scattering has mainly been investigated at high photon energies [3], in order to match the Bragg law for the typical lattice spacings of crystals. In the soft X-ray range, even larger effects are expected, working for instance at the 2p edges of transition metals of the first row or at the 3d edges of rare earths (300-1500 eV), but the corresponding long wavelengths prevent the use of single crystals. Two approaches have been recently adopted in this energy range: i) the study of the Bragg diffraction from artificial structures of appropriate 2d spacing [4]; ii) the analysis of the specular reflectivity, which contains analogous information but has no constraints related to the lattice spacing [5]. Both approches have their own specific advantages: for instance, working under Bragg conditions provides information about the (magnetic) periodicity in ordered structures, while resonant reflectivity can easily be related to electronic properties and absorption spectra. An important aspect common to all the *resonant* X-ray scattering techniques is the element selectivity inherent to the fact of working at a specific absorption edge: under these conditions, X-ray scattering becomes in fact a spectroscopy.

EXPERIMENT

In August 1996, we performed preliminary measurements to test the feasibility of resonant magnetic scattering experiments using elliptically polarized photons on beamline 6.3.2 at ALS. In order to change the polarization state of the light without changing either the optical alignement of the beamline or the calibration of the energy scale, we simply modified the position of the vertical jaws that define the angular acceptance at the entrance of the monochromator. Linearly polarized light is obtained when selecting a vertical accepted angle symmetric with respect to the orbit plane of the electrons in the ring. To have elliptically polarized light of positive (negative) helicity, only the portion of the beam emitted above (below) the orbit plane should go through the monochromator. A good compromise between flux and polarization rate was found accepting the beam within the 0.2 ± 0.05 mrad angular range above the orbit plane.
Measurements were performed on ex-situ deposited metallic layers, as well as on multilayers and crystals. The samples were magnetized along the intersection between the surface and scattering planes by a permanent magnet placed behind the sample holder. The magnet could be rotated in vacuum around the axis normal to the sample surface, using a stepper motor. In this way we could

change at each scan the relative orientation between photon helicity and sample magnetization, without affecting the sample alignment. In the end station of line 6.3.2 the scattering plane is vertical (i.e. orthogonal to the plane of the ring). The sample and the detector can be rotated around the same axis in an independent or coupled (θ/2θ) mode. We performed both energy scans at fixed scattering angles, and θ/2θ scans at fixed photon energy.

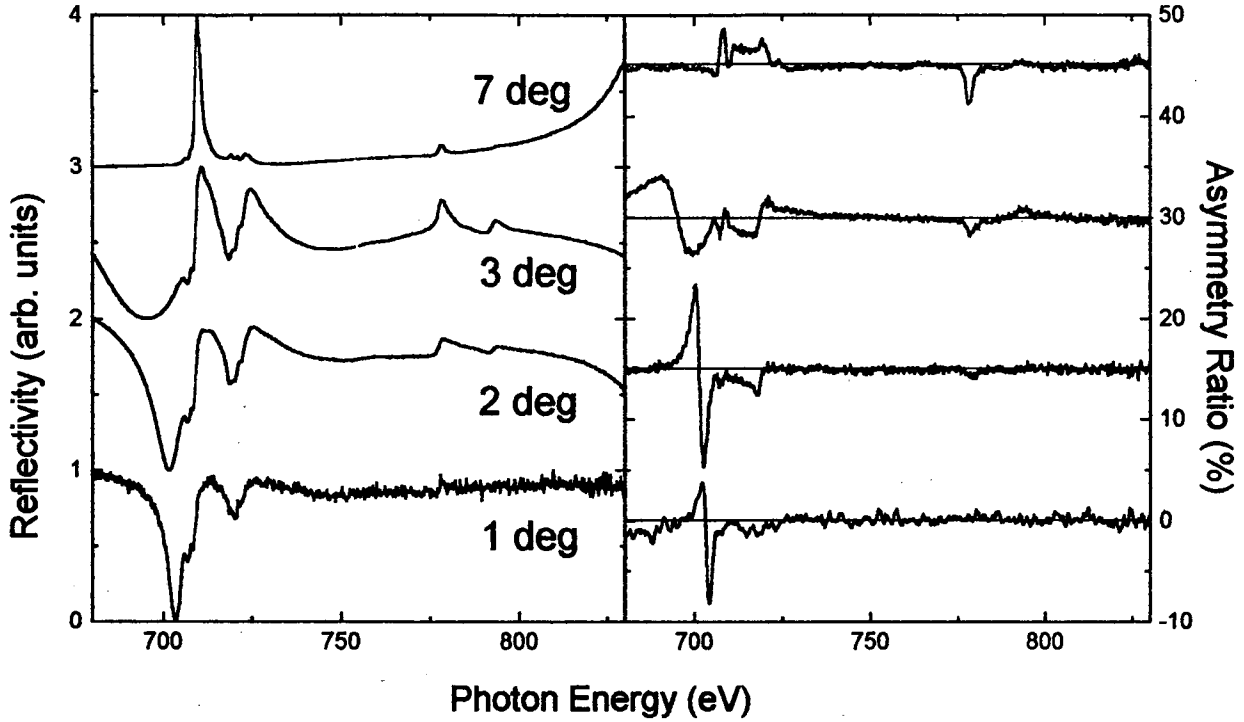

Figure 1. Reflectivity curves (left) taken at different angles of incidence as a function of the photon energy, over a range including the 2p absorption edges of both Fe and Co. The sample is a 11.5 Å Fe / 20 Å Co multilayer. The right panel reports the corresponding asymmetry curves, i.e. the difference divided by the sum of reflectivity measured for a sample magnetization parallel or anti-parallel to the photon helicity.

RESULTS

Fig. 1 reports the magnetization averaged reflectivity curves for an Fe/Co multilayer (11.5 Å Fe / 20 Å Co, Fe terminated), measured at different angles of incidence θ over a photon energy range including both Fe and Co $L_{2,3}$ edges. The right panel of Fig.1 shows the corresponding magnetic part of the resonant scattering, presented as the asymmetry ratio $(I^+ - I^-) / (I^+ + I^-)$, where $I^{\pm}$ is the intensity for the photon helicity (anti-) parallel to the magnetization. The strong angular dependence of both reflectivity and asymmetry curves is related to the interference between the real and imaginary parts of the refractive index through Fresnel's equations. It can also be noted in Fig. 1 that for θ = 1 deg. the reflectivity is almost constant out of the Fe 2p energy region, and the signal from Co (second layer) can hardly be detected. Fig. 2 shows in more detail the reflectivity spectrum measured at θ = 5 deg. for a different Fe/Co multilayer (21.5 Å Fe / 29.5 Å Co): the curves for opposite magnetizations and their difference are reported in the left panel, while on the right we have the asymmetry ratio. Some fine structure can be observed in the reflectivity at the Fe 2p edges: it is not related to noise, but it might originate from the oxidation of the Fe top atomic layers, as suggested by absorption spectroscopy data. On this same sample, we also measured the magnetic effects on Bragg diffraction when the photon energy approaches the 2p resonances.

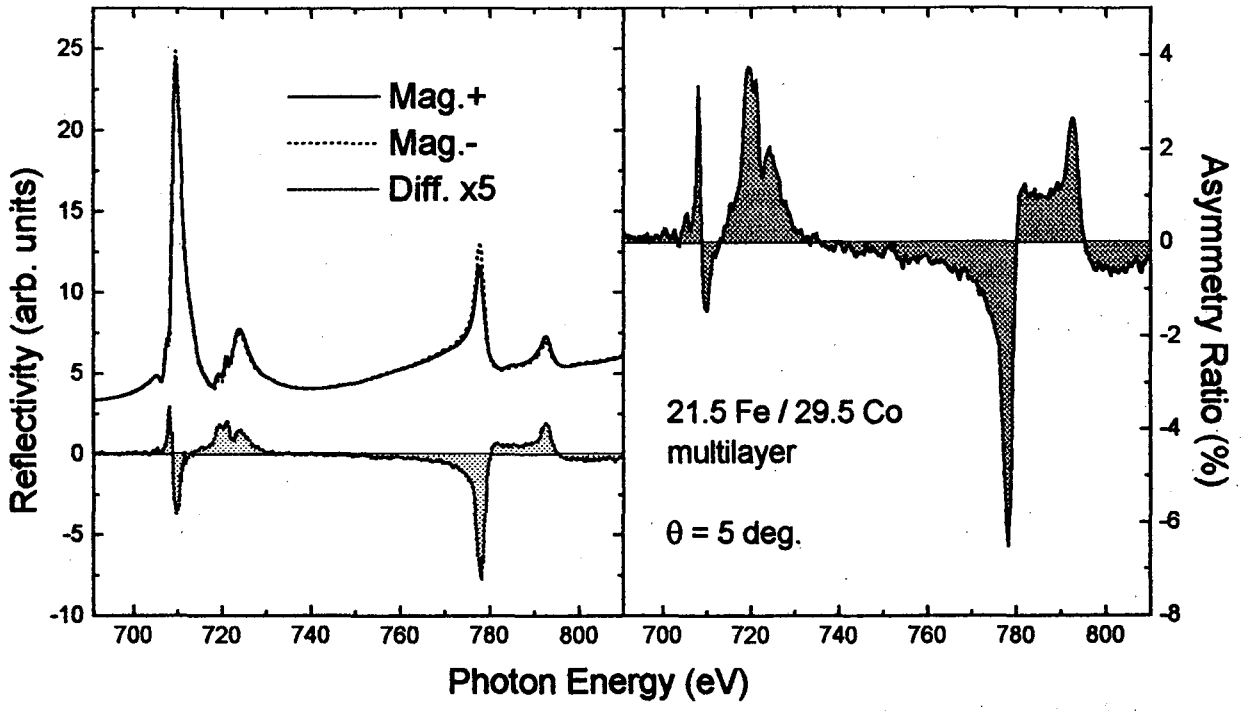

Figure 2. Resonant reflectivity curves for opposite magnetization directions in a 21.5 Å Fe / 29.5 Å Co multilayer. The difference (x 5) and the asymmetry ratio (right panel) curves are also reported.

Fig. 3a shows a few examples of a series of θ/2θ scans taken for various photon energies just below the Fe $2p_{3/2}$ edge. Apart from an increased intensity, there is also an evident enhancement of the variation with the magnetic field when the photon energy gets closer to the edge. We report in Fig. 3b the result of a θ/2θ scan taken at 704 eV, together with the corresponding asymmetry ratio (3c). Even if the analysis of these data is still in progress, a few remarks can be made about Fig. 3 : i) taking the nominal values for the multilayer spacing (51 Å) and for the photon energy (e.g. 704 eV in Fig. 3b), one gets θ_B values in excellent agreement with the experiment; ii) it appears that the main diffraction peak is always flanked by weaker shoulders, also showing a dependence on the magnetic orientation: this could be related to a spread in the layer thicknesses, and/or to interface mixing; iii) larger magnetic effects are expected at the exact $2p_{3/2}$ photon energy (about 709 eV for Fe), but we could not see a diffraction peak there. The reason is that for our sample a photon incident at 9 degrees has to travel through approximately 275 Å of Fe to be reflected at the first Fe/Co interface and come out again. This distance is much larger than the absorption length at the maximum of the Fe L_3 edge, hence photons of 709 eV can hardly feel the periodic structure of the multilayer. In general, the Bragg peak is bound to get broader at resonance, but, if measurable, data can easily be corrected for absorption and still give very useful information [4].

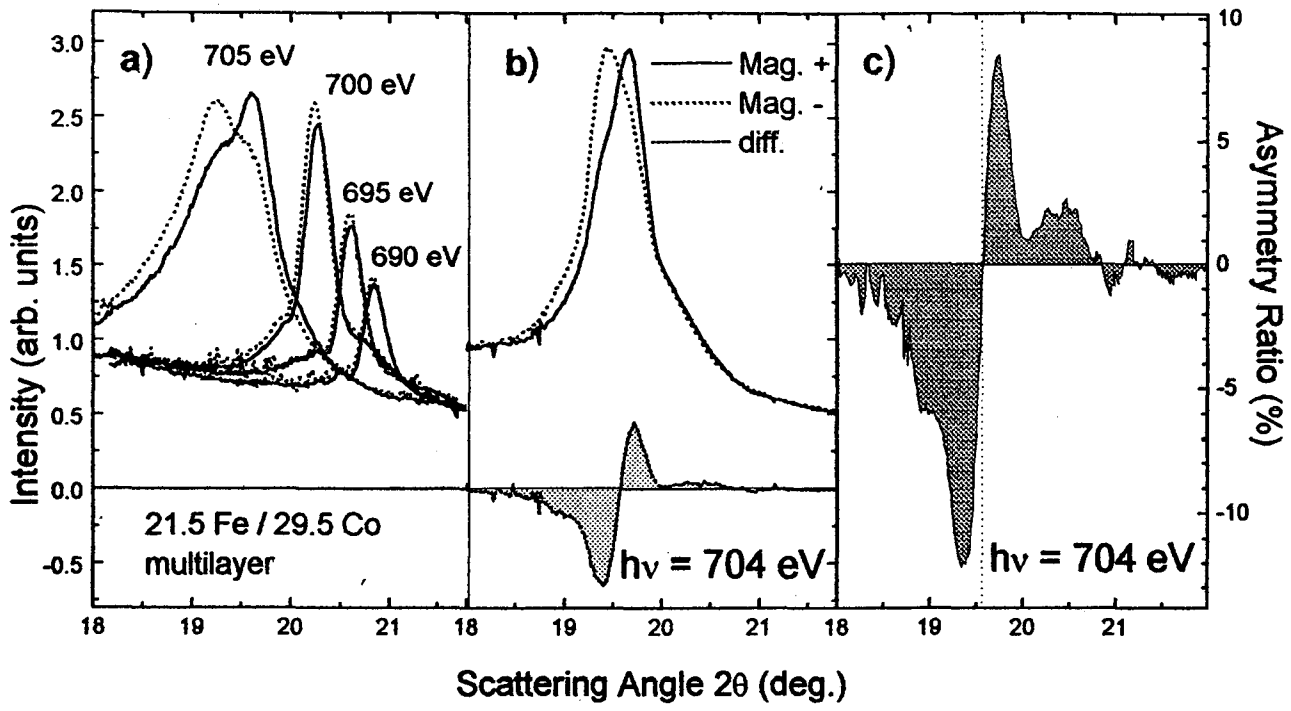

Figure 3. θ/2θ scans at different photon energies close to the Fe L_3 edge. Continuos and dotted lines are for opposite magnetization directions. For hν = 704 eV we also report the difference curve (b) and the asymmetry ratio (c).

CONCLUSIONS

We performed preliminary experiments on Fe/Co multilayers, measuring both specular reflectivity and Bragg diffracion at the 2p resonances. We have shown that the monochromator and the end station of beamline 6.3.2 at ALS are perfectly suited for resonant magnetic scattering experiments in the soft X-ray range. The location of the beamline on a bending magnet source gives, at the price of a lower flux, the possibility of covering a wide energy range with only smooth variations of the incoming intensity. Together with the easy tunability of the polarization state, this represents a major advantage, for this kind of spectroscopy, of a bending magnet over an insertion device delivering high flux in narrow energy bands.

REFERENCES

1. O.Klein and Y.Nishina, Zeit.Phys.**52** (1929) 853; P.M.Platzman and N.Tzoar, Phys.Rev.**B2** (1970) 3556; F.DeBergevin and M.Brunel, Phys.Lett. **39A** (9172) 141
2. D.Gibbs et al., Phys.Rev.Lett. **61** (1988) 1241; J.P.Hannon et al., *ibid.* **61** (1988) 1245; E.D.Isaacs et al., *ibid.* **62** (1989) 1671
3. P.Carra et al., Phys.Rev. **B40** (1989) 7324; D.Gibbs et al., *ibid.* **B43** (1991) 5663; C.Tang et al., *ibid.* **B46** (1992) 5287; F.DeBergevin et al., *ibid.* **B46** (1992) 10772
4. J.M.Tonnerre et al., Phys.Rev.Lett. **75** (1995) 740; C.F.Hague et al., in *Raman Emission by X-rays*, edited by D.Ederer and J.McGuire (World Scientific, Singapore), *in press*
5. C.Kao et al., Phys.Rev.Lett. **65** (1990) 373; Phys.Rev. **B50** (1994) 9599; M.Sacchi et al. J.Mag.Mag.Mater. **147** (1995) L11; Surf.Rev.Lett., *in press*

This work was supported by the Director, Office of Energy Research, Office of Basic Energy Sciences, Chemical Sciences Division of the U.S. Department of Energy under contract No. DE-AC03-76SF00098.

Principal investigator: Maurizio Sacchi, Laboratoire pour l'Utilisation du Rayonnement Electromagnétique, Centre Universitaire Paris-Sud. Email: sacchi@lure.u-psud.fr. Telephone: +33 1 6446 8089.

Role of 3*d* Electrons in Formation of Ionic-Covalent Bonds in II-VI Based Ternary Compounds

K.Lawniczak-Jablonska[1,2], R.J.Iwanowski[1], R.C.C.Perera[2], J. H. Underwood[2], E.M.Gullikson[2]

[1]Institute of Physics, Polish Academy of Sciences, Al. Lotników 32/46, 02-668 Warsaw, Poland.
[2] Lawrence Berkeley National Laboratory, Berkeley, CA 94720, USA.

INTRODUCTION

In the II-VI compounds doped with transition metals (diluted magnetic semiconductors) a substitution of cation by the introduced magnetic ion leads to hybridization of its 3d states with the sp states of the host semiconductor. The degree of hybridization of the 3d states and its interaction with the host material band states has been a subject of numerous discussions [1]. Inner shell absorption spectroscopy provides very useful means of electronic structure analysis in a wide variety of systems. Due to its selectivity for atomic species and the selection rules for electron transitions, the soft X-ray absorption technique offers quite unique opportunity to measure directly the site-selective local density of the unoccupied d states in the compounds studied.

EXPERIMENT AND RESULTS

We report the near-edge soft X-ray absorption spectra for $Zn_{1-x}M_xS$ compounds, where M is Mn, Fe, Co or Ni, and x ranges within the M solubility limit. These include the S- $L_{2,3}$ and L_3 absorption edges of transition metals, measured in the total electron yield mode at the bending magnet beamline 6.3.2 at the Advanced Light Source. The observed changes of the local density of the 3d and s antibonding states, detected in the experiment, indicate that the 3d states effectively participate in formation of the ionic-covalent bond between metal and anion.

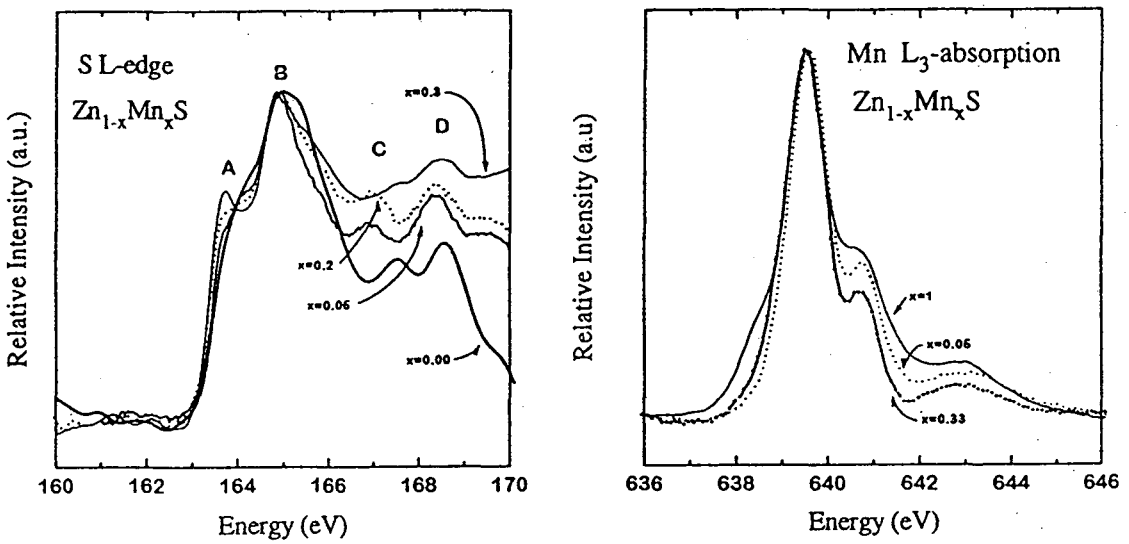

Figure 1. a) $L_{2,3}$ edge of S absorption for $Zn_{1-x}Mn_xS$ normalized at the maximum intensity, x=0.0 - bold line, x=0.05 - middle line, x=0.2 - dotted line, x=0.3 - thin line; b) L_3 -edge of Mn absorption for $Zn_{1-x}Mn_xS$ normalized at the maximum intensity, x=0.05 - dotted line, x=0.33 - bold line, x=1.0 - thin line;

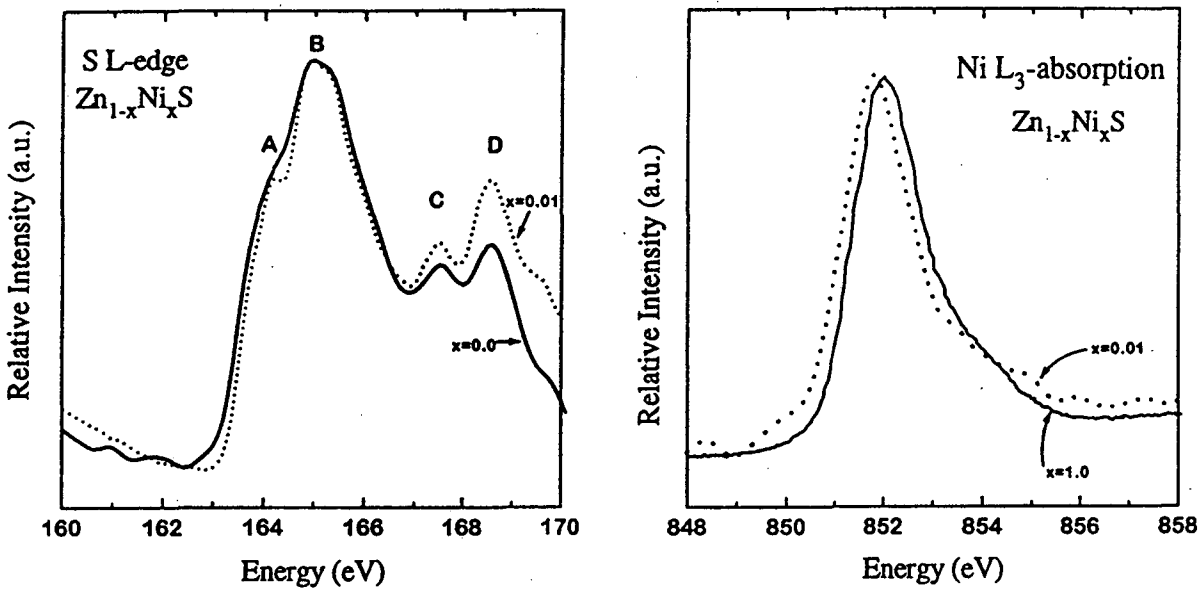

Figure 2. $L_{2,3}$ edge of S absorption for $Zn_{1-x}Ni_xS$ normalized at the maximum intensity, x=0.0 - bold line, x=0.01 - dotted line; L_3 -edge of Ni absorption for $Zn_{1-x}Ni_xS$ normalized at the maximum intensity, x=0.01 - dotted line, x=1.0 - bold line.

The most pronounced changes in sulfur and metal absorption edges were found for Mn- (Fig. 1) and Fe- doped compounds, whereas in the case of Ni dopant (Fig. 2) the effect became the weakest. On the contrary, such behaviour has not been noticed when investigating the unoccupied p-like local DOS in the same materials [2]. Recent results prove that the degree of hybridization between the 3d states of M and the s states of the matrix anion depend on the 3d shell filling.The above evidence was additionally supported by the effective charge transfer estimated from the chemical shifts of the transition metal K-edges. The amount of charge shows direct contribution of the 3d electrons to the ionic bond between cation and anion which also decrease with 3d orbit filling. Therefore, increased occupation of the 3d orbit results in lowering of the contribution to the ionic-covalent bond given by the 3d electrons, which tend to exhibit more core-like character. This can explain a drastic decrease of the solubility limit of the investigated transition metals admixed to the ZnS matrix. The solubility limit, which equals x=0.6 in the case of Mn, falls down to x=0.03 when the Ni dopant is introduced into cation sublattice.

REFERENCES

1. A. Twardowski in Diluted Magnetic Semiconductors, edited by M. Jain (World Scientific, Singapore, 1991), p. 276.
2. K.Lawniczak-Jablonska, R.J.Iwanowski, Z.Gołacki, A.Traverse, S.Pizzini, A.Fontaine, I.Winter and J.Hormes, Phys. Rev. **B 53** (1996) 1119.

This work was supported by the Director, Office of Energy Research, Office of Basic Energy Science, Materials Science Division of the U.S. Department of Energy under Contract No. DE-AC03-76SF00098. Author (K. L-J) kindly acknowledges the financial support of the Fulbright Foundation.
Principal investigator: K. Lawniczak-Jablonska, Institute of Physics, Polish Academy of Sciences, Al Lotnikow 32/46, 02 668 Warsaw, Poland. E-mail:jablo@ifpan.edu.pl. Telephone: 48-22-436034.

X-Ray Absorption and Reflection as Probes of the GaN Conduction Bands: Theory and Experiments

W. R. L. Lambrecht[1], S. N. Rashkeev[1],B. Segall[1],K. Lawniczak-Jablonska[2], T. Suski[3], E. M. Gullikson[4], J. H. Underwood[4], R. C. C. Perera[4],J. C. Rife[5],I. Grzegory [3]and S. Porowski[3], D. K. Wickenden[6]

[1]Department of Physics, Case Western Reserve University, Cleveland, OH 44106-7079
[2]Institute of Physics, Polish Academy of Sciences, 02 688 Warsaw, Poland
[3]UNIPRESS, Polish Academy of Sciences, 01-142 Warszawa, Poland
[4]Lawrence Berkeley National Laboratory, University of California, Berkeley, CA 94720
[5]Naval Research Laboratory, Washington, D. C. 20375
[6]Applied Physics Laboratory, Johns Hopkins Univeristy,Baltimore, MD 20723

INTRODUCTION

X-ray absorption measurements are a well-known probe of the unoccupied states in a material. The same information can be obtained by using glancing angle X-ray reflectivity. In spite of several existing band structure calculations of the group III nitrides [1] and previous optical studies in UV range [2, 3, 4], a direct probe of their conduction band densities of states is of interest. We performed a joint experimental and theoretical investigation using both of these xperimental techniques for wurtzite GaN. A more complete account of this work can be found in [5].

EXPERIMENT AND RESULTS

X-ray absorption and X-ray reflectivity spectra for different incident angles have been collected at the bent magnet 6.3.2. beamline of the Advanced Light Source (ALS). The high photon flux in the N K-edge region and the high energy resolution at this beamline allowed us to resolve fine structure of the X-ray absorption spectra at the K-edges of nitrogen and $M_{2,3}$-edge of Ga and to detect reflected signal even for angles significantly differing from the optimal glancing angle. For measurements in the absorption mode, the direct photocurrent from the sample, positioned perpendicularly to the X-ray beam, was measured as a function of the incoming radiation energy. In the reflection mode, the radiation was detected by GaAsP. Three kinds of GaN samples were used in X-ray absorption experiments to verify the low sensitivity of the photocurrent detection method to the sample surface roughness and contaminations. GaN powder (with particle size smaller than 20 μm available commercially), epitaxial film of about 1 μm thick grown by molecular beam epitaxy (MBE) on sapphire substrate, and bulk single crystal of GaN, grown by a high pressure, high temperature method. The latter sample had the form of a platelet perpendicular to the hexagonal c-axis. The epitaxial films had the same orientation.

First-principles calculations of the (polarization averaged) dielectric response $\varepsilon_2(\omega)$ contributions from the relevant core-level to conduction band transitions and derived spectral functions are used to interpret the data. These calculations are based on the local density approximation (LDA) and use a muffin-tin orbital basis for the band structure and matrix elements. The angular dependence of the X-ray reflectivity was studied and shown to be in good agreement with the theoretical predictions based on Fresnel theory and the magnitude of the calculated X-ray optical response functions (Figs. 1 and 2). The measured intensity of the reflected beam varies drastically with the value of angle θ. The glancing angle corresponding to the maximum of intensity is equal to 5.3°. The rapid decrease of intensity with increasing angles is easily understood on the basis of the Fresnel equations. In fact, the reflectivity would

vary inversely with θ^4. The rapid decrease of signal amplitude for angles below 5.3° is an indication of the rapid decrease of the penetration depth into the bulk. Therefore, for small angles, the oxygen and carbon contamination layers of the surface may overwhelm the GaN signal and only an increase of the background signal can be seen. The simultaneously measured photocurrent for different angles also shows a drastical change of the N K-edge shape and intensity. Besides the obvious variation of the intensity there are also more subtle changes of the spectral shape with angle. One can see that at the larger angles, the spectrum resembles the photocurrent measurements more closely as expected from the theoretical considerations. At the lower angles the characteristic negative dip before the on-set of the spectrum can be seen and maximum intensity is shifted towards higher energies. The calculated spectra at a series of angles are shown in Fig. 2. First of all, we see again that the required intensity multiplication factors vary roughly as expected (θ^4). Secondly, we see that the shoulder A and peaks B and C increase with increasing angle while the peak D decreases. This is consistent with the data and it shows that the Fresnel theory accounts well for the angular dependence.

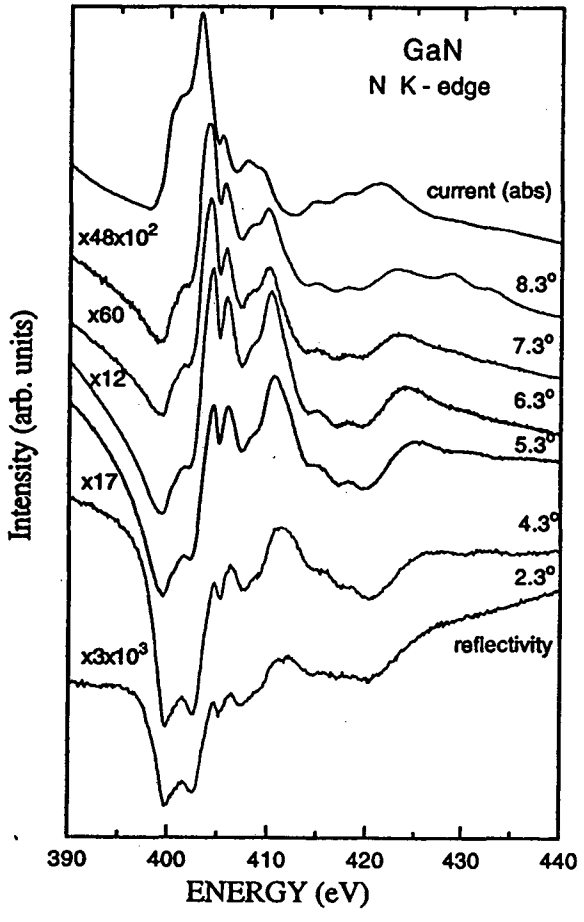

Figure 1. Normalized reflectivity spectra of the nitrogen K-edge as function of angle. Normalization factors are indicated for each curve, except for the 5.3° case where it is one. The spectra are arbitrary shifted vertically for convenience. The topmost curve gives the photoyield measurements of the absorption spectrum for comparison.

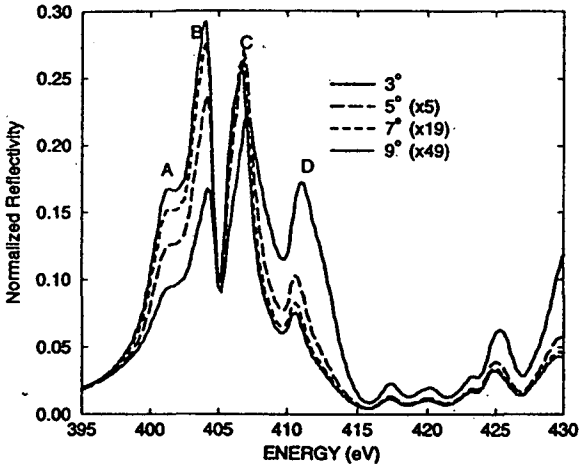

Figure 2. Calculated dependence of the nitrogen K-edge reflectivity spectrum on incident angle. The spectra were multiplied by the factor indicated to make them coincide at 395 eV

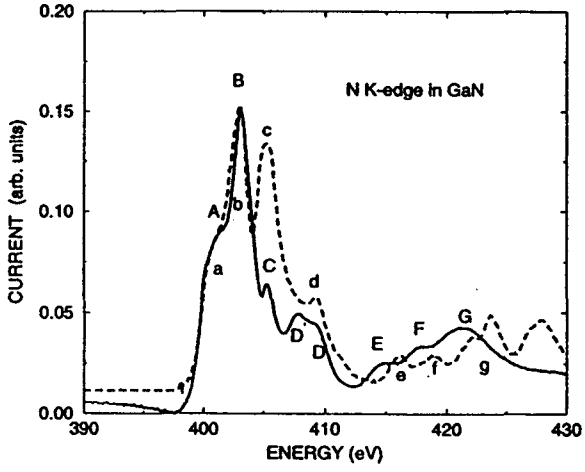

Figure 3. Nitrogen K edge x-ray absorption spectrum of GaN as measured (solid line) compared to the theory (dashed line).

Fig. 3 shows the N-K-edge X-ray absorption spectrum of GaN as measured by total photocurrent compared to the calculated spectrum. The spectrum shown is I/Io after fitting Io to a straight line in the energy range of interest. While the relative peak intensities are somewhat different and also different from the spectrum extracted from X-ray reflectivity, the peak positions are in good agreement at least up to 10 eV above the edge. One expects the N K-edge spectra to be essentially proportional to the N 2p partial density of states (PDOS). By comparison to the band structure, we can to some extent associate the peaks in partial density of states to van Hove singularities at specific points in the Brillouin zone. Fig. 4 shows the band structure of GaN along with the total and N 2p partial density of states. The valence band maximum is chosen as energy reference. For the present purposes only the conduction band is of importance. Several **k**-points or rather the "flat band" regions near to them contribute to each peak. For the first 3 peaks (A--C), no significant differences between theory and experiment are found, indicating that the self-energy correction is approximately constant in that energy range. This is consistent with a previous UV-reflectivity study [6]. In contrast, the GW calculations of Rubio et al. [7] indicate a gradually increasing self-energy shift with increasing energy in the conduction band. The present comparison between LDA theory and experiment does not seem to give any evidence of such a systematic increase in self-energy correction. Fig. 5 shows the Ga-$M_{2,3}$ X-ray absorption spectrum both as measured directly from total photoyield and by KK analysis of the reflectivity data, compared to the calculated results. The separate M_2 and M_3 contributions are also indicated. Good agreement is obtained. The shift applied to the theoretical spectrum in this case is 10.7 eV. This results in a binding energy of the Ga 3p3/2 state with respect to the valence band maximum of 101.9 eV in good agreement with the XPS results which gave 102.6 eV. Our calculated spin-orbit splitting between Ga 3p1/2 and 3p3/2 of 3.65 eV is also in good agreement with the XPS result of 3.7 eV . We note that the A an B peaks correspond to the Ga M_3 spectrum while the C peak is an overlap of the first peak of the M_2 spectrum and the third (much weaker) peak of the M_3 spectrum, peaks D and E correspond to the M_2 spectrum. From the Ga $M_{2,3}$ spectrum we deduce the same equal 2 eV spacing between the first three peaks in the conduction band as was deduced from the N K-spectrum. The peak positions are about 108, 110 and 112 eV for A, B, C corresponding to M_3 and 112, 114 and 116 eV for C, D, E in the M_2 spectrum.

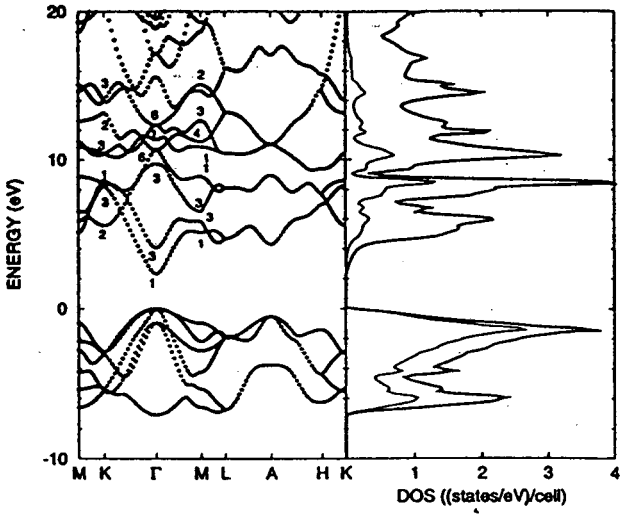

Figure 4. Band structure and density of states (DOS) in wurtzite GaN. Thin line indicates N 2p DOS. Conduction band states at Γ, M, and K are symmetry labelled.

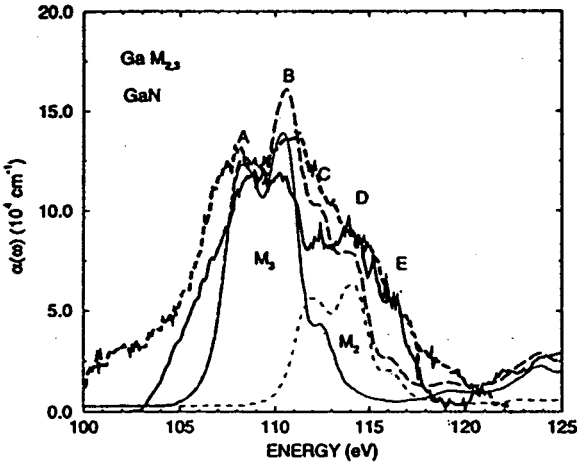

Figure 5. Gallium $M_{2,3}$ edge of x-ray absorption spectrum of GaN as measured by total photo-current (thick short-dashed line), and from KK analysis of reflectivity (thick solid line) compared to theory (long dashed line). Separate calculated c contributions of spin orbit doublet are indicated by thin dashed and thin solid lines.

CONCLUSION

We have performed a systematic study of the N K and Ga $M_{2,3}$ edge spectra in GaN. Aside from some small discrepancies, consistent results were obtained for the peak positions from two different experimental techniques employed to probe these spectra: glancing incidence angle X-ray reflectivity combined with Kramers-Kronig analysis and total photocurrent measurements of the X-ray absorption. Both sets of experimental data agree well with calculated spectra, especially for the transitions to the lower conduction band states up to about 10 eV above the conduction band edge. Even up to 20 eV above the conduction band minima the agreement in spectral shape is rather good with maximum discrepancies between theory and experimental peak positions of about 1 eV. The good agreement in peak positions and the assignment of the peaks to the band structure features allows us to conclude that the self-energy correction beyond the LDA band structure consists essentially of a constant shift for the conduction bands up to about 10 eV above the conduction band minimum. Further differences between theory and experiment may arise from core-hole final state and other many-body effects not included in the present theoretical treatment. Future work to address these questions is planned.

REFERENCES

1. S. Nakamura, M. Senoh, N. Iwasa, and S. Nagahama, Jpn. J. Appl. Phys. 34, L797 (1995); S. Nakamura, M. Senoh, N Iwasa, Nagahama, T. Yamada, and T. Mukai, Jpn. J. Appl. Phys. 34, L1332-5, (1995).
2. S. Nakamura, M. Senoh, S. Nagahama, N. Iwasa, T. Yamada, T. Matsushita, H. Kiyoku, and W. Sugimoto, Jpn. J. Appl. Phys. 35, L74 (1996).
3. See e.g. *Gallium Nitride and Related Materials*, edited by R. D. Dupuis, F. Ponce, S. Nakamura, and J. A. Edmond, Mater. Res. Soc. Symp. Proc. Vol. 395. (MRS, Pittsburgh 1996).
4. W. R. L. Lambrecht and B. Segall, in *Properties of Group III Nitrides*, edited by J. H. Edgar, Electronic Materials Information Service (EMIS) Datareviews Series (Institution of Electrical Engineers, London 1994), Chapt. 4.
5. W. R. L. Lambrecht, S. N. Rashkeev,B. Segall,K. Lawniczak-Jablonska, T. Suski, E. M. Gullikson, J. H. Underwood, R. C. C. Perera,J. C. Rife, I. Grzegory and S. Porowski, D. K. Wickenden, Phys. Rev. B55, 2612 (1997).
6. W. R. L. Lambrecht, B. Segall, S. Strite, G. Martin, A. Agarwal, H. Morkoc, and A. Rockett, Phys. Rev. B 50, 14155 (1994).
7. A. Rubio, J. L. Corkill, M. L. Cohen, E. L. Shirley, and S. G. Louie, Phys. Rev. B 48, 11810 (1993).

The work at CWRU was funded by the National Science Foundation under grants No. DMR 93-22387 and DMR 95-29376. The reflectance measurements were performed at the National Synchrotron Light Source which is sponsored by the U.S.Department of Energy and at the Advanced Light Source which is sponsored by U.S. Department of Energy under Contract No DE-AC03-76SF00098". K.L-J and T.S. kindly acknowledge the financial support of the Fulbright Foundation.

Principal investigator: K. Lawniczak-Jablonska, Institute of Physics, Polish Academy of Sciences, Al Lotnikow 32/46, 02 668 Warsaw, Poland. E-mail:jablo@ifpan.edu.pl. Telephone: 48-22-436034.

X-Ray Photoemission Spectromicroscopy of Titanium Silicide Formation in Patterned Microstructures

S. Singh, H. Solak, and F. Cerrina
Center for X-ray Lithography, University of Wisconsin-Madison, Stoughton, Wisconsin 53589, USA
J.H. Underwood
Center for X-ray Optics, Lawrence Berkeley National Laboratory, Berkeley, California 94720, USA
P. Agnello
IBM Corporation, East Fishkill, New York, USA

INTRODUCTION

Titanium silicide has the lowest resistivity of all the refractory metal silicides and has good thermal stability as well as excellent compatibility with Al metallization.It is used as an intermediate buffer layer between W vias and the Si substrate to provide good electrical contact in ULSI technology, whose submicron patterned features form the basis of the integrated circuits of today and tomorrow, in the ***self* al*igned sil*icide (salicide)** formation process.[1] $TiSi_2$ exists in two phases: a metastable C49 base-centered orthorhombic phase with specific resistivity of 60-90 μΩ-cm that is formed at a lower temperature (formation anneal) and the stable 12-15 μΩ-cm resistivity face-centered orthorhombic C54 phase into which C49 is transformed with a higher temperature (conversion anneal) step.[2,3] C54 is clearly the target for low resistivity VLSI interconnects. However, it has been observed that when dimensions shrink below 1\mic (or when the Ti thickness drops below several hundred angstroms), the transformation of C49 into C54 is inhibited and agglomeration often occurs in fine lines at high temperatures. This results in a rise in resistivity due to incomplete transformation to C54 and because of discontinuities in the interconnect line resulting from agglomeration. [4,5] Spectromicroscopy is an appropriate tool to study the evolution of the TiSi2 formation process because of its high resolution chemical imaging ability which can detect bonding changes even in the absence of changes in the relative amounts of species and because of the capability of studying thick 'as is' industrial samples.

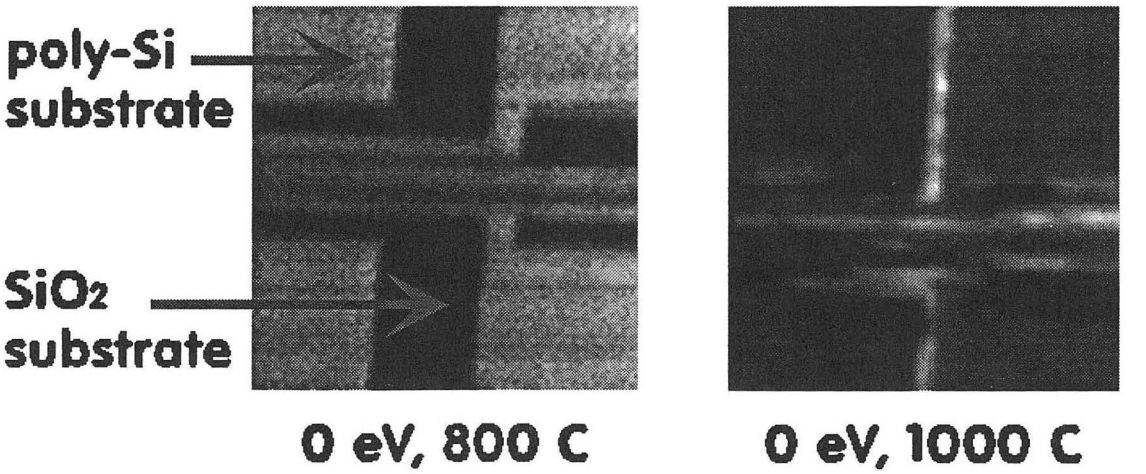

Figure 1. 100 μm × 100 μm , 1 μm step images of SRAM sample after Ti deposition and silicidation acquired with 0 eV photoelectrons after each anneal.

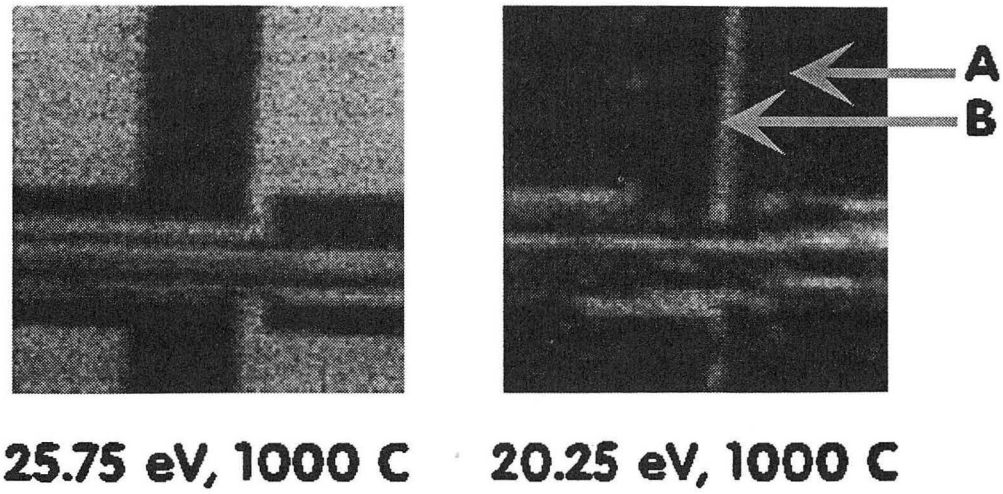

Figure 2. 100 μm × 100 μm , 1 μm step images acquired after the conversion anneal using the unshifted (left panel) and oxide-shifted Si 2p core level photoelectrons.

We have observed the formation of $TiSi_2$ in a patterned SRAM (static random access memory) sample from IBM using the photoelectron spectromicroscope MAXIMUM [6] on ALS Beamline 6.3.2. The sample region studied consists of 200 nm thick polysilicon features patterned atop a 400 nm thick isolation oxide with 50 nm wide silicon nitride sidewall spacers. The sample was chemically cleaned by etching in a 1:200 solution of HF in H_2O for 10 min, before being placed into vacuum. Approximately 30 nm Ti was deposited by evaporation on the surface and the sample was subjected to a ~800 C formation anneal for 30 sec and then to a momentary ~1000 C conversion anneal to form $TiSi_2$. Figure 1 shows secondary electron images of similar areas of the sample taken

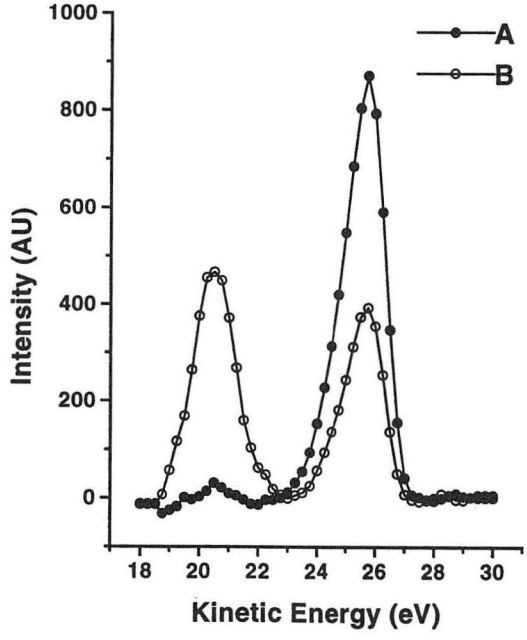

Figure 3. EDC's of the Si 2p acquired at points A and B as marked in Figure 2. A strong oxide-shifted signal is present at point B but not at A.

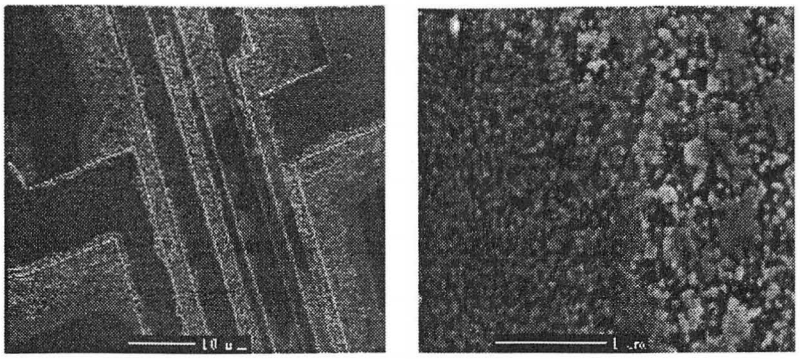

Figure 4. SEM micrographs of silicided sample showing lateral silicide growth and agglomeration.

before and after the conversion anneal. After the 1000 C step, bright colored regions are present next to the silicided polysilicon regions. To investigate lateral differences in chemistry, further photoelectron images of the region shown in the right panel of Figure 1 were acquired using the Si 2p core level photoelectrons. In Figure 2, the left image was acquired at 25.75 eV, the energy of the unshifted Si 2p, and the right image was acquired at 20.25 eV, the energy of the oxide-shifted Si 2p. Point A is on a silicided polysilicon pad and B is on a bright region just outside the pad. Energy distribution curves (EDCs) of the Si 2p core level taken at A and B are shown in Figure 3 and reveal that there is a higher oxide signal at B than at A, where the unshifted signal is higher. Indeed, the bright border regions are not visible in the 25.75 eV image since they have a lower signal than the silicide polysilicon regions. The border regions do, however, have a higher oxide signal, which leads to their being bright in the 20.25 eV image.

These changes result from agglomeration of $TiSi_2$ which has grown laterally a short distance onto the SiO_2 substrate from the polysilicon regions. The agglomeration of the silicide film exposes the underlying oxide substrate, thus leading to a higher oxide signal level in the lateral silicide regions. Agglomeration is not unexpected for the high temperature conversion anneal used, and was confirmed by SEM analysis of the sample. Micrographs showing lateral silicide growth and agglomeration in this SRAM sample are shown in Figure 4.

Clearly, spectromicroscopy is an effective way of studying the technologically important problem of $TiSi_2$ formation. We are planning on carrying out higher resolution experiments that will allow us to not only study local variations in the silicidation reaction, but also to definitively correlate chemical changes with the lateral distribution of C49 and C54 phases in patterned samples. We have already carried out preliminary experiments to this end at SSRL.[7] Future experiments will be carried out on ALS undulator beamline 12.0, where the MAXIMUM endstation is currently being permanently installed.

REFERENCES

1. Jongste, F. Prins, and G. Janssen, "Loss of titanium during formation of self-aligned titanium silicide," Mater. Lett. **8**, 273 (1989).
2. Beyers, D. Coulman, and P. Merchant, "Titanium disilicide formation on heavily doped silicon substrates," J. Appl. Phys. 61, 5110 (1987).

3. H. Jeon, C. Sukow, J. Honeycutt, G. Rozgonyi, and R. Nemanich, "Morphology and phase stability of $TiSi_2$ on Si," J. Appl. Phys. **71**, 4269 (1992).
4. K. Saenger, J.C. Cabral, L. Clevenger, R. Roy, and S. Wind, "A kinetic study of the C49 to C54 $TiSi_2$ conversion using electrical resistivity measurements on single narrow lines," J. Appl. Phys. **78**, 7040 (1995).
5. R. Roy, L. Clevenger, J.C. Cabral, K. Saenger, S. Brauer, J. Jordan-Sweet, J. Bucchignano, G. Stephensen, G. Morales, and J.K.F. Ludwig, "In situ x-ray diffraction analysis of the C49-C54 titanium silicide phase transformation in narrow lines," Appl. Phys. Lett. **66**, 1732 (1995).
6. W. Ng, A. Ray-Chaudhuri, S. Liang, S. Singh, H. Solak, J. Welnak, F. Cerrina, G. Margaritondo, J. Underwood, J. Kortright, and R. Perera, "High resolution spectromicroscopy reaches the 1000 angstrom scale," Nucl. Instr. and Meth. **A347**, 422 (1994).
7. S. Singh, H. Solak, N. Krasnoperov, F. Cerrina, A. Cossy, J. Diaz, J. Stohr, and M. Samant, "An x-ray spectromicroscopic study of the local structure of patterned titanium silicide," Submitted for publication.

This work was supported by the U.S. Department of Energy under Contract No. DE-FG02-96ER45569.

Principal investigator ($TiSi_2$ experiments): Sangeet Singh, Dept. of Electrical and Computer Engineering, University of Wisconsin-Madison. Email: singh@xraylith.wisc.edu. Telephone: 608/265-6074

Principal investigator (MAXIMUM): Franco Cerrina, Dept. of Electrical and Computer Engineering, University of Wisconsin-Madison. Email: cerrina@xraylith.wisc.edu. Telephone: 608/263-4955

Beamline 7.0.1 Abstracts

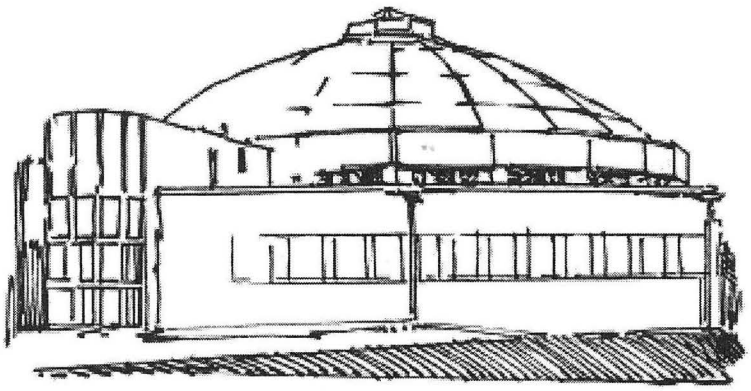

In-Line Phase Retarder and Polarimeter for Conversion of Linear to Circular Polarization

J.B. Kortright,[1] N.V. Smith,[1] J.D. Denlinger,[1] E. Rotenberg,[1] A. Warwick[1]
K.W. Goodman,[2] J.G.Tobin,[2] W.J. Gammon,[3] D.P. Pappas,[3] F.O. Schumann,[4] R.F. Willis[4]
[1]Lawrence Berkeley National Laboratory, Berkeley, CA 94720
[2]Lawrence Livermore National Laboratory, Livermore, CA, 94550
[3]Department of Physics, Virginia Commonwealth University, Richmond, VA 23284-2000
[4]Department of Physics, Pennsylvania State University, University Park, PA, 16802

INTRODUCTION

An in-line polarimeter including phase retarder and linear polarizer was designed and commissioned on undulator beamline 7.0 for the purpose of converting linear to circular polarization for experiments downstream. In commissioning studies, Mo/Si multilayers at 95 eV were used both as the upstream, freestanding phase retarder and the downstream linear polarizer. The polarization properties of the phase retarder where characterized by direct polarimetry and by collecting MCD spectra in photoemission from Gd and other magnetic surfaces.

The resonant birefringence of transmission multilayers results from differing distributions of s- and p-component wave fields in the multilayer when operating near a structural (Bragg) interference condition.[1,2] The resulting phase retardation is especially strong when the interference is at or near the Brewster angle, which is roughly 45° in the EUV and soft x-ray ranges.

EXPERIMENT

The polarimeter is shown schematically in Figure 1, and is conceptually similar to a device already in use at the ALS (described in ref. 3). The new apparatus is installed between the exit slit and refocusing mirrors on beamline 7.0, at a point where the beam is defocused. Following an entrance aperture and I_0 grid is the transmission phase retarder, whose incidence angle θ_R and azimuthal angle α_R can be varied continuously. On a separate azimuthal stage rides the tunable linear polarizer formed by a multilayer with laterally graded period set to reflect at 45° into a Si diode detector. Continuous tuning of the polarizer is achieved by translating it along the period

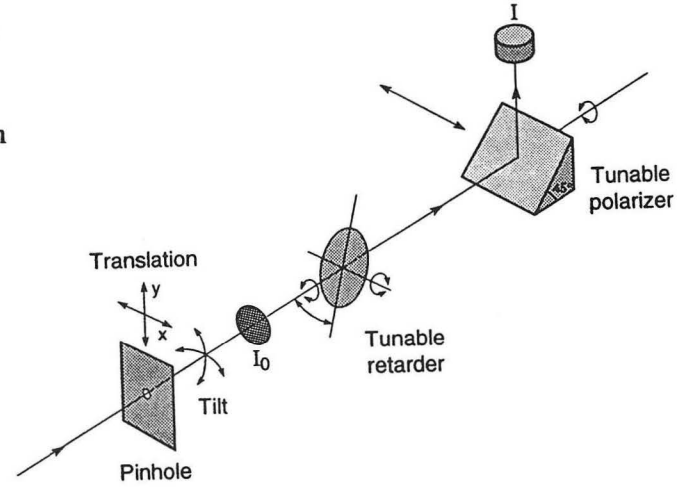

Figure 1. Schematic of the polarimeter. A free-standing transmission multilayer forms the phase retarder, and a reflection multilayer acts as a linear polarizer. The polarizer can be translated out of the beam, allowing it to pass to downstream experiments. The entire apparatus can likewise be translated out of the beam when not in use, allowing the beam to transit the polarimeter uninterrupted.

gradient. Additional translation of the polarizer stage has been added to the current design so the polarizer can be entirely withdrawn from the beam, allowing it to pass through the retarder only to downstream experiments. These motions occur inside of a vacuum chamber housing the optics. In addition, the entire chamber can be translated laterally to withdraw all optical elements from the beam, allowing it to pass uninterrupted through the device. In-line operation of the new apparatus is facilitated by side-mounted feedthroughs to actuate all motions; the earlier version introduces azimuthal rotations from the downstream end, thus precluding in-line operation.

95 eV was chosen for initial operation of the phase retarder because Mo/Si multilayers perform very well just below the Si $L_{2,3}$ edge at 100 eV. Mo/Si multilayers formed both the free-standing phase retarder (d = 87.4 Å, N = 30) and linear polarizer (d = 92.0 Å, N = 30). The calculated retardation showing the general form of the expected phase difference between transmitted s- and p-components for this retarder is shown in Figure 2a. The Bragg condition occurs just above 50°, and a resonance in retardation is clearly evident about this condition.

RESULTS

After initial alignment of the polarimeter to place the optical (azimuthal) axes of the retarder and polarizer along the beam direction, polarizer scans were made to analyze the polarization of the beam transmitted through the retarder at different incidence angles. Figure 2 shows two such scans, one with θ_R near normal incidence and the other with θ_R on the low angle side of the Bragg

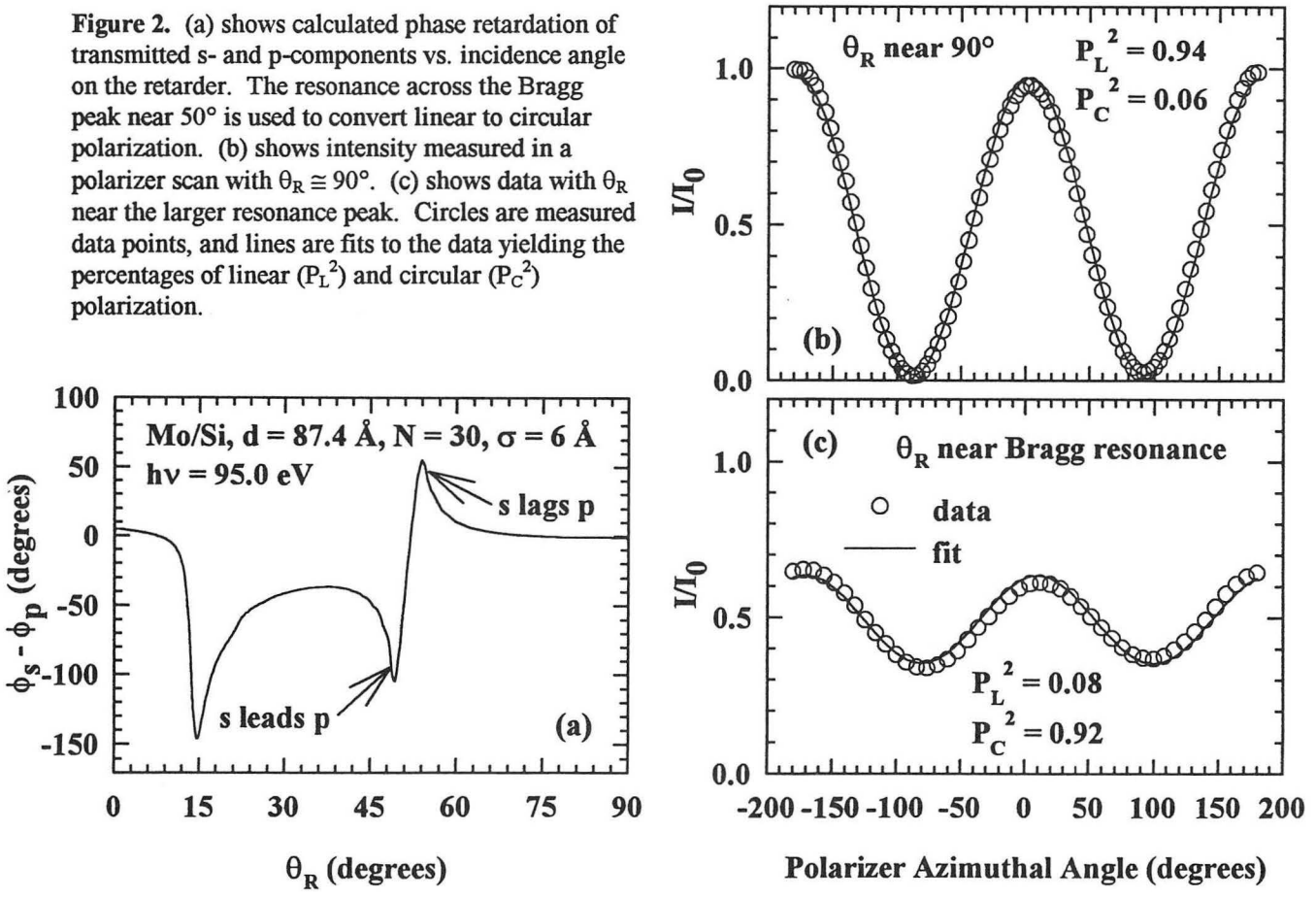

Figure 2. (a) shows calculated phase retardation of transmitted s- and p-components vs. incidence angle on the retarder. The resonance across the Bragg peak near 50° is used to convert linear to circular polarization. (b) shows intensity measured in a polarizer scan with $\theta_R \cong 90°$. (c) shows data with θ_R near the larger resonance peak. Circles are measured data points, and lines are fits to the data yielding the percentages of linear (P_L^2) and circular (P_C^2) polarization.

resonance near the larger retardation peak. (Note that the large retardation peak near 15° occurs at the critical angle for total reflection and is not useful because of low transmission.) Following standard procedures to analyze rotating polarizer scans,[4] we fit the data to obtain the first 3 of 4 Stokes parameters (S_0, S_1, S_2, S_3) that provide directly the degree of linear polarization $P_L \equiv (S_1^2 + S_2^2)^{1/2}/S_0$. The degree of circular polarization $P_C \equiv S_3/S_0$ is obtained indirectly from $P_L^2 + P_C^2 = 1$, assuming no unpolarized component. Polarization measurements at several beamlines at the ALS support the assertion that any unpolarized component is present at levels comparable to measurement uncertainty of about 0.01 in P_L^2 and P_C^2.

The polarization of radiation transmitted through the retarder shows the expected behavior. Near normal incidence (Fig. 2b), the transmitted radiation is predominantly linearly polarized. Incomplete linear polarization may result from residual birefringence near normal incidence or from imperfect optical alignment of the apparatus evident in the data. With θ_R near the Bragg peak (Fig. 2c), the transmitted beam is predominantly circularly polarized.

The sense of circular polarization can be changed from left- to right-circular by rotating the retarder in a prescribed manner keeping the incidence angle θ_R fixed. Data in Figure 2 were collected with the retarder azimuth at 45° with respect to the incoming linear polarization, thus resolving the incident linear beam into equal amounts of s- and p-components at the retarder. By rotation the optic azimuthally about the beam axis to -45°, equal amounts of s- and p-components are again incident on the optic, but the two components have exchanged roles resulting in helicities of opposite sense in the two different settings.

Photoemission experiments downstream verify the performance of the phase retarder and have begun to use its circular polarization routinely. Figure 3 shows valence band photoemission from a clean gadolinium surface excited by circular polarization at 95 eV having opposite helicity. Large shifts in the 4f level are seen, leading to the large MCD (difference) signal in the bottom panel. Under these operating conditions, a loss in flux by roughly a factor of 40 resulted from absorption in the multilayer together with losses in the grid and some occlusion of the beam by the entrance aperture. Even so, the intensity of circular polarization exceeds that available from out-of-plane bending magnet radiation.

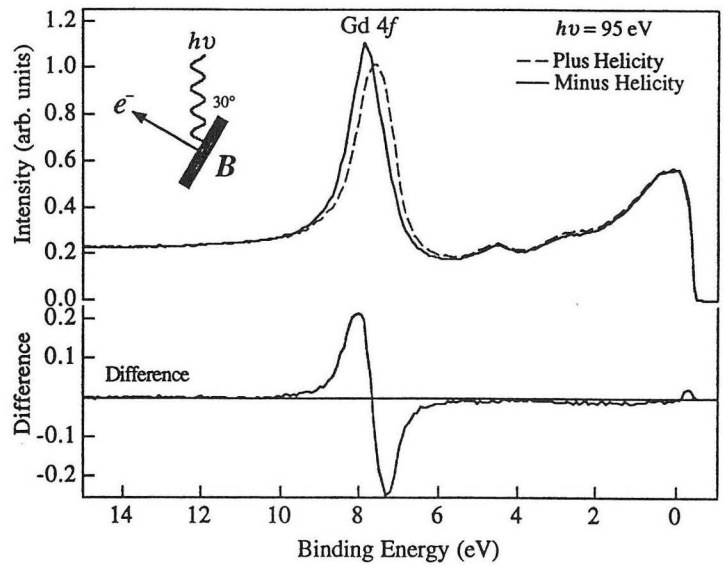

Figure 3. Photoemission spectra (along normal) from an ultrathin Gd film grown on Y (0001) taken with photons of opposite helicity is shown in the top. Changing the sense of circular polarization is accomplished by rotating the phase retarder about the beam to a symmetric position with respect to the incoming polarization. The MCD (difference) spectrum is shown in the bottom. Magnetization lies in-plane.

CONCLUSIONS

This work demonstrates that phase-retarding optical elements can be useful for conversion of linear to circular polarization. To our knowledge this is the first dedicated, in-line phase retarder and polarimeter based on multilayer optics. Free-standing transmission Mo/Si multilayers perform well as retarders up to 100 eV, and it is expected that other multilayer materials will produce large retardation up to 150 eV or so. As energies increase into the soft x-ray the effects of imperfections significantly reduce the interference effects resulting in phase retardation, making near quarter-wave plate operation with multilayers impossible. Other means are currently being investigated to convert linear to circular polarization at higher energies in the soft x-ray range of undulator beamline 7.0.

ACKNOWLEDGMENTS

The multilayer optics were grown in the labs of the Center for X-Ray Optics at LBNL. K.D. Franck provided expert design assistance, and S. Klingler provided expert mechanical support.

REFERENCES

1. J.B. Kortright and J.H. Underwood, Nucl. Instrum. Meth. A **291**, 272 (1992).
2. J.B. Kortright, H. Kimura, V. Nikitin, K. Mayama, M. Yamamoto, and M. Yanagihara, Appl. Phys. Lett. **60**, 2963 (1992).
3. J.B. Kortright, M. Rice, and K.D. Franck, Rev. Sci. Instrum. **66**, 1862 (1995).
4. see J.B. Kortright, M. Rice, Z. Hussain, et al., this report, for expanded discussion of analyzing polarizer scans.

This research was supported by the Director, Office of Energy Research, Office of Basic Energy Sciences, Materials Sciences Division. of the U.S. Department of Energy under Contract No. DE-AC03-76SF00098.

Principal investigator: Jeffrey Kortright, Materials Sciences Division, Lawrence Berkeley National Laboratory
E-mail: JBKortright@lbl.gov. Telephone: (510) 486-5960.

A Scanning Transmission X-Ray Microscope for Materials Science Spectromicroscopy at the ALS

T. Warwick[1], H. Ade[2], S. Cerasari[1,3], A. Garcia[1,2], S. Hayakawa[4], A. Hitchcock[5], E. Rightor[6], S. Seal[1], H. Shin[1,7], R Steele[1], B. Tonner[8] and J. Zhang[1]

[1]Advanced Light Source, Ernest Orlando National Laboratory, University of California, Berkeley California 94720.
[2]Department of Physics, North Carolina State University, Raleigh, North Carolina 27895.
[3]University Trieste, Materials Engineering Department, 34127 Trieste, Italy.
[4]Department of Applied Chemistry, University of Tokyo, Tokyo 113, Japan.
[5]BIMR, McMaster University, Hamilton, Ontario, L8S 4M1, Canada.
[6]DOW Chemical, 2301 N. Brazosport Blvd., Freeport, Texas 77541.
[7]Pohang Accelerator Laboratory, Pohang, Kyungbuk, 790-600, Korea.
[8]Department of Physics, University of Wisconsin, Milwaukee, Wisconsin 53211.

The brightness of the Advanced Light Source will be exploited by several new instruments for materials science spectromicroscopy over the next year or so. The first of these to become operational is a scanning transmission x-ray microscope with which near edge x-ray absorption spectra (NEXAFS) can be measured on spatial features of sub-micron size. Here we describe the instrument as it is presently implemented, its capabilities, some studies made to date and the developments to come.
This work builds on many years of research [1], developing this technique at the National Synchrotron Light Source at Brookhaven National Laboratory.

The Scanning Transmission X-ray Microscope makes use of a zone plate lens [2] to produce a small x-ray spot with which to perform absorption spectroscopy through thin samples. Figure 1 shows the main components of the microscope. The x-ray beam from ALS undulator beamline 7.0 emerges into the microscope vessel through a silicon nitride vacuum window 160nm thick and 300μm square. The vessel is filled with helium at atmospheric pressure. The zone plate lens is illuminated 1mm downstream from the vacuum window and forms an image in first order of a pinhole which is 3m upstream in the beamline. An order sorting aperture passes the first order converging light and blocks the unfocused zero order. The sample is at the focus a few mm downstream of the zone plate and mounted from a scanning piezo stage [3] which rasters in x and y so that an image is formed, pixel by pixel, by an intensity detector behind the

sample. Absorption spectra are measured point-by-point as the photon energy is scanned by rotating the diffraction grating in the monochromator and changing the undulator gap.

Presently, the microscope performs as follows:
The spectral resolution is typically 1 part in 3000, although the beamline can deliver photons at higher resolution (up to one part in 8000). The zone plates now in use are 200μm in diameter with an 80nm wide outer zone. The first order focal length of these zone plate lenses is 4mm at the carbon K edge (300eV). The measured spot size is approximately 150nm FWHM which is about 50% larger than the theoretical diffraction limit. Figure 2 shows a gold test pattern imaged with this scanning microscope.

The instrument can operate with 10^7 photons s^{-1} in the focused spot. This flux is sufficient to allow the use of an analog silicon diode as a detector, the diode current (averaged over a time window of 10 or 20 milliseconds per pixel) provides the pixel intensity in the image. An alternative photon-counting gas proportional counter with a silicon nitride window is provided. This is used at greatly reduced intensity (3×10^5 photons s^{-1}) for samples which are prone to radiation damage. Spectra are measured as the photon energy is scanned with a dwell of hundreds of milliseconds per energy point in order to average out the effects of beam intensity variations (a few percent at frequencies from about 5Hz to 20Hz). The photo-current from the metal order sorting aperture provides a normalization signal which can correct for slow changes in beam intensity from one scan to the next. The absorption spectra of a sub-micron region on the sample is measured by acquiring a spectrum through the sample, then repeating the spectral scan with the sample removed. At the carbon K edge the instrument delivers a spectrum with a 20% dip due to carbon absorption on the windows and mirrors. There is a small dip at the oxygen K edge. Nitrogen 1s spectra can also be measured, at high beam intensity, despite the nitride windows which reduce the spectral signal by about a factor of ten at the nitrogen edge.

The most difficult aspect of the microscope operation is the need to translate the zone plate along the direction of the photon beam in order to remain focused through the range of an absorption spectrum. This motion should occur precisely along the optical axis of the zone plate system, which is the line from the center of the pinhole through the center of the zone plate. Use of the beamline by

other experiments results in continued realignment of the beam into the microscope and the possibility of the pinhole being placed differently each run. The microscope control software includes a feature to compensate for misalignment by shifting the sample transversely to match the unwanted transverse motion of the zone plate with respect to the optical axis as it is translated along the beam direction during a spectral scan. By careful tuning of this algorithm, features can be measured as small as 0.5μm.

Two areas of research seem promising at present. One is polymer science, measuring the distinctive absorption spectra of large organic molecules at the carbon, oxygen and nitrogen K edges. In these experiments great care must be taken to avoid the effects of radiation damage and NEXAFS is superior to electron energy loss techniques which cause more damage [4]. A second area of unique application is the study of the chemistry of hydrated species by absorption spectroscopy. Here we take advantage of the environment of the microscope, which is usually operated in helium at atmospheric pressure, so that it is possible to measure samples which contain water. Hydrated species are very common in environmental science and various trial programs are beginning.

As an example, figure 3 shows some measurements made on sectioned Kevlar fibers at the nitrogen K edge. This illustrates the measurement of polymers in a controlled environment, where the removal of atmospheric nitrogen is essential in order to obtain reliable spectra. These measurements were made at full intensity through the nitride windows, which cause the intensity to drop about a factor of ten at the nitrogen edge, so that very careful normalization is required.

[1] S. Williams, C. Jacobsen, J. Kirz, J. Maser, S. Wirick, X. Zhang, H. Ade and M. Rivers, Rev. Sci. Instrum. 66(1995)1271

[2] E.H. Andersen, V. Boegli and L.P. Muray,
J. Vac. Sci. Tech.13 (1995) 2529

[3] Queensgate Instruments Inc., 90 Merrick Ave., East Meadow, New York 11664.

[4] E.G. Rightor, A.P. Hitchcock, H. Ade, R.D. Leapman, S.G. Urquhart, A.P. Smith, G.E. Mitchell, H.J. Shin, T. Warwick. J. Phys. Chem, 1997, in press.

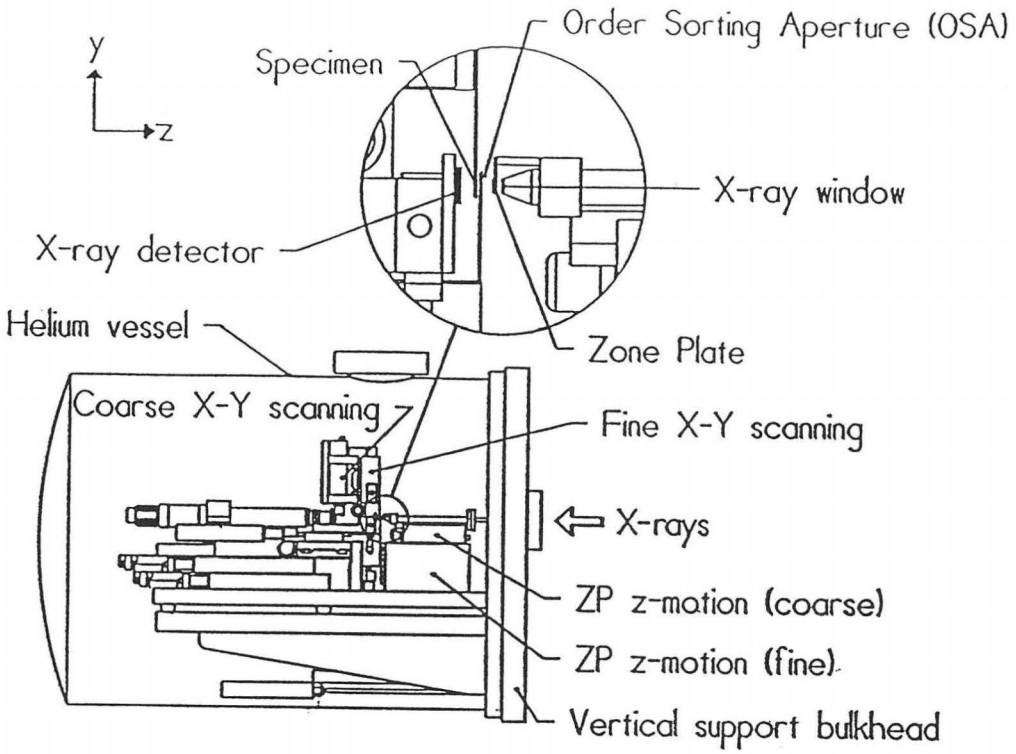

Figure 1. Geometry of the STXM. The helium vessel is shown closed over the microscope from the left and sealed against the vertical support bulkhead.

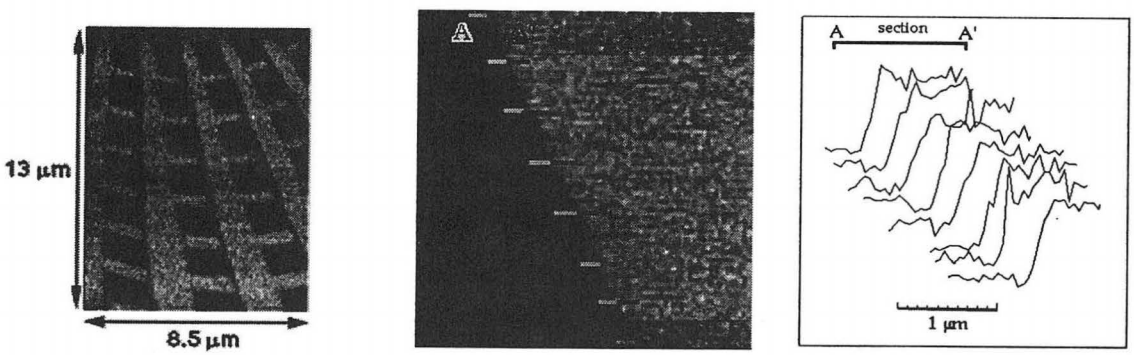

Fig2. Part of an image of a test pattern made by electron beam lithography in gold on a silicon nitride membrane. The profile of image intensity across the etched edge of a silicon wafer is also shown and gives a measure of the size of the x-ray spot; 150nm FWHM.

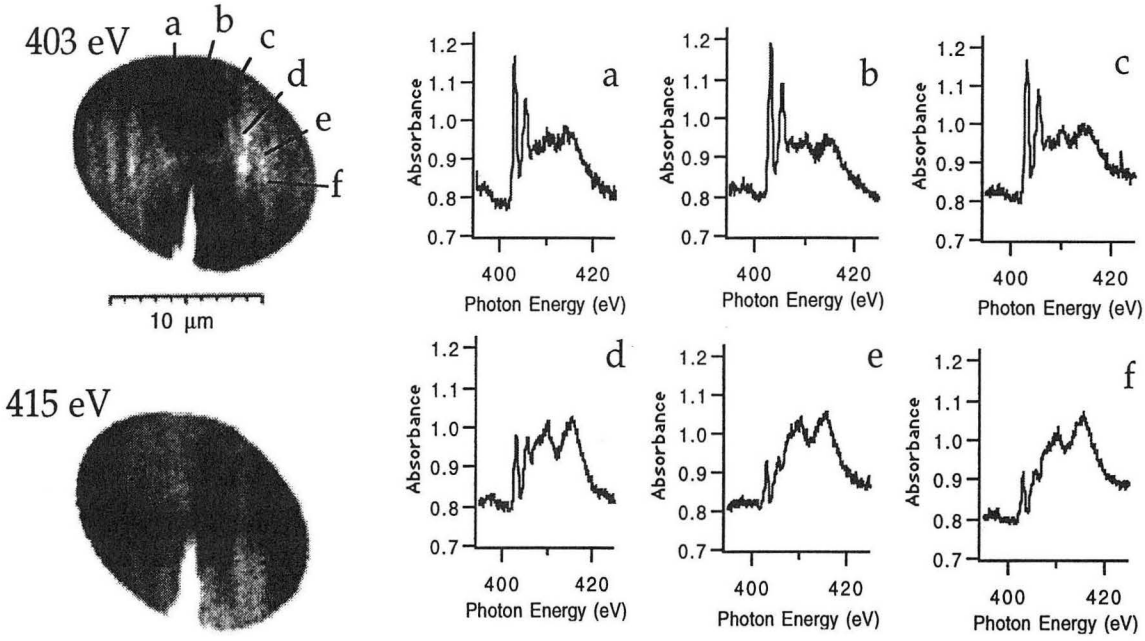

Figure 3. Transmission NEXAFS images of a sectioned Kevlar fiber with radially oriented hydrogen-bonded sheets between adjacent polymer chains shows the sensitivity to the relative orientation between the x-ray polarization plane and the molecular orbitals of nitrogen in the molecule. Nitrogen 1s electrons can be excited into these orbitals only when the orbitals are oriented parallel to the electric vector of the linearly polarized light. π^* orbitals are sharp peaks, the σ^* transition give broader peaks at higher energy. The π^* and σ^* orbitals are pependicular and each gives a cosine^2 intensity distribution with opposite contrast around the fiber, with respect to the horizontal polarization plane.

Principal Investigator: Tony Warwick, ALS, Mailstop 2-414, Ernest Orlando Lawrence Berkeley National Laboratory, 1 Cyclotron Road, Berkeley, CA 94720,
Email: warwick@lbl.gov Telephone: (510) 486 5819

This work was supported by the Director, Office of Energy Research, Office of Basic Energy Sciences, Materials Sciences Division, of the U.S. Department of Energy under Contract No. DE-AC03-76SF 00098

Band Mapping of Surface States vs. Adsorbate Coverage

Eli Rotenberg,[1,2] Steven D. Kevan,[1] J. D. Denlinger,[3] and Jin-Wook Chung[4]

[1]Department of Physics, Univerisity of Oregon, Eugene OR 97403
[2]Advanced Light Source, MS 2-400, Lawrence Berkeley National Laboratory, Berkeley CA 94720
[3]Department of Physics, University of Wisconsin-Milwaukee
[4]Department of Physics, POSTECH, HyoJa-Dong San 31 KyungBuk Pohang, Korea, 790-784

INTRODUCTION

The theory of electron bands, which arises from basic quantum mechanical principles, has been the cornerstone of solid state physics for over 60 years. Simply put, an energy band is an electron state in a solid whose energy varies with its momentum (similar to, but with a more complicated dependence than, how a free electron's energy is proportional to its momentum squared). Much attention over the last 15 years has been given to the study of band structure of surfaces and interfaces, especially as the applications of these two-dimensional systems have become increasingly important to industry and science.[1]

The ultraESCA endstation at beamline 7.01 at the Advanced Light Source was developed for very high-energy- (~50 meV) and angular- (<1°) resolution photoemission studies of materials.[2] The high flux (typically 10^{12} photons/sec) makes the detailed study of the *evolution* of bands possible. We are interested in learning how, when one forms a chemical bond between a metal and an overlaying atom or molecule, the resulting charge transfer to or from the adsorbate affects the surface bands. In some cases of interest, intermediate coverages lead to different band structure than at the extremes of clean and saturated surfaces. Surfaces of tungsten are particularly interesting, as their atomic geometry has been shown to be exquisitely sensitive to both the surface vibrational and electronic properties. In this study, we looked at the surface bands of tungsten ((110) surface, Figure 1), as a function both of *coverage* and *mass* of overlaying atoms. The adsorbed atoms were hydrogen and the alkali atoms lithium and cesium.

EXPERIMENT

The tungsten crystal was cleaned in ultrahigh vacuum using standard surface science techniques. Care was taken to refresh the clean surface after about 20 minutes to ensure no residual gases contaminated the sample. The experimental geometry is discussed in another abstract in this report. Experiments were carried out at Beamline 7.01; the electron spectrometer has an overall angular resolution was better than +/- 0.5 degrees, and the total energy width was kept less than 60 meV; under these conditions spectra of adequate statistics could be acquired in about 30 seconds. Hydrogen exposure was carried out by backfilling the chamber with hydrogen molecules. Alkali exposure was from getter sources (SAES Getters). Coverage was calibrated according to the W 4f surface core-level shifts,[3] as well as from the alkali surface core-level shifts in the case of Li and Cs.

RESULTS

Figure 2 shows the basic idea of the experiment. A photoelectron spectrum (Fig. 2(a)) acquired at angle θ from normal emission is comprised of features, which are identified as either surface- or bulk-related. (For simplicity, we will refer to these features as "states" although some of the surface features are more properly termed "resonances.") The energy and the angle θ of each point have been converted to $k_{||}$, electron momentum parallel to the surface.

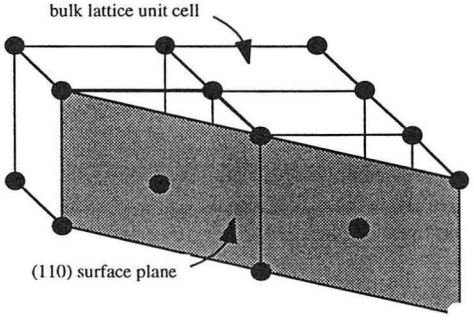

Figure 1. The (110) surface of tungsten.

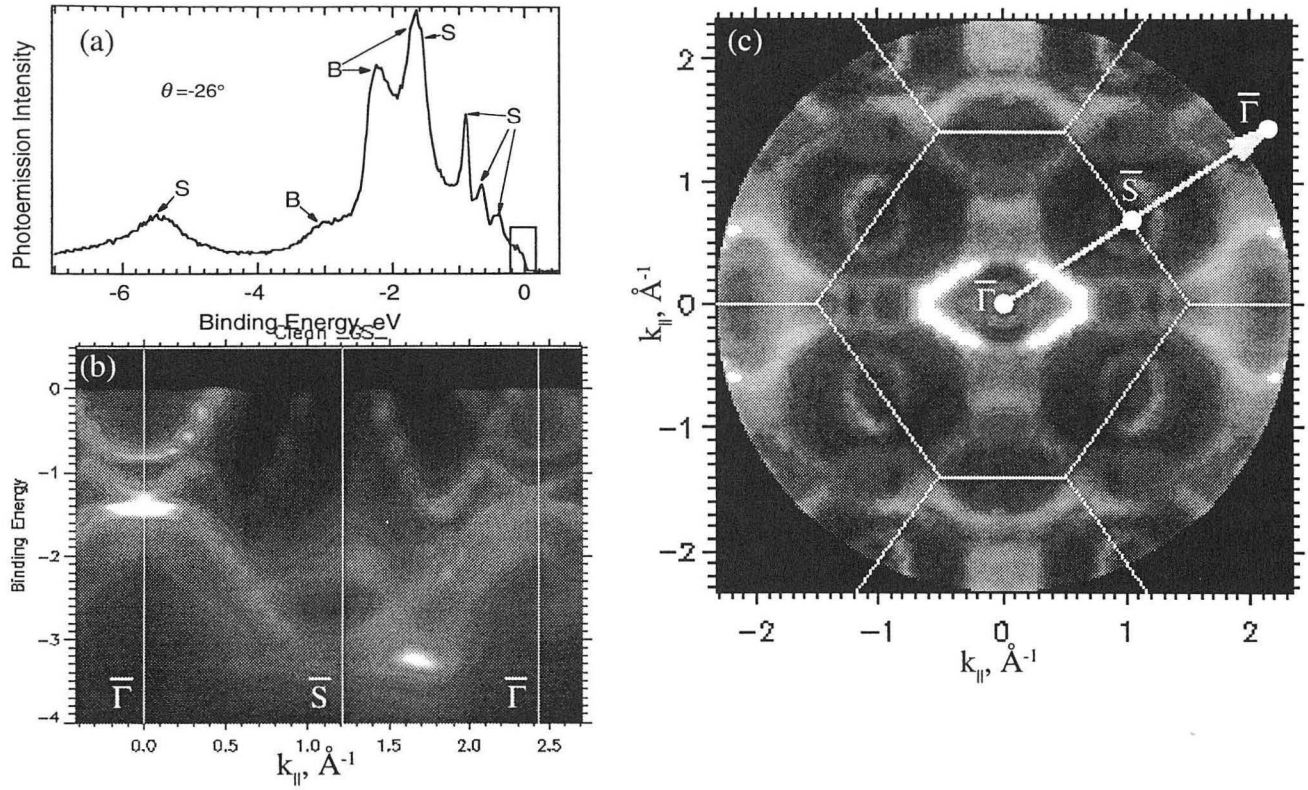

Figure 2. Basic types of spectroscopy used in this experiment. (a) Photelectron spectrum of the valence band for a particular emission angle θ. (b) A mapping of many such spectra into an image relating electron band energy to momentum parallel to the surface, called a band structure plot. (c) Angular map of electrons at zero binding energy (Fermi Level). The intensity along the arrow in (c) is the same as the zero-energy intensity in (b).

When such spectra are repeatedly acquired over a range of angles, each peak's energy varies with its momentum, and the resulting energy *vs.* momentum data are plotted in an intensity map (Fig. 2b), which immediately shows the electronic band structure along a particular azimuth angle ϕ. An alternate way to probe the momentum space is to window the electron detector at the zero-energy, or Fermi-edge level (illustrated by the rectangle in Fig. 2(a)) while sampling both angles θ and ϕ. In this way, one gets a map (see Fig. 2(c)) of the Fermi-Level crossings of the bands in Fig. 2(b). The connection between Figs. 2(b) and (c) is that the intensity along the white arrow in (c) is the same as the intensity near zero energy of (b). In both (b) and (c), the white lines indicate directions of high-symmetry in momentum space.

Figure 3 compares (a) clean to (b) 1/2 and (c) 1 monolayer (ML) hydrogen on this surface band structure. Some bands are completely removed, some new bands are created, and others are modified only by an approximately rigid shift in the binding energy direction, which evolves smoothly with hydrogen coverage.[4] The significance of 1/2 ML is that at this coverage, each W surface atom is accompanied on the average by one hydrogen atom. We observe that the bands which are removed by 1 ML hydrogen are essentially gone already at 1/2 ML. In a molecular picture, what's happening is that the bands that are eliminated are associated with tungsten dangling orbitals which bond directly with hydrogen; the new bands that are created are associated with these new hydrogen-tungsten orbitals, and the bands which shift are essentially unaltered orbitals whose occupation changes as charge is transferred from the hydrogen atoms into the substrate bonds. Complications with this simple interpretation will be discussed in greater detail in a future publication. One should remember that although the data may be interpreted through charge transfer (a real-space property), we measure changes in momentum-space; theoretical modeling is needed to assert the spatial distribution of charge.

Figure 4 shows the effect of hydrogen and lithium adsorption on the Fermi level crossings. The small elliptical figure #1 (among others) in the clean sample's pattern (a) is removed upon 1 ML hydrogen saturation, while there are two surface states #2-3 which split off from the bright bulk-tungsten-related feature in the center. The rate at which they move away from the center as a function of hydrogen coverage can be directly related to the rate that charge is transferred into the underlying bands.

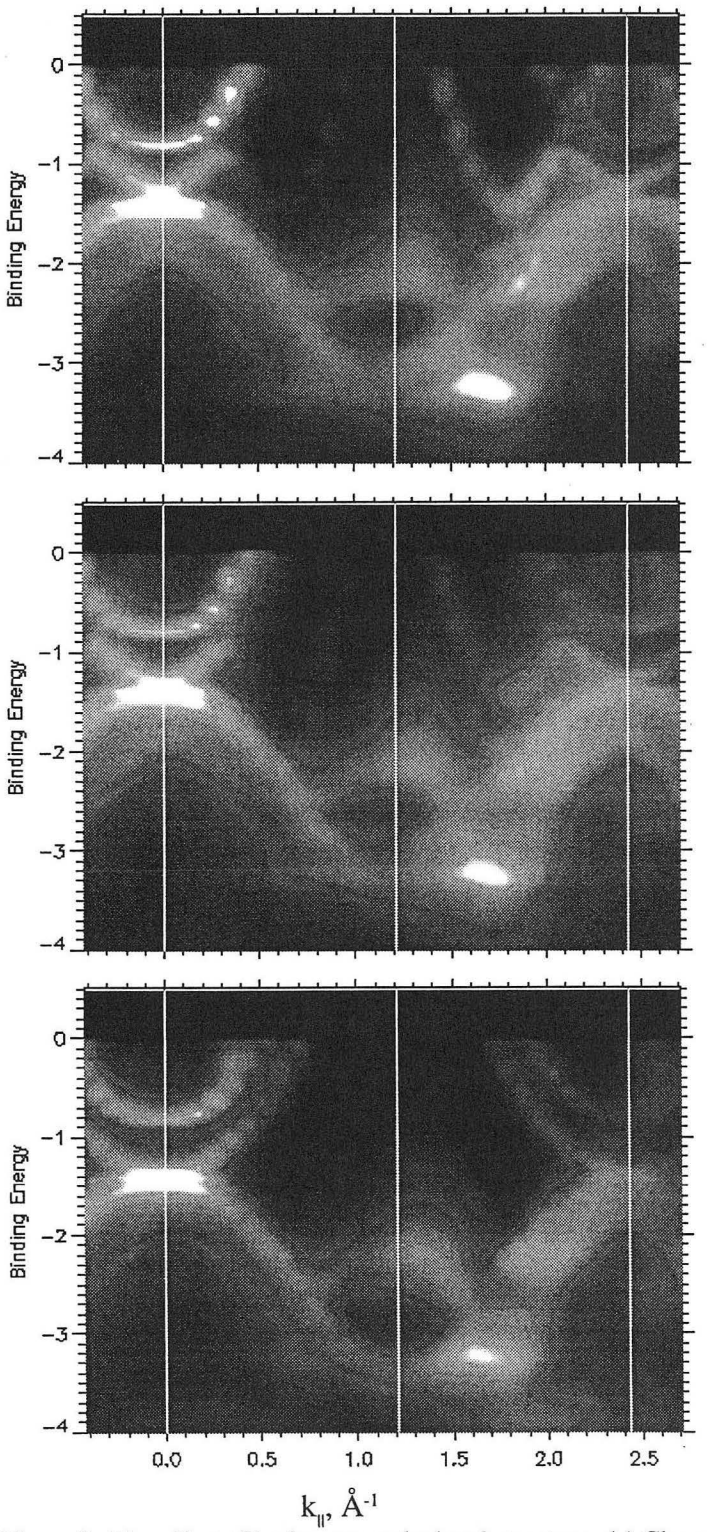

Figure 3. The effect of hydrogen on the band structure. (a) Clean tungsten (b) 1/2 ML hydrogen. (c) 1 ML H.

Chemically speaking, lithium is identical to hydrogen, so one expects similar results. The differences are striking however. The lithium coverage in (c) is only 1/3 that of hydrogen in (b), but already the surface bands have moved roughly the same amount. This suggests a much greater transfer of charge from Li to tungsten bands relative to H. In (d), the bands have moved even further out from the center. The excess charge transfer is associated with a corresponding lack of interaction with the elliptical figure #1, which survives Li coverage apart from only a small change in size. This shows that Li does not interact chemically with the same tungsten orbitals with which hydrogen interacts. Results for cesium, not presented here, come to similar conclusions, although with less overall band motion than in the lithium case.

DISCUSSION

We presented above some examples showing the rich information on chemical bonding and charge transfer one can extract from band structure measurements. In addition to information on electron charge transfer and bonding which we presented above, there are other issues as well, especially related to the exact nature of the Fermi level crossings in Fig. 4, for example. For metals in general, many important properties such as magnetism, vibrations, superconductivity, etc., depend intimately on the response of electrons at the Fermi level to electromagnetic disturbances. This electron response is called screening, and its strength depends on the individual and relative momenta of the electrons involved. The precise shape of the contours in figure 4(b), for example, are

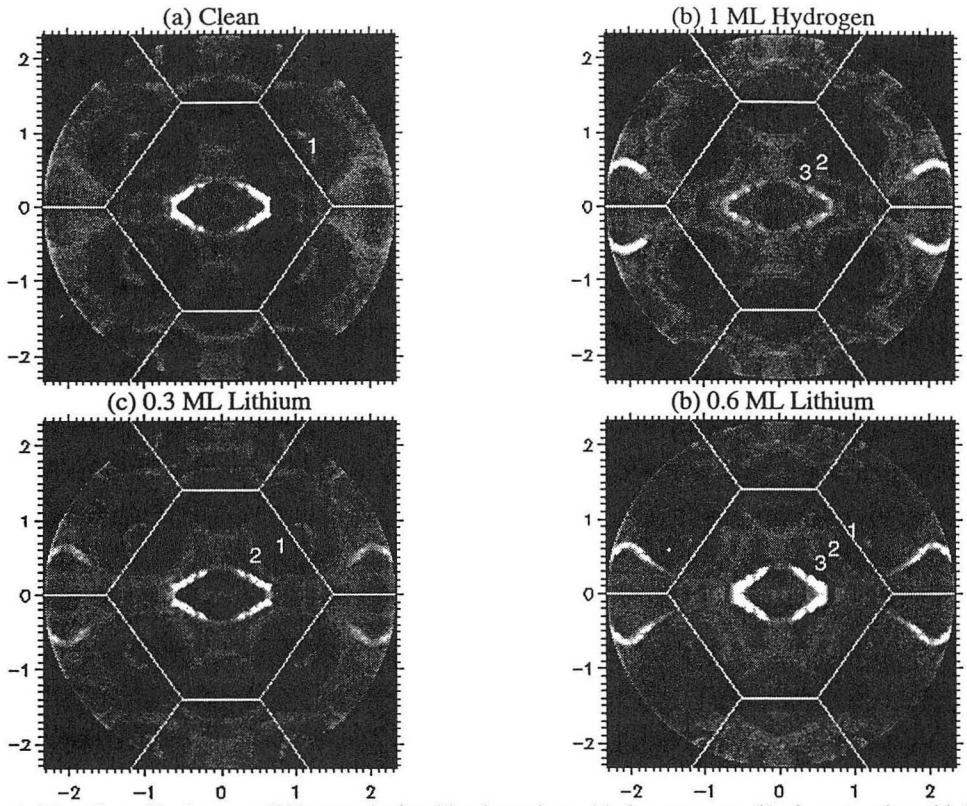

Figure 4. The effect of hydrogen or lithium on the fermi level crossings. (a) clean tungsten (b) after saturating with 1 ML of hydrogen. (c) after depositing ~0.3 ML of lithium. (d) after depositing ~0.6 ML of lithium. Note the images have slightly different intensity scales.

vibrations of the interfacial tungsten atoms in the presence of hydrogen, an issue which we are currently examining. Such anomalies can be strong enough to force a dramatic surface reconstruction which has been suggested.[5]

In the future, we hope to expand the study by correlating the electronic properties of these systems with structural studies using x-ray photoelectron diffraction.[6] We also want to expand the study to other alkalis as well as atoms in other columns of the periodic table.

ACKNOWLEDGEMENTS

We wish to thank K.H. Jeong, M. Scheffler, and P. Ruggerone for useful discussions. JWC acknowledges financial support from the Seo-Am Funds.

REFERENCES

[1] For reviews relevant to this work, see S. D. Kevan and J. W. Chung, in Electronic Surface and Interface States on Metallic Systems, E. Bertel and M. Donath, eds. (World Scientific, 1994).
[2] J. D. Denlinger *et al*, Rev. Sci Instrum. **66**, 1342 (1995); T. Warwick et al, Rev. Sci. Instrum. **66**, 2037 (1995).
[3] E. Rotenberg *et al*, elsewhere in this activity report
[4] A. B. Andrews, D. M. Riffe, and G. K. Wertheim, Phys. Rev. B **49**(12), 8396 (1994).
[5] R. H. Gaylord, K. H. Jeong, and S. D. Kevan, Phys. Rev. Lett. **62**(17)2036 (1989).
[6] J. W. Chung, S. C. Ying, and P. J. Estrup, Phys. Rev. Lett. **56**(7) 749 (1986).
[7] see Len et al, elsewhere in these abstracts.

This work was supported by the U.S. Department of Energy, Division of Materials Science under grant DE-FG06-86ER45275.

Principal investigator: Stephen D. Kevan, Department of Physics, University of Oregon. Email: kevan@oregon.uoregon.edu. Telephone: 541-346-4742.

Chemical Speciation of Polyurethane Polymers by Soft-X-Ray Spectromicroscopy

E.G. Rightor[1], A.P. Hitchcock[2], S.G. Urquhart[2], H. Ade[3], A.P. Smith[3], A. Garcia[3], R. Steele[4], S. Seal[4], S. Cerasari[4], T. Warwick[4] and B.P. Tonner[5]

1. Dow Chemical, Bldg 470, 2301 N. Brazosport Blvd. B-1470, Freeport, TX 77541
2. BIMR, McMaster University, Hamilton, ON L8S 4M1, Canada
3. Department of Physics, North Carolina State University, Raleigh, NC 27895
4. Advanced Light Source, Lawrence Berkeley Lab, Berkeley, CA 94720
5. Dept. of Physics, University of Wisconsin-Milwaukee, Milwaukee, WI 53202

Polyurethane polymers are a versatile class of materials which have numerous applications in modern life, from automotive body panels, to insulation, to household furnishings. Phase segregation helps to determine the physical properties of several types of polyurethanes. Polymer scientists believe that understanding the connections between formulation chemistry, the chemical nature of the segregated phases, and the physical properties of the resulting polymer, would greatly advance development of improved polyurethane materials. However, the sub-micron size of segregated features precludes their chemical analysis by existing methods, leaving only indirect means of characterizing these features. For the past several years we have been developing near edge X-ray absorption spectromicroscopy to study the chemical nature of individual segregated phases. Part of this work has involved studies of molecular analogues and model polymers, in conjunction with quantum calculations, in order to identify the characteristic near edge spectral transitions of important chemical groups [1]. This spectroscopic base is allowing us to study phase segregation in polyurethanes by taking advantage of several unique capabilities of scanning transmission x-ray microscopy (STXM) - high spatial resolution (~0.1 μm), high spectral resolution (~0.1 eV at the C 1s edge), and the ability to record images and spectra with relatively low radiation damage.

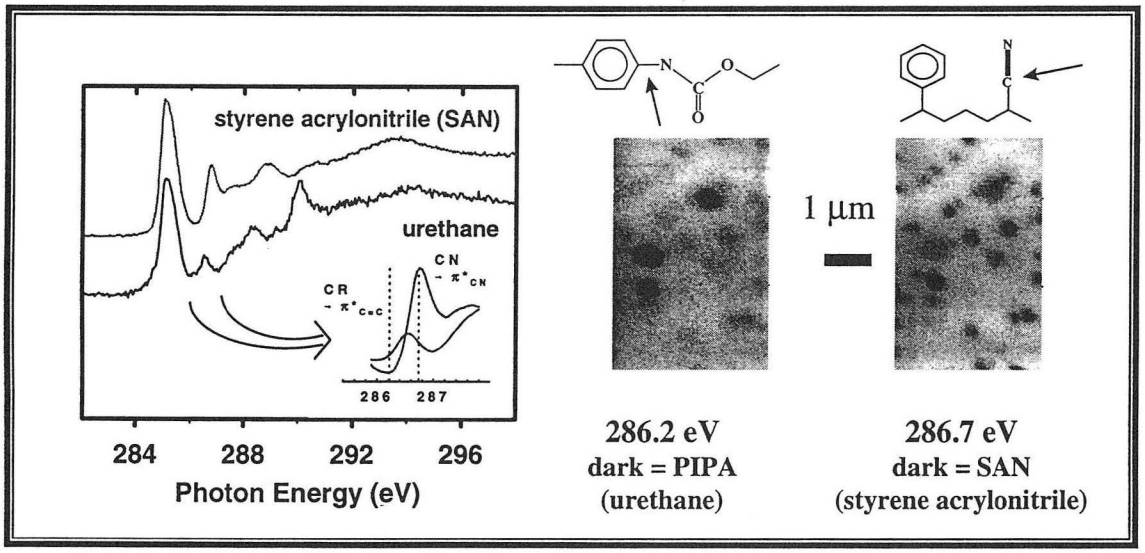

Figure 1. (left) C 1s spectra of SAN and urethane (=carbamate) filler materials. (right) STXM images of a polyurethane polymer containing SAN and carbamate-based fillers. Spectral differences in the 286-287 eV region allow one to distinguish particles, which are indistinguishable at other energies in the C 1s region.

The beamline 7.0 STXM at ALS is being used to study microtomed sections or cast films of polyurethanes. Additional experimental details on the zoneplate microscope and beamline can be found elsewhere [2]. A related study of polyethylene terephthalate involving a direct comparison of STXM and electron energy loss spectroscopy in a transmission electron microscope (TEM-EELS) has shown that, for C 1s spectroscopy, the STXM technique has 500 times less radiation damage than TEM-EELS carried out under similar spectral and spatial resolution [3]. However, experiments with the bright X-ray beam at the ALS STXM have shown that, although the radiation damage to beam sensitive polymers is lower than with other techniques, one still needs to be wary of damage [4]. The development of a high performance gas proportional counter has aided our polymer studies at the ALS.

One method used both to reduce product cost and to control the microstructure and thus the physical properties of polyurethane polymers is the addition of filler particles of various types. Spectroscopic differences between various fillers in polyurethanes can be imaged with STXM by selecting the incident photon energy. Fig. 1 shows an example in which two chemically different segregated particles in a polyurethane are differentiated by imaging at characteristic transitions with highly monochromatized X-rays. There is only 0.5 eV energy difference between characteristic transitions for styrene acrylonitrile (SAN) (286.7 eV), and PIPA, a carbamate-based filler (286.2 eV), but that is enough for STXM to distinguish these particles, even in the presence of a matrix that contributes signal in the region of interest.

STXM can also be used to quantify the amounts of various components using spot analysis. The relative amounts of urea and carbamate (urethane) in polyurethanes is closely linked to formulation and processing, and thus it is an important quantity to measure. Analysis of this ratio is complicated by the presence of polyol (polyether chains) in the polymer which contributes signal in the same spectroscopic region. Using polymer reference standards with known chemical composition, we have isolated the spectral signal corresponding to the urea and urethane components (which is only about 20%) and then quantified the amounts of these two components as shown in Fig. 2. We have carried out validation checks on polyurethane standards at both the ALS and NSLS STXM facilities to confirm the

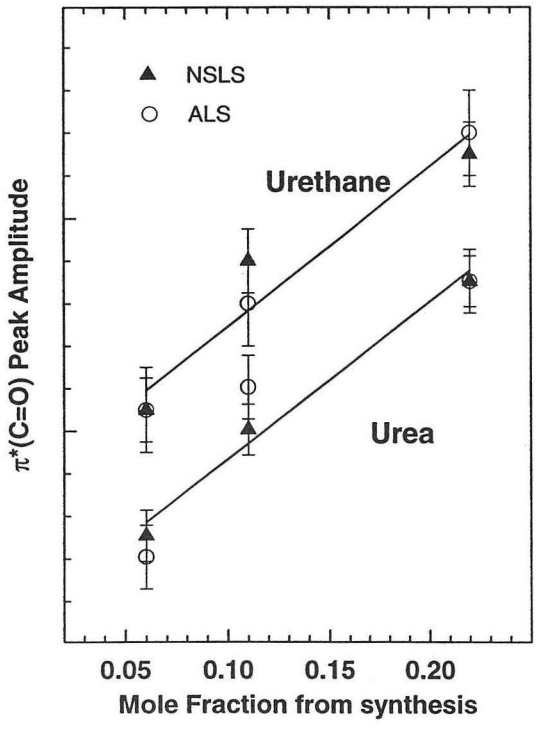

Figure 2. Correlation of peak heights of π*(CO) signals from urea and urethane, with the urea and urethane content predicted from the formulation. Note the good agreement for results from NSLS and ALS.

reproducibility of these results. This has been a major accomplishment of our work. STXM provides a tool that allows chemical composition in complex materials to be studied for the first time at sub-micron scale with low radiation damage.
The BL 7.0 STXM at the ALS is a powerful tool for measuring the microstructure of radiation sensitive organic polymers using spectromicroscopy. Presently we are:

- extending our measurements to other core edges, including N 1s, O 1s and F 1s;
- investigating alternative detection methodologies such as electron and fluorescence yield to complement the transmission detection; and
- exploring the advantages of STXM spectromicroscopy for polymer characterization by investigating different classes of polymer materials.

Based on the pioneering work of Ade, Kirz and collaborators at the NSLS X-1A STXM, as well as our work and that of others at the ALS BL 7.0 STXM, it is clear that scanning X-ray transmission microscopy using soft X-rays can provide information about the chemical origin of phase segregation in radiation-sensitive materials on a sub-micron scale. This information is difficult or impossible to obtain by other means.

REFERENCES

1. S.G. Urquhart, A.P. Hitchcock, E.G. Rightor, R.D. Priester, R.D. Leapman, J. Polymer Sci. B. 33, 1593, (1995).
2. T. Warwick, et al., this report; T. Warwick, et al., Rev. Sci. Inst. (to be published).
3. T. Warwick, H. Padmore, H. Ade, A. P. Hitchcock, E. G. Rightor, B. P. Tonner, J. Elec. Spectr. Rel. Phenom., 1997, in press.
4. E.G. Rightor, A.P. Hitchcock, H. Ade, R.D. Leapman, S.G. Urquhart, A.P. Smith, G.E. Mitchell, H.J. Shin, T. Warwick, J. Phys. Chem, 1997, in press.

The SAN reference spectrum shown in Fig. 1 was acquired at the NSLS X-1A STXM. We thank Brian Tonner (BL 7.0 PRT leader), the other BL 7 PRT members who have assisted our studies, and the ALS staff for their expert operation of the facility. This work was supported by the Director, Office of Energy Research, Office of Basic Energy Sciences, Materials Sciences Division, of the U.S. Department of Energy, under contract No. DE-AC03-76SF00098, Dow Chemical and NSERC (Canada). H. Ade acknowledges an NSF Young Investigator Award (DMR-9458060).

Principal Investigator: Ed Rightor, Dow Chemical, Bldg. 1470, 2301 N. Brazosport Blvd. B-1470, Freeport, TX 77541. Email: egrightor@ldow.com. Telephone: 409-238-3616.

Detection of Subsurface Core-Level Shifts in Si 2*p* Core-Level Photoemission from Si(111)-(1x1):As

J.J. Paggel,[1] M. Hasselblatt,[2] K. Horn,[2] J.D.Denlinger,[3]and E. Rotenberg[4]
[1]Department of Physics, Philipps-Universität Marburg, D-35032 Marburg, Germany
[2]Fritz-Haber Institut der Max-Planck-Gesellschaft, D-14195 Berlin, Germany
[3]Department of Physics, University of Wisconsin-Milwaukee, Milwaukee WI 53201
[4]Department of Physics, University of Oregon, Eugene, OR 97403

The (7 x 7) reconstruction of the Si(111) surface arises from a lowering of energy through the reduction of the number of dangling bonds. This reconstruction can be removed by the *adsorption* of atoms such as hydrogen which saturate the dangling bonds, or by the *incorporation* of atoms, such as arsenic which, because of the additional electron it possesses, can form three bonds and a nonreactive lone pair orbital from the remaining two electrons. Core and valence level photoemission [1,2] and ion scattering [3] data have shown that the As atoms replace the top silicon atoms. Previous core level spectra were interpreted in terms of a bulk and a single surface doublet [1]. Our present results demonstrate that the core level spectrum contains two more lines. We assign these to subsurface silicon layers which also experience changes in the charge distribution when a silicon atom is replaced by an arsenic atom.

A representative spectrum of the Si 2p core level of Si(111)-(1 x 1):As is shown in Figure 1. The data were recorded on beamline 7.0, with Si(111) wafers that were cleaned by a careful flashing procedure, and exposed to a beam of As_4 at a temperature of about 300 C. The spectrum

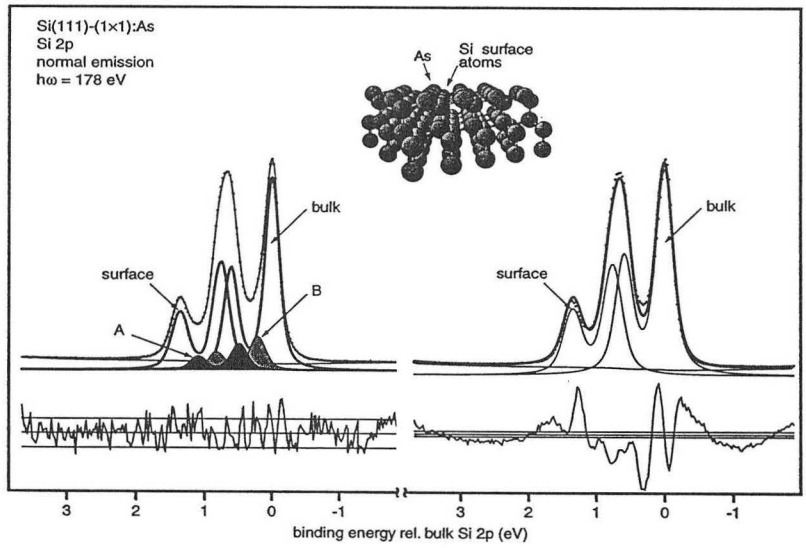

Figure 1: Si 2p core level spectrum of Si(111)-(1 x 1):As with a two-line (right) and four-line fit (left). Also shown are the residuals which clearly demonstrate that more than one surface core level line contribution is present. The lines in the residuum denote the scatter expected from the counting statistics.

is characterized by three sharp peaks, which from their intensity dependence with kinteic energy contain bulk and surface contributions. The right-hand side shows a line shape analysis in terms of one bulk and one surface line, shifted to higher binding energies by about 0.75 eV such as proposed previously. The residual clearly shows that this model function cannot properly describe the spectrum. The left-hand side has a fit in terms of two additional lines (shown in grey). All lines are numerical convolutions of Lorentzians and Gaussians, and the parameters (described in more detail below) were optimized by a nonlinear least squares algorithm based on the Levenberg-Marquardt recipe.

While the weaker lines do not give rise to separate peaks or clear shoulders in the spectra, their presence can be deduced in a straightforward way nevertheless. The (Lorentzian and Gaussian) width of the bulk peak can be derived unambiguously since the additional contributions have only a small contributions to this line. The width of the surface peak can likewise be deduced from the peak at highest binding energy which is hardly influenced by the bulk or the smaller lines. Thus the Gaussian and Lorentzian widths for the surface and bulk contributions are determined experimentally. Spin-orbit splitting and branching ratio are also derived from these intense lines. Thus the only free parameters which remain are the intensities and the peak positions. As seen on the right-hand side of Figure 1, attempts to fit with a bulk and one surface lines leads to large (a factor 20 larger than the statistical deviations) and systematic oscillations in the residuum. These oscillations cannot be removed by the addition of one more line with the width and branching ratio of the surface component, such that we are forced to include two lines as shown in Figure 1. The positions of these lines were arrived at in the following way. First, the least squares were optimized *simultaneously* for two spectra recorded at photon energies where the surface sensitivity is different, such that the intensities of surface and near-surface components are different. Secondly, a set of 40 spectra recorded over a photon energy range of 120 eV was fitted, and the peak positions for the smaller peaks were compared. This resulted in a set of stable fit parameters where the peak positions of the smaller peaks varied by only ± 20 meV. The core level shifts with respect to the bulk line are then -0.75 eV for the line marked "surface", -0.49 eV for line "A", and -0.28 eV for line "B".

Subsurface core level shifts are not unexpected since the modifications of the electronic structure and/or of photohole screening are likely to decay into the bulk and not just to affect the topmost substrate atoms. However, their detection is difficult because of the strong bulk and surface lines, and the fact that they are weaker in view of the larger distance of the emitting atoms from the surface. To our knowledge the only case where subsurface core level shifts have been inferred from a precise analysis of high resolution core level spectra is the Ta(110) surface [4]. We assign the atoms giving rise to peaks "A" and "B" to the second Si layer. As the charge flow from the topmost silicon atom towards the As atoms as inferred from the direction of the core level shift, might continue into the second layer, a sequence of decreasing magnitude of the shift could be related to the increasing distance to the As atom. The line intensities, when averaged over a large range of photon energies in order to average out diffraction effects, actually show that peak "B" is the more intense one throughout. This points towards a reverse assignment, suggesting that the charge rearrangment occurs in an oscillatory manner; an observation important for line assignment which merits further investigation.

The detection of subsurface components suggests that the adsorption of arsenic leads to charge flow also in the second double layer of the Si(111) surface. In view of the difference in atomic radius between As and Si, it was suggested that the (1 x 1):As surface is strained. The presence of charge rearrangement up to the second double layer implies that the atomic coordiantes also exhibit deviations from their ideal Si(111) counterparts, which might be detected through a LEED I/V or photoelectron diffraction analysis.

References

1. M. A. Olmstead, R. D. Bringans, R. I. G. Uhrberg, and R. Z. Bachrach, Phys. Rev. B **34**, 6041 (1986).
2. R. D. Bringans and M. A. Olmstead, J.Vac. Sci.Technol. B **6**, 1132 (1988).
3. R. Gunnella,E. R. Bullock,C. R. Natoli,R. I. G. Uhrberg, L. S. O.Johansson, Surf. Sci. **352-354**, 332 (1996).
4. D. M. Riffe and G. K. Wertheim, Physical Review B **47**, 6672 (1993).

This work was supported by Max-Planck-Gesellschaft, and Deutsche Forschungsgeme inschaft.

Principal investigator: Karsten Horn, Fritz-Haber-Institut der Max-Planck-Gesellschaft, D-14195 Berlin, Germany. Email: horn@fhi-berlin.mpg.de. Telephone: +030-8413-5640.

Direct Surface Magnetometry with Photoemission Magnetic X-Ray Dichroism

J.G. Tobin,[1] K.W. Goodman,[1] F.O. Schumann,[2] R.F. Willis,[2] J. Kortright,[3] J.D. Denlinger,[3] E. Rotenberg,[3] A. Warwick,[3] and N.V. Smith[3]

[1]Lawrence Livermore National Laboratory, Livermore, CA 94550

[2]Pennsylvania State University, University Park, PA 16802

[3]Advanced Light Source, Accelerator and Fusion Research Division, Ernest Orlando Lawrence Berkeley National Laboratory, Berkeley, CA 94720

Element specific surface magnetometry remains a central goal of synchrotron radiation based studies of nanomagnetic structures. One appealing possibility is the combination of x-ray absorption dichroism measurements and the theoretical framework provided by the "sum rules." [1] Unfortunately, sum rule analyses are hampered by several limitations [2], including delocalization of the final state, multi-electronic phenomena and the presence of surface dipoles. An alternative experiment, Magnetic X-Ray Dichroism in Photoelectron Spectroscopy, holds out promise based upon its elemental specificity, surface sensitivity and high resolution. Computational simulations by Tamura et al. [3] demonstrated the relationship between exchange and spin orbit splittings and experimental data of linear and circular dichroisms. Now we [4] have developed an analytical framework which allows for the direct extraction of core level exchange splittings from circular and linear dichroic photoemission data. By extending a model initially proposed by Venus [5], it is possible to show a linear relation between normalized dichroism peaks in the experimental data and the underlying exchange splitting. Since it is reasonable to expect that exchange splittings and magnetic moments track together [6], this measurement thus becomes a powerful new tool for direct surface magnetometry, without recourse to time consuming and difficult spectral simulations. The theoretical derivation will be supported by high resolution linear and circular dichroism data collected at the Spectromicroscopy Facility of the Advanced Light Source. [7,8]

REFERENCES

1. B.T. Thole et al., Phys. Rev. Lett. 68, 1943 (1992); P. Carra et al. Phys. Rev. Lett. 70, 694 (1993).
2. J.G. Tobin et al. Phys. Rev. B 52, 6530 (1995).
3. E. Tamura et al., Phys. Rev. Lett.. 73, 1533 (1994).
4. J.G. Tobin, K.W. Goodman, F.O. Schumann, R.F. Willis, J.B. Kortright, J.D. Denlinger, E. Rotenberg, A. Warwick, and N.V. Smith, submitted to PRL, September, 1996.
5. D. Venus, Phys.. Rev. B 49, 8821 (1994) and references therein.
6. F.J. Himpsel, Phys. Rev. Lett. 67, 2363 (1991).
7. J.G. Tobin et al., J. Appl. Phys. 79, 5626 (1966) and J. Vac. Sci. Tech. B 14, 3171 (1996).
8. J.D. Denlinger et al., Rev. Sci. Instrum. 66, 1342 (1995).

This work was performed under the auspices of the U.S. Department of Energy by LLNL under Contract No. W-7405-ENG-48.

Principal investigator: James G. Tobin, Lawrence Livermore National Laboratory. Email: tobin1@llnl-gov. Telephone: 510-422-7247.

Double and Single Ionization of He and Other Targets Studied Using Cold Target Recoil Momentum Spectroscopy

R.Dörner[1,2], J.M.Feagin[3], C.L.Cocke[2], H.Bräuning[2], O.Jagutzki[1], M.Jung[4], E.P.Kanter[4], H.Khemliche[5], S.Kravis[2], V.Mergel[1], M.H.Prior[5], H.Schmidt-Böcking[1], L.Spielberger[1], J.Ullrich[6], M.Unverzagt[1] and T.Vogt[1]

[1]Institut für Kernphysik, Universität Frankfurt, August- Euler Str.6, 60486 Frankfurt, Germany
[2]Dept. of Physics, Kansas State University, Manhattan, Kansas 66506
[3]Dept. of Physics, California State University - Fullerton, Fullerton, California 92634
[4]Argonne National Laboratory, Argonne, Illinois 60439
[5]Lawrence Berkeley National Laboratory, Berkeley, California 94720
[6]Gesellschaft für Schwerionen Forschung, 64291 Darmstadt, Germany

Double ionization of an atom by a single photon is the simplest and most fundamental many-electron process. The ejection of two electrons following the absorption of one photon is strictly prohibited in an independent electron approximation. Thus determining the probability of double photoionization alone is already a challenging test of our understanding of electron-electron correlation. Furthermore, in the slow breakup of a bound system into three charged particles, the final state wave function must represent a high degree of few-body Coulomb correlation involving the simultaneous interaction of all three particles. The case of double photoionization is again particularly well suited to study this problem as the energy and the angular momentum delivered to the system can be very well controlled.

Helium, as the most basic three body system, has been the target of extensive studies over the past decades. The purpose of this project has been to study double and single ionization using cold target recoil ion momentum spectroscopy (COLTRIMS). This technique has been widely applied within the area of ion-atom collisions to study the dynamics of energy and momentum transfer in collisions between few-electron systems [1], and the entire technical machinery has been transferred to photon-atom collisions [2]. The technique uses space- and time-imaging of He^+ and He^{++} recoil ions created in photon-He collisions to measure the full momentum vector of each ion produced. Event-mode recording is used and a solid angle of nearly 4π is realized, allowing an extremely high data-collection efficiency. In order to reduce the initial momentum spread of the He target a precooled supersonic He jet is used.

For the case of single ionization of He, determination of the He^+ recoil momentum is equivalent to determination of the photoelectron momentum vector. Fig. 1 shows an image of a typical momentum distribution obtained at a photon energy of 80 eV. When double ionization occurs, the channel is uniquely identified by the production of a He^{++} ion but a full determination of the final state of the system requires that in addition to the ion mnomentum the momentum vector of one of the photoelectrons also be determined. This is accomplished using a second imaging detector opposite the ion detector which performs the complimentary momentum vector measurement of one electron. The experiment is run in two-bunch mode, requiring a timing pulse from the beam clock to measure the electron and ion flight times.

Two major projects have been completed to date and published in refs. [3] and [4].

Summaries are given here.

Ratio of Single to Double ionization of He between 80 and 400 eV

The ratio of double to single ionization ($R=\sigma^{++}/\sigma^{+}$) for He has been studied extensively in recent years (for a review, see [5]). In spite of this intense work, the various data sets reported over the last 30 years from threshold (79 eV) to a few hundred eV above are in substantial disagreement. We have used COLTRIMS to remeasure this ratio for photons between 85 and 400 eV. The technique allows the elimination of all known systematic errors discussed previously in the literature on this subject. A detailed discussion about systematic errors can be found in [3]. The results are shown in fig. 2, where they are compared to previous experimental work and to current theoretical calculations (refs. 9–12 in [3]). Our results are about 25% lower than most of the earlier data (refs. 4–7, 13–18 and 23 in [3]), but are in excellent agreement with the most recent calculations.

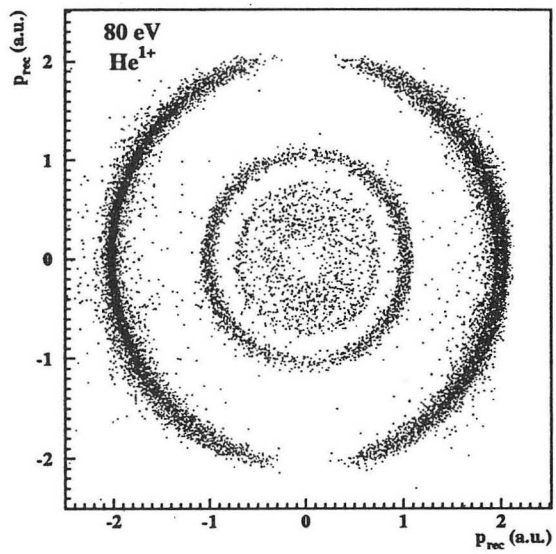

Figure 1: Momentum distribution of He^{+} ions produced by 80 eV photons. The X axis is the direction of the electric field vector of the linearly polarized light. The Y axis is the direction of the gas jet. The data are integrated over a momentum range of ±0.3 a.u. in the direction of the photon beam, the Z axis.

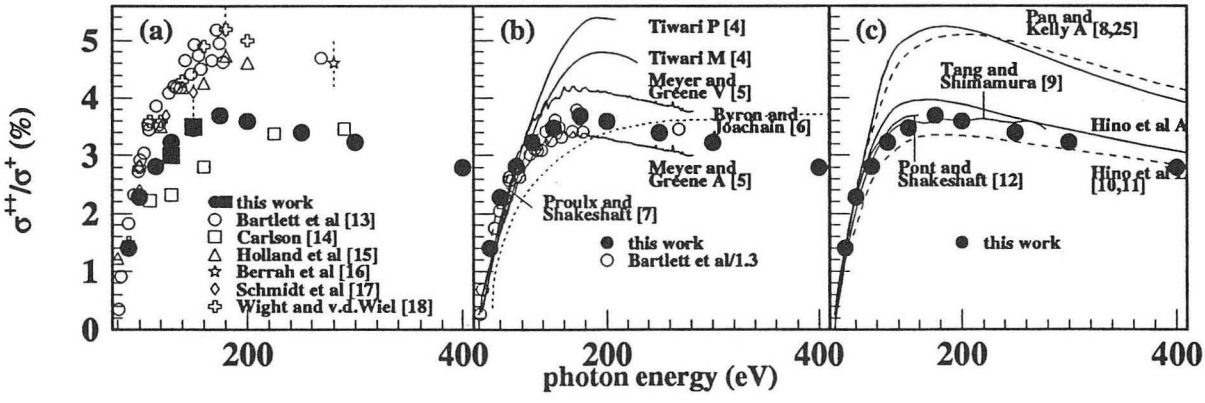

Figure 2: R as a function of photon energy. Full circles: this work (ALS). The open circles in (b) are the same data as in (a) but scaled down by 1.3. V, A, L stand for results obtained in the velocity, acceleration or length form, respectively. The references for the theories and all the older experiments can be found in [3].

Fully differential cross sections for double photoionization of He measured be recoil ion momentum spectroscopy

Several previous experiments have reported differential cross sections for coplanar geometry and for selected cases of equal and unequal energy sharing (refs. 1–6 in [4]). In our work we have for the first time determined fully differential cross sections for double ionization of He near threshold. Here we understand the word fully to mean that, apart from electron spins, the final state of the system is completely kinematically determined and we sample the complete momentum space (4π solid angle) for the ion and one of the electrons. This means that the final momenta of all three particles are determined for *every double ionization event*, with no necessity to choose a priori a particular angle or energy for either electron. Thus the entire final five-dimensional momentum space of the escaping three particles is sampled without prejudice, and the physical process itself determines which parts of this space are the most important.

The results (fig. 3) show that, at an energy of only 1 eV above threshold, the "collective" behavior of the outgoing system is evident in the correlated momenta of the outgoing electrons. The left and right parts of the figure show the data in terms of the Jacobi coordinates $\mathbf{k_r} = \mathbf{k_1} + \mathbf{k_2}$ and $\mathbf{k_R} = \frac{1}{2}(\mathbf{k_1} - \mathbf{k_2})$, where $\mathbf{k_1}$ and $\mathbf{k_2}$ are the momentum vectors of the two electrons. The left figure shows that the recoil ion momentum, the negative of $\mathbf{k_r}$, has a dipole-like distribution, reflecting the dipole-dominated interaction operator. Departure from a pure dipole shape is caused by the absorption of angular momentum into the internal motion of the electron pair, the $\mathbf{k_R}$ motion. The right figure shows the corresponding $\mathbf{k_R}$ distribution. We emphasize that this shows the correlation between the motion of the two electrons, not the motion of the individual electrons. The data reveal that the electrons are preferentially emitted in a direction perpendicular to the recoil momentum. This can be intuitively explained as the result of the electrons trying to move in such a way that neither falls into the He^+ potential, thereby producing single rather than double ionization. These data were found to be in good agreement with a fourth-order Wannier calculation and give an experimental basis for the choice of quantum numbers of the Wannier state populated in the photoionization. In our most recent experiment we obtained fully differential cross sections at 20 eV above threshold. These data show that the Wannier description is still in good agreement with the experiment at this energy. Further detail is given in the publication.

In the future we plan to probe the capabilities of COLTRIMS for the study of other systems. Initial projects include:

1) *double photoionization of Ne* very near the double ionization threshold (62.5–64.5 eV photon energy). In this energy range only the ground state of the Ne^{++} ion can be populated, so the situation is similar to that in He. (Three J values can be populated, however). We wish to investigate to what extent the Wannier patterns observed for He remain for a system in which two of the three potentials are no longer pure Coulomb in nature.

2) *fully differential cross sections for the three body break up of* $H_2 \rightarrow p + e^- + H$ close to threshold. Our experimental technique allows us to measure the energy and angular distribution of the photoelectron with respect to the alignment of the molecular axis with 4π solid angle, delivering the most complete picture of the physical process possible. Such fully differential cross sections will show the details of the electronic motion from the bound to the

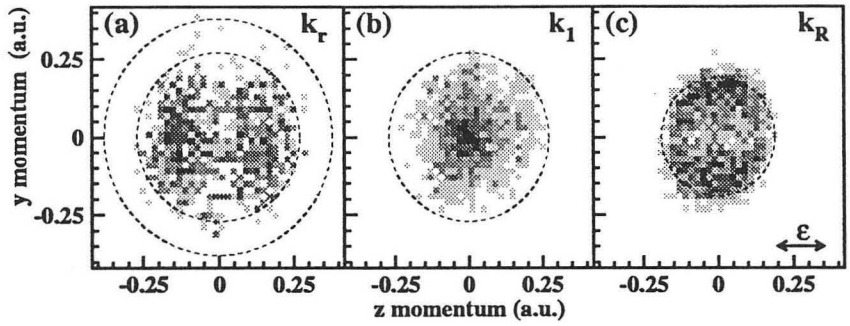

Figure 3: Density plots of projections of the momentum spectra from double ionization of He by 80.1 eV photons. The z and y components of the momentum are plotted on the horizontal and vertical axes, respectively, the polarization vector of the photon is in the z direction and the photon propagates in the x direction. Only events with -0.1< k_{rx} <0.1 are projected onto the plane. (a) The recoil (or $-\mathbf{k_r}$) momentum distribution. The outer circle indicates the maximum calculated recoil momentum, and the inner circle is the locus of events for which the $\mathbf{k_r}$ motion has half of the excess energy. (b) The distribution of single electron momenta ($\mathbf{k_1}$ or $\mathbf{k_2}$). The circle locates the momentum of an electron which carries the full excess energy. (c) The relative electron momentum (or $\mathbf{k_R}$) distribution. The circle identifies the maximum possible value for $\mathbf{k_R}$.

continuum state in the aligned molecular environment like the secondary scattering of the electron at the nuclei of the molecule. Our very high resolution for the ion momentum measurement allows to see the effects of the electron recoil on the nucleus. This will identify from which of the two centers the electron has originally been emitted.

3) *ratio of single to double ionization probabilities for Mg.* This is an extension of the He results discussed above to other systems. No other analogous two-electron system has been studied. We choose Mg because of the convenience of constructing an appropriate oven for producing the atomic beam target. We give up the very high momentum resolution in the direction of motion of the target beam which we have with the cold supersonic He jet, but believe the basic COLTRIMS geometry will remain useful, allowing control of such problems as scattered light, secondary processes, etc. in the same way as for He.

REFERENCES

1. J. Ullrich et al., Comments At. Mol. Phys. **30**, 285 (1994).
2. L. Spielberger et al., Phys. Rev. Lett. **74**,4615 (1995), and references therein.
3. R. Dörner et al., Phys. Rev. Lett. **76**, 2654 (1996).
4. R. Dörner et al., Phys. Rev. Lett. **77**, 1024 (1996).
5. J.H. McGuire et al., J. Phys. B **28**, 913 (1995).

This work was supported by the Division of Chemical Sciences, Office of Basic Energy Sciences, Office of Energy Research, U. S. Dept. of Energy, BMBF,DFG,DAAD, the Max-Planck Preis der Alexander von Humboldt Stiftung and GSI.
Principal investigator: R. Dörner, Institut für Kernphysik der J.W.G.-Universität Frankfurt, August-Euler-Str. 6, 60486 Frankfurt, Germany. Email: doerner@ikf007.ikf.physik.uni-frankfurt.de

Exploring Synchrotron Radiation Capabilities: The ALS-Intel CRADA

F. Gozzo[1,2], A. Cossy-Favre[2], B. Triplett[1], H. Fujimoto[1] and H.Padmore[2]
[1] Component Research, Intel Corporation, Santa Clara, California 95052, USA
[2]Advanced Light Source, Lawrence Berkeley National Laboratory,
University of California, California 94720, USA

Synchrotron radiation spectroscopy and spectromicroscopy were applied, at the Advanced Light Source, to the analysis of materials and problems of interest to the commercial semiconductor industry. We discuss some of the results obtained at the ALS using existing capabilities, in particular the small spot ultra-ESCA instrument on beamline 7.0 [1] and the AMS (Applied Material Science) endstation on beamline 9.3.2 [2].

INTRODUCTION

The continuing trend towards smaller feature size and increased performance for semiconductor components has driven the semiconductor industry to invest in the development of sophisticated and complex instrumentation for the characterization of microstructures. Among the crucial milestones established by the semiconductor Industry Association are the needs for high quality, defect free and extremely clean silicon wafers, very thin gate oxides, lithographies near 0.1 micron and advanced material interconnect structures. The requirements of future generations cannot be met with current industrial technologies. The purpose of this ALS-Intel CRADA (Cooperative Research And Development Agreement) is to explore, compare and improve the utility of synchrotron-based techniques for practical analysis of substrates of interest to semiconductor chip manufacturing. The first phase of the CRADA project consisted in exploring existing ALS capabilities and techniques on some problems of interest. We discuss here some of the preliminary results obtained on Intel samples.

EXPERIMENTS AND RESULTS

We performed a high energy resolution XPS study on thin blanket titanium nitride (TiN) films using the scanning ultra-ESCA spectromicroscope on beamline 7.0 [1]. In addition to its original use as an antireflection coating, titanium nitride has been recognized as an important materials component of metallization structures used in advanced microelectronic devices[3]. It improves adhesion and it is an excellent barrier against diffusion. TiN must conform to the extreme topographies used in devices in order to guarantee void-free plug formation and low junction leakage. It also needs to be very thin in order to reduce interconnect stack thickness and minimize contact and via resistance. However, deposition parameters influence the TiN electronic and chemical properties. Thus, it is important to understand the relationship between these deposition parameters and the electronic and chemical properties and ultimately the way TiN behaves as an adhesion layer and a diffusion barrier. It is also important to study the feature size dependence of its properties because step coverage will only become more challenging as feature sizes decrease and the aspect ratios increase.

Figure 1 shows XPS Ti 2p core level peaks from four different TiN films plus a TiN single crystal used as a reference after sputtering the first surface layers. The films were deposited by reactive sputtering at different N/Ar ratio from 10/90 to 90/10. A low N/Ar ratio may give a better conformality associated to a low sputtering rate. However, the sputtering process may be too slow and inefficient and allow a higher impurity level. By contrast, a high N/Ar ratio may result in a high sputtering rate with an excessively low conformality and undesired stoichiometry. The Ti2p structures in Fig.1 are the convolution of at least two Ti2p components. The main component on the lower binding energy side has been identified as Ti2p in a TiN_x bonding. We observe a shift of this component towards higher binding energy for increasing x values, whereas a shift in the opposite direction was observed in the corresponding N1s core levels. The observed shifts are consistent with the expected increase of ionicity in TiN_x as nitrogen atoms are added to the TiN_x compound. The higher binding energy side component should correspond to some Ti oxidation state (TiO_x with $0<x<2$), since we found clear evidence for the presence of oxygen even after sputter cleaning the surface. Oxygen was also found in the TiN single crystal spectra after sputtering.

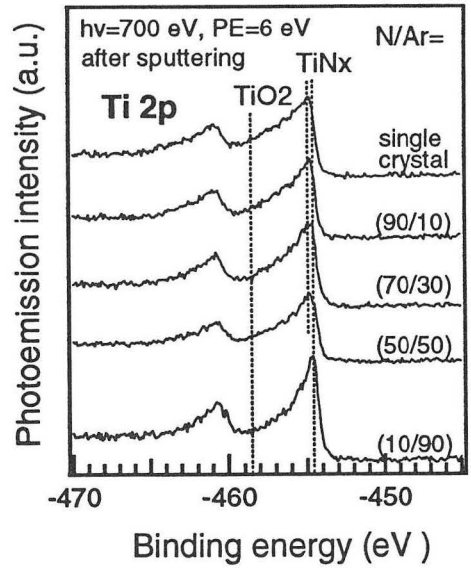

Figure 1. XPS Ti 2p peaks from TiN film with different N/Ar ratios. The signal from a single TiN crystal is taken as a reference.

The need of a good set of XPS data on a clean reference sample for a correct assignment of the XPS peak justified the experiments performed on beamline 9.3.2 using the Applied Materials Science chamber.[2] The main purposes of this experiment were to test a new cleaning procedure which reduces the oxygen and carbon signals and to see how valuable could be a valence band study of TiN films when used to probe the sample stoichiometry and composition. The TiN single crystal surface was first slightly argon etched to remove the natural protective titanium dioxide coating. Then, it was flashed at approximately 700 C for few seconds. Figures 2 and 3 show the oxygen 1s and the titanium 2p XPS core levels. The oxygen peak signal was strongly reduced after the annealing and

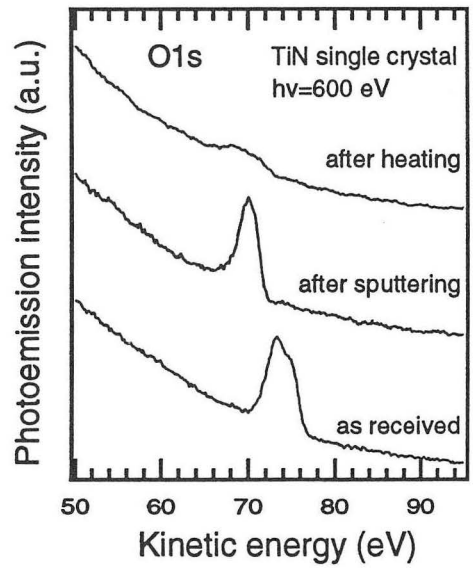

Figure 2. XPS O 1s peaks from a TiN single crystal. Heating the sample at ≈700°C has removed most of the oxygen signal.

the corresponding Ti 2p core levels show a strong change of the peak shape after sputtering and flashing. The second component at the lower kinetic energy side which appears after flashing the sample, may be attributed to a satellite feature as reported by Porte et al.[4] The authors performed a XPS analysis on contaminant-free TiN_x samples for different stoichiometry ($0<x<0.97$). For $x>0.75$, they found a second component at the higher binding energy side of the Ti2p doublet line, which is almost completely absent for lower x values. This component was interpreted as a satellite structure related to the decreasing screening ability of the conduction electrons when the composition approaches the stoichiometric value.

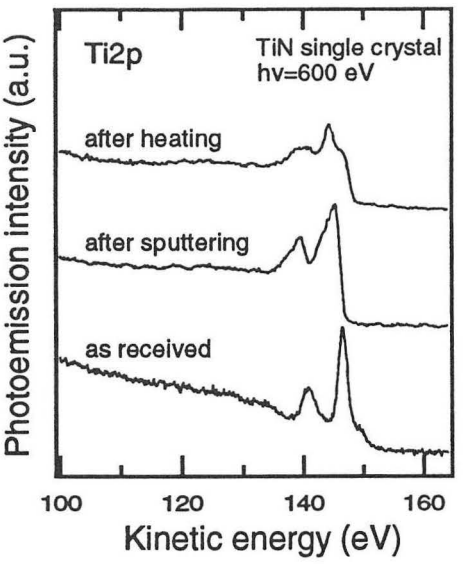

Figure 3. XPS Ti 2p peaks from a TiN single crystal.

Another challenging experiment we performed on beamline 7.0, which took the advantage of the microscopic capabilities of the ultra-ESCA spectromicroscope and of synchrotron radiation, was a depth profiling analysis of a blanket multiple Al/Ti/TiN/SiO_2 interface. We needed to understand the chemistry of the interfaces involved, in particular the Al/Ti interface. Since the sample was a blanket multiple interface, one could simplisticly argue that there was no need for a microscopic XPS. However, an important point which should always be considered when doing depth profiling with a sputter gun, is the extreme difficulties in obtaining uniform sputtered areas over a millimeter scale. When XPS depth profiling is performed with a conventional source, the collected signal is integrated over all the probed areas and does not necessarily correspond to the chemistry under investigation.

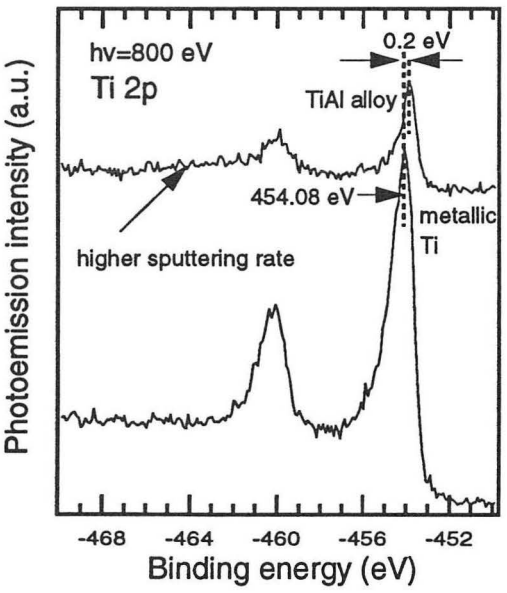

Figure 4. XPS Ti 2p peaks from a Al/Ti/TiN/SiO_2 multiple stack at the Al/Ti interface taken in two different x,y positions. The top spectrum corresponds to a region where the sputtering efficiency was higher.

Our micro-XPS analysis showed evidence of the formation of a Ti_3Al alloy at the Ti/Al interface when looking at the Ti2p core level peak (see Fig.4). Nitrogen was present in both Ti and TiN layers, but where there was the

evidence of Ti_3Al alloy formation, no nitrogen was present. Although the corresponding Al 2p core level binding energies were not consistent with the expected values for the Ti_3Al alloy[5], this was expected since the escape depth for Al2p and Ti2p at the given photon energy (800 eV) is quite different and we were probably comparing different sample layers. The different behavior for the Ti2p and the Al2p core levels at 800 eV, in fact, suggests that the chemistry changes rapidly at the interface and it is very complex.

Another topic of great interest for the semiconductor industry is the search for new low dielectric constants materials (low "k" dielectrics). The chip speed is limited by both the resistance of the metal line and the surrounding insulator. Reducing the metal resistance or the insulating capacitance both push towards the same direction: reaching a higher chip speed. Reducing capacitance also helps minimize crosstalk between adjacent metal lines, an increasingly severe problem.[6]

The push to get to lower dielectric constants has led the industry to investigate two basic approaches. The most easily implemented one, which has the attraction of using existing tools, is to introduce fluorine into more or less standard plasma oxide deposition processes, resulting in fluorinated silicon oxides (SiOF). Although there is an important tradeoff between the amount of fluorine added and the stability of the film, dielectric constants of 3.5 and also 3.2 seem to be achievable with acceptable film stability. The other approach is to use carbon based polymers with designer chemistries tailored to achieve the combination of low dielectric constant and high thermal stability. This approach may ultimately allow a more dramatic reduction of the dielectric constant to perhaps 2 or less. For all of these materials it is important to study their potential for performance improvement against thermal, electrical, chemical and mechanical stability issues which pose reliability risks and interfere with their incorporation into the interconnect system. In all cases, the integration of such materials will be a major development in materials science compared with the well understood integration of plasma and CVD (Chemical Vapor Deposition) SiO_2. In the case of the fluorinated silicon oxides, for example, the higher the fluorine content, the lower the dielectric constant. However, the higher the fluorine content, the higher their tendency to absorb water and release fluorine with a consequent monotonic increase of the dielectric constant and the potential to produce delamination, corrotion, and electromigration failures of the metal lines and vias.

We recently performed a comparative depth profiling XPS study on two SiOF films produced by two different vendors and procedures (sample A and B). One SiOF film was capped after deposition in order to

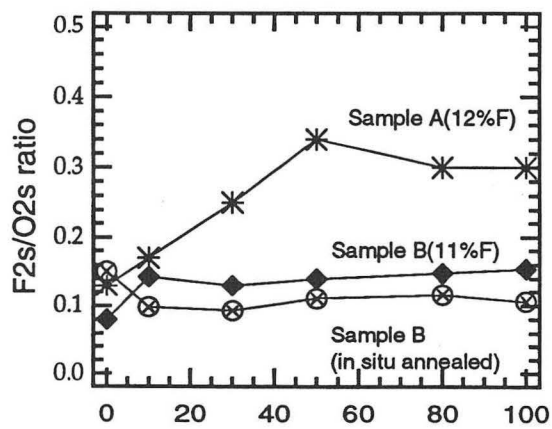

Figure 5. Fluorine over oxygen ratio vs. sputtering time for two SiOF films produced by two different vendors and procedures. Sample b was also *in situ* annealed.

prevent water absorption. Figure 5 shows the fluorine over oxygen ratio as a function of the sputtering time for the two unannealed samples A and B and for sample B after annealing under UHV. Sample A shows the highest F/O ratio and also the strongest variation as a function of the depth profile. The first point value, corresponding to the *as received* sample, is not surprising since sample A was nominally capped. However, the F/O ratio increases rapidly reaching a maximum after 50' sputtering and then it drops and remains quite constant. Different is the behavior of sample B for which the F/O value is quite uniform throughout the film both before and after annealing. Although the sputtering process may have changed the original composition of the film by disrupting some surface chemical bonds, the inhomogeneities observed in the film A should be intrinsic to the film, since the same process does not produce the same effect on the film B.

ACKNOWLEDGMENTS

This work was partially supported by the Swiss National Science Foundation and the Director, Office of Energy Research, Office of Basic Energy Sciences, Materials Sciences Division of the U.S. Department of Energy, under Contract No.DE-AC03-76SF00098. We thank Intel's Materials Technology and Components Research groups for characterizing samples used in the demonstration of the feasibility of X-ray spectromicroscopy applications. We also thank E.Rotenberg, J.Derlinger, S. Cerasari, Xin Zhou and Z.Hussain for their competent help and excellent assistance on beamline 7.0 and 9.3.2.

REFERENCES

[1] J.D.Denlinger, E. Rotenberg, T.Warwick, G.Visser, J.Nordgren, J.-H. Guo, P.Skytt, S.D. Kevan, K.S. McCutcheon, D.Shuh, J.Bucher, N. Edelstein, J.G. Tobin and B.P. Tonner, Rev. Sci. Instrum. **66**(2), 1342 (1995).

[2] Z. Hussain, W. R. A. Huff, S. A. Kellar, E. J. Moler, P. A. Heimann, W. A. McKinney, H. A. Padmore, C. S. Fadley, and D. A. Shirley, J. of Electron Spectrosc. Relat. Phenom. **80**, 401 (1996).

[3] M. Eizenberg, MRS Bulletin **44** (11), 38 (1995).

[4] L. Porte, L.Roux and J. Hanus, Phys. Rev. **B28** (6), 3214 (1983).

[5] D.E. Mercer, Jr, T.R. Hess, T. Mebrahtu, D.L.Cocke and D.G.Naugle, J.Vac.Sci.Technol. A9 (3), 1610 (1991).

[6] P.Singer, Semiconductor International, 88 (May 1996).

Principal investigator: Fabia Gozzo, Component Research, Intel Corporation, SC1-03, 3065 Bowers Ave., Santa Clara, CA 95052. E-mail: FabiaX_Gozzo@ccm.sc.intel.com OR Fabia_Gozzo@macmail.lbl.gov.

Fermi Energy 5*f* Spectral Weight Variation in Uranium Alloys

J. D. Denlinger,[1] J. Clack,[1] J. W. Allen,[1] S.-H. Yang,[2] S.-J. Oh,[2] E.-J. Cho,[3]
W. P. Ellis,[4] D. A. Gajewski,[5] R. Chau,[5] and M. B. Maple[5]

[1]University of Michigan, Dept. of Physics, Ann Arbor, Michigan 98109, USA
[2]Seoul National University, Korea
[3]Chonnam National University, Korea
[4]Los Alamos National Laboratory, Los Alamos, New Mexico 87545, USA
[5]University of California at San Diego, Dept. of Physics, La Jolla, California 92093,USA

INTRODUCTION

Uranium materials display a wide range of thermal, electrical and magnetic properties, often exotic [1]. For more than a decade there have been efforts to use photoemission spectroscopy to develop a systematic and unified understanding of the 5*f* electron states giving rise to this behavior. These efforts have been hampered by a paucity of systems where changes in transport properties are accompanied by substantial spectral changes, so as to allow an attempt to correlate the two kinds of properties within some model. We have made resonant photoemission measurements to extract the 5*f* spectral weight in three systems which show varying degrees of promise of permitting such an attempt, $Y_{1-x}U_xPd_3$, $U(Pd_xPt_{1-x})_3$ and $U(Pd_xCu_{1-x})_5$. We have also measured U 4*f* core level spectra. The 4*f* spectra can be modeled with some success by the impurity Anderson model (IAM), and the 5*f* spectra are currently being analyzed in that framework. The IAM characterizes the 5*f*-electrons of a single site by an *f* binding energy ε_f, an *f* Coulomb interaction and a hybridization V to conduction electrons. Latent in the model are the phenomena of 5*f* mixed valence and the Kondo effect.

EXPERIMENT

Resonant photoemission measurements were performed near the U 5*d* edge on cleaved polycrystalline uranium-alloy samples at the Advanced Light Source Beamline 7.0.1.2. A large order-of-magnitude cross-section enhancement of U 5*f* at the U 5*d* edge allows the U 5*f* spectral weight to be isolated from alloy contributions by subtraction of on- and off-resonance valence spectra. Spectromicroscopy was used to verify the quality and homogeneity of the cleaved samples. First, the sample was aligned and characterized with a standard laboratory x-ray source using a raster-imaging capability of the spectrometer with a 400 μm analysis area. Then the surface was probed further with a 100 μm focused synchrotron beamspot using a 60 meV total instrumental resolution.

The high flux delivered by the undulator beamline allows rapid characterization of the alloy surface with high resolution before appreciable impurities diffuse from the bulk to the surface. Sample homogeneity within the small probe spot is equally important to resolution and surface cleanliness in enhancing the sharpness of the spectra obtained. In addition the high flux allowed measurement of weak uranium intensities down to 1% dilution with good statistics in the $Y_{1-x}U_xPd_3$ system. With the higher resolution and strong signal intensities, new spectral features have been obtained in comparison to previous synchrotron measurements on these alloy systems with instrumental resolutions in the range 0.14 to 0.2 eV and greater.

RESULTS

In $Y_{1-x}U_xPd_3$ it is known from previous work [2,3] that well-defined U^{4+} ions are replaced by Y^{3+} ions. The number of conduction electrons then decreases and the chemical potential is lowered, so that the main weight of the *f*-spectrum (and core levels) moves toward the Fermi energy E_F. Consistent with the Anderson model, this decrease of ε_f leads for $x<0.3$ to Kondo effects which were found to show non-Fermi liquid departures from usual behaviors [4]. Movement of the central weight of the U 5*f* spectra shown in Figure 1 is consistent with previous lower resolution measurements. In addition, finer structures in the U 5*f* spectral shape are revealed, most importantly, a previously unobserved E_F peak which increases in relative spectral weight as *x* decreases. Such E_F weight growth correlated with Kondo behavior is expected in the IAM and has not been observed before in photoemission on uranium materials.

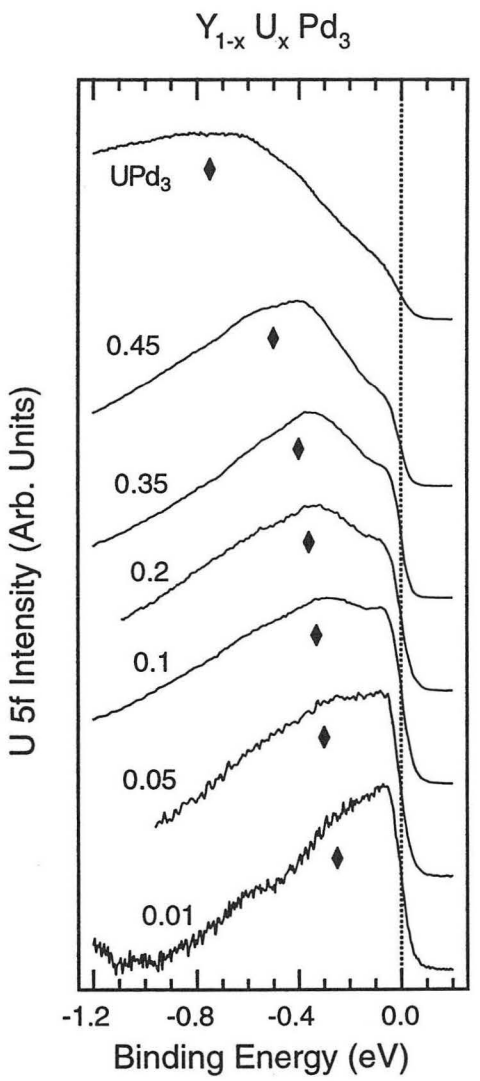

Figure 1. U 5*f* spectral weight for the $Y_{1-x}U_xPd_3$ system obtained from the difference spectra of hν=108 and 102 eV. Spectra were not measured for $0.5<x<0.9$, which is a mixed phase region.

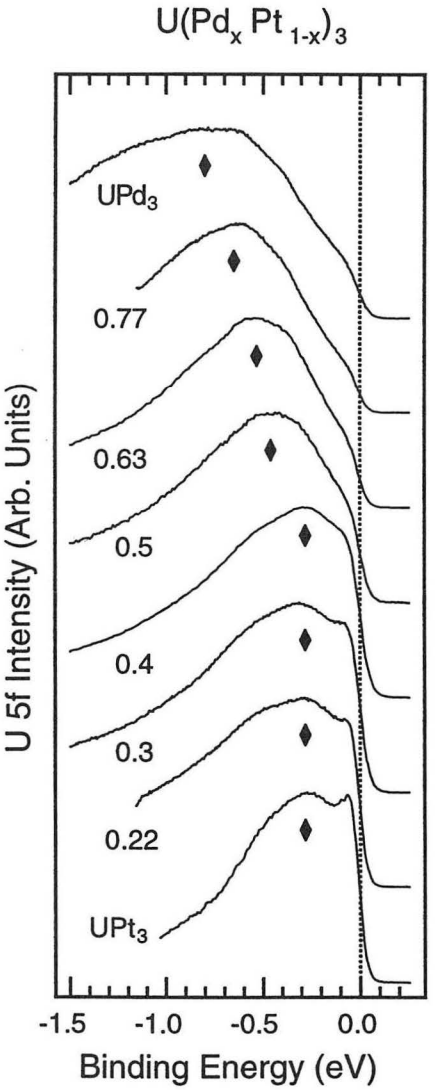

Figure 2. U 5*f* spectral weight for the $U(Pd_xPt_{1-x})_3$ system obtained from the difference spectra of hν=108 and 102 eV. Mixed crystalline phases exist for x=0.5 and 0.63.

The two endpoint materials of the $U(Pd,Pt)_3$ system are very different, including their crystal structures. UPt_3 is a heavy Fermion superconductor with *5f* spectral weight known to peak at E_F [6], whereas UPd_3 is one of few uranium intermetallic compounds that shows a gap around E_F with small *f*-electron density at E_F. A desired goal of studying this alloy system is to correlate core- and *f*-level spectroscopy to a continuous tuning of the conduction electron density contributed by Pd and Pt. Whereas qualitatively the shifting of the U *5f* spectral weight in Figure 2 looks very similar to that of $(Y,U)Pd_3$ in Fig. 1, a more careful examination reveals a discontinuous jump between x=0.4 and x=0.5. This spectral discontinuity correlates with x-ray diffraction data on these samples that indicate a change from the UPt_3 structure for $x<0.4$ to a significant mixture of crystalline phases for x=0.5 and 0.63, and the UPd_3 structure for $x>0.77$. This lack of a smooth transition between the different UPd_3 and UPt_3 crystal structures complicates interpretation of the observed spectral variations. The UPt_3 *5f* resonant photoemission pectrum, measured previously [5] at lower resolution, is resolved for the first time into two distinct peaks. The peak at E_F was observed previously [6] only at lower photon energies where the strength of the Pt emission obscures the deeper binding energy peak so that the complete U *5f* lineshape cannot be discerned. The relative weight of this sharp feature near E_F is seen to decrease upon Pd substitution, while still in the UPt_3 phase.

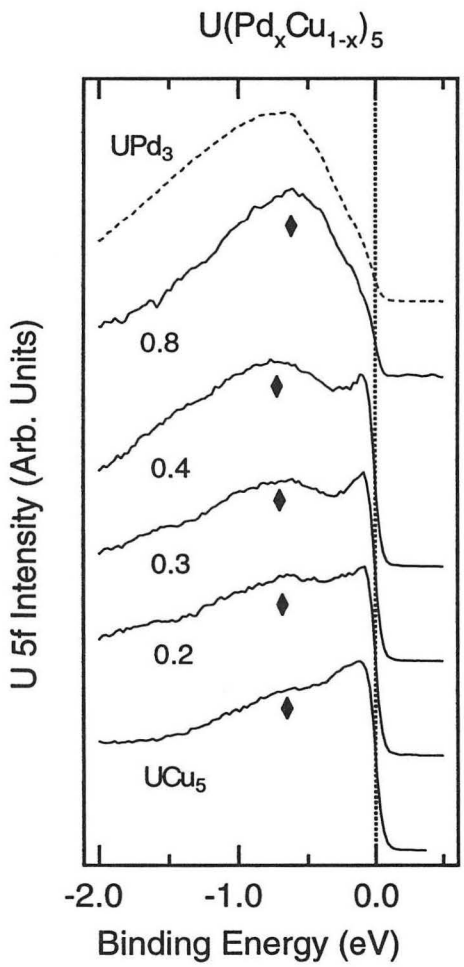

Figure 3. U *5f* spectral weight for the $U(Pd_xCu_{1-x})_5$ system obtained from the difference spectra of hν=108 and 102 eV. A mixed crystalline phase exists for x=0.6.

The same general behavior is seen also for $U(Pd_xCu_{1-x})_5$ in Figure 3. Upon Pd substitution, the sharp U *5f* peak nearest E_F decreases in relative weight to a higher binding energy peak that remains nearly constant in energy while in the UCu_5 crystalline phase. Again, a mixed alloy phase occurs for x=0.6 (not measured), and the spectrum for UPd_4Cu (x=0.8) begins to resemble that of UPd_3.

CONCLUSIONS

Systematic variations in the U *5f* spectral weight in three different U alloy systems have been measured with resonant photoemission. The growth of a narrow *5f* peak at the Fermi level in $(Y,U)Pd_3$, not previously observed, correlated with movement of the main *5f* spectral weight towards E_F and the onset of Kondo transport behavior is generic to the impurity Anderson model and gives promise to its application to the understanding of actinide electronic structure. High resolution photoemission reveals new *5f* spectral features in the $U(Pd,Pt)_3$ and $U(Pd,Cu)_5$ systems, but the presence of a discontinuity with stoichiometry does not allow a simple qualitative interpretation of the spectral variations.

ACKNOWLEDGEMENTS

The authors wish to gratefully acknowledge the support of D. K. Shuh and N. M. Edelstein of the Actinide Chemistry Group, Lawrence Berkeley National Laboratory, in establishing the protocols for radioactive sample handling at the ALS and Beamline 7.0. Also we wish to thank radiation safety monitors K. Heinzelmann and J. Hayes for their support.

REFERENCES

1. G. R. Stewart, Rev. Mod. Phys. **56**, 755 (1984).
2. J.-S. Kang, J. W. Allen, M. B. Maple, et al. Phys. Rev. B **39**, 13529 (1989).
3. L. Z. Liu, J. W. Allen, C. L. Seaman, M. B. Maple, Y. Dalichaouch, J.-S. Kang, M. S.Torikachvili and M. L. Lopez de la Torre, Phys. Rev. Lett. **68**, 1034 (1992).
4. C. L. Seaman, M. B. Maple, B. W. Lee, S. Ghamaty, M. S. Torikachvili, J.-S. Kang, L. Z. Liu, J. W. Allen and D. L. Cox, Phys. Rev. Lett. **67**, 2882 (1991).
5. A. J. Arko, D. D. Koelling, B. D. Dunlap, A. W. Mitchell, C. Capasso and M. del Giudice, J. Appl. Phys. **63**, 3680 (1988).
6. A. J. Arko, C. G. Olsen, D. M. Wieliczaka, Z. Fisk and J. L. Smith, Phys. Rev. Lett. **53**, 2050 (1984).

This work was supported at the University of Michigan by the Director, Office of Basic Energy Sciences, Materials Science Division, of the U. S. Department of Energy under Contract No. DE-FG02-90ER45416 and by the National Science Foundation Grant No. DMR-94-23741; and at UCSD by National Science Foundation Grant No. DMR-91-07698.

Principal Investigator: James W. Allen, Department of Physics, University of Michigan. Email: jwallen@umich.edu. Telephone: 313-763-1150.

Fermi Surface Mapping: Techniques and Visualization

Eli Rotenberg,*§ J. D. Denlinger,** S. D. Kevan,* K. W. Goodman,† J. G. Tobin,†
G. J. Mankey‡
*Department of Physics, University of Oregon, §Advanced Light Source, Lawrence Berkeley National Laboratory, MS 2-400, Berkeley CA 94720, **University of Wisconsin-Milwaukee, †Lawrence Livermore National Laboratory, ‡Department of Physics, Louisiana State University

INTRODUCTION

Angle-resolved photoemission (ARP) of valence bands is a mature technique that has achieved spectacular success in band-mapping metals, semiconductors, and insulators.[1] The purpose of the present study was the development of experimental and analytical techniques in ARP which take advantage of third generation light sources. Here we studied the relatively simple Cu surface[2] in preparation for other metals. Copper and related metals themselves are of current interest, especially due to its role as an interlayer in spin valves and other magnetic heterostructures.[3]major goal of this study was the development of a systematic technique to quickly (i.e. in a few hours of synchrotron beamtime) measure the FS and separate it into bulk and surface FSs. Often, one needs to avoid bulk features altogether, which one can achieve by carefully mapping their locations in k-space. We will also show how we systematically map Fermi surfaces throughout large volumes of k-space, and, by processing the resulting volume data sets, provide intuitive pictures of FSs, both bulk and surface.

Recently, imaging of the FS has been achieved by either scanning the photoelectron emission angle (either by rotating an angle-resolved detector[4] or the sample[5]) or using display-type analyzers.[6,7] Usually these experiments are done at only one or several discrete photon energies and for restricted ranges of emission angle and therefore only map the FS vs. kll. While some experiments have been done with continuously scanned phòton energies,[8] which probes the FS along $k_\perp$, these have been performed at only a few discrete emission angles. In this paper, we present results for simultaneous photon-energy- and angle-dependent scans which probe ~uniformly in both $k_{||}$ and $k_\perp$. For sufficiently high photon energies (>60 eV or so), one can assume free-electron final states, which greatly simplifies data interpretation. However, this requires high angle- and photon energy-resolution. In addition, to acquire data in a reasonable amount of time requires the high brightness of an undulator beamline. Taken together, these requirements can only be met by a third-generation synchrotron such as the Advanced Light Source.

EXPERIMENT AND DISCUSSION

A single-crystal Cu(001) sample was cleaned with standard techniqes. Experiments were performed at the SpectroMicroscopy Facility (Beamline 7.0.1.2) of the Advanced Light Source.[9,10] The instrument consists of a commercial, hemispherical electron analyzer and a five-axis sample goniometer mounted inside an ultra-high vacuum chamber. The angle between the photons and the electron analyzer was held fixed at 60° and the sample was rotated in azimuthal (ϕ) and polar (θ) angles. The total angular acceptance, as measured by the FWHM of the Cu(001) surface state at $\overline{X}$, was better than 1.3°. For FS mapping, the analyzer had a 0.4 eV wide window centered at the Fermi edge. Reducing the energy window's width had little effect on the sharpness of the features observed. The data were taken within a 45° sector, which was then symmetrized using the known 4-fold rotational and mirror-plane symmetries of the Cu(001) surface. Note that this procedure only approximates the full 2π emission, because

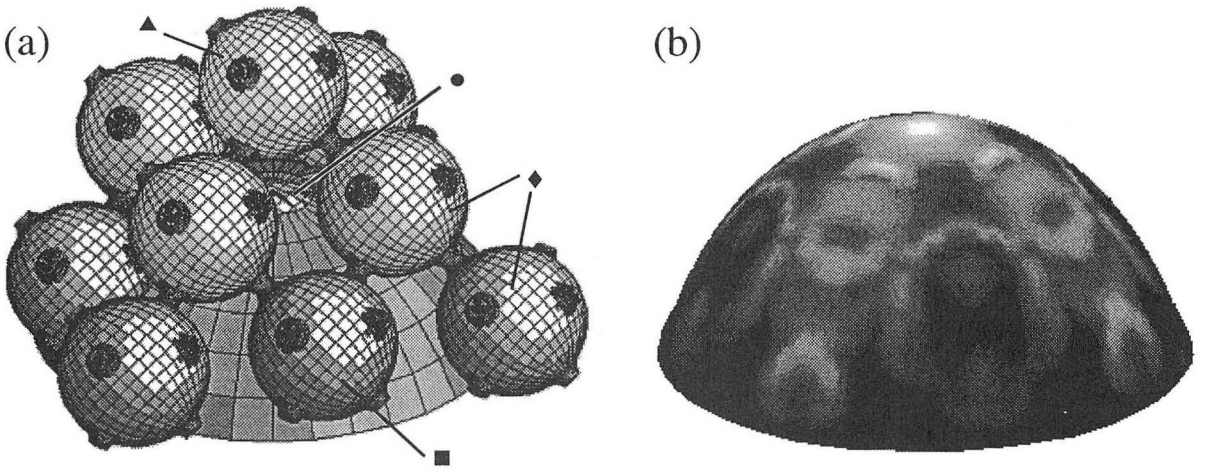

Figure 1. Angle-resolved photoemission measurements of the Cu Fermi Surface at $h\nu$=83 eV. The normal emission direction [001] is upwards. (a) Schematic illustrating the constant k-surface (large hemisphere) intersecting various Fermi Surfaces in the extended zone scheme. (b) Experimental intensity profile for ~2π solid angle, mapped onto the constant-k hemisphere as described in the text. Light shading means high photoemission yield.

the fixed photon polarization vector breaks the mirror plane symmetry, leaving only 4-fold rotational symmetry. This generally has ~10-20% affect on intensities.

Fig. 1(a) shows a schematic of FS mapping for Cu(001) at fixed photon energy. For sufficiently high photon energies, the final states are free-electron-like, and the initial state momentum $\mathbf{k}_{in}$ is related to the measured kinetic energy KE and momentum $\mathbf{k}_{out}$ by

$$k_{in,\parallel} = k_{out,\parallel};\ \mathrm{KE}_{in} = \mathrm{KE}_{out} + V_0 \qquad (1a;b)$$

$$k_{\left\{\begin{smallmatrix}in\\out\end{smallmatrix}\right.}\ [\text{Å}^{-1}] = 0.5124\sqrt{\mathrm{KE}_{\left\{\begin{smallmatrix}in\\out\end{smallmatrix}\right.}\ [\mathrm{eV}]} \qquad (1c)$$

The parameter V_0 is the experimentally-determined inner potential. Therefore an angular pattern obtained at constant kinetic energy appears in k-space as a hemisphere of constant radius k_{in} (shown in Fig. 1(a) for photon energy $h\nu$≈83 eV) cutting through the known bulk FS of Cu. This surface, shown in the extended Brillouin zone (BZ) scheme, consists of a bcc-lattice of approximately spherical-shaped structures. In this figure, normal emission is in the up-direction. The intersections of the constant-k_{in} hemisphere with the FS is detected experimentally using the configuration discussed above. The result of the experiment is shown in Fig. 1(b), which was mapped using V_0=8.8 eV. In this figure the bright lines correspond to high intensity at the Fermi level. The largest polar angle measured was θ=80°, but due to the V_0 term in Eqn. 1(b), the largest polar angle within the crystal was closer to 70°. The various round features may be understood from Fig. 1(a) as due to various degrees of intersection between the constant-k_{in} hemisphere and the ~spherical FSs. The FS in the BZ marked by a square (■), for example, is cut nearly in half and results in a large, round cross section in Fig. 1(b), while those labelled with a diamond (♦) are only slightly intersected, resulting in smaller cross sections. The surface marked with a triangle (▲) is not intersected at all, while the surface marked with a circle (●) is intersected tangentially across the top, resulting in high intensity at the top of Fig. 1(b). The sharp cusp-like features near normal emission at the top of Fig. 1(b) appear to be images of the necks of some of the FSs, although some of the intensity may be due to the $\overline{\mathrm{X}}$ surface state discussed later.

By varying the photon energy, one can access values of $\mathbf{k}_{in}$ within the two nested

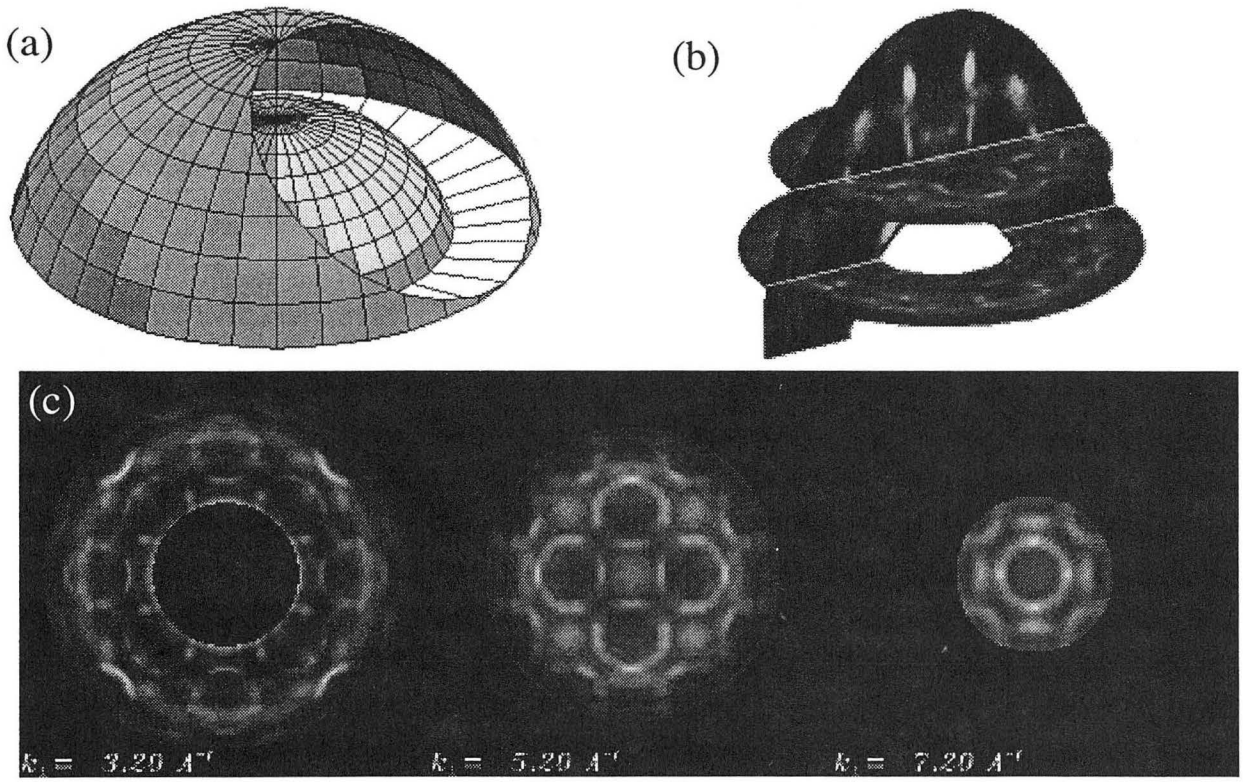

Figure 2. Volume data set of Fermi Surface. (a) Schematic showing the volume of k-space which can be accessed in a typical experiment. (b) Volume data set obtained for Cu(001), with some interesting slices highlighted. (c) Various slices of constant $k_\perp$ for extracted from the data set.

hemispheres illustrated in Fig. 2(a). This entire volume was mapped out for Cu(001) (within a 45° sector) for k_{out}=4.0 to 7.7 Å^{-1} in 0.1 Å^{-1} steps. This corresponds to a photon energy range of ~60 to 225 eV. Having acquired this data, transformed it according to Eqn. 1 into $\mathbf{k}_{in}$, and symmetrized it in the fashion of Fig. 1(b), the data were interpolated into a uniform, 0.1 Å^{-1} spaced grid of k_x, k_y, and k_z within the crystal. This volume data set may then be sampled with arbitrary cuts, as illustrated in Fig. 2(b). A computer animation was also produced, in which each movie frame corresponds to a slice of constant k_z. Plotted in these fashions, one achieves very intuitive images of the FSs, which, especially for large polar angles, can be difficult to perceive from single-photon-energy images like Fig. 1. For example, the alternate stacking sequence (each "layer" of BZs stacked 45° with respect to each other) is clearly evident in Figs. 2(b,c).

Finally, we consider the maps one obtains for constant ϕ, but variable θ and $h\nu$.[5] Representative examples are shown in Fig. 3. In these figures, up is the direction of normal emission, and ϕ is selected to include high-symmetry directions. The utility of acquiring these plots for a new system one is studying cannot be overestimated. They both show the FSs as well as highlight some of the limitations of the simple interpretation we have been using. Fig. 3(a) shows FS data for parts of 5 different BZs. The arrow indicates an instance of "Zone-Selection" rules, whereby the transition intensity near the arrow is much weaker than at the similar point across the BZ at ~5.2 Å-1. This is attributed to a final state effect. The white dashed line, which points along the $[\bar{1}01]$ symmetry direction, indicates a direction in k-space where the transition intensity is weak. Since these regions extend over more than one zone, it appears to be a more strict symmetry-selection rule, probably to be understood with matrix-element calculations which will be reported elsewhere. This calculation should also apply to the other

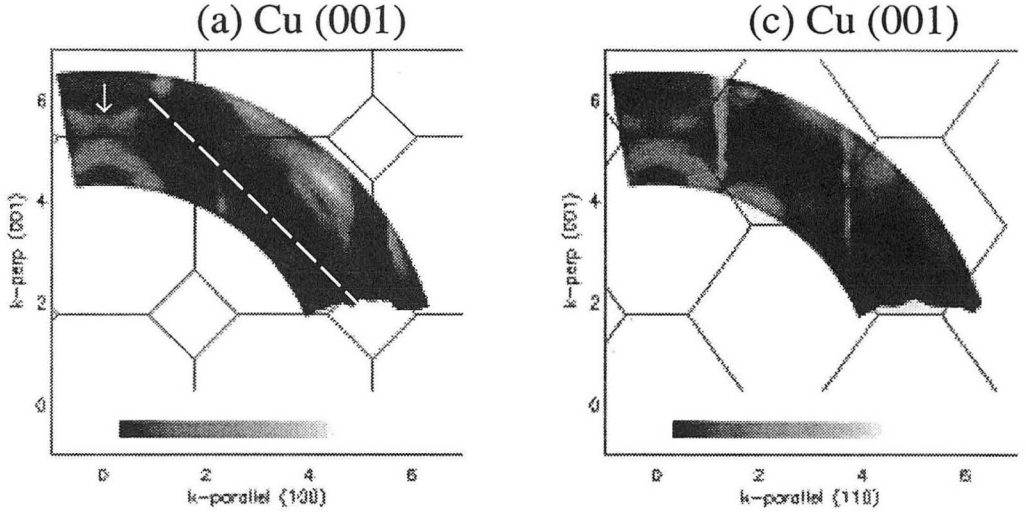

Figure 3. Polar-scan slices of Fermi Surface data for Cu(001) for kll pointing towards (a) [100] and (b) [110]. The features associated with arrows and lines are described in the text.

intensity variations apparent in the figure. Similar effects at other directions in k-space are seen in the volume data set of Fig. 2, which covers a larger volume of k-space. In Fig. 2(c), at $k_{\perp}$=3.2 Å^{-1} for example, the dark and light intensity from Fig. 3(a) appear as dark and light circular bands. Other anomalies in these figures will be discussed later.[11]

Fig. 3(b) shows another slice in k-space along $\mathbf{k}_{||}$=[110]. The most prominent features are a series of vertical lines, which pass through the bulk L-points, or surface $\overline{X}$ points. These lines clearly resemble crystal truncation rods in x-ray diffraction and correspond to surface states. The immediate identification of these surface states in energy-dependent scans is one of the principle reasons to perform the experiments in Fig. 3.

To summarize, we have developed a data acquisition system, together with online visualization and processing, for Fermi surface and band mapping of crystalline materials. While we presented details here for Cu, we have also undertaken studies of unrelated systems, some of which are presented elsewhere in this activity report. While the energy and angular resolution in this study were relatively modest, we have also pushed these to more demanding levels.

REFERENCES

[1] S.D. Kevan, ed., *Angle-Resolved Photoemission,* (Amsterdam, Elsevier, 1992), and references therein.
[2] R. Courths and S. Hüfner, Phys. Rep. **112**(2), 53 (1984), and references therein.
[3] T. Miller, A. Samsavar, G.E. Franklin, and T.-C. Chiang, Phys. Rev. Lett. **61**(12), 1404 (1988).
[4] P. Aebi, J. Osterwalder, R. Fasel, D. Naumovic, L. Schlapbach, Surface Science **307**, 917 (1994).
[5] A.P.J. Stampfl, J.A. Con Foo, R.C.G. Leckey, J.D. Riley, R. Denecke, L. Ley, Surface Science **331**, 1272 (1995).
[6] A. Santoni, L.J. Terminello, F.J. Himpsel, and T. Takahashi, Appl. Phys. A **52**, 229 (1991).
[7] S. Qu, A. Gooneward, K. Subramanian, J. Karunamuni, *et al.*, Surface Science **324**, 133 (1995).
[8] P. Thiry, Ph.D. Thesis, Université Pierre et Marie Curie, 1979.
[9] J.D. Denlinger *et al.*, Rev. Sci. Instrum. **66**, 1342 (1995).
[10] T. Warwick, P. Heimann, D. Mossessian, W. McKinney, and H. Padmore, Rev. Sci. Instrum. **66**, 2037 (1995).
[11] Eli Rotenberg, *et al.,* unpublished.
[12] Eli Rotenberg, *et al.,* elsewhere in this activity report.

This work was supported by the U.S. Department of Energy, Division of Materials Science under grant DE-FG06-86ER45275.

Principal investigator: Stephen D. Kevan, Department of Physics, University of Oregon. Email: kevan@oregon.uoregon.edu. Telephone: 541-346-4742.

Full k-Space Visualization of Photoelectron Diffraction

J. D. Denlinger,[1,2] Eli Rotenberg,[1,3] S. D. Kevan,[2] and B. P. Tonner[3]

[1]Advanced Light Source, Lawrence Berkeley National Laboratory,
University of California, Berkeley, California 94720, USA
[2]University of Oregon, Dept. of Phyiscs, Eugene, Oregon 97403, USA
[3]University of Wisconsin-Milwaukee, Dept. of Physics, Milwaukee, Wisconsin 53211, USA

INTRODUCTION

The development of photoelectron holography has promoted the need for larger photoelectron diffraction data sets in order to improve the quality of real-space reconstructed images (by suppressing transformational artifacts and distortions) [1-3]. The two main experimental and theoretical approaches to holography, the transform of angular distribution patterns for a coarse selection of energies or the transform of energy-scanned profiles for several directions, represent two limits to *k*-space sampling. The high brightness of third-generation soft x-ray synchrotron sources provides the opportunity to rapidly measure large high-density x-ray photoelectron diffraction (XPD) data sets with approximately uniform *k*-space sampling. In this abstract, we present such a photoelectron data set acquired for Cu 3*p* emission from Cu(001) [4].

Cu(001) is one of the most well-studied systems for understanding photoelectron diffraction structure [5] and for testing photoelectron holography methods [6-8]. Cu(001) was chosen for this study in part due to the relatively inert and unreconstructed clean surface, and it served to calibrate and fine-tune the operation of a new synchrotron beamline, electron spectrometer and sample goniometer [9]. In addition to Cu, similar 'volume' XPD data sets have been acquired for bulk and surface core-level emission from W(110), from reconstructed Si(100) and Si(111) surfaces [10], and from the adsorbate system of c(2x2) Mn/Ni(100) [11].

EXPERIMENT

Measurements were performed at the SpectroMicroscopy Facility (Beamline 7.0). The photoelectron diffraction system consists of a high precision two-axis goniometer for sample rotations and a PHI Omni 4 hemispherical electron spectrometer with multi-channel detection and variable-aperture input lens set for an angular acceptance less than ±1°. For rapid scanned-angle XPD measurements of bulk Cu 3*p*, a 0.4 eV wide energy-window was used to take 'snapshots' of the peak and higher kinetic energy background intensities at each sample direction. With dwell times less than 1 second per angle, a 482 point angular intensity pattern could be obtained in less than 15 minutes including ~50% motor motion overhead. Angular distribution patterns were acquired within a 45° azimuthal sector and then mirror- and four-fold symmetrized for Cu(001) to display the full angle hologram. Uniform increments in polar angle to 80° from normal emission and constant solid angle azimuth steps (inversely proportional to polar angle) were used to uniformly sample directions. Automated experimenter control of the undulator gap allows scanned-photon energy experiments to be routinely performed; however, the greater time overhead for undulator and monchromator exit slit motions make this data acquisition mode less efficient. For this reason the large Cu 3*p* XPD data set was acquired by sequential measurement of constant-energy angular distribution patterns.

RESULTS

The full Cu 3*p* XPD data set is represented as a cylindrical volume in Fig. 1. The cylinder is created by stacking 58 angular patterns acquired for an electron momentum range of 3.1 to 8.8 $Å^{-1}$ with 0.1 $Å^{-1}$ steps (37-295 eV kinetic energy range). The full volume represents greater than 185,000 intensities, resulting from the symmetrization of ~28,000 measurements acquired in less than three 8-hour synchrotron shifts. The angles and energies in Figures 1-3 correspond to coordinates outside the crystal and have not been corrected for refraction at the surface due to the crystal inner potential. Cutaways in the cylindrical volume in Fig. 1 show the interior diffraction structure. To highlight the richly detailed intensity variations, contrast has been enhanced by (a) correcting each pattern for inelastic attenuation near grazing emission, (b) normalizing each pattern to a constant integrated intensity, and (c) saturating the intense low kinetic energy peak at normal emission.

A second way of visualizing the data set is by playing a movie sequence of each diffraction pattern. Figure 2 shows a much coarser sampling of ten angular diffraction patterns extracted from the data volume. Energies with ~0.7 $Å^{-1}$ separation have been chosen to maximally illustrate the wide variety of angular patterns. A third way of visualizing the data set is by extracting energy dependent slices at fixed azimuths. Figure 3 shows energy-polar angle slices in two high symmetry azimuths separated by 45°. The slices are additionally mapped into a k_x-k_z coordinates in order to illustrate the polar emission angle.

Large intensity oscillations along the 45° polar emission angle in the {100} planes are observed for energies greater than 100 eV. These energy oscillations are recognized as arising from

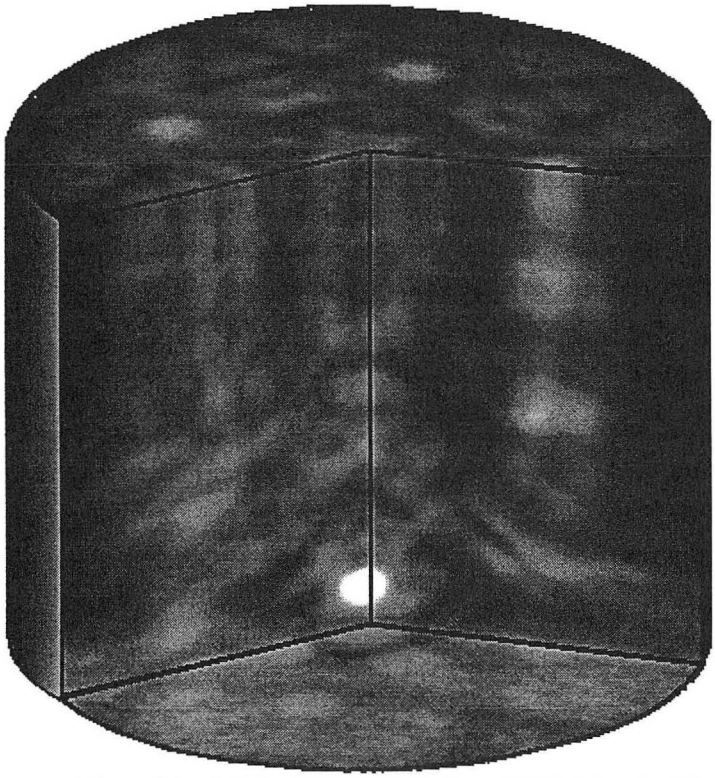

Figure 1. Cylindrical representation of the full Cu(001) Cu 3*p* volume XPD data set with cutaways to show interior diffraction structure. The vertical dimension is linear in electron momentum from k=3.1 to 8.8 Å-1. The radial dimension is linear in polar emission angle from 0° to 80°.

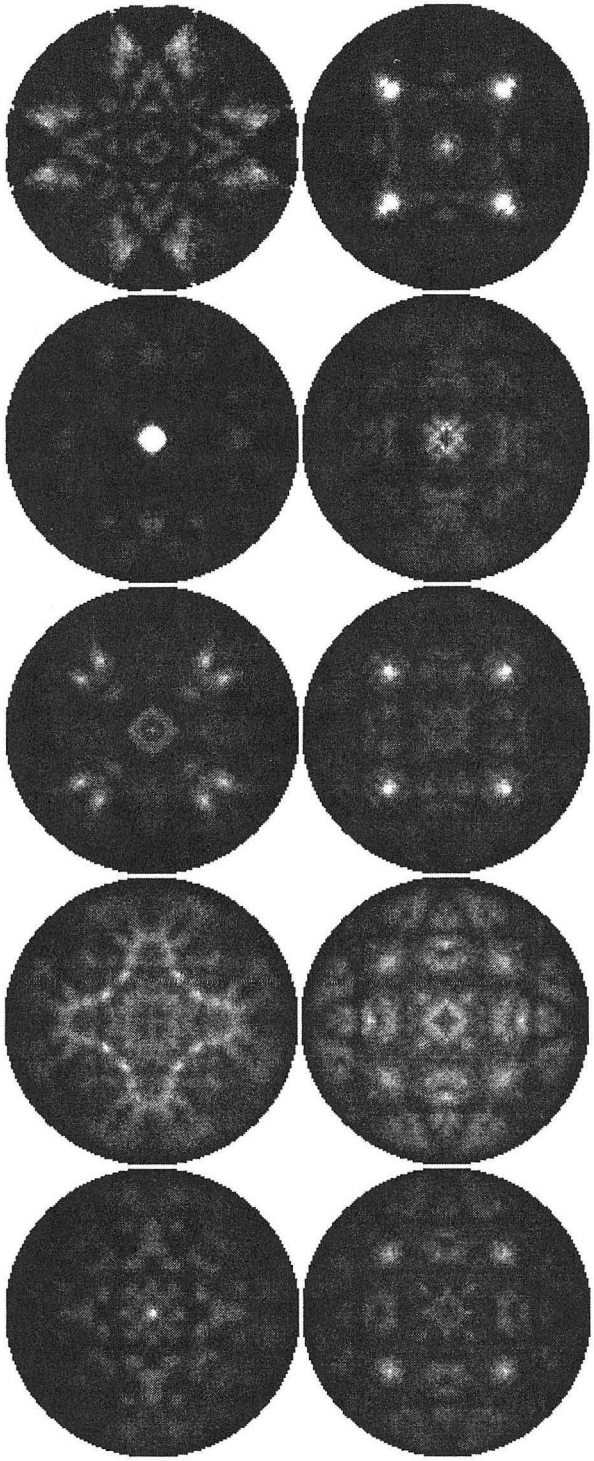

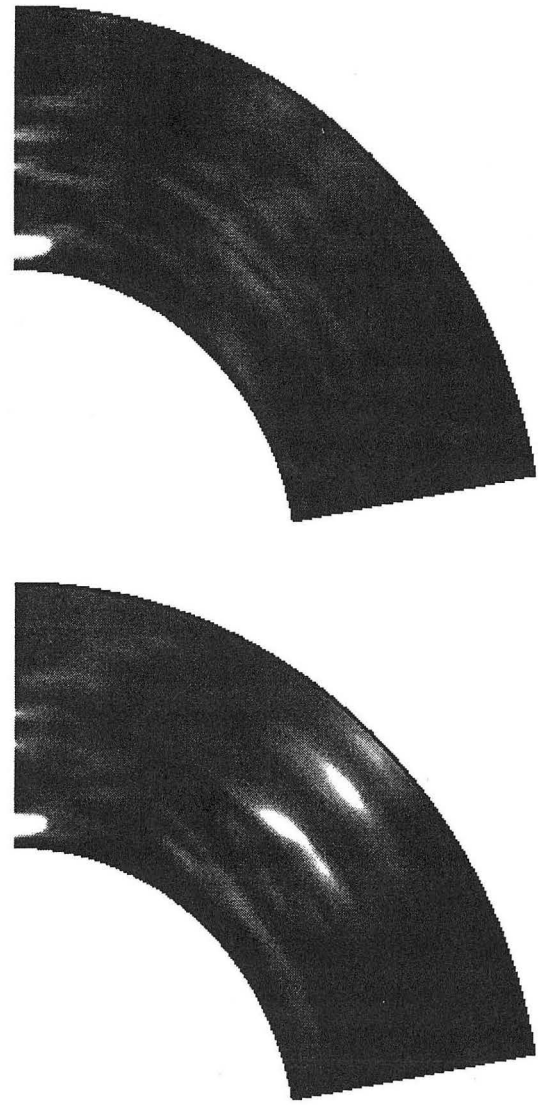

Figure 3. (above) Energy-dependent slices in the [110] (top) and [100] (bottom) emission planes mapped into *k*-space.

Figure 2. (left) Sampling of ten angular distribution patterns with kinetic energies: 39, 52, 67, 84, 111, 142, 176, 214, 250 and 295 eV.

back-scattering from nearest-neighbor atoms [12] along the [101] crystal axis. The path length difference for back-scattered photoelectrons (twice the near-neighbor bond distance) determines the dominant *k*-space period of the oscillations. The (100) energy slice in Fig. 3 also illustrates the angular width (~20°) of this cone of back-scattered intensity. For kinetic energies above 200 eV, the angular patterns in Fig. 2 begin to show the consistent appearance of arcs resulting from emission from atoms in deeper layers below the surface and Kikuchi-like scattering from atoms lying in low-index crystal planes [5].

Below 100 eV, rapidly varying diffraction structure is observed both in the dramatic changes in the angular patterns and in the outwardly sweeping intensity for decreasing energy in the energy slices. Additionally, an intense normal emission peak at 50 eV kinetic energy is observed. Contributing factors to this low energy diffraction behavior include: (i) the enhanced importance of multiple-scattering, (ii) rapid changes in the electron scattering factor, (iii) increased surface sensitivity, and (iv) the increasing effect of surface refraction. The detailed origins of these low energy features are being explored with single- and multiple-scattering calculations.

CONCLUSIONS

The continuous energy and angular variation of photoelectron diffraction intensities has for the first time been experimentally measured and visualized. The *k*-space range for the example presented, Cu 3*p* emission from Cu(001), illustrates the progression from low energies dominated by multiple-scattering to medium energies exhibiting strong back-scattering features. The detailed explanation of the rich diffraction structure will provide a test for scattering simulations. In addition, the data will be used as an experimental test bed for real-space reconstruction algorithms, where optimal *k*-space sampling, energy range selection, algorithm-specific artifacts and other issues are of concern [8].

ACKNOWLEDGEMENTS

This work was supported by the Department of Energy, Materials Science Division, under Grant No. DE-FG02-92ER45468.

REFERENCES

1. J. J. Barton, Phys. Rev. Lett. **67**, 3106 (1991).
2. S. Y. Tong, H. Huang, and C. M. Wei, Phys. Rev B **46** 2452 (1992).
3. H. Wu, G. J. Lapeyre, H. Huang and S. Y. Tong, Phys. Rev Lett. **42**, 251 (1993).
4. J. D. Denlinger, Eli Rotenberg, S. D. Kevan and B. P. Tonner, Mater. Res. Soc. Proceedings, Spring 1996, in press.
5. D. Naumovic, A. Stuck, T. Greber, J. Osterwalder, and L. Schlapbach, Phys. Rev. B 47, 7462 (1993).
6. G. R. Harp, D. K. Saldin, and B. P. Tonner, Phys. Rev B **42**, 9199 (1990).
7. L. J. Terminello, J. J. Barton and D. A. Lapiano-Smith, Phys. Rev. Lett. **70**, 599 (1993).
8. P. M. Len, S. Thevuthasan, A. P. Kaduwela, M. A. Van Hove, and C. S. Fadley, SurfaceScience, in press.
9. J. D. Denlinger, et. al, Rev. Sci. Instrum. **66**, 1342 (1995).
10. J. D. Denlinger, Eli Rotenberg, S. D. Kevan and B. P. Tonner (unpublished).
11. S. Banarjee, S. Ravy, J. D. Denlinger, and B. P. Tonner (unpublished).
12. P.J. Orders and C. S. Fadley, Phys. Rev. B **27**, 6526 (1983).

This work was supported at the University of Michigan by the Director, Office of Basic Energy Sciences, Materials Science Division, of the U. S. Department of Energy under Contract No. DE-FG02-90ER45416 and by the National Science Foundation Grant No. DMR-94-23741; and at UCSD by National Science Foundation Grant No. DMR-91-07698.

Principal Investigator: Brian P. Tonner, Department of Physics, University of Wisconsin-Milwaukee. Email: bptonner@physics.uwm.edu. Telephone: (414) 229-4626.

Holographic Atomic Images from Surface and Bulk W(110) Photoelectron Diffraction Data

P. M. Len[1], J. D. Denlinger[2,3], E. Rotenberg[2,4],
S. D. Kevan[3], B. P. Tonner[4], Y. Chen[5], M. A. Van Hove[5], and C. S. Fadley[1,5]
[1]Physics Department, University of California, Davis, California 95616, USA
[2]Advanced Light Source, Ernest Orlando Lawrence Berkeley National Laboratory, University of California, Berkeley, California 94720, USA
[3]Department of Physics, University of Oregon, Eugene, Oregon 97403, USA
[4]Department of Physics, University of Wisconsin, Milwaukee, Wisconsin 53211, USA
[5]Materials Sciences Division, Ernest Orlando Lawrence Berkeley National Laboratory, University of California, Berkeley, California 94720, USA

Although Gabor originally proposed using electrons in holography to form atomic-resolution images [1], it is only very recently that photoelectron diffraction data have been discussed as a practical method for achieving this [2,3]. Such data enable recording both the amplitudes and phases of the scattered waves (relative to a direct reference wave), thus in principle permitting the holographic reconstruction of atomic positions [2,3]. Photoelectron holography thus holds much promise of at least providing approximate starting structures that can be refined by more conventional comparisons of multiple-scattering calculations with experiment via *R*-factors. Criteria for optimizing the taking of such data and their holographic inversion have recently been published [4]. In the present study, such holographic photoelectron diffraction patterns have been measured for surface and bulk core-level-shifted W $4f_{7/2}$ photoemission from W(110) on ALS beamline 7.0, yielding a data set of unprecedented size and quality. These data have been compared to multiple scattering theory [5], and used as a test case, since the W(110) surface is known not to exhibit significant relaxation in its interlayer spacings relative to the bulk [6]. We have analyzed these experimental and theoretical results holographically in order to demonstrate the capabilities and limitations of photoelectron holography as a structural probe.

The experimental geometry at ALS beamline 7.0 is shown in Fig. 1(a). The W $4f_{7/2}$ photoelectron peak can be resolved into surface and bulk core-level-shifted components, as shown in Fig. 1(b). For each energy E (or wavenumber k) and direction studied, the W $4f_{7/2}$ peak was divided into surface and bulk emission intensities by integrating the areas under the higher-energy and lower-energy flanks of the two W $4f_{7/2}$ peaks, respectively, as shown by the shaded areas in Fig. 1(b). The brightness of the ALS undulator radiation permitted taking one of these spectra in ~10 sec, and doing the simpler area integration over bulk, surface, and high-energy background in ~1 sec.

Figures 2 and 3 respectively show the raw surface and bulk $I(\mathbf{k})$ data sets in $\mathbf{k}$-space, for kinetic energies in vacuum of E = 39eV to 309eV (wavenumbers $k = 3.2\text{Å}^{-1}$ to 9.0Å^{-1}), for a polar takeoff angle range of $10° \leq \theta \leq 90°$(≡ surface normal). A total of ~20,000 unique intensities in the symmetry-reduced 1/4th of the solid angle above the sample was measured.

Figures 4(a) and 5(a) show holographic images reconstructed from the normalized surface and bulk $\chi(\mathbf{k})$ data sets of Figs. 2 and 3 in the vertical $(\bar{1}1\bar{2})$ plane, using the original multi-energy algorithm proposed by Barton [3a], and Tong and co-workers [3b]. The emitter position is indicated by a dashed square, and the ideal positions of the neighboring atoms are indicated by circles.

1. Experimental details

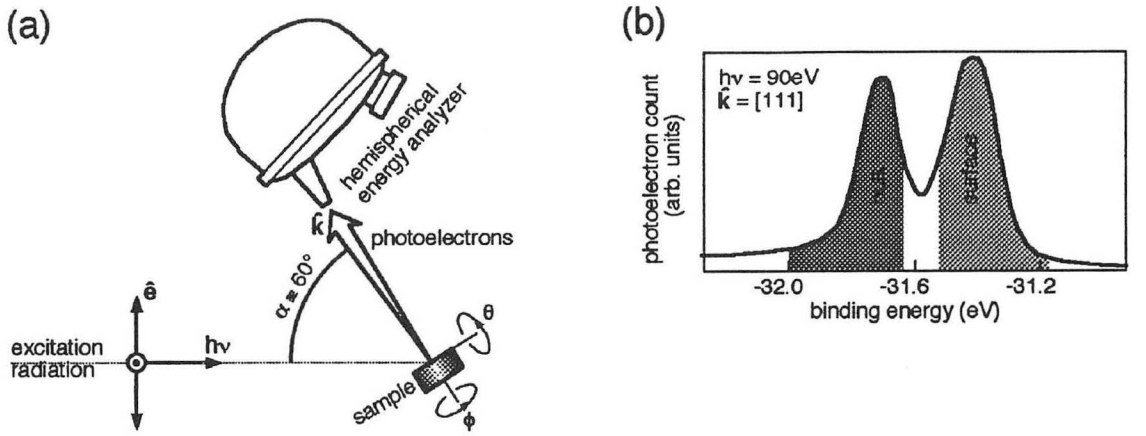

Figure 1. (a) Experimental geometry, including the orientation of the sample (where $\hat{\mathbf{n}}$ is the surface normal) with respect to the horizontal polarization vector ($\hat{\mathbf{e}}$) of the incident excitation radiation $h\nu$, and the exit photoelectron direction. (b) Typical W $4f_{7/2}$ x-ray photoelectron spectrum from W(110), indicating the surface and bulk core-level-shifted contributions used to generate the $I(\mathbf{k})$ intensity data points of Figs. 2-3.

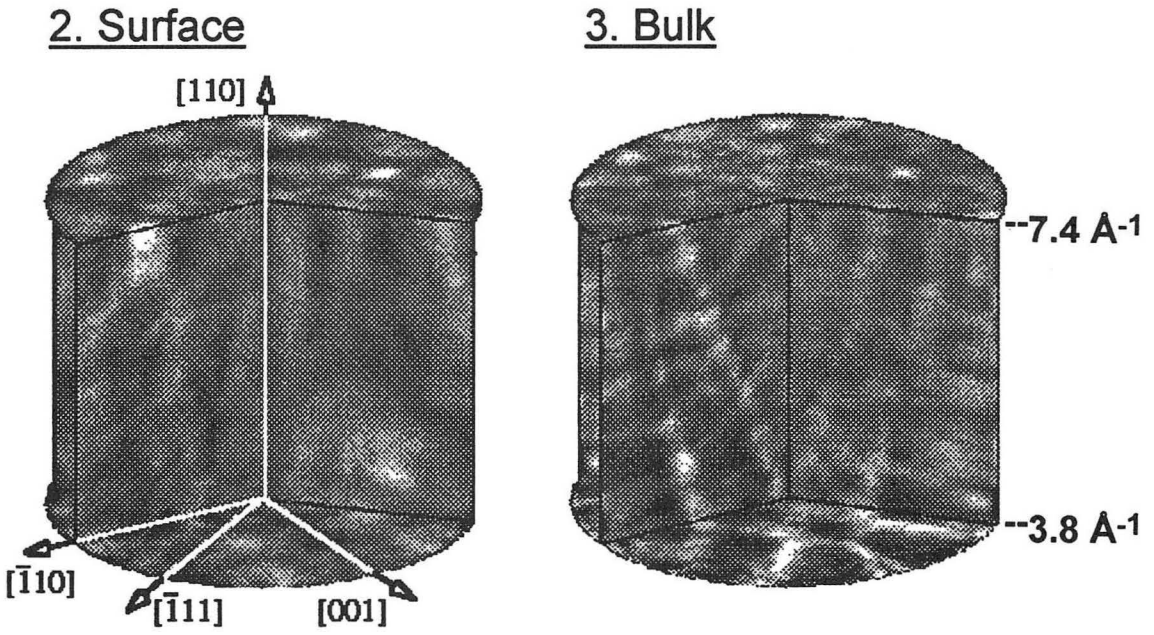

Figures 2-3. Volume representations of the normalized intensity data sets $I(\mathbf{k})$ for W $4f_{7/2}$ emission: 2 = surface and 3 = bulk. The vertical scale is wavenumber varying from 3.8Å^{-1} to 7.4Å^{-1} (corresponding to 56 eV to 211 eV in energy) and each plane is a stereographic projection of a nearly full-hemisphere data set taken over $0°\leq\theta\leq80°$ and ϕ varying over 360°. The energies and polar angles have here all been adjusted to be inside the surface, using an inner potential of V_0 = 14eV.

Figures 4(b) and 5(b) show the equivalent images reconstructed from a fully-converged multiple scattering calculation [5]. There is in general good agreement between experiment and theory. Both surface images very well resolve the backscattering atom below the emitter, and reasonably well resolve the forward scattering atoms above the emitter. The two bulk images exhibit artifactual peaks near the emitter, but agree in the general elongated and slightly doubled shape of the forward scattering images, which are weaker in experiment as compared to theory.

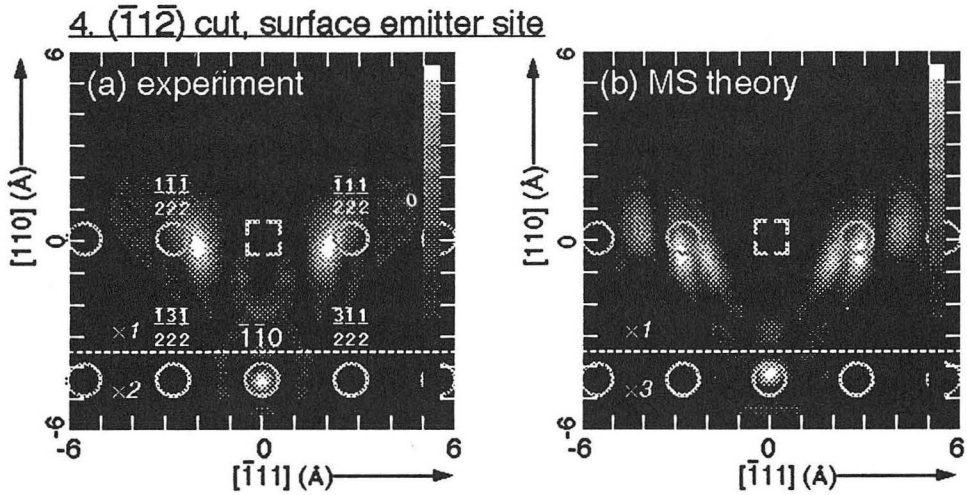

Figure 4. W(110) atomic images in the vertical $(\bar{1}1\bar{2})$ plane, as reconstructed from (a) the experimental W $4f_{7/2}$ surface-emission data set of Fig. 2; and (b) corresponding multiple scattering calculations. The surface emitter site at the origin is indicated by a dashed square, and the positions of the scatterers (assuming no surface relaxation) are indicated by circles. The nearest and next-nearest scattering positions have been labeled in panel (a). Axes are marked off in 1Å units. Image intensities for $z \leq -3.5$Å have been rescaled, with the scale factors indicated on the figures.

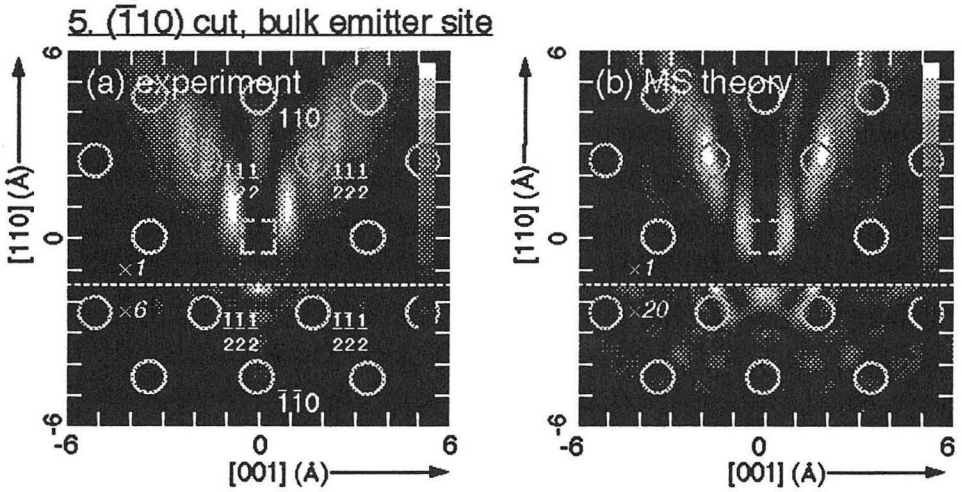

Figure 5. As Fig. 4, but for the bulk emission data set of Fig. 3, $(\bar{1}10)$ plane, and its corresponding multiple scattering simulation. Image intensities for $z \leq -1.5$Å have been rescaled, with the scale factors indicated on the figures.

Although encouraging in several respects, particularly for the case of the surface emitters, both the experimental and theoretical images of Figs. 4-5 suffer from image aberrations and artifacts arising from anisotropies in the photoelectron reference wave and the resultant scattered waves, and possible residual multiple scattering effects. Several modified reconstruction algorithms have

been proposed to account for the anisotropies mentioned, and these are found to exhibit varying degrees of success in improving such holographic images [4a,4b], including those for the present data [7]. Although further research into improved imaging algorithms and more tests against experimental data for other reference cases would certainly be worthwhile, the present data and analysis indicate that photoelectron holography can provide good-to-excellent *ab initio* estimates of the positions of the atoms beside and below surface emitters, and fair-to-good estimates of the positions of the atoms above bulk emitters. Such estimates could then be refined, using *R*-factor comparisons of experiment with model diffraction calculations for various structures.

REFERENCES

1. D. Gabor, Nature (London) **161**, 777 (1948).
2. A. Szöke, in *Short Wavelength Coherent Radiation: Generation and Applications*, T. Attwood, J. Boker (eds.), AIP Conference Proceedings No. 147, (AIP, New York, 1986) p. 361.
3. (a) J. J. Barton, Phys. Rev. Lett. **61**, 1356 (1988), and Phys. Rev. Lett. **67**, 3106 (1991). (b) S. Y. Tong, H. Huang, and C. M. Wei, Phys. Rev. B **46**, 2452 (1992), and references therein.
4. P. M. Len, F. Zhang, S. Thevuthasan, A. P. Kaduwela, M. A. Van Hove, and C. S. Fadley, (a) J. Electron Spec. and Relat. Phenom. **76**, 351 (1995), and (b) submitted to Surf. Sci. (c) P. M. Len, C. S. Fadley, and G. Materlik, to appear in *X-ray and Inner Shell Processes: 17th International Conference*, R. L. Johnson, H. Schmidt-Boeckering, and B. F. Sonntag, eds., AIP Conference Proceedings No. 389 (AIP, New York, 1997), and references therein.
5. SCAT photoelectron diffraction program package, Y. Chen, H. Wu, and D. A. Shirley, including more recent improvements by Y. Chen, private communication.
6. (a) M. Arnold, S. Sologub, G. Hupfauer, P. Bayer, W. Frie, L. Hammer, and K. Heinz, to be published. (b) B. Kim, J. Chen, J. L. Erskine, W. N. Mei, C. M. Wei, Phys. Rev. B **48**, 4735 (1993). (c) R. X. Ynzunza *et al.*, in preparation.
7. P. M. Len, J. D. Denlinger, E. Rotenberg, S. D. Kevan, B. P. Tonner, Y. Chen, M. A. Van Hove, and C. S. Fadley, to be published.

Research at UC-Davis was suppord in part by the Office of Naval Research (Contract Nos. N00014-90-5-1457 and N00014-94-1-0162), by the Director, Office of Energy Research, Office of Basic Energy Sciences, Material Sciences Division of the U.S. Department of Energy (Contract No. DE-AC03-76SF00098), the National Energy Research Supercomputer Center, and by the International Centre for Diffraction Data. Research at the Advanced Light Source Beamline 7.0, Lawrence Berkeley National Laboratory, was supported by the Department of Energy, Materials Sciences Division (Contract Nos. DE-FG02-92ER45468 and DE-AC03-76SF00098). User of a preliminary version of a new multiple-scattering photoelectron diffraction program package was made possible by Y. Chen, H. Wu, and D.A. Shirley.

Principal investigator: P. M. Len, Physics Department, University of California, Davis, CA 95616, USA. Email: len@alohi.ucdavis.edu. Telephone: 916-758-4562. Fax: 916-752-4717.

Ion-Implanted Si-Nanostructures Buried in a SiO_2 Substrate Studied with Soft-X-Ray Spectroscopy

R. Williams, J. -E. Rubensson, S. Eisebitt, J. Lüning, W. Eberhardt,
C. Buchal[1], P. Skytt[2], J. Guo[2], and J. Nordgren[2]

Institut für Festkörperforschung, Forschungszentrum Jülich, D-52425 Jülich, Germany
[1]Institut für Schicht- und Ionentechnik, Forschungszentrum Jülich, D-52425 Jülich, Germany
[2]Department of Physics, Uppsala University, Box 530, S-75121 Uppsala, Sweden

INTRODUCTON

In recent years silicon nanostructures have gained great interest because of their optical luminescence [1], which immediately suggests several applications, e.g., in optoelectronic devices. Nanostructures are also investigated because of the fundamental physics involved in the underlying luminesecence mechanism, especially attention has been drawn to the influence of the reduced dimensions on the electronic structure.

The forming of stable and well-defined nanonstructured materials is one goal of cluster physics. For silicon nanostructures this goal has so far not been reached, but various indirect methods have been established, all having the problem of producing less well defined and/or unstable nanostructures. Ion implantation [2, 3] and subsequent annealing is a promising new technique to overcome some of these difficulties. In this experiment we investigate the electronic structure of ion-implanted silicon nanoparticles buried in a stabilizing SiO_2 substrate.

Soft X-ray emission (SXE) spectroscopy features the appropriate information depth to investigate such buried structures. SXE spectra to a good approximation map the local partial density of occupied states (LPDOS) in broad band materials like Si. This has already been used to study the size dependence of the electronic structure in porous silicon [4, 5]. The use of monochromatized synchrotron radiation (MSR) allows for selective excitation of silicon atoms in different chemical environments. Thus, the emission from Si atom sites in the buried structure can be separated from contributions from the SiO_2 substrate. In this preliminary study strong size dependent effects are found, and the electronic structure of the ion-implanted nanoparticles is shown to be qualitatively different from porous silicon. The results can be interpreted in terms of quantum confinement and chemical shifts due to neighboring oxygen atoms at the interface to SiO_2.

EXPERIMENT

Nanostructures (diameter ≈ 30-50Å) were produced by implanting Si^+-ions at an acceleration voltage of 35 kV into a quartz glass (SiO_2) matrix. A dose of $5x10^{16}$ Si cm^{-2} and subsequent annealing for 1 h. at 700°C produced small nanostructures (Sample S), and a dose of $7x10^{16}$ Si cm^{-2}, followed by annealing for 1 h. at 900°C produced larger clusters (Sample L). Experiments were carried out using MSR (FWHM≈ 50 meV around the Si L edge, E≈ 100 eV) from beamline 7.0 [6] and a grazing incidence Rowland spectrometer [7] (FWHM≈ 250 meV).

RESULTS

The total fluorescence yield Si L absorption spectra of sample S and L and a crystalline silicon (c-Si) reference sample are shown in Fig.1. They derive their intensity from transitions where a 2p electron is promoted to the first empty states, and are related to the density of unoccupied states of Si (s+d) symmetry. The most intense features in the absorption spectra of the implanted samples coincide with the absorption spectrum of SiO_2,(see inset) and can be attributed to the substrate.
Such an interpretation is ruled out for the spectral features found below the SiO_2 absorption threshold (≈104 eV) which we therefore assign to the nanostructures.

These structures show an on-set close to the absorption edge of c-Si. The absorption edges in the spectra of the ion-implanted samples are, however, shifted to higher energies, a shift which is slightly larger for sample S than for sample L. In both samples the absorption structures are broadened and the sharp features are increasingly washed out when the cluster sizes are reduced.

The broadening of the absorption spectra is principally ascribed to contributions from atomic sites in clusters of different sizes. The position of the absorption edges are influenced by the chemical surrounding and quantum confinement effects. A superposition of absorption spectra would hence lead to the observed broadening.

The SXE spectra of high-energy excited ion-implanted samples are dominated by the emission from the SiO_2 substrate. By tuning the excitation energy below the SiO_2 absorption threshold the silicon nanoparticles can be selectively excited. The excitation energies chosen for the emission spectra are indicated as dashed vertical lines in Fig.1. The lowest excitation energy used for the SXE spectra shown in Fig.2, selects the nanostructures exhibiting the lowest absorption threshold.

The intense emission peak at around 100.2 eV in both panels is mainly due to diffuse reflection of the primary beam. Its intensity depends on the reflectivity of the sample, which varies with the

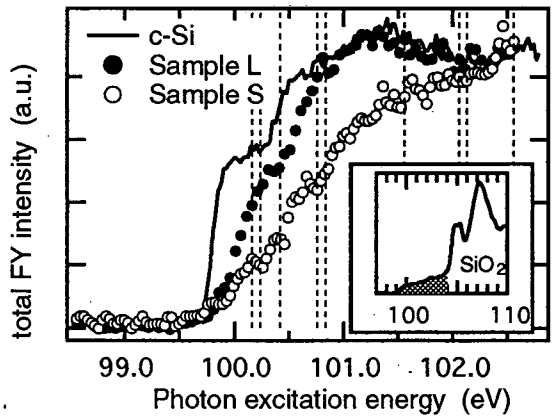

Figure 1. The SXA spectra of sample S (open circles), sample L (filled circles) and a silicon reference sample (line) measured with total fluorescence yield. The dotted vertical lines indicate the energies where emission spectra were recorded.

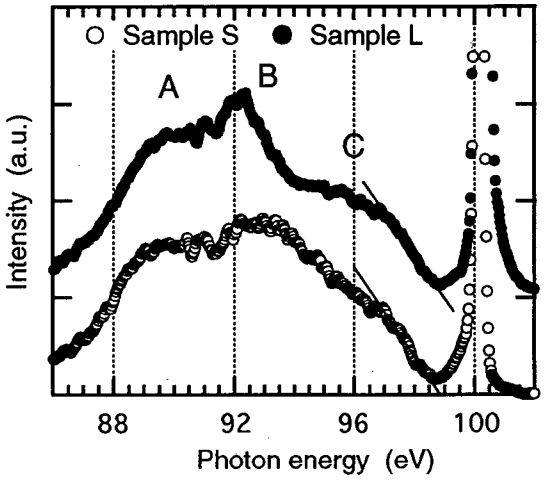

Figure 2. The SXE spectra of sample S (open circles) and sample L (filled circles) excited at 100.2 eV.

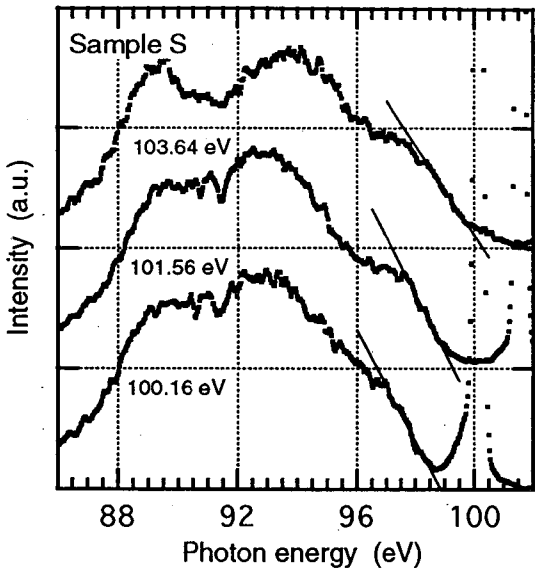

Figure 3. SXE spectra of sample S excited at three different energies below the SiO_2 absorption threshold.

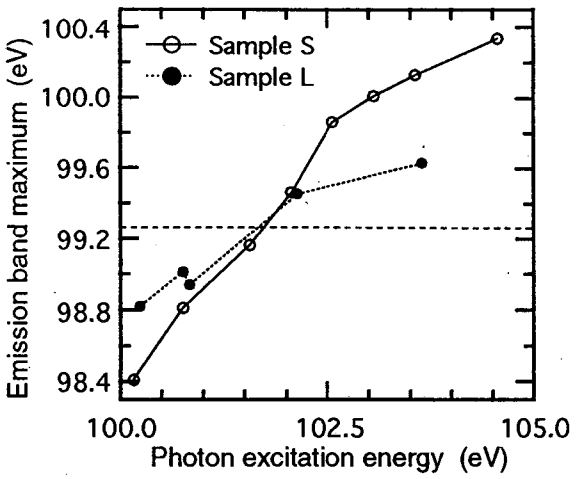

Figure 4. The shift of the Emission band maximum with increasing excitation energy is displayed for sample S (open circles) and sample L (filled circles). The dashed horizontal line indicates the location of the VB maximum for a crystalline Si reference sample.

roughness of the surface. The broader structures at lower energies to a good approximation map the LPDOS of Si (s+d)-symmetry of the nanostructures selectively excited at the lowest energy. The spectrum of sample L in Fig.2 shows three pronounced structures at 89 eV (A), 92 eV (B), and 96 eV (C). The spectrum of sample S has a similar structure, but the maximum (B) has decreased in intensity relative to (A) and intensity is added in the region between (B) and (C).

In both spectra the high-energy cut-off is shifted towards lower energies relative to crystalline Si, and this shift is larger for sample S than for sample L. The quantum confinement model predicts an opening of the band gap with decreasing size. Hence, the observation of the edge shifts in the absorption and emission spectra are in agreement with this model.

The samples inherently contain several inequivalent Si atom sites, e. g., where the oxygen coordination changes from Si in the bulk of the nanostructures to Si at the SiO_2 interface. The lowest excitation energy selects Si atoms without nearest oxygen neighbors, and as a first Ansatz we fit the spectra with spectra from known phases of pure silicon. We find that a superposition of the spectra of crystalline (54%) and amorphous silicon (46%) is in good agreement with the spectrum of sample L. Hence, this sample may contain a mixture of the two phases. No multiphase model is, however, applicable to the spectrum of sample (S). Note that this spectrum also substantially disagrees with spectra of porous Si [4, 5], and it therefore must reflect a modified local structure of silicon, which has earlier not been investigated.

Fig.3 shows the excitation energy dependence of the SXE spectrum of sample S. When the excitation energy increases the peaks (A) and (B) separate, the peak (C) and notably the emission band maximum shifts to higher energies with increasing excitation energy. This shifting effect appears in sample L as well, but is not as pronounced as in sample S. The development of this shift can be seen in Fig.4, where the location of the emission band maximum determined by linear extrapolation to zero is plotted versus excitation energy. The maximum moves almost linearly with a slope of 0.5 for sample S and 0.3 for sample L.

These shifts cannot be attributed to dynamic effects alone, but must be due to emission from different atomic sites in the sample. In the following we develop a simple model in terms of LPDOS to account for this observation.

The quantum confinement model predicts an opening of the bandgap with increasing confinement. When the size of a structure is reduced the CB minimum is shifted to higher energies and simultaneously the VB maximum must shift to lower energy. Assuming the Si 2p core level energy independent of structure size, smaller structures are excited with increasing excitation energy. These smaller structures can thus only contribute to the emission spectra at energies below the energy maximum of the spectra excited at lower energies. Thus the quantum confinement model alone is not sufficient to explain the shift of the VB maximum.

To understand the observed excitation energy dependence a chemical shift of the Si core level must be taken into account. When a Si atom is replaced with an oxygen atom as a nearest neighbor the Si 2p core level is shifted by approximately 1 eV to higher binding energy. If the VB edge locally at these Si atoms is less shifted than the core level, they contribute to the emission spectra at energies above the emission band maximum of the crystalline bulk Si. The shift of the emission band maximum recorded in our spectra can then be assigned to interface regions between the silicon nanostructures and the SiO_2 substrate. A detailed analysis of the excitation energy dependence is in progress.

CONCLUSIONS

Using chemically selective excitation the LPDOS of ion-implanted buried silicon nanostructures in a SiO_2 matrix have been studied. A band gap opening in agreement with the quantum confinement model was observed. The spectra cannot be described in terms known silicon phases, (including porous silicon) but map a modified LPDOS which has earlier not been studied. The excitation energy dependence is related to oxygen terminated regions in the sample, and contains information about the electronic structure of the interface between the silicon nanostructures and the SiO_2 substrate.

REFERENCES

1 L. T. Canham, Appl. Phys. Lett. **57**, 1046 (1990)
2 C. W. White, J. D. Budai, J. G. Zhu, and S. P. Withrow, Mat. Res. Soc. Symp. Pruc. **396**, 377 (1996)
3 Jane G. Zhu, C. W. White, J. D. Budai, S. P. Withrow, and Y. Chen, to be submitted to Journal of Applied Physics.
4 S. Eisebitt, J. Lüning, J.-E. Rubensson, T. van Buuren, S. N. Patitsas, T. Tiedje, M. Berger, R. Arens-Fischer, S. Fronhoff, and W. Eberhardt, Solid State Comm. **97**, 549 (1996),
5. S. Eisebitt, S. N. Patitsas, J. Lüning, J.-E. Rubensson, T. van Buuren, T. Tiedje, and W. Eberhardt, Europhysics Lett., **37**, 133 (1997).
6 T. Warwick, P. Heimann, D. Mossessain, W. MacKinney, and H. Padmore, Rev. Sci. Instrum., **66**, 2037 (1995).
7 J. Nordgren, G. Bray, S.Cramm, R. Nyholm, J. -E. Rubensson, and N. Wassdahl, Rev. Sci. Instrum., **60**, 1969 (1989).

This work was supported by the Swedish Natural Science Research Council and the Goran Gustafssons Foundation for Science and Medicine.

Principal investigator: Jan-Erik Rubensson, IFF-IEE, Forschungszentrum Jülich, Germany. Email: J.Rubensson@KFA-Juelich.De. Telephone: +49-2461-616670.

Lifetime-Vibrational Interference Effects in Resonantly Excited X-Ray Emission Spectra of CO

P. Skytt, P. Glans, K. Gunnelin, J. Guo, and J. Nordgren
Physics Dept., Uppsala University, Box 530, S-751 21 Uppsala, Sweden

INTRODUCTION

The parity selection rule for resonant X-ray emission as demonstrated for O_2 and N_2 [1] (see other abstract in this annual report) can be seen as an effect of interference between coherently excited degenerate localized core states. One system where the core state degeneracy is not exact but somewhat lifted was previously studied at ALS, namely the resonant X-ray emission of amino-substituted benzene (aniline) [2]. It was shown that the X-ray fluorescence spectrum resulting from excitation of the C1s at the site of the "aminocarbon" could be described in a picture separating the excitation and the emission processes, whereas the spectrum corresponding to the quasi-degenerate carbons could not. Thus, in this case it was necessary to take interference effects between the quasi-degenerate intermediate core excited states into account in order to obtain agreement between calculations and experiment.

The different vibrational levels of core excited states in molecules have energy splittings which are of the same order of magnitude as the natural lifetime broadening of core excitations in the soft X-ray range. Therefore, lifetime-vibrational interference effects are likely to appear and influence the band shapes in resonant X-ray emission spectra. Lifetime-vibrational interference has been studied in non-resonant X-ray emission [3], and in Auger spectra [4]. In this report we discuss results of selectively excited soft X-ray fluorescence spectra of molecules, where we focus on lifetime-interference effects appearing in the band shapes.

EXPERIMENT

The experiments were made at the soft X-ray fluorescence end station at beamline 7.0 [5]. A compact grazing incidence grating spectrometer [6] was used to record soft X-ray emission spectra, excited with monochromatized radiation from the SGM monochromator at this undulator beamline [7]. The spectrometer can detect emission either horizontally or vertically, i.e. parallel respectively perpendicular to the polarization vector of the synchrotron radiation. In order to allow gas phase samples to be studied a gas cell was used, which was provided with a silicon nitride input window of diameter 0.2 mm and thickness 1000 Å. A second window made of polyimide, with about the same thickness, was used as exit window for the fluorescence.

RESULTS

Fig.1 shows resonantly excited O K emission of CO in the gas phase [8], excited at different positions within the $2\pi^*$ absorption band. The second spectrum from bottom, 534.2 eV, corresponds to the $2\pi^*$ peak maximum. Plotted in the figure are also the calculated spectra where interference has been omitted respectively included (*direct* respectively *total*). One observes that there are significant deviations between experimental spectra and the ones calculated

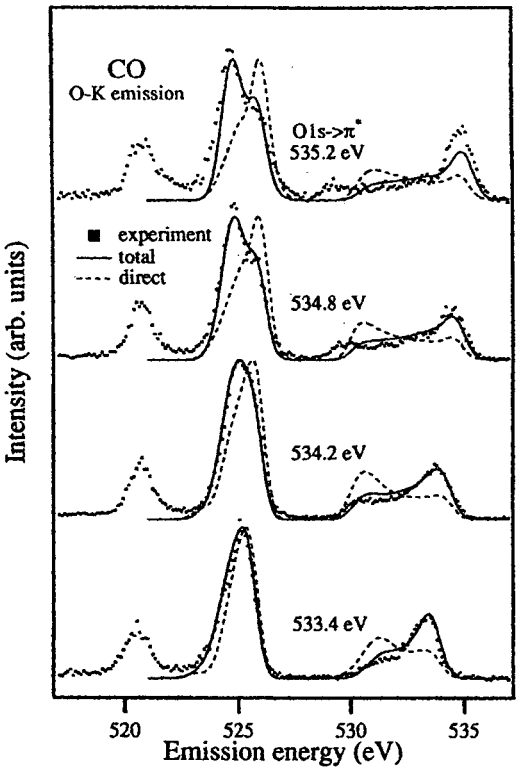

Fig.2 Lifetime-vibration interference effects in the O K emission of CO.

ground state, and thus the 0-0 transition is dominating. Also, the lifetime width of the C 1s state is smaller than that of O1s, and therefore the interference effects are small. Going to higher vibrations the very large difference in absorption cross section between the 0-0 transition and the 0-n transitions will give rise to significant effects, since the tail of the 0-0 peak has significant amplitude at the energy of the 0-1 and 0-2 transitions.

CONCLUSIONS

The presented examples show that it is necessary to include vibrational-interference effects in order to understand the details of resonant soft X-ray emission of molecules. Also in cases where one might not expect significant effects due to a small ratio between lifetime width and vibrational splitting one may have to consider such effects, since tail effects can be substantial.

without interference, whereas quite good agreement is obtained when interference is taken into account.

The appearance of interference effects in the O K emission is not surprising in view of the ratio of lifetime width and vibrational splitting. However, also in cases where one might not expect significant effects due to a small ratio between lifetime width and vibrational splitting one might have to consider such effects, since tail effects can be substantial. In the corresponding C K emission, the situation is different from that of oxygen, see Fig.2. Here essentially no interference effects are observed when exciting to the v=0 vibration of the $2\pi^*$ absorption peak. However, when tuning the excitation to the higher vibrational levels effects start to appear. This can be understood in the following way. The equilibrium bond length of the C1s-$2\pi^*$ state is not very different from that of the

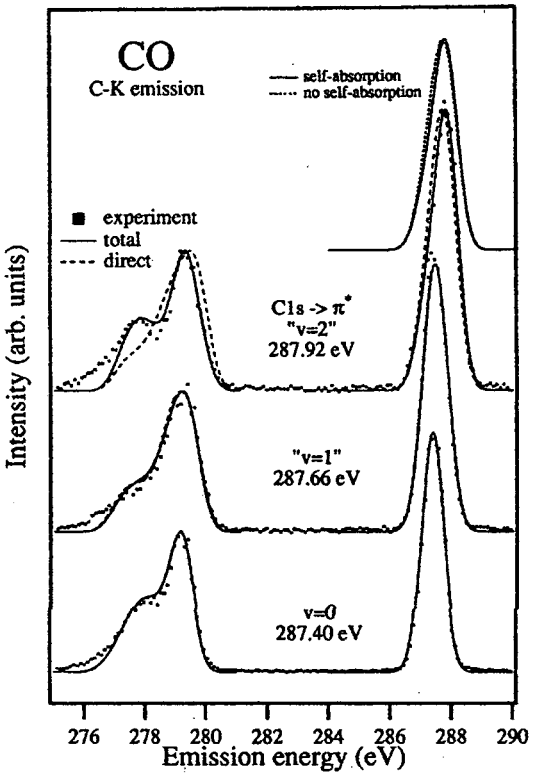

Fig.1 Lifetime-vibrational interference effects in the C K emission of CO.

ACKNOWLEDGEMENTS

We are indebted to T. Warwick, Eli Rotenberg and J. Denlinger for assistance at the beamline and for stimulating interactions.

REFERENCES

1. Skytt, P.; Glans, P.; Guo, J; Gunnelin, K; and others. Phys. Rev. Lett., **77**, 5035 (1996); Glans, P; Gunnelin, K; Skytt, P; Guo, J, and others. Accepted for publ. in J. Elecr. Spectr. Rel. Phenom.
2. Luo, Y; Ågren, H.; Guo, J; Skytt, P.; and others. Physical Review A , **52**, 3730 (1995)
3. Gel'mukhanov, F; Mazalov, L.N.; Kondratenko, A.V.; Chem. Phys. Lett., **46**, 133 (1977); Flores-Riveros, A; Correia, N; Ågren, H; Pettersson, L; and others. J. Chem. Phys., **83**, 2053 (1985).
4. Rubensson, J.-E.; Neeb, M.; Biermann, M; and W. Eberhardt. J. Chem. Phys., **99**, 1633 (1993). See also: Neeb, M; Rubensson; M.; Biermann, M; and W. Eberhardt; and others. Chem. Phys. Lett. 212, 205 (1993). Neeb, M; Rubensson; M.; Biermann, M; and W. Eberhardt. J. Electr. Spectr. 67, 261 (1994).
5. Guo, J.; Wassdahl, N.; Skytt P.; Butorin, S.M.; and others. Rev. Sci. Instrum, **66**, 1561 (1995).
6. Nordgren, J.; Bray G.; Cramm, S; Nyholm R; and others. Rev. Sci. Instrum., **60**, 1690 (1989).
7. Warwick, T.; Heimann, P.; Mossessain, D.; and Padmore, H. Rev. Sci. Instrum., **66**, 2037 (1995).
8. Skytt, P; Glans, P; Gunnelin, K; Guo J; and Nordgren. Phys. Rev. A, **55**, 146 (1997).

This work was supported by the Swedish Natural Science Research Council and the G. Gustafsson Foundation for Science and Medicine.

Principal investigator: E. Joseph Nordgren, Physics Department of Uppsala University, Sweden. E-mail: joseph@fysik.uu.se

Low-Energy *d-d* Excitations in MnO Studied by Resonant X-Ray Fluorescence Spectroscopy

S.M. Butorin; J. Guo; M. Magnuson; P. Kuiper, and J. Nordgren
Physics Dept., Uppsala University, Box 530, S-751 21 Uppsala, Sweden

INTRODUCTION

Resonant soft X-ray emission spectroscopy has been demonstrated to possess interesting abilities for studies of electronic structure in various systems, such as symmetry probing, alignment and polarization dependence, sensitivity to channel interference, etc. (see other abstracts in this Annual Report). In the present abstract we focus on the feasibility of resonant soft X-ray emission to probe low energy excitations by means of resonant electronic X-ray Raman scattering..

Resonant X-ray emission can be regarded as an inelastic scattering process where a system in the ground state is transferred to a low excited state via a virtual core excitation. The energy closeness to a core excitation of the exciting radiation enhances the (generally) low probability for inelastic scattering at these wavelengths [1]. Therefore soft X-ray emission spectroscopy (in resonant electronic Raman mode) can be used to study low energy d-d excitations in transition metal systems. The involvement of the intermediate core state allows one to use the selection rules of X-ray emission, and the appearance of the elastically scattered line in the spectra provides the reference to the ground state.

EXPERIMENT

The experiments were made at the soft X-ray fluorescence end station at beamline 7.0 [2]. A compact grazing incidence grating spectrometer [3] was used to record soft X-ray emission spectra, excited with monochromatized radiation from the SGM monochromator at this undulator beamline [4]. The spectrometer can detect emission either horizontally or vertically, i.e. parallel respectively perpendicular to the polarization vector of the synchrotron radiation. Sample preparation can be made in a separate chamber with transfer capabilities, and a load-lock system allows rapid sample introduction.

RESULTS

Resonant excitation produces dramatically energy dependent spectra when applied to localized systems, such as in the case of the 2p absorption edges of manganese in MnO, see Fig.1 [5]. In its ground state, the five 3d electrons of Mn^{2+} have their spins parallel, forming a ^6S state. When a 2p electron is excited into the 3d shell, it can decay by X-ray emission to its electronic ground state, producing a line at the excitation energy. One also observes a peak 3.5 eV below the excitation energy. This peak is due to processes in which a majority spin electron falls into the core hole. The final states are then quartet states with four spins up and one spin down. Many of these states have an energy about 3 eV above the ground state. At higher excitation energies in the $L_{2,3}$ manifold, the intermediate states contain more quartet states, which explains the increase of quartet and doublet states in the final state spectrum. Quantitatively, the relative intensities of the final states as a function of excitation energy can be calculated by atomic multiplet theory.

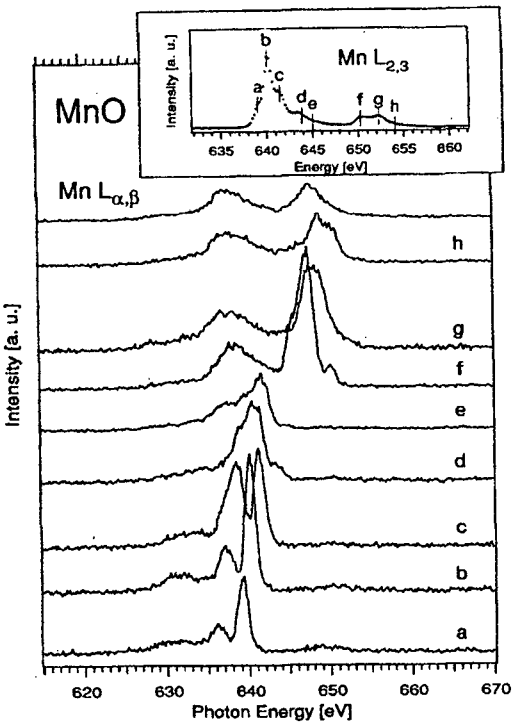

Fig.1 Resonant $L_{2,3}$ emission spectra of MnO. Inset shows $L_{2,3}$ absorption spectrum.

We measured the d-d excitations of Mn^{2+} by resonant electronic soft X-ray Raman spectroscopy. The energy differences that we found do not depend on the core hole or its life time. They are the same as those obtained by optical spectroscopy or electron-energy loss spectroscopy (EELS). Working with core level resonances has the advantages that the d-d excitations are allowed by parity and spin selection rules, and that it is not difficult to calculate their intensities. With improved resolution, this technique can be expected to provide element specific information about low energy excitations in complex solids and molecules.

CONCLUSIONS

By recording the soft X-ray emission spectra of MnO, resonantly excited over the $L_{2,3}$ absorption edge, we obtain the spectrum of low energy d-d-excitations, which are allowed by parity and spin selection rules in this two-photon scattering process. Energies and intensities of observed structures are well described in terms of atomic calculations.

ACKNOWLEDGEMENTS

We are indebted to T. Warwick, Eli Rotenberg and J. Denlinger for assistance at the beamline and for stimulating interactions.

REFERENCES

1. Åberg, T.; and Crasemann. B.; (*X-ray Resonant Scattering*. Eds. K. Fisher, G. Materlik, and C. Sparks, Elsevier, Amsterdam 1994).
2. Guo, J.; Wassdahl, N.; Skytt P.; Butorin, S.M.; and others. Rev. Sci. Instrum, **66**, 1561 (1995).
3. Nordgren, J.; Bray G.; Cramm, S; Nyholm R; and others. Rev. Sci. Instrum., **60**, 1690 (1989).
4. Warwick, T.; Heimann, P.; Mossessain, D.; and Padmore, H. Rev. Sci. Instrum., **66**, 2037 (1995).
5. Butorin S.M.; Guo J.; Magnuson M.; Kuiper P.; and Nordgren J., Physical Review B, **54**, 4405 (1996).

This work was supported by the Swedish Natural Science Research Council and the G. Gustafsson Foundation for Science and Medicine.

Principal investigator: E. Joseph Nordgren, Physics Department of Uppsala University, Sweden. E-mail: joseph@fysik.uu.se

Magnetic X-Ray Dichroism in Ultrathin Epitaxial Films

J.G. Tobin,[1] K.W. Goodman,[1] T.R. Cummins,[2] G.D. Waddill,[2] S. Mishra,[3] J. Gammon,[3] D.P. Pappas,[3] F.O. Schumann,[4] S. Wu,[4] G. Mankey,[4] R.F. Willis,[4] J.D. Denlinger,[5] E. Rotenberg,[5] A. Warwick,[5] J. Kortright,[5] and N.V. Smith[5]

[1]Lawrence Livermore National Laboratory, Livermore, CA 94550
[2]University of Missouri-Rolla, Rolla, MO 65401-0249
[3]Virginia Commonwealth University, Richmond, VA 22284
[4]Pennsylvania State University, University Park, PA 16802
[5]Advanced Light Source, Ernest Orlando Lawrence Berkeley National Laboratory, Berkeley, CA 94720

We have used Magnetic X-ray Linear Dichroism (MXLD) and Magnetic X-ray Circular Dichroism (MXCD) to study the magnetic properties of epitaxial overlayers in an elementally specific fashion. Both MXLD and MXCD Photoelectron Spectroscopy were performed in a high resolution mode at the Spectromicroscopy Facility of the ALS. Circular Polarization was obtained via the utilization of a novel phase retarder (soft x-ray quarter wave plate) based upon transmission through a multilayer film. Our samples were low temperature Fe overlayers, magnetic alloy films of NiFe and CoNi, and Gd grown on Y. Our results include a direct comparison of high resolution angle resolved Photoelectron Spectroscopy performed in MXLD and MXCD modes as well as structural studies with photoelectron diffraction.

This work was performed under the auspices of the U.S. Department of Energy by Lawrence Livermore National Laboratory under contract number W-7405-ENG-48. The Spectromicroscopy Facility and the Advanced Light Source were constructed and are operated under support of the U.S. Department of Energy.

Principal investigator: James G. Tobin, Lawrence Livermore National Laboratory. Email: tobin1@llnl.gov. Telephone: 510-422-7247.

Magnetic X-Ray Linear Dichroism in Resonant and Non-Resonant Gd 4*f* Photoemission

S. Mishra,[1] W.J. Gammon,[1] D.P. Pappas,[1] K.W. Goodman,[2] J.G. Tobin,[2] F.O. Schumann,[3] R.F. Willis,[3] J.D. Denlinger,[4] E. Rotenberg,[4] A. Warwick,[4] and N.V. Smith[4]

[1]Department of Physics, Virginia Commonwealth University, Richmond, VA 23284-2000

[2]Lawrence Livermore National Laboratory, Livermore, CA, 94550

[3]Department of Physics, Pennsylvania State University, University Park, PA 16802

[4]Advanced Light Source, Ernest Orlando Lawrence Berkeley National Laboratory, Berkeley, CA 94720

The enhancement of the magnetic linear dichroism in resonant 4f photoemission (MLDRPE) is studied from a 50 monolayer film of Gd/Y(0001). The ALS at beamline 7.0.1 provided the source of linearly polarized x-rays used in this study. The polarized light was incident at an angle of 30 degrees relative to the film plane, and the sample magnetization was perpendicular to the photon polarization. The linear dichroism of the 4f core levels is measured as the photon energy is tuned through the 4d-4f resonance. We find that the MLDRPE asymmetry is strongest at the resonance. Near the threshold the asymmetry has several features which are out of phase with the fine structure of the total yield.

This work was done under the auspices of the U.S. Department of Energy by Lawrence Livermore National Laboratory under contract number W-7405-ENG-48. This work is based on work supported by the National Science Foundation under grant No. DDMR-9458004. Additional support from Research Corporation under grant No. CC3778 and the Jeffress Trust, No. J338 is also acknowledged.

Principal investigator: James G. Tobin, Lawrence Livermore National Laboratory. Email: tobin1@llnl.gov. Telephone: 510-422-7247.

Magnetic X-Ray Linear Dichroism of Ultrathin Fe-Ni Alloy Films

F.O. Schumann,[1] R.F. Willis,[1] K.W. Goodman,[2] J.G. Tobin,[2]
J.D. Denlinger,[3] E. Rotenberg,[3] and A. Warwick[3]

[1]Department of Physics, Pennsylvania State University, University Park, PA 16802
[2]Lawrence Livermore National Laboratory, Livermore, CA 94550
[3]Advanced Light Source, Accelerator and Fusion Research Division, Ernest Orlando Lawrence Berkeley National Laboratory, Berkeley, CA 94720

We have studied the magnetic structure of ultrathin Fe-Ni alloy films as a function of Fe concentration by measuring the linear dichroism of the 3p-core levels in angle-resolved photoemission spectroscopy. The alloy films, grown by molecular-beam epitaxy on Cu(001) surfaces, were fcc and approximately four monolayers thick. The intensity of the Fe dichroism varied with Fe concentration, with larger dichroisms at lower Fe concentrations. The implication of these results to an ultrathin film analogue of the bulk Invar effect in Fe-Ni alloys will be discussed. These measurements were performed at the Spectromicroscopy Facility (Beamline 7.0.1) of the Advanced Light Source.

The Spectromicroscopy Facility and the Advanced Light Source were constructed and are operated under the support of the U.S. Department of Energy. This work was performed under the auspices of the U.S. Department of Energy by Lawrence Livermore National Laboratory under Contract No. W-7405-ENG-48.

Principal investigator: James G. Tobin, Lawrence Livermore National Laboratory. Email: tobin1@llnl-gov. Telephone: 510-422-7247.

Photoelectron Diffraction k-Space Volumes of the c(2x2) Mn/Ni(100) Structure

S. Banerjee[1], S. Ravy[1,2], J. Denlinger[1], X. Chen[1], D. K. Saldin[1] and B. P. Tonner[1]

[1]Department of Physics, University of Wisconsin-Milwaukee, P.O. Box 413 Milwaukee, WI 53201, U.S.A
[2]Laboratoire de Physique des solides (CNRS URA 2), Université Paris-Sud 91405 Orsay, France

Traditionally, x-ray photoelectron diffraction (XPD) studies have either been done by scanning the diffraction angle for fixed kinetic energy (ADPD), or scanning the kinetic energy at fixed exit angle (EDPD). Both of these methods collect subsets of the full diffraction pattern, or volume, which is the intensity of photoemission as a function of momentum direction and magnitude. With the high intensity available at the *Spectromicroscopy Facility* (BL 7.0) "ultraESCA" station, we are able to completely characterize the photoelectron diffraction patterns of surface structures, up to several hundred electron volts kinetic energy. This large diffraction 'volume' can then be analyzed in many ways. The k-space volume contains as a subset the energy dependent photoelectron diffraction spectra along all emission angles. It also contains individual, hemispherical, diffraction patterns at specific kinetic energies. Other 'cuts' through the data set are also possible, revealing new ways of viewing photoelectron diffraction data, and potentially new information about the surface structure being studied.

In this article we report a brief summary of a structural study being done on the c(2x2) Mn/Ni(100) surface alloy. This system is interesting for both structural and magnetic reasons. Magnetically, the Mn/Ni(100) surface alloy exhibits parallel coupling of the Mn and Ni moments, which is opposite to the reported coupling for the bulk, disordered, alloy. Structurally, the Mn atoms are believed to lie well above the surface plane. This rumpling of the Mn atoms is contrary to expectations based on free atom sizes, since the Mn atom should be smaller than the Ni substrate atoms, leading to an expected contraction. If the Mn atoms have a large local magnetic moment, however, this may lead to an effectively large atomic radius, which could explain the outward motion. Our XPD measurements are being used to test various structural models for this surface.

The experiments were performed on the *SpectroMicroscopy* PRT beamline at the Advanced Light Source, which is optimized for photon energies in the range from 60 eV to about 1000 eV[1]. A custom designed photoelectron diffraction system was employed, which has a computer controlled five-axis manipulator, and a high angular resolution, 16 channel detector hemispherical energy analyzer. The energy resolution of the electron analyzer was 0.06 eV, and had an angular resolution of less than $\pm 1^{\circ}$. The energy resolution of the x-ray beam was less than 0.04 eV, for an overall energy resolution of less than 72 meV. The photon beam is incident in the horizontal direction, with p-polarization and a 30° grazing angle of incidence, and the electron detection axis is in the horizontal scattering plane, with an angle of 60° to the incident photon beam. The axis of rotation for polar angle scans is horizontal, which gives perfect symmetry around normal emission and makes it easy to identify absolute emission angles in the XPD data. This geometry is also optimized for signal intensity at grazing angles of incidence for the photon beam, and grazing exit angles for the electron beam[2].

Photoelectron diffraction patterns were acquired by measuring the photoemission spectrum from the Mn 3p, Ni 3p, and inelastic background at each setting of emission angle and incident photon energy. At each photon energy, a diffraction pattern was measured by stepping through a sequence of emission angles in a 90° azimuthal sector. The angle scan pattern consisted of a se-

quence of azimuthal scans of a quadrant, after which the polar angle of emission is increased and the next azimuthal scan implemented. The range of polar angles collected was from θ=0 (normal emission) to θ=80 degrees. The polar (θ) and azimuthal (ϕ) angular steps were chosen to uniformly sample the quarter-hemisphere of emission angles. The total number of distinct emission angles in the quarter hemisphere was 550, with precision in setting angular positions of 0.2°, from which the hemispherical diffraction pattern was created by a four-fold rotation (no mirror symmetry is applied).

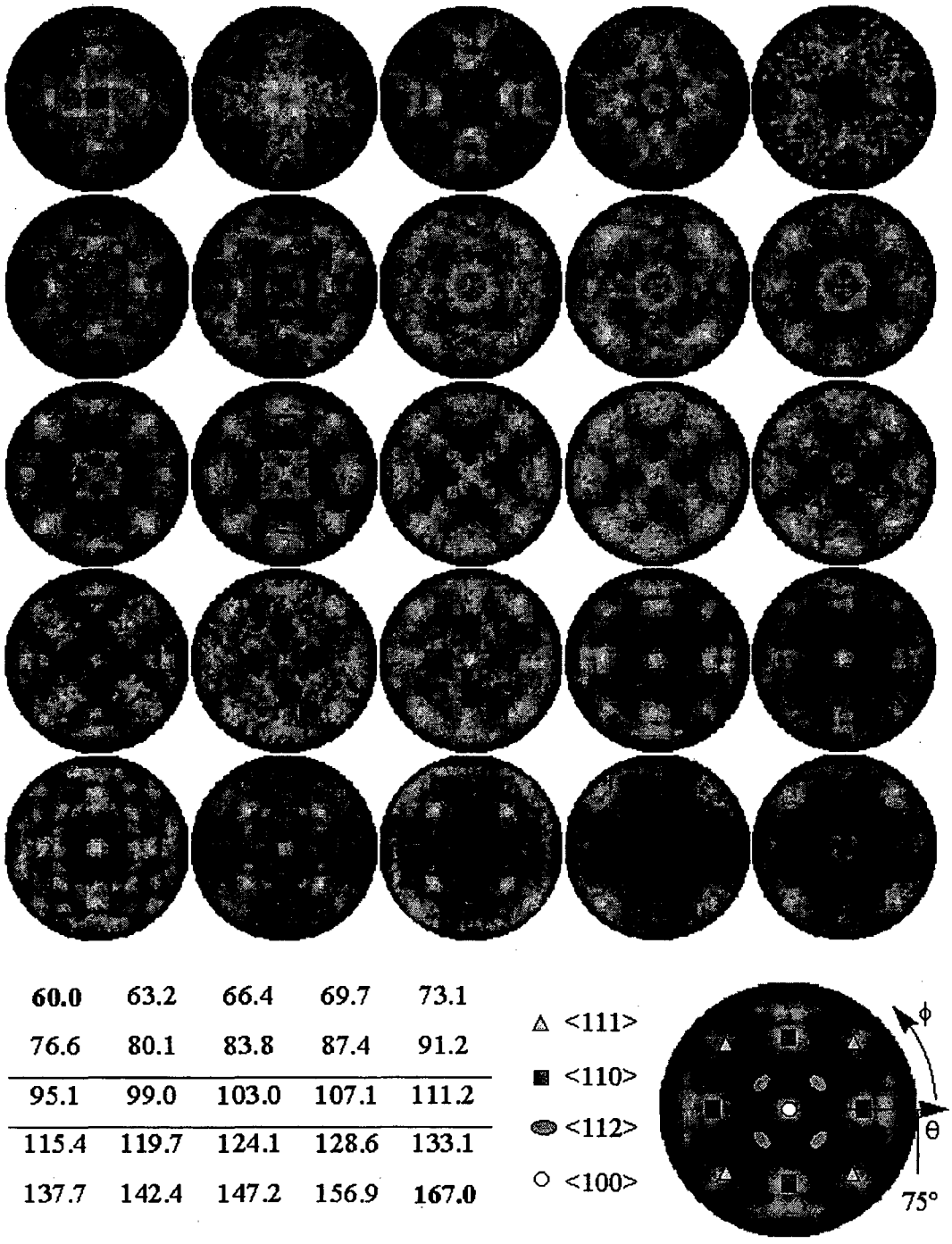

Fig. 1: Experimental diffraction patterns from a c(2×2) Mn/Ni(001) surface alloy for the Mn emitter. 25 diffractograms are shown for Kinetic Energy=60eV to 167eV, equispaced in total momentum by 0.1Å^{-1} from **k**=4.0 to 6.2 Å^{-1} and by 0.2 Å^{-1} from **k**=6.2 to 6.6 Å^{-1}.

Linearly polarized soft x-rays with photon energies ranging from 50 eV to 550 eV were used to measure XPD patterns from both the valence band and core-levels, spanning a range in electron kinetic energy from very surface sensitive at low energy to a forward-scattering limit at high kinetic energy. In addition, a series of 25 diffraction patterns from the Mn and Ni core-levels were accumulated as a function of incident photon energy, with the photon energies selected to produce constant differences in total electron momentum from pattern to pattern. This 'diffraction volume' can be used for direct inversion techniques (holography) with a complete experimental data set. Finally, energy dependent photoelectron diffraction (EDPD) curves were taken at several different emission angles. These EDPD curves matched the synthetic EDPD curves which can be extracted from the diffraction volume.

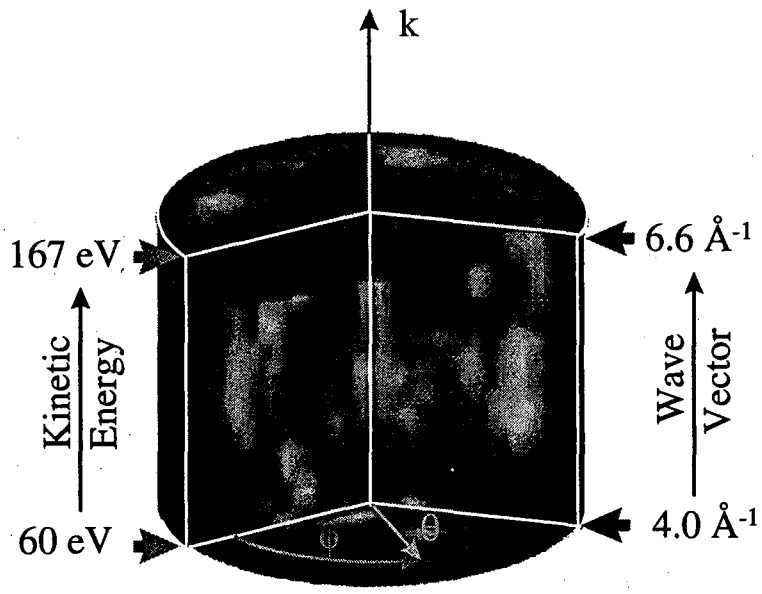

Fig. 2: Photoelectron diffraction k-space volume assembled from the data of the previous figure. Planar horizontal cuts are individual diffraction patterns at a fixed energy, plotted as an orthographci projection. Vertical planes show energy-dependent diffraction at various emission angles, scaled to momentum space.

An electropolished Ni(001) substrate was used, which was cleaned by alternating cycles of Ar ion bombardment followed by electron-beam annealing at 600 °C. The surface was examined for absence of S, O and C impurities by surface-sensitive XPS, and for surface order by LEED. Overlayers were prepared by evaporating Mn from an aluminum oxide crucible which was resistively heated. Ordered c(2x2) Mn/Ni(100) surfaces were found after deposition of one-half monolayer equivalents of Mn, followed by annealing to 400 °C. Thicker surface alloy films, up to 4 ML in thickness, were also studied by XPD and these results will be reported elsewhere.

A sample of the individual Mn emitter experimental diffraction patterns is shown in Fig. 1, for a range of kinetic energy from 60 eV to 167 eV. The patterns show a high level of fine structure, and a strong dependence on kinetic energy, particularly at the lowest kinetic energies. The reproducibility of the fine structure was explicitly tested by repeating several of the diffraction patterns on different surface preparations. The data shown is a composite of results from three separate runs, in which data from different runs is interlaced in energy. The continuity of change in the diffraction patterns as a function of energy is indicative of the reproducibility achieved.

The inset to Fig. 1 shows a high energy, forward scattering diffraction pattern from the substrate Ni. The location of some of the low index directions of the substrate are marked with symbols; these correspond to rows of atoms in the crystal. These directions would produce forward scattering peaks at high kinetic energy in the Mn diffraction patterns, if there were buried Mn atoms. In both these experiments, and other experiments using conventional x-ray sources, we do not

see forward scattering features associated with Mn in sub-surface sites, so we conclude that this preparation technique produces only surface Mn atoms.

The diffraction features in Fig. 1 primarily arise from the interference of backscattered electrons (as opposed to forward scattering at higher kinetic energy). The patterns show that changes of only a few electron volts can produce large differences in the observed diffraction patterns. This sensitivity was used to optimize the theoretical value of the inner potential and electron energy in the calculations.

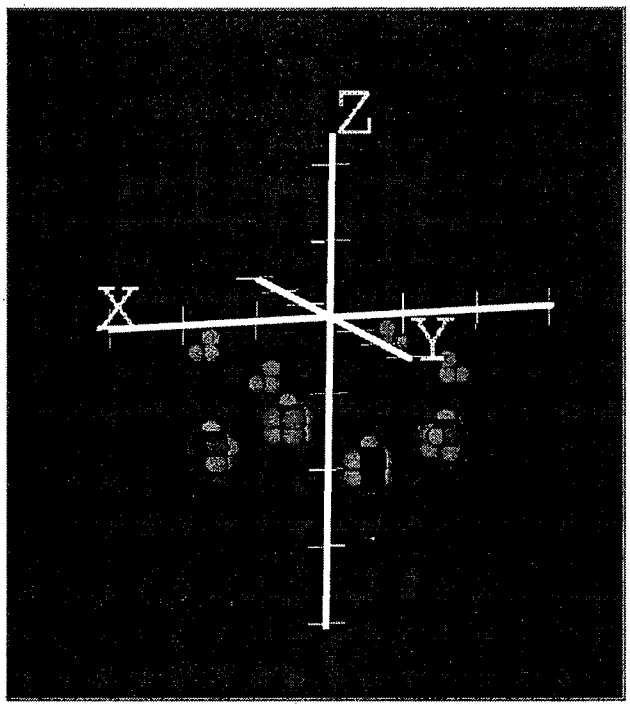

Fig. 3: Reconstructed atomic image of the Ni atoms surrounding a Mn surface atom, by direct inversion of the diffraction volume data from the previous figure. Two sets of 4 Ni atoms are visible; the outward motion of the Mn atom is correctly reconstructed.

The individual diffraction patterns are assembled into a k-space diffraction 'volume' by numerical interpolation to span the 'missing' data between the sampled energies. In order to improve the reliability of this interpolation, the original data set is acquired at kinetic energies chosen to produce equal steps in total electron momentum for the Mn core-level emission line. The diffraction volume can be displayed in a number of ways. A convenient format that we often use has a mixed coordinate system, shown in Fig. 2. The horizontal planes in this figure are orthographic projections of the hemispherical diffraction pattern at fixed kinetic energy; that is, the same as in Fig. 1. Vertical planes show energy-dependent photoelectron diffraction features at various emission angles. The scaling in the vertical axis is chosen to be linear in momentum, rather than energy, since this is the relevant scale for viewing EDPD oscillations.

Full multiple scattering simulations have been performed on several of the diffraction patterns in Fig. 1, with good agreement. The subtle changes from one energy to the next are reproduced theoretically, as well as the more obvious changes in peak appearance and disappearance over wide energy changes.

We have also performed a direct inversion of the diffraction data, using a straightforward photoelectron holographic Fourier-like integral[3]. Because the data set covers a large range of momentum space in three directions (two angles and magnitude of |k|), the reconstructed image, shown in Fig. 3, shows very few artifacts, without any need for correction factors.

REFERENCES

1. J.D. Denlinger, E. Rotenberg, T. Warwick, G. Visser, J. Nordgren, J.-H. Guo, P. Skytt, S.D. Kevan, K.S. McCutcheon, D. Shuh, J. Bucher, N. Edelstein, J.G. Tobin, and B.P. Tonner. Rev. Sci. Inst. 66:1342, 1995.
2. J.D. Denlinger, J. Zhang, and B.P. Tonner. Nucl. Inst. and Methods Phys. Res. A 347:475, 1994.
3. G.R. Harp, D.K. Saldin, and B.P. Tonner. Phys. Rev. Lett. 65:1012, 1990.

This work was supported by the Laboratory for Surface Studies, UW-M, the National Science Foundation under Grant DMR-9413475, and the U.S. Department of Energy under Grant DE-FG-2-92ER-45468.

Principal Investigator: Brian Tonner, Department of Physics, Laboratory for Surface Studies, University of Wisconsin-Milwaukee. Email: tonner@csd.uwm.edu.

Probing Structure-Property Relationships in Perpendicularly Magnetized Fe/Cu(001) Using MXLD and XPD

T.R. Cummins,[1] G.D. Waddill,[1] K.W. Goodman,[2] J.G. Tobin,[2]
J.D. Denlinger,[3] E. Rotenberg,[3] and A. Warwick[3]

[1]University of Missouri-Rolla, Rolla, MO
[2]Lawrence Livermore National Laboratory, Livermore, CA 94550
[3]Ernest Orlando Lawrence Berkeley National Laboratory, Berkeley, CA 94720

Magnetic X-ray Linear Dichroism (MXLD) in Photoelectron Spectroscopy and X-Ray Photoelectron Diffraction (XPD) of the Fe3p core level have been used to probe the magnetic structure-property relationships of perpendicularly magnetized Fe/Cu(001), in an element-specific fashion. A strong MXLD effect was observed in the high resolution photoelectron spectroscopy of the Fe3p at "normal" emission and was used to follow the loss of perpendicular ferromagnetic ordering as the temperature was raised toward room temperature. In parallel with this, "Forward Focussing" in XPD was used as a direct measure of geometric structure in the overlayer. These results and the implications of their correlation will be discussed. Additionally, an investigation of the effect of Mn doping of the Fe/Cu(001) will be described. These measurements were performed at the Spectromicroscopy Facility (Beamline 7.0.1) of the Advanced Light Source.

This work was performed under the auspices of the U.S. Department of Energy by Lawrence Livermore National Laboratory under Contract Number W-7405-ENG-48. The Spectromicroscopy Facility and the Advanced Light Source were constructed and are operated under support of the U.S. Department of Energy.

Principal investigator: James G. Tobin, Lawrence Livermore National Laboratory. Email: tobin1@llnl-gov. Telephone: 510-422-7247.

Probing Symmetry and Symmetry Breaking in Resonant Soft-X-Ray Fluorescence Spectra of Molecules

P. Glans[1], K. Gunnelin, J. Guo, P. Skytt, C. Såthe, J. Nordgren,
F. Gel'mukhanov[2], A. Cesar[2], and H. Ågren[2]
Uppsala University, Physics Dept., Box 530, S-751 21 Uppsala, Sweden
[1] Present adress: Manne Siegbahn Laboratory, Stockholm University, Frescativ. 24, S-104 05 Stockholm, Sweden
[2] Institute of Physics and Measurement Technology, Linköping University, S-581 83, Linköping, Sweden

INTRODUCTION

Conventional *non-resonant* soft X-ray emission brings about information about electronic structure through its symmetry and polarization selectivity, the character of which is governed by simple dipole rules. For centro-symmetric molecules with the emitting atom at the inversion center these rules lead to selective emission through the required parity change. For the more common classes of molecules which have lower symmetry or for systems with degenerate core orbitals (delocalized over identical sites), it is merely the local symmetry selectivity that provides a probe of the local atomic orbital contribution to the molecular orbital. For instance, in X-ray spectra of first row species the intensities essentially map the p-density at each particular atomic site, and, in a molecular orbital picture, the contribution of the local p-type atomic orbitals in the LCAO description of the molecular orbitals.

The situation is different for *resonant* X-ray fluorescence spectra. Here strict parity and symmetry selectivity gives rise to a strong frequency dependence for all molecules with an element of symmetry. In addition to symmetry selectivity the strong frequency dependence of resonant X-ray emission is caused by the interplay between the shape of a narrow X-ray excitation energy function and the lifetime and vibrational broadenings of the resonantly excited core states. This interplay leads to various observable effects, such as linear dispersion, resonance narrowing and emission line (Stokes) doubling. Also from the point of view of polarization selectivity, the resonantly excited X-ray spectra are much more informative than the corresponding non-resonant spectra.

EXPERIMENT

The present experiments were made at the soft X-ray fluorescence end station at beamline 7.0 [1]. A compact grazing incidence grating spectrometer [2] was used to record soft X-ray emission spectra, excited with monochromatized radiation from the SGM monochromator at this undulator beamline [3]. The spectrometer can detect emission either horizontally or vertically, i.e. parallel resp. perpendicular to the polarization vector of the synchrotron radiation. In order to allow gas phase samples to be studied a gas cell was used, which was provided with a silicon nitride input window of diameter 0.2 mm and thickness 1000 Å. A second window made of polyimide, with about the same thickness, was used as exit window for the fluorescence.

RESULTS

Resonant x-ray emission is useful for investigations of symmetry problems. This is because the discrete nature of the core-excitation prepares the symmetry for the emission step, and the

dipole character of the emission then leads to simple selection rules for the full absorption-emission process. For inversion symmetric systems the parity selection rule connects initial and final states either as *gerade-gerade* or *ungerade-ungerade*. If the inversion symmetry would be broken upon the core electron excitation, the parity selection rule evidently does not hold. For the O_2 molecule, it was recently shown that *ungerade* final states indeed were absent in the X-ray emission resulting from excitation to the first absorption state, which is of *ungerade* symmetry, reflecting an unbroken symmetry throughout the entire X-ray fluorescence process [4].

Experimental verification of strict symmetry - selective character of resonant X-ray emission spectra has also been demonstrated for N_2 [5], which is a molecule with only one totally symmetric vibrational mode as well. In Fig.1 is shown N K emission of N_2 excited at different discrete absorption state energies, and also above ionization threshold. The lowermost spectrum is excited at the "white line" energy, i.e. promoting a 1s electron to the lowest unoccupied molecular orbital (LUMO), $1\pi_g$. Apart from the recombination line (participator) only one line is observed, and the same thing occurs for excitation to a higher absorption state of *gerade* symmetry. For excitation at an energy corresponding to an *ungerade* state, the $3p\pi_u$, two lines appear, and finally when exciting at high energy three lines appear. It turns out that the observed behavior reflects strict symmetry selection of the resonant soft X-ray scattering. Exciting to a *gerade* state probes *gerade* occupied orbitals, and vice versa. No deviation from the rule is observed, in agreement with the observations for O_2.

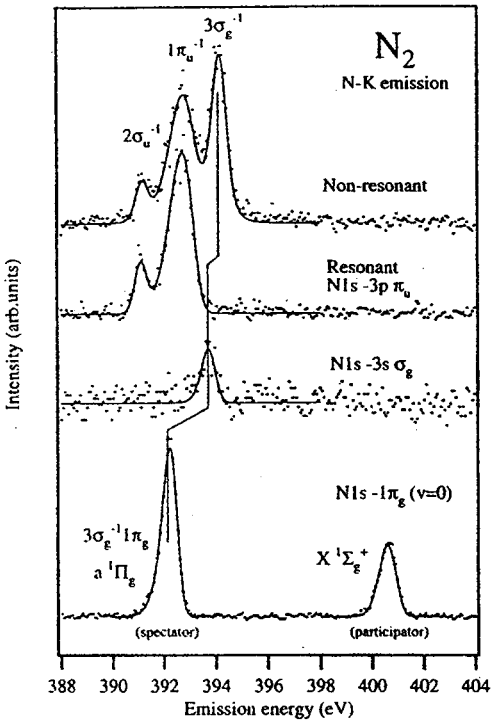

Fig.1 N K emission of N_2 excited to the v=0, vibration of the $C1s^{-1}2\pi^*$ state, to a grade resp. ungerade Rydberg state, and above the ionization threshold.

The presence of non-totally symmetric vibrational modes, as in polyatomic molecules, could introduce dynamical symmetry breaking through vibronic coupling into forbidden symmetries. This would manifest itself by the appearance of forbidden spectral lines. In the following we discuss deviation from the strict selection rules due to dynamical symmetry breaking.

The addition of a carbon atom between the two oxygen atoms of O_2 introduces an antisymmetric stretch mode which can couple the "allowed" $1\sigma_g^{-1}2\pi_u$ and the "forbidden" $1\sigma_u^{-1}2\pi_u$ oxygen core-excited states in the X-ray excitation process and, therefore, break the parity selection rule in the resonant X-ray emission. The relative intensity of the x-ray emission resulting from the "forbidden" state gives a measure of the strength of the symmetry breaking [6].

In the upper part of Fig.2 is shown the O K emission of CO_2 excited at the $2\pi_u$ resonance and above ionization threshold, respectively. One observes that the "forbidden" $1\pi_g^{-1}2\pi_u$ final state appears in the resonant spectrum, although with reduced relative intensity compared with the π_g line for non-resonant excitation. This shows that the parity selection rule is not

valid, which indicates that inversion symmetry is broken in the core excited state, in contrast to the case of O_2.

At the time of primary excitation (t = 0) the core hole is equally distributed over the two oxygen centers keeping the inversion symmetry, which for both O_2 and CO_2 can be described as a superposition of two states with left and right hole localization. The vibronic coupling via the antisymmetric stretch mode between the close lying *gerade* and *ungerade* electronic core hole states of CO_2 leads at time t = t′ to an effective shift of the molecular equilibrium with the inversion symmetry broken and to localization of the core hole to one of the terminal oxygen atoms. For the O_2 or N_2 molecule, the totally symmetric vibrational motion cannot break the electronic symmetry, and the core-excited state remains a superposition of two hole states with retained inversion symmetry at all times.

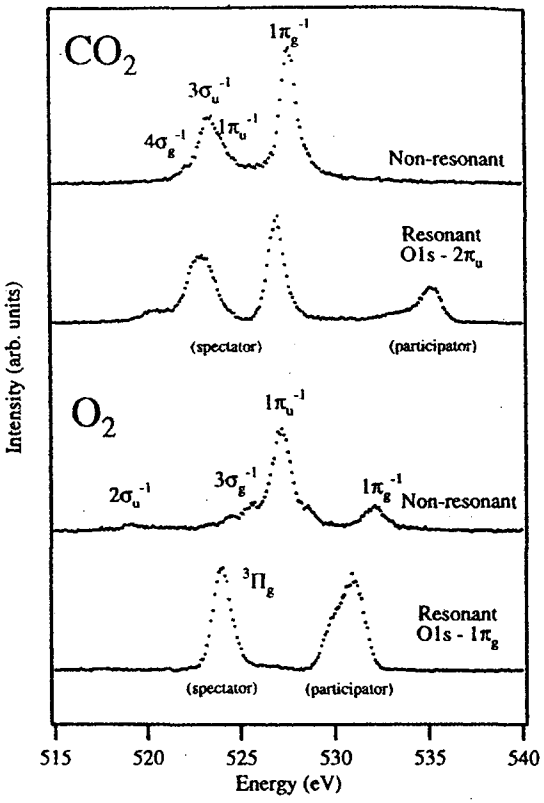

Figur 2 Oxygen K emission spectra of CO_2 and O_2, excited on the first X-ray absorption resonance and at energies above ionization threshold.

The symmetry breaking process is not instantaneous and the degree of symmetry breaking therefore critically depends on the duration of the X-ray scattering process and the vibrational frequency. If the duration time is much smaller than the vibrational time period, the molecule has not enough time to execute the antisymmetric vibration that introduces forbidden parity in the electronic wave function through the vibronic coupling.

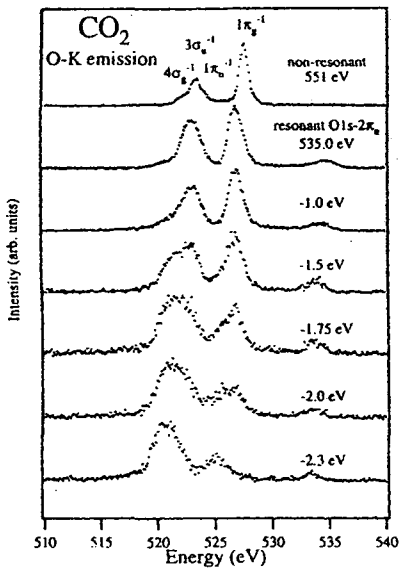

Fig.3 Oxygen K emission of CO_2 excited at first X-ray absorption resonance, and at increasingly lower energies.

One can introduce a time concept related to the excitation energy by considering the extreme cases of exciting on resonance, respectively far from resonance (in analogy with resonant and nonresonant photoemission). In the latter case we are dealing with a prompt process (Raman scattering), whereas on resonance the lifetime of the resonant state determines the interaction time (Resonant Raman scattering) Tuning away from resonance shortens the duration of the process, and one probes preferentially transitions associated with shorter lifetimes, and vibronic symmetry breaking will be less and less effective. Thus, by detuning the excitation of resonant X-ray emission one can tune the effective interaction time of the scattering process [7]. In Fig.3 is shown a series of O K emission spectra of CO_2 excited at the O1s-$2\pi_u$ resonance energy and at downwards increasingly

detuned energies. One observes that the "forbidden" $1\pi_g^{-1}2\pi_u$ line decreases in intensity with increased detuning, in agreement with the discussion above. The larger the detuning, the shorter the effective interaction time and thus the lower the intensity of the emission line that requires symmetry breaking to pick up intensity. At significant detuning the time is too short to permit the carbon atom to move enough to cause appreciable symmetry breaking. By studying emission excited at detuned energies in this way one can thus obtain a "clock" which operates in the femtosecond and sub-femtosecond range.

CONCLUSIONS

The present report demonstrates the symmetry selectivity of resonant soft X-ray fluorescence spectra for molecules. It shows how the soft X-ray process singles out emission valence band states of the same symmetry as the X-ray absorption state in molecules with inversion symmetry. In cases where vibronic coupling can lower the symmetry of the core excited state deviations from this rule are observed. By detuning the excitation away from resonance one can restore the symmetry by virtue of a shortening of the effective scattering time. This finding might offer a new means to study molecular dynamics in the sub-femtosecond range.

ACKNOWLEDGEMENTS

We are indebted to T. Warwick, Eli Rotenberg and J. Denlinger for assistance at the beamline and for stimulating interactions.

REFERENCES

1. Guo, J.; Wassdahl, N.; Skytt P.; Butorin, S.M.; and others. Rev. Sci. Instrum, **66**, 1561 (1995)
2. Nordgren, J.; Bray G.; Cramm, S; Nyholm R; and others. Rev. Sci. Instrum., **60**, 1690 (1989).
3. Warwick, T.; Heimann, P.; Mossessain, D.; and Padmore, H. Rev. Sci. Instrum., **66**, 2037 (1995).
4. Glans, P.; Gunnelin, K.; Skytt, P.; Guo, J.-H.; and others. Phys. Rev. Lett., **76**, 2448 (1996).
5. Glans, P; Gunnelin, K; Skytt, P; Guo, J, and others. Accepted for publ. in J. Elecr. Spectr. Rel. Phenom.
6. Cederbaum, L.S. J. Chem. Phys. **103**, 562 (1995).
7. Skytt, P.; Glans, P.; Guo, J; Gunnelin, K; and others. Phys. Rev. Lett., **77**, 5035 (1996).

This work was supported by the Swedish Natural Science Research Council and the G. Gustafsson Foundation for Science and Medicine.

Principal investigator: E. Joseph Nordgren, Physics Department of Uppsala University, Sweden. E-mail: joseph@fysik.uu.se

Resonant X-Ray Emission from Gas-Phase $TiCl_4$

C.F. Hague[1], M. Tronc[1], F. De Groot[2], H. Ogasarawa[3], A. Kotani[3], J.H. Guo[4] and C. Såthe[4]
[1]Laboratoire de Chimie Physique-Matière et Rayonnement URA 176
Université Pierre et Marie Curie, 11 rue P. et M. Curie, 75231Paris Cedex 05, France
[2]Solid State Physics,
University of Groningen, Nijenborgh 4, 9747 AG, Gröningen, Netherlands
[3]Institute for Solid State Physics,
University of Tokyo, 7-22-1 Roppongi, Minalo-ku, Tokyo 106, Japan
[4]Department of Physics,
University of Uppsala, Box 530, S-751-21 Uppsala, Sweden

INTRODUCTION

Resonant x-ray emission spectroscopy (RXES) has proved to be a powerful tool for studying the electronic structure of condensed matter. Over the past few years it has been used mainly for studying the valence bands of solids [1,2] and condensed molecules [3,4]. Very recently the advent of high brightness photon beams provided by third generation synchrotron radiation source undulators, associated with efficient x-ray emission spectrometers [5] has made it possible to perform experiments on free diatomic molecular systems [6-8]. RXE spectra of free molecules are of prime importance to gain insight into their electronic structure and bonding as they reflect the symmetry of orbitals engaged in the two-electron, two-step process with the $l = 0, \pm 2$ parity-conserving selection rule, and are free from solid state effects which can introduce difficulties in the interpretation. They provide information (more so than XAS) on the core excited states, and, when performed at fixed incident photon energy as a function of the emitted photon energy, on the electronic excitation (charge transfer, multiplet states). Moreover the anisotropy of the angular distribution of resonant x-ray emission affects the relative intensity of the emission peaks and provides information concerning the symmetries of final states [8].
This is a preliminary report on what are the first RXE spectra of a 3*d* transition metal complex in the gas phase. The experiment concerns the Ti $3d \rightarrow 2p$ emission spectrum of $TiCl_4$ over the 450 to 470 eV region.

EXPERIMENT

The experiment was performed on beam line 7.0 at ALS, using the Uppsala x-ray emission spectrometer and gas cell [9].The experimental resolution depends on the monochromator and spectrometer settings. Both were set to approximately 1 eV. Spectra for three typical values of the incoming photon energy are shown in figure 1. Just below the L_3 absorption resonance, at 456.8 eV, the spectrum consists of a single peak corresponding to the L_3 emission (figure 1a). It reaches its maximum intensity referred to that of the elastic peak at this energy i.e., ~ 2 eV below the L_3 resonance. At the L_2 resonance (figure 1b) the spectrum displays a multiplet structure with a giant resonance ~7 eV above normal L_3 emission. At higher energies the intensity of this strong emission line becomes comparable to other x-ray emission structures. This giant resonance is probably associated with an extra valence hole (Coster-Kronig transition).

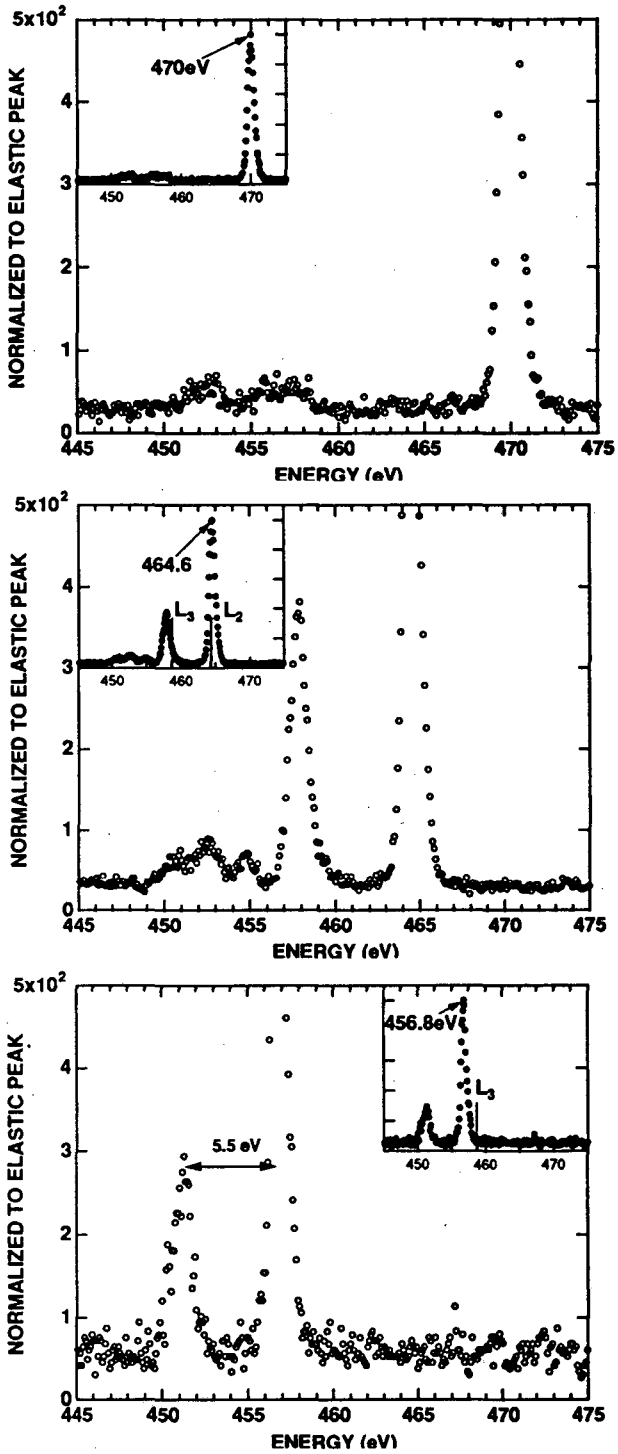

Figure 1. Ti $L_{2,3}$ resonant x-ray emission spectra taken at three different incident photon energies: a) The excitation energy is ~2 eV below the L_3 threshold; b) excitation energy to L_2 threshold; c) excitation well above L_2 threshold (corresponds to normal fluorescence). The insets show the $L_{2,3}$ thresholds and intensities relative to the elastic peak.

DISCUSSION

The $2p$ absorption spectrum of $TiCl_4$ has already been studied using ISEELS[10], but the current theoretical models [11,12], dealing with electronic structure of transition metal complexes (crystal field theory, and molecular orbital theory) fail to fully explain the branching ratio of the Ti L_3 and L_2 multiplets. This branching ratio, is far from the statistical value of 2/1 because of a combination of spin-orbit coupling, $2p$-$3d$ correlations, and correlations within the 3d band (multiplet effects) inducing a strong mixing of the j=3/2 and j=1/2 configurations and a rearrangement of the spectral shape incompatible with a single-particle picture.

The ground state is approximated as $3d^0 + 3d^1\underline{L}$ ($3d^2\underline{L}^2$ configurations are neglected here). The intermediate 2p-hole state is given as $2p^5 3d^1 + 2p^5 3d^2\underline{L}$, and the resonant XES process decays back to $3d^0 + 3d^1\underline{L}$. Excitation to the L_3 edge (not shown) gives a strong elastic peak plus a satellite approximately 6 eV below the excitation energy. Following the picture emerging from the analysis of RXE spectra of cerium [13], this 6 eV satellite is expected to be of the charge-transfer type, related to $3d^1\underline{L}$ character, or more accurately to the anti-bonding combinations of $3d^0$ and $3d^1\underline{L}$. The excitation energy of this satellite (with respect to the elastic peak) increases while scanning through the L_3 edge from 5.5 eV to 6.5 eV, in accord with the theoretical simulations, and related to the energy-differences between E_g and T_{2g} satellites. From this analysis the charge-transfer picture seems appropriate for $TiCl_4$ too. However this picture is strongly challenged by the observation of the RXES structure when exciting at the charge-transfer satellites in the X-ray absorption spectrum. Following ref. 13 charge-transfer satellites in XAS are expected to strongly enhance inelastic scattering. In contrast experiment shows essentially only elastic scattering (plus non-resonant scattering) and virtually no inelastic resonant scattering. This observation challenges the assignment of the XAS satellites.

An alternative assignment to these structures in the XAS spectrum is to assume they are transitions to 4s-states. Because these states are rather delocalised, this would also explain their stronger non-resonant XES contributions. However, it does not change the charge-transfer interpretation of excitation to the main peaks. This emerging dilemma might in fact be very important to further interpretation into the nature of the satellites in XAS and also into the nature of the ground state for transition metals in molecules and ionic solids. Work is in progress to investigate this in more detail. We also intend to extend our measurements to gas phase vanadium complexes ($VOCl_3$, $C_5H_5V(CO)_4$, VCl_4).

CONCLUSION

The, at present, unique characteristics of the Advanced Light Source, make it possible to investigate gas phase RXE processes for the first time with satisfactory resolution. This is proving to be a new challenge to the theorist even in the case of a "textbook example" such as this nominally d^0 transition metal complex.

ACKNOWLEDGEMENTS

The CFH and MT are indebted to Joseph Nordgren for making available his unique experimental set-up at ALS and to the ALS staff who made these experiments possible.

REFERENCES

[1] J. H. Guo et al. Phys Rev B **49**, 1376 (1994)
[2] P. Skytt et al. Phys Rev B **50**, 10457 (1994)
[3] P. Skytt et al. Phys Rev A **52**, 3572 (1995)
[4] J. H. Guo et al. Phys Rev B **52**, 10681(1995)
[5] J.Nordgren et al., Rev.Sci. Instrum. **60**, 1690 (1989)
[6] P. Glans et al. Phys Rev Lett **76**, 2448 (1996)
[7] P. Glans et al. J. Elect. Spect. **82**, 193 (1996)
[8] P. Skytt et al. Phys Rev A 1997 in press
[9] P. Skytt, Uppsala Dissertations, Faculty of Science and Technology **214**, 1996
[10] A. T. Wen and A. P. Hitchcock. Can. J. Chem **71**, 1632 (1993)
[11] F. M. F. de Groot et al. Phys Rev B **41**, 928 (1990)
[12] P. Decleva et al. Chem Phys. **186**, 1 (1994)
[13] S. Butorin et al. Phys Rev Lett **77**, 574 (1996)

This was supported by the French CNRS and the Swedish Science Foundation.

Principal Investigator: Coryn Hague, University Pierre et Marie Curie, Laboratoire de Chime Physique-MR
Email : hague@ccr.jussieu.fr Telephone: +33-1-44276625

Role of Screening and Angular Distributions in Resonant Soft-X-Ray Emission of CO

P. Skytt, P. Glans[1], K. Gunnelin, J. Guo, J. Nordgren, Y. Luo[2], and H. Ågren[2]
Uppsala University, Physics Dept., Box 530, S-751 21 Uppsala, Sweden
[1] Present adress: Manne Siegbahn Laboratory, Stockholm University, Frescativ. 24, S-104 05 Stockholm, Sweden
[2] Institute of Physics and Measurement Technology, Linköping University, S-581 83, Linköping, Sweden

INTRODUCTION

In the present work we focus on two particular properties of resonant X-ray emission, namely core hole screening of the excited electron, and anisotropy caused by the polarization of the exciting synchrotron radiation. The *screening* of the core hole by the excited electron causes energy shifts and intensity variations in resonant spectra compared to the non-resonant case. The linear polarization of the synchrotron radiation and the dipole nature of the absorption process create a preferential alignment selection of the randomly oriented molecules in the case of resonant excitation, producing an anisotropy in the *angular distribution* of the emitted X-rays. We have chosen CO for this study because this molecule has previously served as a showcase for non-resonant X-ray emission, mapping the valence electronic structure differently according to the local selection rules. With the present work we take interest in how this characteristic feature of the spectroscopy is represented in the resonant case.

EXPERIMENT

The experiments were made at the soft X-ray fluorescence end station at beamline 7.0 [1]. A compact grazing incidence grating spectrometer [2] was used to record soft X-ray emission spectra, excited with monochromatized radiation from the SGM monochromator at this undulator beamline [3]. The spectrometer can detect emission either horizontally or vertically, i.e. parallel respectively perpendicular to the polarization vector of the synchrotron radiation. In order to allow gas phase samples to be studied a gas cell was used, which was provided with a silicon nitride input window of diameter 0.2 mm and thickness 1000 Å. A second window made of polyimide, with about the same thickness, was used as exit window for the fluorescence.

RESULTS

By studying the angular dependence of X-ray emission spectra from ordered systems of non-cubic symmetry one can obtain information about orbital symmetries and bond directions. This is a useful property for instance in the study of molecular adsorbates, a class of problems that has recently become accessible for soft X-ray emission spectroscopy [4].

Resonant X-ray emission allows studies of polarization effects also for systems that are not ordered, in contrast to e.g. X-ray absorption spectroscopy, which is often applied for polarization studies of ordered systems. In previous investigations of K_β X-ray emission of gaseous samples polarization effects were observed when monochromatized synchrotron radiation was used for the excitation and the state of the polarization of the emitted radiation was detected. Correspondingly, the polarization manifests itself also in the angular distrubution of the emission [5].

Fig.1 illustrates how anisotropy comes about in X-ray emission of free carbon monoxide molecules [6]. If excitation is tuned to a resonance of σ symmetry, there will be a preferential selection of excited molecules which happen to be aligned with their molecular axes along the polarization vector. Since the lifetime associated with X-ray emission is short compared to molecular rotation times the emitted X-ray spectrum will reflect a frozen picture of the ensemble of molecules as they happened to be oriented at the excitation. The emitted radiation is then distributed with respect to the frozen orientation, thus with preference for a certain direction. At emission angles along the molecular axis for CO, we will then preferentially see emission associated with π orbitals, and in perpendicular directions both π and σ orbitals contribute.

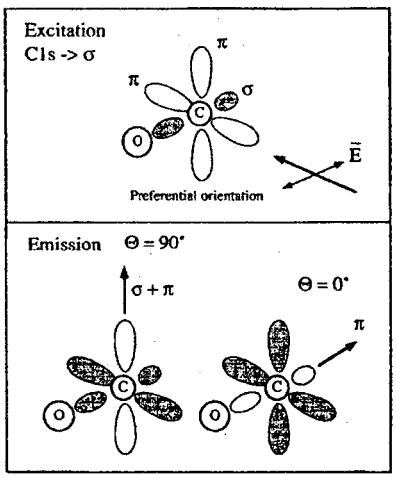

Fig.1 Illustration of the angular dependence of resonant X-ray emission of gaseous molecules

In Fig.2 are plotted a series of C K emission spectra of gaseous CO, excited at various energies, as indicated in the figure, and separating between emission recorded parallel to the exciting radiation polarization (0°), respectively perpendicular (90°). (*En passant* we note that there is a substantial difference between the two spectra corresponding to core exciting to the ground vibration respectively to the first excited vibration. As seen in the figure this is well reproduced by the simulation of the profiles.) The observed anisotropy is in qualitative agreement with the discussion above, and, furthermore in excellent agreement with calculations, shown as solid thin or thick lines in the figure.

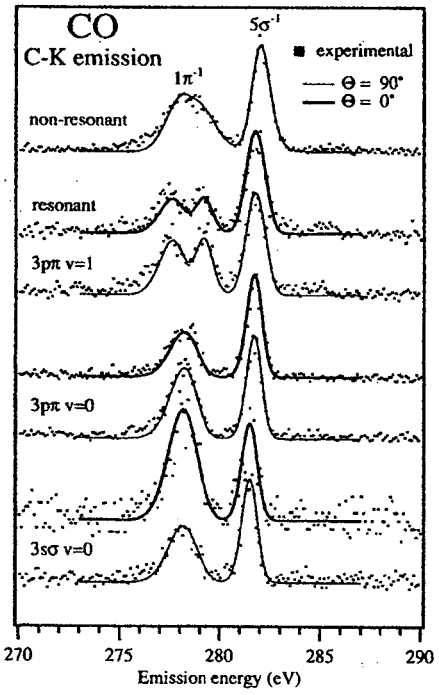

Fig.2 Angular dependent carbon K emission of gaseous CO excited to the 3sσ (v=0) and 3pπ (v=0 and v=1) Rydberg resonances.

One observes that there is a shift in emission energy between the resonantly excited spectra and the spectrum excited above ionization threshold (uppermost spectrum i figure 2). An even larger shift appears when comparing with the emission corresponding to the first X-ray absorption state or LUMO, the $^1\Sigma^+$ state, see Fig.3. The 5σ line in the regular C K emission (top spectrum) has its counterpart in the $^1\Pi$ line at 2.9 eV lower energy in the spectrum excited to the first X-ray absorption state. The 1π band is split into three bands going from the non-resonant case to the resonant case, and two of those, the $^1\Delta$ and $^1\Sigma^-$, appear as shown, whereas the third, $^1\Sigma^+$ is expected to be very weak. In this case the shift is 0.6 eV as measured to the center of gravity of the $^1\Delta$ / $^1\Sigma^-$ band.

The X-ray energy shifts observed can be explained by the screening brought about by the excited electron. Exciting to the LUMO results in a substantial X-ray emission shift compared to non-resonant emission because the excited electron is likely to penetrate the valence electron orbitals appreciably. For Rydberg excitations the situation is more like ionization as seen in the figure, since the Rydberg orbitals should have minor penetration.

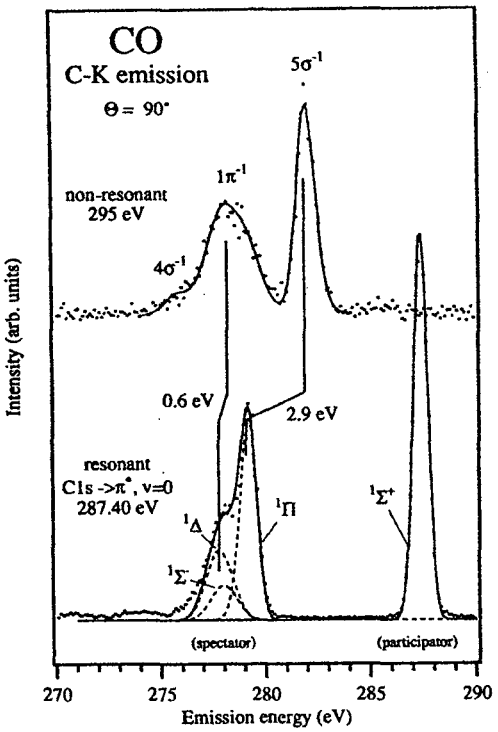

Fig.3. Non-resonant (top) and resonant (bottom) C K emission spectra of gaseous CO. Solid lines are simulated band profiles.

It is interesting to compare the LUMO-excited C K emission of CO with the spectrum from CO adsorbed on a Ni(100) surface [4]. In the adsorbate case there is also a substantial shift of the 5σ peak, which is in accordance with the notion of the population of the empty π* orbital upon binding to the metal surface. The low energy shift of X-ray emission excited below the ionization threshold, compared to non-resonant X-ray emission, is a general phenomenon of electron screening. One can understand the sign of the screening effect by considering the difference between the energies of the core excited respectively the core ionized state in comparison with the difference between the corresponding valence states, see Fig.4. The shift is greater between the core states, since the ionization energy for a valence electron is larger in this case due to the core hole attraction.

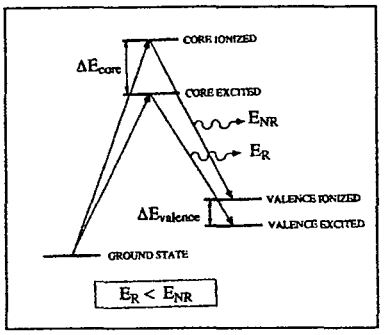

Fig.4 Diagram of states involved in resonant and non-resonant X-ray emission.

The difference between shifts occurring in the carbon respectively the oxygen X-ray emission spectra (see the full publication for details [6]) depend on the localization of the orbitals. This is also the case for the differences that appear between the 5σ and π orbitals.

CONCLUSIONS

As shown here non-resonant and resonant X-ray spectra of CO are quite similar when the resonant core excitation involves a Rydberg orbital. The interaction of a spectator electron in a Rydberg orbital with the remaining electron cloud is thus not sufficiently large to change neither energies nor intensities in the X-ray emission spectra to any appreciable extent. We find that the relative intensities and vibrational band shapes can be simulated with good agreement using the same potential curve parameters and relative intensities as used to simulate the non-resonant carbon spectrum. The energy shifts in the Rydberg-excited spectra are found to be 0.5 eV or less.

In the LUMO excited spectra, on the other hand, the spectator transitions have large energy shifts in comparison to their corresponding transitions in the non-resonant spectra, which can be attributed to the screening nature of the *penetrating* excited electron. Because of the localization of the orbitals involved in the RXE process, with respect to the core-hole site, the screening effects are different when the core hole is situated on the carbon or oxygen site and whether a 5σ or a 1π electron fills the core hole. Energy shifts calculated by multi-configuration self-consistent field theory were found to compare well with experimental data.

Regarding the angular distributions we find that the discrete nature of the core excited states prepares favored directions for the X-ray emission, and that the dipole character of the absorption/emission then leads to a specific angular distribution pattern (specific polarization anisotropy, specific parity selection) with no counterpart in non-resonant emission spectra. In the non-resonant case the core electron is excited to the continuum, which is infinitely degenerate representing all symmetries. This makes the non-resonant process much less selective with respect to any of the processes here mentioned.

ACKNOWLEDGEMENTS

We are indebted to T. Warwick, Eli Rotenberg and J. Denlinger for assistance at the beamline and for stimulating interactions.

REFERENCES

1. Guo, J.; Wassdahl, N.; Skytt P.; Butorin, S.M.; and others. Rev. Sci. Instrum, **66**, 1561 (1995).
2. Nordgren, J.; Bray G.; Cramm, S; Nyholm R; and others. Rev. Sci. Instrum., **60**, 1690 (1989).
3. Warwick, T.; Heimann, P.; Mossessain, D.; and Padmore, H. Rev. Sci. Instrum., **66**, 2037 (1995).
4. Wassdahl, N.; Nilsson, A.; Wiell, T.; Tillborg, H.; and others. Phys. Rev. Lett., **69**, 812 (1992); See also Tillborg, H.; Nilsson, A.; Wiell, T.; Wassdahl, N.; and others. Phys. Rev. B, **47**, 16464 (1993); Nilsson, A.; Bennich, P.; Wiell, T.; Wassdahl, N.; and others. Phys. Rev. B, **51**, 10244 (1995).
5. Lindle, D.W.; Cowan, P.L.; LaVilla, R.D.; Jach, T; and others. Phys. Rev. Lett., **60**, 1010 (1988); Southworth, S.; Lindle, D.W., Meyer, R.; Cowan, P.L. Phys. Rev. Lett., **67**, 1098 (1991).
6. Skytt, P; Glans, P; Gunnelin, K; Guo, J; and others. Phys. Rev. A, **55**, 134 (1997).

This work was supported by the Swedish Natural Science Research Council and the G. Gustafsson Foundation for Science and Medicine.

Principal investigator: E. Joseph Nordgren, Physics Department of Uppsala University, Sweden. E-mail: joseph@fysik.uu.se

Scanned-Energy Mode Photoelectron Diffraction Measurements at Beamline 7.0.1

R. Toomes[1], O. Schaff[2], N.A. Booth[1], J. Denlinger[3], E. Rotenberg[4], A.M. Bradshaw[2] and D.P. Woodruff[1]

[1] Physics Department, University of Warwick, Coventry CV4 7AL, UK
[2] Fritz-Haber-Institut der Max-Planck-Gesellschaft, Faradayweg 4-6, 14195 Berlin, Germany
[3] University of Wisconsin-Milwaukee Physics Dept., 1900 E. Kenwood Blvd., Milwaukee, WI 53211, USA
[4] Advanced Light Source, MS2-400, Lawrence Berkeley Natl. Lab., Berkeley, CA 94720, USA

INTRODUCTION

This report covers the results of our first experimental run, in May 1996, conducted to explore the advantages offered by the high spectral resolution available at the SpectroMicroscopy Facility on beam line 7.0 to conduct scanned-energy mode photoelectron diffraction (PhD). This technique is now a well-established method for the determination of local structure of atomic and molecular adsorbates on well-characterised surfaces [1]. The directly-emitted component of an adsorbate core-level photoelectron wavefield interferes coherently with components of the same wavefield elastically scattered by surrounding atoms, leading to a modulation in the photoemission intensity as a function of kinetic energy in any specific emission direction. A series of such PhD modulation spectra, each typically covering energies from 50-500 eV, for a series of different emission directions, provides the basis for a quantitative structure determination of the emitter-scatterer geometry. Within the last years we have developed an integrated approach to extract the structural information from these photoelectron diffraction (PhD) spectra in a quantitative way [2]. A direct data inversion technique (the so-called Projection method [3]) provides a first-order estimate of the local adsorbate geometry in the form of an'image' of the scatterer atoms which are nearest neighbours to the emitter. This information is then used as a starting model for optimisation of the structural parameters by comparing the experimental PhD spectra with the results of multiple scattering simulations using a code developed by Fritzsche [4]. The optimisation uses an automated trial-and-error procedure by minimising a reliability factor which provides an objective measure of the quality of agreement between experiment and theory. We have successfully applied this approach to the structure determination of about 30 adsorption systems.

A particular strength of PhD is its elemental and chemical specifity. PhD spectra recorded from core level photoemission from the different elements within a molecular adsorbate allow the local sites of the component atoms to be determined independently. Atoms of the same element which reside in chemically different environments can also be investigated separately by utilising the induced chemical shift of the core levels of these atoms. This potential for Chemical Shift PhD has so far been limited, however, by the relatively low spectral resolution ($E/\Delta E \sim 300$) available to us on the high energy toroidal grating monochromator (HE-TGM 1) beamline at BESSY, the second generation storage ring light source in Berlin. Demonstration experiments, for example on coadsorbed PF_3, PF_2 and PF on Ni(111) [5], for which large (~3 eV) chemical shifts occur, have been possible, but such shifts are more typically around 1 eV or less, and the combined requirements of high flux and high resolution require a high resolution monochromator coupled to an undulator at a third generation light source such as the ALS. Our first run at the ALS was undertaken to explore the potential of beamline 7.0 for such studies. Our results identified several issues which will influence our future work (including the need for a special low-temperature manipulator - now being constructed) but also provided clear evidence of the advantages offered by this station for our future work, including improved ability to remove substrate Auger peaks and thus work with a wider range of substrates.

AUGER ELECTRON PEAK BACKGROUND REMOVAL

One problem with the scanned-energy mode of the photoelectron diffraction technique is the role of (fixed-energy) Auger electron peaks in the electron energy spectrum background. Separating the photoemission peak from these background features can be particularly troublesome when strong Auger peaks from the substrate occur in the 50-500 eV energy range. A recent example we have encountered in our work at BESSY is the case of CO adsorbed on Pd(111) [6]. The problem is rather generally bad for second row transition metal substrates, many of which are of chemical interest. Our preliminary PhD results for CO on Pd(110) obtained at the ALS show that the higher spectral resolution enables us to separate the photoemission and Auger emission peaks far more effectively, and thus to remove the usual artifacts from the PhD spectra. Fig. 1a shows an example of PhD data measured at a low energy resolution (average 3.5 eV) measured in normal emission from Pd(111)c(4×2)-CO using the HE-TGM 1 beamline in Berlin. This raw PhD spectrum comprises a set of C 1s photoemission energy spectra recorded at different photon energies; the full data set comprised 210 single C 1s spectra taken at photon energies from 320 to 740 eV in 2 eV steps; the figure shows only every fourth such spectrum. Each individual spectrum was fitted with a sum of a Gaussian peak, a step function and a background function. Fig. 1b shows the intensity of the Gaussian line (and thus of the C 1s core level photoemission signal) as a function of electron kinetic energy, normalised by a smooth polynomial. This modulation function is the PhD spectrum which is to be used for the structure determination described above. At 240, 270 and 330 eV the modulation function shows strong artifacts induced by the MNN Auger lines of the Pd substrate. Fig. 2a shows an enlarged section of the spectrum in fig. 1a in the region around the strongest Auger line together with the corresponding section of the modulation function. By contrast, fig. 2b shows the same energy range for the measurement of CO on Pd(110) at beamline 7.0 of the ALS, together with the modulation function belonging to it. These data were recorded from a surface likely to several adsorption sites [7] obtained by dosing the surface with 20 L CO at approximately 300 K; attempts to prepare the (2×1)p2mg-CO structure which has an associated coverage of 1 ML with all CO molecules in symmetrically equivalent sites were unsuccessful due to inadequate sample cooling. Nevertheless, the C 1s lines are clearly much narrower due to the better energy resolution (0.7 eV in average), and

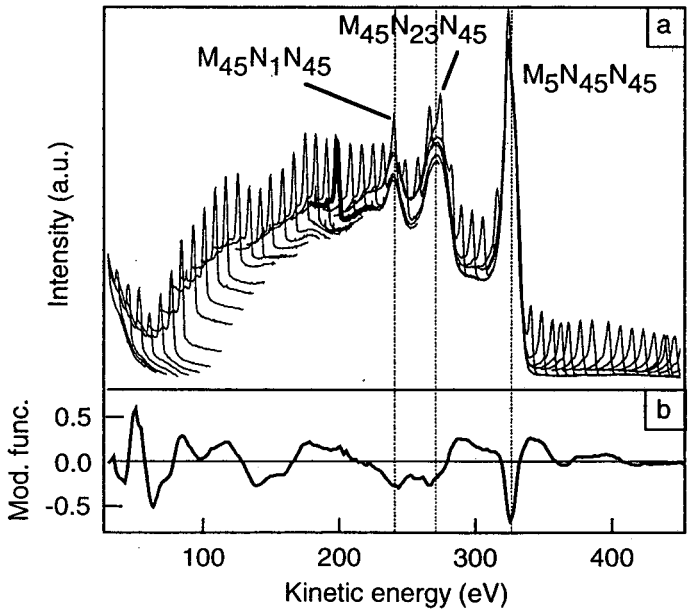

Fig.1: a): raw PhD spectrum from the C 1s core level of Pd(111)c(4×2)-CO measured with an average energy resolution of 3.5 eV at the Berlin synchrotron BESSY I. The spectrum consists of a series of EDCs around the C 1s line, one of which is shown bold. b): modulation function extracted from a) (see text).

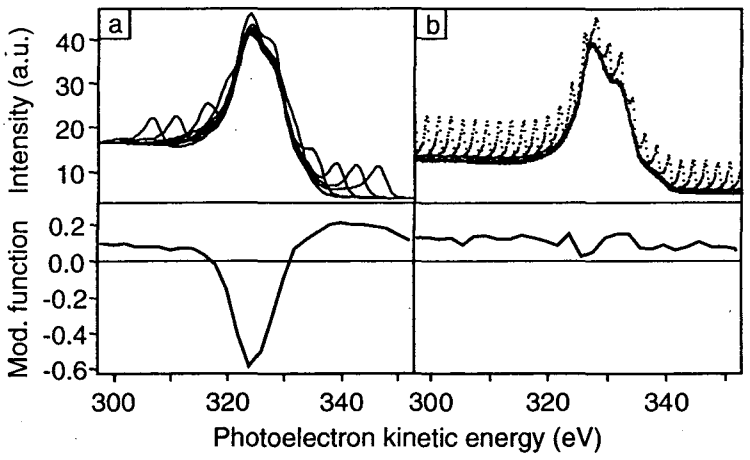

Fig.2: a) gives an enlarged section of the spectrum from fig. 1 together with the corresponding section of the modulation function. b) shows the same region of a PhD spectrum measured at beam line 7.0 for CO on Pd(110).

can now be far more easily separated from the substrate Auger peak which is intrinsically broader, leading to far more reliable PhD spectra. These measurements show the clear advantage of high resolution, such as that available at beamline 7.0 of the ALS, for PhD studies from adsorbates on an important range of substrates which display strong Auger electron emission in the key 50-500 eV kinetic energy range.

CO DISSOCIATION ON Ni(100)

In addition to measurements on the Pd(110)/CO system, a study of Ni(100)/CO was also undertaken. Our original objective was a study of the Ni(100)c($5\sqrt{2}\times\sqrt{2}$)-CO structure, a system where the CO molecules are believed to reside in different adsorption sites [8], and which should therefore be interesting for C 1s and O 1s chemical shift PhD studies. However, the results of our first preparations indicated that the Ni(100) crystal we used was dissociating a large portion of the adsorbed CO even at room temperature. One potential hazard, of course, of very high incident photon flux densities on molecular adsorbates is the possibility of photon stimulated dissociation or desorption, and the small focal spot on beamline 7.0 could make this a particular problem. In fact we did see evidence for beam-induced dissociation of CO on Ni(100) on the timescale of minutes, but we also found what appears to be spontaneous dissociation on this surface. Fig 3 shows photoelectron spectra in the binding energy region of the C 1s and O 1s core levels measured immediately after dosing 0.7 L CO at room temperature. Each spectrum clearly shows two peaks, separated by 2.8 eV and 1.8 eV for C 1s and O 1s, respectively. We assign the peaks at lower binding energies to atomic C and O and those at higher binding energies to intact CO molecules. The relative intensity of the atomic and molecular peaks was found to depend strongly on the position of the photon beam on the crystal. The observed high probability of spontaneous dissociation at room temperature is unexpected and has not been reported previously in the literature, although such an effect has been found to occur at surface steps [9]. Even though the crystal showed a clear (1×1) LEED pattern, we suppose that the atomic C and O arise from CO molecules which dissociated at surface defects. An important feature of the high resolution spectra demonstrated by these results is that they provide a level of surface characterisation well beyond that available in more conventional studies, and also permit PhD structural studies to be made of individual species in complex coadsorption systems. The results suggest that a future study of CO adsorption on a vicinal Ni surface would be of considerable interest, particularly if the measurements could be made at a sufficiently low temperature to detect CO step-edge adsorption prior to dissociation.

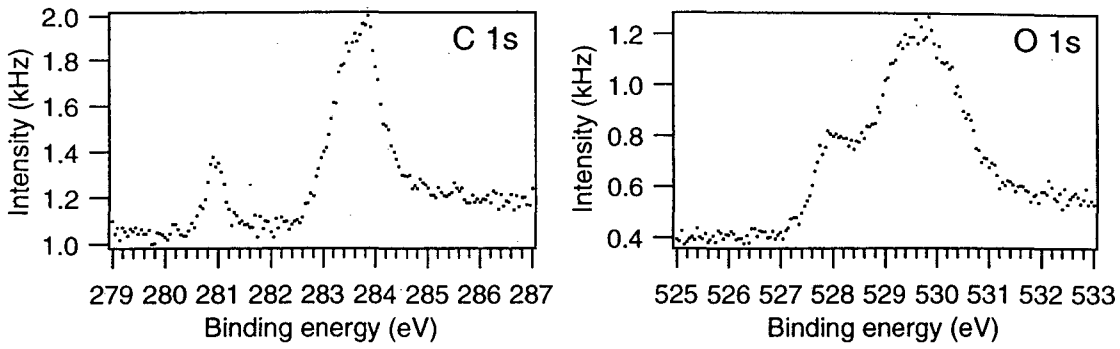

Fig.3: C 1s and O 1s photoelectron spectra from 0.7 L CO dosed onto Ni(100) at room temperature, measured directly after preparation.

In summary, our first photoelectron diffraction measurements in scanned energy mode at beamline 7.0 have provided several examples of the advantages of high energy resolution for PhD structural studies of molecular adsorption studies on a wider range of adsorbate and substrate systems. Future work, particularly with a capability to work at lower sample temperatures, should capitalise on this potential.

REFERENCES

1. D.P. Woodruff and A.M. Bradshaw, Rep. Prog. Phys. **57**, 1029 (1994).
2. D.P. Woodruff, R. Davis, N.A. Booth, A.M. Bradshaw, C.J. Hirschmugl, K.-M. Schindler, O. Schaff, V. Fernandez, A. Theobald, Ph. Hofmann and V. Fritzsche, Surface Sci. **357-358**, 19 (1996).
3. Ph. Hofmann, K.-M. Schindler, S. Bao, A.M. Bradshaw and D.P. Woodruff, Nature **368**, 131 (1994).
4. V. Fritzsche, J. Phys.: Condens. Matter **2**, 9735 (1990).
5. K.-U. Weiss, R. Dippel, K.-M. Schindler, P. Gardner, V. Fritzsche, A.M. Bradshaw, D.P. Woodruff, M.C. Asensio and A.R. González-Elipe, Phys. Rev. Lett. **71**, 581 (1993).
6. T. Gießel, V. Fernandez, S. Bao, C.J. Hirschmugl, R. Lindsay, O. Schaff, K.-M. Schindler, A. Theobald, V. Fritzsche, A.M. Bradshaw, C.J. Baddeley, A.F. Lee, R.M. Lambert, D.P. Woodruff, to be published.
7. R. Raval, S. Haq, M.A. Harrison, G. Blyholder and D.A. King, Chem. Phys. Lett. **167**, 391 (1990).
8. H. Antonsson, A. Nilsson, N. Mårtensson, I. Panas and P.E.M. Siegbahn, J. Electr. Spectr. Rel. Phen. **54/55**, 601 (1990).
9. W. Erley and H. Wagner, Surface Sci. **74**, 333 (1978).

This work was supported by the EPSRC of the UK. AMB and DPW thank the Max-Planck-Gesellschaft and the Alexander von Humboldt-Stiftung for the award of a Max-Planck Forschungspreis.

Principal investigator: D.P. Woodruff, Physics Department, University of Warwick, Coventry CV4 7AL, UK. Email: Phil.Woodruff@Warwick.ac.uk.

Screening Dynamics in Doped Titanates

J-E. Rubensson,[1] J. Lüning,[1] S. Eisebitt,[1] R. Williams,[1] W. Eberhardt,[1]
J. Guo,[2] P. Skytt,[2] S. Butorin,[2] J. Nordgren,[2] N. Shanti,[3] and D. D.Sarma[3]
[1]IFF-IEE, Forschungszentrum Jülich, D-524 25 Jülich, Germany
[2]Department of Physics, Box 530, Uppsala University, S-75221 Uppsala, Sweden
[3]Solid State and Structural Chemistry Unit, Indian Institute of Science, Bangalore 560012, India

INTRODUCTION

The time scale for carrier relaxation in semiconductors is on the same order of magnitude as the life time of shallow core hole states (a few femtoseconds). Resonant Inelastic soft X-ray scattering (RIXS) which involves (virtual) excitations of core levels consequently contains information about the time development of the electronic structure on this time scale. In many cases one can treat the scattering in an absorption (SXA) -followed-by-emission (SXE) picture, where simply the rates for various processes can be compared with the intermediate core hole state decay rate as an internal "clock".

By variation of x ($0<x<1$) in $La_xSr_{1-x}TiO_3$, the amount of Ti d electrons in the system can be controlled. $SrTiO_3$ ($x = 0$) is an insulator with an empty Ti d band. With increasing x, electrons are doped into the Ti d-band, and $LaTiO_3$ ($x = 1$) is a Mott Hubbard insulator with a Ti $3d^1$ configuration.

In this work we demonstrate that the rate for Ti 2p core hole screening in $La_xSr_{1-x}TiO_3$ is doping dependent. The screening rate increases with the availability of Ti 3d electrons, and we estimate it to be $3.8*10^{13}$/s in $La_{0.05}Sr_{0.95}TiO_3$.

EXPERIMENT

Monochromatized synchrotron radiation (FWHM ≈ 0.4 eV) from beamline 7.0 [1] was used for excitation and the emission was analyzed in a grazing incidence spectrometer [2] (FWHM ≈ 0.7 eV). The samples were polycrystalline ingots prepared in an inert gas arc furnace.

RESULTS

The Ti L absorption spectra of $La_xSr_{1-x}TiO_3$ ($x = 0.01$ and $x = 0.05$) in Fig. 1a are very similar to the absorption spectrum of stochiometric $SrTiO_3$. This spectrum is well-described within a quasi-atomic approach as the excitation from a $3d^0$ ground state to $2p^{-1}3d$ final states [3]. The 2p spin-orbit and the crystal field interactions give rise to four dominating states, which in a simplifying picture can be denoted $2p_{3/2}{}^{-1}t_{2g}$, $2p_{3/2}{}^{-1}e_g$, $2p_{1/2}{}^{-1}t_{2g}$, and $2p_{1/2}{}^{-1}e_g$ in order of increasing energy.

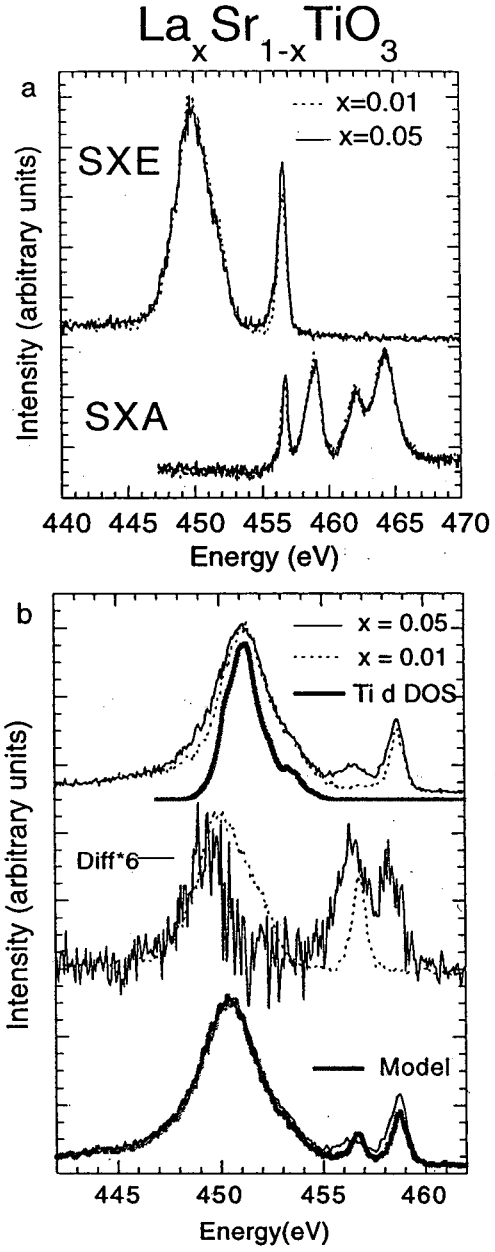

Fig. 1. (a) The SXA and SXE spectra of $La_xSr_{1-x}TiO_3$ (x = 0.01 and x = 0.05) excited below the ionization threshold. (b) SXE spectra excited above the ionization threshold. The calculated DOS is shifted 457 eV to compare to the emission spectra.

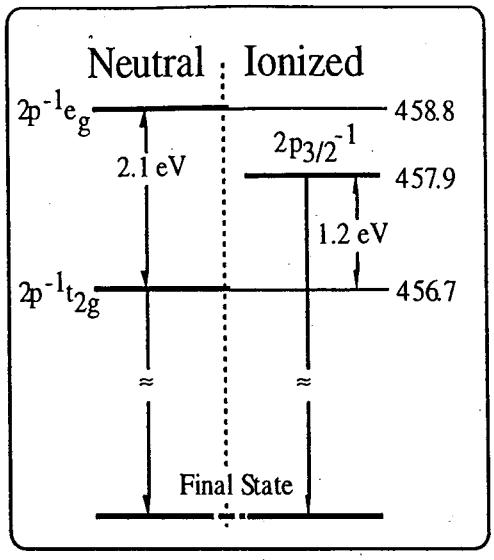

Fig. 2. Energy scheme for illustration of the determination of the 2p ionization energy, and the exciton binding energy. It is assumed that the same final states are reached. Energies are given in eV.

In Fig. 1a we also show the SXE spectra of the two compounds when the excitation is tuned, below the ionization limit, to the first ($2p3/2^{-1}t_{2g}$) resonance. The spectra are dominated by a 3 eV wide peak at 450 eV, which is assigned to transitions from states of primarily oxygen p character. These states are the most intense in the spectra due to their overlap with d-symmetry on the Ti sites, and due to the low occupancy of the non-bonding Ti d states. The energy position of the sharp peak at 456.7 eV coincides with the excitation energy. We assign this peak to atomic-like recombination and diffuse reflection, although the relative contributions of the two processes cannot be separated. The small difference between the two spectra in this energy region may thus be due to a different contribution of diffuse reflection, which is dependent on the surface roughness. In all other respects the two spectra are identical within the measurement accuracy.

We now turn our attention to the spectra excited at 458.8 eV, on the $2p3/2^{-1}e_g$ resonance (upper curves of Fig. 1b). The sharp peak at the excitation energy is, again, due to recombination and diffuse reflection. The main peaks are shifted 1.2 eV relative to the spectra in Fig. 1a, leaving the maxima at 451.2 eV. This shift does not directly correspond to a Raman shift because the primary energy is shifted across the ionization limit. Assuming that the same final states are reached at the two excitation energies, i. e., neglecting the coupling between the initially excited electron and the oxygen p states which dominate the

spectra, we can construct the energy scheme in Fig. 2. From this scheme the $2p_{3/2}$ core level binding energy and the $2p_{3/2}^{-1}t_{2g}$ exciton binding energy can be estimated to be 457.9 eV and 1.2 eV, respectively.

At 456.5 eV, a peak appears in the spectrum of the compound with the higher doping, which is virtually absent in the spectrum of the lower doped compound. A closer inspection of the spectra also reveals that the main peak in the x = 0.05 spectrum is slightly broader than in the x = 0.01 spectrum. The differences are shown in the center part of Fig. 1b. The difference spectrum shows similarities to the spectrum excited below the ionization limit (plotted as a dashed curve): It has a broad maximum around 450 eV, and a double structure between 455 the 460 eV. The feature at 456.5 eV almost coincides with the sharp peak in the spectrum excited below the ionization threshold.

This observation leads us to interpret the spectrum of the x = 0.05 compound, excited above threshold, as a superposition of transitions in the neutral and the ionized system [4]. It indicates a core hole screening mechanism where doping electrons are captured in the excitonic $2p_{3/2}^{-1}t_{2g}$ state. The rate of this process can now be directly compared to the core hole decay rate. Adopting a multi-step picture (Fig. 3), and assuming that the X-ray decay rates are the same for the ionized and the excitonic states, the screening rate is simply

$$\Gamma_{screening} = \frac{I(neutral)}{I(ionized)} \cdot \Gamma_A(neutral),$$

where I(neutral) and I(ionized) are the measured intensities. The lifetime width of the Ti $2p_{3/2}$ hole state, Γ_A(neutral), has been estimated to be 0.1 eV in titanium metal [5], which is also the parameter for the Lorentzian broadening used to fit the $2p_{3/2}^{-1}t_{2g}$ absorption peak in various titanium oxides [6].

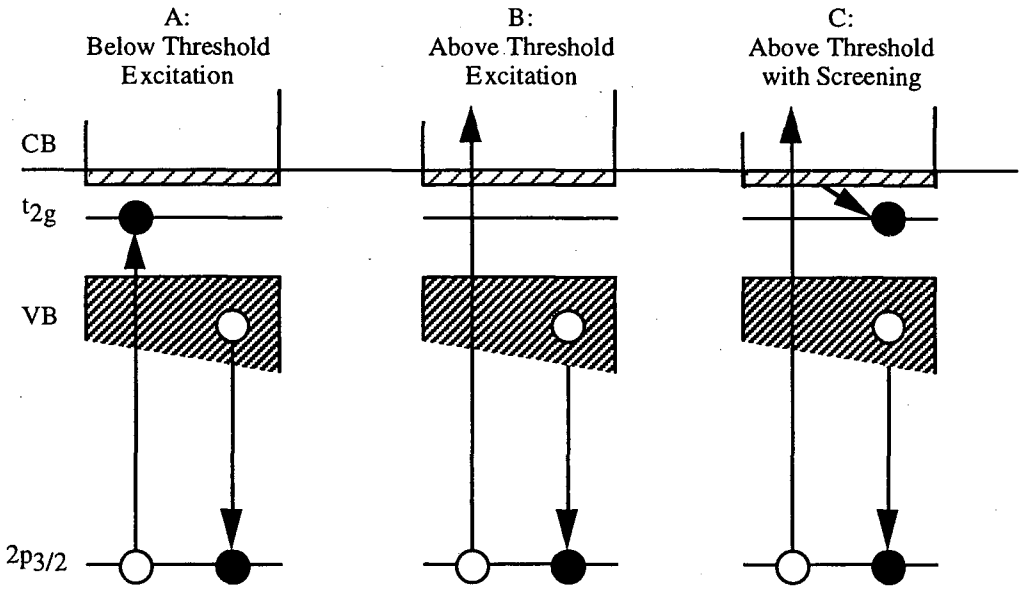

Fig.3 Energy scheme illustrating the screening process. In (A) emission is measured from the directly excited excitonic state. In (B) the system is ionized, and emission from the ionized system is observed, as well as (C) emission from states populated via screening from the Ti d states.

To estimate the intensity ratio we fit the x = 0.05 spectrum excited above threshold as a superposition of the spectrum excited below threshold (neutral), and the x = 0.01 spectrum excited above threshold. The latter is assumed to represent the emission from ionized unscreened states. The best fit (Fig 2c) is achieved with weighting factors corresponding to the intensity ratio I(neutral)/I(ionized)=1/4 which gives a screening rate of $3.8*10^{13}$/s. This corresponds to the increase in screening rate due to the 0.04 additional Ti d electrons, going from x = 0.01 to x = 0.05.

The recombination peak, after ionization and screening, is broadened and shifted relative to the directly excited $2p_{3/2}^{-1}t_{2g} \rightarrow$Ground State recombination. This is due to vibrational excitations associated with the changes in charge state. Vibrations may also have an impact on the main structure in the spectrum, which introduces an uncertainty in the determination of $\Gamma_{screening}$.

CONCLUSIONS

RIXS can be used to study relaxation processes on the time-scale of the core hole lifetime. In lightly doped titanates we have separated transitions from screened and unscreened core hole states, and estimated the core hole screening rate. This result will be followed up by a systematic study of series of doped titanates.

REFERENCES

1. T. Warwick, P. Heimann, D. Mossessain, W. MacKinney, and H. Padmore, Rev. Sci. Instrum., **66**, 2037 (1995).
2. J. Nordgren, G. Bray, S. Cramm, R. Nyholm, J-E. Rubensson, and N. Wassdahl., Rev. Sci. Instrum., 60, 1969 (1989).
3. M. Abbate, F: M. F. de Groot, J. C. Fuggle, A Fujimori, Y. Tokura, Y. Fujishima, O. Strebel, M. Domke, G. Kaindl, J. van Elp, B. T. Thole,, G. A. Sawatzky, M. Sacchi, and N. Tsuda, Phys. Rev. B., 44, 5419 (1991).
4. An interpretation in terms of changes in the local partial density of states can be ruled out, because the feature at 456.5 eV is absent in the spectrum excited below threshold.
5. R. Nyholm, N. Mårtensson, A. Lebugle, and U. Axelsson., J. Phys. F, **11**, 1727 (1981).
6. F. M. F. de Groot, J. C. Fuggle, B. T. Thole, and G. A. Sawatzky, Phys. Rev. B., **42**, 5457 (1990).

This work was supported by the Swedish Natural Science Research Council and the Goran Gustafssons Foundation for Science and Medicine.

Principal investigator: Jan-Erik Rubensson, IFF-IEE, Forschungszentrum Jülich, Germany. Email: J.Rubensson@KFA-Juelich.De. Telephone: +49-2461-616670.

Spectromicroscopy of Fe Distributions in Clay Microcrystals

T. Grundl[1], S. Cerasari[2], A. Garcia[2], T. Warwick[2], H. Ade[3] and B. P. Tonner[2,4,5]

[1]Center for Great Lakes Studies, University of Wisconsin-Milwaukee, PO Box 413, Milwaukee WI 53201
[2]Advanced Light Source, LBNL, 1 Cyclotron Rd., Berkeley, CA 94720
[3]Dept. of Physics, North Carolina State University, Raleigh, NC
[4]Center for X-ray Optics, LBNL, 1 Cyclotron Rd., Berkeley, CA 94720
[5]Dept. of Physics, University of Wisconsin-Milwaukee, PO Box 413, Milwaukee WI 53201

INTRODUCTION

Clays are ubiquitous crystalline particles found in nature that are responsible for contributing to a wide range of chemical reactions in soils. The structure of these mineral particles changes when the particle is hydrated ("wet"), from that when it is dry. This makes a study of the microscopic distribution of chemical content of these microcrystals difficult using standard techniques that require vacuum. In addition to large structural changes, it is likely that chemical changes accompany the drying process. As a result, spectroscopic measurements on dried clay particles may not accurately reflect the actual composition of the material as found in the environment. In this work, we extend the use of the ALS *Spectromicroscopy Facility* STXM to high spectral and spatial resolution studies of transition metal L-edges in environmental materials.

We are studying mineral particles of montmorillonite, which is an Fe bearing clay which can be preprared with a wide distribution of Fe concentrations, and with Fe occupying different substitutional sites. The reactivity of these particles in the environment is related to the charge state of the active Fe sites, and to the distribution of these charge states in the particles themselves (basal surface, edges, or interior sites). This article reports the initiation of a new research direction in high resolution soft x-ray spectroscopy of environmental materials. It relys on the new capability demonstrated at BL7-STXM, to image and perform soft x-ray spectroscopy on wet cell samples, with an energy resolution sufficient to resolve the fine structure in absorption spectra of transition metals. The L-edges of transition elements contain a rich structure of 2p-3d transitions, which can be used to identify the transition metal atom charge state distribution. The methods we developed here for montmorillonite, which is important both practically and as a model system in environmental science, will be applicable to many related problems in soil science, as well as in studies of the basic physical chemistry of geological problems.

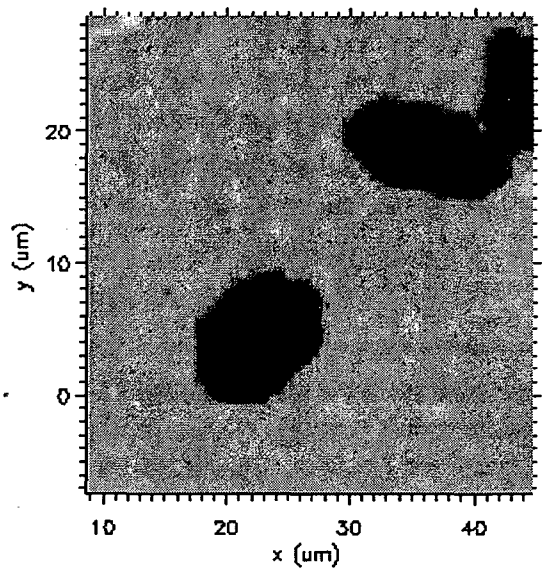

Fig. 1: BL7-STXM image of SWA-1 layered mineral crystallites of clay.

EXPERIMENT

Recent test experiments at the ALS *SpectroMicroscopy Facility* have demonstrated that high resolution soft x-ray absorption spectroscopy can now be extended to include systems in hydrated, aqueous, environments (examples are shown here). This is done by placing the specimens into "wet cells", which are sealed, x-ray transparent, membranes containing the specimen and a thin layer of water. The transmission of soft x-rays through this cell is large enough to obtain

spectra with high energy resolution, sufficient to distinguish between various chemical valences of transition elements in the sample. Although spectroscopy of wet samples has been done before at very high x-ray energies, wet-cell spectroscopy in the soft x-ray region is a recent development. In the case of some transition-metal compounds, the line-widths and chemical specificity is better with soft x-rays (L-edges) than for hard x-rays (K-edges). The wet-cell STXM experiments allow us to look at samples which change their chemistry and shape from wet preparations to dry. In environmental applications, this is of key importance.

An example of such systems are clay particles, which are layered crystalline minerals that play an important role in chemical reactions (both inorganic and biologically mediated) in soils. The catalytic properties of these particles depends on the chemical state of various substituted atoms in the crystal structure, and on the interlayer spacing of the particles which determines which sites are in contact with the fluid medium. The interlayer spacing and surface chemistry of clay particles is very sensitive to hydration. Although 'dry' studies are valuable, we expect to make new discoveries with 'wet cell' spectro-microscopy.

A brief trial experiment has been done to check the feasibility of this research. An image, taken on the BL7 scanning transmission x-ray microscope (STXM) is shown in Fig. 1. This is an Fe-substituted clay particle, montmorillonite, in which we are attempting to determine the lateral distribution of Fe concentration and valence using spectromicroscopy. The particle sizes occur in a wide range. We show 5-10 micron particles in Fig. 1, and we can study them down to the micron range with a spatial resolution of about 0.2 microns. The spectrum of the Fe L-edge from the center of a particle is shown in Fig. 2. The Fe concentration in this specimen was initially 17%. We believe that this sample was only partially hydrated, and therefore the signal from the Fe is reduced.

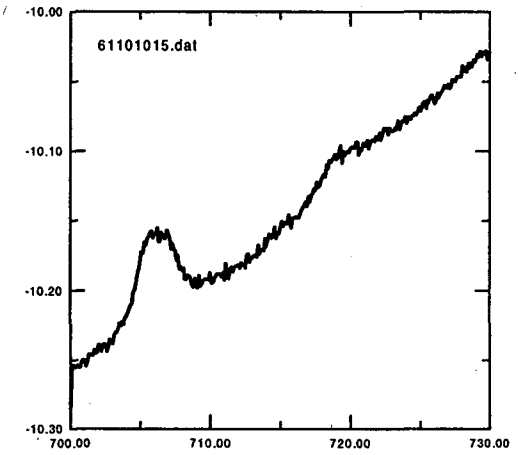

Fig. 2: Spectrum from center of clay particle in previous figure, showing Fe L-edge absorption peaks.

GEOCHEMISTRY OF CLAYS

The immediate purpose of this study is to investigate the process of electron exchange in iron bearing montmorillonite. Numerous studies have established the redox lability of these clay minerals. Stucki, et al., [1] reviews oxidation and reduction reactions of montmorillonites. Various chemical reductants are known, including hydrogen sulfide, sodium dithionate, hydrazine, sodium sulfide and sodium thiosulfate [2,3,4]. In addition, bacterial reduction has been reported [5]. The exact mechanism of electron transfer remains unclear. Essentially all structural iron in montmorillonite is found in the central octahedral layer, therefore electrons must be transferred across the tetrahedral layer or at edge sites where the octahedral layer is in contact with the solution. Electron transfer at edge sites requires electron mobility through the octahedral layer. Electron mobility of this sort is possible in ordered Fe(II-III) structures such as magnetite [6], but is difficult to envision in montmorillonite in which less than 1/3 of the octahedral sites contain iron. Electron transfer across the tetrahedral layer requires a long range interaction between the aqueous reductant (or bacteria) and iron in the montmorillonite structure.

The mapping of iron distribution and charge state before and after reduction will help elucidate which reduction mechanism is operative. Montmorillonites are very sensitive to drying and therefore require spectroscopy to be performed under environmental (as opposed to high vac-

uum) conditions. A better understanding of electron transfer and transport in montmorillonites could have important ramifications in their industrial use as catalysts and will improve the understanding of their chemistry in natural environments where redox reactions are cyclic.

We expect that this study of fully hydrated Fe bearing clays to be useful as a model for studies of environmentally relevant materials, including soils. The planned experiments in the near term will concentrate on the following problems:

1. Determine the particle size range for which spectro-microscopy is now practical. Particles of 5-10 micron in size were imaged in a short test run. We will dedicate some time to methodology of imaging smaller, 1 micron size, particles. This means developing methods for locating sparsely deposited particles of small size in the STXM.
2. Measure high resolution Fe L-edge spectra for natural and artificial clay samples, both fully hydrated, and in the dry state, to identify the chemical changes that accompany drying.
3. Measure distributions of Fe density and line-shape changes as a function of position in particles, to determine if there are differences between the Fe oxidation state at the edges of the particles and that in the center.
4. Measure changes in Fe charge state distributions and lateral distributions in the particles as factors such as pH of the water are changed, or as other solvated ions are added or removed from the water.

Other related projects (ie. studying the electron movement in and out of clays) that will require the use of spectroscopy under environmental conditions include:

- The role of electron donor-acceptor surface complexes in the adsorption of nitroaromatic pollutants to clay minerals.
- The mechanisms behind surface mediated reduction of nitroaromatic pollutants by aqueous Fe(II) at montmorillonite surfaces.
- The selective dissolution of structural Fe(II) out of montmorillonites upon exposure to mildly acidic conditions (pH 2-3).

REFERENCES

1. Stucki, J.W., Bailey, G. and Gan, H. (1995) "Redox reactions in phyllosilicates and their effects on metal transport in Metal Speciation and Contamination in Soils," Allen, Herbert, ed., Lewis Publishers.
2. Rozenson, I. and Heller-Kellai, L. (1976a) "Reduction and oxidation of Fe(III) in dioctahedral smectites 1: reduction with hydrazine and dithionate." Clays and Clay Minerals 24:271-282.
3. Gan, H., Stucki, J., and Bailey, G. (1992) "Reduction of structural iron in ferruginous smectite by free radicals." Clays and Clay Minerals 40:659-665.
4. Lear, P. and Stucki, J. (1989) "Effects of iron oxidation state on the specific surface area of nontronite." Clays and Clay Minerals 37:547-552.
5. Wu, J., Roth, C. and Low, P. (1988) "Biological reduction of structural iron in sodium-nontronite." Soil Sci. Soc. of Am. J. 52:295-296.
6. Jolivet, J: and Tronc, E. (1988) "Interfacial electron transfer in colloidal spinel iron oxide-Conversion of Fe_3O_4-Fe_2O_3 in aqueous medium." J. of Colloid and Interfacial Chem. 125:688-701.

This work was supported by the Laboratory for Surface Studies and Center for Great Lakes Studies (UW-M), the ALS and CXRO (LBNL), and the Department of Energy under grant DE-FG-2-92ER-45468.

Principal investigator: Brian Tonner, Department of Physics, Laboratory for Surface Studies, University of Wisconsin-Milwaukee. Email: tonner@csd.uwm.edu.

Spectromicroscopy of Self-Assembled Protein Clusters

O. Schonschek[1], J. Hormes[1], and V. Herzog[2]

[1]Institute of Physics, University of Bonn, Nussallee 12, D - 53115 Bonn, Germany

[2]Institute of Cell Biology, University of Bonn, Ulrich - Haberland - Str. 61a, D - 53121, Bonn, Germany

The aim of this project is to use synchrotron radiation as a tool to study biomedical questions concerned with the thyroid glands.
The biological background is outlined in a recent paper [1]. In short, Thyroglobulin (TG), the precursor protein of the hormone thyroxine, forms large (20 - 500 microns in diameter) clusters in the extracellular lumen of thyrocytes. The process of the cluster formation is still not well understood but is thought to be a main storage mechanism of TG and therefore thyroxine inside the thyroid glands.
For human thyroids, the interconnections of the proteins inside the clusters are mainly disulfide bondings. Normally, sulfur bridges are catalyzed by an enzyme called Protein Disulfide Bridge Isomerase (PDI). While this enzyme is supposed to be not present in any extracellular space, the cluster formation of TG takes place in the lumen between the thyrocytes. A possible explanation is the autocatalysis of TG.
As shown by immunoflourescence microscopy there is a clear lateral variation concerning protein - packing inside the clusters, which can be interpreted as some kind of hysteresis effect showing the history of hormone production and demand along time. It is suspected that the disulfide bridge density varies as well inside the clusters. The knowledge of the chemical environments of sulfur in the TG clusters could be helpful to understand the building mechanism and could be different for pathological thyroids.
Using the ALS Spectromicroscopy Facility at Beamline 7.0.1 we try to get sulfur images of ultrathin sections of TG clusters with high lateral resolution and local micro - XANES of different regions inside the clusters.
In our first shifts (November 13 to 18, 1996) we operated the Scanning Transmission X-Ray Microscope (STXM) for the very first time at energies as low as 160 eV (Sulfur L-edge). Running the STXM at very low energies showed a so-called shadowing effect resulting from a slight misalignment of the Order Sorting Aperture (OSA). Besides, the short focal distance makes a cautious operation of the microscope inevitable.

It should be pointed out that it was possible to get low energy photons through the samples and to take micro - XANES spectra of good quality. For the well established energy region of Oxygen and Nitrogen the contrast between the TG proteins and the embedding material in the thin sections is only very slight. As the sulfur concentration in the focus point is very low, it is necessary to locate the cluster before the sulfur micro - XANES measurements. Therefore we used special "TEM - letter - grids" and tried to get some optical images to select the right locations for STXM measurements. As the optical contrast between proteins and embedding material is small as well, immunoflourescence marking will be used in the future.
So far it hasn't been possible to get reliable sulfur images and spectra. In our next shifts (January/February 1997) we plan to improve the sample preparation and to use reference samples with higher and well-known sulfur contents. We will also work on improving the capabilities of the STXM at low energies.

ACKNOWLEDGMENTS

The authors wish to thank Brian P. Tonner (University of Wisconsin, Milwaukee) for his support, the whole staff of ALS Beamline 7.0.1 for the cooperation and Ulrich Berndorfer and Christoph Bauer (University of Bonn) for the sample preparation.

REFERENCES

1. U. Berndorfer and V. Herzog, Journal of Clinical Endocrinology and Metabolism, Vol. 83, No. 5, p. 1918 - 1926

This work was supported by Heinrich Hertz - Stiftung, Duesseldorf, Germany

Principal Investigator: Josef Hormes, Institute of Physics, University of Bonn, Germany.
Email: hormes@pib1.physik.uni-bonn.de
Telephone: X - 49 - 228 - 732796, Fax: X - 49 - 228 - 737869 .

Structural Origin of Si-2*p* Core-Level Shifts from Si(100)-c[4x2] Surface: A Spectral X-Ray Photoelectron Diffraction Study

X. Chen[1], J. Denlinger[1,2], E. Rotenberg[2,3], S. D. Kevan[3], and B. P. Tonner[1]

[1]Department of Physics, Laboratory for Surface Studies, University of Wisconsin-Milwaukee, WI 53211
[2]Advanced Light Source, LBNL, 1 Cyclotron Rd., Berkeley, CA 94720
[3]Dept. of Physics, University of Oregon, Eugene, OR

ABSTRACT

We have performed angle-resolved x-ray photoelectron diffraction (XPD) from a Si(100)-c[4x2] surface to study the structural origin of Si-2*p* core-level shifts. In the experiment, the highly resolved surface Si-2*p* core-level spectra were measured as a fine grid of hemisphere and photon energies, using the *SpectroMicroscopy Facility* "ultraESCA" instrument. By carefully decomposing the spectra into several surface peaks, we are able to obtain surface-atom resolved XPD patterns. Using a multiple scattering analysis, we derived a detailed atomic model for the Si(100)-c[4x2] surface. In this model, the asymmetric dimers were found tilted by 11.5±2.0° with bond length of 2.32±0.05Å. By matching model XPD patterns to experiment, we can identify which atoms in the reconstructed surface are responsible for specific photoemission lines in the 2p spectrum.

1. INTRODUCTION

The Si(100) crystal surface has a complex surface reconstruction [1-5], which leads in turn to a complex core-level photoemission spectrum. The fundamental interest in the basic physics of this surface has resulted in many publications on both experiments [6-9] and theories [10-14]. Due to the surface sensitivity and unique feature of chemical specificity, high resolution x-ray photoemission spectroscopy (XPS) is well suited for the study of this surface. By combining photoemission technique with diffraction, it becomes a even more powerful tool as x-ray photoelectron diffraction (XPD) [15-16], which thus allows us to explore the atomic arrangement around emitters of interest. The challenge of this experiment is to measure, with very high statistics and spectral resolution, the Si-2p core level spectrum as a function of emission angle. This technique, which may be called "spectral XPD", makes it possible to separate out the unique diffraction patterns of atoms of the same element, but in different sites.

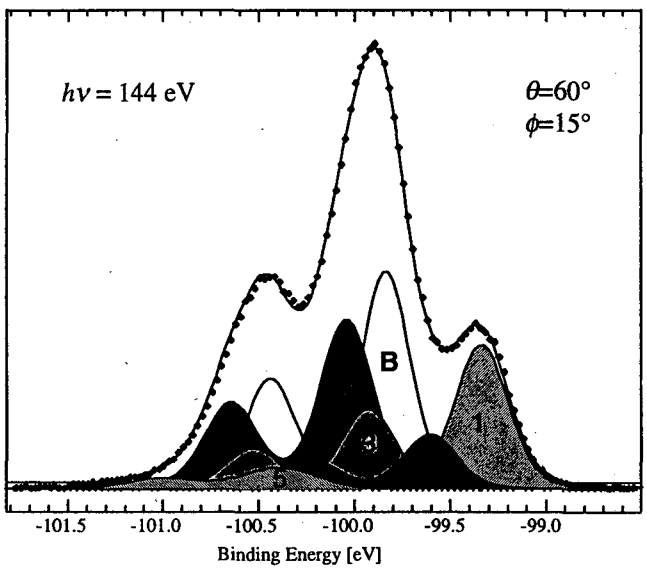

Fig.1: High resolution Si-2*p* core-level photoemission spectrum from Si(100)-c[4x2] surface. The spectrum is decomposed into 6 components.

A surface core-level shift of Si-2*p* at the lowest binding was studied by a prior work of Bullock *et al* [15] and was assigned to Si upper dimer atoms on the Si(100) surface. In their study, one azimuth curve of XPD at hν=130 eV has been measured to confirm the present of asymmetric Si dimers on the surface as proposed by

a theoretical work of Northrup *et al* [11]. However, the structural origins of other surface core-level shifts still remain unknown. In this study, we have measured XPD patterns with spectral quality sufficient to resolve 4 main surface Si 2p peaks, to explore the structural origin of other surface core-level shifts.

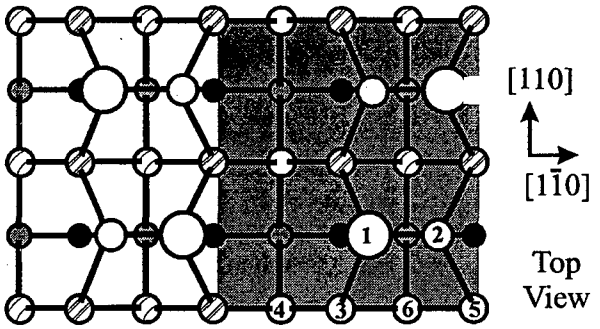

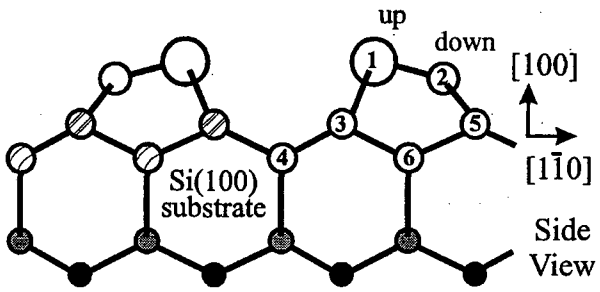

Fig.2 Schematic model for a reconstructed Si(100)-c[4x2] surface. Shaded region represents a unit cell.

2. EXPERIMENTAL

A mirror-polished Si(100) crystal was cleaned by etching followed by cycles of in-situ resistive heating up to 1160°. The surface was checked by XPS measurements and low energy electron diffraction (LEED). A sharp two-domain c[4x2] LEED pattern with well-defined quarter order spots and low background was found. Spectral XPD measurements were made at BL 7.0. High resolution Si-*2p* photoemission spectra were measured over the emission hemisphere on fine angular grids, at 29 different photon energies. Overall more than 20,000 spectra were taken for photon energies from 115.2 eV to 286.6 eV with fine polar angles from θ=0° up to 80° and azimuth angles from ϕ=0° to 90°. A typical high resolution Si-*2p* photoemission spectrum from this experiment is shown in Fig.1.

The decomposition of the Si-*2p* photoemission spectra is done by a quantitative least-squares fitting procedure, where a spectrum is decomposed into 6 components consisting of spin-orbit split (double peak). In the fitting, all the components were assigned to have the same spin-orbit split with Lorentzian-Gaussian type, but freely relaxed in peak ratio. In Fig.1, component S_1, S_2, S_3, S_4, and S_5 are the surface peaks with binding energy shifted by -0.50, -0.23 0.06 0.22, 0.42 eV relatively to the position of the bulk component, B. Therefore, in order to study the core-level shifts separately, we may obtain the surface-resolved XPD's, which are labeled as S_1-XPD, S_2-XPD, S_3-XPD, S_4-XPD, and S_5-XPD. It is found that these diffraction patterns vary significantly from one to another, indicating differences in their structural origin.

3. MULTIPLE SCATTERING CLUSTER SIMULATIONS

The multiple scattering (MS) cluster method we used in simulating these XPD patterns is based on an efficient and accurate concentric-shell-algorithm (CSA), developed by Saldin *et al* [17]. For simulating XPD, we choose a surface model, as shown in Fig.2, where buckled dimers are arranged in a c[4x2] periodicity on an almost intact Si(100) surface. In this model, we assume that dimers are buckled alternatively in the same row (along [110]) and adjacent dimer rows are in an anti-phase configuration.

For a simple and quick approach to the problem, simulations were to focus on a single energy S_1-XPD pattern at hν=160 eV where the emitters are assumed to be the top dimer atoms. During the optimization procedure, we vary all the coordinates of the surface atoms in the model except those restricted by the c[4x2] symmetry. A trial-and-error method is used to

minimize the reliability factor (R-factor) [18] which is an indicator of the goodness of fitting between the experiments and simulations.

Specifically, we vary one atomic coordinate at a time while keeping others unchanged until a local minimum of R-factor is reached. Then we repeat the same procedure on one of other parameters in turn until any changes in those parameters will result in an increase in R-factor. An R-factor of 5.8% is obtained for the optimized c[4x2] model. After the optimization, the buckled dimer is found to be tilted by an angle of 11.5±2.0° with bond length of 2.32±0.05 Å. In addition, the bond lengths between top dimer atom and its two substrate neighbors are found to be 2.44±0.05 Å.

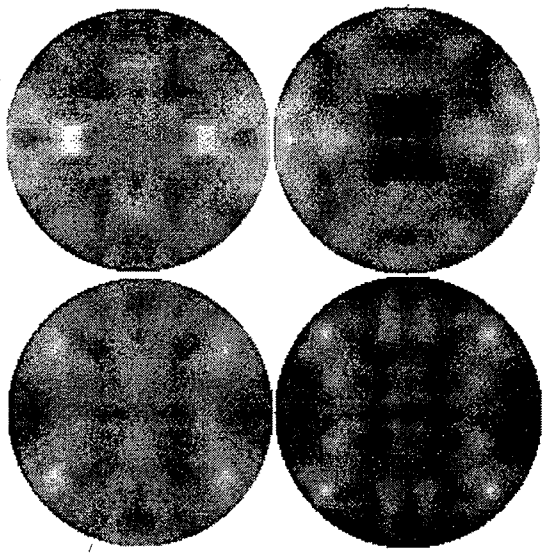

Fig. 3: S_1-XPD (left) and MS simulations (right) at hν=140 (top) and 160 eV (bottom).

Furthermore, we have extended our MS simulations on other photon energies (120 ~ 170 eV) using the same optimized c[4x2] model. It is found that our simulations can reproduce the experimental patterns of S_1-XPD reasonably well on those energy energies. We show in Fig. 3 two S_1-XPD patterns at hν=140 and 160 eV (left) and the MS simulations (right). It is seen in the figure that the agreement between experiment and theory is fairly good for both energies.

In the MS simulations, cluster radii of 7~ 8 Å, which includes 5 shells of total 40 Si atoms, were chosen. The phase shifts of silicon atoms were obtained from muffin-tin potential calculation with input atomic wave-function obtained from a Herman-Skillmann calculation. The maximum angular momentum number of phase shifts is set to be L_{max}=5. The calculated patterns are symmetrized to account for a major/minor domain ratio of 80/20, which is roughly in accordance with the observed LEED patterns.

To check if the diffraction pattern is due to down dimer atoms, we have carried out MS for down dimer atoms using a c[4x2] model, and found an R-factor of 20.5% which is quite large and indicates that S_1 component originates solely from upper dimer atoms.

4. CONCLUSION

As studied by Bullock *et al.* [15], the core-level shift, S_1, was found to be originating from top dimer atoms. But other surface components are still unknown. In the earlier study, the buckled Si dimers were found to be tilted at 19.0° with bond length of 2.24Å where only one azimuth XPD scan data at hν=130 eV were measured. In the current study, a much larger data set of spectral diffraction patterns was measured. Due to the largely improved signal to noise ratio in our XPD measurements, it is possible for us to determine more accurately the atomic arrangement on the surface and to further explore the structural origin of other components.

Since the surface peak S_1 is farther away from the main bulk of the Si-*2p* spectrum, and hence can easily be resolved from the spectrum, the optimized model of c[4x2] structure obtained from MS study of S_1-XPD should be reliable and a good starting point in tracking down the origin of other surface components. We have carried out MS simulations including all emitters from the surface atoms to a depth of 3Å under the surface. MS simulations from

various emitters were then used to compare with experimental patterns of S_2-XPD, S_3-XPD, S_4-XPD and S_5-XPD. It was found that there is a good agreement between the patterns of the S_4-XPD and MS simulations of a substrate silicon atom. This substrate atom is labeled as atom 4 in Fig.2 and is 2.7 Å below top dimer atoms.

In summary, synchrotron radiation surface Si-2*p* spectral XPD patterns from Si(100)-c[4x2] surface have been obtained for the study of this surface. In this study, we have confirmed the structural origin of surface core-level shift, S_1, which is due to the upper Si atoms. We also take advantage of our large number of data acquisition to obtain a detailed c[4x2] atomic arrangement for the surface, and found that the bond length and tilting angle of buckled dimers on this surface are 2.32Å and 11.5°. Through further comparison of our MS simulations using our established c[4x2] model, we are able to identify the structural origin of another core-level, S_4, which results from atoms in the substrate.

REFERENCES

[1] J. Ihm, D. H. Lee, J. D. Joannopoulos, and J. J. Xiong, PRL 51, 1872 (1983).
[2] R. J. Hamers, R. M. Tromp, and J. E. Demuth, PRB 34, 5343 (1986).
[3] T. Tabata, T. Aruga, and Y. Murata, Surf. Sci. 179, L63 (1987).
[4] R. Wiesendanger, D. Burgler, G. Tarrach, and H.-J Guntherodt, Surf. Sci. 232, 1 (1990).
[5] R. A. Wolkov, PRL 68, 2636 (1992).
[6] F. J. Himpsel, F. R. McFeely, A. Taleb-Ibrahimini, J. A. Yarmoff, and G. Hollinger, PRB 38, 6084 (1988).
[7] G. K. Wertheim, D. M. Riffe, J. E. Rowe, and P. H. Citrin, PRL 67, 120 (1991).
[8] D.-S. Lin, T. Miller, and T.-C Chiang, PRL 67, 2187 (1991).
[9] Erik Landemark, C. J. Karlsson, Y.-C. Chao, and R. I. G. Uhrberg, PRL 69, 1588 (1992).
[10] Z. Zhu, N. Shima, and M. Tsukada. PRB 40, 11868 (1989).
[11] J. E. Northrup, PRB 47, 10032(1993).
[12] J. Dabrowski and M. Scheffler, Appl. Surf. Sci. 56, 15 (1992).
[13] K. Kobayashi, Y. Morikawa, K. Terakura, and S. Blugel, PRB 45, 3469 (1992).
[14] P. Kruger and J. Pollmann, PRB 47, 1898 (1993).
[15] E. L. Bullock, R. Gunnella, L. Patthey, T. Abukawa, S. Kono, C. R. Natoli, and L.S. O. Johansson, PRL 74, 2756 (1995).
[16] B. P. Tonner, J. Zhang, X. Chen, Z.-L. Han, G. R. Harp, and D. K. Saldin, JVST B10(4), 1992.
[17] D. K. Saldin, G. R. Harp, and X. Chen. Phys. Rev. B 48, 8234 (1993).
[18] X. Chen, T. Abukawa, and S. Kono, Surf. Sci. 356, 28 (1996).

This work was supported by the Laboratory for Surface Studies, UW-M, the National Science Foundation under Grant DMR-9413475, and the Department of Energy under Grant DE-FG-2-92ER-45468.

Contact Author: X. (Sean) Chen, Advanced Light Source, MS 7-222, LBNL, xchen@grace.lbl.gov .

The Structure of the c(2x2) Mn/Ni(001) Surface Alloy by Quantitative Photoelectron Diffraction

S. Banerjee[1], S. Ravy[1,2], J. Denlinger[1], X. Chen[1], D. K. Saldin[1] and B. P. Tonner[1]

[1]Department of Physics, University of Wisconsin-Milwaukee, P.O. Box 413 Milwaukee, WI 53201, U.S.A

[2]Laboratoire de Physique des solides (CNRS URA 2), Université Paris-Sud 91405 Orsay, France

INTRODUCTION

Surface alloys are two-dimensional metallic systems that can have structures that are unique to the surface, and have no counterpart in the bulk binary phase diagram. A very unusual structure was reported for the Mn-Ni system, based on a quantitative LEED structure determination, which showed that the Mn atoms were displaced out of the surface by a substantial amount[1,2]. This displacement was attributed to a large magnetic moment on the Mn atoms. The structure of the Mn-Ni surface alloy was proposed to be based on a bulk termination model. Magnetic measurements on the Mn-Ni surface alloys, however, showed conclusively that the magnetic structure of these surface alloys is completely different from the bulk alloy analogs[3,4]. For example, bulk MnNi is an antiferromagnet, whereas the surface alloy is ferromagnetic. This suggests that the proposed structure based on bulk termination, may not be correct. X-ray Photoelectron Diffraction (XPD) techniques were used to investigate this structure, using both a comparison to multiple scattering calculations and photoelectron holography. In this article we present some of the results from the quantitative analysis of individual diffraction patterns by comparison to theory.

Earlier structural studies of both Mn/Ni(001) [1,2] and Mn/Cu(001) [5] at half-monolayer coverage by LEED reported a surface structures which consisted of Mn atoms in the substitutional sites, shown schematically in Fig. 1. A displacement of the Mn atoms out of the surface plane was determined, with a somewhat larger value of displacement for Mn on Cu(001), 0.3Å, than on Ni(001), 0.25Å. This is unusual, since the atomic radius of a Mn atom is similar to that of both Cu and Ni, leading to possibly a small buckling of the Mn atoms, but not to a large outward displacement.

We have studied the structure of c(2x2) Mn/Ni(001) using photoelectron diffraction from the Mn and Ni 3p core-levels. The core-level selectivity of XPD is an advantage in a structural study like this, where the scattering strength of the two components in the surface is similar. The study was completed using synchrotron radiation, which provides the additional flexibility of being able to vary the electron kinetic energy. This can be used to enhance the cross section of the surface atoms, improving the signal to background ratio, and increasing the sensitivity of the technique to structural changes right at the surface layer. The synchrotron experiments collected full hemisphere XPD patterns at more than 25 different electron kinetic energies. This large set of diffraction data corresponds to a measurement of photoelectron diffraction intensity as a func-

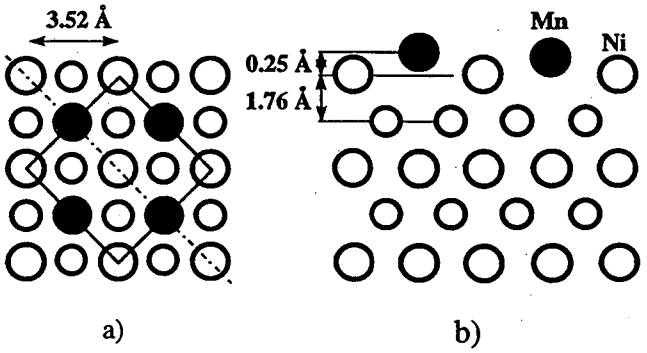

Fig. 1: The structure of 0.5 ML Mn/Ni(001) c(2x2) surface alloy. (a) Top view showing Ni and Mn (black) atoms in the surface layer and first subsurface layer (small white circles) of the substrate. (b) Side view along the dashed line in (a), [110] direction, showing two adjacent planes of atoms (large and small circles).

tion of three momentum space directions; we call such data sets 'diffraction volumes' for this reason. The data set was analyzed using a full multiple scattering cluster calculation, summarized here, as well as a direct (holographic) inversion technique.

The structure of Mn/Ni(001) for coverages from one-half monolayer up to four monolayers coverage was also studied by conventional, laboratory x-ray source XPD. These results will be reported elsewhere.

EXPERIMENT

These experiments were performed on the *SpectroMicroscopy Facility* beamline 7.0 at the Advanced Light Source, which is optimized for photon energies in the range from 60 eV to about 1000 eV[6]. A custom designed photoelectron diffraction system was employed, which has a computer controlled five-axis manipulator, and a high angular resolution, 16 channel detector hemispherical energy analyzer. The energy resolution of the electron analyzer was 0.06 eV (3 eV pass energy), and had an angular resolution of less than $\pm 1^{\circ}$. The energy resolution of the x-ray beam was less than 0.04 eV, for an overall energy resolution of less than 72 meV. The photon beam is incident in the horizontal direction, with p-polarization and a 30° grazing angle of incidence, and the electron detection axis is in the horizontal scattering plane, with an angle of 60° to the incident photon beam. The axis of rotation for polar angle scans is horizontal, which gives perfect symmetry around normal emission and makes it easy to identify absolute emission angles in the XPD data. This geometry is also optimized for signal intensity at grazing angles of incidence of the photon beam, and grazing exit angles for the electron beam[7].

Photoelectron diffraction patterns were acquired by measuring the photoemission spectrum from the Mn 3p, Ni 3p, and inelastic background at each setting of emission angle and incident photon energy. At each photon energy, a diffraction pattern was measured by stepping through a sequence of emission angles in a 90° azimuthal sector. The range of polar angles collected was from $\theta=0$ (normal emission) to $\theta=80$ degrees. The polar (θ) and azimuthal (ϕ) angular steps were chosen to uniformly sample the quarter-hemisphere of emission angles. The total number of distinct emission angles in the quarter hemisphere was 550, with precision in setting angular positions of 0.2°, from which the hemispherical diffraction pattern was created by a four-fold rotation (no mirror symmetry is applied).

Linearly polarized soft x-rays with photon energies ranging from 50 eV to 550 eV were used to measure XPD patterns from both the valence band and core-levels, spanning a range in electron kinetic energy from very surface sensitive at low energy to a forward-scattering limit at high kinetic energy. In addition, a series of 25 diffraction patterns from the Mn and Ni core-levels were accumulated as a function of incident photon energy, with the photon energies selected to produce constant differences in total electron momentum from pattern to pattern. This 'diffraction volume' can be used for direct inversion techniques (holography) with a complete experimental data set. Finally, energy dependent photoelectron diffraction (EDPD) curves were taken at 3 different emission angles. These EDPD curves matched the synthetic EDPD curves which can be extracted from the diffraction volume.

THEORY

The large data set we have accumulated can be analyzed in a number of ways. For the present, we have chosen to calculate theoretical simulations of individual diffraction patterns at specific electron kinetic energies, for a subset of the total data set. We expect that the low kinetic energy

diffraction patterns will be most sensitive to the structural parameters of the outermost c(2x2) layer, while the higher kinetic energy patterns may be simpler to calculate since the effects of multiple scattering become less pronounced.

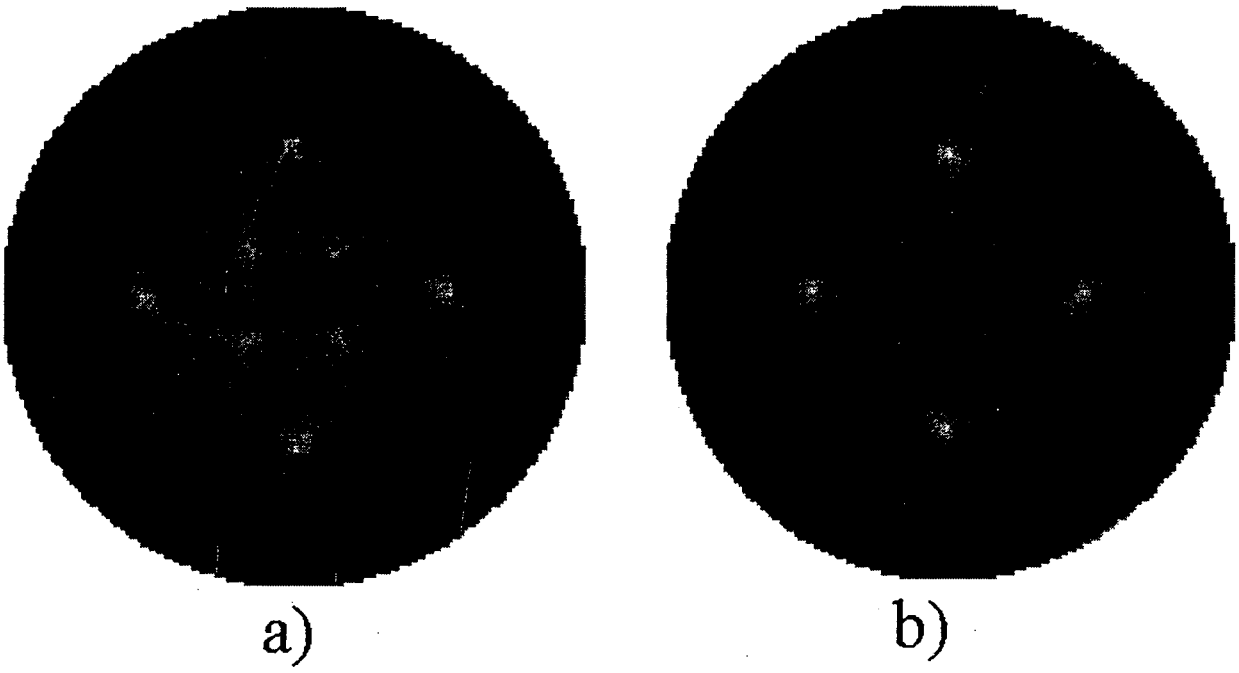

Fig. 2: Comparison of experimental pattern to optimized theoretical simulation at 60eV Kinetic Energy. (a) Experimental pattern at 60eV from the Mn emitter for the c(2˙2) Mn/Ni(001) surface alloy. (b) Optimized diffraction pattern at 60eV shows the surface alloy to have surface Ni atoms displaced inward to have an interlayer spacing of 1.6Å from the subsurface layer whereas the surface Mn atoms are displaced outward by 0.4Å.

Our calculation uses a full multiple-scattering cluster method, known as the concentric shell algorithm, CSA [8]. This is a real-space Green's function method, which makes use of the fact that electron attenuation results in a finite size of the cluster used to model scattering from a solid. In the CSA scheme, the cluster of atoms is divided into shells of atoms that lie at approximately the same radius from the photoemitter atom (which is not generally at the center of the cluster). For a single site model of c(2x2)Mn/Ni(001), only one emitter atom is needed to model the diffraction pattern for the Mn 3p level. For the Ni XPD pattern, a calculation is needed for Ni atoms in each layer of the cluster.

The model cluster was a half-hemisphere of atoms with a radius of 8Å, which intersects five layers of the sample, including the surface layer, for a total of 115 atoms. The surface layer of the cluster contains 8 c(2x2) unit cells. Full multiple scattering is calculated in a series of steps. The scattering of all atoms within a specific shell is calculated as a scattering matrix centered on the emitter atom. Then, the scattering matrices for all shells are combined to include inter-shell scattering to all orders. The cluster consisted of seven shells of atoms. At each atom, scattering phase shifts up to l=6 were included at 60 eV kinetic energy; for the final, emitter-centered scattered wave matrix spherical waves up to l=34 were used.

The experimental geometry is incorporated into the calculation through the dipole matrix elements, which include all allowed s- and d-wave final states for the 3p initial state. The scattering phase shifts were calculated starting from the atomic potential of Hermann and Skillman[9], which is input to a self consistent muffin-tin potential approximation (MUFPOT). In this first stage of data analysis, we concentrated on the diffraction pattern from Mn 3p at a photon energy

of 111.2 eV, corresponding to an electron kinetic energy of about 60 eV. The inner potential, Debye temperature of the Mn and Ni atoms, mean free path, and cluster size were 11 eV, 410K, 450K, 3Å and 8Å, respectively.

RESULTS

The experimental diffraction pattern for 60 eV kinetic energy electrons from the Mn surface atoms is shown in Fig. 2a. This pattern is one of more than 25 diffraction patterns measured over a range of 100 eV in kinetic energy. The individual patterns show a strong sensitivity to kinetic energy; a change of only a few electron volts is enough to cause strong features to completely disappear. This sensitivity is matched in the theoretical calculations, and it places stringent constraints on the values of the inner potential and other non-structural parameters used in the calculation.

Two basic types of structural models were considered. In the first, the Mn atoms were placed as adatoms in four-fold hollow sites at the surface. In the second model, the Mn atoms were in substitutional sites in the outer layer of Ni atoms, with the possibility for different heights of the Mn and Ni atoms in this layer.

We find that the greatest sensitivity to the difference between these two structures is found at the lower kinetic energies where backscattering is strongest, and multiple scattering effects must be included in the simulation. The adatom model gives very poor agreement with experiment. The in-plane, substitutional model gives good agreement between theory and experiment, as is seen in the comparison shown in Fig. 2. The principle characteristics of the patterns is the presence of two nested square arrays of peaks, one rotated by 45° with respect to the other. These structures, which appear only at 60 eV kinetic energy, are found only in the in-plane Mn model, and furthermore are only correctly reproduced with an outward displacement of the Mn atoms (as in Fig. 1).

REFERENCES

1 M. Wuttig, T. Flores and C. C. Knight, Phys. Rev. B **48**, 12082 (1993).
2 M. Wuttig and C. C. Knight, Phys. Rev. B **48**, (1993) 12130.
3 W. L. O'Brien and B. P. Tonner, Phys. Rev. B **50**, 2963-2969 (1994).
4 W. L. O'Brien and B. P. Tonner, Phys. Rev. B **51**, 617 (1995).
5 M. Wuttig, Y. Gauthier and S. Blugel, Phys. Rev. Lett **70**, (1993) 3619.
6 J. D. Denlinger, E. Rotenberg, T. Warwick, G. Visser, J. Nordgren, J.-H. Guo, P. Skytt, S.D. Kevan, K. S. McCutcheon, D. Shuh, J. Bucher, N. Edelstein, J. G. Tobin and B. P. Tonner, Rev. Sci. Instrumen. **66** (1995) 1342.
7 J. D. Denlinger, J. Zhang and B. P. Tonner, Nucl. Inst. and Methods in Phys. Res. A **347**, 475 (1994).
8 D. K. Saldin, G. R. Harp, and X. Chen, Phys. Rev. B **48**, 8234 (1993).
9 F. Herman and S. Skillman, *Atomic Structure Calculations* (Prentice Hall, Englewood Cliffs, NJ, 1963).

This work was supported by the National Science Foundation, Division of Materials Research, under grants DMR-9413475 (BPT) and DMR-9320275 (DKS), and by the UW-M Laboratory for Surface Studies.

Principal investigator: Brian Tonner, Department of Physics, Laboratory for Surface Studies, University of Wisconsin-Milwaukee. Email: tonner@csd.uwm.edu.

Beamline 8.0.1 Abstracts

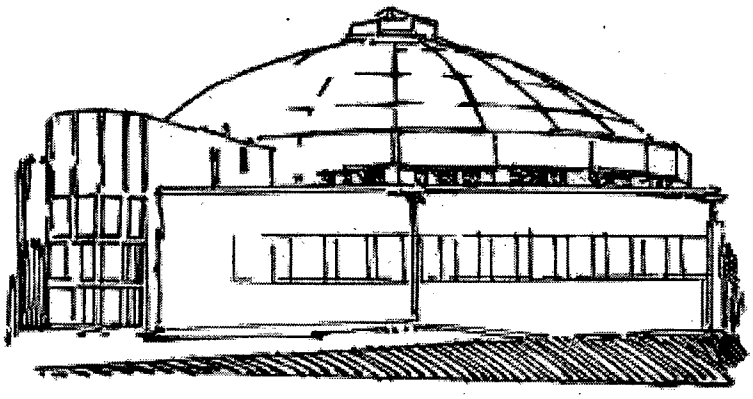

Application of High-Resolution Photoelectron Spectroscopy: Vibrational Resolved C 1*s* and O 1*s* Spectra of CO Adsorbed on Ni(100)

A. Föhlisch[1], A. Nilsson[1], N. Mårtensson[1], D. Menzel[2]
N. Wassdahl[1], O. Karis[1], J. Stöhr[3] and M. Samant[3]
[1]Department of Physics, Uppsala University, Box 530, S-751 21 Uppsala, Sweden
[2]Department of Physics E20, TU München, 85748 Garching, Germany
[3]IBM Research Division, Almaden Research Center 650 Harry Road, San Jose, California 95120, USA

There are various effects which determine the line shape of a core-level electron spectrum [1]. These are due to the finite life-time of the core hole, inelastic scattering of the outgoing photoelectron, electronic shake-up and shake-off processes and vibrational excitations. For free atoms and molecules the different contributions to the observed line shapes can often be well separated. For solids, surfaces and adsorbates the line shapes are in general much broader and it has in the past been assumed that no separation of the various contributions can be made. In the present report we will show that this is indeed not the case. Surprisingly the vibrational fine structure of CO adsorbed on Ni(100) can be resolved in the C1s and O1s electron spectra (fig. 1). This was achieved by the combination of highly monochromatized soft X-rays from Bl.8.0 with a high resolution Scienta 200 mm photoelectron spectrometer. X-ray photoelectron spectroscopy (XPS) with tunable excitation energy yields as a core level spectroscopy atomic and site-specific information. The presented measurements allow for a determination of internuclear distances and potential energy curves in corehole ionized adsorbed molecules.
Our analysis of the c(2x2) phase CO/Ni(100) on "top" yielded a vibrational splitting of 217 ± 2 meV for C1s ionization. For O1s ionization a splitting of 173 ± 8 meV was found (fig. 1).

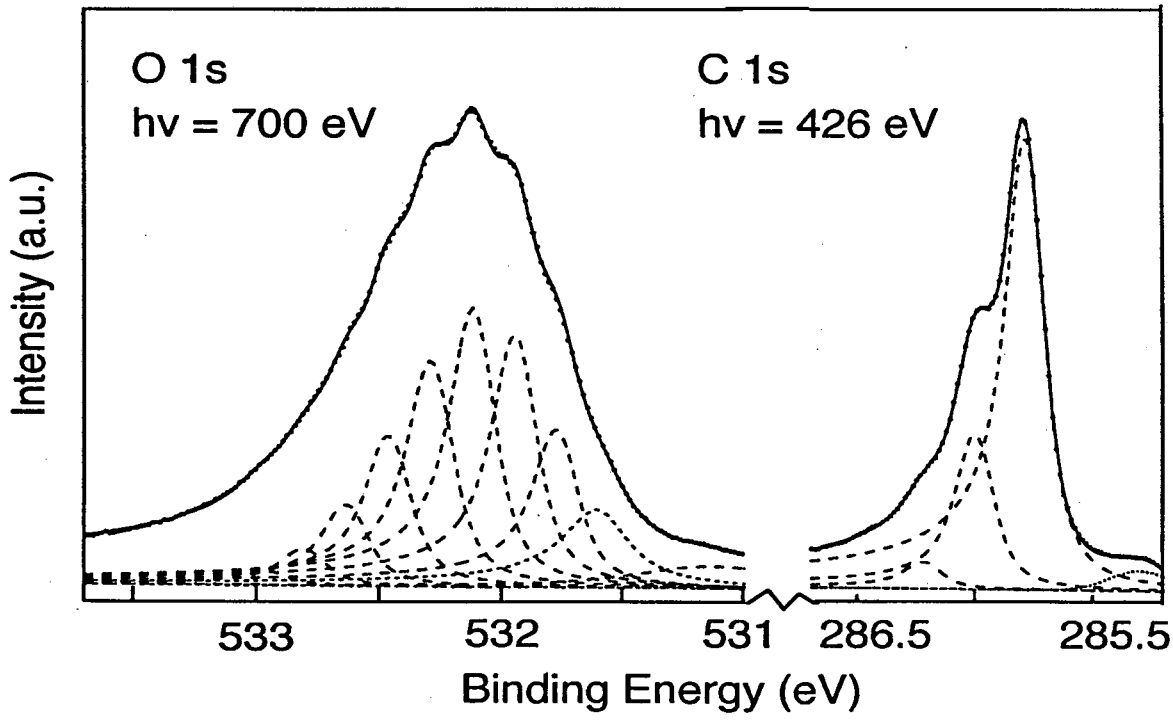

Figure1. Vibrationally resolved photoelectron spectra of CO adsorbed on Ni(100) c(2x2) "on top". Excitation energy for C1s ionization 426 eV, for O1s ionization 700 eV. Vibrational splitting for C1s ionization 217 meV, for O1s ioniztion 173 meV. Shown are datapoints with the individual peaks of the least square fit.

At sufficiently high excitation energy (sudden limit) the nuclear co-ordinates remain unmodified on the timescale of the photoionization process (Born Oppenheimer approximation). If the equilibrium geometry of the molecule changes upon ionization vibrational motion will be excited to accomodate the difference between initial and final state geometry. In a Franck Condon picture vibrational fine structure in XPS results from the electronic transition between the molecular potentials associated with the initial, ground state and the core ionized final state. Core ionized CO is seen in the equivalent core approximation (Z+1) as electronically equivalent to NO for C1s ionization and to CF for O1s ionization.

When a molecule is adsorbed on a surface new vibrational modes appear which are related to the translational and rotational degrees of freedom in the free molecule. In CO adsorbed "on top" on Ni(100)c(2x2) one finds in the ground state the CO strech with 256 meV [6], the substrate molecule strech with 59 meV [6], 2 frustrated translational modes with ca. 3.5 meV [7] and 2 frustrated rotations with 35 meV [6]. The low energy frustrated translational and rotational modes do not much contribute to the broadening unless they are thermally excited in the ground state.

The experiments were performed on beamline 8.0 with approx. 50 meV bandwidth of the soft X-ray monochromator and the Scienta SES 200 photoelectron spectrometer. The direction of photoelectron detection was parallel to the polarization of the exciting radiation. All measurements were performed at 80 K. The Ni(100) substrate was cleaned by standard procedures (Oxygen treatment, sputtering). Preparation of CO on top, bridge and hollow adsorption sites has been presented and characterized in Ref. [2]

In order to extract the vibrational splitting a curve analysis was undertaken. The employed least square fit used a lineprofile composed from a lorenzian with Doniach Sunjic asymmetry convoluted with a gaussian. For all vibrational quantumnumers ν'=0,1,2,3 the same lineprofile was assumed (linked parameters). The lifetime broadening of the C1s core hole was estimated to be 92 meV.

A comparison of the vibrationally resolved C1s and O1s main lines with respect to overall lineprofile and vibrational splitting reveils large differences between XPS taken on CO/Ni(100)c(2x2) and on CO in gas phase [3,4](fig.2). However, XPS taken on the adsorbate system has striking similarities with XAS measured on CO in gas phase [5](fig.2).
These findings can be understood comparing the initial and final states of the different spectroscopies and employing the final state rule which states that the shape of a spectrum is determined by the final state of the spectroscopy (fig.3). The initial state of XAS and XPS on CO in gas phase are identical. In the adsorbate system the surface chemical bond leads to a mixing of the Ni spd-band and the CO π-system in the initial state. Upon ionization charge from the Ni spd-band is transfered into the $2\pi^*$ molecular orbital. This relaxation effect, called metallic screening, leads to a final state which is very similar to the 1s -> $2\pi^*$ core excited final state of XAS in gas phase. The final state of XPS in gas phase is given by the fully core ionized molecule with no population of the $2\pi^*$ orbital .

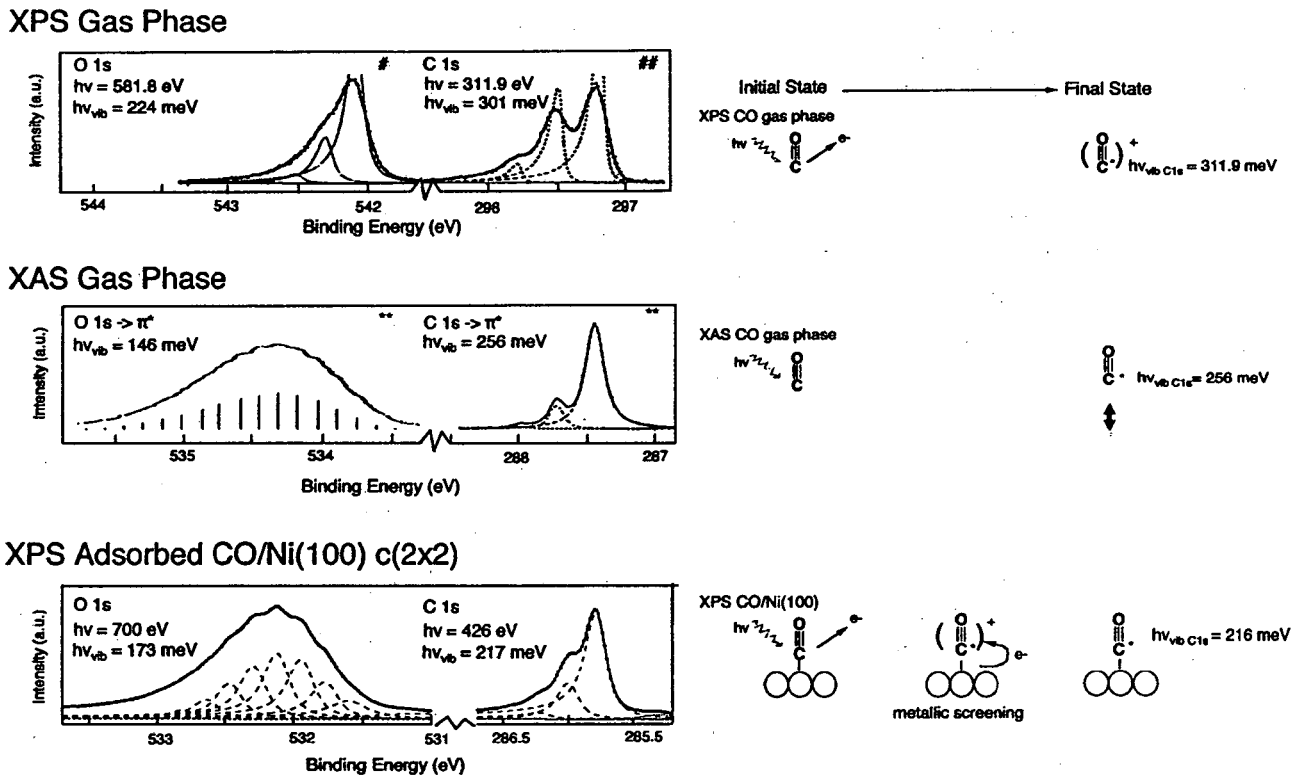

Figure 2. Comparison of XPS on CO/Ni(100)c(2x2) adsorbed on "top" to gas phase measurements taken from references #[3], ##[4],**[5]. Strong similarities between XPS on adsorbate and XAS in gas phase due to similar final states.

Figure 3. Scematic depiction of initial and final states for the corresponding measurements in fig.2. Metallic screening in the adsorbate system leads to a comparable final state than XAS in gas phase.

Comparison of the CO phase on top with CO adsorbed on bridge and hollow reveils interesting differences. The disordered CO/H/Ni(100) phase on "bridge" exhibits a vibrational splitting energy of 195 $\pm$ 6 meV for C1s ionization. The vibrational splitting for C1s ionization of the CO/H/Ni(100)c($2\sqrt{2}$ x $2\sqrt{2}$)R45° phase "hollow" was found to be158 $\pm$ 7 meV. Determination of the vibrational splitting for O1s ionization in the "bridge" and "hollow" systems seemed not appropriate as the observed structures were too washed out.

The observed dependency of decreasing vibrational splitting energy for C1s excitation versus increasing coordination number can be understood as increasing hybridization between the Ni spd-band and the molecular $2\pi^*$ leading to a weakening of the internal CO bond which is in the core ionized final state electronically equivalent to NO. The stronger the CO bond, the larger is the vibrational splitting of the CO strech. On "top" the CO molecule interacts mainly with one

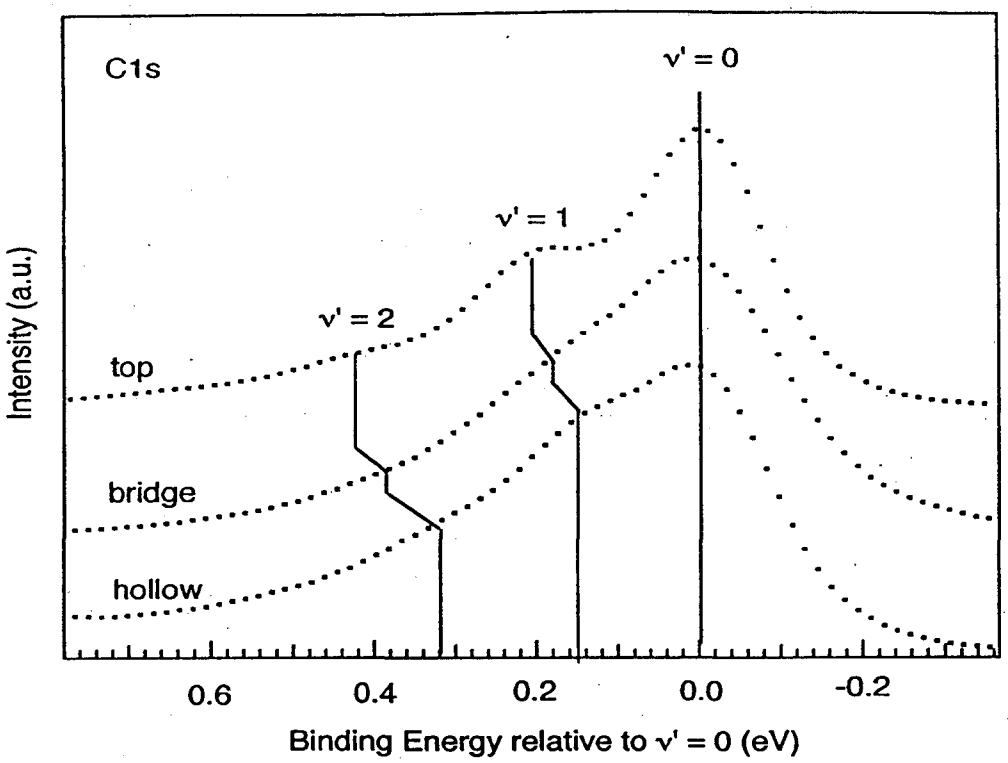

Figure 4: Vibrationally resolved C1s ionized CO on three different adsorption sites. top, bridge and hollow. Excitation energy 426 eV

Ni-atom, on "bridge" with two and on "hollow" with four. In this order the hybridization increases and the CO bond is weakend, therefore leading to smaller vibrational splitting.

The authors wish to thank the ALS staff for their assistance. This work was supported by the Swedish Natural Science Research Council (NFR) and the Göran Gustafsson Foundation for Research in Natural Science and Medicine

REFERENCES

1. N. Mårtensson and A. Nilsson in *Applications of Synchrotron Radiation* editedby W. Eberhardt, Vol. 33 Springer Series in Surface Science (Springer, Berlin, 1995).
2. H. Tillborg, A. Nilsson and N. Mårtensson., Surf. Sci. **47**, 273 (1992).
3. A. Bradshaw, priv. com.
4. K. Randall,A. L. D. Kilcoyne, H. M. Köppe, J. Feldhaus, A. M. Bradshaw, J.- E. Rubensson, W. Eberhardt, Z. Xu, P.D. Johnson, Y. Ma, Phys. Rev. Lett. **71**, 1156 (1993).
5. M. Domke, C. Xue, A. Puschmann, T. Mandel, E. Hudson, D. A. Shirley, G. Kaindl, Chem. Phys. Lett. **173**, 122 (1990).
6 P. Uvdal, P. A. Karlsson, C. Nyberg, A. Andersson and N. V. Richardsson, Surf. Sci. **202**, 167 (1988).
7 R. Berndt, J. P. Toennies and Ch. Wöll, J Electron Spectr., **44**, 183 (1987).

Principal investigator: Anders Nilsson, Department of Physics, Uppsala University, Sweden and the ALS E-mail: Anders.Nilsson@fysik.uu.se Telephone: 510-8419903

An Atom-Specific Look at the Surface Chemical Bond Using X-Ray Emission Spectroscopy

A. Nilsson[1], N. Wassdahl[1], M. Weinelt[1], O. Karis,[1] T. Wiell,[1] P. Bennich,[1]
J. Hasselström[1], A. Föhlisch[1], J. Stöhr[2]and M. Samant[2]
[1]Department of Physics, Uppsala University, Box 530, S-751 21 Uppsala, Sweden
[2]IBM Research Division, Almaden Research Center 650 Harry Road, San Jose, California 95120, USA

CO and N_2 adsorbed on the late transition metals have become prototype systems regarding the general understanding of molecular adsorption. It is in general assumed that the bonding of molecules to transition metals can be explained in terms of the interaction of the frontier HOMO and LUMO molecular orbitals with the d-orbitals. In such a picture the other molecular orbitals should remain essentially the same as in the free molecule. For the adsorption of the isoelectronic molecules CO and N_2 this has led to the so called Blyholder model i. e. a synergetic σ (HOMO) donor and π (LUMO) backdonation bond [1]. Our results at the ALS shows that such a picture is oversimplified.

The direct observation and identification of the states related to the surface chemical bond is an experimental challenge. For noble and transition metal surfaces, the adsorption induced states overlap with the metal d valence band. Their signature is therefore often obscured by bulk substrate states. This complication has made it difficult for techniques such as photoemission and inverse photoemission to provide reliable information on the energy of chemisorption induced states and has left questions unanswered regarding the validity of the frontier orbitals concept

In the following contribution we will show how x-ray emission spectroscopy (XES), in spite of its inherent bulk sensitivity, can be used to investigate adsorbed molecules [2]. Due to the localization of the core-excited intermediate state, XE spectroscopy alllows an atom specific separation of the valence electronic states. Thus the molecular contributions to the surface chemical bond can be separated from those of the substrate. Furthermore, angle dependent measurements make it possible to determine the symmetry of the molecular states, i.e. the separation of π and σ type states [3]. In all we can obtain an atomic view of the electronic states involved in the formation of the chemical bond to the surface.

It is important not only to observe new electronic states related to the surface chemical bond but also to study changes in the contribution from different atoms to the molecular orbitals upon adsorption. The upright adsorption geometry of the N_2 molecule on Ni(100) in on top site leads to two chemically inequivalent N atoms. If a separation between the two atoms can be made it is an ideal case to study how the electronic states redistribute in a homonuclear molecule upon adsorption.

The experiments were performed on beamline 8.0 at the ALS. The x-ray spectrometer, which can be rotated around an axis parallell to the incoming beam, is based on three interchangeable grazing incidence gratings in combination with a movable multichannel detector [4]. It was operated with a resolution of about 0.5 eV.

Previous work has shown that the x-ray absorption spectrum for N_2 on Ni(100) exhibits two 1s to $2\pi^*$ resonances at 400.6 and 401.0 eV [5] corresponding to the outer and inner N atoms, respectively. Hence, by using different excitation energies, site-specific XE spectra can be recorded. The resulting XE spectra for the outer and inner N atoms are shown in Fig. 1. The spectra are plotted on a common binding energy scale relative to the Fermi level, obtained by subtracting the N 1s core-level photoemission binding energies of the two atoms (outer atom: 399.4 eV; inner: 400.7 eV) from the emission energies. The figure is divided in an upper part, displaying states of σ symmetry (obtained by suitable linear combinations of the normal and grazing emission spectra) and a lower part, displaying states of π symmetry (the normal emission spectra).

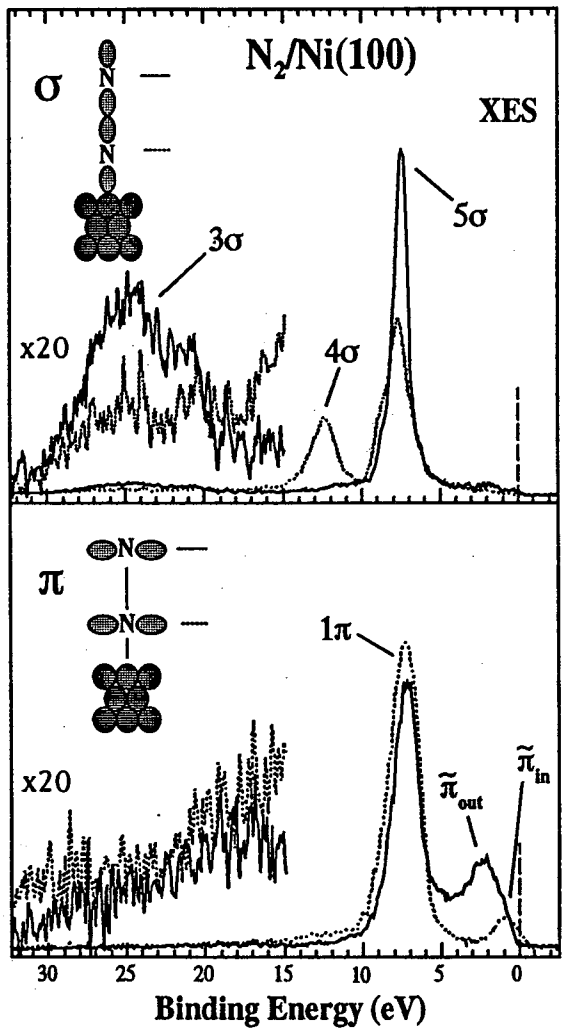

Figure 1. Symmetry resolved XE spectra for the inner and outer N atoms for N_2/Ni(100).

The novel information contained in Fig. 1 is the large difference in the states located on the inner and outer N atoms and the clearly resolved structures within 5 eV binding energy, i.e. in the Ni d band region. All spectral peaks, representing the 2p atom-projected molecular orbitals, exhibit different intensities or shapes for the inner and outer N atoms. Even the 3σ, located about 25 eV below the Fermi level, shows an intensity difference for the two atoms demonstrating that the chemisorption bond affects even the inner valence levels. Other interesting findings are the localization of the 4σ state to the inner N atom, with no visible spectral intensity from the outer N atom, and the larger 5σ localization to the outer N atom. Near the Fermi level we find the molecular states which are important for the surface chemical bond. These states arise from interaction of molecular π states with the Ni d states. The state located on the outer N atom is centered at about 2.5 eV binding energy while the state located on the inner N atom is centered at about 1 eVdenoted $\tilde{\pi}_{out}$ and $\tilde{\pi}_{in}$., resectively. These states are non-bonding with respect to the N-N bond and do not have much resemblance with the original orbitals of the free molecule. We can only generate these states through a linear combination of the original 1π and $2\pi^*$ orbitals. We picture the $\tilde{\pi}_{in}$ state to be strongly Ni-N bonding whereas the $\tilde{\pi}_{out}$ state is essentially a N 2p lone pair. It may contain some non-bonding Ni contribution.

In the spectra we do not see any new occupied states of 5σ symmetry and in previous XA spectra of adsorbed N_2 there are no indications of any new states above the Fermi level [6]. Thus we do not observe any bonding and anti-bonding states indicating a significant 5σ contribution to the surface chemical bond. This supports the cluster calculations of Bagus et al. [7], which show the σ contribution to be mainly repulsive. Our spectra show the repulsion effects as a redistribution

of the molecular σ system upon formation of the surface chemical bond. The 4σ state becomes polarized on the inner- and the 3σ and 5σ states on the outer nitrogen atoms. Surprisingly, all valence states, down to the 3σ state around 25 eV binding energy, are affected by the formation of the chemisorption bond. Despite the relative weakness of the chemisorption bond (≈ 0.4 eV) relative to the intra-molecular bond (≈ 8 eV) the intra-molecular bonding is completely changed upon chemisorption.

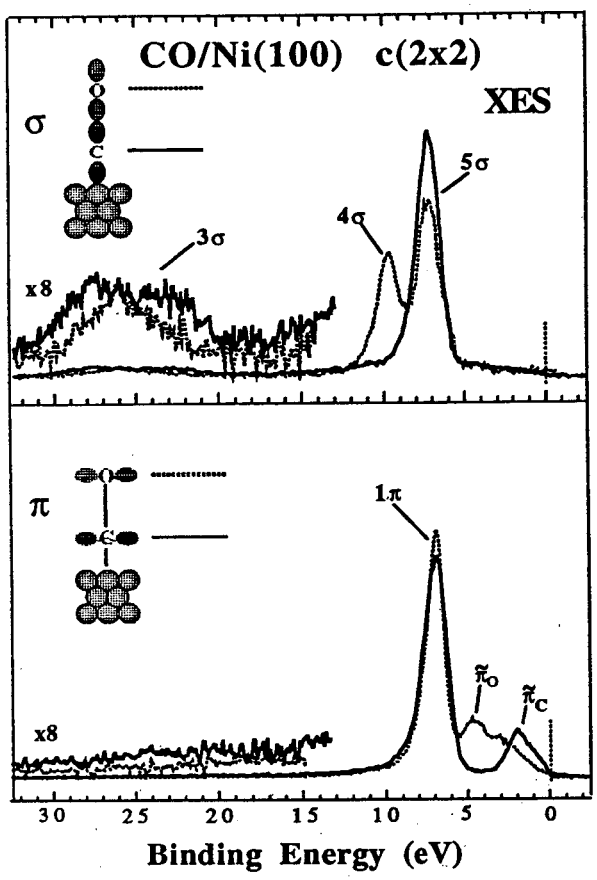

Figure 2. Symmetry resolved XE spectra for the C atom and O atom for CO/Ni(100)

The isoelectronic CO molecule adsorbs in the same way as N_2 in an on top site with the carbon end down. In this case the chemisorption bond is much stronger (≈ 1.5 eV). Fig. 3 shows the XE spectra for the carbon and oxygen atoms on a common binding energy scale relative to the Fermi level . The upper part shows states of σ symmetry while the lower part shows states of π symmetry. We observe that the 5σ state is mainly located at the inner carbon atom and the 4σ on the outer oxygen atom. At first sight this appears to be the reverse situation com pared with N_2. However, the distribution of the molecular orbitals in the free molecule is very different. In the oxygen XE spectrum of free CO the intensity of the 4σ state is about 5 times larger than the 5σ [8]. From Fig. 4 we can observe that upon adsorption the intensity of the 5σ state becomes slightly larger than the 4σ. The 5σ slightly redistribute itself in the same manner as seen in adsorbed N_2 due to the repulsive interaction with the substrate. The 4σ state stays completely localized on the outer oxygen atom as in the free molecule. In the π system we also observe two new states, $\tilde{\pi}_C$ (C-Ni bonding state) on the inner carbon atom and $\tilde{\pi}_O$(O lone pair state) on the outer oxygen atom similar to N_2. The energy splitting between the two states is larger in CO than in adsorbed N_2 , 3 eV and 1.5 eV, respectively. This can be attributed to the energy difference of the atomic 2p levels in carbon and oxygen. As can be seen in the oxygen XE spectrum, the $\tilde{\pi}_C$ state is not entirely localized on the carbon atom. The observed changes in the π system upon chemisorption resemble those between free CO and H_2CO.When two hydrogen atoms are added to CO to form H_2CO one of the π orbitals breaks up into a local C-H bonding orbital ($1b_1$) and an O 2p non-bonding lone pair orbital ($2b_1$), in analogy to the inner π and outer π states in both adsorbed CO and N_2.

The two adsorption examples above nicely demonstrate how oversimplified a frontier orbital concept is in the description of surface chemical bonding. The bond is not only related to the appearance of new orbitals. It is also important to consider changes in the complete molecular orbital framework. The resulting electronic structure of the chemisorption complex is well described in an atom-based picture which x-ray emission spectroscopy (XES) provides.

REFERENCES

1. G. Blyholder, J. Phys. Chem. **68**, 2772 (1964).
2. N. Wassdahl, A. Nilsson, T. Wiell, H. Tillborg, L. C. Duda, J. H. Guo, N. Mårtensson, J. Nordgren, J. N. Andersen and R. Nyholm, Phys. Rev. Lett. **69**, 812 (1992).
3. A. Nilsson, P. Bennich, T. Wiell, N. Wassdahl, N. Mårtensson, J. Nordgren, O. Björneholm and J. Stöhr, Phys. Rev. B**51**, 10244 (1995).
4. J. Nordgren, G. Bray, S. Cramm, R. Nyholm, J. E. Rubensson and N. Wassdahl, Rev. Sci. Instrum. **60**, 1690 (1989).
5. A. Sandell, O. Björneholm, A. Nilsson, E. Zdansky, H. Tillborg, J. Andersen, and N. Mårtensson, Phys. Rev. Lett. **70**, 2000 (1993).
6. O. Björneholm, A. Nilsson, E. Zdansky, A. Sandell, H. Tillborg, J. N. Andersen and N. Mårtensson, Phys. Rev. B**47**, 2308 (1993).
7. P. S. Bagus and G. Pacchioni, Surf. Sci. **278**, 427 (1992).
8. P. Skytt, P. Glans, K. Gunnelin, J. Guo, J. Nordgren, Y. Luo and H. Ågren, to be published.

This work was supported by the Swedish Natural Science Research Council (NFR) and the Göran Gustafsson Foundation for Research in Natural Sciences and Medicine.

Principal investigator: Anders Nilsson, Department of Physics, Uppsala University, Sweden and the ALS
E-mail: Anders.Nilsson@fysik.uu.se Telephone: 510-8419903

An Autoionization Study of the Argon 2*p* Satellites Excited Near the Argon 2*s* Threshold

H. Wang,[1] P. Glans,[1] O. Hemmers,[1] S.B. Whitfield,[1] D.W. Lindle,[1]
R. Wehlitz,[2] I.A. Sellin,[2] J. Levin,[2] G.B. Armen,[2] and R.C.C. Perera[3]

[1]Chemistry Department, University of Nevada, Las Vegas, Box 454003, Las Vegas, Nevada 89154-4003, USA
[2]Department of Physics and Astronomy, University of Tennessee, Knoxville, Tennessee 37996-1200, USA
[3]Advanced Light Source, Lawrence Berkeley National Laboratory, Berkeley, California 94720, USA

The dynamics of near-threshold photoionization is a complex phenomenon in which the many-electron character of the wavefunctions plays an important role [1]. According to generalized time-independent resonant scattering theory [2], the transition matrix element from an initial state to a final state is the summation of the amplitudes of direct photoionization and an indirect term in which intermediate states are involved and the resonant behavior is embedded. Studies of the interference effects of intermediate states have been explored in the cases where the direct term is negligible [3,4].

In the present work, electron time-of-flight spectra of the Ar *2p* satellites were measured at two angles (magic and 0°) in the dipole plane with the exciting photon energy tuned in the vicinity of the Ar *2s* threshold. For excitation far below or above the *2s* threshold, the *2p* satellites spectrum is dominated by *3p* to *np* shakeup contributions upon the ionization of a *2p* electron [5]. On the other hand, the same $[2p3p]n'p$ final states can also be reached *via spectator* L_1-$L_2M_{2,3}$ Coster-Kronig transitions following *2s* to *np* excitations. In addition, because the life time width of *2s* is larger than the energy separation between the *2s* to *np* resonant states individual

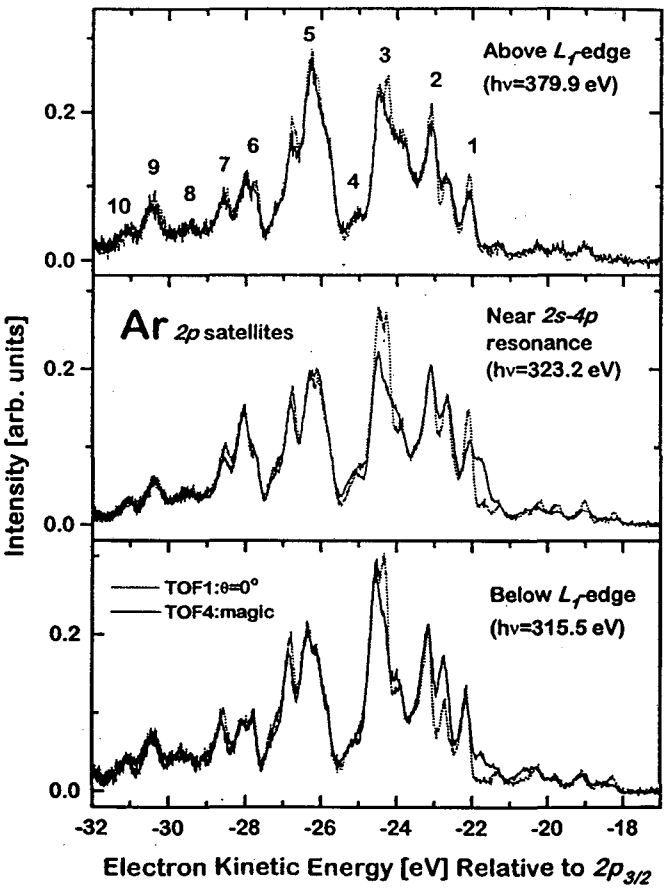

Figure 1. Photon-energy and angular dependence of the Ar *2p* satellites. The spectra were taken at both the magic and 0° in relative to the beam-polarization vector in the dipolar plane, tuning the photon energy across the Ar *2s* threshold. The spectra are normalized to the satellites total intensity.

resonances cannot be excited separately. Furthermore, because the final states $[2p3s]ns\varepsilon'l'$ are embedded in the $[2p3p]$ εl $\varepsilon'l'$ continuum and the latter is enhanced strongly above the *2s* threshold because of Coster-Kronig transitions, in addition to direct double photoionization, interference between these final states also may occur. Therefore, the Ar *2p* satellites excited in the vicinity of the Ar *2s* threshold are examples of a more general case in which interferences between direct and indirect channels, between different intermediate states, and between 'discrete' and continuous final states are intermingled.

REFERENCES

1. U. Fano and J. W. Cooper, Rev. Mod. Phys. **40**, 441(1968).

2. T. Aberg and B. Crasemann, in *Resonant Anomalous X-ray Scattering: Theory and Applications,* edited by G. Materlik, C. J. Sparks, and K. Fischer (North-Holland, Amsterdam, 1994) p.431.

3. M. Neeb, J-E. Rubensson, M. Biermann, A. Bringer, W. Eberhardt, in *Atomic and Molecular Photoionization*, edited by A. Yagishita and T. Sasaki (Universal Academy Press, Inc., Tokyo-Japan, 1996) p.109 and references therein.

4. G. B. Armen, J. C. Levin, and I. A. Sellin, Phys. Rev. **A 53**, 772 (1996).

5. S. Svensson, B. Eriksson, N. Martensson, G. Wendin, and U. Gelius, J. Electr. Spectrosc. Relat.Phenom. **47**, 327 (1988).

Support from NSF (PHY-9303915), Nevada DOE EPSCoR, Research Corporation, The Petroleum Research Fund, and the German DFG is gratefully acknowledged. The experiment was performed at the beamline 8.0 of the Advanced Light Source, which is supported by DOE (DE-AC03-76SF00098).

Corresponding author: HonghongWang, e-mail: wangh@nevada.edu; fax: +1 702 895 4072

The Band Width and Multiple-Angle Valence-State Mapping of Diamond

I. Jiménez,[a,1] L. J. Terminello[1], D. G. J. Sutherland[1], J. A. Carlisle[1], E. L. Shirley[2], F. J. Himpsel[3]
[1]*Lawrence Livermore National Laboratory, Livermore, CA 94551*
[2] *National Institute of Standards and Technology, Gaithersburg, MD 20899, USA.*
[3]*Department of Physics, University of Wisconsin-Madison, Madison, WI 53706 USA*

INTRODUCTION.

The band width may be considered the single most important parameter characterizing the electronic structure of a solid. The ratio of band width and Coulomb repulsion determines how correlated or delocalized an electron system is. Some of the most interesting solids straddle the boundary between localized and delocalized, e.g. the high-temperature superconductors. The bulk of the band calculations available today is based on local density functional (DF) theory.[1] Even though the Kohn-Sham eigenvalues[2] from that theory do not represent the outcome of a band-mapping experiment, they are remarkably similar to the bands mapped via photoemission. Strictly speaking, one should use an excited state calculation that takes the solid's many-body screening response to the hole created in photoemission into account.

Angle-resolved photoemission experiments have become accurate enough to see many-body effects on the band width by comparing the data with DF and Quasi-Particle (QP) calculations. For sodium, a prototype metal, the measured occupied band width was found smaller than DF calculations but close to QP results.[3] On the other hand, the band width in a prototype insulator, such as LiF, was found to be larger than in the DF result, but in agreement with the QP results.[4] One might also consider many-body effects on the band width of semiconductors. Because their band structures are intermediate between those of metals and insulators, it is not even clear whether such effects will be negative or positive. Diamond is a useful prototype semiconductor because of its low atomic number and large band width, which has made it a long-time favorite for testing band theory. Yet, the two experimental values of the band width of diamond have error bars of ±1 eV and differ by 3.2 eV.[5,6]

To obtain an accurate valence band width for diamond, we use a band-mapping method that collects momentum distributions instead of the usual energy distributions. This method has undergone extensive experimental and theoretical tests in determining the band width of lithium fluoride.[4] An efficient, imaging photoelectron spectrometer[7] is coupled with a state-of-the-art undulator beam line at the Advanced Light Source (ALS) to allow us collecting a large number of data sets. Since it takes only a few seconds to take a picture of the photoelectrons emitted into a 84° cone, we can use photon energies as high as 350 eV where the cross section for photoemission from the valence band is already quite low, but the emitted photoelectrons behave free-electron-like. This makes it much easier to locate the origin of the inter-band transitions in momentum space.

The result of our band mapping is a band width of 23.0 ±0.2 eV, which agrees well with QP results by Hybertsen and Louie (23.0 eV) and by Rohlfing et al. (22.88 eV). The band widening of 1.5 eV (7%) compared to the DF band width (21.67 eV by

[a] Present address: Instituto de Ciencia de Materiales de Madrid (CSIC). Cantoblanco, E-28049, Spain.

Hybertsen and Louie, 21.35 eV by Rohlfing et al.) is clearly visible. The origin of this band widening might be understood as an increasing localization of the electronic states towards the bottom of the band. The energy of such localized, correlated states comes out consistently too high in DF calculations.

II. EXPERIMENT

The imaging electron spectrometer used for this work is an improved version of a display analyzer described previously. It combines an ellipsoidal repelling mirror as low-pass with a spherical retarding grid as high-pass. Photoelectrons emitted within a 84° cone around the sample normal are imaged onto a channel plate with optical readout. A new feature is a segmentation of the ellipsoidal mirror into five elements with three slightly different bias voltages, which compensates for the change in angle of incidence along the elliptical direction of the electron mirror. This produces a three times higher resolving power or, alternatively, better homogeneity of the band pass across the field of view. The instrument is operated at beam line 8.0 a 5 cm undulator beam line at the ALS where the data acquisition time is reduced to about 30 seconds per picture, compared to about 30 minutes at a second generation light source. The intensity is normalized to the transmission of the analyzer measured using the emission of secondary electrons, taken at higher photon energy but with the same analyzer settings. Threefold symmetrization suppresses inhomogeneities and polarization effects. All features discussed here are clearly visible in the raw data. The normalized images are converted into momentum distributions numerically, using the analyzer geometry and reference data from the sharp Fermi surface of graphite for calibration.

A hydrogen-terminated diamond(111)-1×1 surface was prepared from a naturally boron-doped, type IIb diamond cleavage surface as described earlier (diamond Refs., Van der Veen, etc.). Slight heating in ultrahigh vacuum to 900 K sharpened the C1s core level spectrum without destroying the hydrogen termination of the broken bonds. The clean 2×1 surface obtained after further heating to 1300 K showed a well resolved surface component of the C(1s) signal and introduced surface states into the valence band spectra. They interfere with the identification of bulk features and blur angular distributions by introducing extra momentum transfer via the 2×1 surface lattice. Therefore, only the hydrogen-terminated 1×1 surface was used for determining the bulk band width.

Our data are pictures of the momentum distribution of photoelectrons emitted with a given kinetic energy. Such pictures were taken for many combinations of electron and photon energies (about 100). As explained in more detail below, the final state kinetic energy of the photoelectrons was selected first. Thereby, the momentum normal to the surface, $k^{\perp}$, was set to a value equivalent to the Γ-point in the bulk Brillouin zone, where the valence band maximum and minimum are (Fig. 1). Then, a series of constant-final-state pictures was obtained at several photon energies, to probe different initial-state energies across the valence band (Fig. 2). As one approaches the valence band maximum or the minimum from within the band, the momentum distribution of the photoelectrons shrinks to a point, which allows one to determine energies of band edges.

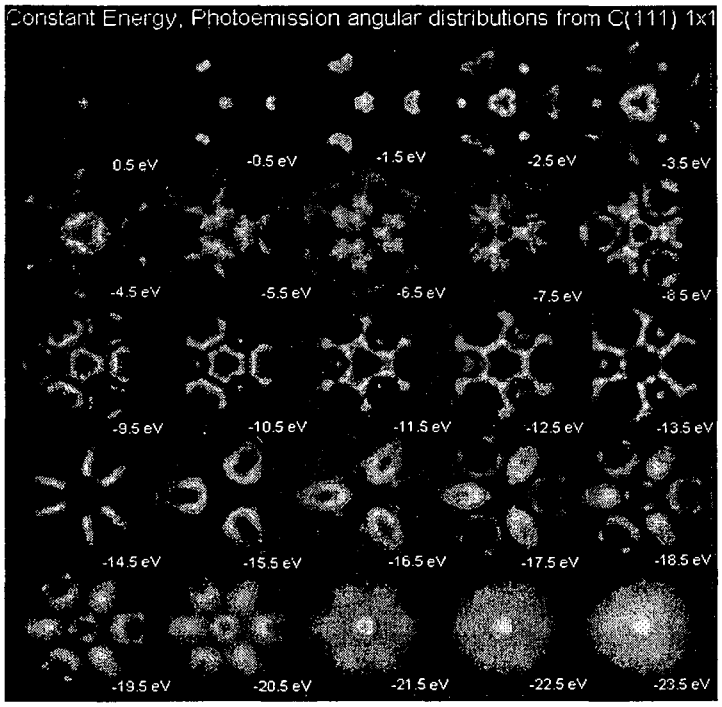

Fig. 1 Pictures of the momentum distribution of photoelectrons for several of initial-state energies across the entire valence band of diamond and a constant final-state at the (222) Γ-point. The emission pattern shrinks to a point at the center when the two band edges are approached. The energy values refer to the valence band maximum.

Fig. 2 Experimental quasiparticle band structure (including lifetime broadening) obtained from a series of momentum distributions across the valence band of diamond. These have been redrawn as traditional band energy dispersion curves.

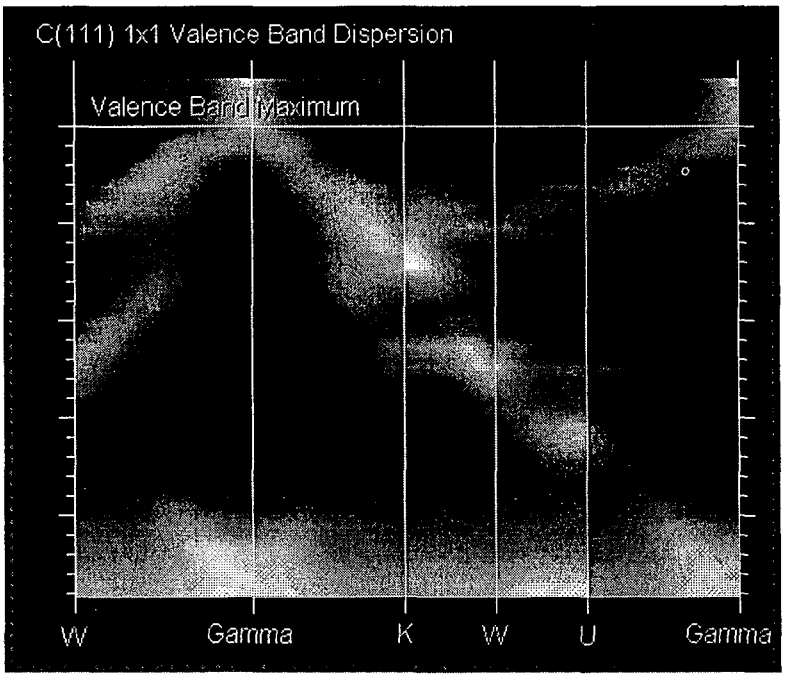

Direct comparison with experiment is done by inverting the pictures to assemble a more traditional rendering of energy-vs-crystal-momentum band dispersion curves. That is, having a rather complete set of momentum distributions at various energies we are able to display the experimental equivalent to the calculated $E(\mathbf{k}^{\parallel})$ energy bands -i.e. the intensity distributions in the E, $\mathbf{k}^{\parallel}$ - plane (Fig. 8). Unlike the sharp, calculated $E(\mathbf{k}^{\parallel})$

relations, the actual data also show effects of lifetime broadening, which is a many-body effect, not yet as fully modeled as the increased band width. The broadening represents the imaginary part of the electron self-energy.

ACKNOWLEDGMENTS.

We would like to thank J. Yurkas, R. Hill, and A. Ellis for their help with the construction of the electron spectrometer. This work has been supported by the Division of Materials Sciences, Office of Basic Energy Science, and performed under the auspices of the U.S. Department of Energy by Lawrence Livermore National Laboratory under contract No. W-7405-ENG-48, and at the Advanced Light Source, LBNL under Contract No. DE-AC03-76SF00098. One of the authors (I.J.) acknowledges financial support from the Spanish Ministerio de Educación y Ciencia.

References:

[1] P. Hohenberg and W. Kohn, Phys. Rev. 136, B864 (1964).
[2] W. Kohn and L. J. Sham, Phys. Rev. 140, A1133 (1965).
[3] E. Jensen and E. W. Plummer, Phys. Rev. Lett. 55, 1912 (1985).
[4] F.J. Himpsel, L.J. Terminello, D.A. Lapiano-Smith, E.A. Eklund, and J.J. Barton, Phys. Rev. Lett. **68**, 3611 (1992), and E. L. Shirley, L. J. Terminello, J. E. Klepeis, and F. J. Himpsel, Phys. Rev. B 53, 10296 (1996).
[5] F.J. Himpsel, J.F. van der Veen, and D.E. Eastman, Phys. Rev. B **22**, 1967 (1980).
[6] F.R. McFeely, S.P. Kowalczyk, L. Ley, R.G. Cavell, R.A. Pollak, and D.A. Shirley, Phys. Rev. B **9**, 5268 (1974).
[7] D.E. Eastman, J.J. Donelon, N.C. Hien, and F.J. Himpsel, Nuclear Instrum. and Methods **172**, 327 (1980).

Principal Investigators: Franz J. Himpsel, University of Wisconsin, Madison (Email himpsel@comb.physics.wisc.edu, Telephone 608-263-5990); Louis J. Terminello, Lawrence Livermore National Laboratory (Email terminello@llnl.gov, Telephone 510-423-7956).

Coherent and Incoherent Processes in Resonant Photoemission

M. Magnuson, O. Karis, M. Weinelt, N. Wassdahl, A. Nilsson and N. Mårtensson

Department of Physics, Uppsala University, P. O. Box 530, S-751 21 Uppsala, Sweden

J. Stöhr and M. Samant

IBM Research Division, Almaden Research Center, 650 Harry Road, San Jose, CA 95120, USA

In this contribution we present the distinction between coherent and incoherent processes in resonant photoemission. As a first step we determine whether an autoionization process is photoemission-like or Auger-like. The discussion is based on measurements for a weakly bonded adsorption system, Ar/Pt(111) [1]. This type of system is well adapted to investigate these effects since it yields distinctly shifted spectral features depending on the nature of the process. After this, the question of resonant photoemission in metallic systems is addressed. This is done in connection with measurements at the $2p$ edges for Ni metal. Ni has been one of the prototype systems for resonant photoemission. The resonances have been discussed in connection with the strong correlation and d-band localization effects in this system [2]. Based on the results some general comments about the appearance of resonant effects in metallic systems are made.

The experiments were performed using beamline 8.0 at the *Advanced Light Source*. This undulator beam-line is equipped with a modified 'Dragon' monochromator with a resolving power of up to 10^4. The end-station was built at Uppsala University and comprises two rotatable spectrometers, a Scienta SES200 electron spectrometer [3] and a high-resolution grazing incidence grating spectrometer for x-ray fluorescence studies [4] . In the Ar measurements the resolution was set to 100 meV for the monochromator and to 200 meV for the spectrometer. In the Ni measurements the resolution was 100 eV for both the monochromator and the spectrometer. The spectra for Ar/Pt(111) were measured at low temperatures using a liquid He flow cryostat.

Fig. 1 shows electron emission (autoionization) spectra of Ar for a number of photon energies around the $2p_{3/2}\rightarrow 4s$ x-ray absorption spectroscopy (XAS) resonance. The overall spectral shape changes with photon energy. Two sets

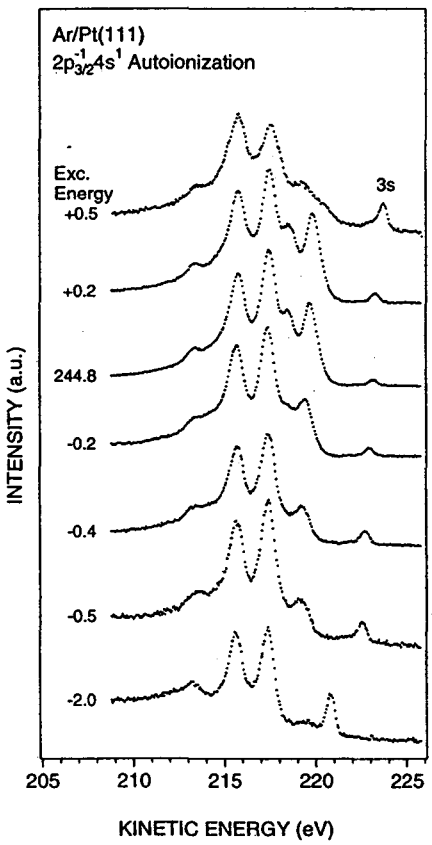

Fig. 1: Ar/Pt(100) autoionization spectra for several photon energies around the $2p_{3/2}\rightarrow 4s$ resonance.

of spectral features can be identified, one which stays at constant kinetic energy and one which moves with the photon energy. The shapes of the two parts of the spectra seem to be independent of the excitation energy. The relative weights of the two parts, however, vary.

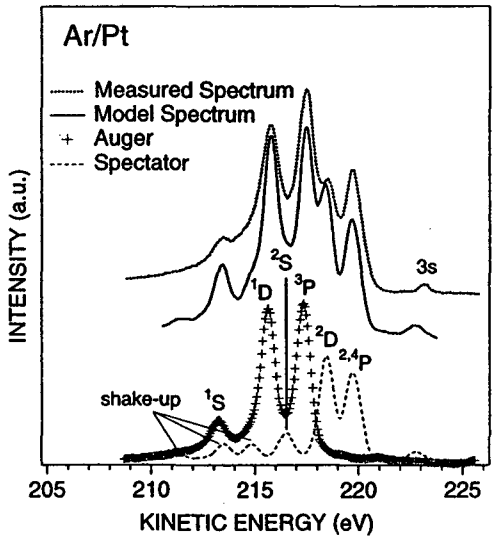

Fig. 2: A fit of the autoionization spectrum for an excitation energy at the resonance maximum.

Fig. 2 shows an analysis of the spectrum recorded at the resonance maximum (244.8 eV). The spectrum can be accurately reproduced by a summation of two model spectra. The curve denoted by (+) corresponds to a $2p_{3/2}$ Auger spectrum recorded for the Ar/Pt sample using a photon energy well above the XAS resonance. The different peaks in the spectrum are due to the multiplet levels of the $3p^4$ final state configuration as denoted in the figure. The dashed curve is a gas phase autoionization spectrum following the excitation of the $2p_{3/2}^{-1}4s^1$ state. The identification of the peaks is given in the figure. The spectrum has been convoluted with a Gaussian of width 0.3 eV and shifted to achieve the best possible fit. By summing these spectra with appropriate weight factors we obtain a model spectrum given by the solid line. As can be seen this curve mimics all essential features of the experimental Ar/Pt autoionization spectrum. The remaining small differences appear mainly in the shake-up part of the autoionization spectrum. This is due to the interaction of the Ar orbitals with the substrate which modifies especially the extended orbitals involved in the shake-up processes. There may also be slight differences in the remaining parts of the spectra caused by small modifications of the splittings and relative intensities of the multiplet components. Similar decompositions have been performed for the decay spectra over the entire $4s$ resonance profile, reaching the same type of agreement. Each spectrum may thus be thought of as consisting of two parts, one with an Auger-like $3p^{-2}$ final state and one with a $3p^{-2}4s^1$ spectator-like final state.

Fig. 3 shows in detail Ni spectra recorded for photon energies around the $2p_{3/2}$ core-level threshold in the photoemission geometry. In this case the spectra are plotted on a binding energy scale. Below threshold, the whole spectrum stays at constant binding energy and the intensities of the different parts of the spectra changes. Immediately above threshold, we observe how the 6 eV feature starts to move to higher binding energies as the photon energy increases. This immediately shows that final states are produced which are not identical to the photoemission final states. This is completely analogous to the situation with the appearance of Auger-like features in Ar/Pt(111) as discussed above. We can also discuss this as an apparent loss of coherence in the process [1]. There are excitations in the system which we do not detect. Also in the valence band region we observe how a weak shoulder develops from the Fermi-level cut-off and starts to disperse with photon energy. This demonstrates the appearance of Auger-type features in the band-like part of the spectrum.

In order to probe the character of the resonant process we follow the photon energy dependence of the intensity for a region in the valence band spectrum close to the Fermi level and for an energy window around the 6 eV satellite. In Fig. 4 this has been done both for the 'Auger' and for the 'photoemission' geometries, i.e. with the E-vector in two different orientations.

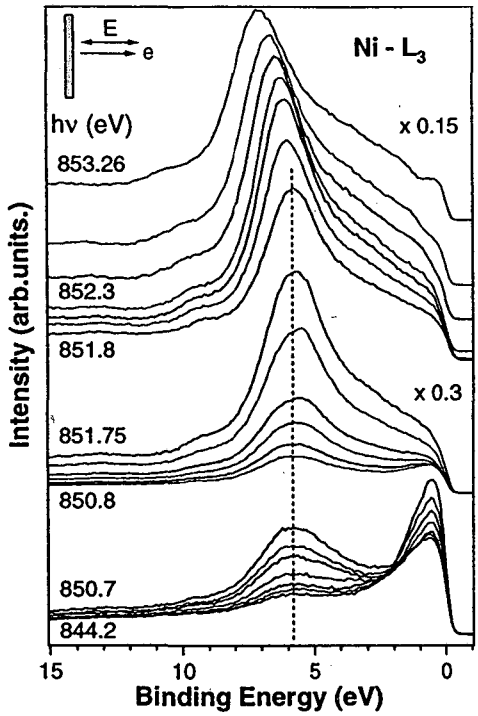

Fig. 3: Valence electron spectra around the $2p_{3/2}$ core-level threshold on a binding energy scale measured in the 'photoemission geometry'. The photon energy increment is about 0.2 eV except for the lower set of data (844.2, 848.0, 849.0, 849.8, 850.3, 850.5, 850.7).

The two top curves show the valence band intensity in the 'photoemission' (top) and 'Auger' (middle) geometries. It is immediately seen that the intensities show characteristic Fano-like profiles [5, 6]. The results for the 6 eV satellite is shown at the bottom. The curves for the 'Auger'- and 'photoemission' geometries are plotted together. Looking at the individual curves there is no clear indication of a resonance line-shape. However, when comparing the measurements for the two geometries (see inset) differences in the profiles are observed which are characteristic of Fano profiles with different q. This shows that there are interference effects also in these spectra. The interference term is small but this is due to the fact that the autoionization channel is dominating so strongly. We have therefore demonstrated that the absence of visible interference effects is not a good criterion for the absence of interference. This may instead be due to the total dominance of one of the spectroscopic channels.

It is found that q is smallest for the valence band, in particular in the 'photoemission' geometry ($q \sim 1.5$ at the $2p_{3/2}$ resonance). This channel is the majority channel in photoemission and the minority one in autoionization. For the satellite, the opposite situation is true and consequently much larger q-values are found ($q \gtrsim 20$ and $q \sim 9$ in the 'Auger' and 'photoemission' geometries, respectively). Going to the $2p_{1/2}$ edge, we find in all cases more pronounced Fano-like profiles corresponding to smaller q-values (e.g. $q \sim 0.5$ for the valence band in the 'photoemission' geometry) as expected due to the weaker absorption and larger lifetime width of the $2p_{1/2}$ level. The trends are fully consistent with the expectations from the Fano model and we therefore conclude that the shapes of the resonance profiles are due to interference.

To summarize, we have investigated the basis for resonant photoemission for two prototype systems, one weakly bonded adsorption system and one transition metal. We find that for Ar/Pt(111) there are two types of features in the spectator autoionization spectra. One of these shows resonant Raman behavior and has to be treated in a one-step picture. The other one shows a normal Auger-like behavior and can be described in a two-step picture. This branching is due to the quasi-localized character of the intermediate state. The intermediate state is localized enough to yield a constant binding energy feature for excitation energies over the entire resonance, although of varying relative strength. The Auger-like feature dominates at most energies and corresponds to final states in which the spectator electron is located in the substrate. The spectator electron may have a distribution of energies and the scattering process can be viewed as the creation of two particles which share energy. Since we observe only one of these we recognize this as a loss of coherence and as an apparent loss of conservation of energy.

We have also performed measurements of the resonant photoemission for a Ni(100) sample with special emphasis on the possible interference between the autoionization and the direct photoemission channels. We observe clear signatures of interference both for the main valence

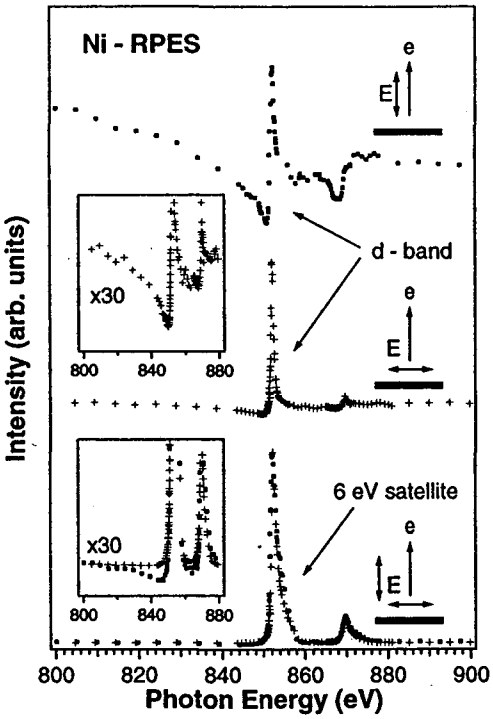

Fig. 4: Intensity of the valence-band emission (top two curves) and the 6 eV satellite (bottom set of curves, plotted together) as function of photon energy in the 'photoemission' and 'Auger' geometries.

band emission and for the 6 eV satellite. The spectra show resonantly enhanced photoemission-like spectral features only in the region before threshold. For photon energies above threshold the emission features rapidly transform into features which appear at constant kinetic energy. In terms of the possible interference with the direct photoemission process this corresponds to a loss of coherence. This implies furthermore that a large fraction of the totally observed resonantly enhanced intensity is incoherent. The results indicate that the resonance behavior is not explained by any strongly localized intermediate state in the resonant scattering process. This also implies that resonance phenomena and especially the interference effects may occur also in systems with very delocalized excited states.

This work was supported by the Swedish Natural Science Research Council (NFR), the Göran Gustavsson Foundation for Research in Natural Sciences and Medicine and the Swedish Institute (SI). ALS is supported by the U.S. Department of Energy, under contract No. DE-AC03-76SF00098.

References

[1] O. Karis, A. Nilsson, M. Weinelt, T. Wiell, C. Puglia, N. Wassdahl, N. Mårtensson, M. Samant, and J. Stöhr, Phys. Rev. Lett. **76**, 1380 (1996).

[2] M. Weinelt, A. Nilsson, M. Magnuson, T. Wiell, N. Wassdahl, O. Karis, A. Föhlisch N. Mårtensson, M. Samant, and J. Stöhr, Phys. Rev. Lett. **78**, 967 (1997).

[3] N. Mårtensson, P. Baltzer, P. A. Brühwiler, J. O. Forsell, A. Nilsson, A. Stenborg, and B. Wannberg, J. Electr. Spectr. **70**, 117 (1994).

[4] J. Nordgren and R. Nyholm, Nucl. Instr. Methods **A246**, 242 (1986); J. Nordgren, G. Bray, S. Cramm, R. Nyholm, J.-E. Rubensson, and N. Wassdahl, Rev. Sci. Instrum. **60**, 1690 (1989).

[5] U. Fano, Phys. Rev. Lett **124**, 1866 (1961); U. Fano, and J. W. Cooper, Rev. Mod. Phys. **40**, 630 (1968).

[6] C.-O. Almbladh and L. Hedin, *Handbook on Synchrotron Radiation*, Vol. 1, edited by E. E. Koch, (North-Holland, Amsterdam, 1983), and references therein.

Principal investigator: Martin Magnuson, Department of Physics, Uppsala University, Box 530, S-75 21 Uppsala, Sweden. Telephone: +46 18 183552. Fax: +46 18 183524.

Core-Level Photoabsorption Study of Defects and Metastable Bonding Configurations in Boron Nitride

I. Jiménez,[a,1] A. F. Jankowski[1], L. J. Terminello[1], D. G. J. Sutherland[1], J. A. Carlisle[1], G. L. Doll[2], W. M. Tong[3],D. K. Shuh[3],F. J. Himpsel[4]

[1]*Lawrence Livermore National Laboratory, Livermore, CA 94551*

[2]*Materials Research Department, Timken Research, Canton OH 44706*

[3]*Lawrence Berkeley Laboratory, Berkeley, CA 94720*

[4]*Department of Physics, University of Wisconsin-Madison, Madison, WI 53706 USA*

INTRODUCTION.

Boron nitride is an interesting material for technological applications and for fundamental solid state physics investigations. It is a compound isoelectronic with carbon and, like carbon can possess sp^2 and sp^3 bonded phases resembling graphite and diamond. BN crystallizes in the sp^2-bonded hexagonal (h-BN), rhombohedral (r-BN) and turbostratic phases, and in the sp^3-bonded cubic (c-BN) and wurtzite (w-BN) phases[1]. A new family of materials is obtained when replacing C-C pairs in graphite with isoelectronic B-N pairs, resulting in C_2BN compounds.[2, 3] Regarding other boron compounds, BN is exceptional in the sense that it has standard two-center bonds with conventional coordination numbers, while other boron compounds (e. g. B_4C) are based on the boron icosahedron unit with three-center bonds and high coordination numbers.[4, 5]

The existence of several allotropic forms and fullerene-like structures for BN suggests a rich variety of local bonding and poses the questions of how this affects the local electronic structure and how the material accommodates the stress induced in the transition regions between different phases. One would expect point defects to play a crucial role in stress accommodation, but these must also have a strong influence in the electronic structure, since the B-N bond is polar and a point defect will thus be a charged structure. The study of point defects in relationship to the electronic structure is of fundamental interest in these materials. Recently, we have shown that Near-Edge X-ray Absorption Fine Structure (NEXAFS) is sensitive to point defects in h-BN, and to the formation of metastable phases even in amorphous materials.[6] This is significant since other phase identification techniques like vibrational spectroscopies or x-ray diffraction yield ambiguous results for nanocrystalline[7] and amorphous samples.[8] Serendipitously, NEXAFS also combines chemical selectivity with point defect sensitivity.

In this work we take advantage of the local sensitivity of the core level photoabsorption technique to identify the presence of both nitrogen vacancies and interstitials in connection to c-BN growth, and to address some questions concerning the bonding structure of boron nitride in intermediate situations between ordered hexagonal and cubic phases. These metastable and defective phases are attained by ion sputtering, ion bombardment and annealing treatments of hexagonal BN thin films. We will demonstrate the capabilities of NEXAFS to characterize point defects following a simple quantitative

---

[a] Present address: Instituto de Ciencia de Materiales de Madrid (CSIC). Cantoblanco, E-28049, Spain.

analysis, and illustrate the possibility to obtain orientational information by angle resolved NEXAFS.

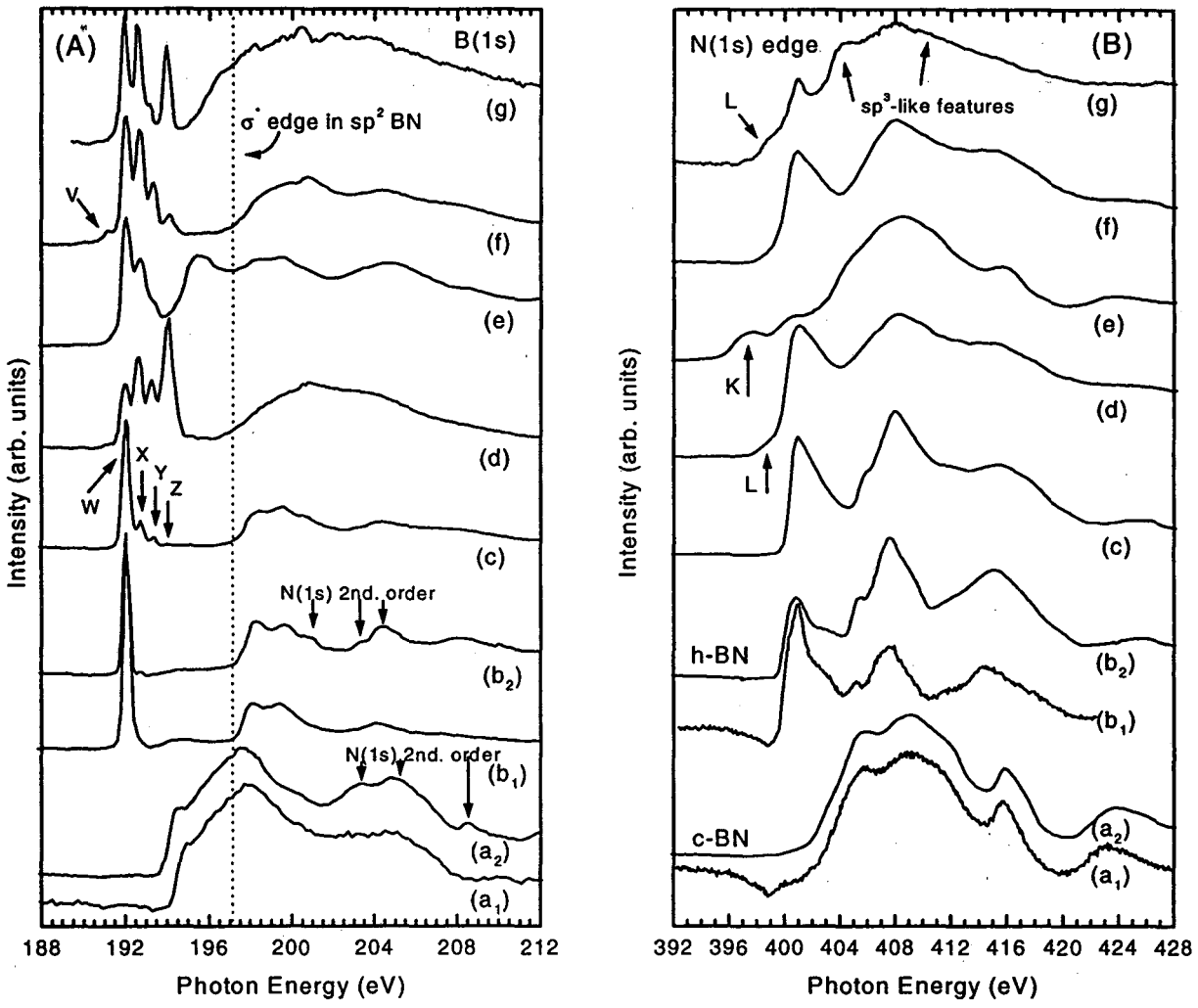

Figure 1. B(1s) and N(1s) photoabsorption spectra corresponding to a variety of local environments in the boron nitride system. The same letter in each panel corresponds to the same sample. Curves (a_1) and (a_2) represents a crystalline c-BN reference measured with filtered light to avoid higher orders of diffraction from the monochromator and with unfiltered light respectively. Curves (b_1) and (b_2) represent a crystalline h-BN reference measured with filtered and unfiltered light respectively. Note the N features in the B region in second order for the unfiltered measurements, conditions under which the rest of the samples were measured. Curves (c) represent a h-BN thin film grown by pulsed laser deposition exhibiting W-Z peaks in the π^* region, (d) a Ne^+ implanted h-BN thin film, (e) a film RF-sputter deposited film in an Ar/N_2 mixture from a boron target with an RF bias applied to the substrate to form sp^3 BN, (f) a N_2^+ implanted thin film, and (g) a N_2^+ implanted thin film containing a new metastable phase.

RESULTS AND DISCUSSION.

Figure 1 shows a series of B(1s) and N(1s) absorption spectra corresponding to a variety of local environments found in the boron nitride system. Curves (a_1, a_2) and (b_1, b_2) are reference spectra from crystalline powders of c-BN and h-BN respectively, the most stable phases with sp^2 and sp^3 bonding. Throughout this work, the c-BN and h-BN standards will be used to compare against the unknown films to determine their bonding. We have calibrated the energy position of the boron and the nitrogen π^* features in h-BN (curves b_1 and b_2) obtaining values of 192.0 ± 0.1 eV and 400.9 ± 0.1 eV respectively.

The boron absorption edge in the *c*-BN spectrum (curves a_1, a_2) appears at 194 eV and corresponds to transitions from the B(1s) core level to the σ^* states in the conduction band. The NEXAFS spectrum shows a sharp peak -with its maximum at 194.5 eV- near the absorption edge, followed by a broad absorption maximum at 198 eV.

Curves (c-g) are representative of BN thin films (~100 nm thick) grown on a Si(100) substrate by pulsed laser deposition. The additional features in the π^* region labeled X-Z correspond to N-void defects in the hexagonal bonding, as we have shown previously.[6] In the thin films, one finds four different local environments of boron atoms, since these may be bonded to three nitrogen atoms, two nitrogens, one nitrogen and no nitrogen, and they show up in the NEXAFS spectra as features W-Z respectively.

ACKNOWLEDGEMENTS.

We are indebted to R. Hill for his technical support, and the SSRL and ALS staffs for their help. We would like to thank Dr. J. V. Mantese and his group at GM Research Labs for implanting the BN films,and D. Chance for his technical support. This work has been supported by the Division of Materials Sciences, Office of Basic Energy Science, and performed under the auspices of the U.S. Department of Energy by Lawrence Livermore National Laboratory under contract No. W-7405-ENG-48, and the Advanced Light Source, LBNL under Contract No. DE-AC03-76SF00098. One of the authors (I. J.) acknowledges financial support from the Spanish Ministerio de Educación y Ciencia.

REFERENCES

[1]L.J. Terminello, A. Chaiken, D.A. Lapiano-Smith, G.L. Doll, and T. Sato, J. Vac. Sci. Technol. A 12:2462 (1994).
[2]K. Kobayashi and N. Kurita, Phys. Rev. Lett. 70:3542 (1993).
[3]M.O. Watanabe, S. Itoh, K. Mizushima, and T. Sasaki, Appl. Phys. Lett. 68:2962 (1996).
[4]K. Wade, *Electron Deficient Compounds*, (Nelson, London, 1971).
[5]D. Emin, Phys. Today 40:55 (1987).
[6]I. Jiménez, A. Jankowski, L.J. Terminello, J.A. Carlisle, D.G.J. Sutherland, G.L. Doll, J.V. Mantese, W.M. Tong, D.K. Shuh, and F.J. Himpsel, Appl. Phys. Lett. 68:2816 (1966).
[7]R.J. Nemanich, S.A. Solin, and R.M. Matin, Phys. Rev. B, 23:6348 (1981).
[8]D.M. Gruen, A.R. Krauss, C.D. Zuiker, R. Csencsits, L.J. Terminello, J.A. Carlisle, I. Jiménez, D.G.J. Sutherland, D.K. Shuh, W.M. Tong, and F.J. Himpsel, Appl. Phys. Lett. 68:1640 (1996).

Principal investigator: Louis J. Terminello, Lawrence Livermore National Laboratory. Email: terminello@llnl.gov. Telephone: 510-423-7956.

Electronic Raman Scattering with Excitation Between Localized States Observed in the Zinc $M_{2,3}$ Soft X-Ray Spectra of ZnS

L. Zhou,[1] T.A. Callcott,[1] J.J. Jia,[1] D.L. Ederer,[2] and R.C.C. Perera[3]

[1]Department of Physics, University of Tennessee, Knoxville, Tennessee 37996, USA

[2]Department of Physics, Tulane University, New Orleans, Louisiana 70118, USA

[3]Advanced Light Source, Ernest Orlando Lawrence Berkeley National Laboratory, University of California, Berkeley, California 94720, USA

INTRODUCTION

Zn $M_{2,3}$ soft x-ray fluorescence (SXF) spectra of ZnS and $ZnS_{.5}Se_{.5}$ excited near threshold show strong inelastic scattering effects that can be explained using a simple model and an inelastic scattering theory based on second order perturbation theory. This scattering is often called electronic resonance Raman scattering. Tulkki and Aberg have developed this theory in detail for atomic systems, but their treatment can be applied to solid systems by utilizing electronic states characteristic of solids rather than of atomic systems.[1,2]

EXPERIMENTAL RESULTS

These experiments were performed on undulator beamline 8.0 of the Advanced Light Source using the soft x-ray emission spectrometer operated the the Tennessee/Tulane/ LBNL/LLNL collaboration.[3] The Zn $M_{2,3}$ spectrum displayed here is from a $ZnS_{.5}Se_{.5}$ sample, but essentially identical results are seen in ZnS. A detailed description of these results has been presented elsewhere.[4,5]

The Zn $M_{2,3}$ SXF spectra excited near threshold are shown in Figure 1. The spectrum at the bottom of the figure is a normal fluorescence spectrum excited with 148 eV photons, which is far above the excitation threshold of the Zn $M_{2,3}$ spectrum. The narrow peak located at 74 eV is a second order image of elastically scattered incident photons. The 2.8 eV separation between the broad peaks is the splitting of the Zn $3p_{1/2}$ and $3p_{3/2}$ core levels and the width of the peaks may be attributed to the large lifetime broadening of these levels.

The remaining spectra are excited with near threshold energies between 89 and 98 eV. The sharp peaks at higher energies are produced by elastically scattered incident photons and the peaks at lower energies by inelastically scattered photons. As the photon energy is increased within this range, a strong inelastic peak less than 2 eV wide moves through the energy region of the normal fluorescence spectrum. Several of its features are noteworthy. First, within experimental resolutions and accuracy, it exactly tracks the elastic peak at about 12.4 eV lower energy. Second, its overall width of less than 2 eV is much less than that of the normal fluorescence spectrum. Third, its relative intensity as it moves through the normal fluorescence spectrum is proportional to the intensity of the

normal fluorescence spectrum, reaching maxima at energies of about 78 and 81 eV, the peak positions of the normal spectrum.

Each of these features are consistent with an electronic resonance Raman process in which the incident photon is scattered through a real intermediate state. The 12.4 eV energy loss is associated with an electronic excitation between localized levels, as illustrated schematically in Figure 2. It occurs from Zn d-bands located between the upper (UVB) and lower (LVB) valence bands of this compound and a narrow exciton state located near the conduction-band edge. The theory requires that the energy loss is equal to the energy difference between the electron and hole states *in the final state* of the scattering process, so that the narrow exciton state is not a core exciton, but a valence exciton in which a hole in the d band binds an electron in a localized orbital. Because the energy difference is associated with the final state of the scattering process, the width of the observed spectra is not limited by the core-hole lifetime, which broadens the normal fluorescence spectrum. The width of the peak is given by a convolution of the energy profile of the exciting light with the widths of the Zn 3d and exciton levels. Finally, the energy uncertainly associated with the limited core-hole lifetime allows the resonant inelastic scattering to occur over an energy range of the normal fluorescence spectrum. These features are more carefully related to the precise mathematical form of the inelastic scattering theory in another publication.[5] The location of Zn d-bands in this compound using SXF measurements is described elsewhere[4], and in another abstract of this volume.[6]

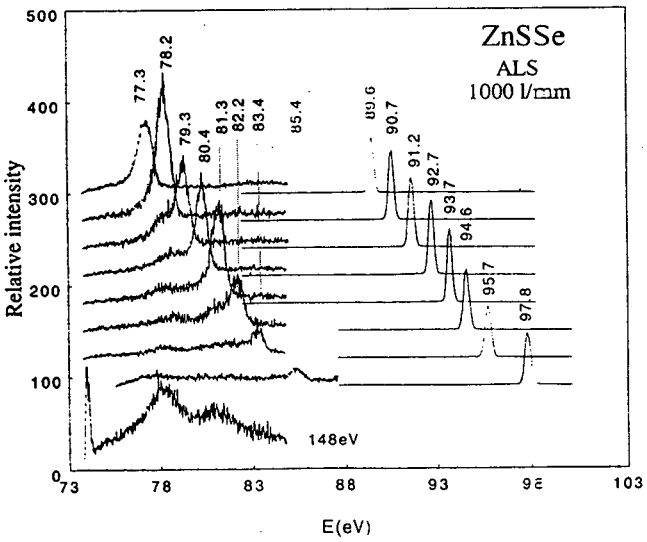

Figure 1. The Zn $M_{2,3}$ spectrum of $ZnS_{.5}Se_{.5}$ excited near threshold

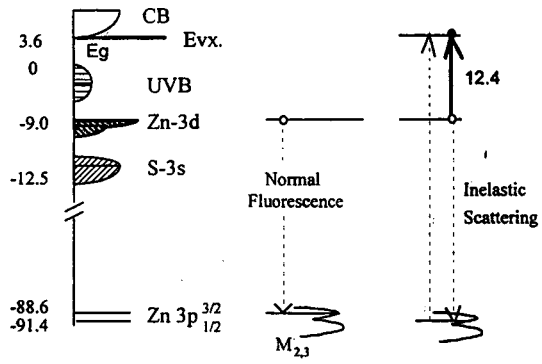

Figure 2. Schematic diagram of normal fluorescence and electronic resonance Raman processes contributing to photon-excited Zn $M_{2,3}$ spectra

REFERENCES

1. J. Tulkki and T. Aberg, J. Phys. B 15, L435 (1982).
2. J. Tulkki, Phys. Rev. A 27,3375 (1983).
3. For properties of beamline and endstation, see ALS First Phase Scientific Program, LBNL publication LBL PUB-706, pp. 11-16, 1992.
4. L. Zhou et al., Phys. Rev. B 55(8), (1997).
5. T.A. Callcott et al., in Proc. of workshop on *Raman Emission by X-ray Scattering*, edited by D.L. Ederer and J.H. McQuire (World Scient. Publ., Singapore, 1996) p. 133.
6. L. Zhou et al., "Sulfur $L_{2,3}$ SXF spectra of CdS and ZnS," (Abstract in this volume).

This work was supported by National Science Foundation grant DMR-9420425 and by the authors institutions, and was carried out at the Advanced Light Source at Lawrence Berkeley National Laboratory operated under Contract No. DE-AC03-76SF00098 with the U.S. Department of Energy.

Principal investigator: T.A. Callcott, Department of Physics, University of Tennessee. Email: tcallcott @utk.edu. Telephone: 423-974-6765.

The Electronic Structure of Benzene Adsorbed on Ni and Cu Surfaces

M. Weinelt[1], A. Nilsson[1], N. Wassdahl[1], O. Karis,[1] T. Wiell,[1]
J. Hasselström[1], J. Stöhr[2]and M. Samant[2]
[1]Department of Physics, Uppsala University, Box 530, S-751 21 Uppsala, Sweden
[2]IBM Research Division, Almaden Research Center 650 Harry Road, San Jose, California 95120, USA

Benzene has for a long time served as a prototype adsorption system of large molecules. It adsorbs with the molecular plane parallel to the surface. The bonding of benzene to a transition metal is typically viewed to involve the π system. Benzene adsorbs weakly on Cu and strongly on Ni. It is interesting to study how the adsorption strength is reflected in the electronic structure of the adsorbate-substrate complex. We have used X-ray Emission (XE) and X-ray Absorption (XA) spectroscopies to selectively study the electronic states localized on the adsorbed benzene molecule. Using XES the occupied states can be studies and with XAS the unoccupied states.

We have used beamline 8.0 and the Swedish endstation equipped with a grazing incidence x-ray spectrometer and a partial yield absorption detector. The resolution in the XES and XAS were 0.5 eV and 0.05 eV, respectively.

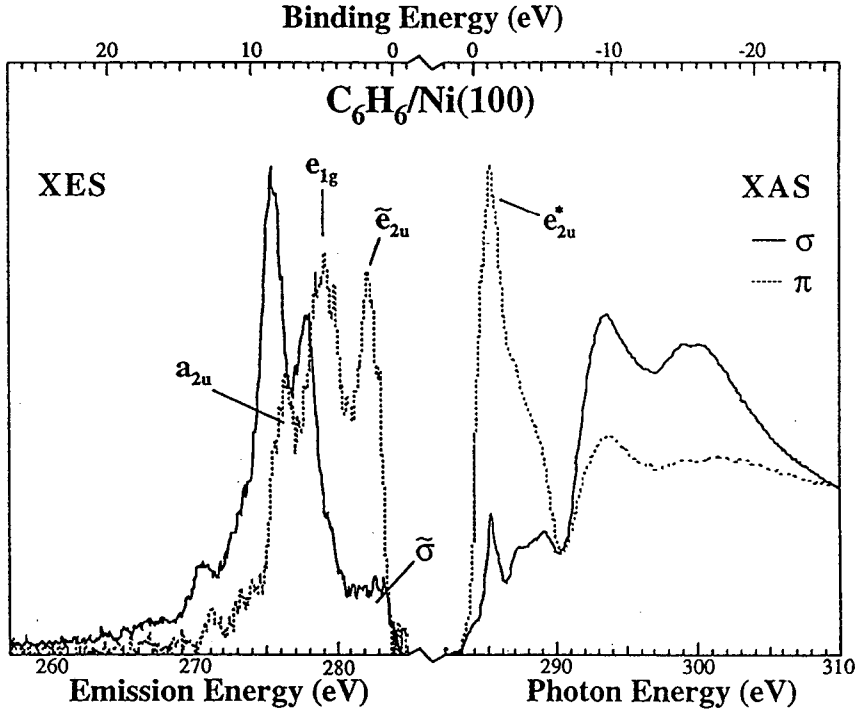

Fig.1 Symmetry resolved x-ray emission and x-ray absorption spectra for benzene on Ni(100). The σ symmetry XES spectrum is the normal emission x-ray emission spectrum, theπ symmetry spectrum was obtained by a suitable linear combination of the grazing and normal emission spectra. The π symmetry peaks in the spectra are labelled by the corresponding molecular orbitals, empty states being designated by an asterisk. New orbitals arising from the surface chemical bond are indicated by a tilde symbol.

XE and XA spectra for benzene on Cu(110) and Ni(100) are shown in Fig. 1 and 2. XE spectra were taken at an excitation energy corresponding to the C1s to $\pi^*(e_{2u})$ transition. The spectra areplotted on a photon energy as well as valence hole binding energy scale (C1s binding energies of 284.1 eV and 284.9 eV for benzene adsorbed on Ni and Cu, respectively). The assignment of

the XE features with binding energies larger than 4 eV is known from the literature and it is given in the figures for the π-system. The pronounced polarization dependence of the XA spectrum shows that benzene is adsorbed with the molecular plane parallel to the surface [1]. Based on this adsorption geometry, the XE spectra shown in Fig. 1 and 2 corresponding to pure σ and π symmetries, were obtained in the same way as described earlier for CO and N_2.

If we start with states of π symmetry (dashed lines) we find three distinct peaks. The $1a_{2u}$ and $1e_{1g}$ π-like orbitals are essentially intact from the gas phase, while the third state, labelled e_{2u}, is not seen for the free molecule. The inversion symmetry of the molecule seems to be partly conserved upon adsorption [2]. It was shown that peaks corresponding to gerade or ungerade symmetry states changed their relative intensity depending on the symmetry of the excited intermediate state. The spectra in Fig. 1 and 2 correspond to a (u) excited state and therefore peaks of (u) symmetry in the XE spectra are slightly enhanced compared with spectra excited just above the onset of the ionization continuum. The results shows that the third state have (u) symmetry for adsorption on both Cu and Ni. We conclude that this is a LUMO (e_{2u})-substrate hybrid.

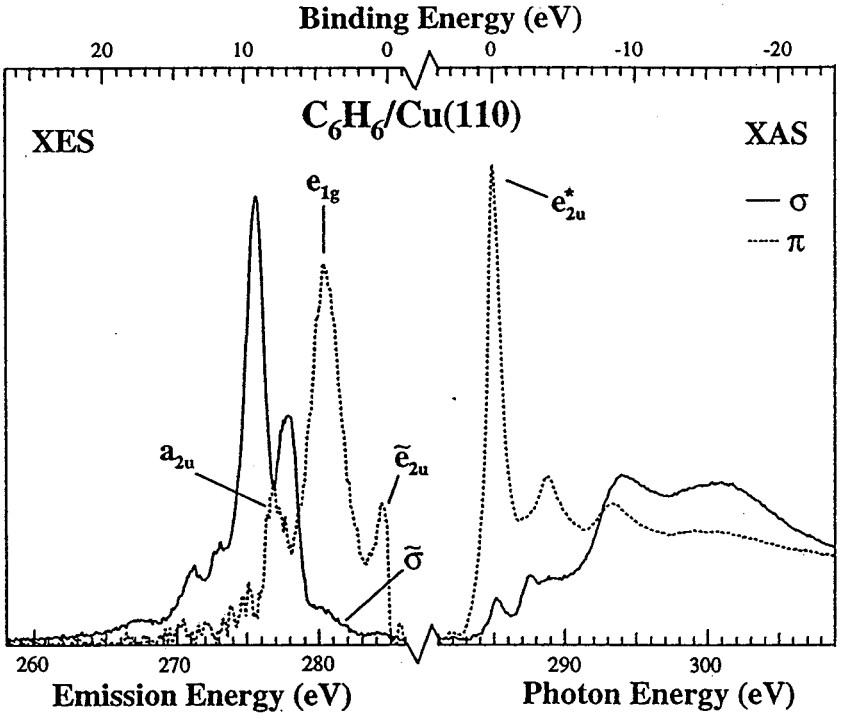

Fig.2 Symmetry resolved x-ray emission and x-ray absorption spectra for benzene on Cu(110). See Fig.1.

The new occupied e_{2u} state appears differently in the spectra from benzene on Cu and Ni. In the case of adsorption on Ni (Fig. 1), the new π state is located 1.7 eV below the Fermi level and hence overlapping the Ni d band region. The fraction of adsorbate character of this state has to be of similar magnitude as that of the higher binding energy π orbitals since the observed emission intensity is of comparable strength. The origin of the e_{2u} state is easily understood in a simple frontier orbital picture. The interaction of the e_{2u} orbital with Ni d states results in an occupied bonding orbital observed in XE, and an empty anti-bonding orbital, the e_{2u}* state observed in XA. The strong molecular character of the bonding e_{2u} state implies that the corresponding anti-bonding e_{2u}* state has significant metal character. This is confirmed by the reduced intensity of the e_{2u}* XA peak relative to the e_{2u} resonance in the gas phase spectrum [1]. The formation of a single bonding state rather than a band suggests that the e_{2u} orbital interacts

mainly with a narrow distribution of states, i.e. the Ni d band. For benzene adsorbed on Cu (Fig. 2), the new occupied e_{2u} orbital is located just below the Fermi level. It seems to be a cut off at the Fermi level. The adsorbate character in this orbital is rather low. This is also reflected in the relatively strong peak from the anti-bonding orbital in the XA spectrum in Fig. 2. Our observations suggest that the unoccupied e_{2u}* orbital interacts with a broad continuum of metal states and becomes broadened with a tail extending below the Fermi level. There is no distinct separation between the bonding and anti-bonding part.

The interaction between an electron level in the adsorbate and the band like distribution of substrate levels has been separated into two extreme cases [3-5]. If the inter-atomic Coulomb interaction (the driving force for generating bonding and anti-bonding states) is smaller than the band width of the substrate states no well separated bonding-anti-bonding states are formed, only a broadened adsorbate induced resonance level is formed. If, on the other hand, the Coulomb interaction is larger than the band width, discrete bonding and anti-bonding states are obtained. The former situation represents a weak coupling case such as benzene on Cu whereas the latter correspond to strong coupling as in benzene on Ni.

In the σ symmetry XE spectra in Fig. 1 and 2 (solid lines), we find, at binding energies larger than 5 eV, an orbital structure identical to the free molecule [6,7]. In addition we find for benzene on Cu, Fig. 2, two new weak structures at binding energies below 5 eV. These structures appear at the same binding energies as the $1e_{1g}$ and e_{2u}, orbitals seen in the π symmetry spectrum. We can anticipate some symmetry mixing due to rehybridization. For benzene adsorbed on Ni the σ symmetry spectrum is different. Here we find significant σ intensity all the way to the Fermi level, marked σ in Fig 1. A simple admixture of σ and π states is not sufficient to explain the appearance of new σ states in the spectrum, since then we would expect a σ electron distribution which resemble the π states with a peak at 1.7 eV (the backbonding e_{2u} orbital). The 2p valence states parallel to the surface must therefore interact with the metal somewhat differently than the perpendicular 2p states. The band-like character of the σ states indicates a hybridization of benzene σ states with the broad Ni sp band in addition to the d band. Since the HOMO and LUMO σ orbitals involve C-H contributions we expect that the presence of these new states could affect the C-H bond. This might have direct implications for the important hydrogenation and dehydrogenation reactions of aromatic hydrocarbons on metal surfaces.

REFERENCES

1. J. Stöhr, NEXAFS Spectroscopy, Vol. 25 of Springer Series in Surface Science (Springer, Heidelberg, 1992).
2. M. Weinelt, T. Wiell, J. Hasselström, O. Karis, N. Wassdahl, A. Nilsson, L.G.M. Pettersson, H. Ågren, J. Stöhr and M. Samant, to be published.
3. P. W. Anderson, Phys. Rev. 124, 42 (1961).
4. D. M. News, Phys. Rev. 178, 1123 (1969).
5. J. R. Schrieffer and D. C. Mattis, Phys. Rev. 140, 1412 (1965).
6. P. Skytt, J. Guo, N. Wassdahl, J. Nordgren, Y. Luo and H. Ågren, Phys. Rev. A52, 3572 (1995).
7. W. Huber, H. P. Steinrück, T. Pache and D. Menzel, Surf. Sci. 217, 103 (1989).

This work was supported by the Swedish Natural Science Research Council (NFR) and the Göran Gustafsson Foundation for Research in Natural Sciences and Medicine.

Principal investigator: Anders Nilsson, Department of Physics, Uppsala University, Sweden and the ALS
E-mail: Anders.Nilsson@fysik.uu.se Telephone: 510-8419903

Incoherent X-Ray Emission of Titanium Diboride at the Boron Site

D.L. Ederer[1], J.J. Jia[2], R. Winarski[1], Ling Zhou[3], T.A. Callcott[3], R.C.C. Perera[4], A. Moewes[5], L.J. Terminello[6], A. Asfaw[7], and J.van Ek[1]

[1]Tulane University, New Orleans, LA 70118
[2]IMP, Inc. 2830 N. First St., San Jose , CA 95134
[3]University of Tennessee, Knoxville , TN 37996
[4] Advanced Light Source ,Lawrence Berkeley Laboratory, Berkeley, CA 94720
[5] Center for Advanced Microstructures and Devices, Baton Rouge, LA 70888
[6]Lawrence Livermore National Laboratories Livermore, CA 94551
[7]Physics Department, University of Addis Abbaba, Addis Abbaba, Ethiopia.

INTRODUCTION

Our group has made a study of a large number of transition metal diborides and hexaborides. As an example we would like to consider one of them. This class of compounds are of technical interest because they are quite hard, metallic, and chemically stable, and have high melting points.(1) In addition to the technical importance of the borides, our group is interested in compounds of this type because of the very strong 1s $\rightarrow$ p* resonance that has been observed and associated with the boron atom(2-5).

Several calculations have been carried out for the hexaborides and the diborides.(6-8). Titanium diboride has been chosen for the example to be presented here. As $h\nu_1$ was scanned between 188 eV and 197 eV, resonant Raman or spectator emission as it sometimes called (3,4) was observed at the 1s $\rightarrow$ p* core-exciton resonance. At a photon energy of about 197 eV the emission spectrum is representative of the valence band density of states having p type symmetry. The crystal structure of TiB_2 is designated as C32 and is characterized by alternating layers of titanium and boron atoms. The boron is arranged in hexagonal nets with a titanium atom centered above each hexagon (9,10). In this compound the three valence electrons form sp-s and p-p orbitals. The strong s bonding occurs between the boron atoms in the net whereas the s and d electrons in the transition metal form into orbitals with four symmetry classes: s, d_{Z^2}, d_{XZ}, and d_{YZ}, and $d_{X^2-Y^2}$ and d_{XY}. The s orbital will bond with the s band, and d_{Z^2} interacts strongly with the lowest lying p orbital while the d_{XZ}, and d_{YZ} orbitals bond with the two higher-lying p levels. The $d_{X^2-Y^2}$ and d_{XY} orbitals are directed in a plane parallel to the boron layers and thus form bonds within the transition metal layer, and are non bonding with respect to the boron layer(9,10). The $d_{X^2-Y^2}$ and d_{XY} orbitals are unoccupied and form resonances low in the conduction band. This is in contrast to the D^4_{6h} symmetry of the lattice of hBN.(11). In h-BN the bonds between the BN atoms in a layers are s and p and just p between the layers. The difference in bonding between h-BN and TiB_2 is undoubtedly the reason why the emission by boron in h-BN is so different than that of boron in TiB_2. even though both compounds have a hexagonal crystal structure, The emission spectrum of oriented h-BN also shows a strong asymmetry in the valance band x-ray emission as a function of the fluorescence emission angle relative to the c axis(12,13) due to the preferred emission direction from bands of s and p symmetry.

RESULTS

The valence emission band obtained from a pressed powder sample at an excitation energy of 197 eV is shown in Figure 1 as the data points. Our observations are in excellent agreement with the results of Holliday(14) and Lyakhovskaya *et al* (15) who published the K emission spectrum of B in this compound obtained by electron bombardment of the sample. Fischer (16) obtained the titanium $L_{II,III}$ spectrum in TiB_2. The scaled experimental data is compared with the recent calculations of Tian et al (1) who used a Linear Muffin Tin Orbital (LMTO) calculation technique to obtain the density of states with p symmetry at the boron site (light curve). Our group has made a similar LMTO calculation within the atomic sphere approximation (17), and it is shown as the heavy curve in Figure 1. The calculated p-type density of states is in good semi quantitative agreement with the measurements. Both calculations obtain very nearly the same band width as the observations and the calculations and the measurements show the same features: a low density of states near the Fermi energy a sharp peaking of the density of states a few eV below the Fermi energy and a tailing off of the density of states deep within the band. Just as with previous example of yttrium and yttria a one electron LMTO calculation accounts for the main features of the density of states in a semiquantitative way.

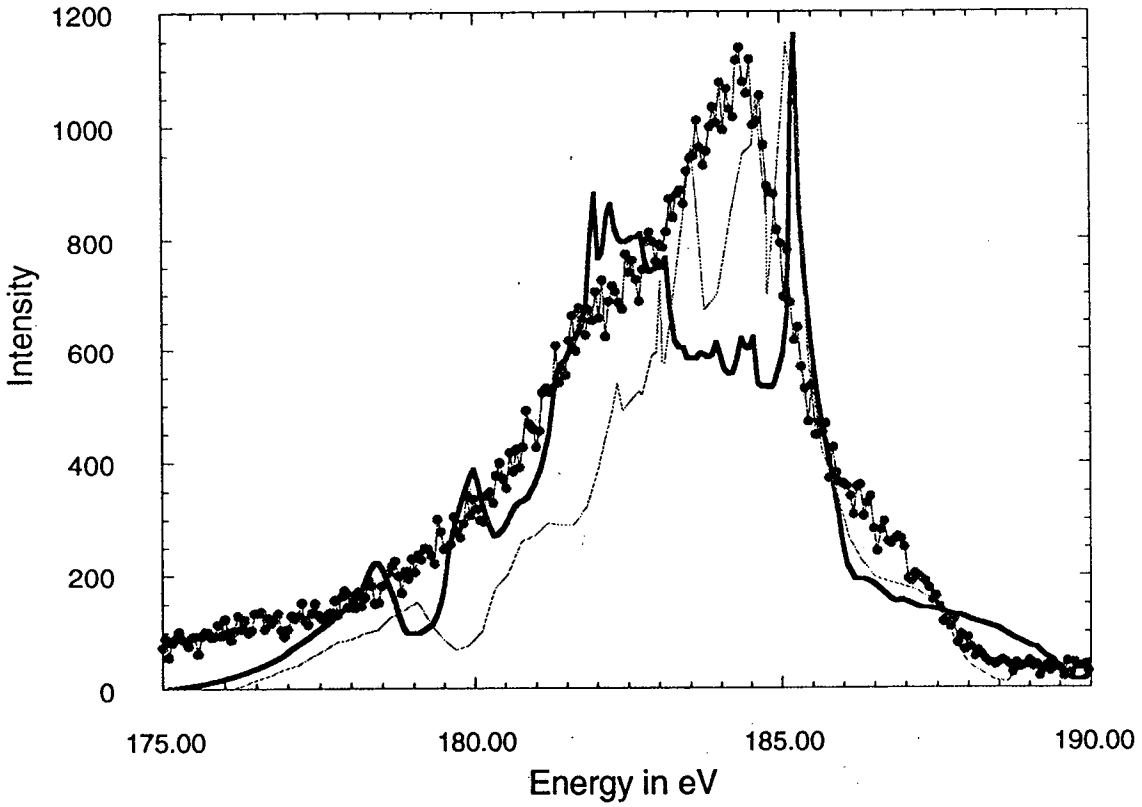

FIGURE 1. Soft X-ray emission spectra for transitions from the valence band into boron 1s vacancies in TiB_2 shown as dotted curves. The calculated p-type density of states at the boron site are shown as: present calculation heavy curve, calculation of Tian et al (Ref. 1) light curve.

ACKNOWLEDGMENTS

The authors are especially grateful to Mr. S. Stadler, and Ms. Tao Shu, for their assistance in taking and reducing some of the data. The authors would like to acknowledge support from NSF grant DMR-9017997, the University of Tennessee Science Alliance and a DoE-EPSCoR cluster research grant DoE-LEQSF (1993-95)-03. The Advanced Light Source is supported by Department of Energy grants DE-AC03-76SF00098.

REFERENCES

1. D.-C. Tian, and X-B. Wang, J. Phys: Condens Matter **4**, 8765-8771 (1992).
2. J.J.Jia, T.A. Callcott, E.L. Shirley, J.A. Carlisle, L.J. Terminello, A. Asfaw, D.L. Ederer, F.J. Himpsel, and R.C.C. Perera, Phys. Rev. Letters, **76**, 4054-4059 (1996).
3. Y. Muramatsu, M. Oshima, and H. Kato, Phys. Rev. Lettrs. **71**, 448-452 (1993).
4. W.L. O'Brien, J.J. Jia, Q.-Y. Dong, T.A. Callcott, K.E. Miyano, D.L. Ederer, D.R. Mueller, and C.-C. Kao, Phys. Rev. Lettrs. **70**, 238-242 (1993).
5. S. Shin, A. Agui, M. T. Fujisawa, Y. Yezuka, T. Ishii, Y. Minagawa, Y. Suda, A. Ebina, O. Mishima, and K. Erqa, Phys Rev. B **52**, 11853-11857 (1995).
6. P.G. Perkins, D.R. Armstrong, and A. Breeze, J. Physics C:Solid State Physics, **8**, 3558-3564 (1975).
7. H. Ihara, M. Hirabayashi, H. Nakagawa, Phys. Rev. B **16**, 726-730 (1977).
8. X-B. Wang, D.-C. Tian, and L.-L. Wang, J. Phys.: Condens. Matter **6**, 10185-10190 (1994).
9. D.D. Vvedensky, M.E. Eberhart, L. Christodoulou, and J.M. MacLaren, Materials Science and Engineering, **A126**, 33-38 (1990).
10. J.K. Burdett, E. Canadell, and G., J. Miller, Am. Chem. Soc. **108**, 6561-6566 (1986).
11. J. Robertson, Phys. Rev. B **29**, 2131-2142 (1984).
12. E. Tegeler, N. Kosuch, G. Wiech, and A. Faessler, Phys. Stat. Sol. (b) **84**, 561-573 (1977).
13. A. Mansour, S.E. Schnatterly, Phys. Rev. B **35**, 9234-9237 (1987).
14. J. E. Holliday, Adv. X-ray Analysis **9**, 365-374 (1966).
15. I.I. Lyakhovskaya, T.M. Zimkina, and V.A. Fomichov, Soviet Physics-Solid State **12**, 138-143 (1970).
16. D.W. Fischer, and D.W. Baun, J. Appl. Phys. **39**, 4757-4763 (1968).
17. O.K. Andersen, Phys. Rev. B. **12**, 3060-3068 (1975).

Principal investigators: David L. Ederer, Physics Department, Tulane University, New Orleans, LA 70118. E-mail dlederer@mailhost.tcs.tulane.edu and Thomas A. Callcott, Physics Department, University of Tennessee-Knoxville,TN 37996. E-mail : tcallcott@utk.edu

Inelastic Scattering at the B K Edge of Hexagonal BN

J.J. Jia[1], J.A. Carlisle[2], E.L. Shirley[3], T.A. Callcott[1], L.E. Terminello[4], L. Zhou[1], D.L. Ederer[5] and R.C.C. Perera[6]

[1] Department of Physics, University of Tennessee, Knoxville, Tennessee 37996, USA
[2] Department of Physics, Virginia Commonwealth University, Norfolk, Virginia 23284 , USA
[3] National Institutes of Standards and Technology, Gaithersberg, Maryland 20899, USA
[4] Lawrence Livermore National Laboratory, Livermore, California 94550, USA
[5] Department of Physics, Tulane University, New Orleans, Louisiana 70118, USA
[6] Advanced Light Source, Ernest Orlando Lawrence Berkeley Laboratory, University of California, Berkeley, California 94720, USA

INTRODUCTION

Many recent soft x-ray fluorescence (SXF) studies have shown that inelastic scattering processes make important contributions to the observed spectra for excitation near the x-ray threshold. These effects are all attributed to a process, usually called and electronic Raman scattering (ERS) process, in which energy is lost to an electronic excitation. The theory has been described using second order perturbation theory by Tulkki and Aberg[1,2]

In different materials, the detailed nature of the electronic excitation producing the energy loss may be very different. In crystalline Si,[3] diamond[4] and graphite,[5] changes in spectral shape and dispersion of spectral features with variation of the excitation energy are observed, which are attributed to k conservation between the photoelectron generated in the excitation process and the valence hole remaining after the coupled emission process. Hence the process is strongly localized in k-space. In hexagonal boron nitride (h-BN), which has a lattice and band structure very similar to graphite, inelastic scattering produces very different effects on the observed spectra. Here, the inelastic losses are coupled to a strong resonant elastic scattering process, in which the intermediate state is a localized core exciton and the final state is a localized valence exciton, so that the electronic excitation is strongly localized in real rather than reciprocal space. Detailed descriptions of the experimental and theoretical description of inelastic scattering in h-BN have been published elsewhere.[6,7]

EXPERIMENTAL RESULTS

These experiments were performed on undulator beamline 8.0 of the Advanced Light Source using the soft x-ray emission spectrometer operated the the Tennessee/Tulane/ LBNL/LLNL collaboration.[8]

The boron K spectra of h-BN excited near threshold are plotted in Figure 1. h-BN has a layered structure similar to that of graphite and a similar band structure. The principal

difference is that h-BN has a large band gap and is an insulator, which permits h-BN to support a localized exciton state with an energy level within the band gap. The presence of this exciton state produces remarkably different effects in its inelastic scattering spectra. The spectra are labeled with the excitation energies. They show a remarkably strong localized excitonic resonance at an excitation energy of 192 eV, which is about 1.5 eV below the conduction band threshold. The high energy quasi-elastic peak marked E reaches a maximum amplitude about 500X larger than other spectral features at the resonance energy. Theoretical studies indicate that this core exciton is derived from π^* states near the conduction band minimum at the M point of the 2D hexagonal Brillouin zone, and is localized within about two lattice spacings from the core excited atom.[6]

The studies further indicate that the final state of the inelastic scattering process is a similarly localized *valence* exciton state in which the electron is bound to a valence hole. The inelastic spectra excited at photon energies below the strong elastic resonance and between the resonance and the conduction band threshold are electronic Raman spectra. The peaks labeled A and B exactly track the elastic energies at energies approximately 16 and 11 eV below the elastic peak. The scattering process is illustrated schematically to the left of the figure. As this diagram indicates, the spectra are essentially a map of the σ-p density of states, produced by energy loss to electronic Raman excitation from the σ-p

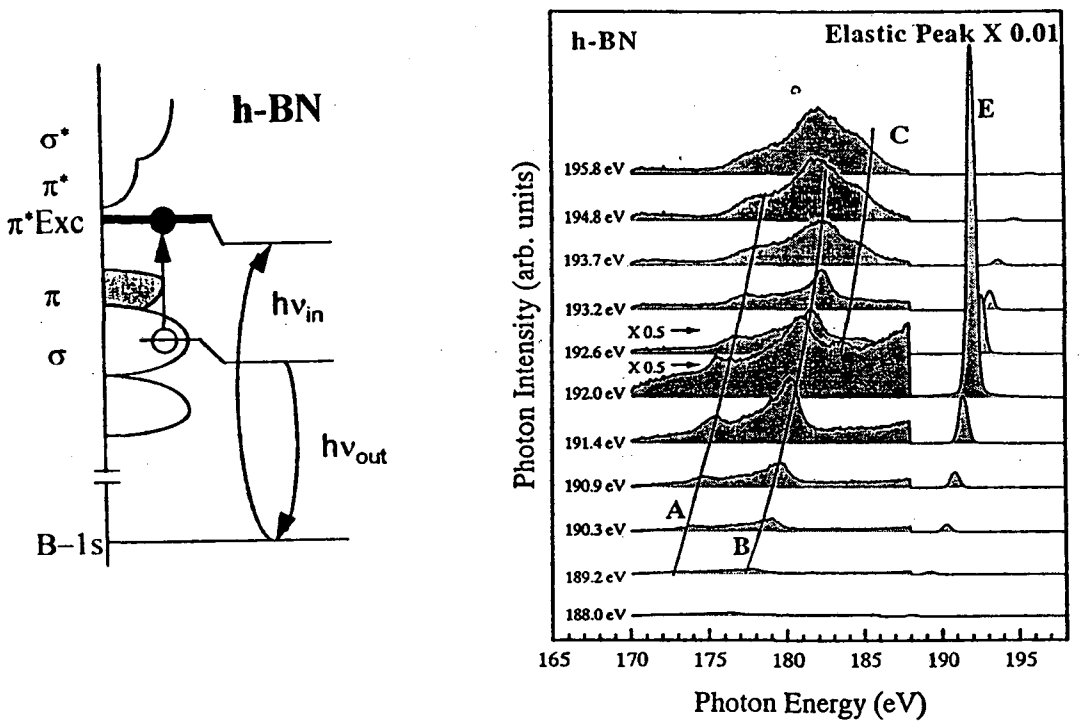

Figure 1. The boron K spectra of h-BN excited near threshold. The excitation process is diagrammed to the left. Spectra are labeled with excitation energies. Peak E is a strong elastic scattering peak associated with scattering through a core exciton state. Below the exciton resonance at 192 eV, peaks A and B result from an electronic Raman scattering process. Peak C, observed on resonance in in normal fluorescence spectra excited above 194 eV, is symmetry forbidden in the inelastic scattering process.

valence bands to a localized valence exciton derived from π^*-p conduction band states. π-p to π^*-p states are forbidden by symmetry in the ERS process. It should be emphasized that the excitons associated with the intermediate and final states of this process are different, the strong resonance in the elastic peak being associated with a core exciton in the intermediate state, and the final state having a localized valence exciton. For excitation on the excitonic resonance at 192 eV and to final states in the conduction band, the spectra show a third peak C associated with transitions from π-p states, which is present in normal SXF spectra, but is forbidden in the inelastic scattering process. This is a clear example of how alternative decay channels are available when the intermediate state is coincident with a real excited state of the system, which can relax the selection rules that control the pure ERS process.

REFERENCES

1. J. Tulkki and T. Aberg, J. Phys. B. **15**, L435 (1982).
2. J. Tulkki, Phys. Rev. A **27**, 3375 (1983).
3. K.E. Miyano et al., Phys. Rev. B **48**, 1918 (1993).
4. Y. Ma et al., Phys. Rev. Letters **69**, 2598 (1992).
5. J.A. Carlisle et al., Phys. Rev. Letters **74**, 1234 (1995).
6. J.J. Jia et al., Phys. Rev. Letters **76**, 4054 (1996).
7. E.L. Shirley in Proc. of workshop on *Raman Emission by X-ray Scattering,* ed. by D.L. Ederer and J.H. McGuire (World Scient. Publ., Singapore, 1996) p. 71.
8. The beamline is described in ALS First Phase Scientific Program, LBNL publication LBL PUB-706, pp. 11-16, 1992.

This work was supported by National Science Foundation grant DMR-9420425 and by the authors institutions, and was carried out at the Advanced Light Source at Lawrence Berkeley National Laboratory operated under Contract No. DE-AC03-76SF00098 with the U.S. Department of Energy.

Principal investigator: T.A. Callcott, Department of Physics, University of Tennessee. Email: tcallcott @utk.edu. Telephone: 423-974-6765.

Observation of Core-Level Binding Energy Shifts Between (100) Surface and Bulk Atoms of Epitaxial $CuInSe_2$

A.J. Nelson[1], G. Berry[2], Angus Rockett[2], D.K. Shuh[3], J.A. Carlisle[4], D.G.J. Sutherland[4] and L.J. Terminello[4]

[1]Department of Physics, Colorado School of Mines, Golden, CO 80401
[2]Department of Materials Science, University of Illinois at Urbana-Champaign Urbana, IL 61801
[3]Lawrence Berkeley National Laboratory, Berkeley, CA 94720
[4]Lawrence Livermore National Laboratory, Livermore, CA 94550

Core-level and valence band photoemission from semiconductors[1-6] has been shown to exhibit binding energy differences between surface atoms and bulk atoms, thus allowing one to unambiguously distinguish between the two atomic positions. Quite clearly, surface atoms experience a potential different from the bulk due to the lower coordination number – a characteristic feature of any surface is the incomplete atomic coordination. Theoretical accounts of this phenomena are well documented in the literature for III-V and II-VI semiconductors.[7,8] However, surface state energies corresponding to the equilibrium geometry of (100) and (111) surfaces of Cu-based ternary chalcopyrite semiconductors have not been calculated or experimental determined. These compounds are generating great interest for optoelectronic and photovoltaic applications, and are an isoelectronic analog of the II-VI binary compound semiconductors.

Surface core-level binding energy shifts depend on the surface cohesive energies, and surface cohesive energies are related to surface structure. For ternary compound semiconductor surfaces, such as $CuInSe_2$, one has the possibility of variations in surface stoichiometry.[9] Applying standard thermodynamical calculations which consider the number of individual surface atoms and their respective chemical potentials should allow one to qualitatively determine the magnitude of surface core-level shifts and, consequently, surface state energies.

One expects that the largest surface atom core-level shift would come from a surface plane that has the lowest coordination number. In bulk $CuInSe_2$, each Se anion is coordinated by two Cu and two In cations (generally with unequal bond lengths).[10] However, the Se atoms at the surface would have twofold coordination (threefold if reconstructed with Se dimers). Comparison with ZnSe(100) surface structures would imply that a moderately Se-rich $CuInSe_2$ surface may result in a stable structure with (2 x 1) symmetry terminated by a full monolayer of Se dimers.[3,11] The Se-terminated (2 x 1) surface would have two filled Se dangling bonds per dimer. For the II-VI isoelectronic analogs to $CuInSe_2$, the occupied dangling-bond state lies below or just at the valence band maximum (VBM) and the empty dangling-bond state lies above or just at the conduction band minimum (CBM).[3,6] Thus, this chalcopyrite semiconductor should provide an ideal system for the

observation of surface states. In addition, the existence of these surface states and their position relative to the VBM may yield information related to improving photovoltaic/optoelectronic device operation. For example, sulfur passivation of these surface states is being proposed as the mechanism and the means of increasing device efficiency for these important technological materials.[12]

We present the first high-resolution X-ray photoemission measurements for the (100) surface of $CuInSe_2$ which clearly show Se 3d surface core-level binding energy shifts. Growth of the $CuInSe_2$ epilayers on GaAs(100) is described in detail elsewhere.[13] This work was performed on the IBM/TENNESSEE/TULANE/LLNL/LBNL beam line 8.0 at the Advanced Light Source (ALS). Photoemitted electrons were analyzed using an ellipsodial mirror display analyzer with a total angular acceptance of 85°. This analyzer acquires angle resolved spectra simultaneously due to its energy filtering/angle preserving characteristics. Photoemission spectra were collected with hv=135 and 300 eV. The combined energy resolution of the monochromator and the analyzer was $\Delta E \approx 50$ meV. The $CuInSe_2$ epilayers were flashed at ≈600°C under 10^{-10} Torr vacuum prior to analysis in order to remove any residual surface contamination.

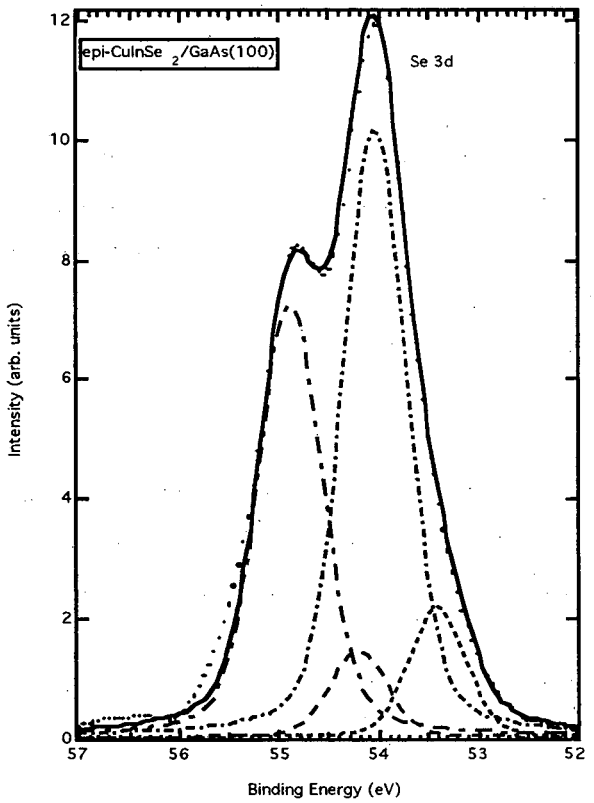

Figure 1. Deconvolved Se 3d core-level spectrum showing showing bulk and surface atom emissiom components.

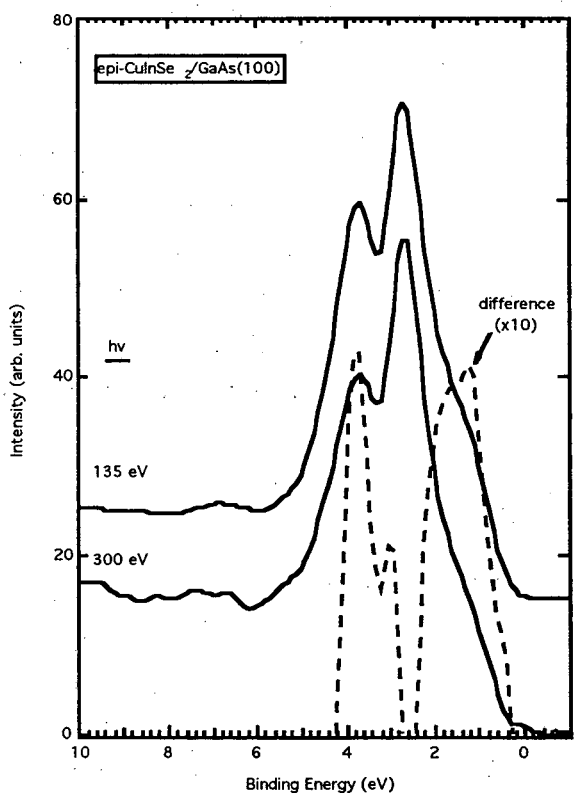

Figure 2. Valence band spectra acquired at the hv=135 and 300 eV from epitaxial $CuInSe_2$/GaAs(100).

The deconvolved Se 3d spectrum acquired at hν=135 eV is shown in Figure 1. Standard Gaussian-Lorentzian curve fitting and background subtraction procedures were followed. The results of the Se 3d difference spectrum were used to isolate the binding energy of the spin-orbit components due to surface emission. Results of this deconvolution show that the Se 3d core level has only a single surface component, which indicates that all Se surface atoms are chemically equivalent. Also, the surface components are shifted by 0.60 eV toward lower binding energy, which is consistent with the magnitude for anion surface shifts observed for III-V and II-VI surfaces.[2-6] These observations are compatible with the proposed (2 x 1) Se terminated surface, but are certainly not conclusive.

Occupied Se surface state emission near the VBM of $CuInSe_2$ would enhance the leading edge of the VB DOS. However, considering the low intensity of the Se 3d feature assigned to a Se surface state, this enhancement would be small. In addition, the photoionization cross sections at these photon energies for Se p state emission from the VB are quite low. Therefore, to enhance the differences and determine their source, the two VB spectra acquired at hν=300 eV and at hν=135 eV were normalized and subtracted and are displayed in Figure 2. The difference spectrum displays two separate doublet structures - one near the VBM (peaks at 0.8 eV and 1.2 eV relative to E_{vbm}) and one under the peaks corresponding to the two branches of the Cu *d* bands (smaller peak at 2.6 eV and larger peak at 3.3 eV relative to E_{vbm}). Thus, the energy separation between these two doublet structures is 1.8–2.1 eV.

The VB of $CuInSe_2$ consists of a mixture of Cu 3d(10) and Se 4p(4) orbitals. The Se 4p orbitals form a threefold degenerate state in the presence of the tetragonal chalcopyrite crystal field. Cu 3d states with the same threefold symmetry interact, forming a lower bonding and upper antibonding state. This antibonding combination forms the VBM and the bonding-antibonding energy separation is on the order of 3–4 eV. Therefore, comparing experiment with theory, and noting the low photoionization cross sections for Se p state emission, we assign the doublet structures of the difference spectrum with cation bonding-antibonding state emission. The difference in theoretical versus experimental energy separation of the doublets may provide a clue on the chemical environment of the surface cations (i.e. Cu) due to the redistribution of surface valence charge.

REFERENCES

1. D.E. Eastman and W.D. Grobman, Phys. Rev. Lett. **28**, 1378 (1972).
2. G.V. Hansson and R.I.G. Uhrberg, Surf. Sci. Reports **9**, 197 (1988)

3. T. Takahashi and A. Ebina, Applications of Surface Science **11-12**, 268 (1982).
4. W. Chen, A. Kahn, P. Soukiassian, P.S. Mangat, J. Gaines, C. Ponzoni, and D. Olego, J. Vac. Sci. Technol. **B12**, 2639 (1994).
5. R.Z. Bachrach, R.S. Bauer, S.A. Flodstrom, and J.C. McMenamin, Nuovo Cimento **B39**, 704 (1977).
6. A. Ebina, T. Unno, Y. Suda, H. Koinuma, and T. Takahashi, J. Vac. Sci. Technol. **19**, 301 (1981).
7. J.R. Chilikowsky and M.L. Cohen, Phys. Rev. **B20**, 4150 (1979).
8. C. Calandra and G. Santoro, J. Vac. Sci. Technol. **13**, 773 (1976).
9. A. J. Nelson, A.M. Gabor, M.A. Contreras, J.R. Tuttle, R. Noufi, P.E. Sobol, P. Asoka-Kumar and K.G. Lynn, J. Appl. Phys. **78(1)**, 269 (1995).
10. J.E. Jaffe and A. Zunger, Phys. Rev. **B28**, 5822 (1983).
11. Alberto Garcia and John E. Northrup, J. Vac. Sci. Technol. **B12**, 2678 (1994).
12. A.J. Nelson, C. R. Schwerdtfeger, G.C. Herdt, D. King, M. Contreras and K. Ramanathan, Thin Films for Photovoltaics, Materials Research Society Conference Proceedings No. **426**, (1996).
13. L. Chung Yang, L.J. Chou, A. Agarwal, and A. Rockett, *Proceedings of the 22nd IEEE Photovoltaic Specialists Conference, Las Vegas* (IEEE, New York, 1991), p.1185.
14. A.J. Nelson, A. Rockett, E. Colavita, M. Engelhardt, and H. Höchst, Phys. Rev. **B42**, 7518 (1990).

This work is supported by the Office of Basic Energy Sciences, U.S. Department of Energy, under Contract No. DE-AC03-76SF00098.

Principal investigator: Art J. Nelson, Physics Department, Colorado School of Mines. Email: ajnelson@wheeze.mines.edu. Telephone: 303-273-3830.

Occupied and Unoccupied Orbitals of C_{60} and C_{70} Probed with C 1*s* Emission and Absorption

J.A. Carlisle,[1] L.J. Terminello,[1] E.A. Hudson,[1] E.L. Shirley,[1] F.J. Himpsel,[2] J.J. Jia,[3] T.A. Callcott,[3] R.C.C. Perera,[4] S.G. Louie,[5] J. Stöhr,[6] M.G. Samant,[6] D.L. Ederer[7]

[1]*Lawrence Livermore National Laboratory, Livermore, CA 94550*
[2]*IBM Research Division, Thomas J. Watson Research Center, Yorktown Heights, NY 10598*
[3]*University of Tennessee, Knoxville, TN 37996*
[4]*Lawrence Berkeley Laboratory, Berkeley, CA 94720*
[5]*Department of Physics, U.C. Berkeley, CA 94720*
[6]*IBM Research Division, Almaden Research Center, 650 Harry Road, San Jose, CA 95120-6099*
[7]*Tulane University, New Orleans, LA, 70118*

INTRODUCTION

The aim of our work is to characterize the orbital structure of the fullerenes, and to pursue its evolution from a cluster to the infinite solid. For obtaining a complete picture of the electronic structure we compare a variety of experimental techniques, i.e. photoemission and core level emission for occupied orbitals and inverse photoemission and core level absorption for unoccupied orbitals [1-6]. Our experimental results focus on optical probes involving the C1s core level, i.e. absorption via transitions from the C1s level into unoccupied π^* and σ^* orbitals and emission involving transitions from occupied orbitals into a C1s hole. Due to the simplicity of the C1s level there exist clear selection rules. For example, only transitions to and from orbitals with p-character are dipole-allowed. These results on the p-projected density of states are compared with inverse photoemission and photoemission results, where the selection rules are less definitive. In addition, a first-principles quasiparticle calculation of the density of states is used to assign the orbital features. The spectra from C_{60} and C_{70} are still far from their infinite analog, i.e., graphite, which is also measured with the same techniques. In order to determine the effect of electron transfer onto C_{60}, as in superconducting alkali fullerides, we are studying resonant emission of C_{60}. An electron is placed in the lowest unoccupied molecular orbital (LUMO) by optical absorption from the C1s level and the C 1s emission detected in the presence of this spectator electron.

ORBITAL STRUCTURE OF C_{60}

Figure 1 compares the spectra of occupied (left) and unoccupied (right) orbitals of condensed C_{60} obtained with different techniques, i.e. C1s emission and photoemission for occupied orbitals and C1s absorption and inverse photoemission (from Ref. 3) for unoccupied orbitals. In addition, the density of states (DOS) is given, using state-of-the-art quasiparticle theory [7]. In general one can distinguish π and σ manifolds, with a larger bonding-antibonding splitting for the more strongly interacting σ bands. The assignments to π- and σ-states can be made either by detailed comparison with calculations (Fig. 1), or by analogy with graphite, where well-defined onsets are observed for the π^* and σ^* states in the absorption spectrum (Fig. 2 right). Similar onsets are seen in the fullerene absorption spectra, except for a downwards shift of about 1 eV. In the C 1s emission spectra (Fig. 2 left) the distinction between π and σ states is not so clear. The graphite spectrum shows only σ states, due to the experimental geometry, where emission along the c-axis of graphite is detected. In this case dipole selection rules do

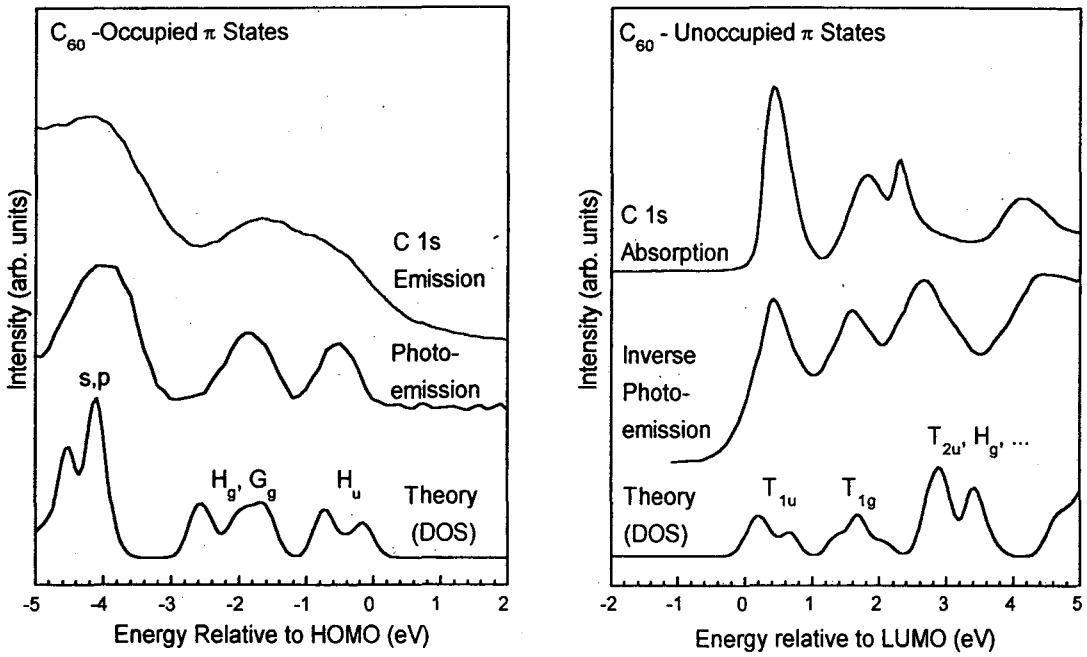

Figure 1: Comparison of various spectroscopies for obtaining the spectrum of occupied (left) and unoccupied (right) π orbitals of condensed C_{60}. The energies are referenced to the HOMO and LUMO, respectively. These data are compared with the density of states (DOS) from first principles quasiparticle calculations (shown at the bottom of each figure), which allows an assignment of the orbitals.

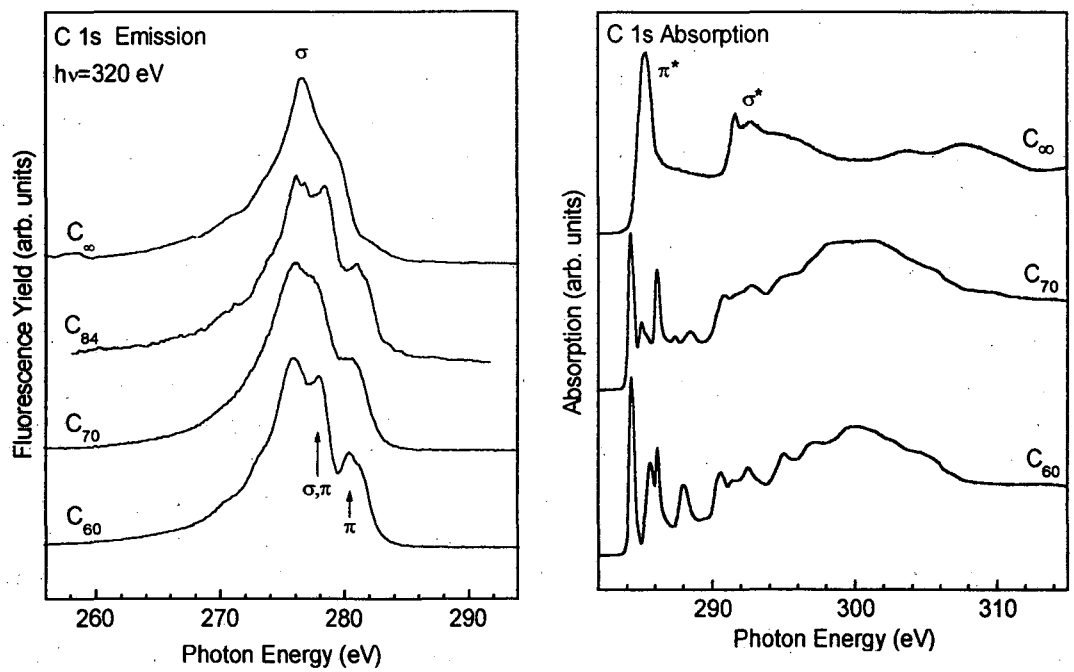

Figure 2: Fluorescence and absorption spectra from the C 1s core level for C_{60}, C_{70}, and their infinite analog graphite. Significant differences are seen between all three materials, showing that the orbital structure varies with cluster size, even for large clusters, and that C_{70} is still far from the limit C_{∞}.

not allow transitions from π orbitals to the C 1s (see Ref. 6). For the fullerenes which can be thought of as having curved carbon sheets, emission from both σ and π orbitals is allowed. Extra π emission features show up at the top of the spectrum. For a detailed analysis we use a comparison with the calculated density of states in Fig. 1.

Various calculations [7-9] both in the solid state and for the free C_{60} molecule, have been published, which allow an identification of the observed peaks in terms of molecular orbitals. We use a state-of-the-art quasiparticle calculation for the density of states of condensed C_{60} in the Fm3 structure [7]. It is based on local density theory, and adds the self-energy that is induced by creating a hole in an occupied band or adding an electron to an unoccupied band. Condensing C_{60} molecules into a thin film broadens molecular orbitals into bands, giving rise to multiple density-of-states peaks per orbital (Fig. 1 bottom). Nevertheless, the intermolecular interaction is weak enough to prevent overlap of neighboring bands near the fundamental gap. Therefore, we can assign the observed peaks in terms of the icosahedral orbital symmetry of the C_{60} molecule, in particular the H_u HOMO, the T_{1u} LUMO, and the next higher T_{1g} orbital. Farther away from the fundamental gap the bands from different orbitals start overlapping. All structures shown in Fig. 1 are π orbitals, except for one near -4.0 eV, which is a combination of σ and π orbitals.

EFFECT OF CLUSTER SIZE

An interesting aspect of carbon clusters is the possibility to follow the transition from an isolated atom to the solid over a wide range of well-defined cluster sizes. As demonstrated in Fig. 2 for C_{60}, C_{70}, and C_{∞} (graphite), there are significant differences between the two cluster sizes, e.g. in the structure of the lower π orbitals seen with C 1s absorption (compare Ref. 4). Both clusters are far from reaching the continuous spectrum of the infinite solid. The sharpness of the molecular orbitals suggests an extension of these experiments to larger fullerenes, and even carbon tubules. In addition to the discrete–to–continuous transition one also expects a chemical transition from non-aromatic to aromatic. The resonant bonding structure normally exhibited by hexagon rings is disrupted by the presence of single-bonded pentagons in the fullerenes [9,10], and it would be interesting to know how much the five-fold rings have to be diluted in order to recover a resonant bonding structure.

ACKNOWLEDGMENTS

This work was supported by the Division of Materials Science, Office of Basic Energy Sciences, and performed under the auspices of the U.S. Department of Energy by Lawrence Livermore National Laboratory under contract No. W-7405-ENG-48. This work was performed at the NSLS, SSRL, and ALS, which are also supported by the Office of Basic Energy Sciences, U.S Department of Energy.

REFERENCES

[1] J.H. Weaver, J. Phys. Chem. Solids **53**, 1433 (1992).

[2] P.A. Brühwiler, A.J. Maxwell, A. Nilsson, R.L. Whetten, and N. Mårtensson, Chem. Phys. Lett. **193**, 311 (1992).
[3] T. Takahashi, S. Suzuki, T. Morikawa, H. Katayama-Yoshida, S. Hasegawa, H. Inokuchi, K. Seki, K. Kikuchi, S. Suzuki, K. Ikemoto, and Y. Achiba, Phys. Rev. Lett. **68**, 1232 (1992).
[4] L.J. Terminello, D.K. Shuh, F.J. Himpsel, D.A. Lapiano-Smith, J. Stöhr, D.S. Bethune, and G. Meijer, Chem. Phys. Lett. **182**, 491 (1991).
[5] Peter Glans, PhD thesis, Uppsala University (1993).
[6] G. Wiech, in: *Inner-Shell and X-Ray Physics of Atoms and Solids*, ed. by D.J. Fabian, H. Kleinpoppen, and L.W. Watson, Plenum (New York 1981), p. 815. These graphite data have been used to calibrate the photon energy in our emission spectrograph. Using Ref. 5 as calibration our energies for the emission spectra would be about 1 eV higher.
[7] E.L. Shirley and S.G. Louie, Phys. Rev. Lett. **71**, 133 (1993).
[8] N. Trouillier and J.L. Martins, Phys. Rev. B **46**, 1754 (1992).
[9] R.C. Haddon, Science **261**, 1545 (1993).

Principal investigator: John A. Carlisle, Department of Physics, Virginia Commonwealth University. Email: jacarlis@vcu.edu. Telephone: 804-828-5443.

Partial Cross Sections of Helium Satellites at Medium Photon Energies

R. Wehlitz,[1] I.A. Sellin,[1] O. Hemmers,[2] S.B. Whitfield[2], P. Glans,[2] H. Wang,[2] D.W. Lindle,[2] B. Langer,[3] N. Berrah,[3] J. Viefhaus,[4] and U. Becker[4]

[1]Department of Physics and Astronomy, University of Tennessee, Knoxville, Tennessee 37996-1200, USA

[2]Department of Chemistry, University of Nevada, Las Vegas, Nevada 89154-4003, USA

[3]Department of Physics, Western Michigan University, Kalamazoo, Michigan 49008-5151, USA

[4]Fritz-Haber-Institut der Max-Planck-Gesellschaft, Faradayweg 4-6, D-14195 Berlin, Federal Republic of Germany

Still of current interest is the important role of single ionization with excitation compared to single ionization alone. The coupling between the electrons and the incoming photon is a single-particle operator. Thus, an excitation in addition to an ionization, leading to a so-called satellite line in a photoelectron spectrum, is entirely due to electron–electron interaction and probes the electron correlation in the ground and final state. Therefore we have undertaken the study of the intensity of helium satellites $He^+n\ell$ ($n = 2 - 6$) relative to the main photoline ($n = 1$) as a function of photon energy at photon energies well above threshold up to 900 eV [1]. From these results we could calculate the partial cross-sections of the helium satellites.

The experiments were performed at the Hamburger Synchrotronstrahlungslabor (HASYLAB) at the undulator beam line BW-3 and at the Advanced Light Source (ALS) at the undulator beam line 8.0. In both cases, we took advantage of the timing mode of the storage rings (1-bunch or 2-bunch mode). Two angle-resolving electron time-of-flight (TOF) spectrometers were employed to analyze the kinetic energy of the photoelectrons emerging from the interaction region defined by the photon beam intersecting an effusive gas beam. The TOF analyzers used at the ALS were designed for high-retardation capability which is crucial for this experiment in order to resolve the satellite states at high photon energies up to 900 eV.

With the help of absolute total photoionization cross-section measurements of Samson *et al.* [2], we calculated the partial cross-sections $\sigma(n)$ of the helium satellites from the satellite-to-1s ratios $R(n)$, using the formula

$$\sigma(n) = R(n) \times \frac{\sigma_{tot}}{1 + R^{2+}} \Big/ \left(1 + \sum_{n=2}^{\infty} R(n)\right) \qquad (1)$$

with σ_{tot} as the total photoionization cross-section and R^{2+} as the double-to-single photoionization ratio. Note that the accuracy of the double-to-single ionization ratio is of minor importance here, because it is only a small correction to our cross-section data. In order to calculate the *total* satellite intensity relative to the 1s line, i.e. $\sum_{n=2}^{\infty} R(n)$, we added the measured satellite-to-1s ratios plus the extrapolated ratios $R(n)$ for higher n to $n \rightarrow \infty$ assuming that $R(n)$ changes as n^{-3} for $n \geq 4$. The resulting partial cross-sections, shown in Fig. 1, are on almost straight lines for each satellite on a log-log scale with a

slope of -3.52(10) except for $n = 2$, which has a slope of -3.23(5). Theory predicts at high photon energies E a slope of -3.5 since the cross section is expected to vary as $E^{-3.5}$.

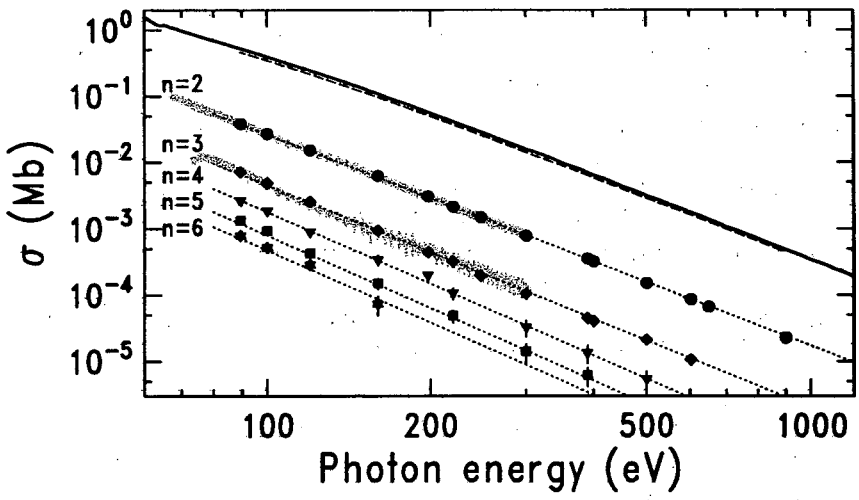

Figure 1. Partial photoionization cross-sections of the satellites $He^+n\ell$ for $n = 2-6$ as a function of photon energy using the absolute total cross-section measurements of Ref. 2 (solid line) for normalization. The gray data points are the recommended cross sections of Ref. 3. The dashed line is the partial photoionization cross-section of the $1s$ main line and the dotted lines are fitted curves as described in the text.

It is interesting to note, that the satellites with $n \geq 3$ keep their high-energy behavior with an exponent close to -3.5 down to very low kinetic energies, whereas the $1s$ main line clearly changes around 300 eV to the low energy behavior with an exponent of about -2.7. The behavior of the satellite $n = 2$ is somewhat between these two limiting cases. This observation shows that the increase of the satellite-to-main line ratio towards lower kinetic energies is basically due to the reduced increase of the $1s$ line towards threshold rather than to an increase of the satellite intensity. Because the agreement between the exponential description of the partial cross-sections and the experimental data is so excellent, there is a very low probability that this could be accidental. We propose here the following simple explanation for the observed behavior. The exponent for the high-energy behavior of the cross section is derived from the Born-approximation of plane waves in the continuum. This approximation fails to describe the photoionization behavior of the $1s$ line at lower kinetic energies, resulting in a change of the exponent. However, this argument can not be simply applied to the satellites because the ℓ-degeneracy of the hydrogenic final ionic state gives rise to a superpostion of many ℓ-wave components in the outgoing photoelectron wave. This superposition of higher and higher angular-momentum components with increasing principal quantum number n reaches the plane wave approximation at much lower energies than the $1s$ line does. Only the first satellite $n = 2$ is in an intermediate situation.

In order to test the consistency of our satellite-to-$1s$ ratios with published double-to-single photoionization ratios, we calculated the double-to-single photoionization ratio from our measured ratios using the theoretical energy-distribution curves of Chang and Poe [4] and Le Rouzo and Dal Cappello [5] which proved to be valid for photon energies below 120 eV [6]. These calculated double-to-single ionization ratios are presented in Fig. 2 and agree fairly well with recent ion measurements [7, 8]. In the lower photon energy range our ratios agree better with the ratios of Dörner *et al.* [8] while for higher photon energies the

agreement is better with the values of Levin *et al.* [7]. One should bear in mind that at lower photon energies the energy distribution of photoelectrons originating from the double-photoionization process is less critical because it is only slightly U-shaped. The uncertainty in the double-to-single ionization ratio introduced by the theoretical energy distribution curves is not included in our error bars.

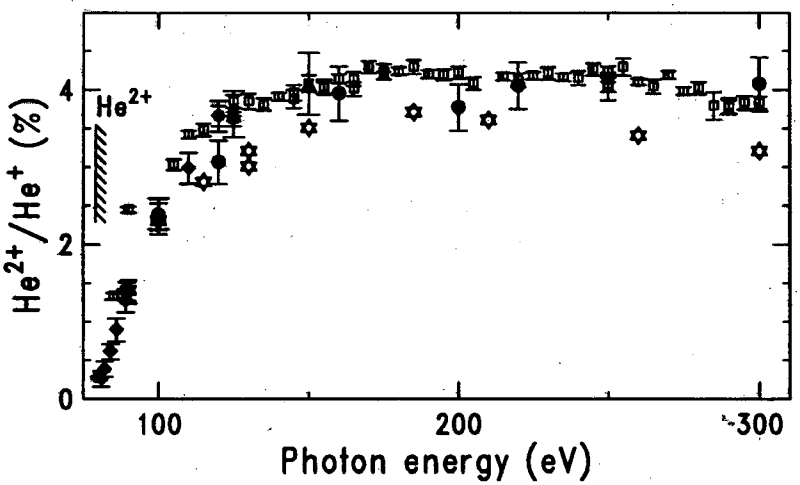

Figure 2. Double-to-single photoionization ratios (full circles) calculated from our satellite-to-1s ratios together with some selected experimental values of other authors (diamonds, Wehlitz *et al.* [6]; squares, Levin *et al.* [7]; stars, Dörner *et al.* [8]; triangles, Schmidt *et al.* [9]).

REFERENCES

1. R. Wehlitz, I.A. Sellin, O. Hemmers, S.B. Whitfield, P. Glans, H. Wang, D.W. Lindle, B. Langer, N. Berrah, J. Viefhaus, and U. Becker, J. Phys. B, in press (1997).
2. J.A.R. Samson, Z.X. He, L. Yin, and G.N. Haddad, J. Phys. B **27**, 887 (1994).
3. J.M. Bizau and F.J. Wuilleumier, J. Elec. Spec. Rel. Phenom. **71**, 205 (1995).
4. T.N. Chang and R.T. Poe, Phys. Rev. A **12**, 1432 (1995).
5. H. Le Rouzo and C. Dal Cappello, Phys. Rev. A **43**, 318 (1991).
6. R. Wehlitz, F. Heiser, O. Hemmers, B. Langer, A. Menzel, and U. Becker, Phys. Rev. Lett. **67**, 3764 (1991).
7. J.C. Levin, G.B. Armen, and I.A. Sellin, Phys. Rev. Lett. **76**, 1220 (1996).
8. R. Dörner *et al.*, Phys. Rev. Lett. **76**, 2654 (1996).
9. V. Schmidt, N. Sandner, H. Kuntzemüller, P. Dhez, F. Wuilleumier, and E. Källne, Phys. Rev. A **13**, 1748 (1976).

This work was supported by the BMBF, the NSF, the DOE, the Research Corporation and The Petroleum Research Fund. RW and BL gratefully acknowledge a Feodor-Lynen-Fellowship of the A. v. Humboldt Foundation and OH acknowledges financial support by the DFG.

Principal investigator: Dennis Lindle, Department of Chemistry, University of Nevada, Las Vegas. Email: Lindle@nevada.edu. Telephone: 702-895-4426.

Photoelectron Spectroscopy and the Dipole Approximation

O. Hemmers,[1] P. Glans,[2] D.L. Hansen,[1] H. Wang,[1] S.B. Whitfield,[3]
R. Wehlitz,[4] J.C. Levin,[4] I.A. Sellin,[4] R.C.C. Perera,[5] and D.W. Lindle[1]
[1]*Department of Chemistry, University of Nevada, Las Vegas, NV 89154-4003*
[2]*Department of Physics, Stockholm University, Stockholm, Sweden 10405*
[3]*Department of Physics, University of South Alabama, Mobile, AL 36688-0002*
[4]*Department of Physics and Astronomy, University of Tennessee, Knoxville, TN 37996-1200*
[5]*Lawrence Berkeley National Laboratory, Berkeley, CA 94720*

Photoelectron spectroscopy is a powerful technique because it directly probes, via the measurement of photoelectron kinetic energies, orbital and band structure in valence and core levels in a wide variety of samples. The technique becomes even more powerful when it is performed in an angle-resolved mode, where photoelectrons are distinguished not only by their kinetic energy, but by their direction of emission as well. Determining the probability of electron ejection as a function of angle probes the different quantum-mechanical channels available to a photoemission process, because it is sensitive to phase differences among the channels. As a result, angle-resolved photoemission has been used successfully for many years to provide stringent tests of our understanding of basic physical processes underlying gas-phase and solid-state interactions with radiation.

One mainstay in the application of angle-resolved photoelectron spectroscopy is the well-known *electric-dipole approximation* for photon interactions. In this simplification, all higher-order terms, such as those due to electric-quadrupole and magnetic-dipole interactions, are neglected. The dipole approximation was first applied to angle-resolved photoemission at a time when most experiments used relatively low photon energies, i.e., UV and far-UV radiation. Since that time, however, many applications have been extended to higher and higher photon energies without considering the validity of the dipole approximation at x-ray energies.

As the photon energy increases, however, effects beyond the dipole approximation become important. To best determine the range of validity of the dipole approximation, photoemission measurements on a simple atomic system, where extra-atomic effects cannot play a role, were performed at BL 8.0. The measurements show that deviations from "dipole" expectations in angle-resolved *valence* photoemission are observable for photon energies down to at least 0.25 keV, and are quite significant at energies around 1 keV. From these results, it is clear that non-dipole angular-distribution effects may need to be considered in any application of angle-resolved photoelectron spectroscopy that uses x-ray photons of energies as low as a few hundred eV.

To see how non-electric-dipole interactions can affect photoelectron angular distributions, it is helpful to first look at the consequences of the dipole approximation for angle-resolved photoemission. The dipole approximation leads to the following expression for the differential photoionization cross section:

$$\frac{d\sigma}{d\Omega} = \frac{\sigma}{4\pi} \left[1 + \frac{\beta}{2} (3\cos^2\Theta - 1) \right] , \qquad (1)$$

which describes the angular distribution of photoelectrons from a randomly oriented sample

(e.g., a gas) created by 100% linearly polarized light. Here, σ is the partial photoionization cross section for a particular subshell, and the angle Θ is measured between the polarization vector of the ionizing radiation and the momentum vector of the ejected electron. The parameter ß, which can only have values in the range from -1 to 2, completely describes the angular distribution of photoelectrons within the dipole approximation.

Electric-quadrupole and magnetic-dipole corrections to the dipole approximation lead to so-called *non-dipole* effects in the angular distributions of photoelectrons, which are described by

$$\frac{d\sigma}{d\Omega} = \frac{\sigma}{4\pi}\left[1 + \frac{\beta}{2}(3\cos^2\Theta - 1) + (\delta + \gamma\cos^2\Theta)\sin\Theta\cos\phi\right] \quad (2)$$

for 100% linearly polarized light. The angle ϕ is measured between the propagation vector of the ionizing radiation and the projection of the photoelectron's momentum vector into the plane perpendicular to the photon polarization. The non-dipole angular-distribution parameters γ and δ result directly from the effects of electric-quadrupole and magnetic-dipole interactions.

To test the range of validity of the dipole approximation, Ne 2s and 2p valence photoemission spectra were measured over the photon-energy range from 0.25 to 1.2 keV using a new apparatus specially designed to measure non-dipole effects in gas-phase photoemission. At each photon energy, a total of 15 spectra, all at different Θ and/or ϕ angles, were collected. Each set of 15 spectra provides enough information to determine simultaneously the polarization characteristics of the incident beam and the angular-distribution parameters ß, γ, and δ. In the process, it was determined that BL 8.0 delivers essentially 100% linearly polarized light over the entire range of the experiment, provided the maximum of the undulator peak corresponds to the selected photon energy.

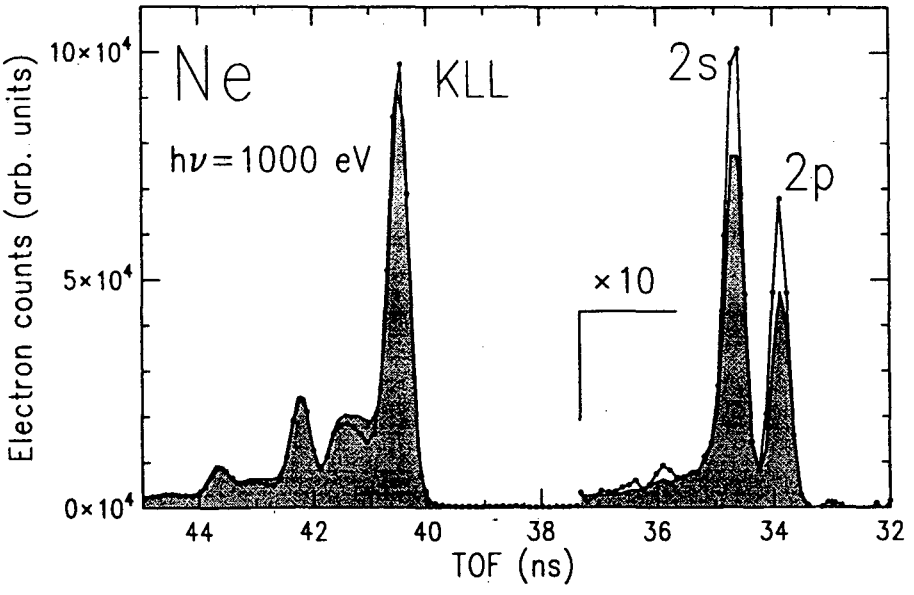

Fig. 1. Photoelectron spectra of Ne measured at a photon energy of 1 keV. The gray spectrum was taken with the dipole magic-angle analyzer and the clear spectrum with the non-dipole analyzer.

As one example of the observed non-dipole angular-distribution effects in Ne, the figure shows two superimposed photoemission spectra taken with $h\nu$ = 1 keV, one at the dipole magic angle (Θ=54.7°, ϕ=90°), in the ϕ=90° plane where non-dipole effects vanish [see Eq. (2)], and the other at an orientation sensitive to non-dipole effects (Θ=54.7°, ϕ=0°). The spectra are scaled to the area of the Ne KLL Auger lines because Auger lines arising from an intermediate state with an *s* hole in a closed-shell atom must have isotropic angular distributions (i.e., $\beta = \gamma = \delta = 0$). The obvious intensity differences between the Ne 2s and 2p peaks in the two spectra are due entirely to non-dipole effects, because both spectra are at the magic angle (Θ=54.7°) where the β parameter has no influence [see Eqs. (1) and (2)]. Clearly, significant changes in ejection probability as a function of angle can be observed due to effects beyond the dipole approximation, even for valence-shell photoemission and for what is commonly considered "low" photon energies ($\leq$1 keV).

Higher-order interactions such as these observed in Ne can, in principle, affect all measurements in the field of angle-resolved photoelectron spectroscopy not made in the ϕ=90° (dipole) plane, even at photon energies below 1 keV. This includes not only measurements on gas-phase targets, but also surface, adsorbate, and condensed-matter targets as well. It is conceivable that any application of photoelectron spectroscopy that relies on angle-dependent differences of photoemission intensities (e.g., much work on atoms and molecules, band-mapping in solids, photoelectron-diffraction and holography, orientation studies of adsorbates, etc.) may benefit from the consideration of non-dipole effects in their analysis.

Support from NSF, Nevada DOE EPSCoR, Research Corporation, and The Petroleum Research Fund is gratefully acknowledged. OH and RW acknowledge support from the DFG and the AvH Foundation, respectively. This work was performed at the ALS, which is supported by DOE (DE-AC03-76SF00098).

Principal investigator: Dennis W. Lindle. E-mail: lindle@nevada.edu. Telephone: 702-895-4426.

Probing the Graphite Band Structure with Resonant Soft-X-Ray Fluorescence

J.A. Carlisle,[1] Eric L. Shirley,[1] E.A. Hudson,[1] L.J. Terminello,[1] T.A. Callcott,[2] J.J. Jia,[2] D.L. Ederer,[3] R.C.C. Perera,[4] and F.J. Himpsel[5]

[1]*Lawrence Livermore National Laboratory, Livermore, CA 94551*
[2]*University of Tennessee, Knoxville, TN 37996*
[3]*Tulane University, New Orleans, LA 70118*
[4]*Lawrence Berkeley Laboratory, Berkeley, CA 94720*
[5]*IBM Research Division, Thomas J. Watson Research Center, Yorktown Heights, NY 10598*

INTRODUCTION

Soft x-ray fluorescence (SXF) spectroscopy using synchrotron radiation offers several advantages over surface sensitive spectroscopies for probing the electronic structure of complex multi-elemental materials [1]. Due to the long mean free path of photons in solids (~1000 Å), SXF is a bulk-sensitive probe. Also, since core levels are involved in absorption and emission, SXF is both element- and angular-momentum-selective. SXF measures the local partial density of states (DOS) projected onto each constituent element of the material. The chief limitation of SXF has been the low fluorescence yield for photon emission, particularly for light elements. However, third generation light sources, such as the Advanced Light Source (ALS), offer the high brightness that makes high-resolution SXF experiments practical. In the following we utilize this high brightness to demonstrate the capability of SXF to probe the band structure of a polycrystalline sample.

In SXF, a valence emission spectrum results from transitions from valence band states to the core hole produced by the incident photons. In the *non-resonant* energy regime, the excitation energy is far above the core binding energy, and the absorption and emission events are uncoupled. The fluorescence spectrum resembles emission spectra acquired using energetic electrons, and is insensitive to the incident photon's energy. In the *resonant* excitation energy regime, core electrons are excited by photons to unoccupied states just above the Fermi level (E_F). The absorption and emission events are coupled, and this coupling manifests itself in several ways, depending in part on the localization of the empty electronic states in the material. In boron nitride, the valence emission spectrum at resonance is shifted, and reflects the influence of an electron excited to a *localized,* excitonic state (a π^* state) [2]. The presence of the localized electron screens the valence electrons, resulting in a shift of the valence emission to lower photon energies. Emission is also observed from (normally unoccupied) excitonic (quasibound) states above E_F. Resonant SXF experiments involving *delocalized* final states in Si [3] and Diamond [4], have found dispersive effects and intensity modulations in the valence emission spectrum as the incident photon energy is varied.

COHERENT FLUORESCENCE IN GRAPHITE

The coupling between absorption and emission in delocalized materials allows one to probe band structure in a unique way. Resonant versus off-resonant fluorescence spectra that were measured from highly oriented pyrolytic graphite (HOPG) at the ALS are shown in Fig. 1a. The take-off angle for these data was 35°, and the width of the excitation energy was approximately 0.3 eV. The uppermost spectrum is characteristic for the non-resonant case, far above threshold ($h\nu_{in}$ = 400 eV). Peaks in the off-resonant spectrum derive primarily from flat regions in the band structure

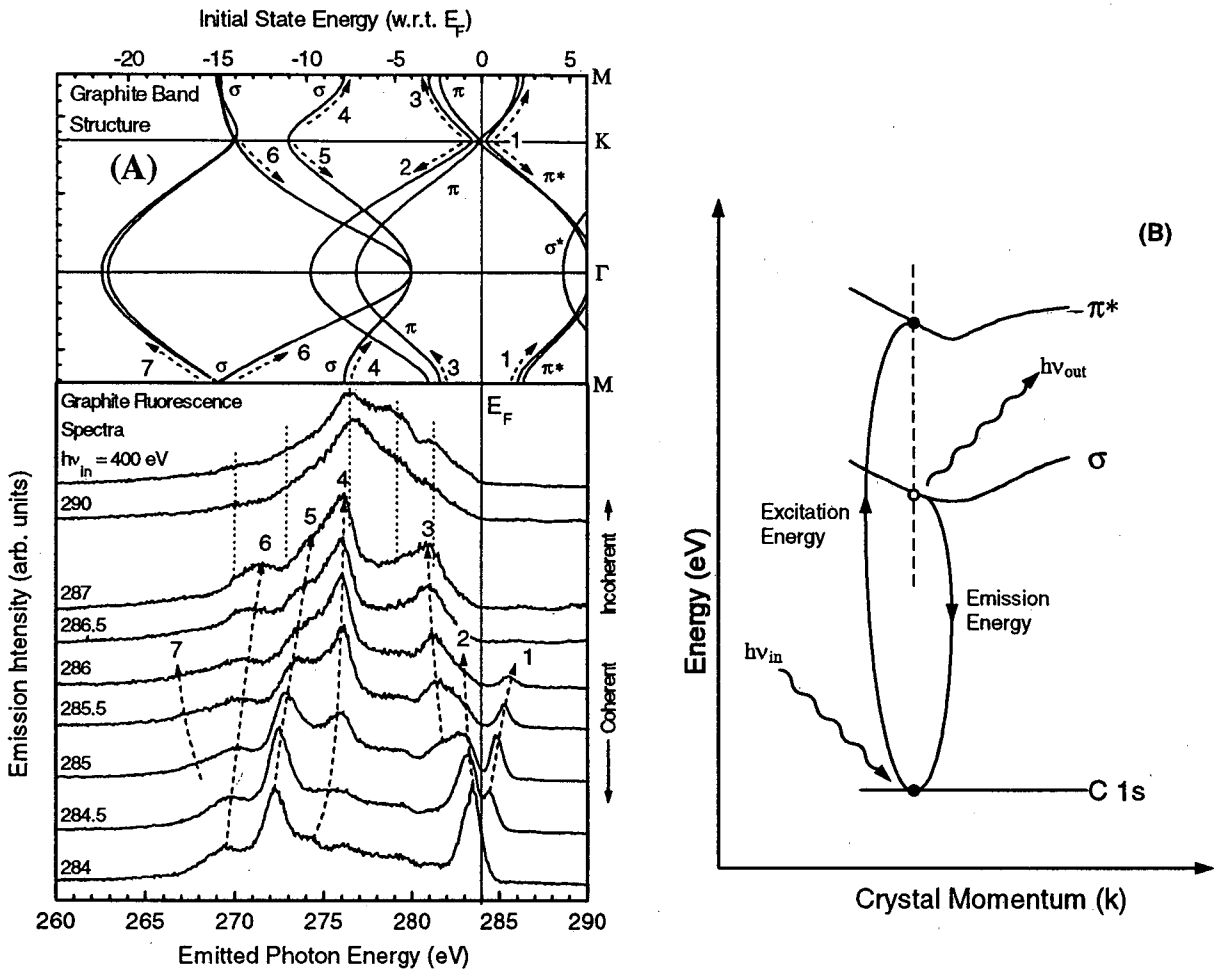

Figure 1 (a) Resonant and non-resonant fluorescence spectra from highly-oriented pyrolytic graphite at incident energies $h\nu_{in}$. The upper panel displays the graphite band structure with the energy axis matched to the photon energy axis of the fluorescence data. The dispersive features labeled 1-7 in the resonant spectra are associated with the portions 1-7 of the graphite band structure indicated by dashed lines and arrows in the upper panel. (b) Schematic representation of coherent fluorescence. After the incident photon excites the core electron to the empty π^* band, only emission from occupied states with the same crystal momentum (vertical line) is allowed

(such as around critical points), which are regions having a high DOS. The resonant spectra are shown below the non-resonant spectrum. Most of these spectra have a drastically different line shape compared to the non-resonant one. Instead of intensity fluctuations observed in other delocalized materials, most of the emission peaks appear to disperse. Their *emitted* photon energies ($h\nu_{out}$) change as $h\nu_{in}$ is varied from 284 eV to 287 eV. These dispersive peaks are highlighted by the dashed lines and are numbered 1-7 in Fig. 4a. The changes in the emission spectrum are most dramatic when $h\nu_{in}$ is varied by just 0.5 eV, from 284.5 eV to 285 eV. The intensities of features 3 and 4 abruptly increase, while peaks 2 and 3 diminish substantially. Such large changes in the spectrum due to such small changes in $h\nu_{in}$ cannot be accounted for solely by simple intensity modulations, which have been explained in terms of sweeping through critical points in the Brillouin zone [4,6].

The $h\nu_{in}$-dependent emission features are the result of transitions from states with a well defined crystal momentum. The upper panel of Fig. 1a shows the band structure of graphite along the high symmetry directions as derived from a tight-binding parametrization of quasiparticle calculations [5]. The σ and π molecular orbitals give rise to the bands labeled in Fig. 1a, and correspond to the different types of bonding (σ or π bonding) which arise between carbon atoms in the graphite sheets. In this figure the band structure has been rotated and the binding energy axis aligned to the lower panel's photon energy axis.

Fig. 1b shows schematically the coherent absorption-emission process [4,5]. Control over $h\nu_{in}$ allows one to select the crystal momentum of the photoelectron's final state in the conduction band. Thus the allowed transitions from occupied states to fill the core hole lie on a vertical line through the band structure having the same crystal momentum as the electron in the π^* conduction band. One may predict the dispersive behavior of the emission peaks graphically in Fig. 1b by constructing sets of vertical lines whose **k**-values are determined by which **k**-point in the π^* band the core electron is excited to by $h\nu_{in}$. The allowed transitions (along the high symmetry directions only) are determined by where the lines intersect the bands. The result of such an analysis leads in a straightforward way to the association of different portions of the graphite band structure in the upper panel of Fig. 1a, which are labeled 1-7, with the emission features labeled 1-7 in the lower panel. Clearly, there is a correlation between the dispersive emission features and the σ and π bands of the HOPG band structure.

ACKNOWLEDGMENT

This work was supported by the Division of Materials Science, Office of Basic Energy Sciences, and performed under the auspices of the U.S. Department of Energy by Lawrence Livermore National Laboratory under contract No. W-7405-ENG-48, by National Science Foundation Grant No. DMR-9017996 and DMR-9017997, by a Science Alliance Center for Excellence Grant from the University of Tennessee, and by the U.S. Department of Energy (DOE) Contract No. DE-AC05-84OR21400 with Oak Ridge National Laboratory. This work was performed at the Advanced Light Source, which is also supported by the Office of Basic Energy Sciences, U.S Department of Energy, under contract No. DE-AC03-76SF00098..

REFERENCES

[1] D.L. Ederer, T.A. Callcott, and R.C.C. Perera, *Synchrotron Radiation News* **7**, 29 (1994).

[2] W.L. O'Brien, J. Jia Q.-Y. Dong, T.A. Callcott, K.E. Miyano, D.L. Ederer, D.R. Mueller, and C.-C. Kao, *Phys. Rev. Lett.* **70**, 238 (1993).

[3] J-E. Rubensson, D. Mueller, R. Shuker, D.L. Ederer, C.H. Zhang, J. Jia, and T.A. Callcott, *Phys. Rev. Lett.* **64**, 1047 (1990); K.E. Miyano, D.L. Ederer, T.A. Callcott, W.L. O'Brien, J.J. Jia, L. Zhou, Q.-Y. Dong, Y. Ma, J.C.Woicik, and D.R. Mueller, *Phys. Rev. B* **48**, 1918 (1993).

[4] Y.Ma, N. Wasshahl, P. Skytt, J. Guo, J. Nørdgren, P.D. Johnson, J-E. Rubensson, T. Boske, W. Eberhardt, and S. D. Kevan, *Phys. Rev. Lett.* **69**, 2598 (1993); P.D. Johnson, Y. Ma, *Phys. Rev. B* **49**, 5024 (1994).

[5] X. Zhu and S. G. Louie, unpublished; see also I.T. McGovern, W. Eberhardt, E.W. Plummer, and J.E. Fischer, *Physica* **99B**, 415 (1980), and R.F. Willis, B. Feuerbacker, and B. Fitton, *Phys. Rev. B* **4**, 2441 (1971).

Principal investigator: Louis J. Terminello, Lawrence Livermore National Laboratory.
For more information, contact John A. Carlisle, Virginia Commonwealth University. Email: jacarlis@vcu.edu. Telephone: 804-828-5443.

Raman Scattering in Transition Metal Compounds: Titanium and Compounds of Titanium

J. Jimenez[1], D.L. Ederer[1], J.J. Jia[2], T. Shu[1], Ling Zhou[3], T.A. Callcott[3] R.C.C. Perera[4], L.J. Terminello[5], A. Asfaw[6] and J. van Ek[1]

[1]Tulane University, New Orleans, LA 70118

[2]IMP, Inc. 2830 N. First St., San Jose , CA 95134

[3]University of Tennessee, Knoxville , TN 37996

[4] Advanced Light Source ,Lawrence Berkeley Laboratory, Berkeley, CA 94720

[5] Center for Advanced Microstructures and Devices, Baton Rouge, LA 70888

[6]Lawrence Livermore National Laboratories Livermore, CA 94551

[7]Physics Department, University of Addis Abbaba, Addis Abbaba, Ethiopia.

INTRODUCTION

The transition metal compounds form a very interesting and important set of materials. The diversity arises from the many states of ionization the transition elements may take when forming compounds. This variety provides ample opportunity for a large class of materials to have a vast range of electronic and magnetic properties (1). The x-ray spectroscopy of the transition elements is especially interesting because they have unfilled d bands that are at the bottom of the conduction band with atomic like structure.(2-4) Our group embarked on the systematic study of transition metal sulfides(5) and oxides (6). As an example of the type of spectra observed in some of these compounds we have chosen to showcase the $L_{II,III}$ emission and Raman scattering in some titanium compounds obtained by photon excitation.

RESULTS

As in h-BN and graphite the exciton levels provide a means to promote Raman scattering with these excitonic states acting as the intermediate state, and the electrons in the valence band providing many final states. Figure 1 is an example of Raman scattering in TiO and TiO_2, where the $L_{II,III}$ emission is plotted on the abscissa for different input photon energies as the ordinate. Each spectrum is displaced according to the value of the excitation photon energy shown on the ordinate. At input photon energies much greater than the $L_{II,III}$ absorption threshold ($\approx$455 eV), the spectra resemble those obtained by Fischer and Baun (7) obtained by electron beam excitation. In these examples the Raman scattering follows the classic pattern as described by Åberg and Tulkki (8), and reviewed by Åberg and Crasemann. (9) The cross section, derived from second order time dependent perturbation theory is he generalized Kramers-Heisenberg (K-H) equation and is given by the following equation as:

$$\frac{d\sigma(\upsilon_1,\upsilon_2)}{d\Omega} = r_e^2 \frac{\upsilon_2}{\upsilon_1} \sum_F \left| \langle F | e^{i(k_1 - k_2)\cdot r} | I \rangle + \frac{1}{m_e} \sum_\eta \frac{\langle F|p\cdot\varepsilon_2|\eta\rangle\langle\eta|p\cdot\varepsilon_1|I\rangle}{E_\eta - E_I - h\nu_1 - i\Gamma_\eta/2} + \frac{1}{m_e} \sum_\eta \frac{\langle F|p\cdot\varepsilon_1|\eta\rangle\langle\eta|p\cdot\varepsilon_2|I\rangle}{E_\eta - E_I + h\nu_1} \right|^2 \times \delta(E_F - E_I + h\nu_1 - h\nu_2) \quad (1)$$

In this equation the first term is the Compton scattering, the second is resonant and the third term is non resonant, and does not contribute significantly to the scattering amplitude. The scaling factor for the inelastic scattering cross section is the square of the classical radius of the

electron,r_e,which has a magnitude of $7.0 \times 10^{-24} cm^2$. In the spectral energy region of interest, this cross section is small compared to the first order photoionization processes and only the resonant term dominates the scattering. In many cases the resonant scattering is characterized by a single intermediate state.(10) The delta function in the K-H equation insures the conservation of energy in the scattering process. The indices, I and F, represent the initial and final states respectively. The energy of the input photon is $h\nu_1$. The quantities $\mathbf{e_1}$ and $\mathbf{e_2}$ are the polarization directions and $\mathbf{k_1}$ and $\mathbf{k_2}$ are the propagation directions of the input and output photons respectively. The energies E_η and E_I are the energy of the intermediate state η and the energy of the initial state respectively. The amplitudes are summed over the intermediate states, η, and the cross section is summed over the final states, F.

This scattering is not limited to atomic levels but has been observed to modify the band emission of solids near threshold. The phenomena was explained by Ma et al(11) as a process that involved not only energy conservation, i.e.: $h\nu_1 - h\nu_2 = E_F - E_I$ but crystal momentum conservation as well so that two equations apply in solids, namely:

$$h\nu_1 - h\nu_2 = E_c(\kappa_c) - E_v(\kappa_v), \quad (2)$$

$$\mathbf{q_1} + \kappa_v = \kappa_c + \mathbf{q_2} = \mathbf{G}. \quad (3)$$

In these expressions the quantities $E_c(\kappa_c)$ and $E_v(\kappa_v)$ are the conduction band and valence band binding energies indexed to the crystal momentum vectors κ_c and κ_v of the conduction band and the valence band electron, respectively. Thus, Raman scattering can involve states localized in real or momentum space. Raman scattering from states localized in momentum space can occur either below(6,12) or above the threshold(13,14), while Raman scattering involving electrons localized in real space occur when the energy of the incident photon is close to but less than the energy for a localized core excitation.

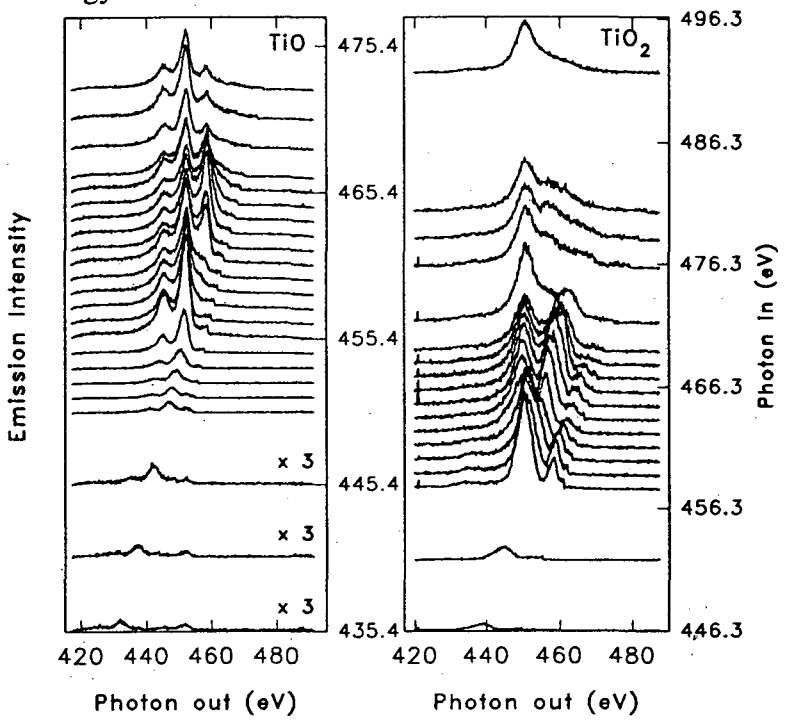

FIGURE 1. Evolution of the TiO (left panel) and TiO_2 (right panel) $L_{II,III}$ emission spectra. All curves show the normalized x-ray emission as a function of the emission energy $h\nu_2$ plotted as the abscissa. The scale on the right give the excitation energy $h\nu_1$. The intensity of the lower three spectra in TiO was multiplied by a factor of three. (From Ref. 6)

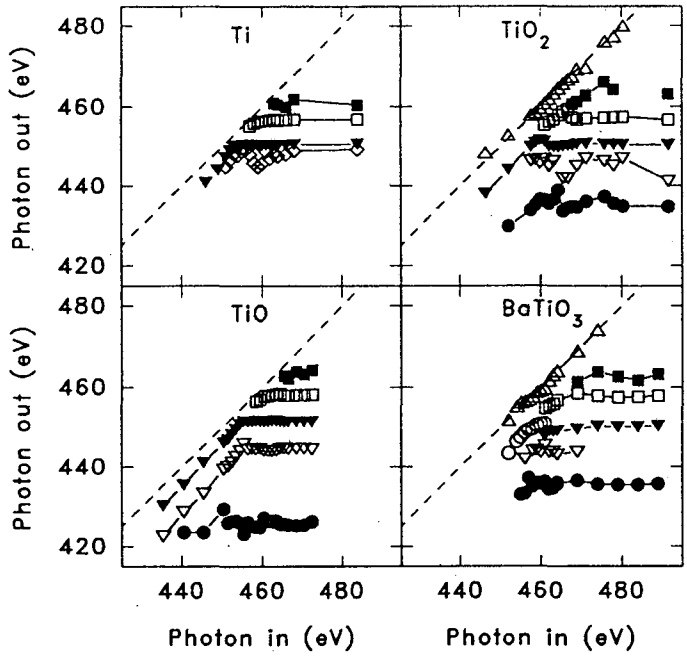

FIGURE 2. Peak position as a function of the excitation energy for all Ti compounds studied. The symbols are grouped as follows. Solid circle: L_{III} valence band (2s subband), open triangle down: L_{III} valence band, solid triangle down: L_{III} valence band, open square: L_{II} valence band, open triangle up: elastic peak, open circle: Raman peak, diamond: extra peak needed in the fitting routine. The exciting photon energy is indicated by a dotted line. (From Ref. 6)

The energy positions of the $L_{II,III}$ emission versus the input energy is shown in Figure 2. Just as in h-BN the *entire band* participates in the scattering constrained by the localization in momentum space defined by Eq(2) and Eq(3). The Raman scattering observed in the titanium compounds is an example of the momentun localized Raman scattering observed below threshold in h-BN reviewed here.(11) It is somewhat surprising that in some compounds the Raman scattering is visible up to *30* eV below the ionization threshold, as can be seen clearly in Figure 2. The Raman loss energies for the titanium compounds studied range between 7 and 20 eV. These Raman losses correspond to energies required to excite a valence exciton, and should be of particular value when making computations that include the valence-exciton state.

ACKNOWLEDGMENTS

The authors are especially grateful to Mr. S. Stadler, and Mr. R. Winarsky, for their assistance in taking and reducing some of the data. The authors would like to acknowledge support from NSF grant DMR-9017997, the University of Tennessee Science Alliance and a DoE-EPSCoR cluster research grant DoE-LEQSF (1993-95)-03. The Advanced Light Source is supported by Department of Energy grants DE-AC03-76SF00098.

REFERENCES

1. D.W.A. Sharp, *Transition Metals*, (London Butterworths, Baltimore University, Park Press)
2. X-B. Wang, D.-C. Tian, and L.-L. Wang, J. Phys.: Condens. Matter **6**, 10185-10190 (1994).

3. D.D. Vvedensky, M.E. Eberhart, L. Christodoulou, and J.M. MacLaren, Materials Science and Engineering, **A126**, 33-38 (1990).
4. F.M.F. de Groot, J.C. Fuggle, B.T. Thole, and G.A. Swatzky, Phys. Rev. B**42**, 5459-5458 (1990).
5. L. Zhou, T.A. Callcott, D.L. Ederer, R.C.C. Perera, submitted to Phys. Rev. B, 1996.
6. J. Jimenez-Mier, D.L. Ederer, U. Diebold, A. Moewes, T.A. Callcott, L. Zhou, J.J. Jia, J. Carlisle, E. Hudson, L.E. Terminello, F.J. Himsel, and R.C.C. Perera, Proceedings of the Workshop: *Raman Emission by X-Rays* , edited by D.L. Ederer, and J.H. McGuire (World Scientific Publishing 1996)pp. 71-80.
7. D.W. Fischer, and D.W. Baun, J Appl. Phys. **39**, 4757-4763 (1968).
8. T. Åberg, and B. Crasemann, *Resonant Anomalous X-ray Scattering: Theory and Applications*, edited by G. Materlik, C.J. sparks, and K Fischer (Amsterdam: Elsevier Science B.V., 1994) pp. 431-448.
9. T. Åberg, and J. Tulkki, *Atomic Inner Shell Physics*, editor B. Crasemann (Plenum Publishing Corp., New York 1985) pp. 419-462.
10. P. Cowan, *Resonant Anomalous X-ray Scattering: Theory and Applications*, editors G. Materlik, C.J. sparks, and K. Fischer,(Elsevier Science B.V., Amsterdam 1994) pp. 449-472.
11. Y. Ma, N. Wasshahl, P. Skytt, J. Guo, J. Nørdgren, P.D. Johnson, J.-E. Rubensson, T. Boske, W. Eberhardt, and S.D. Kevan, Phys. Rev. Lett. **69**, 2598-2602 (1992).
12. J.J. Jia, T.A. Callcott, E.L. Shirley, J.A. Carlisle, L.J. Terminello, A. Asfaw, D.L.Ederer, F.J. Himpsel, and R.C.C. Perera, Phys. Rev. Letters, **76**, 4054-4059 (1996).
13. K.E. Miyano, D.L. Ederer, T.A. Callcott, W.L. O'Brien, J.J. Jia, L. Zhou, Q.-Y. Dong, Y. Ma, J.C. Woicik, and D.R. Mueller, Phys. Rev. **B48**, 1918-1922 (1993-I).
14. J.A. Carlisle, E.L. Shirley, E.A. Hudson, L.E. Terminello, T.A. Callcott, J.J. Jia, D.L. Ederer, R.C.C. Perera, and F.J. Himsel, Phys. Rev. Letters **74**, 1234-1238 (1995).

Principal investigators: David L. Ederer, Physics Department, Tulane University, New Orleans, LA 70118. E-mail dlederer@mailhost.tcs.tulane.edu and Thomas A. Callcott, Physics Department, University of Tennessee-Knoxville,TN 37996. E-mail : tcallcott@utk.edu

Resonant Inelastic Scattering in Dilute Magnetic Semiconductors by X-Ray Fluorescence Spectroscopy

K. Lawniczak-Jablonska[1,2], J.J.Jia[1], L. Lin[3], T.A. Callcott[3], A. Asfaw[4], J.A. Carlisle[4], L.J. Terminello[4], D.L. Himpsel[5], D.L. Edeler[6], J.H. Underwood[1] and R.C.C. Perera[1]

[1]Lawrence Berkeley Laboratory, Berkeley, CA 94720
[2]Institute of Physics, Polish Academy of Science, 02 668 Warsaw, Poland
[3]University of Tennessee, Knoxville, TN 37996
[4]Lawrence Livermore National Labolatory, Livermore, CA 94551
[5] IBM T.J. Watson Research Center, Yorktown Heights, NY 10598
[6] Tulane University, New Orleans, LA 70118

INTRODUCTION

As modern, technologically important materials have become more complex, element specific techniques have become invaluable in studying the electronic structure of individual components from the system. Soft x-ray fluorescence (SXF) and absorption (SXA) spectroscopies provide a unique means of measuring element and angular momentum selective density of electron states, respectively, for the *valence* and *conducting* bands in complex materials. X-ray absorption and the decay through x-ray emission are generally assumed to be two independent one -photon processes. Recent studies, however have demonstrated that SXF excited near the absorption threshold generate an array of spectral features that depend on nature of materials, particularly on the localization of excited states in s and d-band solids and that these two processes can not be longer treated as independent. Resonant SXF offers thus the new way to study the dynamics of the distribution of electronic valence states in the presence of hole which is bond to the electron low lying in the conduction band. This process can simulate the interaction between hole-electron pair in wide gap semiconductors. Therefore such studies can help in understanding of transport and optics phenomena in the wide gap semiconductors.

EXPERIMENT AND RESULTS

We report the result of Mn and S -L resonant emission in $Zn_{1-x}Mn_xS$ (with x=0.2 and 0.3) and MnS as the energy of exciting radiation is tuned across the Mn and S $L_{3,2}$ absorption edge, along with the resonant excited spectra from elemental Mn as a reference. High resolution x-ray emission spectra were recorded on the Advanced Light Source beamline 8.0 a 5.0 cm period undulator beamline with a spherical grating monochromator operating between 70 eV and 1200 eV. The energy resolution of the monochromator was set to be about 0,3 eV during these measurements. The soft x-ray fluorescence endstation includes a Rowland circle grating spectrometer coupled to photoncounting area detector.

In Fig. 1 we present, as an example, the Mn L -emission spectra of $Zn_{0.8}Mn_{0.2}S$. The sharp resonant with three well resolved peaks, significantly different from the spectrum obtained for "normal" emission, at the Mn L_3 line in MnS and ZnMnS compounds was detected. This indicates on the existence of the well localize 3d Mn antibonding states which are coupled to the hole in valence band. After increasing energy by 3 eV, the three peaks structure disappeared and "normal" spectrum was observed. Additionally, a strong resonant with at the L_2 line was detected for all investigated samples.

In the case of L_3 spectra of elemental Mn and at the S L-emission only systematic appearance of new structure in the spectra with the increase of excitation energy was observed. ZnS is a semiconductor with a wide gap. The substitution of Mn in the position of Zn added the well localized 3d states which have character similar to the well localized excitonic states observed in the insulator. Therefore, we can suspect a atomic like coupling between a hole and excited electron. The significant modification of the resonant emission spectra occurs in very narrow range of excitation energy (3 eV) indicating that the coupling between hole in the valence band and the electron in the conduction bands take place only for states close to the bottom of the conduction band.

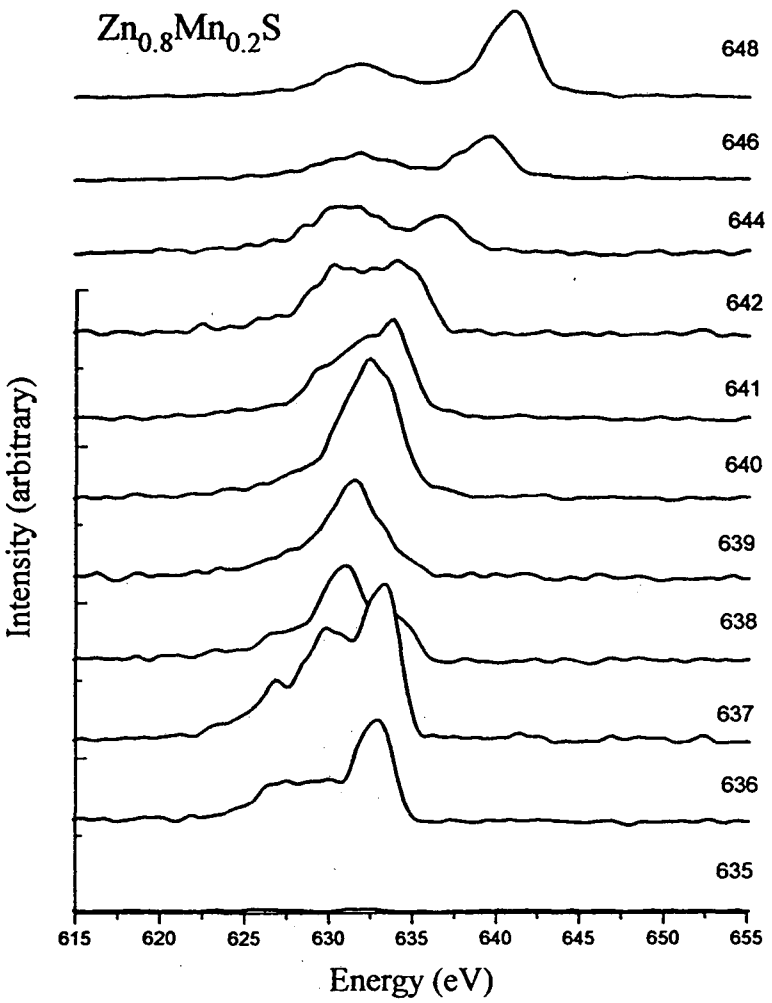

Figure 1. Resonant excited Mn L 2,3 emission spectra of $Z n_{0.8}Mn_{0.2}S$. The exciting radiation energy was tuned from 630 eV to 685 eV, as indicated in the figure.

This work was supported by the Director, Office of Energy Research, Office of Basic Energy Science, Materials Science Division of the U.S. Department of Energy under Contract No. DE-AC03-76SF00098. Author (K. L-J) kindly acknowledges the financial support of the Fulbright Foundation.
Principal investigator: K. Lawniczak-Jablonska, Institute of Physics, Polish Academy of Sciences, Al Lotnikow 32/46, 02 668 Warsaw, Poland. E-mail:jablo@ifpan.edu.pl. Telephone: 48-22-436034.

Soft-X-Ray Fluorescence Study of Buried Silicides in Antiferromagnetically Coupled Fe/Si Multilayers

J.A. Carlisle,[1] A. Chaiken,[1] R.P. Michel,[1] L.J. Terminello,[1] T.A. Callcott,[2] J.J. Jia,[2] D.L. Ederer,[3] R.C.C. Perera,[4] and F.J. Himpsel[5]

[1]Lawrence Livermore National Laboratory, Livermore, CA 94551, USA
[2]University of Tennessee, Knoxville, TN 37996, USA
[3]Tulane University, New Orleans, LA 70118, USA
[4]Lawrence Berkeley National Laboratory, Berkeley, CA 94720, USA
[5]IBM Research Division, Thomas J. Watson Research Center, Yorktown Heights, NY 10598, USA

INTRODUCTION

Multilayer films made by alternate deposition of two materials play an important role in electronic and optical devices such as quantum-well lasers and x-ray mirrors.[1] In addition, novel phenomena like giant magnetoresistance and dimensional crossover in superconductors have emerged from studies of multilayers. While sophisticated x-ray techniques are widely used to study the morphology of multilayer films, progress in studying the electronic structure has been slower. The short mean-free path of low-energy electrons severely limits the usefulness of photoemission and related electron spectroscopies for multilayer studies.

Soft x-ray fluorescence (SXF) is a bulk-sensitive photon-in, photon-out method to study valence band electronic states.[2] Near-edge x-ray absorption fine-structure spectroscopy (NEXAFS) measured with partial photon yield can give complementary bulk-sensitive information about unoccupied states.[3] Both these methods are element-specific since the incident x-ray photons excite electrons from core levels. By combining NEXAFS and SXF measurements on buried layers in multilayers and comparing these spectra to data on appropriate reference compounds, it is possible to obtain a detailed picture of the electronic structure.

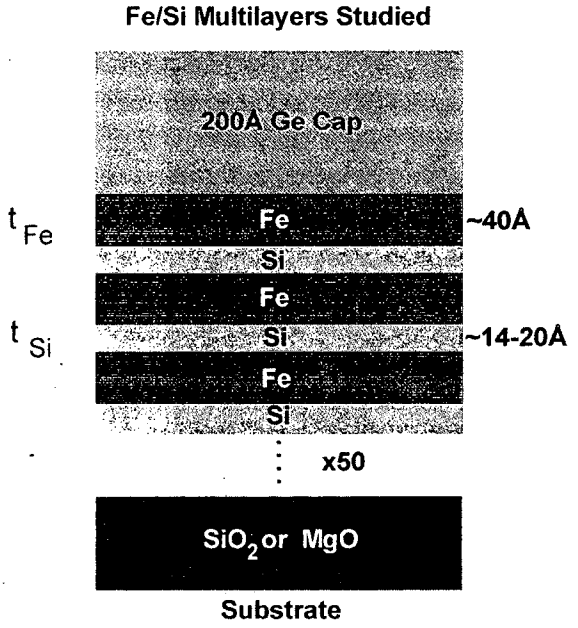

Figure 1. Schematic of the Fe/Si multilayers studied in this work.

The Fe/Si multilayer system (shown in Fig. 1) well illustrates the power of combining the SXF and NEXAFS techniques. Fe/Si multilayers exhibit a large antiferromagnetic (AF) interlayer exchange coupling that is apparently similar to that previously observed in metal/metal multilayers like Fe/Cr.[4] The observation of strong antiferromagnetic coupling was initially surprising, since this coupling is believed to be a manifestation of spin-density oscillations in the non-magnetic metallic spacer layer of a multilayer.[5] The interpretation of the Fe/Si coupling data was hampered by lack of knowledge about the strongly intermixed iron silicide spacer layer, which was variously hypothesized to be a metallic compound in

the B2 CsCl structure[4] or a Kondo insulator in the more complex B20 structure.[6] If the spacer layer is not metallic, then the usual theories of interlayer exchange coupling do not apply[5] and the coupling must involve a novel mechanism. Using transmission electron microscopy (TEM), the spacer layer has been identified as a metastable cubic iron silicide closely lattice-matched to bulk Fe.[7] However, since the exact stoichiometry of the silicide was not determinable by diffraction means, the question of whether the spacer layer is a metal or not has remained unanswerable. SXF and NEXAFS are ideal techniques to resolve exactly this type of issue.

EXPERIMENT

SXF and NEXAFS measurements were performed on five different Fe/Si multilayer films at the Advanced Light Source on beamline 8.0, which is described in detail elsewhere.[8] SXF data has previously been used to study buried layers of BN[9] and Si.[10] Data taken at the Fe L-edge closely resembles bulk Fe for all Fe/Si multilayers. NEXAFS spectra were acquired by measuring the total Si L-emission yield with the same detector used for fluorescence. The resulting data are expected to be comparable to those acquired by electron counting.[3] The films used in this study were grown using ion-beam sputtering (IBS) in a chamber with a base pressure of 2×10-8 torr. The deposition conditions were the same as those used in previous studies.[8] All multilayers were characterized using x-ray diffraction and magnetometry. Reference spectra were obtained from a crystalline silicon (c-Si) substrate piece, an amorphous silicon (a-Si) film made by IBS, and a fragment of an FeSi2 sputter target.

RESULTS

Figure 2 shows the Si L emission spectra and Si L-edge NEXAFS spectra for a crystalline Si reference film and for an epitaxial Fe/Si multilayer grown on an MgO substrate. This multilayer exhibited the high saturation field and low remanent magnetization that are characteristic of antiferromagnetic interlayer exchange coupling [7]. The spectra from the single crystal Si reference clearly show the presence of the fundamental gap, as expected. In comparison to the reference data, the L-emission from the multilayer is quite different, and clearly suggests that the spacerlayers are an Fe silicide (probably Fe-rich) [11]. Furthurmore, the more than 1 eV of overlap between the valence -band features from the SXF and the conduction-band features from NEXAFS is convincing evidence that the silicide is metallic. The data lay to rest any speculation that the interlayer exchange coupling in Fe/Si

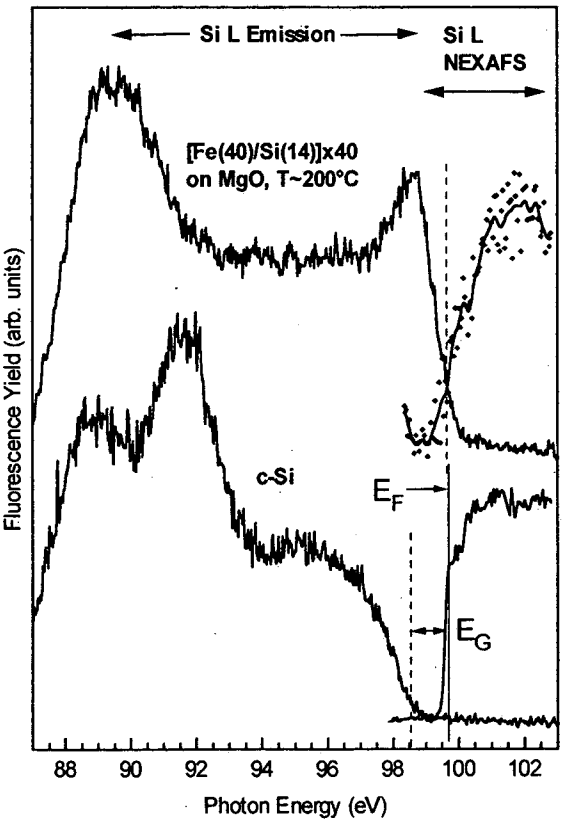

Figure 2. Si L emission and absorption spectra from a single-crystal Si reference (bottom) and an epitaxial Fe/Si multilayer which exhibited antiferromagnetic coupling.

multilayers involves a novel mechanism. In addition, these results on thin buried silidicid layers illustrates the power of photon-in, photon-out spectroscopies with their intrinsic bulk sensitivity, for the study of multilayer films.

ACKNOWLEDGEMENTS

We would like to thank P.E.A. Turchi, P.A. Sterne and J. van Ek for helpful discussions. This work was supported by the Division of Materials Science, Office of Basic Energy Sciences, and performed under the auspices of the U.S. Department of Energy by Lawrence Livermore National Laboratory under contract No. W-7405-ENG-48, by National Science Foundation Grant No. DMR-9017996 and DMR-9017997, by a Science Alliance Center for Excellence Grant from the University of Tennessee, by the U.S. Department of Energy (DOE) Contract No. DE- AC05-84OR21400 with Oak Ridge National Laboratory and by the Louisiana Educational Quality Support Fund and DOE-EPSCOR Grant LEQSF (93-95)-03 at Tulane University. This work was performed at the Advanced Light Source, which is also supported by the Office of Basic Energy Sciences, U.S Department of Energy, under contract No. DE-AC03-76SF00098.

REFERENCES

1. Synthetic Modulated Structures, eds. L.L. Chang and B.C. Giessen, Academic Press, Orlando (1985).
2. D.L. Ederer, T.A. Callcott and R.C.C. Perera, Synchr. Rad. News 7, 29 (1994).
3. J. Stöhr, NEXAFS Spectroscopy, (Springer Verlag, New York, 1992).
4. E.E. Fullerton, J.E. Mattson, S.R. Lee, C.H. Sowers, Y.Y. Huang, G. Felcher, S.D. Bader, and F.T. Parker, J. Appl. Phys. 73, 6335 (1993).
5. K.B. Hathaway in Ultrathin Magnetic Structures, eds. J.A.C. Bland and B. Heinrich, (Springer Verlag, New York, 1994).
6. J.E. Mattson, S. Kumar, E.E. Fullerton, S.R. Lee, C.H. Sowers, M. Grimsditch, S.D. Bader and F.T. Parker, Phys. Rev. Lett. 71, 185 (1993).
7. A. Chaiken, R.P. Michel, and M.A. Wall, Phys. Rev. B, "Structure and Magnetism of Fe/Si Multilayers Grown by Ion-Beam Sputtering," in press.
8. IBM/TENN/TULANE/LLNL/LBL beamline, described further in J.J. Jia, T.A. Callcott, J. Yurkas, A.W. Ellis, F.J. Himpsel, M.G. Samant, J. Stöhr, D.L. Ederer, J.A. Carlisle, E.A. Hudson, L.J. Terminello, D.K. Shuh and R.C.C. Perera, Rev. Sci. Instrum. 66, 1394 (1995).
9. J.A. Carlisle, L.J. Terminello, E.A. Hudson, R.C.C. Perera, J.H. Underwood, T.A. Callcott, J.J. Jia, D.L. Ederer, F.J. Himpsel, and M.G. Samant, Appl. Phys. Lett. 67, 34 (1995).
10. R.C.C. Perera, C.H. Zhang, T.A. Callcott and D.L. Ederer, J. Appl. Phys. 66, 3676 (1989); P.O. Nilsson, J. Kanski, J.V. Thordson, T.G. Andersson, J. Nordgren, J. Guo and M. Magnuson, Phys. Rev. B52, R8643 (1995).
11. J.J. Jia, T.A. Callcott, W.L. O'Brien, Q.Y. Dong, D.R. Muller, D.L. Ederer, Z. Tan, and J.I. Budnick, Phys. Rev. B46, 9446 (1992).

Principal investigator: John A. Carlisle, Department of Physics, Virginia Commonwealth University. Email: jacarlis@vcu.edu. Telephone: 804-828-5443.

Sulfur $L_{2,3}$ Soft-X-Ray Fluorescence of CdS and ZnS

L. Zhou,[1] T.A. Callcott,[1] J.J. Jia,[1] D.L. Ederer,[2] and R.C.C. Perera[3]
[1]Department of Physics, University of Tennessee, Knoxville, Tennessee 37996, USA
[2]Department of Physics, Tulane University, New Orleans, Louisiana 70118, USA
[3]Advanced Light Source, Ernest Orlando Lawrence Berkeley National Laboratory, University of California, Berkeley, California 94720, USA

INTRODUCTION

The II-VI sulfur compounds CdS and ZnS have important electro-optics applications. In addition, they have well characterized and relatively simple structures so that they are good candidates for theoretical model development in solid-state physics. Some experimental results on density of states have been reported, mostly determined from photoemission measurements, and theoretical calculations are available for both materials. Nevertheless the electronic properties of these elements are still not completely understood. It has been established that the d-bands, derived from Cd or Zn, lie in a subband gap between a lower valence band (LVB) derived from the S 3s orbital and an upper valence band (UVB) derived from the 3p states of S and the 4(3)s states of Cd(Zn). The locations of these bands within the gap disagree with the best available calculations, however.

The principal problem is that experimental photoemission meaurements[1] locate the d-bands about 2 eV lower in the band gap than the best available calculations.[2-4] Some authors argue that the hole in the d-band in the final state of the photoemission process increases the binding of the d-electrons. In any case, band gaps, band widths and the precise location of d-bands are important parameters for comparing experiment and theory, and no current calculations give good agreement with all of these parameters. Moreover, photoemission data does not adequately define all of these experimental parameters, because the d-state photoemission dominates that from s and p states and sample charging effects can modify the energy of emitted electrons. A few soft x-ray absorption and emission results have been reported.[5,6] These e-beam excited K and $L_{2,3}$ spectra of CdS are of very good quality, but are not accurately interpreted.[6]

In this abstract, we report photon excited soft x-ray fluorescence (SXF) S $L_{2,3}$ spectra from CdS and ZnS. Using excitation between the L_2 and L_3 thresholds, the L_2 spectrum is suppressed, which permits us to accurately determine features of the UVB and LVB as well as the placement of the Cd(Zn) d-bands between the UVB and LVB. We note that these spectra are produced by dipole transition to the S 2p core levels so that they provide a measure of the angular momentum resolved (s and d)-like local partial density of states ([s+d]-LPDOS) at the S site. Further details of these experimental results have been published elsewhere.[7]

EXPERIMENTAL RESULTS

These experiments were carried out on undulator beamline 8.0 at the Advanced Light Source (ALS) using the Soft X-ray spectrometer endstation operated by the Tennessee/ Tulane/LBNL/LLNL collaboration.[8] Spectra were excited with monochromatized photons from the undulator having energies from 160 to 185 eV and a resolution of 0.4 eV. The emission spectrometer is a Rowland circle design fitted with a photon counting area detector. At the energy of these spectra (142-162 eV), the detector could be centered at 152 eV to record the full spectrum without moving the detector. Spectral resolution is about 0.2 eV.

In Figure 1, sulflur emission spectra from CdS excited by 3 KeV electrons and 174 eV photons are compared. Spectral regions associated with the UVB (155-160 eV), LVB (145-151 eV) and with overlap transitions from the Cd d-bands (151-153 eV) may be identified. A significant feature is that the photon excited spectra are sharper and better resolved than the e-beam excited spectra. These $L_{2,3}$ spectra are produced by transitions to S $2p_{1/2}$ and $2p_{3/2}$ core levels having a separation of 1.1 eV. The doubling of the spectra with a relative magnitude of approximately 2:1 is clearly seen in the d band peaks d1 and d2, and in broadening at the upper edge of the LVB.

Figure 2 illustrates the suppression of the SL_2 spectrum in CdS with photon excitation between the L_3 and L_2 thresholds. With 163 eV photons, only the L_3 spectrum is excited. The d-band peak d2 is completely suppressed, as is the high energy shoulder of the LVB. An important result of this suppression is that an additional feature of the d-band (d3) is uncovered.

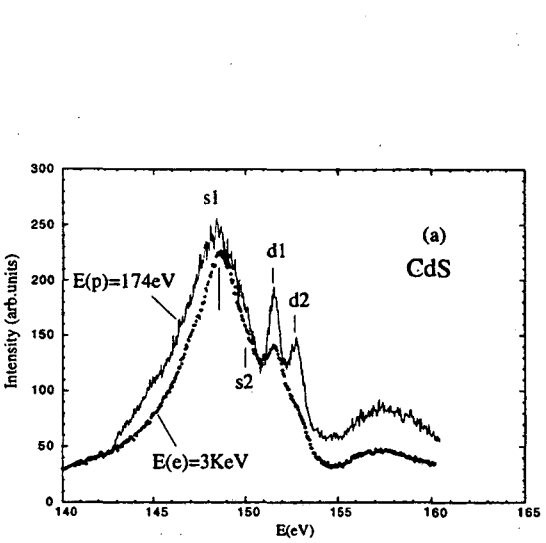

Figure 1. Comparison of S $L_{2,3}$ spectra of CdS for 3 keV electron-beam and 174 eV photon excitation.

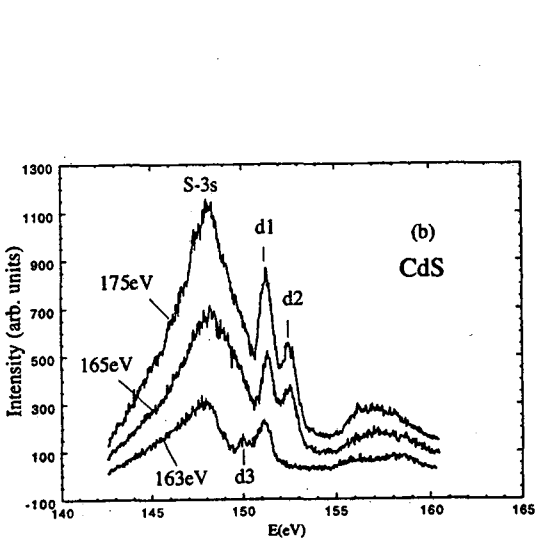

Figure 2. S $L_{2,3}$ spectra of CdS with photon excitation near threshold. The L_2 spectrum is suppressed with 163 eV excitation.

In Figures 3 and 4, we display the clean L_3 spectra of CdS and ZnS on an energy scale with zero at the top of the UVB and identify significant spectral features. The top and bottom and other features of the UVBs are clearly resolved, as is the peak of the LVBs. The d-bands in both compounds are shown to have a doublet structure and are accuratedly located with respect to both the UVB and LVB. In Table I, the energy positions of significant spectral features are determined and compared with published calculations. As with photoemission results, the major discrepancy is in the position of the d-bands in the subband gap.

Table I. Energy positions of principal features in the S L_3 spectra of CdS and ZnS in units of eV. UT, upper edge of the UVB; UB, lower edge of the UVB; U1,U2,U3, peaks in the UVB; Calc., results from theory; Expt., our data.

Spectral Feature	CdS (Expt.)	CdS (Calc.)[a]	ZnS (Expt.)	ZnS (Calc.)[b]
UT	0.0	0.0	0.0	0.0
U1	-1.8	-1.1	-1.9	-2.0
U2	-3.8	-4.3	-3.0	
U3			-4.7	-4.5
UB	5.4		6.0	
d1	-9.0	-7.8	-8.4	
d3	-10.1		-9.1	
S 3s	-12.2	-11.6	-12.4	-12.0
ΔE (d1-d3)	1.05	<0.6	0.6	
Ratio (d1/d3)	0.40		0.41	
ΔE (d1-d2)[c]	1.15	1.18	1.18	

[a]Reference 3. [b]Reference 2. [c]2p spin splitting from $L_{2,3}$ spectra.

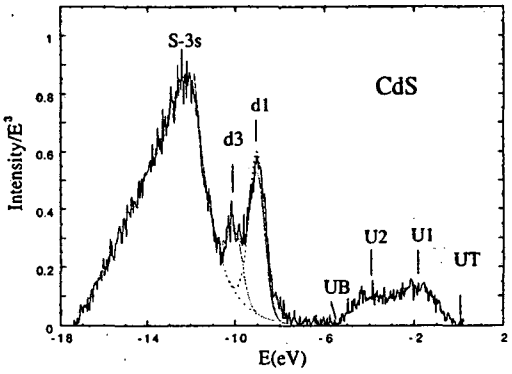

Figure 3. The S L_3 spectrum of CdS with excitation between the L_3 and L_2 thresholds.

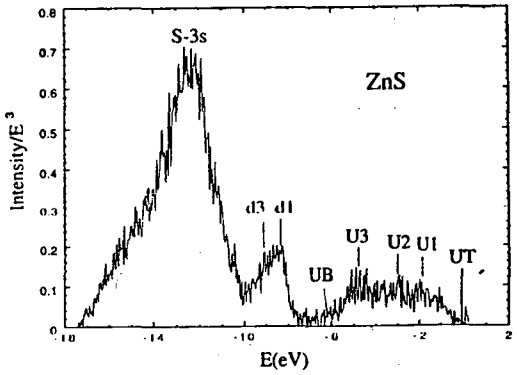

Figure 4. The S L_3 spectrum of ZnS with excitation between the L_3 and L_2 thresholds.

In Figure 5, the L_3 spectrum of CdS is compared with experimental and theoretical results. The e-beam excited S-K spectrum, which provides a measure of the p-like partial density of states (p-LPDOS), resolves the UVB and barely sees the d-bands, but is blind to the LVB. The XPS spectrum is dominated by the d-bands and resolves the UVB, but is also blind to the LVB. The L_3 spectrum, which is a measure of the [s+d]-LPDOS at the S site resolves all three valence regions, and accurately locates the d-bands with respect to the UVB and LVB. We note that both XPS and SXF measurements locate the d-bands in the same position with respect to the UVB, which is not surprising since both processes have the same final state, which includes a valence hole.

The interested reader is referred to the journal publication for a more detailed discussion of these results.[7] It is clear, however, from the data presented that SXF fluorescence studies can make important contributions to our understanding of the electronic properties of compounds.

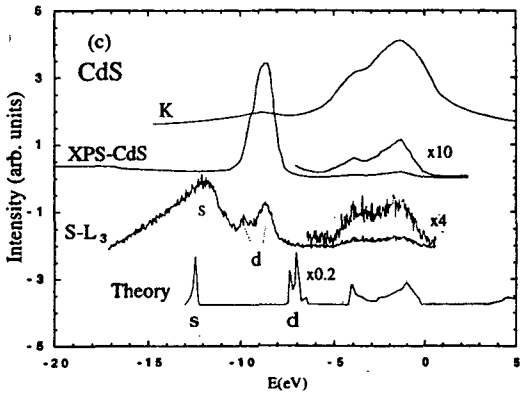

Figure 5. Comparison of experimental and theoretical results for CdS.

REFERENCES

1. L. Ley et al., Phys. Rev. B **9**, 600 (1974).
2. M.-Z. Huang and W.Y. Ching, Phys. Rev. B **47**, 9449 (1993).
3. Y.-N. Xu and W.Y. Ching, Phys. Rev. B **48**, 4335 (1993).
4. P. Schroer et al., Phys. Rev. B **47**, 6971 (1993).
5. C. Sugiura et al., J. Phys. Soc. Jap. **29**, 1645 (1970).
6. C. Sugiura et al., J. Phys. Soc. Jap. **31**, 1784 (1971).
7. L. Zhou et al., Phys. Rev. B **55**(8), (1997).
8. For a description of beamline and endstation, see ALS First Phase Scientific Program, LBL publication LBL-PUB-706, pp. 11-16 (1992).

This work was supported by National Science Foundation grant DMR-9420425 and by the authors institutions, and was carried out at the Advanced Light Source at Lawrence Berkeley National Laboratory operated under Contract No. DE-AC03-76SF00098 with the U.S. Department of Energy.

Principal investigator: T.A. Callcott, Department of Physics, University of Tennessee. Email: tcallcott @utk.edu. Telephone: 423-974-6765.

X-Ray Emission Spectroscopy Applied to Glycine Adsorbed on Cu(110): An Atom and Symmetry Projected View

J. Hasselström[1], O. Karis[1], M. Nyberg[2], M. Weinelt[1], N. Wassdahl[1], A. Nilsson[1], L. G. M. Pettersson[2], J. Stöhr[3] and M. Samant[3]

[1]Dept. of physics, Uppsala University, Box 530, S-75221 Uppsala, Sweden
[2]Institute of theoretical physics, University of Stockholm, Vanadisvägen 9, S-113 46 Stockholm, Sweden
[3]IBM Research division, Almaden research center, 650 Harry Road, San Jose, California 95120-6099, USA

When a molecule is adsorbed on a metal surface by chemical bonding new electronic states are formed. For noble and transition metals these adsorption-induced states overlap with the much more intense metal d-valence band, making them difficult to probe by for instance direct photoemission. However, it has recently been shown that X-ray emission spectroscopy (XES) can be applied to adsorbate systems [1]. Since the intermediate state involves a core hole, this technique has the power to project out the partial density of states around each atomic site. Both the excitation and deexcitation processes are in general governed by the dipole selection rules. For oriented system, it is hence possible to obtain a complete separation into $2p_x$, $2p_y$ and $2p_z$ contribution using angular resolved measurements.

We have applied XES together with other core level spectroscopies to glycine adsorption on Cu(110). Glycine (NH_2CH_2COOH) is the smallest aminoacid and very suitable to study by core level spectroscopy since it has several functional groups, all well separated in energy by chemical shifts. Its properties are furthermore of biological interest.

The experiments were carried out at the undulator beamline 8.0 at the Advanced Light Source (ALS), Lawrence Berkeley Laboratory using a modified spherical grating monochromator. The experimental station consist of two UHV chambers, one for sample preparation and one for analysis. The analyze chamber consist of an electron analyzer (Scienta SES 200) and an X-ray Emission spectrometer both mounted perpendicular to the incoming beam. It also houses a partial yield detector for XAS measurements. All measurements were performed using grazing incidence. Glycine was evaporated from a well outgassed, resistively heated Knudssen cell. The sample temperature was kept at 400 K during the evaporation.

Glycine adsorbs on a clean Cu(110) surface via loss of the acidic hydrogen atom. It exhibits a sharp (3x2) LEED pattern. The Cu(110) surface has two-fold symmetry where the copper atoms in the first layer are oriented in characteristic rows along the [110]-azimuth. Two crystals were mounted, rotated 90° with respect to each other, enabling us to measure absorption- and X-ray emission-spectra in three different directions.

X-ray absorption spectroscopy, also denoted NEXAFS, has been shown to be a powerful technique for determination of molecular orientations on surfaces [2]. In Fig. 1 we show the C 1s, N 1s and O 1s XA spectra in three directions. These results, together with the obtained LEED pattern enabled us to determine the adsorption geometry of the molecule [3]. The proposed geometry is further supported by density functional calculations. Glycine adsorbs with the carboxylic group aligned along the closed packed Cu [110]-rows in a geometry close to parallel to the surface, bonding not only with the oxygen atoms but also with the nitrogen end on the neighboring Cu [110]-row.

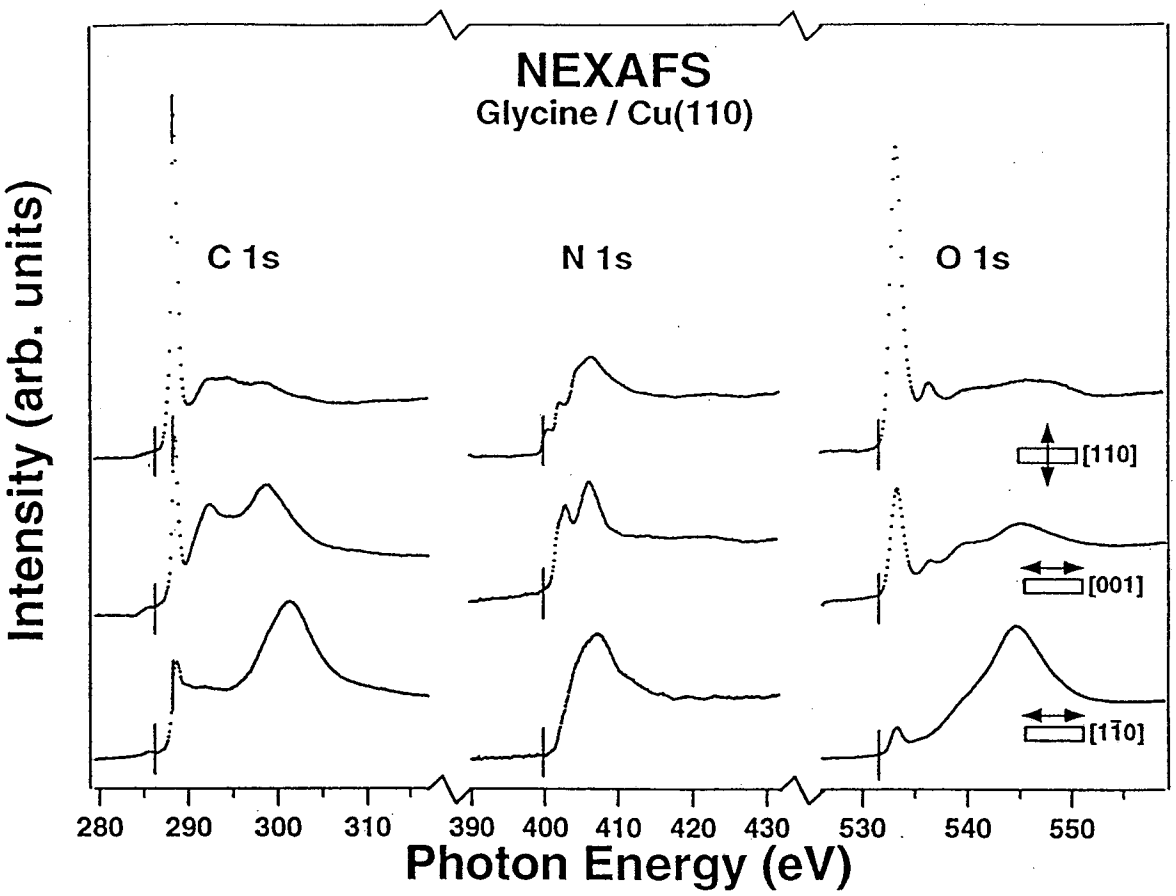

Fig. 1 O 1s, C 1s and N 1s absorption spectra obtained for glycine adsorbed on Cu(110). Using two crystals oriented 90° with respect to each other enabled us to obtain absorption spectra along three different azimuths. The respective XPS binding energies are marked with a line in the figure.

The absorption spectra are furthermore important when applying XES to the system. If the photon energy used to create the corehole in the first process is far above the excitation threshold there is a large probability of creating multi-electron excited states. The presence of additional initial states for the decay process will give rise to X-ray satellites overlapping the pure "one electron" states. However, by using a tuneable synchrotron radiation source, threshold excitation can be performed, thereby suppressing the multiply excited states. The presence of the extra electron will, for chemisorbed system, not modify the spectra [4]. On the timescale of the decay the electron becomes delocalized, creating a fully relaxed initial corehole state. For intensity reasons both the excitation energy and geometry used in this study have been tuned to match the most intense absorption features, usually the π^*-resonance's.

As mentioned, the two carbon atoms in glycine shows a core level chemical shift. It is therefore possible to selectively excite each core level separately. Fig. 2 shows angular resolved XE spectra measured on 4 different atomic sites [5]. The spectra have been put on a binding energy scale by using the corresponding XPS binding energy as Fermi level. This gives us the possibility to directly observe the hybridization of the molecular orbitals and further determine the weight of a specific orbital on the different atoms in the molecule. Hence, states which are best described as being lone-pair orbitals will only be observed on one specific atom. Regarding the bonding to the surface we directly observe new hybrid states between the substrate metal valence bands and the glycine valence levels, close to the Fermi level. Hybridization mainly occurs between orbitals of $2p_x$ and $2p_z$ character whereas orbitals of $2p_y$-type to a large extend keeps its molecular character. In fact, the obtained result is like an experimental version of the LCAO (linear combination of atomic orbitals) approach for molecular orbital theory.

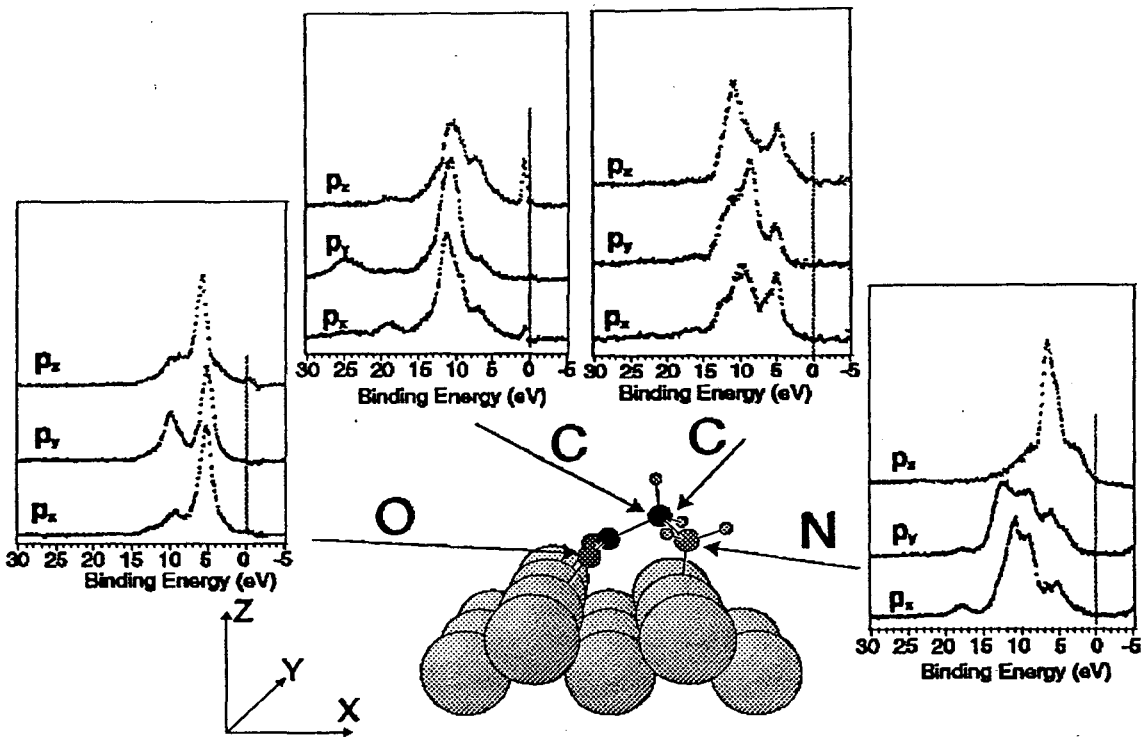

Fig. 2 $2p_X$, 2py and $2p_Z$ symmetry resolved X-ray emission spectra for glycine adsorbed on Cu(110). Inserted is a structural model of the adsorption complex [3]. The spectra are measured at the O atom, both C atoms and the N atom. The valence $2p_X$, $2p_Y$, $2p_Z$ orbitals were obtained by a suitable linear combination of XE spectra measured at different emission angles.

In summary, we have shown that it is possible to apply XES to more complicated molecular adsorbates. The assignment of different electronic states is however not as straight forward as for simple diatomic molecules. For a complete understanding of the redistribution and formation of new electronic states associated with the surface chemical bond, experimental data must be compared to theoretical calculations.

The authors wish to thank the ALS staff for all their assistance. This work was supported by the Swedish Natural Science Research Council (NFR) and by Göran Gustafsson Foundation for Research in Natural Science and Medicine.

REFERENCES

1. N. Wassdahl, A. Nilsson, T. Wiell, H. Tillborg, L. C. Duda, J. H. Guo, N. Mårtensson, J. Nordgren, J. N. Anderssen and R. Nyholm Phys. Rev. Lett. **69**, 812 (1992)
2. J. Stöhr, NEXAFS spectroscopy (Springer Verlag, Heidelberg, 1992)
3. J. Hasselstöm, O. Karis, M. Nyberg, M. Weinelt, N. Wassdahl, A. Nilsson, L. G. M. Pettersson, J. Stöhr and M. Samant to be published
4. A. Sandell, O. Björneholm, A. Nilsson, J. N. Anderssen, B. Hernnäs and N. Mårtensson Phys. Rev. **B49**, 10136 (1994)
5. M. Nyberg, O. Karis, J. Hasselström, M. Weinelt, N. Wassdahl, A. Nilsson, L. G. M. Pettersson, J. Stöhr and M. Samant to be published

Principal investigator: Anders Nilsson, Department of physics, Uppsala University. Email: anders.nilsson@fysik.uu.se. Telephone: +46 18 183609

Beamline 9.0.1 Abstracts

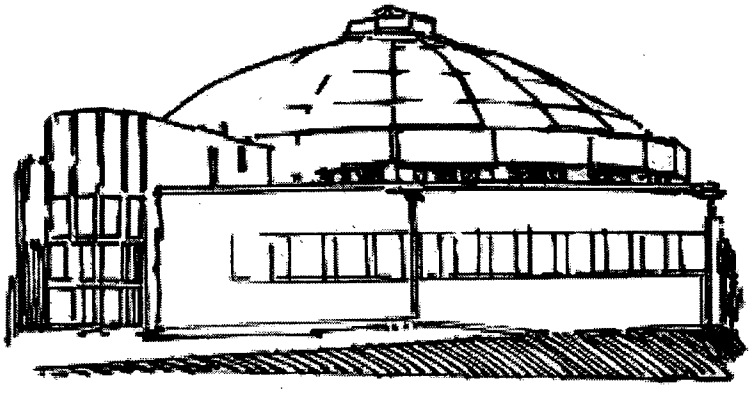

An Electron Spectrometer for Gas-Phase Spectroscopy

J.D. Bozek and A.S. Schlachter

Advanced Light Source, Ernest Orlando Lawrence Berkeley National Laboratory,
University of California, Berkeley, California 94720, USA

INTRODUCTION

An electron spectrometer for high-resolution spectroscopy of gaseous samples using synchrotron radiation has been designed and constructed. The spectrometer consists of a gas cell, cylindrical electrostatic lens, spherical-sector electron energy analyzer, position-sensitive detector and associated power supplies, electronics and vacuum pumps. Details of the spectrometer design are presented together with some representative spectra.

DESIGN OF THE SPECTROMETER

The spectrometer is represented schematically in Fig. 1. A differentially pumped gas cell is aligned with the photon beam axis and forms the interaction region for the spectrometer. The interaction volume in the gas cell is contained within a differentially pumped 7mm diameter cylindrical hole in a block of copper. Beam throttles are attached to the front and back of the interaction volume, a slit is oriented towards the lens, and an electron dump is fitted opposite the slit to reduce the number of back scattered electrons reaching the analyzer.[1] A four element cylindrical electrostatic lens transports, focuses and accelerates the electrons towards the energy

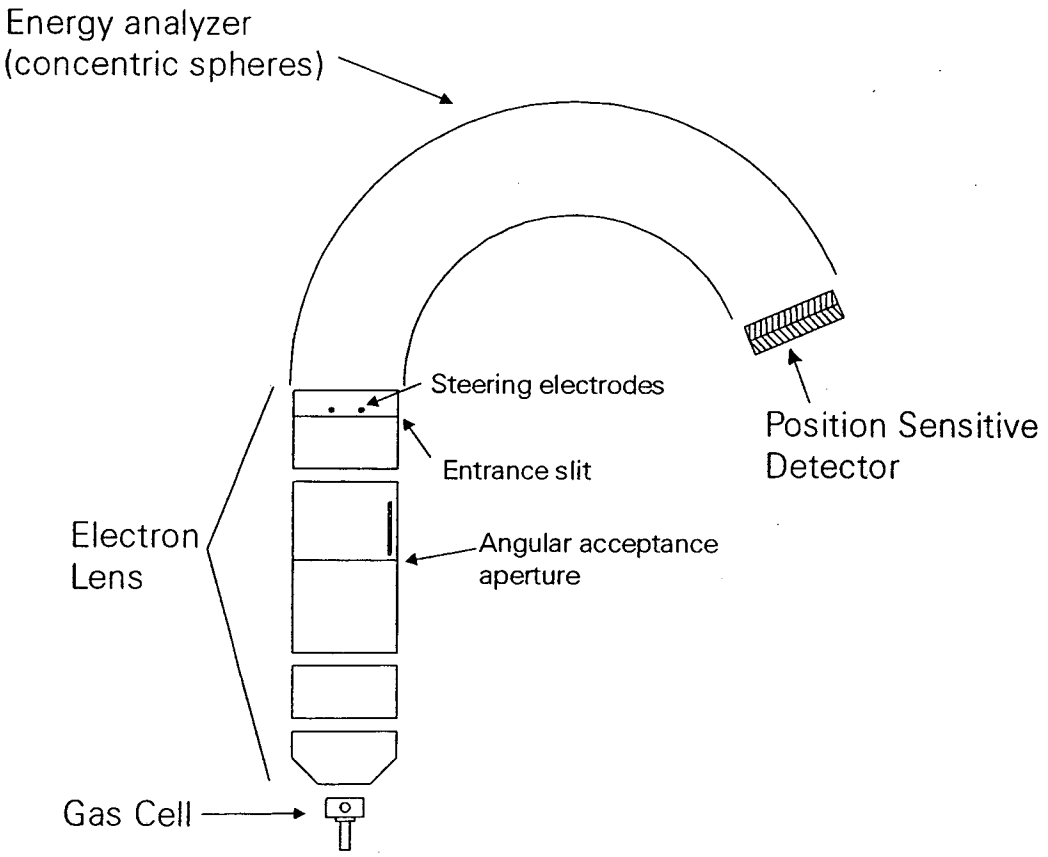

Figure 1. Schematic drawing of the electron spectrometer.

analyzer. The dimensions of the lens elements and the voltages applied to them were determined based on electrostatic modeling calculations carried out using SIMION.[2] The first element of the electrostatic lens contains an aperture to control the angular acceptance of the spectrometer as well as provide differential pumping of the lens. Another aperture in the third element of the lens serves to further control the angular acceptance of the lens. The entrance slit for the electron energy analyzer is fitted into the forth element of the lens and followed by two cylindrical electrodes for steering purposes.[1]

Electrons transported by the lens and passed through the entrance slit are dispersed in energy by a large spherical-sector electron energy analyzer. Spherical-sector electrodes from a McPherson ESCA-36 spectrometer were modified for the purpose. The 36cm mean radius spherical-sector electrodes (157° tangential, 60° azimuthal) were modified with Herzog plates and azimuthal field terminating electrodes to facilitate their use as a pass energy filter for the spectrometer. A two dimension 25mm active area resistive anode position sensitive detector from Quantar Technology Inc.[3] is used as the detector for the system. The second dimension of the detector (in the non-dispersive direction) proved essential for tuning the resolution of the spectrometer allowing the shape of the lines at the detector to be adjusted.

To achieve the required accurate and stable voltages to all of the electrostatic elements in the spectrometer, a custom made computer controlled power supply was designed and constructed at LBNL by J. Katz and Y. Zaninovich. The power supply provides voltages of up to 1000V with 1.5meV resolution. The power supply was designed so that all of the voltages for the spectrometer float on the retarding voltage and the interdependence of various potentials in the spectrometer was taken into account.

PERFORMANCE OF THE SPECTROMETER

The performance of the spectrometer was determined by measuring various photoelectron lines and Auger lines of simple gaseous samples using beamline 9.0.1. A photoelectron spectrum of the Ar3p lines measured at 39.6eV is shown in Fig. 2. The width of the lines, which contain contributions from the natural width of the state, the photon band pass and the electron

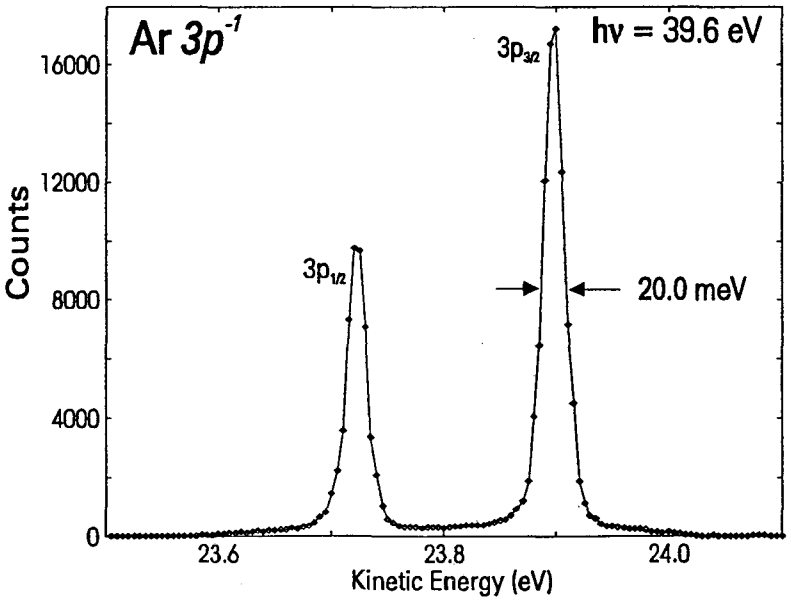

Figure 2. Photoelectron spectrum of the Ar 3p levels measured with 39.6 eV photons from beamline 9.0.1.

spectrometer resolution is dominated by the contribution from the electron spectrometer. The spectrum in Fig. 2 represents the best resolution achieved with the spectrometer to date, 20meV, but future improvements in the magnetic shielding should yield improvements in the resolution.

Photoelectron spectra of molecular core levels measured with the resolution of this spectrometer will often show vibrational fine structure. A photoelectron spectrum of the C 1s level of CH_4 measured using a photon energy of 305eV is shown in Fig. 3. The series of photoelectron bands in this spectrum are due ionization of the C 1s electrons accompanied by excitation of C—H symmetric stretching vibrations in the ion state.[4] The vibrational bands in this spectrum have a full width at half maximum (FWHM) of approximately 188meV and are spaced about 390 meV apart.

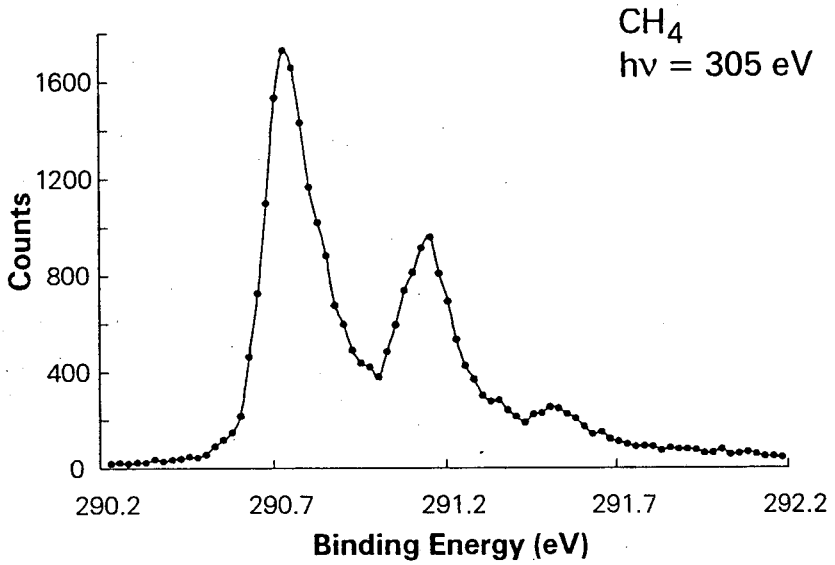

Figure 3. Photoelectron spectrum of methane measured with 305eV photons from beamline 9.0.1.

SUMMARY

A high-resolution electron spectrometer for gas phase spectroscopy at the ALS has been built and tested. The spectrometer performs adequately for vibrationally resolved photoelectron spectroscopy of core levels, although improvements in the resolution can be made.

REFERENCES

1. P. Baltzer, L. Karlsson, M. Lundquist, and B. Wannberg, Rev. Sci. Instrum, **64**, 2179 (1993).
2. D.A. Dahl and J.E. Delmore, computer code SIMION)Idaho National Engineering Laboratory, EG&G Idaho Inc., Idaho Falls, ID, 1988.
3. Quantar Technology Incorportated, 3004 Mission Street, Santa Cruz, CA 95060.
4. U. Gelius, L. Asplund, E. Basilier, S. Hedman, K. Helenelund and K. Siegbahn, Nucl. Instrum. And Methods, **B1**, 85 (1984).

This work was supported by the Director, Office of Energy Research, Office of Basic Sciences, Materials Science Division, of the U.S. Department of Energy under Contract No. DE-AC03-76SF00098.

Principal investigator: John Bozek, Advanced Light Source, Ernest Orlando Lawrence Berkeley National Laboratory. Email: JDBozek@lbl.gov. Telephone: 510-486-4967.

Beamline 9.0.1—A High-Resolution Undulator Beamline for Gas-Phase Spectroscopy

J.D. Bozek, P.A. Heimann, and D. Mossessian

Advanced Light Source, Ernest Orlando Lawrence Berkeley National Laboratory
University of California, Berkeley, California 94720, USA

INTRODUCTION

Beamline 9.0.1 at the Advanced Light Source is an undulator beamline with a Spherical Grating Monochromator (SGM) which provides very high resolution and flux over the photon energy range 20-320eV. The beamline has been used primarily by the atomic and molecular science community to conduct spectroscopy experiments using electron, ion and fluorescence photon detection. A description of the beamline and its performance will be provided in this abstract.

OPTICAL CONFIGURATION

The optical configuration of beamline 9.0.1 is represented schematically in Fig. 1 where the positions and mirror radii of the important elements in the beamline are also indicated. The beamline was first commissioned in August, 1994 when an 8 cm period undulator in the ALS storage ring was used as the source for the beamline. The 8cm period undulator was replaced with a 10cm period undulator in January, 1995 to accommodate the Chemical Dynamics beamline which shares the undulator. A horizontal beam defining aperture (HBDA), which consists of two motor driven jaws which can open and close about the photon beam axis, is located between the undulator and the first mirror in the beamline. The HBDA can be used to reduce the power load on the optics by masking unwanted off-axis radiation from the undulator. The first mirror, M1, is a spherical mirror which forms a horizontal image of the source at the sample position. The second mirror, M2, also spherical, vertically condenses the photon beam onto the entrance slit with an 8:1 demagnification. The demagnification of the source preserves the high flux of the undulator beam through the narrow slits required for high resolution with the monochromator. The entrance slit is fixed in position but has a variable (0-100μm) width. One of three spherical gratings with line densities of 380, 925 and 2100 lines/mm is selected, depending upon the photon energy, to disperse the radiation. The 380, 925 and 2100 lines/mm gratings cover the approximate photon energy ranges 20-60, 40-120 and 100-300 eV respectively. The M1, M2, entrance slit and gratings are all water cooled to reduce thermal distortions. Following the grating, the exit slit translates over a range of ~700mm to satisfy the grating focus condition. The M3 mirror is a bendable mirror with a variable radius of 35-65m and refocuses the beam vertically from the exit slit to the experimental interaction region. Two plane mirrors, M4 and M5, can be translated into the beam to deflect the photon beam horizontally into one of the side branches of the beamline.

PERFORMANCE OF BEAMLINE 9.0.1

The design goals for beamline 9.0.1 were to provide 10^{12} photons per second with a resolving power ($\lambda/\Delta\lambda = h\nu/\Delta h\nu$) of 10,000.[1] The photon flux through the beamline was verified during the commissioning of the beamline by monitoring the flux at the end of the beamline using a GaAsP photodiode.[2] The entrance and exit slits were set for a slit-limited resolving power of 10,000 for the flux measurements. The measured results are show in Fig. 2 together with the photon flux

determined from calculations based on the output of the undulator, the reflectivity of the mirrors and the efficiencies of the gratings.[1]

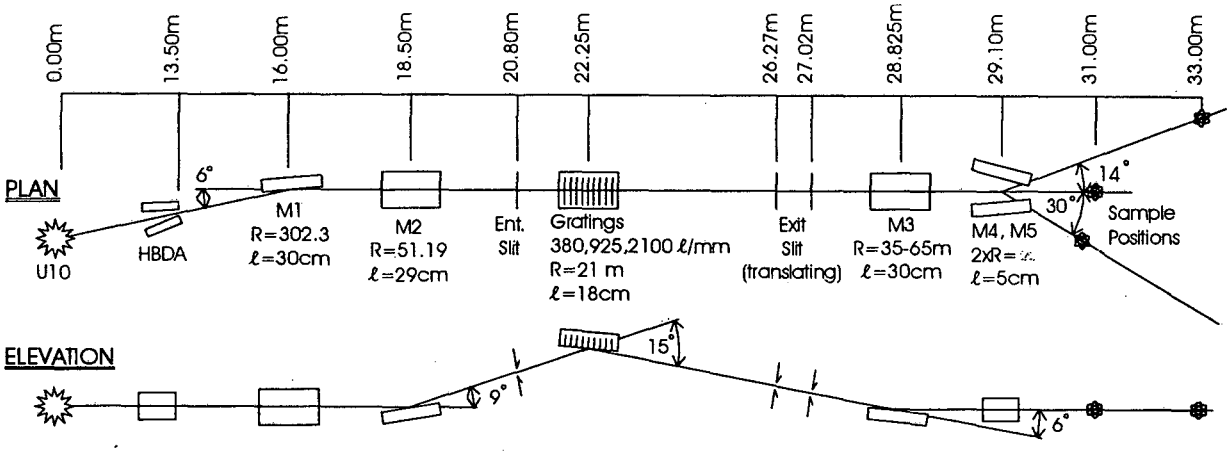

Figure 1. Schematic representation of Beamline 9.0.1. The distances of each of the components from the center of the source point (undulator) is given along the top of the figure. The radii and polished lengths of the mirrors and gratings are given.

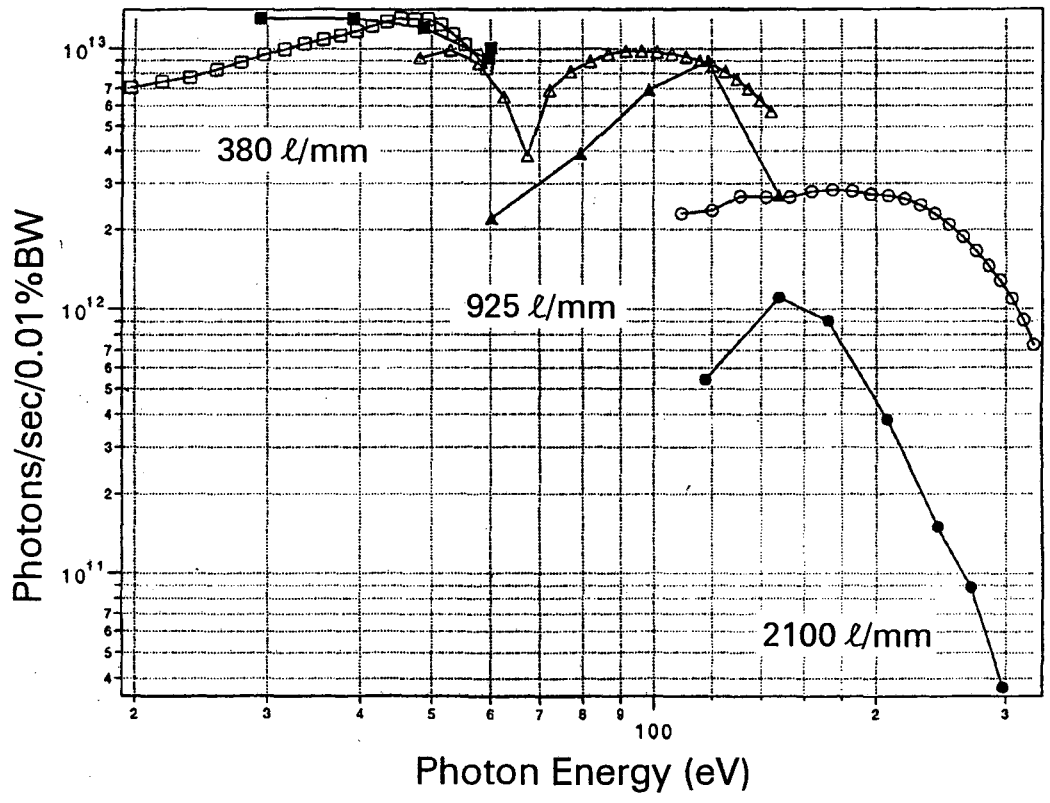

Figure 2: Photon flux of beamline 9.0.1 with the slits set for a resolving power of 10,000 over the energy range from 20-300 eV. Measured data points are shown by the solid symbols while the calculated flux is shown with the open symbols for each of the three gratings.

The size of the photon beam at the focus was characterized using a 20μm diameter pinhole located 31m from the source.[2] The pinhole was translated vertically and horizontally through the focus on an XY stage. The beam was found to have a Gaussian cross section in the horizontal direction with a FWHM of 675μm, a result in satisfactory agreement with the expected beam size. The vertical image size was found to be 30μm which is close to the expected value resulting from the 20μm pinhole and the 20μm exit slit setting that was used.

The beamline 9.0.1 SGM was designed with the goal of achieving or surpassing a resolution ($\Delta\lambda/\lambda = \Delta E/E$) of 10^{-4} over the entire photon energy range.[1] Several factors contribute to the resolution of an SGM, the dispersion of the grating, the widths of the entrance and exit slits, the figure of the gratings and contributions from the various aberrations. At most photon energies, coma is the aberration which has the greatest contribution to the resolution of an SGM. The calculated resolution of the beamline 9.0.1 SGM is shown in Fig.3, where contributions from coma are shown by dashed lines and contributions from 10μm slits are shown by solid lines for each of the three gratings in the beamline. It can be seen that a resolving power of greater than 10,000 can be achieved at all photon energies above 25eV. Below 80eV, coma is the resolution limiting factor at most energies except those close to the Rowland circle energies. At the Rowland circle energy the coma vanishes and the resolution of the SGM is limited by the width of the slits and other usually less important aberrations of the spherical grating. Contributions from these other aberrations are not shown here, but at energies other than the Rowland circle energies their contribution to the resolution of the SGM is about an order of magnitude less than that of coma. Very high resolving power can be achieved near those energies where the coma drops to zero. In a dramatic examples of high spectral resolution near the Rowland circle energy for the 925 lines/mm grating, a very narrow doubly excited state of He, the $(2,-1_3)$ state, occurring at a photon energy of 64.119 eV was measured to have a width of 1.0 meV.[3] This corresponds to a resolving power of 64,000.

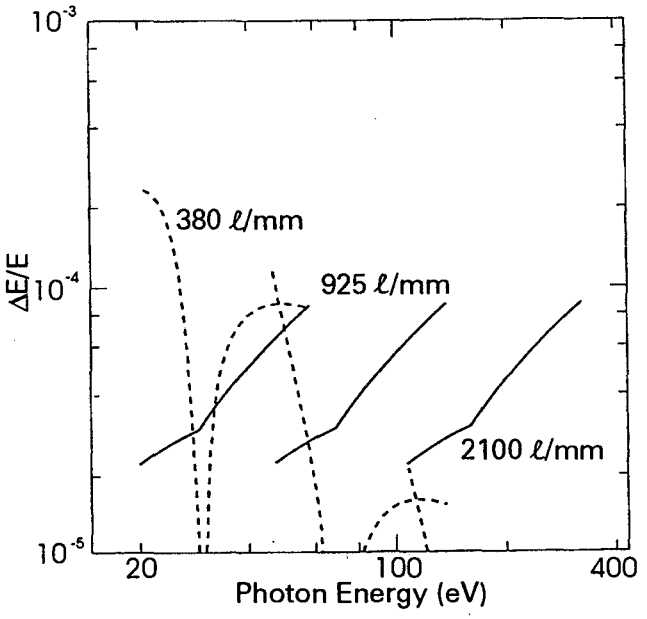

Figure 3. Resolution of the beamline 9.0.1 SGM showing contributions from coma by dashed lines and from 10μm entrance and exit slits by the solid lines for each of the three gratings.

Photoionization yield spectra of the rare gases Ar, Kr and Xe are shown in Figs. 4 - 7 to illustrate the performance of the beamline for all three gratings. The spectra were measured using a parallel plate ion yield gas cell. The gas of interest is charged into a section of vacuum chamber isolated from the ultra-high vacuum of the beamline by a thin window, in this case aluminum. One of two parallel plates inside the gas cell is biased with approximately 100V and the current of the ions striking the other plate is monitored as a function of photon energy. The Ar 3s → np window resonances,[4] which occur around 30 eV and are shown in Fig. 4, are excellent candidates for testing the resolution of the 380 line/mm grating, as they occur close to the Rowland circle energy for this grating. In the spectrum shown in Fig. 4 the $Ar3s^{-1}29p$ resonance can be resolved and the n=22 lines is observed to have a full width at half maximum of 0.7eV, corresponding to a

resolving power of approximately 42,000. In Figs. 5 and 6, ion yield spectra of the Xe 4d and Kr 3d edges measured using the 925 l/mm grating are shown. In Fig. 7 an ion yield spectrum of the 2p edge in Ar measured with the 2100 l/mm grating is shown.

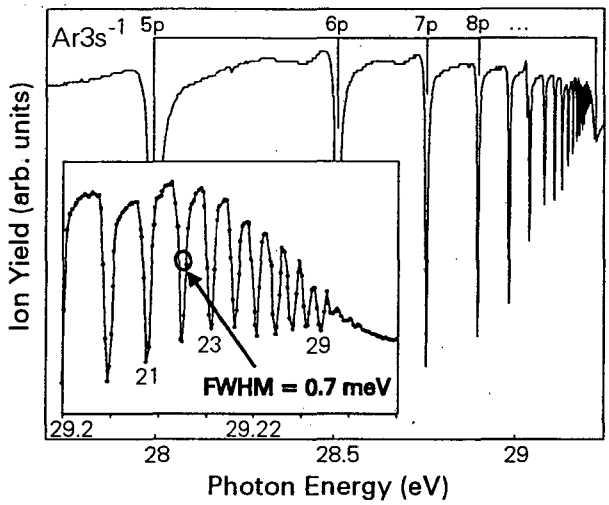

Figure 4. Photoionization yield spectrum of the Ar3s^{-1}np resonances.

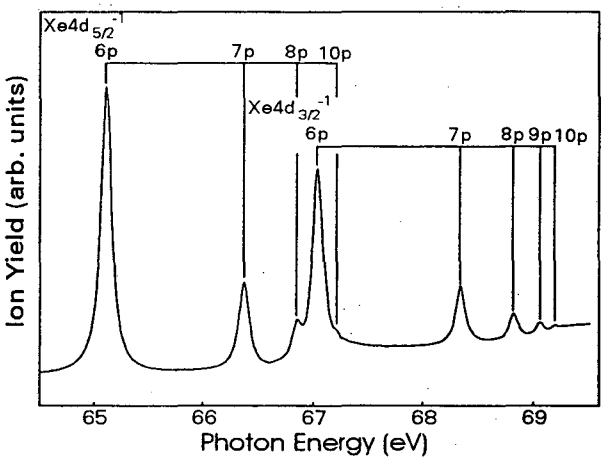

Figure 5. Photoionization yield spectrum of Xe4d^{-1} resonances.

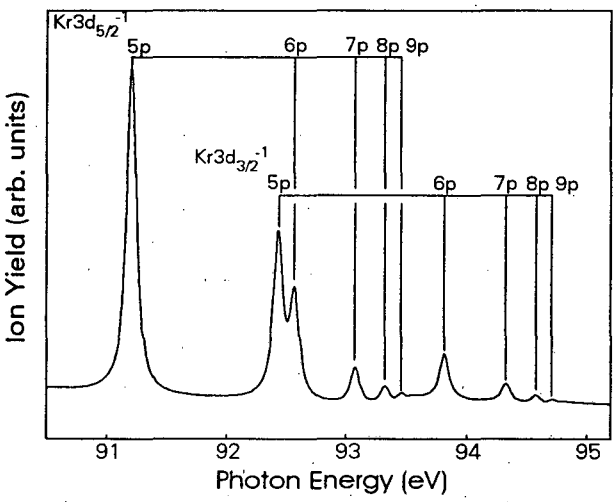

Figure 6. Photoionization yield spectrum of Kr3d^{-1} np resonances.

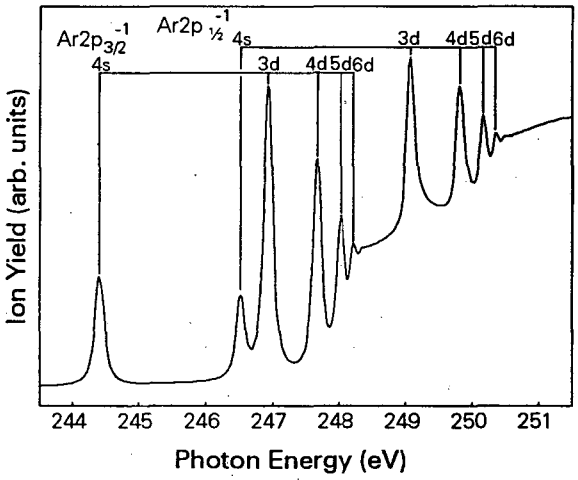

Figure 7. Photoionization yield spectrum of Ar2p^{-1} 4s,nd resonances.

REFERENCES

1. P. Heimann, T. Warwick, M. Howells, W. McKinney, D. DiGennaro, B. Gee, D. Yee and B. Kincaid, Nucl. Instrum. And Methods **A319**, 106 (1992).
2. P.A. Heimann, D. Mossessian and J. Bozek, LSBL-239 (1995).
3. K. Schulz, G. Kaindl, M. Domke, J.D. Bozek, P.A. Heimann, A.S. Schlachter and J.M. Rost, Phys. Rev. Lett., **77**, 3086 (1996).
4. N. Berrah, B. Langer, J. Bozek, T.W. Gorzyca, O. Hemmers, D.W. Lindle and O. Toader, J. Phys. B, **29**, 5351 (1996).

This work was supported by the Director, Office of Energy Research, Office of Basic Sciences, Materials Science Division, of the U.S. Department of Energy under Contract No. DE-AC03-76SF00098.

Principal investigator: John Bozek, Advanced Light Source, Ernest Orlando Lawrence Berkeley National Laboratory. Email: JDBozek@lbl.gov. Telephone: 510-486-4967.

Alignment of Ar^+ $[^3P]4p^2P^0_{3/2}$ Satellite State From the Polarization Analysis of Fluorescent Radiation After Photoionization

O. Yenen[1], K. W. McLaughlin[1], D. H. Jaecks[1], A. S. Schlachter[2], and J. Bozek[2]
[1] Department of Physics, University of Nebraska-Lincoln, Lincoln NE 68588-0111, USA
[2] Advanced Light Source, Ernest Orlando Lawrence Berkeley National Laboratory, University of California, Berkeley, CA 97420, USA

The measurement of the polarization of radiation from satellite states of Ar^+ formed after the photoionization of Ar provides detailed information about the nature of doubly excited states, magnetic sublevel cross sections and partial wave ratios of the photo-ejected electrons. Since the formation of these satellite states is a weak process, it is necessary to use a high flux beam of incoming photons. In addition, in order to resolve the many narrow doubly excited Ar resonances, the incoming photons must have a high resolution. The characteristics of the beam line 9.0.1 of the Advanced Light Source fulfill these requirements.

We determined the polarization of 4765 Å fluorescence from the Ar^+ $[^3P]$ 4p $^2P^0_{3/2}$ satellite state formed after photoionization of Ar by photons from the 9.0.1 beam line of ALS in the 35.620-38.261 eV energy range using a resolution of approximately 12,700.

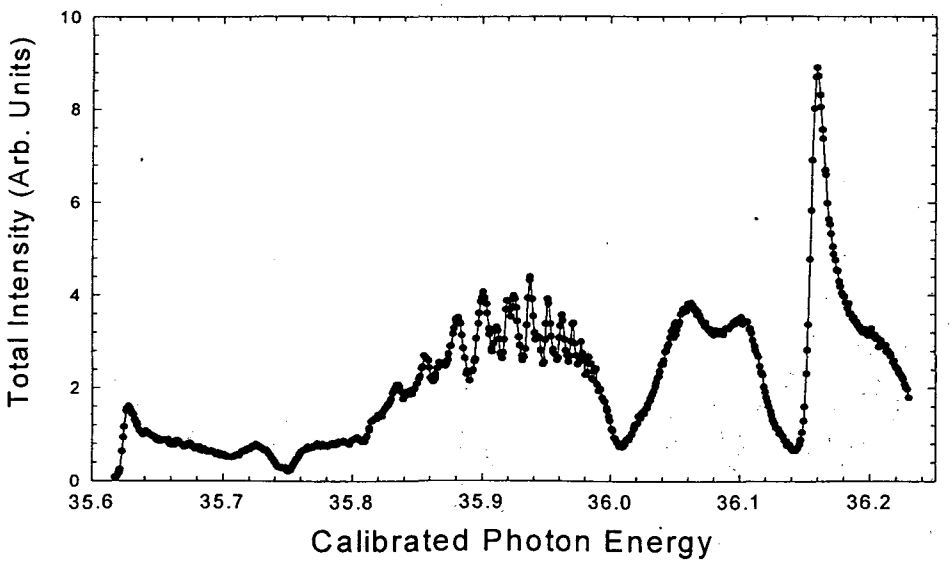

Figure 1. Total Intensity of 4765 A fluorescent radiation corrected for the polarization.

This is accomplished by measuring the intensities of the fluorescent light polarized parallel ($I_\parallel$) and perpendicular ($I_\perp$) to the polarization axis of the incident synchrotron radiation using a Sterling Optics 105MB polarizing filter. The optical system placed at

90° with respect to the polarization axis of the incident light had a narrow band interference filter ($\Delta\lambda$=0.3 nm) to isolate the fluorescent radiation. The calibration of the monochromator of the 9.0.1 beam line was performed using $3s\,3p^6 np\ ^1P_1^o$ series of window-type resonances [1] of Ar from n=6 to n=20, and the threshold onsets of 4658 Å, 4765 Å, 4727 Å, 4880 Å, 4590 Å, and 4610 Å satellite lines of Ar^+.

From the measurements we determined the intensity $I(90) = I_{\parallel} + I_{\perp}$ and the polarization $P(90) = (I_{\parallel} - I_{\perp})/(I_{\parallel} + I_{\perp})$ of the satellite line as measured at 90° with respect to the polarization axis of the incident light. The total intensity of the $^2P^0_{3/2}$ satellite line emitted to 4π solid angle is obtained from [2]:

$$I_{tot} = 4[1 - \frac{P(90)}{3}]\, I(90)$$

and is shown in Fig. 1. The total alignment coefficient A_0^c, defined as [3], $\langle 3J_z^2 - J^2 \rangle / J(J+1)$ is related to the measured polarization P(90) by [4]:

$$A_0^c = \frac{4\,P(90)}{h^{(2)}\,[3 - P(90)]}$$

where $h^{(2)}$ is the ratio of two 6-j symbols. A_0^c is a measure of the distribution of different $|m_j|$ sublevels. Fig. 2 show A_0^c as a function of the incoming photon energy. From the definition of the total alignment coefficient, for j=3/2 states, it can be shown that the magnetic substate cross sections $\sigma(m_j = 3/2)$ and $\sigma(m_j = 1/2)$ are given by:

$$\sigma\,(m_j = 3/2) = \frac{4 + 5A_0^c}{8} I_{tot} \qquad \text{and,} \qquad \sigma\,(m_j = 1/2) = \frac{4 - 5A_0^c}{8} I_{tot}$$

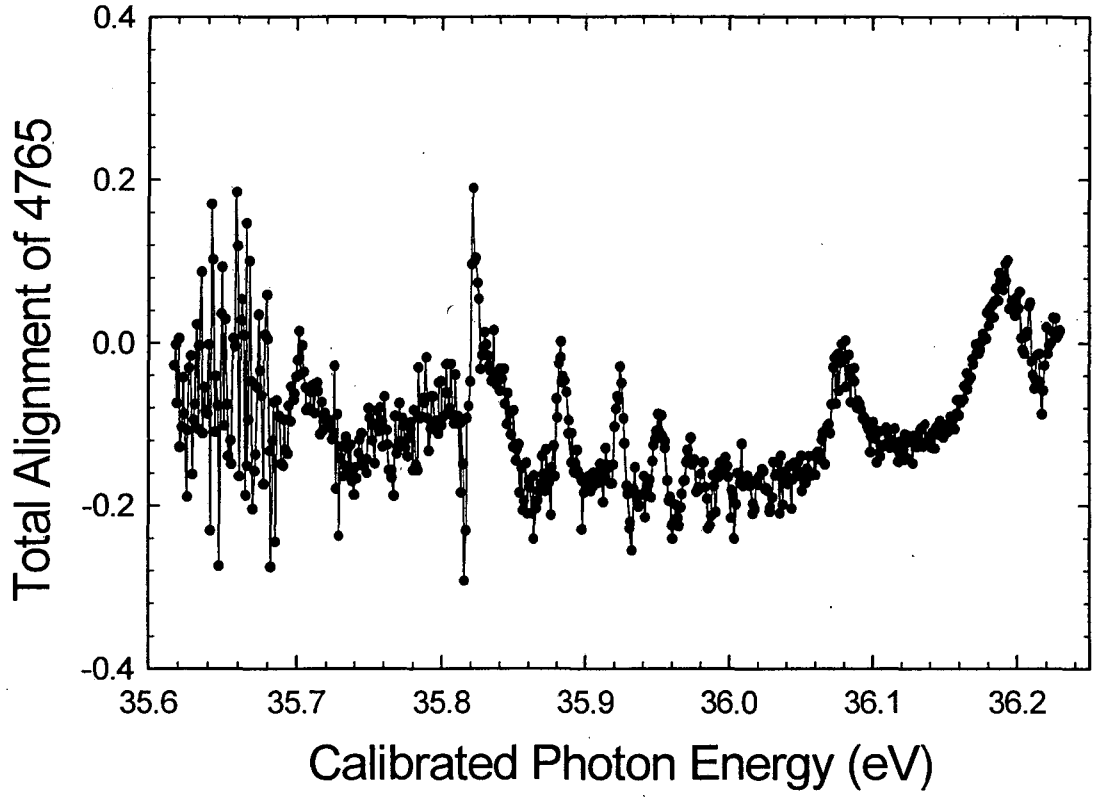

Figure 2. Total alignment parameter as a function of incident photon's energy.

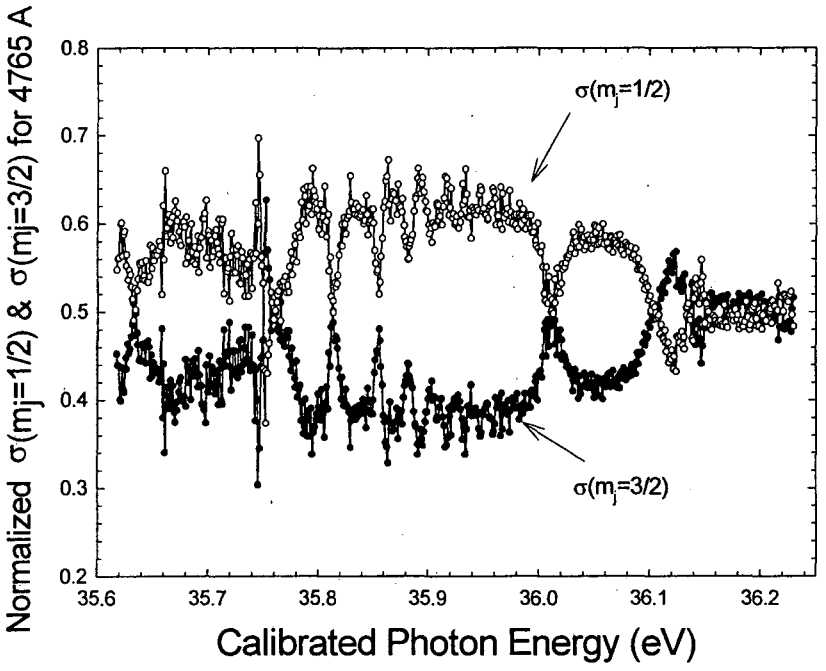

Figure 3. Substate cross sections normalized to their sum.

Since the measurement of I_{tot} is in arbitrary units, we show in Fig. 3 the $\sigma(m_j = 3/2)$ and $\sigma(m_j = 1/2)$ cross sections normalized to their sum.

For $^2P^0_{3/2}$ satellite states, the angular momentum and parity conservation rules limit the orbital angular momentum ℓ of the electron to 0 or 2. In this case, the total alignment coefficient A_0^c can further be related to the ratio of the s-wave to d-wave cross sections of the photoelectron [5]. By expanding the total final state wave function of excited ion plus outgoing electron, using a coupling scheme where total angular momentum **j** of the ion is

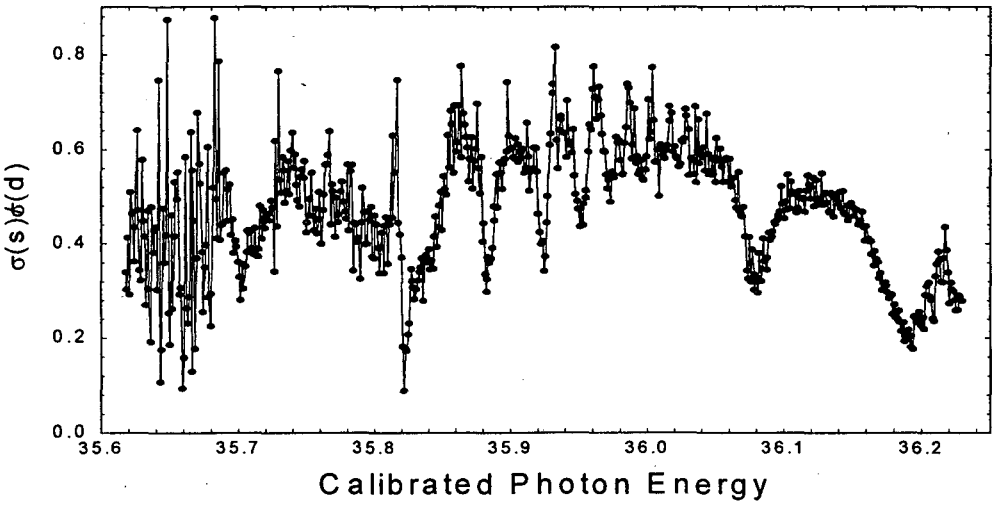

Figure 4. The ratio of the s-wave to d-wave cross sections for the partial waves of the emitted electron.

coupled to the total angular momentum $\mathbf{j}_e = \ell_e + \mathbf{s}_e$ of the free electron, one can readily calculate the ratio of the s-wave to d-wave cross sections of photoelectron in terms of the measured alignment parameter. These ratios are presented in Fig. 4.

These results show that the primary process for satellite-state formation is through autoionizing resonances of Ar. The total alignment parameter, as a function of the incoming photon's energy, displays Fano-profile type of variations and resonance series sometimes absent on the intensity spectrum. We also show that the alignment parameter and the angular distribution of the photoelectron vary rapidly over resonances.

REFERENCES

1. R.P. Madden, D.L. Ederer, and K. Codling, Phys. Rev. **177**, 136 (1969)
2. J.A. Smit, Physica **2**, 104 (1935)
3. U. Fano and J.H. Macek, Rev. Mod. Phys. **45**, 553 (1973)
4. B.W. Moudry, O. Yenen, D.H. Jaecks, and J.H. Macek, Phys. Rev. A **54**, 4119 (1996)
5. J. Jimenez-Mier, C.D. Caldwell, and D.L. Ederer, Phys. Rev. Lett. **57**, 2260 (1986)

This work is supported by the National Science Foundation under Grant PHY-9419505

Principal investigator: Duane H. Jaecks, Department of Physics, University of Nebraska-Lincoln. Email:djaecks@unlinfo.unl.edu. Telephone (402) 472-3274

Angle-Resolved Study of Ar $2p_{1/2,3/2}^{-1}$ *ns,d* Resonant Auger Decay

A. Farhat[1], M. Humphrey[1], B. Langer[1] ,N. Berrah[1] and J. D. Bozek[2]

1Physics Department, Western Michigan University, Kalamazoo, MI 49008
2Lawrence Berkeley National Laboratory, Advanced Light Source,
Mail Stop 2-400, Berkeley, CA 94720

INTRODUCTION

The Auger decay of core excited states in rare gases has been subject to rather intense investigation over a number of years due to its complex nature.

We have measured the intensity distributions and angular distributions (β parameters) for the Auger decay spectra following each of the $2p_{1/2,3/2} \rightarrow$ 4s, 3d, 4d resonant excitations in argon. This report presents our result only for the angular distributions (β parameters) of the $2p_{1/2}^{-1}$4s resonance.

EXPERIMENT

Experimental results were obtained at the Advanced Light Source at Lawrence Berkeley National Laboratory using double bunch operation. The measurements were performed using the 8-cm-55-period U8 undulator of beamline 9.0.1 which uses a spherical grating monochromator. Two time-of-flight (TOF) analyzers were mounted to a rotatable chamber whose axis of rotation was coaxial with the photon beam. For the measurements described in this work, the TOF analyzers were fixed at 0° and 54.7° (the magic angle) with respect to the electric field vector of the incident radiation. This configuration, allows for two complete spectra to be taken simultaneously at different angles. As a result, angular anisotropies can be measured and the β parameters can be extracted for the individual final ionic states. In order to improve the resolution at the kinetic energy region of interest, a 201 V retarding potential was applied to the flight tube to increase the flight time of the electrons [1].

RESULTS

The $2p_{1/2}^{-1}$4s Resonant Auger Spectra

Figures 1 depict portions of the $2p_{1/2}^{-1}$ 4s spectra. Each of the prominent features is labeled with a number, and each individual LS term is labeled by a numbered letter. Here, the same binding energy region is viewed from two different angles (0° and 54.7° with respect to the synchrotron light's electric field). For each resolved final ionic state, a Gaussian peak has been fit, with the relative spacing between the peaks assigned using optical data of Minnhagen [2]. Once the data from each spectrometer has been normalized to the spectrometers' relative efficiency (to compensate for transmission differences

between them), a comparison of the areas of a particular peak at the two angles allows the determination of the β parameter.

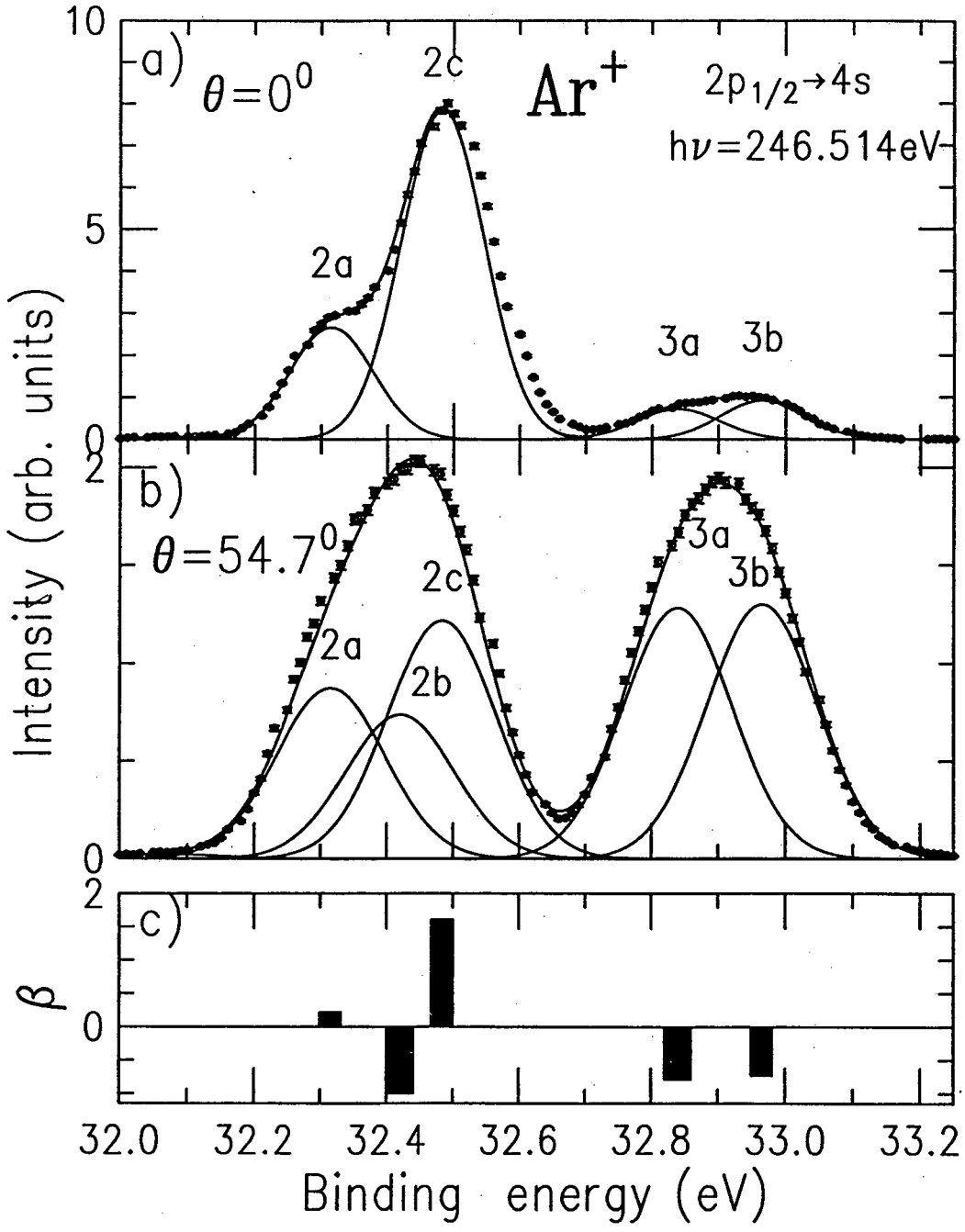

Fig. 1. Auger decay for Ar $2p_{1/2}^{-1}$ 4s resonance shown at (a) $\theta = 0^{\circ}$ and (b) $\theta = 54.7^{\circ}$. The peak labels correspond to those states listed in table 1. The angular distribution anisotropy parameters (β) are shown in (c).

A complete listing of β parameters for nearly all $3p^4nl$ final ionic states is given in Table 1 for the $2p_{1/2}^{-1}4s$ decays. In order to compare our results with previously unresolved work, we have listed both the individual β components and their average β value (shown in the boldface) which includes the sum of all overlapping peaks in a given LS term. For each value, the statistical uncertainty in the last digit is given in parentheses following the value. It should be noted, however, that this uncertainty does not take into account any additional unquantifiable uncertainties such as that due to peak overlap. It can be seen that most β parameters are small positive or negative, the latter indicating a preferred emission in the direction perpendicular to the electric field vector of the radiation. This is due to the enhanced population of final ionic states which can be reached via parity unfavored transitions only through the resonant Auger processes [3]. These results are compared with previous lower resolution measurements from Carlson et al. [4], and Menzel et al. [5], and are compared with theoretical calculations of Cooper [6], Hergenhahn et al. [7], and Chen [8]. In his work, Cooper has treated the Auger decay as a single-step process, Hergenhahn et al. have considered excitation and decay of the resonant state as a two-step process and predicts the resonant Auger decay based on the spectator model. Chen used a multiconfiguration Dirac-Fock method in intermediate coupling with configuration interaction, also a two-step model. In general, our results differ considerably from those of Carlson et al. [4], and we attribute this to the lack of resolution in the previous experiments. However, our results agree quite well with those of Menzel et al. [5] who didn't resolve the individual components. When compared with calculations, we find good agreement with Hergenhahn et al. [7], and very good agreement with Chen [8]. It should therefore be noted that the β parameters agree best with the two-step process calculations [7,8].

CONCLUSION

Angular-resolved measurements of the Ar $2p_{1/2}^{-1}4s$, resonant Auger decays have been reported. The angular distribution anisotropy parameters (β) have been reported for nearly all of the $3p^4nl$ final ionic states, and a comparison of these measurements with previous results demonstrates good agreement. It has been shown that a large majority of the β parameters are either small positive or negative, due to parity unfavored transitions, and as predicted by the spectator model, the averaged β is isotropic in the case of the $2p_{1/2}^{-1}4s$ resonance. A complete report on the $2p_{1/2,3/2} \rightarrow 4s,3d,4d$ resonant Auger decay can be found in [9].

ACKNOWLEGMENTS

We would like to thank Ant Wills and Uwe Becker for Useful discusssions and comments.

Final State $3p^4nl$		β Parameters : $2p_{1/2} \rightarrow 4s$					
			Experiment		*Theory*		
No	LS-term	β This work	β Carlson[4]	β Menzel[5]	β Hergenhahn[7]	β Chen[8]	
2a	$3p^4(^3P)4s^4P_{5/2}$	0.21(3)					0.19
2b	$3p^4(^3P)4s^4P_{3/2}$	-1.0					-0.81
2c	$3p^4(^3P)4s^4P_{1/2}$	1.61(7)					1.8
2a,b,c	**$3p^4(^3P)4s^4P_{5/2,3/2,1/2}$**	**0.54(4)**	**0.1**	**0.56**	**0.69**		**0.62**
3a	$3p^4(^3P)4s^2P_{3/2}$	-0.79(1)					-0.79
3b	$3p^4(^3P)4s^2P_{1/2}$	-0.73(1)					-0.72
3a,b	**$3p^4(^3P)4s^2P_{3/2,1/2}$**	**-0.75(1)**	**-0.37**	**-0.57**	**-0.66**		**-0.75**
2a,b,c	**$3p^4(^3P)4s^4P_{5/2,3/2,1/2}$**						
3a,b	**$3p^4(^3P)4s^2P_{3/2,1/2}$**	**-0.09(2)**	**-0.17**	**0.01**	**0.01**	**0.00**	**-0.007**
7a	$3p^4(^1D)4s^2D_{3/2}$	-1.0					
7b	$3p^4(^1D)4s^2D_{5/2}$	0.05(3)					
8a	$3p^4(^3P)3d^2F_{7/2}$	α					
8b	$3p^4(^3P)3d^2F_{52}$	-0.52(1)					
9a	$3p^4(^3P)3d^2D_{3/2}$	-0.15(2)					
9b	$3p^4(^3P)3d^2D_{5/2}$	-0.04(2)					
7a,b	**$3p^4(^1D)4s^2D_{5/2,3/2}$**						
8a,b	**$3p^4(^3P)3d^2F_{7/2,5/2}$**	**-0.03(2)**	**-0.22**	**0.01**	**0.00**	**0.00**	**0.006**
9a,b	**$3p^4(^3P)3d^2D_{5/2,3/2}$**						
12a	$3p^4(^1S)4s^2S_{1/2}$	0.07(3)	-0.20	0.00	0.00	0.00	0.001

28. Menzel et. al. [5] using two different energies, 246.0 eV and 246.5 eV.
α. Strongly positive β.

Table 1. Experimental and theoretical angular distribution anisotropy Parameters (β) for the Ar $2p_{1/2}^{-1}4s$.

REFRENCES

[1] B. Langer, A. Farhat, B. Nessar, N. Berrah, O. Hemmers, and J. D. Bozek, *in Proceedings of the "Atomic Physics with Hard X-rays from High Brilliance Synchrotron Light Sources" Workshop*, ANL/APS/TM-16, p. 245 (1996).

[2] L. Minnhagen, *Arkiv För Fys.* **25** 203 (1963).

[3] B. Langer, J. Viefhaus, O. Hemmers, A. Menzel, R. Wehlitz, and U. Becker, *Phys. Rev. A.* **51**, R882 (1995).

[4] T. A. Carlson, D. R. Mullins, C. E. Beall, B. W. Yates, J. W. Taylor, D. W. Lindle, and F. Grimm, *Phys. Rev. A* **39**, 1170 (1989).

[5] A. Menzel, Ph.D. Thesis, Technische Universität Berlin (1990, unpublished).

[6] J. W. Cooper, *Phys. Rev. A* **39**, 3714 (1989).

[7] U. Hergenhahn, N. M. Kabachnik, and B. Lohmann, *J. Phys. B: At. Mol. Opt. Phys.* **24**, 4759 (1991).

[8] M. H. Chen, *Phys. Rev. A* **47**, 3733 (1993).

[9] A. Farhat, M. Humphery, B. Langer, N. Berrah, and J. Bozek submitted to *Phys. Rev. A.*

This work was supported under contract NO DE-FG02-95ER 14299 by the US Department of Energy, Office of Basic Energy Science, Division of Chemical Sciences. B.L. is indebted to the Alexander von Humboldt Foundation for partial financial support under the Feodor Lynen program.

Principal investigator: Nora Berrah, Western Michigan University, Physics Department, Kalamazoo, MI 49008. Email: Berrah@wmich.edu. Telephone: 616-387-4955.

Auger Resonant Raman Spectroscopy Used to Study the Angular Distributions of the Xe $4d_{5/2} \rightarrow 6p$ Decay Spectrum

B. Langer[1], N. Berrah[1], A. Farhat[1], O. Hemmers[2], and J.D. Bozek[3]

[1]Western Michigan University, Kalamazoo, MI 49008
[2]University of Nevada, Las Vegas, NV
[3]Lawrence Berkeley National Laboratory, Berkeley, CA

INTRODUCTION

Auger resonant Raman spectroscopy [1] is a powerful tool for studying the resonant Auger decay processes with a resolution narrower than the natural lifetime width of the initial inner-shell hole state. This effect has been used to analyze branching ratios of resonantly excited atoms and molecules. In this paper, we present results of a study of angular distributions of the spectator decay lines of Xe following $4d_{5/2} \rightarrow 6p$ excitation using the Auger resonant Raman effect and highly resolved photons from the Advanced Light Source (ALS).

EXPERIMENT

The experiment was performed under double bunch operation on beamline 9.0.1. Xenon atoms were excited and ionized by monochromatic synchrotron radiation from an 8-cm, 55-period undulator and spherical grating monochromator. Figure 1 shows electron spectra taken simultaneously at different angles (θ=0°, 54.7°) by two time of flight spectrometers, which were mounted on a rotatable chamber. A retarding voltage was used on these spectrometers to increase the flight time of the electrons and therefore improve their energy resolution. Figure 2 shows a section of the decay spectrum recorded with a 32-V retarding potential at three different angles (θ=0°, 54.7°, 90°). From the well separated (^{3}P)6p($^2P_{3/2}$) peak (line 26 in Fig. 1) the kinetic-energy resolution of this experiment was found to be 1.1% and 1.0% of the final kinetic electron energy with retarding voltages of 30 and 32 V, respectively.

RESULTS

The results for the relative intensities and the angular distribution parameters ß are shown in Table 1 together with theoretical calculations from Tulki et al. [2], Chen [3] and Hergenhahn et al. [4]. All the theoretical calculations have in common that both the direct photoionization and the participator decay are neglected, and these approximations have been verified experimentally [5,6].

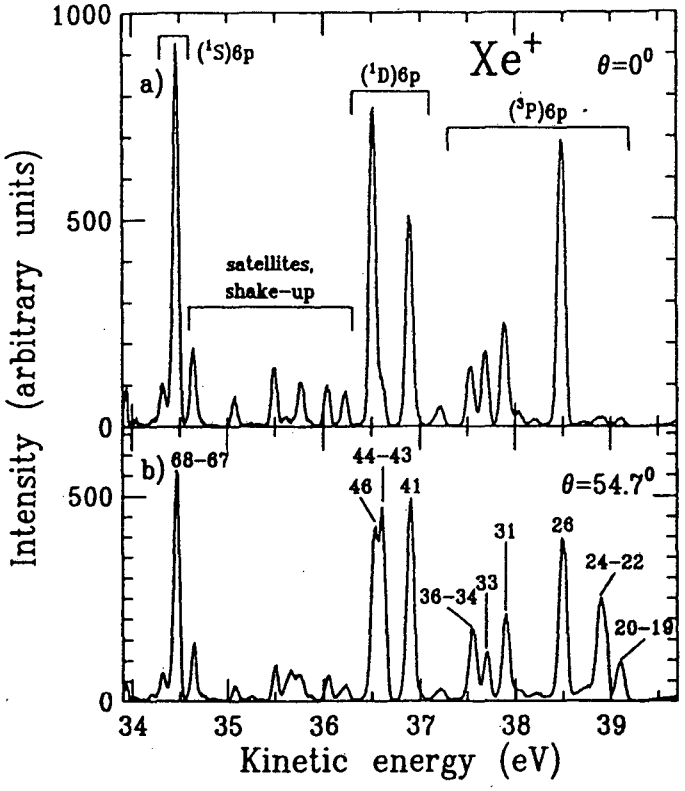

Figure 1. Xe $5p^4nl$ decay spectra after $4d_{5/2} \rightarrow 6p$ resonant excitation at (a) 0° and (b) 54.7° with respect to the polarization of the incident photons. The spectra were recorded with a 30-V retarding potential, which corresponds to a spectrometer resolution of between 45 and 70 meV in the displayed region.

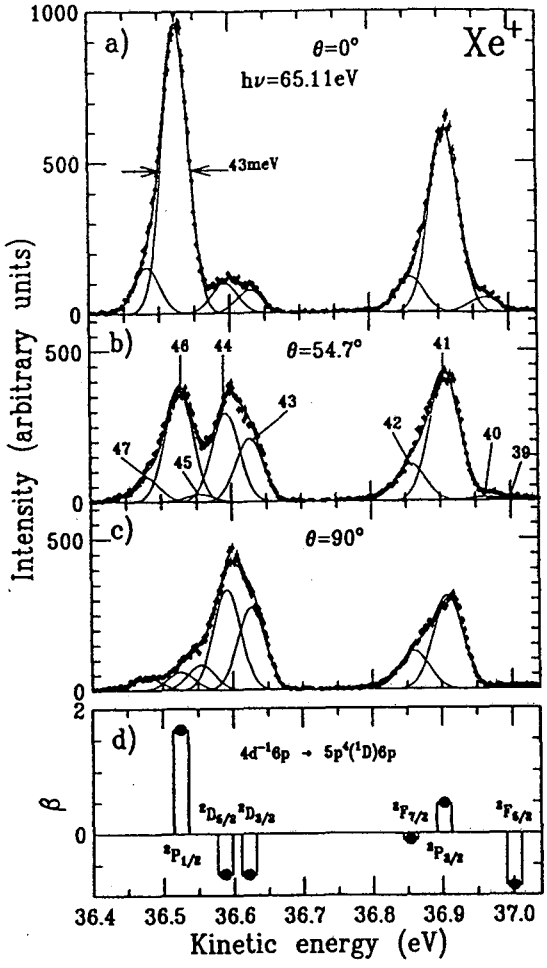

Figure 2. Xe $5p^4nl$ decay spectra after $4d_{5/2} \rightarrow 6p$ resonant excitation in the kinetic-energy range of 36.4-37.1 eV at (a) 0°, (b) 54.7°, and (c) 90° with respect to the polarization of the incident photons. The spectra were measured with a 32-V retarding potential corresponding to a spectrometer resolution of between 43 and 50 meV in the displayed region. (d) shows the angular distribution parameter β for the $5p^4(^1D)6p$ spectator lines.

Besides the $5p^46p$ spectator lines, Table 1 also includes some pure satellite lines. There is fair agreement between our intensities and those reported by Aksela et al. [7] at least for the most intense lines. For small lines that are close to a strong line, our intensities tend to be larger than those of Aksela et al. [7]. This may be due to the fact that we used Gaussian profiles, which drop more rapidly than the Lorentzian profiles used by Aksela et al. [7].

Comparing our results [8] to the different calculations, we find that the agreement varies between excellent and poor, depending on the configuration and method used. (Our omplete work can be found in [8]).

Table 1. Intensities and β parameters of the electron spectrum of Xe after $4d_{5/2}\rightarrow 6p_{3/2}$ excitation (65.110 eV). Intensities are normalized relative to the well separated (^{3}P)6p($^2P_{3/2}$) line (line 26). The statistical uncertainty of the last digits is given in brackets. The identification of the peaks from Chen [3] was done with respect to their calculated energies. Peaks where the leading LS terms differ from that given by Aksela et al. [7] also used by Tulkki, Aksela, and Kabachnik [2] are marked with an asterisk (*).

Final ionic state Term[b]		Line in experiment[b]	Kinetic energy (eV)[b]	Relative intensity	β	β theory[a] Ref. [19]	Ref. [18]	Ref. [17]	Ref. [16]
$5p^4(^3P)6p$	$^4P_{3/2}$	19	39.119	2.0(5)	1.4(6)	1.045	0.984	0.061	1.014
$(^3P)6p$	$^4P_{5/2}$	20	39.098	23.2(7)	−0.85(3)	−0.994	−1.000	−0.999	−0.998
$(^3P)6s$	$^2D_{3/2}$	21[c]	38.975	0.82(12)	2.0(3)				
$(^3P)6p$	$^2D_{5/2}$	22	38.906	37.5(8)	−0.967(12)	−0.994	−1.000	−1.000	−0.998
$(^3P)6p$	$^2S_{1/2}$	23	38.886	17.1(6)	−0.69(3)	−0.448	0.215*	0.157*	0.451*
$(^3P)6p$	$^4D_{7/2}$	24	38.882			−0.588	−0.974	−0.923	−0.932
$(^1D)5d$	$^2G_{9/2,7/2}$	25[c]	38.738	4.0(2)	−0.16(3)				
$(^3P)6p$	$^2P_{3/2}$	26	38.501	100	1.30(2)	1.030	1.018	0.972	1.014
$(^1D)5d$	$^2F_{5/2}$	27[c]	38.216	2.9(2)	0.60(11)				
$(^3P)6p$	$^2P_{1/2}$	28	37.988	5.0(2)	1.03(7)	0.984	0.962*	0.749*	NA[d]*
$(^3P)6p$	$^4P_{1/2}$	30	37.955	7.1(3)	−0.13(6)	0.233	0.774*	0.927	1.000
$(^3P)6p$	$^2D_{3/2}$	31	37.899	42.8(5)	0.73(3)	0.656	0.653*	0.910*	0.800*
$(^3P)6p$	$^4D_{5/2}$	32	37.716	1.3(4)	0.3(6)	−0.188	−0.331	−0.323	0.737
$(^3P)6p$	$^4S_{3/2}$	33	37.627	24.0(6)	1.13(5)	0.745*	0.955	0.557	−0.861
$(^3P)6p$	$^4D_{3/2}$	34	37.570	22.1(5)	−0.14(3)	−0.536*	−0.860*	−0.764*	−0.861*
$(^3P)5d$	$^2G_{5/2}$	35[c]	37.567						
$(^3P)6p$	$^2D_{1/2}$	36	37.535	19.5(4)	0.52(3)	0.593	0.935*	0.817*	1.000*
$(^1D)5d$	$^2P_{1/2}$	37[c]	37.232	5.6(2)	1.36(6)				
$(^1D)5d$	$^2D_{3/2}$	38[c]	37.169	2.7(2)	0.69(11)				
$(^1D)6p$	$^2F_{5/2}$	39	37.001	2.10(14)	−0.85(10)	−0.875	−0.860	−0.914	−0.928
$(^1D)6s$	$^2S_{1/2}$	40[c]	36.959[e]	3.0(2)	2.0(3)				
$(^1D)6p$	$^2P_{3/2}$	41	36.902	82.7(10)	0.47(2)	0.175	0.073	−0.319	−0.399
$(^1D)6p$	$^2F_{7/2}$	42	36.853	24.3(5)	−0.11(3)	0.246	0.052	0.116	0.112
$(^1D)6p$	$^2D_{3/2}$	43	36.621	39.0(7)	−0.66(2)	−0.553	−0.529	−0.375	−0.399
$(^1D)6p$	$^2D_{5/2}$	44	36.587	51.0(8)	−0.65(2)	−0.888	−0.882	−0.930	−0.928
$(^3P)7s$	$^4P_{5/2}$	45[c]	36.550	6(1)	SN[f]				
$(^1D)6p$	$^2P_{1/2}$	46	36.521	63.1(6)	1.66(2)	1.503	1.307	0.550	0.373
$(^3P)7s$	$^2P_{3/2}$	47[c]	36.232	13.9(3)	0.94(4)				
$(^1S)6p$	$^2P_{1/2}$	65	34.602	1.6(3)	0.73(4)	0.130	−0.139	−0.035	NA[d]
$(^1S)6p$	$^2P_{3/2}$	67 68	34.479 34.456	98.9(6)	1.17(4)	0.829	0.847	0.754	0.800

[a]The originally given σ_2 values are multiplied by $-\sqrt{2}$.
[b]According to Aksela *et al.*
[c]Satellite line.
[d]Not allowed.
[e]Energy taken from Hansen and Persson
[f]Strongly negative.

CONCLUSIONS

We have reported high-resolution angular distribution measurements of the Xe spectator lines following Xe $4d_{5/2}\rightarrow 6p$ excitation. The Auger resonant Raman effect was utilized to obtain energy resolutions well below the natural line width of the 4d inner-shell hole. Our results appear to remove the existing experimental discrepancy. Comparisons with different theoretical calculations show partly good agreement, but there is room for improvements for some lines.

ACKNOWLEDGMENTS

We wish to thank the ALS for providing an excellent source of photons. B.L. is indebted to the Alexander von Humboldt Foundation for partial support.

REFERENCES

1. G. S. Brown, M. H. Chen, and B. Crasemann, Phys. Rev. Lett, **45**, 1937 (1980).
2. J. Tulkki, H. Aksela, and N. M. Kabachnik, Phys. Rev. A **50**, 2366 (1994).
3. M. H. Chen, Phys. Rev. A **47**, 3733 (1993).
4. U. Hergenhahn et al. J. Phys. B. **26** L117 (1993).
5. H. Aksela et al. Phys. Rev. A **33**, 3867 (1986).
6. U. Becker et al. Phys. Rev. A **33**, 3891 (1986).
7. H. Aksela et al. Phys. Rev. A **51**, 1291 (1995).
8. B. Langer, N. Berrah, A. Farhat, O. Hemmers, and J. D. Bozek, Phys. Rev. A **53**, R1946 (1996).

This work was supported by the DOE, Office of Basic Energy Sciences, Division of Chemical Sciences under contract No. DE-FG02-95ER14299.

Principal Investigator: Nora Berrah, Western Michigan University, Physics Departmemt, Kalamazoo, MI 49008. Email:Berrah@wmich.edu. Tel: 616-387-4955.

Dynamics of Two-Electron Excitations in Helium

C.D. Caldwell,[1] A. Menzel,[1] S. P. Frigo,[1] S.B. Whitfield,[1] M.O. Krause,[2]
J.-Z. Tang,[3] and I. Shimamura[3]

[1]Department of Physics, University of Central Florida, Orlando, FL 32816-2385
[2]Oak Ridge National Laboratory, Oak Ridge, TN 37831-6201
[3]Institute of Physical and Chemical Research (RIKEN), Wako, Saitama 351-01, Japan

Excitation of both electrons in helium offers a unique window for studying electron correlation at the most basic level in an atom in which these two electrons and the nucleus form a three-body system. We utilized the first light available at the U-8 undulator-SGM monochromator beamline to investigate the dynamic parameters, partial cross sections, differential cross sections, and photoelectron angular distribution parameters (β), with a high resolving power for the photon beam and at the highly differential level afforded by the use of our electron spectrometer. In parallel, we carried out detailed calculations of the relevant properties by a theoretical approach that is based on the hyperspherical close-coupling method.

Partial photoionization cross sections σ_n and photoelectron angular distributions β_n were measured for all possible final ionic states $He^+(n)$ in the region of the double excitations $N(K,T)^A$ up to the N=5 threshold. At a photon energy bandpass of 12 meV below the thresholds N=3,4, and 5, this level of differentiation offers the most critical assessment of the dynamics of the two-electron excitations to date. The experimental data were seen to be very well described by the most advanced theoretical calculations. Weaker double-excitation series with K=N-4 are clearly visible in the β_n data, and even previously unobserved extremely weak series members with A=-1 can be discerned, showing the high sensitivity of the angularly resolved measurements. The shapes of the resonance-induced variations of σ_n or β_n in the double excitations below a given threshold N change radically depending on the final ionic state n but display striking similarities when comparing the satellite states with n=N-1 and n=N-2 below each threshold N. These systematic patterns are in agreement with the theoretical results. Similarly, the peculiarities induced by the interference of two excitation series, primarily the higher members of the series converging to the $He^+(n=5)$ ionization threshold and the lowest member of the series converging to the $He^+(n=6)$ threshold, are delineated in both experiment and theory. This most critical assessment of the dynamics of the two-electron excitations in the prototype element helium has been discussed in three papers published in 1995 and 1996 [1-3].

REFERENCES

1. C. D. Caldwell, A. Menzel, S. P. Frigo, S. B. Whitfield, and M. O. Krause, Sync. Rad. News **8**, Nr. 1, 23 (1995).
2. A. Menzel, S. P. Frigo, S. B. Whitfield, C. D. Caldwell, M. O. Krause, J.-Z. Tang, and I. Shimamura, Phys. Rev. Lett. **75**, 1479 (1995).
3. A. Menzel, S. P. Frigo, S. B. Whitfield, C. D. Caldwell, and M. O. Krause, Phys. Rev. A **54**, 2080 (1996).

This work was supported by NSF under grant numbers PHY-9207634 and PHY-9507573 and by DoE Basic Energy Sciences under contract No. DE-AC0584OR21400 with Martin-Marietta Energy Systems. The Special Researcher's Basic Science Program of RIKEN provided support for J.-Z. Tang and I. Shimamura.

Principal Investigator: C. Denise Caldwell, Department of Physics, University of Central Florida
Email: cdc@phys.physics.ucf.edu. Telephone: 407-823-2325

Fluorescence Excitation Involving Multiple Electron Transition States of N_2 and CO_2

C. Y. Robert Wu, F. Z. Chen, Tom Hung and D. L. Judge
Department of Physics and Astronomy and Space Sciences Center
University of Southern California, Los Angeles, CA 90089-1341

INTRODUCTION

The electronic states and electronic structures of N_2 and CO_2 in the 8-50 eV energy region have been studied extensively both experimentally and theoretically. In the energy region higher than 25 eV there exists many electronic states including multiple electron transition (MET) states which are responsible for producing most of the dissociative photoionization products [1-10]. The electronic states at energies higher than 50 eV have been mainly determined by Auger spectroscopy, double charge transfer, photofragment spectroscopy and ion-ion coincidence spectroscopy [e.g.,10-13]. The absorption and ionization spectra of these molecules at energies higher than 50 eV mainly show a monotonic decrease in cross section values and exhibit structureless features [14-16].

The decay channels of MET and Rydberg (or superexcited) states include autoionization, ionization, dissociative ionization, predissociation, and dissociation while those of single ion and multiple ion states may involve predissociation and dissociation processes. The study of fluorescence specifically probes electronically excited species resulting from the above-mentioned decay channels and provides information for understanding the competition among these channels.

EXPERIMENTAL METHODS

Two fluorescence detectors were used to monitor the fluorescence emitted by electronically excited species. One is a solar blind photomultiplier which monitors fluorescence in the 1060-3000 Å region. The other detector is an UV-visible photomultiplier which mainly monitors molecular emissions in the UV-visible region [e.g.,5]. The incident photon flux was monitored by the combination of a sodium salicylate window and a 1P28 PMT.

The beamline 9.0.1 of the Advanced Light Source, Lawrence Berkeley Laboratory, Berkeley, California, was used in this task. Photon counting systems were used to measure the detected fluorescence intensities. A data acquisition system was employed to process the data from the two fluorescence channels and the incident photon flux, as a function of incident photon energy, for a given flow cell pressure. The relative fluorescence excitation function was obtained by dividing the fluorescence intensity by the corresponding incident photon flux. The carbon and silicon edges were used for incident photon energy calibration and provided an accurate of ± 0.2 eV.

RESULTS AND DISCUSSION

Fluorescence excitation functions for the production of emission in the 1060-3000 Å region through photoexcitation of N_2 in the 28-100 eV region were obtained at a temperature of 650 K. The results are shown in Fig. 1. There are three major broad

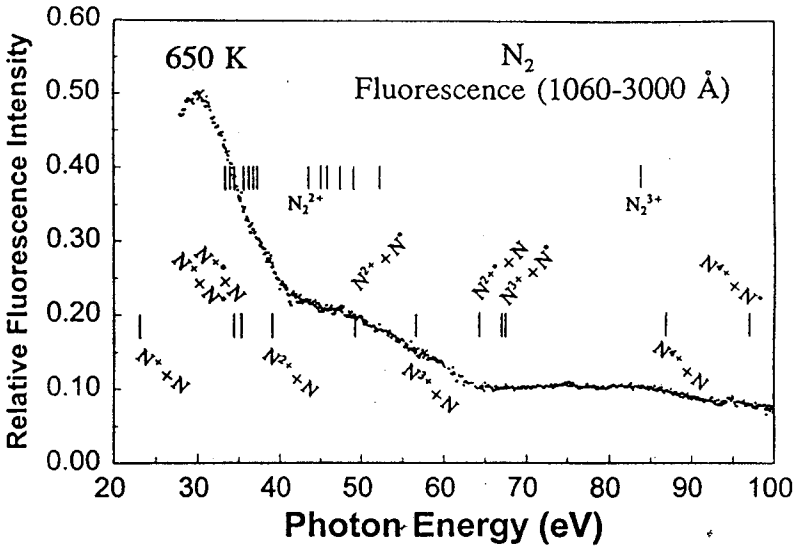

Fig. 1. Fluorescence excitation functions for the production of emission in the 1060-3000 Å region through photoexcitation of N_2.

fluorescence peaks that can be easily seen from the high temperature VUV fluorescence excitation function. The processes for producing the first fluorescence peak in the 28-40 eV region correlates with the decay of MET states of N_2 [7]. Theoretical calculations of N_2 predict that the weak broad absorption peak in the 35.4 eV region, the so-called H bands, consists of either a large number of $^2\Sigma_g^+$, $^2\Sigma_u^+$, and $^2\Pi_u$ ion states of N_2^+ [16] or members of the Rydberg series of N_2^+ [17] converging to the ground state of N_2^{2+} whose limit is at 43.6 eV. It appears that decay from both possibilities contribute to the observed fluorescence [4-8]. The second fluorescence excitation peak lies approximately at 40 to 65 eV which correlates very well with the N^+/N_2 dissociative photoionization channels [1,18]. The detected VUV fluorescence could result from products including excited NI and NII photofragments produced through decay of electronic states of $(N_2^{2+})^*$ and $(N_2^+)^*$ Rydberg states. The third fluorescence excitation peak extends from 65 to 100 eV. There exist many known electronic states of N_2^{2+} and their dissociating products may be responsible for producing some of the detected emission. The ionization potential (IP) of N_2^{3+} is at 84 eV [13]. Thus, there should be excited electronic states and Rydberg states converging to N_2^{3+}, and hence, we expect that they too contribute to the observed fluorescence. However, further studies are required.

In Fig. 2 we show the fluorescence excitation functions of emission in the 1060-3000 Å region produced through photoexcitation of CO_2 in the 28-100 eV region obtained at a temperature of 295 K and that in the 28-60 eV region at 650 K, respectively. There are two major (28-45 and 45-70 eV) and one minor (70-100 eV) broad fluorescence peaks that can be seen in the 295 K VUV fluorescence excitation function. The first and second peaks correlate very well with the specific fragment channels of CO^+, C^+, and O^+ produced through dissociative photoionization of CO_2 [15]. The third peak, however, does not correspond to the typical structureless absorption and ionization spectra of CO_2 [e.g.,11] in the 70-100 eV region. The processes for producing the first fluorescence peak in the 28-45 eV region correlates with the MET states of CO_2 as previously discussed [3,9]. In analogy to the case of N_2 it is likely that the most probable electronic states for producing the observed second and third fluorescence peaks are MET states,

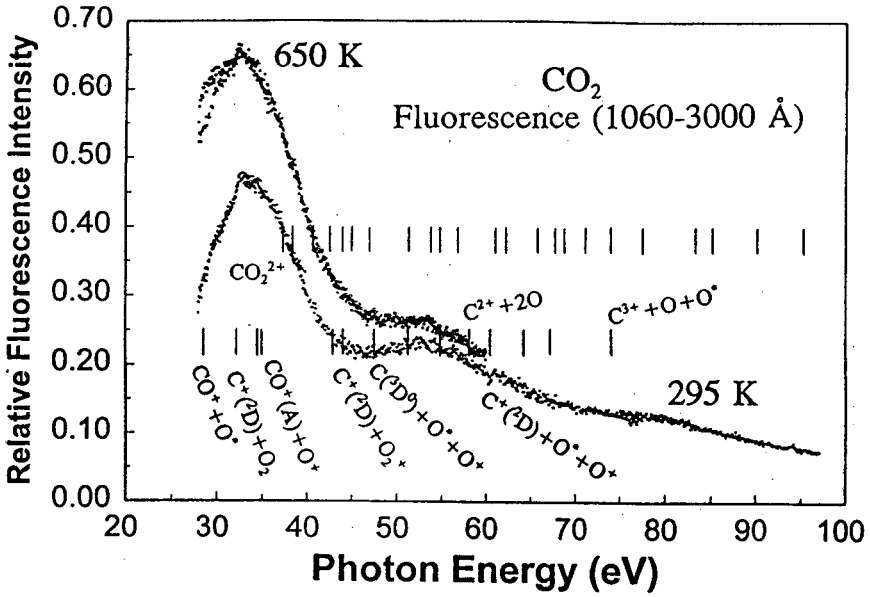

Fig. 2. Fluorescence excitation functions for the production of emission in the 1060-3000 Å region through photoexcitation of CO_2.

excited electronic states of multiply charged CO_2^{m+} [19], and Rydberg states converging to excited states of CO_2^{m+} for m=1-3. However, a definite assignment has to await further refined fluorescence and related studies.

The temperature effect on the production of VUV fluorescence is surprisingly large. As one can see from Fig. 2 there is an increase in the relative fluorescence yield by 48% and 31% at 30 and 32.5 eV, respectively, when the temperature of CO_2 increases from 295 K to 650 K. At 45 and 55 eV the increase is 23% and 9%, respectively. The temperature effect appears to be significant and can probably be attributed to hot bands.

CONCLUDING REMARKS

We have observed fluorescence excitation peaks in the 50-100 eV region and have speculated that the observed fluorescence is produced through decay processes of MET states, in addition to Rydberg and ion states of multiply charged molecules. Further study such as dispersed fluorescence to identify the electronic states of the emitting species may allow us to correlate them with molecular electronic states.

Fluorescence excitation functions of photofragments have previously been shown to provide useful information in the identification of Rydberg states which were not observable in *structureless* regions of absorption and photoionization spectra of N_2 [8,14,16,18,20] and CH_4 [21]. The present work further shows that fluorescence spectrometry can be a very powerful technique for revealing electronic states in the multiply charged region. This happens because there is no background emission from the ionization continua for which the cross sections are normally orders of magnitude larger than the specific excitation channels that lead to the production of fluorescence. We plan to improve our resolution and S/N ratio in order to resolve electronic states in the 50-100 eV region.

In the future we shall carry out an absolute calibration in order to determine absolute

fluorescence cross sections and hence the branching ratios for the fluorescence channels. With the bright undulator beamline we also plan to carry out dispersed fluorescence studies.

ACKNOWLEDGEMENTS

We are grateful to the staff of the Advance Light Source and especially Dr. John Bozek for helpful assistance.

REFERENCES

1. Y. Morioka, T. Akahori, T. Hayaishi, T. Namioka, T. Sasaki, and M. Nakamura, J. Phys. B. **19** (1986) 1075.
2. L.C. Lee, R.W. Carlson, D.L. Judge, and M. Ogawa, Chem. Phys. Lett., **19** (1973) 183 and J. Chem. Phys., **61** (1974) 3261.
3. L.C. Lee, R.W. Carlson, D.L. Judge, and M. Ogawa, J. Chem. Phys., **63**, (1975) 3987.
4. J.A.R. Samson, Y. Chung, and E-M. Yee, J. Chem. Phys., **95** (1991) 717.
5. C.Y.R. Wu, and D.L. Judge, Trends Chem. Phys., **1**, (1991) 51.
6. C.Y.R. Wu, J.K. Chen, and D.L. Judge, J. Geophys. Res., **88** (1983) 2163.
7. C.Y.R. Wu, J. Geophys. Res., **99** (1994) 8971.
8. M. Ukai, K. Kameta, N. Kouichi, Y. Hatano, and K. Tanaka, Phys. Rev. A, **46** (1992) 7019.
9. M. Ukai, K. Kameta, N. Kouichi, Y. Hatano, and K. Tanaka, J. Chem. Phys., **97** (1992) 2835.
10. P. Erman, A. Karawajczyk, E. Rachlew-Kallne, S.L. Sorensen, C. Stromholm, and M. Kirm, J. Phys. B, **26** (1993) 4483.
11. W.F. Chan, G. Cooper, and C.E. Brion, Chem. Phys., **170** (1993) 401.
12. D. Stalherm, B. Cleff, H. Hillig, and W. Mehlhorn, Z. Naturforsch, **24a** (1969) 1728.
13. W.E. Moddeman, T.A. Carlson, M.O. Krause, B.P. Pullen, W.E. Bull, and G.K. Schweitzer, J. Chem. Phys., **55** (1971) 2317.
14. W.F. Chan, G. Cooper, R.N.S. Sodhi, and C.E. Brion, Chem. Phys., **170** (1993) 81.
15. A.P. Hitchcock, C.E. Brion, and M.J. van der Wiel, Chem. Phys., **45** (1980) 461.
16. P.W. Langhoff, S.R. Langhoff, T.N. Rescigno, J. Schirmer, L. Cederbaum, W. Domcke, and W. von Niessen, Chem. Phys., **58** (1981) 71.
17. H. Sambe and D.E. Ramaker, Chem. Phys., **107** (1986) 351.
18. J.A.R. Samson, T. Masuoka, P.N. Pareek, and G.C. Angel, J. Chem. Phys., **86** (1987) 6128.
19. M.J. Besnard, L. Hellner, G. Dujardin, and D. Winkoun, J. Chem. Phys., **88** (1988) 1732.
20. C.Y.R. Wu and D.L. Judge, J. Chem. Phys., **75** (1981) 172.
21. C.Y.R. Wu, L.C. Lee, and D.L. Judge, J. Chem. Phys., **80** (1984) 4682.

This work was supported by NSF grant ATM-9322384 and NASA grant NAGW-1924.

Principal investigator: C. Y. Robert Wu, Department of Physics and Astronomy and Space Sciences Center, University of Southern California. Email: robertwu@lism.usc.edu. Telephone: 213-740-6332. FAX: 213-740-6342.

Identification of Weak Autoionizing Resonances Observed through Fluorescence from the Satellite States of Ar^+

K.W. McLaughlin[1], O. Yenen[1], J.A.R. Samson[1], D.H. Jaecks[1], A.S. Schlachter[2], and J. Bozek[2]
[1] Department of Physics & Astronomy, University of Nebraska-Lincoln, Lincoln NE 68588-0111, USA
[2] Advanced Light Source, Ernest Orlando Lawrence Berkeley National Laboratory, University of California, Berkeley, CA 97420, USA

INTRODUCTION

Photoionization accompanied by excitation of the residual ionic state violates an independent electron model since, according to QED, photons interact only with individual electrons. By allowing measurements at a threshold event with high resolution, the observation of the fluorescence from the decay of these excited states (*satellite states*) is a sensitive method in the study of electron-electron interactions, providing complementary information to photoelectron spectroscopy. In the measurements reported here, an atomic beam of argon has been photoionized with 34 to 39 *eV* synchrotron radiation at beamline 9.0.1 of the Advanced Light Source. This energy range encompasses the $3p^4\,[^3P]\,4p\,{}^4P$, ^2P and ^2D as well as the $[^1D]\,4p\,{}^2F$ satellite states of Ar^+. By observing the fine-structure resolved fluorescence from these satellite states, new Rydberg series and extensions of previously known series have been resolved with an energy resolution of 3 *meV*. With the high photon flux available from the high resolution monochromator of beamline 9.0.1, even the weakly excited $[^3P]\,4p\,(^2S)\,ns,d$ autoionizing structure has been observed for the first time.

EXPERIMENT

A schematic of the experimental apparatus is shown in Fig. 1. An atomic beam of argon effuses from a demagnetized stainless-steel needle intersecting a beam of synchrotron radiation at right angles. The linear polarization axis of the synchrotron radiation is aligned along the atomic beam axis. Fluorescence was observed along two collection axes. One of these is aligned perpendicular to the plane defined by the synchrotron radiation and atomic beam propagation axes (the COLLISION PLANE). The other is aligned within this plane, 30° off axis from the propagation direction of the synchrotron radiation. Each fluorescence collection system consisted of a photomultiplier coupled to the interaction region by a $f/1.9$ lens along with a linear polarizer and 0.3 *nm* bandwidth interference filter. By measuring the polarization of the satellite state fluorescence the total intensity emitted into 4π solid angle can be calculated[1]. Therefore, with the appropriate interference filters, two fine-structure resolved fluorescent measurements were acquired simultaneously. Addressed in a separate ALS abstract[2], the polarization measurement of the satellite state fluorescence further allows the alignment parameters[3] of these excited states to be assessed. The fluorescence spectra are normalized to the incident ionizing photon flux monitored with an aluminum diode as the synchrotron radiation exits the interaction region.

With 20×25 μm slits on the spherical-grating monochromator of beamline 9.0.1, the resolution was nominally 3 *meV* in the 34 to 39 *eV* energy range. Calibration of this ionizing photon

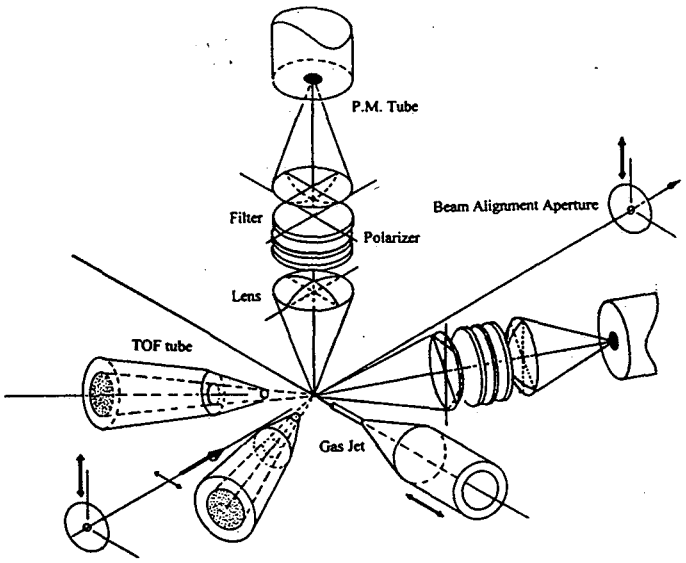

Figure 1. Schematic of the experimental apparatus used, in conjunction with beamline 9.0.1 of the Advanced Light Source, to measure the polarization of the fluorescence from the satellite states of Ar^+.

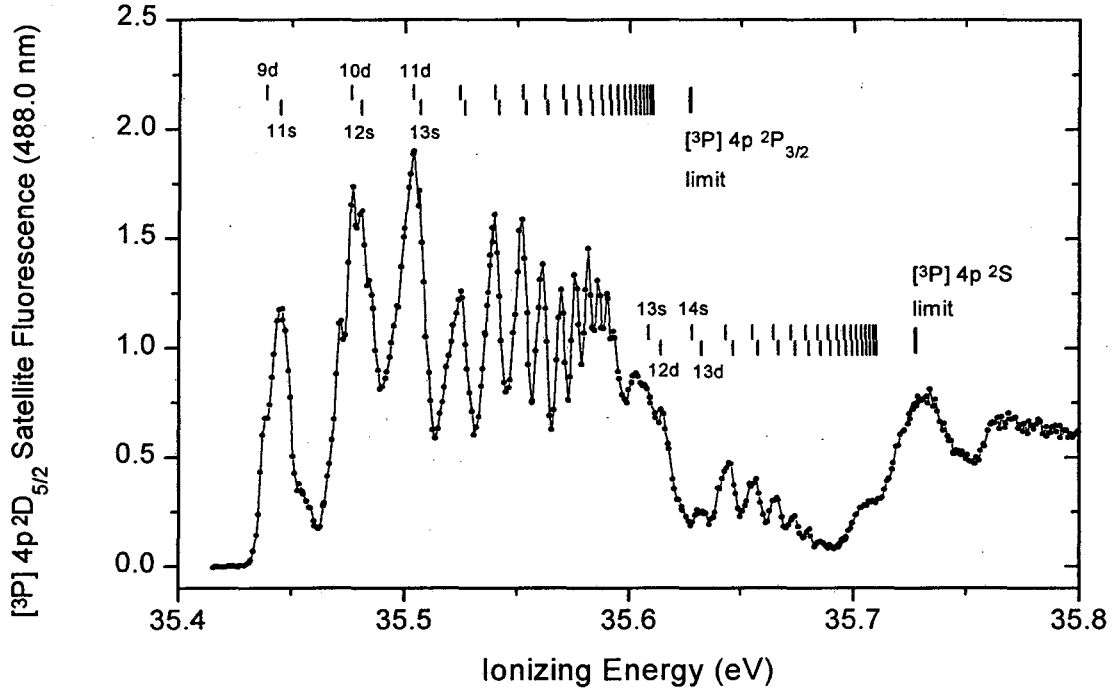

Figure 2. Total intensity of the 488.0 *nm* satellite fluorescence in the immediate vicinity of the threshold for this $[^3P]\ 4p\ ^2D_{5/2}$ satellite state of Ar^+.

energy was accomplished by monitoring the photoelectron signal from the $3s\,3p^6\,np\ ^1P$ window resonances[4] of Ar from $n = 6$ to 20 along with the threshold onsets[5] of the fine-structure resolved fluorescence from the $3p^4\,[^3P]\,4p\ ^2P$, ^2D and $[^1D]\,4p\ ^2F$ satellite states of Ar^+. Photoelectrons are detected by dual microchannel plates in a chevron arrangement. The microchannel plates follow a 10 *cm* time-of-flight column for coarse energy analysis in future photoelectron-photoion fluorescence coincidence studies. Photoelectrons are detected within the COLLISION PLANE along two collection axes: aligned at 45° and at the magic angle, both with respect to the linear polarization axis of the synchrotron radiation. The interaction region was magnetically shielded by 1.6 *mm* thick μ-metal dual shields (both interior and exterior to the vacuum chamber) which attenuates the ambient field by a factor of 10^2.

RESULTS

The fine-structure resolved fluorescence from the $Ar^+\ 3p^4\,[^3P]\,4p\ ^4P_{3/2,5/2}$, $^2P_{1/2,3/2}$ and $^2D_{3/2,5/2}$ as well as the $[^1D]\,4p\ ^2F_{5/2,7/2}$ satellite states has been measured within the ionizing energy range 34 to 39 *eV*. New Rydberg series and extensions of previously known series have been resolved with an ionizing energy resolution of 3 *meV*. Some of the highlights of these measurements is illustrated in Fig. 2 which testifies to the density of the autoionizing structure in this ionizing energy region. Depicted is the intensity of the 488.0 *nm* line representing the $[^3P]\,4p\ ^2D_{5/2} \rightarrow 4s\ ^2P_{3/2}$ fluorescence in the immediate vicinity of the threshold for this satellite state at 35.435 *eV*. The autoionizing $[^3P]\ 4p\ (^2P_{3/2})\ ns$ and n'd Rydberg series is identified up to the $n = 22$ and $n' = 20$ overlapping terms. The 9d term is obscured by the onset to the $^2D_{5/2}$ threshold but the 12s and 10d terms are partially resolved for the first time. This series was absent in early transmission studies[3]. Previous broadband fluorescence measurements[6] had registered broad features indicative of the presence of the early members of this series but had failed to resolved the *n*s and *n'*d terms. Observed for the first time is the weakly excited series $[^3P]\,4p\,(^2S)\,ns,d$. This Rydberg series, observable due to the high photon flux available from the high resolution monochromator of beamline 9.0.1, is weak due to the fact that it violates the *L-S* coupled requirement of a ^1P symmetry for the final state of the system.

REFERENCES

1. J.A. Smit, Physica **2**, 104 (1935).
2. O. Yenen, K.W. McLaughlin, D.H. Jaecks, A.S. Schlachter, and J. Bozek, ALS Compendium of User Abstracts (1997).
3. U. Fano and J.H. Macek, Rev. Mod. Phys. **45**, 553 (1973).
4. R.P. Madden, D.L. Ederer, and K. Codling, Phys. Rev. **177**, 136 (1969).
5. C.E. Moore, *Atomic Energy Levels*, U.S. National Bureau of Standards Circular 467 (1958).
6. J.A.R. Samson, E.-M. Lee, and Y. Chung, J. Elec. Spec., **66**, 75 (1993).

This work is supported by the National Science Foundation under Grant PHY-9419505

Principal investigator: Prof. Duane H. Jaecks, Dept. of Physics & Astronomy, University of Nebraska-Lincoln, Lincoln NE 68588-0111, USA. Email: djaecks@unlinfo.unl.edu. Telephone: 402-472-3274.

Photoionization Study of Doubly-Excited Helium at Ultra-High Resolution

G. Kaindl[1], K. Schulz[1], J.D. Bozek[2], A.S. Schlachter[2], P.A. Heimann[2], and M. Domke[1]
[1]Institut für Experimentalphysik, Freie Universität Berlin
Arnimallee 14, D-14195 Berlin, Germany
[2]Advanced Light Source, Ernest Orlando Lawrence Berkeley National Laboratory
University of California, Berkeley, California 94720, USA

INTRODUCTION

Ever since the pioneering work of Madden & Codling [1] and Cooper, Fano & Prats [2] on doubly-excited helium in the early sixties, this system may be considered as prototypical for the study of electron-electron correlations [3]. More detailed insight into these states could be reached only much later, when improved theoretical calculations of the optically-excited $^1P^o$ double-excitation states became available [4] and sufficiently high energy resolution (ΔE=4.0 meV) was achieved [5,6]. This allowed a systematic investigation of the double-excitation resonances of He up to excitation energies close to the double-ionization threshold, I_∞=79.003 eV [7,8], which stimulated renewed theoretical interest into these correlated electron states [9-11].

We report here on striking progress in energy resolution in this grazing-incidence photon-energy range of grating monochromators and its application to hitherto unobservable states of doubly-excited He. By monitoring an extremely narrow double-excitation resonance of He, with a theoretical lifetime width of $\leq$5 μeV, a resolution of ΔE=1.0 meV (FWHM) at 64.1 eV could be achieved. This ultra-high spectral resolution, combined with high photon flux, allowed the investigation of new Rydberg resonances below the N=3 ionization threshold, I_3, as well as a detailed comparison with ab-initio calculations [14].

EXPERIMENT

The experiments were performed at beamline 9.0.1 of the ALS, using the 925-lines/mm spherical grating of this Dragon-type monochromator [15]. Energy was calibrated by fitting the principal series below I_2 and I_3 to the Rydberg series of Fano profiles, and adjusting the energy-defining monochromator parameters to match the correct threshold energies, I_2=65.4007 eV and I_3=72.9589 eV. The photoionization measurements were done with a gas cell containing two parallel charge-collecting plates of 10-cm active length, filled with He at pressures from 2 to 500 μbar, and separated from the monochromator vacuum by a window of 1500-Å Al(1% Si) [1200-Å carbon] for $h\nu<I_2$ [$h\nu>I_2$]. All spectra were normalized to the incident photon flux monitored with a gold grid in front of the gas cell. The electric current in the gas cell and on the gold grid (10^{-11} - 10^{-10} A) were measured with sensitive current amplifiers (Keithley model 428).

RESULTS AND DISCUSSION

The photoionization spectrum below I_2 is shown in Fig. 1, where the states are denoted by N,K_n; N and n (or n', n") refer to the principal quantum numbers of the inner and outer electrons, respectively, and K to a correlation quantum number, as defined in [3,4]. The principal series, $2,0_n$, shown in (a) for n≥4, was resolved up to n=26 [see inset in (a)]. The stronger secondary series, $2,1_{n'}$, shown on an expanded energy scale in (b) and (c), was observed up to n'=12, and the weaker secondary series, $2,-1_{n''}$, up to n"=7. While most spectra were recorded with 5-μm

wide entrance and exit slits, corresponding to $\Delta E \approx 2$ meV, the $2,1_4$ and $2,-1_3$ resonances were measured with 2.5-μm wide slits at highest resolution. The $2,-1_3$ state is ideally suited for determining monochromator resolution due to its narrow width, calculated as ≤5 μeV[8]. The inset in (b) shows this resonance on an expanded energy scale, with a total width of 1.0 meV (FWHM), corresponding to a resolving power of $E/\Delta E$=64,000 at hν=64.1 eV; this is by a factor of four better than previously obtained with the SX700/II monochromator at BESSY [6]. The photon flux at this ultra-high resolution was measured with a Si photodiode to be $\approx 8 \times 10^9$ photons/s at 62 eV (300 mA ring current; 2.5 μm slits), which is about one order of magnitude higher than at the SX700/II beamline at ΔE=4 meV. The spectra in Fig. 1 were least-squares fitted with independent Fano profiles convoluted with the monochromator function; the solid lines through the data points represent the fit results. The derived resonance energies, lifetime widths, and Fano-q parameters in general agree well with the results of advanced calculations [10,14].

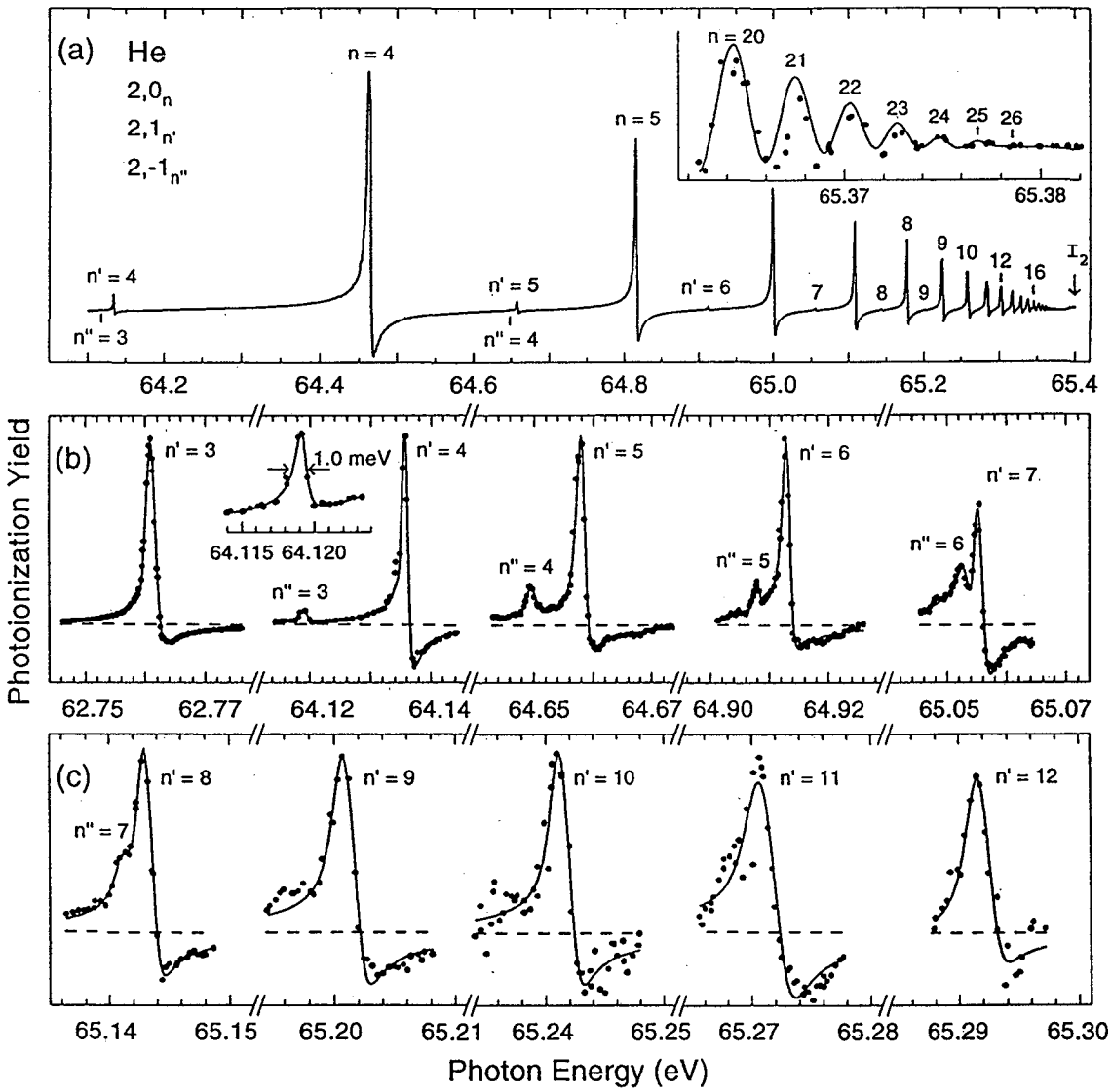

Figure 1: Autoionizing resonances of doubly-excited He below I_2: (a) overview spectrum, with resonances of all three $^1P^o$ Rydberg series; (b), (c) resonances of the secondary series $2,1_{n'}$ and $2,-1_{n''}$. Smooth backgrounds, which are caused by neighboring principal resonances, have been subtracted from the data.

With this substantial improvement in resolution and photon flux, we searched for previously unobservable double-excitation resonances. Fig. 2(a) shows an overview spectrum below I_3, dominated by the principal series, $3,1_n$, and the lowest resonance, $3,-1_3$, of the strongest secondary series; the energies of the newly discovered resonances of the secondary series $3,2_n$, and $3,0_n$ (see below) have been marked by vertical arrows. Fig. 2(b) shows the principal series, $3,1_n$ for $n \geq 14$, resolved up to n=24 at $\Delta E \approx 2.3$ MeV.

The $3,2_n$ and $3,0_n$ resonances are shown in Fig. 3; both series have the correlation quantum numbers T=0 and A=-1, and are "quasi forbidden" [3,14]. A search for the extremely narrow lowest resonance of the fifth n=3 series, $3,-2_n$ (with T=0 and A=0), with a strongly reduced excitation cross-section [10], was unsuccessful. Hence all series with T=1 or 0 and A=+1 or -1 below I_2 and I_3 have now been observed. The series with T=1, A=+1 are the most intense ones, exhibiting also the largest lifetime widths. The series with T=0, A=-1 are weaker and narrower, and the weakest and narrowest resonances have A=0, which could be monitored for N=2 only. Again, the experimental parameters are in good agreement with the results of state-of-the-art calculations, with the exception of the q-parameters of the $3,2_n$ series [14].

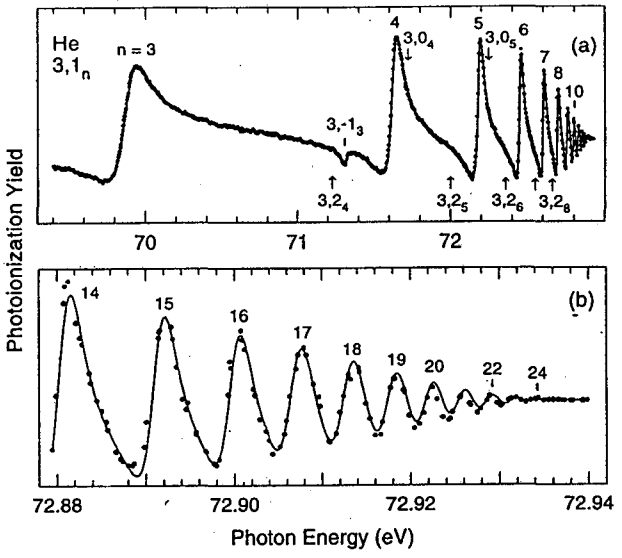

Figure 2: Autoionizing resonances below I_3: (a) overview (from Ref. [8]); (b) upper region of the Rydberg series shown on an expanded energy scale (present work).

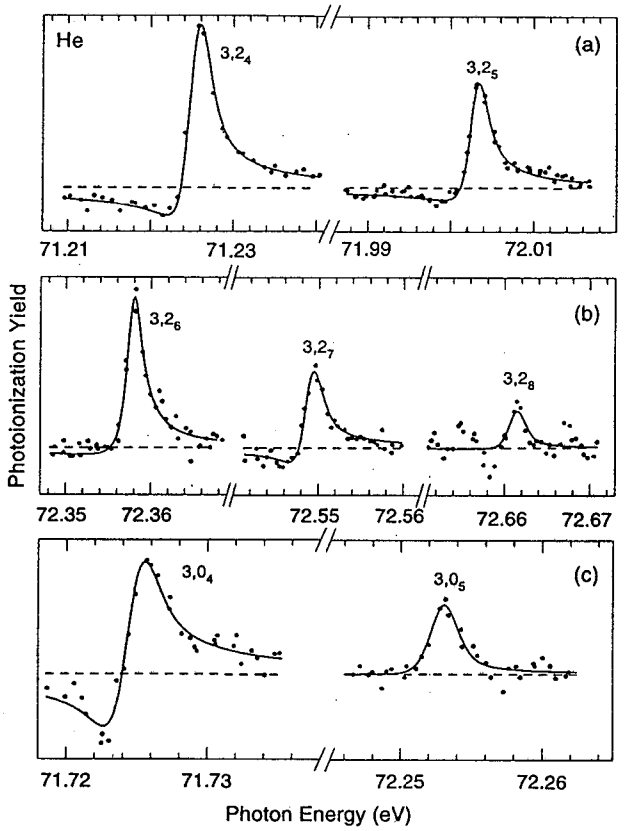

Figure 3: Newly observed resonances of two secondary series below I_3: (a), (b) $3,2_n$ series up to n=8; (c) $3,0_n$ series up to n=5. Smooth backgrounds, caused by neighboring resonances, have again been subtracted.

CONCLUSIONS

The ultimate resolving power of beamline 9.0.1 is 178,000, given by the number of grooves in the 925 lines/mm grating. However, several factors degrade resolution, including the finite widths of the entrance and exit slits, the coma aberration, figure errors of the optical surfaces, and the finite mechanical stability. Even though the coma error is small at 64.1 eV (the Rowland-circle condition is fulfilled at ≈71 eV with the grating used), the results reflect the extraordinary quality of the optical grating (with a figure error better than 0.5 μrad rms). Beamline 9.0.1 at the ALS is thus a powerful new tool for ultra-high resolution spectroscopy of atoms, molecules, and condensed matter.

ACKNOWLEDGMENTS

The authors acknowledge expert help by the operating staff of ALS as well as valuable discussions with H. Padmore, T. Warwick, D. DiGennaro, and W. McKinney.

REFERENCES

1. R.P. Madden and K. Codling, Phys. Rev. Lett. **70**, 516 (1963); Astrophys. J. **141**, 364 (1965).
2. J.W. Cooper, U. Fano, and F. Prats, Phys. Rev. Lett. **10**, 518 (1963).
3. D.R. Herrick and O. Sinanoglu, Phys. Rev. A **11**, 97 (1975).
4. C.D. Lin, Phys. Rev. A **29**, 1019 (1984).
5. M. Domke, C. Xue, A Puschmann, T. Mandel, E. Hudson, D.A. Shirley, G. Kaindl, C.H. Greene, H.R. Sadeghpour, and H. Petersen, Phys. Rev. Lett. **66**, 1306 (1991).
6. M. Domke, G. Remmers, and G. Kaindl, Phys. Rev. Lett. **69**, 1171 (1992).
7. M. Domke, K. Schulz, G. Remmers, R. Gutierrez, G. Kaindl, and D. Wintgen, Phys. Rev. A **51**, R4309 (1995).
8. M. Domke, K. Schulz, G. Remmers, G. Kaindl, and D. Wintgen, Phys. Rev. A **53**, 1424 (1996).
9. J.-Z. Tang, S. Watanabe, M. Matsuzawa, and C.D. Lin, Phys. Rev. Lett. **69,** 1633 (1992).
10. D. Wintgen and D. Delande, J. Phys. B**26**, L399 (1993); and private communication.
11. T.N. Chang, Phys. Rev. A **47**, 3441 (1993).
12. G. Kaindl, K. Schulz, P.A. Heimann, J.D. Bozek, and A.S. Schlachter, Synchrotron Radiation News **8**(5), 29 (1995).
13. K. Schulz, G. Kaindl, J.D. Bozek, P.A. Heimann, and A.S. Schlachter, J. Electr. Spectr. Rel. Phenom. **79**, 253 (1996).
14. K. Schulz, G. Kaindl, M. Domke, J.D. Bozek, P.A. Heimann, A.S. Schlachter, and J.M. Rost, Phys. Rev. Lett. **77**, 3086 (1996).
15. P.A. Heimann, T. Warwick, M. Howells, W. McKinney, D. Digenarro, B. Gee, D. Yee, and B. Kincaid, Nucl. Instr. Meth. A **319**, 106 (1992).

This work was supported by the Director, Office of Energy Research, Office of Basic Energy Sciences, Materials Science Division, of the U.S. Department of Energy under Contract No. DE-AC03-76SF00098. The work in Berlin was supported by the Bundesminister für Bildung, Wissenschaft, Forschung und Technologie, project No. 05-650-KEA, and the Deutsche Forschungsgemeinschaft, project Do-561/1-1.

Principal investigator: Günter Kaindl, Institut für Experimentalphysik, Freie Universität Berlin, Germany. Email: kaindl@physik.fu-berlin.de; Telephone: ++49-30-838-2977; Fax: ++49-30-838-6560.

Precision Angle-Resolved Autoionization Resonances in Ar and Ne

N. Berrah[1], B. Langer[1], T.W. Gorczyca[1], R. Wehlitz[2], A. Farhat[1], D.W. Lindle[3] and J.D. Bozek[4]

[1]Physics Department, Western Michigan University, Kalamazoo, MI 49008
[2]University of Tennessee, Physics Department, Knoxville, TN 37996-1200
[3]Chemistry Department, University of Nevada, Las Vegas, NV 89154
[4]Lawrence Berkeley Laboratory, Advanced Light Source Mail Stop 2-400, Berkeley, CA 94720

INTRODUCTION

Theoretical work has shown that the electron angular distribution [1] and the shape of the autoionization resonances [2] are crucial to the understanding of certain types of electron-electron correlation. Autoionization resonances in Ne (Ar) result from the decay of the excited discrete state $Ne^* 2s2p^6$ np ($Ar^* 3s3p^6$ np) into the continuum state $Ne^+ 2s^22p^5 + e^-$ (ks,kd) ($Ar^+ 3s^23p^5 + e^-$ (ks,kd)). Since the continuum can also be reached by direct photoionization, both paths add coherently, giving rise to interferences that produce the characteristic Beutler-Fano line shape.

In this work, we report on quantitative angle-resolved electron spectrometry studies of (a) the Ne $2s^2\ 2p^6 \rightarrow 2s2p^6$ np (n=3-5) autoionizing resonances and the $2s^22p^6 \rightarrow 2p^43s3p$ doubly excited resonance, (b) the Ar $3s^23p^6 \rightarrow 3s3p^6$ np (n=4-9) autoionization resonances and (c) extended R-matrix calculations of the angular-distribution parameters for both Ne and Ar measurements. Our results are compared with previous theoretical work by Taylor [3].

EXPERIMENT

Two components of instrumentation were needed in these photoemission measurements: high-resolution and high-brightness beamline and an angle-resolved technique to measure the angular distribution of the emitted photoelectrons. The experiment was performed in two-bunch operation at the Advanced Light Source (ALS) at Lawrence Berkeley Laboratory on beamline 9.0.1. The monochromator bandpass was 19 meV in the resonance region of Ne and 6 meV in the case of Ar. We determined the degree of linear polarization P_l of the monochromatic light in the resonance region to be P_l=0.99. The tilt of the polarization plane with respect to the experimental system was measured to be zero. Details of the experimental apparatus are described in another work [4]

RESULTS

The Case of Neon

The aim of this work is to extract the angular distribution parameters. We have done this by fitting our total cross section data using the parameterization of Kabachnik and Sazhina [5]. The results for the total photoionization cross-section are shown in Fig. 1 for one double-excitation and three single-excitation autoionization resonances.

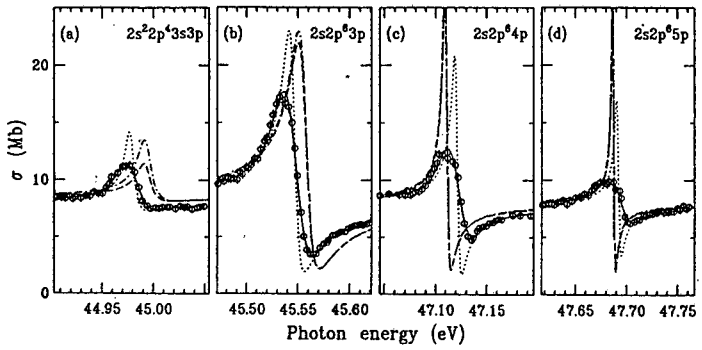

Figure 1. Cross section behavior of the Ne $2s^22p^6$ (a) $2s^22p^43s3p$ and (b-d) $2s2p^6np$ (n=3-5) autoionization resonances. The circles are the experimental data taken at the magic angle. The solid lines represent a Fano curve fit to our data. The dotted lines are created using the Fano parameters without bandpass; the dot-dashed and the dashed lines are our theoretical R-matrix calculations in length and velocity form, respectively.

The fitting parameters, the width Γ, the line profile q and the correlation coefficient ρ^2 for the photoionization cross section in the region of the first 4 resonances were extracted and can be found in Langer [6].

The pronounced behavior of the angular distribution parameter β as a function of the photon energy is shown in Fig. 2 for the $2s2p^6$ (^2S) np resonances, the strong $2p^43s3p$ resonances and the weak $2p^4nln'l'$ resonances.

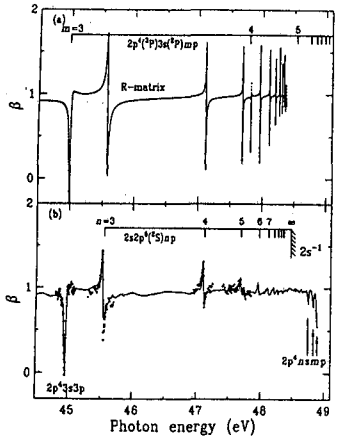

Figure 2. (a) Theoretical calculations and (b) experimental results of the angular distribution anisotropy parameter β for the Ne 2p line in the region of the autoionization resonances below the 2s threshold. In (a), the dotted line and the solid lines, which are nearly identical on this scale, show the length and the velocity forms of our calculation, respectively. In (b), the solid line represents the β parameter as obtained from our scans.

In Fig. 2, angular distribution data are shown for the $2p^2 \rightarrow 3s3p$ resonance as well as the $2s \rightarrow np$ (n=3-5) resonances and are compared with a fit curve. As can be seen from Fig. 2, the parameterization of Kabachnik and Sazhina [5] gives a very good fit to the experimental angular distribution data. The angular distribution has also been compared with the never experimentally tested R-matrix results of Taylor [3] and our R-matrix results. These results can be found in reference [7].

We found that the entire Rydberg series $2s2p^6np$ generated by our calculations lines up well with the experimental values, indicating that our computed quantum defect μ is quite reasonable. Also, the calculated widths of these resonances, the degree of interference with the background, and the shape of the background itself all show good agreement with experiment. We found excellent agreement between the data and both theories. The parameters X, Y and Z produced by our fit and our calculations are listed in Table 1 along with the results from Taylor [3] available only for n=3-4.

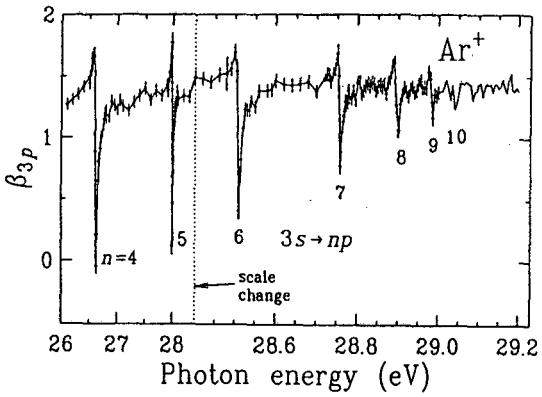

Figure 3. Angular distribution anisotropy parameter β measurements of the Ar $3s^23p^6$ np autoionization resonances.

Table 1. Angular distribution profile parameters for the Ne $2s^22p^6$–$2s^22p^43s3p$ and $2s2p^6np$ (n=3-5) autoionization resonances compared with theoretical calculations.

	Method	$2s^22p^43s3p$			$2s2p^63p$		
		X	Y	Z	X	Y	Z
Taylor (1977)	CI (L)				-0.35	1.23	-1.27
	CI (V)				-0.26	0.96	-0.84
present results	theo. (L)	-0.28	-0.14	0.35	-0.28	1.06	-1.02
	theo. (V)	-0.28	-0.14	0.21	-0.28	1.12	-1.17
	exp.	-0.291(1)	-0.22(1)	0.23(3)	-0.285(1)	1.08(6)	-1.06(4)
	Method	$2s2p^64p$			$2s2p^65p$		
		X	Y	Z	X	Y	Z
Taylor (1977)	CI (L)	-0.33	1.33	-1.37			
	CI (V)	-0.29	1.04	-0.93			
present results	theo. (L)	-0.27	1.14	-1.23	-0.27	1.16	-1.32
	theo. (V)	-0.27	1.12	-0.97	-0.27	1.14	-1.28
	exp.	-0.312(1)	1.02(15)	-0.92(10)	0.301(1)	0.7(3)	-0.8(3)

The Case of Argon

We have fit both the total photoionization cross section data and the angular distribution parameter as in the neon case. The variation of β as a function of photon energy is shown in Fig. 3. Our calculation appeared shifted to higher energies with respect to the measurements for the n=4 resonance but this shift almost vanishes for higher resonances. The parameters X, Y, and Z produced by our fit are listed in Table 2 for n=4 to n=9 along with the results from Taylor [3]. From Table 2, one can note the excellent agreement between the data and the CI calculations. It is clear that the CI calculation is indeed a better model for the data because, in the case of n=4, the single configuration calculation did not even predict the correct sign of the Y parameter. We also would like to point out that our R-matrix calculations tried, unlike others, to obtain the energies position. The result is fair for the low resonances but agrees better with the measurements for the higher resonances. Details of this work can be found in Berrah et al. [8].

CONCLUSION

We have observed the Ne 2s→np (n=3-5) and the Ne $2p^2$→nln'l' resonances. The analysis of the differential cross-section resonances agree well with previous measurements [9]. The angular distribution shows pronounced resonances, more pronounced than in previous measurements. Comparisons of the extracted parameters with Taylor's results [3] and with our R-matrix results are very good. We have also made detailed angle-resolved measurements of the Ar $3s^23p^6$→$3s3p^6$np autoionization resonances as well as R-matrix calculations. The comparison of our results with our R-matrix calculations and those of Taylor [3] is found to be excellent.

	Method	$3s \rightarrow 4p$			$3s \rightarrow 5p$			$3s \rightarrow 6p$		
		X	Y	Z	X	Y	Z	X	Y	Z
Taylor (1978)	SC(L)	-1.53	-2.88	-1.21						
	SC(V)	-0.81	-0.81	-0.09						
	CI (L)	-1.79	1.85	-0.44	-1.77	1.33	-0.14			
	CI (V)	-1.47	1.44	-0.31	-1.46	1.01	-0.06			
present results	theory (L)	-1.73	1.99	-0.56	-1.67	1.55	-0.41	-1.66	1.40	-0.34
	theory (V)	-1.41	1.73	-0.54	-1.36	1.35	-0.39	1.35	1.22	-0.32
	experiment	-1.567(12)	1.49(2)	-0.322(12)	-1.483(11)	1.00(2)	-0.158(13)	-1.46(2)	0.95(4)	-0.10(2)

	Method	$3s \rightarrow 7p$			$3s \rightarrow 8p$			$3s \rightarrow 9p$		
		X	Y	Z	X	Y	Z	X	Y	Z
present results	theory (L)	-1.65	1.36	-0.35	-1.64	1.22	-0.26	-1.63	1.29	-0.33
	theory (V)	-1.34	1.19	-0.33	-1.33	1.08	-0.25	-1.32	1.13	-0.31
	experiment	-1.507(10)	0.97(4)	-0.15(3)	-1.489(14)	0.79(7)	-0.13(6)	-1.49(2)	0.56(9)	-0.46(8)

Table 2. Comparison of the fitted (solid line through the data), and calculated angular-distribution parameters for the $3s3p^6$ 4p and 5p $^1P^0$ resonances in Ar

REFERENCES

1. M. Ya. Amusia, Atomic photoeffect (plenum, New York) (1990).
2. H. Feshbach, Ann. Phys. 19, 287 (1962).
3. K. T. Taylor, J. Phys. B: At. Mol. Opt. 10, L699 (1977).
4. B. Langer, A. Farhat, B. Nessar, N. Berrah, O. Hemmers, and J. D. Bozek, "Resonant Raman effect in the study of Xe" in Proc. Fourth Workshop on Atomic Physics with hard X-Rays from High Brilliance Synchrotron Light Sources (1996).
5. N. M. Kabachnik, and I. P. Sazhina, J. Phys. B: At. Mol. Opt. Phys. 9, 1681 (1976).
6. B. Langer, N. Berrah, R. Wehlitz, T. W. Gorczyca, J. D. Bozek, and A. Farhat, J. Phys. B: At. Mol.Opt. Phys. 29, 1 (1996).
7. N. Berrah, B. Langer, J. D. Bozek, T.W. Gorczyca, O. Hemmers, D. W. Lindle, and O. Toader, J. Phys. B: At. Mol. Opt. Phys. **29**, 5351 (1996)

This work was supported by the US Department of Energy, Office of Basic Energy Science, Division of Chemical Science under contract No. DE-FG02-92ER14299. B.L. and R.W. are indebted to the Alexander von Humboldt Foundation for partial support.

Principal Investigator: Nora Berrah,Western Michigan University, Physics Department, Kalamazoo, MI 49008. Email:Berrah@wmich.edu. Tel. 616-387-4955.

Beamline 9.0.2 Abstracts

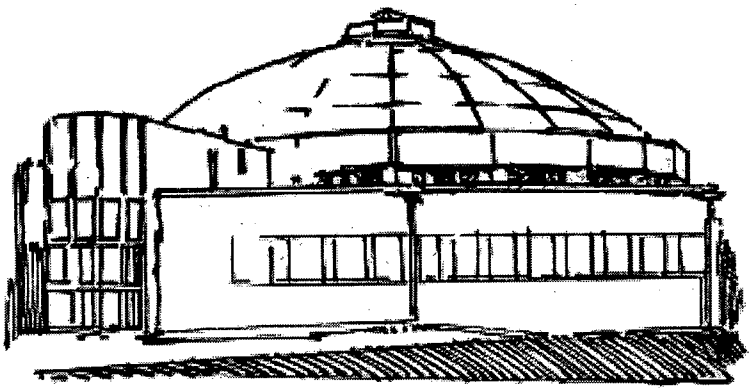

High-Resolution Pulsed-Field Ionization Photoelectron Spectroscopy Using Multi-Bunch Synchrotron Radiation

C.-W. Hsu[1], M. Evans[2], P.Heimann[3], and C.Y. Ng[2]

[1]Chemical Science Division, Lawrence Berkeley National Laboratory, Berkeley, CA 94720, USA
[2]Ames Laboratory, USDOE and Department of Chemistry, Iowa State University, Ames, Iowa 50011, USA
[3]Advanced Light Source and Accelerator and Fusion Research Division, Ernest Orlando Lawrence Berkeley National Laboratory, Berkeley, CA 94720, USA

INTRODUCTION

BL9.0.2.2 is the newly constructed experimental End Station 2 at the Chemical Dynamics Beamline 9.0.2 of the Advanced Light Source (ALS). It is dedicated to the high resolution photoionization study of molecules of interest to atmospheric and combustion chemistry. This End Station is equipped with a high resolution scanning monochromator, which has been demonstrated to have a world record resolution of $E/\Delta E$=70,000 [1, 2]. Taking the advantage of the high resolution ALS light, we have improved the energy resolution in threshold photoelectron spectroscopy (TPES) to 0.8 meV [3]. The TPES is a popular technique for photoionization experiments at all synchrotron radiation facilities due to its high energy resolution as compared to that of traditional photoelectron spectroscopy (PES). TPES achieves higher energy resolution by preferentially detecting near zero kinetic energy photoelectrons resulting from threshold photoionization. However, the spectra obtained from the TPES technique generally are complicated by the simultaneous detection of electrons with nonzero kinetic energy, which are not fully discriminated against.

On the other hand, the spectra obtained from pulsed field ionization photoelectron spectroscopy (PFI-PES) are completely free of the contamination from kinetic electrons. The PFI-PE technique basically involves the detection of the photoelectrons from field ionization of the very high-n Rydberg states, a few cm^{-1} below the ionization energy (IE), by applying a delayed pulsed electric field. Within a delay of a few microseconds, all the prompt electrons formed from direct ionization will escape from the photoionization region and will not be collected. The technique has been a triumph for experiments using tunable pulsed dye lasers. However, experiments using synchrotron radiation have encountered major difficulties in applying this technique because of its high repetition rate light pulses (> 1 MHz), making it difficult for the placement of a delayed pulsed electric field and for the discrimination of the prompt electrons. The experimental scheme for PFI-PES has been demonstrated at the BESSY facility using multi-bunch synchrotron radiation [4]. The prompt electrons and the electrons produced from field ionization of the high-n Rydberg states were separated using the electron time-of-flight technique. A resolution of 3-6 meV was obtained in their experiment, which is insufficient to resolve the rotational structure for most diatomic molecules.

EXPERIMENT

In a recent development, we have overcome this difficulty and successfully incorporated the PFI-PE technique with multi-bunch VUV synchrotron radiation [3]. Fig. 1 shows the timing structure for the implementation of the PFI-PE technique using the 478 MHz ALS light pulses. The time separation between two consecutive light pulses is 2 ns, which acts like a quasi-continuous light source. However, a gap of 48 ns exists between the quasi-continuous light pulses in a period of 656 ns. A pulsed electric field (40 ns, 0.55 V/cm), coinciding with the appearance of this gap, is applied to the photoionization region in order to field ionize all the high-n Rydberg states. Upon the application of a pulsed electric field, the prompt electrons formed from direct ionization have already moved away from the center of the photoionization region. Therefore, they acquire energies different from those electrons produced from field ionization of the high-n Rydberg states. The use of a hemispherical electron energy analyzer (ESA), shown in Fig. 2, is a key element for eliminating the detection of kinetic electrons due to its high energy sensitivity. Theoretically, a prompt electron will possess an energy out of the energy selection range of the ESA after if it has traveled within the ionization region for more than 7 ns. This prediction is confirmed by the experimental observation described below.

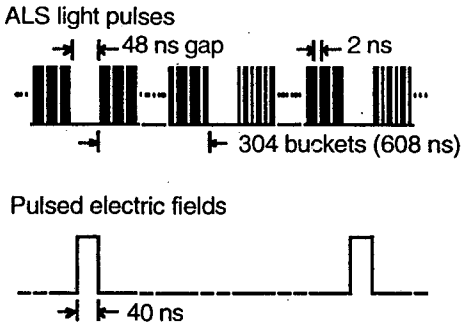

Figure 1. The timing structures for the ALS light bunches in the multi-bunch mode and the electric field (0.55V/cm, width=40 ns) applied to the repeller lens. The time separation between adjacent electric field pulses is 1312 ns.

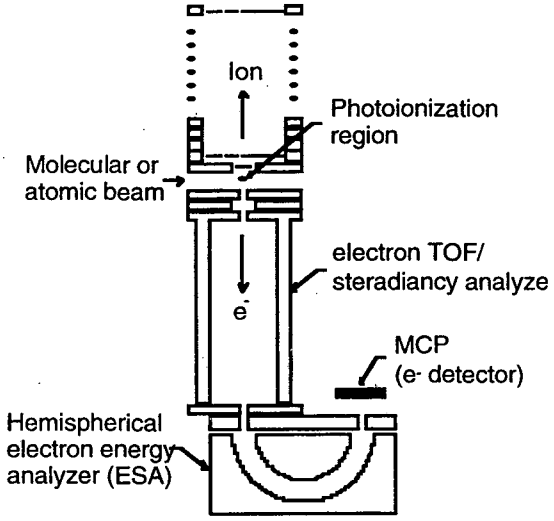

Figure 2. The schematic diagram showing the electr static lens arrangement,the steradiancy analyzer, tl hemisphere electron energy analyzer, and the micr channel plate (MCP) electron detector.

RESULTS

Fig. 3 compares the PFI-PE and TPE spectra of $Ar^+(^2P_{3/2})$ [3]. An energy resolution of 0.5 meV was obtained in the PFI-PE spectrum, approaching the resolution obtained in the PFI-PE experiments using tunable dye lasers. Obviously, the 11s' autoionization resonance, existing in the TPE spectrum, is completely suppressed in Ar PFI-PE spectrum. The $Ar^+(^2P_{3/2})$ threshold peak in the PFI-PE spectrum is red-shifted. This observation is consistent with the fact that the electrons detected in the PFI-PE experiment are from field ionization of the very high-n (n>150) Rydberg states, and the ionization potential is lowered by a few cm^{-1} due to the Stark effect. The combination of PFI-PE and synchrotron radiation manifests its great importance when it is employed to study the photoionization of molecules in their ionic excited states, especially for those states with ionization energy above 18 eV, which is very difficult to reach using tunable dye lasers [5].

CONCLUSION

The experiment scheme developed at the ALS is very easy to set up and implement. It is generally applicable to PFI-PE experiments using multi-bunch synchrotron radiation at other synchrotron radiation facilities. Due to the ease of tuning the synchrotron radiation in the full VUV photon energy range of 6-25 eV, it is expected to have a significant impact on photoelectron spectroscopic studies.

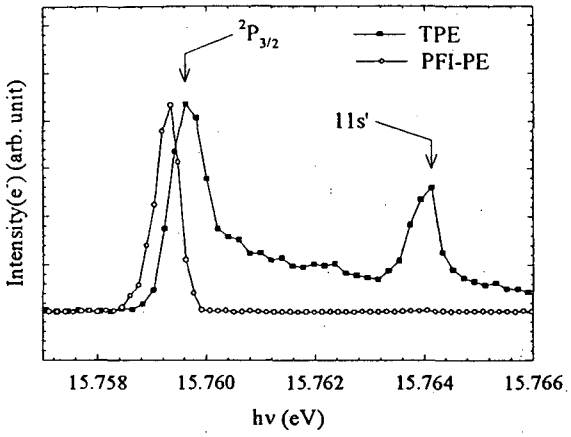

Figure 3. Comparsion of the TPE and PFI-PE spectra for Ar in the photon energy range 15.757-15.766 eV obtained with a 48-ns gap. The intensities for the TPE and PFI-PE peaks for $Ar^+(^2P_{3/2})$ are normalized to the same value.

REFERENCES

1. P. A. Heimann, M. Koike, C. -W. Hsu, M. Evans, C. Y. Ng, D. Blank, X. -M. Yang, C. Flaim, A. G. Suits, and Y. T. Lee, SPIE Proceedings 2856 (1996).
2. C.-W. Hsu, M. Evans, P. Heimann, K. T. Lu, and C. Y. Ng, J. Chem. Phys. 105, 3950 (1996).
3. C.-W. Hsu, M. Evans, C. Y. Ng, and P. Heimann, Rev. Sci. Instrum, in print.
4. E. Waterstradt, R. Jung, H. -J. Dietrich, and K. Muller-Dethlefs, Rev. Sci. Instrum. 64, 3104 (1993).
5. C.-W. Hsu, P. Heimann, M. Evans, S. Stimson, P. T. Fenn, and C. Y. Ng, J. Chem. Phys. to be submitted.

This work was supported by the Director, Office of Energy Research, Office of Basic Energy Sciences, Chemical Science Division of the U.S. Department of Energy under Contract No. W-7405-Eng-82 for the Ames laboratory and Contract No. DE-AC03-76SF00098 for the Lawrence Berkeley National Laboratory.

Principle investigator: Cheuk-Yiu Ng, Ames Laboratory, USDOE and Department of Chemistry, Iowa State University. Email: cyng@ameslab.gov. Telephone: 515-294-4225.

Free Radical Hydrogen Atom Abstraction from Saturated Hydrocarbons: A Crossed-Molecular-Beams Study of the Reaction $Cl + C_3H_8 \rightarrow HCl + C_3H_7$

D. A. Blank, N. Hemmi, A. G. Suits, and Y. T. Lee
Chemical Sciences Division, Lawrence Berkeley Laboratory, University of California, Berkeley, CA 94720

The abstraction of hydrogen atoms from saturated hydrocabons are reactions of fundamental importance in combustion as well as often being the rate limiting step in free radical substitution reactions. We have begun studying these reactions under single collision conditions using the crossed molecular beam technique on beamline 9.0.2.1, utilizing VUV undulator radiation to selectively ionize the scattered hydrocarbon free radical products (C_xH_{2x+1}).

The crossed molecular beam technique involves two reactant molecular beams fixed at 90°. The moleular beam sources are rotatable in the plane defined by the two beams. The scattered neutral products travel 12.0 cm where they are photoionized using the VUV undulator radiation, mass selected, and counted as a function of time.[1] In our initial investigations we are using halogen atoms as protypical free radicals to abstract hydrogen atoms from small alkanes. Our first study has been looking at the reaction of Cl + propane → HCl + propyl radical. In our preliminary efforts we have measured the laboratory scattering angular distribution and time of flight spectra for the propyl radical products at collision energies of 9.6 kcal/mol and 14.9 kcal/mol. Figure 1 shows the laboratory angular distribution for C_3H_7 products at a collision energy of 14.9 kcal/mol.

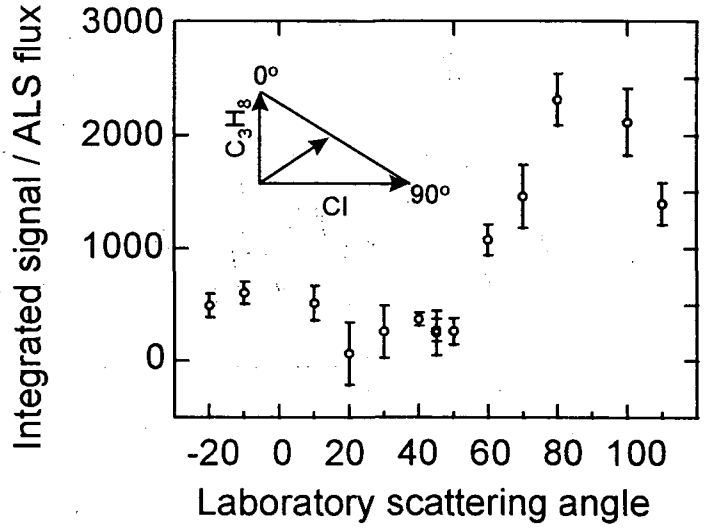

Figure 1. Laboratory scattering distribution for propyl radical products at a collision energy of 14.9 kcal/mol

The laboratory angular distributions show two distinct components in the forward and backward scattering directions. The two components demonstrate a different dependence on collision energy with the backward scattered propyl radical products showing enhancement at higher collision energy. We believe the forward and backward scattered products represent two different reaction mechanisms. Time of flight spectra for C_3H_7

products scattered in the forward direction with respect to the propane reactant are shown in figure 2. The TOF spectra are composed of a single feature and show a large fraction of the available energy, ~50% on average, is partitioned into translation. The TOF spectra for propyl radical products scattered in the backward direction with respect to the propane reactant (not shown) are slightly slower than the forward scattered products reflecting greater internal excitation in the products.

We intend to measure the photoionization onset of the propyl radical products as a function of scattering angle to help identify the n-propyl radiacal ($CH_2CH_2CH_3$) and iso-propyl (CH_3CHCH_3) radical components and further elucidate the reactions mechanism(s).

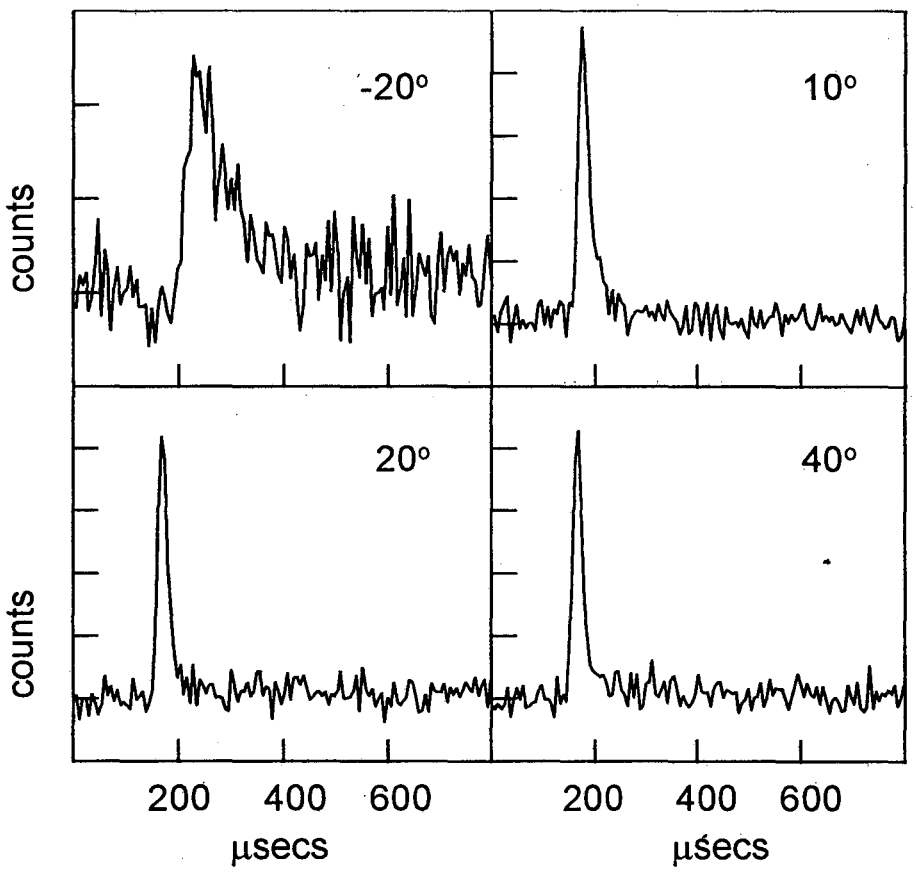

Figure 2. Time of flight spectra for C_3H_7 products scattered in the forward direction with respect to the propane reactant. See figure 1 for the laboratory angular distribution. The spectra are at laboratory angles -20°, 10°, 20°, and 40°. The collision energy is 14.9 kcal/mol.

REFERENCES

1. 1. Y. T. Lee, J. D. McDonald, P. R. LeBreton, and D. R. Herschback, Rev. Sci. Instrum. **40**, 1402, (1969); N. R. Daly, *ibid.* 31, 264 (1960).
A. M. Wodtke and Y. T. Lee, J. Phys. Chem. **89**, 4744 (1985).

This work was supported by the Director, Office of Energy Research, Office of Basic Energy Sciences, Chemical Sciences Division, of the U.S. Department of Energy under Contract No. DE-AC03-76SF00098.

Pricipal investigators: Yuan T. Lee, Office of the President, Academica Sinica, Taipei, Taiwan, 10764. Arthur G. Suits, Chemical Sciences Division, Lawrence Berkeley Laboratory, Berkeley, CA, 94720, phone: 510 486 4754, email: arthur@leea.cchem.berkeley.edu.

High-Resolution Mass-Analyzed Threshold Ion Spectrum of Argon Obtained on Beamline 9.0.2.2

C.-W. Hsu[1], K.T. Lu[1], M. Evans[2], Y.J. Chen[2], C.Y. Ng[2], and P. Heimann[3]

[1]Chemical Sciences Division, Ernst Orlando Lawrence Berkeley National Laboratory, University of California, Berkeley, CA 94720, USA
[2]Ames Laboratory, USDOE and Dept. of Chemistry, Iowa State University, Ames, IA 50011, USA
[3]Advanced Light Source, Accelerator and Fusion Research Division, Ernst Orlando Lawrence Berkeley National Laboratory, University of California, Berkeley, CA 94720, USA

INTRODUCTION

The first mass analyzed threshold ion (MATI) spectrum using dc electric fields and a continuous wave light source has been obtained on End Station 2 of the Chemical Dynamics Beamline (9.0.2.2) at the Advanced Light Source[1]. MATI provides researchers with fundamental spectroscopic information about atomic and molecular ions with the added advantage of mass analysis. The MATI technique involves the detection of ions formed by field ionization of long-lived high-n Rydberg states approaching an ionization threshold.

EXPERIMENT

The MATI apparatus of End Station 2 is shown in Figure 1. It consists of a differentially pumped supersonic molecular beam source (not shown), a photoionization region followed by a series of electrostatic lenses, a quadrupole mass spectrometer (QMS), and a Daly-type detector. The supersonic beam intersects the vacuum ultraviolet light in region 1, defined by V1 and V2, where a small reverse biased electric field (<1 V/cm) is applied to retard any prompt ions formed by direct ionization or by fast autoionization processes. Rydberg states with a lifetime long enough to travel into region 2, defined by V2 and V3, are then field ionized. By applying a consecutive lower voltage on V3 and V4 than for V2, the ions are guided by forward biasing into the QMS and then detected by the Daly detector.

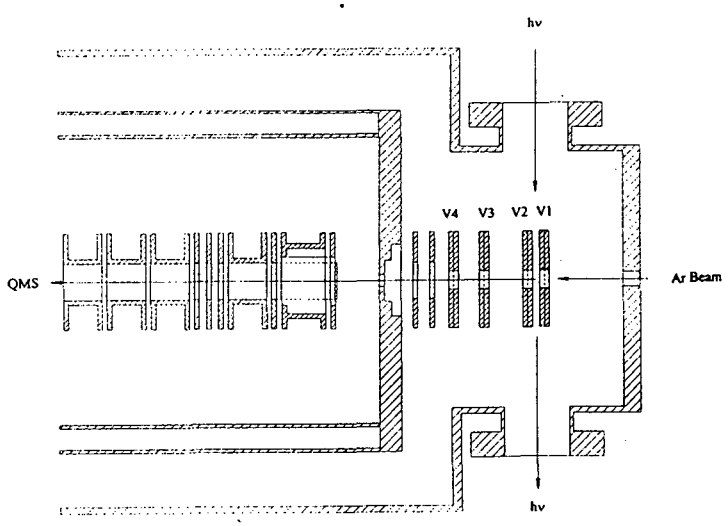

Figure 1. MATI Apparatus: Schematic diagram of the ion lens arrangement of the quadrupole mass spectrometer (QMS).

RESULTS

Figure 2 shows the MATI spectrum of Ar in the photon energy range of 15.74-15.97 eV. This spectrum shows only a MATI peak for the $Ar^+(^2P_{3/2})$ state, but not one for the $Ar^+(^2P_{1/2})$ state. The known ionization energies for the $Ar^+(^2P_{3/2})$ and $Ar^+(^2P_{1/2})$ states are indicated by arrows. The reason for the observation of a MATI peak for only the $Ar^+(^2P_{3/2})$ state has to do with the lifetime of the Rydberg states approaching the $Ar^+(^2P_{3/2})$ ionization continuum. The average speed for a pure Ar supersonic beam is estimated to be $5.6x10^{-4}$ cm/s, yielding the time it takes to go from region 1 to region 2 to be 8 μs. The observation of a strong MATI peak for the $Ar^+(^2P_{3/2})$ state is consistent with the conclusion that the lifetime values for the Rydberg states (n=150) converging to the $Ar^+(^2P_{3/2})$ state are longer than 8.0 μs. The failure to observe the MATI peak for the $Ar^+(^2P_{1/2})$ state indicates that the Rydberg states (n=150) formed at a few cm^{-1} below the IE of $Ar^+(^2P_{1/2})$ have lifetimes <8.0 μs.

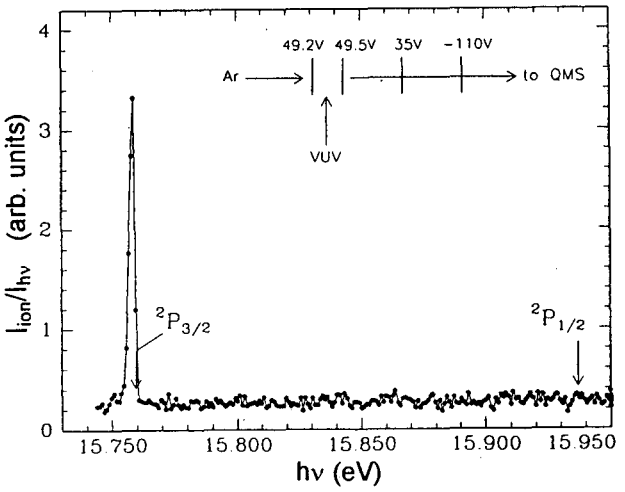

Figure 2. MATI spectrum of Ar in the photon energy range of 15.74-15.97 eV. The IEs for the formation of Ar^+ in the $^2P_{3/2}$ and $^2P_{1/2}$ states are marked.

In contrast, Figure 3 shows the photoionization efficiency (PIE) spectrum of Ar in which no reverse bias was used and all ions were detected. The autoionization features approaching the $Ar^+(^2P_{1/2})$ state are clearly visible. Such autoionization structures are undesirable when performing high resolution spectroscopic studies of a threshold ionization process.

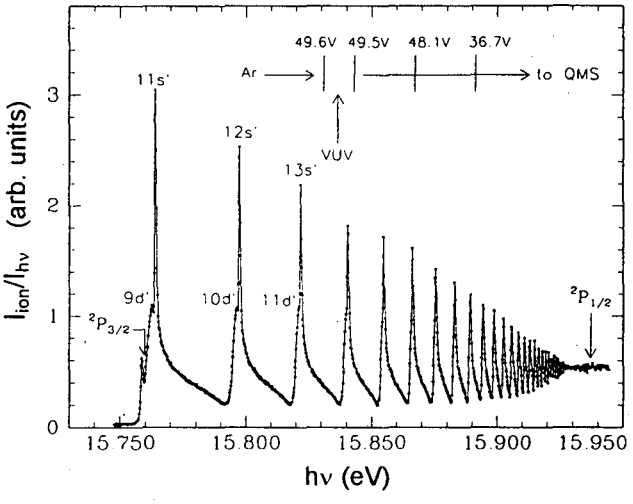

Figure 3. PIE spectrum of Ar in the photon energy range of 15.748-15.950 eV. The IEs for the formation of Ar^+ in the $^2P_{3/2}$ and $^2P_{1/2}$ states are marked.

CONCLUSIONS

As shown, the MATI technique can be used to probe the Rydberg states approaching an ionization continuum and yield information about the lifetimes of these states. In addition, MATI could be used to obtain the spectrum of a single species present in a sample mixture due to the mass

selective nature of the experiment. MATI could also be used to form mass selected and state specific ions for use in ion molecule reaction experiments.

ACKNOWLEDGEMENTS

C.Y.N. is grateful to Professor Phil Johnson for helpful discussions concerning the MATI experiment.

REFERECES

1. C.-W. Hsu, K.T. Lu[1], M. Evans, Y.J. Chen, C.Y. Ng, and P. Heimann, J. Chem. Phys., **105**, 3950 (1996).

This work was supported by the Director, Office of Energy Research, Office of Basic Energy Sciences, Chemical Sciences Division of the U.S. Department of Energy under Contract No. DE-AC03-76SF00098 for the Lawrence Berkeley National Laboratory and Contract No. W-7405-Eng-82 for the Ames Laboratory.

Principal Investigator: Prof. C.Y. Ng, Ames Laboratory, USDOE and Department of Chemistry, Iowa State University. Email: cyng@ameslab.gov. Telephone: 515-294-4225.

A High-Resolution Pulsed-Field Ionization Photoelectron Study of O_2

C.-W. Hsu[1], M. Evans[2], P.Heimann[3], S. Stimson[2], and C.Y. Ng[2]
[1]Chemical Science Division, Lawrence Berkeley National Laboratory, Berkeley, CA 94720, USA
[2]Ames Laboratory, USDOE and Department of Chemistry, Iowa State University, Ames, Iowa 50011, USA
[3]Advanced Light Source and Accelerator and Fusion Research Division, Lawrence Berkeley National Laboratory, Berkeley, CA 94720, USA

INTRODUCTION

There have been numerous photoionization studies of O_2 over the past 10 years. Using the pulsed field ionization (PFI) photoelectron spectroscopy (PES) technique, the electronic ground state of $O_2^+(X\ ^2\Pi_g^-)$ has been well studied on the rotationally resolved level by several groups [1, 2]. However, due to the difficulty of producing photon energies above 18 eV using the tunable lasers, the electronic excited states of O_2^+ have been mostly studied on the vibrationally resolved level using the threshold photoelectron spectroscopy (TPES) and the synchrotron radiation [3].

Recently, we developed a new technique for performing the PFI-PE experiments using multi-bunch synchrotron radiation at the Chemical Dynamics Beamline of the Advanced Light Source (ALS) [4, 5]. Using the high resolution VUV light from the ALS, we have obtained the PFI-PE spectra of O_2 between 12 and 24 eV. In this abstract, we report for the first time the rotationally resolved spectra of $O_2^+(\ b^4\Sigma_g^-,\ v^+=0)$.

EXPERIMENT

The experimental arrangement was described in detail previously [4]. The pure O_2 molecular beam was produced by supersonic expansion through a continuous nozzle (dia=0.127mm) with a stagnation pressure of 760 Torr. The rotationally resolved PFI-PE spectrum of $O_2^+(b^4\Sigma_g^-,\ v^+=0)$ [5] is displayed on the lower trace in Fig. 1. The energy resolution of the PFI-PE spectrum is ~0.5 meV. The TPE spectrum in the same energy range is displayed on the upper trace as a comparison. The rotational structure is clearly resolved in the O_2 PFI-PE spectrum, while it is obscured by autoionization in the TPE spectrum.

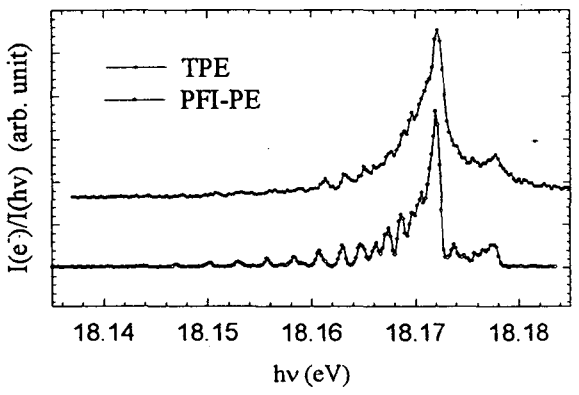

Figure 1. Comparison of the TPE and PFI-PE spectra for $O_2^+(b^4\Sigma_g^-,v^+=0)$

RESULTS

Fig. 2 and 3 show the $O_2^+(b^4\Sigma_g^-)$ PFI-PE spectra for the $v^+=0$ and 4, respectively, along with the simulated spectra. The experimental spectra have been normalized to the photon flux. The pulsed field of 0.55 V/cm used here corresponds to a Stark shift of 0.3 meV for a PFI-PE peak. This shift has been corrected for in the figures. The experimental spectra were well reproduced by the simulated spectra. The assignment is shown on top of each spectrum. The rotational branch is designated as ΔN ($=N^+-N''$), which is the change in the core angular momentum apart from spin in the ion (N^+) and the molecule (N''), similar to that in optical rotational transitions. Due to nuclear spin statistics, the states for an even level of N'' in $O_2(X)$ and an even level of N^+ in $O_2^+(b)$ do not exist. Therefore, only the rotational branches originating from the odd N'' with ΔN=even are possible. Only the rotational branches ΔN=0, ±2 (O, Q, and S branches) are observed in the spectra. The adiabatic ionization potential for b state was determined to be 145973.2 cm^{-1} from the PFI-PE spectrum. The observed ionization energies for transitions $O_2^+(b^4\Sigma_g^-,v^+=0\text{-}9) \leftarrow O_2(X^3\Sigma_g^-,v^+=0)$ are well predicted using a Morse potential with ω_e = 1196.77 cm^{-1} and $\omega_e\chi_e$ = 17.09 cm^{-1}, and the observed ionization potential of the b state given above.

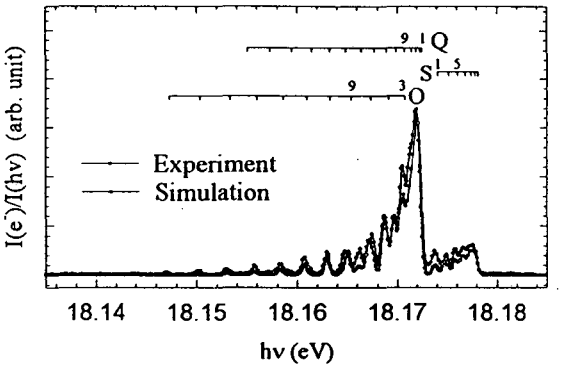

Figure 2. Comparison of the simulated and experimental PFI-PE bands for $O_2^+(b^4\Sigma_g^-,v^+=0)$.

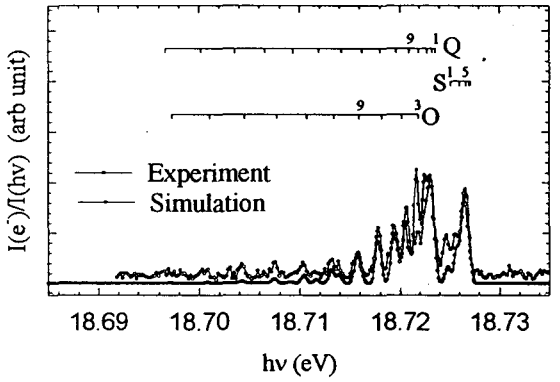

Figure 3. Comparison of the simulated and experimental PFI-PE bands for $O_2^+(b^4\Sigma_g^-,v^+=4)$.

The experimental spectra were simulated using the BOS model. From the simulation, we found that only the s and d orbitals can have significant contributions to the transitions $O_2^+(b^4\Sigma_g^-,v^+) \leftarrow O_2(X^3\Sigma_g^-)$. The partial waves of the outgoing electrons ejected in the photoionization process are restricted to l = 1 and 3. The Q branch gains most of its intensity through the excitation of an s orbital electron. However, the O and S branches can only acquire their intensities through the photoexcitation of a d orbital electron. Since these two branches involve the excitation of the electron in the same orbital, they are expected to have the same transition dipole moment. This indicates that O and S branches should have equal intensities. The large intensity observed for the Q branch, compared to those for the O and S branches, indicates that photoelectrons were predominately generated from the excitation of an s orbital electron. This is observed for most of the

vibrational states except $v^+ = 4$ and 5. Unlike all the other states where the Q branch is more pronounced, the intensity of the S branch is comparable to that of the Q branch for $v^+ = 4$ and 5. This suggests that the rotational branch intensities for $v^+ = 4$ and 5 receive a greater contribution from the photoexcitation of a d orbital electron of the molecular ground state.

CONCLUSION

A rotational resolved PFI-PE spectrum of excited ionic states will help researchers to have better understanding on the dynamics of the photoionization process in greater detail. The O_2^+ PFI-PE spectra for all the states, including X, a, b, B, and C states, are still being analyzed.

REFERENCES

1. R. G. Tonkyn, J. W. Winniczek, and M. G. White, Chem. Phys. Lett., 164, 137 (1989).
2. W. Kong, and J. W. Hepburn, Can. J. Phys., 72, 1284 (1994).
3. F. Merkt, P.M. Guyon, and J. Hepburn, Chem Phys., 173, 479 (1993).
4. C.-W. Hsu, M. Evans, C. Y. Ng, and P. Heimann, Rev. Sci. Instrum, in print.
5. C.-W. Hsu, P. Heimann, M. Evans, S. Stimson, P. T. Fenn, and C. Y. Ng, J. Chem. Phys. to be submitted.

This work was supported by the Director, Office of Energy Research, Office of Basic Energy Sciences, Chemical Science Division of the U.S. Department of Energy under Contract No. W-7405-Eng-82 for the Ames laboratory and Contract No. DE-AC03-76SF00098 for the Lawrence Berkeley National Laboratory.

Principle investigator: Cheuk-Yiu Ng, Ames Laboratory, USDOE and Department of Chemistry, Iowa State University. Email: cyng@ameslab.gov. Telephone: 515-294-4225.

High-Resolution Threshold Photoelectron-Photoion Coincidence Experiments Performed on Beamline 9.0.2.2: Kinetic Energy Release Study of the Process $SF_6 + h\nu \longrightarrow SF_5^+ + F + e^-$

M. Evans[1], C.-W. Hsu[2], P. Heimann[2], and C.Y. Ng[1]

[1]Ames Laboratory, USDOE and Department of Chemistry, Iowa State University, Ames, Iowa 50011, USA
[2]Chemical Sciences Division and Advanced Light Source, Accelerator and Fusion Research Division, Lawrence Berkeley National Laboratory, Berkeley, California 94720, USA

INTRODUCTION

Vacuum ultraviolet (VUV) photoionization mass spectrometry has been used extensively to determine the energetics of neutral radicals and radical cations, as well as to study the dynamics of the dissociative photoionization process. Very often these measurements are concerned with determining the appearance energy (AE) for a dissociative ionization process, as well as determining the heats of formation of the species involved. One such photoionization mass spectrometric technique employed on End Station 2 of the Chemical Dynamics Beamline (9.0.2.2) at the Advanced Light Source is the threshold photoelectron-photoion coincidence (TPEPICO) method. TPEPICO involves measuring the time-of-flight (TOF) mass spectrum of a given cation in coincidence with threshold photoelectrons at a known photoionization energy.

EXPERIMENT

The TPEPICO apparatus of End Station 2 is shown in Figure 1. It consists of a double-differentially pumped supersonic molecular beam production system (not shown), an ion and electron lens system, a threshold photoelectron spectrometer, a TOF mass spectrometer, and microchannel plates (MCP's) for electron and ion detection. The threshold photoelectron spectrometer consists of a steradiancy analyzer and a hemispherical energy analyzer in a tandem arrangement. The VUV light used to ionize the gas phase species of interest is dispersed by a 6.65m off-plane Eagle monochromator and focused by a toroidal mirror into the photoionization chamber. The VUV light and the molecular beam intersect in the photoionization region

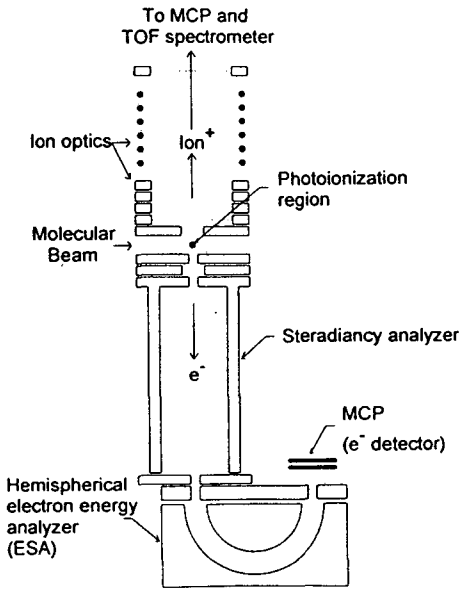

Figure 1. Schematic diagram showing the TPEPICO apparatus on Beamline 9.0.2.2.

at 90° and are perpendicular to the axes of the threshold photoelectron spectrometer and the TOF mass spectrometer. The detection of the generated threshold electron defines the start time for determining the TOF of the corresponding ion. This is possible due to the fact that the electron flight time is much shorter than that of its corresponding ion, which has a much larger mass. The VUV spot size in the photoionization region is ≈ 0.24x0.36 mm^2 for $h\nu \leq 1000$ Å.

RESULTS

The thermochemical data obtainable using the TPEPICO technique on End Station 2 is demonstrated in the recent high-resolution kinetic energy release study[1] of the process

$$SF_6 + h\nu \longrightarrow SF_5^+ + F + e^- \qquad (1).$$

The thermochemical threshold for this process can be determined by measuring the center-of-mass (c.m.) kinetic energy ($E_{c.m.}$) release of SF_5^+, which involves measuring the width of the SF_5^+ TPEPICO TOF mass spectrum. The TOF mass spectrum of SF_5^+ obtained at two different photon energies is shown in Figures 2(a) and 2(b). The width of the TOF peak, which corresponds to the turn around time (Δt) of the most energetic SF_5^+ ions moving away from the TOF ion detector, is related to the $E_{c.m.}(SF_5^+)$ by the relation

$$E_{c.m.}(SF_5^+) = [1/(2m)][(\Delta t)qV/(2d)]^2 , \qquad (2)$$

where m is the mass of SF_5^+, q is the charge of SF_5^+, V is the extraction voltage, and d is the distance between the electrodes which define the ionization region. After calculating the $E_{c.m.}$ release for process (1) at each photon energy and then subtracting this value from its corresponding photon energy, the average AE for process (1) was determined to be 14.11±0.08 eV. This value yields 18.5±1.9 and -202.9±2.2 kcal/mol for the heats of formation at 0 K for SF_5^+ and SF_5, respectively. It should be noted that the uncertainty in the TOF spectra is only 45 ns (FWHM), as observed in the TPEPICO spectrum of Xe^+ under the same experimental conditions. This value sets the lower limit for the uncertainty of the $E_{c.m.}$ release measurements. The high TOF resolution is achieved in part due to the small VUV spot size.

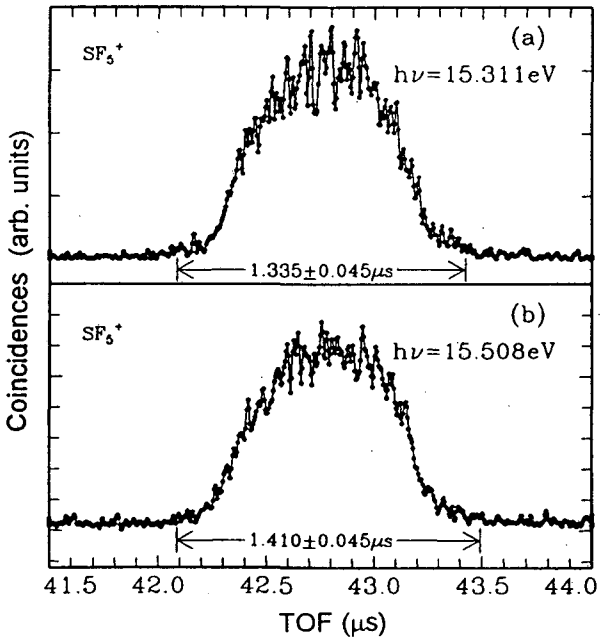

Figure 2. TPEPICO TOF mass spectrum for SF_5^+ formed by process (1) at (a) hν = 15.311 eV and (b) hν = 15.508 eV. Threshold photoelectron energy bandwidth = 9 meV (FWHM).

The dynamics of the dissociative ionization process can also be deduced from the TPEPICO TOF mass spectrum. The SF_5^+ TOF peaks obtained at two different photon

energies (Figures 2(a) and 2(b)) are essentially symmetric. The symmetric peak shape observed is consistent with the conclusion that upon absorption of the ionizing photon the dissociation of SF_6 is prompt. Analysis of the TPEPICO TOF spectra obtained at higher photon energies will also provide valuable insight into whether SF_4^+ and SF_3^+ are formed by sequential fragmentation of SF_5^+, or by a direct process.

CONCLUSIONS

High resolution $E_{c.m.}$ measurements using the TPEPICO technique on End Station 2 allow researchers to determine important thermochemical data with great accuracy. This is due to the high TOF and photon energy resolutions obtainable on the Chemical Dynamics Beamline (9.0.2.2). The dynamics of the dissociative ionization process can also be easily studied. In the future, hydrocarbon radicals, as well as other species related to combustion and atmospheric chemistry, will be studied on 9.0.2.2 using the TPEPICO technique. Valuable insight into the combustion process and the energetics of the species involved will then be possible.

ACKNOWLEDGEMENTS

The authors are grateful to J. Keister and Professor T. Bear for valuable discussions and comments about the experiment.

REFERENCES

1. M. Evans, C.-W. Hsu, P. Heimann, and C.Y. Ng, J. Chem. Phys., **106**, 978 (1997)

This work was supported by the Director, Office of Energy Research, Office of Basic Energy Studies, Chemical Sciences Division of the U.S. Department of Energy under contract No. W-7405-Eng-82 for the Ames Laboratory, and Contract No. DE-AC03-76SF00098 for the Lawrence Berkeley National Laboratory. M. Evans is a GAANN Fellowship recipient, 1993-1995 and 1996-1997.

Principal Investigator: Prof. C.Y. Ng, Ames Laboratory, USDOE and Department of Chemistry, Iowa State University. Email: cyng@ameslab.gov. Telephone: 515-294-4225.

Photoinitiated Decomposition of Substituted Ethylenes: The Photodissociation of Vinyl Chloride and Acrylonitrile at 193 nm

D. A. Blank[1], A. G. Suits[1], Y. T. Lee[1], S. W. North[2], and G. E. Hall[2]
[1]Chemical Sciences Division, Lawrence Berkeley Laboratory, University of California, Berkeley, CA 94720.
[2]Chemistry Department, Brookhaven National Laboratory, Upton, NY, 11973-5000.

Ethylene and its sustituted analogues (H_2CCHX) are important molecules in hydrocarbon combustion. As the simplest π-bonded hydrocarbons these molecules serve as prototypical systems for understanding the decomposition of this important class of compounds. We have used the technique of photofragment translational spectroscopy at beamline 9.0.2.1 to investigate the dissociation of vinyl chloride (X=Cl) and acrylonitrile (X=CN) following absorption at 193 nm. The technique uses a molecular beam of the reactant seeded in helium which is crossed at 90 degrees with the output of an excimer laser operating on the ArF transition, 193.3 nm. The neutral photoproducts which recoil out of the molecular beam travel 15.1 cm where they are photoionized by the VUV undulator radiation, mass selected, and counted as a function of time.[1] The molecular beam source is rotatable about the axis of the dissociation laser. We have directly observed all four of the following dissociation channels for both systems:

$$H_2CCHX \rightarrow H + C_2H_2X \quad (1)$$
$$H_2CCHX \rightarrow X + C_2H_3 \quad (2)$$
$$H_2CCHX \rightarrow H_2 + C_2HX \quad (3)$$
$$H_2CCHX \rightarrow HX + C_2H_2 \quad (4)$$

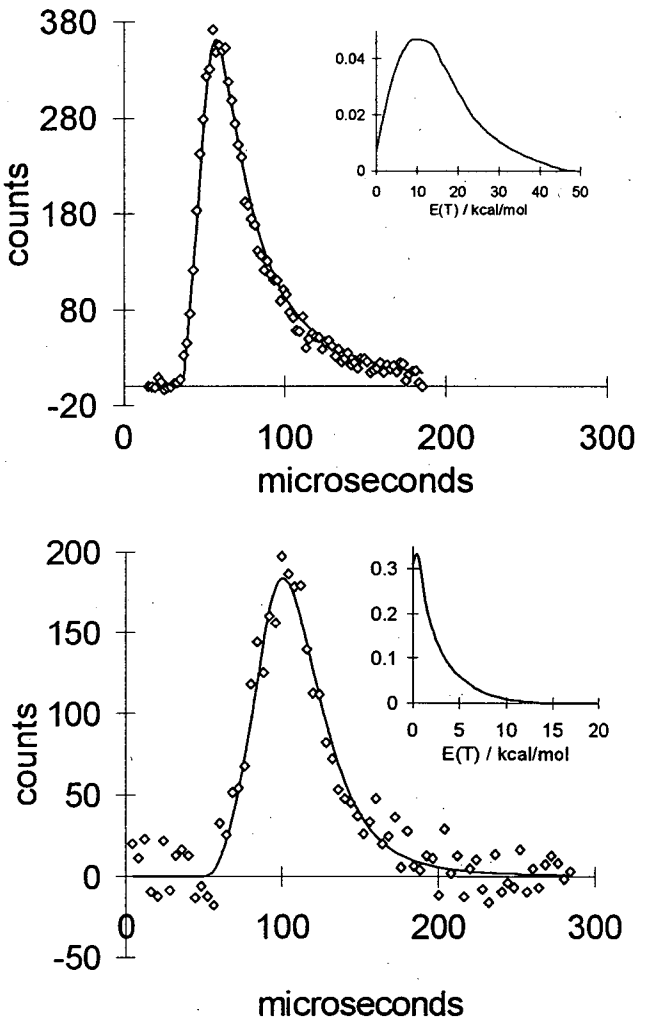

Figure 1. Time of flight spectra (TOF) from the dissociation of acrylonitrile at 193 nm. (top) TOF for m/e 27 at a scattering angle of 30° and a photoionization energy of 15.0 eV. (bottom) TOF for m/e 27 at a scattering angle of 10° and a photoionization energy of 10.0 eV. Inset plots show the center of mass translational energy distributions determined from the fits to the TOF data.

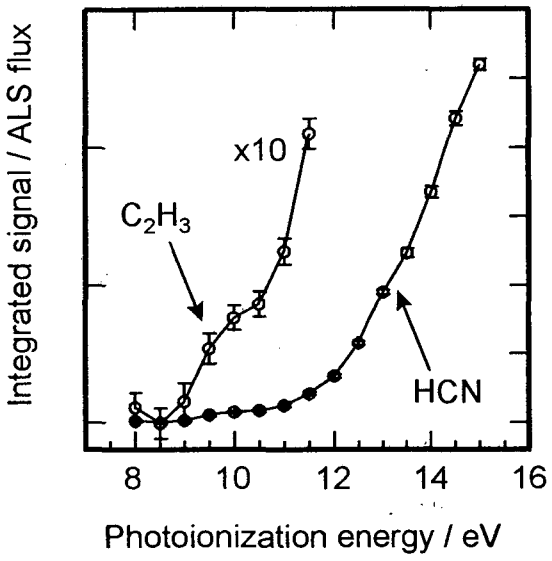

Figure 2. Photoionization spectrum for m/e 27 photoproducts from the dissociation of acrylonitrile at 193 nm at a scattering angle of 15°.

We measured translational energy distributions for all of the observed channels and measured the photoionization onset for many of the photoproducts which provided information about their chemical identity and internal energy content. In the case of acrylonitrile, selective product photoionization provided the ability to discriminate between channels 2 and 4 which result in the same product mass combination. Figure 1 shows time of flight spectra for m/e 27 at photoionization energies above and below the I.P. for HCN and Figure 2 shows the photoionization curve for m/e 27 photoproducts at a scattering angle of 15°. There are two distinct onsets which result from channel 2 and channel 4.

For acrylonitrile all of the observed dissociation channels were found to occur on the ground electronic surface following internal conversion from the initially excited $\pi\pi^*$ electronic state. The dissociation of vinyl chloride was complicated by a low lying σ^*(C-

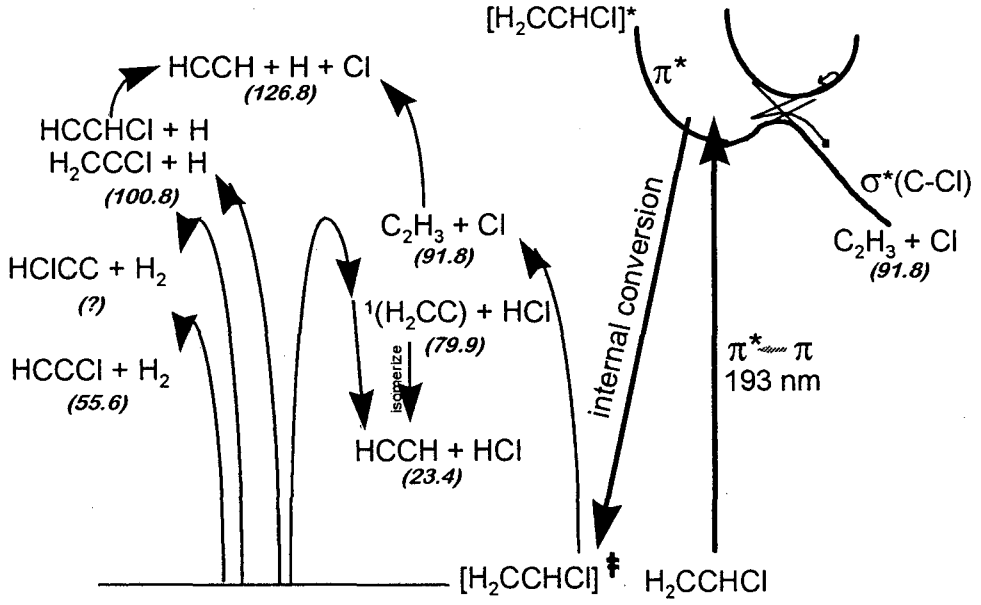

Figure 3: Summary of the observed dissociation channels from the photodissociation of vinyl chloride at 193 nm. The numbers in parenthesis are relative energies relative to vinyl chloride in kcal/mol.

Cl) excited electronic surface. Following the initial $\pi \leftarrow \pi^*$ excitation about half of the excited molecules cross out of the Franck-Condon region and dissociate on the excited σ^* surface, greatly enhancing the yield of channel 2 as compared with acrylonitrile, where exclusive competition on the ground electronic surface allows the thermodynamically more favorable channel 4 to dominate. The other half undergo internal conversion and dissociate on the ground electronic surface. The lower C-X bond energy in vinyl chloride also makes secondary decomposition thermodynamically available for the C_2H_3 and C_2H_2X primary photoproducts. We have observed both of these secondary dissociation processes, $C_2H_3 \rightarrow C_2H_2 + H$ and $C_2H_2Cl \rightarrow C_2H_2 + Cl$, and we have made a direct measurement of the barrier height to C_2H_2Cl dissociation. A summary of the dissociation of vinyl chloride at 193 nm is shown in figure 3.

REFERENCES

1. Y. T. Lee, J. D. McDonald, P. R. LeBreton, and D. R. Herschback, Rev. Sci. Instrum. **40**, 1402, (1969); N. R. Daly, *ibid.* 31, 264 (1960).
   A. M. Wodtke and Y. T. Lee, J. Phys. Chem. **89**, 4744 (1985).

This work was supported by the Director, Office of Energy Research, Office of Basic Energy Sciences, Chemical Sciences Division, of the U.S. Department of Energy under Contract No. DE-AC03-76SF00098.

Pricipal investigators: Yuan T. Lee, Office of the President, Academica Sinica, Taipei, Taiwan, 10764. Arthur G. Suits, Chemical Sciences Division, Lawrence Berkeley Laboratory, Berkeley, CA, 94720, phone: 510 486 4754, email: arthur@leea.cchem.berkeley.edu. Gregory E Hall, Chemistry Department, Brookhaven National Laboratory, Upton, NY, 11937, phone: 516 344 4376.

Three-Body Dissociations: The Photodissociation of Dimethyl Sulfoxide at 193 nm

D. A. Blank, S. W. North, D. Stranges, A. G. Suits, and Y. T. Lee
Chemical Sciences Division, Lawrence Berkeley Laboratory, University of California, Berkeley, CA 94720

When a molecule with two equivalent chemical bonds is excited above the threshold for dissociation of both bonds, how the rupture of the two bonds is temporally coupled becomes a salient question. Following absorption at 193 nm dimethyl sulfoxide (CH_3SOCH_3) contains enough energy to rupture both C-S bonds. This can happen in a *stepwise* (reaction 1) or *concerted* (reaction 2) fashion where we use rotation of the $SOCH_3$ intermediate prior to dissociation to define a stepwise dissociation.[1]

$$CH_3SOCH_3 \rightarrow 2CH_3 + SO \qquad (1)$$

$$CH_3SOCH_3 \rightarrow CH_3 + SOCH_3 \qquad (2a)$$
$$SOCH_3 \rightarrow SO + CH_3 \qquad (2b)$$

Recently, the dissociation of dimethyl sulfoxide following absorption at 193 nm was suggested to involve simultaneous cleavage of both C-S bonds on an excited electronic surface. This conclusion was inferred from laser induced fluorescence (LIF) and resonant multiphoton ionization (2+1 REMPI) measurements of the internal energy content in the CH_3 and SO photoproducts and a near unity quantum yield measured for SO.[2] Since this type of *concerted* three body dissociation is very interesting and a rather rare event in photodissociation dynamics, we chose to investigate this system using the technique of photofragment translational spectroscopy at beamline 9.0.2.1. The soft photoionization provided by the VUV undulator radiation allowed us to probe the $SOCH_3$ intermediate which had not been previously observed and provided good evidence that the dissociation of dimethyl sulfoxide primarily proceeds via a two step dissociation, reaction 2.

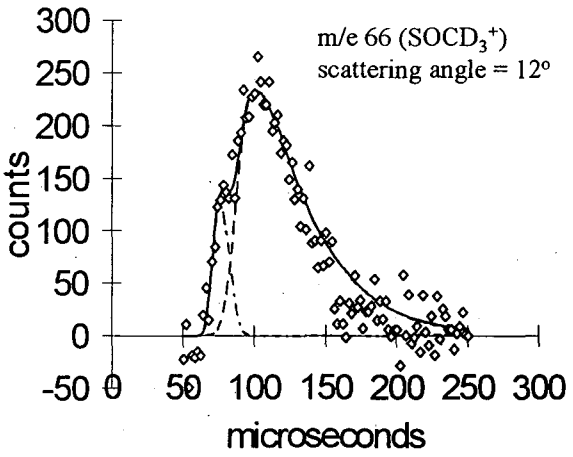

Figure 1. Time of flight spectrum for m/e 66 photofragments from the dissociation of DMSO-d_6 at a scattering angle of 12°. The fit is from the $P(E_T)$ shown in figure 2.

Figure 1 shows the time of flight spectrum (TOF) for m/e 66 ($SOCD_3^+$) photofragments from the dissociation of DMSO-d_6 via reaction 2a. The spectrum contains two separate components. The peak at faster arrival times is the result of dissociation on an excited electronic surface and the broader peak at later arrival times is the result of dissociation on the ground electronic surface following internal conversion. The center of mass

translational energy distributions obtained from the m/e 66 TOF spectra are shown in figure 2.

We found that ~50% of the $SOCH_3$ products from the ground state dissociation were stable with respect to secondary dissociation and ~50% went on to thermally decompose. This results in a quantum yield of 1.4 for CD_3 in excellent agreement with recent transient absorption measurements.[3]

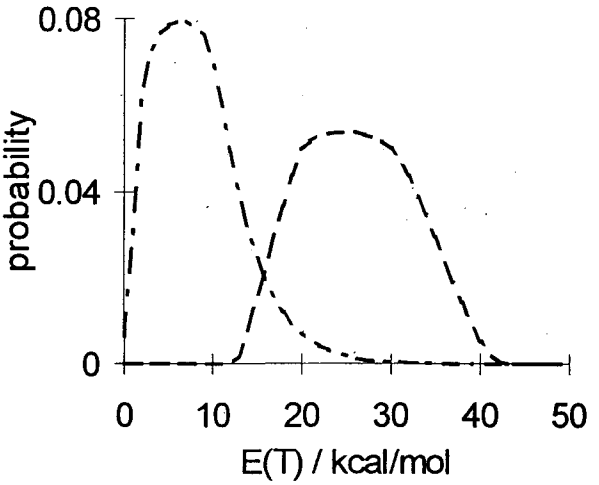

Figure 2. Center of mass translational energy distributions obtained from the m/e 66 TOF spectra. These are the distributions for reaction 2a occurring on the ground electronic surface, dash-dot line, and on an excited electronic surface, dashed line.

The TOF spectrum for m/e 18 (CD_3^+) is shown in figure 3 and shows three contributions. The peak at the earliest times is from reaction 2a on the excited electronic surface. The peak at the latest arrival times is from reaction 2a on the ground electronic surface, and the middle peak is from secondary decomposition of $SOCD_3$ intermediates, reaction 2b.

The translational energy distributions for the dissociation products demonstrated no correlation between the recoiling vectors for SO and the two CH_3 photofragments in the first and second steps. This provides direct evidence that the $SOCH_3$ intermediates survive for more than a rotational period on average before undergoing secondary decomposition and, therefore, dissociation to two methyl radicals and SO proceeds via a *stepwise* mechanism.

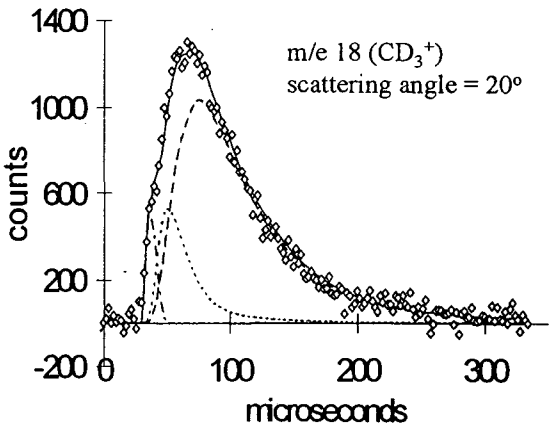

Figure 3. Time of Flight spectrum for m/e 18 photoproducts from the dissociation of DMSO-d_6 at a scattering angle of 20°.

Measurements of the photoionization onset for the scattered SO photoproducts confirmed previous measurements of the internal energy content[2] and demonstrated that the secondary decomposition of the $SOCH_3$ intermediates is strongly mediated by exit channel effects with an ~8 kcal/mol barrier to recombination. Using the VUV undulator radiation for

product ionization also allowed us to observe a competing minor secondary decomposition channel involving C-H bond cleavage in the $SOCH_3$ intermediates.

REFERENCES

1. C.E.M. Strauss and P.L. Houston, J. Phys. Chem. **94**, 8751 (1990).
2. X. Chen, H. Wang, B.R. Weiner, M. Hawley, and H.H. Nelson, J. Phys. Chem. **97**, 12269 (1993).
3. R.N. Rudolph, S.W. North, G.E. Hall, T.J. Sears, J. Chem. Phys. **106**, 1346, (1997).

This work was supported by the Director, Office of Energy Research, Office of Basic Energy Sciences, Chemical Sciences Division, of the U.S. Department of Energy under Contract No. DE-AC03-76SF00098.

Pricipal investigators: Yuan T. Lee, Office of the President, Academica Sinica, Taipei, Taiwan, 10764. Arthur G. Suits, Chemical Sciences Division, Lawrence Berkeley Laboratory, Berkeley, CA, 94720, phone: 510 486 4754, email: arthur@leea.cchem.berkeley.edu.

Universal Imaging: Dissociative Ionization of Polyatomic Molecules, Chemical Dynamics Beamline 9.0.2.

Musa Ahmed, Daniel Chen and Arthur G. Suits*
Chemical Sciences Division, Ernest Orlando Lawrence Berkeley National Laboratory,
University of California, Berkeley CA 94720

A third endstation was recently added to the Chemical Dynamics Beamline[1], designed to exploit the high flux broadband undulator light for a range of studies of reactive scattering, photochemistry and photoionization processes using time-of-flight mass spectroscopy coupled with position-sensitive detection. The apparatus[2] is schematically presented in Fig. 1. Two molecular beam sources are fixed at right angles, with the undulator light, or laser beams, intersecting the molecular beams at 45°.

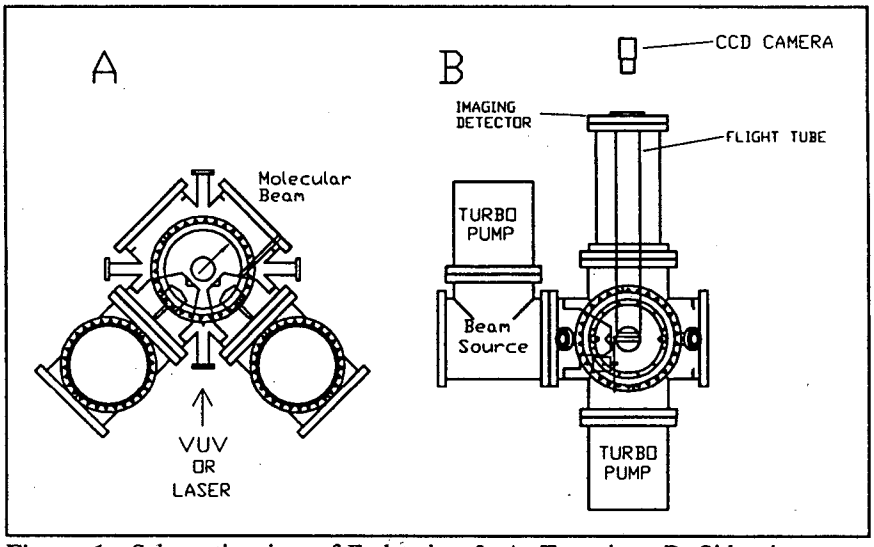

Figure 1. Schematic view of Endstation 3, A. Top view, B. Side view.

To date, beamline experiments have included a study of dissociative photoionization of a variety of molecules including N_2O and SF_6. In this mode, a single molecular beam source is used, with the tunable undulator light inducing, in SF_6 for example, the process $SF_6 \rightarrow SF_6^+ + e^- \rightarrow SF_5^+ + F + e^-$. The SF_5^+ ions are accelerated up the flight tube, mass selected and detected as a function of position on a phosphor screen viewed by a CCD camera. The position directly reveals the recoil speed (or translational energy release) and angular distribution for the dissociative ionization process. Furthermore, this measurement is obtained for all recoil speeds and angles simultaneously. Such detailed angular information has not previously been obtained for dissciative ionization processes; typically ion time-of-flight profiles are deconvoluted to yield rough insight into the angular distributions[3]. The recorded image is actually a 2-dimensional projection of the nascent 3-dimensional velocity distribution, but established tomographic techniques[4] enable us to reconstruct the 3-D distribution.

Figure 2 shows a raw image recorded for SF_5^+ from dissociative ionzization of SF_6 at 15.8 eV. The sizable energy release and strongly anisotropic angular distribution imply a very rapid dissociation process, faster than the rotational period of the parent molecule. In addition, the anisotropy of the angular distribution, with the SF_5^+ recoiling preferentially along the polarization direction of the undulator light, provides information about the nature

of the electronic states involved in the dissociation process. Analysis of the image yields the translational energy and angular distributions shown in Figure 3. The energy release is given as the total center of mass kinetic energy in the process. The angular distributions are fitted to the dipole distribution $I(\theta) = 1+\beta(P_2(\cos(\theta))$, where P_2 is the second Legendre polynomial, to derive the β value indicated. Future studies will employ a high-throughput monochromator and measurement of the ions in coincidence with the electrons for definition of the internal energy of the parent ion prior to dissociation, while providing a higher data acquisition rate.

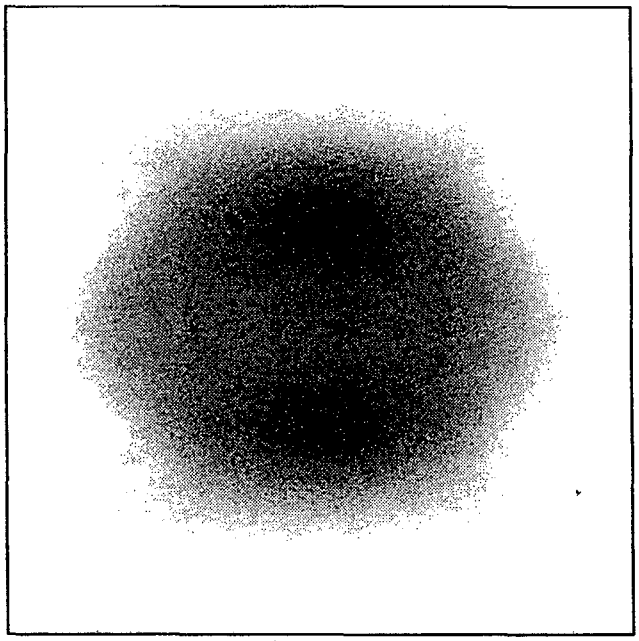

Figure 2. Image of SF_5^+ from dissociative ionization of SF_6 at 15.8 eV. VUV polarization is vertical in the plane of the figure. See text for details.

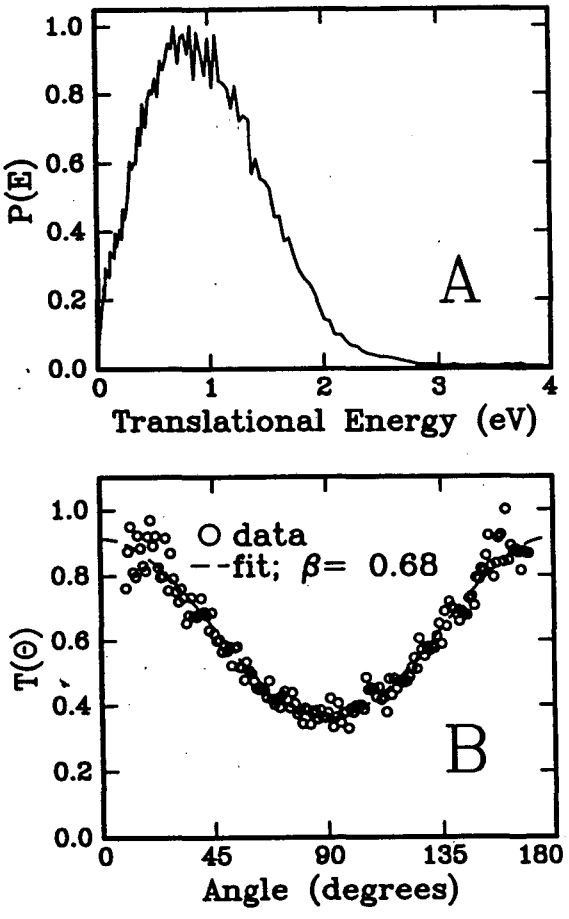

Figure 3. A. Translational energy release for SF_5^+ + F from ionization of SF_6 at 15.8 eV. B. Angular distribution of SF_5^+ for this process.

REFERENCES

1. P. A. Heimann, M. Koike, C. W. Hsu, M. Evans, C. Y. Ng, D. Blank, X. Yang, C. Flaim, A. G. Suits and Y. T. Lee, in **Optics for High-Brightness Synchrotron Beamlines II**, Proc. SPIE, **2856**, 90 (1996).
2. M. Ahmed, D. Blunt, D. Chen and A. G. Suits, J. Chem. Phys. **106** XX, (1997).
3. See, e.g., I. Powis, O. Dutuit, M. Richard-Viard and P.M. Guyon, J. Chem. Phys. **92** 1643 (1990).
4. R. N. Strickland and D. W. Chandler, Appl. Opt. **30**, 1811 (1991).

This work was supported by the Director, Office of Energy Research, Office of Basic Energy Sciences, Chemical Sciences Division, of the U. S. Department of Energy under contract No. DE-AC03-76F00098.

Principal investigator: Arthur G. Suits, E. O. Lawrence Berkeley National Laboratory. Telephone: 510-486-4754. Email: arthur@leea.cchem.berkeley.edu.

Beamline 9.3.1 Abstracts

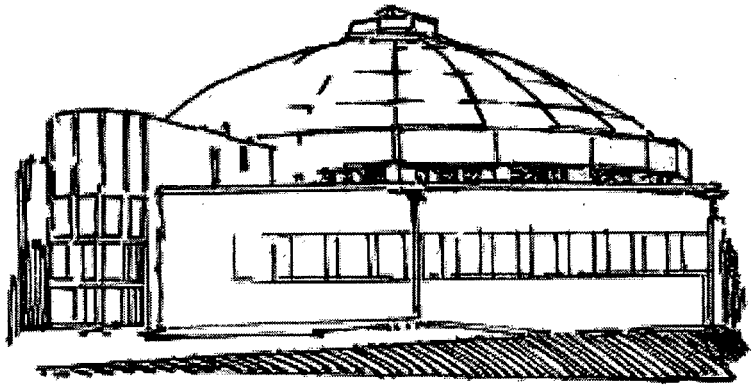

Design and Performance of the ALS Double-Crystal Monochromator

G. Jones,[1] S. Ryce,[1] D.W. Lindle,[1,2] B.A. Karlin,[3] J.C. Woicik,[4] and R.C.C. Perera[1]

[1]Advanced Light Source, Lawrence Berkeley National Laboratory, Berkeley, California 94720
[2]Department of Chemistry, University of Nevada, Las Vegas, Las Vegas, Nevada 89154
[3]National Synchrotron Light Source, Brookhaven National Laboratory, Upton, New York 11973
[4]National Institute of Standards and Technology, Gaithersburg, Maryland, 20899

ABSTRACT

A new "Cowan type" double-crystal monochromator, based on the boomerang design used at NSLS beamline X-24A, has been developed for beamline 9.3.1 at the ALS, a windowless UHV beamline covering the 1-6 keV photon-energy range. Beamline 9.3.1 is designed to simultaneously achieve the goals of high energy resolution, high flux, and high brightness at the sample. The mechanical design has been simplified, and recent developments in technology have been included. Measured mechanical precision of the monochromator shows significant improvement over existing designs. In tests with x-rays at NSLS beamline X-23A2, maximum deviations in the intensity of monochromatic light were just 7% during scans of several hundred eV in the vicinity of the Cr K edge (6 keV) with the monochromator operating without intensity feedback. Such precision is essential because of the high brightness of the ALS radiation and the overall length of beamline 9.3.1 (26 m).

INTRODUCTION

Third-generation synchrotron-radiation sources provide a unique opportunity for advancements in x-ray spectroscopy of atoms, molecules, and solids, owing to the high brightness available.[1] In order to take full advantage of this opportunity, a stable monochromatic x-ray beam is required, which in turn requires a high-precision mechanism for scanning photon energy with the monochromator. This challenge is exemplified in beamline 9.3.1 at the Advanced Light Source (ALS), a windowless beamline covering the 1-6 keV photon-energy range designed for use by the ALS x-ray atomic and molecular spectroscopy program. Beamline 9.3.1 is designed to achieve the goals of high energy resolution and high flux as well as to preserve the high brightness of the ALS source radiation. Design details of this beamline are presented elsewhere.[2]

In order to maintain high brightness at a distant sample while scanning the photon energy, it is desirable to have the monochromator mechanism as precise as possible. For spectroscopy applications, in fact, it is best to operate the monochromator without the usual intensity feedback system to eliminate any possible intensity variations induced by the feedback circuit. In addition, even small feedback corrections can alter the path of the beam through the optical system of the beamline, leading to changes in image quality at the sample. This desire for feedback-free running necessitates the use of a mechanical linkage in the monochromator mechanism. In order to attain the high precision necessary, it also is desirable to have as simple a drive mechanism as possible. Hence, the boomerang design[3,4] used at beamline X-24A at the National Synchrotron Light Source (NSLS), in which a single linear motion actuates scanning of

the monochromator, was taken as a model. An added benefit of this design is that it readily accomodates operation at low photon energies [e.g., near 2 keV with Si(111) crystals].

Performance of the beamline X-24A monochromator mechanism has been documented.[4] Photon-energy scanning is accomplished from outside vacuum by a single linear feed through with 15 cm of total movement. One benchmark for measuring the performance of this device is the degree of non-parallelism, in the dispersion plane, of the two monochromator crystals as a function of this linear motion. Measurements on the original mechanism before it was placed in beamline X-24A exhibited an error of approximately 2 arcsec/cm of linear travel. In practice, actual results were a little worse (4 arcsec/cm of linear travel).[5] Nevertheless, as far as we know, this is as good or better than other existing mechanisms.

DESIGN OF THE ALS DOUBLE-CRYSTAL MONOCHROMATOR

The basic design principles[6] of the new and improved "Cowan type" monochromator are identical to the original design[3], but several significant enhancements have been introduced. The primary change is the removal of all bearings from the mechanism, particularly the crossed-roller bearings used in the original design. Movement of the crystal mounts along the boomerang arms as well as all other linear motions use dovetail slides made of aluminum/bronze sliding on bases made of 304 stainless steel, with both surfaces treated chemically with a vacuum-compatible lubricant. This combination of materials is known not to seize even in ultra-high vacuum (UHV), and the hardness of the materials permits high-precision repetitive motion. We believe that replacement of the crossed-roller bearings is the primary reason for improved performance of the new design relative to the original.

Other design modifications include a significant reduction in the number of parts and use of more robust components. Reduction in the number of parts was accomplished by eliminating the crossed-roller bearings, by eliminating unneeded adjustments in the mechanism[5], and by consolidating multiple pieces into integrally machined components wherever possible. A photograph of the assembled monochromator including the crystal mounts in the small angle configuration is shown in Fig.1. Robustness was achieved simply by making many parts heavier or larger or using ribs for added strength in some larger components. Ease of alignment also has been enhanced by liberal use of fiducial marks throughout the mechanism, its support base, and the monochromator vacuum chamber. Finally, all precision parts were machined using numerically controlled techniques with specially prepared and matched machine tools. This latter effort was necessary to guarantee precise mating of the dovetail slides.

PERFORMANCE OF THE MONOCHROMATOR

To test the precision of the monochromator while scanning, a bench-top approach was used. A two-axis auto-collimator was aligned (< 1 arcsec) with respect to a right-angle mirror. The monochromator, equipped with mirrors in place of the two crystals, was positioned between the right-angle mirror and the auto-collimator with the axis of its linear motion parallel (10-20 arcmin) to the axis of the auto-collimator. As the monochromator is scanned, angular misalignments between the two mirrors riding on the mechanism, both parallel (theta) and perpendicular (chi) to the diffraction plane, can be measured using the auto-collimator.

Results of this test illustrate that the desired precision in theta has been met. For example, over 15 cm of linear travel in the boomerang mechanism, the two crystals (mirrors) remain parallel to

within 10 arcsec. This is at least 3 times better than the original design for the same amount of linear motion[4,5]. In addition, the change in angle is smooth and monotonic over this range. Over the entire range of motion of the new boomerang (23 cm), performance degrades by a factor of 2. Additional adjustment and testing is underway to improve these results.

Tests with x-ray synchrotron radiation were performed at beamline X-23A2 at the NSLS. Absorption spectra at the Cr and Ti K edges taken with the new mechanism are shown in Figs. 2-3. These results agree very well with standard spectra at these edges. Both measurements were taken with unfocused synchrotron radiation, thus only providing a test of theta alignment. Nevertheless, these spectra were recorded with the piezoelectric feedback system turned off, and the measured monochromatic flux varied by only 7-10% over the photon-energy ranges of the scans.

SUMMARY

Beamline 9.3.1 at the ALS is a windowless beamline, covering the 1-6 keV photon-energy range, designed to achieve the goals of high energy resolution, high flux, and preservation of the high brightness from third generation synchrotron radiation sources like the ALS. For atomic and molecular spectroscopy experiments, a stable monochromatic x-ray beam is required. Hence, the beamline has to be equipped with a suitable monochromator. A double-crystal monochromator based on the boomerang design used at NSLS Beamline X-24A has been developed for this beamline. The measured mechanical precision of this new "Cowan type" monochromator shows significant improvement over existing designs, without having to use intensity feedback available with piezoelectric devices. In tests with x-rays, this new mechanism provided monochromatic light with an intensity variation of as little as 7% over several hundred eV in photon energy near the Cr K edge without feedback. We are confident that this monochromator will provide a bright, high-resolution, and stable x-ray beam for use in x-ray spectroscopy at the ALS.

ACKNOWLEDGMENTS

We would like to thank P.L. Cowan for his help and encouragement in development of this monochromator and W. Ng for assistance in testing the monochromator. Tests with x-ray synchrotron radiation were performed at NSLS, which is supported by the U.S. Department of Energy under Contract No. DE-AC020-76CH00016.

FIGURE CAPTIONS

Fig. 1 Photograph of the assembled unit including the crystal mounts in the small angle configuration.

Fig. 2 Chromium K absorption spectrum measured without using an intensity feedback system.

Fig. 3 Titanium K absorption spectrum measured without using an intensity feedback system.

REFERENCES

1. B. Crasemann and F. Wuilleumier, **Physics Today**, p34, volume 37 (1984); D.L. Ederer, T. A. Callcott and R.C.C. Perera, Synchrotron Radiation News **7**, 29 (1994).
2. R. C. C. Perera, G. Jones and D. W. Lindle, Rev. Sci. Instrum. (In press).
3. J.A. Golovchenko, R.A. Levesque and P.L Cowan, Rev. Sci. Instr. **52** , 509 (1981).

4. P.L. Cowan, J.B. Hastings, T. Jach, and J.P. Kirkland, Nucl. Instr. and Meth. **208**, 349 (1983).
5. P.L. Cowan (Private communication).
6. A right-angle linkage system (references 3 and 4) was used to avoid the difficulties of independently manipulating the six degrees of freedom for two crystals in vacuum while maintaining the crystals Bragg planes parallel (within a rocking curve width) to each other, as the monochromator is scanned. This is necessary to provide a spatially constant and high throughput beam throughout the full energy range.

Principal investigator: R.C.C. Perera, Ernest Orlando Lawrence Berkeley National Laboratory. Email: rupert@lbl.gov.

This work was supported by the Director, Office of Energy Research, Office of Basic Energy Sciences, Materials Sciences Division of the U.S. Department of Energy under Contract No. DE-AC03-76SF00098.

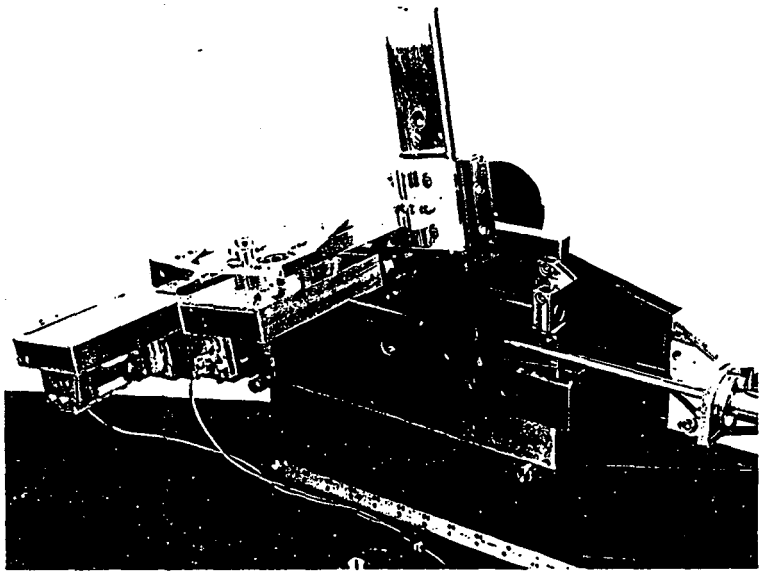

Figure 1

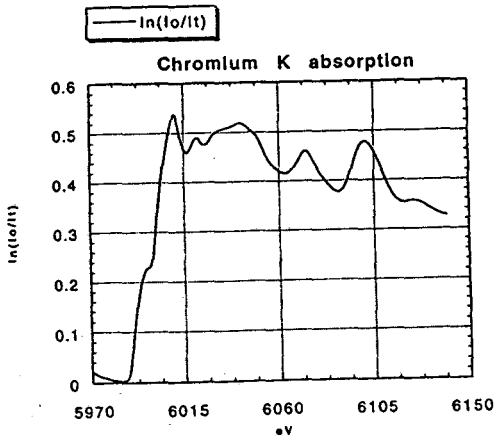

Figure 2

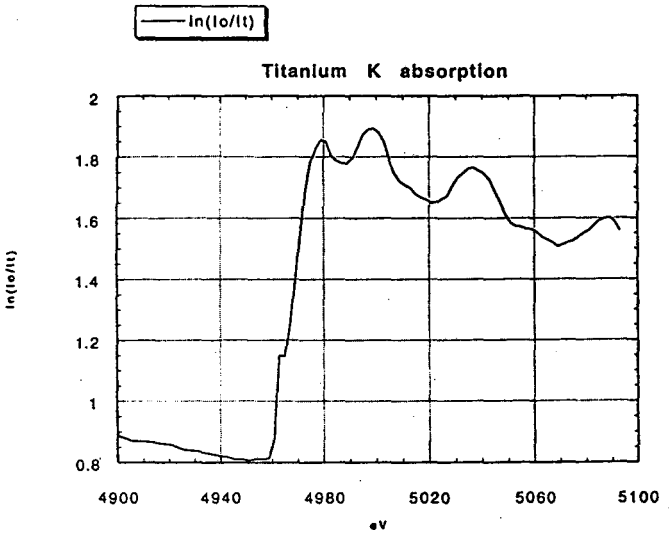

Figure 3

First Results from the High-Brightness X-Ray Spectroscopy Beamline at ALS

R. C. C. Perera, W. Ng and G. Jones
Advanced Light Source, Lawrence Berkeley National Laboratory
Berkeley, CA 94720

D. Hansen, J. Daniels, O. Hemmers, P. Glans, S. Whitfield, H. Wang and D. W. Lindle
Department of Chemistry, University of Nevada, Las Vegas
Las Vegas, NV 89154-4003

Beamline 9.3.1 at the Advanced Light Source (ALS) is a windowless beamline, covering the 1-6 keV photon-energy range, designed to achieve the goal of high brightness at the sample for use in the X-ray Atomic and Molecular Spectroscopy (XAMS) science, surface and interface science, biology and x-ray optical development programs at ALS. X-ray absorption and time of flight photo emission measurements in 2 - 5 keV photon energy along with the flux, resolution, spot size and stability of the beamline will be discussed. Prospects for future XAMS measurements will also be presented..

INTRODUCTION

Third-generation synchrotron-radiation sources like the Advanced Light Source (ALS) in Lawrence Berkeley National Lab. provide a unique opportunity for advancements in x-ray spectroscopy of atoms, molecules, and solids, because of the high brightness available[1]. Beamline 9.3.1 at the ALS is a windowless beamline, covering the 1-6 keV photon-energy range. The beamline is designed to achieve the goals of high flux, and preservation of the high brightness from ALS. The brightness will be an order-of-magnitude higher than presently available in this energy range. The anticipated beam size is about 0.4 mm in diameter, and the flux at the focus is expected to be 10^{11} ph/s in 0.5 eV bandpass. The beamline was commissioned in the spring of 1995, we will discuss the initial operation of the beamline.

BEAMLINE DESIGN

The first mirror (M1) in beamline 9.3.1 at the ALS is located 11.75 m from the source, it collimates the beam vertically and horizontally from bend magnet 9.3. The second mirror (M2), is located 15.50 m from the source, focuses the beam vertically and horizontally onto the sample at 27.25 m from the source. The two-crystal monochromator is located 13.63 m from the source. This configuration allows for high resolution and high brightness by passing a collimated beam through the monochromator, and by focusing the ALS source on the sample with unit magnification. The maximum horizontal acceptance of BL 9.3.1 is 8 mrads, but smaller horizontal acceptance of bend magnet radiation can be used to minimize the dominant mirror (spherical) aberrations. The sagittal and tangential radii of both toroidal mirrors (M1 and M2) are the same. The sagittal (minor) radius is 0.2585 m and the tangential (major) radius is adjustable from 1000 m to ∞ (flat) in increments of 1% (approx.) by elastically bending the mirror. The nominal tangential radius of the mirror is 2136 m when the mirror is positioned such that the glancing incidence angle for the principle ray is 11 mrads. A detail study of the optical design of this beamline is presented elsewhere[2,3]. Both M1 and M2 are mounted rigidly to the vacuum tank. The mirror and the vacuum tank are mounted on a motorized 6 struts HEXAPOD system [4]. Each strut in the system uses a stepping motor in conjunction with a linear scale closed loop feed

back system. All 6 struts are controlled by a window based software system. A very attractive aspect of the HEXAPOD system is its ability to define the origin of its coordinate system anywhere within its range of travel. In our case, the origin was defined to be the center of the mirror surface. The designed range of travel and rotation and resolution of the HEXAPOD are shown in Table 1.

	Range	Resolution
X	10mm	10μm
Y	20mm	0.1mm
Z	20mm	5μm
rX	8°	1μrad
rY	1°	0.01°
rZ	1°	0.005°

Table 1 Range and resolution of the HEXAPOD system in the X,Y, Z direction as well as rotation about these axis.

MONOCHROMATOR DESIGN

The design of our double crystal monochromator is based on the original "Cowan type" monochromator [5,6], but several significant enhancements have been introduced. The primary change is the removal of all bearings from the mechanism, particularly the crossed-roller bearings used in the original design. Movement of the crystal mounts along the boomerang arms as well as all other linear motions use dovetail slides made of aluminum/bronze sliding on bases made of 304 stainless steel, with both surfaces treated chemically with a vacuum-compatible lubricant. This combination of materials is known not to seize even in ultra-high vacuum (UHV), and the hardness of the materials permits high-precision repetitive motion. Other design modifications include a significant reduction in the number of parts and use of more robust components. Reduction in the number of parts was accomplished by eliminating the crossed-roller bearings, by eliminating unneeded adjustments in the mechanism, and by consolidating multiple pieces into integrally machined components wherever possible. Robustness was achieved simply by making many parts heavier or larger or using ribs for added strength in some larger components. Ease of alignment also has been enhanced by liberal use of fiducial marks throughout the mechanism, its support base, and the monochromator vacuum chamber. Photon-energy scanning is accomplished from outside vacuum by a single linear feed through with 15 cm of total movement. The angle of the first crystal is monitored by vacuum compatible tilt Sensor[7]. The resolution of the sensor is in the μrad range. The response time of the tilt sensors are in the minute range, which is not suitable for closed loop operation but they are very useful as an absolute reference. The monochromator is controlled by a Labview based data acquisition program. The alignment of the second crystal can be adjusted in-situ in both θ and χ. The motions are actuated by vacuum compatible pico-motors[8], which have a range of 0.5" and a resolution of 30nm. A closed loop feedback system designed to keep the final focus to within a fraction of the beam size will be installed. The system uses a 4 sector photodiode and a system of differential and summing amplifiers to feed back into the pico-motor. The monochromator operates at a based vacuum of 2 $x10^{-9}$ torr. A thin carbon foil is installed between the monochromtor tank and M1 and M2 mirror tank as a vacuum barrier. The vacuum of M1 and M2 chambers are maintained in 2 $x10^{-10}$ torr, which allows fast turn around time for crystal set change.

EXPERIMENTAL AND RESULTS

The mechanical components of beamline 9.3.1 were commissioned in the spring of 1995. The M1 mirror was installed in Apr. The M2 mirror is expected to be deliver in the winter of 1995. The experiments reported here is done with the beamline in this unusual configuration. The SR source is collimated by M1 and monochromatized by the monochromator. The exit beam is collimated and is 3cm x 1cm. The first set of experiments was done with a gas absorption cell in order to check the energy calibration and resolution of the monochromator. Ion current of the sample gas is collected by a two plate gas cell. Fig. 1 shows an absorption spectra for Ar K edge (5 torr). The spectra is not normalized and the feed back loop was not used. This data demonstrate the resolution and stability of the monochromator mechanism.

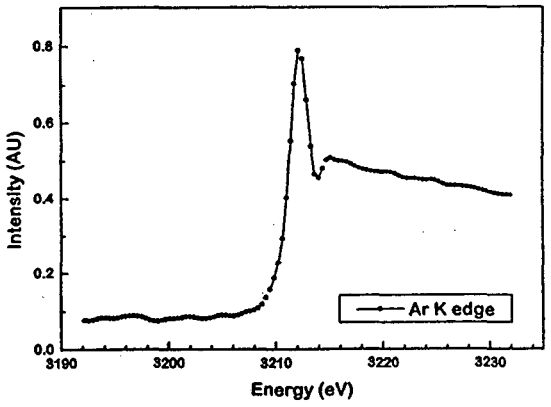

Fig. 1. The Ar K absorption spectra

The first time of flight (TOF) experiment on BL 9.3.1 was obtained during ALS two-bunch operation in August 1995. Since the exit beam of 9.3.1 is not focus at this time, the beam was apertured to 1mm x 1mm for this experiment. The flux delivered to the gas jet is only a fraction of the expected flux in a focused beam. Even in this configuration we were able to obtained TOF spectra with reasonable count rate. Fig. 2 shows a spectrum taken at a photon energy above the argon K-shell threshold. The data were collected using a space-focused ion time-of-flight mass spectrometer. Because of the double-bunch mode of operation, two spectra, indicated by labels above or below the baseline, respectively, are shown. The time axis is scaled to give the correct flight time for the peaks with labels below the spectrum. All of the peaks in the second spectrum (labels above the spectrum) are shifted by 328 ns, the time separation between the two ALS bunches. The maximum time resolution for the experiment can be determined from the width of the prompt peaks resulting from light scattered from the sample onto the detector. These peaks, which actually have a flight time near zero, have a full width at half maximum (FWHM) of only 200 ps. The most intense peak in the spectrum, Ar^{+4}, shows a FWHM of 840 ps, while Ar^{+7}, which is the most efficiently space focused peak, shows a FWHM of 600 ps. The high degree of time resolution observed is a result of the excellent timing characteristics of the ALS, proper handling of the timing signal in the ion-TOF analyzer and associated electronics, and the optimization of the analyzer space-focusing parameters.

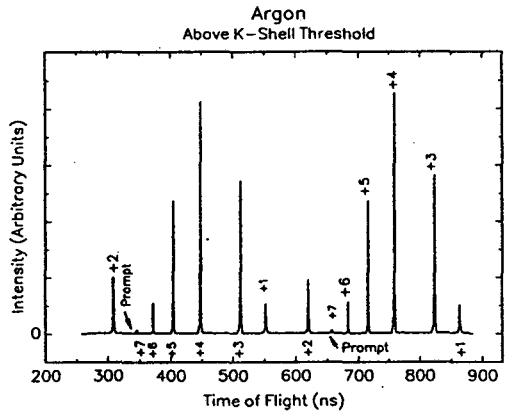

Fig. 2. This figure shows a time of flight spectrum taken at a photon energy above the argon K-shell threshold (3205 eV). The data were collected using a space-focused ion time-ot-flight spectrometer. Because of the double-bunch mode of operation, two spectra are shown in Fig. 2, indicated by labels above or below the baseline, respectively.

SUMMARY

We have designed a windowless beamline at ALS, covering the 1-6 keV photon-energy range, to achieve the goals of high energy resolution, high flux, and high brightness at the sample. When completed later this year, it will be the first ALS monochromatic hard-x-ray beamline providing flux and resolution comparable to any other beamline now in operation. The brightness will be an order-of-magnitude higher than presently available in this energy range. To achieve these goals, two technical improvements, relative to x-ray beamlines, a somewhat novel optical design for x-rays, in which matched toroidal mirrors are positioned before and after the double-crystal monochromator, was adopted, and a new "Cowan type" double-crystal monochromator

ACKNOWLEDGMENTS

We would like to thank P.L. Cowan for his help and encouragement in development of this monochromator. and E.M. Chow for assistance in ray tracing the optical system. We would also like to thank the staff at the ALS of assistance in different parts of the commissioning of the beamline.

REFERENCES

1. ALS Handbook, Lawrence Berkeley Laboratory, Berkeley, CA. PUB-643 Rev. (1989).
2. G. Jones, S. Ryce, D. W. Lindle, B.A. Karlin, J.C. Woicik, W. Ng, and R. C. C. Perera (to be published),
3. E.M. Chow and R.C.C. Perera, Lawrence Berkeley Laboratory, Berkeley, CA. LSBL-215 (1994).
4. Kaman Aerospace Corp. 3480 East Britnia Dr. Suite 120, Tucson, AZ 85706
5. J.A. Golovchenko, R.A. Levesque and P.L Cowan, Rev. Sci. Instr. **52** , 509 (1981).
6. P.L. Cowan, J.B. Hastings, T. Jach, and J.P. Kirkland, Nucl. Instr. and Meth. **208**, 349 (1983).
7. Applied Geomechanics 1336 Brommer St. Santa Cruz, CA 95062
8. New Focus, 2630 Walsh Ave Santa Clara, CA 95051

Principle Investigator, R.C.C. Perera, Lawrence Berkeley National Laboratory, 1 Cyclotron Rd., MS 2-400, Berkeley, CA 94720. Rupert@lbl.gov

This work was supported by the Director, Office of Energy Research, Office of Basic Energy Sciences, Materials Sciences Division of the U.S. Department of Energy under Contract No. DE-AC03-76SF00098.

High-Brightness Beamline for X-Ray Spectroscopy at the ALS

R. C. C. Perera[1], G. Jones[1], and D. W. Lindle[2]

[1]Advanced Light Source, Ernest Orlando Lawrence Berkeley National Laboratory, Berkeley, CA 94720
[2]Department of Chemistry, University of Nevada, Las Vegas, NV 89154-4003

ABSTRACT

Beamline 9.3.1 at the Advanced Light Source (ALS) is a windowless beamline, covering the 1-6 keV photon-energy range, designed to achieve the goals of high energy resolution, high flux, and high brightness at the sample. When completed later this year, it will be the first ALS monochromatic hard x-ray beamline, and its brightness will be an order of magnitude higher than presently available in this energy range. In addition, it will provide flux and resolution comparable to any other beamline now in operation. To achieve these goals, two technical improvements, relative to existing x-ray beamlines, were incorporated. First, a somewhat novel optical design for x-rays, in which matched toroidal mirrors are positioned before and after the double-crystal monochromator, was adopted. This configuration allows for high resolution by passing a collimated beam through the monochromator, and for high brightness by focusing the ALS source on the sample with unit magnification. Second, a new "Cowan type" double-crystal monochromator based on the design used at NSLS beamline X-24A was developed. The measured mechanical precision of this new monochromator shows significant improvement over existing designs, without using positional feedback available with piezoelectric devices. Such precision is essential because of the high brightness of the radiation and the long distance (12 m) from the source (sample) to the collimating (focusing) mirror. This combination of features will provide a bright, high resolution, and stable x-ray beam for use in the x-ray spectroscopy program at the ALS.

INTRODUCTION

Beamline 9.3.1 at the Advanced Light Source (ALS) is a windowless beamline, covering the 1-6 keV photon-energy range. The beamline is designed to achieve the goals of high energy resolution, high flux, and preservation of the high brightness from third generation synchrotron radiation (SR) sources like the ALS. This beamline will provide flux and resolution (10^{11} ph/s in ~ 0.5 eV bandpass) comparable to those of any other beamline now in operation. The brightness will be an order of magnitude higher than presently available in this energy range. The anticipated beam size is about 0.4 mm in diameter.

For the ALS, operating at 1.5 GeV, the approximate vertical opening half-angle of the radiation at the critical energy is:

$$1/\gamma = m_e c^2 / E = 0.34 \text{ mrad}$$

The vertical electron beam size is at its smallest value at all bend magnet 2 (BM 2) and BM 3 positions in the storage ring lattice. The bend magnet field is B = 1.069 T. The critical energy is given by:

$$\varepsilon_c(\text{keV}) = 0.665\ E^2\ (\text{GeV})\ B(\text{T}) = 1.60\ \text{keV}$$

The ALS storage ring has a natural rms horizontal emittance[1] of 3.4 x 10^{-9} mrad and a 10% emittance ratio into the vertical direction. The electron beam emittances are:

$$\varepsilon_h = 3.4 \times 10^{-9}\ \text{mrad}\ ,\ \varepsilon_V = 3.4 \times 10^{-10}\ \text{mrad}$$

In BM 3 the horizontal and vertical beta functions ($\int_h$ and $\int_V$) take the values 0.8545m and 1.4575 m, respectively,[1] and the horizontal dispersion, D_h, is 0.0944. The relative momentum spread, Îp/p, is 8 x 10^{-4}. Hence the rms photon beam dimensions are:

$$\sigma_h = [\varepsilon_h\ \beta_h + (\ D_h\ \Delta p/p)^2]^{1/2} = 93\ \mu\text{m}$$

and

$$\sigma_V = (\varepsilon_V \beta_V)^{1/2} = 22\ \ \mu\text{m}.$$

The electron beam emittances and photon beam dimensions taken together completely define the source.

OPTICAL DESIGN

The optical layout of the ALS beamline 9.3.1 is shown in Figure 1. The first mirror (M1), located 11.75 m from the source, collimates the beam vertically and horizontally from bend magnet 9.3. The second mirror (M2), located 15.50 m from the source, focuses the beam vertically and horizontally onto the sample at 27.25 m from the source. The two-crystal monochromator will be located 13.63 m from the source. This configuration allows for high resolution and high brightness by passing a collimated beam through the monochromator, and by focusing the ALS source on the sample with unit magnification. The optical design used at NSLS beamline X-24A, the brightest source of x-rays presently available in this spectral range, was not good enough to preserve the high brightness of ALS. The maximum horizontal acceptance of BL 9.3.1 is 8 mrads, but smaller horizontal acceptance of bend magnet radiation can be used to minimize the dominant mirror (spherical) aberrations. A detail study of the optical design of this beamline is presented elsewhere.[3] A summary of the ray tracings of the beamline will be presented in the next section.

The sagittal and tangential radii of both toroidal mirrors (M1 and M2) are the same. The sagittal (minor) radius is 0.2585 meters and the tangential (major) radius is adjustable from 1000 meters to ∞ (flat) in increments of 1% (approx.) by elastically bending the mirror. The nominal tangential radius of the mirror is 2136 meters when the mirror is positioned such that the glancing incidence angle for the principle ray is 11 mrads.

The best configuration to combine the action of two mirrors has been studied by several authors.[2] The configurations used in BL 9.3.1 radically violate the Abbe′ sine condition, because the angle to the axis increases at the outgoing side, when the angle to the axis decreases on the incoming side. But, this design results in approximate cancellation of the spherical aberrations originating from the non-unity magnification values used in the design of the beamline. This effect was first

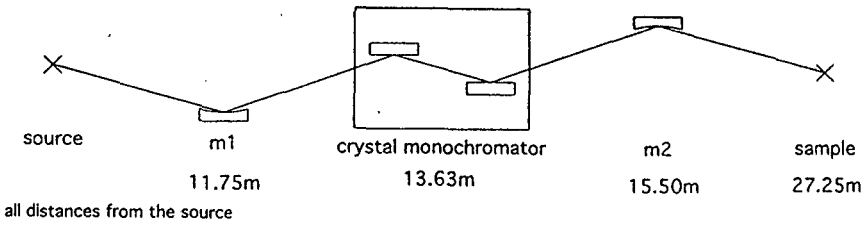

Figure 1. A schematic diagram of the beamline 9.3.1 at ALS.

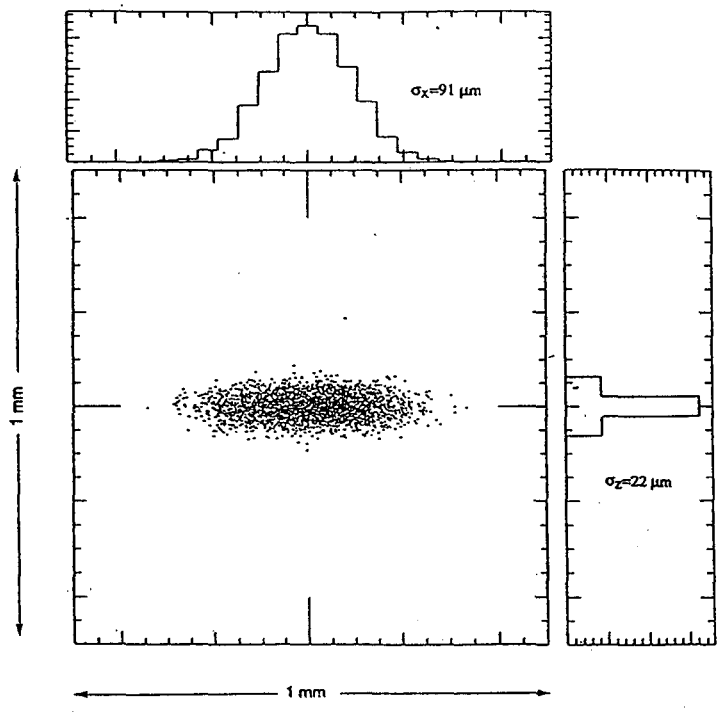

Figure 2. The cross-section of the synchrotron radiation source at the waist of the ALS BM3 modeled by the ray-tracing program SHADOW.

Figure 3. The image at the sample computed by SHADOW neglecting figure errors of the two mirrors.

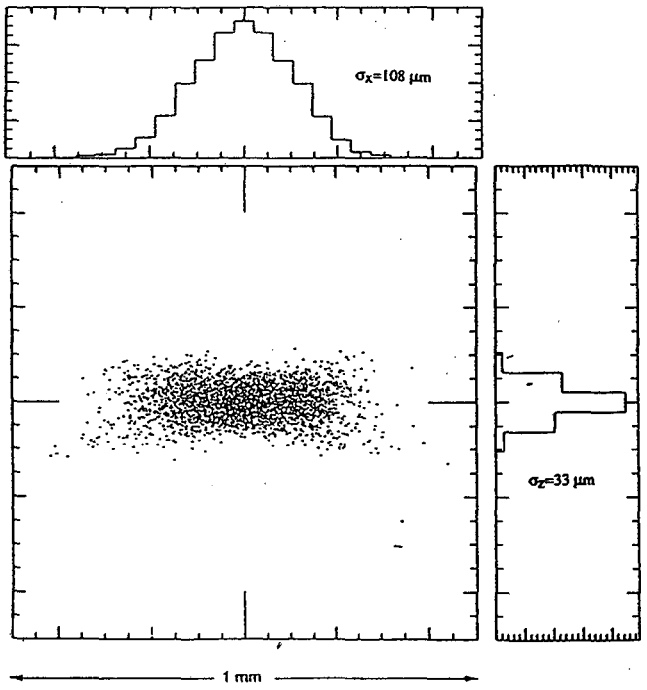

observed during the initial ray tracing studies performed to determine the optimum optical layout for this beamline.

RAY TRACING THE BEAM LINE

In principle, the optical properties of a beamline can be analytically described. With matrices, each corresponding to an optical element, operating on a representation of the beam in four-dimensional phase space (two position and two angular coordinates), the net effect of an optical system can be determined. Since these calculations are generally very complex, a more practical approach is to use the ray-tracing method based on the propagation of randomly generated rays of equal amplitude, weighted with appropriate distribution functions.

The x-ray optics ray tracing program[4] SHADOW, based on the geometrical optics tracings of the rays propagating through an optical system formed by sequential surfaces, was used. The ALS BM3 source was modeled assuming random (Monte Carlo) distributions in both real and momentum space. The parameters used in generating the BM3 source using SHADOW are presented in Table 1 and the cross-section of the synchrotron radiation source at the waist of the BM3 is shown in Figure 2. Ray tracing of the imaging system for an acceptance of 4 mrad bendmagnet radiation was performed. Figure 3 shows the image plane computed by the ray tracing program, neglecting the figure errors of the two mirrors. The rms beam dimensions at the image plane, shown in Figure 3, are $\sigma_h = 108\mu m$ and $\sigma_v = 33$ μm, compared to $\sigma_h = 93$ μm and $\sigma_v = 22$ μm at the waist of the bendmagnet source, which indicates that the image quality is extremely good.

If the M2 mirror shown in Figure 1 is rotated by 180° along the beam axis, the two toroidal mirrors are configured to obey the sine condition. The ray tracing performed on such an optical system showed that the final image is highly abberated and beam dimensions are $\sigma_h = 206$ μm and $\sigma_v = 626$ μm. This illustrate that the dominant aberrations (spherical) would not be improved by satisfying the sine condition, which led into a detailed study of aberration - canceling schemes for SR beamline mirror systems.[5]

FIGURE ERRORS

Figure errors in the optical components need to be minimal to preserve the high brightness of the ALS. The two mirrors in ALS BL 9.3.1 will have a slope error deviation from best-fit sphere of 5 μrads or better (including thermal distortions) over a frequency range of 5 mm to the size of the clear aperture. The errors of the mirror surfaces were modeled with a sine wave with origin at the center of the mirror. Slope errors were considered only in the tangential directions, as the saggital slope errors have a negligible effect, due to the forgiveness factor. For worst-case RMS displacement of 5 μrads and ripple wavelengths of 0.1, 1.0, and 10 cm, the ray tracings were performed. As expected, σ_h remained unchanged, and the resulting σ_v for the three cases are 169, 168, and 183 μm, respectively.

POWER LOADING

When operating at 1.5 GeV and 400 mA, the ALS produces 37.2 kW of total bend magnet power, distributed over the 2π radians. Therefore, in BL 9.3.1, when accepting 8 mrads of bend magnet radiation, receive 47.4 watts. The first mirror and first crystal in the monochromator accept most

of this power. The first mirror will nominally be operating between 11 and 14 mrads of grazing incidence. The power absorbed by the optical components in the beamline was calculated using SHADOW for the worst case (8 mrads of acceptance) for 11 and 14 mrads of grazing incidence of M1. The first mirror will absorb 11.7 to 19.4 watts, whereas the first crystal will absorb 35.4 to 28.0 watts, respectively. The power absorbed on the M1 is distributed over a 9.5 cm by 80 cm area of the mirror. Based on this analysis and other thermal calculations, M1 is not cooled, but the first crystal in the monochromator needs to be cooled.

MONOCHROMATOR

A new "Cowan type" double-crystal monochromator based on the design[6,7] used at NSLS beamline X-24A was developed. The measured mechanical precision of this new monochromator shows significant improvement over existing designs, without using positional feedback available with piezoelectric devices. Such precision is essential because of the high brightness of the radiation and the long distance (12 m) from the source (sample) to the collimating (focusing) mirror. Design details and the measured performance of the monochromator are presented elsewhere.[8]

CONCLUSION

We have designed a windowless beamline at ALS, covering the 1-6 keV photon-energy range, to achieve the goals of high energy resolution, high flux, and high brightness at the sample. When completed later this year, it will be the first ALS monochromatic hard-x-ray beamline providing flux and resolution comparable to any other beamline now in operation. The brightness will be an order-of-magnitude higher than presently available in this energy range. To achieve these goals, two technical improvements, relative to existing x-ray beamlines, a somewhat novel optical design for x-rays, in which matched toroidal mirrors are positioned before and after the double-crystal monochromator, was adopted, and a new "Cowan type" double-crystal monochromator based on the design used at NSLS beamline X-24A was developed. The beamline 9.3.1 at ALS will provide a bright, high resolution, and stable x-ray beam for use in the x-ray spectroscopy program at the ALS.

TABLE 1. Source Description of ALS Bend Magnet 3

Random Source.
Generated total 5000 rays.
Source assumed TRIDIMENSIONAL.
Source Spatial Characteristics: GAUSSIAN
Sigma X : 0.92 E-04 m Sigma Z : 0.22 E-04 m
Depth: SYNCHROTRON SOURCE.

Source Emission Characteristics
Distribution Type: SYNCHROTRON
Distribution Limits. X : 4.0 mrad
Z : 1.0 mrad
Magnetic Radius = 4.81 m. Beam Energy = 1.5 GeV.
Distance from Waist. X: 0 Z: 0
Polarization Used: SR TOTAL

Source Photon Energy Distribution: BOX DISTR
from Photon Energy: 1000 eV to 10000 eV

ACKNOWLEDGMENTS

We would like to thank P.L. Cowan for his help and encouragement in designing the beamline and E.M. Chow for assistance in ray tracing the optical system.

REFERENCES

1. ALS Handbook, Lawrence Berkeley Laboratory, Berkeley, CA. PUB-643 Rev. (1989).
2. W.R. Hunter, Proc. SPIE. 315, 19 (1981); D.E. Aspens, Appl. Opt. 21, 2642 (1982).
3. E.M. Chow and R.C.C. Perera, Lawrence Berkeley Laboratory, Berkeley, CA. LSBL-215 (1994).
4. B. Lai and F. Cerrina , Nucl. Inst. Meth. A246, 337 (1986).
5. M.R. Howells, Lawrence Berkeley Laboratory, Berkeley, CA. LBL-34750 (1993).
6. J.A. Golovchenko, R.A. Levesque and P.L Cowan, Rev. Sci. Instr. 52 , 509 (1981).
7. P.L. Cowan, J.B. Hastings, T. Jach, and J.P. Kirkland, Nucl. Instr. and Meth. 208, 349 (1983).
8. G. Jones, S. Ryce, D. W. Lindle, B.A. Karlin, J.C. Woicik, W. Ng, and R. C. C. Perera (to be published).

This work was supported by the Director, Office of Energy Research, Office of Basic Energy Sciences, Materials Sciences Division of the U.S. Department of Energy under Contract No. DE-AC03-76SF00098.

Principal investigator: Rupert Perera, Advanced Light Source, Ernest Orlando Lawrence Berkeley National Laboratory. Email: rupert@lbl.gov. Telephone: 510-486-5680.

Performance of Beamline 9.3.1 at the ALS: Flux and Resolution Measurements

Y. Uehara,[1] G. Fischer[2], J. Kring,[2] and R.C.C. Perera[2]

[1]Department of Chemistry, University of Nevada, Las Vegas, NV 89154
[2]Advanced Light Source, Ernest Orlando Lawrence Berkeley National Laboratory, Berkeley, CA 94720

INTRODUCTION

Beamline 9.3.1 at the ALS is a windowless beamline, covering the 1-6 keV photon-energy range[1]. This beamline is the first monochromatic hard x-ray beamline in the ALS, and designed to achieve the goals of high energy resolution, and preservation of the high brightness from the ALS. It consists of a new "Cowan type" double-crystal monochromator and two toroidal mirrors which are positioned before and after the monochromator.

The construction of the beamline was completed in December of 1995, with imperfect mirrors. In this report, we describe the experimental results of absolute flux measurements and x-ray absorption measurements of gases and solid samples using the present set of mirrors.

EXPERIMENT

Flux measurements were performed using a silicon photo diode[2], AXUV-100. The photo diode has been developed for applications in the 7 to 6000 eV spectral region, with large dynamic range (over eight orders of magnitude). The diode is a normal p-n junction type, without a doped dead-region, which results in near theoretical quantum efficiencies to XUV photons. For majority of XUV photons, about 3.63 eV of energy is required to generate one electron-hole pair. Thus, the electric current seen by an external circuit is:

$$I\,(A) = \text{Flux (Ph/s)} \times (E\,(eV) / 3.63) \times 1.6 \times 10^{-19}$$

If the photon flux at 3 keV is about 10^{10} ph/s, current of 1.32×10^{-6} A will be observed. AXUV-100 has a square sensitive area of 100 mm^2. The photo diode was placed just after a horizontal slit and a vertical slit. The beam size on the detector is about 2 x 2 mm. The output of the photo diode was amplified by a Keithley 427 (or 428) current amplifier and read by a multimeter.

X-ray absorption measurements of gases were performed using a gas absorption cell by measuring the total electron yield. Ion current from sample gases was collected by a metal plate, and the current was amplified by a Keithley® amplifier. A thin gold foil was placed just before the gas cell to monitor the in-coming flux. Measurements of solid samples were performed in transmission mode using a sample chamber with a liner feed through as the sample holder. Powder samples were spread onto 2μm thick kapton tape. The transmitted intensity was detected by the silicon photo diode.

RESULTS AND DISCUSSION

Flux measurement

Photon energy, tilt sensor's read-out voltage, the photon flux, the ring current, and the normalized flux are presented in Tables 1 and 2 for 1.5 GeV and 1.9 Gev operations. The monochromator is controlled by a Lab VIEW program[3], based on the stepping motor position, which is related to the photon energy, which can be calculated from the Bragg angle. The read-out voltage of the tilt sensor, which is mounted on the first crystal, is related to the Bragg angle by:

$$\theta_{Bragg} = AV^2 + BV + C$$

where, A = -0.018027, B = -5.2849 and C = 34.992.

The values of A, B, and C were obtained using the energy values of absorption spectra.

It is clear from the figures that the photon flux gradually decreases up to 4500 eV, then falls down rapidly. When the ring is operated in 1.9 GeV, the flux was constant up to about 4500 eV,(about 2 x 10^{10} ph/s), which is higher than that obtained with 1.5 GeV operation. However, flux decreases rapidly above 4500 eV.

Considering the calculated properties of the bend-magnet radiation from the ALS and the reflectivity of nickel-coated mirrors, we can expect more flux up to around 5000 eV, when the mirrors take the glancing angle of 11 mrad. On the other hand, the surface roughness of the mirrors affects a lot on the reflectivity. This indicates that the rapid decrease of the flux from about 4500 eV should be due to the rough surface of the second mirror. More flux will be expected with a better second mirror and/or the usage of germanium (Ge) as the monochromator crystals.

Absorption Spectra of Gases

Figure 1 shows the absorption spectra of the Cl K edge of CF_3Cl, CF_2Cl_2, and $CFCl_3$ (2 - 3 torr). This spectrum is normalized with the currents of the I_0 monitor. From the full width at half maximum (FWHM) of the first resonance peak, the energy resolution is estimated to be lower than 1.0 eV. The fine structure of these results agrees very well with the previously published data[4].

CONCLUSION

We described performance tests of BL9.3.1. More than 2 x 10^{10} photons/sec of photons can be obtained from 2000 to 4500 eV, when the storage ring is operated in 1.9 GeV. The photon flux decreases dramatically above 4500 eV. This should be due to the surface roughness of the second mirror. The absorption spectra of several gases and solid samples show that the energy resolution of less than 1 eV can be obtained on the energy range of 2000 to 5000 eV.

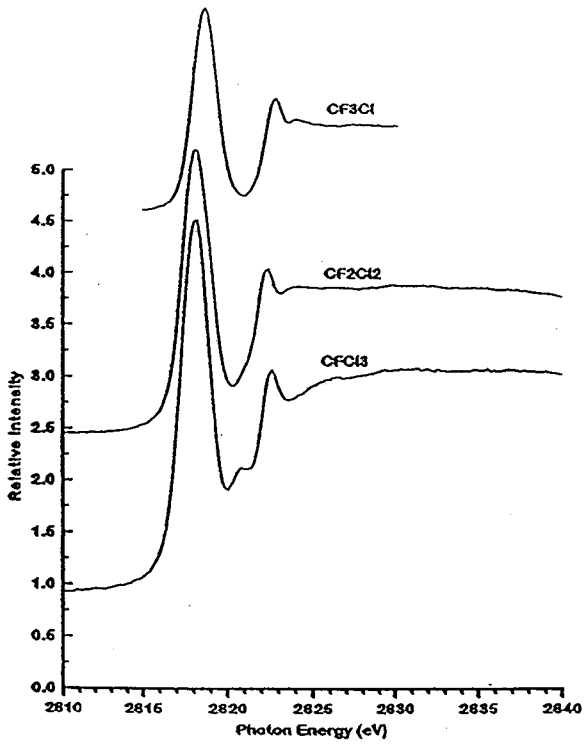

Figure 1. The Cl K absorption spectra of CF_3Cl, CF_2Cl_2, and $CFCl_3$.

Table 1. Tilt sensor, photon flux, ring current, and photon flux normalized to 400 mA at various energies for 1.5 GeV.

Photon Energy (eV)	Tilt Sensor Voltage (V)	Photon Flux (photons/sec)	Ring Current (mA)	Normalized Flux @ 400mA
2124.2	-6.4398	2.2120 E10	308	2.8727 E10
2169.3	-5.8904	2.1011 E10	313	2.6851 E10
2231.9	-5.2465	2.0310 E10	322	2.5230 E10
2321.1	-4.4866	2.1054 E10	330	2.5520 E10
2390.8	-3.9825	2.1484 E10	338	2.5425 E10
2445.7	-3.6270	2.1667 E10	344	2.4939 E10
2507.3	-3.2632	2.0649 E10	346	2.3872 E10
2576.9	-2.8894	1.9528 E10	350	2.2317 E10
2653.9	-2.5143	1.9124 E10	353	2.1670 E10
2739.5	-2.1366	1.8162 E10	361	2.0124 E10
2834.5	-1.7580	1.7649 E10	365	1.9341 E10
2884.1	-1.5748	1.2114 E10	264	1.8355 E10
2936.6	-1.3908	1.0932 E10	268	1.6316 E10
2992.7	-1.2039	1.0742 E10	271	1.5855 E10
3048.9	-1.0264	1.0433 E10	276	1.5120 E10
3112.3	-0.8366	1.0825 E10	261	1.6590 E10
3173.3	-0.6633	1.0567 E10	258	1.6383 E10
3237.2	-0.4911	1.0218 E10	257	1.5904 E10
3304.4	-0.3192	9.6329 E9	256	1.5051 E10
3376.0	-0.1456	9.0589 E9	255	1.4210 E10
3441.7	0.0058	8.5167 E9	253	1.3465 E10
3513.6	0.1632	7.8454 E9	252	1.2453 E10
3587.8	0.3178	7.4048 E9	251	1.1800 E10
3660.1	0.4610	1.0054 E10	368	1.0928 E10
3735.0	0.6022	9.4395 E9	366	1.0316 E10
3812.8	0.7421	8.7351 E9	364	9.5990 E9
3891.4	0.8766	7.9582 E9	355	8.9669 E9
3971.1	1.0066	7.3929 E9	357	8.2833 E9
4050.8	1.1308	6.3624 E9	349	7.2921 E9
4131.2	1.2503	5.6620 E9	347	6.5268 E9
4215.0	1.3694	4.8336 E9	342	5.6533 E9
4298.0	1.4821	3.9326 E9	326	4.8253 E9
4382.5	1.5920	2.7230 E9	324	3.3618 E9
4466.6	1.6967	1.5797 E9	310	2.0383 E9
4552.5	1.7991	6.3291 E8	307	8.2464 E8
4638.3	1.8972	3.4729 E8	303	4.5846 E8

Table 2. Tilt sensor, photon flux, ring current, and photon flux normalized to 250 mA at various energies for 1.9 GeV.

Photon Energy (eV)	Tilt Sensor Voltage (V)	Photon Flux (photons/sec)	Ring Current (mA)	Normalized Flux @ 250mA
2280.2	-4.8157	1.8271E10	182	2.5097 E10
2519.6	-3.1932	1.9065 E10	180	2.6279 E10
2956.0	-1.3242	1.7202 E10	173	2.4859 E10
3269.1	-0.4074	1.6993 E10	175	2.3847 E10
3440.2	0.0035	1.9753 E10	215	2.2969 E10
3596.3	0.3360	1.9091 E10	213	2.2406 E10
3762.2	0.6529	1.7206 E10	209	2.0582 E10
3934.2	0.9481	1.6674 E10	206	2.0235 E10
4114.8	1.2274	1.5114 E10	201	1.8799 E10
4300.7	1.4868	1.2066 E10	190	1.5876 E10
4496.5	1.6107	1.0730 E10	187	1.4345 E10
4693.9	1.7307	1.0093 E10	183	1.3789 E10
4595.4	1.8496	9.0560 E9	176	1.2864 E10
4697.2	1.9632	7.0823 E9	174	1.0176 E10
4798.3	2.0707	4.1103 E9	170	6.0445 E9
4901.9	2.1759	2.9172 E9	164	4.4469 E9
5007.0	2.2776	1.4128 E9	161	2.1938 E9

REFERENCE

1. R.C.C. Perera, G. Jones, and D.W. Lindle, Rev. Sci. Instrm. **66**, 1745 (1995).
2. International Radiation Detectors Co.
3. National Instruments Co., LavVIEW for windows commercial software, (1993).
4. R.C.C.Perera, P.L.Cowan, D.W.Lindle, R.E.La Villa, T.Jach, and R.D.Deslattes, Phys. Rev. A **43**, 3609 (1991).

This work was supported by the Director, Office of Energy Research, Office of Basic Energy Sciences, Materials Science Division, of the U.S. Department of Energy under Contract No. DE-AC03-76SF00098.

Principal investigator: Rupert Perera, Advanced Light Source, Ernest Orlando Lawrence Berkeley National Laboratory. Email: rupert@lbl.gov. Telephone: 510-486-5680.

Ca and S K-Edge XANES Studies of Calcite-Acid Mine Water Interactions

Satish C. B. Myneni, Rupert C. C. Perera[1]

Earth Sciences Division, Lawrence Berkeley National Laboratory, Berkeley, CA 94720
[1] Advanced Light Source, Lawrence Berkeley National Laboratory, Berkeley, CA 94720

INTRODUCTION

Heavy metal-rich acidic waters (SO_4^{2-}, AsO_4^{3-}, SeO_4^{2-}, Fe^{2+}, Fe^{3+}, Al^{3+}, Cu^{2+}, Zn^{2+}, Cd^{2+}) and related ochreous coatings are common around abandoned sulfide and coal mine sites[1-3]. This is mainly caused by the natural weathering of pyrite (FeS_2), arsenopyrite (FeAsS), and other metal sulfide containing shales. Acid generation in the case of pyrite can be explained by a general reaction:

$$FeS_2 + 3.5\ O_2 + H_2O \Leftrightarrow Fe^{2+} + SO_4^{2-} + 2H^+$$

Also, these low pH waters interact with the soils, and mobilize their soluble elements. One of the common remediation strategies is to allow these acid waters to react with limestone ($CaCO_3$-rich rock) and neutralize the pH and precipitate out soluble metals. Yet, the associated problem is the precipitation of Fe and Al oxides and hydroxy sulfate coatings on limestone surfaces, which block calcite reactive sites, and make them ineffective few hours after initiation of treatment. The main objectives of this research are to examine: 1) the chemistry of limestone surface coatings, and 2) their toxic metal uptake and the conditions that inhibit their formation.

Previous molecular studies using X-ray diffraction, and vibrational spectroscopy[4] on limestone surface coatings (sampled from Athens, OH) indicate that the surface-most layer (the layer in contact with water) is composed of schwertmannite (Fe(III)-hydroxy sulfate) like phases[2]. However, white, X-ray amorphous; Al-, sulfate- and carbonate-rich; and Ca-poor phases appeared at the interface between the limestone and the iron oxide coatings. The structure, morphology, and coordination chemistry of component major and trace elements of these white precipitate phases have not previously been examined.

METHODS

Iron-rich acidic mine drainage (AMD) samples were collected from Iron Mountain, CA and were reacted with 1 cm diameter limestone pieces and reagent grade, fine grained $CaCO_3$. The experiments in the case of $CaCO_3$ were also conducted at different pH values by varying the concentration of $CaCO_3$ added. In addition, AMD reacted naturally occurring limestone samples were also collected from Iron Mountain, CA, and Athens, OH.

Ca and S K-edge XANES studies were measured at the Beamline 9.3.1, Advanced Light Source (ALS). The XAS spectra were collected in transmission mode and under ~ 10^{-7} torr pressure. The scan ranges for S and Ca were 2460-2510 eV, and 4030-4100 eV, respectively, with 0.2 eV step size. These studies were conducted at both 1.5 GeV (for S) and 1.9 GeV (for Ca) multi-bunch mode. The XANES studies were also performed at ambient pressure and humidity conditions at the Stanford Synchrotron Radiation Laboratory (SSRL, B.L 6-2), to examine the influence of

water presence on sample S- XANES. At SSRL, the sample fluorescence was collected using a Lytle detector and the scan conditions were similar to those of ALS mentioned above.

RESULTS

S-XANES

The data collected at ambient and UHV conditions suggest that the S-XANES features a few eV above the edge were dissimilar for minerals with high structural water, such as ettringite ($Ca_6Al_2(SO_4)_3(OH)_{12}.26H_2O$) (Fig. 1). Ettringite samples also took longer time to equilibrate with the vacuum conditions of the sample chamber, which may have been due to slow escape of structural water molecules. However, solid phases with little crystalline water did not exhibit major changes in the spectra (e.g. Ferric sulfate). Also, the transmission spectra are useful for concentrated samples, which exhibit self-absorption for fluorescence spectra.

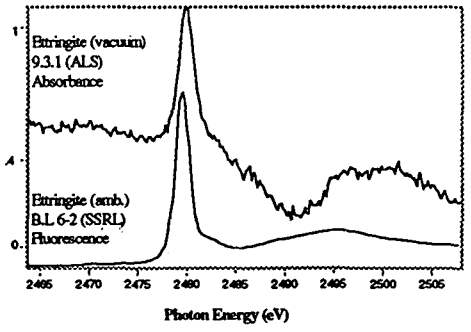

Fig. 1 S K-edge XANES of ettringite in vacuum and atmospheric pressures. The spectra were calibrated against S=S white line features (2469.2 eV) of sodium thiosulfate, and were not subtracted for background.

The AMD reacted limestone and ochreous precipitate samples were examined and compared with different S structural models (not shown here). The data indicate that a) the energy position of the white line is sensitive to the S oxidation state and complexing cation, b) all of the field and laboratory samples indicate S in +VI oxidation state (Fig. 2), and c) poorly crystalline white precipitates have sulfate, dominantly complexed to Al.

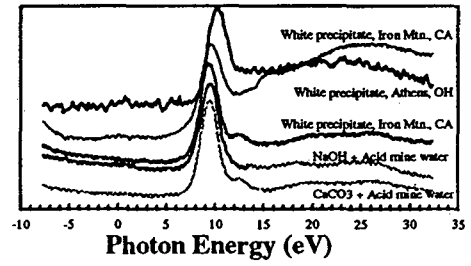

Fig. 2 S K-edge XANES (absorption) of AMD reacted samples. Edge is calibrated against S=S features in Na-thiosulfate (2467.9 eV).

Ca XANES

Compounds with Ca in different coordination and ligand environment were examined to evaluate their influence on the white line shifts and other spectral features in the XANES region. The Ca K-edge spectra of these compounds exhibit contrasting features and are similar to those reported by Quatrieri *et al.*[5]. Octahedral Ca, coordinated to "O" (e.g. $CaCO_3$) exhibits a stronger 1s → np transition (f1 in Fig. 3). With increases in coordination (e.g. 8 in $CaSO_4.2H_2O$; and 9 in $Ca(NO_3)_2.4H_2O$), the intensity of this feature decreases. Compounds with Ca in 8 coordination, but with different local geometry also exhibit major changes in Ca-XANES spectra (e.g. Ca and Al polyhedra linkage in

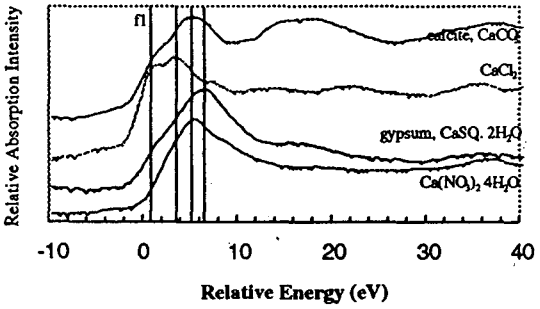

Fig. 3 Ca K-edge XANES of common Ca salts. The spectra were calibrated against calcite white line (4052.7 eV).

ettringite; and Ca and SO_4 in $CaSO_4.2H_2O$). Ca coordination to strong electronegative elements (e.g. Cl), also produced major changes in 1s → np transition.

White precipitates sampled from field sites were relatively poor for Ca concentration and thus their XANES transmission spectra were noisy and no distinguishable features could be recorded. However, XANES spectra of laboratory samples (AMD reacted with $CaCO_3$) suggest that the sample1s → np transition are intermediate between $CaCO_3$ and $CaSO_4.2H_2O$ (Fig. 4). Also, the XANES features a few eV above the edge (~ 25 eV) were different from these models.

CONCLUSIONS

The present study shows that: 1) sample modifications can occur under UHV conditions and natural samples with high crystalline water are not suitable for studying under vacuum, 2) The sensitivity of Ca and S XANES to the local coordination environment can be used for interpreting these element bonding in complex and poorly crystalline natural materials, and 3) Ca and S XANES of field and laboratory samples indicated that Al/Al-Ca rich sulfates form on limestone surfaces and their coordination is different from the known well crystalline models. More structure related studies (EXAFS, and theoretical XANES calculations) have to be conducted to identify the coordination environment around Ca and S.

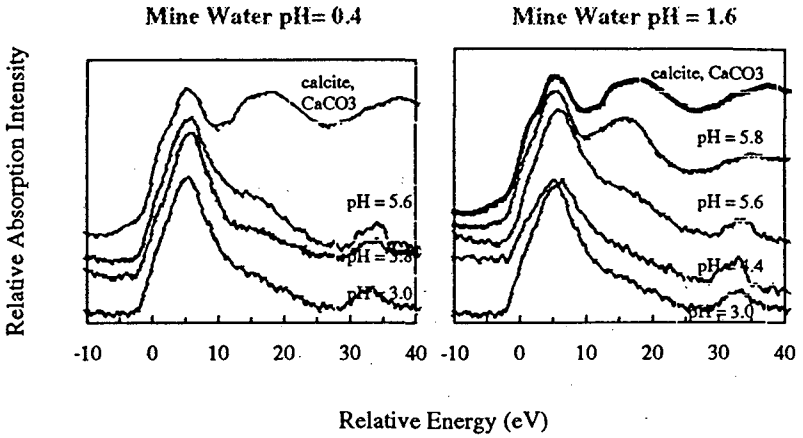

Fig. 4. Fine grained $CaCO_3$ reactions with AMD. The sample edges were calibrated against $CaCO_3$ white line, 4052.7 eV.

ACKNOWLEDGEMENTS

S. C. B. Myneni would like to acknowledge Drs. Tetsu K. Tokunaga (LBNL) and Jerry M. Bigham (The Ohio State University) for their encouragement in this study.

REFERENCES

1. Nordstrom D. K., Jenne E. A., and Ball J. W. 1979. ACS Series. 93, 51.
2. Bigham J.M., Schwertmann U., Carlson L., Murad E. 1990. Geoc. Cosmoch. Acta. 54, 2743.
3. Bowell R. J., and Bruce I. 1995. Ap. Geochem. 10, 237.
4. Myneni, S. C. B. 1997. To be published.
5. Quatrieri S., Chaboy J., Merli M., Oberti R., Ungarett L. 1995. Phys. Chem. Mineral., 22, 159.

This study was supported by the Office of Basic Energy Science, Geoscience Program, DOE: DE-ACO3-76SF00098.
Principal Investigator: Satish C. B. Myneni, Earth Sciences Division, Lawrence Berkeley National Laboratory. Email: smyneni@lbl.gov. Tel: (510) 486-4591.

Dissociation of Deep-Core-Excited CH_3Cl

D.L. Hansen,[1] J.P. Cotter,[2] G.R. Fisher,[3] K.T. Leung,[4] R. Martin,[1] P. Neill,[2]
W. Ng,[3] R.C.C. Perera,[3] M. Simon,[5] Y. Uehara,[6]
B. Vanderford,[1] S.B. Whitfield,[7] and D.W. Lindle[1]

[1]Department of Chemistry, University of Nevada, Las Vegas, NV 89154-4003, USA
[2]Department of Physics, University of Nevada, Reno, NV 89557-0058, USA
[3]Lawrence Berkeley National Laboratory, Berkeley, CA 94720, USA
[4]Department of Chemistry, University of Waterloo, Canada
[5]LURE, Bâtiment 209D, Université Paris-Sud, 91405 Orsay Cedex, France
[6]Mitsubishi Electric Corp., Amagasaki, Hyogo, 661 Japan
[7]Department of Physics, University of South Alabama, Mobile, AL 96688, USA

Using x-rays from B.L. 9.3.1, a space-focused time-of-flight (TOF) mass spectrometer was used to study photofragmentation of CH_3Cl following excitation in the neighborhood of the Cl K-shell threshold (~2.8 keV). Multi-ion coincidence measurements were used to search for selective dissociation of specific bonds in the molecule. Such selectivity has been observed for excitation near outer-core-level thresholds (e.g., Cl $2p$), but this is the first study in deep core levels, where very-short core-hole lifetimes and Auger cascade effects may influence fragmentation. Both high-resolution time-of-flight spectroscopy and multi-coincidence photoelectron-photoion-photoion (PE- PIPICO), as well as photoelectron-photoion-photoion-photoion (PE3PICO) measurements were performed. Dramatic changes in the line shapes for different fragment ions are observed as a function of the excitation energy, and are attributed to selective dissociation of the CH_3Cl molecule along the C-Cl bond. In addition, pronounced angular distributions of the ejected ions

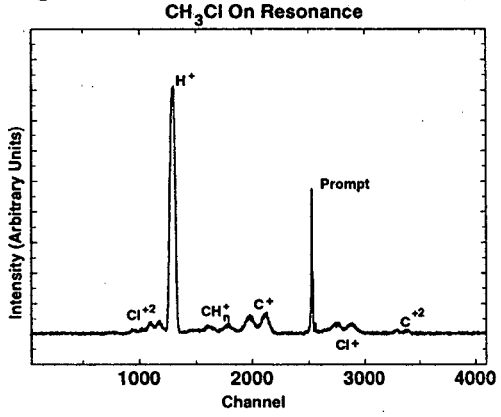

FIG. 1. CH_3Cl Spectrum taken on the $1a_1 \rightarrow 8a_1$ resonance.

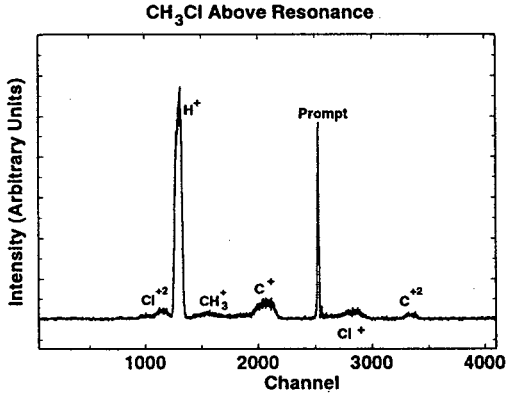

FIG. 2. CH_3Cl Spectrum taken above the Cl K-threshold.

are observed on resonance. This can be seen by comparing figures 1 and 2. Figure 1 represents data taken at photon energy corresponding to excitation to the Cl a_1 antibonding orbital ($1a_1 \rightarrow 8a_1$). A distinct splitting of the peaks is observed as a result of the alignment of the core-excited molecule on the $8a_1$ resonance. Because of this alignment, ions produced in the fragmentation of the molecule are ejected towards, and away from the detector. Figure 2 represents data taken above the K-shell resonance, where no such splitting is observed due to isotropic fragmentation of the molecule.

Support from NSF (PHY-9303915), Nevada DOE EPSCoR, Research Corporation, and The Petroleum Research Fund is gratefully acknowledged. This work was performed at the Advanced Light Source, which is supported by DOE (DE-ACO3-76SF00098).

Team Leader: D.W. Lindle, e-mail: lindle@nevadu.edu; fax: +1 702 895 4072

Fragmentation of HCl Following Excitation at the Chlorine K Edge

D.L. Hansen, M.E. Arrasate, J.P. Cotter[1], G.R. Fisher[2], K.T. Leung[3], J.C. Levin[4], R. Martin, P. Neill[1], R.C.C. Perera[2], I.A. Sellin[4], M. Simon[5], Y. Uehara[6], B. Vanderford, S.B. Whitfield[7], and D.W. Lindle

Department of Chemistry, University of Nevada, Las Vegas, NV 89154-4003, USA

[1] *Department of Physics, University of Nevada, Reno, NV 89557-0058, USA*

[2] *Lawrence Berkeley National Laboratory, Berkeley, CA 94720, USA*

[3] *Department of Chemistry, University of Waterloo, Canada*

[4] *Department of Physics, University of Tennessee, Knoxville, TN 37996, USA*

[5] *LURE, Bâtiment 209D, Université Paris-Sud, 91405 Orsay Cedex, France*

[6] *Mitsubishi Electric Corp., Amagasaki, Hyogo, 661 Japan*

[7] *Department of Physics, University of South Alabama, Mobile, AL 36688, USA*

A space-focussed time-of-flight (TOF) mass spectrometer was used to study the relaxation dynamics of HCl following excitation in the vicinity of the Cl-K edge (~2.8 keV) using x-rays from B.L. 9.3.1. At the lowest resonant excitation to a σ^* antibonding orbital ($1\sigma \rightarrow 6\sigma$), a significant fraction of the excited molecules decay by emission of a neutral H atom. While neutral-H emission has been observed for shallow core levels (e.g. Cl 2p in HCl), we believe this to be the first observation of neutral-atom emission as a significant decay channel following resonant excitation of a deep core hole. The dissociation of neutral hydrogen atoms raises the issue of how effectively dissociation competes with Auger decay in the relaxation of these deep core levels (i.e. Cl 1*s*). The figure shows the evidence for this neutral dissociation. For this figure, peaks in the TOF spectra were integrated and their fractional yield was plotted as a function of photon energy. The most prominent feature in this graph is the dip in the fraction of hydrogen and the corresponding jump in the fraction of Cl^{3+} detected on resonance. These changes correspond to a 40% decrease in the amount of H^+ detected. In addition, trends in fractional ion yields from Photo-Ion Photo-Ion COincidence (PIPICO) spectra suggest the presence of post-collision interaction (PCI). While, electron spectroscopy studies are required to confirm the observation of this effect, we believe this to be the first evidence of PCI moderated dissociation in molecules.

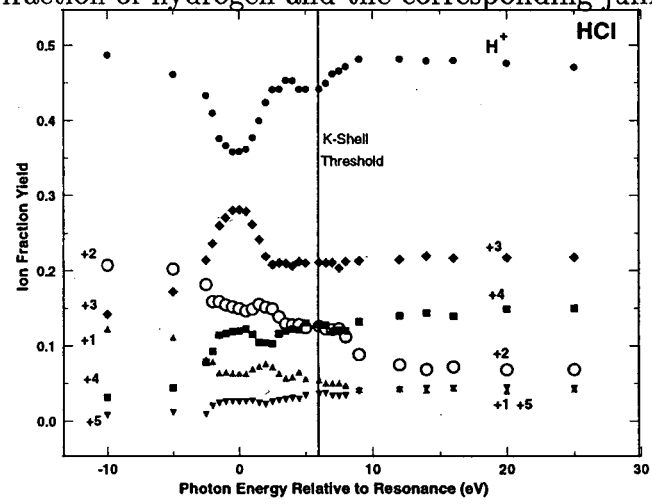

FIG. 1. Fractional ion yield as a function of excitation energy relative to the ($1\sigma \rightarrow 6\sigma$) resonance in the chlorine *K* near-edge region.

Support from NSF (PHY-9303915), Nevada DOE EPSCoR, Research Corporation, and The Petroleum Research Fund is gratefully acknowledged. This work was performed at the Advanced Light Source, which is supported by DOE (DE-AC03-76SF00098) and at the National Synchrotron Light Source, supported by DOE (DE-AC020-76CH00016).

Principal investigator: D.W. Lindle. Email: lindle@nevada.edu. Fax: +1 702 895 4072.

Beamline 9.3.2 Abstracts

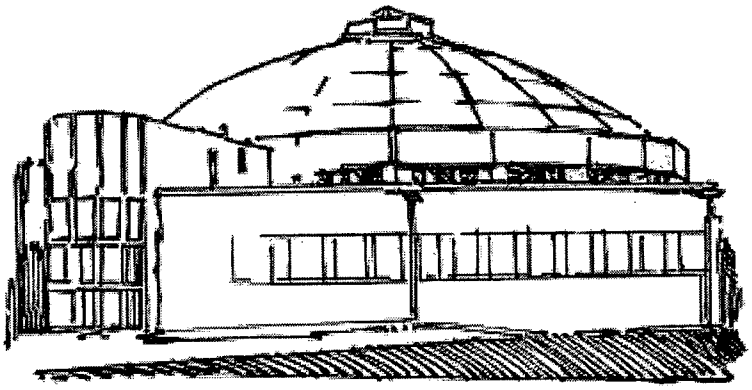

An Advanced Photoelectron Spectrometer/Diffractometer for Studies of the Atomic, Electronic, and Magnetic Structure of Surfaces, Interfaces, and Nanostructures

R.X. Ynzunza[1,2], E.D. Tober[1,2], Z. Wang[1,2], F. J. Palomares[1,2,3], J. Morais[2], R. Denecke[1,2], S. Ryce[2], J. Zaninovich[2], C. Westphal[2,4], C.E. Miner[5], A. Kay[1,2], D. Leech[6], M. Mellon[6], K. Shaw[7], D.M. Lind[7], J. Liesegang[2,8], Z. Hussain[9], N.V. Smith[9], D.A. Shirley[10], and C.S. Fadley[1,2]

[1]Department of Physics, University of California, Davis, Davis, CA 95616, USA
[2]Materials Sciences Division, Lawrence Berkeley National Laboratory, Berkeley, CA 94720, USA
[3]ICMM-CSIC, Cantoblanco E-28049, Madrid, Spain
[4]Department of Physics, University of Muenster, Muenster, Germany
[5]Datassist Computing Service, Winters, CA 95694
[6]Quantar Technology Inc., Santa Cruz, CA 95060
[7]Department of Physics, Florida State University, Tallahassee, FL 32306
[8]School of Physics, Latrobe University, Bundoora, VIC 3083, Australia
[9]Advanced Light Source, Lawrence Berkeley National Laboratory, Berkeley, CA 94720
[10]Pennsylvania State University, University Park, PA 16802

INTRODUCTION

A next-generation experimental end station for surface and interface science studies has been developed with the aim of making full utilization of the capabilities of a third generation synchrotron radiation facility such as the Advanced Light Source. This system, the Advanced Photoelectron Spectrometer/[Diffractometer (APSD) [1], has initially been installed on one half of the rotating platform on the bending magnet beamline 9.3.2 [2] and is planned to be moved to the Elliptical Polarized Undulator (EPU) beamline 4.0.1 in the latter part of 1997. The first phase of the APSD system is completely commissioned and it has been routinely used by both the PRT and independent investigators since November, 1994 for numerous studies, as discussed in a number of other reports in this compendium [3-10]. The following is a brief description of the important characteristics of this experimental end station as it now stands, together with the various improvements and additions for enhancing its capabilities that are either underway or planned.

SYSTEM CHARACTERISTICS AND PERFORMANCE

In Fig. 1, we show a schematic view of the APSD. It has been configured for high-resolution, high-intensity photoelectron spectroscopy, diffraction, and holography measurements. Fig. 2 shows a photograph of the system, with major components labelled. The electron energy analyzer is a tuneable-resolution large-diameter hemispherical electrostatic system (Scienta ES200) [11] that has been incorporated into a main analysis chamber which can rotate over 60 degrees in the plane of the electron storage ring. This rotation is made possible by a large-diameter bellows linking the main chamber to the beamline, as shown in these figures. Such in-plane analyzer rotation, although common for much smaller analyzers mounted inside the vacuum system, has not been attempted before in such an *ex situ* mounting, and it here permits selectively probing the angular variation of the differential photoelectric cross section, keeping the photon-sample geometry fixed while measuring intensities over a large fraction of the 2π solid angle above the surface, and scanning the analyzer synchronously with the sample polar-angle motion so as to

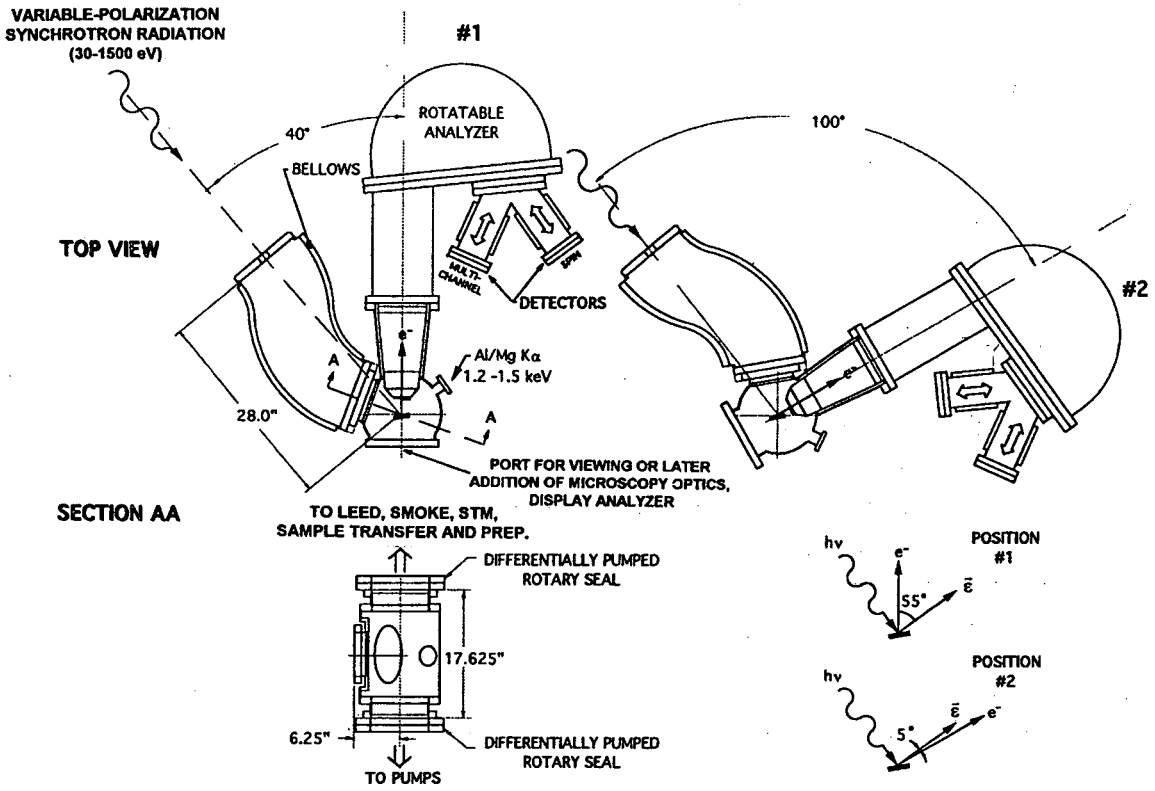

Figure 1. Schematic drawing of the Advanced Photoelectron Spectrometer/Diffractometer (APSD), with various components labelled. The rotation of the main chamber, including electron analyzer, and the range of photon-electron geometries possible are also indicated.

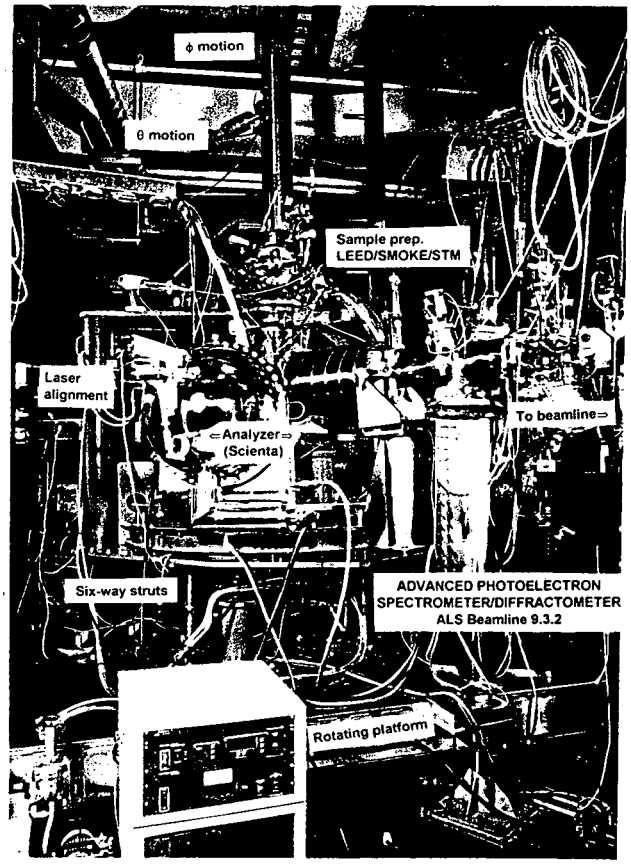

Figure 2. Photograph of the APSD system, with various components labelled.

keep the photoelectron escape process from the surface constant while varying the photon incidence geometry (e.g. while going into a condition of total reflection from the surface).

The spherical grating monochromator of beamline 9.3.2 [2] and the analyzer (operated with a typical 10:1 pre-retardation of the electrons in energy) [1] are together capable of operating at energy resolutions of $\Delta E/E_{kin} \sim 1:10^4$. This performance has been directly verified for our system, with linewidths as low as 3 meV being measured for an analyzer pass energy of 2 eV. The analyzer is also equipped with a demountable collimator at its entry to limit the solid angle of acceptance to ±1.5° for high angular resolution studies. This collimator also has the desirable effect of limiting the area of the sample seen by the analyzer, thus eliminating any emission from the adjacent parts of the sample holder that could affect quantitative analyses of surface compositions. The main chamber is also equipped with a standard AlKα/MgKα x-ray source that can be used for offline quantitative analysis and x-ray photoelectron diffraction measurements, and a low-energy electron flood gun for neutralizing charge in studies of insulating samples. Examples of data obtained with this system appear elsewhere [3-10].

The sample preparation and characterization chamber situated at the top of the system is separated from the main chamber by a gate valve. This chamber incorporates a variety of instrumentation: low energy electron diffraction (LEED) optics, an ion sputtering gun, Knudsen cells for metal deposition, a quartz crystal oscillator for monitoring growth, and a large-gap *in situ* electromagnet for magnetizing samples and carrying out surface magnetooptic Kerr effect (SMOKE) measurements. A high-precision long-travel sample goniometer with computer control of both polar and azimuthal motions and ~±0.3° accuracies in both motions translates samples between the two chambers and permits automated scanning of angle-resolved photoelectron spectra. This can accommodate up to eight samples on a carousel, with *in situ* transfer to the measurement position being possible via a wobble stick. The choice of different kinds of sample holders allows heating the sample with non-inductive resistive heating, resistive heating by direct-current passage through the sample, or electron-bombardment heating for highest temperatures up to 2300 K. A preliminary liquid nitrogen cooling system also permits lowering temperatures to ~ 200-220K.

ADDITIONAL IMPROVEMENTS IN PROGRESS

The analyzer is presently equipped with the standard Scienta multichannel detector that is only capable of an integrated count rate of ~100 kHz over its full counting area, or ~600-700 kHz when operated in a new "grey-scale" mode. These limits on count rate are often found to prevent taking full advantage of the photon flux as delivered by this bend-magnet beamline at the ALS, with these problems expected to be at least 10x worse in the future siting of this system on the EPU. Thus, it is desirable to replace the existing detector with a much higher speed multichannel detector that can operate at up to the GHz rate. A first version of this high-speed multichannel detector with 192 channels and projected to be capable of operating at about 200 MHz will be tested shortly; this has been developed in collaboration with Quantar Technology, Inc. A second more powerful version capable of operating in the GHz range is also under parallel development at LBNL. In addition, an alternative single-channel spin detector of the so-called microMott type has been fabricated and this is currently undergoing first tests and commissioning. The multichannel detector and the spin detector can also be interchanged *in situ* via a novel design utilizing a large differentially-pumped rotary seal, together with two sets of linear drives. This permits positioning either one of the two detectors at the detection plane of the Scienta analyzer

without breaking vacuum. This spin detector will be used, together with circular polarized excitation, in the study of magnetic materials, with some first results of this type being discussed elsewhere in this compendium [6,8,9]. Another important development underway is the replacement of the original data acquisition system and analysis package with a much more user friendly and rapidly responding software/hardware system, as needed for example for time-resolved studies of surface reaction kinetics [4].

Other characterization techniques including SMOKE and scanning tunneling microscopy (STM) are also ready to be added to the analysis and preparation chamber in the near future.

As a final very important improvement to this system during the current year, we will replace and/or modify the sample goniometer to include more efficient cryogenic cooling down to ~20K and higher angular accuracies of $\pm 0.1°$ or better, without sacrificing any of the aforementioned heating options.

REFERENCES

1. A preliminary account of this system appears in: C.S. Fadley, M.A. Van Hove, Z. Hussain, and A.P. Kaduwela, J. Elec. Spec. and Rel. Phen. **75**, 273 (1995).
2. Z. Hussain, W. R. A. Huff, S. A. Keller, E. J. Moller, P. A. Heimann, W. McKinney, H. A. Padmore, C. S. Fadley, and D. A. Shirley, J. Elec. Spec. and Rel. Phen. **80**, 401 (1996) and abstracts by E.J. Moler et al. and J. Kortright et al. elsewhere in this volume.
3. R.X. Ynzunza et al., abstract in this volume discussing the structure of clean W(110).
4. R.X. Ynzunza et al., abstract in this volume discussing the oxygen kinetics and the structure of oxygen on W(110).
5. S. Kellar et al., abstract in this volume discussing the structure of oxygen on W(110).
6. R.X. Ynzunza et al., abstract in this volume discussing circular dichroism in photoelectron emission from oxygen on W(110)
7. E.D. Tober et al., abstract in this volume discussing interface photoelectron diffraction for Fe/W(110) and Gd/W(110).
8. E.D. Tober et al., abstract in this volume discussing spin-polarized photoelectron diffraction for Gd(0001).
9. R. Denecke, J. Morais et al., abstract in this volume discussing magnetic circular dichroism in photoelectron emission from Gd(0001).
10. S. Thevuthasan, S.A. Chambers, et al., abstract in this volume discussing the structure of formate on TiO_2(110).
11. N. Mårtensson, P. Baltzer, P.A. Brühwiler, J.-O. Forsell, A. Nilsson, A. Stenborg, and B. Wannberg, J. Elec. Spec. and Rel. Phen. **70**, 117 (1994).

This work was supported by DOE, OER, BES, Mat. Sci. Div. (Contract DE-AC03-76SF00098), ONR (Contract N00014-94-1-0162), CNPq (Brazil), and DFG (Germany).

Principal investigator: C.S. Fadley, Materials Sciences Division, Lawrence Berkeley National Laboratory, Mailstop 2-100, Berkeley, CA 94720. Email: fadley@lbl.gov. Telephone: (510) 486 5774.

Beamline 9.3.2—A High-Resolution, Bend-Magnet Beamline with Circular Polarization Capability

E. J. Moler, Z. Hussain, M. R. Howells, S. A. Kellar, M. A. Rice, J. B. Kortright, R. X. Ynzunza, G. Andronaco, P. Heimann, W. McKinney, C. Cummings, T. Lauritzen, J. P. McKean, F. J. Palomares, H. Wu, Y. Zheng, A. T. Young, M. R. Howells, S. C. Irick, R. X. Ynzunza, H. Daimon, E. D. Tober, H. A. Padmore, C. S. Fadley, D. A. Shirley
Lawrence Berkeley National Laboratory, Berkeley, CA 94720

Beamline 9.3.2 is a high resolution, SGM beamline on an ALS bending magnet with access to photon energies from 30-1500 eV. Features include circular polarization capability, a rotating chamber platform that allows switching between experiments without breaking vacuum, an active feedback system that keeps the beam centered on the entrance slit of the monochromator, and a bendable refocusing mirror. Figure 1 shows a schematic of the beamline. The beamline optics consist of horizontally and vertically focussing mirrors, a Spherical Grating Monochromator (SGM) with movable entrance and exit slits, and a bendable refocussing mirror. In addition, a movable aperature has been installed just upstream of the vertically focussing mirror which can select the x-rays above or below the plane of the synchrotron storage ring, allowing the user to select circularly or linearly polarized light.

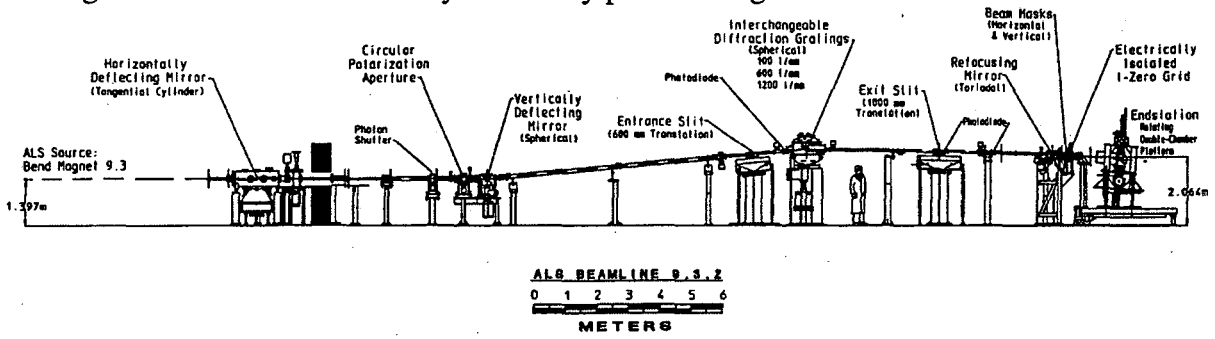

Figure 1. Schematic of Beamline 9.3.2 with Circular Polarization Aperature and Bendable Refocussing Mirror.

CIRCULAR POLARIZATION

Circularly polarized x-rays are used to study the magnetic properties of materials. Beamline 9.3.2 can supply left and right circularly polarized x-rays by a computer controlled aperture which may be placed above or below the plane of the synchrotron storage ring. The degree of linear and circular polarization has been measured and calibrated (see J. B. Kortright, et. a. in this compendium for details). The figure below shows the calculated and measured values for

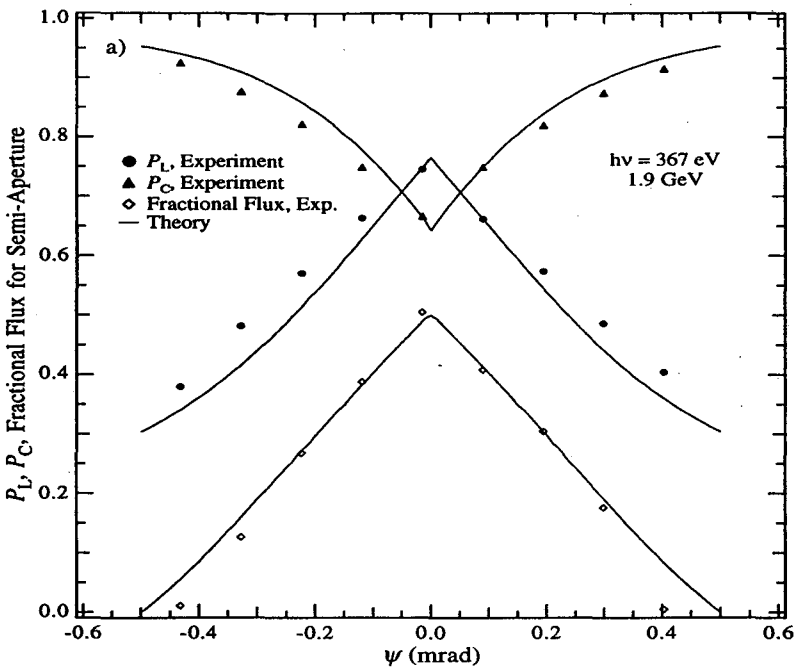

Figure 2. Measured and calculated flux for circularly polarized x-rays (see text)

the degree of linear (P_L) and circular (P_C) polarization and the fractional flux as the aperture was stepped across the vertical opening angle for 367 eV photon energy.

BENDABLE REFOCUSSING MIRROR

A bendable refocusing mirror was recently installed on Beamline 9.3.2. Preloaded micrometers allow precise and accurate control of all six degrees of freedom. A rotary vacuum feedthrough drives the in-vacuum bender via a flexible shaft. The mechanism allows bending of the mirror from infinity to an 80 meter focal length. The bend only changes the vertical focus. The horizontal focus is adjusted by tilting the mirror to vary the angle of incidence. Once the horizontal focus is set, the mirror is bent to bring the vertical focus to the same plane.

ACTIVE BEAM-POSITION FEEDBACK

The beamline is designed for high resolution work. Consequently, the entrance aperature of the monochromator is often used at >10 μm opening. Because of the 2:1 demagnification of the source, the image on the entrance slit is ~50 μm. These two characteristics lead to very tight tolerances on maintaining the positon of the beam at the entrance slit. Beam and mirror drift were found to be a significant hindrance to stable operation of the beamline. We solved that problem by introducing a feedback mechanism on the vertically deflecting M2 mirror that keeps the beam centered on the exit slit via a computer controlled loop. The figure below shows the resulting flux at the exit of the monochromator with and without the feedback control system operating.

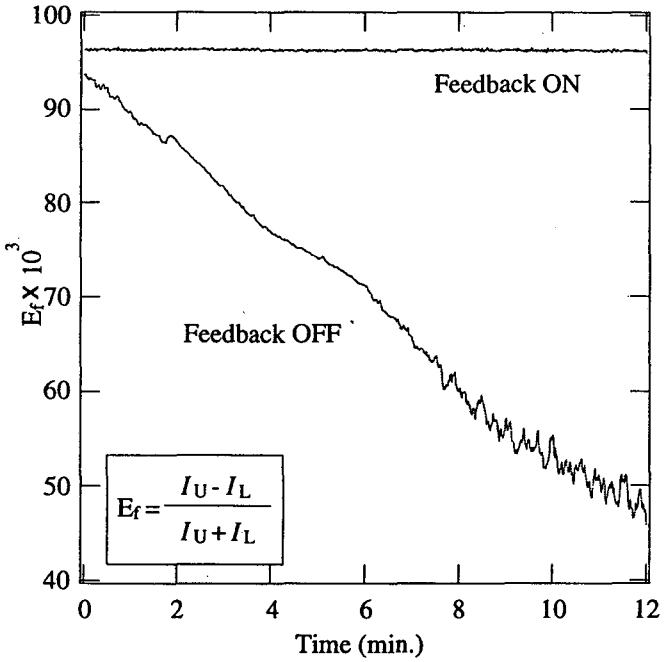

Figure 3. Error function vs. Time with and without feedback control of the M2 mirror pitch.

ELECTRON BEAM MOTION DIAGNOSTICS

The feedback system works well as a diagnostic tool for electron beam motion. We have been able to identify correlations between the synchrotron electron beam motions and environmental factors by monitoring the control voltage of the feedback loop. The figure below identifies the

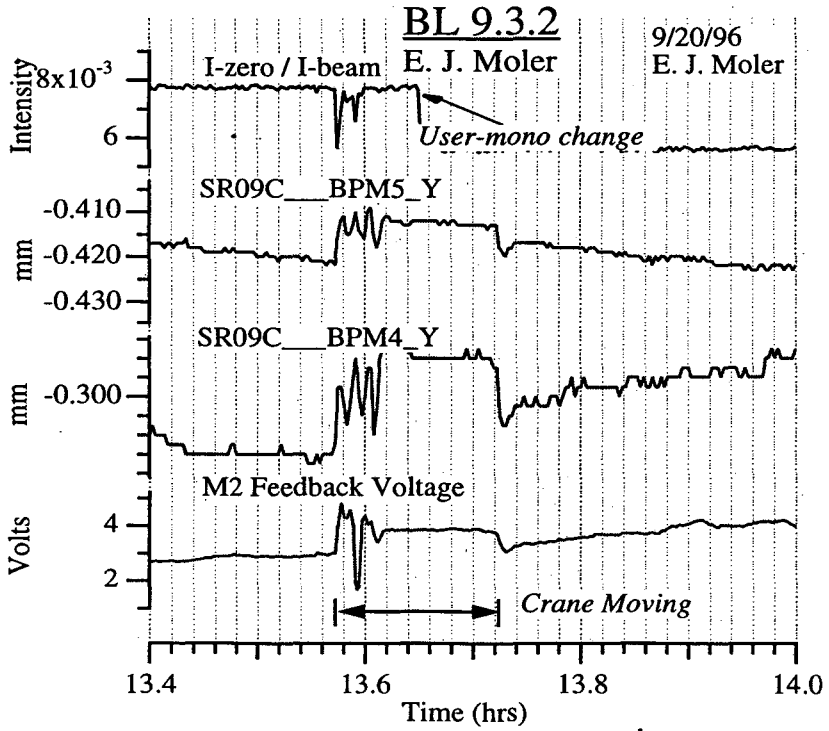

Figure 4. Flux, beam position from SR BPM's, and feedback-control-voltage vs. time during crane operation

cause of a beam motion as being from the crane which was operated during the time marked. Several other features that correlate x-ray flux changes with electron beam motions and their correction by the M2 feedback system have been identified.

REFERENCES

1 Z. Hussain, W.R.A. Huff, S.A. Kellar, E.J. Moler, P.A. Heimann, W. McKinney, H.A. Padmore, C.S. Fadley, and D.A. Shirley, "*High Resolution Soft X-Ray Bending Magnet Beamline 9.3.2 with Circularly Polarized Radiation Capability at the Advanced Light Source.*" (11th International Conference on Vacuum Ultraviolet Radiation Physics, Tokyo, Japan, 27 Aug.-1 Sept. 1995), Journal of Electron Spectroscopy and Related Phenomena, May 1996, vol.80:401-4.

2 Z. Hussain, W.R.A. Huff, S.A. Kellar, E.J. Moler, P.A. Heimann, W. McKinney, C. Cummings, T. Lauritzen, J.P. McKean, F.J. Palomares, H. Wu, Y. Zheng, A.T. Young, H.A. Padmore, C.S. Fadley, and D.A. Shirley, "*High Resolution Beamline 9.3.2 in the Energy Range 30-1500 eV at the Advanced Light Source; Design and Performance,*" Rev. Sci. Instrum. 67(9),1996, SR95 CD-ROM Proceedings.

3 J. Kortright, M.A. Rice, Z. Hussain, H.A. Padmore, A.T. Young, A. Adamson, W.R.A. Huff, E.J. Moler, S.A. Kellar, R.X. Ynzunza, F.J. Palomares, H. Diamon, E.D. Tober, and C.S. Fadley, "*Polarization Measurement and Vertical Aperture Optimization for Obtaining Circularly Polarized Bend-Magnet Radiation.*" Rev. Sci. Instrum. 67(9), 1996, SRI95 CD-ROM Proceedings.

4 Z. Hussain, W. R. A. Huff, S. A. Kellar, E. J. Moler, P. A. Heimann, W. McKinney, M. R. Howells, J. B. Kortright, M. A. Rice, C. Cummings, T. Lauritzen, J. P. McKean, S. C. Irick, F. J. Palomares, R. X. Ynzunza, Z. Wang, G. Andronaco, N. Hartman, E. D. Tober, H. Wu, Y. Zheng, A. Adamson, A. T. Young, H. Daimon, H. A. Padmore, C. S. Fadley, D. A. Shirley, *"High-Resolution Soft X-Ray (hv= 30-1500 eV) Bending Magnet Beamline 9.3.2 with Circularly Polarized Radiation Capability at the Advanced Light Source: Design, Performance, and Operation,"* LSBL-336 (June 1996).

5 Z. Hussain, T. Huff, E. Moler, S. Kellar, Pat McKean, and H. Wu, "*Characterization of BL 9.3.2: I. The Spherical Vertical Focusing Mirror M2 and the ALS Bending Magnet Source Size.*" Lawrence Berkeley National Laboratory, LSBL -217 (September 1994).

This work was supported by the Director, Office of Energy Research, Office of Basic Energy Sciences, Materials Sciences Division, of the U.S. Department of Energy under Contract No. DE-AC03-76SF00098.

Principal investigator: Charles S. Fadley, Advanced Light Source, Ernest Orlando Lawrence Berkeley National Laboratory. Email: fadley@lbl.gov. Telephone: 510-486-5774.

Design and Performance of a Soft-X-Ray Interferometer for Ultra-High-Resolution Fourier Transform Spectroscopy

E.J. Moler, Z. Hussain, R.M. Duarte, M. R. Howells
Lawrence Berkeley National Laboratory, Berkeley, CA 94720

A Fourier Transform Soft X-ray spectrometer (FT-SX) has been designed and is under construction for the Advanced Light Source (ALS) at Lawrence Berkeley National Laboratory as a branch of beamline 9.3.2. The spectrometer is a novel soft x-ray interferometer designed for ultra-high resolution (theoretical resolving power E/ΔE~106) spectroscopy in the photon energy region of 60-120 eV. This instrument is expected to provide experimental results which sensitively test models of correlated electron processes in atomic and molecular physics. The design criteria and consequent technical challenges posed by the short wavelengths of x-rays and desired resolving power are discussed. The fundamental and practical aspects of soft x-ray interferometry are also explored.

1. INTRODUCTION AND SCIENTIFIC MOTIVATION

Correlated electron motion is at the center of any chemical process and thus constitutes a very important arena of basic scientific research. The many-body nature of the problem precludes analytical solutions leaving only approximations to the quantum problem potentially tractable. The central problem in theoretical electron correlation studies is to find the appropriate approximations that describe all of the main characteristics of the experimentally observed features of such systems. It is natural to start with excitations of the helium atom since this is the simplest correlated electron system and, with the availability of synchrotron radiation sources, increasingly detailed experimental observations have become available. The FT-SX spectrometer has been designed to probe this prototypical system with unprecedented resolving power. Of particular interest are the regions of overlapping double excitation series where classically chaotic behavior is mixed with quantization effects [1].

2. SYNCHROTRON RADIATION AND RESOLUTION LIMITS OF STANDARD SOFT X-RAY MONOCHROMATORS

Synchrotron radiation has proved to be an extremely useful tools in basic atomic and molecular physics studies. The high photon flux and tunable photon energy enables detailed studies of excitation processes which are considerably challenging to the theoretical physics community. Third generation light sources, such as the Advanced Light Source (ALS) at Lawrence Berkeley National Laboratory, coupled with high resolution beam lines are providing extremely detailed observations of scientifically important systems such as the helium double excitation series, a correlated electron system, in the soft x-ray range. However, there is more to be gained with increased resolving power in x-ray absorption experiments.

The highest resolving power soft x-ray beam lines available consist of a low emittance synchrotron source and a highly optimised, grating based monochromator, usually a Spherical Grating Monochromator (SGM). The low emittance source allows for relatively high photon flux while using the small aperatures necessary to operate the SGM at maximum resolving power. While the claim of experimentally achieved resolving power can vary depending on the interpretation of the data and caution of the investigators, it is apparent that the theoretically maximum resolving power of a spherical grating monochromator [2], (E/ΔE≈50,000) has been closely approached by Kaindle, et al. in the region of the helium double excitations (~ 65 eV)[2].

3. SOFT X-RAY INTERFEROMETRY AND ESSENTIALS OF FOURIER TRANSFORM SPECTROMETRY

To achieve a higher resolving power, a different approach must be used other than the "traditional" grating based monochromator. It has been known in optics for a long time that interferometers can

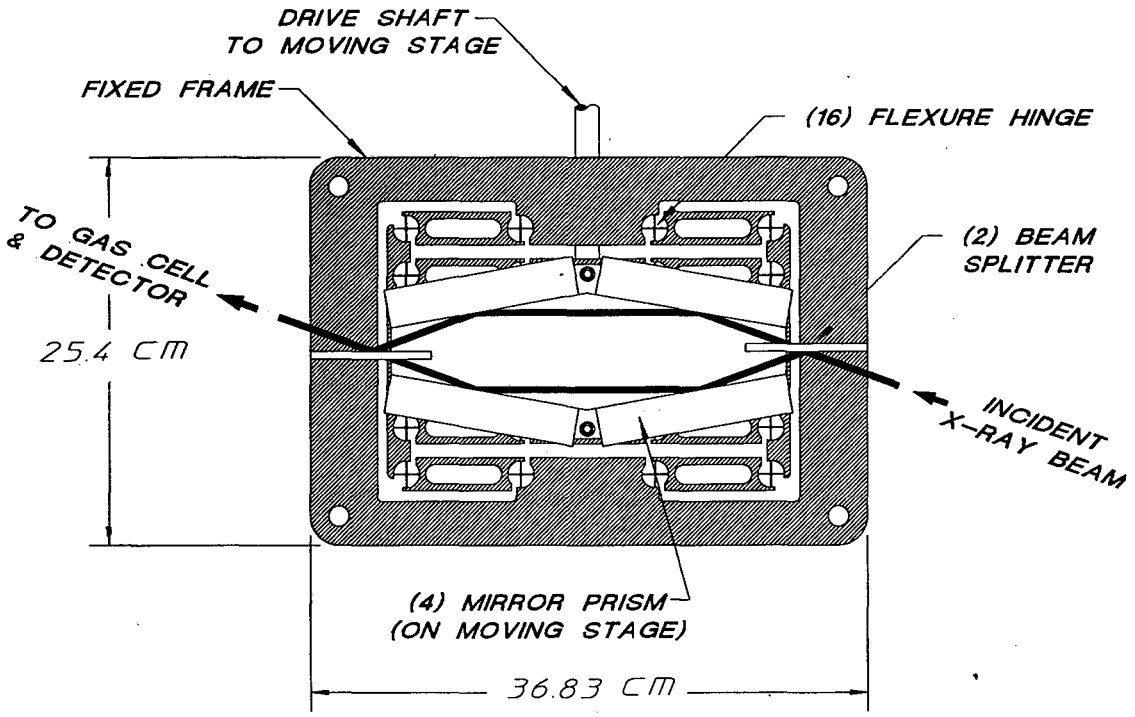

Figure 1. Schematic of Soft X-ray Interferometer.

always, in principle, outperform gratings in terms of maximum resolving power or phase space acceptance for equivalent resolving power[3]. In practice, interferometry with x-rays is very difficult due to the short wavelengths. It is only recently that the mechanical, optical, and metrological technology have advanced enough to practically build a soft x-ray interferometer for Fourier transform spectrometry.

The basic operation of a Fourier transform spectrometer is to split an incident beam into two parts and recombine them coherently after introducing a phase delay. The Fourier transform of the resulting interference pattern, as a function of phase delay or path-length difference, gives the energy spectrum of the incident beam. The Michelson interferometer, which is widely used in infra-red spectroscopy, is the most common example of such an instrument. The path-length-difference is introduced by moving one or more mirrors to vary the geometric distance between the beam splitter(s) and the detector. The key components of any interferometer are the beam splitters, which usually determine the optical aperature and operating range of an interferometer, and the mirror translation stage, which determine the maximum resolution of the instrument.

The resolution of any optical spectrometer depends on the maximum path length difference introduced between the various parts of the beam. More precisely,

$$\delta\nu = \frac{1}{2\Delta L}$$

where ΔL is the maximum path-length-difference introduced and $\delta\nu$ is the maximum resolution in wavenumber. If one can maintain the alignment of the mirrors to ensure proper overlap of the beams at the detector, the resolution of an interferometer can be arbitrarily small by simply increasing ΔL. A grating, on the other hand, has a limit to the

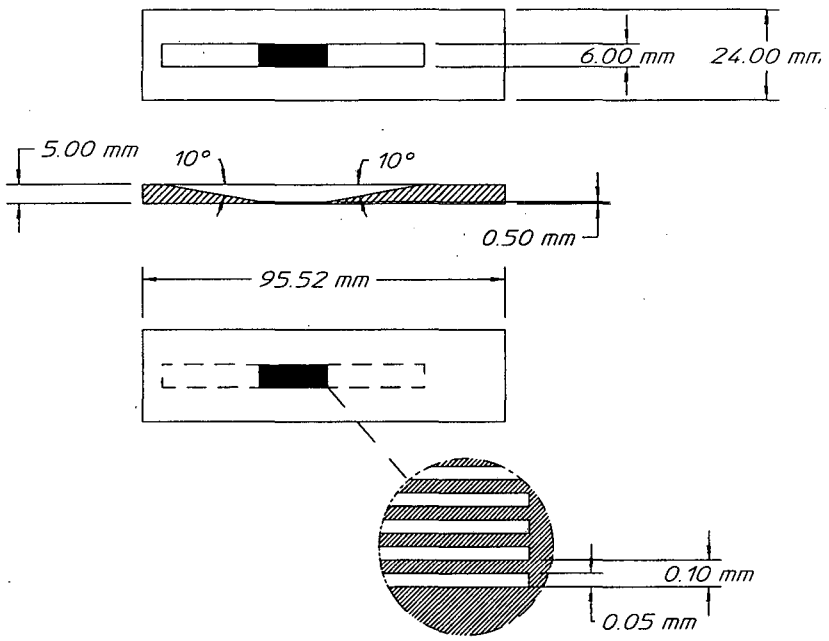

Figure 2. Silicon Beam Splitter

maximum path-length-difference which it can accomodate.

4. OVERVIEW OF FT-SX BRANCHLINE

The FT-SX spectrometer is a modified Mach-Zehnder type interferometer designed to operate in the 60-120 eV photon energy range (wavelength 10-20 nm) with a theoretical resolution of ~65 μeV.It is a permanent end-station branch of beamline 9.3.2 at the ALS. The synchrotron radiation is first pre-filtered by the SGM monochromator, operated in a moderate resolution mode with a 100 l/mm grating, to improve the signal/noise ratio of the absorption spectrum measured by the interferometer. The x-rays are then deflected by a simple plane mirror downstream of the monochromator exit slit then pass through the FT-SX spectrometer and a conventional gas ionization cell and impinge on a solid state detector. The entire interferometer is mounted in a high-vacuum chamber separated from the UHV beamline by a thin foil window. The vacuum vessel is mounted on an optical table to damp vibration. The moving mirror stage is driven by a double action, hydraulic piston which is external to the vacuum vessel. The mirror position in the interferometer is measured with a commercially available HEWLITT-PACKARD heterodyne laser interferometer with a resolution of 3 Å and an actual rms noise of 4.5 Å. Both the piston drive and the laser interferometer are mounted on the optical table. The heart of the spectrometer is a flexture-hinged linear motion stage upon which is mounted four mirrors permanently aligned by optical contacting to a custom, high precision prism.

5. SOME TECHNICAL CHALLENGES AND SOLUTIONS

A detailed discussion of the design and specification considerations for a soft x-ray interferometer is beyond the scope of this paper. Here we present just a few of the key features of the FT-SX spectrometer.

BEAM SPLITTERS

Beam splitters for soft x-rays are not readily available. We have chosen to use a wavefront dividing beamsplitter which is essentially an x-ray quality mirror with slots. The difficulty in fabricating such a device is to maintain a tolerable slope error on the reflecting parts (flatness <1 μrad

and surface roughness ~3 Å rms) while creating slots which are small enough to allow coherent splitting of the incident x-ray beam. Additionally, the thin "bars" of mirror left between the slots must have an optical coating to achieve reasonable reflectivity. Based on the coherence properties of the incident x-ray beam we determined a slot width of 50 μm and a period of 100 μm was sufficient to split the x-ray beam coherently. The scheme developed to fabricate the beam splitters is as follows:

a) a single crystal Si wafer is polished to an x-ray quality finish with a specific orientation relative to the (110) crystal plane.

b) the back side of the wafer is ultrasonically machined to thin the center of the wafer where the slots will be and to cutout chamfers to allow the grazing incident x-rays to pass through the slots.

c) the wafer is masked and the slots are chemically etched with an etchant that preferentially cuts along the [110] direction.

d) the optical coating is applied in a manner to maintain a stress free thin film. For the ALS spectrometer we have selected molybdenum.

The beam splitters have been successfully fabricated by Rockwell Power Systems Division of Rockwell International.

THE MECHANICAL MIRROR STAGE

The mirror stage must allow enough motion to introduce the desired path-length-difference between the two halves of the x-ray beams and must maintain an angular alignment which ensures coherent recombination of the two beams at the detector. For the FT-SX spectrometer the total range of motion is ~ 1 cm and the angular tolerance is ±0.1 arc-seconds across the entire range. We have achieved this by using "cartwheel" type flexural hinges (see fig. 1) which were wire-EDM cut from a monolithic maraging steel slab.

6. CONCLUSION

An FT-SX spectrometer is currently under construction at the Advanced Light Source at Lawrence Berkeley National Laboratory. The technical challenges posed by the short wavelength of the x-rays and the desired, ultra-high resolving power have been met using state-of-the-art mechanical, optical, and metrological technology. We believe this general scheme may be adapted to other uses such as high throughput and high resolving power x-ray flourescence spectrometers.

ACKNOWLEDGEMENTS

We wish to thank the ALS designers, engineers, and technicians. This work was supported by U.S. DOE contract number DE-AC03-76SF00098.

REFERENCES

[1]M. Domke, C. Xue, A. Puschman, T. Mandel, E. Hudson, D. A. Shirley, G. Kaindl, C. H. Greene, and G. R. Sadeghpour, "Extensive Double-Excitation States in Atomic Helium," Physical Reveiw Letters **66**, 3441-3443 (1991).

[2]G. Kaindl, "Ultra-High Resolution Spectroscopy of the He Double Excited States," presented at the Oji International Seminar on Atomic and Molecular Photoionization, Tsukuba, Japan, 1995 (unpublished).

[3]J. Chamberlain, *The Principles of Interferometric Spectroscopy* (John Wiley and Sons, Chichester, 1979).

Principal Investigator: David A. Shirley.

This work funded by Director, Office of Energy Research, Office of Basic Energy Sciences, Materials Science Division, of United States Department of Energy under contract No. DE-AC03-76SF00098.

Diffraction Patterns of the Beam Splitters Used in a Soft-X-Ray Interferometer with He-Ne Laser

C.H. Oh,[1,2] D.U. Choi, S.J. Park,[1] S.S. Suk,[1] M.R. Howells,[2]
Z. Hussain,[2] E.J. Moler,[2] and J. Spring[2]

[1]Kyungpook National University, Taegu, 702-701, Korea
[2]Advanced Light Source, Ernest Orlando Lawrence Berkeley National Laboratory,
UC Berkeley, California 97420.USA

Two 50% reflection-50% transmission-grating beam splitter(B.S.) are being used in the soft x-ray interferometry[1,2] at Beamline 9.3.2 of ALS. They are consisted of a rigid flat mirror with a series of slots width 50 ㎛ etched in part(5×18 ㎟) of the area.

The diffraction patterns of the first B.S. and both B.S.s were investigated with He-Ne laser in both cases of normal incident and 20° grazing incident to the B.S.[Fig. 1]. The intensities of each diffraction patterns were measured with a radiation power meter(ORIEL 70260, 70261)

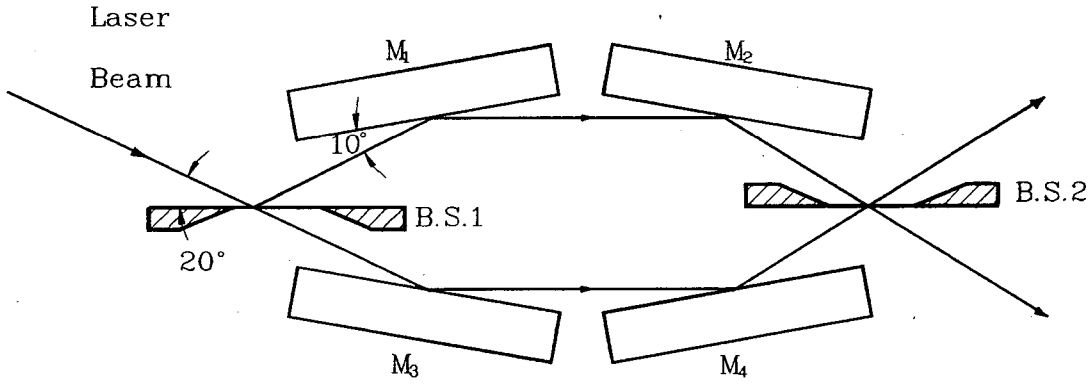

Figure 1. Optical path of the interferometer

The normal incident pattern is straight line and shows nearly same intervals, and the intensities of them are similiar to that of the double slits with Fraunhofer diffraction theory. The diffraction patterns of grazing incident[3] show a circle spot line. The transmitted patterns and reflected patterns show a symmetric arc on a long distance screen, whose radii are same and confirm a modified diffraction equation[Fig. 2].

The intensities of all the fringes of the B.S. also follows to the Fraunhofer diffraction theory. Patterns of the grating were affected strongly by the single slit effect. It was observed that only 3 fringes of each pattern were illuminated on the 2nd beam splitter. For the soft x-ray(λ =10 ㎚), the number of fringes illuminating on the 2nd B.S. was calculated from the results of He-Ne laser beam(λ =632.8 ㎚) experiment, and showed x=0.0314 ㎜(fringe interval), n=±95.5(number of order) and therefore the total number was 191 fringes.

The patterns produced by the 2nd beam splitter were also investigated in intensities and positions of them. Both patterns of upper beam and lower beam are same direction and same radii of circle[Fig. 3]. It was found that each fringe was consisted of fine fringes which was caused by two fringe beams that was arrived at the 2nd beam splitter.

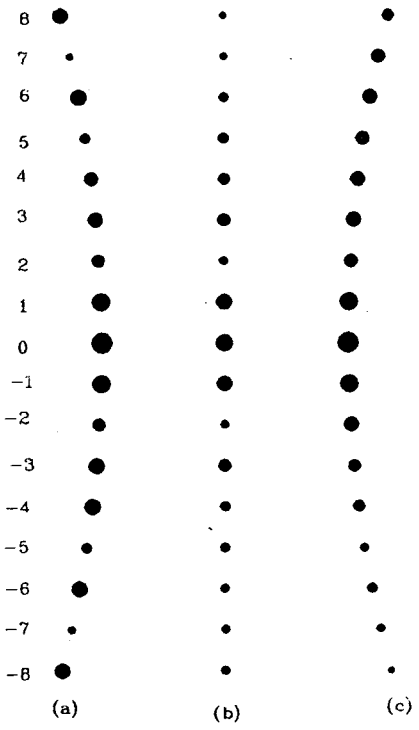

Figure 2. Diffraction pattern of B.S.
(a) transmitted
(b) normal
(c) reflected

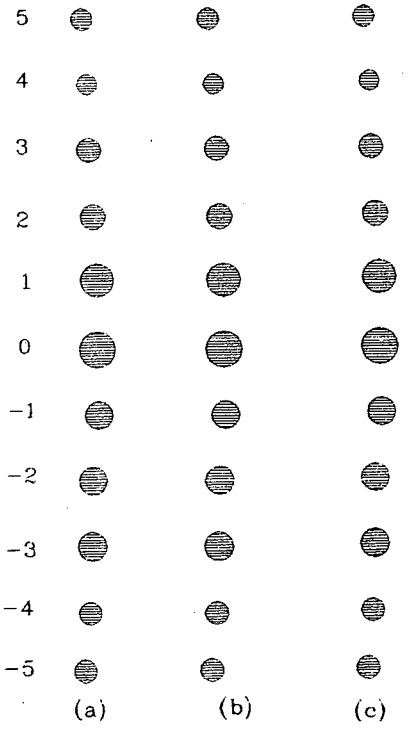

Figure 3. Diffraction fringes through the interferometer
(a) transmitted beam
(b) interferometer beam(a+c)
(c) reflected beam

References

1. E.J. Moller, Ph. D. Design and Characterization of High Resolution Fourier Transform Soft x-ray spectrometer for sychroton radiation(Lawrence Berkeley Laboratory, University of Califonia, Berkeley,1995)
2. M.R. Howells, K, Frank, Z. Hussain, E.J. Moler, T. Reich, D. Moller, and D.A. Shirey, Toward a soft x-ray Fourier-Transform spectrometer, Nuclear Instruments and Methods in Physics Research A 347, 182-191(1994).
3. Webster Cash, Applied Optics 21, 710(1982).

This work was supported by the Director, Office of Energy Research, Office of Basic Energy Sciences, Materials Science Division, of the U.S. Department of Energy under Contract No. DE-AC03-76SF00098; and by Kyungpook National University, Korea.

Principal investigators: Malcolm Howells, Advanced Light Source, Ernest Orlando Lawrence Berkeley National Laboratory (Email mrhowells@lbl.gov, Telephone 510-486-4949); Zahid Hussain, Advanced Light Source, Ernest Orlando Lawrence Berkeley National Laboratory (Email zhussain@lbl.gov, Telephone 510-486-7591).

Polarization Measurement and Vertical Aperture Optimization for Obtaining Circularly Polarized Bend-Magnet Radiation

J.B. Kortright,[1] M. Rice,[1] Z. Hussain,[2] H.A. Padmore,[2] A. Adamson,[2] W.R.A. Huff,[3] A.T. Young,[2] E.J. Moler,[3] S.A. Kellar,[3] R.X.Ynzunza,[4,5] F.J. Palomares,[4] H. Daimon,[6] E.D. Tober,[2,5] C.S. Fadley[4,5]

[1]*Center for X-Ray Optics,* [2]*Advanced Light Source,* [3]*Chemical Sciences Division,*
[4]*Materials Sciences Division, Lawrence Berkeley National Laboratory, Berkeley, CA 94720*
[5]*Physics Department, Univerisity of California-Davis, Davis, CA 95616*
[6]*Department of Material Physics, Osaka University, Osaka, Japan*

INTRODUCTION

Growing interest in utilizing circular polarization prompted the design of bend-magnet beamline 9.3.2 at the Advanced Light Source, covering the 30-1500 eV spectral region, to include vertical aperturing capabilities for optimizing the collection of circular polarization above and below the orbit plane.[1] After commissioning and early use of the beamline, a multilayer polarimeter[2] was used to characterize the polarization state of the beam as a function of vertical aperture position. This report partially summarizes the polarimetry measurements and compares results with theoretical calculations intended to simulate experimental conditions. A more complete discussion can be found in ref. 3.

EXPERIMENT

ALS bend-magnet beamline 9.3.2 was designed to collect out-of-plane circular polarization using variable apertures upstream of the first vertically deflecting optical element. A narrow (0.037 mrad) vertical aperture is much smaller than the vertical beam width. Two wide apertures (1.9 mrad) can pass the entire beam when centered vertically, and can block the beam from above or below to define an arbitrary vertical aperture. All apertures are precisely positioned by computer. Both the narrow and wide apertures were systematically stepped across the beam and the polarimeter was used to determine the degrees of linear and circular polarization as a function of vertical aperture position.

The polarimeter uses linear polarizers based on multilayer interference structures with Bragg peaks at the 45° Brewster angle.[2] The polarimeter is capable of translating a laterally graded multilayer to form a continuously tunable polarizer for spectroscopic measurements. In these measurements we utilized three separate uniform multilayers which could be translated in vacuum to measure the polarization at three widely separated energies. These multilayers were designed to operate at 97 eV (Mo/Si multilayer), 367 eV (W/B_4C), and 722 eV (W/B_4C). Using a 12 Å period W/B_4C multilayer, these were the first direct polarization measurements of bend magnet radiation at energies above 700 eV. The polarimeter can house a transmission multilayer phase retarder[4] which can experimentally distinguish between unpolarized and circularly polarized radiation. A phase retarder was not used in this case, and we have learned that the amount of unpolarized radiation is smaller than the uncertainty in our measurements.

RESULTS

Polarization was measured as the narrow and wide vertical apertures were systematically stepped through the beam's vertical opening angle ψ. Measurements were made after a systematic alignment of the beamlines optical components, which effectively centered them on the vertical center of the beam. Only results from the highest energy studied are reported here.

The intensity reflected from the polarizer as a function of azimuthal angle α is given by

$$I(\alpha) = S_0(R_S + R_P)/2 + 0.5(R_S - R_P)[S_1\cos 2\alpha + S_2 \sin 2\alpha]$$

where R_S and R_P are reflectivities of s- and p-component radiation from the polarizer, and S_0, S_1 and S_2 are the first three of four Stokes parameters that define the intensity and polarization state of the beam. Thus we measure directly the degree of linear polarization, $P_L = (S_1^2 + S_2^2)^{1/2}/S_0$. Circular polarization is represented by the fourth Stokes parameter, S_3, and the degree of circular polarization $P_C = S_3/S_0$. P_C is determined from $P_L^2 + P_C^2 \leq 1$, with the equality holding in the case of no unpolarized radiation.

Figure 1 shows results at 722 eV of scanning the narrow vertical aperture through the beam. Symbols are experimental values and lines are theoretical values from calculations that include effects of non-zero slit width and the finite length of optical elements. The degree of linear polarization is in good agreement with theory over the entire vertical opening angle. In particular, the agreement of measurement with theory near $\psi = 0$ is within measurement error and indicates that the degree of linear polarization (0.999) is essentially complete. We measure no unpolarized radiation near $\psi = 0$, and we assert that there is little reason to expect an increase in any unpolarized component away from $\psi = 0$. Thus we conclude that any unpolarized radiation present is at or below our detection limit, and we use the equality above to determine the degree of circular polarization. The P_C values measured and calculated show good agreement. Similarly good agreement was obtained at the lower photon energies.

Figure 1. Measured and calculated degrees of linear (P_L) and circular (P_C) polarization transmitted through a 0.037 mrad vertical aperture as it is scanned vertically through the vertical fan of bend magnet radiation.

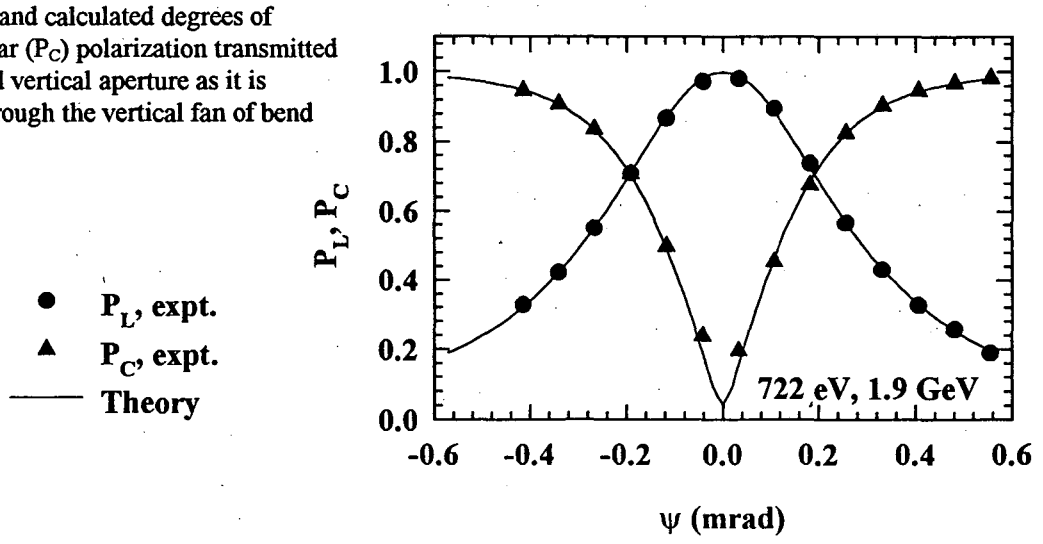

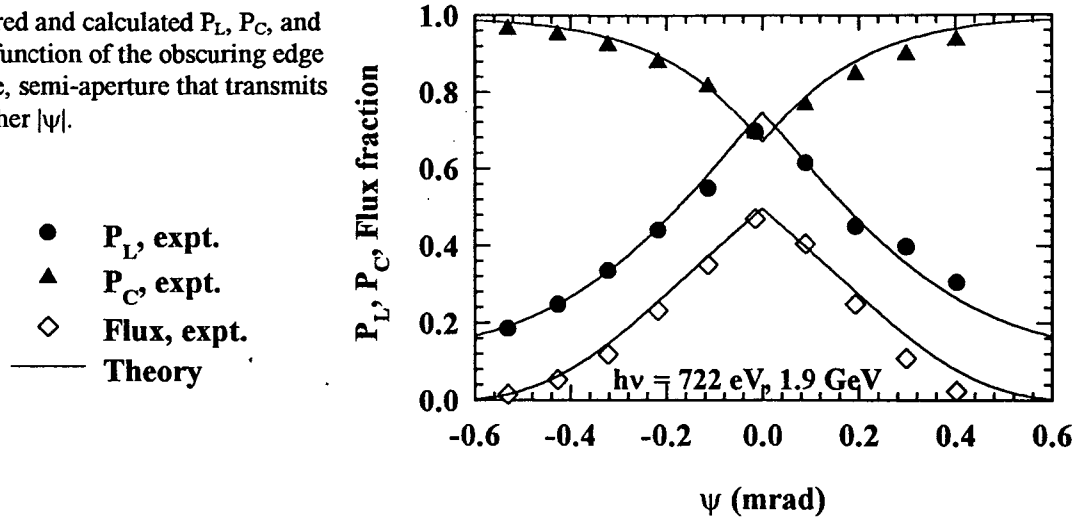

Figure 2. Measured and calculated P_L, P_C, and relative flux as a function of the obscuring edge position of a wide, semi-aperture that transmits all photons to higher $|\psi|$.

Figure 2 shows polarization and flux results at 722 eV as the wide aperture is scanned through the beam. For positive ψ values this semi-aperture obscures the beam from below, while for negative ψ values the semi-aperture obscures the beam from above. Symbols are experimental values. Lines are calculated theoretical values. The agreement between measurement and theory is reasonably good, although somewhat less good than was the case with the narrow vertical aperture. This is because the measurements with the wide, semi-aperture are more difficult to simulate accurately in the calculation because of the uncertain transmission of out-of-plane radiation with increasing $|\psi|$. Reduced transmission at larger $|\psi|$ would result in reduced circular polarization and increased linear polarization, as is observed. The flux fraction is that fraction of flux transmitted through the semi-aperture compared to the flux transmitted with the aperture removed. Evidently the beamline transmission a large positive ψ was somewhat reduced, consistent with the above interpretation. With the semi-aperture removed to transmit the entire beam, measured values of the degree of linear and circular polarization equal those measured with the aperture edge at $\psi = 0$, confirming that the radiation of opposite helicity from above and below the orbit plane shows no coherence, as expected.

The semi-aperture data allow us to investigate and optimize a generalized figure of merit of interest in experiments utilizing circular polarization. For photon-limited measurements a figure of merit often used is $P_C \cdot I^{1/2}$, where I is the intensity in the incident beam. Here we substitute the fractional flux passing through the semi-aperture for I to investigate this figure of merit as the aperture position is varied. Measured and calculated quantities are in Figure 3, and both have the same general shape. A shallow minimum at $\psi = 0$ is predicted but does not appear to be observed experimentally. Out-of-plane effects mentioned above cause the measured figure of merit to fall more rapidly with ψ than predicted. The figure of merit is optimized with the semi-aperture at or just beyond $\psi = 0$. Thus experiments using left or right circular polarization are best illuminated with only roughly a factor of 2 loss in total intensity, assuming this figure of merit overrides other experimental considerations. For many experiments, a high value of P_C may be more important than this figure of merit, in which case a more extreme out-of-plane aperture may be selected.

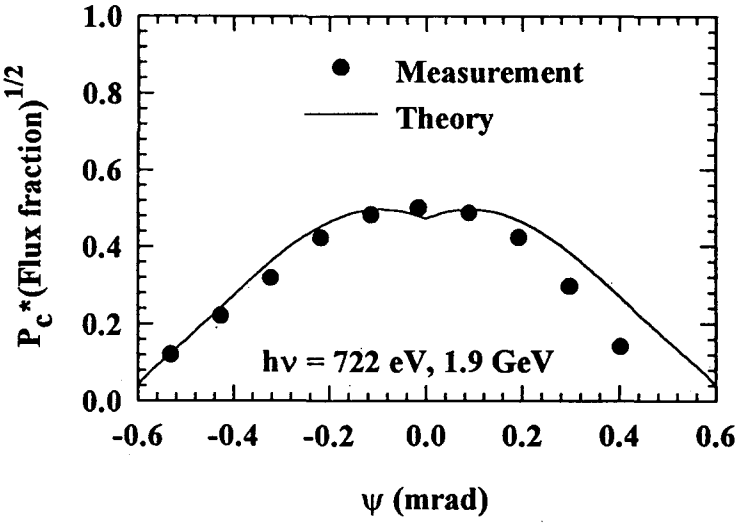

Figure 3. Measured and calculated values of a figure of merit given by the square root of the flux fraction times the degree of circular polarization as the wide, semi-aperture is stepped across the vertical opening angle at 722 eV.

CONCLUSIONS

Multilayer linear polarizers enable the direct measurement of polarization in a range from roughly 50 to at least 1000 eV spanning the EUV and soft x-ray. Even with low reflectivities at the higher photon energies, intense synchrotron beams are easily measured. The degrees of linear and circular polarization measured with the well-defined, narrow vertical aperture are in very good agreement with theoretical predictions. Any unpolarized radiation that may be present has intensity smaller than our experimental uncertainty. Further work is necessary to quantify any small residual unpolarized component. Thus, careful vertical aperturing and well aligned optics produce beams whose polarization is measured to be quite close to theoretical predictions. Conversely, users of bend-magnet radiation without careful alignment, aperturing and polarimetry are likely to be using beams of unknown polarization state. To obtain a beam with $P_L \cong 1$, a narrow slit on axis must be used. The figure of merit given by $P_C * I^{1/2}$ is maximized with the semi-aperture edge on the orbit plane, so that only half of the total available flux is lost in optimizing this figure of merit.

REFERENCES

1. Z. Hussain, W.R.A. Huff, S.A. Kellar, E.J. Moller, P.A. Heimann, W. McKinney, C. Cummings, T. Lauritzen, J.P. McKean, F.J. Palomares, H. Wu, Y. Zheng, A.T. Young, H.A. Padmore, C.S. Fadley, and D.A. Shirley, Rev. Sci. Instrum. **67(9)** (1996), SRI'95 CDROM Proceedings.
2. J.B. Kortright, M. Rice, and K.D. Franck, Rev. Sci. Instrum. **66**, 1567 (1995).
3. J.B. Kortright, M. Rice, Z. Hussain, H.A. Padmore, A. Adamson, W.R.A. Huff, A.T. Young, E.J. Moler, S.A. Kellar, R.X.Ynzunza, F.J. Palomares, H. Daimon, E.D. Tober, C.S. Fadley, Rev. Sci. Instrum. **67(9)** (1996), SRI'95 CDROM Proceedings.
4. J.B. Kortright, H. Kimura, V. Nikitin, K. Mayama, M. Yamamoto, and M. Yanagihara, Appl. Phys. Lett. **60**, 2963 (1992).

This research was supported by the Director, Office of Energy Research, Office of Basic Energy Sciences, Materials Science Division of the U.S. Department of Energy under Contract No DE-AC03-76SF00098.

Principal investigator: Jeffrey Kortright, Materials Sciences Division, Lawrence Berkeley National Laboratory
E-mail: JBKortright@lbl.gov. Telephone: (510) 486-5960.

Adsorption Site and Structure Determination of c(2x2) N_2/Ni(100) Using Angle-Resolved Photoemission Extended Fine Structure

Edward J. Moler[1], Scot A. Kellar[1], W. R. A. Huff[1],
Zahid Hussain[1], Yu Zheng[2], Eric A. Hudson[3], Yufeng Chen[4], David A. Shirley[4]

[1]Advanced Light Source, Lawrence Berkeley National Laboratory, Berkeley, CA 94720
[2]Qualop Systems Corp., 568 Weddell Drive, Suite 8, Sunnyvale, CA 94089
[3]Lawrence Livermore National Laboratory, Livermore, CA 94551
[4]Departments of Chemistry and Physics, The Pennsylvania State University, University Park, PA 16802

We have determined the atomic spatial structure of c(2x2) N2/Ni(100) with Angle-Resolved Photoemission Extended Fine Structure (ARPEFS) from the nitrogen 1s core level using monochromatized x-rays from beamline 6.1 at SSRL and beamline 9.3.2 at the ALS. The chemically shifted N 1s peak intensities were summed together to obtain ARPEFS curves for both nitrogen atoms in the molecule. We used a new, highly-optimized program based on the Rehr-Albers scattering matrix formalism to find the adsorption site and to quantitatively determine the bond-lengths. The nitrogen molecule stands upright at an atop site, with a N-Ni bond length of 2.25(1) Å, a N-N bond length of 1.10(7) Å, and a first layer Ni-Ni spacing of 1.76(4) Å. The shake-up peak shows an identical ARPEFS diffraction pattern, confirming its intrinsic nature and supporting a previous use of this feature to decompose the peak into contributions from the chemically inequivalent nitrogen atoms. Comparison to a previously published theoretical treatment of N-N-Ni and experimental structures of analogous adsorbate systems demonstrates the importance of adsorbate-adsorbate interactions in weakly chemisorbed systems.

INTRODUCTION

Angle-Resolved Photoemission Extended Fine Structure (ARPEFS) is a well established technique for determining the spatial structure of atomic and molecular adsorbates on metal surfaces[1-3]. We have used ARPEFS to determine the adsorption site and bond lengths of c(2x2) molecular nitrogen on Ni(100). Nilsson and Mårtensson found two sharp peaks in the photoemission spectrum of the N 1s core-level corresponding to the two chemically inequivalent nitrogen atoms in the molecular adsorbate[4]. They also investigated the broad satellite peak 6 eV below the main peaks and concluded that it was a shake-up peak associated with final-state molecular excitations. Their analysis of the shake-up satellite was based on the implicit assumption that the satellite peak showed identical scattering characteristics to the main peak. This assumption has not been previously established.

SURFACE STRUCTURE DETERMINATION

The photoemission intensities were extracted from the XPS spectra in the standard method[1]. We have performed full Multiple Scattering Spherical Wave (MSSW) calculations using the formalism of Rehr and Albers[5] to determine the best match of adsorption site and bond lengths to the experimental ARPEFS χ-curve. The program, developed entirely within our group, is highly optimized for obtaining a best fit to experimental data including multiple emitters[6]. We used second order matrices (6x6) and up to 8th order scattering, which produce a convergent calculation at these energies and inter-atomic distances. The best fit was defined by the conventional R-factor

analysis[1]. We show the experimental chi-curve and the best fit for each of the three adsorption sites in figure 1.

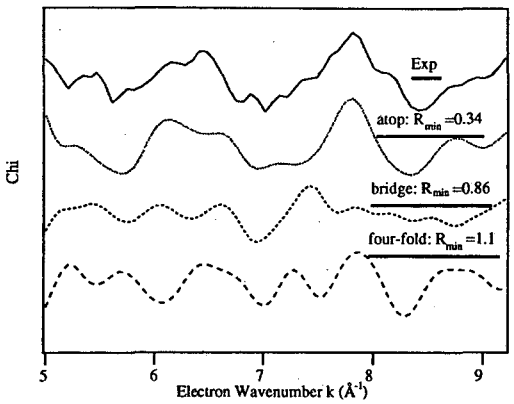

Figure 1. Experimental ARPEFS curve and best fit calculation for each adsorption site. The experimental curve is derived from the sum of the intensities from the two main peaks in the XPS spectrum. Clearly the atop adsorption site gives the best fit with an R-factor of 0.34.

To obtain these fits we allowed the N-N and N-Ni distances and the spacing between the first two nickel layers to vary. We also allowed the inner potential, the Debye temperatures of the near surface layers, and the tilt of the N-N molecule to vary. Clearly the atop site is the best fit, with an R-factor of 0.34. The N-Ni bond length is found to be 2.25 Å and the N-N bond length is found to be the gas-phase nitrogen value of 1.10 Å. Interestingly, the spacing between the first two nickel layers is found to be the bulk nickel value of 1.76 Å, in contrast to the contracted clean-metal layer spacing of 1.60 Å as reported by Frenken, et. al.[7] . Oed, et. al. have found the clean metal contraction to be ~1%, a spacing of 1.74 Å[8]. A surface debye temperature of 220 K and an inner potential of 15.1 eV were found to give the best fit.
To examine the sensitivity to the layer spacings and establish error bars we calculated the R-factor for various interlayer spacings and inner potentials. It has been shown that the inner potential may affect the derived layer spacings and must be included in the R-factor analysis[9]. The uncertainty is reported as one standard deviation, i.e. a confidence level of 0.68, and is written in parentheses following the last significant digit. All other layer spacings were optimised to the best fit for each fixed parameter value in the R-factor determination. Figure 2 shows the R-factor contour for the N-Ni layer spacing and inner potential and for the first layer Ni-Ni spacing and inner potential..

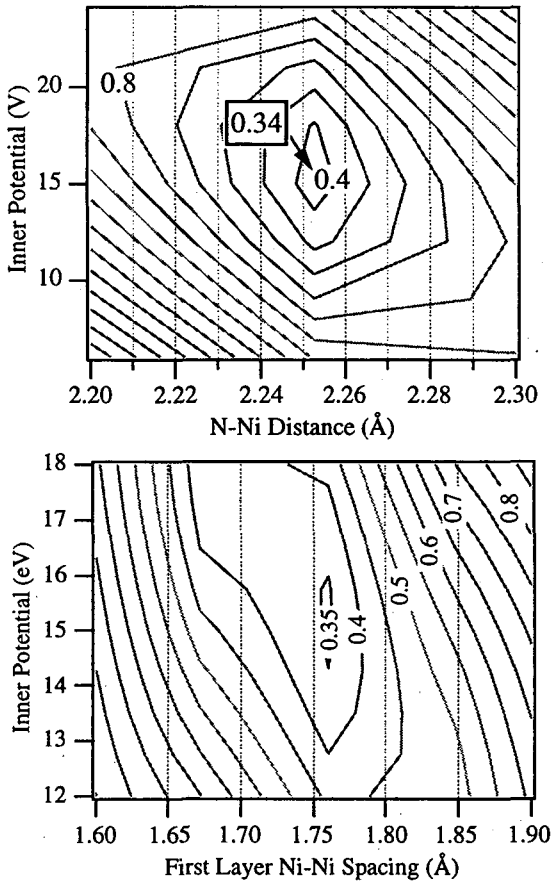

Figure 2. R-factor vs. inner potential and N-Ni layer spacing. The minimum is at a layer spacing of 2.255 Å. R-factor vs. inner potential and spacing between the first and second nickel layers.

Extraction of the error bars from the R-factor analysis has been discussed previously[10]. We conclude from these analyses that the error in the N-Ni layer spacing is 0.01 Å , the Ni-Ni layer spacing is 0.04 Å, and the N-N bond length is 0.07 Å.

THE SATELLITE PEAK

An interesting feature of the photoemission spectra is the broad, intense peak at 6 eV below the main peaks. Nilsson and

Mårtensson assigned this peak as an intrinsic satellite feature, and shows that it contains contributions from both of the main peaks by spectrum subtraction, making use of the variation in peak intensities with emission angle[7]. In fig. 5 we compare the χ-curve of the sum of the main peaks to the χ-curve of the 6 eV satellite.

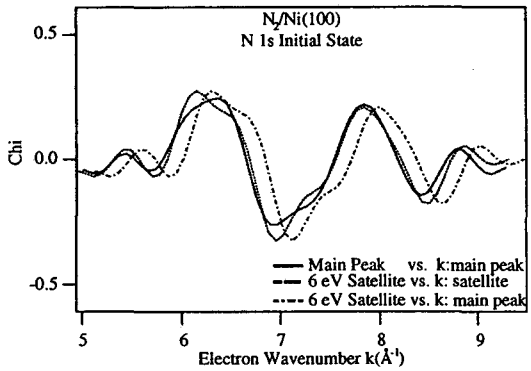

Figure 3. Comparison of ARPEFS chi-curves for the main peaks and the satellite peak. The curves have been Fourier smoothed to a 13 Å cutoff to facilitate comparison.

The main peak curve (solid) and the satellite curve (dotted) are each plotted against the k-value of its corresponding peak. The peak 3 curve is also plotted vs. the k-value of the main peak (dash-dotted). The peak 3 chi-curve, plotted vs. its own k-value, follows the summed main peak chi-curves very closely, showing that it displays an identical ARPEFS diffraction pattern to the main peaks, including identical amplitudes. We infer that the 6 eV peak arises from intrinsic satellite structures, each having the same intensity ratio as its main peak.

CONCLUSION

We have measured the nitrogen 1s ARPEFS oscillations from c(2x2) N_2/Ni(100). We find that the nitrogen molecule adsorbs in an atop site with the N-N bond normal to the surface with a N-N length of 1.10(7) Å. The N-Ni bond length is 2.25(1) Å and the first Ni-Ni layer spacing is 1.76(4) Å . The satellite peak intensity shows the same chi curve as the sum of the two main peaks, confirming that the component satellite peaks are intrinsic, and with the same intensity ratio as the main peaks. Comparison with theoretical treatments of the N-N-Ni system and experimental structures of analogous adsorbate systems suggests that a quantitative theoretical treatment of weakly adsorbed systems must include lateral interactions between adsorbates.

ACKNOWLEDGMENTS

We would like to thank the staff and management of the Stanford Synchrotron Radiation Laboratory in Stanford, CA and the ALS at Lawrence Berkeley National Laboratory for their support and help with the experimental work.

REFERENCES

1 J. J. Barton, C. C. Bahr, C. C. Robey, Z. Hussain, E. Umbach, and D. A. Shirley, Physical Review B **15**, 3807 (1986).

2 C. C. Bahr, J. J. Barton, Z. Hussain, S. W. Robey, J. G. Tobin, and D. A. Shirley, Physical Review B **35**, 3773 (1987).

3 L. G. Terminello, X. S. Zhang, S. Kim, A. E. Schach von Wittenau, K. T. Leung, and D. A. Shirley, Physical Review B **38**, 3879 (1988).

4 Anders Nilsson, Helena Tillborg, and Nils Martensson, "Electronic Structure of Adsorbates from Core-level Shake-up Spectra: N2 on Ni(100)," Physical Review Letters **67** (8), 1015 (1991).

5 J. Rehr and Albers, Physical Review B **41**, 8139 (1990).

6 E. J. Moler .

7 J. W. M. Frenken and J. F. van der Veen, "Relation between Surface Relaxation and Surface Force Constants in Clean and Oxygen-Covered Ni(001)," Physical Review Letters **51** (20), 1876-1879 (1983).
8 W. Oed, H. Lindner, U. Starke, K. Heinz, and K. Muller, "Adsorbate-Induced Relaxation and Reconstruction of c(2x2)O/Ni(100): A Reinvestigation by LEED Structure Analysis," Surface Science **224**, 179-194 (1989).
9 W. R. A. Huff, Y. Zheng, Z. Hussain, and D. A. Shirley, Journal of Physical Chemistry **98**, 9182-9186 (1994).
10 Z. Huang, "Structural Studies of Molecular Metallic Overlayers Using Angle-Resolved Photoemission Extended Fine Structure," Ph. D. Thesis, University of California, Berkeley, 1992.

This work was supported by the Director, Office of Energy Research, Office of Basic Energy Sciences, Chemical Sciences Division of the U. S. Department of Energy under contract No. DE-AC03-76SF00098.
Principle Investigator: David A. Shirley, Lawrence Berkeley National Laboratory

Angle and Temperature Dependence of Magnetic Circular Dichroism in Core-Level Photoemission from Gd(0001)

R. Denecke[1,2], J. Morais[1], R. X. Ynzunza[1,2], J.G. Menchero[1,3], J. Liesegang[1*], M. Rice[1], J. Kortright[1], Z. Hussain[1], and C. S. Fadley[1,2]

[1]Lawrence Berkeley National Laboratory, Berkeley, California 94720, USA
[2]Department of Physics, University of California, Davis, Davis, California 95616, USA
[3]Department of Physics, University of California, Berkeley, Berkeley, California 94720 USA

INTRODUCTION

Magnetic dichroism in core-level photoelectron emission from solids represents a promising new element-specific probe of surface and interface atomic structure and magnetic order. One way of measuring such effects is by using photoelectrons excited by circular polarized radiation, thus leading to magnetic circular dichroism (MCD) if the intensity with right-circular polarized (RCP) light is not equal to that with left-circular polarized (LCP) light. The spin-integrated photoelectron intensity in a certain emission direction also in general depends on the direction of the magnetization in a magnetic material. In fact, if the magnetization lies in a surface mirror plane, then inverting its direction can provide a second way of measuring MCD. Purely atomic theoretical models have been successful in explaining many aspects of such data [1]. By varying the emission direction one also probes the geometric structure of the sample. But such MCD in photoelectron angular distributions (MCDAD) then has to be interpreted also in terms of photoelectron diffraction. Measuring the temperature dependence of such MCD effects also provides a useful tool for studying magnetic transition temperatures. We have here studied such effects in core-level emission from Gd(0001).

EXPERIMENT

The experiments have been performed on beamline 9.3.2 [2a] using the advanced photoelectron spectroscopy/diffraction endstation [2b]. Photoelectron spectra were measured with a Scienta-200 electron analyzer, and with an overall photon-plus-analyzer energy resolution of about 1 eV. All spectra shown have been taken at a photon energy of about 450 eV yielding Gd 4d photoelectron energies of about 290-298 eV. The helicity of the photons can be chosen by moving an aperture above or below the plane of the storage ring, with the degree of circular polarization being about 80-85% [2a]. In the experiments presented here, we have largely used LCP light, but spot checks were also made to see if inverting magnetization in a mirror plane yielded the same effects as switching to RCP light.

The samples used were atomically thick films of Gd evaporated at room temperature onto a clean W(110) substrate. The thickness of the Gd films was chosen to be 100ML (≅300Å), as monitored by a quartz crystal microbalance, with final annealing at 700 K to insure monatomically flat surfaces. The cleanliness and crystalline order of the substrate and the final films were checked by x-ray photoelectron spectroscopy (XPS) and low energy electron diffraction (LEED), respectively. The Gd films have been studied with remanent in-plane magnetization, as induced by an in-situ magnetic field of about 200 G lying along a high-symmetry direction containing a mirror-plane of the crystal. During photoemission measurements, the light impinged on the

sample at an angle of 20° relative to the surface. Photoelectrons were collected either in normal emission or in emission at 20° with respect to the surface normal, and the sample was rotated stepwise about its surface normal so as to vary the azimuthal emission angle. The geometry is shown as an inset in Figure 1; the photon incidence direction **q**, the surface normal **n**, and the photoelectron wave vector **k** all lie in a plane. The MCD measurements were performed by inverting the magnetization direction; this was done simply by rotating the sample by 180° around the surface normal. The angle varied in the angle-dependent spectra shown below (Φ_M) is thus also the angle between the magnetization directions and the plane defined by **q**, **n**, and **k**.

RESULTS

Figure 1 shows an example of Gd 4d core-level spectra taken with the two different orientations of the magnetization axis (here denoted as parallel (p) and anti-parallel (a)). Also shown is a normalized MCD difference or asymmetry curve obtained from these two spectra. This asymmetry curve agrees very well with a free-atom theoretical description by van der Laan et al. [1], although the present data better resolve the individual final states of the Gd^+ ion than the experimental results presented in this prior study. As an overall measure of the MCD effect, we

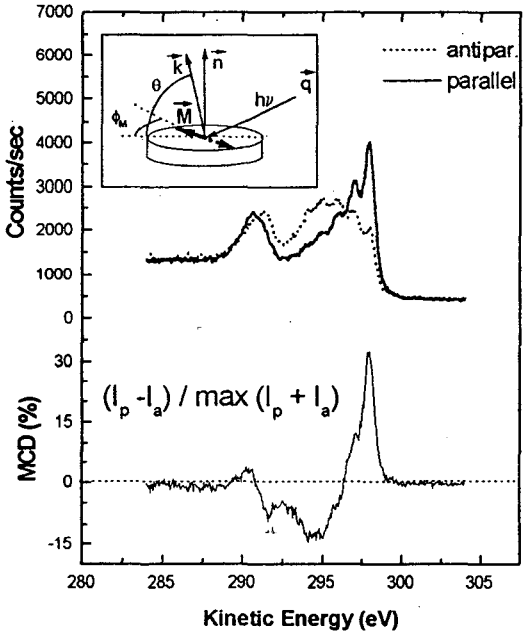

Fig.1: Gd 4d core-level photoemission spectra taken at a photon energy of 450 eV using left circular polarized light. The solid line spectrum was taken with the sample magnetization parallel to the azimuth of the light indicence direction (Φ_M=0°), and the dotted line spectrum with an antiparallel arrangement (Φ_M = 180°). The lower curve is the normalized difference or MCD asymmetry. The inset shows the experimental geometry.

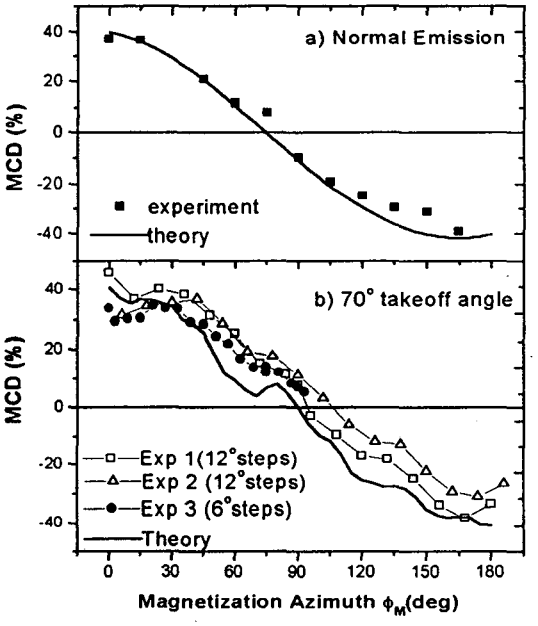

Fig.2: Angle dependence of the overall MCD effect for Gd 4d core-level emission. (a) Normal emission, (b) Electron takeoff angle = 70° (20° from normal). In both cases the solid lines show theoretical curves calculated for the respective cases. In (a) the calculation is for a free atom, in (b) it is for emission from an atomic cluster three layers thick in order to account for photoelectron diffraction effects.

have taken the difference between the maximum and minimum values of MCD curves such as that in the bottom panel of Fig. 1. For normal emission , Fig. 2(a) shows this overall MCD as a function of Φ_M. The same quantity for emission at 20° off normal is shown in Fig. 2(b).

The data in Fig. 2(a) basically exhibit a cosine-like behavior which would be expected from the free atom case, and there is excellent agreement with calculations based on such a free-atom model. However, the MCD behavior in Fig. 2(b) shows noticeable deviations from free-atom behavior, and this is reproducible over three different samples studied. The additional MCD modulations riding on the overall cosine-like curve are due to photoelectron diffraction. In order to learn more about the scattering processes involved, we have performed simulations using single-scattering and multiple scattering cluster calculations and including spin-orbit splitting and exchange splitting in the initial state [3]. The results of these calculations are shown in Fig. 2(b) as a dotted line. The theory well reproduces the additional modulations found in the experiment and clearly identifies them as diffraction features.

Turning now to the temperature dependent data, we note that the Curie temperature for bulk Gd material is about 293K. Thus, our samples were initially cooled to approximately 260K and then heated up to about 340 K in order to determine the manner in which the magnetic order disappears. Some preliminary results are shown in Fig. 3, where we plot the overall MCD asymmetry as a function of temperature for two runs on different samples. As temperature is increased, one clearly observes the decrease of the MCD signal to a negligibly small value when T_C has been exceeded, with the second run having a slightly higher transition temperature by about 10K. Shown also in Fig. 3 are magneto-optical Kerr effect (MOKE) measurements for two different annealing temperatures in preparing the Gd that span our choice of 700K [4]; these confirm the transition temperature seen in our first run, which is essentially the bulk value. Since MOKE penetrates a number of atomic layers into the sample, it is not surprising that it yields a bulk transition temperature for such a thick film. However, photoemission is a surface sensitive probe, so we might also expect to detect a surface-specific transition temperature, if it is in fact higher than that of the bulk by 20-60K, as has been proposed previously [5]. There may be some indication of this in the data for our second MCD run, which in fact had a cleaner surface, but further measurements will be necessary to confirm this suggestion.

CONCLUSIONS

For thick Gd(0001) films grown on W(110), we have obtained angle-dependent magnetic circular dichroism (MCD) data which vary by as much as ±35%. These data also reveal modulations of ~ ±5% which are verified as due to photoelectron diffraction effects by comparison with diffraction calculations. Additionally, we have measured the temperature dependence of the MCD amplitude. This clearly shows the bulk Curie temperature, and perhaps an indication of a higher surface Curie temperature. More investigations of these issues, from both experimental and theoretical viewpoints, are underway.

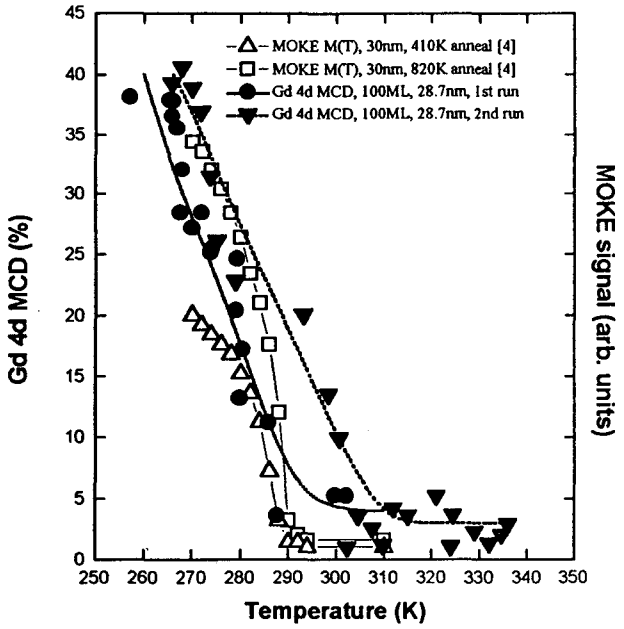

Fig.3: Temperature dependence of the MCD asymmetry for a takeoff angle of 70°. Shown are two different experimental MCD runs and MOKE measurements for comparison [4]. The sample surface in the first run was slightly contaminated, and shows a lower transition temperature by about 10K.

REFERENCES

*Permanent address: Department of Physics, La Trobe University, Bundoora 3083, Australia

1. G. van der Laan, E. Arenholz, E. Navas, A. Bauer, G. Kaindl, Phys. Rev. B**53**, R5998 (1996)
2. (a) Z. Hussain, W. R. A. Huff, S. A. Keller, E. J. Moller, P. A. Heimann, W. McKinney, H. A. Padmore, C. S. Fadley, and D. A. Shirley, J. Elec. Spec. and Rel. Phen. **80**, 401 (1996) and abstracts by E.J. Moler et al. and J. Kortright et al. elsewhere in this volume; (b) C.S. Fadley, M.A. Van Hove, Z. Hussain, and A.P. Kaduwela, J. Elec. Spec. and Rel. Phen. **75**, 273 (1995) and abstract by R.X. Ynzunza et al. elsewhere in this volume.
3. (a) M.A. Van Hove, A.P. Kaduwela, H. Xiao, W. Schattke, and C.S. Fadley, J. Elec. Spec. and Rel. Phen. 80, 137 (1996); (b) J. Menchero, J. Morais, R. Denecke, M.A. Van Hove, and C. S. Fadley (to be published)
4. M. Farle, W. A. Lewis, J. Appl. Phys. **75**, 5604 (1994)
5. H. Tang, D. Weller, T. G. Walker, J. C. Scott, C. Chapert et al., Phys. Rev. Lett. **71**, 444 (1993) and references therein.

This work was supported by DOE, OER, BES, Mat. Sci. Div. (Contract DE-AC03-76SF00098), ONR (Contract N00014-94-1-0162), CNPq (Brazil), and DFG (Germany).

Principal investigators: Jonder Morais, Reinhard Denecke, MSD, Lawrence Berkeley National Laboratory. Email: jonder@electron .lbl.gov, denecke@electron.lbl.gov. Telephone: (510) 486 4581.

Characterization of Combustion Chamber Products by Core-Level Photoabsorption Spectroscopy

S.A. Kellar,[1,2] W.R.A. Huff,[1,2] E.J. Moler,[1,2] S. Yeh,[3] and Z. Hussain[2]

[1]Department of Chemistry, University of California, Berkeley, California 94720
[2]Advanced Light Source, Lawrence Berkeley National Laboratory, University of California, Berkeley, California 94720
[3]Chevron Research and Technology Company, 100 Chevron Way, Richmond, CA 94802

The lubricating performance of motor oil is adversely affected by the carbon soot contamination that is a natural by-product of the combustion process. Particularly in diesel engines, 'blow-by' is a problem that greatly decreases the longevity of the engine-lubricating oil. Motor oil manufactures spend considerable resources developing new oil formulations that counteract the adverse affects of this combustion soot. At present, the only effective way to test new formulations is in a working engine. This process is obviously expensive and not especially efficient. In this ongoing work in collaboration with Chevron Research and Technology, our goal is to find a form of carbon that chemically resembles the soot created by the 'blow-by' in a diesel engine. The chemically correct soot substitute can be used in bench tests to replace the expensive full motor testing for new formulations. The final testing would still be done in the test motors but only with promising candidates.

To these ends, Near Edge X-ray Adsorption spectroscopy Extended Fine Structure (NEXAFS) is an attractive technique in that it has chemical specificity through the core-level binding energy and because it probes the chemically important unoccupied molecular orbitals of the material. Core-level photoabsorption has been used to characterize the empty electronic states of a wide variety of materials. Specifically, the near-edge region of the photoabsorption process has been used to determine the relative quantity of sp^2 and sp^3 bonding in carbon films[1].

These experiments were performed on Beamline 9.3.2 at the Advanced Light Source (ALS) in Berkeley. The samples were fine grained powders pressed into pellets. The C(1s) absorption spectra were collected from each sample by measuring the total electron yield from the sample as a function of photon energy. The absorption intensity was normalized to the incoming photon flux by measuring the photoyield from a fine gold mesh. Clean gold was evaporated on to the grid before starting the data collection.

Figure 1 compares the absorption spectra for three related carbon black samples. R760 is a commercialy available carbon black (Raven 760) that was added to two oil formulations, A and B, as a soot surrogate. These oils were tested in a diesel engine, and samples, RA and RB recovered from the oil after the test interval. These spectra show very similar structure above the adsorption edge in the σ^* region (above 289 eV). However, the uppermost sample, labeled R760, shows significantly different structure before the edge. Many past carbon NEXAFS studies have shown this region to correspond to 1s-π^* transitions associated with the p-type unoccupied molecular orbitals[2-4]. The differences shown in Fig 1. suggest that these samples differ in their π-bonding. The energy shift of the most prominent peak in this region could be due to π-bonding to atoms other than carbon.

Figure 2. compares the R760 and the RA carbon black samples to several model compounds, acetylene black, vulcan black, and graphite. The RA sample is most similar to the vulcan black model compound with a single

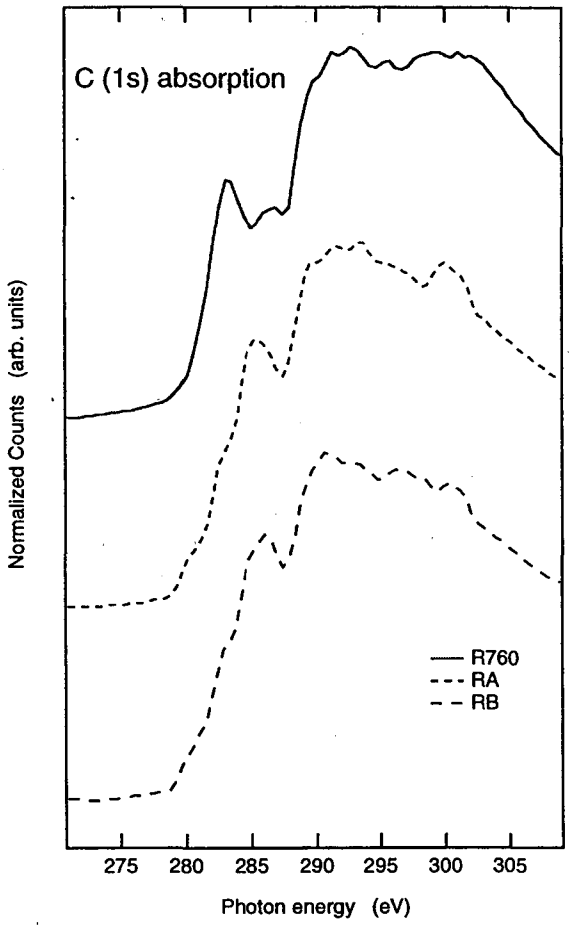

Figure 1. Normalized C(1s) photoabsorption measured by total electron yield. R760, a commercially available carbon black was added to fully formulated motor oils A and B. The oils were run in a diesel test engine, and soots RA and RB recovered from the used oils. The spectra are very similar above the edge at 289 eV. However, below the edge the recovered soot differs from the parent compound in the region where the π-bonding is probed.

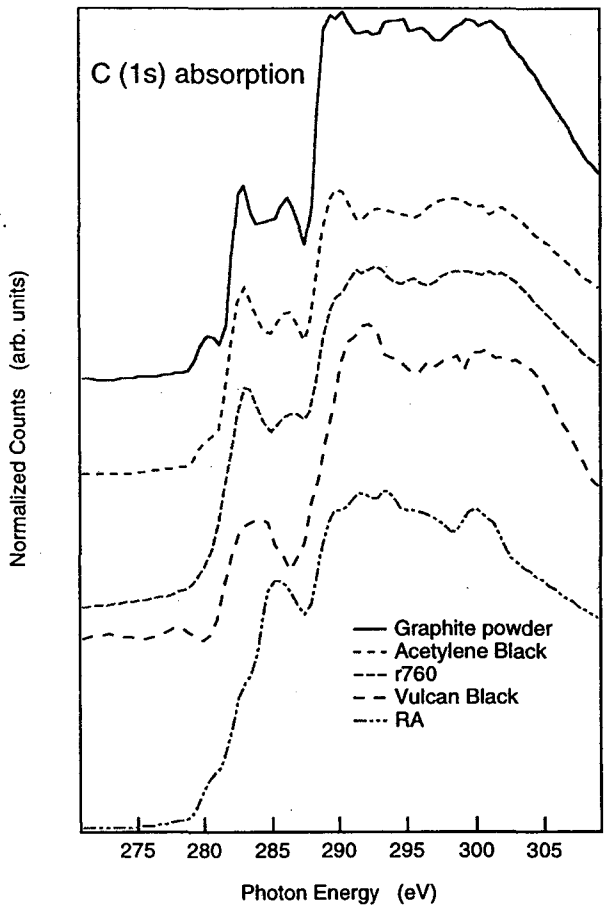

Figure 2. Normalized C(1s) NEXAFS spectra comparing assorted carbon blacks, including recovered soot from a dieseltest engine, RA. The R760 most closely resembles the acetylene black. Both show two pre-edge peaks in the π^* region, with the peaks in the R760 compound shifted 400 meV to higher energy. The size of the edge jump is also similar. The RA sample resembles the vulcan black with one π^* resonance, shifted 1.5 eV higher in energy.

σ^* peak, though the position of the peak in the vulcan black sample is shifted to lower energy by 1.5 eV. The R760 sample seems to be most like the acetylene black, with two pre-edge peaks at 283 and 286 eV respectively. These positions are shifted from those in the acetylene black by 400 meV toward higher binding energy.

References:

1. C.D. Zuiker, A.R. Krauss, D.M. Gruen, J.A. Carlisle, L.J. Terminello, S.A. Asher, R.W. Bormett, Mat. Res Soc. Symp. Proc. **437**, 211 (1996)
2. Y.Wang, H. Chen, and R.W. Hoffman, J. Vac. Sci Tech. A , **9**,1153 (1991)
3. J. Nithianandam, J.C. Rife, and H. Windischmann, Appl. Phys. Lett. **60**,135 (1992)

This work was supported by the Director, Office of Energy Research, Office of Basic Energy Sciences, Materials Science division, of the U.S. Department of Energy under Contract No. DE-AC03-76SF00098 and Chevron Research and Technology company, 100 Chevron Way, Richmond, California
Principal Investigator: Zahid Hussain, Advanced Light Source, Ernest Orlando Lawrence Berkeley National Laboratory. Email: zhussain@lbl.gov. Telephone 510-486-7521

Characterization of Heterogeneous Nickel Sites in CO Dehydrogenase from *Clostridium thermoaceticum* by Nickel L-Edge X-Ray Spectroscopy

C. Y. Ralston,[1] M. Kumar,[2] S. W. Ragsdale,[2] and S. P. Cramer[1,3]

(1) Department of Applied Science, University of California, Davis, CA 95616
(2) Department of Biochemistry, University of Nebraska, Lincoln, NE 68583
(3) Lawrence Berkeley National Laboratory, Berkeley, CA 94720

L-edge x-ray absorption spectroscopy (XAS) is a useful spectroscopic technique for determining the electronic state of transition metals. For first row transition metals, the L-edge represents a transition from 2p core levels to 3d valence levels. Coulomb and exchange interactions between the core hole and 3d valence electrons make the L-edge sensitive to the number and configuration of 3d electrons, hence to the metal spin state and oxidation state. We have used L-edge XAS to characterize the Ni sites in the carbon monoxide dehydrogenase (CODH) enzyme from *Clostridium thermoaceticum*. This CODH catalyzes both CO oxidation and acetyl-CoA synthesis at two Ni and Fe containing centers, C and A, respectively [1,2]. Since the enzyme exhibits complex EPR signals that never integrate to one spin per Ni, there is evidence for heterogeneity in the types of Ni present.

The Ni L-edge protein spectra were recorded at ALS beamline 9.3.2. The photon energy resolutions used for protein samples and for Ni model compound spectra were 350 and 270 meV respectively. During data collection the sample chamber was maintained at less than 5×10^{-9} Torr using a helium cryopump. Model compound spectra were measured using total electron yield detection, while protein spectra were recorded using fluorescence detection with a windowless 13-element germanium detector, and were calibrated using the total electron yield spectrum of NiF_2 or NiO. Each protein spectrum presented represents the sum of approximately 40 15-minute scans.

In previous L-edge XAS studies of metalloproteins [3], computer simulations of the L-edge multiplet structure were used to derive information about the metal oxidation state and ligand field. However, in many of the CODH spectra the multiplet structure is not observable, and other properties of the spectra must be exploited. We have used the property of chemical shift with oxidation state (L_3 centroid) and "branching ratio", the ratio of L_3 intensity to overall intensity, $I(L_3) / [\, I(L_2) + I(L_3) \,]$, to systematically study Ni model compounds in a variety of symmetries, oxidation, and spin states. Using these two properties, we have created a two-dimensional diagram mapping the different types of Ni compounds. As shown in Figure 1, Ni(I) and Ni(II) can be clearly distinguished by the shift in L_3 centroid position, and high spin and low spin Ni(II) can be distinguished using the difference in branching ratio.

We next applied the technique to the study of a Ni protein. The L-edges of CODH under native, CO-treated, and CO+phen-treated conditions are shown in Figure 2. The native enzyme spectrum falls within the low spin Ni(II) region of the correlation diagram. The current data suggest that a significant fraction of Center C Ni is also low spin, and since tetrahedral Ni(II) is generally high spin, a 5-coordinate Center C Ni seems favored. The spectrum of the CO-treated sample shows a clear low-energy shoulder at the L_3 edge as compared with the spectra of the native enzyme.

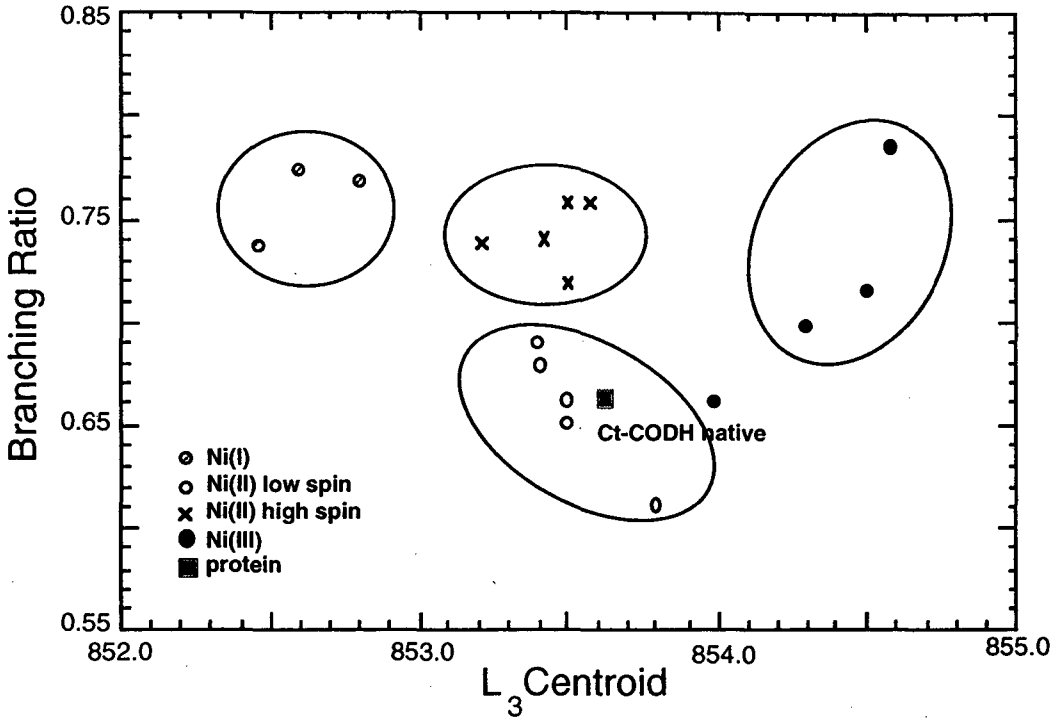

Figure 1. Two dimensional correlation diagram of Ni model compounds of known oxidation and spin state, and several Ni proteins. Compounds are plotted as a function of L3 centroid position and branching ratio. Ellipses are drawn only to guide the eye, and do not represent error margins.

This shoulder appears in the Ni(I) energy region, suggesting that a fraction of nickel in CODH is reduced to Ni(I) upon CO treatment. We were able to fit the spectrum of CO-treated CODH with a combination of Ni(I) and Ni(II) model compounds. The best fit uses a mix of Ni(I) and low spin Ni(II) (Figure 2, inset). Since several high spin Ni(II) complexes showed L3 absorption maxima (but not centroids) at energies close to those of Ni(I) compounds, we also attempted to fit the CODH spectrum with a combination of high spin and low spin Ni(II), as shown in Figure 2. Although high spin spectra can fit the CODH spectrum well near the center of the L3 peak, they cannot reproduce the low energy tail of the L3 edge. In addition, since phen treatment selectively removes the Ni from Center A [4], and since much of the low energy shoulder feature disappears in the CO+phen-treated sample spectrum, the data suggests that the CO-induced Ni(I) feature is from a form of Center A Ni.

We have found that by using L-edge XAS we are able to distinguish between different spin and oxidation states of Ni compounds. We have used this result to characterize the Ni containing CODH protein in various states. The L-edge spectra are consistent with other results showing that when CODH is reacted with CO, the metal centers undergo reduction. The EPR spectrum of the adduct between CO and Center A shows a low spin quantitation of 0.25 - 0.35 spins per dimer, which is consistent with our finding from the L-edge spectra of incomplete conversion to Ni(I). Resonance Raman[5], and infrared [6] spectroscopic studies have shown that CO binds end-on to an Fe (not Ni) site within Center A. The Ni L-edge spectra are consistent with a model in which binding of CO to Center A converts Ni^{2+}-X-[Fe4S4] to Ni^{1+}-X-[Fe4S4]-CO, with spin density from the Ni distributed over the other components of Center A. The experimental sensitivity of L-edge spectroscopy is now adequate for obtaining good spectra on proteins, and the technique should be a valuable complement to other types of spectroscopy.

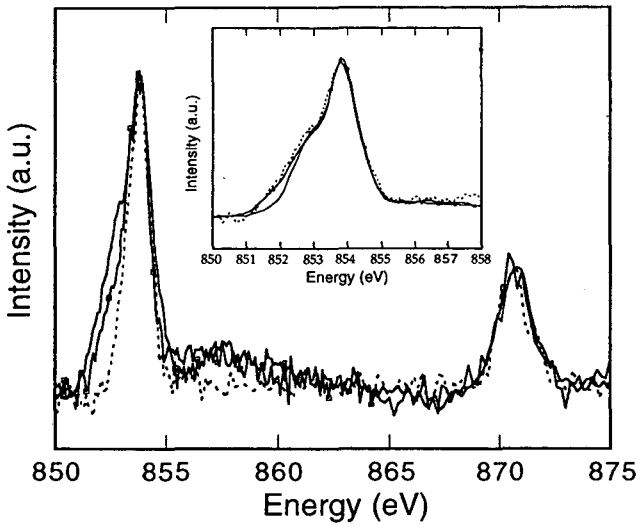

Figure 2. L-edge spectra of CO-treated CODH (solid line), native CODH (dashed line) and CO+phen-treated CODH (solid line with squares). Inset: L_3 edge of CO-treated CODH (dashed line) as compared to a sum of 30% Ni(I) and 70% low spin Ni(II) spectra (solid line with squares), and a sum of 30% high spin Ni(II) and 70% low spin Ni(II) spectra (solid line).

We gratefully acknowledge the following people for supplying Ni model compounds used in this study: Dr. E. Fujita, Prof. J.A. Kovacs, Dr. M. Woomer and Prof. T.J. Collins, Dr. C.A. Marganian and Prof. P.K. Mascharak, Prof. M.J. Maroney, Prof. M.W.W. Adams, and Mr. J. Allman.

REFERENCES

1. S. A. Raybuck, N.R. Bastian, W.H. Orme-Johnson, and C.T. Walsh, Biochemistry **27**, 7698 (1988).
2. M. Kumar, W.-P. Lu, L. Liu, and S.W. Ragsdale, J. Am. Chem. Soc. **115**, 11646 (1993).
3. S. J. George, J. van Elp, J. Chen, Y. Ma, C. T. Chen, J.-B. Park, M. W. W. Adams, B. G. Searle, F. M. F. deGroot, J. C. Fuggle, and S. P. Cramer, J. Am. Chem. Soc. **114**, 4426 (1992).
4. W. Shin, and P. A. Lindahl, Biochemistry **31**, 12870 (1992).
5. D. Qiu, M. Kumar, S. W. Ragsdale, and T. G. Spiro, Science **264**, 817 (1994).
6. M. Kumar, and S. W. Ragsdale, J. Am. Chem. Soc. **114**, 8713 (1992).

This work was supported by the National Institutes of Health Grant GM-44380 and the DOE Office of Health and Environmental Research.

Principal investigator: Stephen P. Cramer, Advanced Light Source, Earnest Orlando Lawrence Berkeley National Laboratory. Email: SPcramer@lbl.gov. Telephone: 510-486-4720.

Circular Dichroism in Core Photoelectron Emission from (1x1) Oxygen on W(110): Experiment and Theory

H. Daimon[1,4], R.X. Ynzunza[1,2], F.J. Palomares[1,2,3], E.D. Tober[1,2], Z. Wang[1,2], J. Morais[1], R. Denecke[1,2], M. Rice[2], J.B. Kortright[2], Z. Hussain[2], M.A. Van Hove[1], and C.S. Fadley[1,2]
[1]Lawrence Berkeley National Laboratory, Berkeley, CA 94720
[2]Department of Physics, University of California-Davis, Davis, CA 95616
[3]ICMM-CSIC, Cantoblanco E-28049, Madrid, Spain
[4]Department of Materials Physics, Osaka University,Toyonake, Osake 560, Japan

INTRODUCTION

One of the several advantages of using synchrotron radiation is the possibility of varying it from linear polarization (LP) to left and right circular polarization (LCP and RCP), and we have used beamline 9.3.2 at the ALS [1(a)] to exploit this capability in high-resolution core-level photoelectron emission. This beamline is the only one at the ALS presently capable of varying polarization over a broad energy range from ~30 to 1500 eV. In connection with core photoelectron emission from surfaces, it then becomes possible to look for circular dichroism effects in which the intensity with LCP excitation (I_{LCP}) is not equal to the intensity with RCP excitation (I_{RCP}). Such effects are known to occur for both non-magnetic [2,3] and magnetic [4,5] systems. For the latter, they constitute a novel element-specific way of studying both atomic structure and local magnetic order [4,5], but the question then arises of clearly distinguishing non-magnetic from magnetic circular dichroism effects [2(b),3].

In order to better understand the interrelationship between non-magnetic circular dichroism [2,3] and magnetic circular dichroism [4,5], we have performed circular dichroism measurements for the non-magnetic system of a (1x1) oxygen overlayer on W(110). This incipient-oxide overlayer corresponds to a coverage of 1 ML of oxygen, leads to a (1x12) superstructure in its LEED pattern, and exhibits W 4f core spectra that are easily resolvable into "oxide" and bulk components separated by ~0.73 eV [6]. Such non-magnetic circular dichroism in core photoelectron angular distributions (CDAD) was first observed by Schönhense et al. from CO/Pd(111) [2(a)]. This experiment showed that, even in what are overall non-chiral atomic geometries, circular dichroism may be present in core photoelectron emission. Subsequent to this, Daimon et al. observed similar effects in core emission from Si(100) [3(a)], and we will relate our experimental findings for O/W to a theoretical model for these effects introduced by them, as well as to more accurate multiple scattering photoelectron diffraction calculations of such effects.

EXPERIMENT

The experiment was performed at beamline 9.3.2 of the ALS [1(a)], with angle-resolved and chemical-state-resolved photoelectron spectra being measured using its advanced photoelectron spectrometer/diffractometer [1(b)]. The (1x1)-(1x12) oxygen overlayer was prepared on a clean W(110) surface by a method described elsewhere [6]. The experimental geometry is shown in Fig. 1(a). The photons were incident normal to the sample surface and were chosen to be linearly polarized, left circularly polarized, or right circularly polarized. A degree of circular polarization of 85% can be achieved by means of a movable aperture at the entrance to the beamline [1(a)]. The first photon energy was 366 eV, leading to W 4f photoelectrons at 335-339 eV which were

analyzed using a Scienta SES 200 spectrometer [1(b)]. A typical spectrum is shown in Fig. 1(b), and each member of the 5/2, 7/2 doublet consists of a bulk peak and an oxide peak that is shifted to higher binding energy (lower kinetic energy) by ~0.73 eV. Separate photoelectron diffraction patterns have been measured for these two types of photoelectron peaks. The sample was rotated in azimuthal angle (ϕ) and the analyzer was rotated in polar angle (θ) over a range of approximately 27.5°so as to preserve the normal incidence of the light. In this way, both intensities could be measured over a θ range (as measured with respect to the surface) of 16.5° to 44° and a solid angle corresponding to ~41% of the 2π steradians above the surface.

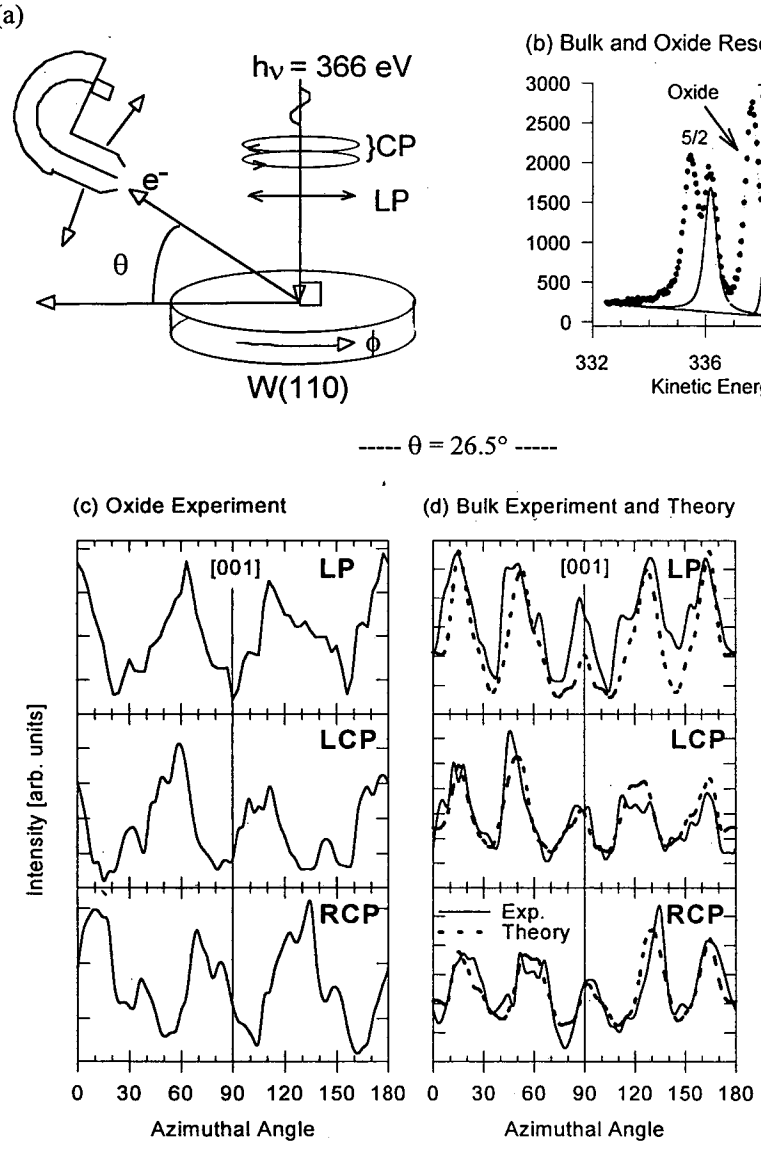

Figure 1. Circular dichroism in the angular distributions (CDAD) of photoelectrons from a (1x1) oxygen overlayer on W(110) with a (1x12) oxide superstructure: (a) The experimental geometry, with radiation incident normal to the surface and a rotating Scienta spectrometer being used to measure at various takeoff angles θ; (b) A typical W 4f spectrum with oxide and bulk peaks resolved in both the 5/2and 7/2 components; (c) Azimuthal scans at a takeoff angle of 26.5° for the oxide W4f component for linearly polarized light (LP), left circularly polarized light (LCP), and right circularly polarized light (RCP); (d) Comparison of the analogous experimental curve for bulk emission with theoretical photoelectron diffraction calculations.

Azimuthal photoelectron diffraction patterns at a 26.5° polar takeoff angle are shown in Figs. 1(c) and (d) for oxide and bulk emission in all three polarizations. Comparing the diffraction patterns for LCP and RCP excitation for either oxide or bulk, we see that some features appear to exhibit azimuthal peak "rotations" across the [001] mirror plane at $\phi = 90°$, with the diffraction peaks for LCP being shifted to the left and those for RCP being shifted to the right. However, other differences between the LCP and RCP curves do not follow such a simple characterization. Fig. 2 shows a full data set for both oxide and bulk emission, with the photon energy here being 280 eV. Similar azimuthal peak rotations (especially visible in the oxide data) and other more complex changes between LCP and RCP can be seen here as well. The sum of I_{LCP} and I_{RCP} is

also found to be very nearly equal to I_{LP}, a result which is not rigorously true for all cases, but can be shown to be a good approximation for W 4f in our geometry and for our kinetic energy range.

Such diffraction peak rotations with changing circular polarization were first observed and theoretically interpreted in terms of a physically intuitive model by Daimon et al. [3(a)]. This model relies on the dipole selection rules for circularly polarized light ($\Delta m = m_f - m_i = -1$ for LCP and $\Delta m = +1$ for RCP), combined with an estimate of the relative strengths of the various allowed transitions to different $|\ell_f, m_f> = |\ell_i \pm 1, m_f>$ final states. This leads to final-state wave functions that are for many cases dominated by $|\ell_f, m_f> = |\ell_i + 1, \ell_i \pm 1>$, with the two signs holding for the two different circular polarizations. The spherical harmonics associated with these wave functions in turn have an azimuthal dependence of $\exp(im_f\phi)$, and they thus yield spiraling surfaces of constant phase in azimuth, rather than the simpler spherical surfaces of constant phase that are more often seen in the radial dependence of the wave functions. Since the photoelectron current will be carried perpendicular to these constant phase surfaces, the photoelectron diffraction features are predicted to be rotated in opposite directions by the two polarizations. Simple formulas for estimating these rotations have been presented elsewhere and compared to experimental data, where they are found to well reproduce Si(001) peak shifts [3].

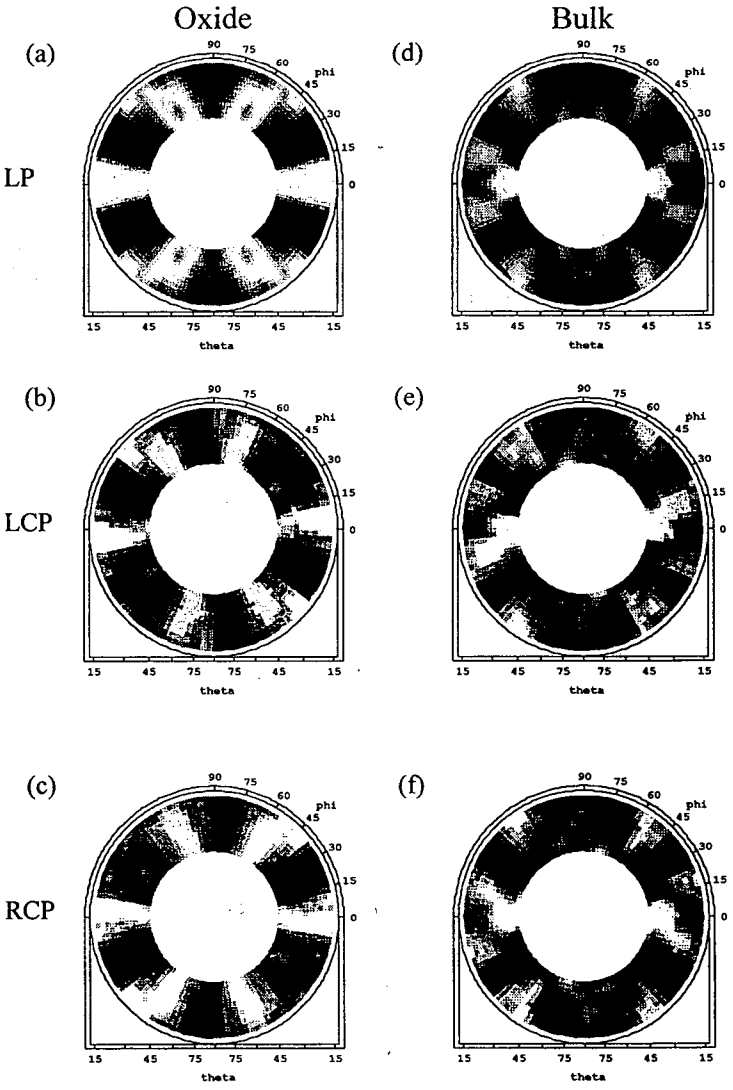

Figure 2. Large-solid-angle photoelectron diffraction patterns for oxide ((a),(b),(c)) and bulk ((d),(e),(f)) W 4f emission from a (1x1)-(1x12) oxygen overlayer on W(110). Panels (a) and (d) are for excitation with linearly polarized light, (b) and (e) are for left circularly polarized light, and (c) and (f) are for right circularly polarized light. Note the apparent rotations of certain major features in the patterns between left and right circular polatization.

A more accurate picture of these effects is to include all allowed transitions with their precise weightings, as well as single and multiple scattering of the outgoing photoelectron wave. Such calculations have been applied successfully to Si(001) by Kaduwela et al. [7], and we here apply them to our data for O/W. These calculations were performed using a program developed by Kaduwela et. al. [7] and based on the Rehr-Albers approximation for treating multiple scattering. The preliminary calculated curves in Fig. 1(d) were obtained for bulk emission. Even though the atomic cluster used did not include the O atoms (a reasonable first

approximation due to their being much weaker scatterers than W), this theory correctly predicts not only the gross motion of certain features that one can describe as rotations, but also various other peak distortions beyond this simple description. It is thus clear that, although the model of Daimon et al. [3(a)] correctly describes the basic physics of the peak rotation phenomenon, a fully quantitative description of such non-magnetic CDAD effects will require a complete treatment of the excitation matrix elements, including photoelectron scattering and diffraction.

CONCLUSIONS

Circular dichroism in core photoelectron angular distributions for non-magnetic systems can result in large differences in I_{LCP} and I_{RCP} of up to ±50%, and such effects are expected to be very generally observable. Our results for O/W show that these effects can arise for different chemical states in a single sample and that they can be predicted quantitatively by photoelectron diffraction calculations. Such non-magnetic circular dichroism effects due to photoelectron diffraction must also be included in any interpretation of analogous MCD experiments with magnetic materials. For example, in the 2p levels of the 3d ferromagnetic metals, MCD is only ± a few % in magnitude [4], and thus potentially much smaller than the non-magnetic contributions [2(b)]. For the high-spin 4f ferromagnet Gd, MCD has been found to be about ±35%, and thus about 7 times larger than the non-magnetic diffraction contributions [5]; nonetheless, even for this case the non-magnetic diffraction effects cannot be fully neglected.

REFERENCES

[1](a) Z. Hussain, W. R. A. Huff, S. A. Keller, E. J. Moler, P. A. Heimann, W. McKinney, H. A. Padmore, C. S. Fadley, and D. A. Shirley, J. Elec. Spec. and Rel. Phen. **80**, 401 (1996) and abstract by E.J.Moler et al. elsewhere in this volume. (b) C.S. Fadley, M.A. Van Hove, Z. Hussain, and A.P. Kaduwela, J. Elec. Spec. and Rel. Phen. **75**, 273 (1995) and abstract by R.X. Ynzunza et al. elsewhere in this volume.

[2] (a) G. Schönhense, Phys. Scr. **T31**, 255 (1990); J. Bansmann et al., Phys. Rev. B**46**, 13496 (1992). (b) C. Westphal, A.P. Kaduwela, C.S. Fadley, and M.A. Van Hove, Phys. Rev. B **50**, 6203 (1994).

[3] (a) H. Daimon, T. Nakatani, S. Imada, S. Suga, Y. Kagoshima, and T. Miyahara, Jpn. J. Appl. Phys. **32**, L1480 (1993); H. Daimon, T. Nakatani, S. Imada, and S. Suga, J. Elec. Spec. Rel. Phen. **76**, 55 (1995); (b) .A.P. Kaduwela, H. Xiao, S. Thevuthasan, C.S. Fadley, and M.A. Van Hove, Phys. Rev. B **52**, 14927 (1995).

[4] L. Baumgarten, C.M. Schneider, H. Peterson, F. Schäfers, and J. Kirschner, Phys. Rev. Lett. **65**, 492, (1990).

[5] R. Denecke, J. Morais et al., abstract elsewhere in this volume.

[6] K.E. Johnson, R.J. Wilson, and S. Chiang, Phys. Rev. Lett. **71**, 1055 (1993); R. Ynzunza et al., abstract elsewhere in this volume.

[7] A.P. Kaduwela, D.J. Friedman, and C.S. Fadley, J. Elec. Spectrosc. and Relat. Phenom. **57**, 223 (1991).

This work was supported by the Director, Office of Energy Research, Office of Basic Energy Sciences, Materials Science Division, of the U.S. Department of Energy under Contract No. DE-AC03-76SF00098; and by ONR (Contract N00014-94-0162).

Principal investigator: R.X. Ynzunza, Materials Sciences Division, Lawrence Berkeley National Laboratory. Email: ramon@photon.lbl.gov. Telephone: 510-486-4581.

Evidence of the Nature of Core-Level Photoemission Satellites Using Angle-Resolved Photoemission Extended Fine Structure

Edward J. Moler[1], Scot A. Kellar[1], W. R. A. Huff[1],
Zahid Hussain[1], Zhengqing Huang[2], Yufeng Chen[3], David A. Shirley[3]

[1]Advanced Light Source, Lawrence Berkeley National Laboratory, Berkeley, CA 94720
[2]Department of Chemistry and the James Franck Institute, The University of Chicago, Chicago IL 60637
[3]Departments of Chemistry and Physics, The Pennsylvania State University, University Park, PA 16802

ABSTRACT

We present a unique method of experimentally determining the angular momentum and intrinsic/extrinsic origin of core-level photoemission satellites by examining the satellite diffraction pattern in the Angle Resolved Photoemission Extended Fine Structure (ARPEFS) mode. We show for the first time that satellite peaks not associated with chemically differentiated atomic species display an ARPEFS intensity oscillation. We present ARPEFS data for the carbon 1s from ($\sqrt{3}$x$\sqrt{3}$)R30 CO/Cu(111) and p2mg(2x1)CO/Ni(110), nitrogen 1s from c(2x2) N_2/Ni(100), cobalt 1s from p(1x1) Co/Cu(100), and nickel 3p from clean nickel (111). The satellite peaks and tails of the Doniach-Sunjic line shapes in all cases exhibit ARPEFS curves which indicate an angular momentum identical to the main peak and are of an intrinsic nature.

INTRODUCTION

The nature of core level photoemission satellites from clean metals has been an active area of investigation for many years[1-10]. The interpretation of satellites from molecular adsorbates on metal surfaces have been employed as a probe into the nature of the surface chemical bond on a variety of systems[11-17]. Generally, these satellites are interpreted as correlated excitations of valence level electrons into either unoccupied bound states (shake-up or electron-hole pair excitations) or into the continuum (shake-off) which are associated in some way with the photoemission process. There are, however, open questions regarding the nature of these satellite structures.

Two questions often arise in the interpretation of core-level satellites in solid and adsorbate systems. One question is whether the peak is intrinsic, i.e. a shake-up or shake-off peak, or extrinsic, from an inelastic scattering process encountered before the electron leaves the solid, e.g. a plasmon loss. The second question concerns the character of the valence excitation, which can be to a HOMO-LUMO type transition, for example, or an excitation into a Rydberg-like state, each of which involves transitions to a state of some specific angular momentum.

We show in this paper that both of these questions can be approached by examining the Angle Resolved Photoemission Extended Fine Structure (ARPEFS) curves associated with the main peak and its satellites. ARPEFS is a well known technique for finding the spatial atomic structure of surfaces to very high accuracy[18]. It is based on measuring the intensity of a core level photoelectron with an angle-resolved electron energy analyzer while varying the electron kinetic energy. This technique is also known as scanned-energy photoelectron diffraction. We have found that the satellite structures not associated with a chemically differentiated atomic species can display an ARPEFS diffraction pattern and can thus be used to infer certain features of the origin of these peaks.

EXPERIMENTAL

The CO/Cu(111) experiment was performed on beam line 9.3.2 at the Advanced Light Source (ALS) at Lawrence Berkeley National Laboratory. The N_2/Ni(100) experiment was performed on beam line 6.1 at the Stanford Synchrotron Radiation Laboratory (SSRL). The clean nickel and CO/Ni(110) experiments were performed using beam line U3-C at the National Synchrotron Light Source (NSLS) at Brookhaven National Laboratory. The Co/Cu(100) experiment was performed using beam line 6-2 at SSRL.

DATAREDUCTION

An example XPS spectra for each system is shown in Fig. 1 top. The experimental data points are shown as circles. The best fit lines and fitting components are also shown. These fits are used to extract the peak intensities for the ARPEFS curves. The region of integration, if not a peak, is demarcated by vertical solid lines. The integrated intensity above the background in these regions are used to extract the ARPEFS curves. The ARPEFS curve, representing the intensity oscillation for each peak in the XPS spectrum, is shown below the respective spectrum. The abscissa is the electron wave-number, in $Å^{-1}$, for each peak.

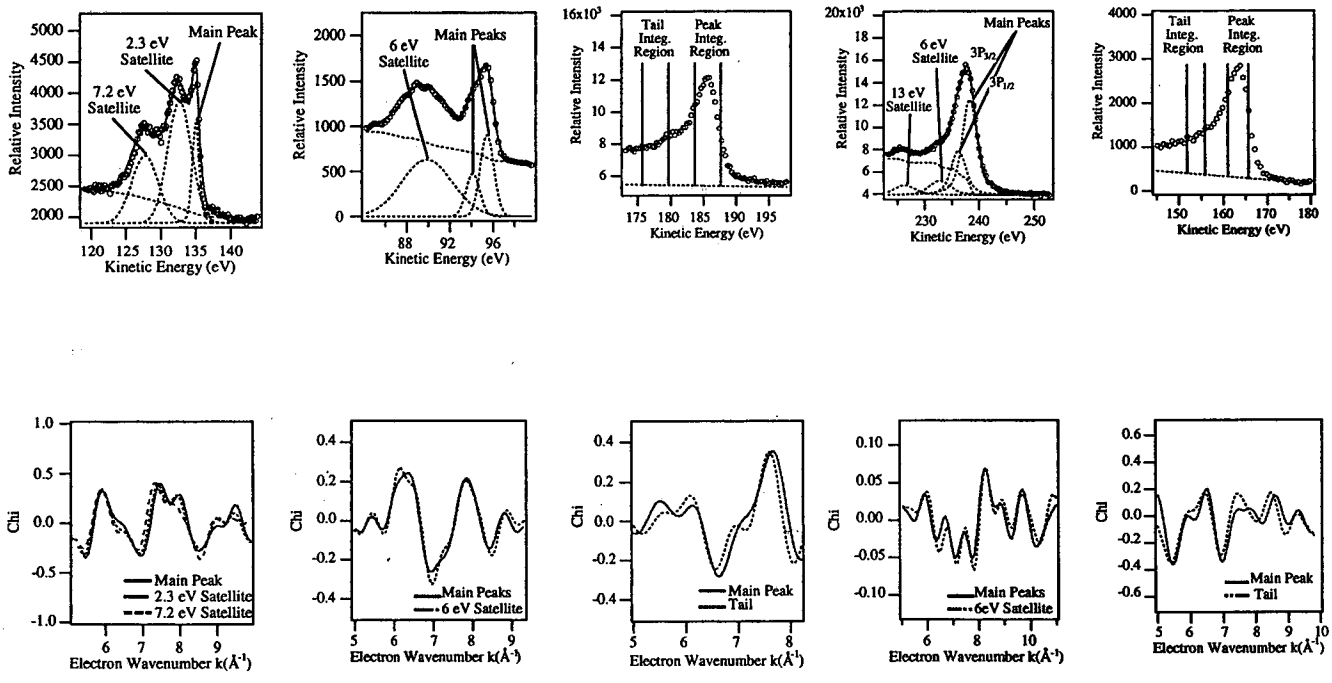

Figure 1. XPS regions used to extract chi (top). The ARPEFS curves are compared, each plotted vs. the k-value of its respective peak.

It is clear from the figures that the satellite peaks exhibit the same ARPEFS diffraction pattern as the main peak with the exception of the nickel 13 eV satellite, which will be discussed further below. The ARPEFS curves for the p2mg(2x1)CO/Ni(110) and p(1x1) Co/Cu(100) systems have been Fourier smoothed to 10 Å to aid comparison.

RESULTS AND DISCUSSION

Two important conclusions can be drawn from the similarities between the main and the satellite peak ARPEFS curves. The first is that these satellite peaks and the DS tails must be intrinsic. This stems from the extreme sensitivity of ARPEFS to the position of the outgoing electron wave's origin, which is ~ 0.01 Å. An inelastic scattering event from valence electrons would most likely lead to an outgoing electron wave which is not centered at an equivalent ion core and thus would exhibit a very different diffraction pattern, if any at all. The fact that we find these peaks to be intrinsic is compatible with the interpretation of Tillborg, Nilsson, and Martensson that the molecular adsorbate satellites are due to shake-up transitions which originate from a single-step process[12]. This interpretation considers the final state of the remaining electrons to be strongly influenced by the newly created core-hole. This state is not an eigenstate of the unperturbed system, leading to a final state which is a sum of the new eigenstates of the adsorbate-plus-core-hole system and thus has significant probability of valence excitations. The nickel 6 eV satellite is also intrinsic. This is consistent with the current understanding of its origin as being due to an excitation of a single d-level electron correlated with the 3p core excitation into the continuum, leaving a $3d^9$ valence configuration in the final state[3]. The DS line shape is also derived assuming an intrinsic excitation of the Fermi sea in the core-hole creation process. Our results confirm the intrinsic origin of the DS tail.

The second conclusion which can be drawn from the similarities in the ARPEFS curves is that the satellite peaks have the same angular momentum as the main peak. The dipole selection rules of photoemission are known to be valid for the main peaks and have been used to successfully model the diffraction curves from many systems. The similarity of the ARPEFS curves indicates that the angular momentum of the satellites are the same as that of the main peak. This restricts the valence excitations to monopole transitions for single electrons and a net zero angular momentum change for two electron excitations in these systems. This agrees well with previous theoretical investigations into the 6 eV nickel satellite where a d-d transition is considered the most likely origin of that satellite structure[3]. It has been suggested that there may be excitations to s and d-like Rydberg states in the carbon 1s XPS of c(2x2) CO/Ni(100)[12], which is closely related to the CO/Cu(111) system. It is apparent from our data that there is essentially no angular momentum transfer and that the transitions to np states dominate.

CONCLUSION

We have shown for the first time that photoemission satellite peaks from multi-electron excitations exhibit an ARPEFS diffraction pattern. Examination of this pattern leads to unique information on the angular momentum and intrinsic/extrinsic nature of the satellite. We find that the core level satellite peaks of carbon 1s from ($\sqrt{3}$x$\sqrt{3}$)R30 CO/Cu(111), nitrogen 1s from c(2x2) N2/Ni(100), and nickel 3p from clean nickel(111) are all intrinsic peaks with final state angular momenta identical to that dictated by the photoemission selection rules. Similarly, the tail of the Doniach-Sunjic line shapes in cobalt 1s from p(1x1) Co/Cu(100) and p2mg(2x1) CO/Ni(110) also originate from an intrinsic process and have a final state angular momentum identical to the maximum of the peak.

ACKNOWLEDGMENTS

We would like to thank the staff and management of the ALS at Lawrence Berkeley National Laboratory for their support and help with the experimental work.

REFERENCES

[1]O. Bjorneholm, J. N. Andersen, C. Wigren, and A. Nilsson, "Resonant photoemission at core-level shake-up thresholds: Valenc-band satellites in nickel," Physical Review B **41** (15), 10408-10412 (1990).
[2]L. C. Davis and L. A. Feldkamp, "New Mechansim for Resonant Photoemission," Physical Review Letters **44** (10), 673-676 (1980).
[3]W. Eberhardt and E. W. Plummer, "Angle-resolved photoemission determination of the band structure and multielectron excitations in Ni," Physical Review B **21** (8), 3245-3255 (1980).
[4]M. Iwan, F. J. Himpsel, and D. E. Eastman, "Two-Electron Resonance at the 3p Threshold of Cu and Ni," Physical Review Letters **43** (24), 1829-1832 (1979).
[5]B. W. Jepsen, F. J. Himpsel, and D. E. Eastman, "Single-step-model analysis of angle-resolved photoemission from Ni(110) and Cu(100)," Physical Review B **26** (8), 4039-4051 (1982).
[6]Y. Liu, Z. Xu, and P. D. Johnson, "Spin-orbit coupling, exchange interaction, and hybridization in the photoexcitation of the Ni 3p core level," Physical Review B **52** (12), R8593-R8596 (1995).
[7]M. F. Lopez, A. Gutierrez, C. Laubschat, and G. Kaindl, "Resonant 3p and 3s Core-Level Photoemission at the 2p Thresholds of Ni and Co Metal," Solid State Communications **94** (8), 673-676 (1995).
[8]Nils Martensson and Borje Johansson, "Valence-Band and Core-Level Satellites in Nickel and Related Elements," Physical Review Letters **45** (6), 482-485 (1980).
[9]Nils Martensson, Ralf Nyholm, and Borje Johansson, "Four-hole satellites in the L3VV Auger and the valenc-band spectra from nickel," Physical Review B **30** (4), 2245-2248 (1984).
[10]G. van der Laan, M. Surman, M. A. Hoyland, C. F. J. Flipse, B. T. Thole, U. Seino, H. Ogasawara, and A. Kotani, "Resonant photoemission at the Ni 2p core level as a probe of electron correlation effects in nickel," Physical Review B **46** (15), 9336-9340 (1992).
[11]H. Ueba, "Theory of core-hole-decay dynamics of adsorbates on metal surfaces: Role of the $2\pi^*$ level of a chemisorbed CO molecule," Physical Review B **45** (7), 3755-3768 (1992).
[12]Helena Tillborg, Anders Nilsson, and Nils Martensson, "Shake-up and shake-off structures in core level photoemission spectra from adsorbates," Journal of Electron Spectroscopy and Related Phenomena **62**, 73-93 (1993).
[13]D. Lovric and B. Gumhalter, "Extra-adsorbate screening in XPS of C 1s core levels of CO/Cu," Surface Science **278**, 108 (1992).
[14]Anders Nilsson, Helena Tillborg, and Nils Martensson, "Electronic Structure of Adsorbates from Core-Level Shake-up Spectra: N2/Ni(100)," Physical Review Letters **67** (8), 1015-1018 (1991).
[15]Anders Nilsson, "Core Level Electron Spectroscopy Studies of Surfaces and Adsorbates," Ph. D. Thesis, Uppsala University, 1989.
[16]J. Schirmer, G. Angonoa, S. Svensson, D. Nordfors, and U. Gelius, "High-energy Photoelectron C 1s and O 1s shake-up spectra of CO," Journal of Physics B: Atomic and Molecular Physics **20**, 6031-6040 (1987).
[17]J. C. Fuggle, E. Umbach, D. Menzel, K. Wnadelt, and C. R. Brundle, "Adsorbate Line Shpaes and Multiple Lines in XPS: Comparison of Theory and Experiment," Solid State Communications **27**, 63-69 (1978).
[18]W. R. A. Huff, Y. Zheng, Z. Hussain, and D. A. Shirley, "Final-State Effects in the Angle-Resolved Photoemission Extended Fine Structure of c(2x2)S/Ni(001)," Journal of Physical Chemistry **98**, 9182-9186 (1994).
[19]Z. Huang, Z. Hussain, W. R. A. Huff, E. J. Moler, and D. A. Shirley, Physical Review B **48**, 1696 (1993).
[20]S. Doniach and M. Sunjic, "Many-electron singularity in X-ray photoemission and X-ray line spectra from metals," Journal of Physics C: Solid State Physics **3**, 285-291 (1970).

This work was supported by the Director, Office of Energy Research, Office of Basic Energy Sciences, Chemical Sciences Division of the U.S. Department of Energy under contract No. DE-AC03-76SF00098.

Principal investigator: David A. Shirley, Ernest Orlando Lawrence Berkeley National Laboratory. Email: dshirley@lbl.gov.

First Observation of a Ferromagnetic-to-Paramagnetic Phase Transition on a Ferromagnetic Surface Using Spin-Polarized Photoelectron Diffraction

E.D. Tober[1,2], F. J. Palomares[2,3], R.X. Ynzunza[1,2],
Z. Wang[1,2], Z. Hussain[4], and C.S. Fadley[1,2]

[1]Department of Physics, University of California at Davis
Davis CA 95616 USA
[2]Materials Sciences Division, Lawrence Berkeley National Laboratory
Berkeley, CA 94720
[3]ICMM-CSIC, E-28049, Madrid, Spain
[4]Advanced Light Source, Lawrence Berkeley National Laboratory
Berkeley, CA 94720

INTRODUCTION

Spin-polarized photoelectron diffraction (SPPD) has been used previously by our group to study two antiferromagnetic surfaces ($KMnF_3$(011) and MnO(001)); these measurements provided evidence of a surface and/or short-range-order magnetic transition significantly above the bulk transition temperature [1]. We here report the first use of SPPD to study the order-disorder transitions on a ferromagnetic surface: Gd(0001). Prior work on Gd(0001) suggests that it is unusual in having a surface transition temperature that is 20-60 K above the bulk transition temperature [2], but there is still not total agreement on the existence of this effect and its origins. We have thus used the multiplet-split Gd 4s and Gd 5s photoelectron spectra as sources of spin-polarized photoelectrons to study this magnetic transition.

EXPERIMENT

The experiments were performed with the advanced photoelectron spectrometer/diffractometer [3a] on ALS beamline 9.3.2 [3b]. Photon energies of 120 eV and 565 eV were used to excite photoelectrons from the Gd 4s and 5s levels at kinetic energies of ~78 eV and ~189 eV, respectively. The two multiplet peaks present in both of these spectra correspond to low-spin ^7S and high-spin ^9S states of the final Gd^+ ion, and yield highly spin-polarized photoelectrons that are predominantly parallel (up) and anti-parallel (down), respectively, as measured with respect to the 4f spin of the emitting Gd atom. These spectra were measured as a function of temperature from 220K to 520K, thus spanning both the bulk Curie temperature T_{cb} = 293K and the supposed surface Curie temperature T_{cs} about 20-60K above this. Some example 5s and 4s spectra with a linear background subtracted are shown for several temperatures in Fig. 1, and small changes in the relative intensities of the two peaks with temperature of the order of a few % are evident there. Four different emission directions were studied in detail as a function of temperature: three for 5s emission, and one for 4s emission.

RESULTS AND DISCUSSION

The spin-up/spin-down intensity ratios in these multiplets are found to exhibit distinct and systematic changes as a function of temperature that are consistent with the existence of short-range magnetic order up to 60-80 K above the bulk Curie temperature. Some of these data, expressed as a normalized spin asymmetry, are shown in Fig 2. Denoting the spin-up intensity as I(up), the spin-down intensity as I(down), and their ratio at a given measurement temperature as

R(T) = I(up)/I(down), we define this asymmetry as A(T) (in %) = 100[R(T)-R(T_{max})]/R(T_{max}), where T_{max} is the highest temperature reached. For three of the cases shown in Fig. 2 ((a),(b), and (d)), there are distinct changes in the asymmetry over the full range of temperatures from T_{cb}

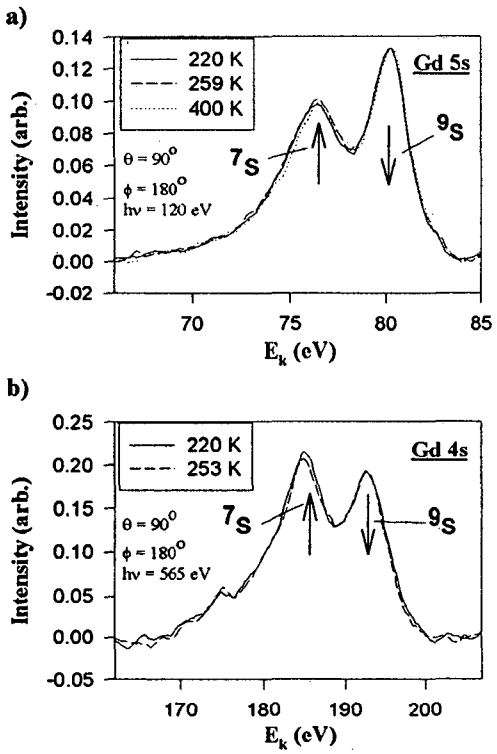

Figure 1. Photoelectron spectra taken at normal emission (θ = 90°) of (a) Gd 5s excited from Gd(0001) with hν = 120 eV and at three temperatures of interest: 220 K (solid line), 259 K (dashed line), and 400 K (dotted line). (b) Gd 4s excited with hν = 565 eV at two temperatures of interest: 220 K (solid line) and 253 K (dashed line). All spectra have had the inelastic background subtracted and are normalized to have equal ^{9}S intensity. A small peak due to N 1s appears at ~175 eV in (b); this corresponds to <0.01 ML of nitrogen on the surface.

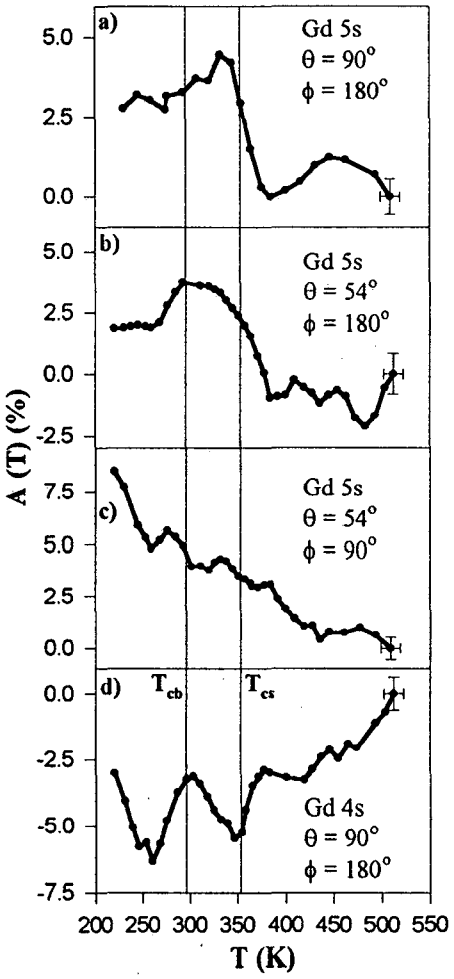

Figure 2. Experimental spin asymmetry A(T) derived from ^{7}S and ^{9}S intensity ratios as a function of temperature T for (a) Gd 5s emission along the normal (θ = 90°, φ = 180°, the "c" axis), (b) Gd 5s emission (θ = 54°, φ = 180°, along the "-b" axis), (c) Gd 5s emission (θ = 54°, φ = 90°, along the "a" axis), and (d) Gd 4s emission (θ = 90°, φ = 180°, along the "c" axis)

to what has been reported previously as T_{cs}. In the 5s results of (a) and (b), there is a broad peak with a sharp dropoff at ~375K; in the 4s results of (d) there are two distinct peaks very near the expected positions of T_{cb} and T_{cs}. For the fourth case in Fig. 2(c), no significant change in the asymmetry is observed, beyond a slow monotonic decrease as temperature is raised. Comparison of these results to theoretical calculations based on spin-dependent photoelectron scattering using a method proposed previously [1] also yields semi-quantitative agreement with

experiment: the magnitudes of the effects in Figs. 2(a), (b), and(d) are well predicted, as is the strong directionality that leads to a lack of a significant effect along the direction in Fig. 2(c).

An additional effect seen for the first time in our data is a temperature dependence in the energy separation of the two multiplet peaks. In particular, this separation in the 5s multiplet is found to decrease slightly (by ~20-60 meV out of 3.9 eV) on going through both T_{cb} and T_{cs}, with small dips being reproducibly seen near both temperatures for all three of the cases in Figs. 2(a)-(c). This effect also indicates the presence of two magnetic transitions, and suggests further the existence of interesting temperature- and spin- dependent configuration-interaction and/or electron-screening effects around the final Gd^+ ionic states. These effects will be studied more quantitatively in the future.

CONCLUSIONS

Our results thus confirm the existence of a surface or near-surface magnetic transition for Gd(0001) that occurs 60-80K above the bulk transition temperature, in agreement with, but slightly higher than, the temperatures reported in previous studies. This work also suggests the future utilization of both SPPD and multiplet peak separations for studying magnetic transitions on other ferromagnetic surfaces and interfaces.

REFERENCES

1. B. Sinkovic, B. Hermsmeier, and C. S. Fadley, Phys. Rev. Lett. 55, 1227 (1985); B. Hermsmeier, J. Osterwalder, D. J. Friedman, and C. S. Fadley, Phys. Rev. Lett. 62, 478 (1989); B. D. Hermsmeier, C. S. Fadley, M. O. Krause, J. Jiminez-Mier, P. Gerard, and S. T. Manson, Phys. Rev. Letters 61, 2592 (1988); B.D. Hermsmeier, J. Osterwalder, D. J. Friedman, T. Tran, and C. S. Fadley, Phys. Rev. B 42, 11895 (1990)
2. D. Weller, S. F. Alvarado, W. Gudat, K. Scröder, and M. Campagna, Phys. Rev. Lett. 54, 1555 (1985); B. Kim, A. B. Andrews, J. L. Erskine, K. J. Kim, and B. N. Harmon, Phys. Rev. Lett. 68, 1931 (1992); H. Tang, D. Weller, T. G. Walker, J. C. Scott, C. Chapert et al., Phys. Rev. Lett. 71, 444 (1993); C. Rau and M. Robert, Phys. Rev. Lett. 58, 2714 (1987);C. Rau, J. Mag. and Mag. Mat. 31-34, 874 (1983);C. Rau and S. Eichner, Phys. Rev. B 34, 6347 (1986) & in "Nuclear Methods in Materials Research", eds. K. Bethge, H. Burman, H. Jex, and F. Rauch (Viewig, Braunschweig, 1980), p. 354.
3. (a) C.S. Fadley, M.A. Van Hove, Z. Hussain, and A.P. Kaduwela, J. Elec. Spec. and Rel. Phen. 75, 273 (1995) and abstract by R.X. Ynzunza et al. elsewhere in this volume: (b) Z. Hussain, W. R. A. Huff, S. A. Keller, E. J. Moller, P. A. Heimann, W. McKinney, H. A. Padmore, C. S. Fadley, and D. A. Shirley, J. Elec. Spec. and Rel. Phen. 80, 401 (1996) and abstract by Z. Hussain et al. elsewhere in this volume.

Support for these studies was provided by the Director, Office of Energy Research, Div. of Basic Energy Sciences, Materials Sciences Div., of the U.S. Dept. of Energy, under Contract No. DE-AC03-76SF00098; the Office of Naval Research under Contract (N00014-94-0162); and the National Energy Research. Supercomputing Center.

Principal investigator: E.D. Tober, IBM Almaden Research Center, Dept. K11B, Bldg 080/D1-415B, 650 Harry Rd., San Jose, CA 95120. Email: tober@almaden.ibm.com. Telephone: (408)927-2243.

Full-Solid-Angle Photoelectron Diffraction from Bulk and Surface Atoms of Clean W(110)

R.X. Ynzunza[1,2], E.D. Tober[1,2], F.J. Palomares[1,3], Z. Wang[1,2], H. Daimon[1,4], Y. Chen[1]
Z. Hussain[1], M.A. VanHove[1], and C.S. Fadley[1,2]
[1]Lawrence Berkeley National Laboratory, Berkeley, CA 94720
[2]Department of Physics, University of California-Davis, Davis, CA 95616
[3]ICMM, CSIC, Cantoblanco E-28049, Madrid, Spain
[4]Department of Materials Physics, Osaka University, Toyonaka, Osaka 560, Japan

INTRODUCTION

We have studied the atomic structure of the clean W(110) surface by means of site-resolved scanned-angle W4$f_{7/2}$ photoelectron diffraction (PD) data obtained over nearly the full 2π solid angle above the surface. Prior to the availability of high-brightness sources such as the Advanced Light Source, such large high-resolution data sets were prohibitively time consuming to obtain. The well characterized W(110) system [1-5] was used as a reference case to check the accuracy of structure deteminations from such scanned-angle data via R-factor comparisons of experiment with theoretical multiple scattering calculations. The photoelectron kinetic energy of ~40 eV used was also lower than in many prior PD studies, providing further challenges to theory. The influence of various non-structural theoretical input parameters (e.g., scattering phase shifts, electron inelastic attenuation length, and inner potential) was thus also assessed. A final optimized structure is presented, together with comments on the future applications of this method.

EXPERIMENT

These experiments were performed on bend-magnet beamline 9.3.2 at the ALS [6(a)] using its advanced photoelectron spectrometer/diffractometer experimental station [6(b)].

The sample was prepared by an initial oxygen reduction at a temperature of 1200°C and a pressure of $1x10^{-7}$ torr O_2 to reduce the amount of carbon from the near-surface region. This was followed by repeated flashing at up to 2200 °C by electron bombardment heating. Sample cleanliness was then monitored by x-ray photoelectron spectroscopy (XPS), low energy electron diffraction (LEED), and most sensitively by the surface core level shift (SCLS) between the bulk and surface atoms, which reaches a maximum value of ~320 meV for a fully clean surface [1(b)]. Fig. 1 shows (a) the schematic experimental geometry and (b) a typical spectrum. For a given sample preparation, the actual data collection time was limited to 30 minutes to maintain adequate cleanliness. The base pressure during measurements was $1.3x10^{-10}$ torr.

The photoelectrons were excited by 70 eV linear-polarized light from a spherical-grating monochromator [6(a)]. This resulted in W 4$f_{7/2}$ photoelectrons at a kinetic energy of ~39-40 eV, as shown in Fig. 1(b). The angle between the incident radiation and the analyzer (which is in fact variable for this system [6(b)]), was for this experiment fixed at 70°. To enable the most accurate measurement of the bulk and surface peak intensities, individual spectra were obtained at each direction and stored for later analysis by peak fitting. Data were obtained over the nearly full 2π

solid angle above the surface by rotating the sample on two perpendicular axes for polar takeoff angle θ and azimuthal angle ϕ. The data consisted of twenty-eight azimuthal scans spanning takeoff angles with respect to the surface from 9° to 90° (=normal emission) and with 3° steps in takeoff angle. The azimuthal step size was adjusted with takeoff angle such that the final data set consisted of 892 spectra representing roughly equal solid-angle increments. Angles below 9° were not used due to the much lower count rates and thus longer counting times involved. Due to the symmetry of the crystal surface, only a 90° azimuthal scan is in principle needed to provide information on the full 360° intensity profile. However, to increase accuracy and average over any small sample misalignments, we collected data over 180° in azimuth, and then mirror-averaged this into a 90° sector that was finally used to generate full 360° representations of our data. At each direction, a W $4f_{7/2}$ photoelectron spectra was taken with a Scienta SES 200 hemispherical electrostatic spectrometer [6(b)]; the high luminousity of this spectrometer permitted taking a single high-resolution spectrum in ~20 seconds. Any variations of radiation flux with time were normalized out in determining the final intensities.

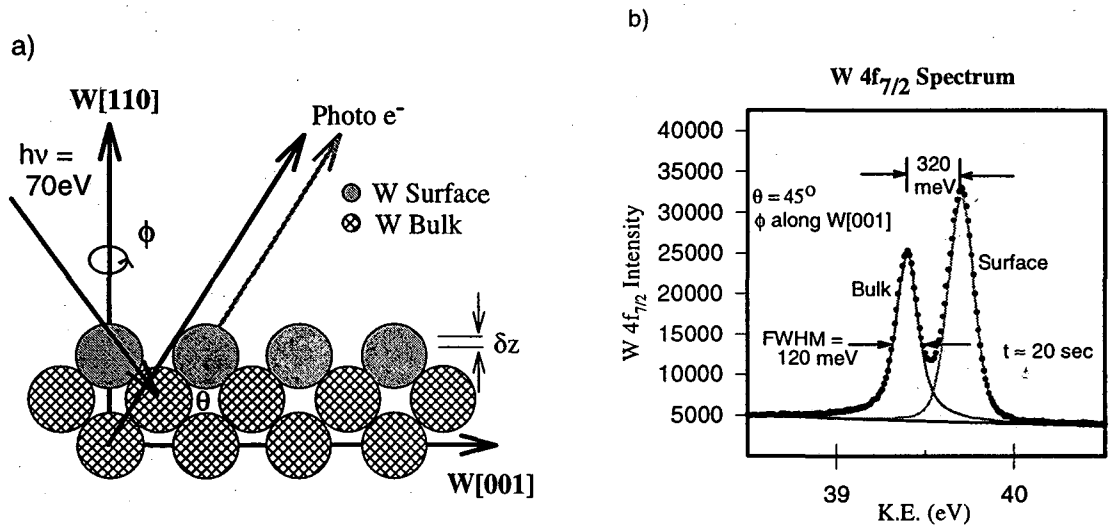

Figure 1. (a) A schematic of the experimental geometry, showing the two types of tungsten atom sites studied. (b) A W $4f_{7/2}$ photoelectron spectrum, showing the two component due to bulk atoms and surface atoms, with a surface core level shift (SCLC) between the two of 320 meV. Emission was at a takeoff angle with respect to the surface of $\theta = 45^{o}$ and an azimuthal angle of $\phi = 90^{o}$ (lying along the [100] direction in the W(110) surface).

RESULTS

The easily resolvable surface core level shift in Fig. 1(b) permits deriving site-specific photoelectron diffraction patterns from both the tungsten atoms in the surface layer and the tungsten atoms below the surface layer. The 39-40 eV kinetic energy range of the photoelectrons is also very near the minimum in their inelastic attenuation length, which we have estimated from an analysis of the takeoff-angle dependence of the surface/bulk intensity ratio [7] to be only 3.0-4.0 Å. This very small value enhances the surface contribution, making it stronger than that for the bulk in many emission directions, as illustrated in Fig. 1(b). Due to the different local

geometry around the two types of atoms, the bulk and the surface diffraction patterns are also strikingly different, as seen in the full-solid-angle patterns presented in Figs. 2(a),(c).

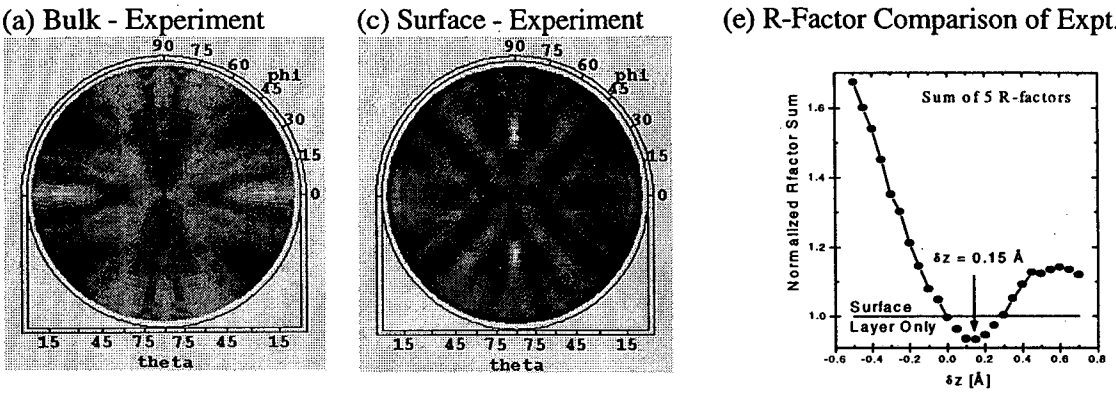

Figure 2. Full-solid-angle W4f$_{7/2}$ photoelectron diffraction patterns: (a) bulk-resolved experiment, (b) bulk theory for the optimum interlayer distance, (c) surface-resolved experiment, and (d) surface theory for the optimum interlayer distance. (e) R-factor comparison between experiment and multiple-scattering theory for the surface-atom W 4f$_{7/2}$ photoelectron diffraction pattern of Fig. 2(b). The curve represents a normalized sum of five R-factors defined in ref. 10(b). The horizontal line corresponds to an R-factor for calculations in which no bulk scatterers were present.

Multiple scattering diffraction calculations were performed using a program developed by Chen et. al. [8] and based on the previously-used Rehr-Albers approximation for treating the multiple scattering of photoelectrons [9]. Because of its high atomic number, tungsten is a very strong scatterer, particularly for low-energy electrons [9b]. Thus, several different sets of calculated scattering phase shifts were tried, along with variations in other non-structural parameters such as the electron attenuation length and the inner potential. Experiment was compared to theory via a set of 5 R-factors originally suggested for LEED analyses [10(a)] and later modified for PD analyses [10(b)]. The trial atomic geometries in theory involved a series of outward relaxations or inward contractions of the surface layer with respect to the second layer below, with the relevant distance being defined as δz (measured relative to the unrelaxed bulk interlayer distance). Fig. 2(e) shows the variation of a normalized sum of these five R-factors with δz. All five R factors are found to yield very nearly the same structure, with the overall conclusion being a small 0.15 ± 0.05 Å outward relaxation of the surface layer from its normal bulk termination. This is thus 6.7% of the bulk interlayer distance of 2.23 Å. The excellent final agreement between experiment and theory for surface emission is illustrated in Figs. 2(c) and (d). The analogous comparison for bulk emission in Figs. 2(a) and (b) shows good agreement, with further calculations for this more complex multi-layer emission problem still in progress. Another interesting aspect of the surface-atom analysis is that theory and experiment are in general in very good agreement if only the surface layer of scatterers is included in the calculation (i.e., if no bulk scatterers are present); this is represented by the horizontal line in Fig. 2(e). However, with a proper calculation including all scatterers, the influence of the bulk scatterers is evident: the minimum R-factors are slightly lower for the optimum geometry, and the values for interlayer distances more than about 0.7 Å away

from the optimum are significantly higher, such that the agreement decreases. Our final structural conclusion for this structure agrees with prior PD results by Jugnet et al. based on a much smaller data set , which show no relaxation to within ± 0.2Å [2]. Our structure is also in general agreement with prior LEED studies of this surface, which have reached conclusions varying from a small contraction of 0.07Å[3] to no relaxation at all [4,5].

CONCLUSIONS

This study thus has applied site-resolved full-solid-angle photoelectron diffraction to the well-defined test case of the clean W(110) surface, for which the surface and bulk diffraction patterns can be measured separately. Multiple scattering theory is found to provide an excellent description of the surface data, even at a low kinetic energy of ~40 eV, and R-factor comparisons of experiment and theory permit deriving structural information with an accuracy of ~±0.05 Å. Future applications of such large-scale site-resolved data sets to various surfaces and interfaces are thus promising.

REFERENCES

1. (a) Tran Minh Duc, C. Guillot, Y. Lassailly, J. Lecante, Y. Jugnet, and J.C. Vedrine, Phys. Rev. Lett., **43**, 789 (1979); (b) D.M. Riffe, G.K. Wertheim, and P.H. Citrin, Phys. Rev. Lett., **63**, 1976 (1989).
2. Y.Jugnet, N.S. Prakash, L. Porte, Tran Minh Duc, T.T.A. Nguyen, R. Cinti, H.C. Poon and G. Grenet, Phys. Rev. B, **37**, 8066 (1988).
3. M. Arnold, S. Sologub, G. Hupfauer, P. Bayer, W. Frie, L. Hammer, and K. Heinz (private communication).
4. M.A. Van Hove and S.Y. Tong, Surf. Sci. **54**, 91 (1976).
5. J.C. Buchholz, G.C. Wang, and M.G. Lagally, Surf. Sci. **49**, 508 (1975).
6. (a) Z. Hussain, W. R. A. Huff, S. A. Keller, E. J. Moller, P. A. Heimann, W. McKinney, H. A. Padmore, C. S. Fadley, and D. A. Shirley, J. Elec. Spec. and Rel. Phen. **80**, 401 (1996) and abstract by E.J. Moler et al. elsewhere in this volume. (b) C.S. Fadley, M.A. Van Hove, Z. Hussain, and A.P. Kaduwela, J. Elec. Spec. and Rel. Phen. **75**, 273 (1995) and abstract by R.X. Ynzunza et al. elsewhere in this volume.
7. C.S. Fadley, Prog. in Surf. Sci. **16**, 275 (1984).
8. H. Wu, Y. Chen, and D.A. Shirley, with subsequent improvements by Y. Chen.
9. (a) J.J. Rehr and R.C. Albers, Phys. Rev. B, **41**, 81139 (1990); (b) A.P. Kaduwela, D.J. Friedman, and C.S. Fadley, J. Elec. Spectrosc. and Relat. Phenom. **57**, 223 (1991).
10. (a) M.A. Van Hove, S.Y. Tong, and M.H. Elconin, Surf. Sci., **64**, 85 (1977); (b) R.S. Saiki, A.P. Kaduwela, M. Sagurton, J. Osterwalder, D.J. Friedman, and C.S. Fadley, Surf. Sci., **282**, 33 (1993).

This work was supported by the Director, Office of Energy Research, Office of Basic Energy Sciences, Materials Science Division, of the U.S. Department of Energy under Contract No. DE-AC03-76SF00098; ONR (Contract N00014-94-0162); and the National Energy Research Computing Center.

Principal investigator: R.X. Ynzunza, Dept. of Physics, UC Davis and Materials Sciences Division, Lawrence Berkeley National Laboratory. Email: ramon@photon.lbl.gov. Telephone: 510-486-4581.

Interface Structures of Ordered Fe and Gd Overlayers on W(110) from Site-Specific Photoelectron Diffraction

E. D. Tober[1,2],R. X. Ynzunza[1,2], F. J. Palomares[1,2,3], Z. Wang[1,2],
Z. Hussain[4], M. A. Van Hove[2], and C. S. Fadley[1,2]

[1]Department of Physics, University of California at Davis
Davis, CA 95616 USA
[2]Materials Sciences Division, Lawrence Berkeley National Laboratory
Berkeley, CA 94720
[3]ICMM-CSIC, E-28049, Madrid, Spain
[4]Advanced Light Source, Lawrence Berkeley National Laboratory
Berkeley, CA 94720 USA

INTRODUCTION

A key advantage of photoelectron diffraction (PD) as a surface structure probe is in permitting state-resolved or site-specific structural determinations via core level binding energy shifts [1]. This method has not been applied previously to metal-metal interfaces, and we here report site-specific and full-solid-angle photoelectron diffraction data from interface W atoms just beneath ordered (1x1) Fe and (7x14) Gd monolayers on W(110) [3]. These data were obtained by utilizing core level shifts in the W $4f_{7/2}$ spectrum. Shinn et al. [3] first observed interface core-level shifts (ICLS's) in W $4f_{7/2}$ photoelectron spectra from W(110) surfaces covered with one monolayer (ML) of Ni, Pt, or Fe in pseudomorphic (1x1) structures. In the case of (1x1) Fe, the W $4f_{7/2}$ spectrum consists of three components: one from the interfacial W layer shifted by -225 meV from the bulk position, another from what appears to be the second W layer shifted by -80 meV, and a third from the bulk W atoms situated below (which is found to remain at the same distance from the Fermi level as for the clean surface) [3]. In this study, we have examined both the pseudomorphic (1x1) Fe monolayer on W(110) [3] and the non-pseudomorphic (7x14) Gd monolayer on W(110), which forms a Moiré pattern with long-range order [4]. Comparison of our experimental data with multiple scattering calculations permits determining the Fe adsorption site and the relative interlayer spacing to the first and second W layers [2]. These Fe results are also compared to those from the very different Gd overlayer and from the clean W(110) surface which has recently been studied by Ynzunza et al. as a reference case [5].

EXPERIMENT

The PD measurements were performed with the advanced photoelectron spectrometer/diffractometer [6] situated on bend magnet beamline 9.3.2 of the ALS [7]. This system couples a high-resolution spherical grating monochromator to a high-resolution/high-luminosity Scienta SES-200 analyzer, and it is possible with it to acquire individual photoelectron W $4f_{7/2}$ spectra with both excellent statistics (~40,000 peak counts) and resolution (≤80 meV) in the short data acquisition times (~40 s/spectrum) required for large-scale PD measurements.

RESULTS

The W $4f_{7/2}$ photoelectron spectra for the clean W(110) surface, the (1x1) Fe-covered surface, and the (7x14) Gd-covered surface are shown in Figs. 1(a), (b), and (c), respectively. All of these spectra were obtained with $\theta = 45°$ as measured with respect to the surface and with ϕ pointing along the W [001] direction in the sample plane ($\phi = 90^{o}$ in our notation). For each of the three spectra, there exist two prominent peaks, one at higher E_b corresponding to emission from the bulk W atoms (or 2nd layer W atoms for the (1x1) Fe-covered surface) and a second at lower E_b due to emission solely from the top layer of W atoms (which can be at the free surface or at the metal-metal interface). In the case of the Fe or Gd covered surface, the PD effects associated with this lower E_b feature thus allow us to probe directly the local environment of the W atoms at the interface. The clean W(110) surface shift is measured to be -320 meV, while the ICLS's for the (1x1) Fe covered surface are -235 meV and -90 meV for the interface and the 2nd layer, respectively, in excellent agreement with prior measurements [3]. The ICLS for (7x14) Gd is -390 meV, a noteworthy result because this is the largest shift yet observed for surface or metal-metal interface atoms on W(110).

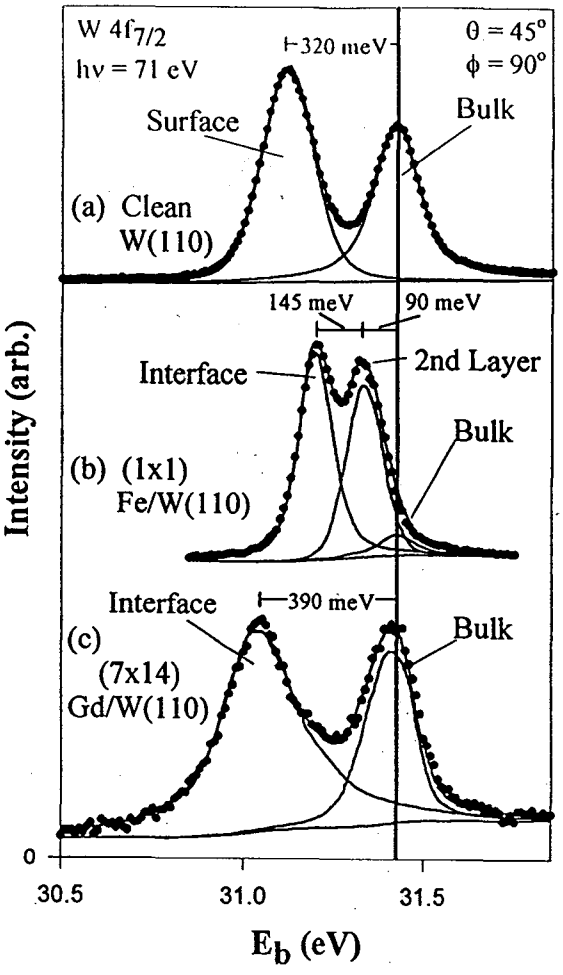

Figure 1. W $4f_{7/2}$ photoelectron spectra taken with $h\nu = 71$ eV, $\theta = 45°$, and ϕ along the W [001] azimuth from (a) the clean W(110) surface, (b) 1.2 ML of Fe in a(1x1) overlayer on W(110), and (c) 1.2 ML of Gd in a (7x14) Moiré structure on W(110).

Considering first the Gd overlayer, we note that prior STM and LEED results show that it consists of a hexagonal overlayer which is very close to Gd(0001) in atomic arrangement, with only a 1.2% expansion along W[001] and a 0.6% contraction along W[-110]. The resulting Moiré pattern or coincidence lattice forces the Gd into 24 different adsorption sites and leaves the underlying W interface atoms largely undercoordinated in 32 inequivalent emitter sites. Thus, the Gd to first order looks like a loosely bound overlayer capable of screening the core hole formed in W 4f emission, and this qualitatively explains the decrease in binding energy of the interface W atoms relative to the clean-surface W atoms. In addition, the multiplicity of adsorption sites and emitter types means that the Gd overlayer acts as a source of more or less diffuse background scattering, as far as the interface and bulk W atoms are concerned. Therefore, the W PD patterns with the Gd overlayer are not expected to be very different from those of the clean surface, and this is in fact what we observe. Figs. 2(a),(c),(f), and (g) show some individual azimuthal diffraction data which illustrate this point.

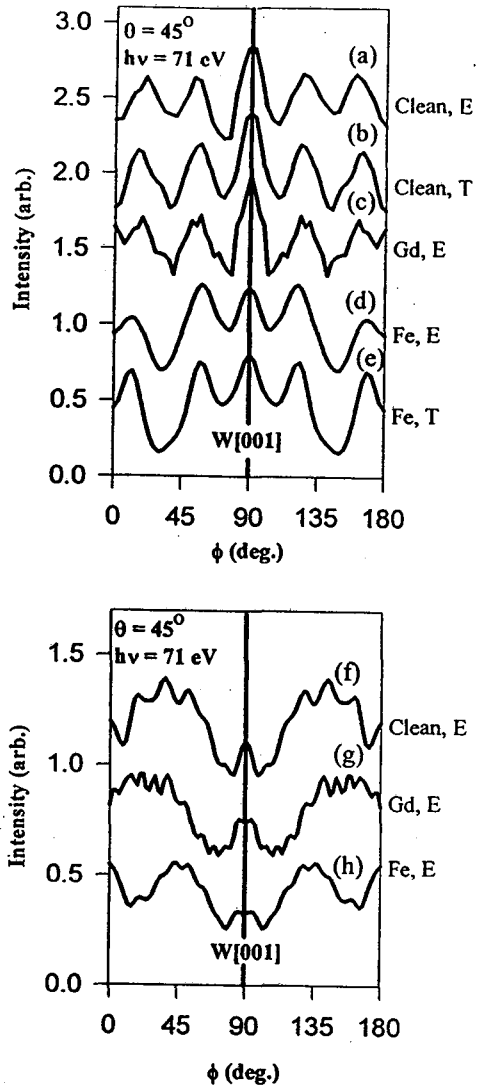

Figure 2. Single W $4f_{7/2}$ azimuthal scans taken with hν = 71 eV, and θ = 45° from (a) experiment for the -320 meV-shifted clean-surface peak; (b) theory for the clean surface peak in (a) (from ref. 4); (c) experiment for the -390 meV-shifted interface peak of (7x14) Gd/W(110); (d) experiment for the -225 meV-shifted interface peak of (1x1) Fe/W(110); (e) theory for the Fe/W case in (d), with Fe at the optimum positions in the twofold bridge site; (f) experiment for the clean W(110) bulk peak; (g) experiment for the bulk peak of (7x14) Gd/W(110); and (h) experiment for the 2nd layer peak of (1x1) Fe/W(110).

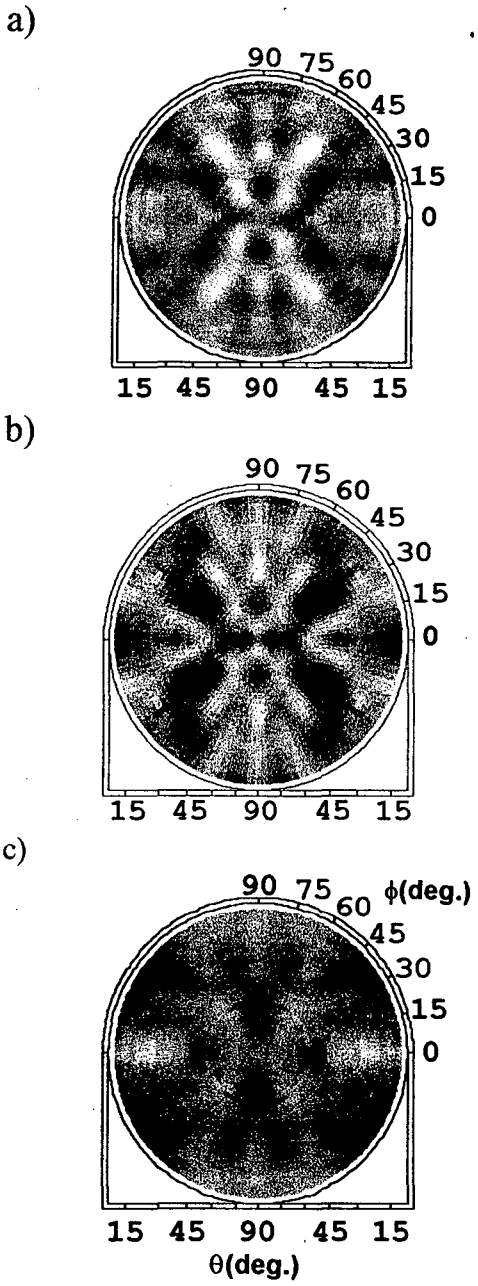

Figure 3. Full-solid-angle W $4f_{7/2}$ PD patterns for the (1x1) Fe/W(110) system taken from (a) experimental data for the -235 meV-shifted W interface peak, (b) theoretical multiple scattering calculations for the (1x1) Fe/W(110) interface with an optimized twofold bridge adsorption site for the Fe, and (c) experimental data for the -90 meV-shifted W 2nd-layer peak. The photoelectron kinetic energy outside the surface was E_k = 40 eV in all cases. The data shown span takeoff angles relative to the surface from 12° to 90°(normal emission), and the W(100) azimuth is toward the top of the page in each of these stereographic projections.

For the Fe overlayer however, the W atoms all have a definite coordination to the Fe, and the strength of the bond formed is illustrated by the considerable perturbation of both the interface and the second-layer W binding energies, as shown in Figs. 1(a) and (b). Full-solid-angle PD patterns were measured for this overlayer for both the interface and second-layer peak, and Figs. 3(a) and 3(c) show our results for these two cases, respectively. These data were analyzed by using R-factors to compare them to multiple scattering calculations for different atomic geometries in which both the Fe-W interface vertical distance (z_{12}) and the distance between the interface and second-layer W atoms (z_{23}) were varied to achieve the best fit to experiment. The best fit was found for Fe sitting in a two-fold bridge site which is equivalent to continuing the bulk W structure, with a distance $z_{12} = 2.17$ Å and a z_{23} corresponding to a slight expansion (~0.05 Å) relative to bulk W. The theoretical diffraction pattern for this optimized geometry is shown in Fig. 3(b).

CONCLUSIONS

The structure of a metal-metal interface ((1x1) Fe on W(110)) has thus been determined quantitatively for the first time by means of site-specific photoelectron diffraction. This study thus opens up the possibility of using such high-resolution site-specific photoelectron diffraction to study a variety of metal-metal interface systems.

REFERENCES

1. C.S. Fadley, S. Thevuthasan, A.P. Kaduwela, C. Westphal, Y.J. Kim, R. Ynzunza, P. Len, E.D. Tober, F. Zhang, Z. Wang, S. Ruebush, A. Budge, and M.A. Van Hove, J. Elec. Spec. and Rel. Phen. **68**, 19 (1994).
2. E. D. Tober, R. X. Ynzunza, F.J. Palomares, Z. Wang, Z. Hussain, M. A. Van Hove, and C. S. Fadley, submitted to Physical Review Letters.
3. N. D. Shinn, B. Kim, A. B. Andrews, J. L. Erskine, K. J. Kim, and T.-H. Kang, Mat. Res. Soc. Symp. Proc. **307**, 167 (1993)
4. E. D. Tober, R. X. Ynzunza, C. Westphal, and C. S. Fadley, Phys. Rev. B **53**, 5444 (1996)
5. R. X. Ynzunza, E.D. Tober, F.J. Palomares, Z. Wang, H. Daimon, Z. Hussain, M.A. Van Hove, and C.S. Fadley, in preparation, and see additional abstract in this volume.
6. C.S. Fadley, M.A. Van Hove, Z. Hussain, and A.P. Kaduwela, J. Elec. Spec. and Rel. Phen. **75**, 273 (1995).
7. Z. Hussain, W. R. A. Huff, S. A. Keller, E. J. Moller, P. A. Heimann, W. McKinney, H. A. Padmore, C. S. Fadley, and D. A. Shirley, J. Elec. Spec. and Rel. Phen. **80**, 401 (1996)

Support for these studies was provided by the Director, Office of Energy Research, Division of Basic Energy Sciences, Materials Sciences Division, of the U.S. Dept. of Energy, under Contract No. DE-AC03-76SF00098; the Office of Naval Research under contract (N00014-94-0162); and the National Energy Research Supercomputing Center at LBNL.

Principal investigator: E.D. Tober, IBM Almaden Research Center, Dept. K11B, Bldg 080/D1-415B, 650 Harry Rd., San Jose, CA 95120. Email: tober@almaden.ibm.com. Telephone: (408)927-1653.

Photoelectron Spectroscopy of Iodine-Covered Si(001)

W. K. Wang,[1] T.D. Liu,[1,2] H.-F. Lai,[1,2] J. A. Yarmoff,[1,2] A. A. Baski,[3] E. J. Moler,[4] J. Morais,[5,6] R. Denecke,[5,6] and C. S. Fadley[5,6]

[1]Department of Physics, University of California, Riverside, CA 92521
[2]Materials Sciences Division, Ernest Orlando Lawrence Berkeley Laboratory, Berkeley, CA 94720
[3]Department of Physics, Virginia Commonwealth University, Richmond, VA 23284
[4]Advanced Light Source, Ernest Orlando Lawrence Berkeley Laboratory, Berkeley, CA 94720
[5]Department of Physics, University of California, Davis, CA 95616
[6]Materials Sciences Division, Ernest Orlando Lawrence Berkeley Laboratory, Berkeley, CA 94720

The interactions of halogens with semiconductor surfaces are of interest in both fundamental physics and modern technology. In this study, the chemisorption of I_2 on Si(001)-2x1 is investigated using high-resolution soft x-ray photoelectron spectroscopy. A clean Si(001) surface was exposed in UHV to I_2 produced *in situ* from a solid-state electrochemical cell [1]. Photoelectron spectra were collected from the iodine-saturated surface as a function of both azimuthal and polar angles.

High-resolution Si 2p core level spectra indicate that I_2 dissociatively chemisorbs on Si(001) surface, forming SiI surface species. At saturation coverage, ~ 1 ML of iodine is adsorbed. These results imply that each Si surface atom is bonded to a single I atom. A 2¥1 LEED pattern was observed from the saturated surface, which indicates that the dimer bonds remain intact. All these observations are consistent with the results of ref. [2].

Core-level photoelectron diffraction is a very sensitive method for investigating surface geometrical structure [3,4]. Figure 1 shows three representative high-resolution Si 2p core-level spectra which were collected as a function of azimuthal angle. It is clearly seen that the relative SiI intensity is dependent on the angle. This dependence results from photoelectron diffraction, and the data therefore contain information on the detailed surface structure, such as the Si-I bond angle. Our next step will be to compare our results to multiple scattering calculations [5] in order to quantitatively determine the surface structural parameters.

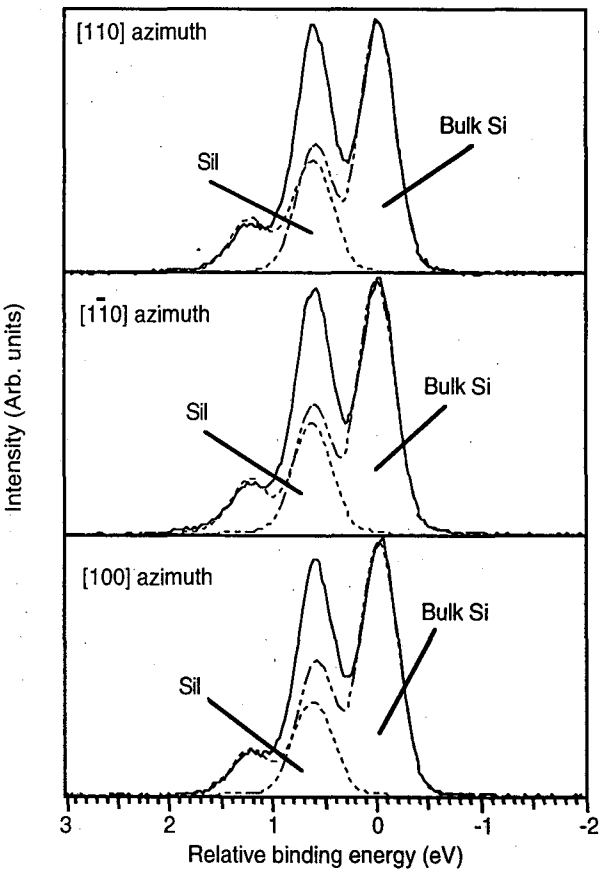

Figure 1. Comparison of Si 2p core-level photoelectron spectra collected from an I-saturated Si(001)-(2x1) surface at different azimuthal angles. All the data were collected with a photon energy of 150 eV. The incident photon and electron emission angles were both 45° from the surface normal

REFERENCES

1. N.D. Spencer, P.J. Goddard, P.W. Davies, M. Kitson and R.M. Lambert, J. Vac. Sci. Technol. A **1** (1983) 1554.
2. D. Rioux, F. Stepniak, R.J. Pechman and J.H. Weaver, Phys. Rev. B **51** (1995) 10981.
3. C.S. Fadley, M.A. Van Hove, Z. Hussain and A.P. Kaduwela, J. Elect. Spect. **75** (1995) 273.
4. E.L. Bullock, R. Gunella, L. Patthey, T. Abukawa, S. Kono, C. R. Natoli and L.S.O. Johansson, Phys. Rev. Lett. **74** (1995) 2756.
5. S. Gota, R. Gunnella, Zi-Yu Wu, G. Jezequel, C.R. Natoli, D. Sebilleau, E.L. Bullock, F. Proix, C. Guillot and A Quemerais, Phys. Rev. Lett. **71** (1993) 3387.

This work was supported by the Director, Office of Energy Research, Office of Basic Energy Sciences, Materials Sciences Division of the U.S. Department of Energy under Contract No. DE-AC03-76SF00098, and by the Army Research Office under Grant No. DAAH04-94-G-0410.

Principal Investigator: Jory A. Yarmoff, Department of Physics, University of California-Riverside. Telephone: 909-787-5336.

Spatial Structure Determination of ($\sqrt{3}$ x $\sqrt{3}$)R30° and (1.5 x 1.5)R18° CO on Cu(111) Using Angle-Resolved Photoemission Extended Fine Structure

Edward J. Moler[1], Scot A. Kellar[1], W. R. A. Huff[1],
Zahid Hussain[1], Yu Zheng[2], Eric A. Hudson[3], Yufeng Chen[4], David A. Shirley[4]

[1]Advanced Light Source, Lawrence Berkeley National Laboratory, Berkeley, CA 94720
[2]Qualop Systems Corp., 568 Weddell Drive, Suite 8, Sunnyvale, CA 94089
[3]Lawrence Livermore National Laboratory, Livermore, CA 94551
[4]Departments of Chemistry and Physics, The Pennsylvania State University, University Park, PA 16802

We report a study of the spatial structure of ($\sqrt{3}$ x $\sqrt{3}$)R30° (low coverage) and (1.5 x 1.5)R18° (intermediate coverage) CO adsorbed on Cu(111), using the Angle-Resolved Photoemission Extended Fine Structure (ARPEFS) technique at beamline 9.3.2 at the Advanced Light Source. The CO molecule adsorbs on an atop site for both adsorption phases. Full multiple-scattering spherical-wave (MSSW) calculations were used to extract the C-Cu bond length and the first Cu-Cu layer spacing for each adsorption phase. We find that the C-Cu bond length remains unchanged with increasing coverage, but the 1st Cu-Cu layer spacing contracts at the intermediate coverage. We calculate the bending mode force constant in the (1.5 x 1.5)R18° phase to be κ_δ=2.2 (1) x 10^{-12} dyne·cm/rad from our experimentally determined bond lengths combined with previously published infra-red absorption frequencies.

INTRODUCTION

The adsorption of carbon monoxide on transition-metal surfaces has been extensively studied, both experimentally[1-12] and theoretically[13-19], with the goal of gaining a basic understanding of the surface chemical bond. Experimentally determined spatial structures of CO adsorbates provide important tests of theoretical models for these systems. We have determined the carbon-copper bond length and the first copper-copper layer spacing for two different, well-ordered coverage phases of CO on Cu(111) using Angle-Resolved Photoemission Extended Fine Structure (ARPEFS)[20].

The ARPEFS structure determination technique is based on the oscillatory variation in the angle-resolved photoemission intensity from the core levels of near-surface atoms with the electron kinetic energy. It has been successfully used to study the local structure of adsorbed atoms and molecules and to determine the substrate layer relaxation[7,20-24]. The surface structure can be determined quantitatively by fitting the experimental data with multiple-scattering spherical-wave calculations[7,20,24,25].

SURFACE STRUCTURE DETERMINATION

The ARPEFS curves for both the ($\sqrt{3}$ x $\sqrt{3}$) R30° and (1.5 x 1.5) R18° overlayers are shown in Fig. 1. Their similarity suggests that the adsorption site is the same for both structures with only small differences in the interlayer spacings, in agreement with previous FT-IR and EELS results which indicate only one kind of adsorption site for these structures[8].

We have performed full Multiple Scattering Spherical Wave (MSSW) calculations to quantitatively extract the inter-layer spacing between the overlayer and substrate and between the near-surface substrate layers. The calculation program is based on the formalism of Rehr and Albers (RA)[25]. The best fit was defined by the conventional R-factor analysis[20].

The results of the MSSW calculations with lowest R-factor for each structure are shown in Fig. 1. The R-factor is 0.12 for both structures. The carbon-copper layer spacing for both structures were found to be the same, 1.91 Å. The first copper-copper layer spacing was found to be 2.07 Å and 2.01 Å for the ($\sqrt{3}$ x $\sqrt{3}$) R30° and (1.5 x 1.5) R18° overlayer structures, respectively. These derived parameters proved to be insensitive to the C-O bond-length and tilt.

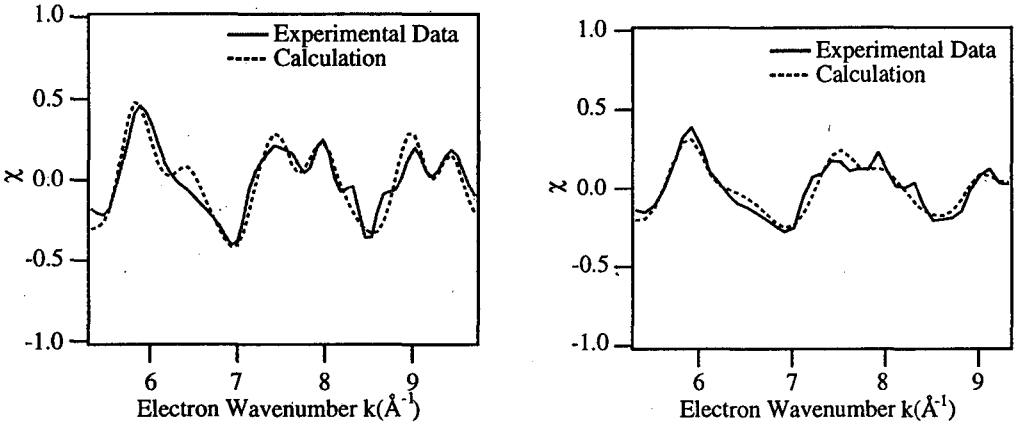

Figure 1. Comparison of experimental data and MSSW calculation for the low coverage (left) and intermediate coverage (right) of CO/Cu(111).

RESULTS AND DISCUSSION

The results of this work are summarized in Table I. The chi curve based on the atop adsorption site of the CO molecule with the carbon end down shows excellent agreement (R=0.12) between the MSSW calculations and the experimental data, confirming the previous findings for the two lowest-coverage phases[5,6,8,11,12]. The C-Cu bond length is the same for both coverages, 1.91 Å. The first copper-copper layer spacing does not show any change from the clean copper surface spacing of 2.07(2) Å[26] for the lower coverage ($\sqrt{3}$ x $\sqrt{3}$) R30° phase, within experimental uncertainty. There is a distinct contraction of the surface layer for the higher coverage (1.5 x 1.5) R18° phase to 2.01(4) Å.

LEED Structure	C-Cu Bond Length	First Cu-Cu Layer Spacing
clean Cu(111) metal	----------	2.07(2) Å ref 26
($\sqrt{3}$ x $\sqrt{3}$) R30°	1.91(1) Å	2.07(3) Å
(1.5 x 1.5) R18°	1.91(2) Å	2.01(4) Å

Table 1. Summary of experimentally determined structural parameters for CO/Cu(111)

The fact that the Cu-C bond length remains constant for both adsorption coverages while the 1st Cu-Cu layer spacing changes has interesting implications regarding the energetics and dynamics of the two overlayers. The difference in Gibbs free energy between the adsorbed state and the same state activated for desorption has been shown to have a dramatic increase with decreasing coverage between the (1.5 x 1.5) R18° and the ($\sqrt{3}$ x $\sqrt{3}$) R30° phases[11], while the change is less steeply sloped at lower and higher coverages. The coverage-dependent isosteric heat of adsorption also has a significant inflection in the region between the (1.5 x 1.5) R18° and the ($\sqrt{3}$ x $\sqrt{3}$) R30° phases, with a nearly constant values of 50 kJ/mole at lower coverages and 38 kJ/mole at higher coverages[6]. The authors of Reference 8 noted that this inflection could indicate the onset of a different adsorption site, but pointed out that this hypothesis did not explain why the heat of adsorption then remained constant throughout the high coverage region. Subsequent work showed that only atop species exist for these phases[8]. It has also been suggested that

competition for back-donated metal d-electrons may weaken the Cu-CO bond with increasing coverage[6]. Our results indicate that the Cu-CO bond does not weaken with greater coverage but that the changes in energy of adsorption are related to an adsorbate-induced contraction of the first substrate layer. There is little if any contraction of the first Cu-Cu layer up to a coverage of 0.33 monolayer. The onset of the inflections in the thermodynamic properties occur at approximately this coverage.

Hirschmugl, et. al. observed an IR adsorption band at ~285 cm^{-1} which was assigned to a bending (frustrated rotation) mode of the Cu-C-O complex in the (1.5 x 1.5) R18° structure. Calculation of the force constant of the bending-mode vibration, υ_2, of a linear molecule requires knowledge of the bond lengths between the atoms.Using our results and the frequency measurements of Hurschmugl, we can determine the bending mode force constant from the equations of Herzberg[5,27]. The values of the IR absorption frequencies for three isotopes as measured by Hirschmugl, et. al. are 285(8) cm^{-1}, 273(8) cm^{-1}, and 285(6) cm^{-1} for $^{12}C^{16}O$, $^{13}C^{18}O$, and $^{12}C^{18}O$, respectively. We find the force constant to be k_δ=2.2(1) x 10^{-12} dyne·cm/rad. The uncertainty was estimated by propagation of the experimental uncertainties[28].

CONCLUSION

We have determined the spatial structure of CO/Cu(111) for two coverages, characterized by (1.5 x 1.5) R18° and (√3 x √3) R30° LEED patterns, using ARPEFS. The CO molecule adsorbs on an atop site at both coverages with a C-Cu bond length of 1.91 Å, with an uncertainty of ±0.01 Å and ±0.02 Å for the two respective structures. The first Cu-Cu layer spacings were found to be 2.07 (3) Å and 2.01(4) Å for the (1.5 x 1.5) R18° and (√3 x √3) R30° structures, respectively. The bending mode force constants for the Cu-C-O complex in the (1.5 x 1.5) R18° structure is calculated from the bond-lengths and published IR absorption frequencies to be k_δ=2.2(1) x 10^{-12} dyne·cm/rad.

ACKNOWLEDGMENTS

We would like to thank the staff and management of the ALS at Lawrence Berkeley National Laboratory for their support and help with the experimental work.

REFERENCES

[1]S. Andersson and J. B. Pendry, "The structure of c(2x2) CO adsorbed on copper and nickel (001) surfaces," Journal of Physics C **13**, 3547-3561 (1980).
[2]H. Antonsson, A. Nilsson, and N. Martensson, "Vibrational Motion and Geometrical Structure in Adsorbed CO Studied by Core Level Photoelectron Spectroscopy," Journal of Electron Spectroscopy and Related Phenomena **54/55**, 601-613 (1990).
[3]A. M. Baro and H. Ibach, "New Study of CO adsorption at low temperature (90 K) on Pt(111) by EELS," Journal of Chemical Physics **71** (12), 4812-4817 (1979).
[4]J. E. Demuth and D. E. Eastman, "Photoemission Observation of Two Molecular Phases of CO Absorbed on Cu(100)," Solid State Communications **18**, 1497-1500 (1976).
[5]C. J. Hirschmugl, G. P. Williams, F. M. Hoffmann, and Y. J. Chabal, "Adsorbate-Substrate Resonant Interactions Observed for CO on Cu(100) and (111) in the Far-IR using Synchrotron Radiation," Journal of Electron Spectroscopy and Related Phenomena **54/55**, 109-114 (1990).
[6]P. Hollins and J. Pritchard, "Interactions of CO Molecules Adsorbed on Cu(111)," Surface Science **89**, 486-495 (1979).
[7]Z. Huang, "Structural Studies of Molecular Metallic Overlayers Using Angle-Resolved Photoemission Extended Fine Structure," Ph. D. Thesis, LBNL report LBL-33040, University of California, Berkeley, 1992.
[8]R. Raval, S. F. Parker, M. E. Pemble, P. Hollins, J. Pritchard, and M. A. Chesters, "FT-RAIRS, EELS and LEED Studies of the Adsorption of Carbon Monoxide on Cu(111)," Surface Science **203**, 353-377 (1988).

[9]A. Sandell, P. Bennich, A. Nilsson, B. Hernnas, O. Bjorneholm, and N. Martensson, "Chemisorption of CO on Cu(100), Ag(110), and Au(110)," Surface Science **310**, 16-26 (1994).
[10]A. G. Yodh and H. W. Tom, "Picosecond linear vibrational spectroscopy of CO adsorbed on Cu(111) by phase-sensitive polarization modulation," Physical Review B **45** (24), 302-307 (1992).
[11]W. Kirstein, B. Kruger, and F. Theime, "CO Adsorption Studies on Pure and Ni-covered Cu(111) Surfaces," Surface Science **176**, 505-529 (1986).
[12]B. J. Hinch and L. H. Dubois, "Time-Resolved EELS Studies of Molecular Surface Residence Times: the CO/Cu(111) Desorption System," Journal of Electron Spectroscopy and Related Phenomena **54/55**, 1990 (1990).
[13]C. Rong and C. Satoko, "Adsorption of N2, CO, and No on Fe(111) Surface: Model Calculation by DV-X-Alpha Method," Surface Science **223**, 101-118 (1989).
[14]J. Paul and A. Rosen, "Electronic Structure of CO adsorbed on a Cu(111) surface analyzed with molecular cluster models.," Physical Review B **26** (8), 4073-4077 (1982).
[15]A. C. Pavao, M. Braga, C. A. Taft, B. L. Hammond, and W. A. Lester, "Theoretical Study of the CO interaction with 3d-metal surfaces," Physical Review B **43** (9), 6962-6966 (1991).
[16]C. W. Bauschlicher, "A theoretical study of CO/Cu(100)," Journal of Chemical Physics **101** (4), 3250-3254 (1994).
[17]E. Miyoshi, Y. Sakai, and S. Katsuki, "A molecular orbital study for CO coadsorbed with K on Cu(001) and Ag(001)," Surface Science **242**, 531-537 (1991).
[18]M. A. Nygren and P. E. M. Siegbahn, "Theoretical Study of Chemisorption of CO on Copper Clusters," Journal of Chemical Physics **96**, 7579-7584 (1992).
[19]R. A. Van Santen, "Coordination of Carbon Monoxide to Transition-metal Surfaces," Journal of the Chemical Society, Faraday Transactions **81**, 1915-1934 (1987).
[20]J. J. Barton, C. C. Bahr, C. C. Robey, Z. Hussain, E. Umbach, and D. A. Shirley, "Adsorbate-geometry determination by measurement and analysis of angle-resolved-photoemission extended-fine-structure data: application to c(2*2)S/Ni(001)," Physical Review B **34** (6), 3807-3819 (1986).
[21]J. J. Barton, S. W. Robey, C. C. Bahr, and D. A. Shirley, "Surface Structure Determination with ARPEFS," in *The Structure of Surfaces(Springer Series in Surface Sciences)*, edited by M. A. Van Hove and S. Y. Tong (Springer Verlag, New York, 1985), Vol. 2, pp. 191-198.
[22]S. W. Robey, J. J. Barton, C. C. Bahr, G. Liu, and D. A. Shirley, "Angle-resolved-photoemission extended-fine-structure spectroscopy investigation of c(2x2) S/Ni(011)," Physical Review B **35** (3), 1108 (1987).
[23]K. T. Leung, L. J. Terminello, Z. Hussain, X. S. Zhang, T. Hayashi, and D. A. Shirley, "Surface-bonding geometry of (2x1)S/Ge(001) fby the normal-emission angle-resolved photoemission extended-fine-structure technique," Physical Review B **38** (12), 8241 (1988).
[24]L. Q. Wang, A. E. Schach von Wittenau, Z. G. Ji, Z. Q. Huang, and D. A. Shirley, "c(2x2) Cl/Cu(001) adsorbate geometry and substrate-surface relaxation using low-temperature angle-resolved photoemission extended fine structure," Physical Review B **44**, 8241 (1991).
[25]J. Rehr and Albers, "Scattering-matrix formulation of curved-wave multiple-scattering theory: Application to x-ray-absorption fine structure," Physical Review B **41** (12), 8139 (1990).
[26]J. M. MacLaren, J. B. Pendry, P. J. Rous, D. K. Saldin, G. A. Somorjai, M. A. Van Hove, and D. D. Vvedensky, *Surface Crystallographic Information Service: A Handbook of Surface Structures* (D. Reidel Publishing Company, Boston, 1987).
[27]G. Herzberg, *Molecular Spectra and Molecular Structure II. Infrared and Raman Spectra of Polyatomic Molecules* (Van Nostrand Reinhold Company, New York, 1945).
[28]P. R. Bevington, *Data Reduction and Error Analysis for the Physical Sciences* (McGraw-Hill, San Francisco, 1969).

This work was supported by the Director, Office of Energy Research, Office of Basic Energy Sciences, Chemical Sciences Division of the U.S. Department of Energy under contract No. DE-AC03-76SF00098.

Principal investigator: David A. Shirley, Ernest Orlando Lawrence Berkeley National Laboratory. Email: dshirley@lbl.gov.

The Structural Determination of Au(1ML)/Fe(15ML)/Au(100) Using Angle-Resolved Photoemission Extended Fine Structure

S.A. Kellar[1,2], W.R.A. Huff[1,2], E.J. Moler[1,2], Y. Chen[3], Z. Hussain[2], D.A. Shirley[3]

[1]Department of Chemistry, University of California, Berkeley, California 94720
[2]Advanced Light Source, Lawrence Berkeley National Laboratory, University of California, Berkeley, California 94720
[3]Departments of Chemistry and Physics, The Pennsylvania State University, University Park, Pennsylvania 16802

A great amount of attention has been given to investigating thin magnetic films and magnetic multilayers, especially systems involving iron and the noble metals[1-8]. In most of these studies the authors assume that the Fe layers will maintain bulk spacing even at interfaces. However, it is well known that for the clean metal the first and second layer spacing is contracted from the bulk value, and that absorbates can significantly expand this spacing[9-20]. Atomic structural details about these interfaces is important because the electronic states that are localized at the interface between the two different materials are critical in determining the magnetic properties of ultra-thin films and multilayers[21, 22]

In this study we use Angle-Resolved Photoemission Extended Fine Structure (ARPEFS) to investigate thin (*ca.* 10 and 15 monolayers) Fe films grown on a Au(100) single crystal. ARPEFS is a well established technique for determining the atomic structure of atomic and molecular adsorbates on metal surfaces[18, 19, 24-27]. The technique's advantages are its atomic selectivity due to the unique binding energies of core level electrons, the large oscillations, which in this study are ± 40%, and its inherent accuracy. In the past, structural determinations have only been done with ARPEFS signals from initial states with zero angular momentum because of the difficulties in treating non-s initial states in the scattering calculations. This study presents the first structure determination of a bimetalic system using the ARPEFS from non-s initial states. We report results from a new computer simulation and fitting procedure based on the Rehr and Albers formalism[28]. This program, developed by our group, uses second-order matrices (6x6) and up to eighth-order scattering to produce a convergent calculation at these electron energies and inter-atomic distances[29].

The experiment was performed at the Advanced Light Source (ALS) on the bend magnet beamline 9.3.2, which covers the photon energy range of 30 eV to 1500 eV. The system studied and reported here is for 15 monolayers (ML) of Fe grown on the Au(100) single crystal. Breaks in the slope of the Fe 3p photoemission intensity *vs.* evaporation time curves confirm the layer-by-layer growth reported by other authors (Fig. 1). Comparison of the Fe and Au photoemission intensities as well as sputtering studies confirm that the Fe layers grow with one ML of Au atoms, acting as a surfactant, on the top of the growing Fe layers.

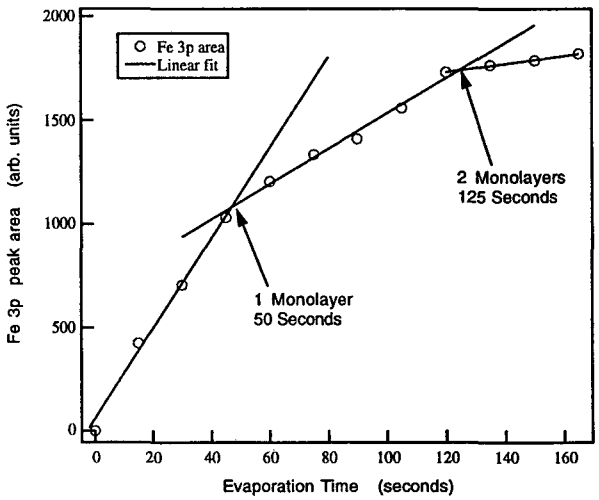

Figure 1. The Fe 3p photoemission intensity plotted against the Fe evaporation time. The breaks in the slope of the curve indicate layer-by-layer growth. One ML of Au atoms, acting as a surfactant, remains on top of the growing Fe layers. The LEED pattern is 1x1

We collected the ARPEFS intensity modulations, I(k), from the Au $4f_{7/2}$ core level along the normal and the 45° off-normal emission directions. This function I(k) has two components; a

slowly varying, atomic-like portion, $I_0(k)$, upon which is superimposed a rapidly oscillating beat pattern that arises from the interference between the primary wave propagating directly to the detector and waves which scatter elastically off nearby atomic potentials before reaching the detector. diffraction curves, $\chi(k)$ are obtained by removing the slowly varying $I_0(k)$ portion from I(k).

$$\chi(k) = \frac{I(k) - I_0(k)}{I_0(k)}$$

Figure 2. shows the experiemntal $\chi(k)$ curves.

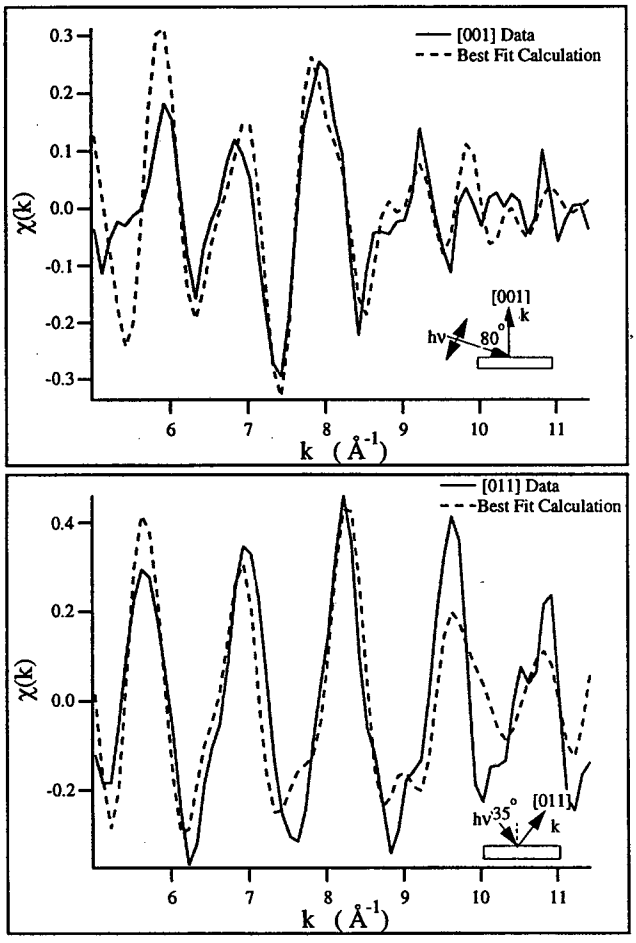

Figure 2. The Au $4f_{7/2}$ ARPEFS data from Au(1ML)/ Fe(15ML)/Au(100) collected along the [001] and [011] emission directions. Schematics of the experimental geometry are shown. Dashed lines are the best fit multiple scattering calculation results. The largest-amplitude oscillations in each curve arise from strong backscattering off the nearest-neighbor Fe atoms in the [001] and [011] directions, respectively. See Fourier transforms in Fig. 3.

The auto-regressive linear-prediction based Fourier transform (ARLP-FT), shown in Fig. 3, transforms the diffraction data from momentum space to real space[30]. In ARPEFS, the positions of the strong backscattering peaks in ARLP-FTs from adsorbate/substrate systems can be predicted with very good accuracy using the single-scattering cluster model together with the concept of strong backscattering from atoms located within a cone around 180° from the emission direction. The ARLP-FT peaks correspond to path-length differences between that component of the wave which propagates directly to the detector and those components which are first elasticly scattered by the atomic potentials. Analysis of the ARLP-FT provides information about the adsorption site as well as the bonding distance of the gold atoms. Figure 3 shows the ARLP-FT for Fe/Au(100)

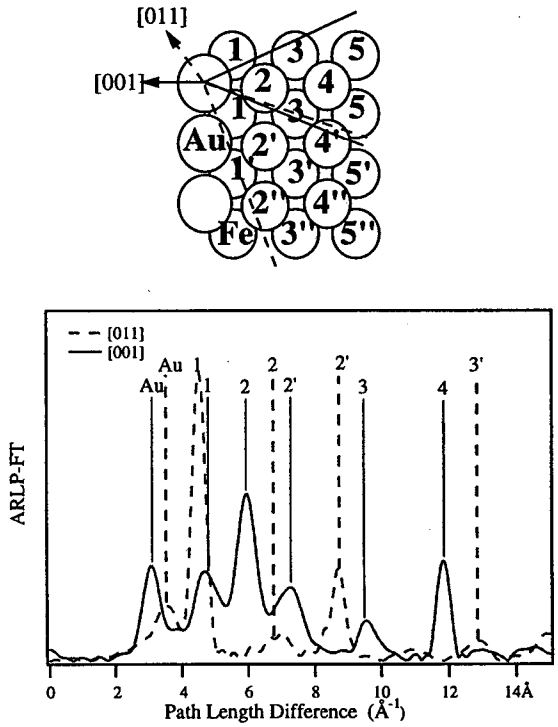

Figure 3. ARLP-FTs of the ARPEFS [001] data (solid line) and the [011] data (dashed line). A model of the lattice with the backscattering cones for each emission direction indicates the scattering atoms coresponding to the FT peaks. Note the excellent agreement between peak positions and calculated values.

The observed peaks in the ARLP-FT are most consistant with a structural model where the Au atoms sit in the four-fold hollow site, 1.6 Å above the surface plane of the bulk Fe. The ARLP-FT shows peaks corresponding to scattering events from as far away as the fourth iron layer.The fact that we see such long PLD is an indication of the qualitiy of the Fe films and the sharpness of the Fe-Au interface. The very good agreement between the predicted and the observed peaks in the ARLP-FT and the presence of sharp ARLP-FT peaks due to scattering from the fourth Fe layer, shows the Fe lattice to be very like the Fe bulk.

Fitting the experimental diffraction curves to a multiple-scattering model yields more precise structural parameters than that given by the Fourier analysis alone. Chen *et al.* recently developed a new multiple-scattering code, based on the Rehr-Albers formalism, which can model initial states with arbitrary angular momentum and which is fast enough to allow practical fitting to be done[28, 29].This calculation requires both structural and non-structural parameters. We used the structural parameters determined by the Fourier analysis as the initial guesses in the fitting procedure. The non-structural parameters include the initial-state angular momentum, the atomic scattering phase-shifts, the crystal temperature, the inelastic mean free path, the emission and light polarization directions, the electron analyzer acceptance angle, and the inner potential.

The best fits determine the Au-Fe1 spacing to be 1.67 Å, and the Fe1-Fe2, and the Fe2-Fe3 spacing to be that of the bulk iron, 1.43 Å, within the experimental error limits. It is interesting to note that this value is a slight expansion of interlayer spacings realatiave to the clean metal[31].

References

[1] F. Ciaccacci and S. D. Rossi, Physical Review B **51**, 11538-11545 (1995).

[2] E. Vescovo, O. Rader, J. Redinger, S: Blugel, and C. Carbone, Physical Review B**51**, 12418-12424 (1995).

[3] F. J. Himpsel, Physical Review B **44**, 5966-5969 (1991).

[4] J. M. Maclaren, M. E. McHenry, S. Crampin, and M. E. Eberhart, Journal of Applied Physics **67**, 5406-5411 (1990).

[5] S. D. Bader and E. R. Moog, Journal of Applied Physics **61**, 3729-3734 (1987).

[6] W. Gerts, Y. Suzuki, T. Katayama, K. Tanaka, K. Ando, and S. Yoshida, Physical Review B **50**, 12581-12586 (1994).

[7] Y.-L. He, Y.-F. Liew, and G.-C. Wang, Journal of Applied Physics **75**, 5580-5582 (1994).

[8] W. Heinen, C. Carbone, T. Kachel, and W. Gudat, Journal of Electron Spectroscopy and Related Phenomena **51**, 701-712 (1990).

[9] W. Arabczyk, H.-J. Müssig, and F. Storbeck, Surf. Sci. **251/252**, 804-808 (1991).

[10] W. Arabczyk, T. Baumann, F. Storbeck, H. J. Müssig, and A. Meisel, Surf. Sci. **189/190**, 190-198 (1987).

[11] S. R. Chubb and W. E. Pickett, Solid State Commun. **62**, 19-22 (1987).

[12] S. R. Chubb and W. E. Pickett, Phys. Rev. B **38**, 10227-10243 (1988).

[13] R. Imbihl, R. J. Behm, G. Ertl, and W. Moritz, Surf. Sci. **123**, 129-140 (1982).

[14] K. O. Legg, F. Jona, D. W. Jepsen, and P. M. Marcus, Phys. Rev. B **16**, 5271-5276 (1977).

[15] K. O. Legg, F. Jona, D. W. Jepsen, and P. M. Marcus, Surf. Sci. **66**, 25-37 (1977).

[16] R. S. Saiki, G. S. Herman, M. Yamada, J. Osterwalder, and C. S. Fadley, Phys. Rev. Lett. **63**, 283-286 (1989).

[17] S. Tang, A. J. Freeman, and G. B. Olson, Phys. Rev. B **47**, 2441-2445 (1993).

[18] X. S. Zhang, L. J. Terminello, A. E. S. v. Wittenau, S. Kim, Z. Q. Huang, Z. Z. Yang, D. A. Shirley, F. M. Tao, and Y. K. Pan, (Lawrence Berkeley National Laboratory, 1987).

[19] X. S. Zhang, L. J. Terminello, S. Kim, Z. Q.

Huang, A. E. S. v. Wittenau, and D. A. Shirley, J. Chem. Phys. **89**, 6538-6546 (1988).
[20] J. M. V. Zoest, J. M. Fluit, T. J. Vink, and B. A. V. Hassel, Surf. Sci. **182**, 179-199 (1987).
[21] A. J. Freeman and R. Wu, Journal of Magnetic Materials **100**, 497 (1991).
[22] L. H. Bennet and R. E. Watson, (World Scientific, Singapore, 1993).
[23] K. Totland, P. Fuchs, J. C. Groebli, and M. Landolt, Physical Review Letters **70**, 2487 (1993).
[24] J. J. Barton, S. W. Robey, and D. A. Shirley, Phys. Rev. B **34**, 778-791 (1986).
[25] J. J. Barton, C. C. Bahr, S. W. Robey, Z. Hussain, E. Umbach, and D. A. Shirley, Phys. Rev. B **34**, 3807-3819 (1986).
[26] Z. Huang, Ph.D. Thesis (University of California, Berkeley, 1992).
[27] W. R. A. Huff, Y. Zheng, and Z. Hussain, Journal of Physical Chemistry (1994).
[28] J. J. Rehr and R. C. Albers, Physical Review B **41**, 8139-8149 (1990).
[29] Y. F. Chen, W. Wu, and D. A. Shirley, (To be published).
[30] J. J. Barton, Ph.D. Thesis, (The University of California, Berkeley, 1985).

This work was supported by the Director, Office of Energy Research, Office of Basic Energy Sciences, Chemical Sciences Division of the U.S. Department of Energy under contract No. DE-AC03-76SF00098.

Principal investigator: David A. Shirley, Ernest Orlando Lawrence Berkeley National Laboratory. Email: dshirley@lbl.gov.

The Structure of Formate on TiO2(110) by Scanned-Energy and Scanned-Angle Photoelectron Diffraction

S. Thevuthasan,[1] Y.J. Kim,[1] G.S. Herman,[1] S.A. Chambers,[1] C.H.F. Peden,[1]
Z. Wang,[2,3] R.X. Ynzunza,[2,3] E.D. Tober,[2,3] J. Morais,[2] and C.S. Fadley[2,3]
[1]Pacific Northwest National Laboratory, Richland, Washington 99352, USA
[2]Ernest Orlando Lawrence Berkeley National Laboratory, Berkeley, California 94720, USA
[3]Department of Physics, University of California-Davis, Davis, California 95616, USA

INTRODUCTION

There is a considerable interest in understanding the interaction of small organic molecules with oxide surfaces. The chemistry of formate interactions with TiO_2(110) has been investigated by several groups [1-5], but there is little information on the structure of the adsorbate/surface complex. Recently we combined high-energy x-ray photoelectron diffraction (XPD) measurements at PNNL with low-energy scanned-angle and scanned-energy photoelectron diffraction measurements at the ALS to investigate the structure of the formate ion on TiO_2(110) in detail [6-8]. The high-energy XPD results reveal that formate binds through the oxygens in a bidentate fashion to Ti cation rows along the [001] direction with an O-C-O bond angle of about 126°. Low-energy photoelectron diffraction data, which is briefly described below, was used to identify the specific bonding geometry, including the bond length between the Ti cation and the oxygen in the formate.

EXPERIMENT

Low-energy photoelectron diffraction experiments were carried out on beam line 9.3.2 at the ALS. The end station at this beam line was equipped with a Scienta SES 200 hemispherical analyzer for collection of photoelectron spectra, along with a five-axis sample manipulator and in situ sample cleaning capabilities. A vacuum-reduced TiO_2(110) surface [2-4] was cleaned and ordered by cycles of light Ar^+ ion sputtering at 500 eV and annealing in oxygen at a pressure of $1x10^{-6}$ torr and a temperature of 900 K. 96% pure formic acid, purified by several freeze-pump-thaw cycles, was dosed onto the substrate at room temperature by backfilling the chamber to ~$2x10^{-7}$ torr with formic acid vapor from a liquid reservoir for 150 seconds. This leads to a saturation coverage of 0.5 ML of formate anions with respect to the exposed five-coordinate Ti^{+4} cations on the surface. Theoretical simulations were carried out using spherical wave single and multiple scattering cluster theory for select trial geometries [9] with the partial wave phase shifts being computed

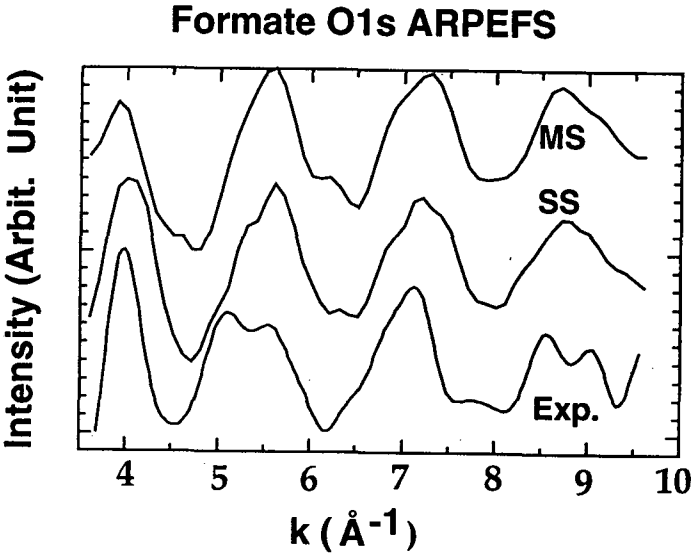

Fig. 1: Experimental formate O1s ARPEFS scan taken 10° off normal toward [001] with calculated scans using single scattering (SS) and multiple scattering (MS) for the cluster with the vertical distance between Ti and formate oxygen of Z=2.05 Å.

using the program FEFF [10]. The cluster size was 773 atoms (21 OCO moieties and 710 substrate atoms) for the single scattering calculations. The multiple scattering calculations were limited to a 230 atom wedge shaped cluster (18 OCO moieties and 176 substrate atoms) spanning only a 180° azimuthal angle range due to computer memory limitations.

RESULTS

Our ALS experimental results are summarized in Figs. 1 and 2. Fig. 1 shows the experimental formate O1s scanned energy photoelectron diffraction data, or angle-resolved photoemission fine structure (ARPEFS), after a four-point smoothing, along with the calculated single and multiple scattering intensities using the optimized cluster geometry. Hartree-Fock calculations predicted the bond length between the Ti cation and the formate O to be 2.05 Å [6]. Several geometries were considered with different Ti-O bond lengths in the single scattering calculations and the variation of the five distinct R-factors used [11] are shown in Fig. 3(a). From this analysis we can conclude that the R-factor minimum can be obtained for the vertical distance between the Ti cation and formate oxygen, Z, of 2.1±0.1 Å.

Experimental scanned-angle data for takeoff angles of 25°, 30°, and 35° are shown in Fig. 2, along with the calculated single and multiple scattering intensities using the optimized cluster geometry. Again, several geometries were considered for these calculations and a detailed R-factor analysis was carried out with single scattering. The R-factors for the three angles are summed and the average R-factors as a function of Z are shown in Fig. 3(b). In this case the R-Factors minimum can be obtained as 1.9±0.1 Å. The width of the R-factor minimum is larger in the scanned-angle results as compared to the ARPEFS data and the difference in the widths may be caused by the relatively high angular acceptance (±6°) of the analyzer. Overall we can conclude that the optimum Z would be 2.0±0.2 Å.

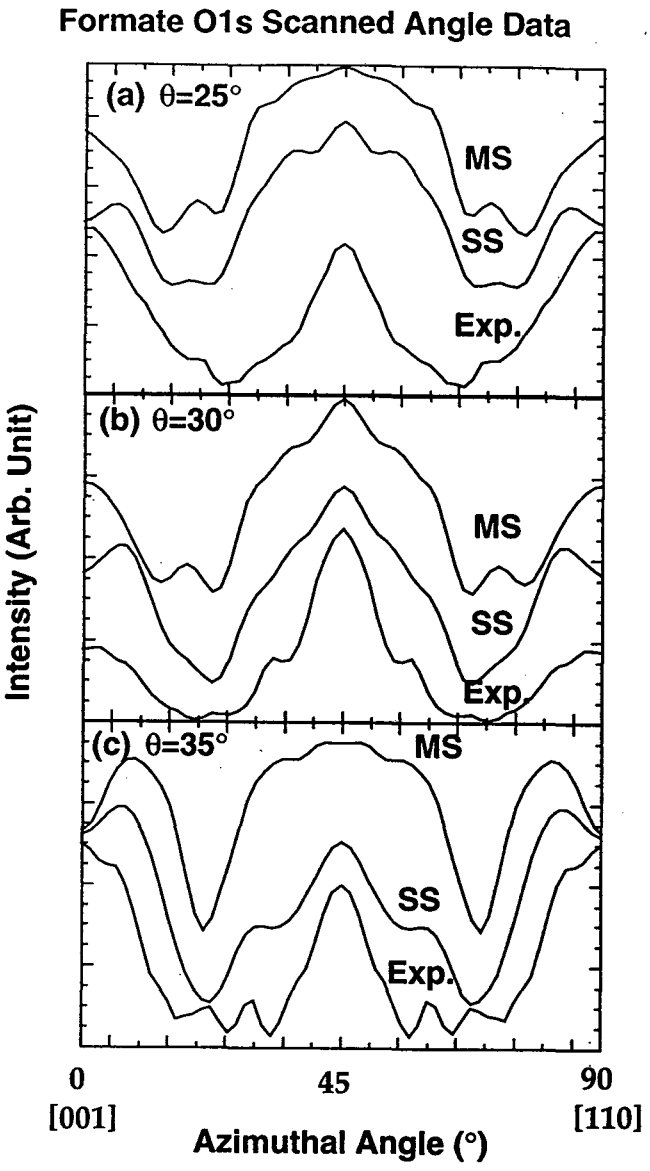

Fig. 2: Experimental azimuthal scans at an energy of 77 eV and takeoff angles of (a)θ=25°, (b)θ=30°, and (c) θ=35°, with the calculated scans using single scattering (SS) and multiple scattering (MS) for clusters with the vertical distance between Ti and formate oxygen of Z=2.05 Å.

CONCLUSIONS

In conclusion, we have used photoelectron diffraction to determine the chemisorption geometry of formate on TiO_2(110). The experimental scanned-energy and scanned-angle data agree very well with theoretical simulations and are in agreement for the adsorption site and the adsorbate-substrate bond length predicted by Hartree-Fock theory.

ACKNOWLEDGEMENTS

The authors gratefully acknowledge partial support from US Department of Energy, Office of Basic Energy Sciences, Materials Science Division under Contract Nos. DE-AC06-76RLO 1830 (PNNL) and DOE-AC03-76SF00098 (LBNL & UC Davis).

REFERENCES

[1] Also at University of California at Davis, Davis, CA 95616.
[2] Present address: IBM Almaden Research Center, San Jose, CA 95120

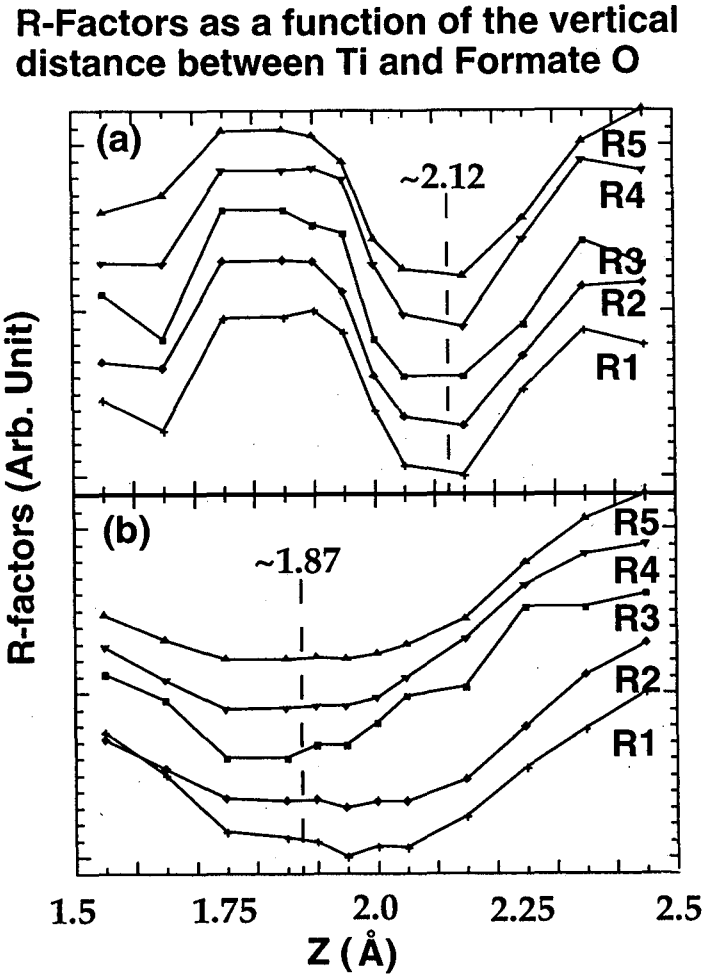

Fig. 3: The R-Factors as a function of the vertical distance (Z) between the Ti cation and the adsorbed formate oxygen: (a) scanned-energy, and (b) scanned angle.

1. H. Onishi, T. Aruga, and Y. Iwasawa, J. Catal. 146 (1994) 557.
2. K.S. Kim, M.A. Barteau, Langmuir 6 (1990) 1485.
3. M.A. Henderson, J. Phys. Chem. 99 (1995) 15253.
4. M.A. Henderson, J. Phys. Chem. 1996 submitted.
5. H. Onishi, and Y. Iwasawa, Chem. Phys. Lett. 226, (1994) 111.
6. S.A. Chambers, M.A. Henderson, Y.J. Kim, and S. Thevuthasan, Surf. Rev. Lett. (1996) to appear.
7. S.A. Chambers, S. Thevuthasan, Y.J. Kim, G.S. Herman, Z. Wang, E. Tober, R. Ynzunza, J. Morais, C.H.F. Peden, K. Ferris, and C.S. Fadley, Chem. Phys. Lett. (1997) to appear.
8. S. Thevuthasan, Y.J. Kim, G.S. Herman, S.A. Chambers, C.H.F. Peden, Z.Wang, R.X. Ynzunza, E.D. Tober, J. Morais, and C.S. Fadley, in preparation.
9. D.J. Friedman, and C.S. Fadley, J. Electron Spectrosc. Relat. Phenom. 51 (1990) 701; A. P. Kaduwela, D.J. Friedman, and C.S. Fadley, J. Electron Spectrosc. Relat. Phenom. 57 (1991) 223.
10. J. Mustre de Leon, J.J. Rehr, S.I. Zabinsky, and R.C. Albers, Phys. Rev. B44 (1991) 4146.
11. R.S. Saiki, A.P. Kaduwela, M.Sagurton, J. Osterwalder, D.J. Friedman, C.S. Fadley and C.R. Brundle, Surf. Sci. 282 (1993) 33.

Principal investigator: Scott A. Chambers, Pacific Northwest National Laboratory. Email: sa_chambers@pnl.gov. Telephone: 509-375-2220.

A Study of Angle-Resolved Photoemission Extended Fine Structure as Applied to the Ni 3*p*, Cu 3*s*, and Cu 3*p* Core Levels of the Respective Clean (111) Surfaces

W. R. A. Huff[1], Edward J. Moler[1], Scot A. Kellar[1],

Zahid Hussain[1], Yu Zheng[2], Eric A. Hudson[3], Yufeng Chen[4], David A. Shirley[4]

[1]Advanced Light Source, Lawrence Berkeley National Laboratory, Berkeley, CA 94720

[2]Qualop Systems Corp., 568 Weddell Drive, Suite 8, Sunnyvale, CA 94089

[3]Lawrence Livermore National Laboratory, Livermore, CA 94551

[4]Departments of Chemistry and Physics, The Pennsylvania State University, University Park, PA 16802

The first non-*s* initial state angle-resolved photoemission extended fine structure (ARPEFS) study of clean surfaces for the purpose of further understanding the technique is reported. The surface structure sensitivity of ARPEFS applied to clean surfaces and to arbitrary initial states is studied using normal photoemission data taken from the Ni 3*p* core levels of a Ni(111) single crystal and the Cu 3*s* and the Cu 3*p* core-levels of a Cu(111) single crystal. The Fourier transforms of these clean surface data are dominated by backscattering. Unlike the *s* initial state data, the *p* initial state data show a peak in the Fourier transform corresponding to in-plane scattering from the six nearest-neighbors to the emitter. Evidence was seen for single-scattering events from in the same plane as the emitters and double-scattering events.

Using a newly developed, multiple-scattering calculation program, ARPEFS data from clean surfaces and from *p* initial states can be modeled to high precision. Although there are many layers of emitters when measuring photoemission from a clean surface, test calculations show that the ARPEFS signal is dominated by photoemission from atoms in the first two crystal layers. Thus, ARPEFS applied to clean surfaces is sensitive to surface reconstruction. The known contraction of the first two Cu(111) layers is confirmed. The best-fit calculation for clean Ni(111) indicates an expansion of the first two layers.

To better understand the ARPEFS technique, we studied s and non-s initial state photoemission from clean metal surfaces. As expected, the Cu 3s $\chi(k)$ curve is roughly 180° out of phase from the Cu 3p $\chi(k)$ curve. The clean surface ARPEFS data resemble data for adsorbate systems, showing strong backscattering signals from atoms up to four layers below the source atoms. In addition to the backscattering, the Ni 3p data and Cu 3p data show a peak in the FT at ~2.5 Å corresponding to in-plane single-scattering of the photoemission wave

Although there were many layers of emitters in this clean surface study, the ARPEFS fitting process was sensitive to the surface relaxation. The spacing between the first two nickel layers is

2.09(1) Å which is a 3% expansion from the bulk nickel value. By contrast, the spacing between the first two copper layers is 2.06(5) Å which is a 1.5% contraction from the bulk copper value.

For the Cu(111) 3s and 3p fitting, the R-factor was minimized as a function of fe and qe. These contour plots indicate that the Cu 3p photoemission intensity is more directional than the Cu 3s photoemission intensity. This in turn indicates that the photoemission intensity from the Cu 3p core-levels must have mostly d-wave character.

To study the scattering processes in more detail, two types of test calculations were completed. A cluster with a single emitter adsorbed on a layer of scattering potentials was used to investigate the possibility of detecting double-scattering events directly in the FT. To this end, the Cu 3p test results were more convincing than the Cu 3s test results. A second test system used a ten-layer cluster and a single emitter moved successively through the first six layers. Although the signal from the deeper layers may modulate the high-frequency oscillation magnitudes slightly, the photoemission signal comes principally from the first two crystal layers.

It has been shown that photoelectron holography signals from clean surfaces are dominated by forward scattering, with atomic positions being imaged up to three layers ahead of the emitting atom. A combination of these two photoelectron diffraction techniques would therefore provide a very good method for studying ordered interfaces.

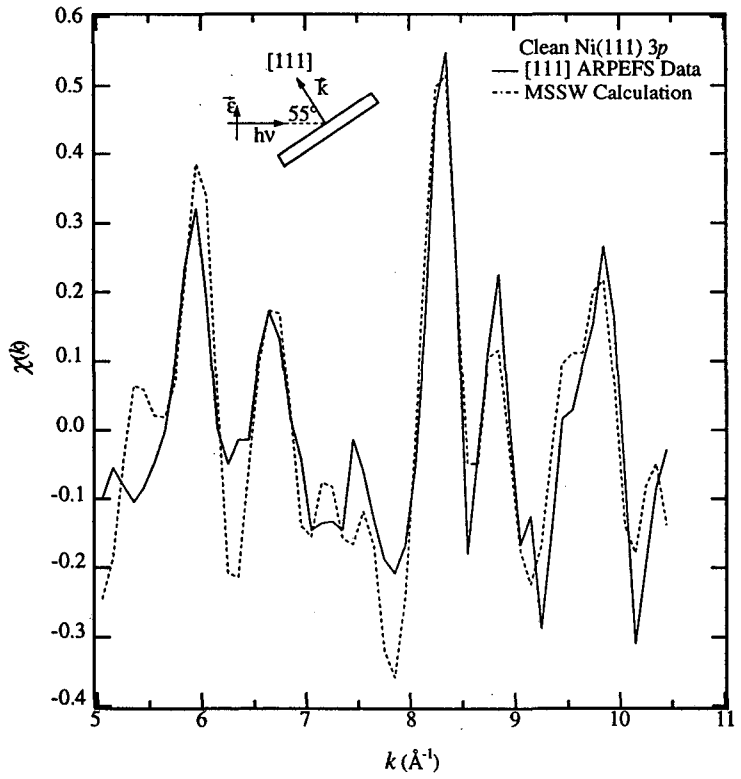

Figure 1: Ni(111) 3*p* ARPEFS $\chi(k)$ data (solid line) and best fit (dashed line). A schematic of the experimental geometry is shown.

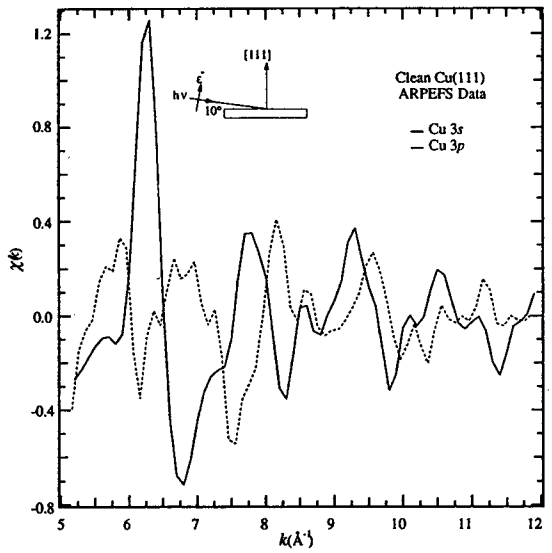

Figure 2. Ni(111) 3*p* ARPEFS $\chi(k)$ data (solid line) and best fit (dashed line). A schematic of the experimental geometry is shown.

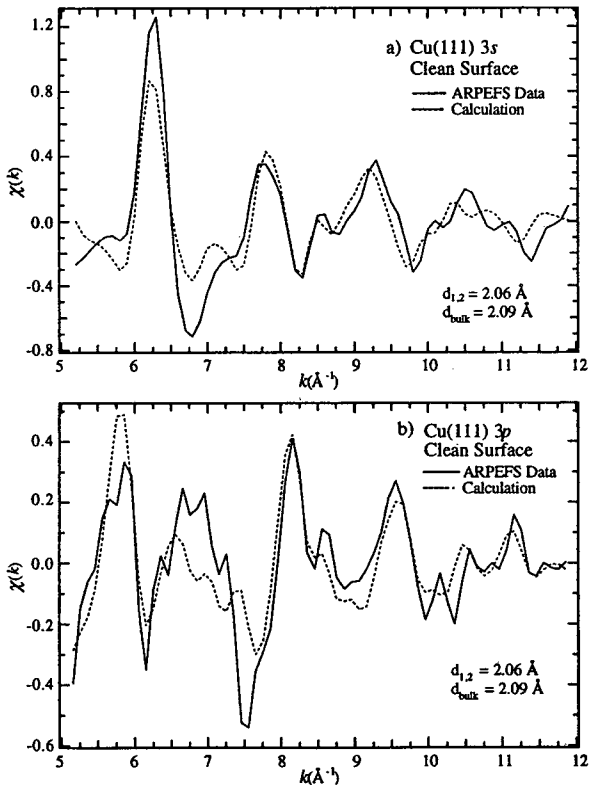

Figure 3. ARPEFS $\chi(k)$ data (solid line) and the MSSW best fit (dashed line) for a) Cu(111) 3*s* and b) Cu(111) 3*p*.

This work was supported by the Director, Office of Energy Research, Office of Basic Energy Sciences, Chemical Sciences Division of the U.S. Department of Energy under contract No. DE-AC03-76SF00098.

Principal investigators: Zahid Hussain, Ernest Orlando Lawrence Berkeley National Laboratory (Email hussain@lbl.gov, Telephone 510-486-7591); David A. Shirley, Ernest Orlando Lawrence Berkeley National Laboratory (Email dshirley@lbl.gov).

Study of the Oxidation of W(110) by Full-Solid-Angle Photoelectron Diffraction with Chemical State and Time Resolution

R.X. Ynzunza[1,2], F.J. Palomares[1,2,3], E.D. Tober[1,2], Z. Wang[1,2], J. Morais[1], R. Denecke[1,2], H. Daimon[1,4], Y. Chen[1], Z. Hussain[1] J. Liesegang[1,5], M.A. VanHove[1], and C.S. Fadley[1,2]
[1]Lawrence Berkeley National Laboratory, Berkeley, CA 94720
[2]Department of Physics, University of California-Davis, Davis, CA 95616
[3]ICMM, CSIC, Cantoblanco E-28049, Madrid, Spain
[4]Department of Materials Physics, Osaka University, Toyonaka, Osaka 560, Japan
[5]Department of Physics, La Trobe University, Bundoora 3083, Australia

INTRODUCTION

The brightness of third-generation synchrotron radiation from beamline 9.3.2 at the Advanced Light Source [1(a)] has been combined with the high-intensities and energy resolutions possible with its advanced photoelectron spectrometer/diffractometer experimental station [1(b)] in order to study the time dependence of the oxidation of the W(110) surface. This has been done via chemical-state-resolved core-level photoelectron spectroscopy and diffraction. This system has been studied previously by other methods such as LEED and STM [3-6], but several questions remain as to the basic kinetics of oxidation and the precise adsorption structures involved. By studying the decay and growth with time of various peaks in the W $4f_{7/2}$ photoelectron spectra, it should be possible to draw quantitative conclusions concerning the reaction kinetics involved. We have also measured full-solid-angle photoelectron diffraction patterns for the two oxygen-induced W states, and these should permit fully defining the different structures involved in this oxidation process.

RESULTS AND DISCUSSION

The surface of a clean W(110) surface at room temperature was reacted with oxygen at a pressure $3x10^{-9}$ Torr O_2; the base pressure in the chamber before beginning to leak in oxygen was $1.3x10^{-10}$ Torr. The W $4f_{7/2}$ spectrum taken for the clean W(110) surface at the onset of oxidation is shown in Fig. 1(a). This figure shows two well-resolved peaks, with a 320meV binding energy shift between them and the peak at higher kinetic energy (lower binding energy) being attributed to the top layer of tungsten atoms with no overlying adsorbate [2]. Spectra such as this were taken every 20 sec over a period of 70 min. Figs. 1(b) and (c) show later spectra taken at 35 min and 70 min. By 35 min., the surface peak is gone, indicating that the top layer of tungsten is completely covered by some first adsorption state(s) of hydrogen [2] and/or oxygen. There are two chemically shifted peaks, one at a higher binding energy with +350 meV shift relative to bulk that we assign to a first and more weakly bound chemisorbed species, and the other with a +730 meV that we assign to a second and more strongly bound "incipient-oxide-like" species. The 730 meV peak is found to persist up to a 1 monolayer (ML) oxygen coverage where, with oxidation at higher temperature and pressure, it forms a highly ordered (1x1)-(1x12) long-range structure as seen in both scanning tunneling microscopy (STM) [6] and low energy electron diffraction (LEED) [7]. Figs. 1(b) and (c) make it clear that the 350 meV state grows in first, but that the 730 meV state becomes dominant by the end of the time interval. Fitting peak shapes to this set of spectra now permits determining the quantitative time dependence of all four of the peak intensities observed, as shown in Fig. 1(d). From this figure, we can see that the decay of the surface peak occurs over the first 10-15 min., that it is accompanied by a growth of the bulk peak,

and that it is only after the 350 meV peak reaches a maximum at about 20-25 min. that the 730 meV peak begins to grow in, at the expense of the 350 meV peak. These results clearly suggest a linkage in the kinetics of these adsorption and oxidation processes. We are presently analyzing these first-of-a-kind data in order to derive a more precise kinetic model.

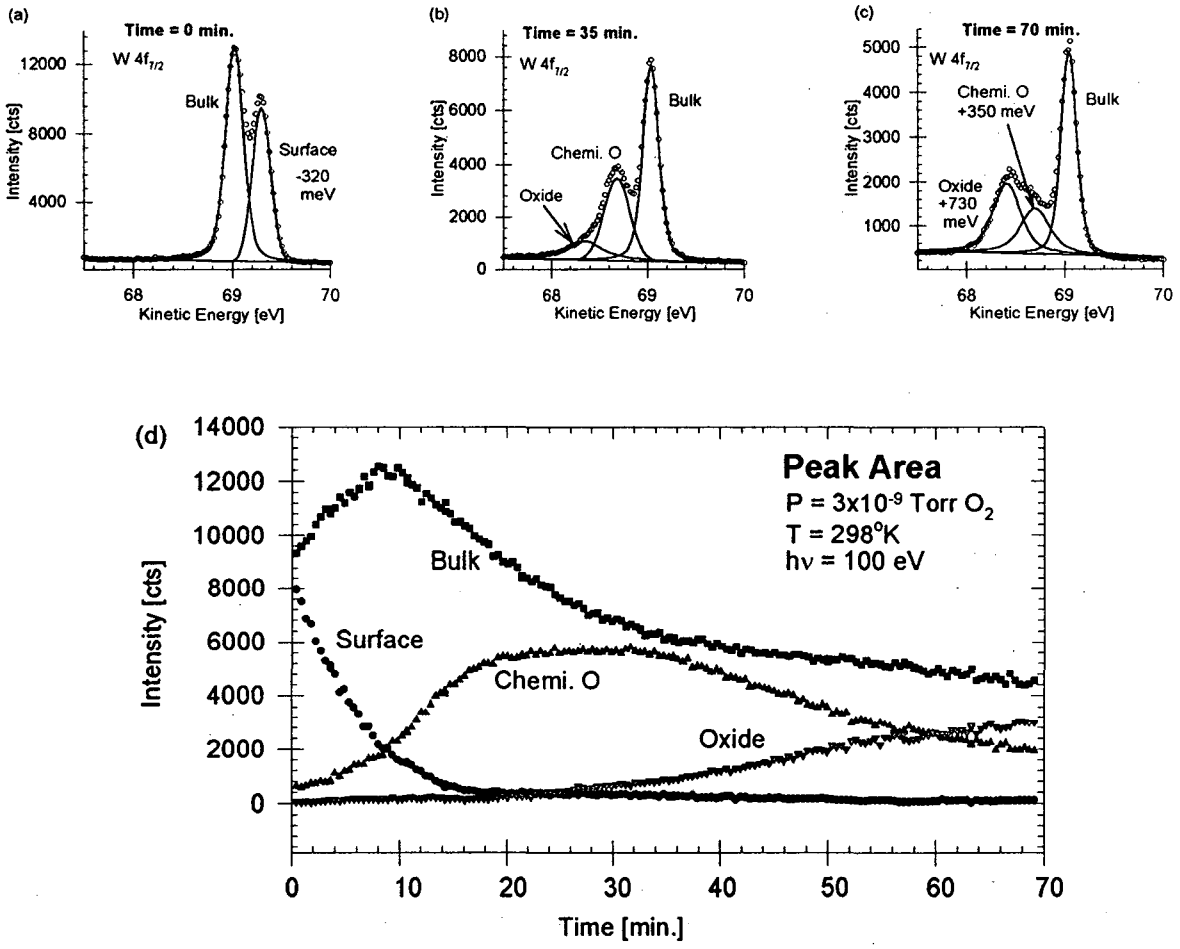

Figure. 1. Time and state resolved W $4f_{7/2}$ photoelectron spectra for a clean W(110) surface exposed to oxygen: (a) t = 0 min.--Initial clean surface showing the surface core level shifted peak at -320 meV with respect to bulk; (b) t = 35 min.--Surface after 35 min. exposure showing the two oxygen-induced peaks at +350 meV and +730 meV; (c) t = 70 min.--Final spectrum of the series after 70 min., showing the increase of the oxide peak at the expense of the chemisorbed oxide peak; (d) The time dependence of the four peaks observed in these spectra.

We have also measured full-solid-angle photoelectron diffraction patterns for both the chemisorbed and oxide peaks in the W $4f_{7/2}$ spectrum, with these then permitting a direct structural determination for the two W states involved. The structure of the oxide state at 730 meV has not been determined before, beyond the indication of a threefold adsorption site from STM [6(a)], although LEED has been used to determine the structure of what is probably the 350 meV state [6(b)]. The LEED pattern shows superstructure spots whose symmetry depends on the oxygen coverage and the heat treatment during and after adsorption [this work and 6(b)]. For our study, one monolayer of oxygen is deposited, so that, by the end of the exposure, the LEED exhibits a (1x1)-(1x12) pattern. We here discuss the results for the oxide peak at 730 meV associated with this (1x12) structure, with analysis for the other peak at 350 meV currently in progress. This oxide was formed in a purer state by doing a separate surface reaction at a pressure of $1.3x10^{-6}$ Torr of oxygen and a temperature of 700°C, a recipe used in a prior STM

study [6] and leading to a sharp (1x1)-(1x12) LEED pattern [7]. For this case, only a single oxide peak at 730 meV was observed, together with the bulk peak. The angle between the linearly-polarized incident radiation and the electron emission direction was fixed at 70°, with the sample being rotated on two perpendicular axes to obtain the full diffraction pattern. The excitation energies used were 127 eV and 170 eV, via third- and fourth- order light from the spherical grating monochromator on beamline 9.3.2 [1(a)]. We have measured ~900 W $4f_{7/2}$ spectra over nearly the full solid angle above the surface, spanning the takeoff angle range from θ = 9° to 90° (=normal emission) in 3° steps and the 180° azimuthal angle range from W [1-10] to [-110]. Fitting these spectra with appropriate peak shapes then permitted deriving separate diffraction patterns from each peak. The variation of radiation flux with time was normalized out in determining the final intensities. The experimental diffraction pattern for the oxide peak with 170 eV excitation is shown in Fig. 2(a).

The data in Fig. 2(a) have been analyzed by comparing experiment to theory via R-factors, with corollary structural information coming as well from a similar analysis of an experimental diffraction pattern obtained with higher-energy x-ray excitation at 1,487 eV [7]. The final optimum structure is for the oxygen in this incipient oxide structure to sit in a quasi-threefold hollow site on the W(110) surface, with an interlayer separation from the first W layer of 0.95 ± 0.05 Å and a W-O bond distance of 1.79 Å that is very close to that found in bulk W oxides. The final theoretical diffraction pattern for the best fit geometry is shown in Fig. 2(b), and it is in excellent agreement with experiment. Analysis of the data obtained with 127 eV excitation leads to a similar structural conclusion.

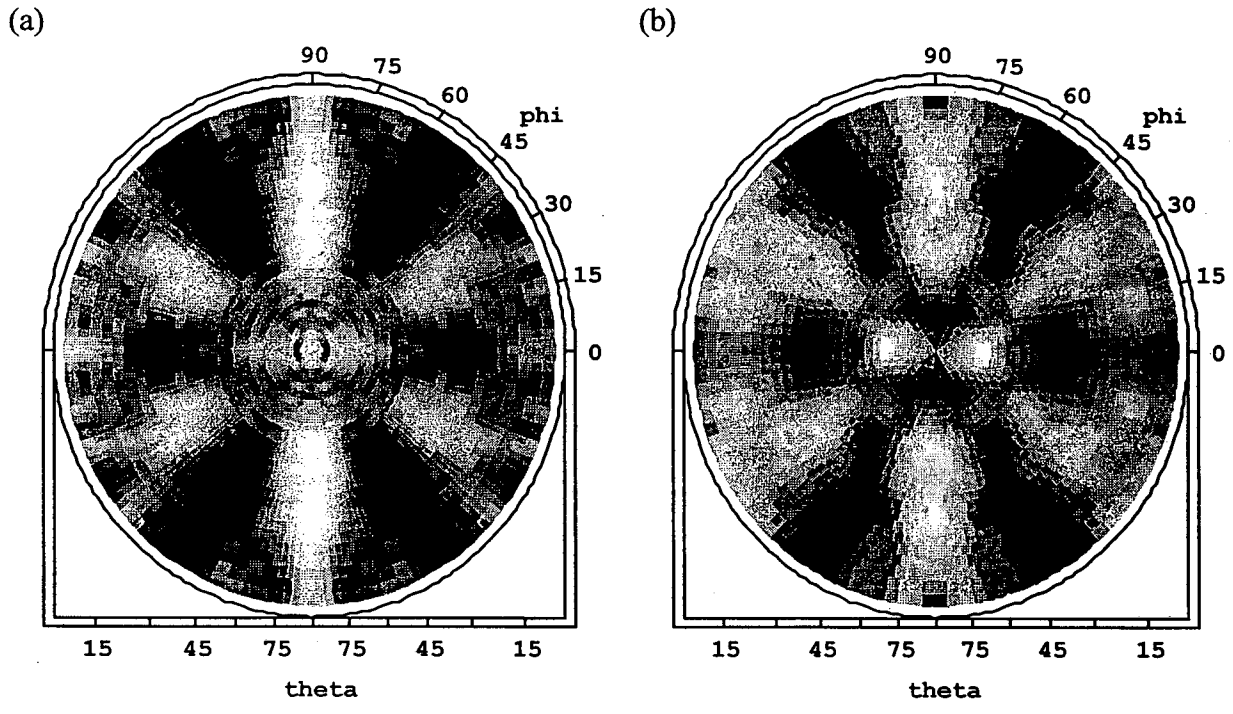

Figure 2. Full-solid angle diffraction from the top layer of atoms of O/W(110) (1x1)-(1x12); (a) experimental data; (b) multiple scattering theory with oxygen atoms occupying the threefold hollow sites at a bond distance of 1.79 Å, and an interlayer distance of 0.95 Å.

CONCLUSIONS

This study thus demonstrates the considerable potential of time and chemical-state resolved photoelectron spectroscopy at a third-generation synchrotron radiation source for studying surface reaction kinetics, as illustrated for the four-state system involved in the oxidation of clean W(110). Being able to simultaneously use photoelectron diffraction to determine the local atomic geometries around species with different chemical states, as illustrated here for the incipient oxide state in the O/W(110) system, represents another unique capability that should be broadly applicable to various surface reactions and epitaxial growth processes.

REFERENCES

1. (a) Z. Hussain, W. R. A. Huff, S. A. Keller, E. J. Moler, P. A. Heimann, W. McKinney, H. A. Padmore, C. S. Fadley, and D. A. Shirley, J. Elec. Spec. and Rel. Phen. **80**, 401 (1996) and abstract by E.J. Moler et al. elsewhere in this volume. (b) C.S. Fadley, M.A. Van Hove, Z. Hussain, and A.P. Kaduwela, J. Elec. Spec. and Rel. Phen. **75**, 273 (1995) and abstract by R.X. Ynzunza et al. elsewhere in this volume.
2. (a) Tran Minh Duc, C.Guillot, Y.Lassailly, J.Lecante, Y.Jugnet, and J.C. Vedrine, Phys. Rev. Lett., **41**, 1425 (1978); (b) D.M. Riffe, G.K. Wertheim, and P.H. Citrin, Phys. Rev. Lett., **63**, 1976 (1989).
3. L.H. Germer and J.W. May, Surf. Sci. **4**, 452 (1966).
4. E. Bauer, Surf. Sci. **7**, 351 (1967).
5. E. Bauer and T. Engel, Surf. Sci. **71**, 695 (1978).
6. (a) K.E. Johnson, R.J. Wilson, and S. Chiang, Phys. Rev. Lett. **71**, 1055 (1993); (b) M.A. Van Hove and S.Y. Tong, Phys. Rev. Lett. **35**, 1092 (1975).
7. H. Daimon, J. Palomares, R.X. Ynzunza, and C.S. Fadley, unpublished.

This work was supported by DOE, OER, BES, Mat. Sci. Div. (Contract DE-AC03-76SF00098), ONR (Contract N00014-94-1-0162), and the National Energy Research Supercomputer Center.

Principal investigator: Ramon Ynzunza, UC Davis Dept. of Physics, and MSD, Lawrence Berkeley National Laboratory. Email: ramon@photon.lbl.gov. Telephone: (510) 486-4581.

The Surface Structure of (1x1)O/W(110)x12 Determined by Angle-Resolved Photoemission Extended Fine Structure

S.A. Kellar[1,2], W.R.A. Huff[1,2], E.J. Moler[1,2], R. Ynzunza[3], Z. Xin[2,4], Y. Chen[2,4], C.S. Fadley[2,3], Z. Hussain[2], D.A. Shirley [4]

[1]Department of Chemistry, University of California, Berkeley, California 94720

[2]Advanced Light Source, Lawrence Berkeley National Laboratory, University of California, Berkeley, California 94720

[3]Department of Physics, University of California, Davis, California 95616

[4]Departments of Chemistry and Physics, The Pennsylvania State University, University Park, Pennsylvania 16802

Oxygen adsorption on tungsten is one of the earliest and most studied model adsorption systems[1]. Researchers have identified multiple coverage-dependent phases on the W(110) face [2,3]. The three ordered phases are the (2x1) with a coverage of $\theta = 0.5$ monolayer (ML), the (2x2) with $\theta = 0.75$ ML, and the (1x1) with $\theta = 1.0$ ML. The higher coverage phases are considered to be two-dimensional oxides with the oxygen arranged along the close-packed substrate directions. Previous researchers found that annealing these high-coverage phases led to additional superstructures in LEED[2]. These additional LEED spots were interpreted as due to a compressed "misfit" oxygen overlayer[2]. This structure would be extremely difficult to determine with a diffraction technique like Angle-Resolved Photoemission Extended Fine Structure (ARPEFS), because of the number of different scattering geometries. Recently however, using scanning tunneling microscopy (STM), Chiang *et al.* showed that these high-order diffraction spots were instead due to very regularly spaced domain walls[4]. These walls separate domains where the oxygen adsorption site switches from the left side to the right side of the unit cell. This configuration leads to domain walls which alternated between higher oxygen concentration and lower concentration than the rest of the surface. Figure 1 shows an illustration of these domain walls as well as the high-symmetry adsorption sites. The distance between the walls is *ca.* 10 atomic units[4]. Fadley *et al.* labeled this LEED structure [(1x1)O/W(110)]x12[5].

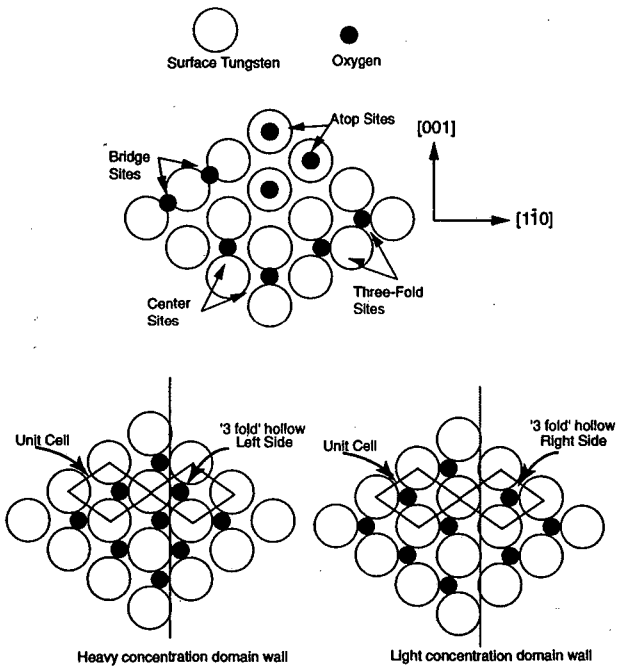

Figure 1. Top panel: Surface structure of the (1x1) O/W(110) showing possible high-symmetry adsorption sites. The bottom panel shows the oxygen atoms adsorbed into the quasi-threefold hollow site. The site exchange domain walls were proposed by Chiang *et al.* to explain the additional LEED superstructure seen when the (1x1)O/W(110) surface is annealed. The adsorption site exchange leads to alternating domain walls with light or heavy oxygen concentration. The LEED pattern for this structure is 12x1

While the STM study showed the origin of these higher-order diffraction spots,

no detailed atomic-structural study has been done for this system to date. In the present study we use Angle-Resolved Photoemission Extended Fine Structure (ARPEFS) to determine the adsorption site and local atomic structure of [(1x1) O/W(110)] x 12. ARPEFS is a well established technique for determining the atomic structure of atomic and molecular adsorbates on metal surfaces[6-12]. The technique's advantages are its elemental selectivity through the binding energies of core level electrons, the large oscillations in intensity, and its inherent accuracy.

These experiments were performed at the Advanced Light Source (ALS) on beamline 9.3.2, a bend magnet beamline with a spherical grating monochromator (SGM). Three gratings span an energy range from 30 eV to 1200 eV, with a maximum resolving power, $E/\Delta E$ = 10,000[13].

The (1x1)x12 oxide preparation method is from Diamon[15]. After the cleaning process, the crystal is warmed to 1000 K and exposed to 2 x 10^{-6} Torr of O_2 for 11 minutes 40 seconds. The resulting LEED pattern is 1x1 with extra superstructure diffraction features. These higher-order spots align along the $[1\bar{1}3]$ direction. After the sample preparation, the crystal was still free from carbon or sulfur contamination and will remain so for literally days due to the passivation of the surface by the oxygen. The ARPEFS data were taken on this surface structure at room temperature. During the data collection the crystal was oriented such that the polarization vector, ε, of the synchrotron radiation was along the <001> azimuth. The photoemission spectra were taken at two different angles, normal emission and 45° from normal emission along the <001> azimuth. In the rest of this paper we will describe these directions as normal emission and off-normal emission, respectively.

We collected the ARPEFS intensity modulations, I(k), from the O 1s core level along the normal and the 45° off-normal emission directions. This function I(k) has two components; a slowly varying, atomic-like portion, $I_0(k)$, upon which is superimposed a rapidly oscillating beat pattern that arises from the interference between the primary wave propagating directly to the detector and waves which scatter elastically off nearby atomic potentials before reaching the detector. diffraction curves, $\chi(k)$ are obtained by removing the slowly varying $I_0(k)$ portion from I(k).

$$\chi(k) = \frac{I(k) - I_0(k)}{I_0(k)}$$

The auto-regressive linear-prediction based Fourier transform (ARLP-FT) transforms the diffraction data from momentum space to real space[16]. In ARPEFS, the positions of the strong backscattering peaks in ARLP-FT from adsorbate/substrate systems can be accurately predicted using the single-scattering cluster model together with the concept of strong backscattering from atoms located within a cone centered at 180° from the emission direction. The effective solid angle of this backscattering cone is approximately 30° to 40°, though signals from scattering atoms very close to the source atom may be observable even if the scatters lie outside the nominal backscattering cone. The ARLP-FT peaks correspond to path-length differences between that component of the wave which propagates directly to the detector and those components which are first elastically scattered by the atomic potentials within this backscattering cone.

Analysis of the ARLP-FT provides information about the adsorption site as well as the bonding distance between the oxygen and tungsten atoms. Figure 2 shows the ARLP-FT for each emission direction. The 1x1 LEED structure suggests that oxygen adsorbs to a high-symmetry site on the W(110) surface. Using plane geometry and ignoring phase-shift effects, one can then calculate the path-length differences (PLD) and scattering angles for strong scattering events for each adsorption site geometry. Comparison of the predicted peak positions to the observed peaks in the ARLP-FT usually favors one adsorption site. In this study we consider the atop, bridge, center and quasi threefold site as possible O adsorption sites. The off-normal ARLP-FT is dominated by one

peak at a PLD = 3.5 Å. The strength of this peak immediately suggests a site with very strong backscattering geometry at 45° emission, eliminating the atop site. The normal-emission peaks at 3.1 and 6.7 Å are most consistent with the center or the threefold hollow sites. We cannot distinguish between the center and threefold hollow sites by comparison of the PLD because the scattering geometries are too similar. The Fourier analysis agrees best if the O atom adsorbs in the center or three fold hollow site approximately 1.15 Å above the first-layer tungsten. For this geometry the predicted PLD and the observed ARLP-FT peaks are in good agreement and the relative peak strengths are reasonable for the scattering angles.

In order to distinguish between the center and threefold sites and to extract more precise structural parameters than determined by the ARLP-FT analysis, we fitted the diffraction data to a full multiple-scattering model. The results of the fitting routine for the normal emission and off-normal emission data are shown in Fig. 3. The quasi threefold hollow site is clearly the best structure. The calculation code for this fitting routine was recently developed by Chen, Wu and Shirley and is based on the Rehr-Albers formalism[17,18]. This calculation requires both structural and non-structural parameters as input. We used the structural parameters determined by the ARLP-FT analysis as the starting point for the mul-

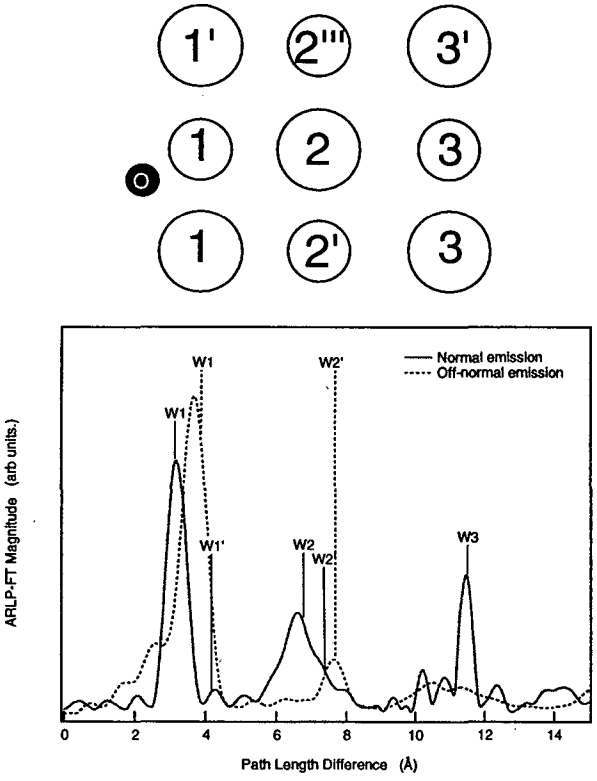

Figure 2. ARLP-FT of the experimental $\chi(k)$ curves for the O 1s normal emission (solid line) and 45° off-normal emission (dashed line). The model indicates the scattering atoms contributing to peaks in the ARLP-FT. In the model the relative size of the W atoms indicates its position relative to the plane of the paper and the O plane. The larger atoms are sticking out of the paper plane and the smaller are into the paper plane.

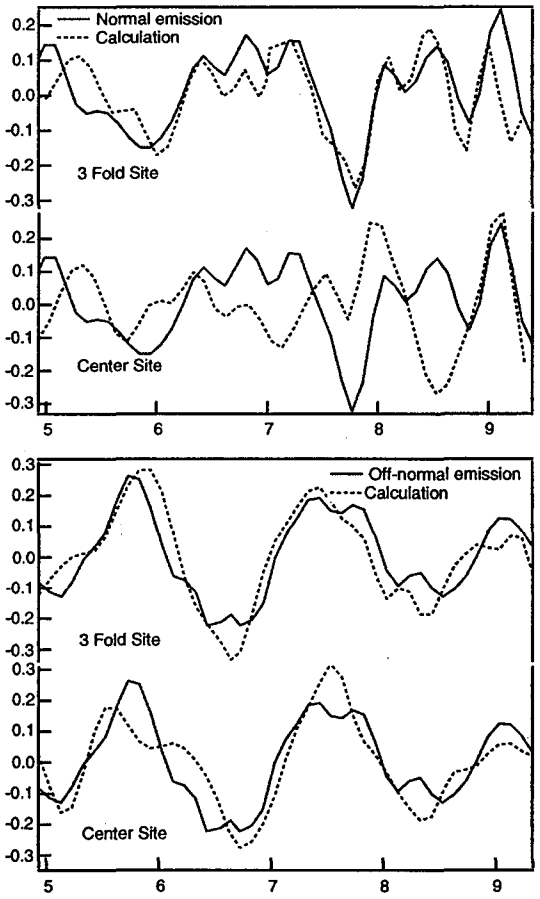

Figure 3. Best-fit calculations to the normal emission O 1s $\chi(k)$ to the threefold hollow and center sites. The normal and off-normal curves were fitted simultaneously. The threefold hollow is the best fit with an R-factor equal to 0.43. The best-fit parameters are O-W1 = 1.21 Å; W1-W2 = 2.19 Å; adsorption site 0.48 Å from center position along $[1\bar{1}0]$.

tiple-scattering calculations. The non-structural parameters include the initial-state angular momentum, the atomic scattering phase-shifts, the crystal temperature, the inelastic mean free path, the emission and light-polarization directions, the electron-analyzer acceptance angle, and the crystal's inner potential.

The threefold-hollow site is obviously the best fit to the experimental data with an R-factor equal to 0.43. The best fits determine the O-W1 interlayer spacing to be 1.21 Å, and the W1-W2 spacing to be 2.19 Å. The O-adsorption site is very close to the ideal threefold site, located 0.46 Å from the center of the long axis, along $[1\bar{1}0]$. The true threefold site, equally distant from each of the three W atoms, is 0.56 Å from the center site along the $[1\bar{1}0]$. A surface Debye temperature of 400 K and an inner potential of 8.01 V were found to give the best fit.

The results of the MSSW calculations are very similar to those found by a previous LEED study for a different O/W(110) phase. These researchers found for the (2x1)O/W(110) phase that the oxygen adsorbs near the threefold site. They reported the distance of the O atoms above the surface to be 1.25 Å. This previous study did not report a value for the distance between the first and second layer tungsten. We find that the local geometry is the same for [(1x1)O/W(110)]x12 phase as for the (2x1)O/W(110) phase independent of the long range order of the oxide layer. We report the oxygen adsorption site to be near the threefold hollow, 1.21 ± 0.04 Å above the surface-tungsten plane.

References

[1] I. Langmuir, Journal of the American Chemical Society **35**, 105 (1913).
[2] E. Bauer and T. Engel, Surface Science **71**, 695-718 (1978).
[3] T. Engle, H. Niehus, and E. Bauer, Surface Science **52**, 237 (1975).
[4] K. E. Johnson, R. J. Wilson, and S. Chiang, Physical Review Letters **71**, 1055-1058 (1993).
[5] C. S. Fadley, M. A. V. Hove, Z. Hussain, *et al.*, Journal of Electron Sprctroscopy and Related Phenomena **75**, 273-297 (1995).
[6] J. J. Barton, C. C. Bahr, Z. Hussain, *et al.*, Phys. Rev. Lett. **51**, 272-275 (1983).
[7] J. J. Barton, C. C. Bahr, S. W. Robey, *et al.*, Phys. Rev. B **34**, 3807-3819 (1986).
[8] L. J. Terminnello, X. S. Zhang, S. Kin, *et al.*, Physical Review B **38**, 3879-91 (1988).
[9] L.-Q. Wang, A. E. Schach von Wittenau, Z. G. Ji, *et al.*, Physical Rev. B **44**, 1292-1305 (1991).
[10] L.-Q. Wang, Z. Hussain, Z. Q. Huang, *et al.*, Physical Review B **44**, 13711-19 (1991).
[11] X. S. Zhang, L. J. Terminello, A. E. S. v. Wittenau, *et al.*, (Lawrence Berkeley National Laboratory, 1987).
[12] X. S. Zhang, L. J. Terminello, S. Kim, *et al.*, J. Chem. Phys. **89**, 6538-6546 (1988).
[13] Z. Hussain, W. R. A. Huff, S. A. Kellar, *et al.*, Journal of Electron Spectroscopy and Related Phenomena **80**, 401-404 (1996).
[14] R. X. Ynzunza, Ph.D. Thesis (University of California, Davis, 1997).
[15] H. Diamon, Personal Communication, 1995).
[16] J. J. Barton, Ph.D. Thesis (The University of California, Berkeley, 1985).
[17] Y. F. Chen, W. Wu, and D. A. Shirley, (To be published).
[18] J. J. Rehr and R. C. Albers, Physical Review B **41**, 8139-8149 (1990).

Principal Investigator: David A. Shirley.

This work funded by Director, Office of Energy Research, Office of Basic Energy Sciences, Materials Science Division, of United States Department of Energy under contract No. DE-AC03-76SF00098.

X-ray Absorption Measurements of Charge-Ordered $La_{0.5}Sr_{1.5}MnO_4$

T. Saitoh,[1] P. M. Villella,[1] D. S. Dessau,[1] Y. Moritomo,[2,*] Y. Tokura,[2] X. Zhou[3], E.J. Moler[3], and Z. Hussain[3]

[1]Department of Physics, University of Colorado, Boulder, Colorado 80309-0390, USA
[2]Joint Research Center for Atom Technology, Tsukuba, Ibaraki 305, Japan and Department of Applied Physics, University of Tokyo, Bunkyo-ku, Tokyo 113, Japan
[3]Advanced Light Source, Ernest Orlando Lawrence Berkeley National Laboratory, Berkeley, California 94720, USA

INTRODUCTION

Perovskite and "layered perovskite"-type manganese oxides show a variety of electronic and magnetic properties such as the colossal magnetoresistance (CMR) [1,2]or the charge ordering [3]. Among them, $La_{0.5}Sr_{1.5}MnO_4$ (K_2NiF_4 structure) which has 0.5 holes per Mn site ($d^{3.5}$) shows the charge-order transition at ~220 K [3,4] below which Mn^{3+} and Mn^{4+} sites are believed to order in the *CE*-type [4,5]. Although the charge ordering phenomenon has also been observed in the perovskite manganites $Pr_{0.5}Sr_{1.5}MnO_3$ or $Pr_{0.5}Ca_{1.5}MnO_3$ [6], the present system has another advantage that it has a layered structure. This enables us to address the issue of the orbital symmetry which should be directly related to the charge ordering. In this report, we present the results of x-ray absorption spectroscopy (XAS) on $La_{0.5}Sr_{1.5}MnO_4$ for two polarization angles and two (above and below the transition temperature T_{CO}) temperatures.

EXPERIMENTAL

High quality single crystals of $La_{0.5}Sr_{1.5}MnO_4$ were grown by the floating-zone method [3]. The experiment has been performed on ALS beamline 9.3.2. at two(290 K and 50 K) temperatures in the AMC chamber. The absorption intensity was obtained by measuring the partial electron yield. The photon energy was calibrated so that the first peak of the O 1s XAS spectrum of NiO should be located at 531.8 eV [7]. The spectral intensity has been normalized at ~600 eV photon energy where no polarization effect was observed, after subtracting a constant background. At the same time, two crystal orientations were employed to detect in-plane or out of-plane unoccupied states: the normal incidence, in which the photon beam is perpendicular to the MnO_2 planes, gives spectra sensitive to the in-plane states and the grazing incidence (the photon beam is 20 degrees away from the complete grazing) gives information of the out of-plane states. The crystals were cleaved *in situ* in a vacuum of 2×10^{-10} torr at approximately 50 K by knocking off a post glued to the top of the sample. The energy resolution was typically about 0.1 eV.

RESULTS

Figure 1 shows the O 1s XAS spectra of $La_{0.5}Sr_{1.5}MnO_4$ for two polarizations at two temperatures. The spectra are similar to those of $La_{0.6}Sr_{1.4}MnO_4$ ($d^{3.6}$) by a recent study [8]. The broad structures located between 540 eV and 547 eV have been assigned to Mn 4*sp*-related features and the peak at ~536 eV originates from hybridization to La 5*d* and Sr4*d* states [9]. The peak at 532.5 eV which

shows large polarization dependence is characteristic of layered systems [8]. The recent study has shown that the intensity of the peak systematically changes from a single layered compound to a cubic one, suggesting that the peak is due to La(Sr)-O sheets between Mn-O planes [8]. At both the (i) high and (ii) low temperatures the spectra show large polarization dependence in a large energy scale from the absorption edge up to ~545 eV, showing the layered nature of the electronic structure. The first peak located at ~528 eV, originating from Mn 3*d* states, also shows a large polarization effect. Because the grazing incidence spectra are sensitive to the out of-plane states, $d_{3z^2-r^2}$ states (z is perpendicular to the MnO_2 plane, namely the sample surface) would be dominant in the leading edge and the intensity around the top of the first peak would have mainly $d_{x^2-y^2}$ state origin. On the other hand, the temperature dependence of the spectra in both the orientations is quite weaker than the polarization effect although the charge-order temperature T_{CO}~220 K is between the two temperatures.

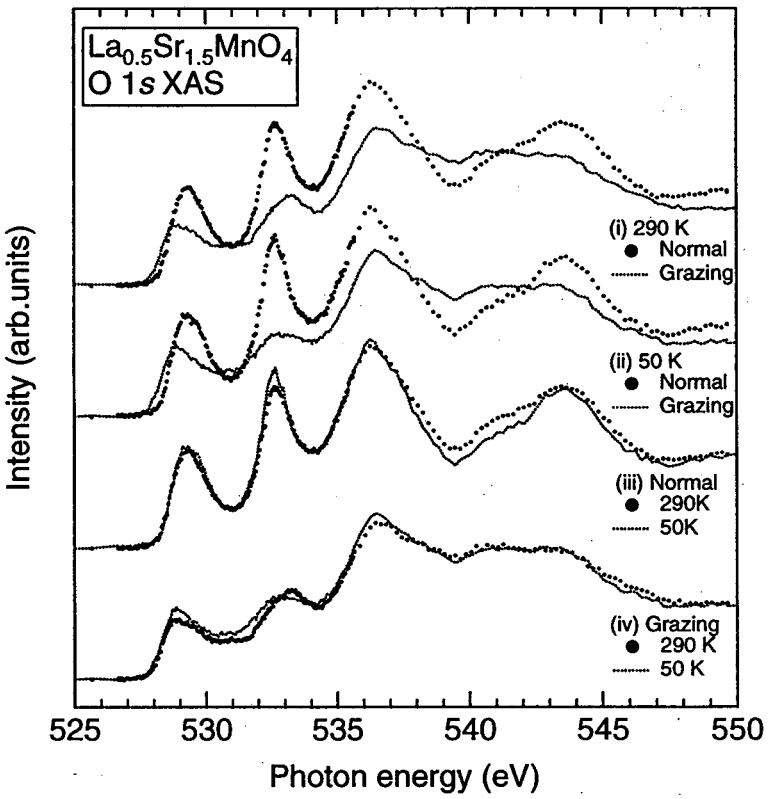

Figure 1. O 1*s* XAS spectra of $La_{0.5}Sr_{1.5}MnO_4$ at 290 K and 50 K. "Normal" and "Grazing" indicate that the photon beam was normal to the MnO_2 plane and 70° away from the normal incidence, respectively.

However, small but observable changes can be seen near the absorption edge in the grazing spectra (iv); the first peak of the 50 K spectrum has more intensity than the 290 K spectrum, which may correspond to $d_{x^2-y^2}$ states rather than the $d_{3z^2-r^2}$ states according to (i) and (ii) in the figure, whereas the absorption edge itself ($d_{3z^2-r^2}$ states) does not show any significant change. This could be an observation of the charge-order transition because in the ordered state (*CE*-type ordering) the $d_{3x^2-r^2}$ and the $d_{3y^2-r^2}$ (in-plane) orbital ordering was proposed [10]. In this scenario, however, the very tiny change with temperature in the normal-incidence spectra (iii) should be explained at the same time. Also, Mn 2*p* XAS spectra (not shown) did not show large changes with temperature. Further analysis and investigation should be needed.

SUMMARY

We have measured the O 1*s* XAS spectra of $La_{0.5}Sr_{1.5}MnO_4$ above and below the charge-order transition temperature. The spectra showed strong polarization effects at both the room temperature

and 50 K. Small temperature-dependent change was observed in the grazing incidence spectra, which could be related to the charge ordering.

REFERENCES

1. R. von Helmont, J. Wecker, B. Holzapfel, L. Schultz, and K. Samwer, Phys. Rev. Lett. **71**, 2331 (1993); K. Chahara, T. Ohno, M. Kasai, and Y. Kozono, Appl. Phys. Lett. **63**, 1990 (1993); Y. Tokura, A. Urushibara, Y. Moritomo, T. Arima, A. Asamitsu, G. Kido, and N. Furukawa, J. Phys. Soc. Jpn. **63**, 3931 (1994).
2. Y. Moritomo, A. Asamitsu, H. Kuwahara, and Y. Tokura, Nature **380**, 141 (1996).
3. Y. Moritomo, Y. Tomioka, A. Asamitsu, and Y. Tokura, Phys. Rev. B **51**, 3297 (1995).
4. B. J. Sternlieb, J. P. Hill, U. C. Wildgruber, G. M. Luke, B. Nachumi, Y. Moritomo, and Y. Tokura, Phys. Rev. Lett. **76**, 2169 (1996).
5. E. O. Wollan and W. C. Koehler, Phys. Rev. **100**, 545 (1955).
6. Y. Tomioka, A. Asamitsu, Y. Moritomo, H. Kuwahara, and Y. Tokura, Phys. Rev. Lett. **74**, 5108 (1995).
7. This gives the same photon energy as Ref. 8. Another work adopted 531.7 eV for NiO. (F. M. F. de Groot, M. Grioni, J. C. Fuggle, J. Ghijsen, G. A. Sawatzky, and H. Petersen, Phys. Rev. B **40**, 5715 (1989).)
8. C. H. Park, D. S. Dessau, T. Saitoh, Z. -X. Shen, Y. Moritomo, and Y. Tokura, unpublished.
9. M. Abbate, F. M. F. de Groot, J. C. Fuggle, A. Fujimori, O. Strebel, F. Lopez, M. Domke, G. Kaindl, G. A. Sawatzky, M. Takano, Y. Takeda, H. Eisaki, and S. Uchida, Phys. Rev. B **46**, 4511 (1992).
10. Z. Jirák, S. Krupicka, Z. Simsa, M. Dlouha, and S. Vrátislav, J. Magn. Magn. Mater. **53**, 153 (1985).

* Current Address: Center for Integrated Research in Science and Engineering, Nagoya University, Nagoya 464-01, Japan

This work was funded by Office of Naval Research Young Investigator grant N00014-96-I-0768.

Principal investigator: Daniel S. Dessau, Department of Physics, University of Colorado, 80309. Email: dessau@spot.colorado.edu. Telephone: 303-492-1607.

X-Ray Magnetic Circular Dichroism and X-Ray Absorption Spectroscopy of Novel Magnetic Thin Films

M.A. Brewer[1], H.L. Ju[1], Kannan M. Krishnan[1], A.T. Young[2], V. Martynov[2], E. Moler[2], X. Zhou[2], S. Kellar[2], and Z. Hussain[2]

[1]Materials Sciences Division, Ernest Orlando Lawrence Berkeley National Laboratory, University of California, Berkeley, California 94720, USA

[2]Advanced Light Source, Ernest Orlando Lawrence Berkeley National Laboratory, University of California, Berkeley, California 94720, USA

The optimization of the magnetic properties of materials for a wide range of applications requires a dynamic iteration between synthesis, property measurements and characterization at appropriate length scales. In addition, atomically engineered thin films and nanostructures offer new opportunities to elucidate the physics of magnetism, test theories and most importantly build new materials with unique properties. Our interest arises both from the increased appreciation of the degree to which magnetic properties can be influenced by tailored microstructures and the ability to characterize them by x-ray scattering/dichroism techniques. Preliminary results of our work at the ALS on "giant" moment in α"-$Fe_{16}N_2$ and "colossal" magnetoresistance in manganite perovskites is presented here.

It has recently been claimed [1] that α"-$Fe_{16}N_2$ possesses a giant magnetization of 2.9 T (~2300 emu/cc) when grown on lattice-matched $In_{0.2}Ga_{0.8}As$(001) and Fe/GaAs(001). However, attempts at growth on simpler substrates have resulted in only a modest enhancement in moment [2] and often in multiphase mixtures. Theoretical calculations [3] based on the band structure of $Fe_{16}N_2$ predict values for the magnetization around 2.3 T (~1780 emu/cc), well below Sugita's claims, but consistent with the magnetization reported by several other workers. We have carried out preliminary XMCD measurements on the Fe $L_{2,3}$ and N K edges of iron nitrides grown on Si(001). Using appropriate sum rules applied to the integrated MCD spectrum, we hope to determine the magnetic moment of the iron species in the α"-$Fe_{16}N_2$ films and other phases and resolve the orbital and spin contributions to the moment.

There is also rapidly growing interest in the "colossal magnetoresistance" effect observed in manganese oxides for both fundamental and commercial applications [4,5]. Detailed understanding of these phenomena, including the nature of the charge carriers and spin polarized conduction band, is far from satisfactory. To address some of these issues we have measured the electron energy loss spectra (EELS) of manganese perovskites at room temperature. Our EELS results show a prepeak (O 2p hole) at the threshold of O 2p [6] and the peak intensity proportional to the conductivity. The EELS results imply that in this material there is a significant O 2p hole-driven conductivity contrary to the current "double exchange" theory which is based on mixed Mn valence of Mn^{3+} and Mn^{4+} and their interactions through filled oxygen 2p states. Further, the precise relationship between the transport (metal to insulator) transition and magnetic (ferromagnetic to antiferromagnetic) transition is not yet understood. We hope that temperature dependent XMCD and XAS measurements of the Mn $L_{2,3}$ edge would shed light on these questions.

We have recently developed a crystallographic template for the growth of the range of Fe-N phases on Si(001) by lattice matching on Ag underlayers [7]. Epitaxial films of pure α-Fe, γ'-Fe_4N and α'-Fe_8N (N martensite) were grown individually by the optimization of reactive N_2 sputtering parameters. Annealing the α'-Fe_8N films resulted in the formation of α'-Fe_8N/α"-$Fe_{16}N_2$

mixtures. Quantification of x-ray diffraction peak intensities confirmed that the α'/α" mixtures contained as much as 46 vol% α" (remaining α'). VSM measurements of the α' and of the α'/α" mixture indicate enhanced magnetic moments for both the α' and α" phases with respect to α-Fe. Mössbauer experiments have confirmed that the iron in α"-$Fe_{16}N_2$ occupies three distinct sites in agreement with the proposed crystal structure.

We have also grown epitaxial $La_{1-x}Sr_xMnO_3$ on $LaAlO_3$ (100) thin films by both sol-gel technique and pulsed laser deposition. Undoped $LaMnO_3$ is insulating for the entire temperature range we have investigated. $La_{1-x}Sr_xMnO_3$ with doping $0.2<x<0.5$ becomes metallic and ferromagnetic. The EELS result shows a prepeak in O K edges for metallic manganese oxides and the prepeak diminishes for insulating manganese oxides. Any noticeable changes in Mn $L_{2,3}$ edges are not observed within the resolution of EELS.

XMCD experiments were performed on beamline 9.3.2, which has circularly polarized soft x-rays available, in September 1996. XMCD experiments were performed by collecting the total electron yield (sample photoelectric current). An external magnetic field of 3 Tesla was applied in these experiments, using a vacuum chamber with a built-in superconducting magnet. Figure 1(a) shows the absorption spectra of the iron $L_{2,3}$ edges in a pure α-Fe film. The solid spectrum was obtained with the photon polarization and magnetic field direction parallel, while the dashed spectrum was obtained with the polarization and field anti-parallel. The spectra were normalized both by I_0 and to fit the background values at zero on the left and one on the right. Figure 1(b) shows the MCD spectrum (solid line, the difference between the curves in Figure 1(a)) and its integrated curve (dashed line). Sum rules applied to the integrated curve give a ratio of $m_{orb}/m_{spin} \sim 0.03$, in agreement with the range of literature values for Fe[8]. XMCD of high-moment α'/α" films indicates an increase in this ratio, suggesting an increase in the orbital contribution to the moment. This is an unexpected result and calls for further study. Further studies using improved samples (capped to avoid oxidation) and improved signal collection are planned for our upcoming sessions on beamline 9.3.2.

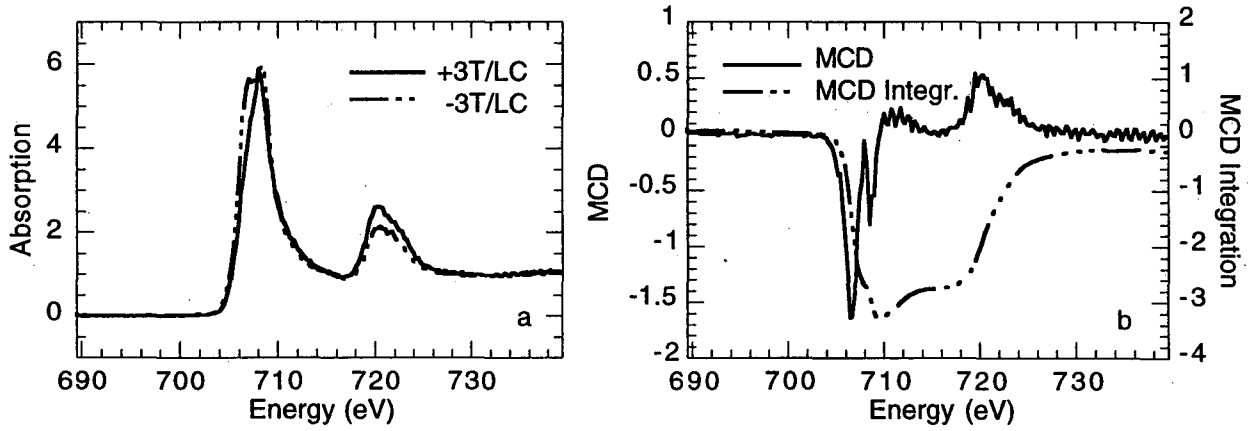

Figure 1. (a) X-ray absorption spectra of the Fe $L_{2,3}$ edges in a pure α-Fe film. The solid spectrum was obtained with the photon polarization and magnetic field direction parallel, while the dashed spectrum was obtained with the polarization and field anti-parallel. (b) MCD spectrum (solid line, the difference between the curves in (a)) and its integrated curve (dashed line).

We have also carried out preliminary XMCD and XAS on Mn $L_{2,3}$ edges and O K edges of manganese oxide $La_{1-x}Sr_xMnO_3$ thin films. With the XAS measurement, we would like to investigate the doping, temperature, and field dependence of the prepeak intensity in the O K edge and the white line ratio $I(L_3)/I(L_2)$ in Mn $L_{2,3}$ edges, which depends on the Mn oxidation state [9]. We hope to resolve the unoccupied electron density of states on the oxygen and manganese sites, for different divalent doping (and/or oxygen content) and as a function of temperture (77 K < T < 350 K). In particular, with the XMCD measurements we hope to investigate the correlation between the magnetic and transport properties of these novel materials. Preliminary experiments (Figure 2) show the dichroism effect in the Mn $L_{2,3}$ edges in $La_{0.7}Sr_{0.3}MnO_3$ very clearly.

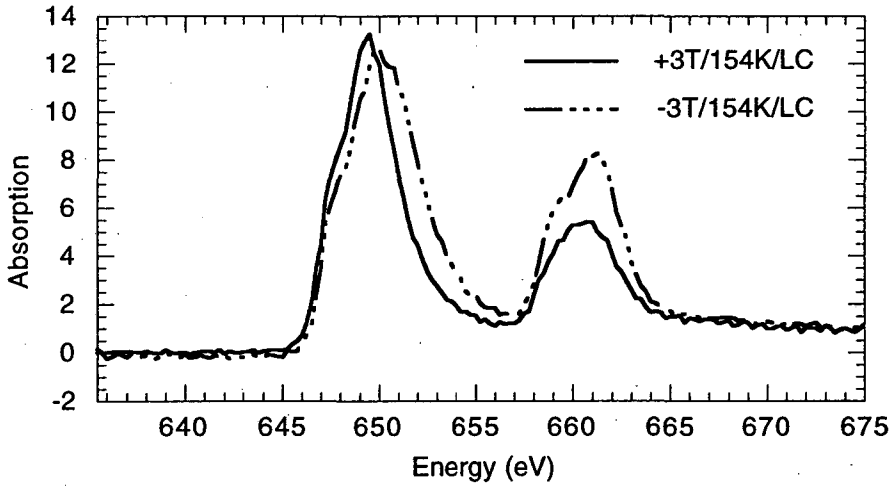

Figure 2. X-ray absorption spectra of the Mn $L_{2,3}$ edges in a $La_{0.7}Sr_{0.3}MnO_3$ film. The solid spectrum was obtained with the photon polarization and magnetic field direction parallel, while the dashed spectrum was obtained with the polarization and field anti-parallel.

REFERENCES

1. Y. Sugita, K. Mitsouka, M. Komuro, H. Hoshiya, Y. Kozono, and M. Hanazono, *J. Appl. Phys.* **70**, 5977 (1991).
2. C. Ortiz, G. Dumpich, and A.H. Morrish, *Appl. Phys. Lett.* **65**, 2737 (1994).
3. R. Coehoorn, G.H.O. Daalderop and H.J.F. Jansen, *Phys. Rev. B* **48**, 3830 (1993).
4. R. von Helmolt, J. Wecker, B. Holzapfel, L. Schultz, and K. Samwer, Phys. Rev. Lett. **71**, 2331 (1993).
5. G.C. Xiong, Qi Li, H.L. Ju, S.N. Mao, L. Senapati, X.X. Xi, R.L. Greene, and T. Venkatesan, Appl. Phys. Lett. **66**, 1427 (1995).
6. H.L. Ju, Hyunchul Sohn, Kannan M. Krishnan, Phys. Rev. Lett. submitted.
7. M. A. Brewer, Kannan M. Krishnan and C. Ortiz, *J. Appl. Phys.* **79**, 5321 (1996).
8. C.T. Chen, Y.U. Idzerda, H.-J. Lin, N.V. Smith, G. Meigs, E. Chaban, G.H. Ho, E. Pellegrin, and F. Sette, *Phys. Rev Lett.* **75** (1), 152 (1995).
9. H. Kurata and C. Colliex, Phys. Rev. B **48**, 2102 (1993).

This work was supported by the U.S. Department of Energy under contract No. DE-AC03-76SF00098.

Principal investigator: Kannan M. Krishnan, Materials Sciences Division, Ernest Orlando Lawrence Berkeley National Laboratory. Email: krishnan@lbl.gov. Telephone: 510-486-4614.

Beamline 10.3.1 Abstracts

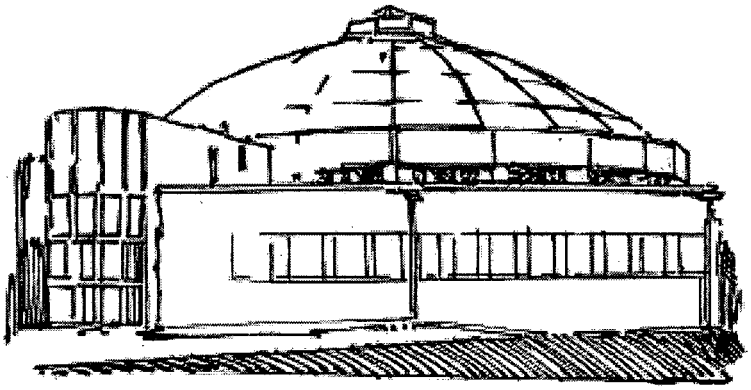

Focusing X Rays to a 1-μm Spot Using Elastically Bent, Graded Multilayer Coated Mirrors

J. H. Underwood,[1] A. C. Thompson, [1] J. B. Kortright, [1] K. C. Chapman,[1] and D. Lunt[2]
[1]Center for X-ray Optics, Ernest Orlando Lawrence Berkeley National Laboratory,
University of California, Berkeley, California 94720, USA
[2]Photon Sciences Ltd., 32 Athol St., Douglas, Isle of Man, British Isles

INTRODUCTION

In the x-ray fluorescent microprobe [1,2] at beamline 10.3.1, the ALS bending magnet source is demagnified by a factor of several hundred using a pair of mirrors arranged in the Kirkpatrick-Baez (K-B) configuration. These are coated with multilayers to increase reflectivity and limit the pass band of the x-rays striking the sample. The x-rays excite characteristic fluorescent x-rays of elements in the sample, which are analyzed by an energy dispersive Si-Li detector, for a sensitive assay of the elemental content. By scanning the focal spot, the spatial distribution of the elements is determined; the spatial resolution depends on the size of this spot. When spherical mirrors are used, the spatial resolution is limited by aberrations to 5 or 10 μm. This has been improved to 1 μm through the use of an elliptical mirror formed by elastically bending a plane mirror of uniform width and thickness with the optimum combination of end couples.

The principles for constructing an x-ray microscope using multilayer coated K-B optics with spherical mirrors are developed in [1]. Although astigmatism is corrected by the crossed-mirror K-B arrangement, residual aberrations remain. Since in the x-ray microprobe we demagnify an on-axis "point" source, i.e. there is no significant object field, the resolution of the microprobe is limited primarily by the spherical aberration of the mirrors, which is very significant at high demagnification. The two K-B mirrors focus independently in the horizontal and vertical directions, and we need consider only the focusing in the meridional plane of either mirror. Consider a mirror designed to demagnify a source at an object distance u = 34 m. to an image at a distance v = 100 mm, i.e. at a demagnification $M = v/u = 1/340$. A glancing angle of incidence θ of 1° allows the mirror to operate at 10 keV with a multilayer mirror having a d-spacing of 35.46 Å (using the Bragg equation $2d\sin\theta = n\lambda$ without correcting for refraction). A mirror of length L= 25 mm gives a collection aperture 440 μm wide, and hence a gain of about 10^5 in intensity over a 1 μm pinhole, assuming 50% efficient optics. A spherical mirror requires a radius R of 11.426 m., as calculated from the paraxial equations. The transverse spherical aberration $\Delta y'$ for the extreme rays of a mirror of half-aperture $\psi = L/2R$ may be estimated from the formula of Kirkpatrick and Baez [3]. We find that $\Delta y'$ is about 20 μm; this represents the maximum extent of the characteristic asymmetric flare of the spherically aberrated image. Since the x-ray energy in this flare excites fluorescence over a large area surrounding a very small feature, it must be minimized in a microprobe application.

Although the ideal surface for focusing from a single object point to an image point is an ellipse or ellipsoid, it is difficult to achieve the desired elliptical figure accuracy and a surface finish smooth enough for coating with multilayer mirrors by conventional grinding and polishing. However a high-quality optical flat can be elastically bent into an a close approximation of an ellipse [4]. Whereas a beam of uniform cross-section bent by two *equal* end couples bends into a circle, the application of *unequal* end couples to such a beam creates a bending moment varying linearly along the length, and the resultant linear variation of curvature may be used to approximate any arbitrary desired mirror figure such as an ellipse. From the standard equation of the ellipse, the

semi-axes a and b may be calculated from the focusing geometry, and hence y, the slope $\partial y/\partial x$, and the radius of curvature ρ as a function of x. In Fig. 1(a) section is plotted as a function of the position along the mirror. The pole of the mirror (coordinate zero) is 34 meters from the source. The horizontal line represents the circle of radius $R = 11.462$ m. derived from the paraxial equation, or the radius of the ellipse at its center. The dashed curve represents the best least squares fit of a mirror whose curvature varies linearly along its length. The fit is excellent, and the bent mirror is clearly superior to the constant radius counterpart. To illustrate this quantitatively we compare slope errors. The bent mirror, whose second derivative changes linearly, will have a quadratic slope variation along its length. The slope of a circular or spherical mirror changes only linearly along the mirror, and hence has one less parameter to obtain a fit. Fig. 1(b) shows the difference in slope between the ideal ellipse, the circular mirror and the optimum bent mirror. The slope errors at the ends of the bent mirror are about 3 μrad, more than a factor of 10 smaller than those for the spherical mirror, and are comparable in magnitude with the slope errors encountered in polishing flat and spherical mirrors for synchrotron radiation optics. These small errors could be corrected by varying the breadth profile of the mirror slightly along its length [4], but this was not required in the present case, since for an image distance of 100 mm, a 3 μrad slope error represents a transverse aberration of 0.6 μm.

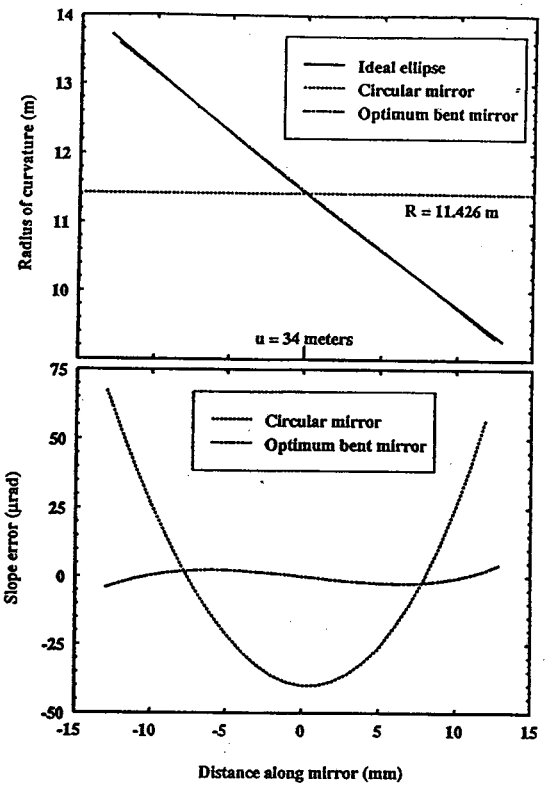

Figure 1(a). Variation of the radius of curvature of various mirrors along their length for the text example $u = 34$ m, $v = 100$ mm, $\theta = 1°$. Horizontal line: circular mirror. Bold curve: the ideal elliptical mirror. Dash-dot curve, best fit of a mirror with a linearly varying radius, as obtained by bending a uniform beam. Figure 1(b). Comparison of slope errors. Dotted curve: difference in slope between ideal ellipse and circular mirror. Dashed curve: difference in slope between ideal ellipse and best fit bent mirror.

THE MIRROR BENDER

The mirror bender (Fig. 2) was fabricated as a single part by electrical discharge machining (EDM), and a mirror (25 x 10 mm) of single crystal silicon was glued to it. The bender was made from 39% nickel-iron alloy to match the coefficient of thermal expansion of silicon at room temperature. The ends of the mirror pivot on two flexure hinges; the right hand hinge H1 is of the single or "notch" type while the left hinge H2 is a double-ended or "strip" style hinge. This avoids the build-up of compressional stress in the beam that would result if both hinges were of the single type. The leaf springs demagnify the force on the levers and decrease the sensitivity of the adjustment to the motion of the two bending screws, pushing through wobble pins. The screw S1 controls the mean radius of the mirror while S2 adds a bias to vary the radius along the length. Using this scheme the required elliptical shape was obtained relatively easily using a long trace profiler [6].

GRADED MULTILAYER COATINGS

The x-ray reflecting multilayers allow an increase in the glancing angle (hence decreased aberrations), and act as a monochromator for the x-rays. If the multilayer coatings are uniform, the Bragg angle, and therefore the energy of the x-rays reflected, varies across the face of each mirror, and the reflected energies match only at the center points of the mirrors, resulting in a loss of flux. This is avoided by grading the multilayers so that each ray passing through the two-mirror system encounters the correct angle and d-spacing for efficient reflection of the required energy. Two sets of mirrors were designed and coated with W/B_4C multilayers for operation at 8.5 or 12 keV. The grading of both mirrors increases the throughput by about a factor of 9.

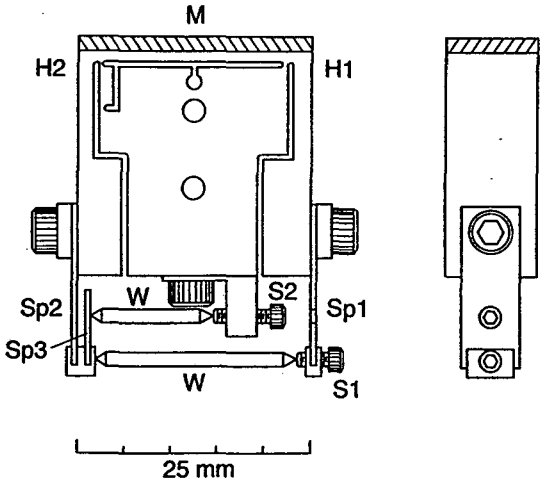

Figure 2. Tiny bendable mirror (TBM) mechanism. Key: M; mirror surface, H1, H2; flexure hinges, S1, S2; adjustment screws, W; wobble pin, L; locking screws. Sp1, Sp2, Sp3; leaf springs.

MIRROR PERFORMANCE

The mirrors were pre-bent to the correct elliptical profile using a long trace profiler [5] before mounting in the microprobe. The mirrors are mounted in a simple fashion on a double sine bar; this arrangement allows rapid and easy alignment of the mirrors, leaving only determination of the best focus to be carried out *in situ*. This was done by scanning both edges of a gold-coated tungsten wire, 20 to 25 μm in diameter, through the focal region using the scanning stage of the microprobe. The derivative of this data represents the one-dimensional spread function of the corresponding mirror. This procedure was carried out with scans in perpendicular directions to obtain the resolution of both the vertically and horizontally focusing mirrors. Here we show only the data obtained with the vertically focusing mirrors, but with both mirrors installed during the measurements. Fig. 3(a) is the result of a vertical wire scan across the focal region of the spherical mirrors with ungraded multilayer coatings, using a 25 μm diameter wire and steps of 1 μm. The FWHM of the differentiated scan yields a "resolution" of 1.8 μm. However, the resolution as measured by, for example, the RMS spot size, would be considerably worse. The spread function of each mirror is characterized by the classic spherical aberration "flare"

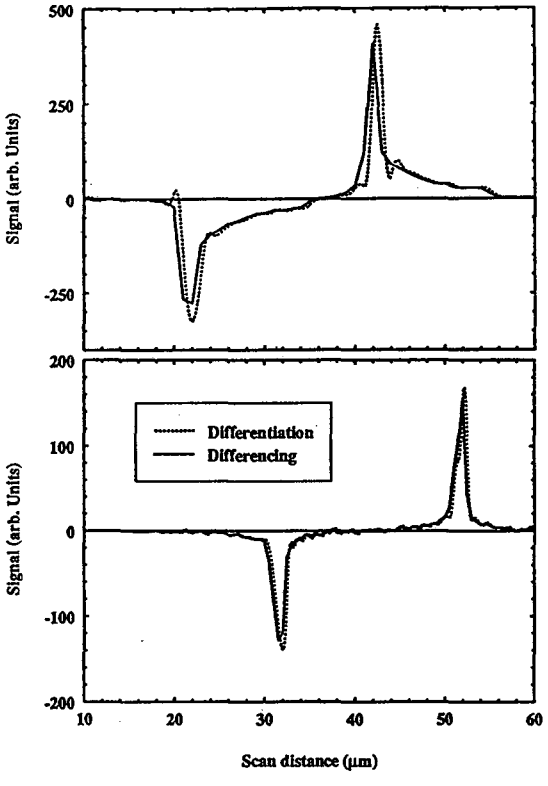

Figure 3. Vertically focusing mirror resolution from wire scans. The bold curves are obtained by differencing adjacent points in the data, the dotted curves by numerical differentiation. Both edges of the wire are shown. Above: Spherical, ungraded mirrors. Below: Bent and graded mirrors.

which extends almost 25 μm, in good agreement with the Kirkpatrick-Baez formula. Fig. 3(b) is the differentiated data from a vertical scan of the focal region of the bent, graded mirrors using a 21 μm wire and an 0.5 μm step. The FWHM spot size has improved to 1.3 μm, but in addition the flare resulting from spherical aberration has essentially disappeared. Correcting for the finite step size and the contribution from the vertical FWHM size of the ALS source, the resolution of the mirror alone is 1.15 μm. The performance of the horizontally focusing mirrors, and of those designed for 12 keV operation, was similar.

CONCLUSIONS

Flat mirrors of uniform cross-section can be bent, with the optimum combination of unequal end couples, into a very good approximation of an ellipse. Used in an x-ray fluorescence microprobe, such mirrors provide a solution to the spherical aberration problem encountered with fixed spherical mirrors at high demagni-fication, and improve the resolution of the microprobe to the order of 1 μm. It should be possible to improve this by a factor of 2 or 3 by width profiling of the mirrors. Grading the multilayer d-spacing increases the throughput and narrows the pass band of the microprobe. These features allow the microprobe to take maximum advantage of high brightness third generation synchrotron radiation sources. This bending scheme offers a method for constructing elliptical mirrors with low slope errors for a variety of hard and soft x-ray applications.

ACKNOWLEDGMENTS

We thank Phil Batson for mechanical design, and Steve Irick for his assistance in adjusting the mirrors using the long trace profiler.

REFERENCES

1. J. H. Underwood, A. C. Thompson, Y. Wu and R. D. Giauque, Nucl. Instr. Meth. **A 266**, 318 (1988).
2. A. C. Thompson, J. H. Underwood, Y. Wu, R. D. Giauque, R. G. Futernick, and M. L. Rivers, in *X-ray Microscopy in Biology & Medicine*, edited by K. Shinohara *et al.* (Japan Sci. Soc. Press, Tokyo/Springer-Verlag, Berlin, 1990), p. 119.
3. P. Kirkpatrick and A.V. Baez J. Opt. Soc. Am. **39**, 766 (1948)
4. J. H. Underwood; Space Sci. Instr. **3**, 259 (1977).
5. S. C. Irick; Proc. S.P.I.E. **2515**, 37 (1995)

This work was supported by the Director, Office of Energy Research, Office of Basic Energy Sciences, Materials Science U.S. Department of Energy, under contract number DE-AC03-76SF00098.

Principal investigator: A.C. Thompson, Center for X-ray Optics, Ernest Orlando Lawrence Berkeley National Laboratory. Email: underwoo@lbl.gov. Telephone: 510-486-5590.

Spectral Response of Multi-Element Silicon Detectors

B. A. Ludewigt,[1] C. S. Rossington,[2] and Karen Chapman*[3]

[1]Life Sciences Division, Ernest Orlando Lawrence Berkeley National Laboratory, University of California, Berkeley, CA 94720, USA
[2]Engineering Division, Ernest Orlando Lawrence Berkeley National Laboratory, University of California, Berkeley, CA 94720, USA
[3]Center for X-ray Optics, Ernest Orlando Lawrence Berkeley National Laboratory, University of California, Berkeley, CA 94720, USA

INTRODUCTION

Multi-element silicon strip detectors, in conjunction with integrated circuit pulse-processing electronics, offer an attractive alternative to conventional lithium-drifted silicon Si(Li) and high purity germanium detectors (HPGe) for high count rate, low noise synchrotron x-ray fluorescence applications. One of the major differences between the segmented Si detectors and the commercially available single-element Si(Li) or HPGe detectors is that hundreds of elements can be fabricated on a single Si substrate using standard silicon processing technologies. The segmentation of the detector substrate into many small elements results in very low noise performance at, or near, room temperature, and the count rate of the detector is increased many-fold due to the multiplication in the total number of detectors. Traditionally, a single channel of detector with electronics can handle ~100 kHz count rates while maintaining good energy resolution; the segmented detectors can operate at >MHz count rates merely due to the multiplication in the number of channels [1]. One of the most critical aspects in the development of the segmented detectors is characterizing the charge sharing and charge loss that occur in between the individual detector strips, and determining how these affect the spectral response of the detectors.

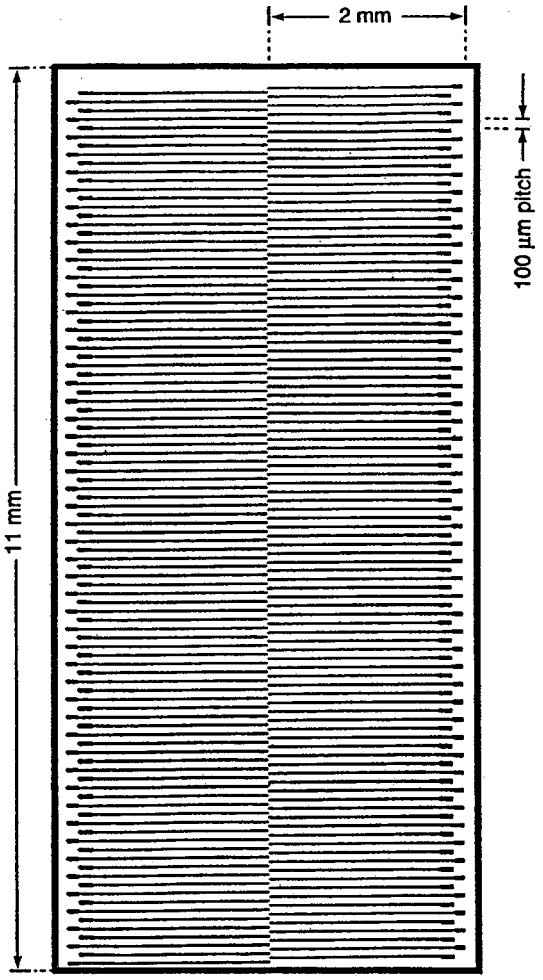

Figure 1. Schematic of the top surface of a silicon strip detector used for these measurements. Strips are 2 mm long, 10 microns wide, on a 100 micron pitch. Substrate is high purity silicon, 300 microns thick.

EXPERIMENT

We used the microprobe beam line (10.3.1) with a 5 micron spot size and 8.5 keV beam to scan the multi-element silicon stripdetector and map the spectral response as a function of position

on the detector. Fig. 1 shows a schematic of the segmented side of the strip detector used for these measurements. Fig. 2a shows the x-ray response when the x-ray beam was directly on the strip, and Fig. 2b shows the x-ray response when the x-ray beam was directly in between the strips. (Strips were 10 microns wide on a 100 micron pitch.) The enhanced spectral background occurring in the spectrum collected when the beam was in between the detector strips. Fig. 2b is a result of both charge *sharing* between strips and charge *loss*. When the detector is used in a typical x-ray fluorescence (XRF) application, with the x-ray flux covering the full detector area, the spectral background is higher than is desirable for optimum XRF measurements, and thus must be reduced in order for the detectors to perform adequately.

CONCLUSIONS

We used the microprobe x-ray beam, and additional measurements, to fully characterize the spectral response of a multi-element silicon detector and have used these results to develop new detector designs with improved spectral response. Fig. 3 shows a typical x-ray spectrum from a ^{55}Fe source from one of the new improved detectors. In addition to the low spectral background, an excellent energy resolution of ~200eV FWHM (at 5.9 keV, 2 microseconds amplifier peaking time, -25°C) has been achieved [2].

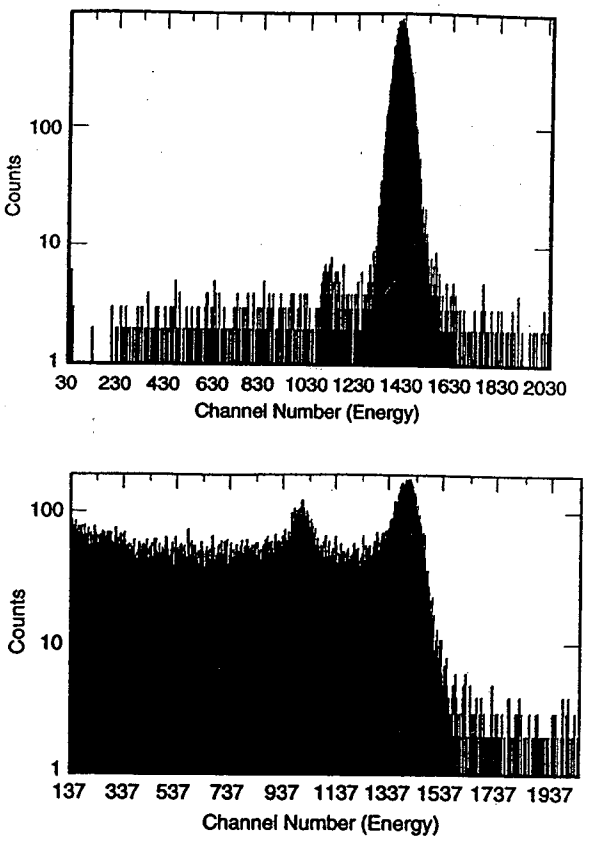

Figure 2. (a) Spectral response of silicon strip detector when 8.5 keV, 5 micron beam is directly on the detector strip. (b) Same, when beam is directly in between two strips.

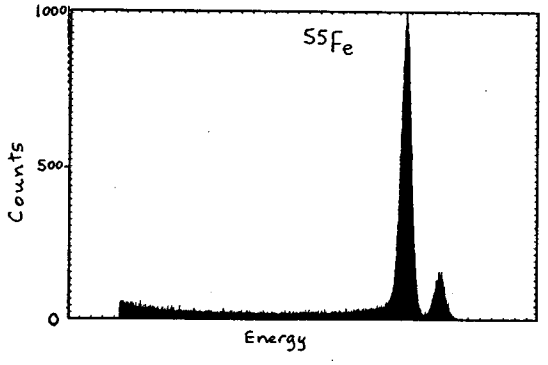

Figure 3. ^{55}Fe x-ray spectrum from a new detector, showing improved spectral response.

REFERENCES

1. B. Ludewigt, J. Jaklevic, I. Kipnis, C. Rossington and H. Spieler, "A High Rate, Low Noise X-Ray Silicon Strip Detector System," IEEE Trans. Nucl. Sci, **41 (4)** 1037-1041 (1994). LBL-34060

2. B. Ludewigt, C. Rossington, I. Kipnis and B. Krieger, "Progress in Multi-Element Silicon Strip Detectors for Synchrotron XRF Applications," IEEE Trans. Nucl. Sci. **43** (1996) 1442-1445.

This work was supported by the Director, Office of Energy Research, Office of Health and Environmental Research, Medical Applications and Biological Research Division, of the U.S. Department of Energy, under Contract No. DE-AC03-76SF00098.

*Now at: Kevex Inc., San Carlos, California, USA.

Principal investigators: C.S. Rossington, Engineering Division, Ernest Orlando Lawrence Berkeley National Laboratory (Email csrossington@lbl.gov, Telephone 510-486-7827); B.A. Ludewigt, Life Sciences Division, Ernest Orlando Lawrence Berkeley National Laboratory (Email baludewigt@lbl.gov, Telephone 510-486-7733).

Characterization of Quaternary Metal Oxide Films by Synchrotron X-Ray Fluorescence Microprobe

D. L. Perry,[1] A. C. Thompson,[2] R. E. Russo,[3] X. L. Mao,[3] and K. L. Chapman[2]

[1]Earth Sciences Division, Ernest Orlando Lawrence Berkeley National Laboratory, University of California, Berkeley, CA 94720, USA
[2]Center for X-ray Optics, Ernest Orlando Lawrence Berkeley National Laboratory, University of California, Berkeley, CA 94720, USA
[3]Environmental Energy Technologies Division, Ernest Orlando Lawrence Berkeley National Laboratory, University of California, Berkeley, California 94720, USA

INTRODUCTION

A high demand for thin films in industrial technology has been responsible for the creation of new techniques for the fabrication of such films. One highly effective method for the syntheses of variable composition thin films is pulsed-laser deposition (PLD). The technique has a large number of characteristics which make it an attractive approach for making films. It offers rapid deposition rates, congruent material transfer, simple target requirements from which to make the films, in situ multilayer deposition, and no gas composition or pressure requirements. Additionally, the technique can also afford crystalline films and films with novel structures. Pulsed-laser deposition can be used to make films of semiconductors[1-3], insulators [4], high-temperature superconductors [5-9], diamond-like films [10, 11], and piezoelectric materials [12].

Quaternary metal oxides involving calcium, nickel, and potassium have been shown to be quite effective in the catalysis of coal gasification and methane coupling. The catalysts can be synthesized by a variety of techniques, including thermal decomposition of the metal salts, high-temperature annealing of the mixed oxides, and high-temperature dehydration/heating of a mixture of the metal hydroxides. An inherent problem with these traditional, high-temperature syntheses, however, is the much higher melting and boiling points of the calcium and nickel oxides relative to those of potassium oxides, resulting in the loss of potassium from the catalysts at much lower temperatures than those that are necessary to form homogeneous oxide phases from the starting materials. A major consequence of this problem is that it is extremely difficult to synthesize highly reproducible samples of the quaternary metal oxides using traditional, standard thermal techniques [13] such as those listed above.

One approach to incorporating all three of the metal oxides into one phase is the use of laser ablation to prepare films [14, 15] of the catalysts so that they may be used for coatings, smooth surfaces on which to conduct detailed studies of gas-solid interface reactions that are involved in catalytic processes, and other applications. The problem of dissimilar boiling points of the three metal oxides system is overcome, since the laser ablation process effects the volatilization of all three components from the laser target essentially simultaneously.

Although the three metal oxides are indeed effectively vaporized and deposited simultaneously during the two processes, there is strong interest in gaining an understanding of the chemical and morphological aspects of the films that are deposited. Phenomena such as lattice defects and chemical heterogeneity are of interest, especially in the films studied here where the composition of each of the elements varies so widely. In this case, it is of interest to learn if the potassium—which has the lowest boiling point and is the smallest metal oxide component of the

system—is homogeneously spread throughout the matrix of the film, if there is any segregation of it in localized regions, or if any clustering of it with either of the other two metal ions occurs. Too, it is of interest to observe any islands of segregation involving either of the other two metals in the system. Thus, because of the micron-level lateral spatial resolution and elemental sensitivity of the synchrotron x-ray fluorescence microprobe technique used here, the investigator is able to answer these questions at a level that has heretofore been impossible.

EXPERIMENTAL

Films of calcium-nickel-potassium oxide were fabricated by pulsed laser deposition as previously described [15]. The films were analyzed using the x-ray fluorescence microprobe at the Advanced Light Source (ALS). A pair of multilayer-coated spherical mirrors in a Kirkpatrick-Baez configuration are used to focus and monochromate (with 6 % bandpass) the beam. The $K\alpha_1$ emission lines of potassium, calcium, chromium, iron, and nickel were measured simultaneously with a Si(Li) detector. With the mirrors set to 8.5 keV, the focused beam intensity was 3 x 10^9 photons/second when the ALS was operating at 1.0 GeV and 250 mA. The spot size was 2 μ x 2 μ. The samples were scanned in a series of long, one-dimensional scans of about 3 mm in which the step size between the points was 5 microns, and the counting time at each point was 1-3 seconds. At each point, the complete energy spectrum was analyzed with a peak fitting program to find the net intensity in all of the elemental peaks.

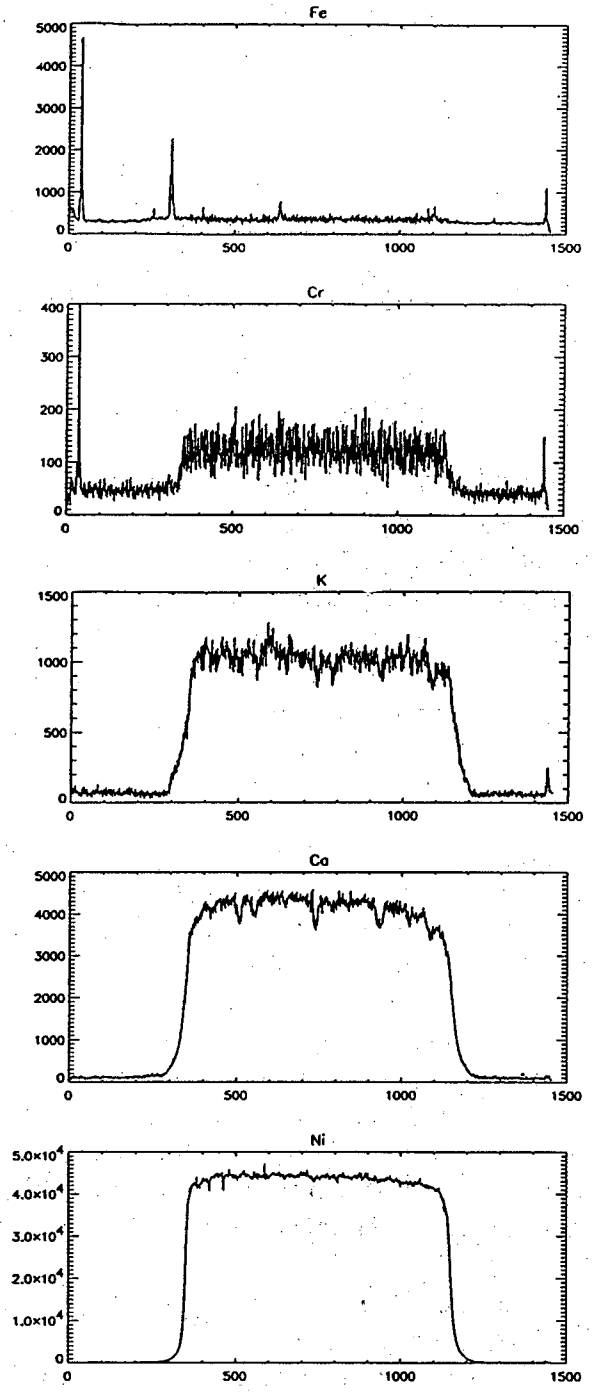

Figure 1. X-ray fluorescence microprobe lateral elemental profiles for iron, chromium, potassium, and calcium, nickel. The shown profiles represent 3.25 mm in width across the surface of the sample.

RESULTS AND DISCUSSION

The experimental data discussed here are restricted to the matrix homogeneity of the films themselves for films which were void of these microparticles. Although some very slight variations in the individual elemental profiles of calcium, nickel, and potassium in the laser ablation-generated films studied here were observed and thus indicated enriched microdomains, most of the areas of the matrices appeared to be mostly homogeneous with respect to the three elements. Trace quantities of chromium and ironwere also dispersed throughout the films, their

presence being due to their introduction as contaminants in the chemical reagents used to make the original laser targets.

Fig. 1 shows the results of looking at a line analysis across the face of one typical film. Elemental ratios in these profiles show good consistency with general homogeneity of the elements throughout the overall film matrix. The result is illustrative of the concept that films of the type fabricated here can be many millimeters in width and exhibit *macro*homogeneity and function well for their intended purpose (such as membranes) while at the same time also exhibiting chemical *micro*heterogeneity with respect to isolated micron-size domains.

REFERENCES

1. M. I. Baleva, M. A. Maksimov, S. M. Metev, and M. S. Sendova, J. Mater. Sci. Lett.**5**, 533(1986).
2. J. L. Dubowski, P. Morman, P. B. Sewell, D. F. Williams, F. Krolicki, and M. Lewicki, Thin Solid Films **147**, 533(1986).
3. H. S. Kwok, P. Mattocks, D. T. Shaw, S. Witanachchi, and J. P. Zheng, Appl. Phys. Lett. **52**, 1095(1988).
4. H. Sankar, Mater. Res. Soc. Symp. Proc. **29**, 373(1984).
5. D. Dijjkamp, T. Venkateson, X. D. Wu, S. A. Shaheen, N. Jisrawi, Y. H. Min-Lee, W. L. Mclean, and M. Croft, Appl. Phys. Lett. **51**, 619(1987).
6. D. K. Fork, J. B. Boyce, F. A. Ponce, R. I. Johnson, G. B. Anderson, G. A. N. Connell, C. B. Eom, and T. H. Geballe, Appl. Phys. Lett. **53**, 337(1988).
7. M. Balooch, D. R. Olander, and R. E. Russo, Appl. Phys. Lett. **55**, 197(1989).
8. X. L. Mao, R. E. Russo, H. B. Liu, and J. C. Ho, Appl. Phys. Lett. **57**, 2591(1990).
9. R. P. Reade, X. L. Mao, and R. E. Russo, Appl. Phys. Lett. **59**, 739(1991).
10. C. L. Marquardt, R. T. Williams, and D. J. Nagel, Mater. Res. Soc. Symp. Proc. **38**, 325(1985).
11. S. S. Wagal, E. M. Juengerman, and C. B. Collins, Appl. Phys. Lett. 53, 187(1988).
12. R. E. Leuchtner, K. S. Grabowski, D. B. Chrisey, and J. S. Horwitz, Appl. Phys. Lett.,1193(1992).
13. D. L. Perry, P. Berdahl, and C. Perrino, J. Mater. Res.,**9**, 2993(1994).
14. D. L. Perry, X. L. Mao, and R. E. Russo, J. Mater. Res. **8**, 2400(1993).
15. X. L. Mao, D. L. Perry, and R. E. Russo, High Temp. Mater. Sci., *33*, 117(1995).

This work was supported by the Assistant Secretary for Fossil Energy, Office of Technical Coordination, through the Morgantown Energy Technology Center, Morgantown, WV, 26505; and by the Director, Office of Energy Research, Office of Basic Energy Sciences, Materials Sciences Division, all of the U. S. Department of Energy, under Contract No. DE-AC03-76SF00098.

Principal investigator: Dale L. Perry, Earth Sciences Division, Ernest Orlando Lawrence Berkeley National Laboratory. Email: dlperry@lbl.gov. Telephone: 510-486-4819.

Deep-Etch X-Ray Lithography at the ALS: First Results

C. Kahn Malek*,[1] K.H. Jackson,[1] R.A. Brennen,[2] M.H. Hecht,[2] W.D. Bonivert,[3] and J. Hruby[3]

[1]Center for X-ray Optics, Ernest Orlando Lawrence Berkeley National Laboratory, University of California, Berkeley, CA 94720, USA
[2]Center for Space Microelectronics, Jet Propulsion Laboratory, Pasadena, CA 91109, USA
[3]Materials Synthesis Department, Sandia National Laboratories, Livermore, CA 94551, USA

INTRODUCTION

The fabrication of high-aspect-ratio and three-dimensional (3D) microstructures is of increasing interest in a multitude of applications in fields such as micromechanics, optics, and interconnect technology. Techniques and processes that enable lithography in thick materials differ from the planar technologies used in standard integrated circuit processing. Deep x-ray lithography permits extremely precise and deep proximity printing of a given pattern from a mask into a very thick resist. It requires a source of hard, intense, and well collimated x-ray radiation, as is provided by a synchrotron radiation source. The thick resist microstructures so produced can be used as templates from which ultrahigh precision parts with high aspect ratios can be mass-produced out of a large variety of materials (metals, plastics, ceramics). This whole series of techniques and processes has been historically referred to as "LIGA," from the German acronym for lithography, electroforming (Galvanoformung), and plastic molding (Abformung), the first development of the basic LIGA process having been performed at the Nuclear Research Center at Karlsruhe in Germany [1].

DEEP X-RAY LITHOGRAPHY SETUP

Initial experiments in deep etch lithography were performed on the x-ray microprobe beamline [2] installed on the 10.3 bending magnet of the Advanced Light Source (ALS) at the Ernest Orlando Lawrence Berkeley National Laboratory. Beamline 10.3, consisting of two independent lines beyond the injection shutter, is shown in Fig 1. Branch 10.3.1, which was used for these experiments, is a dedicated x-ray fluorescence microprobe beamline operated by the Center for X-ray Optics in the Materials Science Division. It has been designed with a 0.77-mrad horizontal acceptance angle to transport a white radiation beam. A 125μm-thick beryllium window has been installed to isolate the beamline from the synchrotron and to protect the ring (10^{-10} Torr) from accidental venting of the beamline. A second 125-μm Kapton™ window ends the beamline. All components in the beamline were aligned using an x-ray collimator to an accuracy of 0.2 mrad. Variable horizontal and vertical slits determine the size of the beam entering the hutch. The

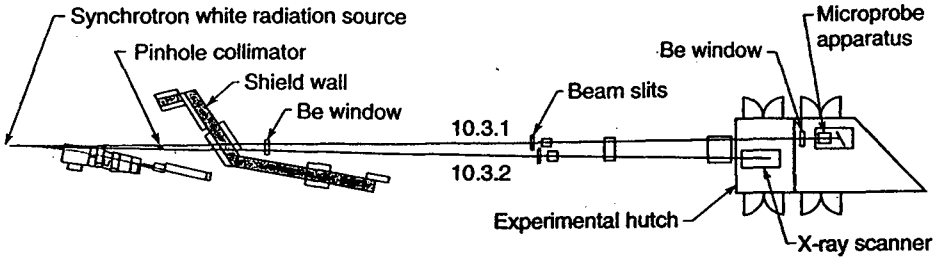

Figure 1. Schematics of the microprobe beamline at the ALS.

transmitted flux and horizontal beam density distribution were measured with an ion chamber placed at the end of the beamline. Maximum exposure area is 25(H)×16(V) mm^2 at the end station located 33 m from the source. The exposure is performed by putting the mask in contact with the substrate and holding the ensemble close to the kapton window to limit the air path. A factor of 6 between the surface and bottom doses [dose bracket 3-20 kJ/cm^3 [3] was obtained when exposing 800 μm Plexiglas™ with a stencil metallic mask and 250-μm Kapton™ filters. A simple scanner moved the sample at 0.2 mm/s over 60 mm in the vertical direction and reduced the local heating. With typical operating current between 300 and 400 mA, an exposure time on the order of 100 min was needed to completely expose an 800-μm-thick Plexiglas™ sample in a 12-mm scan.

A second branch line (10.3.2) is under construction. It has a wide aperture, allowing an exposure area of 60 mm×20 mm at the exposure station situated 30 m from the point source. The first window in this branch line is replaced with a low conductance aperture, allowing more flux to be delivered. An x-ray scanner allowing the exposure of a 6 in.×6 in. area with a scanning speed of 1 to 100 mm/s has been constructed by Surface/Interface, Inc. of Mountain View, CA. The scanner can be aligned to the x-ray beam to within 0.3 mrad and will allow exposures of tilted samples.

STENCIL MASKS

A technology for high contrast masks with thick absorber pattern at 2-5 Å is currently under investigation. Initially, stencil masks chemically or laser etched in metal sheets were used. These included 180-μm-thick chemically etched brass (thermal sensor) and 80-100-μm thick chemically etched stainless steel (hole array). The minimum feature size in such masks was about 20 μm. The advantage of these masks is that they are relatively easy to produce, inexpensive, and have a very high contrast.

RESIST PROCESSING

Previously reported resists for deep etch lithography [4,5] consisted of self-cast layers of high molecular weight PMMA. Prepolymerized PMMA was dissolved in the methyl methacrylate (MMA) monometer with initiator and cross-linking agents, and then was fully polymerized *in situ* at room temperature and thermally cured. In this work, however, we used commercially available cast sheets of PMMA such as Plexiglas™ with a molecular weight of 1 to 2 million amu.

For development, we immersed the sample in "GG" developer [6] with agitation. This developer, based on a mix of morpholine/2-aminoethanol/2-(2-butoxyethoxyt)ethanol/water, was especially formulated to obtain a high selectivity between exposed and unexposed PMMA areas. Free-standing Plexiglas™ sheets allow the developer to penetrate both sides of the exposed area, which allows deeper structures to be developed at a higher rate.

METAL FORMING IN ACRYLIC SHEETS

The PMMA microstructures (Fig. 2a) produced by deep etch x-ray lithography are used as a primary mold or template to produce secondary metallic microstructures. In particular, metals such as copper, nickel, nickel alloys, or gold can be electrodeposited in these patterns. The structure shown in Fig. 2b and 2c was electroformed using a free-standing acrylic mask. The PMMA mask was placed on a stainless disk which was attached to a rotating electrode using a Teflon™ fixture. This assembly was then rotated at 800 rpm in an acid copper sulfate solution. Current density on the order of 21 mA/cm^2 at 22°C was used. The electroformed structure was then removed from the stainless base creating a free-standing part.

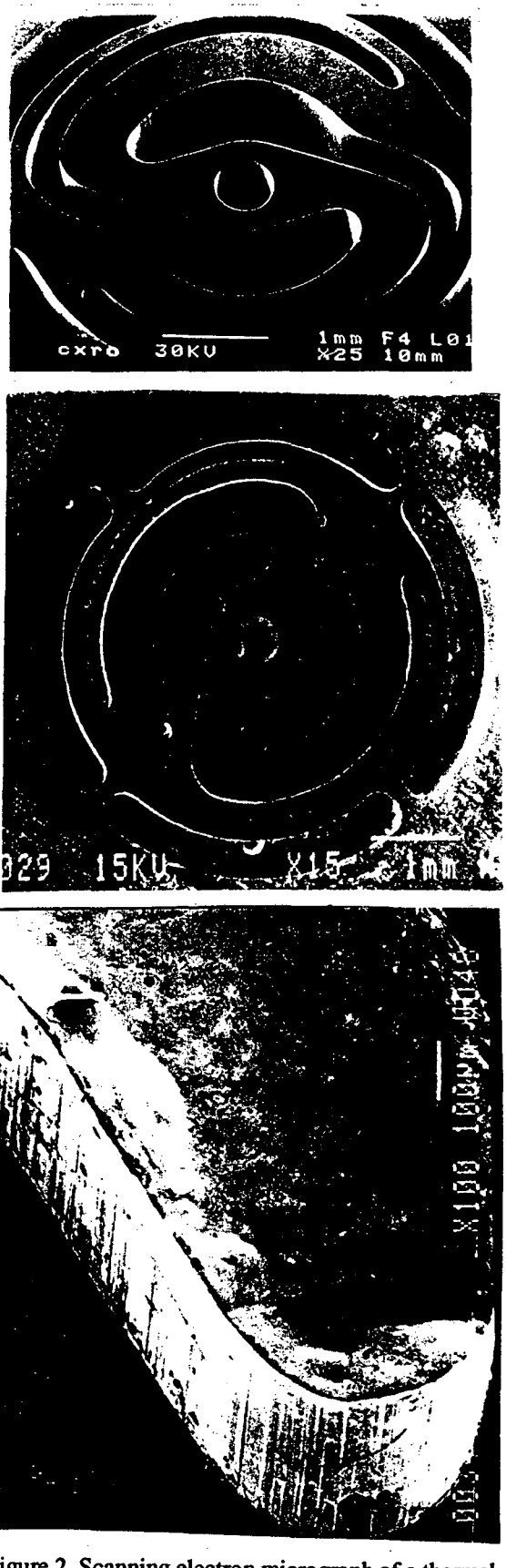

Figure 2. Scanning electron micrograph of a thermal sensor: (a) 800μm-thick acrylic template, (b) 300-μm-thick copper replica, and (c) blow-up of (b).

ACKNOWLEDMENTS

The authors would like to acknowledge the support of Al Thompson, CXRO, for providing access to the X-ray Microprobe beamline 10.3 for this experiment, and acknowledge the use of the Berkeley Microfabrication Laboratory in the development of masks for this project. Resonetics, Inc. and the Photofabrication shop of the Engineering Technology Department of the Ernest Orlando Lawrence Berkeley National Laboratory, are thanked for providing us, respectively, with laser etched masks and chemically etched masks. Two of the authors (R.A.B. and M.H.H.) acknowledge the Stanford Synchrotron Radiation Laboratory where complementary efforts have been carried out. Their findings will be published elsewhere.

REFERENCES

1. Becker, W. Ehrfeld, P. Hagmann, A. Maner, and D. Munchmeyer, Microelectron. Eng **4**, 35 (1986).
2. Thompson, K.L. Chapman, and H.J. Underwood, SPIE **1740, 191** (1992).

3. Bley, J.Gottert, M. Harmening, M. Himmelhaus, W. Menz, J. Mohr, C. Muller and U. Wallrabe, Microsystem Technologies **91**, Berlin, Germany, Oct. 29-Nov. 1, 1991.
4. Mohr, W. Ehrfeld, D. Munchmeyer, and A. Stutz, Macromol. Symp. **24**, 231 (1989).
5. Guckel, T.R. Christenson, K.J. Scrobis, D.D. Denton, B. Choi, E.G. Lowell, J.W. Lee, S.S. Bajikar, and T. W. Chapman, Technical Digest Solid State Sensor and Actuator Workshop Digest, Hilton Head, SC, 4-7 June 1990, p. 188.
6. Ghia and W. Glashauser, Offenlegungsschrift DE3039110, Siemens AG, Munich, Germany.

This work was supported in part by the Director, Office of Energy Research, Office of Basic Energy Sciences, of the U.S. Department of Energy under Contract No. DE-AC03-76SF00098; and by the DOD/ARPA Advanced Lithography Program; and by the National Aeronautics and Space Administration.

*Now at Center for Advanced Microstructures and Devices, Louisana State University, 3990 West Lakeshore Drive, Baton Rouge, LA 70803, USA

Principal investigator: Keith H. Jackson, Center for X-ray Optics, Ernest Orlando Lawrence Berkeley National Laboratory. Email: khjackson@lbl.gov. Telephone: 510-486-6894.

The Effects of Synchrotron X Rays on the Local Structure and the Recrystallization of Ion-Damaged Si

Kin Man Yu, Lei Wang, and W. Walukiewicz
Center for Advanced Materials, Materials Sciences Division
Lawrence Berkeley National Laboratory, Berkeley, CA 94720

Ion implantation is used extensively as a routine, controllable and reproducible doping technique for semiconductor processing. In Si, the amorphization by ion beams as well as the subsequent thermally induced solid phase epitaxy (SPE) and the electrical activation of the implanted dopants have been studied extensively.[1,2] It has been well established that the SPE of amorphous Si (α-Si) layers created by implantation is initiated by thermal annealing at temperatures $\geq$ 400°C and proceeds in a planar fashion. The kinetics of the SPE process was found to follow an Arrhenius equation with an activation energy of 2.7eV.[2] Various models have been proposed to explain the SPE process.[3,4] In most cases, the mechanism leading to SPE is expected to involve the formation and/or motion of defects at or near the amorphous/crystalline interface. In this work we explore the effects of an intense x-ray beam generated by a synchrotron source on the SPE process of ion amorphized Si layers.

A layer of amorphous Si was created near the surface of a single crystal Si to a depth of ~2000Å by 180keV Zn ion implantation. The sample was then irradiated at beam line 10-3 (microprobe beamline) at the Advance Light Source (ALS) for 5-16 hours. The irradiations were carried out with a current of ~300mA at an electron energy of 1.5 GeV in the storage ring. The peak x-ray energy was ~4.0 keV. For 5-16 hours irradiation, the total photons absorbed by the α-Si film was ~ 0.3-1 photon/Si atom (for 4keV photons). After irradiation the samples were annealed at 450-535°C for 1 hr. in a flowing N_2 ambient.

Figure 1 shows the Raman spectra of Si samples with (X) and without (un-X) x-ray irradiation prior to thermal annealing. Notice that in the as-implanted (un-X) sample, the Raman peak of crystalline Si at 521 cm^{-1} is still observable but is shifted to a lower wave number (511.6 cm^{-1}) indicating that in the as-implanted sample, crystalline regions are still present in the amorphous layer and that these crystalline regions are under tensile stress. The Raman spectrum from the X sample shows a completely amorphous layer with no crystalline peak. These results suggest that the ion implanted layer is not completely amorphous and that x-ray irradiation completely amorphizes the layer.

The minimum yield, χ profiles derived from the Rutherford backscattering spectrometry in the <111> channeling orientation (c-RBS) performed on the samples annealed at 535°C are shown in Fig. 2. χ is a measure of the crystalline quality of a crystal and a χ=1 indicates an amorphous (or polycrystalline) structure.[5] The χ value in the X sample is much lower than that in the un-X sample indicating that a much better crystalline layer is obtained by x-ray irradiation prior to thermal annealing. A peak is observed at ~600-700Å below the surface in the χ profiles from both of the annealed samples. This depth corresponds to the maximum in the nuclear energy deposition in the Zn implantation process as calculated using the Monte Carlo computer package TRIM-91.[6]

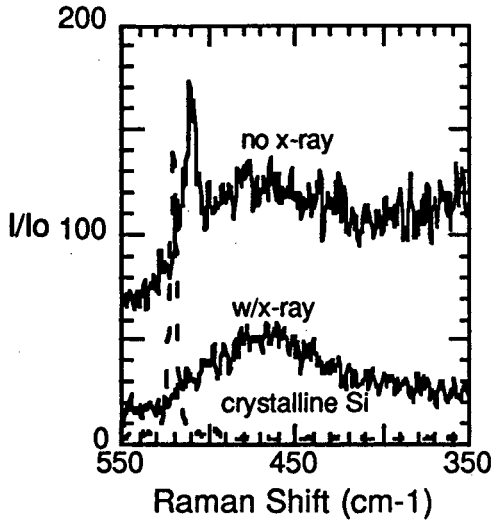

Figure 1. Raman spectra from a crystalline Si sample and the Zn implanted Si samples before and after x-ray irradiation prior to thermal annealing.

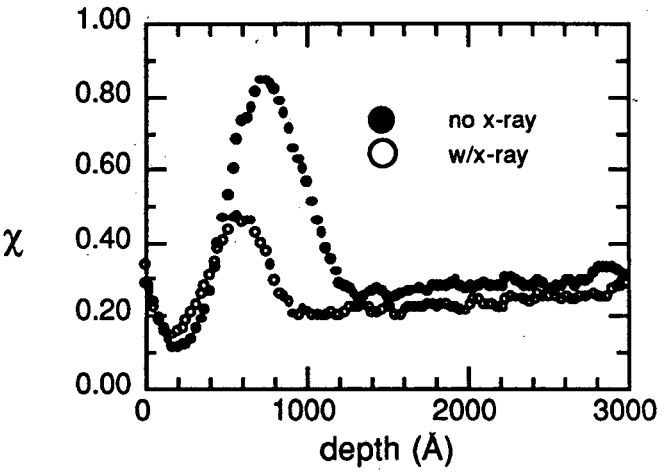

Figure 2. The χ profiles measured by c-RBS in the <111> direction for the Zn implanted Si samples, with and without x-ray irradiation, after annealing at 535°C for 1 hr.

The peaks in χ indicate a high residual damage concentration in the regrown layers. The thickness of these buried defective layers are estimated to be ~600Å and 350Å for the un-X and X samples, respectively. The intensity of the dechanneling peak is dramatically lower for the X sample in comparison to the un-X sample. Annealing these samples at higher temperature (575°C) results in a perfectly regrown layer for the X sample, while a defective region at ~700Å still exists in the un-X sample. c-RBS shows that the SPE of the un-X layer results in a highly defective layer at the region where the nuclear energy deposition is maximum while with x-ray irradiation prior to thermal annealing a much more perfect crystal can be regrown.

The exact mechanism of this x-ray assisted annealing is unknown. We believe that it is related to the K-shell photo-absorption of the Si atoms. Unlike energetic ion beams, the photon beam does not physically amorphize crystalline Si by displacing host atoms in the lattice. Instead the photons are absorbed by the host atoms and the energy is dissipated through various radiative and non-radiative processes. The excitation of the atoms in the α-Si layer through x-ray absorption provides adequate energy for the Si atoms to locally rearrange from a "damaged amorphous" layer into a homogeneously amorphous state. In other words, the crystallites in the α-Si and also at the c/a interface were "dispersed" by the x-rays. This is consistent with the generally believed models on SPE which involve the existence and motion of defects at the c/a interface.[3,4]

The structural change of the α–Si due to x-ray irradiation was further investigated by EXAFS technique. The EXAFS experiments were performed on Si wafers implanted with 180 keV Ga to $1x10^{15}/cm^2$ both as-implanted (Ga un-X) and irradiated with x-ray (Ga-X) (0.7 photons/Si atom) without thermal treatment. The Ga-Si bond distance, R_{Ga-Si} for the Ga un-X and Ga-X samples are very similar and are 2.37Å and 2.39Å, respectively. This measured R_{Ga-Si} are longer than the Si-Si bond distance in the matrix (2.35Å) and are in perfect agreement with the calculated[7] and experimentally obtained[8] value for R_{Ga-Si} in Ga doped Si (2.38Å). The coordination number, CN

of the Ga-X sample (3.6±0.3) is, however significantly higher than that of the Ga un-X sample (3.0±0.3). These results suggest that the Ga atoms in the α-Si created by ion implantation are three-fold coordinated, similar to those reported in Dent et. al.[8] Upon x-ray irradiation, the photons absorbed by the α-Si provide enough energy to locally re-arrange the atoms to close to a four-fold coordinated environment.

In conclusion, we have studied the effect of intense x-ray irradiation on Si layers amorphized by ions and the subsequent SPE single crystal Si. We found that in ion amorphized Si layers, although the ion dose is well above the amorphization threshold, small crystallites are still present. The absorption of x-ray by the Si atoms provides enough energy to disperse the small crystallites in the amorphous Si, reducing the number of interfacial defects as well as locally re-arrange the atoms to form a homogeneously amorphous layer with close to four-fold coordinated environment. This re-arrangement in local structure of the α-Si results in nearly a defect-free crystal after SPE.

We thank K. Jackson and A. Thompson for their coorporation in the use of the beamline at the ALS for the irradiation. We also like to acknowledge C. Kisielowski for the TEM work, K. Roderick for the ion implantation, L. Hsu for assistance in the EXAFS experiments, and E. Haller for helpful discussion.

REFERENCES

1. J. M. Poate and J. S. Williams, in :*Ion Implantation and Beam Processing*, edit. J. S. Willaims and J. M. Poate, (Academic Press, Australia, 1984) pp. 13-57, and references therein.
2. G. L Olson and J. A. Roth, in: *Handbook of Crystal Growth*, vol. 3, edit. D. T. J. Hurle, (Elsevier, The Netherlands, 1994) pp. 257-312, and references therein.
3. F. Spaepen and D. Turnbull, in *Laser-Solid Interactions and Laser Processing*, edited by S. D. Ferris, H. J. Leamy, and J. M. Poate (AIP, New York, 1978), p.73.
4. J. S. Williams and R. G. Elliman, Phys. Rev. Lett. **51**, 1069 (1983).
5. see for example L. C. Feldman, J. W. Mayer, and S. T. Picraux, *Materials Analysis by Ion Channeling-submicron crystallography* (Academic, New York, 1982).
6. J. F. Ziegler, J. P. Biersack and U. Littmark, *The Stopping and Ranges of Ions in Matter* (Pergamon, Oxford, 1985).
7. F. Bechstedt and W. A. Harrison, Phys. Rev. **B39**, 5041 (1989).
8. A. J. Dent, B. R. Dobson, G. N. Greaves, S. Kalbitzer, C. Derst, and G. Müller, Mat. Res. Soc. Symp. Proc. **307**, 21 (1993).

This work was supported in part by the Laboratory Directed Research and Development Program at the Lawrence Berkeley Laboratory and by the Director, Office of Energy Research, Office of Basic Energy Sciences, Materials Science Division of the U. S. Department of Energy under Contract No. DE-AC03-76SF00098. SSRL and ALS are supported by the Office of Basic Energy Sciences of the US Department of Energy.

Principal Investigator: Kin Man Yu, Materials Sciences Division, E. O. Lawrence Berkeley National Laboratory. Email: KMY@lbl.gov. Telephone: 510-486-6656.

Interactions of Structural Defects with Metallic Impurities in Multicrystalline Silicon

S.A. McHugo [1], A.C. Thompson [2], H. Hieslmair [3], E.R. Weber [3], M.D. Rosenblum [4] and J.P. Kalejs [4]

[1] Advanced Light Source Center, Lawrence Berkeley National Laboratory, Berkeley, CA 94720
[2] Center for X-Ray Optics, Lawrence Berkeley National Laboratory, Berkeley, CA 94720
[3] Dept. of Materials Science and Mineral Eng., University of California, Berkeley, CA 94720
[4] ASE Americas Inc., Billerica, MA 01821

Multicrystalline silicon is one of the most promising materials for terrestrial solar cells. The material's low cost and good efficiency make it cost competitive without inherent environmental disposal difficulties. However, it is critical to getter impurities from the material as well as inhibit contamination during growth and solar cell processing. Standard solar cell processing steps such as, phosphorus in-diffusion for p-n junction formation and aluminum sintering for backside ohmic contact fabrication, intrinsically possess gettering capabilities [1-5]. These processes have been shown to improve L_n values in regions of multicrystalline silicon with low structural defect densities but not in highly dislocated regions, suggesting that if impurities are present at these dislocations they are not effectively gettered [6-10]. Recent Deep Level Transient Spectroscopy (DLTS) results indirectly reveal higher concentrations of iron in highly dislocated regions [11] while further work suggests that the release of impurities from structural defects, such as dislocations, is the rate limiting step for gettering in multicrystalline silicon [11-13]. The work presented here directly demonstrates the relationship between metal impurities, structural defects and solar cell performance in multicrystalline silicon

Edge-defined Film-fed Growth (EFG) multicrystalline silicon in the as-grown state and after full solar cell processing was used in this study. Standard solar cell processing steps were carried out at ASE Americas Inc. As-grown cast multicrystalline silicon was also used for comparison. Samples were subjected to a piranha cleaning (5:H_2SO_4, 1:H_2O_2 @ 120°C) for 15 minutes in order to remove organics and metal impurities, prior to all Surface Photovoltage (SPV) and X-Ray Fluorescence (XRF) micro-probe measurements. Metal impurity concentrations and distributions were determined by use of the x-ray fluorescence microprobe (beamline 10.3.1) at the Advanced Light Source, Lawrence Berkeley National Laboratory. The sample was at atmosphere so only elements with Z greater than silicon could be detected, which includes all metal impurities of interest. Multi-layer mirrors arranged in a Kirkpatrick-Baez

orientation focused the x-rays down to ≤ 1μm. The typical sampling depth for metal impurities in silicon is ≈ 50μm. Standard samples with known amounts of various impurities ranging from Al to Zn were used to quantify the impurity concentration in the multicrystalline silicon samples. This system allowed for micron-scale mapping of metal impurities with sensitivities far surpassing conventional techniques. It should be noted that observations of metal impurity agglomerates have been observed with this apparatus previously [14], however, correlation with structural defects was not achieved. Structural defect densities were determined by preferential etching and surface analysis using a Scanning Electron Microscope (SEM) in secondary electron mode. Mapped areas were exactly relocated between the XRF and SEM to allow for direct comparison of impurity and structural defect distributions.

Minority carrier diffusion length (L_n) values were measured on a number of as-grown EFG samples using SPV. Typical L_n values ranged from 10-100μm. XRF studies of this material as well as other as-grown multicrystalline silicon materials reveal the presence of Fe and Ni. The observation of Fe in as-grown multicrystalline silicon are in accord with indirect measurements of other work [11]. An XRF map of Fe is shown below in Figure 1a.

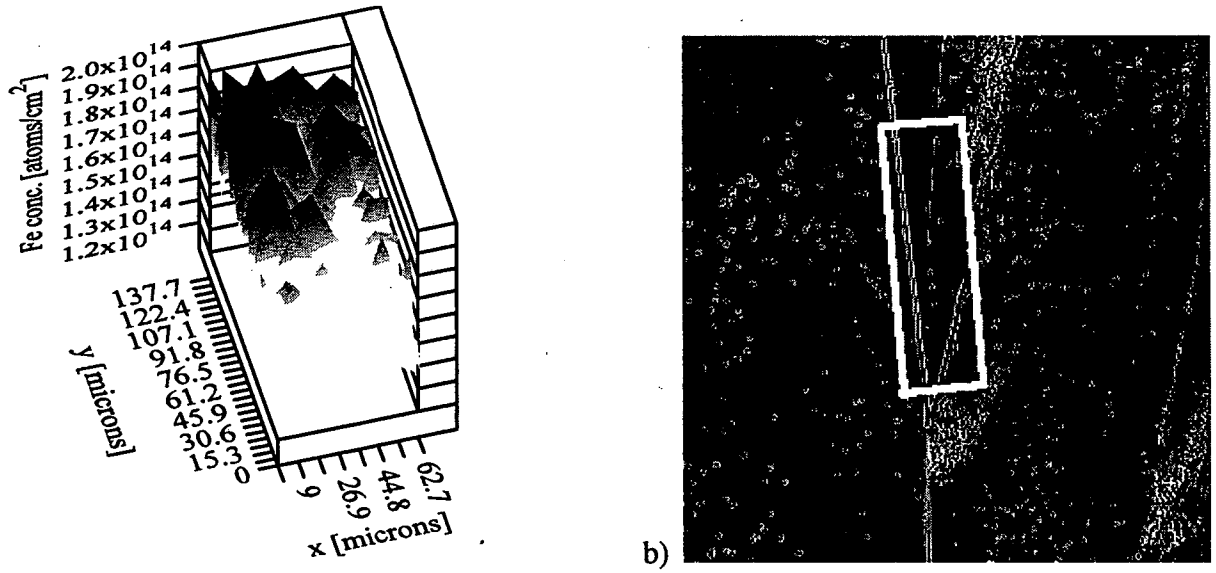

Figure 1: a) X-Ray Fluorescence map of Fe in an EFG multicrystalline silicon sample b) SEM micrograph of a preferentially etched EFG sample showing dislocations and grain boundaries. The XRF scan area of Figure 1a is denoted by the white box.

Following the XRF mapping, the sample from Figure 1a was preferentially etched and analyzed with an SEM in secondary electron mode as shown in Figure 1b where the lines are etched-out grain boundaries and the pits delineate dislocations. By comparison of Figures 1a and b, it is apparent that the Fe is primarily present along two grain boundaries. This is direct evidence that

metal impurities agglomerate at structural defects in as-grown multicrystalline silicon. One would expect this agglomeration since any impurities present during the slow cool from crystal growth would prefer to precipitate at the highly disordered core of a grain boundary. This defect seems to provide an extraordinarily low energy site for Fe which would be required in order to trap impurities at high growth temperatures when the impurities are highly mobile and the impurity supersaturation is low. This concept has been shown for Cu precipitation at structural defects in single and multicrystalline silicon [15,16].

SPV measurements of L_n were also taken on fully processed EFG, as shown in Figure 2.

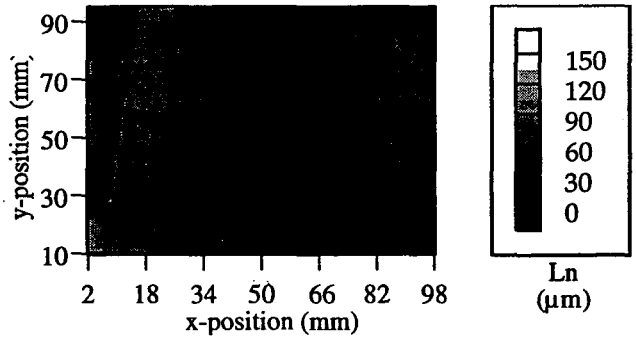

Figure 2: SPV map of L_n across a 10x10 cm EFG solar cell after complete solar cell processing.

Of particular interest is the one poorly performing region down the center of the wafer which is along the growth direction. This region has drastically reduced the solar cell efficiency by ≈ 3% absolute. XRF line scans were taken across this poor region as well as other good regions. A summed spectra taken in the poor region, shown in Figure 3, reveals the presence of Ni and Fe.

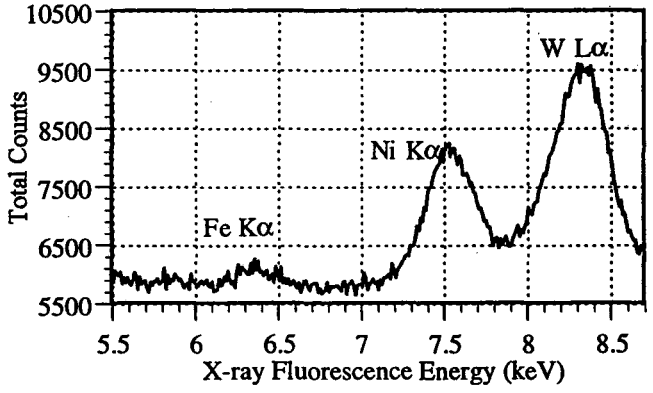

Figure 3: XRF spectra of a fully processed EFG solar cell. This spectra is the sum of 228 spectra taken over a line scan through the low L_n regions in Figure 2.

For this scan, 228 points in 1.25 μm steps were taken with a 5 minute dwell time at each point. The W Lα is a stray signal from the apparatus. XRF scans taken in good regions detected neither these impurities nor any other impurities. The Ni was widely distributed while the Fe signal was

too weak at any point for spatial resolution. This is direct proof that metal impurities are not adequately gettered during typical solar cell processing steps.

Considering the results presented here and other past work [11-13], which show incomplete gettering for lengthy anneal times such that impurity diffusion from the original site to the gettering layer should be sufficient, it is highly probable that these impurities are not gettered from this material because of sluggish impurity release from defects. Further work must be carried out to determine the cause for the slow release.

ACKNOWLEDGMENTS

The authors would like to thank S.M. Myers, F.G. Kirscht and T. Heiser for wonderfully enlightening conversations.

REFERENCES

1. L. Baldi, G. Cerofolini and G. Ferla, J. Elec. Chem. Soc. **127**, 164 (1980)
2. W. Schröter and R. Kühnapfel, Appl. Phys. Lett. **56**, 2207 (1990)
3. E.Ö. Sveinbjörnsson, O. Engström and U. Södervall, J. Appl. Phys. **73**, 7311 (1993)
4. R.D. Thompson and K.N. Tu, Appl. Phys. Lett. **41**, 440 (1982)
5. M. Apel, I. Hanke, R. Schindler and W. Schröter, J. Appl. Phys. **76**, 4432 (1994)
6. B.L. Sopori, L. Jabstrzebski, T. Tan and S. Narayanan: in *Proc. of the 12th European Photovoltaic Solar Energy Conference*, Netherlands, 1994, p. 1003
7. S.A. McHugo, J. Bailey, H. Hieslmair and E.R. Weber: in *1994 IEEE First World Conf. on Photovoltaic Energy Conversion,* Waikoloa, Hawaii, U.S.A., 1994, p. 1607
8. M. Loghmarti, R. Stuck, J.C. Muller, D. Sayah and P. Siffert, Appl. Phys. Lett. **62**, 979 (1993)
9. O. Porre, M. Stemmer and M. Pasquinelli, Materials Science and Eng. B24, 188 (1994)
10. S.A. McHugo, H. Hieslmair and E.R. Weber: in *Defects in Semiconductors 18, International Conference on Defects in Semiconductors,* edited by M. Suezawa and H. Katayama-Yoshida, Sendai, Japan (1995) p. 1979
11. S.A. McHugo, H. Hieslmair and E.R. Weber: Applied Physics A, Feb, 1997
12. M. Seibt and W. Schröter: *6th Workshop on the Role of Impurities and Defects in Silicon Device Processing,* Aug. 1996
13. S.A. McHugo, H. Hieslmair and E.R. Weber: ibid 17
14. A.C. Thompson and R. Holm, to be published
15. S.A. McHugo and W.D. Sawyer, Appl. Phys. Lett. **62**, 2519 (1993)
16. B. Shen, T. Sekiguchi, J. Jablonski and K. Sumino, J. Appl. Phys. **76**, 4540 (1994)

This work was supported by the Director, Office of Energy Research, Office of Basic Energy Sciences, Materials Sciences Division, of the U.S. Department of Energy, under Contract No. DE-AC03-76SF00098.

Principal Investigator: Scott McHugo, Advanced Light Source Center, Ernest Orlando Lawrence Berkeley National Laboratory. E-mail: samchugo@lbl.gov, Tel: 510-486-4874

Metallic Impurities in Gallium Nitride Grown by Molecular Beam Epitaxy

S.A. McHugo[1], J. Krueger[2], C. Kisielowski[2], E.R. Weber[2] and M. Rubin[3]

[1] Advanced Light Source Center, Lawrence Berkeley National Laboratory, Berkeley, CA 94720
[2] Materials Sciences Division, Lawrence Berkeley National Laboratory, Berkeley, CA 94720
[3] Energy and Environment Division, Lawrence Berkeley National Laboratory, CA 94720

Transition metals are often encountered in trace amounts in semiconductors. They have been extensively studied in most elemental and compound systems, since they form deep donor and/or acceptors levels which usually degrade the electronic and optical material properties. For example, in the early days of GaAs bulk growth, Cr has been used to achieve semi-insulating GaAs material. Only very little is known about transition metals in recent III-V semiconducting materials, such as GaN, AlN and InN. These few studies have been done exclusively on Metal-Organic Chemical Vapor Deposition-(MOCVD) or Hybrid Vapor Phase Epitaxy HVPE-grown GaN [1-2].

Preliminary x-ray fluorescence studies at the Advanced Light Source, beamline 10.3.1, Lawrence Berkeley National Laboratory have revealed that GaN materials grown by Molecular Beam Epitaxy (MBE) have Fe, Ni and Cr as the dominant transition metal contaminants as shown below in Figure 1.

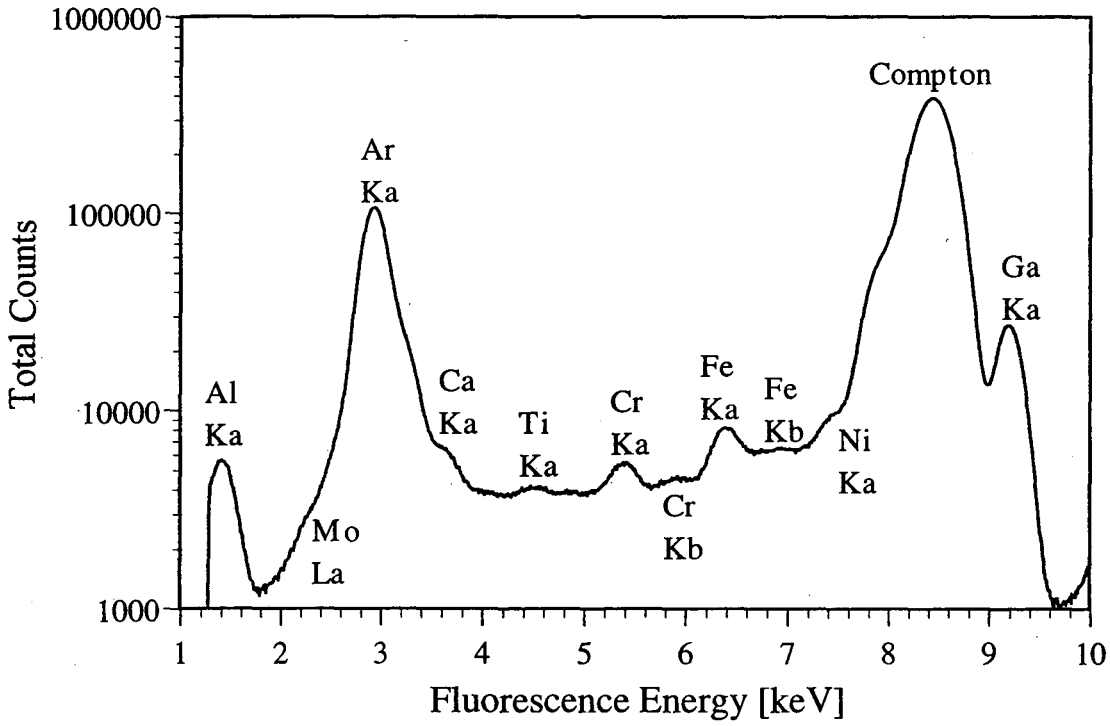

Figure 1: X-ray Fluorescence spectra of a MBE-grown GaN thin film intentionally doped with Ca. The spectra is a sum of 81 points, each with a 5 minute dwell time. The substrate is sapphire (Al_2O_3). The Ar and Compton peaks originate from the experimental apparatus. Of particular interest are the large Fe, Cr and Ni signals.

This finding is commensurate with the extremely high concentrations of hydrogen, carbon and oxygen (up to 10^{20} cm^{-3}) measured by Secondary Ion Mass Spectroscopy (SIMS). This indicates that GaN films are contaminated with a variety of elements.

Preliminary work using the mapping capabilities of the x-ray fluorescence microprobe revealed the metal impurities were inhomogeneously distributed over the film. An example is shown below in Figure 2.

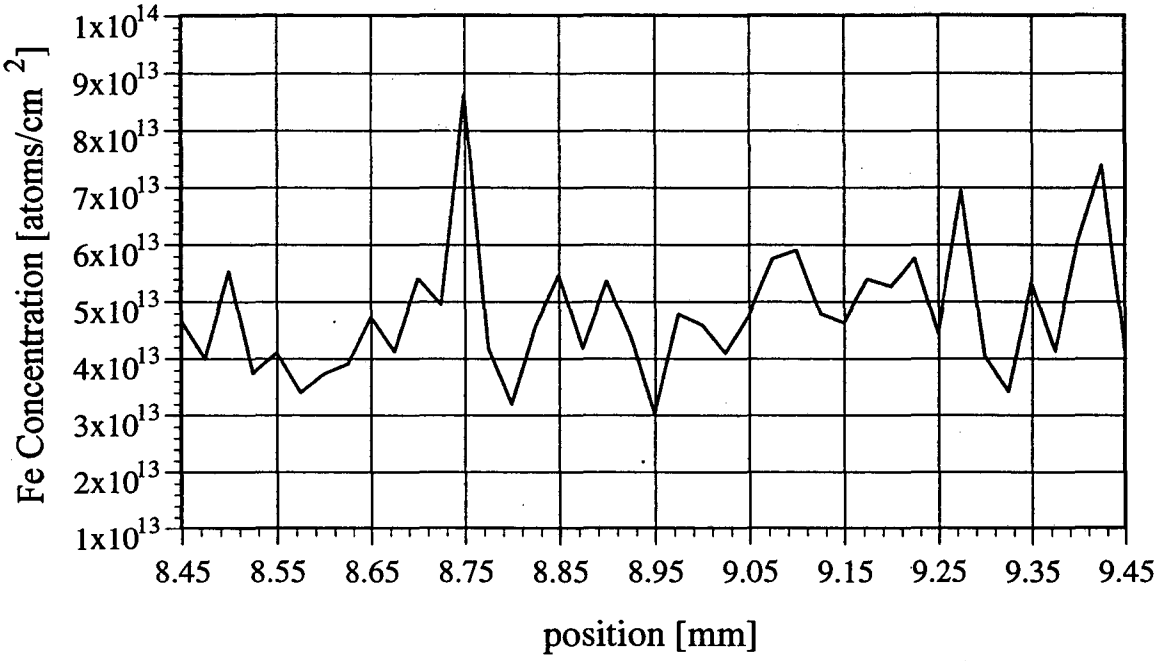

Figure 2: Fe concentration profile across 1mm of a GaN film with 25μm steps. X-ray spot size was 2.1μm. Distinct Fe spikes are seen at 8.75, 9.275 and 9.425mm.

Future work of this collaboration will be to find a correlation between the existence of transition metals in our MBE films, as revealed by x-ray fluorescence, and Photoluminescence (PL) spectra taken in the infrared region. Also, we will make use of the 1μm spatial resolution of x-ray microprobe to locate the contaminants in relation to structural defects in the GaN films. Because of the large strain caused by the lattice mismatch between the GaN films and the substrates, the films grow in a columnar order with high densities of grain boundaries and dislocations. These structural defects offer preferential sites for metal precipitation or agglomeration which could degrade the optical properties of this material more so than if the impurities were left dissolved in the GaN.

ACKNOWLEDGMENTS

The authors would like to thank A.C. Thompson.

REFERENCES

1. Baur, J.; Maier, K.; Kunzer, M.; Kaufmann, U. etal, "Infrared luminescence of residual iron deep level acceptors in gallium nitride (GaN) epitaxial layers", Appl. Phys. Lett., **64** (7), pgs. 857-9

2. Pressel, K.; Heitz, R.; Eckey, L.; Loa, I. etal, "Identification of transition metals in GaN", in: Gallium Nitride and Related Materials. First International Symposium, Boston, MA, USA, 27 Nov.-1 Dec. 1995. Edited by: Ponce, F.A.; Dupuis, R.D.; Nakamura, S., Edmond, J.A. Pittsburgh, PA, USA: Mater. Res. Soc, 1996. p. 491-6.

This work was supported by the Director, Office of Energy Research, Office of Basic Energy Sciences, Materials Sciences Division, of the U.S. Department of Energy, under Contract No. DE-AC03-76SF00098.

Principal Investigator: Scott McHugo, Advanced Light Source Center, Ernest Orlando Lawrence Berkeley National Laboratory. E-mail: samchugo@lbl.gov, Tel: 510-486-4874

The Rate-Limiting Mechanism of Transition Metal Gettering in Multicrystalline Silicon

S.A. McHugo*, A.C. Thompson*, M. Imaizumi**, H. Hieslmair*** and E.R. Weber***
* Lawrence Berkeley National Laboratory, Advanced Light Source, Berkeley, CA 94720, USA
**Toyota Technological Institute, Nagoya 468, JAPAN
***Dept. of Materials Science, University of California at Berkeley, CA 94720, USA

Multicrystalline silicon is a very interesting material for terrestrial solar cells. Its low cost and respectable energy conversion efficiency (12-15%) makes it arguably the most cost competitive material for large-volume solar power generation. However, the solar cell efficiency of this material is severely degraded by regions of high minority carrier recombination which have been shown to possess both dislocations and microdefects. These structural defects are known to increase in recombination activity with transition metal decoration. Therefore, gettering of metal impurities from the material would be expected to greatly enhance solar cell performance. Contrary to this rationale, experiments using frontside phosphorus and/or backside aluminum treatments have been found to improve regions with low recombination activity while having little or no effect on the high recombination regions and in turn only slightly improving the overall cell performance [1-4]. The goal of this research is to determine the mechanism by which gettering is ineffectual on these high recombination regions.

We have performed studies on integrated circuit (IC) quality single crystal and multicrystalline solar cell silicon (mc-silicon) in the as-grown state and after a variety of processing/gettering steps. With Surface Photovoltage measurements of the minority carrier diffusion length which is inversely proportional to carrier recombination (Figure 1), we have seen that aluminum gettering is effective for improving IC quality material but ineffective for improving the regions of initially low diffusion lengths (high recombination rates) in mc-silicon.

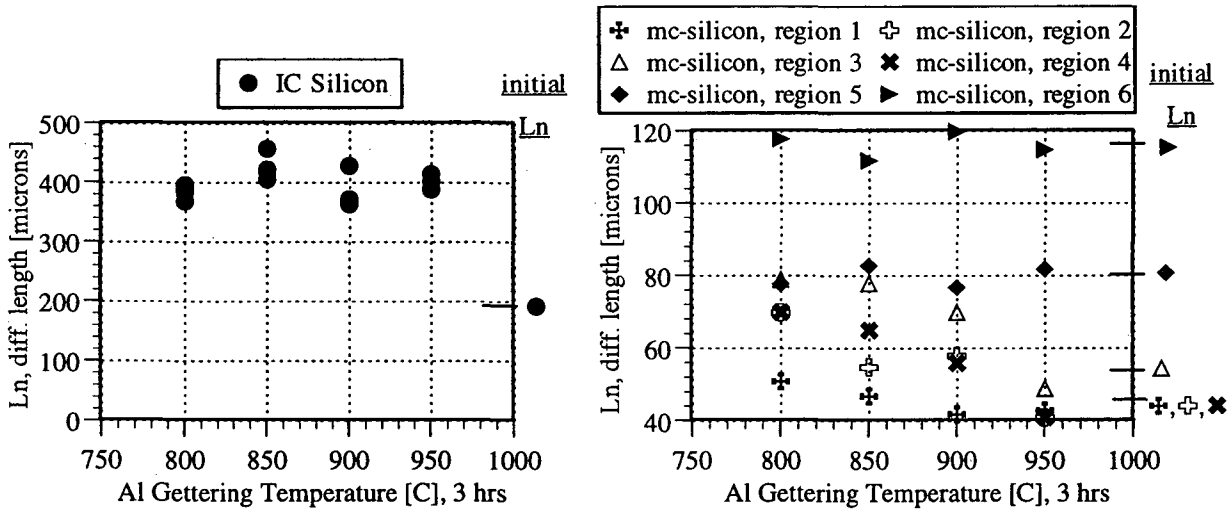

Figure 1: Minority carrier diffusion length (Ln) measurements on IC quality single crystal silicon and solar grade multicrystalline silicon (mc-silicon).

Of particular interest is the great increase in diffusion length for IC material as compared to the mc-silicon. Clearly the IC material has benefited to a greater extent from the gettering procedure than the mc-silicon. Also, the mc-silicon regions of moderate to high initial diffusion length are

unaffected by the gettering treatments while the initially poor diffusion length regions are moderately improved but to a lesser extent at higher temperatures. In regions 1-4 of the mc-silicon have a high dislocation density while regions 5 and 6 have a very low dislocation density. This suggests dislocations drastically increase carrier recombination rates in as-grown material and after gettering treatments.

From our Deep Level Transient Spectroscopy (DLTS) results, shown in Figure 2, we have determined that, in as-grown mc-silicon, metal impurities primarily dwell in regions of high dislocation density. These regions are seen to have significant carrier recombination rates. Since DLTS can only detect dissolved impurities and not impurities precipitated/agglomerated at structural defects, heat treatments were employed to reveal the impurities. The samples were annealed at 1100°C for 4 minutes to dissolve any impurities into the silicon matrix and rapidly quenched to room temperature to leave the impurities in a dissolved state.

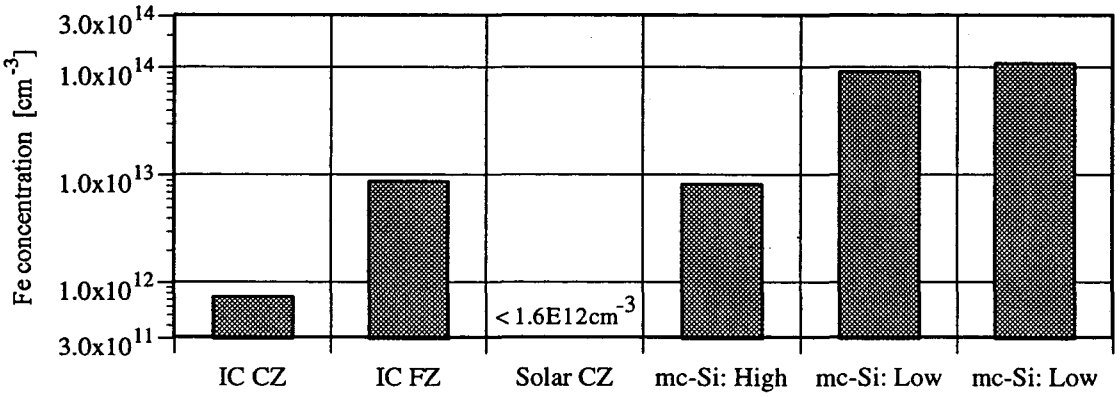

Figure 2: DLTS results from as-grown IC grade Czochralski (CZ), Float Zone (FZ), solar grade CZ, multicrystalline silicon (mc-Si) with high and low dislocation densities. The high dislocation and low dislocation density materials possessed diffusion lengths of ≈ 40μm and 130μm respectively. The Solar CZ Fe concentration could only be determined to be lower than $1.6x10^{12}$ atoms/cm^3 due to an intrinsic limitation of the DLTS apparatus.

These results provide indirect proof that a large concentration of Fe atoms reside predominantly at dislocations in mc-silicon where minority carrier diffusion lengths are low. In order to directly prove this assumption we have used synchrotron-based x-ray fluorescence mapping, beamline 10.3.1 at the Advanced Light Source Lawrence Berkeley National Laboratory, and correlated structural analysis. From this work we have concluded that metal impurities reside in discrete agglomerations, suggesting the impurities are precipitated at structural defects. An example of Ni agglomerations is shown in Figure 3. Previous work has shown Fe agglomerations at dislocations and grain boundaries in another manufacturer's material, see other Advanced Light Source abstract entitled "Interactions of Structural Defects with Metallic Impurities in Multicrystalline Silicon".

We have annealed the sample of Figure 3 at 500°C for 30 seconds with a rapid quench to room temperature in order to freeze in the kinetics of impurity dissolution. Based on diffusion data of Ni in silicon, [5], one would expect significant diffusion of the Ni for this anneal temperature and time. Following this anneal we have scanned the same region as in Figure 3 using the x-ray fluorescence microprobe. These results are shown in Figure 4.

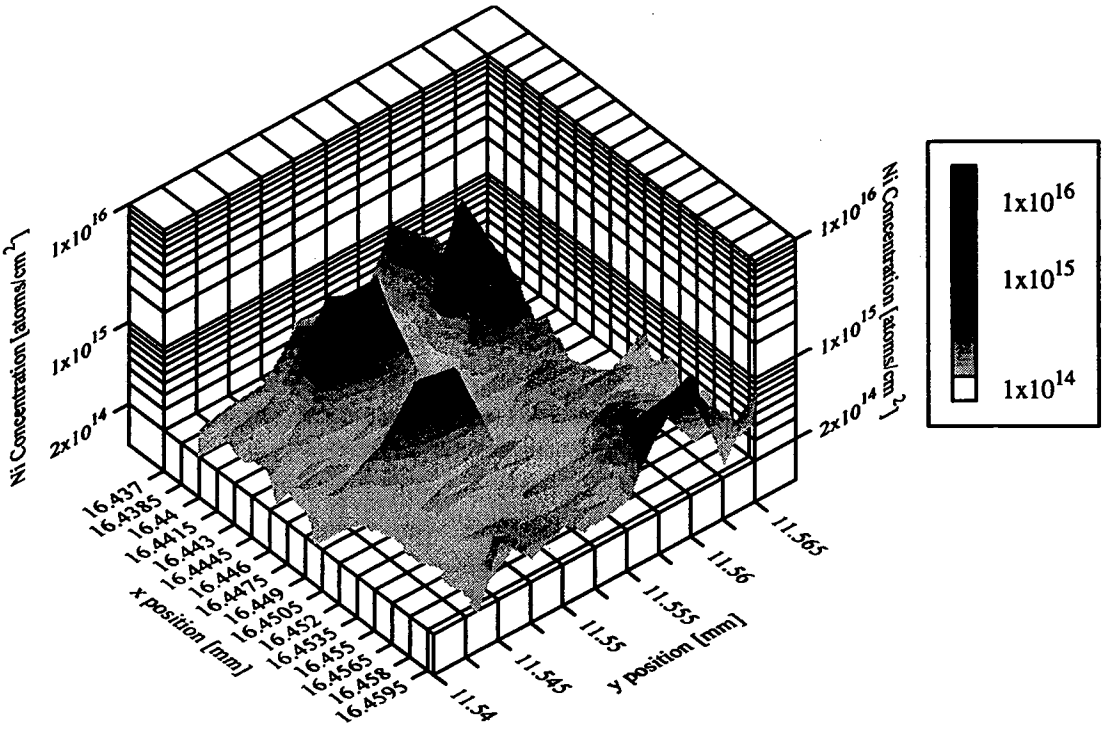

Figure 3: Ni distribution across as-grown multicrystalline silicon. Note the discrete agglomerations of impurities. The scan range is 23μm x 25μm in the x and y directions respectively.

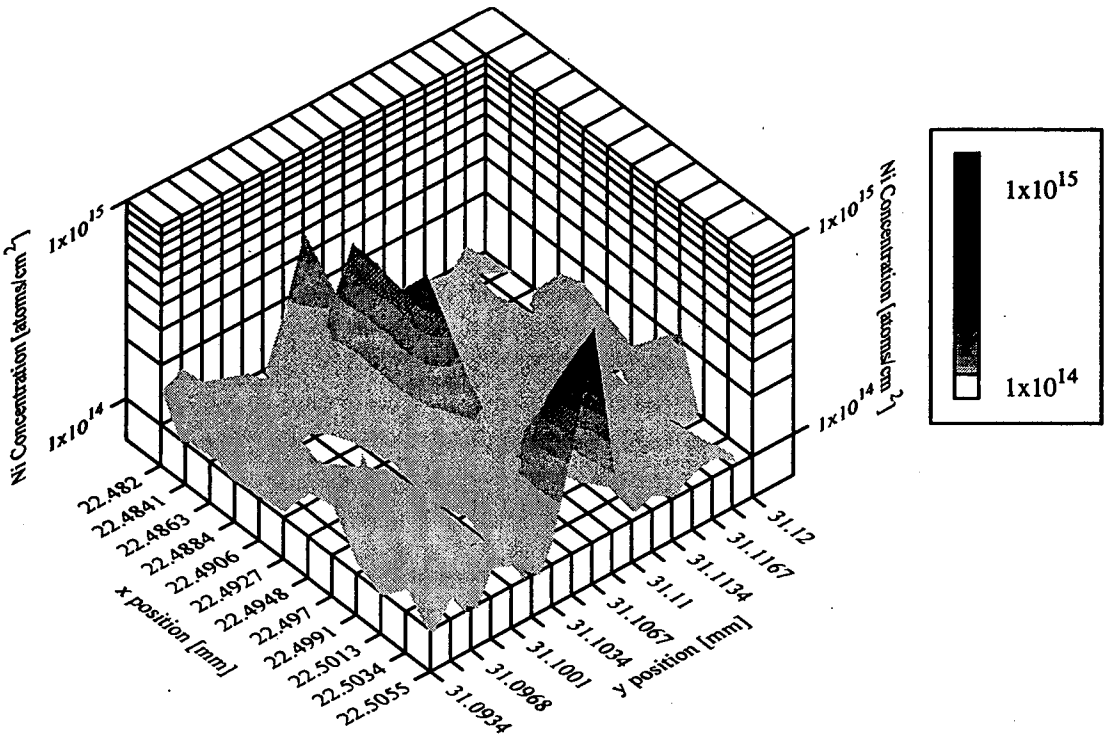

Figure 4: Ni distribution across multicrystalline silicon that has been subjected to a 500°C-30 second anneal. Note the continued presence of discrete agglomerations of impurities and the decrease of the Ni concentration compared to Figure 3. The scan range is 23.5μm x 26.6μm in the x and y directions respectively. This region is approximately the same region as scanned in Figure 3.

It must be noted that the x and y coordinates are labeled differently between the two figures but the scans took place over approximately the same regions. A nice correspondence is seen between the "ridge" of Ni at 31.105mm in Figure 4 and the ridge at 11.56mm in Figure 3. The scan in Figure 4 does not contain the area where the additional Ni agglomerations are seen in Figure 3. Of particular interest we see the Ni concentration along the ridge has decreased with the 500°C-30 second anneal. This is understandable as Ni is expected to rapidly diffuse during the heat treatment, e.g., the typical diffusion length of this impurity ($\sqrt{4Dt}$) is ≈109μm. However, complete dissolution of the nickel precipitate has not occurred. Theoretical modeling of nickel diffusion at this temperature and time will be carried out to determine if complete dissolution would be expected.

Our immediate future work will consist of impurity mapping the region in Figures 3&4 after the material has undergone a gettering treatment. Following the impurity mapping, the sample will be preferentially etched to reveal structural defects and a correlation between Ni distributions and defects can be achieved. Additionally, multicrystalline silicon with Fe intentionally introduced during the growth process will be subjected to experiments similar to that of the material in Figures 3-4.

From this work, one could possibly conclude that gettering as applied to multicrystalline silicon is limited by the *release* of the impurity from structural defects. This fact suggests the metal could be in the form of a stable metal carbide or oxide which is not easily dissolved or possibly as a metal atom or metal silicide that is highly stabilized by the strain field of the structural defect. In the future, it would be desirable to learn the chemical nature of the metal atom at these structural defects with the use of soft x-ray fluorescence or x-ray absorption studies with similar mapping capabilities.

ACKNOWLEDGMENTS

The authors would like to thank Sumitomo SiTiX Corp. for providing the multicrystalline silicon for this work.

REFERENCES

[1] M. Loghmarti, R. Stuck, J.C. Muller, D. Sayah, P. Siffert, Appl. Phys. Lett., **62**, 979 (1993)
[2] O. Porre, M. Stemmer, M. Pasquinelli, Mat. Sci. & Eng. **B24**, 188 (1994)
[3] B.L. Sopori, L. Jastrzebski, T. Tan, S. Narayanan in *Proc. of the 12th European Photovoltaic Solar Energy Conf.,* Netherlands, 1994, p. 1003
[4] S.A. McHugo, H. Hieslmair, E.R. Weber, Appl. Phys. A, Feb. 1997
[5] E.R. Weber, Appl. Phys. A **30**, 1 (1983)

This work was supported by the Director, Office of Energy Research, Office of Basic Energy Sciences, Materials Sciences Division, of the U.S. Department of Energy, under Contract No. DE-AC03-76SF00098.

Principal Investigator: Scott McHugo, Advanced Light Source Center, Ernest Orlando Lawrence Berkeley National Laboratory. E-mail: samchugo@lbl.gov, Tel: 510-486-4874

X-Ray Fluorescence Microtomography of SiC Shells

G.E. Ice,[1] J.-S. Chung,[1] and M. Nagedolfeizi[2]
[1]Oak Ridge National Laboratory, Oak Ridge, TN, USA
[2]University of Tennessee, Knoxville, TN, USA

INTRODUCTION

TRISCO coated fuel particles contain a small kernel of nuclear fuel encapsulated by alternating layers of C and SiC as shown in Fig. 1. The TRISCO coated fuel particle is used in an advanced fuel designed for passive containment of the radioactive isotopes. The SiC layer provides the primary barrier for radioactive elements in the kernel. The effectiveness of this barrier layer under adverse conditions is critical to containment.

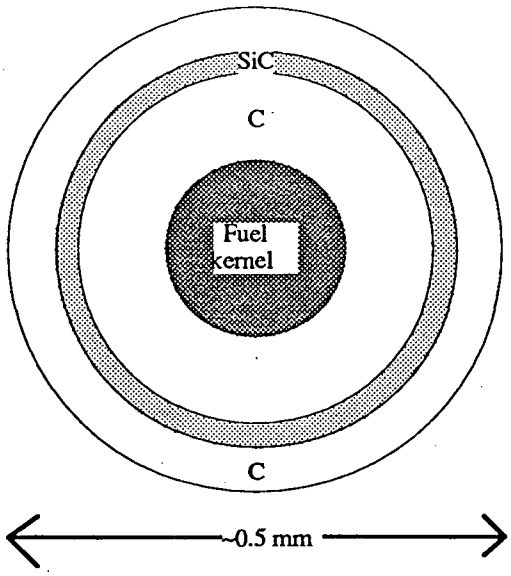

Figure 1. Schematic of TRISCO fuel element.

We have begun the study of SiC shells from TRISCO fuel. We are using the fluorescent microprobe beamline 10.3.1. The shells under evaluation include some which have been cycled through a simulated core melt-down. The C buffer layers and nuclear kernels of the coated fuel have been removed by laser drilling through the SiC and then exposing the particle to acid. Elements of interest include Ru, Sb, Cs, Ce and Eu. The radial distribution of these elements in the SiC shells can be attributed to diffusion of elements in the kernel during the melt-down. Other elements in the shells originate during the fabrication of the TRISCO particles.

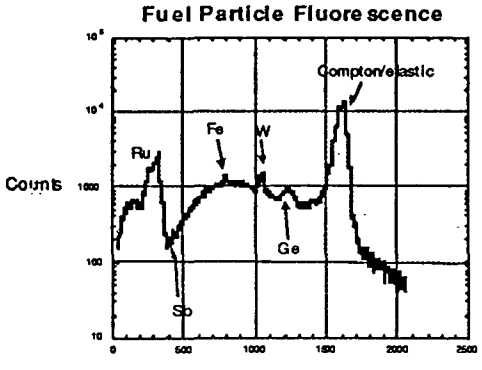

Figure 2. Typical fluorescence spectra from a TRISCO fuel sphere.The observed peaks are tentatively identified.

X-ray fluorescence microtomography is an ideal tool for this work because it is nondestructive, it is sensitive to heavy elements in a low Z matrix, and because it provides a 3-D picture of the elemental distribution. This observed elemental distribution can be correlated with flaws and defects in the SiC shell. The elemental distribution from a typical fuel particle is shown in Fig. 2. We have measured the 2-D distribution of 10 elements in a slice through the center of the SiC shell. This data is presently being analyzed.

This work was sponsored in part by the Laboratory Directed Research and Development Program of the Oak Ridge National Laboratory and the Division of Materials Sciences, U.S. Department of Energy under contract DE-AC05-96OR22464 with Lockheed Martin Energy Research Corporation and by the U.S. Department of Energy BES Materials Science under Contract No. W-31-109-ENG-38.

Principal investigator: Gene E. Ice Oak Ridge National Laboratory, Oak Ridge, TN, USA Email: gei@ornl.gov. Telephone: 423-574-2744

Beamline 10.3.2 Abstracts

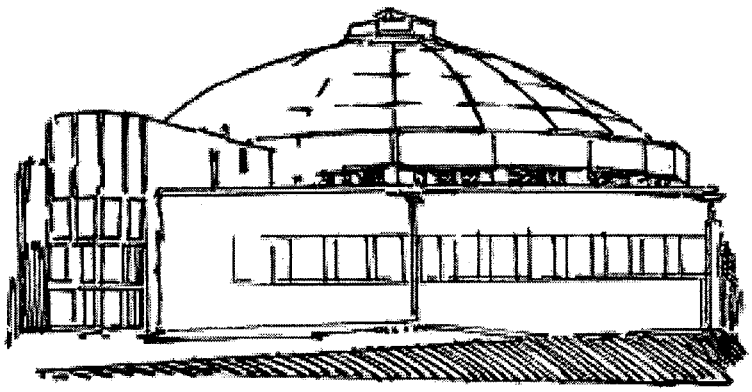

Ultrafast Laser Pump/X-Ray Probe Experiments

J. Larsson,[1] P.A. Heimann,[2] Z. Chang,[3] E. Judd,[1] P.H. Bucksbaum,[1,3]
H.C. Kapteyn,[3] R.W. Lee,[4,1] A. Machacek,[5] M.M. Murnane,[3] H.A. Padmore,[2]
P.J. Schuck,[1] J.S. Wark,[5] and R.W. Falcone[1]

[1]Department of Physics, 366 LeConte Hall, University of California Berkeley,
Berkeley CA 94720-7300, USA, E-mail: jorgen@physics.berkeley.edu

[2]Advanced Light Source, Accelerator and Fusion Research Division,
Lawrence Berkeley National Laboratory, Berkeley, California 94720, USA

[3]Center for Ultrafast Optical Science, University of Michigan, Ann Arbor, MI 48109, USA

[4]L-399, Lawrence Livermore National Laboratory, P.O. Box 808, Livermore, CA 94551, USA

[5]Department of Physics, Clarendon Laboratory, University of Oxford, Parks Road,
Oxford OX1 3PU, U.K.

In an ongoing project aimed at probing solids using x-rays obtained at the ALS synchrotron with a sub-picosecond time resolution following interactions with a 100 fs laser pulse, we have successfully performed pump-probe experiments limited by the temporal duration of ALS-pulse. We observe a drop in the diffraction efficiency following laser heating. We can attribute this to a disordering of the crystal. Studies with higher temporal resolution are required to determine the mechanism. We have also incorporated a low-jitter streakcamera as a diagnostic for observing time-dependant x-ray diffraction. The streakcamera triggered by a photoconductive switch was operated at kHz repetition rates. Using UV-pulses, we obtain a temporal response of 2 ps when averaging 5000 laser pulses. We demonstrate the ability to detect monochromatized x-ray radiation from a bend-magnet with the streak camera by measuring the pulse duration of a x-ray pulse to 70 ps.

Our experimental set-up is shown in Fig. 1.The source of x-ray radiation was the beamline 10.3.2. Most of the experiments were performed with the ALS operating in double-bunch mode, for which the repetition frequency is 3†MHz. The divergence was set by a round 0.4 mrad aperture inserted in the beam. The unfocused, white radiation is monochromatized by the first Si (111) crystal, shown in figure 1. A second flat sample crystal is excited by a laser pulse in pump/probe experiments. Both crystals are diffracting in the vertical plane corresponding to s polarisation. For the experiments described here, the Bragg angle of the first crystal was chosen to be 22.5 degrees in order to reflect 5 keV radiation. In order to maximize the signal on the streak camera, the first crystal is bent in order to focus the x-ray radiation onto the streak camera in the horizontal plane. Bending of the crystal was achieved by gluing the wafer onto a cylindrically machined aluminium mandrel. The slope error of the surface of the wafer along the horizontal direction was about 1 mrad, which is about ten times the width of the rocking curve for the used reflection.
A horizontal focus of about 0.4 mm was observed on heat-sensitive paper. Using a Silicon photo diode we measure the number of photons per pulse to be 1500. In future experiments, we expect to be able to achieve about an order of magnitude higher flux levels by using a crystal with a better flatness in the plane direction .

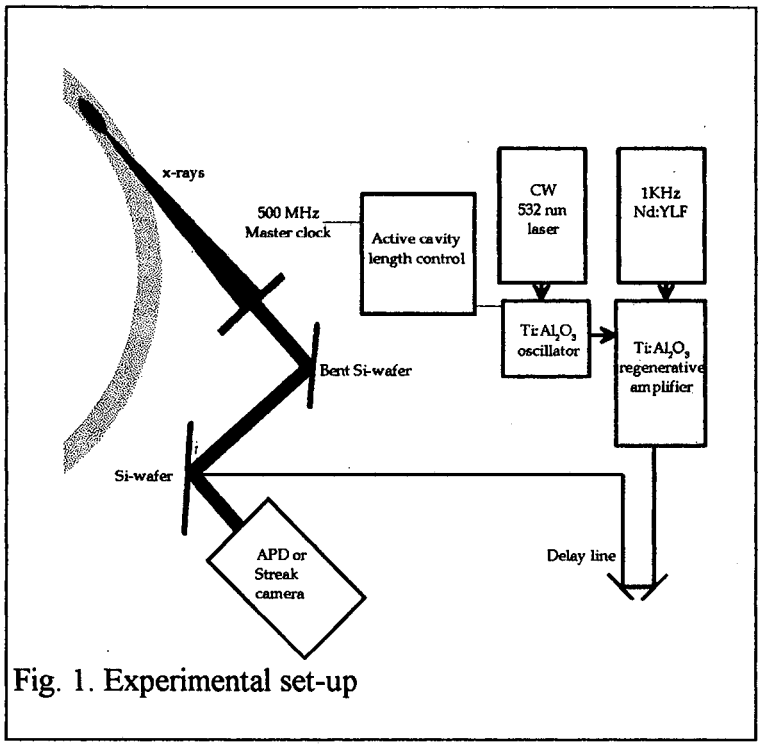

Fig. 1. Experimental set-up

Our laser set-up consists of a non-commercial Ti:Sapphire oscillator pumped by a Millenium Nd:Yag laser and a Positive light Spitfire regenerative amplifier operating at a frequency of 1 kHz. The pulse duration is about 100 fs and the pulse energy is about 0.5 mJ. The synchronisation of the laser to the synchrotron is achieved by locking the laser oscillator frequency to the master clock of the synchrotron[3]. From the error signal in the stabilizing electronics, we estimate the jitter between the laser and the synchrotron to be about 5 ps. The regenerative amplifier is triggered off a subharmonic of the master clock.

We obtain high temporal resolution in one of two ways. It is possible to use a avalanche photodiode to separate consecutive ALS pulses. By varying the temporal delay between the laser and the x-ray pulse using a delay line we can obtain a temporal resolution limited by the ALS pulse.

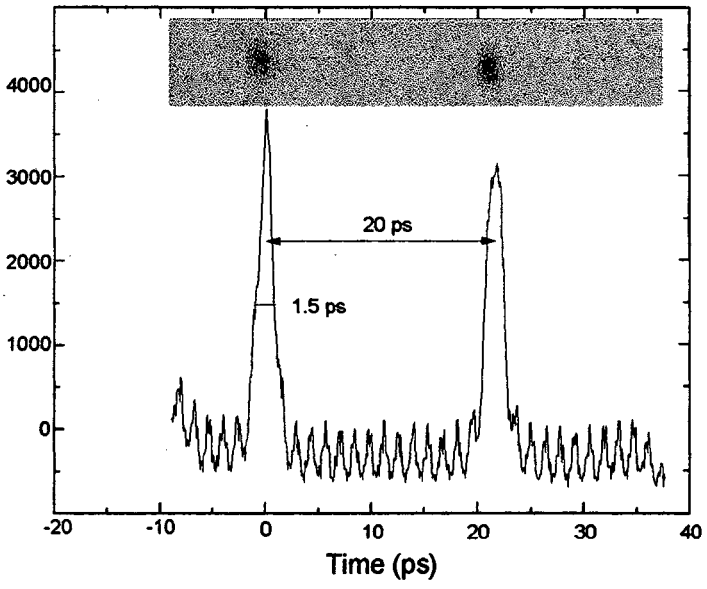

Fig. 2. The temporal response of the streak camera was measured to be 2 ps when averaging 5000 pulses.

In order to improve the time-resolution we use an x-ray streak camera. With a commercial streak camera, we can detect a single pulse from the synchrotron. However, we observe a relatively low number of photons. We estimate that we can detect approximately 15 photoelectrons per pulse, indicating that the quantum efficiency of our 1000 Å thick CsI photo cathode is about 1%. It is clear that a different approach is needed to achieve a good signal-to-noise ratio. One way of achieving this is to average

over multiple pulses. To use this approach, the temporal jitter between the streak camera and laser must be less than the expected time resolution. It has been shown that this can be achieved by triggering the sweep to the deflection plates using a photo conductive switch. [3]. We employed a X-ray streak camera which is capable of operating at kHz repetition rates. This camera has previously been shown to have a single-shot time resolution of 880 fs for x-ray when triggered by a photo-conductive switch [2]. More recently, this resolution was improved to 540 fs by an improved sweep plate design and using a faster sweep speed [4].

The relative jitter of the streak camera to the laser was measured using UV pulses obtained by frequency mixing in KDP crystals. Part of the 800 nm light from the laser, with a pulse energy of about 20 μJ, was used to trigger a GaAs photo-conductive switch. A fused silica window intersected the laser beam, to provide a well-defined delay of 20 ps between two parts of the UV beam incident on the photocathode. The two pulses were then used to calibrate the time response and relative jitter of the streak camera. The integrated temporal response of the streak camera was derived from the data displayed in Fig. 3. Since we did not obtain any single-shot data we cannot give an accurate value for the trigger jitter. We did however determine the temporal multiple shot response to be 2 ps, when averaging 5000 laser pulses.

As a test of our ability to observe picosecond time scale events in the x-ray spectral region with the ultra-fast streakcamera, we measured the pulse duration of the ALS, operating at an electron energy of 1.9 GeV, and at a beam current of 30 mA, in 2-bunch mode. The results of the measurements are shown in Fig.4. The data was obtained by averaging over 2000 pulses. The observed pulse duration of 70 ps is in good agreement with previous measurements of the ALS pulse duration using a fast photo diode and a streak camera sensitive to visible light.

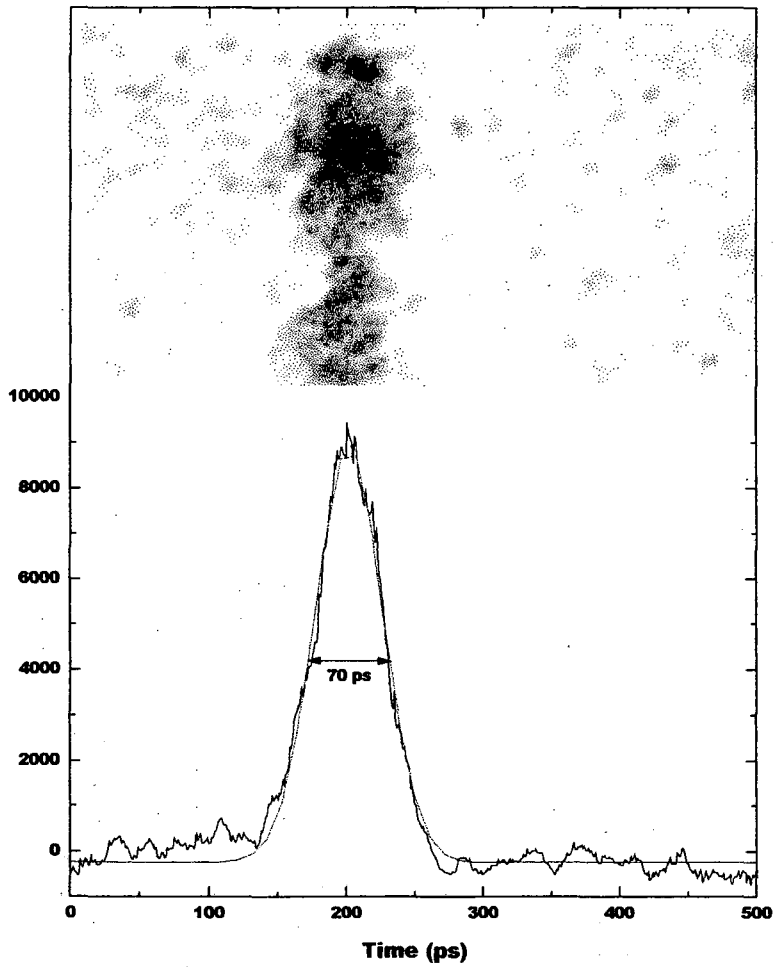

Fig. 3. The pulse duration of the ALS was measured to 70 ps with a streak camera operating an averaging mode.

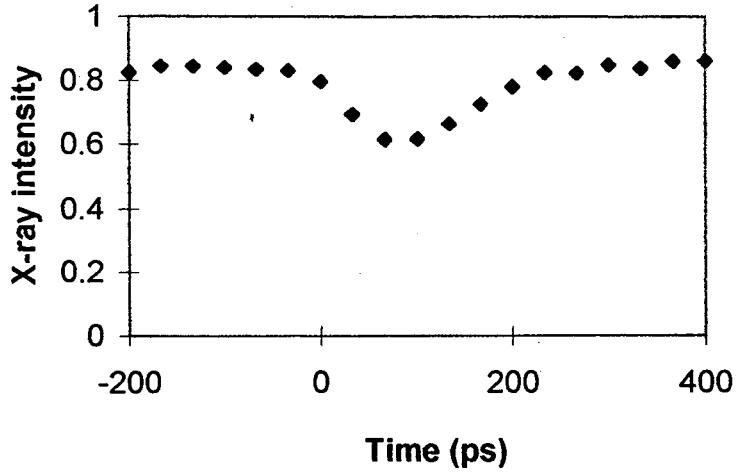

Fig. 4. Diffracted x-ray intensity from a InSb sample as function of delay between laser and x-ray probe.

In experiments using the avalanche photodiode we observe a rapid disordering of a InSb crystal. The diffracted x-ray intensity on the Bragg maximum with variable delay between the laser and the x-ray pulse is shown in Fig. 4. A decrease is observed in a time limited by the ALS pulse length followed by a slower increase. Experiments with higher temporal resolution are in progress.

In conclusion, we show a rapid disordering of a InSb crystal. The resolution was determined by the duration of the ALS pulse. We also demonstrate that we can detect x-ray radiation from a synchrotron source with a temporal resolution of 2 ps, by using an ultrafast x-ray streak camera. Our set-up will allow us to pursue laser pump/x-ray probe experiments to monitor structural changes in materials with ultrafast time resolution.

References

1. D. Bourgeois, T. Ursby, M. Wulff, C. Pradervand, A. Legrand, W. Schildkamp, S Labouré, V. Srajer, T. Y. Teng, M. Roth and K. Moffat: J. Synchrotron Rad. 3, 65 (1996)
2. Z. Chang, A. Rundquist, J. Zhou, M. M Murnane, H. C. Kapteyn, X. Liu, B. Shan, J. Liu, L. Niu, M. Gong and X. Zhang: Appl. Phys. Lett. 69, 133 (1996)
3. A. Maksimchuk, M. Kim, J. Workman, G. Korn, D. Du, D. Umstdter and G. Mourou: Rev. Sci. Instr. 67, 697 (1996)
4. Z. Chang, A. Rundquist, H. Wang H. C:. Kapteyn, M. Murnane, X. Liu, B. Shan, J. Liu, L.Niu, M. Gong, and X. Zhang, R. Lee, The 22nd International Congress on High Speed Photography and Photonics, Santa Fe, (October 1996),
5. R. Keller, T. Renner and D. J. Massoletti: Proceedings of the 7th Beam Instrumentation Workshop, Argonne, IL, May 6-7, 1996

This work was supported by an Academic Research Infrastructure Instrumentation Grant from the National Science Foundation, and the Department of Energy through Lawrence Livermore National Laboratory and Lawrence Berkeley National Laboratory. P.H.B. acknowledges support from the Miller Foundation of the University of Berkeley California. J.L. acknowledges support from the Swedish Natural Science Research Council. H.K. acknowledges support from the Chinese Academy of Sciences. We would like to thank the Center for X-Ray Optics for assisting our independent investigator group in getting access to beamline 10.3.2.

Principal Investigator: Roger W. Falcone, Department of Physics, University of California, Berkeley. Email: Chairman@physics.berkeley.edu.

Fabricating Sub-Collimating Grids for an X-Ray Solar Imaging Spectrometer Using LIGA Techniques

R.A. Brennen,[1] M.H. Hecht,[1] D.V. Wiberg, [1] S.J. Manion, [1] W.D. Bonivert,[2] J.M. Hruby[2], M.L. Scholz,[3] T.D. Stowe, [3] T.W. Kenny, [3] K.H. Jackson,[4] and C. Khan Malek[5]

[1]Jet Propulsion Laboratory, 4800 Oak Grove Drive, Pasadena, CA 91109, USA
[2]Sandia National Laboratory, Livermore, CA 94551, USA
[3]Stanford University, Stanford, CA 94305, USA
[4]Center for X-ray Optics, Ernest Orlando Lawrence Berkeley National Laboratory, University of California, Berkeley, CA 94720, USA
[5]Center for Advanced Microstructures and Devices, Louisiana State University, 3990 West Lakeshore Drive, Baton Rouge, LA 70803, USA

The HESSI mission proposes to perform high resolution imaging and spectroscopy observations in the soft X-ray, hard X-ray, and gamma-ray regimes, with finer angular resolution (nearly 2 arcseconds) and finer energy resolution (approximately 1 keV) than has been previously possible [1]. This combination of imaging and spectroscopy is achieved with a set of Rotating Modulation Collimators placed in front of an array of cooled germanium and silicon detectors. A set of 12 bi-grid collimators, each of which consists of a pair of identically pitched, widely-separated grids, is used to provide the imaging. Each grid consists of a planar array of equally-spaced, parallel, X-ray opaque slats separated by X-ray transparent slits. If the slits of each grid are parallel to each other and the pitch is identical for the two grids, then the transmission through the grid pair depends on the direction of incidence of the incoming X-rays as shown in Fig. 1. For slits and slats of equal width, the transmission varies between zero and 50% depending on whether the shadows of the slats in the top grid fall on the slits or slats of the lower grid. A complete transmission cycle from zero to 50% and back to zero corresponds to a change in source direction

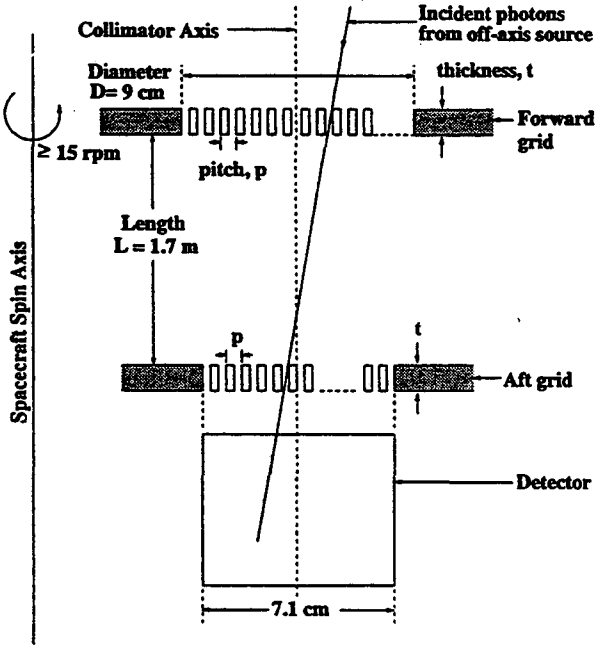

Figure 1. Schematic of forward and aft girds in the Rotation Modulation Collimator. Note off-axis photon path.

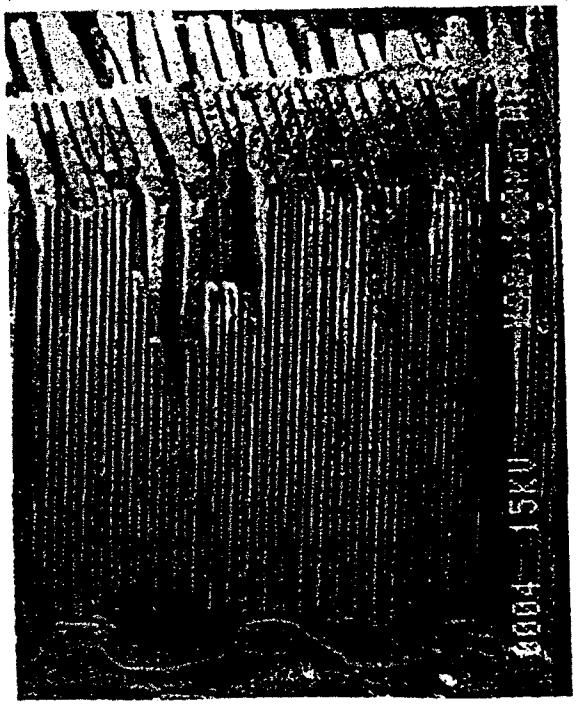

Figure 2. SEM of electroplated copper with original design PMMA grid mold removed.

that is given by p/L, where L is the separation between the grids. The angular resolution is then given by $p/(2L)$. Rotation of a grid pair assembly provides the change in source direction; by using the 12 differently pitched grid pairs, a two dimensional image of the source can be reconstructed from the Fourier components determined from the modulated signals.

GRID DESIGN AND FABRICATION

The finest angular resolution is a function of the smallest pitch of the grids. For a minimum resolution of 2 arcseconds and a grid separation of 1.7 meters, the pitch of the finest grid must be 34 μm. Each grid must be almost perfectly identical; the RMS pitch of the grids in each pair must correspond to within 1 part in 10000. The tolerances for each grid as to slat width, thickness variation, and slat position are much less stringent, being on the order of 5% to 10%. The active grid area of the lower, or aft, grid must have a diameter of 7.1 cm, and the front grid a diameter of 8.9 cm.

Techniques such as electrodischarge machining (EDM) and tungsten foil stacking using spacers can be used to fabricate grids with pitches from 2 mm down to approximately 100 μm. However, the 10^{-4} correspondence for the RMS pitch for any grid pair has not yet been met by the above methods for grids with pitches below 100 μm. The LIGA processing technique provides a unique and ideal method for fabricating the three required grids with pitches smaller than 100 μm.

Our design consists of a very rigid mold structure which does not require a substrate. A free-standing sheet of PMMA that is not mounted on a substrate is expose such that, after developing, the mold structure is a free-standing single cell grid mold. The open slits in this grid are filled with electroplated metal which acts as the X-ray absorbing collimating grid since the PMMA slats between the metal-filled slits are acceptably transparent to high energy X-rays down to approximately 10 keV photons. This grid can collimate X-rays from 10 keV to 300 keV, meeting the specifications for the 34 μm pitch grid. For lower energy X-rays, a grid must be used that has no material between the absorbing slats [2].

An X-ray mask is fabricated by depositing an electroplating strike onto a silicon wafer. A patterned layer of photoresist is put down on the strike, and gold is then electroplated into this photoresist mold. The X-ray mask is used to pattern the light from a synchrotron radiation source directed at a sheet of PMMA. The exposed areas of the PMMA are developed away and the remaining PMMA, in the form of a grid, is placed on a conducting substrate and used as a mold for electroplating up from the substrate.

X-ray exposures of the PMMA were made on two synchrotrons: the Advanced Light Source (ALS) at the Ernest Orlando Lawrence Berkeley National Laboratory, in Berkeley, California, and the Stanford Synchrotron Radiation Laboratory (SSRL) in Palo Alto, California. The ALS bending magnet photon output has a criticial energy of 1.6 keV when running at 1.5 GeV and a critical energy of 3.1 keV when running at 1.9 GeV. Beamline 10.3.2 at the ALS has an acceptance of 2 mrad and a beamline length of 30 meters, resulting in a horizontal exposure width of 6 cm. SSRL has a characteristic energy of 4.7 keV with an 11 cm exposure spanning 5.5 mrad.

Because the X-ray masks for the grids are currently fabricated only on 200μm thick silicon substrates, grid exposures are carried out only at SSRL and at the ALS during 1.9 GeV operation.

The exposures at SSRL were set such that grid slats defined on the mask ran horizontally. In this manner, the maximum angle of the sidewalls, *due to beam angle,* can be assumed to be 0.5 μm per 1 mm height since the angular spread of the X-ray beam in the vertical direction is 0.5 mrad. Further, since any horizontal pattern edge passes both the top and the bottom of the X-ray beam and the highest energy photons are concentrated vertically in the central portion of the exposure area, the exposed section of the resist can be considered to be better than the above 0.5 mrad.

The target exposure dose is between 2kJ/cm^3 and 20kJ/cm^3 [3]. Since the PMMA absorbs the lower energy photons more readily than high energy ones which can penetrate more deeply into the resist, the front or top of the PMMA stack receives a higher dose than the back. In order that all exposed PMMA receive a dose high enough to be developed while not being overdosed, the ratio between the front and back doses should remain below about 5. The filters through which the synchrotron X-ray beam passes before exposing the PMMA resist include beryllium, aluminum, the silicon substrate of the X-ray mask, and for some exposures, Kapton®. The target dose for the back side of the last PMMA sheet is typically 2.5kJ/cm^3, resulting in maximum doses on the front of approximately 7 kJ/cm^3 for exposures at SSRL and 10 kJ/cm^3 for exposures at the ALS with exposure time of 4 hours and 13 hours, respectively, per 1 cm of vertical scan.

Developing of the exposed resist is performed using the "GG" developer [4]. The samples are developed at 35°C in 1000 ml of the developer using a magnetic stirrer for agitation. They are then rinsed in 1000 ml of 35°C "GG" rinse, 80% 2-(2-butoxyethoxy) ethanol, 20% water, and then rinsed again in 35°C DI water.

Since the exposed samples of resist are free-standing sheets of PMMA and the developed pattern is a self-supporting grid, they can be developed from both sides of the sheet simultaneously. The 800 μm thickness of the sheets, in addition to the unexposed surrounding area, ensures a structurally sound geometry that remains intact through the developing process. The samples are immersed in the developer in way such that the flow over the surface of the resist is parallel to the lines of the grid. Samples in which the flow is perpendicular to the grid develop very slowly. Full development times for parallel flow developing range for an 800 μm thick grid range from 1 hour to 12 hours depending on the exposure dose. These long development times result from the small size of the slits which are nominally 17 μm wide. After the sample develops through, the sample is turned for 10 to 15 minutes such that the flow is perpendicular to the *surface* of the sample. The subsequent rinses are both performed with this perpendicular orientation of the sample, the first rinse for 30 to 60 minutes and the DI water rinse for at least 1 hour.

All electroplating for the HESSI grids is performed using a copper plating bath. Once this process is fully stable, the grids will be plated using a gold bath which has electroplating characteristics similar to that of copper baths.

The developed PMMA grid mold is mounted on a copper plate with a very clean surface. The mold is attached to the plate using a highly conforming, non-conducting tape such that only the

grid portion of the sample is open to the electroplating bath. The sample is immersed in a commercially available acid copper plating bath. Several types of bath agitation have been tested including mechanical agitation, bubbling agitation and simple flow over the surface (not laminar flow). This diffusion is comparatively slow and the plating up of 800 μm of copper takes several days. (See Fig. 2.)

RESULTS AND CONCLUSIONS

The current issues to be examined for this project include the uneven exposure and development of large exposed areas, uneven electroplating in the PMMA grid mold, and methods for increasing the development rate. The energy absorbed by the silicon and gold mask is on the order of 1 watt per horizontal cm at SSRL, totally 6 watts for a 3 inch wafer mask. This can be reduced by either cooling the mask or by using a pre-filter and a mask substrate that is more X-ray transparent than the current 200 μm of silicon.

ACKNOWLEDGEMENTS

The research described in this paper was performed by the Center for Space Microelectronics Technology, Jet Propulsion Laboratory, California Institute of Technology; and by Sandia National Laboratory, Livermore; and was sponsored by the National Aeronautics and Space Administration, Office of Space Access and Technology. Synchrotron X-ray beam time was provided by the Advanced Light Source at the Ernest Orlando Lawrence Berkeley National Laboratory and by the Stanford Synchrotron Radiation Laboratory at the Stanford Linear Accelerator Center.

REFERENCES

1. Lin, Principal Investigator, "The High Energy Solar Spectroscopic Imager (HESSI)," a proposal submitted to NASA in response to the MIDEX Announcement of Opportunity, June 21, 1995.
2. Brennen, M.H. Hecht, D.V. Wiberg, S.J. Manion, W.D. Bonivert, J. Hruby, E. Kruglick, K.S.J. Pister, "Fine pitch grids fo an x-ray solar imaging spectrometer fabricated by optical lithography and XeF_2 etching," to be presented at Micromachining and Microfabrication '95, SPIE, Austin, Oct. 23-24, 1995.
3. Mohr, W. Ehrfeld, D. Munchmeyer, A. Stutz, "Resist technology for deep-etch synchrotron radiation lithography," Makromolekulare Chemie, Macromolecular Symposia Series, V. 24, pp.231-251, 1989.
4. Guckel, T.R. Christenson, K.J. Skrobis, D.D. Denton, B. Choi, E.G. Lovell, J.W. Lee, S.S. Bajikar, and T.W. Chapman, "Deep X-ray and UV lithographies for micromechanics," Technical Digest, IEEE Solid-State Sensor and Actuator Workshop, pp. 118-122, June 4-7, 1990.

This work was supported by the Director, Office of Energy Research, Office of Basic Energy Sciences, Materials Science Division, of the U.S. Department of Energy under Contract No. DE-AC03-76SF00098; and by the National Aeronautics and Space Administration, Office of Space Access and Technology.

Principal investigator: Reid A. Brennen, Jet Propulsion Laboratory. Email: rbrennen@hpl.hp.com. Telephone: 415-852-8502.

Fabrication of Miniaturized Electrostatic Deflectors Using LIGA

K.H. Jackson,[1] C. Khan-Malek,*[1] L.P. Muray,[1] W.D. Bonivert,[2] J.M. Hruby,[2]
J.T. Hachman,[2] and T.H.P. Chang[3]

[1]Center for X-Ray Optics, Ernest Orlando Lawrence Berkeley National Laboratory, University of California, Berkeley, CA 94720, USA

[2]Materials Synthesis Department, Sandia National Laboratory, Livermore, CA 94551-0969

[3]IBM Research Division, T.J. Watson Research Center, Yorktown Heights, NY 10598

INTRODUCTION

Miniaturized electron beam columns ("microcolumns") have been demonstrated to be suitable candidates for scanning electron microscopy (SEM), e-beam lithography and other high resolution, low voltage applications [1]. In the present technology, microcolumns consist of "selectively scaled" micro-sized lenses and apertures, fabricated from silicon membranes with e-beam lithography, reactive ion beam etching and other semiconductor thin-film techniques [1,2]. These miniaturized electron-optical elements provide significant advantages over conventional optics in performance and ease of fabrication. Since lens aberrations scale roughly with size, it is possible to fabricate simple microcolumns with extremely high brightness sources and electrostatic objective lenses, as shown schematically in Fig. 1, with resolution and beam current comparable to conventional e- beam columns. Moreover, since microcolumns typically operate at low voltages (1KeV), the proximity effects encountered in e-beam lithography become negligible. For high throughput applications, batch fabrication methods may be used to build large parallel arrays of microcolumns [3]. To date, the best reported performance with a 1 keV cold field emission cathode, is 30nm resolution at a working distance of 2mm in a 3.5mm column [1].

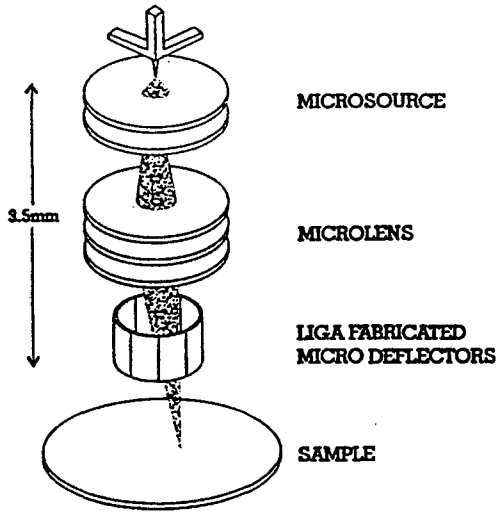

Figure 1. Schematic representation of a miniature electron beam column. The lens and deflector elements are fabricated using surface micromachining and LIGA techniques. Not shown are the apertures and blanking plates.

Fabrication of the microcolumn deflector and stigmator, however have remained beyond the capabilities of conventional machining operations and semiconductor processing technology. Instead, although scaled appropriately, the deflector/stigmator unit is still machined and assembled by hand. Typically, the deflector consists of a precision milled 2mm thick aluminum body and 0.5mm polished copper wire electrodes [4]. This work examines the LIGA process as a superior alternative to fabrication of the deflectors, especially in terms of degree of miniaturization, dimensional control, placement accuracy, run-out, facet smoothness and choice of suitable materials. LIGA is a combination of deep X-ray lithography, electroplating, and injection molding processes which allow the fabrication of microstructures with lateral dimensions in the micrometer range, vertical dimensions several hundred micrometers high, and submicron tolerances.

COLUMN DESIGN CONSIDERATIONS

The function of deflectors is to linearly displace the electron beam in proportion to an applied voltage. The simplest arrangement of electrodes is a set of parallel plates oriented along the x and y axes. However, a large improvement in field distortion and spot aberration may be realized if the main plates are augmented by field-shaping auxiliary plates operated at proportionally lower potentials. The octupole deflector, illustrated in Fig. 2, is typical for this type of design and is currently incorporated into the microcolumn. An additional benefit is that an octupole can correct astigmatism in the beam with no additional electrodes [5]. Higher order deflectors, such as dodekapoles and 20-poles have been considered for LIGA fabrication, but are currently not in use because of compromises in performance and the lack of suitable electronics.

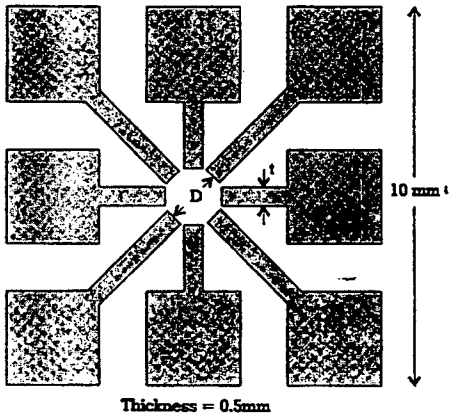

Figure 2. Design of the LIGA mask. Two sets of 500μm thick deflectors were required: i) with D = 1mm, t = 200μm; and ii) D = 0.5mm, t = 100μm. These correspond to aspect rations of 2.5:1 and 5:1, respectively.

The current designs for LIGA-fabricated octupoles are a compromise between drive requirements, scan field size and realizable tolerances. Two sets of octupoles were required with diameters of 1mm and 0.5mm and pole widths of 200 μm and 100 μm, respectively. The electrodes were 500 μm thick with corresponding aspect ratios of 2.5:1 and 5:1. With these parameters, the scan field size was estimated to be 10 μm at 1 mm working distance. Acceptable tolerances in all dimensions were +/- 1μm, including surface roughness. Low stress copper was the material of choice, primarily for its high conductivity. The mask incorporated a retaining ring which held the electrodes in alignment until after transfer to an insulating substrate.

THE LIGA FABRICATION PROCESS

The search for simplicity and low cost has led to developing a LIGA process which, though not optimum in term of physical properties, is simple and inexpensive enough to be used for rapid prototype development. A pattern from a conventional photomask is transferred to a thick (20-30μm) photoresist layer which is then patterned with a gold absorber using electroplating. The X-ray mask carrier is a thinned (100μm thick) silicon <100> wafer. Gold X-ray absorber patterns have been produced with an additive process based on contact photolithography in thick resist and gold electroplating.

X-RAY EXPOSURE AND PATTERN TRANSFER

Pattern transfer with X-ray masks consisting of 100 μm thick silicon mask substrates and 20 μm gold absorber structures was performed on a bending magnet beamline at the Advanced Light Source. This beamline and its particular characteristics have been described elsewhere [6]. The X-ray resist used was PMMA in the form of commercially available sheets of Plexiglas™ 600-800 μm thick. The exposed PMMA was developed in the so-called "GG" developer [7]. This developer was especially formulated so that large thicknesses of PMMA can be developed with a

high selectivity between exposed and unexposed areas. The fidelity of the pattern transfer with a 100 μm thick silicon mask substrate and 20 μm gold absorber structures shows a contrast sufficient for the replication into 800 PMMA μm sheets.

ELECTROPLATING OF OCTUPOLES

The exposed and developed octupoles are bonded to a conducting substrate with epoxy and then immersed in a acid copper sulfate electrolyte bath at room temperature with agitation. The time required to plate the octupole up to a copper thickness of 800μm was 35 hours. After plating the surface of the octupole was polished. The completed octupole lens is shown in Fig. 3. The metal needles observed on the top edges of the octupole are a result of a non-optimized polishing process.

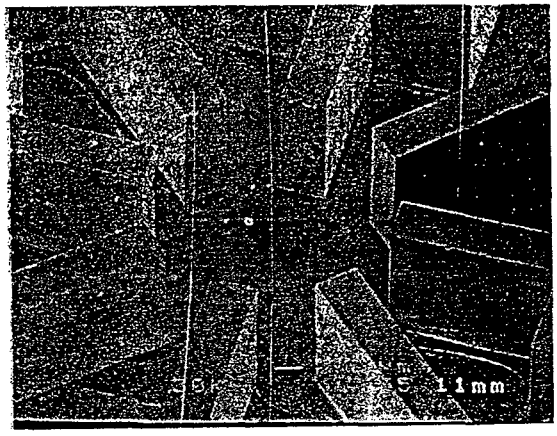

Figure 3. The octupole (top view) after electroplating. The advantage of LIGA in an application like this is its inherent ability to maintain high placement accuracy between adjacent poles of the octupole.

REFERENCES

1. E. Kratschmer, H.S. Kim, M.G.R. Thomson, K.Y. Lee, S.A. Rishton, M.L. Yu, and T.H.P. Chang, J. Vac. Sci. Technol. **B 12**, 3503 (1994).
2. T.H.P. Chang, D.P. Kern, M.A. McCord and L.P. Muray, J. Vac. Sci. Technol. **B 9**, 438 (1991).
3. T.H.P. Chang, D.P. Kern, and L.P. Muray, J. Vac. Sci. Technol. **B 10**, 2743 (1992).
4. L.P Muray, U. Staufer, D.P. Kern, and T.H.P. Chang, J. Vac. Sci. Technol. **B 10**, 2749 (1992).
5. C.H. Schaefer, J. Vac. Sci. Technol. **B 4**, 1237 (1986).
6. C. Khan Malek, K. Jackson, R. A. Brennen, M. H. Hecht, W. D. Bnivert, and J. Hruby, "Deep etch X-ray lithography at the Advanced Light Source: First results," J. Vac. Sci. Technology, **B12(6)**, 4009-4012 (1994).
7. V. Ghia and W. Glashauser, "Verfahren für die Spannungsfreie Entwicklung von Bestrahlten Polymethylmethacrylat-Schichten," Offenlegungsschrift DE3039110, Siemens AG, Munich, Germany.

This work was supported in part by the Director, Office of Energy Research, under the ERLTT program, Basic Energy Sciences, Materials Science Division, of the U.S. Department of Energy under Contract No. DE-AC03-76SF00098 and Sandia National Laboratories under Contract No. DE-AC04-94AL8500. In addition, the authors would like to thank Michael Hecht and Reid Brennen of the Center for Space Microelectronics of the Jet Propulsion Laboratory, for helpful discussion concerning the use of thin silicon wafers as mask carriers.

*Now at Center for Advanced Microstructures and Devices, Louisiana State University, 3990 West Lakeshore Drive, Baton Rouge, LA 70803, USA

Principal investigator: Keith H. Jackson, Center for X-Ray Optics, Ernest Orlando Lawrence Berkeley National Laboratory. Email: khjackson@lbl.gov. Telephone: 510-486-6894.

Masks for High Aspect Ratio X-Ray Lithography

Chantal Khan Malek,[1] Keith H. Jackson,[1] William D. Bonivert,[2] and Jill Hruby[2]

[1]Center for X-Ray Optics, Lawrence Berkeley National Laboratory, University of California, Berkeley, CA 94720, USA
[2]Materials Synthesis Department, Sandia National Laboratories

Fabrication of very high aspect ratio microstructures, as well as ultra-high precision manufacturing is of increasing interest in a multitude of applications. Fields as diverse as micromechanics, robotics, integrated optics, and sensors benefit from this technology. The scale-length of this spatial regime is between what can be achieved using classical machine tool operations and that which is used in microelectronics. This requires new manufacturing techniques, such as the LIGA process, which combines x-ray lithography, electroforming, and plastic molding [1,2,3,4].

X-RAY MASK FABRICATION

The search for process simplicity and low cost has led to developing LIGA masks which, though not optimum in term of physical properties, are simple and cheap enough to be used for process development and high aspect ratio device fabrication. An ultrathin wafer of silicon is used as a simple and inexpensive mask carrier. The wafer is coated with a plating base consisting of a chromium film, acting as an adherence layer, and a gold seed layer. These films are deposited using e-beam evaporation to a thickness of 40nm. Absorber patterns have been produced with an additive process based on contact photolithography in thick resist and gold electroplating, as described in the following sections.

PHOTOLITHOGRAPHY

Patterns with high aspect ratios and steep edges have been produced by conventional near UV contact printing. Thick photoresists of high transparency and viscosity were investigated. The existence of positive and negative resists allows flexible replication of masks of either polarity:

- a positive novolak based resist (Hoechst 4620) developed by immersion in a mildly basic aqueous developer
- a negative photosensitive polyimide resist (OCG 7020) spray-developed in an organic solvent

The mask substrates were singly or multiply spin-coated. For novolak resist this produces a 10 μm layer for a single coating, 20 μm for a double coating. For the polyimide resist, layer thicknesses of 20 μm, 50 μm, 70 μm were obtained for 1, 2 and 3 coatings respectively. The masks were written or only partially printed in such a way that patterns with areas of the same order of magnitude were transferred to the resist in order to insure a more uniform thickness during electroplating.

Steep walls require a very good contact between the printing mask and the photoresist surface. The Hoechst resist was not postbaked, whereas the polyimide was postbaked at 150°C for one hour in air. In addition, oxygen plasma was used to de-scum the bottom of the holes before the electrochemical deposition step. Examples of structures produced in OCG 7020 are given in Fig. 1.

ELECTROPLATING

The gold absorber patterns were deposited in a commercial non cyanide-based gold plating solution This neutral mildly acidic sodium gold sulfite electroplating bath showed good compatibility with both the novolak and polyimide resists. The deposits were fine-grained with low surface roughness on the order of 10nm. The stress in the thin deposited film as determined from the measurement of substrate bending was negligible, varying from a compressive 0 to 5 MPa with gold films 10 and 20 μm thick respectively. Current density and electrolyte flow were adjusted to maintain a uniform height distribution across a 3 inch wafer. Thickness uniformity in micro-plating is strictly geometry dependent; a good thickness uniformity of the gold microstructures was obtained by plating simultaneously only patterns with comparable feature size. After plating, the resist stencil was removed easily by using an organic solvent stripper.

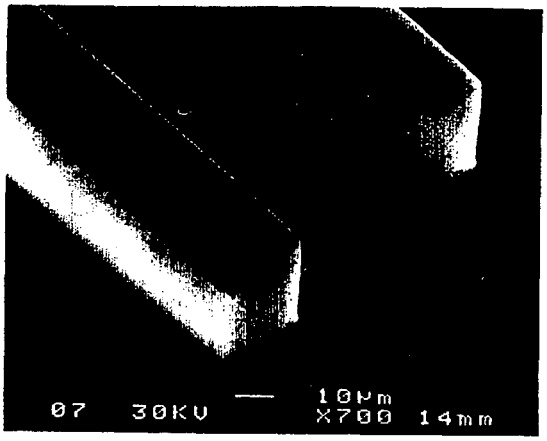

(a)

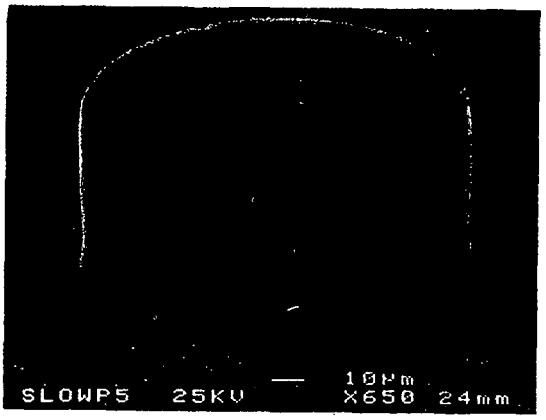

(b)

Fig. 1(a, b). SEM micrograph of microstructures in OCG 7020 resist, minimum feature size: 20μm, resist thickness: 40 μm.

X-RAY MASK TRANSFER IN THICK ACRYLIC SHEET

Simulations of the power density transmitted spectra through various filters have been made using the "CXrL toolset" [5]. The exposure spectra incident on the PMMA resist were calculated with several different mask substrate materials and with the ALS operating at a stored beam energy of 1.5 GeV and 1.9 GeV. The resulting transmitted spectra through the different filter materials in the beampath are plotted in Fig. 2 where the various curves represent:

- The power distribution of the synchrotron radiation emitted at a beam energy of 1.5 GeV and 1.9 GeV respectively and with 400 mA of stored current: curves 1) and 1')
- The exit window consisting of a 127 μm beryllium window followed by a 1000 mm gap filled with helium and a 127 μm Kapton™ window: curves 2) and 2')
- The 100 μm silicon mask carrier: curves 3) and 3')

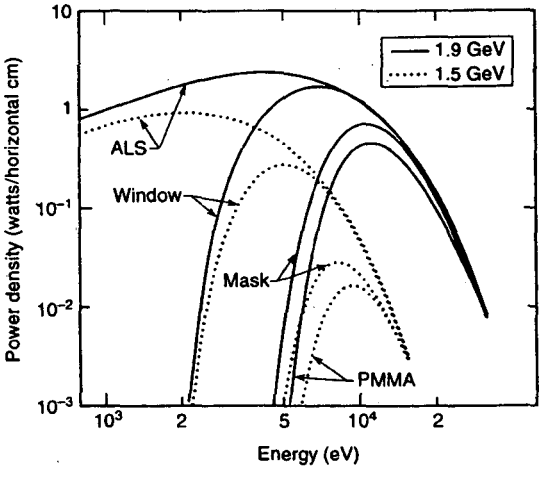

Fig. 2. Power distribution of the spectrum emitted by the synchrotron radiation sources operated with 400 mA with various filters in the beamline.

- The 1000 μm PMMA resist layer: curves 4) and 4')

The window, the mask substrate, and the filters cut off x-rays with wavelength greater than 0.5 nm. The exposure time with the ALS functioning at 1.9 GeV is reduced by a factor of 20 as the spectral distribution of the x-ray flux is shifted towards shorter wavelengths and absorption in the silicon substrate is much less. At 1.5 GeV, exposure time suggests the consideration of a thinner silicon mask carrier, whereas at 1.9 GeV, silicon wafers 100 μm and 200 μm thick are adequate. Table 1 shows the contrast of the masks as a function of gold thickness with various mask blank materials. In particular, a gold thickness on the order of 18-22 μm is necessary to achieve a mask contrast of 200 with 100 μm silicon masks.

Pattern transfer with DXRL masks consisting of 100 μm thick silicon mask substrates and 20 μm gold absorber structures was performed on a bending magnet beamline at the Advanced Light Source. This beamline and its particular characteristics have been described elsewhere [6]. The x-ray resist used was PMMA in the form of commercially available sheets of Plexiglas™ 600-800 μm thick. The exposed PMMA was developed in a mixture of morpholine/2-aminoethanol/2-(2-butoxyethoxy) ethanol/DI water, the so-called "GG" developer [7]. This developer was especially formulated so that large thicknesses of PMMA can be developed with a high selectivity between exposed and unexposed areas. Microstructures fabricated in 800 μm thick Plexiglas™ are shown in Fig. 3. The fidelity of the pattern transfer with a 100 μm thick silicon mask substrate and 20 μm gold absorber structures shows a contrast sufficient for the replication into 800 PMMA μm sheets.

Fig. 3. Optical micrograph of the micro-tumbler replicated in 800 μm thick PMMA.

ACKNOWLEDGMENTS

The use of the Microfabrication Laboratory at the University of California at Berkeley is acknowledged for mask fabrication, with special thanks to one of its member, Gerd Matzen, for his assistance in implementing the spray-development polyimide process. In addition, the authors would like to thank Michael Hecht and Reid Brennen of the Center for Space Microelectronics of the Jet Propulsion Laboratory, respectively, for helpful discussion concerning the use of thin silicon wafers as mask carriers at SSRL, Stanford, and for implementing the "CXRL Toolset" at CXRO, as well as Sam Mukherjee of the Engineering Department at the E. O. Lawrence Berkeley National Laboratory for his CAD work on the masks used. Paul de la Houssave of the Research.

	200 μm Be blank		100 μm Si blank		5 μm Si blank		5 μm diamond blank	
Au thickness μm	1.5 GeV	1.9 GeV	1.5 GeV	1.9 GeV	1.5 GeV	1.9 GeV	1.5 GeV	1.9 GeV
5	103 / 24	33 / 15	8 / 7	5 / 5	91 / 23	29 / 11	133 / 26	39 / 12
10	713 / 139	151 / 46	37 / 27	18 / 15	616 / 131	134 / 44	936 / 151	184 / 47
15	* / *	488 / 143	121 / 87	53 / 43	* / 485	432 / 136	* / 566	597 / 152
20	* / *	* / 387	345 / 242	138 / 111	* / *	* / 368	* / *	* / 411

Table 1. Contrast calculated for various combinations of mask substrate and gold absorber thickness as calculated on the beamline at the ALS.

Development, Technology and Evaluation Division of the Naval Command, Control, and Ocean Surveillance Center is also thanked for his critical reading of the manuscript.

REFERENCES

1. E. W. Becker, W. Ehrfeld, P. Hagmann, A. Maner, and D. Munchmeyer, "Fabrication of microstructures with high aspect ratios and great structural heights by synchrotron radiation lithography, galvanoforming, and plastic molding", Microelectron. Eng. **4**, 35-56 (1986).
2. W. Ehrfeld, P. Bley, F. Gotz, J. Mohr, D. Munchmeyer, W. Schelb, H. J. Baving, and D. Beets, "Progress in deep-etch synchrotron radiation lithography", J. Vac. Sci. technol. **B6(1)** 178-182 (1988).
3. H. Guckel, T. R. Christenson, K.J. Skrobis, D. D. Denton, B. Choi, E. G. Lowell, J. W. Lee, S. S. Bajikar, and T. W. Chapman, "Deep x-ray and UV lithographies for micromechanics," Technical Digest Solid State Sensor and Actuator Workshop Digest, Hilton Head, SC, USA, June 4-7, 1990, pp. 118-122.
4. H. Guckel, T. R. Christenson, and K. J. Skrobis, "Deep X-ray lithography, metal plating assembly as fabrication tools for micromechanics," Proc. IEEE 11th Sensor Symposium, June 92, Tokyo.
5. "The CXrL Toolset Users Guide, Version 1.0," University of Wisconsin-Madison, © 1993.
6. C. Khan Malek, K. Jackson, R. A. Brennen, M. H. Hecht, W. D. Bonnivert, and J. Hruby, "Deep etch X-ray lithography at the Advanced Light Source: First results," J. Vac. Sci. Technology, **B12(6)**, 4009-4012 (1994).
7. V. Polymethylmethacrylat-Schichten," Offenlegungsschrift DE3039110, Siemens AG, Munich, Germany.

Principal investigator: Keith H. Jackson, Center for X-ray Optics, Ernest Orlando Lawrence Berkeley National Laboratory. Email: khjackson@lblgov. Telephone: 510-486-6894

*Now at CAMD (Louisiana State University), Baton Rouge, LA, USA

This work was supported in part by the Director, Office of Energy Research, Office of Basic Energy Sciences, Materials Science Division, of the U.S. Department of Energy under Contract No. DE-AC03-76SF00098.

Total Reflection X-Ray Fluorescence: Determination of an Optimum Geometry

Y. M. Koo[1], C-H. Chang[2] and H. A. Padmore[2]

[1]Pohang University of Science and Technology, Pohang 790-784, Republic of Korea
[2]Advanced Light Source, Ernest Orlando Lawrence Berkeley National Laboratory, Berkeley CA 94720

INTRODUCTION

Total reflection X-Ray Fluorescence (TXRF) is a widely used technique in which the normal trace element detection capability of hard x-ray fluorescence (XRF) is enhanced by use of an x-ray reflective substrate. XRF with photon excitation is more sensitive than electron impact induced XRF, due to the absence of a bremstrahlung background. TXRF is more sensitive than normal photon induced XRF due to the reduction of the substrate scattering and fluorescence signals. This reduction comes about because in total external reflection, the photon field only penetrates about 20 Å into the surface, instead of typically 50μm for a silicon substrate at normal incidence for 10 KeV photons. The technique is used in many fields of trace element analysis, and is widely used in the determination of metal impurity concentrations on and in the surface of silicon wafers [1]. The Semiconductor Industry Association roadmap (SIA) indicates a need for wafer contamination detection at the 10^{7} atoms/cm^{2} level in the next few years. Current commercial systems using rotating anode x-ray sources presently routinely operate with a sensitivity level of around 10^{10} atoms/cm^{2} and this has led to interest in the use of synchrotron radiation to extend the sensitivity by three orders of magnitude. The pioneering work of Pianetta and co-workers at SSRL has clearly shown that this should be possible, using a fully optimized source and detector [2,3].

The purpose of this work is to determine whether ALS would be a suitable source for this type of highly sensitive wafer TXRF. At first look it appears improbable as the SSRL work used a high flux multipole wiggler source, and it is clear that the detected fluorescence for relevant concentrations is small. In addition, SSRL operates at 3.0 GeV rather than 1.9 GeV, and is therefore more naturally suited to hard x-ray experiments. However, TXRF is an experiment in which due to the small grazing angles, brightness (in one direction) is the key parameter. The ALS bending magnet sources are a bright source of x-rays, particularly in the vertical direction, where the beam size is for example 30 μm (FWHM) in the central magnet. The conventional geometry with synchrotron radiation excitation is with the electric vector and the sample surface normal parallel. This is used to minimize Compton scattering. However, although scattering is minimized, a large penalty is paid in terms of flux. Firstly, the source size is usually much larger in the horizontal than the vertical directions, and secondly, in the direction of isotropic emission (horizontal) the collection angle has to be extremely small, given by a small fraction of the critical angle of silicon at 10 KeV. In addition, due to the very low fluorescence signals, usually the detector is designed to collect a large solid angle, and this detracts anyway from the Compton minimizing geometry.

The aim of this work was therefore to establish a theoretical model for the scattering and fluorescence processes, so that we could predict the differences between alternative geometries

and select an optimum configuration. In addition, we have checked the model against experimental results for the horizontal scattering condition.

SCATTERING AND FLUORESCENCE CALCULATIONS

The three geometries considered are shown in Fig. 1.

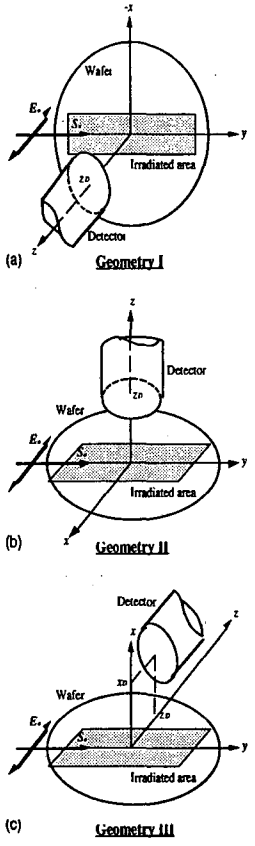

Fig. 1 Three different configurations between the wafer and detector. In all the configurations, the incident beam is along the *y* axis and the axis of detector is along the *z* axis.

To calculate the intensities of fluorescence and scattering in each case the following steps were carried out;

1. flux. The beam is monochromatized using a horizontally focusing multilayer mirror (6:1), followed by a vertically deflecting plane multilayer mirror. The horizontally focusing mirror collects 0.08 mrads (convergence angle onto the wafer in the direction of deflection is therefore 0.48 mrads) and forms a 0.04 mm size beam. The plane multilayer mirror collects 0.12 mrads, giving a 4 mm beam size at the wafer. The theoretical values of reflectivity for the 50 layer pair, 25.6 Å d spacing multilayers were computed, together with the polarized flux output into the above aperture sizes. Beryllium windows and air gaps were included.

2. solid angle. Depending on the geometry of the sample, the detector will see different angular distributions of light. It is therefore important to correctly integrate all emission points on a sample into the detector aperture. This is done for the three different detector geometries shown in Fig. 1.

3. fluorescence. The electric field intensity above, at and inside the surface can be computed from the Fresnel equations. The fluorescence yield is obtained from integration over the whole range of excitation energies given by the multilayer reflectivity and the storage ring spectrum. The isotropic emission is integrated into the acceptance of the detector.

4. scattering. The Compton inelastic as well as the elastic scattering are calculated for the three polarized geometries. Raman and thermal diffuse scattering are small and are ignored here. Both terms are functions of angle, and again, the emission must be carefully integrated over the collection aperture of the detector.

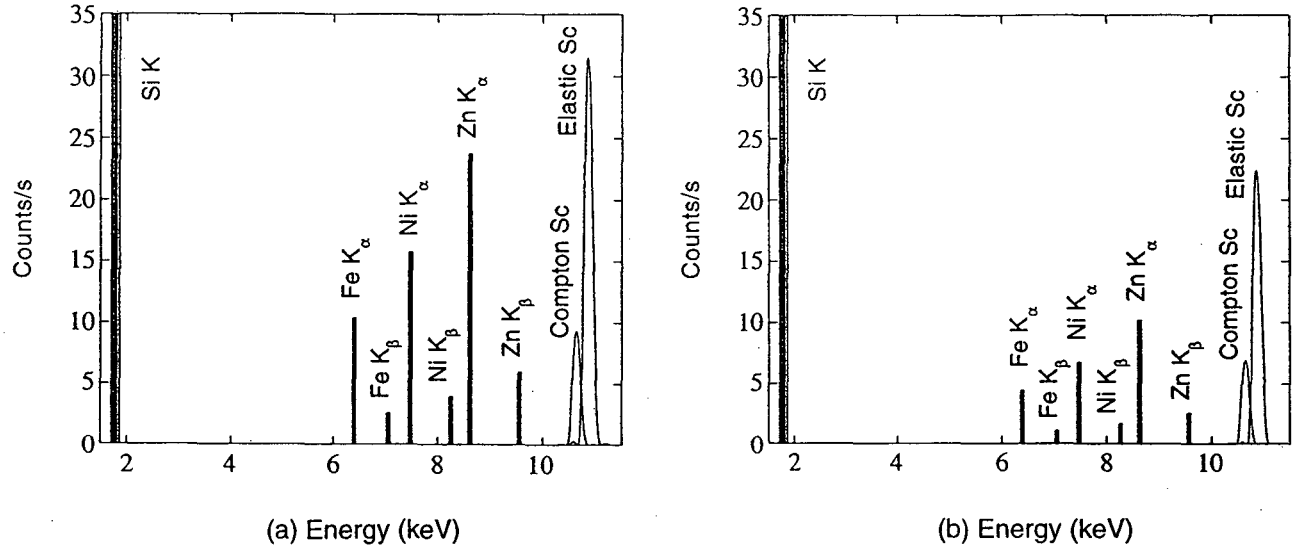

Fig. 2. Calculated spectrum of a silicon wafer contaminated with Fe, Ni, and Zn at a level of 10^{12} atoms/cm^2 at the glancing angle $\varphi_c/2$ (= 1.43 mrad) in two different geometries. For Geometry I (a) the detector is assumed to be located at $z_D = 4\ r_D$. For Geometry III (b), the detector is assumed to be located at $z_D = 4.5\ r_D$ and $x_D = 1.2\ r_D$, where r_D is the radius of the detector, and x_D and z_D give the coordinates of the front of the detector.

An example of the results of this computation are shown in Fig. 2 for the standard perpendicular geometry, and for a vertically reflecting wafer with a horizontal detector, for a wafer with a contamination of 10^{12} atoms/cm^2 for each component. The results here were computed for 1.9 GeV, 30 mA (single bunch running). Data is given for the case where the contamination is on the wafer It can be seen that the fluorescence is approximately halved going from the standard geometry with a perpendicular detector, to one in which the wafer is vertically deflecting, with the detector just above the surface. In addition, it can be seen that the fluorescence to scatter ratio also decreases, approximately by a factor of 1.7.

This result shows that geometry 3, with vertical reflection and horizontal detection is marginally worse, as expected, in comparison to geometry 1. However, with a purpose built optical system, geometry 3 would give a much higher detected signal. The work of Pianetta and co-workers has shown that even in very dilute systems, signal to background ratio is not the primary concern, but rather total fluorescence signal (with the proviso that other scatter sources are minimized). Geometry 3 has two advantages in this respect, firstly that using a 1:1 focusing system, a large horizontal aperture could be collected and focused onto the wafer. In addition to the extra flux,

the integration into a detector would be more efficient, due to the small image size. Collecting 3 mrads would be easily practical, in comparison to the 0.08 mrads used here. In addition, these results do not include the effect of the source asymmetry of 8:1 between the horizontal and vertical beam sizes. This would be reflected directly in an 8 fold increase in flux density in the reflecting direction on the wafer. Together with the better horizontal integration, and the machine running under normal conditions (1.9 GeV, 400 mA), we would have 8000 times the signal predicted here. This indicates that a contamination of around 10^8 atoms / cm^2 would give similar rates. The detector counting rate would be close to 200 KHz from the elastic peak. This is high for a single element detector, but it appears within reach of the latest DSP based detectors.

EXPERIMENTAL

Fig. 3 shows data recorded using geometry 1 on a deliberately contaminated wafer.

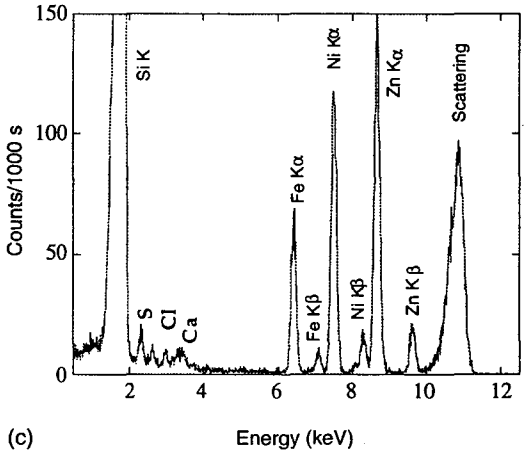

Fig. 3. Fluorescence spectrum for a contaminated wafer at a glancing angle of 2.45 mrads (just less than the critical angle).

It can be seen that we have Fe, Ni, and Zn present, and an asymmetric primary peak, containing the Compton and elastic scattering peaks. If the intensity of the components is plotted as a function of grazing angle, the shape of the function can be used to determine the relative concentrations of material on or in the surface. For Ni for example, this analysis yielded 4×10^{11} and 1×10^{12} atoms / cm^2 on and in the wafer surface respectively. In addition, we can analyze the scaling of the scattering with angle, and compare this to our model.We find excellent agreement, both in terms of absolute magnitude, and in terms of the relative amounts of Si and contaminant fluorescence, and scattering.We therefore feel that we can use the model to predict the performance of other scattering geometries with some confidence.

SUMMARY

We have developed a model that predicts the fluorescence and scattering contributions in TXRF for contaminated wafers.Using the model, we can show that the scatter to fluorescence ratio is less than a factor of 2 higher in the optimum geometry (geometry 1), in comparison to a geometry with vertical deflection and horizontal detection (geometry 3). The latter geometry should however have the great advantage of high horizontal collection aperture and will take advantage of the very high vertical brightness of an ALS dipole source.

ACKNOWLEDGMENTS

The help of Jeff Kortright in performing the experiments and providing the multilayer coating is gratefully acknowledged. The wafer sample was provided by Steve Laderman (HP) and the experiments were performed in collaboration with Steve and the group of Piero Pianetta (SSRL). The work was carried out on CXRO beamline 10.3.2.The assistance of Al Thompson is gratefully acknowledged. This work was supported by the Director, Office of Energy Research,Office of Basic Energy Sciences, Materials Sciences Division of the U.S. Department of Energy, under Contract no. DE-AC03-76SF00098.

REFERENCES

1. R. S. Hockett,"Diagnostic Techniques for Semiconductor Materials and Devices", EGS 92-2, 132(1992).
2. P. Pianetta, N. Takaura, Brennan, W Topkins, S.S. Laderman, A. Fisher-Colbrie, M. Madden, D.C. Wherry, and J.B. Kortight, Rev. Sci. Instrum. 66(2), 1995
3. S. Brennan,W.Topkins, N. Takaura, S.P. Pianetta, S.S. Laderman, A Fisher-Colbrie, J.B Kortight, M.C. Madden, and D.C. Wherry, Nucl. Ins. and Meth. A 347, 417(1994).

Principal investigator: Howard A. Padmore, Advanced Light Source, Ernest Orlando Lawrence Berkeley National Laboratory. Email: HAPadmore@lbl.gov. Telephone: 510-486-5787.

Beamline 12.0.1 Abstracts

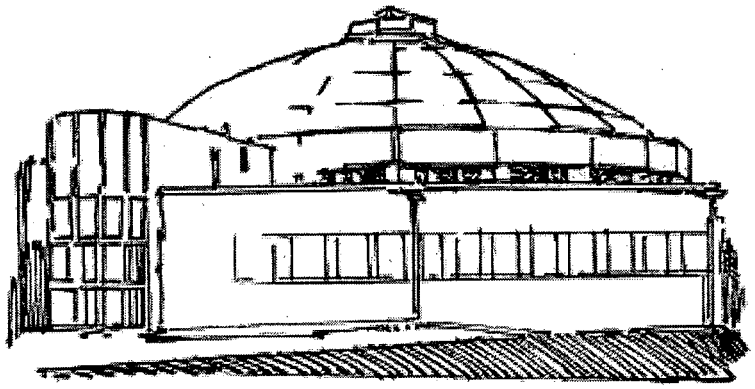

Phase-Shifting Point-Diffraction Interferometry at EUV Wavelengths

Kenneth A. Goldberg,[1,2] Edita Tejnil,[1,3] Sang Lee,[1,3] Hector Medecki,[1] David T. Attwood,[1,3] and Jeffrey Bokor[1,3]

[1]Center for X-Ray Optics, Ernest Orlando Lawrence Berkeley National Laboratory, University of California, Berkeley, CA 94720, USA
[2]Physics Department, University of California, Berkeley, CA 94720, USA
[3]EECS Department, University of California, Berkeley, CA 94720, USA

A novel phase-shifting point-diffraction interferometer (PS/PDI) operating at the Advanced Light Source (ALS) is being used to perform wavefront-measuring metrology at 13.4-nm wavelength to characterize aberrations in a multilayer-coated 10x Schwarzschild objective designed for extreme ultraviolet (EUV) projection lithography experiments. [1]

To achieve 0.1-micron critical dimension pattern transfer with EUV projection lithography at 13.4-nm wavelength, nearly diffraction-limited all-reflective multilayer-coated optical systems with 0.1 numerical aperture are required. The EUV wavefront, determined by the mirror surfaces and the reflective multilayer coatings, is measurable only at the operational wavelength of the system. Our goal is to measure the EUV wavefront to an accuracy of 0.01 waves rms (0.13 nm).

The PS/PDI is a type of point-diffraction interferometer, modified for significantly improved throughput and phase-shifting capability. [2] The interferometer design, shown in Figure 1, utilizes a grating beamsplitter and pinhole spatial filters in the object and image planes of the optical system under test. The 10x-reduction Schwarzschild objective, with image-side numerical aperture of 0.08, is illuminated by a sub-micron pinhole in the object plane. A coarse, 20-micron pitch grating placed between the illumination pinhole and the Schwarzschild system serves a dual role as a small-angle beam-splitter and a phase-shifting element. The first-order diffracted beam from the grating is spatially filtered in the image plane of the Schwarzschild with a sub-100-nm

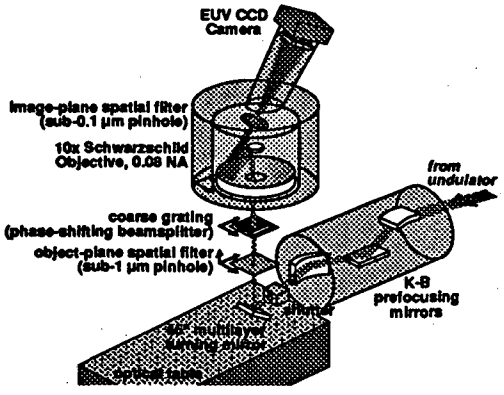

Figure 1. The PS/PDI interferometer at ALS Beamline 12.0

Figure 2. A typical interferogram

pinhole and becomes the 'reference' wave in the interferometer. [3] The zero-order beam is the 'test' wave, and it passes unobstructed through a 4.5-μm window in the image plane. The test

and reference beams are separated by several microns in the image plane to minimize beam overlap. The interference fringes are recorded with a CCD detector placed about 12 cm from the Schwarzschild image plane. Translation of the grating in the direction perpendicular to the rulings introduces a controllable phase-shift between the test and reference beams, enabling analysis with phase-shifting interferometry.

Figure 2 shows a typical interferogram fringe pattern from the measurements of the Schwarzschild objective.

REFERENCES

1. *Phase-Shifting Point Diffraction Interferometry For At-Wavelength Testing Of Lithographic Optics*, E. Tejnil, K. A. Goldberg, H. Medecki, R. Beguiristain, J. Bokor, D. T. Attwood, OSA TOPS Volume on Extreme Ultraviolet Interferometry (1996).
2. "Phase-Shifting Point Diffraction Interferometer," H. Medecki, E. Tejnil, K. A. Goldberg, J. Bokor, Optics Letters, vol.**21**, no.19: 1526-8 (1996)
3. *A 3-D Numerical Study Of Pinhole Diffraction To Determine The Accuracy Of EUV Point Diffraction Interferometry*, K. A. Goldberg, E. Tejnil, J. Bokor, OSA TOPS Volume on Extreme Ultraviolet Interferometry (1996).

This work was supported by the Office of Basic Energy Science of the Department of Energy under contract No. DE-AC03-76SF00098, Intel, and DARPA.

Principal investigator: Jeffrey Bokor, Center for X-Ray Optics, Ernest Orlando Lawrence Berkeley National Laboratory, Email: jbokor@grace.lbl.gov. Telephone: 510-642-4134

Beam Test Facility Abstracts

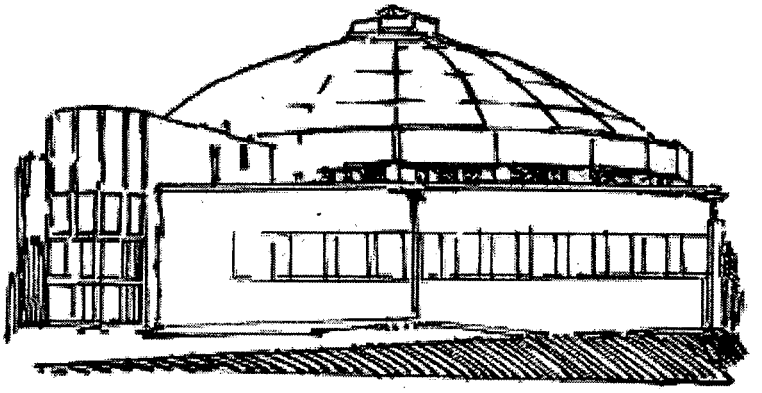

Plasma Lenses for Focusing Relativistic Electron Beams

R. Govil, S. Wheeler, W. Leemans
Accelerator and Fusion Research Division - Center for Beam Physics
Ernest Orlando Lawrence Berkeley National Laboratory
University of California, Berkeley, CA 94720, USA

INTRODUCTION

The next generation of colliders require tightly focused beams with high luminosity. To focus charged particle beams for such applications, a plasma focusing scheme has been proposed[1]. Plasma lenses can be overdense (plasma density, n_p much greater than electron beam density, n_b) or underdense ($n_p < 2\ n_b$). In overdense lenses the space-charge force of the electron beam is canceled by the plasma and the remaining magnetic force causes the electron beam to self-pinch. The focusing gradient is non-linear, resulting in spherical aberrations. In underdense lenses, the self-forces of the electron beam cancel, allowing the plasma ions to focus the beam. Although for a given beam density, a uniform underdense lens produces smaller focusing gradients than an overdense lens, it produces better beam quality since the focusing is done by a plasma ions. The underdense lens can be improved by tapering the density of the plasma for optimal focusing[2]. The underdense lens performance can be enhanced further by producing adiabatic plasma lenses to avoid the Oide limit on spot size due to synchrotron radiation by the electron beam[3].

The plasma lens experiment at the Beam Test Facility (BTF)[4] is designed to study the properties of plasma lenses in both overdense and underdense regimes. In particular, important issues such as electron beam matching, time response of the lens, lens aberrations and shot-to-shot reproducibility are being investigated.

EXPERIMENTAL SETUP

The Beam Test Facility uses the ALS injector which provides 50 MeV electron beam with a charge of 1-2 nC in 15 ps long bunches. The unnormalized emittance is typically 0.2 - 0.3 mm-mrad. The BTF line is equipped with a wide range of diagnostics including integrating current transformers for charge measurement, high bandwidth BPMs, fluorescent screens, and optical transition radiation (OTR) diagnostics[5].

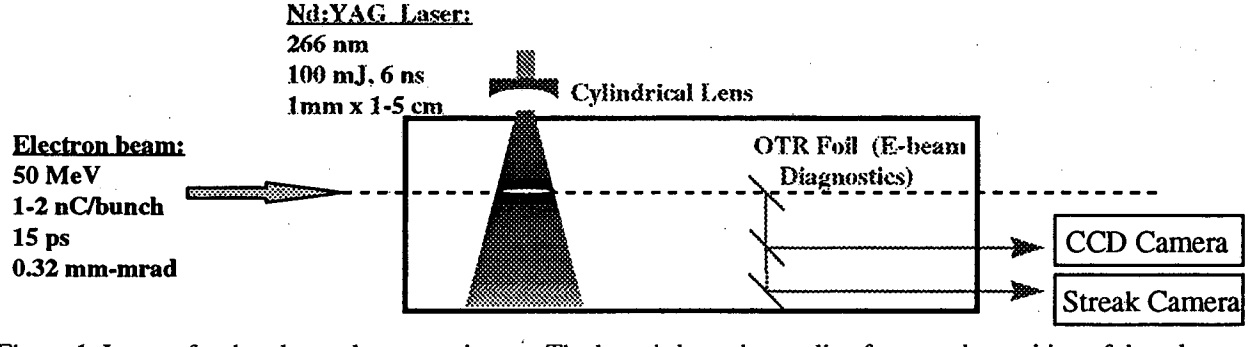

Figure 1. Layout for the plasma lens experiment. The laser is brought to a line focus at the position of the e-beam. Backward OTR is collected for electron beam diagnostics and imaged on to CCD and Streak cameras.

The electron beam is focused into a plasma chamber, that is separated from the ultra-high vacuum beam line by an eight micron thick Kapton window. Plasma is produced in tripropylamine(TPA) vapor through two photon ionization using a 266 nm laser beam. The ionizing laser beam enters the plasma chamber at right angles to the electron beam. The laser is brought to a line focus at the position of the electron beam. The plasma length is adjusted by changing the laser focusing and the density is controlled through the TPA fill pressure and laser intensity.

PLASMA PRODUCTION AND CHARACTERIZATION

For ionizing the vapor, 1064 μm radiation from a Nd:YAG laser is frequency quadrupled to provide 6ns long 266 nm pulses. The two-photon ionization process can be expressed as,

$$n_p = \alpha \frac{n_0 I^2 \Delta t}{h\nu}, \qquad (1)$$

where n_p is the plasma density [cm^{-3}], n_0 is the neutral gas density [cm^{-3}], I is the laser pulse intensity [W/cm^2], Δt is the laser pulse length [s], and $(h\nu)$ the photon energy [Jsec]. Here all the other constants have been absorbed in α, the two-photon ionization coefficient [cm4/W].

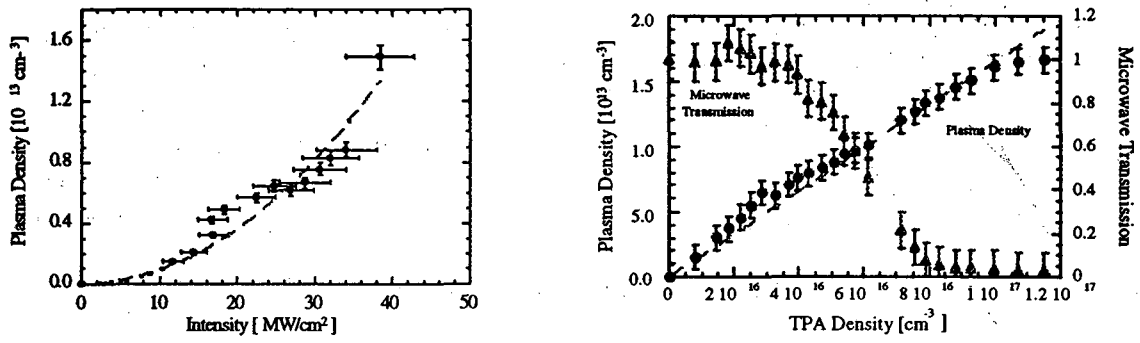

Figure 2. Plasma density (solid dots) scales quadratically with laser intensity and linearly with TPA density. The hollow triangles represent the transmitted microwave signal strength.

To achieve plasma lengths on the order of a few centimeters, the laser beam is defocused horizontally using a cylindrical defocusing lens (Figure 1). To maintain the laser intensity (and therefore, the plasma density), the beam is focused in the vertical direction.

The plasma density is measured through microwave interferometry at 94.3 GHz described previously[5]. The microwave signal is launched transversely to the plasma sheet. The plasma density is calculated by measuring the relative microwave phase shift introduced by the plasma. Since the plasma densities are close to critical density for microwave beam absorption, a two-channel in-quadrature measurement technique[6] is used to compensate for absorption effects. The plasma density was measured as a function of neutral gas fill pressure and laser intensity as shown in Figure 2. The two-photon ionization coefficient, α, was measured to be 2.5×10^{-29} W/cm^4. Plasma densities up to 2×10^{14} cm^{-3} were measured using this technique. At this density the transmitted microwave amplitude was only 3% of the initial amplitude, in agreement with calculations.

ELECTRON BEAM DIAGNOSTICS

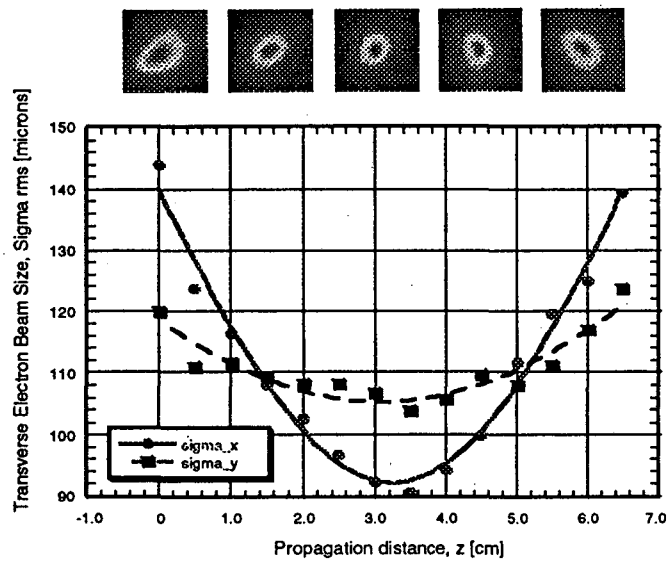

Figure 3. Measurement of beam size through OTR at various positions along the direction of propagation. The solid and dashed lines represent the best fit through the transverse beam size, σ_{rms}, along the x-axis and y-axis, respectively.

The electron beam is diagnosed using optical transition radiation that is produced by a charged particle at it passes through a boundary between two media with different dielectric constants. The radiation contains information about the size, divergence and energy of the source charged particle beam.

A five micron thin nitrocellulose foil coated with high reflectivity aluminum is inserted in the electron beam path. When the beam passes through the foil, it emits transition radiation, which is imaged onto a CCD camera. The OTR foil is mounted on a motorized stage. As the stage is moved along the trajectory of the electron beam, a direct measurement of the beam size as a function of propagation distance is obtained. In the later stages of the experiment, the nitrocellulose foil was replaced by a 1 mm thick quartz plate coated with high reflectivity aluminum. To study the temporal dynamics of the plasma lens, OTR is imaged to a streak camera with 2ps resolution[7].

ELECTRON BEAM FOCUSING BY BEAM-INDUCED PLASMAS

A relativistic electron beam passing through a gas can collisionally ionize the gas. The density of the plasma, n_p, is then given by,

$$n_p = \left|\frac{dE}{dx}\right| \frac{N_b \sigma_z \rho_m}{E_{th}} \qquad (2)$$

where dE/dx is the stopping power of electron beam [eVcm^2/g], N_b is the electron beam density [cm^{-3}], σ_z is the electron bunch length [cm], ρ_{gas} is the mass density of background gas [cm^{-3}], and E_{thresh} is the ionization threshold of the gas [eV]. In our case, this corresponds to a plasma density of approximately 10^{11} - 10^{12} cm^{-3}. Since the plasma is produced by the electron beam, the spatial profile of the plasma follows the evolution of the electron beam and is calculated to be: $n_p(z) = n_{p\max}\beta_0 / \sqrt{\beta_0^2 + s^2}$, where $s=z-ct$ and β_0 is the minimum value of the electron beam beta function in the plasma. The plasmas produced through electron beam ionization are underdense. The focusing strength of an underdense plasma lens is given by $K = 2\pi r_e n_p / \gamma$, where r_e is the classical electron radius, γ the electron beam energy and n_p the plasma density.

Figure 4 shows the measured electron beam size as a function of propagation distance inside the plasma chamber. In vacuum, the beam size at the waist is measured to be 130 μm. As the neutral gas pressure is increased, the beam ionizes the vapor, and is focused by the resulting plasma.

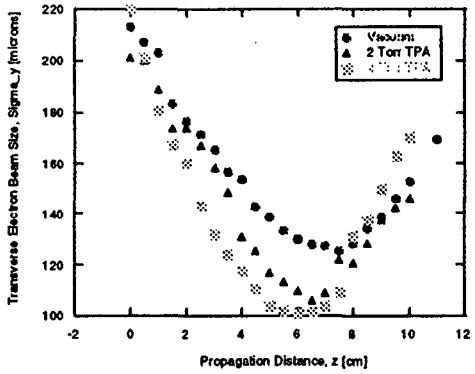

Figure 4. Measured electron beam focusing by beam-ionized plasma. As the neutral gas density increases, so does the induced plasma density and the plasma focusing.

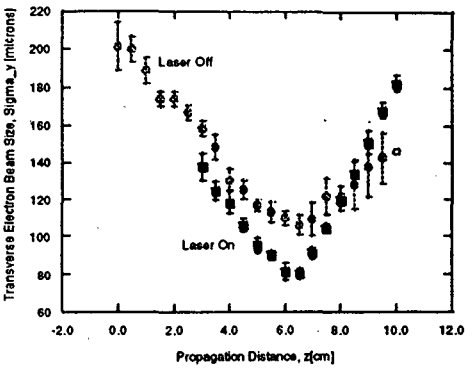

Figure 5. Measured electron beam focusing by laser-produced plasma. When the laser is turned on , the laser produced plasma focuses the electron bunch to a smaller spot size.

ELECTRON BEAM FOCUSING BY OVERDENSE LASER RODUCED PLASMAS

The laser beam is temporally and spatially aligned with the electron beam. The electron beam size as a function of propagation distance is measured with and without the laser beam (Figure 5). When the laser beam is turned on to produce plasma, the electron beam is focused to a smaller spot size. A corresponding increase in electron beam peak intensity is measured using OTR. The strength of focusing is found to depend strongly on electron beam beta function matching into the plasma, in agreement with theoretical calculations.

CONCLUSION

The 50 MeV electron beam from the ALS injector has been focused through plasma lenses at BTF. Electron beam focusing by beam induced plasmas has been studied using optical transition radiation diagnostics. Laser produced overdense plasmas have been observed to focus the electron beam. Both types of lenses show strong dependence on e-beam beta function matching. Currently, highly overdense plasmas are being studied to observe return current cancellation. Detailed simulations are being conducted for comparison with theoretical predictions and temporal dynamics of plasma lenses is being experimentally investigated.

REFERENCES

1 P. Chen, Part. Accel. **20**, 171 (1987).
2 T. Katsouleas, et al., Proc. 1992 Adv. Accel. Workshop (1992).
3 P. Chen, et al., Phys. Rev. Lett. **64**, 1231 (1990).
4 W. Leemans, et al., Proc. 1993 Part. Accel. Conf., 83 (1993).
5 M. de Loos et al., Proc. Eurpoean Part.Accel. Conf. (1994).
6 W. Barry, private communication.
7 R. Govil et al., Proc. Part. Accel. Conf. (1995).

Work supported by the Director, Office of Energy Research, Office of High Energy Physics and Nuclear Research, High Energy Physics Division, U.S. Department of Energy under Contract No. DE-AC03-76SF00098.

Principal investigator: Wim Leemans, Ernest Orlando Lawrence Berkeley National Laboratory. Email: Wim_Leemans@lbl.gov. Telephone: 510-486-7788.

Ultrashort Hard X-Ray Pulses Generated by 90° Thomson Scattering

A.H. Chin[1], R.W. Schoenlein[2], W.P. Leemans[3], P. Volfbeyn[3], T.E. Glover[2], P. Balling[2], M. Zolotorev[3], K.-J. Kim[3], S. Chattopadhyay[3], and C.V. Shank[1,2]

[1]Department of Physics, University of California, Berkeley, California 94720, USA
[2]Materials Sciences Division, Ernest Orlando Lawrence Berkeley National Laboratory, University of California, Berkeley, California 94720, USA
[3]Accelerator and Fusion Research Division, Center for Beam Physics, Ernest Orlando Lawrence Berkeley National Laboratory, University of California, Berkeley, California 94720, USA

INTRODUCTION

Ultrashort x-ray pulses permit observation of fast structural dynamics in a variety of condensed matter systems. We have generated 300 femtosecond, 30 keV x-ray pulses by 90° Thomson scattering between femtosecond laser pulses and relativistic electrons. The x-ray and laser pulses are synchronized on a femtosecond time scale, an important prerequisite for ultrafast pump-probe spectroscopy. Analysis of the x-ray beam properties also allows for electron bunch characterization on a femtosecond time scale.

EXPERIMENT

The experiments are performed in the Center for Beam Physics Beam Test Facility at the Advanced Light Source. Experimental details may be found in Refs. 1 and 2. Briefly, terawatt laser pulses at 800 nm are produced by a Ti:Sapphire based chirped pulse amplification system [3]. These laser pulses Thomson scatter off of relativistic electrons (50 MeV, $\gamma = 98$), produced by the linear accelerator at the Advanced Light Source, to generate highly directed x-rays. For Thomson scattering from a single relativistic electron, the x-rays produced have energies with the following angular dependence

$$E = 2\gamma^2 E_{laser} \frac{(1-\cos\psi)}{(1+\gamma^2\theta^2)} \qquad (1)$$

for $\gamma >> 1$, where ψ is the interaction angle between the electron and laser pulse (90° in our case) and θ is the x-ray emission angle relative to the electron trajectory, as shown in Fig. 1 [1,2].

By choosing a 90° scattering geometry, the duration of the generated x-ray pulse is determined by the transit time of the ultrashort laser pulse (~ 100 fs) across the focused electron beam waist (~ 90 microns), resulting in x-ray pulses of ~ 300 fs in duration. Knowledge of the x-ray pulse duration is based solely on the determination of the electron beam size at the interaction point. This is obtained by imaging the optical transition radiation emitted by the relativistic electrons as they pass through a thin aluminum foil (placed in the electron beam path when the laser is not present) [1,2].

The Thomson scattered x-rays are detected by imaging the visible fluorescence emitted when the x-rays strike a phosphor screen onto a CCD camera. X-ray spectra are obtained by aperturing the x-ray beam and using a solid-state (Ge) detector in photon counting mode, and using pulse-height analysis [1,2].

Because an ultrashort laser pulse is used in the generation of the x-ray pulses, the ultrashort x-ray pulses are automatically synchronized with visible laser pulses. This allows for ultrafast pump-probe experiments, with visible pump and x-ray probe pulses. As x-rays can be used as structural probes (e.g. x-ray diffraction, EXAFS) structural dynamics in condensed matter, initiated by femtosecond laser pulses, may be studied using this x-ray source [1].

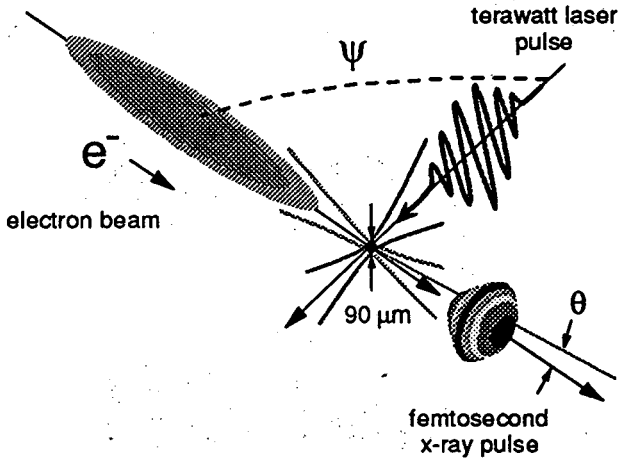

Figure 1. Thomson scattering geometry.

RESULTS

We have obtained spatial and spectral characteristics of the x-ray beam [1,2]. Fig. 2 shows the spatial profile of the x-ray beam striking a phosphor ~ 80 cm from the interaction point. The image corresponds to $\sim 5\times10^4$ x-ray photons per pulse, contained in a divergence of $\sim 1/\gamma = 10$ mrad. Fig. 3 shows x-ray spectra at different observation angles θ relative to the center of the x-ray beam. The spatial profile and spectra closely agree with the Thomson scattering theory, taking into account the emittance of the electron beam (i.e. the distribution of electron trajectories at the focus) [1,2].

Analysis of the x-ray divergence and energy spectrum yields information about the electron bunch divergence. Monitoring the x-ray yield as a function of the temporal and spatial overlap of the electron bunches and laser pulses can be used to determine the temporal and spatial profiles of the electron bunches. Knowledge of both the electron beam divergence and spot size where the laser interacts with the electron beam allows for the determination of the electron beam emittance for femtosecond time slices of the beam, rather than averaged over the entire electron bunch[2].

Ultimately, the Thomson scattering source of ultrashort x-ray pulses is to be used to study ultrafast structural dynamics in condensed matter [1]. One interesting phenomenon is the ultrafast melting of semiconductors under intense, ultrashort laser excitation [4,5]. The ultrafast visible light experiments (see, e.g. Refs. 4 and 5) suggest that loss of long-range order occurs on the femtosecond time scale in semiconductors under intense laser excitation. This loss of order is postulated to occur because of the structural instability created by the promotion of a large fraction (~ 10%) of electrons from bonding (valence band) to anti-bonding (conduction band) states [6,7]. However, as visible light techniques are only indirect probes of structure, this ultrafast structural transformation can only be inferred from these experiments. Performing a time-resolved x-ray diffraction experiment using the Thomson scattering source would more conclusively determine if long-range order is indeed lost on the femtosecond time-scale. As a preliminary step, we have performed x-ray diffraction on semiconductor crystals without laser excitation, using the Ge detector to detect the diffracted x-rays.

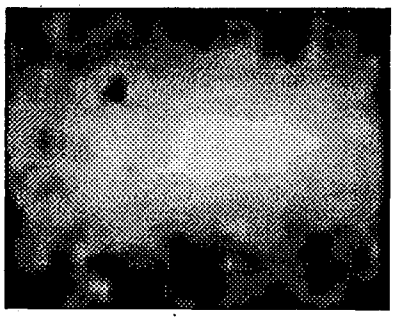

Figure 2. CCD image of the spatial profile of the x-ray beam, taken ~ 80 cm from the interaction point. The horizontal and vertical sizes (FWHM) are ~ 12 mm and ~ 8 mm respectively.

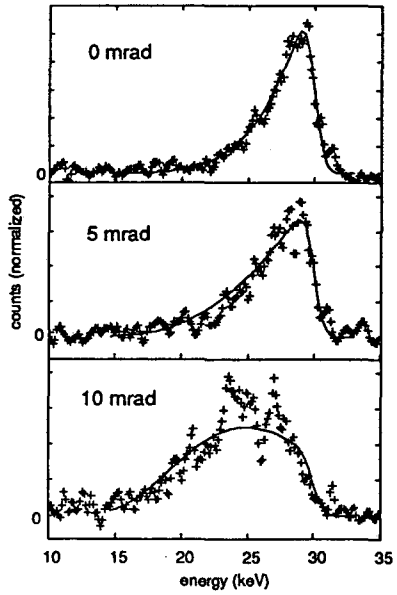

Figure 3. Normalized x-ray spectra at observation angles of 0 mrad, 5 mrad, and 10 mrad from the center of the beam. Solid lines are theoretical predictions.

CONCLUSIONS

We have generated 0.4 angstrom, 300 fs x-ray pulses by right-angle Thomson scattering. This source of ultrashort x-ray pulses is a promising tool for studying ultrafast structural dynamics in condensed matter. Experiments are underway to study the effects of ultrashort, intense laser pulse excitation on the long-range order in semiconductors. Thomson scattering with terawatt laser pulses may also be used to characterize ultrashort time slices of electron bunches.

ACKNOWLEDGEMENTS

The authors wish to acknowledge R. Govil, T. Byrne, and the Advanced Light Source operations crew.

REFERENCES

1. R.W. Schoenlein, W.P. Leemans, A.H. Chin, P. Völfbeyn, T.E. Glover, P. Balling, M. Zolotorev, K.-J. Kim, S. Chattopadhyay, and C.V. Shank, Science **274**, 236 (1996).
2. W.P. Leemans, R.W. Schoenlein, P. Volfbeyn, A.H. Chin, T.E. Glover, P. Balling, M. Zolotorev, K.-J. Kim, S. Chattopadhyay, and C.V. Shank, Phys. Rev. Lett. **77**, 4182 (1996).
3. D. Strickland and G. Mourou, Opt. Commun. **56**, 219 (1985).
4. C.V. Shank, R. Yen, and C. Hirlimann, Phys. Rev. Lett. **50,** 454 (1983); **51,** 900 (1983).
5. E.N. Glezer, Y. Siegal, L. Huang, and E. Mazur, Phys. Rev. B **51**, 6959 (1995); **51**, 9589 (1995).
6. J.A. Van Vechten, R. Tsui, and F.W. Saris, Phys. Lett. **74A**, 422 (1979).
7. P. Stampfli and K.H. Bennemann, Appl. Phys. A **60**, 191 (1995); Phys. Rev. B **46**, 10686 (1992).

This work was supported by the U.S. Department of Energy under Contract No. DE-AC03-76SF00098 and by the National Science Foundation under grant PHY-9512693.

Principal investigators:
Wim Leemans, Acceleration and Fusion Research Division, Center for Beam Physics, Ernest Orlando Lawrence Berkeley National Laboratory. Email: Wim_Leemans@lbl.gov. Telephone: 510-486-7788.
Robert Schoenlein, Materials Sciences Division, Ernest Orlando Lawrence Berkeley National Laboratory. Email: rwschoen@lbl.gov. Telephone: 510-486-6557.

Institutions Funding User Research at the ALS

This list is compiled from the funding institutions users listed in their abstracts for work done from 1993 to 1996.

U.S. Department of Energy

EPSCoR
Office of Energy Research
    Office of Basic Energy Sciences
    Chemical Sciences Division
    Geoscience Program
    Materials Sciences Division
Office of Health and Environmental Research
    Medical Applications and Biological Research Division
Office of High-Energy Physics and Nuclear Research
    High-Energy Physics Division

Other Institutions

Alexander von Humboldt Stiftung, Germany
Army Research Office
Assistant Secretary for Fossil Energy, Office of Technical Coordination
Associated Western Universities, Inc.
AvH Foundation
BMBF
Bundesminister für Bildung, Wissenschaft, Forschung und Technologie, Germany
Chevron Research and Technology Company
Chinese Academy of Sciences
CNPq, Brazil
Deutsche Forschungsgemeinschaft, Germany
Dow Chemical
EPSRC of the United Kingdom
French CNRS
Fulbright Foundation
GAANN Fellowship
Göran Gustafsson Foundation for Research in National Science and Medicine
GSI
Heinrich Hertz-Stiftung, Düsseldorf, Germany
Intel
International Centre for Diffraction Data
Jeffress Trust
Kyungpook National University, Korea
Laboratory for Surface Studies
Laboratory-Directed Research and Development Program of Lawrence Berkeley National Laboratory
Laboratory-Directed Research and Development Program of Oak Ridge National Laboratory
Lockheed Martin Energy Research Corporation
Louisiana Educational Quality Support Fund
Max-Planck-Gesellschaft
National Aeronautics and Space Administration
    Office of Space Access and Technology

Institutions Funding Research at the ALS, cont.

National Energy Research Supercomputing Center at Lawrence Berkeley National Laboratory
National Institute of Standards and Technology
National Institutes of Health
National Science Foundation
    Division of Materials Research
North Atlantic Treaty Organization
NSERC, Canada
Office of Naval Research
Petroleum Research Fund
Research Corporation
Seo-Am Funds
Spanish Ministerio de Educación y Ciencia
Special Researcher's Basic Science Program of RIKEN (Institute of Physical and Chemical Research, Japan)
Swedish Institute
Swedish National Science Research Council (NFR)
Swedish Science Foundation
Swiss National Science Foundation
Tulane University
Unilever plc
University of California-Berkeley
University of Tennessee
University of Wisconsin-Milwaukee
U.S. Department of Defense
    Advanced Research Projects Research Agency
        Advanced Lithography Program
Virginia Commonwealth University

ALS Technical Reports Table of Contents

Introduction

Technical Reports

Report from the ALS Director

"Full Speed Ahead" summarizes the past year's activities of the ALS. Our successful operation and R&D efforts are due to the cooperation of large numbers of people doing work on the leading edge of the synchrotron radiation field. This concentration of skill, talent, and dedication continues to build, as engineers, scientists, and staff at the ALS work to provide a technically excellent machine and a strong base of user support. Our high-powered user community is taking these resources and running with them, generating scientific results at an accelerating pace.

This acceleration is due in part to the Scientific Facilities Initiative initially funded by Congress in October 1995, which boosted FY96 funding for the ALS and other DOE national user facilities. With this boost in funding, we increased the number of operating hours for users 73% and built several new beamlines, with more due to become available soon (Table 1). The demand for those new beamlines, in turn, means our scientific user community and its needs are growing, and ALS management is working closely with the Users' Executive Committee (elected to represent the ALS user community) to see that these needs are met. It is an encouraging sign that maintaining scientific facilities utilization is still among the top priorities for the DOE Energy Research Program in FY98, as this will allow us to continue serving our users effectively while pushing the boundaries of synchrotron research and development.

The success and growth of the ALS scientific program depends directly on the quality of operations the facility provides, and one of the key parameters for our performance is the reliability and quality of the beam delivered. To this end, we brought new coupled-bunch longitudinal and transverse feedback systems on line in March 1996. However, with feedback systems on, the decreased beam size has made some remaining beam-position instabilities more critical. Therefore, since September 1996, a special task force of ALS accelerator physicists, engineers, scientists, operators, and users led by Rod Keller has been working with remarkable success to further stabilize the ALS electron beam and thereby to increase photon-beam stability for users. Many of the ALS technical reports summarize key areas related to improving beam diagnostics and stability.

We have also expanded our range of operating modes in the past year. We now operate at 1.9 GeV more than half the time, and we have increased the maximum current available in this mode from 150 mA to 340 mA. The installation of narrow-gap vacuum chambers in sectors 7 and 8 (May 1997) and longer-period undulators is meeting most experimenters' needs for low-energy photons at 1.5 GeV, so that we no longer need to operate at 1.0 GeV (though we still offer up to a few weeks each year of 1.3-GeV operations). A new "camshaft" fill pattern provides for a range of timing experiments without interfering with more conventional uses of the beam.

	FY94	FY95	FY96	FY97 (Projected)
Users	95	213	296	350
Independent Investigator Proposals	0	7	43	113
User Hours	2222	2686	4461	4600
Operating Beamlines	8	11	14	21

Table 1. Increased funding in FY96 allowed the ALS to expand its operations for users and accelerate the pace of beamline construction.

I am proud to say our beamline and instrumentation development is truly leading the field. Some examples include:

Micro-XPS at Beamline 7.3.1. The micro-XPS (x-ray photoelectron spectroscopy) branchline of this beamline recently received its first light ahead of schedule while exceeding initial specifications, despite the tight construction schedule of only nine months. This beamline, partially funded by Intel and Applied Materials, is designed to serve several specific needs of the semiconductor community and to be inexpensive to replicate in case of increasing demand.

Macromolecular Crystallography and Structural Biology Support Facilities. Beamline 5.0 for macromolecular crystallography is nearing completion and already it is clear there will be a high level of demand for this beamline. Structural Biology Support Facilities to provide lab and computer support for the beamline's users opened in the fall of 1996.

Elliptical Polarization Undulators (EPUs). A working scale model for these new insertion devices, which shift rows of magnets to produce light in any polarization from linear (any orientation) to circular (either helicity), was recently completed. The EPUs will serve Beamline 4.0 which will be dedicated to magnetic spectroscopy and microscopy. The beamline is scheduled to be commissioned in 1998.

Adaptive Optics. The ALS is taking the lead in designing new types of bending mirrors that meet or exceed tough specifications for slope error and spot size, and is also addressing the challenges of designing mirrors with small radii of curvature.

In addition to all this, work at the ALS may well be contributing to the success of future synchrotron radiation facilities. Because of its small transverse beam size, the ALS is one of the first storage rings in the world to be in the position to study the transient regime of ion instabilities. In many future rings, this transient instability is predicted to have very fast growth rates, much faster than the damping rates of existing and proposed transverse feedback systems, and thus is a potential limitation.

Brian M. Kincaid

ALS Operations

The success and growth of the ALS scientific program depends directly on the quality of operations the facility provides. In 1996 the ALS again demonstrated its ability to deliver a high-quality beam to user experiments on a reliable schedule and maintain an efficient and safe work environment for users. The success of these efforts depends on the cooperation among ALS groups and between the ALS and users.

In November 1995 we made a substantial increase in our operations for users and our level of customer support because of increased funding from the Scientific Facilities Initiative. User beamtime now occupies 16 eight-hour shifts per week, an increase of 78% week-by-week as compared to the previous funding-limited schedule. This increased level of funding is key if the ALS is to continue to be able to meet the ever-growing needs of the user community and if it is to be fully utilized as a national user facility.

The remaining 5 shifts per week were 3 for accelerator physics, 1 for maintenance and installation, and 1 for startup and test. There was one two day maintenance period scheduled per month for most of the year which has helped keep the time needed for major installation shutdowns to a minimum. Scheduled versus actual beam availability during the last calendar year was 89.3% overall and 89.4% during user shifts, a total of 6940 hours scheduled and 6124 hours delivered including time deducted for normal storage ring refills (Figure 1). The only "major" cause of beam outage for the year, which was in fact fixed in less than two days with no loss of user beamtime, was a jammed roller screw in the gap drive system for the sector 8 undulator.

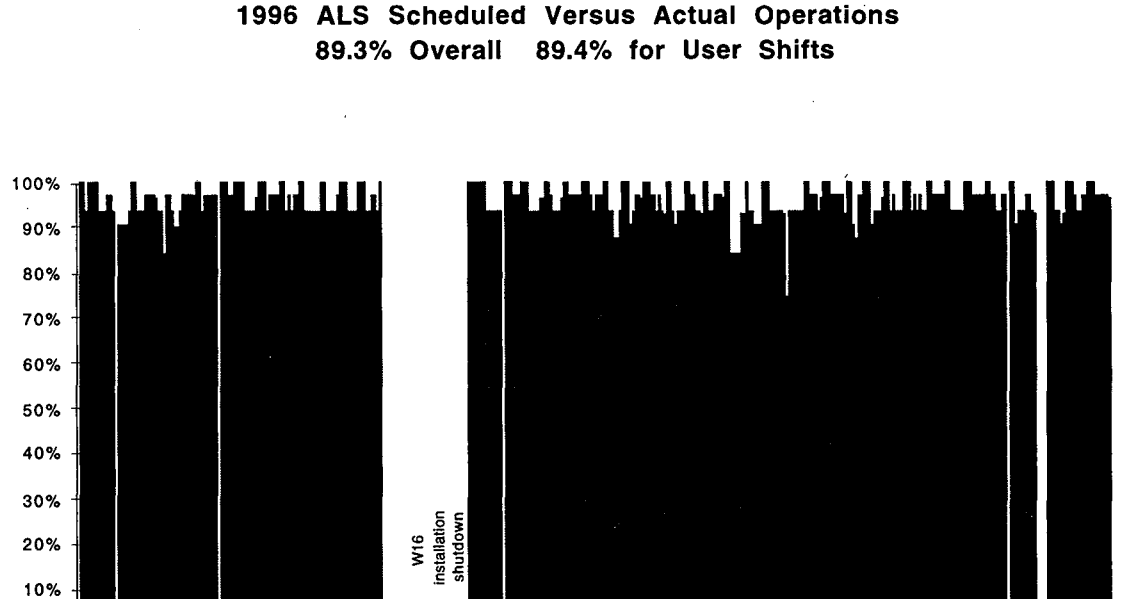

Figure 1. ALS performance for machine operations during 1996.

User operations included operation at 1.1 GeV, 1.3 GeV, 1.5 GeV and 1.9 GeV with fill patterns including 320 bunch, 304 bunch, 288 bunch, with and without a single 20 mA bunch (camshaft), and 2-bunch. The long-term scheduling process is gradually emphasizing operation at the higher energy, 1.9 GeV, as this increases the variety of experiments that can be performed efficiently on ALS beamlines by providing more usable photon flux at high photon energies. In 1996 we increased the maximum current at 1.9 GeV from 260 mA to 340 mA as a result of tests and rf system tuning to allow increased power with the existing rf cavity windows. Scheduling for operations is done at least 6 months in advance with input from users, the Users Executive Committee, and ALS management. Weekly scheduling meetings are held to fine tune the two week rolling schedule.

Continuing improvements of the facilities for the ALS have included low-conductivity water (LCW) system improvements included heat exchanger maintenance, new pump and fan motors with variable frequency drives, replacement of the cooling tower fan and gearbox, installation of stainless steel water lines between the cooling tower and Building 6, and replacement of epoxy coated valves in Building 6 with stainless steel valves. Additionally, a cathodic protection system was installed by Berkeley Lab's Facilities Department on all the LCW water lines connected to the Building 34 cooling tower system.

In addition, beam position monitoring has been upgraded through new, improved electron beam position monitors (BPMs), and hardware and software. This has helped in identifying major causes of temperature related beam movement and evaluating temperature control software changes.

Reported by Bob Miller

Accelerator Physics Overview

In the following technical reports, we describe three activities of the accelerator physics group that vary widely in scope. The first: an improvement to the operational capabilities of the facility, based on the experience and tools developed by the accelerator physicists. The second: an enhancement of the measurement-based modeling tools that are being used to improve the performance of the accelerators. The third: an exciting new development for the accelerator group that builds on our detailed understanding of the way in which the accelerators behave.

Improvements to the ALS's operational capabilities were spurred by our bringing the longitudinal and transverse multibunch feedback systems into routine operation. As a consequence, the fundamental beam parameters of natural emittance and energy spread reached their theoretically predicted values of 4 nm-rad and 0.08% respectively. The vertical emittance (at 1.5 GeV) was particularly small, measured at 0.1 nm-rad. The immediate result of this success was more challenges for the accelerator physicists.

With such low emittance, the lifetime of the densely packed electron bunches becomes dominated by the Touschek effect (collisions of electrons within the bunch that transfer transverse momentum to the longitudinal direction). At around 2 hours, the lifetime was uncomfortably short for the user community, so a compromise was reached in which the small vertical emittance was traded against longer lifetime. This is done by changing the ratio of transverse energies (proportional to the beam emittances) between the horizontal and vertical planes, using skew quadrupole fields (a capability designed into the sextupole magnets). The challenge was to determine the most effective way of controlling this "betatron coupling"—which is very sensitive to the betatron tunes—in the face of tune changes caused by undulators, as they are manipulated by the users. We have successfully identified magnet settings where the coupling changes caused by the undulators have an insignificant effect on electron beam size. The next challenge will arise when the powerful 2-T wiggler is brought into routine operation.

A related issue arose because the users began to take advantage of the better resolution they could achieve with the higher-quality electron beam. This led to a requirement for better electron beam position stability. The improvement was accomplished without closed-orbit feedback (a feat not achieved at any other synchrotron radiation facility), as described under "Orbit Stabilization for the ALS Electron Beam."

Throughout the year we have continued to refine the measurement-based modeling of the storage ring and to understand the limitations of these techniques caused by the real and apparent motion of the beam position monitors (BPMs), which all reside in the massive 10 m long arc vacuum vessels. Many of the improvements that came out of the beam stabilization program, particularly more uniform temperature stabilization in the accelerator tunnels, resulted in more reliable position stability for the BPMs. This, in turn, gave us more confidence in the measurement-based modeling of the storage ring and allowed us to propose improved operating scenarios based on the model. Two examples of such efforts, leading to better injection efficiency and to compensation of the beta-beating induced by the vertical focusing in the W16.0 wiggler, are discussed under "Machine Modeling."

With a better understanding of the storage ring parameters, we have been able to embark on a study of more esoteric effects in the accelerators. One such study has targeted the interaction of the bunched electron beam with the residual ions in the storage ring. These studies are discussed under "Ion Effects in the ALS." One effect is particularly worthy of note: the fast-ion instability. The theory first originated to describe beam emittance growth observed in the Photon Factory in Japan. However, experiments there failed to show any of the predicted parameter-dependent characteristics. At the ALS, a well controlled series of experiments was carried out in collaboration with accelerator physicists from the Stanford Linear Accelerator Center. In these experiments, the instability was unambiguously identified for the first time.

Reported by Alan Jackson

Orbit Stabilization for the ALS Electron Beam

During the design phase of the ALS storage ring, the tolerance for electron beam orbit stability was set to 10% of the nominal beam size, or to standard deviations (1σ) of 20 μm horizontally and 5 μm vertically in the straight sections. An important secondary parameter for these limits is the time scale for which they are meant to apply. For most of the current ALS users, this scale ranges from 0.1 s to the running time between refills (about 4 hours). Up to the fall of 1995, the ALS beam suffered from five kinds of orbit perturbations occurring in the critical time range that all had their characteristic signatures as to amplitude, time, and distribution between the horizontal and vertical planes. The worst amplitudes reached about 300 μm peak-to-peak.

At this point, a task force was constituted from members representing the ALS accelerator physics group, the operations group, diagnostics and control systems, and Berkeley Lab's Engineering and Facilities Divisions. Soon one effect was identified that consisted of vertical orbit perturbations with a period of about 15 minutes caused by oscillations of the low-conductivity water (LCW) temperature. The clue to solving this problem had been a comparison of the oscillation periods of the LCW temperature and the photon beam intensity variations noted by users. After this particular problem was solved, the vertical orbit stability was consistently much better than the horizontal one, and this fact momentarily reduced the pressure on the stability task force to further improve the operating conditions.

Things changed again by the summer of 1996, when new beam position monitors (BPMs) were installed in several straight sections of the storage ring that inherently had much higher sensitivity than the BPMs installed in the curved vacuum chambers, mostly because of their negligible dependence on beam current. At the same time, several user groups had refined their experimental procedures to a point where the remaining orbit perturbations began to seriously compromise their research results. (Figure 1 shows the stability of the electron beam at this time.) The stability task force was therefore reactivated with the mission to improve the orbit stability to the original specifications in the shortest time possible. The time constraint precluded any immediate work on a closed orbit feedback system, for which we estimated a development time of at least 18 months.

Two experiences from the past led to the next major progress made by the stability task force. One was the success with stabilizing the LCW temperature down to 0.1°C peak-to-peak, or one-tenth of its original specification. The other reached much farther back—to the construction phase of the storage ring, in which survey and alignment cycles failed to agree until the ALS building was air conditioned to a precision of 1°C peak-to-peak. The effect of air temperatures exceeding this range was that the 12 m long girders on which the lattice magnets of every arc section are mounted changed their curvature, progressively misaligning the magnets. By modeling this effect with the help of a newly developed simulation code, we were able to identify individual sectors that caused certain large horizontal orbit perturbations. Dedicated experiments with the storage ring itself, involving precision micrometers and inclinometers, showed that changes of 0.2°C in girder temperature could lead to magnet misalignments of about 50 μm and consequently to 300-μm orbit deformations.

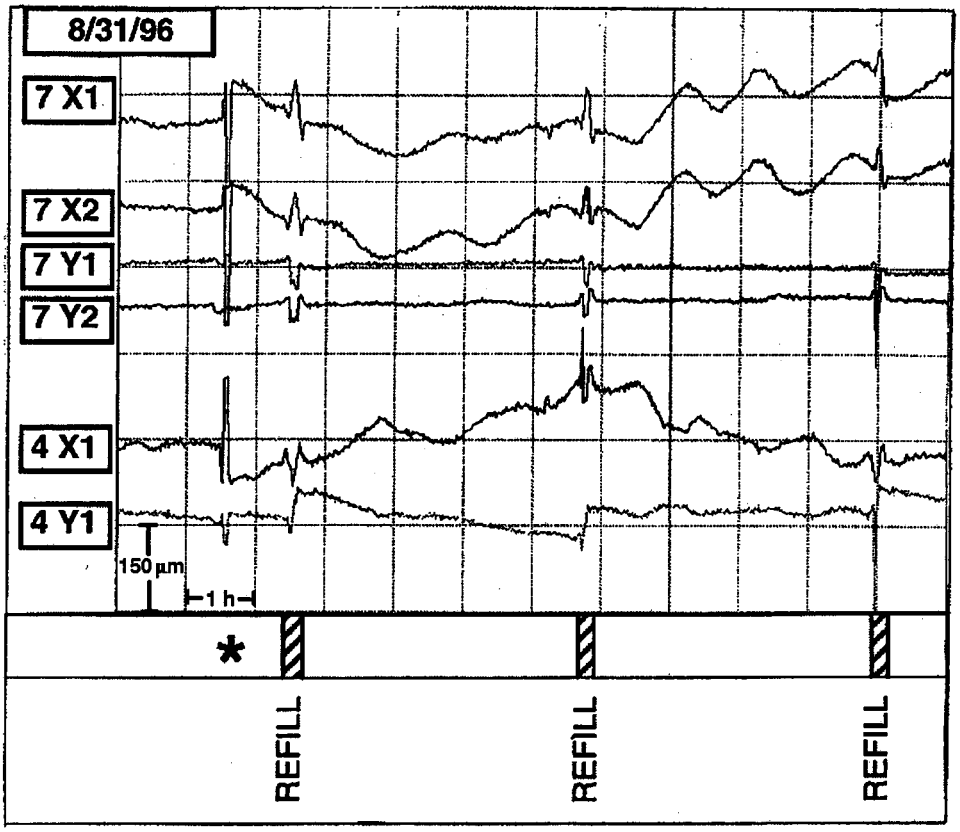

Figure 1. Horizontal and vertical insertion device beam position monitor (ID-BPM) signals observed over a 12-h period on August 31, 1996. Readings from BPMs during fills (hatched areas) are invalid. The asterisk marks an event that would be typical of a crane movement. Most traces also show significant drifts and oscillations with a 1-h period typical of air temperature variations in the storage ring tunnel. The labels on the left-hand side indicate straight sector number, coordinate direction, and position (1 for upstream and 2 for downstream) of each ID-BPM.

At this point it was clear that the air temperature had to be much better stabilized than before, but it took about two months of gradual changes to establish a consistent scenario that led to a dramatic improvement in orbit stability. The main elements of this scenario include keeping the temperature in the storage ring tunnel lower than that of the ALS building; moving the nine temperature controlling sensors in the tunnel from the inner wall to the outer wall, away from the air outlets, and averaging their readings; holding all nine air-handling units that supply the tunnel with cooled air to one common value; and using four large fans positioned around the ring to move the air in the tunnel in a spiral fashion around the storage ring. All these measures reduced the typical remaining orbit perturbations to about 20 µm horizontally and 5 µm vertically peak-to-peak, or 8.5 µm and 2.1 µm standard deviation, respectively. Thus, the established tolerances for beam stability have been substantially exceeded without the help of an orbit feedback system.

There are three other, unrelated effects that influence the electron orbit, one of them well anticipated, and two providing surprises to everyone involved. The first effect occurs whenever an insertion device gap is changed. The device's integral dipole component (caused by magnetic fields that are not exactly balanced) changes slightly and deforms the orbit around

the entire ring. This effect is being cared for satisfactorily by applying compensating steerer fields in a feed-forward mode. The accuracy of the existing BPMs in the arc sections is the limiting factor for this compensation method. To further minimize the influence of insertion device gap changes on the electron orbit, after a refill the operators routinely close all gaps to the width at which they were set at the end of the preceding run.

The second effect is caused by the two large cranes in the ALS building: the polar crane mounted on the former cyclotron yoke and the annex crane serving the experiment stations. It was demonstrated that a change in position of the polar crane perturbs the magnetic field crossing the straight sections enough to create a 50-μm orbit distortion. This effect can be handled well administratively, limiting crane movement to the times when the ring is not being used by experimenters.

The last effect has not yet been fully analyzed, but it is well correlated with excitation changes in the last two dipole magnets of the booster-to-storage-ring transfer line. These magnets are located more than 1.5 m away from the nearest part of the storage ring, but the fact that the orbit perturbations take place predominantly in the horizontal plane suggests that the (vertical) fringe field of either magnet reaches into the iron-free regions of the storage ring in this area and affects the electron beam position.

With dynamic and administrative controls, we have arrived at the satisfactory state of beam stability indicated in Figures 2 and 3.

Several experiments were carried out to monitor the thermal effects on the storage ring vacuum tank. Since the vacuum tank contains the electron BPMs, changes in its position can have important consequences when tracking the electron beam. The position of the end part of the insertion-device vacuum chamber in sector 7 was monitored with both 1-μm-resolution dial indicators and with 1-μrad-resolution inclinometers. This chamber part was found to undergo several characteristic changes during a weekly operation cycle. One change, measured with respect to the adjacent girder, was a 20-30 μm vertical position change during a 6-8 hour cooling down or warming up period before and after weekly shutdowns, see Figure 4. The same figure also shows horizontal and vertical position changes of the observed chamber section, and hence the BPM it carries, that occur on a fill-to-fill basis during operation and are directly correlated with the beam intensity cycle. These changes, again measured with respect to the girder, are 15 μm horizontally and 8 μm vertically and are apparently caused by photon heating of the chamber wall.

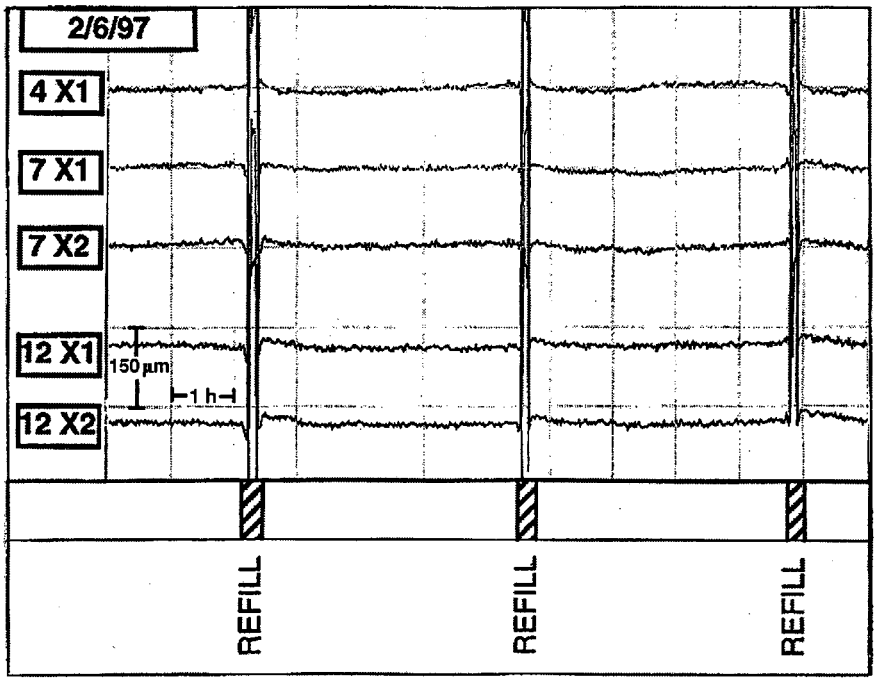

Figure 2. Horizontal ID-BPM position signals observed over a 12-h period on February 6, 1997. Sector-12 ID-BPMs are added to those for sectors 4 and 7, and the substantial gain in stability as compared to the conditions in August 1996 is easy to discern.

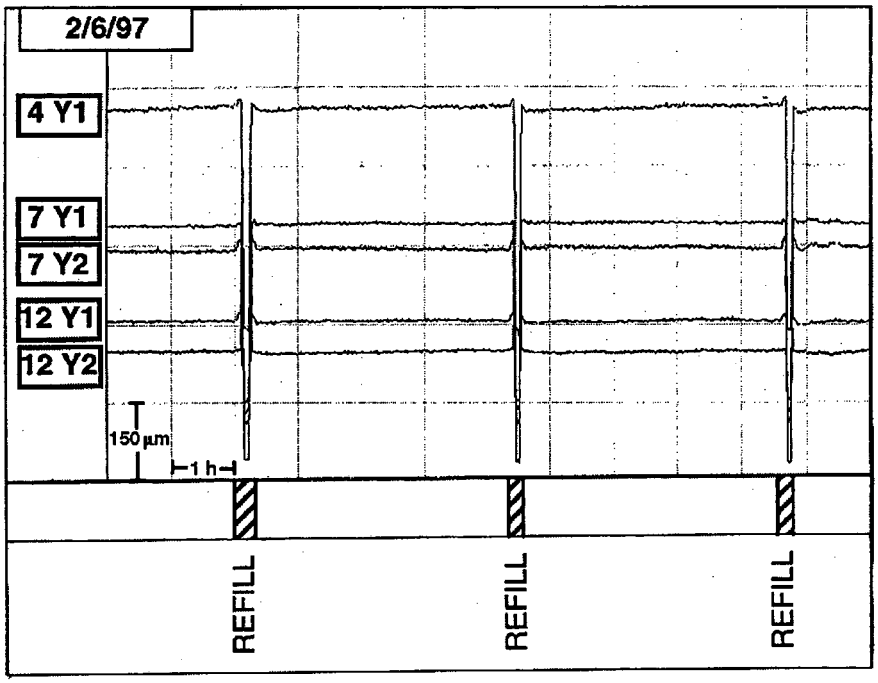

Figure 3. Vertical ID-BPM position signals observed over a 12-h period on February 6, 1997. Again, the improvement as compared to August 1996 is striking. Together with Figure 2, this represents the typical performance of the ALS storage ring to date.

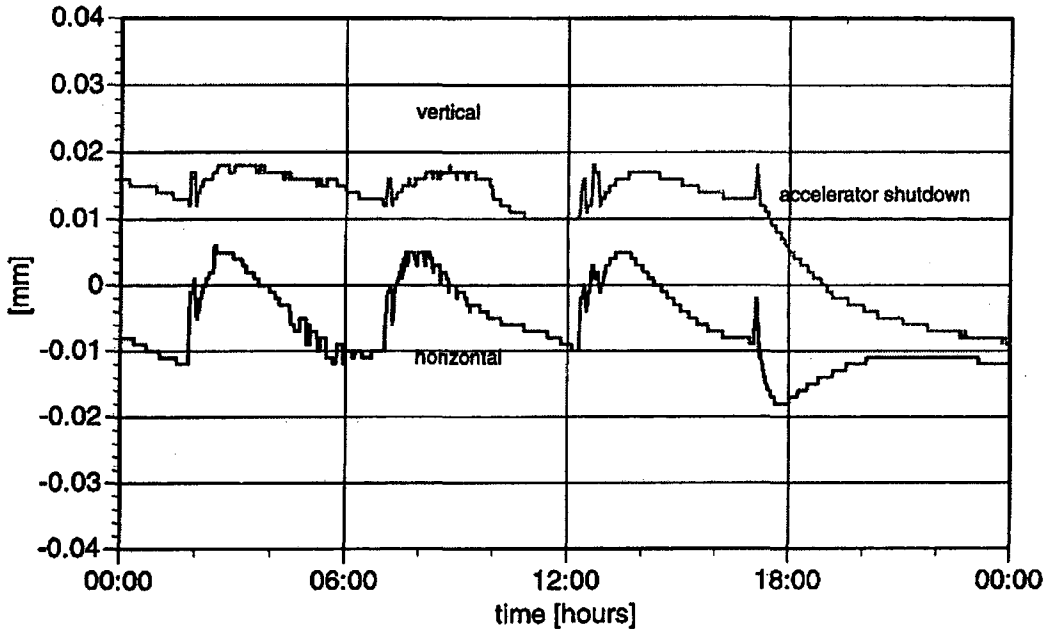

Figure 4. Fill-to-fill and shutdown-induced position changes measured at the end of the insertion-device vacuum chamber in sector 7.

There are three major lines of improvement to be followed in the future. First, the few remaining issues with air temperature control will be solved to guarantee best beam performance under all conditions. Second, a global orbit feedback system will be developed. The expectation is that, with improved mechanical stability of the machine and improved performance of the BPMs, the orbit distortions will be suppressed even more than currently possible. Our goal is 1 μm standard deviation. Third, we will increase the frequency range over which we can measure stability. Beam positions are currently monitored and archived once every minute, leading to the stability values mentioned above. On the high-frequency end (hundreds of megahertz), the electron beam is controlled by the fast longitudinal and transverse feedback systems. With a new orbit feedback system, we will be able to tackle perturbation frequencies up to about 30 Hz. A new class of users, however, aims at employing the infrared part of the ALS photon spectrum, and these users typically scan their monochromators very quickly. Consequently, these users would suffer from beam instabilities in the kHz range. It is presently unclear whether the ALS storage ring exhibits orbit distortions at those frequencies, but we will investigate this question very soon. We are planning to do so by using the diagnostic beamline (Beamline 3.1) with a fast photodiode, observing the intensity behind a narrow slit placed at the flank of the beam cross-section.

Reported by Roderich Keller

Machine Modeling

BEAM-BASED MODEL CALIBRATION

In the early stage of operating the ALS, an idealized model of the machine was used to correct the orbit in the storage ring. Because the ring was not ideal, this form of orbit control was limited. A year or so after commissioning, the control of the machine shifted from "ideal-model-based" orbit control to "beam-based" orbit control. Specifically, orbit response matrices were developed by repeatedly measuring the change in the beam orbit as a function of the change in a steerer magnet's strength. These matrices were then used to predict which steerer magnet strengths would need to be changed in order to correct the orbit. With these measured response matrices (which are more representative of the true machine than the ideal model was), the control over the orbit was vastly improved. In 1996, we entered a third stage of development where orbit response matrices are also being used to improve our machine model. This has vastly improved our understanding of the ring.

The work of modeling the orbit response matrices has been done in collaboration with James Safranek of Brookhaven National Laboratory. Using the technique developed by Safranek, we have fit our model to generate model response matrices that agree with the measured response matrices. This was done by varying many parameters, quadrupole magnet field strengths as well as steerer magnet and electron beam position monitor gains, allowing us to extract the true values for these parameters.

Because there are many parameters in the fit (more than 500), one might question whether this method could find the true parameter values or just another set of values that produces the same matrices. Therefore it is desirable to have an independent check. We made this check in the spring of 1996. At that time we suspected that there was a large variation in the 24 quadrupole defocusing (QD) magnet power supplies, leading to variation in the field strengths of the quadrupoles. We measured the excitation currents for the 24 QD magnets and compared that measurement to the fitted model. The results can be seen in Figure 1. As seen in the figure, there is very good agreement between the two independent measurements. In particular, both measurement techniques showed that four QD magnets (8, 13, 16, and 22) had strengths 1% or more lower than the rest of the quadrupoles. These power supplies were subsequently replaced.

Because of the precision of the ALS electron beam position monitors (< 1 micron with averaging), we have found that it is possible to measure the relative field strengths of the quadrupole magnets to about 0.1% by fitting measured orbit response matrix data.

SYMMETRY RESTORATION AND INJECTION EFFICIENCY

Linear focusing errors (such as the variations in QD magnet strengths discussed above) perturb the storage ring's natural 12-fold symmetry. This can strongly degrade the stability of the electron motion. In particular, the amount of symmetry breaking can determine how far particles can stably oscillate about the center of the beam. This is especially important for injection, where the motion of the injected particles—which must be injected with an initial transverse offset far from the beam center—must be stable. Fortunately, since we can

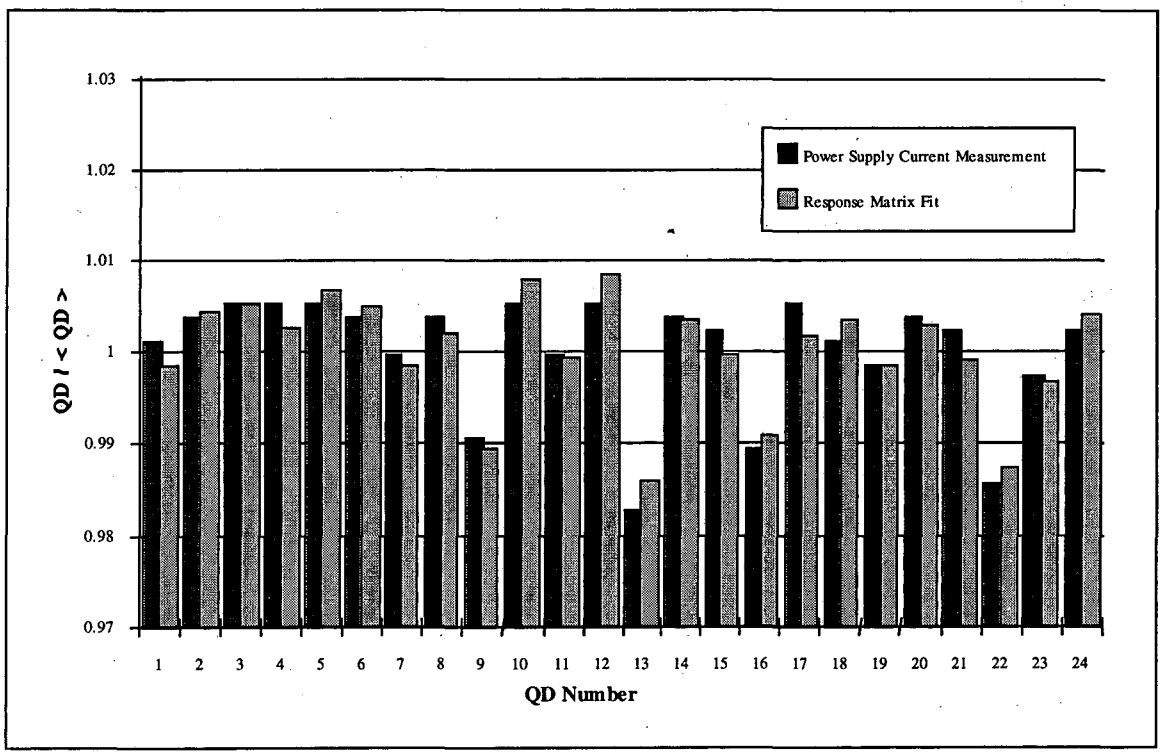

Figure 1. Comparison between measured excitation currents in 24 quadrupole defocusing magnets and fitted orbit response matrix data. Both techniques showed a difference of 1% or more in QD magnet strengths for four particular magnets relative to the others.

measure the linear errors, it is possible to adjust quadrupole strengths to restore the ring's 12-fold symmetry. The effects of symmetry breaking on the beam dynamics have been studied in an ongoing collaboration with the French astronomer Jacques Laskar using his Frequency Map Analysis technique.

In such a study, we track particles to compute a frequency map and the limits of stable motion that define the dynamic aperture. In Figure 2, we show the stability plots for two ring states, one with broken symmetry and the other with restored symmetry. In each model, particles are launched with a variety of initial transverse coordinates and tracked for 1000 turns or until they are lost. The initial transverse coordinates of particles that were stable for 1000 revolutions are plotted in the figure.

The left plot in Figure 2 was generated by including measured quadrupole errors in the model with no adjustments for symmetry. Particles with a horizontal offset greater than 13 mm do not survive in this lattice. The right plot was generated by including measured quadrupole errors plus additional quadrupole adjustments made to restore the lattice symmetry. As evidenced by the larger area covered by the latter plot, particles in the ring with symmetry restored should survive long-term tracking even if injected with an offset out to 18 mm.

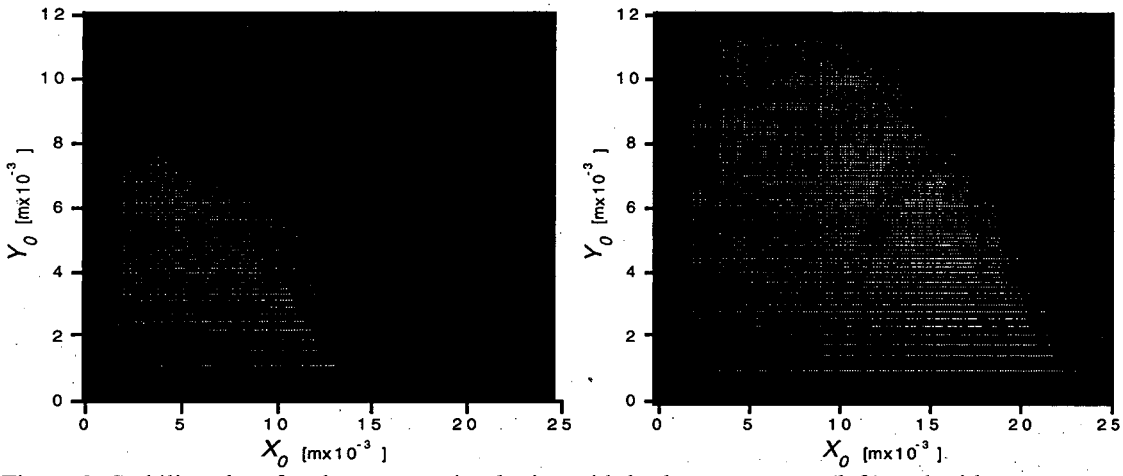

Figure 2. Stability plots for the storage ring lattice with broken symmetry (left) and with symmetry restored (right) by adjusting quadrupole magnet strengths.

An experimental comparison was made between these two lattices by looking at the injection capture efficiency of the two lattices as a function of an injection offset, which increases the resulting oscillation amplitude of the injected electrons. The result can be seen in Figure 3. We found a 40% improvement in efficiency at the nominal injection position (approximately 10 mm from the beam center) in the lattice with restored symmetry. As we increased the offset by 3 mm, it became nearly impossible to inject into the lattice with uncorrected errors, but we could still inject with an acceptable rate into the more symmetric lattice.

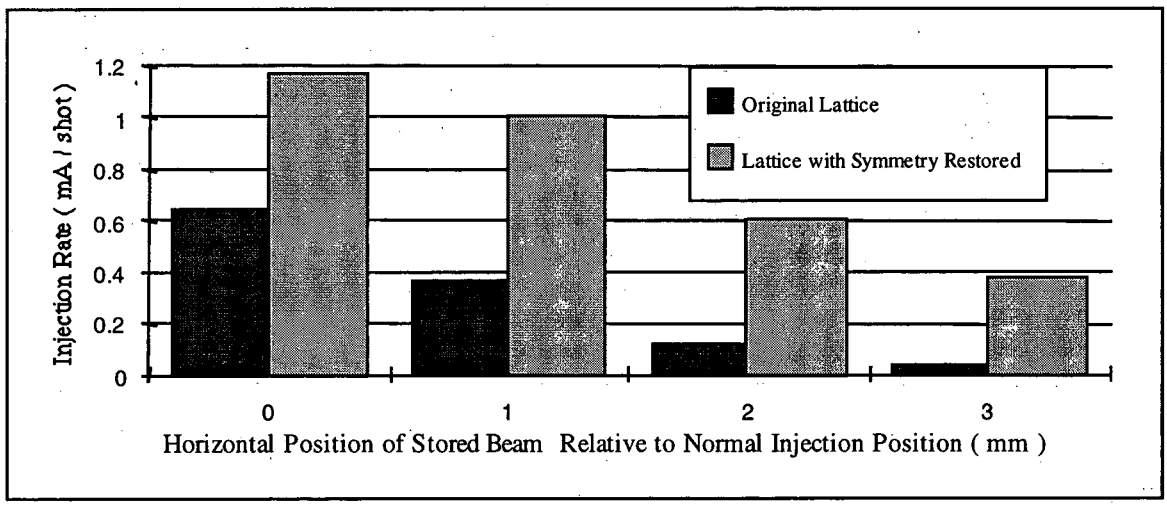

Figure 3. Comparison of injection capture efficiencies for the storage ring lattice with symmetry broken and with symmetry restored.

FOCUSING COMPENSATION FOR THE W16 WIGGLER

In addition to quadrupole field errors, edge focusing caused by a wiggler will also perturb the storage ring symmetry. This does not affect injection, because injection is done with the wiggler gaps open. It does, however, affect the beam size around the storage ring. When the wiggler is closed, the focusing causes a change in the vertical beam size that varies ±20% around the ring—an effect that can be clearly seen by users. To correct for this focusing, one

can adjust 48 individual quadrupole power supplies around the circumference. The difficulty lies in determining how much the fields need to be changed in order to best correct the focusing.

The technique we employed was again based on the measured orbit response matrices. We measured matrices with the wiggler open and closed, then adjusted the quadrupoles to best minimize the discrepancy between the two matrices. A comparison of the vertical beam sizes at the QD magnets (based on measurements of the beta functions) before and after focusing compensation can be seen in Figure 4. In the lattice, the wiggler is located in straight section 5 between the 8 and 9 QD magnets. We found that, with the exception of the sectors surrounding the wiggler, we could reduce the change in size to less than +/- 3%. This compensation will provide minimal change in beam size for users away from the wiggler.

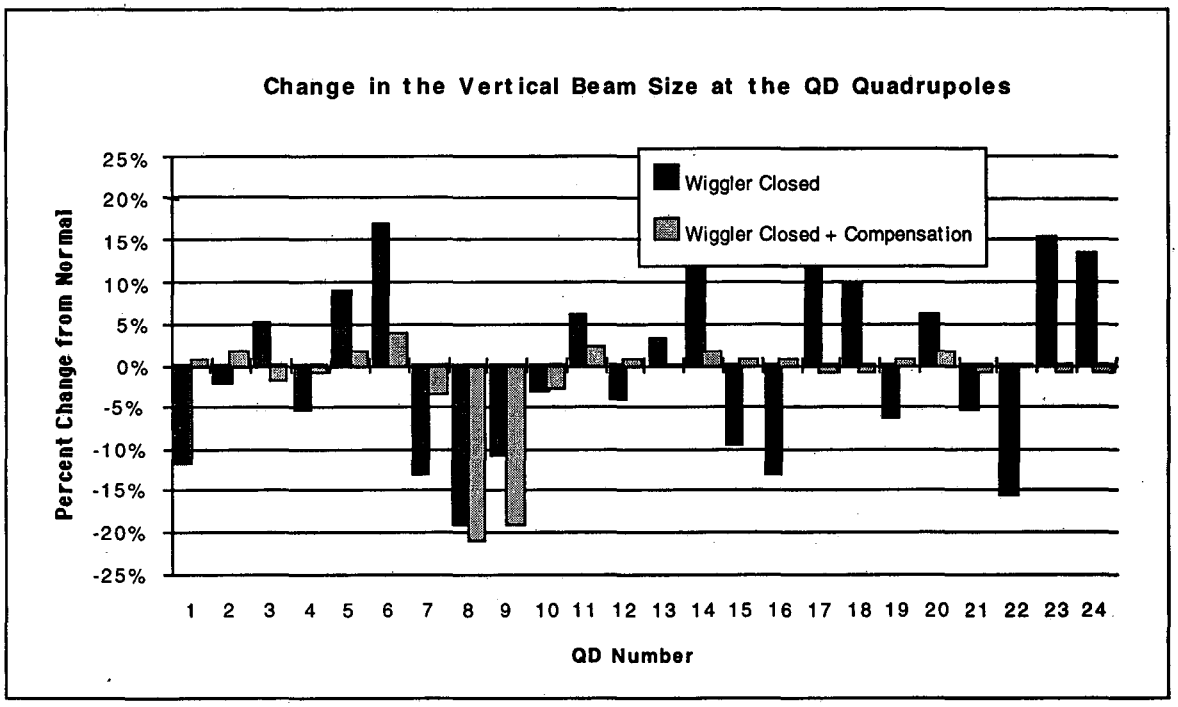

Figure 4. Vertical beam sizes at the storage ring's quadrupole defocusing magnets (based on measurements of the beta functions) before and after compensation for the focusing effect of the W16 wiggler.

Sidebar: The Storage Ring Model and the Response Matrix

The model of the storage ring consists of a beam optics program that maps the position and transverse momentum of a particle at one point in the ring, j, to the position and momentum of the particle at another position, i, such that

$$\begin{pmatrix} x^i \\ p_x^i \\ y^i \\ p_y^i \end{pmatrix} = R^{ij} \begin{pmatrix} x^j \\ p_x^j \\ y^j \\ p_y^j \end{pmatrix} \qquad \text{(Equation 1)}$$

where x and y are the horizontal and vertical positions and px and py are the horizontal and vertical momenta. From the map, R, and knowledge of the ring's dispersion function, h, it is possible to compute the response matrix coefficients, Cij, which relate the change in the closed orbit at the position of a beam position monitor (BPM), i, due to the change in field of a corrector at position j. This leads to

$$C^{ij}_{12/34} = \left[R^{ij} \left(1 - R^{jj} \right)^{-1} \right]_{12/34} - \frac{\eta_i \eta_j}{\alpha L} \qquad \text{(Equation 2)}$$

where 12 refers to the horizontal plane and 34 to the vertical plane, R^{ij} is the transfer matrix between the corrector at j and the BPM at i, R^{ij} is the full-turn matrix starting after the corrector location, η_j and η_i are the dispersions at the location of the corrector and the BPM respectively, α is the ring's momentum compaction factor, and L is the ring's circumference. The first term in Equation 2 is immediately derivable from Equation 1. The second term in Equation 2 comes about because a corrector change in a region of dispersion, η_j, will induce an energy shift in the beam which in turn will be visible as an additional orbit shift in a BPM that is located in a region of dispersion, η_i.

This model of the storage ring can be calibrated by adjusting parameters in the model so that there is better agreement between a response matrix computed by the model, C, and one measured in the machine, $\overline{C}$. This calibration of the model is done in the following way. First, equations are set up that relate the measured $\overline{C}^{ij}$ and the model (C^{ij}) response coefficients in a first-order Taylor series

$$\bar{C}^{ij} = C^{ij} + \sum_{n=1}^{\infty} \frac{\partial C^{ij}}{\partial g_k} \delta g_k + C^{ij} \Delta z^i - C^{ij} \Delta c^j \qquad \text{(Equation 3)}$$

where g_k are the quadrupole gradient errors and Δz and Δc are the change in the BPM and corrector gains from unity. Then, to determine the errors in the model, δg_k, Δz, and Δc are adjusted to minimize the difference between $\overline{C}^{ij}$ and C^{ij} in a least squares sense. This is done by casting Equation 3 into a set of linear equations of the form $\vec{Y} = A\vec{X}$ where $\vec{Y}$ is the difference between the measured and modeled response matrix coefficients and $\vec{X}$ is the vector of parameters that need to be found. The solution is simply $\vec{X} = (A^T A)^{-1} A^T \vec{Y}$ where $(A^T A)^{-1}$ is the covariance matrix, containing the errors on the fitted parameters.

Reported by David Robin

Ion Effects in the ALS

With increasing demands on the performance of storage rings, designs for new synchrotron light sources, colliders, and damping rings are calling for higher beam currents, more bunches, and smaller beam sizes. For each step forward in performance, however, a host of new problems arise. A collaboration between the ALS accelerator physics group and physicists from the Stanford Linear Accelerator Center has used the ALS to study a new regime of ion instabilities in storage rings. The effects are predicted to have potentially limiting consequences in the next generation of storage rings, such as the PEP-II and KEK $B\bar{B}$-factories.

Conventional ion instabilities have been observed for many years. The ions, generated by beam–gas collisions, become trapped in the potential of the beam and accumulate over multiple beam passages. The trapped ions are then observed to cause a number of deleterious effects, the most serious of which is a drastic reduction in beam lifetime. One of the standard solutions used to prevent ion trapping is to include a gap in the bunch train that is long compared to the bunch spacing. In this case, the ions are first strongly focused by the passing electron bunches and then over-focused in the gap. Over multiple beam passages, the ion motion is unstable and the electron beam is unaffected.

A new regime of ion trapping has been predicted where ions generated and trapped during the passage of a single train cause a fast instability, leading to an increase in beam size by up to a factor of two. In this situation, a gap in the bunch train does not help, because the instability develops over a single passage of the beam. The instability mechanism is shown schematically in Figure 1. As a bunch train passes through the storage ring, it ionizes residual gas. A small oscillation of the first electron bunch drives oscillations of the ions, which in turn drive transverse oscillations in subsequent bunches. Through this amplification mechanism, small oscillations at the head of the bunch train drive large oscillations at the tail. In many

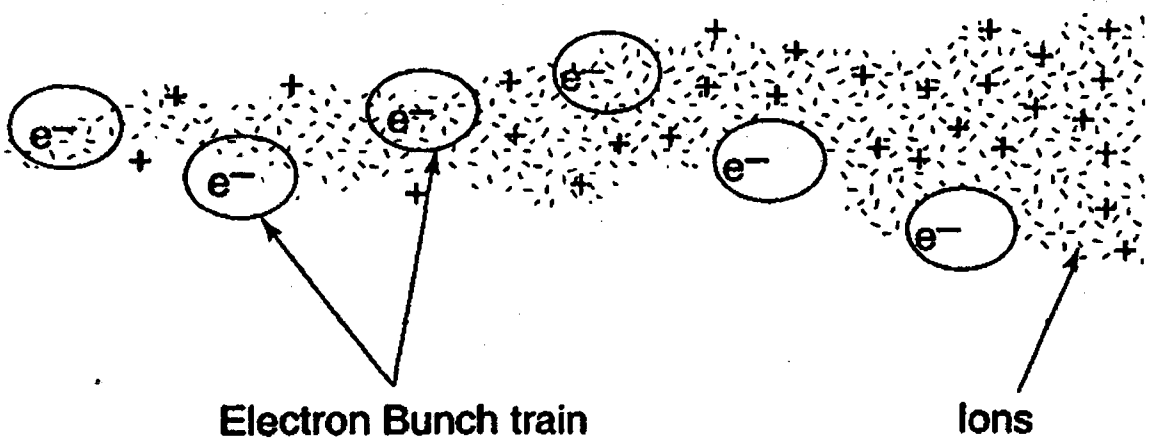

Figure 1. Schematic drawing of the fast beam–ion instability. As a bunch train passes through the storage ring, it ionizes residual gas. A small oscillation of the first electron bunch drives oscillations of the ions, which in turn drive transverse oscillations in subsequent bunches. Thus, small oscillations at the head of the bunch train drive large oscillations at the tail.

future rings, this transient instability is predicted to have very fast growth rates—much faster than the damping rates of existing and proposed transverse feedback systems—and thus is a potential limitation. Because of its small transverse beam size, the ALS is one of the first storage rings in the world capable of studying this regime of ion instabilities.

At the nominal ring pressure of 0.25 nTorr, we do not observe any significant ion effects in the ALS. For small gaps in the fill pattern, we observe small coherent vertical oscillations of the beam indicative of an ion instability that is probably due to residual nitrogen or carbon monoxide. We observe an average increase in the vertical beam size of only 2–3%. As the gap in the fill pattern is increased, the coherent signals disappear and the vertical beam size returns to its natural value.

In order to create a potentially more unstable situation, we added helium gas to the storage ring vacuum up to a pressure of 80 nTorr. Because it is experimentally difficult to distinguish conventional ion trapping from the transient ion instability, we used large gaps in the fill pattern where conventional ion trapping was not expected. Figure 2 gives a comparison of the average transverse beam profiles at the nominal and elevated pressures for a total beam current of 80 mA with only half of the ring filled. All coupled-bunch feedback systems were operational during the experiment. In addition to observing a significant instability, we were

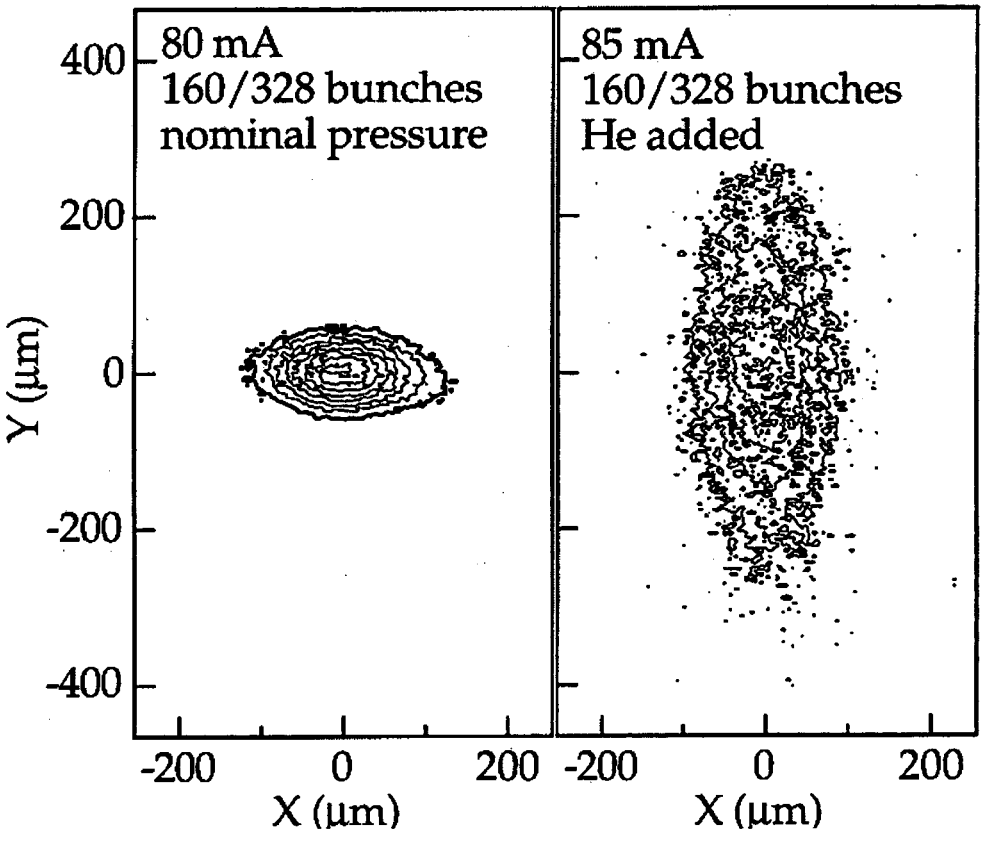

Figure 2. Transverse images of the ALS electron beam at 80 mA with only half of the ALS filled. The image at left was taken with the storage ring at nominal pressure. The right-hand picture shows the vertical beam blowup that occurred with 80 nTorr of helium added to the vacuum. The images were taken at the diagnostic beamline (Beamline 3.1).

also able to observe the instability threshold as we slowly increased the length of the bunch train, as shown in Figure 3. We are continuing studies of the transient ion instability, especially with regard to potential cures.

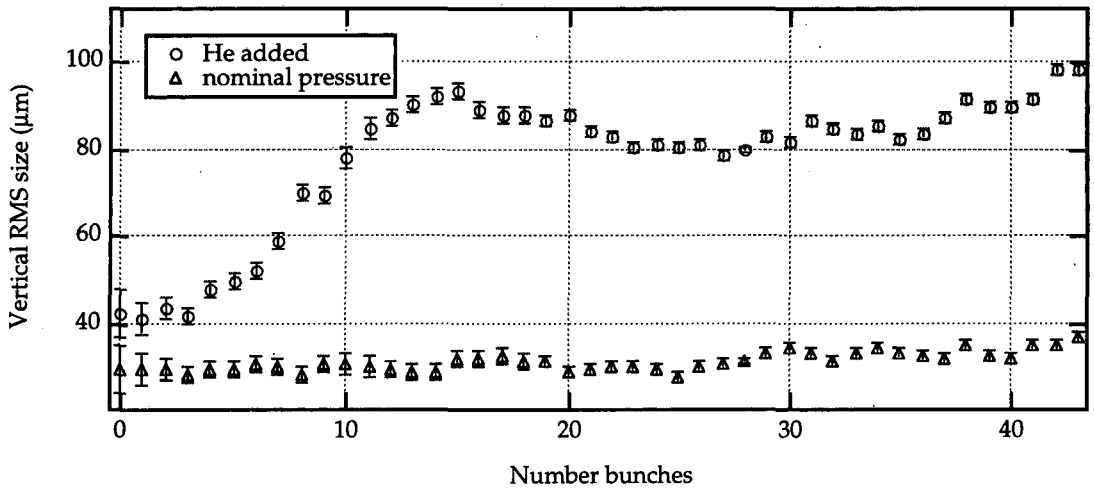

Figure 3. Changes in the average vertical beam size of a bunch train as the number of bunches increases. The threshold of the instability agrees well with the predicted value. Very little increase is observed at nominal pressure.

Sidebar: Theory of the Fast Beam–Ion Instability

A linear treatment of the transient interaction of an electron beam and residual ionized gas was first described by Raubenheimer and Zimmerman (*Phys. Rev. E*, **52**: 5487–5498, 1995). The interaction can be treated as the coupled vertical oscillations of the electron and ion beam. The equation of motion for the centroid vertical position of the electron beam (y_b) as a function of the distance z from the head of the bunch train is given by

$$y_b''(z) + \omega_\beta^2 y_b(z) = K_i\left[y_i(s+z) + y_b(z)\right]\int_{-\infty}^{z} \rho(z')dz'$$

where ω_β is the betatron oscillation frequency, y_i is the centroid vertical position of the ions, and $\rho(z)$ is the longitudinal electron beam density. The constant K_i is given by

$$K_i = \frac{4\lambda_{ion} r_e}{3\gamma\sigma_x(\sigma_x + \sigma_y)}$$

σ_x and σ_y are the horizontal and vertical beam sizes, λ_{ion} is the longitudinal ion density, and r_e is the classical electron radius. The coordinate z denotes the position along the bunch train and s the longitudinal position in the storage ring. A similar equation can be written for the centroid vertical position of the ion beam with a driving term depending on y_b.

A perturbation expansion of the equations of motion yields an approximate solution for the electron beam motion given by

$$y_b(z) \sim \eta(z)^{-1/4} e^{2\sqrt{\eta(z)}} \sin(\omega_i z - \omega_\beta s - \phi)$$

where ω_i is the coherent ion frequency given by

$$\omega_i = \left(\frac{4Nr_p}{3L_{sep}\sigma_y(\sigma_x + \sigma_y)A} \right)^{1/2}$$

where N is the number of electrons per bunch, r_p is the classical proton radius, L_{sep} is the distance between bunches, and A is the atomic number of the ion species; and $\eta(z)$ is given by

$$\eta(z) = \frac{K_i \omega_i z^2 s}{16 L_{train} \omega_\beta}$$

where L_{train} is the length of the bunch train.

The amplitude of vertical oscillations increases along the bunch train with a quasi-exponential dependence and with an oscillation frequency of ω_i. Closer examination of the above shows that the growth is much faster for smaller transverse beam sizes, particularly in the vertical direction. For example, the growth time for the ALS is estimated to be only 2.4 μs (3 turns in the ring). Further considerations, such as decoherence of the ion motion from nonlinearities and from variation of the lattice functions around the ring, increase the growth times significantly and indicate that the instability should saturate at an amplitude near σ_y. Even including these effects, however, the fast beam–ion instability is predicted to be one of the limiting factors in future storage rings, where transverse beam sizes are projected to be at least an order of magnitude smaller than present designs.

Reported by John Byrd

ALS High Resolution Beam Position Monitor

There are 118 electron beam position monitor (BPM) stations in the ALS storage ring. At each station there are four small electrodes called buttons that couple rf signals from the beam to processing electronics. Ninety-six of these monitors are in the 12 curved sections of the storage ring called sector-arcs. In these monitors, the buttons are connected to BPM electronics designed to provide high speed measurements of beam orbit. The remaining 22 BPM stations are in the straight sections, and the original purpose for these buttons was to act as pickups for a beam interlock system. If the electron beam in an insertion device is moved too far out of its normal orbit, it is possible for the powerful photon beam generated by the insertion device to melt areas of the aluminum vacuum chamber. When the interlock function of these BPMs is implemented, the beam will be aborted if a 2 mm orbit shift is detected in any straight section where an insertion device is operational. At present we rely on thermocouples attached to the beam pipe that sense heat generated by a miss-steered photon beam. The thermocouple system can be difficult to test and is designed to be a backup to the BPM interlock system.

High speed measurements are not required to implement the interlock feature, so it was decided to develop a high-resolution, narrow-band, multiplexed BPM instrument for the straight sections of the storage ring. Multiplexing four beam pickup signals into a single receiver at a high rate removes from the measurement many of the errors found in the non-multiplexed sector-arc BPM receivers. An additional feature of the new BPM is self normalization to beam intensity. This means the instrument delivers X and Y signals proportional to beam position regardless of the beam intensity (over normal ALS operating conditions). Because the BPM electronics are to be part of an equipment protection interlock, we chose not to rely on computer software—the electronics are completely analog. In the older BPMs, computers are needed to perform self calibration, correct gain and offset errors, perform normalization to beam intensity, and finally calculate beam position. It would be unwise to rely on such a BPM for an important equipment protection interlock.

The prototype insertion device beam position monitor (IDBPM) electronics were installed on a sector 4 straight section beam position sensor. The IDBPM revealed beam motion which had not been detected with the other BPMs. At that time the sector-arc BPM data were not being archived and no computer application was in use to display long-term beam motion. However, the IDBPM position data along with the temperature of the accelerator's cooling water and storage ring tunnel air were displayed on chart recorders over a period of many hours. From this data, it was quickly determined that the storage ring electron beam moved +/- 4 μm vertically with a period of about 12 minutes. Longer term vertical motion of about 20 μm occurred over several hours. Horizontal motion was larger, +/- 50 μm, with a period of about 2 hours. The chart recorder data showed perfect correlation between 12-minute vertical beam motion and magnet cooling water temperature fluctuations. Improvements were made to the water system temperature control, and the 12 minute beam position oscillations ceased.

The IDBPM electronics were improved to reduce beam intensity dependent errors and another prototype instrument was installed. While BPM studies continued, the electronics design was offered to industry in hopes that a BPM useful to the accelerator community in general would be

developed. The Bergoz company accepted the offer and improved the BPM electronics to the point where beam intensity dependence is almost nil and the input signal dynamic range is almost 10,000 to 1. For the ALS, this means we can obtain position readings over an intensity range of 0.4 A to less than 1 mA. Beam intensity dependence is typically less than 5 μm between 0.4 A and 1 mA when the beam is centered in the pickup electrodes. Resolution of less than 1 μm is easily achieved with signal averaging. As of February 1997, there were 6 Bergoz BPMs operating in the ALS storage ring, soon there will be over 20.

A beam stabilization task force was established at the ALS with the mission of determining the extent and causes of beam motion in the storage ring and to eliminate it if possible. The instruments used in this work are the IDBPMs, many temperature sensors, a number of electronic micrometers, and clinometers (devices capable of measuring very small angular displacement). The IDBPMs were connected to the ALS control system and their data displayed on a 12 hour chart in the control room. Also, the position data are archived along with all other accelerator parameters.

Our measurements have enabled us to reduce beam motion considerably, especially in the horizontal axis, in a relatively short time. The chief reason for this is good air temperature management. Our immediate goal is to stabilize vertical beam position over a filling period to about 2 μm (10% of the beam rms size in an insertion device). While air temperature control certainly helps, we believe we may have to employ a closed-orbit feedback system to achieve the ultimate stability. To implement closed orbit feedback, we require a number of stable position sensors around the storage ring. With 20 IDBPMs we should be able to reduce slow orbit shifts to some degree. For optimum performance, it may be necessary to have more position sensors. This would require additional Bergoz BPMs in place of (or in addition to) existing sector-arc BPMs.

Recent operational experience with the storage ring has shown that the "golden" beam orbit is not necessarily optimum for some insertion device beamline users. Because of their excellent stability, we have been using the IDBPMs to create a static local orbit bump around an insertion device to satisfy experimenters. If global closed-orbit feedback isn't implemented, it may be possible to apply local feedback around an insertion device to stabilize the photon beam. In this case the IDBPMs would be used as pickups for a local orbit bump feedback system.

The insertion device BPMs have been very useful in helping us diagnose undesired beam motion in the ALS storage ring. While they cannot provide the high-speed, single-turn beam position data we obtain from the sector-arc BPMs, they do provide unparalleled stability and resolution for low frequency position measurements. Once all the IDBPMs are functional and have been thoroughly tested, we will design the equipment protection interlock.

Reported by Jim Hinkson

Using Matlab for Accelerator Control

The ALS is a relatively small accelerator, yet the computer control system has the sizable task of continuously monitoring and controlling more than 7000 variables. Given this type of complexity, it is important to have an efficient method to acquire and control data.

The high-level software control of the ALS computer control system has been through a number of evolutions which pace the rapid developments in the computer world. While ALS computer control may lack the standard software development environment enforced at many modern accelerators, it gains in the amount of flexibility available to the application developer. ALS computer control is possible via BASIC, Visual Basic, C, C++ (Borland and Microsoft), FORTRAN, Pascal, Adelphi, TclTk, EPICS, Excel, Toolbook, and the list goes on. Since the variation of software is already large and convoluted, why not add one more—Matlab.

Matlab is a matrix manipulation language originally developed to be an efficient programming environment for using the LINPACK and EISPACK libraries developed in the heydays of FORTRAN. Hence, Matlab has a large number of built-in functions for numerical methods that have proven to be accurate, nearly bug free, and which properly warn the user if a calculation is close to a numerical instability. Matlab shares many similarities with other "high level" languages such as Mathematica, MATHCAD, and IDL. To gain the symbolic manipulation capabilities of languages like Mathematica, a version of Matlab can be purchased with the Maple kernel embedded. One big advantage of Matlab over FORTRAN, Pascal, or C is that matrix algebra is coded very much like one would write the equations on a piece of paper. However, it is very difficult to compare Matlab to a traditional compiled computer language. Matlab functions are compiled, but they run in an active workspace where each function call is interpreted at run time. Interpreted languages can be computationally slow, however, they allow one to create an interactive environment for doing mathematics on a computer. The fact that Matlab's built-in functions are compiled greatly mitigates the speed disadvantage of using an interpreted language.

What makes Matlab so appealing for doing accelerator physics studies is the combination of an active workspace for variables, numerous built-in functions, powerful graphics capability, and platform independence. At the ALS, Matlab is regularly used for global orbit correction, local steering of photon beams, developing insertion device dipole compensation tables, beam-based alignment of the quadrupoles, measuring response matrices, finding beta functions, and many accelerator physics studies. The following example is the entire horizontal global orbit correction routine for the ALS using a singular valued decomposition (SVD) method where only the first 24 singular values of the matrix are used.

```
X = getx;                       % Gets all 96 horizontal BPMs (96x1 vector)
[U, S, V] = svd(Sx);            % Computes the SVD of the response matrix, Sx(96x94)
DeltaAmps = - X / U(:,1:24);    % Find the corrector changes via Gaussian elimination (94x1 vector)
stepsp('HCM', DeltaAmps);       % Changes the current in all 94 horizontal corrector magnets
```

Once the ALS database access functions *getx* and *stepsp* (i.e. step the setpoint) have been written, this relatively involved global orbit correction method can be accomplished in four lines. Ease of use and simplicity allow one to quickly change and experiment with new ideas in a very short period of time. Given the value of machine time at the ALS, this is obviously a valuable tool.

Reported by Gregory J. Portmann

Preliminary Results of Ground Vibration on the ALS Storage Ring and its Effect on Electron Beam Motion

Although the ALS building is a relatively large structure with many thousands of tons of concrete in its foundation, at some level the entire ALS floor is still being jostled around. The problem is not just the magnitude of the ground motion, but how these vibrations get amplified by the various structural bending modes of the ALS components.

If ground motion causes movement of the ALS photon beams, then many experiments at the ALS can be adversely affected. The mechanism for how ground vibration infiltrates into the photon beams is multifaceted. In the user areas, the entire beamline is subject to mechanical vibrations that simply shake the mirrors and endstation hardware. In the storage ring, vibrations move the magnets and vacuum chamber, which causes small field perturbations. These field changes cause electron beam movement, which in turn results in movement of the photon beams. The good news is that the ALS electron beam is inherently quite stable. Fluctuations in the electron beam in the 0.1 to 1000 Hz range are typically 3 to 8 μm rms, which is better than the specified requirement of one tenth of the beam size. This allows the ALS to operate without global or local orbit feedback, which is very unusual for a light source.

The level of ground vibration of the ALS floor is relatively small—typically less than a few tenths of a micron in the 0.1 to 400 Hz frequency range (the bandwidth of the accelerometers used to measure vibration). The problem arises from the mechanical amplification due to the natural bending modes of the magnet support structure and the magnification of magnet motion to electron beam motion due to the strong focusing quadrupole and sextupoles magnets in the storage ring. The magnification of beam motion from magnet motion is magnet family and location specific. Typical amplification factors range between 1 to 15. For instance, the peak electron beam motion for a change in position of a focusing quadrupole (QF family) magnet is a factor of 10 vertically and 6 horizontally greater than the magnet motion.

The aluminum vacuum vessel in the storage ring also influences beam motion. The first effect is beneficial: not all the magnetic field variations from a vibrating magnet will pass through the vacuum chamber. Due to the induced eddy currents in the aluminum, the magnet field as seen by the electron beam will be a low-pass filtered version of the actual perturbation. The exact bandwidths of these filters are magnet location specific and not well known but are likely to be a few Hertz. Unfortunately, the second effect is adverse: if the vacuum chamber is vibrating, the electron beam may pickup the high frequency motions since the eddy currents will oppose fast field changes inside the chamber.

Determining the sources for electron beam motion in the ALS storing ring is a difficult task. Vibration of the 72 quadrupole, 24 sextupole, and 36 bend magnets are likely sources, as well as field perturbations cause by the 216 power supplies in the storage ring (1 bend, 2 sextupole, 49 quadrupole, 94 horizontal corrector, and 70 vertical correctors). Measuring the beam motion is complicated by the fact that the BPMs are fixed in the vacuum chamber which is also vibrating. However, by measuring the electron beam motion, vibration of the magnets, and vibration of the vacuum vessel, the picture gains some clarity.

The upper plot in Figure 1 shows the power spectral density (PSD) function for the vibration of a quadruple focusing magnet (QFA 1 in sector 7), the vibration of the vacuum chamber in the location of the insertion device beam position monitor IDBPM(7,1), and the electron beam motion as measured by IDBPM(7,1). Vibration was measured using a seismic accelerometer from Wilcoxon Research (model 731A) connected to a spectrum analyzer (HP-3563A). Off-line analysis was done using Matlab. The bandwidth of the IDBPM is about 1 kHz. Unfortunately the noise floor of the IDBPM is not fully determined. The integral of the PSD function is the rms change in the time domain (Parseval's Theorem). Hence, using the power spectrum one can gain insight into what frequency bands are causing the greatest amount of beam motion. The lower plot in Figure 1 shows the cumulative integration of the power spectrum. The integration was done in reverse order, 50 Hz to 0.3 Hz, to illustrate the stability improvements if a feedback system was developed. For example, if one could eliminate all electron beam motion below 30 Hz, then the remaining motion would be 0.7 μm. However, this article is not accounting for motion above 50 Hz. Since electron beam motion in the 50 to 1000 Hz range is likely to be submicron, the signal-to-noise ratio of the IDBPM electronics becomes problematic.

The most obvious example of beam motion from vibration in Figure 1 is the 6.4 Hz bending mode of the storage ring girder. The first 4 structural modes of the girder, as measured in Ref. [1], are 6.4, 9.7, 12.7, 15.3 Hz. These 4 modes also show up clearly in the vibration data for the QFA magnet. Since the 6.4 Hz mode is not present in the vacuum chamber where the IDBPM is mounted, it is reasonable to assume that the electron beam is actually moving due to this structural mode. If one integrates the PSD from 5 to 8 Hz (shown in Figure 1, lower plot), the magnitude of this mode is approximately 0.6 μm. However, removing this mode would only reduce the total rms displacement from 3 to 2.9 μm ($\sqrt{3^2 - 0.6^2}$). The 9.7 and 12.7 Hz modes also appear in the beam position spectrum. The 27 Hz peak in the IDBPM data makes a noticeable change in the rms motion, yet its source has not yet been determined.

Interpreting the downward slope in lower plot of Figure 1 from .3 to 5 Hz can be done with the help of Ref. [2]. Fisher has written an excellent survey paper on measuring ground vibration and the effects on accelerators. If the Wilcoxon accelerometers could resolve lower frequencies with a smaller noise floor, one would hopefully find a peak at .15 Hz caused by the ocean waves. Fisher reports that the ground vibration due to the ocean can be seen almost everywhere is the world—it is not just a coastal effect. The IDBPM data does not show this effect since the wavelength is long compared to the size of the ALS. The "bulge" in the data from 5 to 50 Hz is most likely caused by relatively local environmental sources.

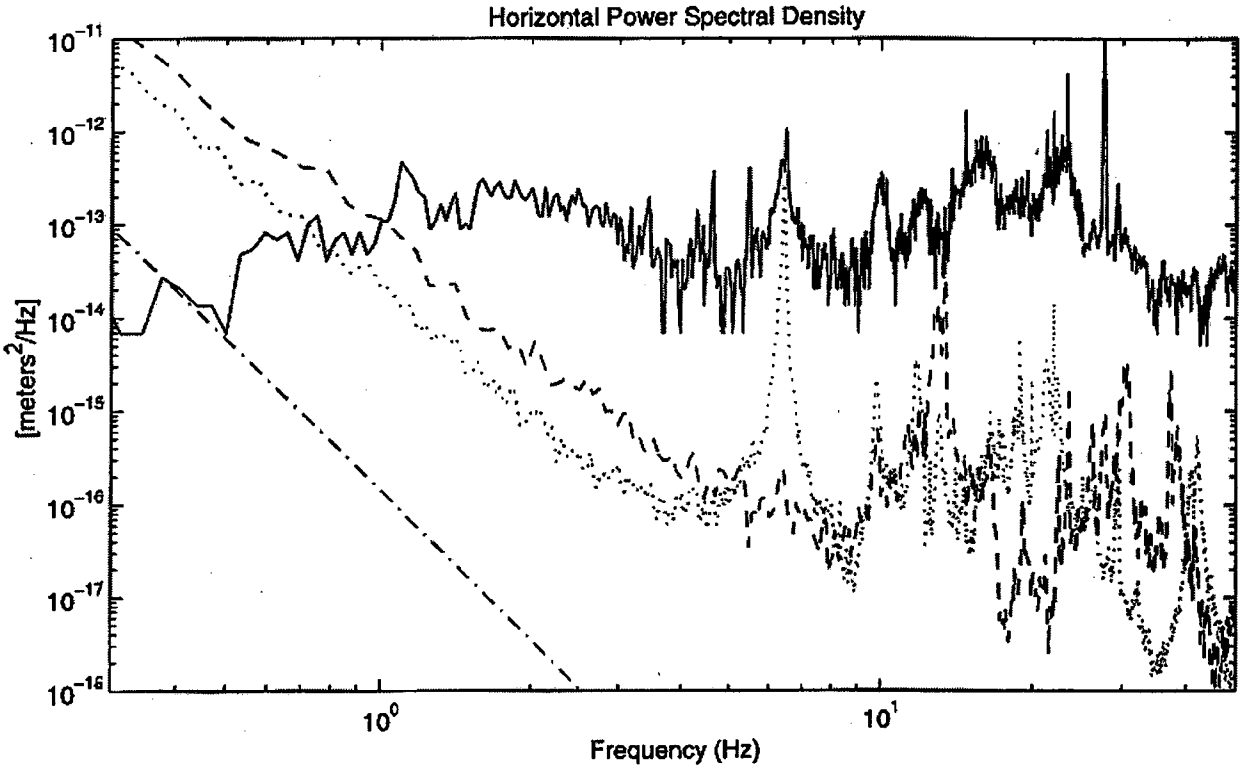

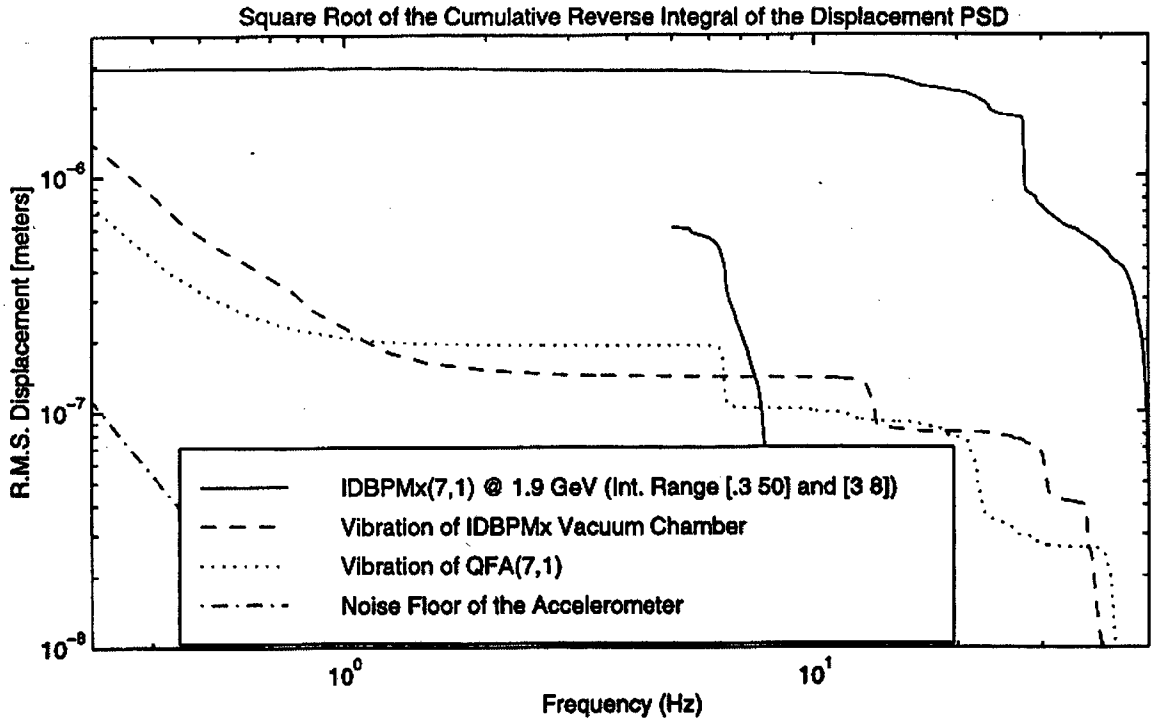

Figure 1. The power spectral density (PSD) function for the vibration of a quadruple focusing magnet [QFA(7,1)], the vibration of the vacuum chamber in the location of the insertion device beam position monitor IDBPM(7,1), and the electron beam motion as measured by IDBPM(7,1).

It is difficult to make a conclusive statement about the effects of vibration on electron beam motion from the limited amount of data presented in this paper. However, we feel it is reasonable to state that the magnitude of the motion caused by vibration is likely to be at the micron level. In order to form a more coherent picture as to the causes of "low" frequency beam motion at the ALS, one needs to combine vibration and power supply stability data with beam position data. Since the total electron beam motion in the .1 to 1000 Hz range is relatively small (a few microns), no serious attempt has been made to accurately determine the sources of the beam motion. If future experiments require electron beam stability below a few microns, then it will be necessary to either track down and eliminate the sources causing the motion or implement a feedback system to actively stabilize the electron and/or photon beams.

REFERENCES

[1] P.A. Manning and R.B. Burdick, "Dynamic Analysis of a Six Strut System," LLNL/SSC Presentation, June 19, 1992.

[2] G.E. Fisher, "Ground Motion and its Effects in Accelerator Design," SLAC Pub. 3392, July 1985.

Reported by Gregory J. Portmann

Mechanical Design of a Pinger System

As more beamlines are added to the ALS, tuning the storage ring for precise electron beam position and stability at all beamlines becomes increasingly difficult. To meet this challenge, ALS accelerator physicists are working to improve their understanding of the complex electron beam dynamics of the storage ring. The new "pinger system," currently in the design and fabrication stage, will be an important tool in this effort.

SPECIFICATIONS

The pinger system will provide a pair of very fast dipole magnets to intentionally perturb the orbit of a single electron bunch in a single pass. The effects of this controlled transverse "kick" will be monitored by an existing system of beam position monitors (BPMs) for validation and improvement of beam dynamics models. In order to accomplish this, the pinger system must deliver calibrated vertical and/or horizontal dipole fields of up to 315 Gauss in a pulse which lasts no longer than 650 ns. This will require single turn dipole magnets, discharging 10 kV to ground. A special ceramic beam tube section is needed so that induced eddy currents will not retard the penetration of the magnet field.

ENGINEERING

As is often the case, the initial intention for this project was to closely duplicate an existing design. The beam kickers in the ALS injection straight perform a similar function, and we hoped to save on engineering costs. However, as is also often the case, a closer study of the injection straight revealed many reasons not to do this. The following is a brief summary of the design evolution of the pinger system (an early concept sketch is shown in Figure 1). As you will see, considerable effort has gone into creating a cost effective, reliable design, with many well-motivated departures from the original concept.

Our reference design, the ALS injection straight, has a rectangular vacuum aperture of 83 x 38 mm^2. Its ceramic vacuum tube was expensive, difficult to manufacture, difficult to align, and the unbalanced vacuum forces are high. For the pinger, an 88-mm ID round ceramic beam tube was chosen to be much stronger and easier to fabricate, and its "square" aperture allows the horizontal and vertical kick magnets to be essentially identical. A further advantage emerged: in the round geometry, beam image currents can be handled by a uniform resistive coating on the tube ID, with no need for the difficult patterned resistive coating used with the rectangular aperture. The optimum coating resistance is a trade-off between minimizing the eddy-current-induced field penetration delay, and living with the steady state I^2R heating of the ceramic tube caused by beam image currents of up to 400 mA. An experimental mock-up indicates that a 2.0-ohm-per-square coating of titanium will allow acceptable field penetration times with a maximum steady state image current heat load of about 100 watts, which will be cooled with an air flow system.

The original electrical joint design used to connect the injection straight resistive coating to the conventional metal beam tube has caused some concern at the ALS. Beam current induced heating at or very near these joints has necessitated forced air cooling. Although the cause of this problem has not been resolved, a leading theory is that small cavities in the electrical joint design

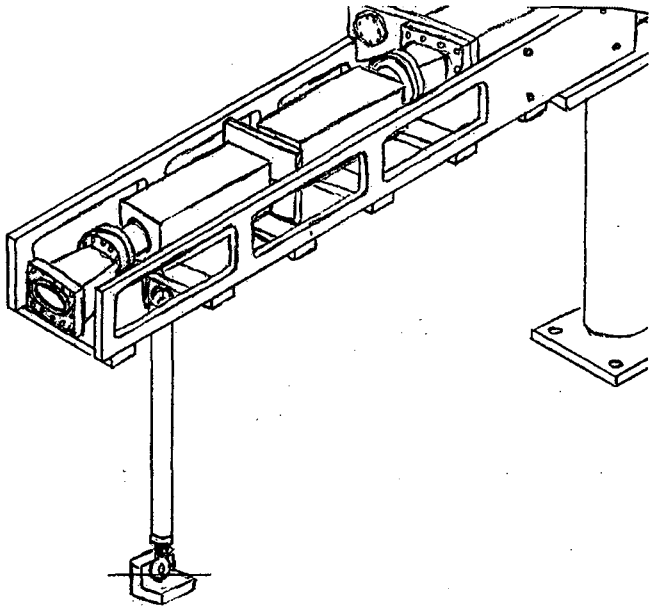

Figure 1. An early concept sketch for the ALS pinger system.

may be coupling with rf energy, resulting in local heating. In the pinger design, only a single, round fingerstock joint is used, with a minimum cavity.

The various risks and expense of the ceramic tube end electrical and vacuum connections motivated a further simplification: a single long ceramic tube threaded through both the horizontal and the vertical kick magnets. A 54-in (1.37 m) tube length is required, with only two end connections, rather than the four which would have been needed with separate tubes for each magnet.

The support and alignment of the ceramic tubes in the injection straight had also been a problem, due to variations in ceramic wall thickness. For the pinger, we will avoid this by not doing it. We plan to rely only on the engagement of the electrical contact sleeve in the neighboring transition piece to flexibly support the 25-lb (11.34 kg) weight of the ceramic tube.

Axial vacuum loads were considerable in the injection straight design because of the difference in cross section between the bellows and the ceramic tube aperture. (The collapsing load of the bellows exerts a sizable tension load on the ceramic tube.) Since the pinger ceramic tube is round, it is possible to use a bellows of only slightly larger area than the tube itself. The calculated vacuum load tension in the pinger ceramic tube is much reduced, only 102 lb (46.27 kg). This load is taken in tension by the Kovar fittings brazed to the ends of the ceramic beam tube. The maximum stress in the critical braze joint was further reduced by making the O.D. of the ceramic backing ring 1.8 mm larger than the ceramic tube. A finite element analysis shows that this small change will reduce the maximum stress in the braze joint by a factor of six. These increased safety margins all work to improve the vacuum integrity of the ALS storage ring.

The pinger system will be installed in ALS straight section 2. The one-piece ceramic tube allows the pinger to be short enough to occupy only the upstream half of the straight section, reserving the downstream half for future diagnostic instruments, or possibly even an insertion device. In this location, photon masking had to be carefully considered; that is, the synchrotron radiation from the upstream bend magnet had to be absorbed by a water cooled photon stop incorporated in the upsteam transition piece. In the course of studying these layouts, a further simplification emerged:

there is no need for the electron beam to be perfectly centered in the ceramic beam tube. By introducing an intentional offset of 10 mm, we were able to reduce the tube inner diameter from 88 mm to only 74 mm. This resulted in a reduced magnet aperture and a reduced pulsed power requirement to drive the magnets. Figure 2 shows the ceramic beam tube design.

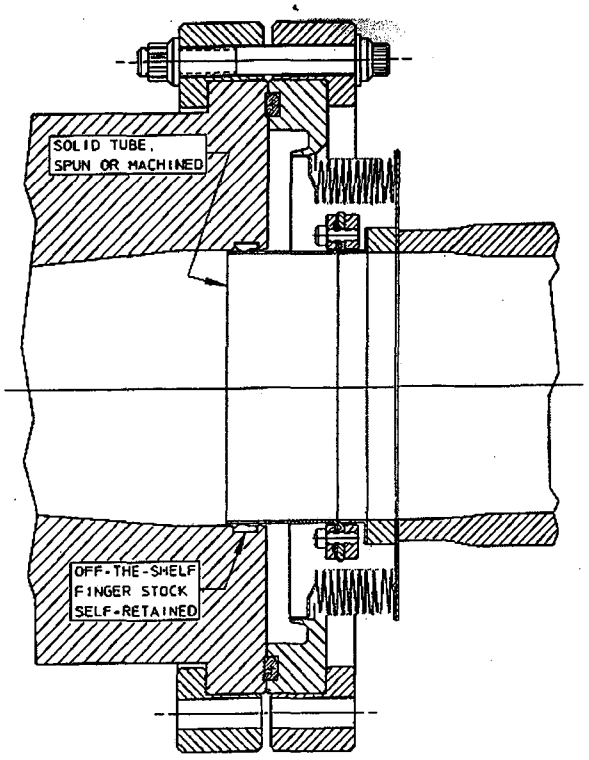

Figure 2. Ceramic beam tube design for the ALS pinger system.

With a robust, conservative design in hand, we confronted the realities of component fabrication. The ceramic tube with its brazed Kovar metal end fittings turned out to be an exceedingly involved fabrication. Over 20 different ceramic, metalization, and brazing vendors were contacted, revealing a wide variety of capabilities and limitations. Ultimately, the 1.35-m-long 99.5% alumina tubes were pressed, fired, and metalized in 0.68-m-long halves by WesGo, Inc. (Belmont, CA), and these were subsequently brazed together and to their Kovar metal end fittings by Alpha Braze (Fremont, CA).

Other design involvements include the "transition pieces" which are EDM'd (Electric Discharge Machined) from solid metal blocks to provide a smooth vacuum chamber transition from the elliptical section of the storage ring to the round ceramic tube, and a carefully thought out support system designed to protect the ceramic beam tube from mechanical stress. We are working hard to bring all the vacuum related components together in time for installation in the May 1997 shutdown of the ALS, and hope to deliver a working pinger system in summer 1997. Like many accelerator upgrade projects, an idea that initially sounded fairly straightforward has spawned a rich mix of engineering complications and challenges.

Reported by William Thur

Experimental Systems Overview

The past year has seen many new and exciting developments on the floor of the ALS. The protein crystallography wiggler beamline, driven by a 2-T multipole wiggler source, is now almost complete. The system is conventional in that it uses collimating and refocusing optics before and after a two crystal scanning monochromator. However, the very high power from the wiggler makes it necessary to intensively cool all the major optical elements, as well as slits and apertures. Even with only 1/3 of the ultimate aperture, the system will be one of the best in the world for crystallography. The first users of the beamline are scheduled to begin work in July 1997.

The scanning transmission x-ray microscope (STXM) on undulator Beamline 7.0 is now a mature instrument and is routinely taking data. This system uses zone plate focusing to produce a micro-focus, and, commensurate with the outer line width of the zone plate, the system is achieving around 1200-Å resolution. It has been used on a wide range of materials science problems, but work has especially concentrated on polymeric systems. The STXM works either in air or with one atmosphere of helium. To complement this instrument, an ultra-high vacuum system has been constructed and is now being commissioned. Again, it uses micro-zone plate focusing but in this case an electron energy analyzer is used for detecting photoelectrons (XPS). In addition to XPS, x-ray absorption spectroscopy (XAS) can be performed by detecting the total or partial yield of photoelectrons.

Bend magnet beamline 7.3.1 is now complete and in use. This beamline has two branches, one wide-aperture branch (7.3.1.1) for a photoelectron emission microscopy (PEEM), and a second branch (7.3.1.2) for micro-focused x-ray photoelectron spectroscopy (μ-XPS). The μ-XPS branch is finished and performing as expected. The system forms a monochromatic focus at an adjustable 20 by 40 μm pinhole, and this acts as an object for the following microscope. The focusing system is a pair of elliptically shaped grazing incidence mirrors, produced by controlled bending, which are within the ultra-high vacuum of the photoemission system. The microscope is designed to perform 1-μm-spatial-resolution scanning XPS on semiconductor wafers. It has many features specially designed for wafer samples, including in-situ high resolution optical microscopy, fast sample interchange, and interferometric encoding of sample position. One of the goals is to be able to introduce wafers into UHV, and go to previously referenced areas of interest to sub-micron accuracy. The development of this system is supported by Intel Corporation and Applied Materials.

Beamline 1.4 for infrared microscopy is nearing completion, the microscope is fully tested, and first beam is expected in April 1997. The system consists of two mirrors (plane and ellipsoidal) inside the shield wall to focus the radiation through a diamond isolation window; a system of collimating mirrors; and a commercial Nicolet interferometer and microscope. The wavelength range of 2–35 μm corresponds to the chemical fingerprinting range for organic species. Eventually, we will construct a second branchline to feed several different experiments including a system for reflection infrared studies of molecular adsorbates on clean single crystal surfaces.

FUTURE DIRECTIONS

The photoelectron emission microscopy beamline (7.3.1.1) is essentially complete and the PEEM system itself has an expected completion date of August. The PEEM endstation is derived from an earlier version produced by an ALS user group but differs in several key respects. It operates at high voltage (30 kV), has 2 projector stages, a stigmator and several deflectors to ensure that the beam passes through the center of the lenses, and fast sample transfer and sophisticated sample manipulation. A thorough theoretical study has shown that the system should be capable of 200-Å resolution and great attention is being paid to vibration isolation.

A second PEEM system is now under intense study and construction will start later this year. The 200-Å resolution limit, and the relative inefficiency of transmission (due to vignetting at the back focal plane aperture), are both consequences of the broad electron energy distribution produced by x-ray induced photoemission and the chromaticity of the electron lenses. It was recently shown by the group of Gertrude Rempfer (U. of Oregon Portland) that an electron mirror can be designed to have equal and opposite chromatic and spherical aberration coefficients to the combined electron optical column, and therefore opens up the possibility of very high spatial resolution with high throughput. The key components are the electron mirror and a magnetic prism to separate the in-going from out-going electron beams. This project is being jointly pursued with a group at Arizona State University. This system will need the very high flux density of the elliptical polarization undulator to reach its potential resolution of 2 nm. We expect completion of this project by fall 1998, commensurate with commissioning of the 4.0.3/4 microscopy beamline.

The first of the elliptical polarization undulator beamlines, 4.0.1/2, is now taking shape and a contract has been placed for construction of its high-power monochromator with Oxford Instruments. This beamline is designed for a wide energy range, 20–1600 eV, and will give very high resolving power for a range of studies on magnetic systems. Several of the optical elements are being fabricated, with the rest of the orders due for placement in spring 1997. The specification for the front end is also complete. ALS engineers are designing the complex mirror system located before the monochromator that will be used to focus radiation from either of the two elliptical polarization undulators into either of the two beamlines (4.0.1/2, 4.0.3/4). We expect operation of the first beamline in April 1998 and we have now started on the optical design of the second monochromator which will be optimized for high spatial resolution microscopy.

Reported by Howard Padmore

Research and Development in Adaptive Mirrors

It is a truism of the field of synchrotron radiation optics that the only beamline components that the *x-rays* ever see are the optical surfaces, many of which are mirrors. This emphasizes the true importance of forming optical surfaces in the best possible way and points first to the classical methods of grinding and polishing rigid glass mirrors. These techniques have been enormously successful in the wider field of optics and are still of value in some beamline applications. However, there are many cases where focusing mirrors must be made with tunable focal properties in which case one needs to make a circularly cylindrical mirror with a tunable radius. Another rationale arises when a mirror with a difficult shape is required. Often the mirror can be made flat and then be formed into an ellipse or other difficult shape by bending. This is not only less expensive than the zone-polishing techniques that would be needed to make a grazing-incidence ellipse, but it provides a superior figure and finish due the use of a full size lap in 100% contact with the mirror surface. Still other cases arise where the adaptive technology provides important correction capability against errors due to gravity, thermal distortion, or manufacturing tolerances.

In the ALS beamline construction program, the use of adaptive mirrors is increasing and the range of designs, materials, and applications is broadening due to an active R&D program by the Experimental Systems Group. At the time the ALS beamline program began, adaptive mirrors were already in use at several other synchrotron radiation laboratories and were also in wide use for optics that must see through the earth's atmosphere. However, the most recent generation of ALS beamlines always seemed to require new levels of optical quality (consequent upon the smallness of the ALS source), new materials properties, new shapes or sizes, or new levels of cost effectiveness. Such requirements (mostly derived directly from the needs of the scientific program) have lead to a number of advances in the art of adaptive mirrors which we describe below.

For adaptive mirrors, metals hold special advantages over ceramics because one can simply bolt them to a bending machine and bend them, to high curvature if needed, without fear of breaking. Ceramics on the other hand can be polished to a superior finish, have a proven dimensional stability, and an established ability to act as substrates for x-ray multilayers. To cover the widest range of possibilities, we need to use both so that we have to find metals that take a superpolish and have high dimensional stability and to establish safe methods of attaching glass and silicon mirrors to a bending machine. All these things have now been done as the following examples show (Table 1).

All three examples have a number of features in common:
The shape is an elliptical cylinder. The advantage of elliptical cylinders over circular ones lies in their aberration properties. For a given tolerance of aberration, the light-gathering power of the ellipse will always be greater, commonly by more than an order of magnitude for systems with a magnification far from unity. In a Kirkpatrick-Baez pair this advantage is squared.

Table 1: Three elliptical mirrors made at the ALS

	XPS* (BL 7.3.1.2)	PEEM (BL 7.3.1.1)	μDIFF* (BL 7.3.3.1)
Conjugates (m)	4, 0.1	20, 1.85	31, 0.1
Grazing angle (°)	1.6	2.5	0.33
Size (mm^3)	75×25×3	1250×100×15	40×10×3
Min radius (m)	4.5	48	32
Achieved slope error (μr)	2.2	5 (partial aperture)	0.6
Achieved finish (Å rms)	2.5	7	5
Projected spot size based on slope error (μm)	1	43	0.5
Material	precipitation-hardening stainless steel (17-4 PH)	fully-annealed, very-low-carbon steel (1006)	ULE™ (ultra-low expansion glass)
Polisher	Dallas Optical Systems	Rockwell (Albuquerque)	Rockwell (Albuquerque)
Attachments	nut and bolt	nut and bolt	glue
Special challenges	extreme curvature	avoid tension, extremely large size	figure accuracy

*Parameters of one of the pair are given as an example.

The elliptical shape is generated by bending a mirror of uniform thickness but variable width. This approach allows the most sensitive parameter (the thickness) to be accurately held uniform by precision grinding, lapping and polishing. The bent shape is determined by the width which is made to a calculated form by numerically-controlled machining.

The bending is carried out by weak leaf springs. This type of bending delivers a prescribed force rather than a prescribed displacement which makes the system tolerant of manufacturing errors or changes in the mirror size (due to thermal expansion for example) so long as they are small compared to the driver motion needed to bend the mirror.

THREE EXAMPLE MIRRORS

The mirror pair for the XPS project were built for microfocusing with a goal of a 1 μm^2 focal spot at 1 keV and the maximum flux allowed by the beam phase space and the needed grazing angles of reflection. This implies elliptical mirrors to control aberrations and a high demagnification factor which in turn leads to a very high mirror curvature. To produce such extreme curvature and have a mirror thick enough to polish implies a high level of stress which suggests a metal substrate preferably without a plated layer. The development of mirrors made of precipitation-hardening stainless steel (17-4 PH) to meet all the needs of this application, including the achievement of a 2.5 Å rms finish on the bare steel, was achieved in a collaboration with small business and was one of the major successes of the program. The achievement of an elliptical mirror with this level of figure and finish was a first. The use of bare steel for such an enterprise was also a first which will have implications far beyond XPS. At time of writing, preliminary x-ray tests have shown a focal width of 3 μm.

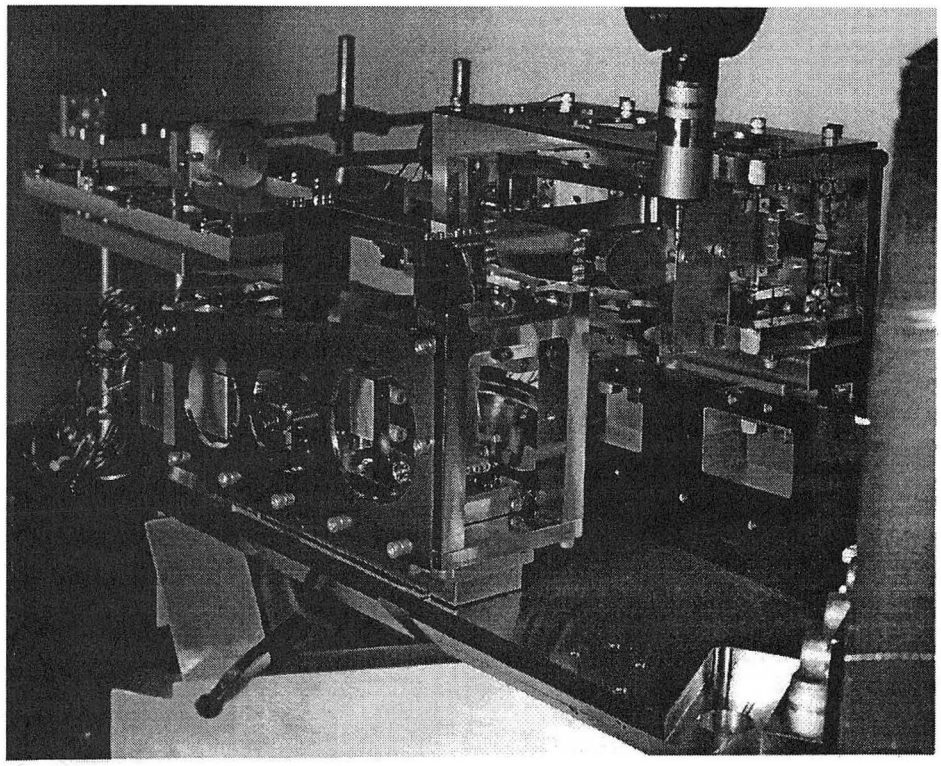

Figure 1. The XPS experiment on Beamline 7.3.1.2 in which a Kirkpatrick-Baez pair of mirrors are used to form a finely focused spot of soft x rays. The two mirrors shown are made from simple stainless steel plates, suitably shaped so that when bending forces are applied, an elliptical-cylinder reflecting surface is formed. Such elliptical reflectors have much higher light gathering power than the corresponding circular ones.

The PEEM mirror offered quite different challenges. It was by far the largest mirror made at the ALS and was specified to as a condenser to illuminate a microscope sample with maximal flux over a field of 30 μm. As before it was necessary to make the mirror thick enough to polish and strong enough to take the bending stresses, and the solution was to use a common mild steel with very low carbon, for dimensional stability. A new type of crossed-leaf-spring bending machine was designed to avoid placing the mirror in tension and a plated layer of electroless nickel (to improve polishability) was applied to all the substrate surfaces. Such a layer could be safely used in this case since the surface stresses were about ten times lower than for the XPS mirror.

Unlike the other two mirrors, the microdiffraction mirror was for hard x-rays. This implied a much smaller grazing angle and a correspondingly weaker curvature to get a similar microfocusing geometry to the XPS system. This was accomplished by means of an edge-profiled ULE mirror glued to metal end pieces for connection to the bending springs. This mirror recently achieved the best slope error yet of 0.6 μr which is, in part, a tribute to a fairly to a significant research and development program in the use of glue for these types of optics. Apart from adequate strength, the adhesive material must have low outgassing and low shrinkage and must be applied so that such shrinkage as does occur is not in the longitudinal (curvature-producing) direction. At time of writing x-ray tests have also just begun on this system and first results show a 2.2 μm spot.

Reported by Malcolm Howells

The Micro-XPS Project

The micro x-ray photoelectron spectroscopy (μ-XPS) project is a joint development with Intel Corporation and Applied Materials. The object is to build an XPS system capable of 1 μm spatial resolution using a bend magnet source. The project grew out of a need identified in the Semiconductor Industry Association Roadmap for a technique capable of surface chemical mapping at high spatial resolution. Of existing techniques, infrared spectromicroscopy has excellent sensitivity and selectivity for organic species, but poor spatial resolution due to the diffraction limit for the long wavelengths used (typically 10-20 μm). On the other hand, scanning Auger microscopy (SAM) has excellent spatial resolution (0.1 μm), but the chemical information that can be obtained is extremely limited because the wide energy width of the Auger lines masks the subtle chemical shifts in binding energy that reveal chemical bonding.

In the semiconductor industry and many other areas where surface chemical information is important, there is a need for the combination of XPS with good spatial resolution. This need has led to the development of highly sophisticated laboratory systems for scanning XPS, and the current state-of-the-art achieves about 10 μm spatial resolution but has very long imaging times due to the limited brightness of the source. Our target was to design a system with a factor of 10 higher spatial resolution (1 μm), with short imaging times, and capable of taking full advantage of the tunability of synchrotron radiation. The selection of photon energy is important in two respects: first, it allows the cross section of the element of interest to be maximized; and second, it allows us to vary the kinetic energy of the photoemitted electrons and hence their escape depth. In this way we can alter the surface sensitivity and minimize radiation damage.

The ultimate goal will be to build a system with a resolution which is a small fraction of next generation microcircuit linewidths (0.25 μm). However, this would require the use of an undulator source and would be expensive. It is important at this stage to demonstrate the techniques in a user friendly system, rather than aim for the highest spatial resolution. The system we have designed addresses many of the concerns of the semiconductor community. For example, the system can accept 2 x 3 inch wafer sections, and, using a high resolution in-situ optical microscope to pick up fiducial points, a positioning accuracy of 1 μm can be achieved with laser interferometric encoding of the sample position. This is important because the patterned wafer samples will be first examined elsewhere using conventional techniques, the points of interest identified, and then the samples will be transferred to the ALS. Here they will pass through a fast entry load lock, through a prep chamber, and into the analysis chamber, while needing to retain the coordinate system of the sample to an accuracy matching our spatial resolution.

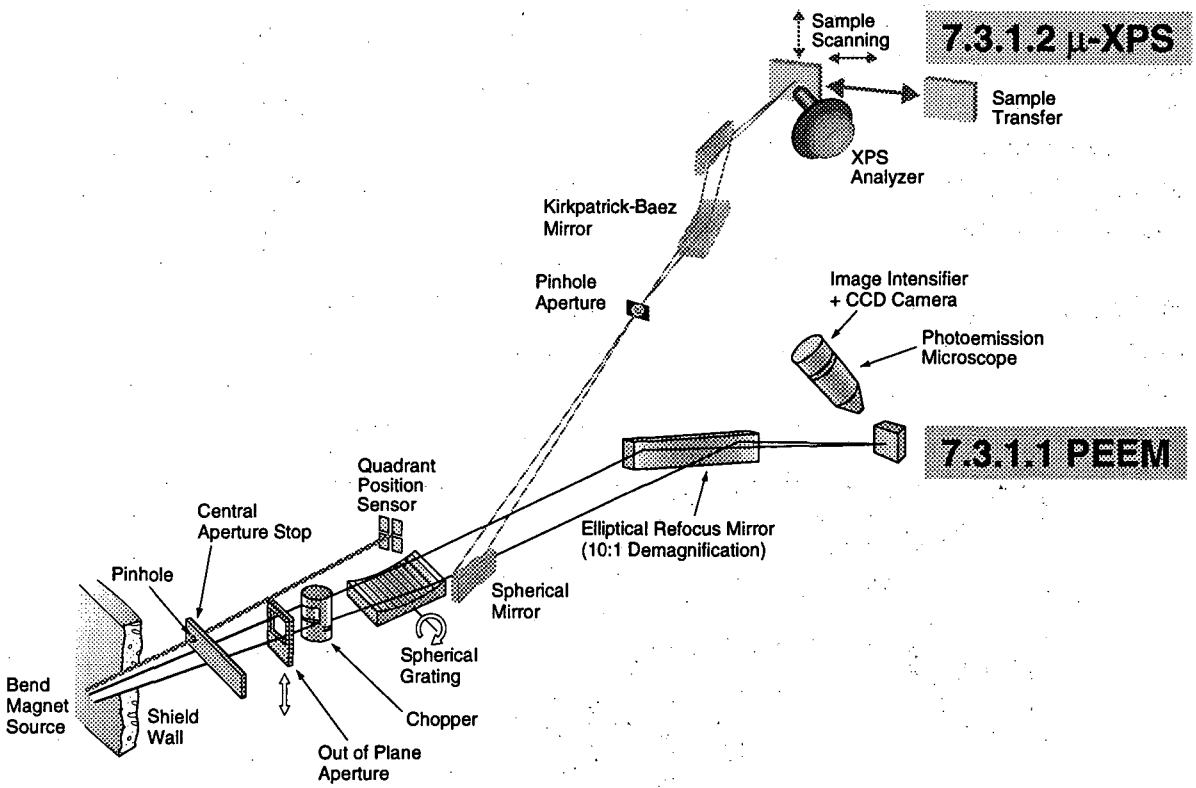

Figure 1. Beamline 7.3.1 is a specialized beamline optimized for spectromicroscopy. It has two branches, one for magnetic imaging with a full-field imaging photoemission microscope (PEEM) and one for x-ray photoelectron spectroscopy (μ-XPS). A spherical mirror diverts part of the light from the main beam into the μ-XPS branch, so that both can be used simultaneously.

The μ-XPS system uses a branchline off an existing monochromator, 7.3.1, in order to reduce the total system cost (see Figure 1). This monochromator, together with a spherical horizontally deflecting branching mirror, delivers a monochromatic focus to an adjustable pinhole that then acts as the object for the μ-XPS imaging system. The micro-focusing is produced by orthogonal elliptical mirrors in a Kirkpatrick-Baez arrangement. These mirrors have to be near perfect to produce the micron-sized focus we desire, and are made by the controlled bending of flats (see "Research and Development in Adaptive Mirrors"). These focus at 40 and 20:1 in the horizontal and vertical directions respectively from the 40 x 20 μm object pinhole. The beam size at the mirrors is 1.25 x 2.5 mm, and, in a 100 and 200 mm image distance respectively, the beam is demagnified to 1 μm. In addition to the challenge of producing the elliptical mirrors, the whole optical system is in ultra-high vacuum and very close to the sample stage. Figure 2 shows a 3D CAD drawing of the system, showing beam entering from the left, the electron energy analyzer, sample manipulator, and sample prep systems.

The system is now complete and undergoing initial commissioning. With almost no adjustment of the mirrors (there are 4 adjustments for each, only 1 of which has so far been used), the spatial resolution at full aperture is 2 x 7 μm. With further adjustment, we are confident of reaching our 1 μm target. In addition it should be noted that the diffraction limit of these mirrors at a photon energy of 1 keV is less than 0.1 μm, and so limited by the available photon flux, we can expect with improved optics and a smaller pinhole to achieve sub-micron resolution.

We anticipate a period of intense activity in which the ALS, Intel, and Applied Materials staff develop the system and apply it to microstructure materials problems. One of our near term goals will be to start work on an 8-in wafer stage, and, ultimately, if the return on investment is adequate, an undulator based system capable of 0.1 μm resolution.

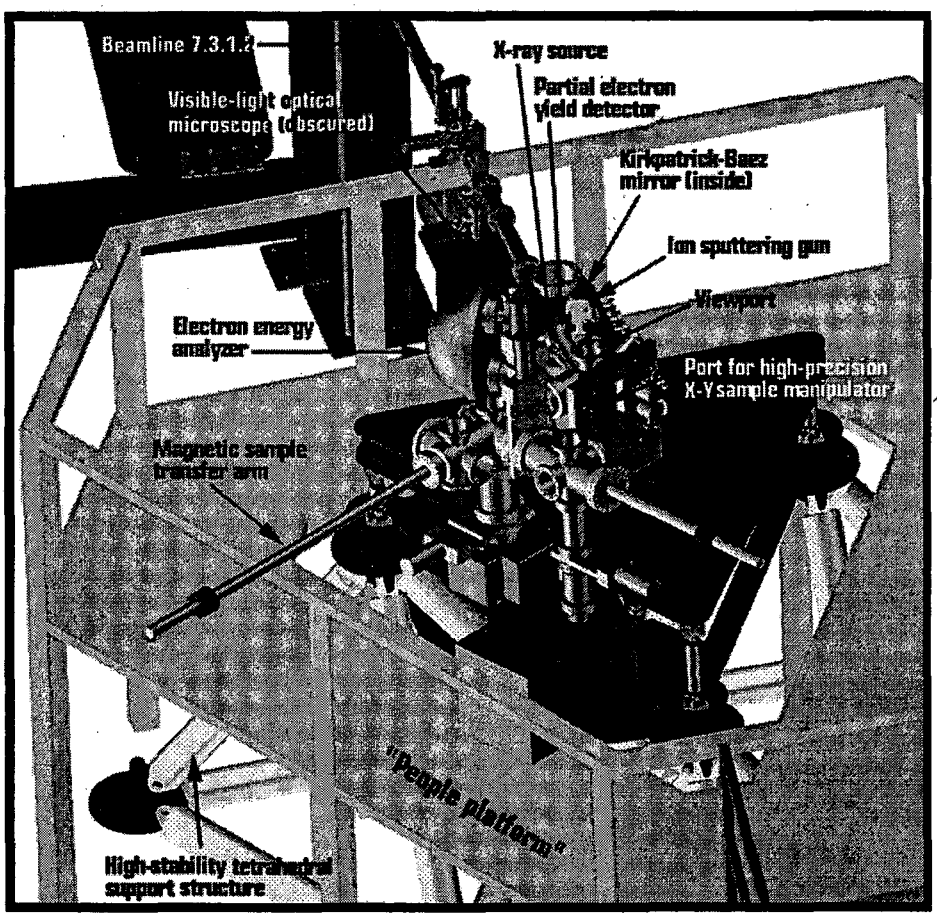

Figure 2. 3D computer aided design was used to accurately determine the interaction of all the precision components in the microXPS endstation and to aid in the measuring and fiducializing process. The endstation system is located approximately 2 m above the floor and supported on a specially designed tetrahedron with a natural frequency of 60 Hz. The endstation was created specifically for analyzing the microstructures and small-area interfaces in integrated circuits (ICs) and the silicon wafers from which ICs are made. It will be used for a variety of tasks in which the surface chemistry of microstructures needs to be determined. These include fundamental issues such as determining the chemical state of reacted surfaces and determining the composition of contaminant species.

Reported by Howard Padmore

ALS Insertion Device Work

The 16-cm-period wiggler (W16) was completed and installed during the spring 1996 shutdown. This brought the total number of insertion devices installed in the ALS to five: four undulators and a wiggler. The wiggler will provide 5–15 keV photons for the Macromolecular Crystallography Facility located at Beamline 5.0. It features a variable gap, hybrid permanent magnet structure. Peak on-axis field is 2.17 T at the 14 mm minimum magnetic gap.

The second small-gap vacuum chamber was completed, this one destined for the U5.0 undulator serving Beamline 8.0. Installation of the chamber, scheduled for the May 1997 shutdown, will allow the undulator to reach 0.85 T peak effective field at the 14 mm minimum magnetic gap, providing photons just below 50 eV when the ALS operates at 1.5 GeV.

We started work on the 10-cm-period undulator (U10) that will serve the Atomic and Molecular Science Beamline to be moved from sector 9 to sector 10 in the later part of 1997. The photon energy range will be 12–1500 eV at 1.9 GeV. Though similar to first U10 undulator now in sector 9, this 43-period device uses the support structure, drive system, control system, and permanent magnet blocks available from the re-directed elliptical wiggler project as well as the vacuum chamber which will be removed from the undulator in sector 8 during the May 1997 shutdown. To reduce cost, the hybrid magnetic structure on this device utilizes iron instead of vanadium permendur for pole material. This is possible because the required peak field is only 0.8 T. The poles are designed to conveniently match the available vacuum chamber shape so additional machining on the chamber is not required.

In conjunction with the Experimental Systems and Accelerator Physics Groups, studies began on special insertion devices for such experimental areas as microdiffraction. Effort to date has been concentrated on determining performance from such devices as in vacuum, short period, small gap undulators; quasiperiodic undulators; superconducting undulators; high field wigglers; and single-pole bends. The goal of this study is to develop design parameters for future ALS insertion devices.

Another one of our key areas of activity is detailed in the technical report "Elliptical Polarization Undulator."

Reported by Egon Hoyer

Elliptical Polarization Undulator

One key area of activity for the ALS insertion device group in 1996 was the construction of the elliptical polarization undulator (EPU) facility at the ALS dedicated to magnetic microscopy and spectroscopy. We completed the final specifications and a detailed design for the first undulator, a 5-cm-period EPU5.0, and we began construction on the device and its related systems.

The 1.9-m-long EPU with 37.5 periods is designed to produce very bright photon beams with variable polarization in the energy range of 100–1500 eV. The EPU facility will eventually include two identical EPU5.0s and a third device with a longer period (approximately 8.0 cm, exact period length not yet determined) to access lower photon energies. The 1.9-m length is chosen to allow two insertion devices to be placed in tandem in a single straight. A third device is accommodated by use of a transverse stage on which one of the EPU5.0's will be mounted along with the longer period device. This arrangement will allow users to switch between the sources. A three magnet chicane system will separate the photon beams from the two insertion device stations by 2.53 mrad. The chicane system includes a magnet at the entrance and exit of the straight section and one between the two insertion devices. The straight section layout is shown in Figure 1.

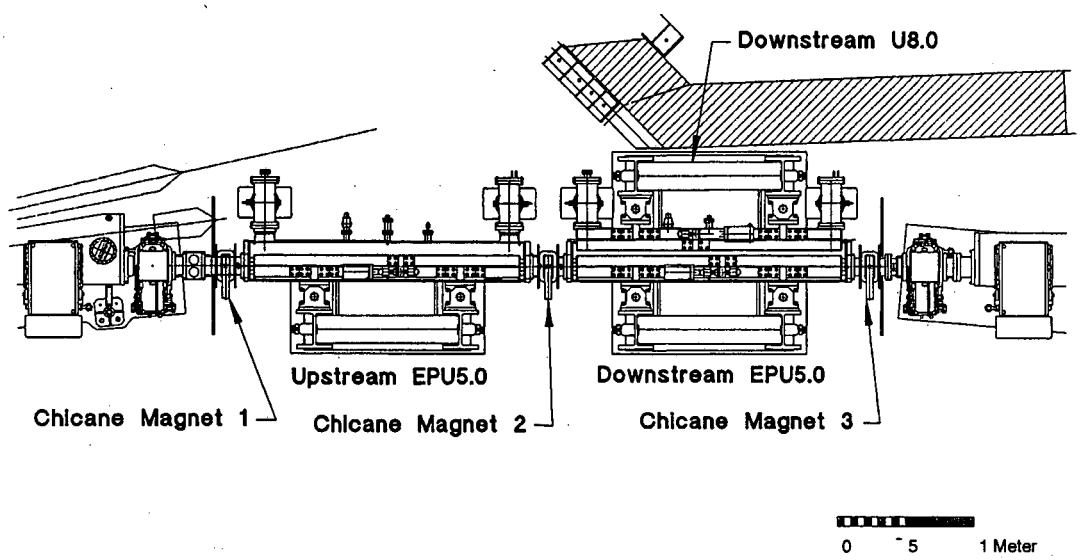

Figure 1. EPU straight sector layout.

The magnetic structure consists of four identical quadrants as shown in Figure 2. Q1 and Q3 are fixed; Q2 and Q4 are allowed to translate parallel to the magnetic axis. The relative translation, called the quadrant phase, χ, of the magnetic quadrants, changes the ellipticity of an electron orbit passing through the device and thus changes the polarization of the emitted radiation. When $\chi = 0$, the magnetic structure is equivalent to a standard linear undulator, only B_y is produced on axis, and the radiation is linearly polarized in the horizontal plane. When $\chi = \lambda/2$, where λ is the

undulator period, only B_x is produced on axis and radiation is linearly polarized in the vertical plane. When χ has any other value, both B_x and B_y are produced on axis, and the radiation is elliptically polarized. When B_x=B_y, radiation is circularly polarized.

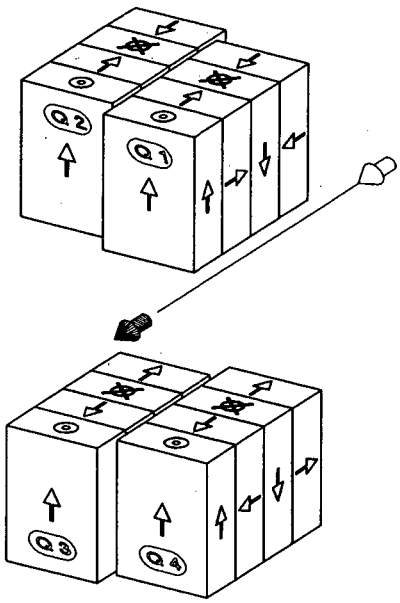

Figure 2. Four quadrant schematic of the EPU.

Notable features of the EPU magnetic design include mechanical adjustability at each magnet to correct magnet errors that contribute to optical phase errors and electron beam trajectory perturbations, and a deflection- and displacement-free entrance and exit. The EPU5.0 is the first pure permanent magnet design for the ALS. It is also the first half-length device designed to accommodate two devices in a straight section.

Several small magnetic models were assembled and used to test the magnetic design. A more elaborate 6.5 period prototype has also been completed. This has all of the magnetic features of the full device, including the ends. The model will be used to commission the new magnet measurement system, and to develop techniques for identifying and correcting magnetic errors. This will also give us our first test of whether or not we can achieve a gap-independent deflection- and displacement-free entrance and exit.

A new support structure and drive system was developed to accommodate as many as four shorter insertion devices in a single straight section: two source locations each with a possible arrangement of two side by side devices, either of which can be selected as the source. The drive system includes three drives: one to control the magnet gap, and two for translating the two moveable quadrants. The philosophy has been to make the design generic so that it may be utilized in future installations where two to four insertion devices per straight section are desired.

Reported by Steve Marks

Publications Based on Work Done at the ALS

If a publication is associated with a particular beamline, the beamline number is given to the left of the reference.

Refereed Journal Articles

9.0.2 Ahmed, M., D. Blunt, D. Chen, and A. Suits, "UV photodissociation of oxalyl chloride yields four fragments from one photon absorption," *J. Chem. Phys.* (1997).

Barat, K., "Obtaining laser safety at a synchrotron radiation user facility: the Advanced Light Source," *Journal of Laser Applications* (in press).

9.0.1 Berrah, N., B. Langer, J.D. Bozek, O.A. Hemmers, D.W. Lindle, and O.F. Toader, "High-resolution angle-resolved photoelectron spectroscopy: the Ar $3s^{-1} \rightarrow$ np (n = 4–16) autoionization resonances," *J. Phys. B* **27** (1996) p. 5351.

9.0.1 Berrah, N., B. Langer, J.D. Bozek, O.A. Hemmers, D.W. Lindle, O.F. Toader, and T.W. Gorczyca, "Angular-distribution parameters and R-matrix calculations of Ar $3s^{-1} \rightarrow$ np (n = 4–16) resonances," *J. Phys. B* **29** (June 1996) pp. 5351–5365.

9.0.1 Berrah, N., O.F. Toader, B. Langer, J.D. Bozek, D.W. Lindle, and O.A. Hemmers, "Autoionization of Ar, Kr and Xi near the ns threshold," *Bull. Am. Phys. Soc.* **40** (1995) p. 1287.

9.0.2.1 Blank, D.A., S.W. North, D. Stranges, A. Suits, and Y.T. Lee, "Unraveling the dissociation of dimethyl sulfoxide following absorption at 193 nm," *J. Chem. Phys.* **106** (August 1996) p. 539.

7.0.1 Butorin, S., D. Mancini, J. Guo, N. Wassdahl, J.E. Nordgren, and R.C.C. Perera *et al* ., "Resonant x-ray fluorescence spectroscopy of correlated systems—A probe of charge transfer excitations," *Phys. Rev. Lett.* **77** (1996) p. 5035.

8.0.1 Butorin, S., J.-H. Guo, M. Magnuson, P. Kuiper, and J.E. Nordgren, "Low-energy d-d excitations in MnO studied by resonant x-ray fluorescence spectroscopy," *Phys. Rev. B* **54**, 7 (August 1996) pp. 4405–4408.

8.0.1 Carlisle, J.A., A. Chaiken, R.P. Michel, L.J. Terminello, J. Jia, T.A. Callcott, and D.L. Ederer, "Experimental determination of the electronic structure of buried silicides in antiferromagnetically coupled Fe/Si multilayers," *Phys. Rev. B* **76** (1996) p. 1762.

8.0.1 Carlisle, J.A., E.L. Shirley, E.A. Hudson, L.J. Terminello, T.A. Callcott, J. Jia, D.L. Ederer, R.C. Perera, and F.J. Himpsel, "Probing the graphite band structure with resonant soft x-ray fluorescence," *Phys. Rev. Lett.* **74**, 7 (February 1995) pp. 1234–1236.

8.0.1 Carlisle, J.A., L.J. Terminello, A.V. Hamza, E.A. Hudson, E.L. Shirley, F.J. Himpsel, D.A. Lapiano-Smith, J. Jia, T.A. Callcott, R.C. Perera, D.K. Shuh, S. Louie, J. Stöhr, M.G. Samant, and D.L. Ederer, "Occupied and unoccupied orbitals of C_{60} and C_{70}," *Mol. Cryst. Liq. Cryst.* **256** (1994) pp. 819–824.

8.0.1 Carlisle, J.A., L.J. Terminello, E.A. Hudson, R.C. Perera, J.H. Underwood, T.A. Callcott, J. Jia, D.L. Ederer, and F.J. Himpsel, "Characterizing buried interfaces using resonant soft x-ray fluorescence," *Appl. Phys. Lett.* (in press).

7.0.1 Cesar, A., F. Gel'mukhanov, Y. Luo, H. Agren, P.I. Skytt, P.N. Glans, J. Guo, K.M. Gunnelin, and J.E. Nordgren, "Resonant x-ray scattering beyond the Born-Oppenheimer approximation: symmetry breaking in the oxygen resonant x-ray emission spectrum of carbon dioxide," *J. Chem. Phys.*

9.0.1 Cubaynes, D., S. Diehl, L. Journel, B. Rouvellou, J. Bizau, S. Al Moussalami, F. Wuilleumier, N. Berrah, L. VoKy, P. Faucher, A. Hibbert, C.P. Blancard, E.T. Kennedy, T.J. Morgan, J.D. Bozek, and A.S. Schlachter, "First photoexcitation measurements and R-matrix calculations of even-parity hollow states in laser-excited lithium atoms," *Phys. Rev. Lett.* **77**, 11 (September 1996) p. 2194.

7.0.1 Denlinger, J., E. Rotenberg, T. Warwick, G. Visser, J.E. Nordgren, J. Guo, P.I. Skytt, S.D. Kevan, K.S. McCutcheon, D.K. Shuh, J.J. Bucher, N.M. Edelstein, J.G. Tobin, and B.P. Tonner, "First results from the spectromicroscopy beamline at the Advanced Light Source," *Rev. Sci. Instrum.* **66**, 2 (1995) p. 1342.

7.0.1 Denlinger, J., J. Zhang, and B.P. Tonner, "Angular instrument response for photoelectron diffraction using focused, plane-polarized synchrotron beams," *Nucl. Instrum. Methods* **A347** (1994) pp. 475–479.

9.0.1 Diehl, S., D. Cubaynes, J. Bizau, L. Journel, B. Rouvellou, S. Al Moussalami, F. Wuilleumier, E.T. Kennedy, N. Berrah, C.P. Blancard, T.J. Morgan, J.D. Bozek, A.S. Schlachter, L. VoKy, P. Faucher, and A. Hibbert, "High resolution measurements of partial photoionization cross-section in hollow lithium: a critical comparison with advanced many-body calculations," *Phys. Rev. Lett.* **76**, 21 (May 1996) p. 3915.

7.0.1 Doerner, R., J. Feagin, H. Braening, O. Jagutzki, M.B. Jung, E.P. Kanter, H. Khemliche, S.D. Kravis, V. Mergel, M.H. Prior, H. Schmidt-Böcking, L. Spielberger, J.H. Ullrich, M. Unverzagt, T. Vogt, and C.L. Cocke, "Fully differential cross sections for double photoionization of He measured by recoil ion momentum spectroscopy," *Phys. Rev. Lett.* **77** (November 1996) pp. 1024–1026.

7.0.1 Doerner, R., T. Vogt, V. Mergel, H. Khemliche, S.D. Kravis, C.L. Cocke, J.H. Ullrich, M. Unverzagt, L. Spielberger, M. Damrau, O. Jagutzki, I. Ali, B. Weaver, K. Ullmann, C.C. Hsu, M.B. Jung, E.P. Kanter, B. Sonntag, M.H. Prior, E. Rotenberg, J. Denlinger, T. Warwick, S.T. Manson, and H. Schmidt-Böcking, "Ratio of cross sections for double to single ionization of He by 85–400 eV photons," *Phys. Rev. Lett.* **76**, 15 (April 1996) pp. 2654–2657.

7.0.1 Droubay, T.C., G. Mursky, and B.P. Tonner, "High resolution x-ray absorption micro-spectroscopy of lamellar phases in natural ilmenite," *J. Electron Spectros. Relat. Phenom.* (in press).

7.0.1 Duda, L.C., P. Isberg, Ph. Andersson, B. Hjörvarsson, J. Guo, C. Såthe, and J.E. Nordgren, "Hydrogen induced changes of the electronic states in ultra-thin single crystal vanadium layers," *Phys. Rev. B* (in press).

7.0.1 Duda, L.C., P. Isberg, S. Mirbt, J. Guo, B. Hjörvarsson, P. Granberg, and J.E. Nordgren, "Soft x-ray emission study of Fe/V(001) superlattices," *Phys. Rev. B* **54** (1996) p. 10303.

8.0.1 Ederer, D.L., J.A. Carlisle, I. Jimenez, J. Jia, K.D. Osborn, T.A. Callcott, R.C. Perera, J.H. Underwood, L.J. Terminello, A. Asfaw, and F.J. Himpsel, "Study of buried interfaces by soft x-ray fluorescence spectroscopy excited by synchrotron radiation," *J. Vac. Sci. Technol. A* **14** (1996) p. 859.

9.0.2 Evans, M.D., C.Y. Ng, C. Hsu, and P.A. Heimann, "A high resolution energy-selected kinetic energy release study of the process $SF_6 + h\nu$; $SF_5^+ + F + e^-$: heat of formation of SF_5^+," *Chem. Phys. Lett.* **106** (1997) p. 978.

9.3.2 Fadley, C.S., M.A. Van Hove, Z. Hussain, and A. Kaduwela, "Photoelectron diffraction: new dimensions in space, time, and spin," *J. Electron Spectros. Relat. Phenom.* **75** (November 1995) pp. 273–297.

9.0.1 Francis, J.T., C.C. Turci, T. Tyliszczak, G.G. De Souza, N. Kosugi, and A.P. Hitchcock, "Electron impact core excitation of SF_6: Part I: S 2p, S 2s and F 1s spectroscopy," *Phys. Rev. A* **52**, 6 (December 1995) pp. 4665–4677.

7.0.1 Gammon, W.J., S.R. Mishra, K.W. Goodman, J.G. Tobin, F.O. Schumann, R.F. Willis, J. Denlinger, E. Rotenberg, T. Warwick, and N.V. Smith, "A comparison of magnetic linear dichroism in 4f photoemission and 4d-4f photoemission from Gd on Y(0001)," *J. Vac. Sci. Technol.* (in press).

7.0.1 Glans, P.N., K.M. Gunnelin, P.I. Skytt, J. Guo, N. Wassdahl, J.E. Nordgren, H. Agren, F.Kh. Gel'mukhanov, T. Warwick, and E. Rotenberg, "Resonant x-ray emission spectroscopy of molecular oxygen," *Phys. Rev. Lett.* **76**, 14 (April 1996) pp. 2448–2451.

7.0.1 Glans, P.N., P.I. Skytt, K.M. Gunnelin, J. Guo, and J.E. Nordgren, "Selectively-excited x-ray emission spectra of N2," *J. Electron Spectros. Relat. Phenom.* **82**, 3 (December 1996) pp. 193–201.

8.0.1 Gruen, D.M., A.R. Krauss, C.D. Zuiker, R. Csencsits, L.J. Terminello, J.A. Carlisle, I. Jimenez, D.G. Sutherland, D.K. Shuh, W.M. Tong, and F.J. Himpsel, "Characterization of nanocrystalline diamond films by core-level photoabsorption," *Appl. Phys. Lett.* **68** (1996) p. 1640.

7.0.1 Guo, J., P.I. Skytt, N. Wassdahl, J.E. Nordgren, Y. Luo, O. Vahtras, and H. Agren, "Resonant and non-resonant x-ray scattering from C_{70}," *Chem. Phys. Lett.* (March 1995) pp. 152–159.

7.0.1 Guo, J., P.N. Glans, P.I. Skytt, N. Wassdahl, J.E. Nordgren, Y. Luo, H. Agren, Y. Ma, T. Warwick, P. Heimann, E. Rotenberg, and J. Denlinger, "Resonant excitation x-ray fluorescence from C_{60}," *Phys. Rev. B* **52** (1995) p. 10681.

8.0.1 Haass, M., J. Jia, T.A. Callcott, D.L. Ederer, K.E. Miyano, R.N. Watts, D. Mueller, C. Tarrio, and E. Morikawa, "Variable groove spaced grating monochromators for synchroton light sources," *Nucl. Instrum. Methods* **A347** (1994) p. 258.

Heimann, P.A., D. Mossessian, T. Warwick, C. Wang, S. Marks, H.A. Padmore, B.M. Kincaid, and E. Gullikson, "Experimental Characterization of ALS Undulator Radiation," *Rev. Sci. Instrum.* **66** (1995) p. 1885.

9.0.2 Heimann, P.A., M. Koike, C. Hsu, M.D. Evans, K. Lu, C.Y. Ng, A. Suits, and Y.T. Lee, "Performance of the chemical dynamics beamline at the Advanced Light Source," *Rev. Sci. Instrum.* (1996).

8.0.1 Hemmers, O.A., G. Fisher, P.N. Glans, D.L. Hansen, H. Wang, S. Whitfield, D.W. Lindle, R. Wehlitz, J.C. Levin, I.A. Sellin, R.C. Perera, E.W.B. Dias, H.S. Chakraborty, P.C. Deshmukh, and S.T. Manson, "Beyond the dipole approximation: angular-distribution effects in valence photoemission," *Phys. Rev. Lett.* (May 1996).

9.0.2 Hemmi, N., and A. Suits, "Photodissociation of oxalyl chloride at 193nm probed via synchrotron radiation," *J. Phys. Chem.* (in press).

8.0.1 Himpsel, F.J., H. Akatsu, J.A. Carlisle, D.G. Sutherland, I. Jimenez, L.J. Terminello, J. Jia, T.A. Callcott, M.G. Samant, J. Stöhr, D.L. Ederer, R.C. Perera, S.Y. Tong, and D.K. Shuh, "Surface and interface analysis at 3rd generation light sources," *Progress in Surface Science* **50**, 1–4 (1995) pp. 37–51.

9.0.1 Hitchcock, A.P., S.G. Urquhart, A.T. Wen, A.L.D. Kilcoyne, T. Tyliszczak, E. Rühl, N. Kosugi, J.D. Bozek, J. Spencer, D.N. McIlroy, and P.A. Dowben, "Inner-shell excitation spectroscopy of closo-carboranes," *J. Chem. Phys.* (October 1996).

Howells, M., "Design strategies for monolithic adaptive metal mirrors," *Optical Engineering* **34**, 2 (February 1995) pp. 410–417.

Howells, M., "Design strategies for monolithic adjustable-radius metal mirrors," *Optical Engineering* **34** (1995) pp. 410–417.

Howells, M., "Some fundamentals of cooled mirrors for synchrotron radiation beamlines," *Optical Engineering* **35**, 4 (August 1994) pp. 1187–1197.

9.3.2 Howells, M., H. Frank, Z. Hussain, E. Moler, T. Reich, D. Möller, and D.A. Shirley, "Toward a soft x-ray Fourier-transform spectrometer," *Nucl. Instrum. Methods* **A347**, 1–3 (August 1994) pp. 182–191.

Hoyer, E., J. Akre, D.E. Humphries, S. Marks, Y. Minamihara, P. Pipersky, D. Plate, and R. Schlueter, "Advanced Light Source elliptical wiggler," *Rev. Sci. Instrum.* **66**, 2, (February 1995).

Hoyer, E., J. Akre, J. Chin, W. Gath, W.V. Hassenzahl, D.E. Humphries, B.M. Kincaid, S. Marks, P. Pipersky, D. Plate, G.J. Portmann, and R. Schlueter, "Undulators at the Advanced Light Source," *Rev. Sci. Instrum.* **66**, 2 (February 1995).

Hoyer, E., S. Marks, P. Pipersky, and R. Schlueter, "Advanced Light Source multiple trim magnets, or "magic fingers," for insertion device field integral correction," *Rev. Sci. Instrum.* **66**, 2 (February 1995).

9.0.2.1 Hsu, C., K. Lu, M.D. Evans, Y.J. Chen, P.A. Heimann, and C.Y. Ng, "A high resolution photoionization study of Ne and Ar: observation of mass analyzed threshold ions using synchrotron radiation and direct current electric fields," *J. Chem. Phys.* **105**, 10 (September 1996) pp. 3950–3961.

9.0.2 Hsu, C.-W., M.D. Evans, C.Y. Ng, and P.A. Heimann, "High resolution threshold and pulsed field ionization photoelectron spectroscopy using multibunch synchrotron radiation source," *Rev. Sci. Instrum.* (1997).

9.0.2 Hsu, C.-W., M.D. Evans, P.A. Heimann, K.T. Lu, and C.Y. Ng, "High resolution photoionization studies on the chemical dynamics beamline at the Advanced Light Source," *J. Chem. Phys.* (in press).

9.0.2 Hsu, C.-W., M.D. Evans, S.L. Stimson, C.Y. Ng, and P.A. Heimann, "A high resolution pulsed field ionization photoelectron study of O_2 using third generation undulator synchrotron radiation," *J. Chem. Phys.* (1996).

9.0.2 Huang, J.-C., Y.-S. Cheung, M.D. Evans, C.-X. Liao, C.Y. Ng, C.-W. Hsu, P.A. Heimann, H. Lefebvre-Brion, and C. Cossart-Magos, "A high resolution VUV photoionization, photoelectron, and pulsed field ionization study of CS_2 near the CS_2^+ ($^2P_{3/2,1/2}$) thresholds," *J. Chem. Phys.* **106** (1997) p. 864.

Huang, Z.Q., Z. Hussain, T. Huff, E. Moler, and D.A. Shirley, "Structural determination of p2mg(2x1) CO/Ni(110) with the use of angle-resolved photoemission extended fine structure," *Phys. Rev. B* **43**, 3 (1993) pp. 1696–1710.

9.3.2 Hudson, E.H., E. Moler, Y. Zheng, S.A. Kellar, P.A. Heimann, Z. Hussain, and D.A. Shirley, "Near-edge sodium and fluorine K-shell photoabsorption of alkali halides," *Phys. Rev. B* **49** (1994) pp. 3701–3708.

9.3.2 Huff, T., Y. Chen, S.A. Kellar, E. Moler, Z. Hussain, Y. Zheng, and D.A. Shirley, "II: A study of angle-resolved photoemission extended fine structure as applied to the Cu 3s and Cu 3p core-levels of a clean Cu(111) surface," *Phys. Rev. B* (in press).

9.3.2 Huff, T., Y. Chen, S.A. Kellar, E. Moler, Z. Hussain, Z. Huang, and D.A. Shirley, "I: Study of angle-resolved photoemission extended fine structure as applied to the Ni 3p core-level of a clean Ni(111) surface," *Phys. Rev. B* (in press).

9.3.2 Huff, T., Y. Chen, X. Zhang, L.J. Terminello, F.M. Tao, Y.K. Pan, S.A. Kellar, E. Moler, Z. Hussain, H. Wu, Y. Zheng, X. Zhou, A.E. Schach von Wittenau, S. Kim, Z. Huang, and D.A. Shirley, "Structure determination of chemisorbed c(2x2)P/Fe(100) using angle-resolved photoemission extended fine structure and self-consistent-field X alpha scattered wave calculations: comparison with C(2x2)S/Fe(100)," *Phys. Rev. B* **55**, 15 (April 1996).

9.3.2 Huff, T., Y. Zheng, Z. Hussain, and D.A. Shirley, "Final-state effects in the angle-resolved photoemission extended fine structure of c(2x2)S/Ni(001)," *J. Phys. Chem.*, Vol. 98, 1994, pp. 9182–9186.

Humphries, D.E., F. Goetz, P. Kownacki, S. Marks, and R. Schlueter, "A multiple objective magnet sorting algorithm for the Advanced Light Source insertion devices," *Rev. Sci. Instrum.* (in press).

8.0.1 Jia, J., E.L. Shirley, J.A. Carlisle, T.A. Callcott, L.J. Terminello, A. Asfaw, D.L. Ederer, F.J. Himpsel, and R.C. Perera, "Resonant inelastic x-ray scattering in h-BN observed by soft x-ray fluorescence spectroscopy," *Phys. Rev. Lett.* **76** (1996) p. 4054.

8.0.1 Jia, J., T.A. Callcott, A. Asfaw, J.A. Carlisle, L.J. Terminello, D.L. Ederer, R.C. Perera, and F.J. Himpsel, "Occupied electronic states of $CaSi_2$ and CaSi: soft x-ray fluorescence spectroscopy," *Phys. Rev.* **52** (March 1995) p. 4904.

8.0.1 Jia, J., T.A. Callcott, J.A. Carlisle, L.J. Terminello, A. Asfaw, D.L. Ederer, F.J. Himpsel, and R.C. Perera, "X-ray raman scattering in h-BN observed by soft x-ray fluorescence spectroscopy," *Phys. Rev. Lett.* (in press).

8.0.1 Jimenez, I., A. Jankowski, L.J. Terminello, D.G. Sutherland, J.A. Carlisle, G.L. Doll, W.M. Tong, D.K. Shuh, and F.J. Himpsel, "Core level photoabsorption study of defects and metastable bonding configurations in boron nitride," *Phys. Rev. Lett.* (1997).

8.0.1 Jimenez, I., A. Jankowski, L.J. Terminello, J.A. Carlisle, D.G. Sutherland, G.L. Doll, J.V. Mantese, W.M. Tong, D.K. Shuh, and F.J. Himpsel, "Near-edge x-ray absorption fine structure study of bonding modifications in BN thin films by ion implantation," *Appl. Phys. Lett.* **68**, 13 (May 1996), pp. 2816–2818.

8.0.1 Jimenez, I., L.J. Terminello, D.G. Sutherland, J.A. Carlisle, E.L. Shirley, and F.J. Himpsel, "The band width of diamond," *Phys. Rev. B* (in press).

8.0.1 Karis, O., A. Nilsson, M.G. Weinelt, T. Wiell, C. Puglia, N. Wassdahl, N. Martensson, M.G. Samant, and J. Stöhr, "One-step and two-step description of de-excitation processes in weakly interacting systems," *Phys. Rev. Lett.* **76**, 8 (February 1996) pp. 1380–1393.

9.0.2 Keister, J.W., T. Baer, M.D. Evans, C.Y. Ng, and C.-W. Hsu, "Methyl loss kinetics of energy-selected butadiene radical photocations," *J. Phys. Chem.* (1997).

10.3.2 Khan-Malek, C.G., K.H. Jackson, R.A. Brennen, M. Hecht, W.D. Bonivert, and J. Hruby, "Deep etch x-ray lithography at the Advanced Light Source: first results," *J. Vac. Sci. Technol. B* **12**, 6 (Nov/Dec 1994) pp. 4009–4012.

10.3.2 Kim, S.K., Y. Koo, V. Chernov, and H.A. Padmore, "Clear evidence for strain changes according to Co layer thickness in Co/Pd multilayers: an extended x-ray absorption fine study," *Phys. Rev. B* **53**, 16 (1995) p. 11.

Kirz, J., C. Jacobsen, and M. Howells, "Soft x-ray microscopes and their biological applications," *Quarterly Reviews of Biophysics* **28** (1995) pp. 33–130.

Kirz, J., H. Ade, E. Anderson, C. Buckley, H. Chapman, M. Howells, C. Jacobsen, C.H. Ko, S. Lindaas, D. Sayre, S. Williams, S. Wirick, and X. Zhang, "New results in soft x-ray microscopy," *Nucl. Instrum. Methods* **B87** (1993) pp. 92–97.

Koike, M., and T. Namioka, "Optimization and evaluation of varied line spacing plane grating monochromators for third-generation synchrotron radiation sources," *J. Electron Spectros. Relat. Phenom.* **80** (1995) pp. 303– 308.

9.0.2 Koike, M., P. Heimann, A.H. Kung, T. Namioka, D. DiGennaro, B. Gee, and N. Yu, "VUV high resolution and high flux beamline for chemical dynamics studies at the Advanced Light Source," *Nucl. Instrum. Methods* (1994).

Kortright, J., S.K. Kim, T. Warwick, and N.V. Smith, "Soft x-ray circular polarizer using magnetic circular dichroism at the Fe L_3 line," *Appl. Phys. Lett.* (in press).

6.3.2 Kosugi, N., R.G. Cavell, and A.P. Hitchcock, "(LS) versus (jj) coupling in P 2p inner-shell excited states of PF_3," *Chem. Phys. Lett.* (November 1996).

Lambrecht, W.R.L., S.N. Rashkeev, B. Segall, K. Lawniczak-Jablonska, T. Suski, E. Gullikson, J.H. Underwood, R.C. Perera, J.C. Rife, I. Graegory, S. Porowski, and D. Wickenden, "X-ray absorption, glancing-angle reflectivity, and theoretical study of the N-K and Ga- M edge spectra in GaN," *Phys. Rev. B* **55** (1997) p. 2612.

9.0.1 Langer, B., N. Berrah, A.H. Farhat, O.A. Hemmers, and J.D. Bozek, "Auger resonant raman spectroscopy used to study the angular distributions of the Xe $4d_{5/2} \rightarrow 6p$ decay spectrum," *Phys. Rev. A* **53**, 4 (1996) p. 1946.

Lawniczak-Jablonska, K., R.C. Perera, J.H. Underwood, E. Gullikson, and R. Iwanowski, "Hybridization of the 3d states of transition metals with the states of the ZnS matrix," *Phys. Rev. B* (1997).

Lawniczak-Jablonska, K., T. Suski, Z. Liliental-Weber, E. Gullikson, J.H. Underwood, T. Drummond, and R.C. Perera, "Anisotropy of the nitrogen conduction states in the group III nitrides studied by polarized x-ray absorption," *Appl. Phys. Lett.* (in press).

BTF Leemans, W., R. Schoenlein, P. Volfbeyn, A.H. Chin, T.E. Glover, P. Balling, M. Zolotorev, K.-J. Kim, and C.V. Shank, "X-ray based sub-picosecond electron bunch characterization using 90° Thomson scattering," *Phys. Rev.* **77**, 4128 (1996).

BTF Leemans, W., R. Schoenlein, P. Volfbeyn, A.H. Chin, T.E. Glover, P. Balling, M. Zolotorev, K.-J. Kim, S. Chattopadhyay, and C.V. Shank, "Interaction of relativistic electrons with ultrashort laser pulses: generation of femtosecond x-rays and microprobing of electron beams," *IEEE J. Quantum Electron.* (in press).

Len, P., F Zhang, S. Thevuthasan, A. Kaduwela, M.A. Van Hove, and C.S. Fadley, "Photoelectron holography: prospects and limitations of direct methods," *J. Electron Spectros. Relat. Phenom.* **76** (1995) pp. 351–357.

Len, P., S. Thevuthasan, A. Kaduwela, M.A. Van Hove, and C.S. Fadley, "Optimization of k-space sampling in atomic imaging by electron emission holography," *Surf. Sci.* **365** (1996) pp. 535–546.

Lindaas, S., M. Howells, C. Jacobsen, and A. Kalinovsku, "X-ray holographic microscopy via photoresist recording and atomic-force microscope readout," *J. Opt. Soc. Am. A* **13**, 9 (September 1996) pp. 1788–1800.

Lindle, D.W., O.A. Hemmers, P.N. Glans, D.L. Hansen, H. Wang, S. Whitfield, R. Wehlitz, J.C. Levin, I.A. Sellin, and R.C. Perera, "The x-ray atomic and molecular spectroscopy program at the Advanced Light Source," *Indian Journal of Physics* (1996).

10.3.2 Ludewigt, B., C.S. Rossington, I. Kipnis, and B. Krieger, "Progress in multi-element silicon detectors for synchrotron XRF applications," *IEEE Trans. Nucl. Sci.* **43**, 3 (1996) pp. 1442–1445.

7.0.1 Luo, Y., H. Agren, F. Gel'mukhanov, J. Guo, P.I. Skytt, N. Wassdahl, and J.E. Nordgren, "Symmetry selective resonant inelastic x-ray scattering of C_{60}," *Phys. Rev. B* **52** (1995) p. 14479.

7.0.1 Luo, Y., H. Agren, J. Guo, P.I. Skytt, N. Wassdahl, and J.E. Nordgren, "Sub-eV chemical shifts and strong interference effects measured in the resonance x-ray scattering spectra of aniline," *Phys. Rev. A* **52**, 5 (November 1995) pp. 3730–3736.

7.0.1 Ma, Q., R.A. Rosenberg, C. Kim, J. Grepstat, P.A. Pianetta, T.C. Droubay, D.J. Dunham, and B.P. Tonner, "Comparative magnetic-field imaging, electric-field imaging, and scanning Auger microscopy study of metal-matrix composites," *J. Electron Spectros. Relat. Phenom.* (in press).

10.3.2 Maier, M.R., B. Ludewigt, C.S. Rossington, H. Yaver, and J.J. Zaninovich, "A 16-channel peak sensing ADC for singles spectra in the FERA format," *IEEE Trans. Nucl. Sci.* **43**, 3 (1996) pp. 1680–1682.

Marks, S., "Magnetic design of trim excitations for the Advanced Light Source storage ring sextupole," *IEEE Trans. Magn.* (July 1996).

Marks, S., and C.W. Cork, "Flux, irradiance, and transmission calculations for the Advanced Light Source wiggler beamline 5.0," *Rev. Sci. Instrum.* (October 1995).

Marks, S., J. Akre, E. Hoyer, D.E. Humphries, T. Jackson, Y. Minimihara, P. Pipersky, D. Plate, and R. Schlueter, "Magnetic design of the Advanced Light Source elliptical wiggler," *IEEE Trans. Magn.* (July 1996).

Marks, S., W.R. McKinney, H.A. Padmore, and A.T. Young, "Optimization design study for an elliptical wiggler at the Advanced Light Source," *Rev. Sci. Instrum.* **66** (1995).

8.0.1 Martensson, N., M.G. Weinelt, O. Karis, N. Wassdahl, A. Nilsson, J. Stöhr, and M.G. Samant, "Coherent and incoherent processes in resonant photoemission," *Appl. Phys. Lett.* (1996).

9.0.2 Mayer, P.M., J.W. Keister, T. Baer, C.-W. Hsu, M.D. Evans, and C.Y. Ng, "The fragmentation of dimethylamine dimer ions: accurate neutral and ionic dimer binding energies by a combined TPEPICO, variation RRKM, and ab initio approach," *J. Phys. Chem.* (1997).

9.0.1 McGuire, J.H., N. Berrah, R.J. Bartlett, J.A.R. Samson, J.A. Tanis, C.L. Cocke, and A.S. Schlachter, "The ratio of cross sections for double to single ionization of helium by high energy photons and charged particles," *J. Phys. B* (in press).

9.0.1 Medecki, H., E. Tejnil, K. Goldberg, and J. Bokor, "Phase-shifting point diffraction interferometer," *Opt. Lett.* **21**, 19 (October 1996) pp. 1526–1528.

9.0.1 Menzel, A., S. Frigo, S. Whitfield, C. Caldwell, M.O. Krause, J.Z. Tang, and I. Shimamura, "Decay paths of interfering two-electron excitations in helium," *Phys. Rev. Lett.* **75**, 8 (August 1995), pp. 1479–1482.

9.0.1 Menzel, A., S.P. Frigo, S. Whitfield, C. Caldwell, and M.O. Krause, "Partial photoionization cross sections and photoelectron angular distributions for double excitations up to the N = 5 threshold in helium," *Phys. Rev. A* **54**, 3 (September 1996) pp. 2080–2089.

6.1.2 Meyer-Ilse, W., and L. Jochum, "Partially coherent imaging with soft x-ray microscopes," *Appl. Opt.* **34** (1995), pp. 4944–4950.

9.3.2 Moler, E., S.A. Kellar, Z. Hussain, T. Huff, Y. Zheng, E.A. Hudson, Y. Chen, and D.A. Shirley, "Adsorption site and structure determination of c(2×2) N_2/Ni(100) using angle-resolved photoemission extended fine structure," *Chem. Phys. Lett.* (May 1996).

9.3.2 Moler, E., S.A. Kellar, Z. Hussain, W.R.A. Huff, Y. Chen, and D.A. Shirley, "Spatial structure determination of ($\sqrt{3} \times \sqrt{3}$) R30° and (1.5 × 1.5) R18° Co on Cu(111) using angle-resolved photoemission extended fine structure," *Phys. Rev. B* **54**, 17 (1996) pp. 10862–10868.

Mossessian, D., and P. Heimann, "Characterization of Advanced Light Source undulator radiation—high k, taper, and the near field effect," *Rev. Sci. Instrum.* **66**, 11 (November 1995) pp. 5153–5161.

Mossessian, D., P. Heimann, E. Gullikson, R.K. Kaza, J. Chin, and J.L. Akre, "Transmission grating spectrometer for characterization of undulator radiation," *Nucl. Instrum. Methods* (1994).

8.0.1 Nelson, A.J., G. Berry, A. Rockett, D.K. Shuh, J.A. Carlisle, D.G. Sutherland, and L.J. Terminello, "Observation of core-level binding energy shifts between the (100) surface and bulk atoms of epitaxial $CuInSe_2$," *Appl. Phys. Lett.* (1997).

8.0.1 Nilsson, A., M.G. Weinelt, T. Wiell, P. Bennich, O. Karis, N. Wassdahl, J. Stöhr, and M.G. Samant, "Local probing of the surface chemical bond using x-ray emission spectroscopy," *Appl. Phys. Lett.* (1996).

7.0.1 Nilsson, P., J. Kanski, J.V. Thordson, T.G. Andersson, J.E. Nordgren, J. Guo, and M. Magnuson, "Electronic structure of buried Si layers in GaAs(001) as studied by soft-x-ray emission," *Phys. Rev. B* **52**, 12 (September 1995), pp. 8643–8645.

7.0.1 Nordgren, J.E., "Soft x-ray emission spectroscopy in the nineties," *J. Electron Spectros. Relat. Phenom.* **78** (1996) p. 25.

7.0.1 Nordgren, J.E., "Soft x-ray emission spectroscopy. The new look.," *Phys. Scr., T.* **61** (1996) pp. 32–37.

7.0.1 Nordgren, J.E., and N. Wassdahl, "Soft x-ray fluorescence spectroscopy using tunable synchrotron radiation," *J. Electron Spectros. Relat. Phenom.* **72** (1995) pp. 273–280.

7.0.1 Nordgren, J.E., P.N. Glans, K.M. Gunnelin, J. Guo, P.I. Skytt, C. Såthe, and N. Wassdahl, "Resonant soft x-ray fluorescence spectra of free molecules," *J. Appl. Phys.* (in press).

8.0.1 Osborn, K.D., and T.A. Callcott, "Two new optical designs for soft x-ray spectrometers using variable-line-space gratings," *Rev. Sci. Instrum.* **66** (May 1995) p. 3131.

Padmore, H.A., and T. Warwick, "New developments in soft x-ray monochromators for 3rd generation synchrotron radiation sources," *J. Electron Spectros. Relat. Phenom.* **75** (1995) p. 9.

8.0.1 Perera, R.C., J. Jia, T.A. Callcott, J.A. Carlisle, L.J. Terminello, F.J. Himpsel, and D.L. Ederer, "Resonant inelastic scattering in localized solid systems by soft x-ray fluorescence spectroscopy," *J. Electron Spectros. Relat. Phenom.* **79** (1996) p. 139.

Reich, T., Z. Hussain, E. Moler, M. Blackwell, G. Kaindl, D.A. Shirley, and M. Howells, "High resolution in the soft x-ray range from a toroidal grating monochromator," *Rev. Sci. Instrum.* **64**, 9 (September 1993).

7.0.1 Rightor, E.G., A.P. Hitchcock, H. Ade, R.D. Leapman, S.G. Urquhart, A. Smith, G.E. Mitchell, D. Fischer, H. Shin, and T. Warwick, "Spectromicroscopy of poly(ethylene terephthalate): comparison of spectra and radiation damage rates in x-ray absorption and electron energy loss," *J. Chem. Phys.* (October 1996).

6.3.2 Samson, J.A.R., W.C. Stolte, Z.X. He, J.N. Cutler, and D.L. Hansen, "Postcollision interactions in the auger decay of the Ar L shell," *Phys. Rev. A* **54**, 3 (September 1996) pp. 2099–2106.

9.0.1 Samson, J.A.R., Z.X. He, R. Moberg, W.C. Stolte, and J.N. Cutler, "Recent experiments in atomic double photoionization," *Can. J. Phys.* (in press).

9.0.1 Samson, J.A.R., Z.X. He, W.C. Stolte, and J.N. Cutler, "Multiple photoionization of free atoms," *J. Electron Spectros. Relat. Phenom.* (1995).

Schlueter, R., "Undulators for short wavelength FEL amplifiers," *Nucl. Instrum. Methods* (1995) pp. 44–47.

Schlueter, R., and S. Marks, "Three dimensional pure permanent magnet undulator design theory," *IEEE Trans. Magn.* (July 1996).

Schlueter, R., D.E. Humphries, and J. Tanabe, "Pure permanent magnet harmonics corrector ring," *Nucl. Instrum. Methods* (April 1995).

Schlueter, R., S. Marks, C. Loper, and K. Halbach, "Passive temperature compensation in hybrid magnets with application to the Fermilab stacker and recycler ring dipole design," *IEEE Trans. Magn.* (July 1996).

BTF Schoenlein, R., W. Leemans, A.H. Chin, P. Volfbeyn, T.E. Glover, P. Balling, M. Zolotorev, K.-J. Kim, S. Chattopadhyay, and C.V. Shank, "Femtosecond x-ray pulses at 0.4 Å by 90° Thomson scattering: a new tool for probing structural dynamics of materials," *Science* **274**, 236 (1996).

9.0.1 Schulz, K., G. Kaindl, M. Domke, J.D. Bozek, P.A. Heimann, A.S. Schlachter, and J.M. Rost, "Observation of new rydberg series and resonances in doubly excited helium at ultrahigh resolution," *Phys. Rev. Lett.* **77**, 15 (October 1996) pp. 3086–3089.

7.0.1 Shin, H.J., K. Jeong, D.C. Johnson, S.D. Kevan, M. Noh, and T. Warwick, "Study of TiSe2/NbSe2 superlattice with use of scanning transmission x-ray microscope," *J. Korean Phys. Soc.* (in press).

7.0.1 Skytt, P., P. Glans, K.M. Gunnelin, J. Guo, and J.E. Nordgren, "Lifetime vibrational interference effects in resonantly-excited x-ray emission spectra of CO," *Phys. Rev. A* **55**, 1 (January 1997) pp. 146–154.

7.0.1 Skytt, P.I., J. Guo, N. Wassdahl, J.E. Nordgren, Y. Luo, and H. Agren, "Probing symmetry breaking upon core excitation with resonant x-ray fluorescence," *Phys. Rev. A* **52**, 5 (November 1995) p. 3572.

7.0.1 Skytt, P.I., P.N. Glans, J. Guo, K.M. Gunnelin, C. Såthe, J.E. Nordgren, F. Gel'mukhanov, A. Cesar, and H. Agren, "Quenching of symmetry breaking in resonant inelastic x-ray scattering by detuned excitation," *Phys. Rev. Lett.* **77**, 25 (December 1996) pp. 5035–5038.

7.0.1 Skytt, P.I., P.N. Glans, K.M. Gunnelin, J. Guo, J.E. Nordgren, and H. Agren, "Combined analysis of x-ray emission and adsorption for spectral assignments: The O-K spectra of CO_2," *Phys. Rev. A.* (in press).

7.0.1 Skytt, P.I., P.N. Glans, K.M. Gunnelin, J. Guo, J.E. Nordgren, Y. Luo, and H. Agren, "Role of screening and angular distributions in resonant x-ray emission of CO," *Phys. Rev. A* **55**, 1 (January 1997) pp. 134–145.

Smith, N.V., and H.A. Padmore, "X-ray magnetic circular dichroism spectroscopy and microscopy," *Mater. Res. Bull.* (April 1995) pp. 41–43.

Smith, N.V., and M. Howells, "Whispering galleries for the production of circularly polarized synchrotron radiation in the XUV region," *Nucl. Instrum. Methods* **347** (1994) pp. 115–118.

6.3.2 Soufli, R., and E. Gullikson, "Reflectance measurements on clean surfaces for the determination of optical constants of silicon in the EUV/soft x-ray region," *Appl. Opt.* (1996).

9.0.2 Suits, A., P.A. Heimann, X. Yang, M.D. Evans, C. Hsu, K. Lu, and Y.T. Lee, "A differentially pumped harmonic filter on the chemical dynamics beamline at the Advanced Light Source," *Rev. Sci. Instrum.* **66**, 10 (October 1995) pp. 4841–4844.

8.0.1 Sutherland, D.G., F.J. Himpsel, L.J. Terminello, K.M. Baines, J.A. Carlisle, I. Jimenez, D.K. Shuh, and W.M. Tong, "The chemisorption of $H_2C[Si(CH_3)_3]_2$ and $Si_6(CH_3)_{12}$ on Si(100) surfaces," *J. Appl. Phys.* (in press).

6.3.2 Sutherland, D.G., H. Akatsu, M. Copel, F.J. Himpsel, T.A. Callcott, J.A. Carlisle, D.L. Ederer, J. Jia, I. Jimenez, R.C. Perera, D.K. Shuh, L.J. Terminello, and W.M. Tong, "Stoichiometry reversal in the growth of thin oxynitride films on Si(100) surfaces," *J. Appl. Phys.* **78**, 11 (December 1995) pp. 6761–6769.

6.3.2 Sutherland, D.G., H. Akatsu, M. Copel, F.J. Himpsel, T.A. Callcott, J.A. Carlisle, D.L. Ederer, J. Jia, I. Jimenez, R.C. Perera, D.K. Shuh, L.J. Terminello, and W.M. Tong, "Stoichiometry reversal and depth-profiling in the growth of thin oxynitride films with N_2O on Si(100) surfaces," *J. Electron Spectros. Relat. Phenom.* **80** (1996) pp. 133–136.

8.0.1 Sutherland, D.G., K. Pakbaz, L.J. Terminello, S.C. Williams, P. Elliker, G. Fox, T.W. Hagler, H.W. Lee, T.A. Callcott, J.A. Carlisle, D.L. Ederer, F.J. Himpsel, J. Jia, I. Jimenez, D.K. Shuh, and W.M. Tong, "Photo-oxidation of MEH-PPV polymers studied by core-level photoabsorption spectroscopy," *Appl. Phys. Lett.* **68** (1996), p. 2046.

7.0.1 Tobin, J.G., K.W. Goodman, F.O. Schumann, R.F. Willis, J. Kortright, J. Denlinger, E. Rotenberg, T. Warwick, and N.V. Smith, "Generalized description of magnetic x-ray circular dichroism in Fe 3p photoelectron emission," *J. Vac. Sci. Technol.* (September 1996).

7.0.1 Tobin, J.G., K.W. Goodman, F.O. Schumann, R.F. Willis, J. Kortright, J. Denlinger, E. Rotenberg, T. Warwick, and N.V. Smith, "Direct extraction of exchange splittings from magnetic x-ray dichroism in photoelectron spectroscopy," *Phys. Rev. Lett.* (in press).

7.0.1 Tobin, J.G., K.W. Goodman, G.J. Mankey, R.F. Willis, J. Denlinger, E. Rotenberg, and T. Warwick, "Magnetic x-ray dichroism in the spectroscopy of ultrathin magnetic alloy films," *J. Vac. Sci. Technol. B* **14**, 4 (July/Aug 1996), pp. 3171–3175.

7.0.1 Tobin, J.G., K.W. Goodman, G.J. Mankey, R.F. Willis, J. Denlinger, E. Rotenberg, and T. Warwick, "Magnetic x-ray linear dichroism in the photoelectron spectroscopy of ultra-thin magnetic alloy films," *J. Appl. Phys.* **79**, 8 (April 1996) p. 5626.

7.0.1 Tonner, B.P., D.J. Dunham, and T.C. Droubay, "A photoemission microscope with a hemispherical capacitor energy filter," *J. Electron Spectros. Relat. Phenom.* (in press).

7.0.1 Tonner, B.P., D.J. Dunham, T.C. Droubay, J. Kikuma, J. Denlinger, E. Rotenberg, and T. Warwick, "Development of electron spectromicroscopy," *J. Electron Spectros. Relat. Phenom.* **75** (1995) pp. 309–332.

Van Dorssen, G.E., M.D. Roper, H.A. Padmore, A.D. Smith, and G.N. Greaves, "Core excitons in silicon and silicon oxides," *Rev. Sci. Instrum.* **66** (1995) p. 1480.

Van Hove, M.A., A. Kaduwela, H. Xiao, W. Schattke, and C.S. Fadley, "Application of photoelectron diffraction theory to circular dichroism and spin-polarized photoelectron emission," *J. Electron Spectros. Relat. Phenom.* **80**, (1996) pp. 137–142.

7.0.1 Warwick, T., H.A. Padmore, H. Ade, A.P. Hitchcock, E.G. Rightor, and B.P. Tonner, "Soft x-ray spectromicroscopy development for materials science at the Advanced Light Source," *J. Electron Spectros. Relat. Phenom.* (in press).

Warwick, T., M. Howells, and M. Shlezinger, "A variable radius mirror for imaging the exit slit of an SGM undulator beamline at the Advanced Light Source," *Rev. Sci. Instrum.* **66** (March 1995) pp. 2270–2272.

Warwick, T., N. Andresen, G.J. Portmann, and A. Jackson, "Performance of photon position monitors for undulator beams at the Advanced Light Source," *Rev. Sci. Instrum.* **66** (1995) p. 1985.

8.0.1 Wehlitz, R., I.A. Sellin, O.A. Hemmers, S. Whitfield, P.N. Glans, H. Wang, D.W. Lindle, B. Langer, N. Berrah, J. Viefhaus, and U. Becker, "Photon energy dependence of ionization-excitation in helium at medium energies," *J. Phys. B* **30** (1997) pp. 51–58.

8.0.1 Weinelt, M.G., A. Nilsson, M. Magnuson, T. Wiell, N. Wassdahl, O. Karis, A. Föhlisch, N. Martensson, M.G. Samant, and J. Stöhr, "Resonant photoemission at the 2p edges of Ni: resonant raman and interference effects," *Phys. Rev. Lett.* **78** (1997) p. 967.

8.0.1 Weinelt, M.G., A. Nilsson, O. Karis, M. Magnuson, T. Wiell, N. Wassdahl, N. Martensson, J. Stöhr, and M.G. Samant, "Resonant photoemission and resonant inelastic x-ray scattering: coherent vs. incoherent processes," *World Scientific* (1996).

9.0.2 Wu, C., F. Chen, T. Hung, and D.L. Judge, "Studies of fluorescence from photoexcitation of N_2 and CO_2 in the 28–100 eV region," *J. Electron Spectros. Relat. Phenom.* **80**, 13 (September 1996) pp. 13–16.

7.0.1 Wu, S.Z., F.O. Schumann, R.F. Willis, K.W. Goodman, J.G. Tobin, and R. Carr, "Magnetic dichroism effect of binary alloys using circularly polarized x-rays," *J. Vac. Sci. Technol.* (in press).

Young, A.T., H.A. Padmore, and N.V. Smith, "X-ray magnetic microscopy and spectroscopy using a third generation synchrotron radiation source," *J. Vac. Sci. Technol. A* (in press).

Zheng, Y., E. Moler, E. Hudson, Z. Hussain, and D.A. Shirley, "Structural determination of NH_3 adsorbed on Ni(100) using angle-resolved photoemission extended fine-structure spectroscopy," *Phys. Rev. B* **48**, 7 (August 1993).

8.0.1 Zhou, L., T.A. Callcott, Q.Y. Dong, J. Jia, K.E. Miyano, D.L. Ederer, and R.C. Perera, "A study of the electronic structure of CdS and ZnS using soft-x-ray emission spectroscopy," *Phys. Rev. B* (1997).

8.0.1 Zhou, L., T.A. Callcott, Q.Y. Dong, K.E. Miyano, D.L. Ederer, and R.C. Perera, "A study of the sulphur $L_{2,3}$ and zinc $M_{2,3}$ soft x-ray emission spectra in CdS and ZnS," *Phys. Rev.* (in press).

Refereed Conference Proceedings

7.0.1 Agren, H., Y. Luo, F. Gel'mukhanov, J. Guo, P.I. Skytt, N. Wassdahl, and J.E. Nordgren, "Symmetry selective resonant inelastic x-ray scattering," in *Physica B*, Proceedings of Conference on x-ray absorption fine structure, August 28–September 2, 1994, Berlin Germany.

12.0 Beguiristain, H., J.H. Underwood, M. Koike, P.J. Batson, H. Medecki, S. Rekawa, K.H. Jackson, and D.T. Attwood, "Characterization of thermal distortion effects on beamline optics for EUV interferometry and soft x-ray microscopy," in *Rev. Sci. Instrum.*, Proceedings of Synchrotron Radiation Instrumentation–95, October 18–25, 1995, Argonne IL.

9.0.1 Berrah, N., "High resolution photoionization and photoexcitation using synchrotron radiation," in *AIP Conference Proceedings 360*, Proceedings of The XIX International Conference on the Physics of Electronic and Atomic Collisions, July 26–August 1, 1995, Whistler, B.C. Canada.

5.0 Beuville, E., C.W. Cork, T. Earnest, W. Mar, J. Millaud, D. Nygren, H.A. Padmore, B. Turko, G. Zizka, P. Datte, and N. Xuong, "A 2D smart pixel detector for time resolved crystallography," in *Rev. Sci. Instrum.*, Proceedings of Synchrotron Radiation Instrumentation–95, October 18–25, 1995, Argonne IL.

5.0.2 Beuville, E., J.-F. Beche, C.W. Cork, V. Douence, T. Earnest, J. Millaud, D. Nygren, H.A. Padmore, B. Turko, G. Zizka, P. Datte, and N. Xuong, "Two-dimensional pixel array image sensor for protein crystallography," in *Optics for High-Brightness Synchrotron Radiation Beamlines II*, Proceedings of 1996 SPIE, August 5–9, 1996, Denver CO.

BTF Chattopadhyay, S., A. Chin, E. Glover, K.-J. Kim, W. Leemans, C.V. Shank, and R. Schoenlein, "Femtosecond X-rays by Orthogonal Thomson Scattering," in *Proceedings* of OSA Conference on High Field Interactions and Short Wavelength Generation, August 1994, St. Malo, France.

8.0.1 Ederer, D.L., K.E. Miyano, W.L. O'Brien, T.A. Callcott, Q.Y. Dong, J. Jia, D.R. Mueller, J. Rubensson, R.C. Perera, and R. Shuker, "Research opportunities in fluorescence with third generation synchrotron radiation sources," in *Series E: Applied Sciences*, Proceedings of NATO Summer School on Applications with Third Generation Synchrotron Sources.

9.0.1 Goldberg, K., E. Tejnil, and J. Bokor, "A 3D numerical study of pinhole diffraction to predict the accuracy of EUV point diffraction interferometers," in *OSA Trends in Optics and Photonics Volume on Extreme Ultraviolet Lithography*, Proceedings of OSA Trends in Optics and Photonics, 1996.

10.3.2 Goldberg, K., H. Beguiristain, J. Bokor, H. Medecki, D.T. Attwood, K.H. Jackson, E. Tejnil, and G. Sommargren, "Progress toward lambda/20 EUV interferometry," in *J. Vac. Sci. Technol. B*, Proceedings of Electron Ion and Photon Beam Conference, May 30–June 3, 1995, Scottsdale AZ.

9.0.1 Goldberg, K., H. Beguiristain, J. Bokor, H. Medecki, K.H. Jackson, D.T. Attwood, G. Sommargren, J.P. Spallas, and R. Hostetler, "At-wavelength testing of optics for EUV," in *Proceedings of the SPIE 2437*, 347, Proceedings of 1995 SPIE Conference on Microlithography, San Jose CA.

9.0.1 Goldberg, K., H. Beguiristain, J. Bokor, H. Medecki, K. Jackson, and D.T. Attwood, "Point diffraction interferometry at EUV wavelengths," in *OSA Trends in Optics and Photonics Volume on Extreme Ultraviolet Lithography*, Proceedings of OSA Trends in Optics and Photonics, 1994.

6.3.2 Gullikson, E., R. Korde, L.R. Canfield, and R.E. Vest, "Stable silicon photodiodes for absolute intensity measurements in the VUV and soft x-ray regions," in *J. Electron. Spectros. Relat. Phenom.*, Proceedings of 11th International Conference on Vacuum Ultraviolet Radiation Physics, August 27–September 1, 1995, Tokyo Japan.

7.0.1 Guo, J., N. Wassdahl, P.I. Skytt, S. Butorin, L.C. Duda, C.J. Englund, and J.E. Nordgren, "An end station for polarization and excitation energy selective soft x-ray fluorescence spectroscopy," in *Rev. Sci. Instrum.*, Proceedings of Synchrotron Radiation Instrumentation–94, July 18–22, 1994, Stony Brook NY.

Heimann, P., D. Mossessian, T. Warwick, C. Wang, S. Marks, H.A. Padmore, B.M. Kincaid, and E. Gullikson, "Experimental characterization of Advanced Light Source undulator radiation," in *Rev. Sci. Instrum.*, Proceedings of Synchrotron Radiation Instrumentation–95, October 18–25, 1995, Argonne IL.

9.0.1 Heimann, P., J.D. Bozek, W.R. McKinney, S.C. Irick, H.A. Padmore, G. Kaindl, and K. Schulz, "Very-high resolution in the soft x-ray region on beamline 9.0.1 at the Advanced Light Source," in *Rev. Sci. Instrum.*, Proceedings of Synchrotron Radiation Instrumentation–95, October 18–25, 1995, Argonne IL.

9.0.2 Heimann, P.A., M. Koike, C. Hsu, M.D. Evans, C. Ng, D.A. Blank, X. Yang, C. Flaim, A. Suits, and Y.T. Lee, "Performance of the VUV high resolution and high flux beamline for chemical dynamics studies at the Advanced Light Source," in *Optics for High-Brightness Synchrotron Radiation Beamlines II*, Proceedings of 1996 SPIE, August 5–9, 1996, Denver CO.

9.0.1 Heiser, F., N. Saito, K. Wieliczek, O.A. Hemmers, N. Berrah, and U. Becker, "Angle resolved fragmentation studies of small molecules," in *AIP Conference Proceedings 360*, Proceedings of The XIX International Conference on the Physics of Electronic and Atomic Collisions, July 26–August 1, 1995, Whistler, B.C. Canada.

8.0.1 Himpsel, F.J., D.A. Lapiano-Smith, H. Akatsu, J.A. Carlisle, E.A. Hudson, L.J. Terminello, T.A. Callcott, J. Jia, M.G. Samant, J. Stöhr, D.L. Ederer, and R.C. Perera, "Surface physics with synchrotron radiation," in *Proceedings* of Symposium of Synchrotron Radiation Techniques in Industrial Research, August 1–5, 1994, Washington D.C.

8.0.1 Himpsel, F.J., H. Akatsu, J.A. Carlisle, L.J. Terminello, E.A. Hudson, J. Jia, T.A. Callcott, R.C. Perera, M.G. Samant, J. Stöhr, and D.L. Ederer, "Core level spectroscopy of thin oxides and oxynitrides," in *Electrochemical Society*, Proceedings of Symposium on Silicon Nitride and Silicon Dioxide Thin Insulating Films, May 1–5, 1994, San Francisco CA.

9.0.1 Hitchcock, A.P., and E. Rühl, "Inner-shell excitation, relaxation and fragmentation of cluster beams and molecules," in *AIP Conference Proceedings 360*, Proceedings of The XIX International Conference on the Physics of Electronic and Atomic Collisions, July 26–August 1, 1995, Whistler, B.C. Canada.

9.3.2 Huff, W.R.A., Y. Chen, S.A. Kellar, E. Moler, H. Wu, Z. Hussain, and D.A. Shirley, "Angle-resolved photoemission extended fine structure: multiple layers of emitters and multiple initial states," in *J. Electron. Spectros. Relat. Phenom.*, Proceedings of 11th International Conference on Vacuum Ultraviolet Radiation Physics, August 27–September 1, 1995, Tokyo Japan.

9.3.2 Hussain, Z., W.R.A. Huff, S.A. Kellar, E.J. Moler, P. Heimann, W.R. McKinney, H.A. Padmore, C.S. Fadley, and D.A. Shirley, "High resolution soft x-ray bending magnet beamline 9.3.2 with circularly polarized radiation capability at the Advanced Light Source," in *J. Electron. Spectros. Relat. Phenom.*, Proceedings of 11th International Conference on Vacuum Ultraviolet Radiation Physics, August 27–September 1, 1995, Tokyo Japan.

9.3.2 Hussain, Z., W.R.A. Huff, S.A. Kellar, E. Moler, P. Heimann, W.R. McKinney, C. Cummings, T. Lauritzen, P. McKean, J. Palomares, H. Wu, W.Y. Zheng, H.A. Padmore, C.S. Fadley, and D.A. Shirley, "High-resolution beamline 9.3.2 in the energy range 30–1500 eV at the Advanced Light Source: design and performance," in *Rev. Sci. Instrum.*, Proceedings of Synchrotron Radiation Instrumentation–95, October 18–25, 1995, Argonne IL.

Irick, S.C., R. Krishna Kaza, and W.R. McKinney, "Obtaining three-dimensional height profiles from a two-dimensional slope measuring instrument," in *Rev. Sci. Instrum.*, Proceedings of Synchrotron Radiation Instrumentation–94, July 18–22, 1994, Stony Brook NY.

Jackson, A., "Operational experiences at the Advanced Light Source," in *Rev. Sci. Instrum.*, Proceedings of Synchrotron Radiation Instrumentation–95, October 18–25, 1995, Argonne IL.

8.0.1 Jia, J., T.A. Callcott, J. Yurkas, A.W. Ellis, F.J. Himpsel, M.G. Samant, J. Stöhr, D.L. Ederer, J.A. Carlisle, E.A. Hudson, L.J. Terminello, D.K. Shuh, and R.C. Perera, "First experimental results from IBM/TENN/TULANE/LLNL/LBL undulator beamline at the Advanced Light Source," in *Rev. Sci. Instrum.*, Proceedings of Synchrotron Radiation Instrumentation–94, July 18–22, 1994, Stony Brook NY.

Jones, G., S. Ryce, D.W. Lindle, B.A. Karlin, J.C. Woicik, and R.C. Perera, "Design and performance of the Advanced Light Source double-crystal monochromator," in *Rev. Sci. Instrum.*, Proceedings of Synchrotron Radiation Instrumentation–94, July 18–22, 1994, Stony Brook NY.

9.0.1 Kaindl, G., K. Schulz, J.D. Bozek, A.S. Schlachter, and P. Heimann, "Double-excited helium studied at ultra-high resolution," in *AIP Conference Proceedings 360*, Proceedings of The XIX International Conference on the Physics of Electronic and Atomic Collisions, July 26–August 1, 1995, Whistler, B.C. Canada.

9.0.1 Kaindl, G., K. Schulz, J.D. Bozek, A.S. Schlachter, and P. Heimann, "Photoionization study of doubly excited helium at ultra-high resolution," in *J. Electron. Spectros. Relat. Phenom.*, Proceedings of 11th International Conference on Vacuum Ultraviolet Radiation Physics, August 27–September 1, 1995, Tokyo Japan.

Koike, M., P.A. Heimann, and T. Namioka, "Design of a high-resolution step-and-scan type monochromator capable of tuning to undulator radiation over a wavelength range of 80–180nm," in *Optics for High-Brightness Synchrotron Radiation Beamlines II*, Proceedings of 1996 SPIE, August 5–9, 1996, Denver CO.

9.3.2 Kortright, J., M. Rice, Z. Hussain, H.A. Padmore, A. Adamson, T. Huff, A.T. Young, E. Moler, S.A. Kellar, R. Ynzunza, J. Palomares, H. Daimon, E.D. Tober, and C.S. Fadley, "Polarization measurement and vertical aperture optimization for obtaining circularly polarized bend-magnet radiation," in *Rev. Sci. Instrum.*, Proceedings of Synchrotron Radiation Instrumentation–95, October 18–25, 1995, Argonne IL.

Krebs, G.F., T. Lauritzen, and W. Thur, "Survey and alignment at the Advanced Light Source," in *Proceedings* of Fourth International Workshop on Accelerator Alignment, November 14–17, 1995, Tsukuba JAPAN.

9.0.1 Langer, B., N. Berrah, J.D. Bozek, O.A. Hemmers, D. Lindle, and O.F. Toader, "High resolution angle resolved photoelectron spectroscopy at the Advanced Light Source: The ar 3s–1 → np resonances," in *AIP Conference Proceedings 360*, Proceedings of The XIX International Conference on the Physics of Electronic and Atomic Collisions, July 26–August 1, 1995, Whistler, B.C. Canada.

Lawniczak-Jablonska, K., J. Jia, L. Lin, T.A. Callcott, A. Asfaw, J.A. Carlisle, L.J. Terminello, F.J. Himpsel, D.L. Ederer, J.H. Underwood, and R.C. Perera, "Resonant inelastic scattering in dilute magnetic semiconductors by soft x-ray fluorescence spectroscopy," in *Proceedings* of the International Workshop on Resonant Inelastic Soft X-ray Scattering, Walberberg Germany.

9.3.2 Len, P., F. Zhang, A. Kaduwela, S. Thevuthasan, M.A. Van Hove, and C.S. Fadley, "Photoelectron holography: prospects and limitations," in *J. Electron. Spectros. Relat. Phenom.*, Proceedings of 11th International Conference on Vacuum Ultraviolet Radiation Physics, August 27–September 1, 1995, Tokyo Japan.

4.0.1 Martynov, V., A.T. Young, and H.A. Padmore, "Elliptically polarizing undulator beamline 4.0.1 for magnetic spectroscopy at the Advanced Light Source," in *Optics for High-Brightness Synchrotron Radiation Beamlines II*, Proceedings of 1996 SPIE, August 5–9, 1996, Denver CO.

Martynov, V., W.R. McKinney, and H.A. Padmore, "An elliptical wiggler beamline for the Advanced Light Source," in *Rev. Sci. Instrum.*, Proceedings of Synchrotron Radiation Instrumentation–95, October 18–25, 1995, Argonne IL.

McKinney, W.R., D. Mossessian, E. Gullikson, and P. Heimann, "Efficiency and stray light measurements and calculations of diffraction gratings for the Advanced Light Source," in *Rev. Sci. Instrum.*, Proceedings of Synchrotron Radiation Instrumentation–94, July 18–22, 1994, Stony Brook NY.

6.1.2 Meyer-Ilse, W., H. Medecki, C. Magowan, R.L. Balhorn, M.M. Moronne, and D.T. Attwood, "Advanced microscopy: the new high resolution zone-plate microscope at the Advanced Light Source in Berkeley," in *JMSA Proceedings Microscopy and Microanalysis 1995*, August 13–15, 1995, Kansas City MO.

9.3.2 Moler, E., Z. Hussain, R.M. Duarte, and M.R. Howells, "Design and performance of a soft x-ray interferometer for ultra-high resolution fourier transform spectroscopy," in *J. Electron. Spectros. Relat. Phenom.*, Proceedings of 11th International Conference on Vacuum Ultraviolet Radiation Physics, August 27–September 1, 1995, Tokyo Japan.

9.3.1 Ng, W., G. Jones, R.C. Perera, D.L. Hansen, J.M. Daniels, O.A. Hemmers, P.N. Glans, S. Whitfield, H. Wang, and D.W. Lindle, "First results from the high-brightness x-ray spectroscopy beamline 9.3.1 at Advanced Light Source," in *Rev. Sci. Instrum.*, Proceedings of Synchrotron Radiation Instrumentation–95, October 18–25, 1995, Argonne IL.

Ng, W., R.C. Perera, J.H. Underwood, S. Singh, H. Sokak, and F. Cerrina, "Installation of the MAXIMUM microscope at the Advanced Light Source," in *Rev. Sci. Instrum.*, Proceedings of Synchrotron Radiation Instrumentation–95, October 18–25, 1995, Argonne IL.

Padmore, H.A., M. Howells, S.C. Irick, R. Sandler, T.R. Renner, and Y. Koo, "Some new schemes for producing high-accuracy elliptical x-ray mirrors by elastic bending," in *Optics for High-Brightness Synchrotron Radiation Beamlines II*, Proceedings of 1996 SPIE, August 5–9, 1996, Denver CO.

5.0 Padmore, H.A., T. Earnest, S. Kim, A.C. Thompson, and A. Robinson, "A beamline for macromolecular crystallography at the Advanced Light Source," in *Rev. Sci. Instrum.*, Proceedings of Synchrotron Radiation Instrumentation–94, July 18–22, 1994, Stony Brook NY.

9.3.1 Perera, R.C., G. Jones, and D.W. Lindle, "High-brightness beamline for x-ray spectroscopy at the Advanced Light Source," in *Rev. Sci. Instrum.*, Proceedings of Synchrotron Radiation Instrumentation–94, July 18–22, 1994, Stony Brook NY.

Renner, T.R., H.A. Padmore, and R. Keller, "Design and performance of the Advanced Light Source diagnostic beamline," in *Rev. Sci. Instrum.*, Proceedings of Synchrotron Radiation Instrumentation–95, October 18–25, 1995, Argonne IL.

Schoenlein, R.W., A.H. Chin, T.E. Glover, C.V. Shank, W.P. Leemans, P. Volfbeyn, K.-J. Kim, and S. Chattopadhyay, "Femtosecond x-rays generated via Thomson scattering of Terawatt laser pulses with relativistic electrons," in *Proceedings* of OSA Conference on Ultrafast Phenomena, May 1996, San Diego, CA.

9.0.1 Schulz, K., G. Kaindl, M. Domke, J.D. Bozek, P.A. Heimann, and A.S. Schlachter, "High resolution photoionization of doubly excited helium," in *Verhandlungen der Deutschen Physikalischen Gesellschaft*, Proceedings of Frühjahrstagung der Deutschen Physikalischen Gesellschaft, March 18–21, 1996, Rostock Germany.

Shirley, D.A., B.L. Petersen, and M. Howells, "Electron spectroscopy into the twenty-first century," in *Proceedings* of the International Conference on Electron Spectroscopy (ICES), Rome Italy.

9.0.1 Tejnil, E., K.A. Goldberg, H. Medecki, H. Beguiristain, J. Bokor, and D.T. Attwood, "Phase-shifting point diffraction interferometry for at-wavelength testing of lithographic optics," in *OSA Trends in Optics and Photonics Volume on Extreme Ultraviolet Lithography*, Proceedings of OSA Trends in Optics and Photonics, 1996.

9.0.1 Tejnil, E., K. Goldberg, E.H. Anderson, and J. Bokor, "Zonal placement errors in zone plane lenses," in *OSA Trends in Optics and Photonics Volume on Extreme Ultraviolet Lithography*, Proceedings of OSA Trends in Optics and Photonics, 1996.

9.3.2 Tober, E., R. Ynzunza, J. Palomares, A. Kaduwela, Z. Wang, F. Zhang, H. Daimon, Z. Hussain, and C.S. Fadley, "Photoelectron diffraction from interface atoms in Gd thin films on W(110)," in *J. Electron. Spectros. Relat. Phenom.*, Proceedings of 11th International Conference on Vacuum Ultraviolet Radiation Physics, August 27–September 1, 1995, Tokyo Japan.

10.3.1 Underwood, J.H., A.C. Thompson, J. Kortright, and K.L. Chapman, "Focusing x-rays to a 1μm spot using elastically bent, graded multilayer coated mirrors," in *Rev. Sci. Instrum.*, Proceedings of Synchrotron Radiation Instrumentation–95, October 18–25, 1995, Argonne IL.

6.3.2 Underwood, J.H., E. Gullikson, M. Koike, P.J. Batson, P.E. Denham, K.D. Franck, R.E. Tackaberry, and W.F. Steele, "Calibration and standards beamline 6.3.2 at the Advanced Light Source," in *Rev. Sci. Instrum.*, Proceedings of Synchrotron Radiation Instrumentation–95, October 18–25, 1995, Argonne IL.

7.0.1 Warwick, T., P. Heimann, D. Mossessian, W.R. McKinney, and H.A. Padmore, "Performance of a high resolution, high flux density SGM undulator beamline at the Advanced Light Source," in *Rev. Sci. Instrum.*, Proceedings of Synchrotron Radiation Instrumentation–94, July 18–22, 1994, Stony Brook NY.

7.3.1 Wheeler, B., W.R. McKinney, Z. Hussain, and H.A. Padmore, "Preliminary optical design of a varied line-space spectograph for the multi-channel detection of near-edge x-ray absorption fine structure (NEXAFS) spectra in the 280–550 eV energy range," in *Optics for High-Brightness Synchrotron Radiation Beamlines II*, Proceedings of 1996 SPIE, August 5–9, 1996, Denver CO.

Winn, B, X. Hao, C. Jacobsen, J. Kirz, J. Miao, S. Wirick, H. Ade, C. Buckley, M. Howells, S.L. Hulbert, I. McNulty, and T. Oversluizen, "Considerations for a soft x-ray spectromicroscopy beamline," in *Optics for High-Brightness Synchrotron Radiation Beamlines II*, Proceedings of 1996 SPIE, August 5–9, 1996, Denver CO.

9.0.2 Wu, C., D.L. Judge, T. Matsui, and K. Ito, "Fluorescence excitation function for producing NI and high-resolution, high-temperature, absorption spectra of N_2 in the EUV region," in *J. Electron. Spectros. Relat. Phenom.*, Proceedings of 11th International Conference on Vacuum Ultraviolet Radiation Physics, August 27–September 1, 1995, Tokyo Japan.

9.0.2 Wu, C., F. Chen, and D.L. Judge, "Temperature-dependent absorption and emission studies of atmospheric gases with application of planetary atmospheres," in *J. Electron. Spectros. Relat. Phenom.*, Proceedings of 11th International Conference on Vacuum Ultraviolet Radiation Physics, August 27–September 1, 1995, Tokyo Japan.

9.3.2 Ynzunza, R., E. Tober, J. Palomares, Z. Wang, H. Xiao, F. Zhang, H. Daimon, Z. Hussain, and C.S. Fadley, "Full-solid-angle photoelectron diffraction on W(110) with surface and bulk resolution," in *J. Electron. Spectros. Relat. Phenom.*, Proceedings of 11th International Conference on Vacuum Ultraviolet Radiation Physics, August 27–September 1, 1995, Tokyo Japan.

Young, T., E.H. Hoyer, S. Marks, V. Martynov, H.A. Padmore, D. Plate, and R. Schlueter, "Elliptically polarizing undulator beamlines at the Advanced Light Source," in *Rev. Sci. Instrum.*, Proceedings of Synchrotron Radiation Instrumentation–95, October 18–25, 1995, Argonne IL.

Conference Proceedings

Attwood, D., H. Medecki, W. Meyer-Ilse, E. Anderson, H.R. Beguiristain, J. Bokor, J. Brown, F. Cerrina, K. Goldberg, J. Heck, C. Magowan, D.K. Shuh, S. Singh, E. Tejnil, B.P. Tonner, J.H. Underwood, and T. Warwick, "X-ray microimaging at the sub-100nm scale," in *Proceedings* of U.S.-Japan Workshop on X-ray Optics "Technical Challenges," November 11–15, 1996.

Belkacem, A., H.A. Gould, B. Feinberg, N. Claytor, T. Dinneen, and R. Bossingham, "Knock-on electron emission in relativistic ion-atom collisions," in *Proceedings* of 1996 Annual Meeting of the Division of Atomic, Molecular, and Optical Physics, May 15–18, 1996, Ann Arbor MI.

Berrah, N., "Recent advances in VUV spectroscopy of atoms," in *Proceedings* of Annual Meeting of the Optical Society of America, Dallas TX.

9.0.1 Berrah, N., B. Langer, A.H. Farhat, O.A. Hemmers, and J.D. Bozek, "Angle resolved high resolution studies of the Xe $4d_{5/2} \rightarrow 6p$ resonances," in *Proceedings* of 17th International Conference on X-ray and Inner Shell Processes, September 9–13, 1996, Hamburg Germany.

9.0.1 Berrah, N., B. Langer, and F. Ahmad, "High resolution photoionization and photoexcitation using synchrotron radiation," in *Proceedings* of 210th American Chemical Society National Meeting, August 20–24, 1995, Chicago IL.

9.0.1 Berrah, N., O.F. Toader, B. Langer, J.D. Bozek, D.W. Lindle, and O.A. Hemmers, "Autoionization of Ar, Kr and Xe near the ns threshold—determination of partial cross section and beta parameter in ns-epsilon p transitions," in *Bull. Am. Phys. Soc.*, Proceedings of DAMOP Meeting of the American Physical Society, May 16–19, 1995, Toronto Canada.

9.0.1 Bozek, J.D., A.S. Schlachter, G. Kaindl, and K. Schulz, "Ultra-high resolution spectroscopy of the He doubly excited states," in *Proceedings* of Oeji International Seminar on Atomic and Molecular Photoionization, September 4–7, 1995, Tsukuba Japan.

9.0.1 Bozek, J.D., A.S. Schlachter, P. Heimann, G. Kaindl, and K. Schulz, "Ultra-high resolution at the Advanced Light Source: recent results from beamline 9.0.1," in *Bull. Am. Phys. Soc.*, Proceedings of DAMOP Meeting of the American Physical Society, May 16–19, 1995, Toronto Canada.

10.3.2 Brennen, R.A., M. Hecht, D. Wiberg, S.J. Manion, W.D. Bonivert, and J.M. Hruby, "LIGA and thick film lithography for thick structures," in *Proceedings* of Digest 28th Annual SCCAVS Symposium, Micromachining Workshop II, Technology and Applications, September 27–28, 1995, Anaheim CA.

10.3.2 Brennen, R.A., M. Hecht, D. Wiberg, S.J. Manion, W.D. Bonivert, J.M. Hruby, K.S. Pister, and E. Kruglick, "Fine pitch grids for an x-ray solar imaging spectrometer fabricated by optical lithography and XeF_2 etching," in *Proceedings* of 1995 SPIE: Microlithography and Metrology in Micromachining, October 23–24, 1995, Austin TX.

10.3.2 Brennen, R.A., M. Hecht, D. Wiberg, S.J. Manion, W.D. Bonivert, J.M. Hruby, M.L. Scholz, T.D. Stowe, T.W. Kenny, K.H. Jackson, and C.G. Khan-Malek, "Fabricating sub-collimating grids for an x-ray solar imaging spectrometer using LIGA techniques," in *Proceedings* of 1995 SPIE: Microlithography and Metrology in Micromachining, October 23–24, 1995, Austin TX.

10.3.2 Brennen, R.A., M. Hecht, D. Wiberg, S. Manion, D. Bonivert, J.M. Hruby, M.L. Scholz, T.D. Stowe, T.W. Kenny, K.H. Jackson, and C.K. Makel, "Fabrication of collimating grids for an x-ray solar telescope using LIGA methods," in *Proceedings* of High Aspect Ratio Microstructure Technology Conference (HARMST '95), July 3–5, 1995, Karlsruhe Germany.

6.1.2 Brown, J., C. Magowan, R.L. Balhorn, J. Heck, and W. Meyer-Ilse, "Biological applications of XM-1," in *Proceedings* of International Conference on X-ray Microscopy and Spectroscopy, August 5–9, 1996, Wurzburg Germany.

9.0.1 Caldwell, C., A. Menzel, S. Frigo, and M.O. Krause, "High-resolution photoemission from simple atoms and molecules," in *Proceedings* of Annual Meeting of the Advanced Light Source Users' Association, October 20–21, 1994, Berkeley CA.

8.0.1 Callcott, T.A., "Soft x-ray fluorescence spectroscopy of solids," in *Proceedings* of Annual Meeting of the Advanced Light Source Users' Association, October 20–21, 1994, Berkeley CA.

8.0.1 Callcott, T.A., J. Jia, J.A. Carlisle, E.L. Shirley, L.J. Terminello, R.C. Perera, and F.J. Himpsel, "Inelastic scattering processes near threshold in soft X-ray fluorescence," in *Proceedings* of International Workshop on Soft X-ray Fluorescence Spectroscopy, March 25–26, 1995, Uppsala Sweden.

8.0.1 Callcott, T.A., J. Jia, L. Zhou, D.L. Ederer, L.J. Terminello, J.A. Carlisle, R.C. Perera, M.G. Samant, F.J. Himpsel, and E.T. Arakawa, "Applications of soft x-ray fluorescence spectroscopy in materials science," in *1996 Spring Meeting Abstracts*, Proceedings of 1996 Materials Research Society Spring Meeting, April 8–12, 1996, San Francisco CA.

8.0.1 Callcott, T.A., L. Zhou, J. Jia, L. Lin, D.L. Ederer, L.J. Terminello, J.A. Carlisle, and R.C. Perera, "The effects of intermediate and final states on electronic resonance Raman scattering observed in the Zn $M_{2,3}$ fluorescence spectra of ZnSSe excited near threshold," in *Proceedings of REX Workshop*, Proceedings of Workshop on Raman Emission by X-Ray Scattering, December 1–4, 1995, New Orleans LA.

8.0.1 Carlisle, J.A., E.L. Shirley, L.J. Terminello, E.A. Hudson, J. Jia, T.A. Callcott, D.L. Ederer, and F.J. Himpsel, "Resonant fluorescence studies of novel materials," in *Materials Research Society*, Proceedings of Materials Research Society Meeting, April 19, 1995, San Francisco CA.

8.0.1 Carlisle, J.A., E.L. Shirley, L.J. Terminello, E.A. Hudson, J. Jia, T.A. Callcott, F.J. Himpsel, D.L. Ederer, and R.C. Perera, "Resonant soft x-ray fluorescence studies of novel materials," in *Materials Research Society*, Proceedings of Materials Research Society Symposium.

8.0.1 Carlisle, J.A., L.J. Terminello, E.A. Hudson, E.L. Shirley, F.J. Himpsel, J. Jia, T.A. Callcott, R.C. Perera, S. Louie, J. Stöhr, M.G. Samant, and D.L. Ederer, "Occupied and unoccupied orbitals of C_{60} and C_{70} with C 1s emission and absorption," in *Materials Research Society*, Proceedings of Materials Research Society Symposium, November 27–December 2, 1994, Boston MA.

8.0.1 Carlisle, J.A., L.J. Terminello, J. Jia, T.A. Callcott, D.L. Ederer, R.C. Perera, and F.J. Himpsel, "Resonant soft x-ray scattering in graphite and hexagonal boron nitride," in *Proceedings of REX Workshop*, Proceedings of Workshop on Raman Emission by X-Ray Scattering, December 1–4, 1995, New Orleans LA.

Caspi, S., R. Schlueter, and R. Tatchyn, "High-field strong-focusing undulator designs for x-ray linac coherent light source (LCLS) applications," in *Proceedings* of Particle Conference & International Conference on High-Energy Accelerators, May 1–5, 1995, Dallas TX.

Chin, A.H., R.W. Schoenlein, T.E. Glover, C.V. Shank, W.P. Leemans, P. Volfbeyn, R. Govil, K.-J. Kim, and S. Chattopadhyay, "Generation of femtosecond x-ray pulses via Thomson scattering of terawatt IR laser pulses with relativistic electrons," in *Proceedings* of CLEO/QUELS, June 1996, Anaheim, CA.

Claytor, N., A. Belkacem, T. Dinneen, B. Feinberg, and H.A. Gould, "Electron capture from pair production at 11 GeV/nucleon," in *Proceedings* of 1996 Annual Meeting of the Division of Atomic, Molecular, and Optical Physics, May 15–18, 1996, Ann Arbor MI.

7.0.1 Cossy, A., J. Diaz, S. Anders, H.A. Padmore, Y. Liu, M.G. Samant, J. Stöhr, H. Brown, and T.P. Russell, "Photoelectron emission microscopy and its application to the study of polymer surfaces," in *Proceedings* of Third International School and Symposium on Synchrotron Radiation in Natural Science (ISSRN '96), May 31–June 8, 1996, Jaszoweic Poland.

7.0.1 Denlinger, J., B.P. Tonner, E. Rotenberg, S.D. Kevan, P. Len, and C.S. Fadley, "Bulk and surface photoelectron diffraction and holography of W(110)," in *American Vacuum Society*, Proceedings of 43rd National Symposium, October 14–18, 1996, Philadelphia PA.

7.0.1 Denlinger, J., B.P. Tonner, E. Rotenberg, S.D. Kevan, P. Len, and C.S. Fadley, "Bulk and surface photoelectron diffraction and holography of W(110)," in *Bulletin of the American Physical Society Program of the 1996 March Meeting*, March 18–22, 1996, St. Louis MO.

5.0 Earnest, T., H.A. Padmore, C.W. Cork, and S. Kim, "The macromolecular crystallography facility at the Advanced Light Source," in *Proceedings* of International Conference on Crystallization of Biological Materials, November 12–17, 1995, Hiroshima Japan.

9.3.2 Fadley, C.S., "Photoelectron and x-ray diffraction and holography: the next generation," in *Proceedings* of VII-th Symposium on Surface Physics, June 30–July 4, 1996, Trest Castle Czech Republic.

9.3.2 Fadley, C.S., "Growth and structure of magnetic surfaces and interfaces," in *American Vacuum Society*, Proceedings of 42nd National Symposium, October 16–20, 1995, Minneapolis MN.

9.0.1 Farhat, A.H., B. Langer, O.A. Hemmers, M.A. Humphrey, and N. Berrah, "Photoionization with excitation of the 4s and 4p subshells in krypton," in *Bull. Am. Phys. Soc.*, Proceedings of DAMOP Meeting of the American Physical Society, May 16–19, 1995, Toronto Canada.

Feinberg, B., "Comparison of conventional and novel quadrupole drift tube magnets inspired by Klaus Halbach," in *The Art and Science of Magnet Design*, Proceedings of Halbach Symposium on Magnet Technology Vol. 1, February 1, 1995, Berkeley CA.

Feinberg, B., A. Belkacem, R. Bossingham, and H.A. Gould, "Capture from pair production as a beam loss mechanism for heavy ions at RHIC," in *Proceedings* of 1993 IEEE Particle Accelerator Conference, May 17–20, 1993, Washington D.C.

7.0.1 Glans, P.N., K.M. Gunnelin, J. Guo, and J.E. Nordgren, "Selection rules in resonant x-ray emission of free molecules," in *Proceedings* of 17th International Conference on X-ray and Inner Shell Processes, September 9–13, 1996, Hamburg Germany.

Gould, H.A., A. Belkacem, N. Claytor, T. Dinneen, and B. Feinberg, "Electron capture and loss by 10 GeV/nucleon gold ions," in *Proceedings* of 1996 Annual Meeting of the Division of Atomic, Molecular, and Optical Physics, May 15–18, 1996, Ann Arbor MI.

Gould, H.A., N. Claytor, A. Belkacem, B. Feinberg, and T. Dinneen, "Capture from pair production at 11 GeV/nucleon," in *Proceedings* of 1996 Joint Meeting of the APS and the AAPT, May 2–5, 1996, Indianapolis IN.

Gozzo, F.G., K. Franck, M. Howells, Z. Hussain, T. Warwick, H.A. Padmore, and B.B. Triplett, "Soft X-ray spectromiscroscopy and its application to semiconductor microstructure characterization," in *Proceedings* of Third International School and Symposium on Synchrotron Radiation in Natural Science (ISSRN '96), May 31–June 8, 1996, Jaszoweic Poland.

8.0.1 Hemmers, O.A., G. Fisher, P.N. Glans, D.L. Hansen, H. Wang, S. Whitfield, D.W. Lindle, R. Wehlitz, J.C. Levin, and I.A. Sellin, "Non-dipolar angular distributions of Ne 2s and 2p valence photoelectrons," in *Bull. Am. Phys. Soc.*, Proceedings of DAMOP Meeting of the American Physical Society, May 15–18, 1996, Ann Arbor MI.

Hemmers, O.A., R. Wehlitz, G. Fisher, P.N. Glans, D.L. Hansen, H. Wang, S. Whitfield, J.C. Levin, I.A. Sellin, and D.W. Lindle, "Electric-quadrupole and magnetic-dipole angular distribution effects on Ne 2s and 2p valence photoemission," in *Proceedings* of 17th International Conference on X-ray and Inner Shell Processes, September 9–13, 1996, Hamburg Germany.

Hinkson, J.A., and K.B. Unser, "Precision analog signal processor for beam position measurements in electron storage rings," in *Proceedings* of Second European Workshop on Beam Diagnostics and Instrumentation for Particle Accelerators, May 28–31, 1995, Travemunde Germany.

9.0.1 Hitchcock, A.P., J.D. Bozek, and E. Ruhl, "Inner-shell excitation and ionic fragmentation of molecules," in *Proceedings* of 78th Canadian Society for Chemistry Conference, May 28–June 1, 1995, Guelph, Ontario Canada.

Howells, M., "Some ideas on the choice of designs and materials for cooled mirrors," in *The Art and Science of Magnet Design*, Proceedings of Halbach Symposium on Magnet Technology Vol. 1, February 1, 1995, Berkeley CA.

Howells, M., C. Jacobsen, and S. Lindaas, "Possibility for one-shot tomography using a high-gain free-electron laser," in *Proceedings* of the Conference on Workshop on Scientific Applications of Coherent X-rays, Stanford CA.

Hoyer, E., J. Akre, D.E. Humphries, T. Jackson, S. Marks, D. Plate, G.J. Portmann, and R. Schlueter, "Wigglers at the Advanced Light Source," in *Proceedings* of Particle Conference & International Conference on High-Energy Accelerators, May 1–5, 1995, Dallas TX.

9.3.2 Huff, T., Y. Chen, X. Zhang, L.J. Terminello, F.M. Tao, Y.K. Pan, S.A. Kellar, E. Moler, Z. Hussain, H. Wu, Y. Zheng, X. Zhou, A.E. Schach von Wittenau, S. Kim, Z. Huang, Z.Z. Yang, and D.A. Shirley, "Angle-resolved photoemission extended fine structure study of chemisorbed c(2x2)P/Fe(100): comparison with self-consistent-field X alpha scattered wave calculations," in *1996 Spring Meeting Abstracts*, Proceedings of 1996 Materials Research Society Spring Meeting, April 8–12, 1996, San Francisco CA.

9.0.1 Humphrey, M.A., A.H. Farhat, B. Langer, N. Berrah, and D. Cubaynes, "High resolution study of Ar $2p \rightarrow ns, d$ resonant auger transitions using the auger resonant raman effect," in *Bull. Am. Phys. Soc.*, Proceedings of DAMOP Meeting of the American Physical Society, May 15–18, 1996, Ann Arbor MI.

Humphries, D.E., J. Akre, E. Hoyer, S. Marks, Y. Minamihara, P. Pipersky, D. Plate, and R. Schlueter, "Design of end magnetic structures for the Advanced Light Source wigglers," in *Proceedings* of Particle Conference & International Conference on High-Energy Accelerators, May 1–5, 1995, Dallas TX.

Hung, T., F.Z. Chen, C.Y.R. Wu, and D.L. Judge, "Study of excited electronic states of multiply charged N_2 using fluorescence spectrometry," in *American Geophysical Union*, Proceedings of The American Geophysical Union 1995 Spring Meeting, May 29–June 2, 1995, Baltimore MD.

Jackson, A., "Operational experience with multi-bunch feedback at the Advanced Light Source," in *Proceedings* of European Particle Accelerator Conference, June 10–14, 1996, Barcelona Spain.

8.0.1 Jiménez-Mier, J., D.L. Ederer, M.P. Diebold, A.P. Moewes, T.A. Callcott, L. Zhou, J. Jia, J.A. Carlisle, E.A. Hudson, L.J. Terminello, A. Asfaw, F.J. Himpsel, and R.C. Perera, "Raman scattering at the L-edge of transition metals," in *Proceedings of REX Workshop*, Proceedings of Workshop on Raman Emission by X-Ray Scattering, December 1–4, 1995, New Orleans LA.

6.1.2 Jochum, L., W. Meyer-Ilse, H. Medecki, and D.T. Attwood, "X-ray microscopy at the Advanced Light Source: partial coherent image modeling," in *Materials Society of America Annual Meeting, 1994.*

9.3.2 Kaduwela, A., M.A. Van Hove, and C.S. Fadley, "Magnetic order on the MnO(001) surface from spin-polarized photoelectron diffraction and spin-polarized photoelectron holography," in *1996 Spring Meeting Abstracts*, Proceedings of 1996 Materials Research Society Spring Meeting, April 8–12, 1996, San Francisco CA.

9.0.1 Kaindl, G., K. Schulz, M. Domke, J.D. Bozek, A.S. Schlachter, and P.A. Heimann, "High-resolution study of double-excitation states in helium," in *Bulletin of Abstracts*, Proceedings of International Symposium on High-Resolution Spectroscopy Using Synchrotron Radiation, August 24–25, 1995, Pohang Korea.

Keller, R., T.R. Renner, and D. Massoletti, "Electron beam diagnostics using synchrotron radiation at the Advanced Light Source," in *Proceedings* of Seventh Beam Instrumentation Workshop, May 6–9, 1996, Argonne IL.

Kim, C., "Modeling of the Advanced Light Source linac," in *Proceedings* of XVIII International Linac Conference, August 26–30, 1996, Geneva Switzerland.

Kortright, J., "Status and limitations of multilayer x-ray interference structures," in *Proceedings* of 2nd International Symposium on Metallic Multilayers, September 11–14, 1995, Cambridge UK.

6.3.2 Kortright, J., and M. Rice, "Element-specific soft x-ray magneto-optic rotation studies of magnetic films and multilayers," in *Proceedings* of 1996 SPIE International Symposium on Polarization Analysis and Applications to Device, June 12–14, 1996, Yokohama Japan.

6.3.2 Kortright, J., and M. Rice, "Soft x-ray optical rotation as element-specific magneto-optical probe," in *Materials Research Society Meeting*, Proceedings of Materials Research Society Meeting, April 19, 1995, San Francisco CA.

Lambrecht, W.R.L., S.N. Rashkeev, B. Segall, K. Lawniczak-Jablonska, T. Suski, E. Gullikson, J.H. Underwood, R.C. Perera, and J.C. Rife, "X-ray absorption and reflection as probes of the GaN conduction bands: theory and experiment of the N-K edge and Ga-$M_{2,3}$ edges," in *Proceedings of the Fall 1996 Materials Research Meeting*, Proceedings of Materials Research Society, December 2–6, 1996, Boston MA.

9.0.1 Langer, B., N. Berrah, A.H. Farhat, O.Y. Nayandin, D. Cubaynes, and J.D. Bozek, "Inner shell autoionization resonances of atomic chlorine studied by angle resolved photoelectron spectroscopy using synchrotron radiation," in *Bull. Am. Phys. Soc.*, Proceedings of DAMOP Meeting of the American Physical Society, May 15–18, 1996, Ann Arbor MI.

9.0.1 Langer, B., O.A. Hemmers, O. Toader, J.D. Bozek, and N. Berrah, "Angle resolved high resolution studies of the Xe $4d_{5/2} \rightarrow 6p$ resonance," in *Bull. Am. Phys. Soc.*, Proceedings of DAMOP Meeting of the American Physical Society, May 16–19, 1995, Toronto Canada.

Laskar, J., and D. Robin, "Application of frequency map analysis to the Advanced Light Source," in Proceedings of International workshop on single-particle effects in large hadron colliders, October 15–21, 1995, Montreux Switzerland.

Lawniczak-Jablonska, K., T. Suski, W.R.L. Lambrecht, S.N. Rashkeev, B. Segall, and J. Rife, "X-ray edge spectra of III-nitrides," in *Proceedings* of American Physical Society Meeting, March 17–21, 1997, Kansas City MO.

Leemans, W., R. Schoenlein, A. Chin, E. Glover, and others, "Femtosecond X-rays from 90 degrees Thomson scattering," in *Proceedings* of the 1995 Particle Accelerator Conference, May 1995, Dallas, TX.

Leemans, W., R. Schoenlein, A. Chin, E. Glover, M. Conde, S. Chattopadhyay, K.-J. Kim, and C.V. Shank, "Femtosecond x-ray generation through 90° Thomson scattering: Status of the LBL experiment," Sixth Advanced Accelerator Concepts Workshop, June 1994, Fontana, WI, *AIP Conference Proceedings* **335**, 209 (1995).

7.0.1 Len, P., C.S. Fadley, and G. Materlik, "Atomic holography with electrons and x-rays," in *Proceedings* of 17th International Conference on X-ray and Inner Shell Processes, September 9–13, 1996, Hamburg Germany.

7.0.1 Len, P., S. Thevuthasan, C.S. Fadley, M.A. Van Hove, J. Denlinger, B.P. Tonner, E. Rotenberg, S.D. Kevan, T. Gog, and G. Materlik, "Photoelectron and x-ray holography: present status and future prospects," in *ICSOS-5 Program and Abstract Book*, Proceedings of 5th International Conference on the Structure of Surfaces, July 8–12, 1996, Aix en Provence France.

Len, P., T. Gog, C.S. Fadley, and G. Materlik, "Atomic imaging with x-ray holography," in *American Vacuum Society*, Proceedings of 43rd National Symposium, October 14–18, 1996, Philadelphia PA.

Len, P., T. Gog, C.S. Fadley, D. Bahr, C. Sanchez-Hanke, and G. Materlik, "Direct reconstruction of atomic images from multi-energy x-ray holography data sets," in *Bulletin of the American Physical Society Program of the 1996 March Meeting*, March 18–22, 1996, St. Louis MO.

Lindaas, S., C. Jacobsen, A. Kalinovsky, and M. Howells, "X-ray Gabor holography: recent progress," in *Proceedings* of the Conference New Orleans, 1994, Proceedings of Microscopy Society of America, 1994, New Orleans LA.

9.3.1 Lindle, D.W., "X-ray fluorescence studies of gaseous molecules," in *Proceedings* of International Workshop on Soft X-ray Fluorescence Spectroscopy, March 25–26, 1995, Uppsala Sweden.

9.3.1 Lindle, D.W., "X-ray atomic and molecular spectroscopy at the Advanced Light Source," in *Bull. Am. Phys. Soc.*, Proceedings of DAMOP Meeting of the American Physical Society, May 16–19, 1995, Toronto Canada.

Lo, C.C., B. Taylor, and K. Baptiste, "The amplitude and phase control of the Advanced Light Source storage ring RF system," in *Proceedings* of Particle Conference & International Conference on High-Energy Accelerators, May 1–5, 1995, Dallas TX.

Marks, S., "Use of the Halbach perturbation theory for the multipole design of the Advanced Light Source storage ring sextupole," in *The Art and Science of Magnet Design*, Proceedings of Halbach Symposium on Magnet Technology Vol. 1, February 1, 1995, Berkeley CA.

Martynov, V., W.R. McKinney, and H.A. Padmore, "Elliptical wiggler beamline with minimum focal spot size at the Advanced Light Source," in *Proceedings* of 1995 SPIE's 40th Annual Meeting on Optical Engineering and Instrumentation, July 9–14, 1995, San Diego CA.

Massoletti, D., C. Kim, and A. Jackson, "Emittance measurements in the Advanced Light Source booster synchrotron," in *Proceedings* of Particle Conference & International Conference on High-Energy Accelerators, May 1–5, 1995, Dallas TX.

10.3.1 McHugo, S., and M. Imaizumi, "Release of impurities from structural defects in polycrystalline silicon solar cells," in *Proceedings* of the Spring 1997 Materials Research Society Meeting, March 31–April 4, 1997, San Francisco CA.

10.3.1 McHugo, S., H. Hieslmair, E.R. Weber, M.D. Rosenblum, and J.P. Kalejs, "Interactions of structural defects with metallic impurities in multicrystalline silicon," in *Proceedings* of the Fall 1996 Materials Research Meeting, December 2–6, 1996, Boston MA.

6.1.2 Meyer-Ilse, W., H. Medecki, J. Brown, J. Heck, E.H. Anderson, C. Magowan, A.D. Stead, T.W. Ford, and D.T. Attwood, "High resolution soft x-ray microscopy," in *Proceedings* of International Conference on Soft X-rays in the 21st Century, January 13–17, 1997, Orem UT.

6.1.2 Meyer-Ilse, W., H. Medecki, J. Brown, J. Heck, E.H. Anderson, C. Magowan, A.D. Stead, T.W. Ford, R.L. Balhorn, D. Arndt-Jovin, T. Jovin, C. Petersen, and D.T. Attwood, "X-ray microscopy in Berkeley," in *Proceedings* of International Conference on X-ray Microscopy and Spectroscopy, August 5–9, 1996, Wurzburg Germany.

Moler, E., and R.L. Watson, "Chemical effects on the k-alpha/k-beta intensity ratio for first row transition metals," in *Proceedings* of 10th Conference on the Application of Accelerators in Research and Industry, November 1–5, 1988, Denton TX.

9.3.2 Moler, E., T. Huff, S.A. Kellar, Z. Hussain, Y.F. Chen, and D.A. Shirley, "Surface structure determination of c(2x2) N_2/Ni(100) and low and intermediate coverages of CO/Cu(111) by angle-resolved photoemission extended fine structure (ARPEFS) using synchrotron radiation," in *Proceedings of the Fall 1996 Materials Research Meeting*, December 2–6, 1996, Boston MA.

9.3.2 Morais, J., R. Denecke, J. Liesegang, R. Ynzunza, and C.S. Fadley, "On the angle- and temperature-dependent magnetic circular dichroism in core photoelectron emission from Gd(0001) on W(110)," in *Proceedings* of VII Annual Workshop of LNLS Users, November 12, 1996, Campinas Brazil.

Nishimura, H., "Taking an object-oriented view of accelerators," in *Proceedings* of Particle Conference & International Conference on High-Energy Accelerators, May 1–5, 1995, Dallas TX.

Nishimura, H., C. Timossi, and M. Valdez, "Accelerator operation management using objects," in *Proceedings* of Particle Conference & International Conference on High-Energy Accelerators, May 1–5, 1995, Dallas TX.

Nishimura, H., L. Schachinger, and H. Ohgaki, "Orbit control at the Advanced Light Source based on sensitivity matrices," in *Proceedings* of Particle Conference & International Conference on High-Energy Accelerators, May 1–5, 1995, Dallas TX.

7.0.1 Nordgren, J.E., "X-ray emission spectroscopy. A modern tool to probe electronic structure and dynamics," in *Proceedings* of Würzburg Röntgen Centennial Meeting, October 9–13, 1995, Würzberg Germany.

7.0.1 Nordgren, J.E., "Soft x-ray fluorescence spectroscopy of molecules," in *Proceedings* of Annual Meeting of the Advanced Light Source Users' Association, October 20–21, 1994, Berkeley CA.

Nuhn, H.-D., E.T. Scharlemann, and R. Schlueter, "Alignment and magnet error tolerances for the LCLS x-ray FEL," in *Proceedings* of Particle Conference & International Conference on High-Energy Accelerators, May 1–5, 1995, Dallas TX.

7.0.1 Padmore, H.A., "Soft-x-ray optics for spectromicroscopy at the Advanced Light Source," in *Proceedings* of 17th International Conference on X-ray and Inner Shell Processes, September 9–13, 1996, Hamburg Germany.

9.3.2 Palomares, J., R. Ynzunza, E. Tober, H. Daimon, Z. Wang, Z. Hussain, A. Kaduwela, Y. Chen, M.A. Van Hove, and C.S. Fadley, "Oxide and metal-interface structures on W(110) from state-resolved and circular dichroic photoelectron diffraction," in *ICSOS-5 Program and Abstract Book*, Proceedings of 5th International Conference on the Structure of Surfaces, July 8–12, 1996, Aix en Provence France.

Portmann, G.J., D. Robin, and L. Schachinger, "Automated beam based alignment of the Advanced Light Source quadrupoles," in *Proceedings* of Particle Conference & International Conference on High-Energy Accelerators, May 1–5, 1995, Dallas TX.

10.3.2 Qiu, C.H., M.W. Leksono, J.I. Pankove, C.S. Rossington, and E.E. Haller, "Effects of x-ray and gamma-ray irradiation on GaN," in *Proceedings* of the Fall 1996 Materials Research Meeting, December 2–6, 1996, Boston MA.

Ritchie, A., D. Oldfather, and A. Lindner, "The Advanced Light Source (ALS) radiation safety system," in *Proceedings* of 1993 IEEE Particle Accelerator Conference, May 17–20, 1993, Washington D.C.

Robin, D., and J. Laskar, "Understanding the nonlinear beam dynamics of the Advanced Light Source," in *Proceedings* of Computational Accelerator Physics Conference, September 24, 1996, McLean VA.

Robin, D., C. Kim, and A. Sessler, "Compton scattering in the Advanced Light Source booster," in *Proceedings* of Particle Conference & International Conference on High-Energy Accelerators, May 1–5, 1995, Dallas TX.

Robin, D., G.F. Krebs, G.J. Portmann, A. Zholents, and W. Decking, "Reduction of nonlinear resonance excitation from insertion devices in the Advanced Light Source," in *Proceedings* of Particle Conference & International Conference on High-Energy Accelerators, May 1–5, 1995, Dallas TX.

Robin, D., J. Safranek, G.J. Portmann, and H. Nishimura, "Model calibration and symmetry restoration of the Advanced Light Source," in *Proceedings* of European Particle Accelerator Conference, June 10–14, 1996, Barcelona Spain.

7.0.1 Rotenberg, E., J. Denlinger, S.D. Kevan, K.W. Goodman, J.G. Tobin, G.J. Mankey, and K. Subramanian, "Fermi surface mapping using a third generation light source," in *1996 Spring Meeting Abstracts*, Proceedings of 1996 Materials Research Society Spring Meeting, April 8–12, 1996, San Francisco CA.

7.0.1 Rotenberg, E., S.D. Kevan, D.K. Shuh, J.J. Bucher, N.M. Edelstein, T. Warwick, J. Denlinger, B.P. Tonner, and J.G. Tobin, "Electron spectroscopy of transuranic oxides by synchrotron radiation techniques," in *Proceedings* of Northern California Chapter of the American Vacuum Society, June 13, 1995, Santa Clara CA.

9.0.1 Samson, J.A.R., J.N. Cutler, Z.X. He, W.C. Stolte, and J.D. Bozek, "High resolution multiple photoionization study of Ar," in *Bull. Am. Phys. Soc.*, Proceedings of DAMOP Meeting of the American Physical Society, May 16–19, 1995, Toronto Canada.

7.0.1 Samson, J.A.R., W.C. Stolte, Z.X. He, J.N. Cutler, R.J. Barlett, and M. Sagurton, "The ratio of He^{2+}/He^{+} near threshold," in *Proceedings* of Workshop on Two-Electron Processes in Photon-Helium Interaction, January 8–9, 1996, Boulder CO.

Schlachter, A.S., "New results in atomic physics at the Advanced Light Source," in *Proceedings* of Fourth U.S./Mexico Workshop on Atomic and Molecular Physics, July 7–10, 1994, Hacienda Galindo Mexico.

Schlachter, A.S., and A. Robinson, "Synchrotron light sources: a powerful tool for science and technology," in *Proceedings* of Regional Workshop on Applications of Synchrotron Radiation, January 3–7, 1996, Bangkok Thailand.

9.0.1 Schlachter, A.S., and J.D. Bozek, "High-resolution VUV spectroscopy: new results from the Advanced Light Source," in *Proceedings* of Workshop on Atomic Physics with Hard X Rays from High Brilliance Synchrotron Light Sources, May 20–21, 1996, Argonne IL.

Schlueter, R., "Field errors in hybrid insertion devices," in *The Art and Science of Magnet Design*, Proceedings of Halbach Symposium on Magnet Technology Vol. 1, February 1, 1995, Berkeley CA.

8.0.1 Shirley, E.L., "Simulating x-ray fluorescence in graphite and boron nitride," in *Proceedings of REX Workshop*, Proceedings of Workshop on Raman Emission by X-Ray Scattering, December 1–4, 1995, New Orleans LA.

7.0.1 Shuh, D.K., J.J. Bucher, N.M. Edelstein, J. Denlinger, B.P. Tonner, E. Rotenberg, and S.D. Kevan, "Electron spectroscopy of transuranic oxides by soft x-ray synchrotron radiation techniques," in *Materials Research Society*, Proceedings of Materials Research Society Symposium, November 27–December 2, 1994, Boston MA.

7.0.1 Shuh, D.K., P.G. Allen, J.J. Bucher, N.M. Edelstein, T. Reich, M.A. Denecke, and H. Nitsche, "Investigation of environmental problems by x-ray absorption spectroscopy," in *Proceedings* of International Conference on Advanced Materials 1995, International Materials Research Society, August 27–September 1, 1995, Cancun Mexico.

8.0.1 Shuh, D.K., W.M. Tong, I. Jimenez, D. Feiler, R.S. Williams, J.A. Carlisle, D.G. Sutherland, L.J. Terminello, and F.J. Himpsel, "Characterization of pulsed laser deposited GaN films by near edge absorption fine structure (NEXAFS)," in *Materials Research Society*, Proceedings of Materials Research Society Symposium, November 27–December 2, 1994, Boston MA.

6.3.2 Stolte, W.C., Y. Lu, J.A.R. Samson, D.L. Hansen, S. Whitfield, P.N. Glans, H. Wang, O.A. Hemmers, and D.W. Lindle, "Effects of post-collision interaction for the auger decay of the oxygen K-shell," in *Bull. Am. Phys. Soc.*, Proceedings of DAMOP Meeting of the American Physical Society, May 15–18, 1996, Ann Arbor MI.

Stover, G.D., "Analysis and design modifications for upgrade of storage ring bump pulse system driving the injection bump magnets at the Advanced Light Source," in *Proceedings* of Particle Conference & International Conference on High-Energy Accelerators, May 1–5, 1995, Dallas TX.

8.0.1 Terminello, L.J., E.S. Hudson, E.L. Shirley, F.J. Himpsel, J. Jia, T.A. Callcott, R.C. Perera, M.G. Samant, and D.L. Ederer, "Occupied and unoccupied orbitals of C_{60} and C_{70} probed with O in emission and absorption," in *Proceedings* of Materials Research Society Symposium, November 27–December 2, 1994, Boston MA.

8.0.1 Terminello, L.J., N.D. Shinn, G.E. Ice, K. D'Amico, and D.L. Perry, "Applications of synchrotron radiation techniques to materials science II," in *Proceedings* of Materials Research Society Symposium, November 27–December 2, 1994, Boston MA.

Teytelman, D., J. Byrd, J. Corbett, and G. Stover, "Operation and performance of the PEP-II longitudinal damping system at the Advanced Light Source," in *Proceedings* of Particle Conference & International Conference on High-Energy Accelerators, May 1–5, 1995, Dallas TX.

Teytelman, D., R. Claus, J.D. Fox, H. Hindi, I. Linscott, S. Prahakar, A. Drago, and G. Stover, "Feedback control and beam diagnostic algorithms for a multiprocessor DSP system," *Seventh Beam Instrumentation Workshop*, May 6–9, 1996, Argonne IL, 1996.

Thur, W., and T. Lauritzen, "Surveying the monument system at Lawrence Berkeley Laboratory's Advanced Light Source accelerator," in *Proceedings* of Particle Conference & International Conference on High-Energy Accelerators, May 1–5, 1995, Dallas TX.

9.3.2 Tober, E., J. Palomares, R. Ynzunza, Z. Wang, Z. Hussain, and C.S. Fadley, "First observation of a ferromagnetic to paramagnetic phase transition on a ferromagnetic surface using spin-polarized photoelectron diffraction," in *ICSOS-5 Program and Abstract Book*, Proceedings of 5th International Conference on the Structure of Surfaces, July 8–12, 1996, Aix en Provence France.

9.3.2 Tober, E., J. Palomares, Z. Wang, R. Ynzunza, Z. Hussain, and C.S. Fadley, "Spin polarized photoelectron diffraction from Gd(0001) films," in *American Vacuum Society*, Proceedings of 43rd National Symposium, October 14–18, 1996, Philadelphia PA.

9.3.2 Tober, E., R. Ynzunza, J. Palomares, A. Kaduwela, Z. Wang, H. Xiao, F. Zhang, H. Daimon, Z. Hussain, and C.S. Fadley, "Interface photoelectron diffraction and angle-resolved valence band spectra from Gd thin films on W(110)," in *1996 Spring Meeting Abstracts*, Proceedings of 1996 Materials Research Society Spring Meeting, April 8–12, 1996, San Francisco CA.

9.3.2 Tober, E., R. Ynzunza, J. Palomares, Z. Wang, Z. Hussain, and C.S. Fadley, "Angle- and energy-dependent valence band photoemission study of Gd thin films on W(110) and clean W(110)," in *Bulletin of the American Physical Society Program of the 1996 March Meeting*, March 18–22, 1996, St. Louis MO.

7.0.1 Tobin, J.G., K.W. Goodman, G.J. Mankey, R.F. Willis, J. Denlinger, E. Rotenberg, and T. Warwick, "Correlation of magnetic dichroism in x-ray absorption and photoemission using ultrathin magnetic alloy films," in *1996 Spring Meeting Abstracts*, Proceedings of 1996 Materials Research Society Spring Meeting, April 8–12, 1996, San Francisco CA.

8.0.1 Tong, W.M., D.K. Shuh, I. Jimenez, D. Feiler, S. Williams, J.A. Carlisle, D.G. Sutherland, L.J. Terminello, R.E. Treece, J.S. Horowitz, and F.J. Himpsel, "NEXAFS of pulsed laser deposited BN, CN_x, and GaN films," in *Proceedings* of American Chemical Society, August 20–25, 1995, Chicago IL.

8.0.1 Tong, W.M., I. Jimenez, D.K. Shuh, D. Feiler, R.S. Williams, J.A. Carlisle, D.G.S. Sutherland, L.J. Terminello, R.E. Treece, J.S. Horowitz, and F.J. Himpsel, "NEXAFS characterization of pulsed laser deposited nitride films," in *Proceedings* of Northern California Chapter of the American Vacuum Society, June 13, 1995, Santa Clara CA.

7.0.1 Urquhart, S.G., A.P. Hitchcock, E.G. Rightor, A. Smith, and H. Ade, "Polymer chemical speciation by NEXAFS spectromicroscopy: insights from molecular modelling," in *1996 Spring Meeting Abstracts*, Proceedings of 1996 Materials Research Society Spring Meeting, April 8–12, 1996, San Francisco CA.

8.0.1 Wang, H., P.N. Glans, O.A. Hemmers, S. Whitfield, and D.W. Lindle, "An autoionization study of the argon 2p satellites excited near the argon 2s threshold," in *Proceedings* of 17th International Conference on X-ray and Inner Shell Processes, September 9–13, 1996, Hamburg Germany.

9.3.2 Wang, Z., A. Kaduwela, F. Zhang, M.A. Van Hove, and C.S. Fadley, "Short range magnetic order on the MnO(001) surface from spin-polarized photoelectron diffraction and holography," in *American Vacuum Society*, Proceedings of 42nd National Symposium, October 16–20, 1995, Minneapolis MN.

9.3.2 Wang, Z., A. Kaduwela, S. Thevuthasan, M.A. Van Hove, and C.S. Fadley, "Imaging short-range magnetic order by spin-polarized photoelectron holography," in *American Vacuum Society*, Proceedings of 41st National Symposium, October 24–28, 1994, Denver CO.

9.3.2 Wang, Z., A. Kaduwela, S. Thevuthasan, M.A. Van Hove, and C.S. Fadley, "Spin-polarized photoelectron holography: imaging short range magnetic order," in *1995 Spring Meeting Abstracts*, Proceedings of 1995 Materials Research Society Spring Meeting, April 17–21, 1995, San Francisco CA.

8.0.1 Wehlitz, R., I.A. Sellin, O.A. Hemmers, S. Whitfield, D.W. Lindle, B. Langer, N. Berrah, J. Viefhaus, and U. Becker, "Ionization-excitation of helium of high photon energies," in *Bull. Am. Phys. Soc.*, Proceedings of DAMOP Meeting of the American Physical Society, May 15–18, 1996, Ann Arbor MI.

9.0.1 Wehlitz, R., J.D. Bozek, B. Langer, A.H. Farhat, and N. Berrah, "High-resolution study of the Ne 2s → np autoionization resonances," in *Bull. Am. Phys. Soc.*, Proceedings of DAMOP Meeting of the American Physical Society, May 16–19, 1995, Toronto Canada.

9.0.2 Wu, C., D.L. Judge, T. Matsui, and K. Ito, "High-resolution, high-temperature absorption spectra of N_2 in the 834 and 917 angstrom regions," in *American Geophysical Union*, Proceedings of The American Geophysical Union 1995 Spring Meeting, May 29–June 2, 1995, Baltimore MD.

9.0.1 Wuilleumier, F., "First photoemission studies of hollow lithium atoms," in *Proceedings* of Oeji International Seminar on Atomic and Molecular Photoionization, September 4–7, 1995, Tsukuba Japan.

9.0.1 Wuilleumier, F., D. Cubaynes, S. Diehl, J. Bizau, B. Rouvellou, L. Journel, S. Al Moussalami, N. Berrah, L. VoKy, P. Faucher, A. Hibbert, T.J. Morgan, E.T. Kennedy, C.P. Blancard, J.D. Bozek, and A.S. Schlachter, "First measurements of hollow lithium states produced by triple excitation of laser-excited lithium atoms," in *Bull. Am. Phys. Soc.*, Proceedings of DAMOP Meeting of the American Physical Society, May 15–18, 1996, Ann Arbor MI.

9.0.1 Wuilleumier, F., S. Diehl, D. Cubaynes, J. Bizau, B. Rouvellou, L. Journel, S. Al Moussalami, T.J. Morgan, E.T. Kennedy, N. Berrah, K. Blanchard, J.D. Bozek, and A.S. Schlachter, "High resolution studies of hollow lithium atoms by photoelectron spectrometry at the Advanced Light Source," in *Bull. Am. Phys. Soc.*, Proceedings of DAMOP Meeting of the American Physical Society, May 15–18, 1996, Ann Arbor MI.

Yamamoto, R., J. Bowers, A. Harvey, R. Holmes, G. James, A. Marcus, A. Libkind, R. Martin, L. Mullins, J. Thomas, W. Wong, S. Aronson, S. Kahn, P. Kroon, T. Shea, R. Schlueter, and W. Sondheim, "The phenix detector magnet subsystem," in *Proceedings* of Magnet Technology Conference, June 11–16, 1995, Tampere Finland.

9.0.2.1 Yang, X., D.A. Blank, J. Lin, P.A. Heimann, A.M. Wodtke, Y.T. Lee, and A. Suits, "Chemical reaction dynamics using the Advanced Light Source," in *Proceedings* of 210th American Chemical Society National Meeting, August 20–24, 1995, Chicago IL.

9.3.2 Ynzunza, R., E. Tober, J. Palomares, Z. Wang, H. Daimon, A. Kaduwela, M.A. Van Hove, and C.S. Fadley, "Full-solid-angle photoelectron diffraction from W(110)," in *1996 Spring Meeting Abstracts*, Proceedings of 1996 Materials Research Society Spring Meeting, April 8–12, 1996, San Francisco CA.

9.3.2 Ynzunza, R., E. Tober, J. Palomares, Z. Wang, H. Daimon, A. Kaduwela, M.A. Van Hove, and C.S. Fadley, "Full-solid-angle photoelectron diffraction from W(110): experiment and theory," in *Bulletin of the American Physical Society Program of the 1996 March Meeting*, March 18–22, 1996, St. Louis MO.

9.3.2 Ynzunza, R., J. Palomares, E. Tober, Z. Wang, H. Daimon, and C.S. Fadley, "State-resolved and circular dichroic photoelectron diffraction on O/W(110)," in *American Vacuum Society*, Proceedings of 43rd National Symposium, October 14–18, 1996, Philadelphia PA.

Young, A.T., D.J. Clark, W.B. Kunkel, K.T. Leung, and C.Y. Li, "A compact permanent magnet cyclotrino for accelerator mass spectrometry," in *The Art and Science of Magnet Design*, Proceedings of Halbach Symposium on Magnet Technology Vol. 1, February 1, 1995, Berkeley CA.

9.3.2 Zhang, F., P. Len, A. Kaduwela, S. Thevuthasan, M.A. Van Hove, and C.S. Fadley, "Photoelectron holography: prospects and limitations," in *IVC-13/ICSS-9*, Proceedings of 13th International Vacuum Congress 9th International Conference on Solid Surfaces, September 25–29, 1996, Yokohama Japan.

9.3.2 Zhang, Z., P. Len, A. Kaduwela, S. Thevuthasan, M.A. Van Hove, and C.S. Fadley, "Photoelectron holography: prospects and limitations," in *American Vacuum Society*, Proceedings of 42nd National Symposium, October 16–20, 1995, Minneapolis MN.

Books

Balhorn, R.L., and et al, "Application of x-ray microscopy to the analysis of sperm chromatin," in *X-ray Microscopy and Spectromicroscopy*, Thieme, J., G. Schmahl, E. Umbach, and D. Rudolph, eds., Springer Heidelberg, 1997.

Cross, J.C., ed., *The art and science of magnet design: a festschrift in honor of Klaus Halbach*, Vol. 1, Lawrence Berkeley Laboratory, Berkeley, CA, 1995.

Ford, T.W., A.M. Page, W. Meyer-Ilse, and A.D. Stead, "A comparative study of the ultrastructure of living cells of the green alga chlamydomonas using both soft x-ray contact and direct imaging systems and an evaluation of possible radiation damage," in *X-ray Microscopy and Spectromicroscopy*, Thieme, J., G. Schmahl, E. Umbach, and D. Rudolph, eds., Springer Heidelberg, 1997.

Heck, J., W. Meyer-Ilse, J. Brown, E. Anderson, H. Medecki, and D.T. Attwood, "Resolution of XM-1," in *X-ray Microscopy and Spectromicroscopy*, Thieme, J., G. Schmahl, E. Umbach, and D. Rudolph, eds., Springer Heidelberg, 1997.

Howells, M., "Mirrors for synchrotron radiation beamlines," in *New Directions in Research using Third Generation Synchrotron Sources* **254**, Applied Science series, Kluwer Academic Publishers, 1993.

Howells, M., and B.M. Kincaid, "The properties of undulator radiation," in *New Directions in Research using Third Generation Synchrotron Sources*, Applied Science series, Kluwer Academic Publishers, 1993.

Howells, M., and C. Jacobsen, "X-ray holographic microscopy using the atomic force microscope," in *X-ray Microscopy IV*, Bogorodski Pechatnik, Helsinki, 1993.

Lindaas, S., B.H. Calef, K. Downing, M. Howells, C. Magowan, D. Pinkas, and C. Jacobsen, "X-ray holography of fast-frozen hydrated biological samples," in *X-ray microscopy and spectroscopy*, Springer-Verlag, Heidelberg, 1997.

Meyer-Ilse, W., D.T. Attwood, and M. Koike, "X-ray microscopy resource center at the Advanced Light source," in *Synchrotron Radiation in the Biosciences*, Chance, B., J. Deisenhofer, S. Ebashi, D. Goodhead, J. Helliwell, H. Huxley, Oxford University Press, 1994, pp. 625–636.

Meyer-Ilse, W., H. Medecki, J. Brown, J. Heck, E. Anderson, C. Magowan, A.D. Stead, T.W. Ford, R.L. Balhorn, C. Petersen, and D.T. Attwood, "X-ray microscopy in Berkeley," in *X-ray Microscopy and Spectromicroscopy*, Thieme, J., G. Schmahl, E. Umbach, and D. Rudolph, eds., Springer Heidelberg, 1996.

Meyer-Ilse, W., M.M. Moronne, C. Magowan, H. Medecki, J. Hearst, D.T. Attwood, P. Guttmann, G. Schneider, and T. Wilheim, "Techniques and applications of x-ray microscopy," in *X-ray Microscopy IV*, Erko, A.I. and V. Aristov, eds., Bogorodski Peschatnik Publishing Co., Chernogolovka, 1994.

Schlueter, R., "Wiggler and undulator insertion devices," in *Synchrotron radiation sources—a technical primer*, Winick, H. ed., World Scientific Publishing Company, River Edge, 1994, pp. 377–408.

Skytt, P.I., P.N. Glans, J. Guo, K.M. Gunnelin, N. Wassdahl, and J.E. Nordgren, "Resonant soft x-ray emission spectroscopy of small molecules," in *Raman Emission of X-rays*, McGuire, J. and D. Ederer, eds., World Scientific 1996, Baton Rouge, 1996.

Stead, A.D., J. Brown, J. Judge, W. Meyer-Ilse, D. Neely, A.M. Page, E. Wolfrum, and T.W. Ford, "Use of soft x-rays to image hydrated and dehydrated bacterial spores using either contact microscopy or soft x-ray transmission microscopy," in *X-ray Microscopy and Spectromicroscopy*, Thieme, J., G. Schmahl, E. Umbach, and D. Rudolph, eds., Springer Heidelberg, 1997.

Stead, A.D., P.A.F. Anastasi, J. Brown, T. Majima, W. Meyer-Ilse, D. Neely, A.M. Page, S. Rondot, H. Shimizu, T. Tomie, and T.W. Ford, "If carbon discrimination is more important to biologists than resolution, will soft x-ray microscopy become a useful biological technique?," in *X-ray Microscopy and Spectromicroscopy*, Thieme, J., G. Schmahl, E. Umbach, and D. Rudolph, eds., Springer Heidelberg, 1997.

Turek, S., ed., *The art and science of magnet design: selected notes of Klaus Halbach*, Vol. 2, Lawrence Berkeley Laboratory, Berkeley, 1995.

Theses based on work done at the ALS

Grush, M.M., "X-ray spectroscopy of manganese clusters," doctoral dissertation, University of California Davis, Davis, CA, 1996, Advisor Prof. Stephen Cramer.

7.0.1 Gunnelin, K.M., "Soft x-ray emission studies of the electronic structure of molecules," licenciat dissertation, Uppsala University, Uppsala, Sweden, 1997, Advisor Prof. Joseph Nordgren.

7.0.1 Guo, J., "Resonant soft x-ray fluorescence spectroscopy applied to high temperature superconductors and carbon systems," doctoral dissertation, Uppsala University, Uppsala, Sweden, 1995, Advisor Prof. Joseph Nordgren.

9.3.1 Hansen, D.L., "A space focused ion time of flight mass spectrometer, and spectroscopy of hydrogen chloride, deuterium chloride, and hydrogen sulfide at "hard" x-ray energies," masters thesis, University of Nevada, Las Vegas, Nevada, 1995, Advisor Prof. Dennis W. Lindle.

9.3.2 Huff, T., "Development of a high-resolution soft x-ray (30–1500 eV) beamline at the Advanced Light Source and its use for the study of angle-resolved photoemission extended fine structure," doctoral dissertation, University of California, Berkeley, CA, 1996, Advisor Prof. David Shirley.

Kellar, S.A., "High-resolution structural studies of ultra-thin transition-metal overlayers and two-dimensional transition-metal oxides using synchrotron radiation," doctoral dissertation, University of California, Berkeley, CA, 1996, Advisor Prof. David Shirley.

9.3.2 Len, P., "Atomic holography with electrons and x-rays," doctoral dissertation, University of California, Davis, CA, 1997, Advisor Prof. Charles Fadley.

9.3.2 Moler, E., "High-resolution spectroscopy using synchrotron radiation for surface structure determination and the study of correlated electron systems," doctoral dissertation, University of California, Berkeley, CA, 1996, Advisor Dr. David Shirley.

9.0.1 Schulz, K., "High-resolution absorption spectroscopy autoionization resonance of helium and neon," doctoral dissertation, Freie Universität Berlin, Berlin, Germany, 1997, Advisor Prof. Dr. Günter Kaindl.

9.3.2 Tober, E., "Studies of magnetic-metal epitaxial growth modes and surface properties by spin-polarized and site-resolved photoelectron diffraction, scanning tunneling microscopy, and low energy electron diffraction," doctoral dissertation, University of California, Davis, CA, 1997, Advisor Prof. Charles Fadley.

9.3.2 Wang, Z., "Short-range magnetic order from spin-polarized photoelectron diffraction and holography: experiment and theory for MnO(001)," doctoral dissertation, University of California, Davis, CA, 1997, Advisor Prof. Charles Fadley.

8.0.1 Wiell, T., "Soft x-ray emission spectroscopy applied to adsorbates and interfaces," doctoral dissertation, Uppsala University, Uppsala, Sweden, 1995, Advisor Prof. Joseph Nordgren.

Contributed News Articles

Bienenstock, A., and A. Robinson, "The impact of synchrotron radiation on materials research," *Beam Line*, **25**, Issue 2, Summer 1995.

9.0.1 Caldwell, C., A. Menzel, S. Frigo, S. Whitfield, and M.O. Krause, "High resolution in electron emission spectrometry," *Synchrotron Radiation News* **8**, 1 (1995) pp. 23–25.

8.0.1 Ederer, D.L., T.A. Callcott, and R.C. Perera, "Soft x-ray fluorescence: a multifaceted window to view the electronic structure of matter," *Synchrotron Radiation News* **7**, 4 (July/Aug. 1994) p. 29.

8.0.1 Hemmers, O.A., P.N. Glans, D.L. Hansen, H. Wang, S. Whitfield, D.W. Lindle, R. Wehlitz, J.C. Levin, I.A. Sellin, and R.C. Perera, "Photoelectron spectroscopy and the dipole approximation," *Synchrotron Radiation News* **9**, 6 (Nov./Dec. 1996) pp. 44–49.

9.0.1 Kaindl, G., K. Schulz, P.A. Heimann, J.D. Bozek, and A.S. Schlachter, "Ultra-high resolution in the soft x-ray region at beamline 9.0.1 at the Advanced Light Source," *Synchrotron Radiation News* **8**, 5 (May 1995) pp. 29–32.

6.1.2 Meyer-Ilse, W., H. Medecki, L. Jochum, E. Anderson, D.T. Attwood, C. Magowan, R.L. Balhorn, M.M. Moronne, D. Rudolph, and G. Schmahl, "New high-resolution zone-plate microscope at Beamline 6.1 of the Advanced Light Source," *Synchrotron Radiation News* **8** (1995) pp. 29–33.

Padmore, H.A., and T. Warwick, "New developments in beamlines for the Advanced Light Source," *Synchrotron Radiation News* **8**, 6 (November 1995) pp. 14–20.

6.1.2 Robinson, A., "Biological x-ray microscopy of the Advanced Light Source," *SIM News* **47**, 1 (Jan/Feb 1997) pp. 5–11.

Robinson, A., "Advanced Light Source Users' Association Ninth Annual Meeting," *Synchrotron Radiation News* **10**, 1 (Jan/Feb 1997) pp. 4–7.

BTF Robinson, A., "Laser techniques for generating femtosecond x-rays at the Advanced Light Source," *Synchrotron Radiation News* **10**, 1 (Jan/Feb 1997) pp. 32–33.

5.0.1 Robinson, A., "High-speed x-ray area detector for the Advanced Light Source," *Synchrotron Radiation News* **9**, 2 (March/April 1996) pp. 10–13.

5.0 Robinson, A., "Protein crystallography facility approved at the Advanced Light Source," *Synchrotron Radiation News* **8**, 2 (March 1995) p. 39.

Robinson, A., "Transition undulator radiation: a bright source of coherent IR," *Synchrotron Radiation News* **8**, 5 (September 1995) pp. 36–37.

7.0.1 Shuh, D.K. *et al* ., "Researchers use Advanced Light Source for TRU analysis," *Energy Research News* **4**, 4 (September 1994).

8.0.1 Studt, T., "Bright Synchrotron Sources Widen the Scope of Materials Research," *Research and Development Magazine* **36** (1994) p. 105.

Becoming an ALS User

The ALS, a Department of Energy national user facility, welcomes researchers from universities, industry, and government laboratories. Qualified users have access either as members of participating research teams (PRTs) or as independent investigators. PRTs (groups of researchers with related interests from one or more institutions) construct and operate beamlines and have primary responsibility for experiment endstation equipment. They are entitled to a certain percentage of their beamline's operating time according to the resources contributed by the PRT. Through a proposal process, the remaining beamtime is granted to independent investigators, who may provide their own endstation or negotiate access to a PRT-owned endstation.

Anyone wishing to explore the potential of synchrotron radiation in their research should review the beamline information given in the next section to gain some familiarity with the beamlines' photon energy ranges and other individual capabilities. To inquire more specifically about a particular beamline, use the contact information given in the individual beamline tables.

Independent Investigator Program

Independent researchers may propose experimental programs or single experiments to be performed on existing beamlines. Proposals may involve bringing experiment chambers to the ALS from other locations, or they may involve the use of chambers provided by the ALS facility or by a PRT. Independent investigators may also establish collaborations with PRT members.

The ALS has two semesters per year for soliciting independent investigator proposals: April–September and October–March. After the proposals are submitted, they are reviewed by ALS personnel for technical feasibility and safety, and PRT members from the appropriate beamline check the proposal for conformance to the beamline's capabilities. If a particular beamline is specified in the proposal, it is strongly recommended that the independent investigator contact the appropriate PRT spokesperson before submitting the proposal. Contact information for the PRT spokespersons and local contacts for each beamline are given in the beamline information tables on pp. 555–587. For information on beamlines available to independent investigators, contact the ALS Program Support Coordinator; for information on the submission process and deadlines, contact the ALS User Administrator (see inside back cover for ALS contact information).

After the ALS and PRT review, the proposals undergo peer review by a five-member Proposal Study Panel, which rates the proposals and makes recommendations on the requisite beam time. Highly rated proposals are allocated beam time by the ALS Scientific Program Head, Neville Smith, in consultation with the spokesperson of the host PRT.

Non-Proprietary Research

The ALS does not charge users for beam access if their research is non-proprietary. For research to be considered non-proprietary, the research results must be published in the open literature. All users are responsible for the day-to-day costs of research (e.g., supplies, phone calls, and technical support).

Proprietary Research

Proprietary research can also be performed at the ALS. Users performing proprietary research will be charged a fee based on cost recovery for ALS usage. In return, the user may choose to take title to any inventions made during the proprietary research program and treat as proprietary all technical data generated during the program. Contact the ALS User Administrator for information on proprietary research proposals (see inside back cover for contact information).

Table of Beamlines at the ALS

No.	Source **	Areas of Research	Energy Range	Avail.	Pages for Abstracts/ Technical Info.
BTF	ALS linac	Beam Test Facility	50 MeV elec.	Now	469/587
1.4	Bend	Infrared spectromicroscopy	0.05–1 eV	1997	–/555
3.1	Bend	Diagnostic beamline	200–280 eV	Now	–/–
4.0.1-2	EPU5	Magnetic spectroscopy	20–2000 eV	1998	–/556
4.0.3-4	EPU5	Magnetic microscopy	100–1600 eV	1998	–/557
5.0.1	W16	Monochromatic protein crystallography	7–14 keV	1998	–/558
5.0.2	W16	Multiple-wavelength (MAD) & monochromatic protein crystallography	3.5–14 keV	1997	–/559
6.1.2	Bend	High-resolution zone-plate microscopy	500–800 eV	Now	1/560
6.3.1	Bend	Calibration and standards, EUV/soft x-ray optics testing, solid-state chemistry	500–2000 eV	1998	–/561
6.3.2	Bend	Calibration and standards; EUV optics testing; atomic, molecular & materials science	50–1000 eV	Now	35/562
7.0.1	U5	Surface and materials science, spectromicroscopy	60–1000 eV	Now	83/563
7.0.2	U5	Coherent optics experiments	70–650 eV	1997	–/567
7.3.1.1	Bend	Magnetic microscopy, spectromicroscopy	260–1500 eV	1997	–/568
7.3.1.2	Bend	Surface and materials science, micro x-ray photoelectron spectroscopy	260–1500 eV	Now	–/569
7.3.3	Bend	Materials science	3–12 keV	1997	–/570
8.0.1	U5	Surface and materials science	60–1000 eV	Now	179/571
9.0.1	U10	Atomic and molecular science, high-resolution gas-phase spectroscopy*	20–310 eV	Now	247/573
9.0.2.1	U10	Chemical reaction dynamics, photochemistry	5–30 eV	Now	283/575
9.0.2.2	U10	Photoionization dynamics	5–30 eV	Now	283/576
9.3.1	Bend	Atomic, molecular, and materials science	2.2–6 keV	Now	307/577
9.3.2	Bend	Chemical and materials science	30–1500 eV	Now	331/580
10.3.1	Bend	Fluorescence x-ray microprobe	3–20 keV	Now	413/582
10.3.2	Bend	X-ray optics development, deep-etch x-ray lithography (LIGA), materials science	3–12 keV	Now	443/583
11.3	Bend	Deep-etch x-ray lithography (LIGA), scanning transmission x-ray microscopy	3–12 keV 260–750 eV	1998	–/584
12.0.1/ 12.0.2	U8	EUV lithography optics testing, interferometry, surface and materials science	60–320 eV	Now	465/585

* The atomic and molecular science beamline will move to 10.0 in early 1998.

** Bend = bend magnet; EPU5 = 5-cm-period elliptical polarization undulator; W16 = 16-cm-period wiggler, Ux = x-cm-period undulator

Beamline 1.4

Beamline/Branchline number	**1.4**
Operational	1997
Research program	Infrared spectromicroscopy
Source characteristics	Bend magnet
Energy range	0.05–1 eV
Frequency range	700 cm^{-1} to 4000 cm^{-1}
Interferometer resolution	0.25 cm^{-1}
Endstations	FTIR, IR microscope (N_2 purged)
Characteristics	Motorized sample stage, micron-resolution transmission and reflection modes
Spatial resolution	Diffraction limited (≈ wavelength)
Detectors	Extended-range MCT (Mercury Cadmium Telluride)
Spot size at sample	10 μm
Samples Preparation	 Stereo microscope and table available
Sample environment	N_2 purged, minimal clean area (no particle specification)
Scientific applications	Particulate contamination, biological samples, forensic studies, laminates, polymers, fibers
Local contact (until July 1997)	Name: Carol J. Hirschmugl Phone: (510) 486-8627 Fax: (510) 486-7696 Email: cjhirschmugl@lbl.gov
Spokesperson	Name: Wayne R. McKinney Affiliation: Advanced Light Source, LBNL Phone: (510) 486-4395 Fax: (510) 486-7696 Email: wrmckinney@lbl.gov

Beamline 4.0.1-2

Beamline/Branchline number	**4.0.1-2**
Operational	1998
Research program	Magnetic spectroscopy
Source characteristics	5.0-cm-period elliptical polarization undulator (EPU5.0), EPU7.5 (planned)
Energy range	20–2000 eV
Monochromator Calculated flux (1.9 GeV, 400 mA) Resolving power (E/ΔE)	Variable included angle PGM 5×10^{13} photons/sec/0.1%BW at 800 eV* 5,000–10,000
Endstations	Total yield, XPS, and fluorescence detectors in UHV chambers with magnets generating fields up to 6 T
Local contact	Name: Anthony T. Young Affiliation: Advanced Light Source, LBNL Phone: (510) 486-7746 Fax: (510) 486-7696 Email: atyoung@lbl.gov

* Polarization is user selectable, from horizontal to vertical and left and right elliptical (or circular) polarization. Value reported is the merit function flux = total flux × (degree of circular polarization)^2.

Beamline 4.0.3-4

Beamline/Branchline number	**4.0.3-4**
Operational	1998
Research program	Magnetic microscopy
Source characteristics	5.0-cm-period elliptical polarization undulator (EPU5.0)
Energy range	100–1600 eV
Monochromator Calculated flux (1.9 GeV, 400 mA) Resolving power (E/ΔE)	SGM 5×10^{13} photons/sec/0.1%BW at 800 eV* 3000
Endstations	Scanning spot microscope Full-field photoemission electron microscope
Local contact/spokesperson	Name: Anthony T. Young Affiliation: Advanced Light Source, LBNL Phone: (510) 486-7746 Fax: (510) 486-7696 Email: atyoung@lbl.gov

* Polarization is user selectable, from horizontal to vertical and left and right elliptical (or circular) polarization. Value reported is the merit function flux = total flux × (degree of circular polarization)^2.

Beamline 5.0.1

Beamline/Branchline number	**5.0.1**
Operational	1998
Research program	Monochromatic protein crystallography
Source characteristics	16-cm-period wiggler (W16)
Energy range	7–14 keV
Monochromator Calculated flux (1.9 GeV, 400 mA) Resolving power (E/ΔE)	 8.5×10^{13} photons/sec/0.1%BW at 12 keV (energy dependent) ≈6000 with Si(111) at 10° asymmetry angle
Endstation	Macromolecular crystallography facility
Detectors	CCD (planned)
Spot size at sample (FWHM)	0.7 mm (h) × 0.3 mm (v)
Samples Format Preparation	 Single crystals of biological molecules Support labs available
Sample environment	Ambient or ≈100°K
Special notes	Computers for data processing and analysis are available
Scientific applications	Biological crystallography; monochromatic
Local contact/spokesperson	Name: Thomas Earnest Affiliation: Structural Biology Div., LBNL Phone: (510) 486-4603 Fax: (510) 486-5664 Email: tnearnest@lbl.gov

Beamline 5.0.2

Beamline/Branchline number	**5.0.2**
Operational	1997
Research program	Multiple-wavelength anomalous diffraction (MAD) and monochromatic protein crystallography
Source characteristics	16-cm-period wiggler (W16)
Energy range	3.5–14 keV
Monochromator Calculated flux (1.9 GeV, 400 mA) Resolving power (E/ΔE)	Double crystal 2.3×10^{13} photons/sec/0.1%BW into 1.5 mrad at 12.4 keV 15,000 for Si(111)
Endstation	Macromolecular crystallography facility
Characteristics	Kappa-geometry camera, CCD detector, low-temperature system
Detectors	2 × 2 array CCD detector
Spot size at sample (FWHM)	3.0 mm (h) × 0.3 mm (v)
Samples Format Preparation	 Single crystals of biological molecules Support labs available
Sample environment	Ambient or ≈100°K
Special notes	Computers for data processing and analysis are available
Scientific applications	Biological crystallography; multiple-wavelength anomalous diffraction (MAD); monochromatic
Local contact/spokesperson	Name: Thomas Earnest Affiliation: Structural Biology Div., LBNL Phone: (510) 486-4603 Fax: (510) 486-5664 Email: tnearnest@lbl.gov

Beamline 6.1.2

Abstracts begin on page 1

Beamline/Branchline number	**6.1.2**
Operational	Now
Research program	High-resolution zone-plate microscopy
Source characteristics	Bend magnet
Energy range	500–800 eV (extended range 250–950 eV)
Monochromator Calculated flux (1.9 GeV, 400 mA) Resolving power (E/ΔE)	Zone plate linear Images with 1000 × 1000 pixels, 1000 photons/pixel are recorded in 3 sec at 517 eV/0.3%BW 200–500 (with 20–5 μm field of view)
Endstation	X-ray microscope (XM-1)
Characteristics	Conventional-type (full-field) soft x-ray microscope
Spatial resolution	40 nm
Detectors	Back-thinned CCD camera
Field of view	5 to 20 μm single field; larger areas can be tiled together like a mosaic
Samples Format Preparation	 Thin samples (up to 10 μm thick) on silicon nitride or other foils, wet chamber provided Sample dependent
Sample environment	Helium at atmospheric pressure, wet or dry, low temperature (cryo) (in preparation)
Special notes	Mutual indexing system with visible-light microscopy provided to position and focus sample
Scientific applications	Biology, environmental sciences, material sciences, polymers
Local contact/spokesperson	Name: Werner Meyer-Ilse Affiliation: Center for X-Ray Optics, LBNL Phone: (510) 486-6892 Fax: (510) 486-4550 Email: w_meyer-ilse@lbl.gov

Beamline 6.3.1

Beamline/Branchline number	6.3.1
Operational	1998
Research program	Calibration and standards, EUV/soft x-ray optics testing, solid-state chemistry
Source characteristics	Bend magnet
Energy range	500–2000 eV
Monochromator Calculated flux (1.9 GeV, 400 mA) Resolving power (E/ΔE)	Double crystal 10^{11} photons/sec/0.01%BW at 1000 eV 5000
Endstation	Reflectometer
Characteristics	VLS-PGM monochromator with fixed exit slit and refocusing mirror; 2-circle goniometer with x, y, z, θ sample mirror
Spatial resolution	Can position to 1 μm
Detectors	Si diode, CEM, MCP, total yield
Spot size at sample	5 × 200 μm
Samples Format	Solid-state, gas phase Foils, powders, etc.
Sample environment	High vacuum or UHV
Scientific applications	Solid-state chemistry to the Al and Si K edges, atomic physics reflectometry, scattering
Local contact/spokesperson	Name: Jim H. Underwood Affiliation: Center for X-Ray Optics, LBNL Phone: (510) 486-4958 Fax: (510) 486-4550 Email: underwoo@lbl.gov

Beamline 6.3.2

Abstracts begin on page 35

Beamline/Branchline number	**6.3.2**
Operational	Now
Research program	Calibration and standards; EUV optics testing; atomic, molecular, and materials science
Source characteristics	Bend magnet
Energy range	50–1000 eV
Monochromator Calculated flux (1.9 GeV, 400 mA) Resolving power (E/ΔE)	VLS-PGM 10^{11} photons/sec/0.01%BW at 100 eV 7000
Endstation	Reflectometer
Characteristics	2-circle goniometer with x, y, z, θ movement of sample
Spatial resolution	Can position to 1 μm
Detectors	Si diode, CEM, MCP, total yield
Spot size at sample	5 × 200 μm
Samples Format	Solid state, gas phase Foils, powders, films
Sample environment	High vacuum or UHV
Scientific applications	Solid-state chemistry, gas phase, atomic physics, reflectometry, scattering
Local contact/spokesperson	Name: Jim H. Underwood Affiliation: Center for X-Ray Optics, LBNL Phone: (510) 486-4958 Fax: (510) 486-4550 Email: underwoo@lbl.gov

Beamline 7.0.1

Abstracts begin on page 83

Beamline/Branchline number	**7.0.1**
Operational	Now
Research program	Surface and materials science, spectromicroscopy
Source characteristics	5-cm-period undulator (U5) (first, third, and fifth harmonics)
Energy range	60–1000 eV
Monochromator Calculated flux (1.9 GeV, 400 mA) Resolving power (E/ΔE)	SGM (gratings: 150, 380, 925 l/mm) $\approx 10^{12}$ photons/sec/0.01%BW (resolution dependent) 3000 typical, 8000 optimized
Endstations	UltraESCA Scanning transmission x-ray microscope (STXM) Scanning photoemission microscope (SPEM) Fluorescence spectrometer

Endstation identifier	**UltraESCA**
Characteristics	High-resolution, angle-resolved XPS spectroscopy; capable of making images by rastering the sample through a fixed spot; sample is rotated for angle-resolved measurements
Spatial resolution	50 μm
Detectors	Hemispherical electron energy analyzer; total electron yield detector
Spot size at sample	50 μm
Samples Format Preparation	 Solid samples, 1" maximum diameter Preparation chamber with sputtering is provided
Sample environment	UHV
Special notes	LEED and in-situ sample heating and cooling available
Scientific applications	XPS, XPD, NEXAFS of solids and surfaces
Local contact	Name: Eli Rotenberg Phone: (510) 486-5975 Fax: (510) 486-2930 Email: erotenberg@lbl.gov
Spokesperson	Name: Professor Brian Tonner Affiliation: University of Wisconsin–Milwaukee Phone: (414) 229-4626 Fax: (414) 229-5589 Email: tonner@csd.uwm.edu

Beamline 7.0.1, cont.

Endstation identifier	Scanning transmission x-ray microscope (STXM)
Characteristics	Used to make x-ray images and NEXAFS spectra of thin samples in transmission in the photon energy range 180–900 eV
Spatial resolution	Scanning microscope with focusing by means of Fresnel zone plates; resolution determined by spot size, which is 150 nm with current zone plates but will improve with new zone plates
Detectors	Gas proportional counter, silicon photodiode
Spot size at sample	150 nm with current zone plates
Samples Format Preparation	Solids Thin sections or thin films (100 nm thick) typically 3 × 3 mm in area No preparation chamber available
Sample environment	Helium at 1 atm
Special notes	Samples may be wet or dirty; thin films may be deposited on silicon nitride widows; optical alignment is provided by looking at the back side of the sample to locate regions of interest from optical micrographs
Scientific applications	Imaging, NEXAFS in small spots
Local contact	Name: Tony Warwick Phone: (510) 486-5819 Fax: (510) 486-7696 Email: t_warwick@lbl.gov
Spokesperson	Name: Professor Brian Tonner Affiliation: University of Wisconsin–Milwaukee Phone: (414) 229-4626 Fax: (414) 229-5589 Email: tonner@csd.uwm.edu

Beamline 7.0.1, cont.

Endstation identifier	**Scanning photoemission microscope (SPEM)** (This instrument is presently being commissioned; we expect to serve independent investigators by the summer of 1997.)
Characteristics	Designed for sub-micron XPS in the photon energy range 200–800 eV
Spatial resolution	Scanning microscope with focusing by means of Fresnel zone plates; resolution determined by spot size, which is 150 nm with current zone plates but will improve with new zone plates
Detectors	Hemispherical electron energy analyzer; total electron yield detector
Spot size at sample	150 nm with current zone plates
Samples Format Preparation	Solids 1" maximum diameter Preparation chamber with sputtering and annealing provided
Sample environment	UHV
Special notes	Optical alignment equipment provided so that visible marks on the sample surface can be used to find an area of interest prior to x-ray measurements; in-situ heating and cooling.
Scientific applications	Imaging, XPS and NEXAFS in small spots
Local contact	Name: Tony Warwick Phone: (510) 486-5819 Fax: (510) 486-7696 Email: t_warwick@lbl.gov
Spokesperson	Name: Professor Brian Tonner Affiliation: University of Wisconsin–Milwaukee Phone: (414) 229-4626 Fax: (414) 229-5589 Email: tonner@csd.uwm.edu

Beamline 7.0.1, cont.

Endstation identifier	**Fluorescence spectrometer**
Characteristics	Grating spectrometer for high-resolution (1:3000) photon-in/photon-out spectroscopy in the 50–1200 eV range
Detectors	Channel-plate photon counter in spectrometer focal plane
Spot size at sample	50 μm
Samples Format Preparation	 Solids or gases in windowed cell No preparation chamber provided
Sample environment	UHV
Special notes	This spectrometer is installed by the group from the University of Uppsala, Sweden. Potential users are asked to contact Professor Nordgren to explore possible collaborations.
Scientific applications	Photon-in/photon-out spectroscopy
Local contact	Name: Tony Warwick Phone: (510) 486-5819 Fax: (510) 486-7696 Email: t_warwick@lbl.gov
Spokesperson	Name: Professor Joseph Nordgren Affiliation: University of Uppsala, Sweden Phone: +46 (0)18 183554 Fax: +46 (0)18 183524 Email: joseph@fysik.uu.se

Beamline 7.0.2

Beamline/Branchline number	**7.0.2**
Operational	1997
Research program	Coherent optics experiments
Source characteristics	5-cm-period undulator (U5)
Energy range	70–650 eV
Monochromator Calculated flux (1.9 GeV, 400 mA) Resolving power (E/ΔE)	None 2.8×10^{15} photons/sec/1%BW/central cone at 457 eV 70
Endstations	General purpose
Detectors	Resist and others
Samples Format Preparation	Any Mount on thin membrane Can be cryo
Sample environment	Clean high vacuum
Special notes	Endstation separated from beamline by cooled window
Scientific applications	Holography, diffraction, coherent scattering, correlation spectroscopy
Local contact/spokesperson	Name: Malcolm Howells Affiliation: Advanced Light Source, LBNL Phone: (510) 486-4949 Fax: (510) 486-7696 Email: mrhowells@lbl.gov

Beamline 7.3.1.1

Beamline/Branchline number	**7.3.1.1**
Operational	1997
Research program	Magnetic microscopy, spectromicroscopy
Source characteristics	Bend magnet
Energy range	260–1500 eV
Monochromator Calculated flux (1.9 GeV, 400 mA) (linearly polarized) Resolving power (E/ΔE)	SGM 3×10^{12} photons/sec/0.1%BW at 800 eV 1800 at 800 eV
Endstation	Photoemission electron microscope (PEEM2)
Characteristics	Imaging of electron emission
Spatial resolution	200 x 200 Å (designed)
Detectors	CCD
Spot size at sample	≤ 50 × 50 μm
Samples Format Preparation	Conductive solids up to 1 cm^2 in area Solid Sputtering, heating, transfer capability
Sample environment	UHV
Special notes	Choice of linearly or circularly polarized radiation (flux of circularly polarized radiation is reduced)
Scientific applications	Real-time study of magnetic, elemental, chemical, and topological properties of materials
Local contact	Name: Simone Anders Phone: (510) 486-5928 Fax: (510) 486-4374 Email: sanders@lbl.gov
Spokesperson	Name: Joachim Stöhr Affiliation: IBM Almaden Research Center Phone: (408) 927-2461 Fax: (408) 927-2100 Email: stohr@almaden.ibm.com

Beamline 7.3.1.2

Beamline/Branchline number	7.3.1.2
Operational	Now
Research program	Surface and materials science, micro x-ray photoelectron spectroscopy
Source characteristics	Bend magnet
Energy range	260–1500 eV
Monochromator Calculated flux (1.9 GeV, 400 mA) Resolving power (E/ΔE)	SGM 3×10^{10} photons/sec/0.1%BW at 800 eV 1800 at 800 eV
Endstation	Micro-XPS
Characteristics	X-ray photoelectron spectroscopy study of 50×50 mm sample with 1-μm^2 spot size
Spatial resolution	1×1 μm (designed)
Spot size at sample	2×2 μm (now)
Detectors	Electron energy analyzer detector, partial electron yield detector
Samples Format Preparation	Up to 50×50 mm Solid Heating, sputtering
Sample environment	UHV
Special notes	In-vacuum fiducialization of sample using optical visible-light microscope; high-precision 2" × 4.5" x-y stage; laser interferometer encoding
Experimental techniques	Micro-XPS, NEXAFS, MCD
Scientific applications	Study of microstructures and interfaces in integrated circuits
Local contact	Name: Zahid Hussain Phone: (510) 486-7591 Fax: (510) 486-7696 Email: hussain@lbl.gov
Spokesperson	Name: Baylor Triplett Affiliation: Intel Corporation Phone : (408) 765-2069 Fax: (408) 765-2949 Email: baylor_b_triplett@ccm.sc.intel.com

Beamline 7.3.3

Beamline/Branchline number	**7.3.3**
Operational	1997
Research program	Materials science
Source characteristics	Bend magnet
Energy range	4–12 keV
Monochromator Calculated flux (1.9 GeV, 400 mA) Resolving power (E/ΔE)	White light and monochromatic Monochromatic (8.5 keV): 1×10^9 photons/sec/μm^2/3×10^{-4}BW 3500 at 8.5 keV (monochromatic)
Endstations	Microdiffraction Femtosecond laser-driven x-ray diffraction
Characteristics	Microprobe, white light, and monochromatic experiments
Spatial resolution	1 μm, 50 × 300 μm for fsec
Detectors	X-ray CCD, fluorescence, fsec streak camera
Spot size at sample	1 μm, 50 × 300 μm for fsec
Samples Format	 Typically < 1 cm^2 × 1 mm thick
Sample environment	Air
Scientific applications	Micro-diffraction applied to measurement of strain, micro-XAS, environmental science, sub-picosecond diffraction
Local contact/spokesperson	Name: A.A. MacDowell Affiliation: Advanced Light Source, LBNL Phone: (510) 486-4276 Fax: (510) 486-7696 Email: macdowel@grace.lbl.gov

Beamline 8.0.1

Abstracts begin on page 179

Beamline/Branchline number	**8.0.1**
Operational	Now
Research program	Surface and materials science
Source characteristics	5-cm-period undulator (U5) (first, third, and fifth harmonics)
Energy range	60–1000 eV
Monochromator Calculated flux (1.9 GeV, 400 mA) Resolving power (E/ΔE)	SGM (gratings: 150, 380, 925 l/mm) $\approx 10^{12}$ photons/sec/0.1%BW (resolution dependent) 3000 typical, 8000 optimized
Endstations	Ellipsoidal-mirror electron energy analyzer Soft x-ray fluorescence spectrometer

Endstation identifier	**Ellipsoidal-mirror electron energy analyzer (EMA)**
Characteristics	Measures 84° of electron emission angles from solid samples with 80 meV resolution
Spot size at sample	100 μm
Samples Format Preparation	Solids < 1 × 1 cm In-situ resistive heating; in-situ evaporation
Sample environment	UHV
Special notes	Sample transfer capabilities; preparation chamber
Scientific applications	XPS, ARPES, NEXAFS of solids and surfaces
Local contact	Name: Lou Terminello Phone: (510) 423-7956 Fax: (510) 423-7040 Email: terminello1@llnl.gov
Spokesperson	Name: Franz Himpsel Affiliation: University of Wisconsin, Madison Phone: (608) 263-5590 Fax: (608) 263-2334 Email: himpsel@comb.physics.wisc.edu

Beamline 8.0.1, cont.

Endstation identifier	**Soft x-ray fluorescence spectrometer**
Characteristics	Measures the soft x-ray emission from solid samples with a dispersive grating spectrometer
Spot size at sample	100 μm
Samples Format	Solids Samples up to 4" in diameter
Sample environment	UHV
Special notes	Sample transfer capabilities
Scientific applications	SXF, fluorescence-yield XAS of solids
Local contact	Name: Melissa Grush Phone: (510) 486-6645 Fax: (510) 486-4773 Email: mmgrush@lbl.gov
Spokesperson	Name: Thomas Callcott Affiliation: University of Tennessee Phone: (423) 974-6765 Fax: (423) 974-3949 Email: tomc@utkux.utcc.utk.edu

Beamline 9.0.1

Abstracts begin on page 247

Beamline/Branchline number	**9.0.1**
Operational	Now
Research program	Atomic and molecular science, high-resolution gas-phase spectroscopy
Source characteristics	10-cm-period undulator (U10) (first and third harmonics)
Energy range	20–310 eV
Monochromator Calculated flux (1.9 GeV, 400 mA) Resolving power (E/ΔE)	SGM (gratings: 380, 925, 2100 l/mm) ≈10^{12} photons/sec/0.01%BW (dependent upon resolution) ≈10,000 (selectable by slit width)
Endstations	Endstations for photoelectron and photoionizaton yield spectroscopy are available; users may bring their own endstations
Characteristics	Optimized for gas-phase spectroscopy using a variety of facility- and user-provided endstations
Detectors	Electron, ion, photon
Spot size at sample	0.75 mm (h) × 0.1–0.5 mm (v) depending on exit slit setting
Samples Format Preparation	 Gas at pressure up to 10^{-5} Torr Vented gas cabinets available for hazardous samples
Sample environment	Differential pumping is provided on the beamline to permit gas pressures in the experimental stations of approximately 10^{-5} Torr without adverse effects on the beamline optics. Potential users of the beamline should check with ALS staff regarding the suitability of the differential pumping for their gases.
Special notes	A parallel-plate ion-yield gas cell is available for beamline calibration
Scientific applications	Atomic and molecular photoelectron spectroscopy, ion spectroscopy, photoionization yield spectroscopy, fluorescence spectroscopy
Local contact	Name: John D. Bozek Phone: (510) 486-4967 Fax: (510) 486-7696 Email: jdbozek@lbl.gov
Spokesperson	Name: Nora Berrah Affiliation: Western Michigan University Phone: (616) 387-4955 Fax: (616) 387-4939 Email: berrah@wmich.edu

Beamline 9.0.1, cont.

Endstation identifier	**Gas-phase photoelectron spectrometer**
Characteristics	Optimized for gas-phase photoelectron spectroscopy with a gas cell, differentially pumped electron lens, and dispersive electron energy analyzer
Detectors	Spherical-sector electron energy analyzer
Spot size at sample	3.0 mm (h) × 0.1–1.0 mm (v)
Samples Format Preparation	 Gases at pressures up to $\approx 10^{-5}$ Torr Gas cabinets available for hazardous samples
Sample environment	Permanent differential pumping is incorporated into the beamline to permit relatively high sample pressures of 10^{-5} Torr in the interaction region.
Special notes	Heating of the gas cell to approximately 400°C is possible
Scientific applications	Atomic and molecular electron spectroscopy
Local contact/spokesperson	Name: John D. Bozek Affiliation: Advanced Light Source, LBNL Phone: (510) 486-4967 Fax: (510) 486-7696 Email: jdbozek@lbl.gov

Beamline 9.0.2.1

Abstracts begin on page 283

Beamline/Branchline number	**9.0.2.1**
Operational	Now
Research program	Chemical reaction dynamics, photochemistry
Source characteristics	10-cm-period undulator (U10) (fundamental)
Energy range	5–30 eV
Monochromator Calculated flux (1.9 GeV, 400 mA) Resolving power (E/ΔE)	None $\approx 10^{16}$ photons/sec/2.5%BW 40
Endstation	Crossed molecular beam
Characteristics	Designed for photofragmentation spectroscopy and reactive scattering; two rotatable molecular-beam sources
Detectors	Time-of-flight spectroscopy by quadrupole mass analyzer
Spot size at sample (calculated)	170 μm (h) × 50 μm (v)
Samples Format Preparation	 Gas sample Molecular beam, seeded in rare gas
Sample environment	Vacuum $\approx 10^{-6}$ Torr
Scientific applications	Photofragmentation spectroscopy, reactive scattering
Local contact	Name: Naoki Hemmi Phone: (510) 486-7635 Fax: (510) 486-5311 Email: naoki@leea.cchem.berkeley.edu
Spokesperson	Name: Arthur Suits Affiliation: Chemical Sciences Div., LBNL Phone: (510) 486-4754 Fax: (510) 486-5311 Email: arthur@leea.cchem.berkeley.edu

Beamline 9.0.2.2

Abstracts begin on page 283

Beamline/Branchline number	**9.0.2.2**
Operational	Now
Research program	Photoionization dynamics
Source characteristics	10-cm-period undulator (U10) (fundamental)
Energy range	5–30 eV
Monochromator Calculated flux (1.9 GeV, 400 mA) Resolving power (E/ΔE)	Off-plane Eagle $\approx 10^{11}$ photons/sec/0.01%BW 70,000
Endstation	Molecular-beam photoelectron/photoion spectroscopy
Characteristics	Multipurpose design for high-resolution photoelectron spectroscopy and photoelectron/photoion coincidence experiments
Detectors	Time-of-flight and quadrupole ion and pulse field ionization electron detector
Spot size at sample (calculated)	360 μm (h) by 240 μm (v)
Samples Format Preparation	 Gas sample Molecular beam, seeded in rare gas
Sample environment	Vacuum $\approx 10^{-6}$ Torr
Scientific applications	Pulse field ionization photoelectron spectroscopy, threshold photoelectron/photoion coincidence
Local contact	Name: Chiawei Hsu Phone: (510) 486-2992 Fax: (510) 486-2930 Email: cwh@me13.lbl.gov
Spokesperson	Name: Cheuk Ng Affiliation: Iowa State University Phone: (515) 294-4225 Fax: (515) 294-5825 Email: cyng@pop.ames.lab.gov

Beamline 9.3.1

Abstracts begin on page 307

Beamline/Branchline number	9.3.1
Operational	Now
Research program	Atomic, molecular, and materials science
Source characteristics	Bend magnet
Energy range	2200–6000 eV with Si(111) crystals
Monochromator Calculated flux (1.9 GeV, 400 mA) Resolving power (E/ΔE)	Double crystal 4.2×10^{10} photons/sec/0.01%BW at 2500 eV 3000–8000
Endstations	X-ray absorption cell Ion time-of-flight spectrometer Angle-resolved time-of-flight electron spectrometer Angle-resolved hemispherical electron analyzer Polarized-x-ray emission spectrometer

Endstation identifier	X-ray absorption cell
Detectors	Photodiode
Spot size at sample	1 × 1 mm
Samples	Powder, 1/2" diameter
Sample environment	UHV
Scientific applications	NEXAFS
Local contact	Name: Rupert Perera Phone: (510) 486-5680 Fax: (510) 486-7696 Email: rupert@lbl.gov
Spokesperson	Name: Dennis Lindle Affiliation: University of Nevada Las Vegas Phone: (702) 895-4426 Fax: (702) 895-4072 Email: lindle@nevada.edu

Beamline 9.3.1, cont.

Endstation identifier	Ion time-of-flight spectrometer
Characteristics	Timing resolution ≈200 ps; capable of coincidence measurement (ion–ion, ion–ion–ion, electron–ion, electron–ion–ion, etc.)
Detectors	Microchannel plates for ions, channeltron for electrons
Spot size at sample	1 × 1 mm
Samples	Gases
Sample environment	Gas-phase flow system
Scientific applications	Ion spectroscopy, total and partial ion yields, PIPICO, PEPICO, PEPIPICO, etc.
Local contact	Name: Rupert Perera Phone: (510) 486-5680 Fax: (510) 486-7696 Email: rupert@lbl.gov
Spokesperson	Name: Dennis Lindle Affiliation: University of Nevada Las Vegas Phone: (702) 895-4426 Fax: (702) 895-4072 Email: lindle@nevada.edu

Endstation identifier	Angle-resolved time-of-flight electron spectrometer
Characteristics	Timing resolution ≈200 ps; chamber rotates about x-ray beam (±100°)
Detectors	4 time-of-flight electron analyzers (0.5 m long)
Spot size at sample	1 × 1 mm
Samples	Gases
Sample environment	Gas-phase flow system
Scientific applications	Photoelectron and Auger spectroscopy, electron–electron coincidence
Local contact	Name: Rupert Perera Phone: (510) 486-5680 Fax: (510) 486-7696 Email: rupert@lbl.gov
Spokesperson	Name: Dennis Lindle Affiliation: University of Nevada Las Vegas Phone: (702) 895-4426 Fax: (702) 895-4072 Email: lindle@nevada.edu

Beamline 9.3.1, cont.

Endstation identifier	**Angle-resolved hemispherical electron analyzer (available late 1997)**
Characteristics	High energy resolution ($E/\Delta E \leq 5000$) and high electron kinetic energies (≤ 5 keV); chamber rotates about x-ray beam and analyzer rotates about a perpendicular axis, allowing coverage of $\approx 1\pi$ steradians
Detectors	2-D position-sensitive detector (microchannel plates plus resistive anode)
Spot size at sample	1×1 mm
Samples	Gases
Sample environment	Gas-phase flow system
Scientific applications	Photoelectron and Auger spectroscopy
Local contact	Name: Rupert Perera Phone: (510) 486-5680 Fax: (510) 486-7696 Email: rupert@lbl.gov
Spokesperson	Name: Dennis Lindle Affiliation: University of Nevada Las Vegas Phone: (702) 895-4426 Fax: (702) 895-4072 Email: lindle@nevada.edu

Endstation identifier	**Polarized-x-ray emission spectrometer (available in 1998)**
Characteristics	High x-ray energy resolution ($E/\Delta E \approx 3000$). Curved-crystal Rowland-circle spectrometer
Detectors	2-D position-sensitive detector (microchannel plates plus resistive anode)
Spot size at sample	1×1 mm
Samples	Gases
Sample environment	Static gas cell with windows
Scientific applications	X-ray emission
Local contact	Name: Rupert Perera Phone: (510) 486-5680 Fax: (510) 486-7696 Email: rupert@lbl.gov
Spokesperson	Name: Dennis Lindle Affiliation: University of Nevada Las Vegas Phone: (702) 895-4426 Fax: (702) 895-4072 Email: lindle@nevada.edu

Beamline 9.3.2

Abstracts begin on page 331

Beamline/Branchline number	**9.3.2**
Operational	Now
Research program	Chemical and materials science
Source characteristics	Bend magnet
Energy range	30–1500 eV
Monochromator Calculated flux (1.9 GeV, 400 mA) Resolving power (E/ΔE)	SGM (gratings: 100, 600, 1200 l/mm) $\approx 10^{11}$ photons/sec/0.1%BW at 400 eV 3000 typical, 8000 max (with 10-μm slits) Capability for circularly polarized radiation
Endstations	Advanced materials chamber (AMC) Advanced photoelectron spectrometer/diffractometer (APSD) Industrial chamber*, ARPES* Users may bring their own endstation *Available June 1997

Endstation identifier	**Advanced materials chamber (AMC)**
Characteristics	PHI analyzer, sample preparation with LEED, XPS, evaporation, sputtering, precision manipulator
Spatial resolution	0.5×1 mm^2
Detectors	16-element multichannel detector, partial electron yield detector
Spot size at sample	0.5×1 mm^2
Samples Format Preparation	Solid 5–10 mm diameter Sputtering, evaporation, XPS, LEED, heating up to 2000°C; cooling down to 80°K
Sample environment	UHV
Special notes	Sample transfer capability
Experimental techniques	Photoelectron diffraction, XPS, NEXAFS, MCD
Scientific applications	Studies of atomic and electronic structure of surfaces
Local contact	Name: Zhou Xin Phone: (510) 486-7633 Fax: (510) 486-4299 Email: xin@ux8.lbl.gov
Spokesperson	Name: Zahid Hussain Affiliation: Advanced Light Source, LBNL Phone: (510) 486-7591 Fax: (510) 486-7696 Email: hussain@lbl.gov

Beamline 9.3.2, cont.

Endstation identifier	**Advanced photoelectron spectrometer/diffractometer (APSD)**
Characteristics	High-resolution rotatable Scienta analyzer, sample preparation with LEED, evaporator, high-precision sample manipulator, sputtering
Spatial resolution	5 μm with pre-lens
Detectors	Multichannel detector and spin-resolved mini Mott
Spot size at sample	0.5×1.0 mm^2
Samples Format Preparation	Solid 5–10 mm diameter, 1–2 mm thick Sputtering, evaporation, LEED, XPS, heating up to 2000°C; cooling down to 150°K
Sample environment	UHV
Special notes	Capability of using either a multichannel detector or a spin detector, analyzer rotatable in horizontal plane
Experimental techniques	Photoelectron diffraction, high-resolution XPS, UPS, MCD
Scientific applications	Studies of the atomic, electronic, and magnetic structure of surfaces, interfaces, and nanostructures
Local contact	Name: Zahid Hussain Phone: (510) 486-7591 Fax: (510) 486-7696 Email: hussain@lbl.gov
Spokesperson	Name: Professor C. S. Fadley Affiliation: Material Sciences Div., LBNL, and UC Davis Phone: (510) 486-5774; (916) 752-8788 Fax: (510) 486-4680 Email: fadley@lbl.gov

Beamline 10.3.1

Abstracts begin on page 413

Beamline/Branchline number	**10.3.1**
Operational	Now
Research program	Fluorescence x-ray microprobe
Source characteristics	Bend magnet
Energy range	3–20 keV (without multilayer mirrors) 6–15 keV (with multilayer mirrors)
Monochromator Calculated flux (1.9 GeV, 400 mA) Resolving power (E/ΔE)	 Multilayer mirrors in Kirkpatrick-Baez configuration 3×10^{10} photons/sec 17 at 12.5 keV
Endstation	Fluorescence x-ray microprobe with white light capability
Characteristics	X-ray fluorescence analysis of samples with high elemental sensitivity and high spatial resolution
Spatial resolution	1.2 × 1.8 μm
Detectors	Si (Li)
Spot size at sample	1.2 × 1.8 μm
Samples Format Preparation	 Almost any sample can be studied since most samples are measured in air. Standard sample holders are available to less than 2 cm diameter. Samples should be flat to within 10 μm
Sample environment	Air
Special notes	By special arrangement, the focusing mirrors can be removed and then the white-light beam can be used for experiments that require white radiation (e.g., testing capillary optics or evaluating x-ray collimators)
Scientific applications	Trace element analysis with high spatial resolution, for example silicon solar cells, GaN, environmental soil samples, and biological samples; testing of x-ray capillary optics and new x-ray detectors
Local contact	Name: Scott McHugo Phone: (510) 486-4874 Fax: (510) 486-7696 Email: samchugo@lbl.gov
Spokesperson (Returning to LBNL in August 1997)	Name: Al Thompson Affiliation: Center for X-Ray Optics, LBNL Phone: (510) 486-5590 Fax: (510) 486-4550 Email: thompson@lbl.gov

Beamline 10.3.2

Abstracts begin on page 443

Beamline/Branchline number	**10.3.2**
Operational	Now
Research program	X-ray optics development, deep-etch x-ray lithography, materials science
Source characteristics	Bend magnet (2 horizontal mrad at 32 m from bend magnet)
Energy range	3–12 keV
Monochromator Calculated flux (1.9 GeV, 400 mA)	None 2.7×10^{13} photons/sec/0.1%BW
Endstation	Large hutch with optical table for experimental equipment
Scientific applications	Many different experiments have been done which use x-ray energies of about 3 keV: past experiments include LIGA, TXRF of silicon wafers, x-ray optical element testing
Local contact	Name: Keith Jackson Phone: (510) 486-6894 Fax: (510) 486-4955 Email: keith_jackson@macmail.lbl.gov
Spokesperson	Name: Al Thompson Affiliation: Center for X-Ray Optics, LBNL Phone: (510) 486-5590 Fax: (510) 486-4550 Email: thompson@lbl.gov

Endstation identifier	**Deep-etch x-ray lithography**
Spot size at sample	4" × 0.05"
Scientific applications	Micromachining of high-aspect-ratio microstructures
Local contact/spokesperson	Name: Keith Jackson Affiliation: Center for X-Ray Optics, LBNL Phone: (510) 486-6894 Fax: (510) 486-4955 Email: keith_jackson@macmail.lbl.gov

Beamline 11.3

Beamline/Branchline number	**11.3**
Operational	1998
Research program	Deep-etch x-ray lithography (LIGA), scanning transmission x-ray microscopy
Source characteristics	Bend magnet
Energy range	3–12 keV (LIGA) 260–750 eV (STXM)
Endstations	LIGA (see Beamline 10.3.2) Scanning transmission x-ray microscope (STXM)
Local contact/spokesperson (for LIGA)	Name: Keith Jackson Affiliation: Center for X-Ray Optics, LBNL Phone: (510) 486-6894 Fax: (510) 486-4955 Email: keith_jackson@macmail.lbl.gov

Beamline 12.0.1/12.0.2

Abstracts begin on page 465

Beamline/Branchline number	**12.0.1/12.0.2**
Operational	Now
Research program	EUV lithography optics testing, interferometry, surface and materials science
Source characteristics	8-cm-period undulator (U8)
Energy range	60–320 eV
Monochromator Calculated flux (1.9 GeV, 400 mA) Resolving power (E/ΔE)	VLG-PGM $\approx 5 \times 10^{13}$ photons/sec/1%BW at 134 eV 200–1000
Endstations	EUV interferometer MAXIMUM

Endstation identifier	**EUV interferometer**
Detectors	GaAsP flux monitor, silicon 1000 × 1000 CCD array
Samples Format	 All-reflective, multilayer-coated EUV optics
Sample environment	10^{-7} Torr or 10^{-4} Torr of O_2
Scientific applications	Interferometric wavefront measurement of optics designed for EUV lithography
Local contact	Name: Kenneth A. Goldberg Phone: (510) 486-4079 Fax: (510) 486-4550 Email: kagoldberg@lbl.gov
Spokesperson	Name: Jeffrey Bokor Affiliation: U.C. Berkeley, Center for X-Ray Optics, LBNL Phone: (510) 642-4134 Fax: (510) 642-2739 Email: jbokor@eecs.berkeley.edu

Beamline 12.0.1/12.0.2, cont.

Endstation identifier	**MAXIMUM**
Characteristics	Scanning photoelectron microscope with multilayer optics at 95 eV or 130 eV
Spatial resolution	0.1 μm
Detectors	CMA-MCP
Spot size at sample	0.1 μm
Samples Format Preparation	 15 × 15 mm maximum sample size Deposition, cleaving, ion beam sputtering, annealing
Sample environment	UHV; in-situ heating and electrical testing
Scientific applications	Semiconductor surfaces and interfaces, microelectronics, metallization, silicides
Local contact	Name: Gian Franco Lorusso Phone: (510) 486-6853 Fax: (510) 486-4550 Email: glorusso@grace.lbl.gov
Spokesperson	Name: Jim H. Underwood Affiliation: Center for X-Ray Optics, LBNL Phone: (510) 486-4958 Fax: (510) 486-4550 Email: underwoo@lbl.gov

Beam Test Facility

Abstracts begin on page 469

Beamline/Branchline number	**Beam Test Facility**
Operational	Now
Electron beam energy	50 MeV
Charge/bunch	1–1.5 nC
Bunch length	25–35 ps
Emittance	0.2–0.5 mm-mrad
Number of bunches/macropulse	1–8
Repetition rate	1, 2 Hz
Minimum spot size	35 μm
Lasers	Ti: Al_2O_3 Nd:YAG λ = 800 nm λ = 1.064 μm, 0.532 μm, 0.266 μm ε = 60 mJ ε = 1 J, 0.5 J, 0.1 J τ = 100 fs τ = 9 ns, 7 ns, 4–5 ns Rep. rate: 10 Hz
Local contact/spokesperson	Name: Wim Leemans Affiliation: Center for Beam Physics, LBNL Phone: (510) 486-7788 Fax: (510) 486-7981 Email: leemans@lbl.gov

Available to DOE and DOE Contractors from the
Office of Scientific and Technical Communication
P.O. Box 62, Oak Ridge, TN 37831
Prices available from (615) 576-8401

Available to the public from the
National Technical Information Service
U.S. Department of Commerce
5285 Port Royal Road, Springfield, VA 22161

☆ U.S. GOVERNMENT PRINTING OFFICE: 1997-584-891/79109

Table of Beamlines at the ALS

No.	Source **	Areas of Research	Energy Range	Avail.	Pages for Abstracts/ Technical Info.
BTF	ALS linac	Beam Test Facility	50 MeV elec.	Now	469/587
1.4	Bend	Infrared spectromicroscopy	0.05–1 eV	1997	–/555
3.1	Bend	Diagnostic beamline	200–280 eV	Now	–/–
4.0.1-2	EPU5	Magnetic spectroscopy	20–2000 eV	1998	–/556
4.0.3-4	EPU5	Magnetic microscopy	100–1600 eV	1998	–/557
5.0.1	W16	Monochromatic protein crystallography	7–14 keV	1998	–/558
5.0.2	W16	Multiple-wavelength (MAD) & monochromatic protein crystallography	3.5–14 keV	1997	–/559
6.1.2	Bend	High-resolution zone-plate microscopy	500–800 eV	Now	1/560
6.3.1	Bend	Calibration and standards, EUV/soft x-ray optics testing, solid-state chemistry	500–2000 eV	1998	–/561
6.3.2	Bend	Calibration and standards; EUV optics testing; atomic, molecular & materials science	50–1000 eV	Now	35/562
7.0.1	U5	Surface and materials science, spectromicroscopy	60–1000 eV	Now	83/563
7.0.2	U5	Coherent optics experiments	70–650 eV	1997	–/567
7.3.1.1	Bend	Magnetic microscopy, spectromicroscopy	260–1500 eV	1997	–/568
7.3.1.2	Bend	Surface and materials science, micro x-ray photoelectron spectroscopy	260–1500 eV	Now	–/569
7.3.3	Bend	Materials science	3–12 keV	1997	–/570
8.0.1	U5	Surface and materials science	60–1000 eV	Now	179/571
9.0.1	U10	Atomic and molecular science, high-resolution gas-phase spectroscopy*	20–310 eV	Now	247/573
9.0.2.1	U10	Chemical reaction dynamics, photochemistry	5–30 eV	Now	283/575
9.0.2.2	U10	Photoionization dynamics	5–30 eV	Now	283/576
9.3.1	Bend	Atomic, molecular, and materials science	2.2–6 keV	Now	307/577
9.3.2	Bend	Chemical and materials science	30–1500 eV	Now	331/580
10.3.1	Bend	Fluorescence x-ray microprobe	3–20 keV	Now	413/582
10.3.2	Bend	X-ray optics development, deep-etch x-ray lithography (LIGA), materials science	3–12 keV	Now	443/583
11.3	Bend	Deep-etch x-ray lithography (LIGA), scanning transmission x-ray microscopy	3–12 keV 260–750 eV	1998	–/584
12.0.1/ 12.0.2	U8	EUV lithography optics testing, interferometry, surface and materials science	60–320 eV	Now	465/585

* The atomic and molecular science beamline will move to 10.0 in early 1998.

** Bend = bend magnet; EPU5 = 5-cm-period elliptical polarization undulator; W16 = 16-cm-period wiggler, Ux = x-cm-period undulator

ALS Contacts

ALS Director
Brian M. Kincaid
Tel: (510) 486-4810
Fax: (510) 486-4960
Email: bmkincaid@lbl.gov

ALS Scientific Program Head
Neville Smith
Tel: (510) 486-5423
Fax: (510) 486-4773
Email: nvsmith@lbl.gov

ALS Head of Operations
Ben Feinberg
Tel: (510) 486-7725
Fax: (510) 486-4960
Email: b_feinberg@lbl.gov

ALS Program Support
Alfred S. Schlachter
Tel: (510) 486-4892
Fax: (510) 486-6499
Email: fred_schlachter@lbl.gov

ALS Administration
Elizabeth Saucier
Advanced Light Source, MS 80-101
Lawrence Berkeley National Laboratory
University of California
Berkeley, CA 94720
Tel: (510) 486-6166
Fax: (510) 486-4960
Email: ecsaucier@lbl.gov

ALS Home Page
http://www-als.lbl.gov

ALS User Executive Committee Chair

1997
Louis J. Terminello
Lawrence Livermore National Laboratory
P.O. Box 808, MS L-357
Livermore, CA 94550
Tel: (510) 423-7956
Fax: (510) 423-7040
Email: terminello@cms1.llnl.gov

1998
Werner Meyer-Ilse
Center for X-Ray Optics, MS 2-400
Lawrence Berkeley National Laboratory
Berkeley, CA 94720
Tel: (510) 486-6892
Fax: (510) 486-4550
Email: w.meyer-ilse@lbl.gov

Ernest Orlando Lawrence Berkeley National Laboratory
Advanced Light Source | University of California
Berkeley, California 94720 | USA